UNIVERSIDAD NACIONAL AUTÓNOMA DE MÉXICO
PROGRAMA DE POSGRADO EN CIENCIAS DE LA TIERRA
CENTRO DE GEOCIENCIAS

Magmatismo y extensión del Mioceno en la porción sur del Golfo de California y sus márgenes

T E S I S
QUE PARA OPTAR POR EL GRADO DE:
DOCTOR EN CIENCIAS DE LA TIERRA
(GEOLOGÍA ESTRUCTURAL Y TECTÓNICA)

P R E S E N T A
JOSE FERNANDO DUQUE TRUJILLO

TUTOR
Dr. LUCA FERRARI PEDRAGLIO
CENTRO DE GEOCIENCAS, UNAM

COMITÉ TUTOR:
Dra. Ma. Teresa Orozco Esquivel, CGeo, UNAM.
Dr. Ángel F. Nieto Samaniego, CGeo, UNAM.
Dr. Luca Ferrari Pedraglio, CGeo, UNAM.

Querétaro, Qro., Febrero, 2015

“(...) Y eso, Maximiliano, me lo enseñaste tú. Tú, que también inventaste a México para mi. Tú que inventaste sus selvas y sus mares. Tú que con tus palabras inventaste el aroma de sus valles y el fuego de sus volcánes”

F. Del Paso (Noticias del imperio)

A Sara y Samuel...

Indice General

Resumen

El proceso de *rifting* al interior de un continente puede tardar entre 80 y 30 m.a. hasta que se complete el proceso de ruptura y una nueva corteza oceánica sea formada. Para el rift del Golfo de California, los modelos clásicos proponen que el comienzo de la extensión ocurre hacia los 12.5 Ma, cuando termina la subducción en la margen occidental de Baja California. Debido a que el proceso de oceanización inició en el Plioceno, esos modelos implicarían que la ruptura de la litósfera en el Golfo de California fue rápida (en ~6-10 m.a.) en comparación con otras zonas de rift continental. Esta alta tasa de deformación se habría dado porque el magmatismo previo del "arco Comondú" habría debilitado la corteza y porque la alta oblicuidad de la divergencia habría permitido un proceso de rifting más eficiente. Este modelo se basa principalmente en trabajos llevados a cabo en la parte oeste del golfo, en Baja California. En el presente trabajo se presenta un modelo geodinámico distinto, basado en un estudio geológico y estructural regional apoyado por una cantidad importante de datos geocronológicos y geoquímicos obtenidos a partir de un muestreo sistemático realizado en ambas márgenes del golfo (estados de Sinaloa, Nayarit y Baja California Sur), y en los bloques continentales actualmente sumergidos en la parte sur del golfo. El trabajo se divide en tres partes principales: 1) un trabajo que revisa la geología y la edad de la actividad tectónica en la margen sureste del golfo, usando principalmente las rocas volcánicas que allí afloran; 2) un estudio de las rocas intrusivas expuestas en ambas márgenes (incluyendo las partes sumergidas) para estimar la distribución, tasa de enfriamiento y exhumación de los plutones del Mioceno, y 3) un análisis cinemático del fallamiento de la margen sureste del Golfo, en el cual se documentan dos fases cinemáticas previas a la transtensión actual. Los resultados de este estudio muestran que el proceso de extensión comienza a finales del Oligoceno en una amplia franja que afectó desde la Sierra Madre Occidental hasta el Golfo de California con una extensión ~E-W entre ~24 y 18 Ma. Posteriormente, entre ~18 y 11 Ma, la deformación se concentra a manera de un rift estrecho, en la zona del actual Golfo de California y sus márgenes con dirección ENE-WSW. Durante estas fases de deformación en la parte sur del golfo y sus márgenes se emplazaron

numerosos plutones que pueden correlacionarse con el segundo pulso ignimbritico de la Sierra Madre Occidental y el grupo Comondú. Una de las principales implicaciones del presente estudio es que una buena parte del proceso de extensión habría ocurrido antes del final de la subducción de la placa Farallón bajo Norteamérica, y que el momento en que la subducción termina y se instala un nuevo límite de placas en la parte Occidental de la placa norteamericana (~12.5 Ma), marca el comienzo de la divergencia transtensional, mas no el comienzo del proceso de rifting como tal. Otra implicación importante es que el magmatismo del mioceno temprano y medio de la Sierra Madre Occidental y del grupo Comondú es sin-extensional y es producido en mayor medida más por la descompresión del manto que por los fluidos liberados por la placa en subducción. En otras palabras, el magmatismo mioceno fue controlado por la extensión litosférica y no al revés.

Abstract

The process of continental rifting may last between 80 and 30 m.y. from the beginning of the lithospheric extension to the formation of a new oceanic crust. In the case of the Gulf of California, conventional models propose that extensión began at ~12.5 Ma, when subduction ended in the western margin of Baja California. Since oceanization began in the Pliocene, the complete rupture of the lithosphere in the gulf would have occurred in just ~6 to 10 m.y., an uncommon anomalous short time span when compared with other continental rifts. This high rate of deformation is traditionally explained by crustal weakening induced by magmatism of the "Comondú arc" and because the high oblique divergence between the Pacific and North America plates would result in a more efficient rupture process. This model was mostly elaborated from studies carried out in the western margin of the gulf, in Baja California. This thesis present a different geodynamic model based on a regional geologic and structural study suppoted by a large number of geochronologic and geochemical data obtained from a systematic sampling along the rift margins (Sinaloa, Nayarit and Baja California Sur states), as well as in the rifted continental blocks presently submerged in the southern part of the gulf. The work is divided in three parts: 1) a regional study which revisit the geology and age of tectonic activity on the southeast margin of the Gulf of California, based on the volcanic record of this margin; 2) a study of the intrusive rocks exposed on both margins (including the submerged parts) that determine the distribution and estimate the cooling rate and time of exhumation of the Miocene plutons, and 3) a kinematic analysis of the southeastern part of the Gulf, which documents two main extensional phases prior to the present transtensional phase. The result of this thesis show that the process of lithosphere rupture began at the end of the Oligoceno in a wide area spanning from the Sierra Madre Occidental up to the present Gulf of California, with an E-W extensional phase between ~24 and 18 Ma. Subsequently, between ~18 and 11 Ma, deformation focused in a narrower belt along the present Gulf of California and its margins with an ENE-WSW direction. During these phases of extension several plutonic rocks correlative with the last ignimbrite pulse of the Sierra Madre Occidental and the Comondú group were emplaced in

the southern part of the gulf and its margins. One of the main implications of this study is that a significant part of the extensional process occurred before the end of subduction of the Farallon plate beneath North America. Therefore, the end of subduction (~12.5 Ma) marks the beginning of the transtensional phase rather than the onset of the rifting. Another implication is that the Early and Middle Miocene magmatism of the Sierra Madre Occidental and the Comondú are syn-extensional and mainly produced by mantle decompression rather than by fluids released from the subducted slab. In other words, Miocene magmatism was controlled by lithospheric extension and not the other way around.

Agradecimientos

Quiero agradecer de manera muy especial a mi asesor Luca Ferrari por las oportunidades que me brindó siempre y por creer en mi, mas de lo que yo mismo. Igualmente a la Dra. Teresa Orozco, asesora y amiga, quien fue un apoyo incondicional siempre en todos los momentos de mi estadía en México y a quien le estaré eternamente agradecido por sus enseñanzas. A la Dra. Margarita López por creer en mis capacidades, permitirme experimentar y enseñarme el fascinante mundo de la geocronología. Soy muy afortunado de haber llegado a un excelente grupo de trabajo que siempre se preocupó por mejorar mis capacidades sin escatimar en recursos. Muchas gracias a todos.

Sin duda le debo un agradecimiento muy especial a Sara, en primer lugar por ser mi soporte en todo momento, por ser mi compañía incondicional, por haberse arriesgado a construir un hogar conmigo. Igualmente, agradezco a Samuel, nuestro hijo, por traernos tantas alegrías y enseñarnos la importancia de las cosas simples en la vida.

Agradezco igualmente a muchas personas que siempre estuvieron apoyando este proceso de aprendizaje. Uwe Martens, gracias por tus palabras, compañía apoyo, etc. Luigi Solari, por sus enseñanzas y excelentes conversaciones desde el fraccionamiento isotópico hasta el color del piso del Cgeo. Roberto Molina, por su admirable coraje, visión de la ciencia y apoyo. Ángel Nieto, por su constante accesoria. Gianluca Norini, por su disposición para enseñarme, su compañía en campo y su amistad. Carlos Ortega, por su ayuda en el lab y en la reducción de datos. Adicionalmente a muchas personas que siempre estuvieron dispuestas a discutir y contribuir de alguna u otra manera. Gracias a Susana, Lucia, Mariano, Marina, Vlad, Carrasco, Dr. Aranda, Juan Martín, Ofelia, Arturo, Carlos Mendoza, Carolina, Jesús, Juanito, Giles, Alex.

A Marta Pereda, le debo un agradecimiento muy especial; sin su ayuda sin horarios, mi titulación no habría sido posible.

A mis compañeros, Chilo, Gore, Kurt, Vero, Lupe, Angelito, Pao, Mária, Jobo, Uru, Bert, Joel, Paty, Isi, Gaby, Merari, Micke, Jaz, Mateo, Rodri, Mario, Aldo, Toño, Edu, Monse, entre muchos otros con quienes compartí clases, campo, depas, cubos, fiestas, etc. Muchas gracias, sin ustedes la vida en México no habría sido igual. A quienes nos han dejado, los llevo en el alma.

Agradezco a mis amigos no geólogos Omar, Erika, Doña Teresita y Don Felipe, quienes me hicieron siempre sentir en casa. Los extrañaré.

Agradezco a mi familia por su apoyo incondicional mientras estuvimos fuera y en nuestro regreso.

A México y a los mexicanos.

1

Generalidades

I. Introducción

El proceso de rifting continental constituye uno de los procesos tectónicos mas importantes de la Tectónica de Placas. La ruptura de un continente implica que la litósfera continental pase por un proceso de extensión, adelgazamiento extremo hasta su ruptura completa y la formación de una nueva corteza oceánica que separe ambos fragmentos (Veevers y Hansen, 1981; Barker y Morgan, 1981). Actualmente el modelo del proceso de rifting es entendido como un proceso dinámico entre dos miembros extremos de rifting pasivo y rifting activo. Estos dos tipos de rifting contribuyen al proceso de ruptura continental en diferente medida, incluso variando a lo largo de la historia de evolución del rift (Neumann y Ramberg, 1978; Sengör y Burke, 1978; Barker y Morgan, 1981; Morgan y Baker, 1983; Mulugeta, 1985; Ruppel, 1995; Huismans et al., 2001).

Tradicionalmente se considera el rift del Golfo de California como un proceso que comienza en el Mioceno Medio (ca. 12.5 a 14 Ma) cuando el proceso de subducción de la Placa de Farallón bajo Norteamérica cesa y Baja California es adosada a esta primera. Este proceso genera una rápida ruptura (~6-10 my) de la corteza continental (Stock y Hodges, 1989; Henry y Aranda-Gómez, 1992, 2000; Umhoefer et al., 2001; Oskin and Stock, 2003; Fletcher et al., 2007; Lizarralde et al., 2007; Seiler et al., 2011; Umhoefer, 2011; Sutherland et al., 2012; Miller and Lizarralde, 2013).

La rapidez del proceso de ruptura continental implícito en el modelo tradicional de formación del Golfo de California, contrasta radicalmente con los registros geológicos globales, en los cuales el proceso de ruptura de la litosfera continental toma entre 25 y 80 My para llegar a la formación de suelo oceánico (Bohannon et al., 1989; Menzies et al., 1997; Abbate et al., 2001; Ziegler and Cloething, 2004; Omar and Steckler, 1995; Pik et al., 2008; Corti, 2009), clasificando el rift del Golfo de California como un rift anómalamente rápido (Umhoefer, 2011). Con la intención de explicar la aparente rapidez del proceso de ruptura continental en la zona del Golfo de California, se han invocado varios factores, entre los cuales se cuentan: 1) el proceso de rifting se habría concentrado a lo largo de una zona previamente debilitada térmicamente debido al magmatismo del arco Comondú, 2) la alta velocidad relativa entre placas, que causara altas tasas de deformación, 3) un régimen de extensión oblicuo en el cual dominan los procesos de fallamiento de rumbo (ver revisión en Umhoefer, 2011).

El hecho de que gran parte de la corteza continental directamente afectada por el proceso de extensión se encuentra actualmente sumergida bajo las aguas del Golfo, hace que el estudio de la corteza distendida sea aun más complicado. Hasta ahora, la mayoría de los estudios en los que se basan los modelos clásicos de apertura del Golfo de California, son esencialmente construidos a partir de evidencias recopiladas a lo largo de la Península de Baja California y la Isla de Tiburón en la parte norte del Golfo (Stock y Hodges, 1989; Martín-Barajas et al., 1995; Fletcher et al., 2000; Oskin et al., 2001; Umhoefer et al., 2002; Oskin y Stock, 2003; Seiler et al., 2011; Mark et al., 2012). Sin embargo, los estudios más recientes realizados en la margen noreste de la Provincia Extensional del Golfo (PEG) en Sonora y Chihuahua occidental, indican que el proceso de extensión habría comenzado notablemente antes que lo indicado en los modelos clásicos, incluso a finales del Oligoceno (Gans, 1997; McDowell et al., 1997; Wong et al., 2010; Murray et al., 2013), afectando un area bastante amplia, y que para los ~18 Ma el proceso de extensión se habría focalizado en la zona donde actualmente se encuentra el Golfo de California (Bryan et al., 2014).

Debido a diversos factores, la margen oeste (Península de Baja California) de la PEG ha sido más estudiada que la margen este (Estados mexicanos de Nayarit, Sinaloa, Jalisco y Durango), donde existe un falta de datos duros a pesar de que existe un registro geológico mas completo de los eventos ocurridos en el Cenozoico en la margen suroccidental de la placa Norteamérica. El presente trabajo busca constreñir la temporalidad del proceso de extensión a lo largo de la porción sur PEG y a la luz de los nuevos datos obtenidos reevaluar la pertinencia de los modelos clásicos de apertura del Golfo de California.

Para lograr el objetivo planteado se realizó un estudio multidisciplinario de geología, geocronología, geotermobarometría, geoquímica y geología estructural en distintos puntos de la margen este del Golfo (Nayarit, Sonora y Jalisco) y de la corteza continental sumergida. Esto permitió obtener una importante cantidad de nueva información sobre el registro magmático en esta región y estudiar la relación entre magmatismo y tectónica de extensión y transtensión.

II. Marco Geológico

La región suroccidental de México, se caracteriza por una prolongada subducción de la placa Farallón bajo Norteamérica (NA) desde el Mesozoico, situación que se invierte a mediados del Oligoceno, cuando la primer interacción de la placa del Pacífico con la margen occidental de NA inicia la formación de una margen transformante y transtensional que se propaga desde el sur de California hacia Baja California al final del Mioceno medio. A partir de esta compleja interacción se genera una serie de importantes estructuras geológicas en la parte occidental de México y suroccidental de los Estados Unidos, tales como la zona de cizalla del oeste de California-Walker Lane, el sistema de fallas San Benito-Tosco-Abreojos al oeste de la península de Baja California, y el rift del Golfo de California (Fig. 1).

En el occidente de México, desde la Faja Volcánica Transmexicana (FVTM) hasta el estado de Sonora, y rodeando el Golfo de California, se encuentran evidencias de una extensión previa a la apertura del Golfo en la provincia de Cuencas y Sierras (Fig. 1) y que corresponde a la prolongación sur de la bien conocida provincia *Basin and Range* de los Estados Unidos. Esta deformación se caracteriza por una zona de intenso fallamiento normal con dirección predominante N-S a NNW-SSE que forma grábenes y semigrabenes rellenos con sedimentos del Cenozoico (Henry, 1989; Henry y Aranda-Gomez, 1992, 2000; Calmus et al., 2010). El límite oeste de la provincia extensional se considera el núcleo no extendido de la SMO (Fig. 1). La extensión de la región del Golfo de California es parte de la llamada provincia Extensional del Golfo (PEG) (Gastil, 1975) o proto-Golfo de California (Karig y Jensky, 1972), la cual se define desde el escarpe principal del Golfo en Baja California (*Main Gulf Escarpment*), hasta el núcleo no extendido de la SMO. Sin embargo, hacia el límite este de la provincia no está bien delimitado en el norte (Sonora-Chihuahua) ni en la parte sur de la SMO (Nayarit-Jalisco), ya que en estas partes la extensión es espacialmente continua y afecta las estribaciones de la SMO.

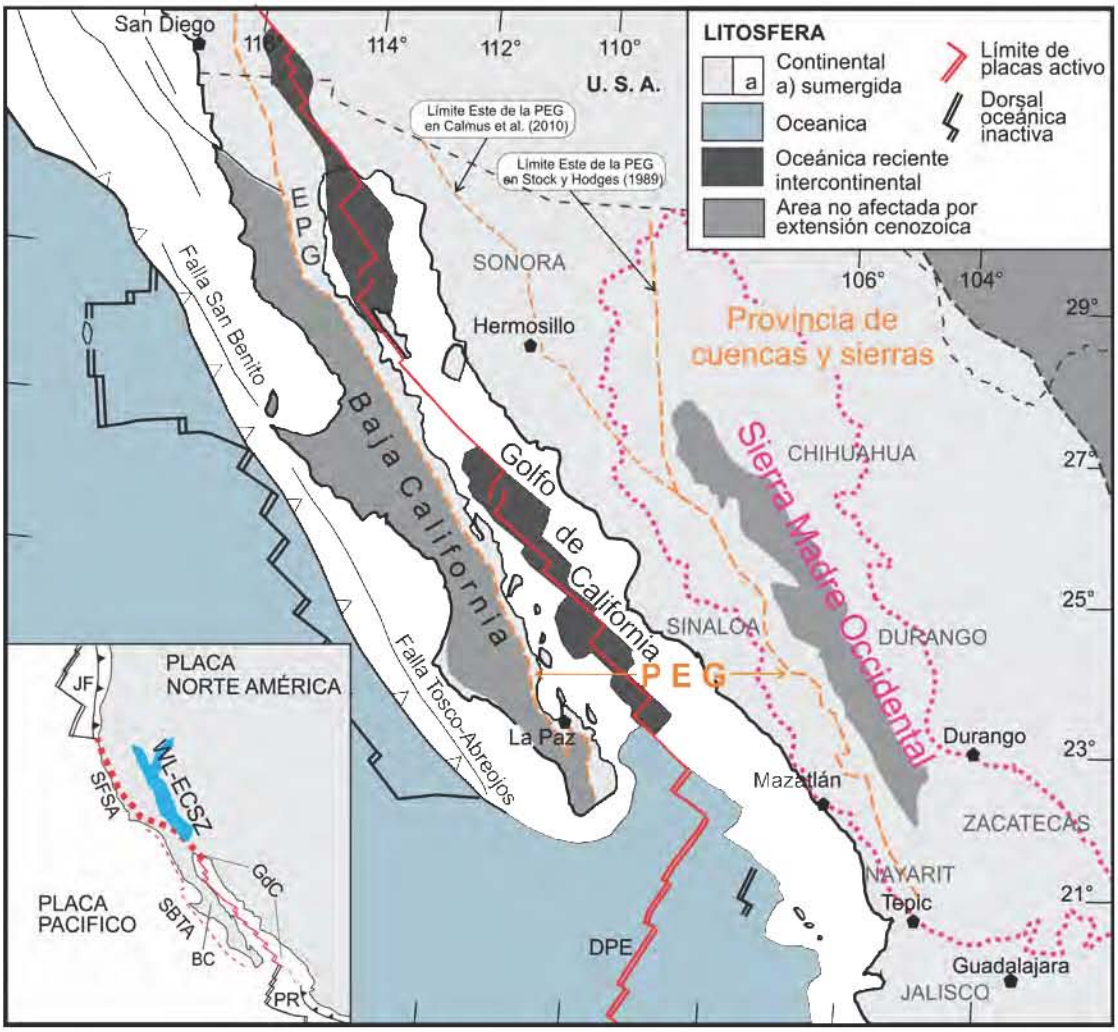

Fig. 1. Mapa tectónico regional del Golfo de California y occidente de México. Se puede apreciar las diferentes tipos de litosfera presentes en la zona y la extensión de la Provincia Extensional del Golfo (línea discontinua naranja) y la Sierra Madre Occidental (línea punteada rosa). Distribución de las diferentes litosferas y el núcleo no extendido de la Sierra Madre Occidental tomado de Ferrari et al. (2013). PEG-Provincia Extensional del Golfo; EPG-Escarpe Principal del Golfo. El mapa inserto muestra los principales sistemas de falla que constituyen el límite de placas en la zona: JF-Placa Juan de Fuca; WL-ECSZ-Walker Lane-East California shear zone; SFSA-Sistema de falla San Andrés; GdC-Sistema de fallas del Golfo de California; SBTA-Sistema de falla San Benito-Tosco Abreojos; BC-Baja California; PR-Placa Rivera.

La temporalidad de la extensión en la PEG y su relación con la subducción es un tema de debate. Los trabajos de Stewart (1998) y Henry (1989) afirman que la extensión en la PEG comienza antes de la formación de un límite de placas entre Farallón y NA, y mientras la subducción era activa. Mientras que el trabajo de Stock y Hodges (1989), intoduce la idea de que la extensión comienza en el Mioceno Medio, cuando la subducción termina, idea que se

ha mantenido en los trabajos subsecuentes (Henry y Aranda-Gómez, 1992, 2000; Umhoefer et al., 2001; Umhoefer, 2011; Fletcher et al., 2007; Lizarralde et al., 2007; Seiler et al., 2011; Sutherland et al., 2012; Miller y Lizarralde, 2013). Aunque ha existido cierto debate en cuanto a la edad a la que comienza la transtensión dentro del Golfo, existe un consenso general en que el inicio del rifting ocurre alrededor de los 12.5 Ma como un proceso completamente post-subducción y relacionado exclusivamente a la divergencia oblicua entre NA y Baja California, a su vez capturada por la Placa del Pacífico (Stock y Hodges, 1989; Nourse, 1994; Gans, 1997; Oskin y Stock, 2003; Vega-Granillo, 2003; Fletcher et al., 2007; Umhoefer, 2011; Miller y Lizarralde, 2013).

La cinemática de la ruptura continental es otro punto de debate en el modelo de apertura del Golfo de California. Inicialmente el modelo de Stock y Hodges (1989) propone que la fase inicial de apertura del Golfo ocurre mediante una partición de la deformación en una componente ortogonal (WSW-ENE) acomodada en el eje del rift y una componente lateral derecha acomodada a lo largo del sistema de fallas Tosco-Abreojos al oeste de Baja California. Posteriormente la deformación se habría concentrado al este de Baja California en una deformación transtensiva, responsable de la ruptura final de la litósfera y la formación del rift al final del Mioceno (8-6.5 Ma). Estudios posteriores pusieron en duda el modelo propuesto por Stock y Hodges, (1989), proponiendo una transtensión lateral derecha a partir de los 12.5 Ma (Gans, 1997; Fletcher et al., 2007). Recientemente Bennet et al., (2013) y Bennet y Oskin (2014) proponen que la deformación se concentró en zonas de cizalla lateral-derecha que facilitaron la ruptura continental, formando el rift del Golfo de California. Todos estos modelos concuerdan en la existencia de una fase transtensional posterior al cese de la subducción (~12.5 Ma).

A lo largo de la margen occidental de México han sido definidas varias provincias magmáticas, las cuales se asocian a diferentes ambientes tectónicos que evidencian la compleja historia tectónica de esta margen. La evidencia más antigua del magmatismo continental asociado a la subducción al oeste de Baja California es la cadena de batolitos peninsulares (Peninsular

Range Batholiths, PRB), una cadena continua de intrusivos que forman el cuerpo principal de la Península de Baja California (Gastil et al., 1975). Esta franja de intrusivos continúa con los batolitos cretácicos expuestos en la parte continental de México (Sinaloa y Jalisco), y representa las raíces de un arco magmático de edad Cretácico a Paleógeno, de al menos 200 km (Gastil, 1975; Schaaf et al., 2000; Ortega-Rivera, 2003; Henry et al., 2003). Posterior a este magmatismo, y marcando un nuevo régimen tectónico, se manifiesta un magmatismo de silícico a bimodal, de edad Oligoceno a Mioceno medio, conocido regionalmente como la Gran provincia Silícica de la Sierra Madre Occidental (Ferrari et al., 2007; Bryan et al., 2014). Esta es la provincia silícica más importante de Norteamérica y la más joven en el mundo (Bryan, 2007; Bryan y Ferrari et al., 2013). Dentro de ella se pueden separar dos eventos eruptivos principales. Un primer evento de edad Oligoceno (~34 y 28 Ma) y un segundo evento del Mioceno temprano (~24 y 18 Ma). Estudios geocronológicos en esta secuencia indican el emplazamiento de grandes volúmenes de ignimbrítas en poco tiempo, implicando una importante tasa de generación de magmas silícicos (McDowell y Keizer, 1977; Ferrari et al., 2002, 2007; Bryan et al., 2008). La energía térmica y los volátiles necesarios para desencadenar estas grandes erupciones son proporcionados por intrusiones de magmas basálticos, tanto hacia la base de la corteza continental como por intrusiones someras, que refunden plutones de anteriores eventos magmáticos, generando grandes volúmenes de rocas riolíticas pobres en cristales que hacen erupción a través de grandes calderas y fisuras (Bryan et al., 2008). Este proceso de intrusión y refusión habría sido facilitado a su vez por la tectónica extensional predominante en esta parte de la placa NA durante su emplazamiento (Ferrari et al., 2007).

Dentro de la PEG se ha identificado otro evento parcialmente coetáneo con la provincia silícica de la SMO. Este evento, de carácter volcánico a volcano-sedimentario, es conocido como “arco” Comondú (Hausback, 1984; Sawlan y Smith, 1984; Sawlan, 1991; Umhoefer et al., 2001). Sus depósitos representan distintos episodios de volcanismo efusivo, lavas de composición intermedia, importantes eventos volcanoclásticos, depósitos epiclásticos y sedimentación fluvial y eólica (Umhoefer et al., 2001). El Grupo Comondú ha sido ampliamente

interpretado como depositado en una cuenca de “fore-arc” formada antes de la apertura del Golfo de California (Hausback, 1984; Umhoefer et al., 2001; Conly et al., 2005; Godinez et al., 2010; Umhoefer, 2011). Recientemente se ha sugerido que el “arco” Comondú no representa un típico magmatismo de supra-subducción sino mas bien la actividad magmática relacionada con la extensión temprana del Golfo de California, y que la composición andesítica-dacítica observada corresponde a una mezcla de basaltos del manto con magmas riolíticos producto de la fusión parcial de la corteza continental durante la fase inicial del proceso de rift (Bryan et al., 2014).

III. Objetivos

El objetivo principal del presente trabajo es el estudio de la deformación y el magmatismo asociado a la transición de un límite de placa convergente a uno divergente en la parte occidental de México, caracterizado por la apertura del rift del Golfo de California. El estudio se centra en la parte sur de la SMO y del Golfo de California, tratando de acotar la temporalidad del proceso de extensión y tener evidencias de la cinemática del proceso de apertura del Golfo. Este trabajo además, aporta información útil para mejorar el entendimiento tanto del proceso inicial de apertura de rifts continentales como de la variación de estos en el tiempo.

Para lograr el objetivo principal, 1) Se realizó una caracterización de las rocas que constituyen la corteza continental del Golfo de California, mediante el muestreo submarino de rocas; 2) Se obtuvieron datos geocronológicos que permitieron reconstruir la historia de enfriamiento de plutones pre- y sinextensionales emplazados en la PEG; 3) Se caracterizó la geometría, cinemática y edad de la deformación en la margen sur-este de la PEG (estados de Nayarit, Sinaloa y Jalisco).

IV. Metodología

Con el objeto de obtener datos duros que permitan evaluar la validez de los modelos de geologia regional propuestos para la apertura del Golfo de California, en este trabajo se integraron diferentes técnicas analíticas que permitan generar una nueva interpretación sobre la manera cómo ocurrieron los eventos que llevaron a la apertura del Golfo de California y la formación de la SMO.

La metodología del presente trabajo fue la realización de un estudio interdisciplinario tanto en la parte emergida como sumergida de las márgenes continentales de la parte sur del rift del Golfo de California, integrando diversas herramientas.

El muestreo de la corteza continental sumergida en la parte sur del Golfo se realizó durante varios cruceros oceanográficos (DANA, ROCA y BEKL) liderados por el Dr. Peter Lonsdale. El muestreo se concentró en los escarpes de fallas altamente reflectivos que suponen una buena exposición de roca dura y una ausencia de depósitos de talud. Durante los cruceros oceanográficos DANA y BEKL el muestreo fue realizado mediante el uso de dragas, las cuales fueron arrastradas a lo largo de los escarpes que se deseaba muestrear. Primero bajando la draga hasta el fondo marino y posteriormente moviendo lentamente el barco en dirección contraria a la pendiente, dejando la draga estacionaria para que esta fuera arrastrada a lo largo de la pendiente por una distancia de entre 150 y 200 m. De esta manera se tiene certeza del sitio donde la draga tocó el fondo marino y en qué dirección fue realizado el muestreo. Por lo tanto se tiene una certeza relativa de la localización de las muestras recuperadas (mas detalles en Duque-Trujillo et al., 2014).

Durante el crucero oceanográfico ROCA se utilizó como método de muestreo el vehiculo no tripulado (Remote Operated Vehicle-ROV) Jason. Éste fue utilizado de manera similar a la draga, realizando una inmersión en un punto determinado para posteriormente dirigirlo remotamente desde el barco manteniendo siempre contacto visual con el fondo marino a través de video, y realizando un perfil de muestreo a lo largo del escarpe seleccionado. Con este método de

muestreo se tuvo perfecto control de la posición espacial y estratigráfica de las muestras, pues Jason tiene posicionamiento 3D en tiempo real y además el registro constante de video permite realizar el control estratigráfico del muestreo. El muestreo se realizó parando el vehiculo en los sitios deseados y colectando la muestra deseada mediante los brazos mecánicos con que cuenta el equipo, permitiendo un muestreo *in situ* (más detalles en Duque-Trujillo et al., 2014). De las muestras recuperadas tanto durante los cruceros oceanográficos, como durante las campañas de muestreo en campo realizadas a lo largo de la margen este del Golfo (Estados de Jalisco, Nayarit y Sinaloa) como de la margen oeste (Península de Baja California e islas del sur del Golfo de California), se seleccionaron las muestras mas estratégicas por composición, textura y localización, tratando de cubrir de la mejor manera la zona sur del Golfo. De las muestras seleccionadas se realizó un análisis petrográfico con el objetivo de obtener su composición modal y características texturales, así como para evaluar su grado de alteración y seleccionar las muestras para análisis geoquímico. Para la mayoría de las muestras se obtuvieron análisis geoquímicos de elementos mayores y trazas. Los análisis de elementos mayores fueron realizados por fluorescencia de rayos X (XRF) en el Instituto de Geología de la Universidad Nacional Autónoma de México (UNAM), usando un equipo Siemens SRS3000, siguiendo el procedimiento descrito por Bernal y Lozano-Santacruz (2005). La preparación de las muestras para los análisis de elementos traza se realizaron en los laboratorios del Centro de Geociencias de la UNAM (CGeo), Campos Juriquilla, Querétaro, en un laboratorio ultralimpio siguiendo los procedimientos descritos por Mori et al. (2007). Adicionalmente se incorporaron dos pasos de digestión en bombas Parr®, con el fin de obtener una disolución completa de los minerales más resistentes (e.g. circón). Las muestras fueron analizadas en el Laboratorio de Estudios Isotópicos del CGeo, usando un espectrómetro de masas cuadrupolo con plasma inductivamente acoplado (ICP-MS) Thermo X Series II. Los análisis de elementos mayores y traza de las muestras DANA y ROCA fueron realizados en el laboratorio GeoAnalytical en Washington State University.

En algunas de las muestras fueron realizados análisis de química mineral con el fin de realizar cálculos termobarométricos. Estos análisis fueron realizados en el Departamento de Ciencias de la Tierra de la Università degli Studi di Milano, usado una microsonda JEOL JXA 8200 equipada con cinco espectrómetros de dispersión de longitud de onda (WDS). El equipo fue usado con un haz de 1µm a 15 kV y 15 nA de corriente. Especimenes naturales y sintéticos de onfacita y albita (Na), olivino (Mg), anortita (Al), wollastonita (Ca, Si), feldespato potásico (K), ilmenita (Ti), cromita (Cr), rodonita (Mn) y fayalita (Fe) fueron usados como estándares de calibración.

Una parte importante del presente trabajo fue aportar nuevos datos de rocas intrusivas y volcánicas aflorantes en la zona de influencia del Golfo de California. Se obtuvieron 117 nuevas edades mediante los métodos U-Pb en circón y $^{40}Ar/^{39}Ar$ en anfíbol, biotita, feldespato potásico, moscovita y matriz. El fechamiento de la misma muestra usando ambos métodos y diferentes minerales se realizó especialmente en muestras con edades de formación previas al Mioceno medio. Los análisis de U-Pb fueron realizados en el Laboratorio de Estudios Isotópicos del CGeo. La separación mineral se realizó usando técnicas convencionales de separación por métodos gravimétricos y magnéticos. Las imágenes de catodoluminiscencia fueron obtenidos con un microscopio binocular adaptado a un luminoscopio ELM-3R. El proceso de ablación láser se realizó usando un equipo Resolution M-50, láser excímero de ArF, operado a 193 nm, 5 Hz y ~6J/cm^2. El análisis isotópico fue realizado en un espectrómetro cuadrupolo Thermo X-Series II (ICP-MS), siguiendo el protocolo descrito por Solari et al. (2010) y usando como estándar de referencia el circón natural Pleišovice (Sláma et al., 2008). El proceso de reducción de datos se realizó usando el script UPb.age bajo el software R (Solari y Tanner, 2011), o usando Iolite (Paton et al., 2011). La manipulación de los datos, cálculos y gráficos se realizó usando el “Add-In” Isoplot 3.7 para Microsoft Excel (Ludwing 2004).

Los análisis de $^{40}Ar/^{39}Ar$ fueron realizados en el Laboratorio de Geocronología del Centro de Investigación Científica y de Educación Superior de Ensenada Baja California (CICESE), México. Las muestras, junto con los estándares fueron irradiados en el reactor nuclear de la Universidad McMaster en Hamilton, Ontario, Canadá. Para el procesado de datos y presentación

de resultados se utilizaron los programas RadAn y AgeCalc desarrollados para el Laboratorio de Geocronología del CICESE.

En rocas plutónicas, las edades U/Pb son consideradas usualmente como indicadoras de la edad de intrusión, esto debido a la temperatura de cierre del sistema U-Pb en el circón (>900°C), temperatura comparable a la cual comenzaría la cristalización de un magma diferenciado (Cherniak and Watson, 2001). Las edades de $^{40}Ar/^{39}Ar$, por otra parte, son usadas para constreñir el momento en el que una roca estuvo a una temperatura determinada. Esta temperatura corresponderá a la temperatura de cierre del sistema K-Ar en el mineral que se esté analizado. Por lo tanto la combinación de análisis de $^{40}Ar/^{39}Ar$ en diferentes minerales podría indicar la trayectoria de enfriamiento de una roca; Indicando por ejemplo, un enfriamiento lento en condiciones de quiescencia tectónica o un enfriamiento rápido debido a exhumación tectónica o emplazamiento somero del magma. Las temperaturas de cierre del sistema $^{40}Ar/^{39}Ar$ mas usadas para los diferentes minerales usados son: hornblenda (400-600°C), biotita (350-400°C), moscovita (300-350°C) y feldespato potásico (150-350°C) (Reiners et al., 2005).

En cuanto al trabajo de geología estructural, éste fue realizado a lo largo de tres transectos que cortan de manera transversal la Sierra Madre Occidental (SMO) con el fin de cortar la mayor cantidad de estructuras posibles. La determinación de la orientación de los planos de fallas y fracturas fue realizada mediante el uso de una brújula para geología. Los planos de falla fueron inspeccionados para encontrar estrías de falla e indicadores cinemáticos. Cada plano se midió en forma de buzamiento y dirección del buzamiento y cada estría de falla se midió como una linea caracterizada por buzamiento y dirección del buzamiento. El análisis de los paleo-esfuerzos se realizó mediante el método de diedros rectos de Angelier (1979, 1984), usando el software Tectonics FP. La suma de los diedros rectos define los cuadrantes de compresión y extensión, dentro de los cuales se encuentran ejes de esfuerzo principal máximo (σ_1) y mínimo (σ_3) (Angelier, 1994). Con el fin de evaluar el grado de confiabilidad de los datos de diedros rectos, se realizaron gráficos de densidad de los diedros rectos para cada uno de los transectos, usando el software Stereo32. Este método fue aplicado en sitios donde se midieron un mínimo de cuatro fallas con indicadores cinemáticos.

2

Extensión del Oligoceno tardío-Mioceno medio y magmatismo sinextensional en la parte suroccidental de la Sierra Madre Occidental: el inicio del rift del Golfo de California

Articulo:

Ferrari, L., López-Martínez, M., Orozco-Esquivel, T., Bryan, S., Duque-Trujillo, J., Lonsdale, P., Solari, L. 2013. Late Oligocene to Middle Miocene rifting and synextensional magmatism in the southwestern Sierra Madre Occidental, México: The beginning of the Gulf of California rift. Geosphere, v. 9, n. 5. doi:10.1130/GES00925.1

Contribuciones individuales de los autores:

- **Luca Ferrari:** Consecución del financiamiento; concepción del estudio; trabajo de campo; análisis e integración de datos geocronológicos; preparación de mapas y perfiles geológicos; reconstrucción paleogeográfica; redacción del manuscrito.
- **Margarita López-Martínez:** Coordinación del proceso de preparación de muestras y fechamiento por el método $^{40}Ar/^{39}Ar$; participación en el análisis y presentación de edades $^{40}Ar/^{39}Ar$; participación en revisión bibliográfica.
- **Teresa Orozco-Esquivel:** Trabajo de campo; coordinación del proceso de preparación de muestras y análisis geoquímicos; análisis y presentación de datos geoquímicos.
- **Scott Bryan:** Consecución del financiamiento para trabajo de campo; contribución en las discusiones fundamentales del modelo presentado; revisión y aporte en la redacción del manuscrito.
- **Jose Duque-Trujillo:** Participación en el rabajo de campo y toma de muestras; participación en la preparación de muestras para fechamiento por U-Pb y $^{40}Ar/^{39}Ar$; participación en el análisis y reducción de datos geocronológicos; participación en elanálisis y presentación de datos geocronológicos de U-Pb y $^{40}Ar/^{39}Ar$.
- **Peter Lonsdale:** Consecución del financiamiento; concepción, planeación y dirección de los cruceros oceanográficos DANA y ROCA.
- **Luigi Solari:** Tutoría en el proceso de preparación de muestras y fechamiento por el método U-Pb; colaboración en la reducción de datos de LA-ICP-MS.

Late Oligocene to Middle Miocene rifting and synextensional magmatism in the southwestern Sierra Madre Occidental, Mexico: The beginning of the Gulf of California rift

Luca Ferrari[1,2,*], Margarita López-Martínez[3], Teresa Orozco-Esquivel[1], Scott E. Bryan[4], Jose Duque-Trujillo[1], Peter Lonsdale[5], and Luigi Solari[1]

[1]*Centro de Geociencias, Universidad Nacional Autónoma de México, Campus Juriquilla, 76230, Querétaro, Qro., Mexico*
[2]*Instituto de Geología, Universidad Nacional Autónoma de México, Ciudad Universitaria, 04510, México Distrito Federal, Mexico*
[3]*Departamento de Geología, Centro de Investigación Científica y de Educación Superior de Ensenada (CICESE), Carretera Ensenada-Tijuana No. 3918, 22860 Ensenada, Baja California, México*
[4]*School of Earth, Environmental and Biological Sciences, Queensland University of Technology, Brisbane, Queensland 4001, Australia*
[5]*Scripps Institution of Oceanography, University of California at San Diego, La Jolla, California 92093, USA*

ABSTRACT

Although Basin and Range–style extension affected large areas of western Mexico after the Late Eocene, most consider that extension in the Gulf of California region began as subduction waned and ended ca. 14–12.5 Ma. A general consensus also exists in considering Early and Middle Miocene volcanism of the Sierra Madre Occidental and Comondú Group as subduction related, whereas volcanism after ca. 12.5 Ma is extension related. Here we present a new regional geologic study of the eastern Gulf of California margin in the states of Nayarit and Sinaloa, Mexico, backed by 43 new Ar-Ar and U-Pb mineral ages, and geochemical data that document an earlier widespread phase of extension. This extension across the southern and central Gulf Extensional Province began between Late Oligocene and Early Miocene time, but was focused in the region of the future Gulf of California in the Middle Miocene. Late Oligocene to Early Miocene rocks across northern Nayarit and southern Sinaloa were affected by major approximately north-south– to north-northwest–striking normal faults prior to ca. 21 Ma. Between ca. 21 and 11 Ma, a system of north-northwest–south-southeast high-angle extensional faults continued extending the southwestern side of the Sierra Madre Occidental. Rhyolitic domes, shallow intrusive bodies, and lesser basalts were emplaced along this extensional belt at 20–17 Ma. Rhyolitic rocks, in particular the domes and lavas, often show strong antecrystic inheritance but only a few Mesozoic or older xenocrysts, suggesting silicic magma generation in the mid-upper crust triggered by an extension-induced basaltic influx. In northern Sinaloa, large grabens were occupied by huge volcanic dome complexes ca. 21–17 Ma and filled by continental sediments with interlayered basalts dated as 15–14 Ma, a stratigraphy and timing very similar to those found in central Sonora (northeastern Gulf of California margin). Early to Middle Miocene volcanism occurred thus in rift basins, and was likely associated with decompression melting of upper mantle (inducing crustal partial melting) rather than with fluxing by fluids from the young and slow subducting microplates. Along the eastern side of the Gulf of California coast, from Farallón de San Ignacio island offshore Los Mochis, Sinaloa, to San Blas, Nayarit, a strike distance of >700 km, flat-lying basaltic lavas dated as ca. 11.5–10 Ma are exposed just above the present sea level. Here crustal thickness is almost half that in the unextended core of the adjacent Sierra Madre Occidental, implying significant lithosphere stretching before ca. 11 Ma. This mafic pulse, with subdued Nb-Ta negative spikes, may be related to the detachment of the lower part of the subducted slab, allowing an upward asthenospheric flow into an upper mantle previously modified by fluid fluxes related to past subduction. Widespread eruption of very uniform oceanic island basalt–like lavas occurred by the late Pliocene and Pleistocene, only 20 m.y. after the onset of rifting and ~9 m.y. after the end of subduction, implying that pre-existing subduction-modified mantle had now become isolated from melt source regions. Our study shows that rifting across the southern-central Gulf Extensional Province began much earlier than the Late Miocene and provided a fundamental control on the style and composition of volcanism from at least 30 Ma. We envision a sustained period of lithospheric stretching and magmatism during which the pace and breadth of extension changed ca. 20–18 Ma to be narrower, and again after ca. 12.5 Ma, when the kinematics of rifting became more oblique.

INTRODUCTION

Over the past 30 m.y. the western North American plate margin has changed from convergence to highly oblique divergence through a complex interaction with the Pacific plate that produced two pairs of parallel structures: the San Andreas fault system and the Eastern California Shear Zone–Walker Lane in the U.S., and the San Benito–Tosco–Abreojos fault system and the Gulf of California rift in Mexico (Fig. 1). Strike-slip deformation in both regions moved inland; currently, the Eastern California Shear Zone–Walker Lane accommodates ~25% and the Gulf of California accommodates ~90% of the Pacific–North America relative plate motion (Wesnousky, 2005; Plattner et al., 2009). Stretching of the continental lithosphere preceded direct interaction of the Pacific and North America plates and produced the Basin and Range composite extensional province (Dickinson, 2002). In Mexico, the Basin and Range

*Corresponding author.

Geosphere; October 2013; v. 9; no. 5; p. 1161–1200; doi:10.1130/GES00925.1; 15 figures; 2 tables; 1 supplemental file.
Received 6 March 2013 ♦ Revision received 31 July 2013 ♦ Accepted 15 August 2013 ♦ Published online 13 September 2013

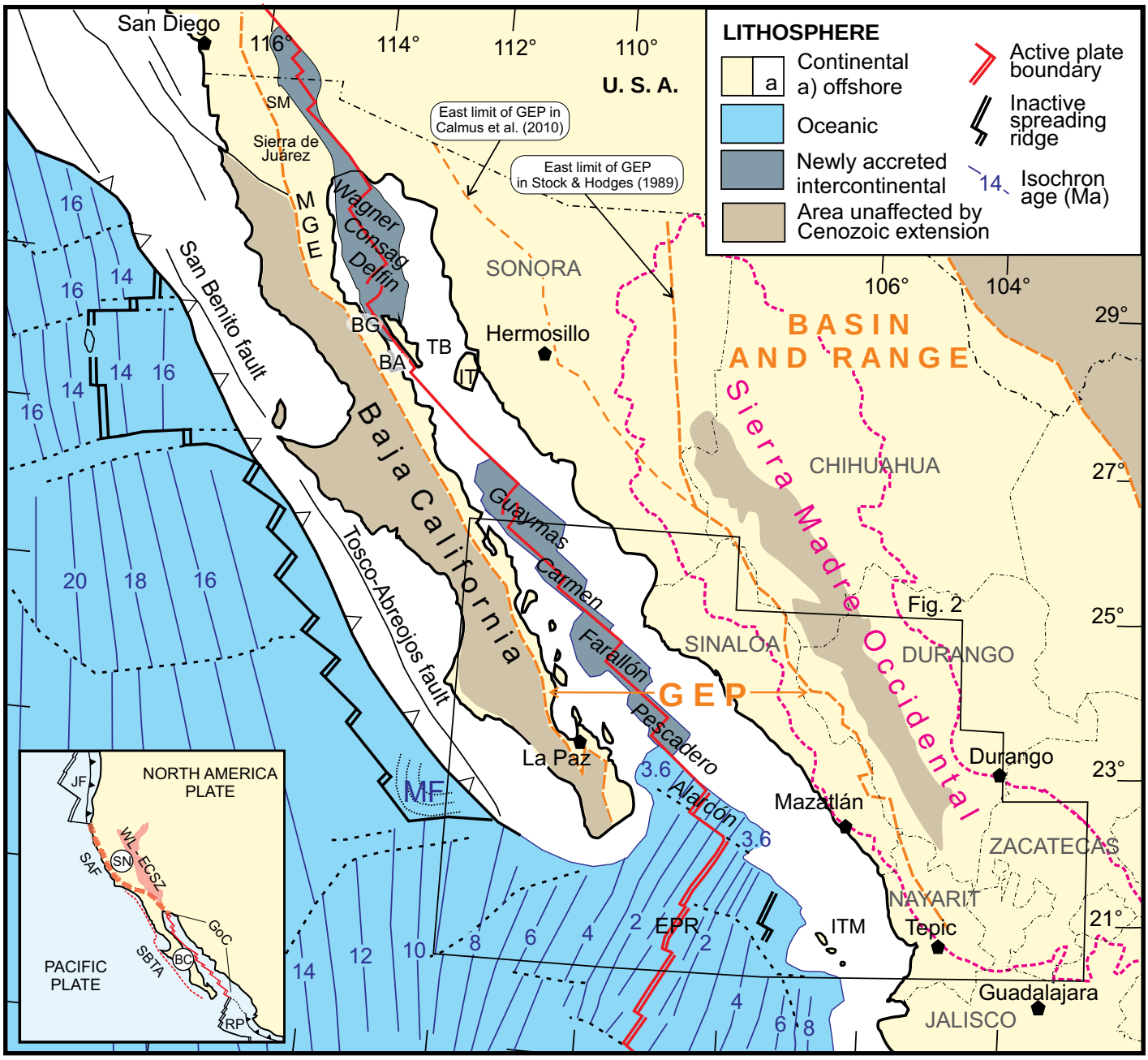

Figure 1. Regional tectonic map of the Gulf of California and adjoining areas showing the different types of lithosphere, extents of the Basin and Range and Gulf Extensional Provinces (dashed orange lines), and preserved extent of the contiguous part of the Sierra Madre Occidental silicic large igneous province (dashed red line). The extent of the unextended core of the Sierra Madre Occidental has been revised according to this study. Patterns of oceanic plate boundaries and crustal isochrons are from Lonsdale (1991) and Tian et al. (2011). GEP—Gulf Extensional Province, where different eastern boundaries in Sonora are based on those defined by Stock and Hodges (1989) and Calmus et al. (2010); MGE—Main Gulf Escarpment; BG—Bahía Guadalupe; BA—Bahía de Los Angeles; IT—Isla Tiburón; TB—Tiburón Basin; ITM—Islas Tres Marias; MF—Magdalena Fan; EPR—East Pacific Rise; SM—Sierra El Mayor. Inset shows the main fault systems currently defining the Pacific–North America plate boundary (SAF—San Andreas fault system; WL-ECSZ—Walker Lane–Eastern California shear zone; SBTA—San Benito–Tosco Abreojos fault system; GoC—Gulf of California fault system) and the Sierra Nevada (SN) and Baja California (BC) microplates; RP—Rivera Plate; JF—Juan de Fuca Plate.

episode of extension is recognized across a wide region north of the Trans-Mexican Volcanic Belt (e.g., Henry, 1989; Henry and Aranda-Gomez, 1992, 2000; Calmus et al., 2010) (Fig. 1), although the western limit of this extension has been poorly defined. More focused extension in the Gulf of California area, bounded to the west by the Main Gulf Escarpment of Baja California and to the east by the unextended core of the Sierra Madre Occidental (SMO), has been referred to as the Gulf Extensional Province (GEP) (Gastil et al., 1975) (Fig. 1) or the proto–Gulf of California (Karig and Jensky, 1972). In earlier studies (e.g., Stewart, 1978; Henry, 1989), it was argued that proto–Gulf of California rifting substantially preceded the formation of a Pacific–North America plate boundary at this latitude (ca. 14–12.5 Ma); i.e., extension occurred when subduction was still ongoing. However, after the influential work of Stock and Hodges (1989), most (e.g., Henry and Aranda-Gómez, 1992, 2000; Umhoefer et al., 2001; Umhoefer, 2011; Fletcher et al., 2007; Lizarralde et al., 2007; Seiler et al., 2011; Sutherland et al., 2012; Miller and Lizarralde, 2013) assumed that extension in the Gulf of California region began only at the end of Middle Miocene time, when subduction ended and the transfer of Baja California to the Pacific plate began. In the past two decades workers have debated the onset of oblique rifting in the Gulf of California (e.g., Stock and Hodges, 1989; Gans, 1997; Oskin and Stock, 2003; Fletcher et al., 2007; Miller and Lizarralde, 2013), but a general consensus has existed where gulf opening was fundamentally a post-subduction event, controlled by the highly oblique, northwestward motion of Baja California that was able to rift the continental lithosphere in ~6–10 m.y. (Umhoefer, 2011).

Separating young extension of the GEP from that of the older Basin and Range is particularly challenging in the northern part of the SMO (Fig. 1) (see discussion in Calmus et al., 2010). In Sonora and Chihuahua, extension has affected the entire volcanically active region, and appears spatially contiguous and temporally continuous, leading to different interpretations on the location of the boundary between the two extensional provinces (Fig. 1). In western Chihuahua, extension is poorly dated but affects ignimbrites as young as ca. 29 Ma (McDowell and Mauger, 1994) and is considered to have started ca. 30 Ma on the basis of basalt geochemistry (Cameron et al., 1989; McDowell and Mauger, 1994). Near the Chihuahua-Sonora border, extension has been recently established as ca. 27–25 Ma (Murray et al., 2013) by detailed geologic mapping and geochronology. In central Sonora, clastic sedimentation in extensional basins as well as development of metamorphic core complexes began almost concurrently along a ~200-km-wide zone at the end of the Oligocene and continued throughout the Middle Miocene (McDowell et al., 1997; Gans, 1997; Gonzalez-León et al., 2000; Vega-Granillo and Calmus, 2003; Nourse et al., 1994; Wong and Gans, 2003; Wong et al., 2010). Low-angle detachment faulting in the core complexes waned by 15 Ma (Wong et al., 2010), but high-angle normal faulting continued until ca. 8.5 Ma in coastal Sonora (McDowell et al., 1997; Mora-Alvarez and McDowell, 2000; Roldán-Quintana et al., 2004). Gastil et al. (1975) placed the eastern limit of the GEP in the coastal region of Sonora. Stock and Hodges (1989) extended it to the western SMO (Fig. 1) to include the belt of core complexes, the age of which was not known at that time; however, they considered that it could be also related to the Late Miocene opening of the Gulf of California. Based on the new knowledge about the ages of the core complexes, Calmus et al. (2010) placed the boundary further to the west at the longitude of Hermosillo (Fig. 1), because this was the boundary of post–12 Ma extension. In this way they reiterated the notion that rifting in the Gulf of California was a postsubduction process.

Pre–Late Miocene extension was also reported from a few locations in the northern Gulf of California, although these examples have generally been neglected because of overprinting by Late Miocene–Pleistocene deformation. In Baja California, Late Oligocene to Middle Miocene extension is reported at Bahía de Guadalupe (ca. 24–14 Ma; Axen, 2003), whereas extension at least partially concurrent with the Basin and Range of central-western Sonora is documented near the Main Gulf Escarpment of northern Baja California at Sierra el Mayor (ca. 15–10 Ma; Axen et al., 2000) and southern Sierra de Juárez (16–11 Ma; Lee et al., 1996) (Fig. 1). Micropaleontological studies of deep wells drilled in the Wagner, Consag, and Tiburón Basins (Fig. 1) also suggest the presence of shallow-marine sedimentation in some areas of the northern Gulf of California in the Middle Miocene (Helenes et al., 2009). These data contrast with the geology of Isla Tiburón (Oskin and Stock, 2003; Bennett et al., 2012) (Fig. 1) that clearly indicates that marine incursion at this site is latest Miocene. Despite contrasting interpretations about the timing of marine sedimentation (see the Discussion), an early onset of extension in the northern Gulf of California region cannot be ruled out and the possibility exists that the Basin and Range and the GEP were at least partly overlapping in space.

Cenozoic magmatism preceding and accompanying the development of the Gulf of California has also been divided into two different episodes, supposedly controlled by the tectonic setting at the plate boundary. Oligocene and Early Miocene silicic to bimodal volcanism of the SMO silicic large igneous province in mainland Mexico, as well as the Middle Miocene intermediate Comondú Group in Baja California, has for many years simply been interpreted as the expression of suprasubduction arc magmatism (e.g., Sawlan and Smith, 1984; Sawlan, 1991; Hausback, 1984; Umhoefer et al., 2001), whereas the appearance of more heterogeneous magma types (e.g., adakites, Nb-enriched basalts, magnesian andesites) after 12 Ma has been associated with the development of the oblique-divergent plate boundary (see reviews in Pallares et al., 2008; Calmus et al., 2010). Implicit in this view is the idea that a given tectonic setting should be promptly and clearly reflected in magma composition. However, the use of geochemistry to track the transition from subduction to rifting has been proved inconclusive in Sonora (Till et al., 2009) and is challenged in Baja California, where calc-alkaline volcanism occurred well after subduction ended, until the Pleistocene (Martín-Barajas et al., 1995; Bigioggero et al., 1995; Schmitt et al., 2006; Calmus et al., 2010).

However, it has been shown that the dominantly silicic SMO volcanics have a strong crustal contribution (Ruiz et al., 1988, 1990; Albrecht and Goldstein, 2000; Bryan et al., 2008; this work), such that the calc-alkaline and other subduction-related signatures like Nb-Ta depletions essentially reflect the composition of the crust involved in partial melting and do not directly provide any constraints on the tectonic setting of magmatism. Rapid large-scale crustal melting during the Oligocene and Early Miocene (Ferrari et al., 2007) is atypical of modern subduction zones and indicates that the SMO cannot be considered a normal volcanic arc (Bryan et al., 2008, 2013). In a similar line of reasoning, the origin of the compositionally distinctive, but volumetrically minor, intermediate volcanism of the Middle Miocene Comondú Group in southern Baja California has recently been questioned, i.e., this volcanism is more consistent with mixing and hybridization in upper crustal reservoirs promoted by ongoing extensional tectonics (Bryan et al., 2013).

Due to poor access and security reasons, the southeastern side of the Gulf of California has been comparatively less studied than the western side in Baja California. This region, comprising the state of Sinaloa, the northern part of Nayarit, and the western part of Durango, Zacatecas, and Jalisco (Fig. 2), includes both the unextended core of the SMO and the GEP (Fig. 1). A better definition of the onset of rifting

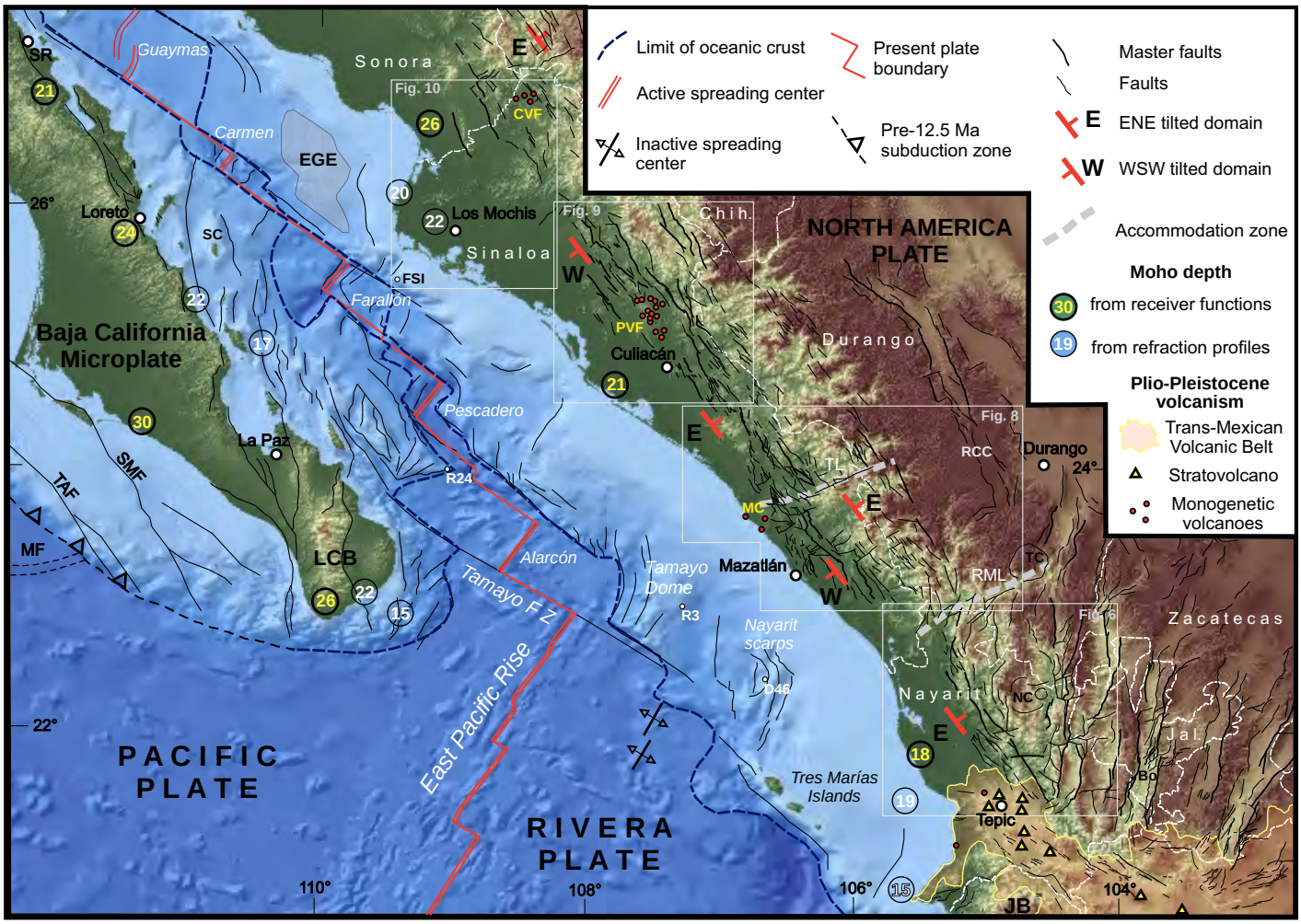

Figure 2. Tectonic map of the south-central Gulf of California and adjoining regions showing the main Neogene faults and crustal thicknesses (from Persaud et al., 2007; Lizarralde et al., 2007). Offshore samples not included in Figures 6 and 8–10 are shown here (R3—ROCA 3J 5; R24—ROCA 24J 33; D46—DANA 46a). RML—Río Mezquital lineament; TL—Tayoltita lineament; Bo—Bolaños graben; RCC—Río Chico–Canatlán graben; NC—Nayar caldera field; TC—Temoaya caldera; MC—Mesa Cacaxtla shield volcano; PVF—Pericos volcanic field; CVF—Choix volcanic field; JB—Jalisco block; TAF—Tosco-Abreojos fault system; SMF—Santa Margarita fault; FSI—Farallón de San Ignacio Island; SC—Santa Catalina Island; SR—Santa Rosalía; EGE—Eastern Guaymas evaporites; LCB—Los Cabos Block; MF—Magdalena Fan; Jal.—Jalisco State.

in the southeastern side of the Gulf of California can help to define the timing of extension in the entire GEP. Henry and Fredrikson (1987) and Henry (1989) suggested that extension in Sinaloa adjacent to the Gulf of California might be as old as Late Oligocene based on the age of a few dated north-northwest–trending dikes in the region, and a maximum age of 17 Ma was reported for extensional faulting. Subsequently, it has been assumed that the GEP in this area developed after the end of the Middle Miocene (Henry and Aranda Gómez, 2000; Ferrari et al., 2002; Aranda Gómez et al., 2003; Sutherland et al., 2012), although geologic studies and radiometric ages to support this interpretation were restricted to a few locations.

We present results of a regional geologic study supported by 43 new ^{40}Ar-^{39}Ar and U-Pb ages (Figs. 3–5) and geochemical data that test the possibility of earlier extension in the southern GEP. We document a latest Oligocene to Middle Miocene phase of extension concurrent with the Early Miocene episode of SMO silicic to bimodal volcanism and show that substantial crustal thinning was accomplished before the end of subduction at 14–12.5 Ma. We conclude that distinguishing Neogene magmatism and extension in western Mexico into two stages with a separate subduction and rifting history is incorrect, as crustal extension and decompression-driven mantle melting and crustal melting have been the controlling factors since at least the end of the Oligocene. In this perspective, Basin and Range extension and particularly the bimodal volcanism of the SMO represent the initial stage of a long rifting process that led to the formation of the Gulf of California.

METHODS

Geologic Mapping

Few geological studies exist for the southeastern border of the Gulf of California and, where available, are mostly at a reconnaissance level (Henry and Fredrikson, 1987; Henry, 1989; Ferrari et al., 2002). The first regional geologic synthesis (presented in Ferrari et al., 2007) was

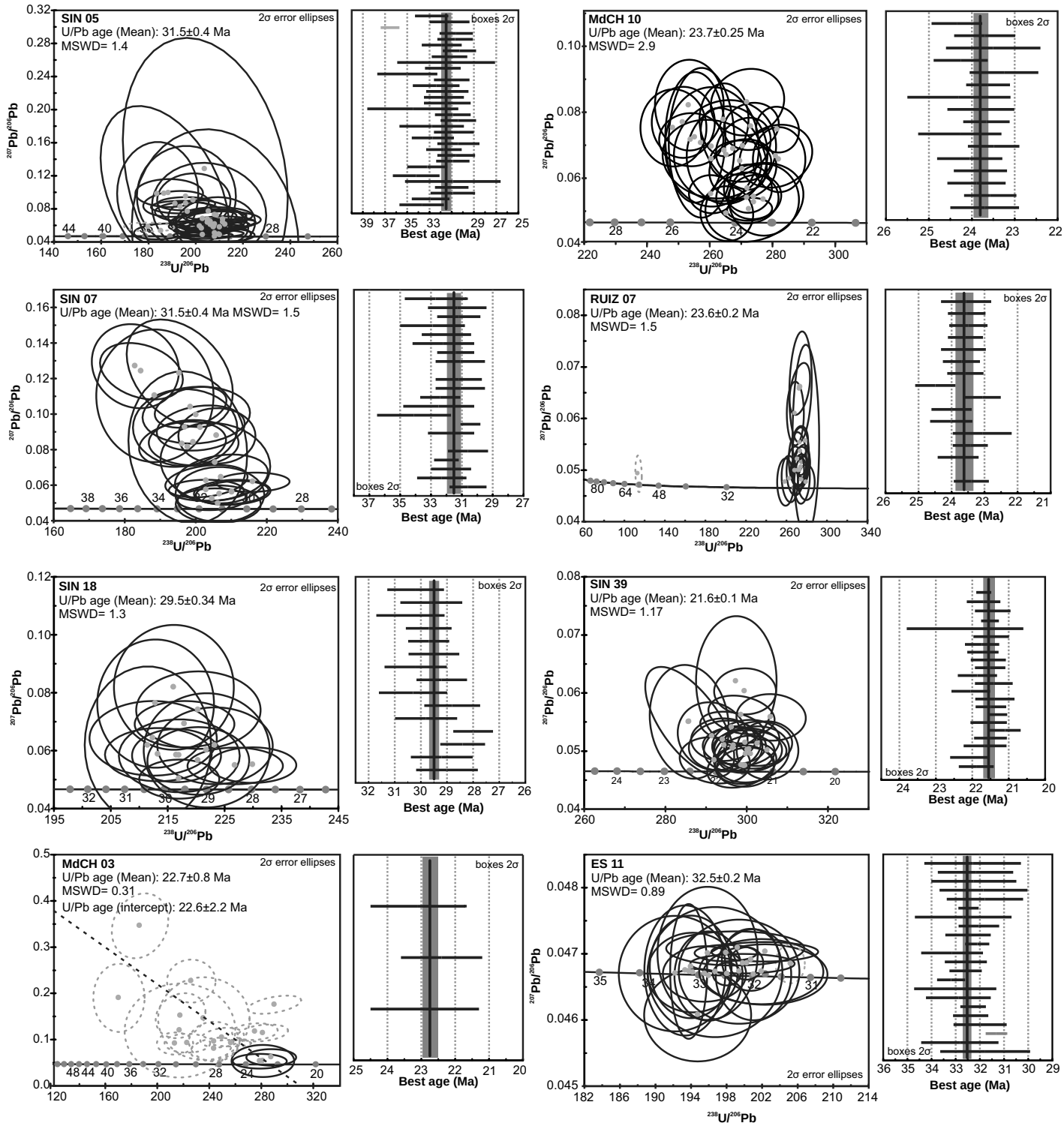

Figure 3 (*on this and following page*). Histograms and concordia diagrams of U-Pb ages for zircons of silicic rocks. Errors in calculated ages are 2σ. Dashed ellipses are data points not used in calculating the weighted mean. Full details of the U-Pb experiments are given in the Supplemental File (see footnote 1).

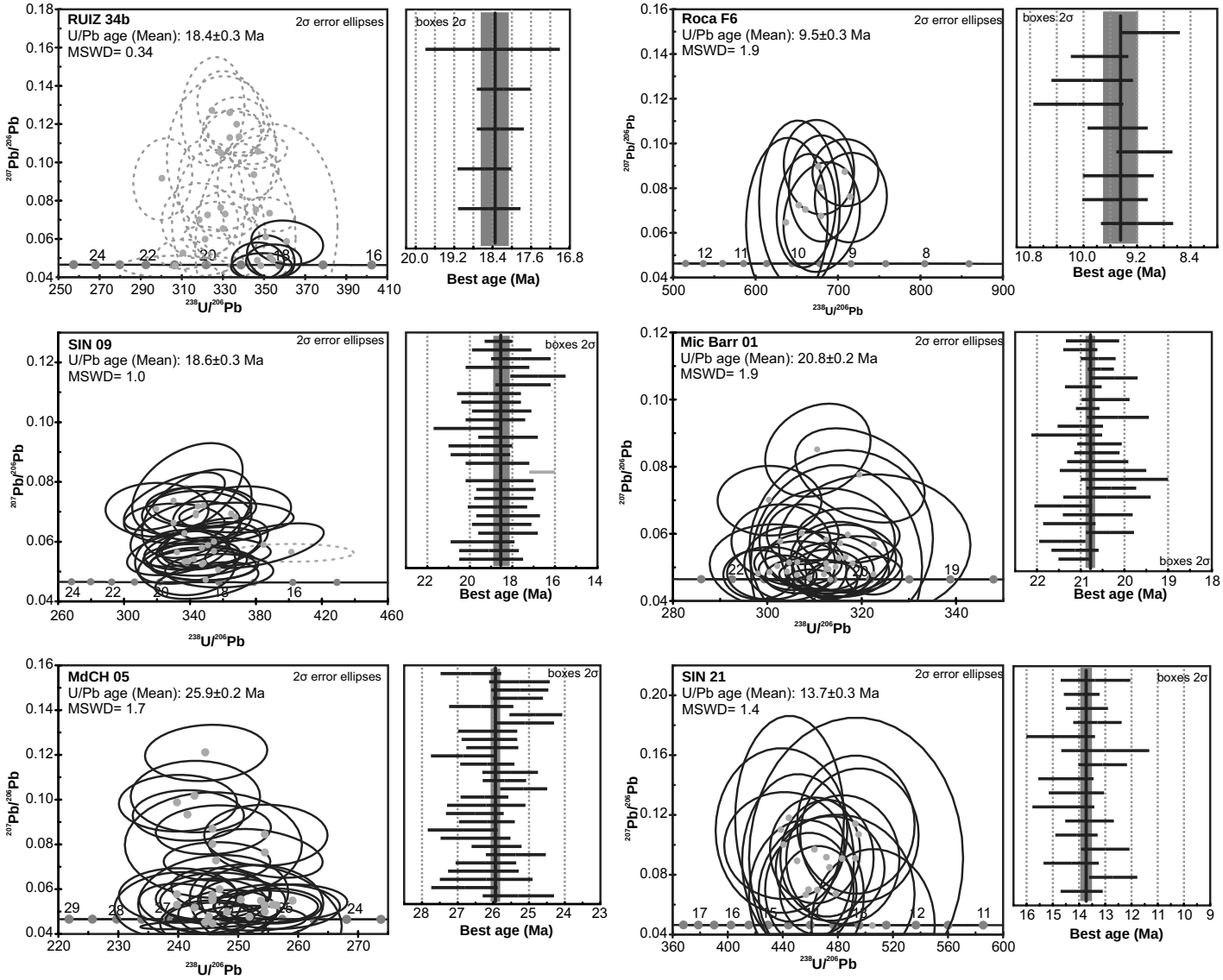

Figure 3 (*continued*).

based on the available literature data and the integration of 1:250,000 scale maps published by Servicio Geológico Mexicano (SGM) completed in 2002. In the past decade, the SGM has systematically mapped many quadrangles at 1:50,000 scale (available at: http://mapserver.sgm.gob.mx/cartas_impresas/productos/cartas/cartas50/geologia50/numcarta50.html), thus improving the regional geologic database. Although these maps generally have good field control, they often lack absolute age information. For the purpose of this study we have compiled a new regional geologic map through the reinterpretation of the 1:50,000 scale maps of SGM incorporating our new geochronologic data and field work carried out between 2006 and 2010. The map design and integration was accomplished through the use of Google Earth Pro (http://www.google.com) and Quantum GIS (geographic information system; http://www.qgis.org/).

Geochronology and Geochemistry

Previous geochronologic data were limited and unevenly distributed across the studied region. McDowell and Keizer (1977) dated (by K-Ar) ignimbrite successions along the Durango-Mazatlán highway in the central SMO and some of these samples were later redated by ^{40}Ar-^{39}Ar (McDowell and McIntosh, 2012), but without any significant change to the assigned ages. Henry and Fredrikson (1987) and Henry et al. (2003) reported U-Pb (thermal ionization mass spectrometer, TIMS), and K-Ar ages for plutonic and volcanic rocks in southern Sinaloa. In Ferrari et al. (2002), ^{40}Ar-^{39}Ar ages of the main ignimbrite sequences in northern Nayarit were provided. Additional sparse K-Ar and ^{40}Ar-^{39}Ar ages mostly without geologic context were presented in Damon et al. (1979), Solé et al. (2007), and Iriondo et al. (2003, 2004). However, large areas of the SMO in Sinaloa still lack geochronologic data.

The main problem with the K-Ar dating method is its inability to detect thermal resetting or excess Ar (Faure and Mensing 2005). As a further complication, laser ablation–inductively coupled plasma–mass spectrometry (LA-ICP-MS) zircon dating of SMO ignimbrites (Bryan et al., 2008) revealed significant age discrepancies, beyond analytical error, between U-Pb zircon and K-Ar or ^{40}Ar-^{39}Ar biotite and feldspar ages. In several cases, the discrepancy

reflected the incorporation of xenocrystic and antecrystic zircons that skewed the population age toward ages older than the eruption. Inheritance signatures are a particular problem for zircons from Early Miocene rhyolites (see also Ramos-Rosique, 2013; Murray et al., 2013), which are suspected to be extensive in the study area. A fundamental conclusion of these recent studies in neighboring areas in the SMO is the importance of stratigraphic control on dated samples and the requirement to double date by both ^{40}Ar-^{39}Ar and LA-ICP-MS techniques to obtain stratigraphically relevant ages (Bryan et al., 2008), an approach that we have followed in this study for critical samples. We are aware that the term antecrysts is not unequivocally used in the literature. In this paper we adopt the definition in a previous paper on the SMO silicic volcanism (Bryan et al., 2008), where it was pointed out that when magmatism has been sustained for 15–20 m.y. at a provincial scale, defining what is antecrystic and what is xenocrystic becomes blurred. For ancient magmatic systems like the SMO where individual volcanoes and their erupted products cannot always be identified and correlated, coupled with the lower precision of the LA-ICP-MS technique, it is not possible to discriminate zircons into antecrystic and xenocrystic at time scales <1 m.y., as has been achieved at modern silicic volcanoes (e.g., Charlier et al., 2005; Schmitt et al., 2010). Within the SMO, any zircon younger than 38 Ma has been produced by magmatism associated with the province (considered as antecrysts in this study), while older zircons have been assimilated from mid-lower crustal rocks and are obviously unrelated to the SMO volcanism (xenocrysts).

For this study we collected a large suite of samples from representative rock units exposed along the southeastern margin of the Gulf of California, with the aim of better constraining extensional faulting and volcanism in space and time. Three samples were also obtained from rifted continental blocks submerged in the Gulf of California during the National Science Foundation–funded DANA and ROCA cruises in 2004 and 2008. We obtained 43 new mineral ages by U-Pb LA-ICP-MS and ^{40}Ar-^{39}Ar methods. U-Pb ages were determined at Centro de Geociencias, Universidad Nacional Autónoma de México (UNAM), campus Juriquilla. Ages are summarized in Table 1. Procedures are described in Appendix 1, and complete analytical results are presented in the Supplemental File[1]. The ^{40}Ar-^{39}Ar dating was performed at the Geochronology Laboratory of the Departamento de Geología, Centro de Investigación Científica y de Educación Superior de Ensenada (CICESE) with the procedures described in Appendix 2.

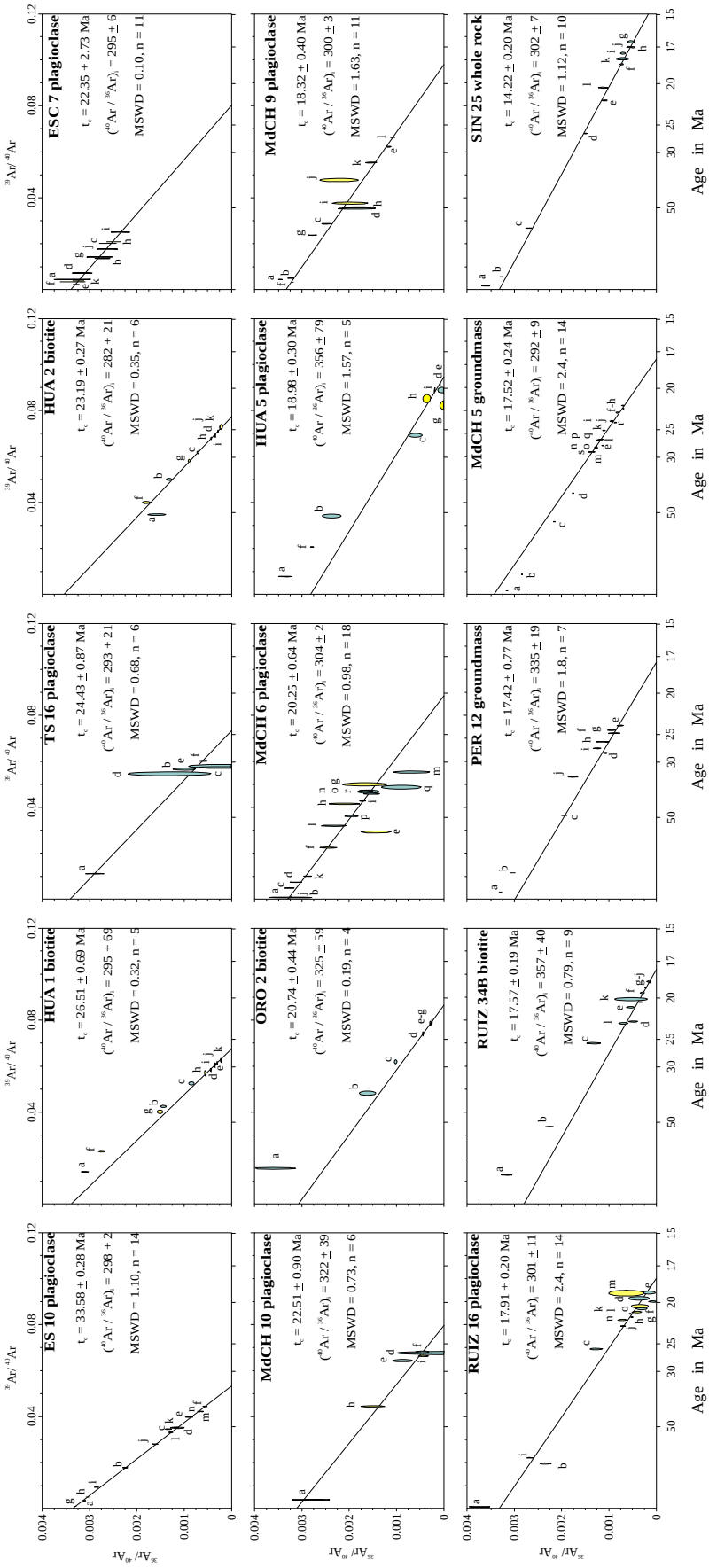

Figure 4 (*on this and following two pages*). ^{36}Ar/^{40}Ar versus ^{39}Ar/^{40}Ar correlation diagrams for the samples analyzed. First experiment is in pale blue and second experiment is in yellow. One-step laser fusion experiments from sample DANA 46a are in pink. Letters on ellipse identify fraction of gas released reported in the Supplemental File (see footnote 1). The isochron age (t_c) and (^{40}Ar/^{36}Ar)$_i$ calculated is given for each sample. MSWD is the mean square of weighted deviates and n is the number of data fitted. Full details of the ^{40}Ar-^{39}Ar experiments are given in the Supplemental File (see footnote 1).

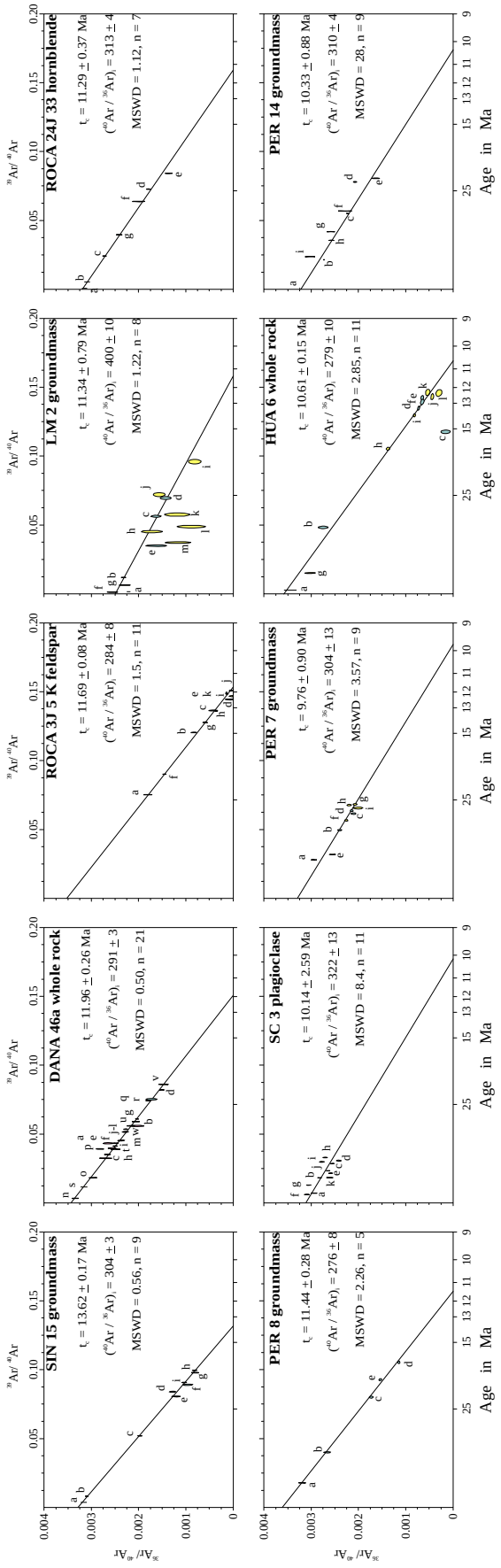

Figure 4 (*continued*).

The ^{40}Ar-^{39}Ar ages are summarized in Table 1. All the relevant ^{40}Ar-^{39}Ar information and a discussion of each experiment are given in the Supplemental File (see footnote 1).

A selection of samples dated in this work and in Ferrari et al. (2002) plus other samples for which we have stratigraphic controls were analyzed for major and trace elements. Major elements were analyzed with a Siemens SRS-3000 X-ray fluorescence instrument at Instituto de Geología (UNAM), following the procedures outlined in Lozano-Santa Cruz et al. (1995). Trace element analyses were obtained by ICP-MS using a Thermo Series XII instrument at Centro de Geociencias (UNAM) Querétaro, Mexico. Major and trace element analysis of samples DANA 46a, ROCA 3J 4, and ROCA 24J 33 were obtained at the GeoAnalytical Laboratory of Washington State University. Results are presented in Table 2. Further details of procedures and measurements are given in Appendix 3.

REGIONAL GEOLOGIC SETTING

The study region encompasses the western part of the southern and central SMO (as defined in Ferrari et al., 2007). The region is here divided into three domains: northern Nayarit (Figs. 6 and 7), southern Sinaloa, and northern Sinaloa (Figs. 8–11), based on the dominant dip and tectonic transport direction during Gulf of California rifting (Fig. 2) (e.g., Axen, 1995) as well as the type of underlying basement. The prevolcanic basement in northern Sinaloa consists of metavolcanic and metasedimentary assemblages of Paleozoic to Late Jurassic age (El Fuerte Group; Mullan, 1978; Vega-Granillo and Vidal-Solano, 2008, 2012; Keppie et al., 2006) covered by shale, marl, and limestone of Berriasian to Turonian age (Servicio Geológico Mexicano, 1999a, 2000). In southern Sinaloa deformed granitoids intruding phyllitic sandstone, quartzite, and quartz-biotite-muscovite schist yielded Jurassic to Early Cretaceous ages (Henry et al., 2003) and are covered by limestone of Albian–Cenomanian age (Bonneau, 1970). In northern Nayarit, prevolcanic basement consists of undated slate and phyllites only exposed in small outcrops 14 km northwest of Acaponeta (Servicio Geológico Mexicano, 1999b) (too small to be shown in Fig. 6). Continental magmatism that formed the rocks of the lower part of the SMO (the lower volcanic complex of McDowell and Keizer, 1977) ranges in age from Cenoma-

[1]Supplemental File. Analytical data for U-Pb and Ar-Ar data. If you are viewing the PDF of this paper or reading it offline, please visit http://dx.doi.org/10.1130/GES00925.S1 or the full-text article on www.gsapubs.org to view the Supplemental File.

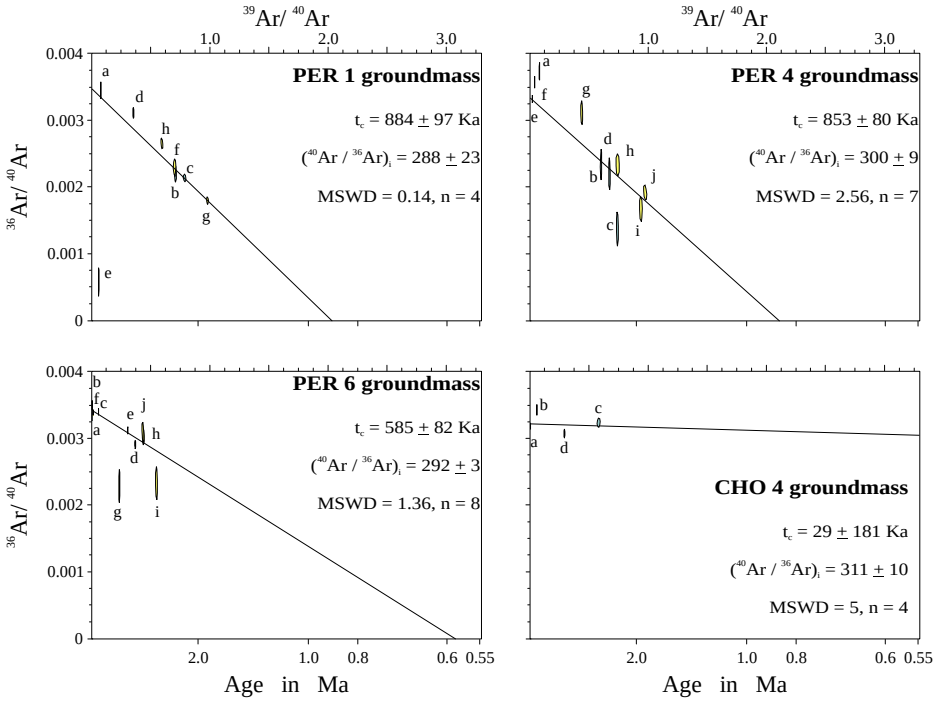

Figure 4 (*continued*).

nian to Early Eocene (Ferrari et al., 2007, and references therein) and has been interpreted to record an inland migration of arc magmatism that produced the Peninsular Ranges batholith of Baja California in Aptian–Albian time (Gastil, 1975; Ortega-Rivera, 2003). The lower volcanic complex is capped by a 1–1.5-km-thick silicic-dominant to bimodal volcanic succession named the upper volcanic supergroup in Durango and Sinaloa (McDowell and Keizer, 1977). Silicic volcanic rocks in this package constitute ~85% of the erupted material and occurred in two pulses or flare-ups ca. 34–28 Ma and ca. 24–18 Ma (Ferrari et al., 2002, 2007; Bryan et al., 2008, 2013); for simplicity, we refer to these as the Oligocene and Early Miocene pulses in the following discussion. The Oligocene pulse is recognized across the entire SMO and its volume is approximately three times larger than the Early Miocene pulse, being mainly observed in the central and southern SMO (Ferrari et al., 2007). Mafic volcanism was less abundant but is found ubiquitously interspersed in the main ignimbrite successions younger than the Late Oligocene. Postignimbritic volcanic rocks consist of basaltic lavas of Late Miocene (11–10 Ma), late Pliocene, and Pleistocene age, mostly located in the coastal area.

The regional volcanic stratigraphy revised by us and constrained by new age data presented herein provides the key basis for establishing the age of extension in the southwestern SMO adjacent to the Gulf of California. The geologic constraints of this early phase of extension in the three rift domains defined here are described in the following, from south to north.

EXTENSIONAL FAULTING AND SYNEXTENSIONAL MAGMATISM IN THE NORTHERN NAYARIT DOMAIN

Geologic and Tectonic Setting

The northern Nayarit domain is bounded to the south by a left-lateral transpressional zone located just to the north of the Trans-Mexican Volcanic Belt (Ferrari, 1995; Ferrari et al., 2002) and to the north by the Río Mezquital lineament, a fault zone accommodating opposite tilting of strata (Fig. 2). The northern Nayarit domain is a footwall segment in the terminology of Axen (1995), with rocks dominantly dipping east to east-northeast due to north-south– to north-northwest–striking, largely west-dipping normal faults (Figs. 6 and 7). The presence of the lower volcanic complex is evidenced by a small granite body 20 km north of Huajicori (Fig. 6) that yielded a late Maastrichtian U-Pb zircon age (Duque-Trujillo et al., 2013), by the occurrence of Late Paleocene detrital zircons in modern sands from the Acaponeta and San Pedro Rivers, the catchment areas of which include inaccessible areas of the southern SMO (Fletcher et al., 2007, their samples SM1 and SM 2), as well as by Late Cretaceous to Paleocene zircon xenocrysts found in Early Miocene rhyolitic domes dated in this study (samples MdCH 10, RUIZ 7, and RUIZ 34b; Table 1; Supplemental File [see footnote 1]).

Most of the northern Nayarit segment is covered by silicic ignimbrites, domes, and basalts of the upper volcanic supergroup. Rocks of the Oligocene pulse were reported only in the northeastern part of the area, where several ignimbrites and a dome were dated as 31.2–27.9 Ma (Ferrari et al., 2002; Fig. 6); however, they may underlie most of the area, as indicated by the ages of an ignimbrite and inherited zircons found by us in the western part of the study area (see following). The rest of the area is covered by rocks associated with the Early Miocene ignimbrite flare-up, ranging between ca. 24 and 17 Ma. These rocks can be grouped into three packages: the Las Canoas ignimbrite succession (24–23 Ma), the Nayar ignimbrite succession and associated rhyolites and basalts (ca. 22–20 Ma), and rhyolitic domes and intrusions emplaced in a belt along the western margin of the SMO (ca. 22–18 Ma; Figs. 6 and 7).

Extensional faulting affected almost the entire region apart from a north-elongated elliptical area, ~25 × 35 km wide, centered in the Mesa del Nayar, where ignimbrites are flat lying. At least two generations of high-angle normal faults can be recognized: (1) north-south–striking faults affecting the entire region and bounding grabens and half-grabens (Atengo, Jesús María, Huajicori, Puente de Camotlán, Huajimic, and Sierra de Alica half-grabens; La Ventana and San Agustín grabens); and (2) north-northwest–striking faults developed along the western margin of the SMO crosscutting the north-south faults (Pochotitán and San Pedro–Acaponeta fault systems; Fig. 6). Constraints on the age of faulting are available in a number of areas and indicate prolonged extension beginning at the Oligocene-Miocene boundary.

Atengo Half-Graben

Faulting in the Atengo half-graben has resulted in tilts to 25° for ignimbrites as young as 28 Ma (Ferrari et al., 2002). On the western side of the half-graben, approximately north-south rhyolitic dikes, 5–10 m thick, cut across the ignimbrite sequence and fed a large rhyolitic dome dated as 27.9 Ma (Ferrari et al., 2002) (Figs. 6, 7A, and 12A). The rhyolitic dikes are emplaced along the flexure separating tilted blocks on the east from flat-lying ignimbrites in the west, so they can be considered to mark the inception of the extension. Several microporphyritic basaltic lavas surround and partly cover the rhyolites. These lavas are only moderately tilted (~10°) and show an intraplate affinity (see Geochemistry discussion),

TABLE 1. SUMMARY OF NEW U-Pb AND Ar-Ar AGES

Sample	Location	Long (W)	Lat (N)	Elevation (m)	Rock type	Material* dated	$^{40}Ar/^{39}Ar$ age	Error (2σ)	U-Pb age (mean $^{206}U/^{238}U$)	Error (2σ)	Observations
Sierra Madre Occidental synextensional volcanism											
ES 10	Andesitic flows below ignimbrite succession of sample ES 11, near San Pablo, Durango	105° 35′ 49″	23° 51′ 29″	1948	Basaltic andesite	Plag	33.82	0.28			Isochron age
ES 11	Pink ignimbrite tilted 35° to the east-northeast by major north-northwest normal fault near San Pablo, Durango	105° 36′ 58″	23° 52′ 16″	1948	Quartz-rich, strongly welded ignimbrite	Zr			32.5	0.21	MSWD = 0.89, n = 21. Crystals in the range 33.4-31.3 Ma
SIN 05	Block and ash flow from dome cut by the Concordia graben faults near El Verde, Sinaloa	106° 5′ 16″	23° 21′ 47″	115	Glassy rhyolite lava	Zr			31.5	0.4	MSWD = 1.4, n = 32. Crystals in the range 36–30 Ma
SIN 07	Rhyolite dome North of San Juan de Jacobo along a possible northeast-trending fault, Sinaloa	106° 8′ 49″	23° 27′ 42″	160	Rhyolite lava	Zr			31.5	0.4	MSWD = 1.5, n = 20. Crystals in the range 35–29 Ma
SIN 18	Las Adjuntas dome along the El Salto–Espinazo del Diablo road, Durango	105° 30′ 45″	23° 45′ 36″	2778	Flow-banded rhyolite lava	Zr			29.5	0.3	MSWD = 1.3, n = 15. Crystals in the range 30.5–28 Ma
HUA 1	Ignimbrite from the lower part of the succession along the Huajicori-Picachos road, Nayarit	105° 16′ 52″	22° 39′ 26″	145	Crystal-rich ignimbrite	Bio	26.48	0.15			Plateau age
MdCH 03	Intermediate lava sequence underlain rhyolite dome of sample MdCH 05, Nayarit	105° 14′ 18″	22° 49′ 9″	730	Dacite lava	Zr			22.7	0.8	Many discordant zircons. MSWD = 0.31, n = 3
TS 16	Basaltic lava flow underlying 23.5 Ma ignimbrite east of Las Canoas, Zacatecas	104° 13′ 31″	22° 37′ 50″	2523	Microporphyritic basalt	Plag	24.38	0.75			Plateau age
RUIZ 7	Lowermost ignimbrite in the hanging wall of San Pedro fault system; road from Estación Ruiz to Mesa del Nayar, Nayarit	104° 53′ 10″	22° 1′ 44″	185	Fine-grained, welded and indurated pink ignimbrite with quartz and sanidine	Zr			23.6	0.2	MSWD = 1.5, n = 15. One 57 Ma xenocryst.
HUA 2	Ignimbrite from the upper part of the succession along the Huajicori-Picachos road, Nayarit	105° 11′ 28″	22° 42′ 31″	1564	Lithic ignimbrite	Bio	22.99	0.14			Plateau age
ESC-7	Eroded lava succession along the Escuinapa–Corral de Piedras road, Sinaloa	105° 40′ 43″	22° 53′ 20″	517	Basaltic andesite lava	Plag	22.39	2.56			Plateau age
MdCH 10	Nuevo León dome, on top of 21.1 Ma ignimbrite plateau, Nayarit	105° 3′ 43″	22° 39′ 7″	1668	Dacite lava	Plag, Zr	22.51	0.90	23.7	0.2	Isochron age. U-Pb MSWD = 2.9, n = 16. Possibly antecrystic inheritance. Four xenocrysts (72–63 Ma).
SIN 39	Silicic domes at northwest tip of Sierra El Infierno, Sinaloa	107° 4′ 35″	24° 21′ 30″	114	Rhyolite lava	Zr			21.6	0.1	MSWD = 1.17, n = 22. Crystals in the range 24.5–21 Ma
ORO 2	Welded ignimbrite at roadcut west of El Cajon Hydroelectric Plant, Nayarit	104° 33′ 2″	21° 27′ 6″	415	Welded Ignimbrite	Bio	20.74	0.44			Isochron age
MicBarr 01	Rhyolitic dome in the hanging wall of the San Pedro–Acaponeta fault system, east of San Miguel, Nayarit	105° 12′ 32″	22° 16′ 16″	170	Rhyolitic dome	Zr			20.8	0.2	MSWD = 1.9, n = 25. Crystals in the range 22.5–20 Ma
MdCH 06	Caramota dome, emplaced in the hanging wall of the Huajicori fault system	105° 17′ 2″	22° 36′ 58″	171	Rhyolitic dome	Plag	20.25	0.64			Isochron age
HUA 5	Poorly welded ash flow at Rio Acaponeta, northern exit of Huajicori, Nayarit	105° 19′ 10″	22° 38′ 52″	85	Ignimbrite	Plag	18.98	0.30			Isochron age
MdCH 09	Mafic lava flow along a normal fault near El Ryito, Nayarit	105° 10′ 12″	22° 40′ 8″	1144	Olivine basalt lava	Plag	18.32	0.40			Isochron age
RUIZ 16	Rhyolitic dome capping the Nayar succession near the inferred caldera rim, west of Mesa del Nayar, Nayarit	104° 44′ 42″	22° 9′ 18″	1592	Rhyolitic dome	Plag	17.91	0.20			Isochron age

(*continued*)

TABLE 1. SUMMARY OF NEW U-Pb AND Ar-Ar AGES (*continued*)

Sample	Location	Long (W)	Lat (N)	Elevation (m)	Rock type	Material* dated	$^{40}Ar/^{39}Ar$ age	Error (2σ)	U-Pb age (mean $^{206}U/^{238}U$)	Error (2σ)	Observations
Sierra Madre Occidental synextensional volcanism (*continued*)											
RUIZ 34b	Rhyolitic dome covering a normal fault at Santa Cruz de Guaybel, road from Estación Ruiz to Mesa del Nayar, Nayarit	104° 48′ 4″	22° 3′ 32″	846	Rhyolite lava	Bio, Zr	17.57	0.19	18.4	0.3	Isochron age. U-Pb age based on 5 youngest overlapping grains. MSWD = 0.34, n = 5
PER12	Eroded mafic lavas interlayered with sediments Batequitos–El Divisadero road, Sinaloa	107° 42′ 36″	25° 18′ 31″	206	Basaltic andesite lava	Gms	17.42	0.77			Isochron age
SIN 09	Sierra El Infierno dome complex, north of El Espinal, Sinaloa	106° 52′ 58″	24° 11′ 48″	155	Rhyolite lava	Zr			18.6	0.3	Concordia age. Single crystals in the 21–16 Ma age range
MdCH 05	Cuchara dome, emplaced along major normal fault, North of Huajicori, Nayarit	105° 15′ 40″	22° 46′ 37″	739	Rhyolite lava	Gms	17.41	0.07	25.9	0.2	U-Pb age dominated by antecrysts ranging between 28.5 and 23.5 Ma (MSWD 1.7, n = 28). Ar-Ar plateau age of groundmass considered the correct eruption age
SIN 25	Mafic lava succession near El Salto reservoir dam, Sinaloa	106° 42′ 4″	24° 7′ 12″	202	Basaltic lava	WR	14.01	0.23			Isochron age
SIN 21	Dome near El Palmito (unit C of McDowell and Keitzer, 1977), Durango-Mazatlán road, Sinaloa	105° 49′ 51″	23° 34′ 21″	2005	Rhyolite lava	Zr			13.7	0.3	MSWD = 1.4, n = 16
SIN 15	Basaltic lava flows covering Sierra el Infierno rhyolitic complex, north of Abuya, Sinaloa	107° 0′ 4″	24° 16′ 8″	154	Microporphyritic basalt	Gms	13.62	0.17			Isochron age
Coastal offshore lavas postdating Sierra Madre Occidental extension											
Dana 46a	Sample dredged on Nayarit scarp	106° 37′ 48″	22° 26′ 24″	–810	Hawaiite diabase	WR	11.96	0.26			Isochron age
Roca 3J 5	ROV sample at Tamayo dome, offshore Nayarit	107° 17′ 54″	22° 58′ 34″	–580	Lithic crystal tuff	Feld	11.70	0.07			Plateau age
LM2	El Muellecito, Sierra Navachiste, Sinaloa	108° 58′ 37″	25° 34′ 41″	5	Dacite lava	Gms, Plg	11.34	0.79			Isochron age
Roca 24J 33	ROV sample south of Pescadero transform	108° 56′ 17″	24° 2′ 28″	–1585	Microdiorite	Hb	11.29	0.37			Isochron age
PER-8	Flat-lying mafic lavas in a quarry west of Quila, Sinaloa	107° 7′ 9″	24° 22′ 53″	91	Basaltic andesite lava	Gms	10.94	0.23			Weighted mean
SC 3	Mafic dike cutting Early Miocene granites and aplite dike on Santa Catalina Island, BC	110° 47′ 19″	25° 41′ 44″	0	Basalt	Plag	10.89	0.52			Weighted mean
PER 7	Lower part of almost flat-lying lava succession at the base of La Piedrera peak, Sinaloa	107° 20′ 51″	24° 42′ 53″	190	Basaltic andesite lava	Gms	10.54	0.20			Plateau age
HUA-6	Flat-lying lava succession at the base of Las Peñitas microwave peak, Nayarit	105° 13′ 14″	21° 56′ 39″	59	Basaltic andesite lava	Gms	10.45	0.15			Plateau age
PER14	Flat-lying mafic lavas south of Guamuchil, Sinaloa	108° 0′ 7″	25° 9′ 2″	33	Basaltic andesite lava	Gms	10.33	0.88			Isochron age
Roca F6	Lower unit at Farallon de San Ignacio, offshore Topolobampo, Sinaloa	109° 22′ 48″	25° 26′ 24″	5	Dacite lava	Zr			9.5	0.3	MSWD = 1.9, n = 9
Pericos Volcanic Field											
PER1	Lava flow near Las Higueras, road to Lopez Mateos reservoir, Sinaloa	107° 31′ 12″	25° 2′ 24″	226	Hawaiite lava	Gms	0.884	0.097			Isochron age
PER-4	Lava flow from cone near Aguamitas de Capirato, Sinaloa	107° 32′ 24″	25° 6′ 36″	425	Hawaiite lava	Gms	0.843	0.074			Plateau age
PER-6	Recent lava flow at arroyo Huicharavito, road to Badiraguato, Sinaloa	107° 37′ 48″	25° 15′ 0″	193	Hawaiite lava	Gms	0.585	0.082			Isochron age
Choix Volcanic Field											
CHO 4	Young basaltic lava flow along the road to Huites reservoir, Sinaloa	108° 23′ 20″	26° 49′ 31″	207	Basaltic lava	Gms	0.138	0.107			One-step age

Note: MSWD—mean square of weighted deviates; ROV—remotely operated vehicle.
*Material abbreviations: Plag—plagioclase; Zr—zircon; Hb—hornblende; Bio—biotite; Gms—groundmass ; WR— whole rock; Feld—feldspar. BC—Baja, California.

TABLE 2. MAJOR AND TRACE ELEMENT ANALYSIS OF SAMPLES FROM THE SOUTHEASTERN MARGIN OF THE GULF OF CALIFORNIA

					Pleistocene				
Sample	CHO 1	CHO 2	CHO 3	CHO 4	PER 1	PER 3	PER 4	PER 5	PER 6
Area	Choix v. f.	Choix v. f.	Choix v. f.	Choix v. f.	Pericos v. f.	Pericos v. f.	Pericos v. f.	Pericos v. f.	Pericos v. f.
Long (°W)	108.3513	108.4335	108.4693	108.3888	107.5185	107.5223	107.5356	107.5642	107.6260
Lat (°N)	26.6634	26.7996	26.7376	26.8253	25.0353	25.0957	25.1084	25.1714	25.2510
Age (Ma)				0.138	0.884		0.843		0.585
Classification	AB	AB	B	AB	H	H	H	H	H
Rock type	lava flow	lava flow	lava flow	lava flow	lava flow	lava flow	lava flow	lava flow	lava flow
Major elements (wt%)									
SiO_2	46.07	46.24	49.39	47.86	46.93	47.54	48.04	47.50	47.85
TiO_2	3.46	2.94	2.46	2.95	2.63	2.60	2.57	2.69	2.56
Al_2O_3	15.48	15.73	16.35	16.59	16.27	15.66	16.65	16.70	16.61
Fe_2O_3	2.67	2.65	2.50	3.48	3.69	3.57	3.60	3.74	3.47
FeO	9.62	9.54	9.01	7.30	7.75	7.50	7.56	7.86	7.29
MnO	0.173	0.182	0.179	0.175	0.188	0.162	0.176	0.182	0.173
MgO	7.08	7.66	5.89	5.65	6.82	8.27	6.38	6.67	6.44
CaO	9.90	10.28	8.62	8.40	8.99	8.81	8.41	8.51	8.51
Na_2O	3.29	2.73	3.36	4.28	4.28	3.70	4.00	3.91	4.30
K_2O	1.62	1.45	1.61	2.33	1.76	1.53	1.75	1.56	2.01
P_2O_5	0.633	0.598	0.620	0.978	0.688	0.669	0.848	0.681	0.781
Mg#	51.2	53.4	48.3	49.2	52.3	57.9	51.3	51.5	52.5
Trace elements (ppm)									
Li	6.46	5.85	7.92	7.89	8.22	7.17	8.76	8.44	8.56
Be	1.79	1.64	1.78	2.60	2.46	2.21	2.52	2.38	2.55
Sc	24.9	26.4	18.9	14.8	21.4	20.5	18.8	20.5	19.7
V	270.2	258.9	181.6	166.4	218.2	203.7	187.3	208.1	197.2
Cr	145.0	181.3	105.3	133.3	121.8	231.0	104.5	101.5	109.9
Ni	92.0	99.2	66.5	71.6	84.9	222.3	71.4	515.7	139.4
Rb	25.6	26.2	29.6	39.9	45.5	34.9	43.1	35.8	51.4
Sr	686	648	573	881	746	694	741	684	773
Y	29.3	29.4	29.9	33.0	31.1	29.0	31.6	30.9	30.7
Zr	225	205	247	360	255	242	265	260	271
Nb	60.3	59.7	67.5	91.0	81.6	66.6	80.8	69.0	85.0
Cs	0.30	0.27	0.26	0.43	0.53	0.34	0.41	0.43	0.46
Ba	395	433	598	527	575	499	604	461	619
La	31.16	33.19	35.66	50.65	44.90	36.85	45.92	38.60	47.83
Ce	67.05	67.81	71.02	103.82	86.50	73.04	88.60	76.46	91.88
Pr	8.56	8.64	8.84	12.90	10.40	8.95	10.58	9.34	10.91
Nd	35.61	34.95	35.04	50.85	39.76	35.15	40.49	36.72	41.36
Sm	8.00	7.55	7.43	10.46	8.08	7.53	8.27	7.95	8.29
Eu	2.44	2.29	2.28	3.11	2.48	2.34	2.53	2.45	2.52
Gd	7.37	6.95	6.86	8.86	7.28	6.90	7.46	7.28	7.35
Tb	1.08	1.02	1.02	1.27	1.07	1.02	1.09	1.07	1.07
Dy	5.93	5.69	5.68	6.78	6.05	5.76	6.16	6.06	6.01
Ho	1.09	1.06	1.07	1.22	1.15	1.08	1.17	1.14	1.13
Er	2.77	2.77	2.81	3.10	3.01	2.81	3.06	2.97	2.98
Yb	2.25	2.35	2.42	2.54	2.68	2.46	2.69	2.60	2.63
Lu	0.32	0.34	0.36	0.36	0.39	0.35	0.39	0.37	0.38
Hf	5.04	4.64	5.18	7.34	5.40	5.18	5.53	5.54	5.72
Ta	3.50	3.40	3.78	5.20	4.94	4.06	4.89	4.23	5.11
Pb	1.95	2.08	2.09	2.97	2.77	2.22	2.67	2.64	2.88
Th	3.55	3.46	3.49	5.43	5.96	4.76	5.92	4.99	6.37
U	1.09	1.06	1.13	1.69	1.71	1.38	1.68	1.50	1.82
CIPW normative minerals (wt%)									
q	–	–	–	–	–	–	–	–	–
c	–	–	–	–	–	–	–	–	–
ne	4.6	1.8		6.0	7.8	3.1	2.9	3.0	6.4
di	18.1	16.9	11.5	13.0	16.2	14.2	11.2	11.6	13.8
hy	–	–	5.9	–	–	–	–	–	–
ol	13.7	15.8	10.2	10.0	11.8	14.8	12.6	13.2	11.6

(*continued*)

suggesting that they were emplaced after extension began. A small amount of plagioclase suitable for dating was separated from one of these basaltic lavas (TS 16). The ^{40}Ar-^{39}Ar analyses yielded a consistent plateau age of 24.38 ± 0.75 Ma (Fig. 5; Supplemental File [see footnote 1]), confirming the inception of extension in the Atengo half-graben in the Late Oligocene. These basalts underlie the Las Canoas ignimbrite succession, dated as 23.5 Ma by K-Ar (Damon et al., 1979) and as 23.3 Ma by ^{40}Ar-^{39}Ar (Ferrari et al., 2002). Similar aged basaltic lavas also occur in the lower part of the ca. 24 Ma El Salto–Espinazo del Diablo ignimbrite sequence, exposed along the Mazatlán-Durango highway 130 km to the northwest (McDowell and Keizer, 1977; age from McDowell and McIntosh, 2012) (Fig. 8), and below the 23.5 Ma Alacrán, ignimbrite exposed in the Bolaños graben 90 km to the southeast (Ramos-Rosique, 2013). In the Bolaños graben, north-south faulting started ~1 m.y. before the emplacement of the Alacrán ignimbrite ca. 23.5 Ma and continued until at least 15 Ma (Ramos-Rosique, 2013). Other correlative basaltic lavas associated with normal faulting are found in the Rodeo half-graben and in the Nazas area (Luhr et al., 2001).

TABLE 2. MAJOR AND TRACE ELEMENT ANALYSIS OF SAMPLES FROM THE SOUTHEASTERN MARGIN OF THE GULF OF CALIFORNIA (*continued*)

					Late Miocene				
Sample	DANA 46a	PER 7	PER 8	PER 14	ES 1	LM 1	ROCA F3	ROCA F1b	ROCA 24J 33
Area	Nayarit scarp	Coastal Sinaloa	Coastal Sinaloa	Coastal Sinaloa	Northeast of Pueblo Nuevo	Sierra Navachiste	Farallón de San Ignacio	Farallón de San Ignacio	South Pescadero transform
Long (°W)	106.6293	107.3476	107.1191	108.0020	105.3206	108.9472	109.3778	109.3778	109.0441
Lat (°N)	22.4363	24.7147	24.3815	25.1506	23.4603	25.5848	25.4362	25.4362	24.0161
Age (Ma)	11.92	10.54	10.94	10.33	10*				11.29
Classification	KTB	BA	BA	A	BA	BA	BA	A	A
Rock type	lava flow	lava flow	lava flow	lava flow	lava flow	lava flow	lava flow	lava flow	subvolcanic
Major elements (wt%)									
SiO_2	51.43	53.49	53.52	57.52	55.44	55.08	56.21	57.23	62.06
TiO_2	3.08	1.11	1.70	1.20	1.40	1.75	1.81	1.76	0.86
Al_2O_3	14.58	19.45	17.90	17.24	17.42	15.49	16.69	16.15	16.28
Fe_2O_3	4.06	2.34	2.77	2.29	2.54	3.25	2.80	3.22	2.17
FeO	8.52	4.90	5.81	4.80	5.34	6.82	5.89	5.38	3.62
MnO	0.189	0.112	0.134	0.113	0.112	0.139	0.136	0.129	0.117
MgO	3.96	4.53	3.74	3.72	4.19	4.88	3.66	3.33	3.41
CaO	7.93	9.27	8.84	7.34	7.44	8.34	6.70	6.43	5.74
Na_2O	3.57	3.42	4.08	4.02	3.26	3.37	4.14	4.34	3.23
K_2O	1.72	1.13	1.15	1.44	2.31	0.61	1.37	1.58	2.34
P_2O_5	0.957	0.253	0.366	0.308	0.572	0.276	0.594	0.448	0.181
Mg#	36.7	53.5	44.6	49.2	49.5	47.2	43.7	41.8	52.2
Trace elements (ppm)									
Li	–	10.03	12.46	11.08	8.37	6.44	8.97	14.93	–
Be	–	1.27	1.44	1.44	1.78	1.03	1.61	1.79	–
Sc	37.2	21.4	25.8	21.5	19.0	21.4	22.3	22.6	20.0
V	341.6	178.2	219.0	163.7	169.8	168.6	187.8	197.1	144.4
Cr	9.3	87.0	24.2	44.5	72.0	89.1	17.5	18.3	39.6
Ni	12.7	40.0	10.6	26.8	39.0	85.7	16.9	16.1	10.7
Rb	28.8	18.8	17.3	22.6	42.5	7.1	22.4	15.5	64.8
Sr	367	542	511	527	775	400	409	405	334
Y	47.7	21.1	31.6	24.7	24.2	24.7	38.1	43.7	27.7
Zr	222	133	172	185	211	135	231	263	201
Nb	14.5	8.0	9.4	8.9	21.3	6.5	12.8	13.9	8.4
Cs	0.32	0.36	0.54	0.56	1.06	0.11	0.54	0.19	1.81
Ba	470	512	740	619	882	383	559	634	769
La	31.48	13.50	17.10	18.25	34.72	11.33	19.23	21.57	25.68
Ce	66.59	29.03	37.65	39.71	68.66	25.19	40.96	48.58	53.57
Pr	8.59	3.86	5.26	5.22	8.77	3.55	5.91	6.66	6.68
Nd	39.26	16.44	23.02	21.60	34.44	16.40	25.86	29.11	26.19
Sm	10.17	3.91	5.66	4.84	6.87	4.60	6.51	7.34	5.85
Eu	3.38	1.21	1.65	1.41	1.94	1.57	1.89	2.08	1.35
Gd	9.97	3.98	5.90	4.73	5.82	5.10	6.87	7.79	5.34
Tb	1.58	0.62	0.91	0.73	0.83	0.80	1.09	1.23	0.87
Dy	9.29	3.83	5.60	4.39	4.54	4.76	6.78	7.69	5.27
Ho	1.82	0.77	1.13	0.88	0.86	0.90	1.36	1.55	1.08
Er	4.79	2.11	3.05	2.42	2.29	2.33	3.75	4.31	2.95
Yb	3.91	2.00	2.83	2.32	2.05	2.01	3.56	4.09	2.65
Lu	0.61	0.29	0.42	0.35	0.31	0.29	0.53	0.61	0.42
Hf	5.74	3.09	4.06	4.16	4.56	3.49	5.31	5.89	5.59
Ta	0.99	0.49	0.59	0.54	1.15	0.38	0.79	0.86	0.62
Pb	7.43	4.97	5.66	6.07	9.05	2.58	4.92	5.35	7.52
Th	4.45	1.37	1.63	1.98	3.86	0.95	2.16	2.39	10.68
U	1.65	0.45	0.52	0.67	1.23	0.32	0.82	0.74	3.04
CIPW normative minerals (wt%)									
q	3.6	3.0	2.3	7.9	6.1	8.5	7.5	8.3	16.7
c	–	–	–	–	–	–	–	–	–
ne	–	–	–	–	–	–	–	–	–
di	11.8	8.0	11.7	7.9	5.7	11.6	5.2	7.4	3.5
hy	11.7	12.8	9.5	10.6	13.3	13.7	12.3	9.3	10.5
ol	–	–	–	–	–	–	–	–	–

(*continued*)

Jesús María Half-Graben

To the west of the Atengo half-graben, the Jesús María half-graben drops the Las Canoas succession ~1700 m to the west, where it is found tilted as much as 30° (Fig. 7B). The Jesús María fault system also downthrows the Nayar ignimbrite succession ~1300 m. As defined in Ferrari et al. (2002), the Nayar succession consists of several ignimbrite sheets that thicken toward the Mesa del Nayar area, where at least 11 cooling units form a 1-km-thick sequence with ^{40}Ar-^{39}Ar ages ranging between 19.9 ± 0.4 and 21.2 ± 0.3 Ma. Basaltic andesitic lavas dated as 21.3 ± 0.3 Ma found along the Jesús María fault system (Ferrari et al., 2002) (Fig. 7B) suggest that extension associated with half-graben formation was ongoing at the time. The top of the flat-lying Nayar succession reaches a maximum of ~1950 m elevation just west of Mesa del Nayar. The Nayar succession is not exposed in the Jesús María footwall block, where the top of the 23.5 Ma Las Canoas ignimbrite succession is at ~2450 m elevation.

TABLE 2. MAJOR AND TRACE ELEMENT ANALYSIS OF SAMPLES FROM THE SOUTHEASTERN MARGIN OF THE GULF OF CALIFORNIA (*continued*)

	Late Miocene			Latest Oligocene to Early Miocene					
Sample	LM 2	R F6	R 3J 4	PER12	ESC 7	TS 16	TS 21	NAY 21	MdCH 10
Area	Sierra Navachiste	Farallón de San Ignacio	Tamayo dome	Badiraguato	Huajicori-Picachos	Atengo	Jesús María	Jesús María	Huajicori-Picachos
Long (°W)	108.9768	109.3800	107.3427	107.7100	105.6786	104.2254	104.5111	104.5780	105.0624
Lat (°N)	25.5779	25.4400	23.0561	25.3085	22.8889	22.6305	22.2524	22.2410	22.6526
Age (Ma)	11.34	9.7	11.7[†]	17.42	22.39	24.38	21.3[§]	23.01	22.51
Classification	D	R	D	BA	BA	B	B	B	D
Rock type	lava flow	lava flow	tuff	lava flow	lava flow	lava flow	lava flow	dike	dome
Major elements (wt%)									
SiO_2	66.26	71.41	–	55.17	55.03	48.66	50.97	50.64	68.24
TiO_2	0.55	0.43	–	1.11	1.09	2.39	1.70	1.54	0.72
Al_2O_3	17.19	14.41	–	18.05	17.16	17.20	16.94	17.85	15.97
Fe_2O_3	1.55	1.55	–	2.58	3.02	2.75	2.19	2.21	1.96
FeO	2.10	1.39	–	5.41	6.35	9.89	7.87	7.97	2.64
MnO	0.077	0.041	–	0.119	0.172	0.154	0.146	0.155	0.044
MgO	0.95	0.66	–	4.30	4.30	5.03	5.97	6.21	0.51
CaO	4.57	1.50	–	8.03	8.27	8.96	8.81	8.79	2.54
Na_2O	4.55	5.02	–	3.89	3.00	3.26	3.02	2.83	3.82
K_2O	2.06	3.51	–	1.08	1.39	1.24	1.73	1.25	3.32
P_2O_5	0.157	0.084	–	0.246	0.214	0.444	0.660	0.555	0.23
Mg#	32.6	29.8		49.8	45.9	42.1	52.0	52.7	17.2
Trace elements (ppm)									
Li	13.39	33.21	–	9.18	18.80	95.35	54.31	–	33.66
Be	1.25	2.94	–	1.15	1.20	1.74	1.73	–	2.17
Sc	9.6	5.7	5.1	21.8	28.5	26.9	25.0	–	11.9
V	88.5	32.6	182.0	205.6	273.6	277.7	224.4	–	60.0
Cr	8.8	3.1	40.9	46.6	40.0	21.5	147.7	–	4.5
Ni	12.3	2.0	7.7	20.1	19.1	33.2	54.1	–	2.7
Rb	41.7	72.5	214.0	20.4	36.8	26.8	32.2	–	112.1
Sr	731	132	103	643	467	618	683	–	304
Y	25.8	42.0	81.7	19.1	22.9	28.2	25.7	–	39.2
Zr	96	262	456	117	106	167	188	–	224
Nb	4.6	14.6	39.7	6.9	5.0	22.2	12.8	–	12.3
Cs	0.84	1.87	3.94	0.49	1.23	3.53	36.91	–	6.02
Ba	3878	722	184	554	527	389	816	–	1089
La	31.63	27.92	70.69	13.19	12.98	23.17	29.72	–	40.49
Ce	35.06	56.71	146.40	29.31	28.26	49.77	62.97	–	69.81
Pr	5.94	6.98	17.75	4.03	3.73	6.64	8.40	–	10.71
Nd	23.57	27.72	66.23	17.64	16.22	27.67	34.20	–	42.27
Sm	4.41	6.23	14.85	4.18	3.85	6.28	7.20	–	8.79
Eu	1.42	0.92	0.55	1.31	1.13	1.92	2.14	–	2.26
Gd	4.55	6.32	13.72	4.08	3.89	6.05	6.29	–	8.01
Tb	0.63	1.05	2.43	0.61	0.62	0.91	0.89	–	1.18
Dy	3.52	6.82	15.08	3.51	3.81	5.30	4.91	–	6.97
Ho	0.73	1.41	3.08	0.69	0.77	1.03	0.94	–	1.35
Er	1.95	4.10	8.53	1.81	2.22	2.71	2.46	–	3.75
Yb	1.62	4.27	7.93	1.61	2.14	2.39	2.17	–	3.53
Lu	0.25	0.63	1.21	0.24	0.34	0.35	0.32	–	0.52
Hf	2.58	7.05	14.48	2.84	2.72	3.93	4.14	–	5.51
Ta	0.37	1.09	2.81	0.40	0.32	1.43	0.72	–	0.86
Pb	8.26	7.67	23.41	5.07	9.05	4.36	6.02	–	15.90
Th	4.08	7.00	22.96	1.49	2.73	2.46	2.44	–	8.34
U	1.35	2.16	8.28	0.54	1.07	0.75	0.92	–	2.90
CIPW normative minerals (wt%)									
q	20.6	24.6	–	4.7	7.4	–	–	–	26.8
c	–	–	–	–	–	–	–	–	2.0
ne	–	–	–	–	–	–	–	–	–
di	1.0	0.4	–	7.8	8.5	10.7	9.7	6.2	–
hy	3.7	2.1	–	13.1	14.2	7.0	16.0	22.0	3.4
ol	–	–	–	–	–	9.2	3.1	0.7	–

(*continued*)

These relations indicate that extension along the approximately north-south faults of the Jesús María half-graben must have initiated before the emplacement of the Nayar succession ca. 21 Ma, so the footwall was already a topographic barrier to the east, preventing further eastward outflow of the Nayar ignimbrites. Extension must have continued for a few million years more to tilt and downthrow the Nayar succession east of Mesa del Nayar (Fig. 7B). Further constraints on the age of faulting in the area just west of Mesa del Nayar come from a rhyolitic dome located 25 km to the southwest, which covers a north-south fault without being cut by the fault (Fig. 12B). A sample from this dome yielded 26 U-Pb ages in the range 23–17 Ma (sample RUIZ 34b; Fig. 3; Table 1). A weighted mean including all the analyses would yield an age of 19.02 ± 0.3 Ma, with a mean square of weighted deviates (MSWD) of 3.7, indicating an age spread beyond the obtained analytical error. A further weighted mean, obtained with the 5 concordant and overlapping youngest analyses, yields an age of 18.4 ± 0.3 Ma (MSWD = 0.34, n = 5), which is interpreted as the best estimation for the last phase of zircon crystallization

TABLE 2. MAJOR AND TRACE ELEMENT ANALYSIS OF SAMPLES FROM THE SOUTHEASTERN MARGIN OF THE GULF OF CALIFORNIA (*continued*)

	Latest Oligocene to Early Miocene							
Sample	MdCH 03	MZ 1	ESC 2	ESC 3	ESC 8	HUA 5	MicBarr 01	MicBarr 03
Area	Huajicori-Picachos	Camino Mazatlán-Miravalle	San Pedro-Acaponeta	West of Llano Grande	Road to Rincón Verde	Huajicori-Picachos	San Pedro-Acaponeta	Northern Nayarit
Long (°W)	105.2383	106.3446	105.1094	105.0757	105.7785	105.3195	105.2091	105.2286
Lat (°N)	22.8192	23.2670	22.1849	22.7600	22.9204	22.6477	22.2715	22.2739
Age (Ma)	25.1		20.9§	21.1§		18.98	20.62	
Classification	R	R	R	D	R	R	R	R
Rock type	lava flow	ash flow	ign.	ign.	ign.	tuff	dome	dome
Major elements (wt%)								
SiO_2	69.92	78.15	74.43	–	74.06	83.04	76.28	80.93
TiO_2	0.51	0.09	0.14	–	0.23	0.11	0.22	0.18
Al_2O_3	15.90	12.32	15.28	–	13.82	9.67	12.69	10.43
Fe_2O_3	1.76	0.59	0.54	–	1.03	0.72	0.69	0.35
FeO	1.58	0.53	0.48	–	0.92	0.65	0.62	0.31
MnO	0.068	0.035	0.024	–	0.065	0.013	0.033	0.009
MgO	0.33	0.18	0.47	–	0.47	0.36	0.23	0.07
CaO	1.52	0.47	0.55	–	1.22	0.22	0.73	0.58
Na_2O	4.61	3.14	3.10	–	4.24	0.71	2.65	0.56
K_2O	3.65	4.48	4.96	–	3.87	4.50	5.82	6.58
P_2O_5	0.14	0.013	0.035	–	0.072	0.013	0.03	0.01
Mg#	15.8	23.5	46.5		31.4	32.9	24.9	16.8
Trace elements (ppm)								
Li	24.75	23.80	57.80	34.77	28.54	14.64	40.15	–
Be	2.58	2.78	2.18	1.32	2.25	1.63	1.75	–
Sc	8.3	1.6	2.5	7.5	3.1	4.1	3.9	–
V	31.9	9.8	3.5	21.4	10.1	0.3	22.2	–
Cr	2.3	2.5	3.0	3.7	3.2	3.3	3.4	–
Ni	0.7	1.7	2.2	3.3	2.2	2.2	1.9	–
Rb	120.9	135.1	156.9	92.5	123.2	102.8	211.6	–
Sr	343	46	77	381	146	36	81	–
Y	39.8	24.8	16.0	14.8	17.0	13.5	11.4	–
Zr	285	104	72	193	121	129	78	–
Nb	13.8	16.2	13.0	7.3	10.3	11.5	11.1	–
Cs	6.30	2.24	3.44	8.74	2.63	3.64	6.56	–
Ba	1254	1049	914	1315	1267	808	1242	–
La	30.83	35.50	33.93	21.26	27.76	30.52	27.55	–
Ce	59.40	62.48	41.60	39.28	48.92	38.85	47.08	–
Pr	8.01	8.02	7.15	5.27	5.68	7.11	5.10	–
Nd	30.87	27.01	23.52	19.75	19.37	25.61	16.38	–
Sm	6.63	5.07	4.05	3.63	3.43	4.06	2.74	–
Eu	1.47	0.50	0.66	0.90	0.66	0.51	0.57	–
Gd	6.37	4.23	3.35	3.04	2.92	3.09	2.25	–
Tb	1.00	0.69	0.50	0.45	0.46	0.43	0.34	–
Dy	6.27	3.94	2.76	2.57	2.69	2.30	1.94	–
Ho	1.28	0.79	0.51	0.49	0.54	0.44	0.40	–
Er	3.71	2.41	1.53	1.48	1.67	1.33	1.12	–
Yb	3.79	2.57	1.52	1.57	1.85	1.23	1.22	–
Lu	0.57	0.40	0.24	0.24	0.29	0.18	0.19	–
Hf	7.12	3.89	2.63	5.31	3.53	4.41	2.39	–
Ta	1.01	1.24	1.19	0.57	0.87	0.98	0.98	–
Pb	14.66	7.53	18.69	6.08	18.40	15.72	17.12	–
Th	13.66	11.62	13.32	8.54	10.22	13.73	13.12	–
U	4.12	3.01	3.73	1.28	3.45	2.02	3.60	–
CIPW normative minerals (wt%)								
q	25.4	41.3	35.5	–	31.2	60.6	36.6	51.2
c	1.9	1.5	3.9	–	0.6	3.3	0.8	1.4
ne	–	–	–	–	–	–	–	–
di	–	–	–	–	–	–	–	–
hy	1.6	0.9	1.4	–	1.8	1.3	0.8	0.2
ol	–	–	–	–	–	–	–	–

Note: Dash indicates not analyzed. Abbreviations: v.f.—volcanic field; A—andesite; AB—alkali basalt; B—basalt; BA—basaltic andesite; D—dacite; H—hawaiite; KTB—potassic trachybasalt; R—rhyolite; ign.—ignimbrite.

*K-Ar age from Solé et al. (2007).

†Age of the lithologically similar sample R3J-5, collected at the same site.

§$^{40}Ar/^{39}Ar$ age from Ferrari et al. (2002). Normative minerals: q—quartz; c—corundum; ne—nepheline; di—diopside; hy—hypersthene; ol—olivine.

for this rhyolite dome. We also dated a biotite concentrate from the same sample by Ar-Ar laser step-heating; the resulting isochron yielded an age of 17.57 ± 0.19 Ma (Table 1; Fig. 4), which we consider as the best estimation of the emplacement age of the dome. We dated a large rhyolite dome capping the Nayar succession west of Mesa del Nayar, which is unfaulted and has a mostly flat top (i.e., does not appear tilted) (sample RUIZ 16; Table 1). Plagioclase separated from the rhyolite was step-heated and yielded an isochron of 17.91 ± 0.20 Ma (Fig. 4), indistinguishable within error from the biotite age of the RUIZ 34b dome. These geologic relations suggest that by ca. 17.6 Ma extension associated with the north-south faults had essentially terminated.

Huajicori-Picachos Fault System

The Huajicori area is located in northwestern Nayarit (Fig. 6). Here, a system of north-south–striking and west-dipping normal faults creates an ~1800 m escarpment that bounds the SMO ignimbrite plateau toward the coastal plain (Huajicori-Picachos fault system; Fig. 7C). The lowermost ignimbrite exposed by the fault system is a pink, crystal-rich welded ignimbrite with biotite, quartz, feldspar, and plagioclase. We dated a biotite concentrate from this ignimbrite (sample HUA 1) by ^{40}Ar-^{39}Ar, obtaining a plateau age of 26.48 ± 0.15 Ma (Fig. 5; Table 1) from the weighted mean of the last four fractions of the second experiment. We have also dated some zircons from an aphyric dacitic lava in the same succession ~20 km to the north of HUA 1 (sample MdCH 03). We performed a total of 27 zircon analyses; once filtered, these yielded 18 concordant to variably discordant ages. In particular, the 3 youngest analyses yielded concordant and overlapping results, with a ^{206}Pb/^{238}U weighted average age of 22.7 ± 0.8 Ma (MSWD = 0.31, n = 3) (Fig. 3), consistent with the stratigraphic position of the sample. A succession of ~1000 m of ignimbrites covers the Oligocene ignimbrite and Early Miocene dacite. We dated one of the highest ignimbrites near the Los Picachos site, a moderately welded and poorly indurated ignimbrite with biotite and feldspar phenocrysts (HUA 2) that forms a distinctive erosional morphology with sharp peaks. Duplicate experiments by laser step-heating on a biotite concentrate gave a well-defined plateau age of 22.99 ± 0.14 Ma and an isochron age of 23.19 ± 0.27 Ma; we consider the former the best estimate age for the emplacement of this sample because of its smaller error (Table 1). The ignimbrite succession is capped by a large dacitic dome, from which we separated 31 zircons that gave concordant to slightly discordant U-Pb ages in the range ca. 28–23 Ma and 4 xenocrysts with ages of 72–63 Ma (sample MdCH 10; Table 1; Fig. 3). The ^{206}Pb/^{238}U weighted mean of 16 crystals yields an age of 23.7 ± 0.2 Ma (MSWD = 2.9). The stratigraphic position of this dome above the HUA 2 ignimbrite dated as 22.99 Ma, combined with obvious inheritance, indicates that the weighted mean age is biased by an antecrystic population and thus provides no constraint on timing of dome emplacement. For this reason we also dated a plagioclase concentrate from the same sample by the ^{40}Ar-^{39}Ar method. The sample yielded an isochron age of 22.51 ± 0.90 Ma and a plateau age of 22.15 ± 0.93 Ma (Figs. 4 and 5; Table 1), consistent with the stratigraphic relations, and confirming that this dacitic lava is dominated by relatively subtle

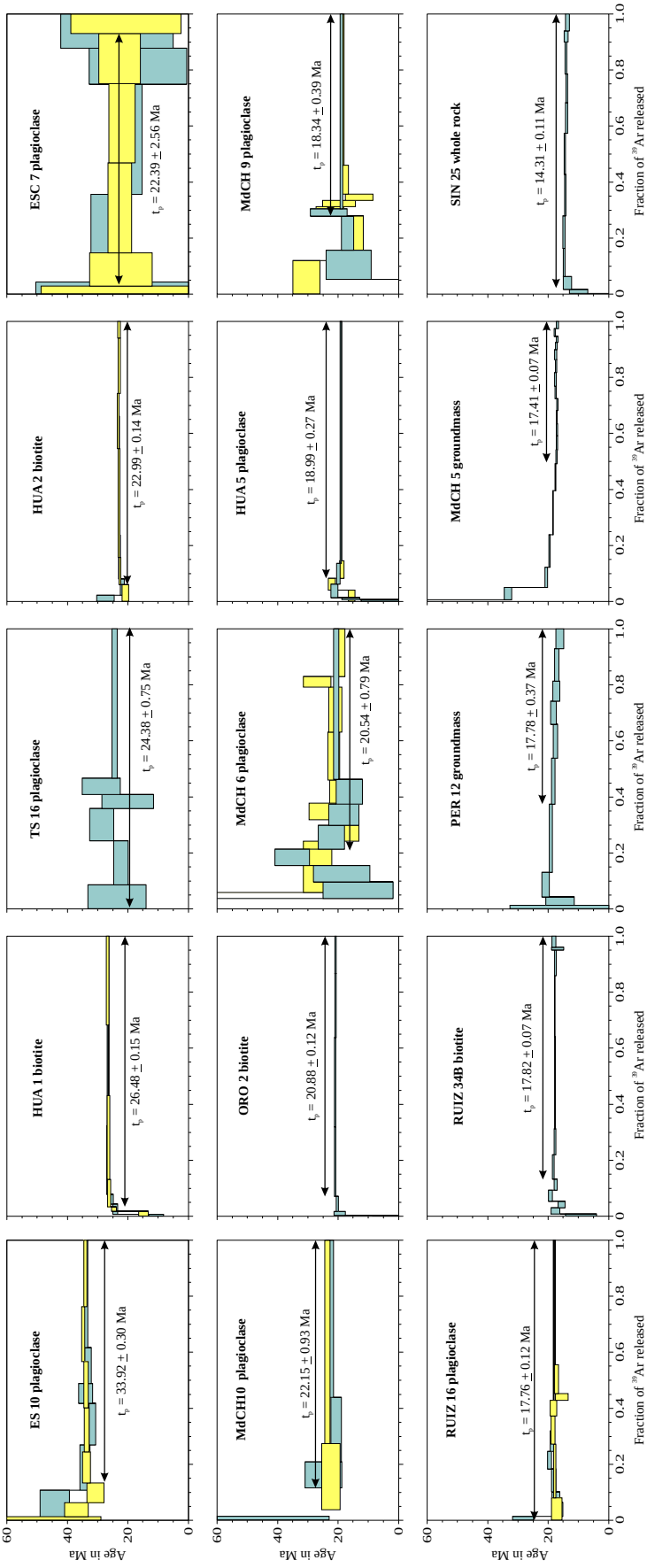

Figure 5 (*on this and following two pages*). ^{40}Ar-^{39}Ar age spectra for the samples analyzed. Full details of the ^{40}Ar-^{39}Ar experiments are given in the Supplemental File (see footnote 1). The plateau age (t_p) given in the figure was calculated with the weighted mean (W_m) of the fractions identified with the horizontal arrow. First experiment is in pale blue and second experiment is in yellow. For illustrative purposes the 13 one-step laser fusion experiments from sample DANA 46a, are plotted as pseudo-age spectrum in pink.

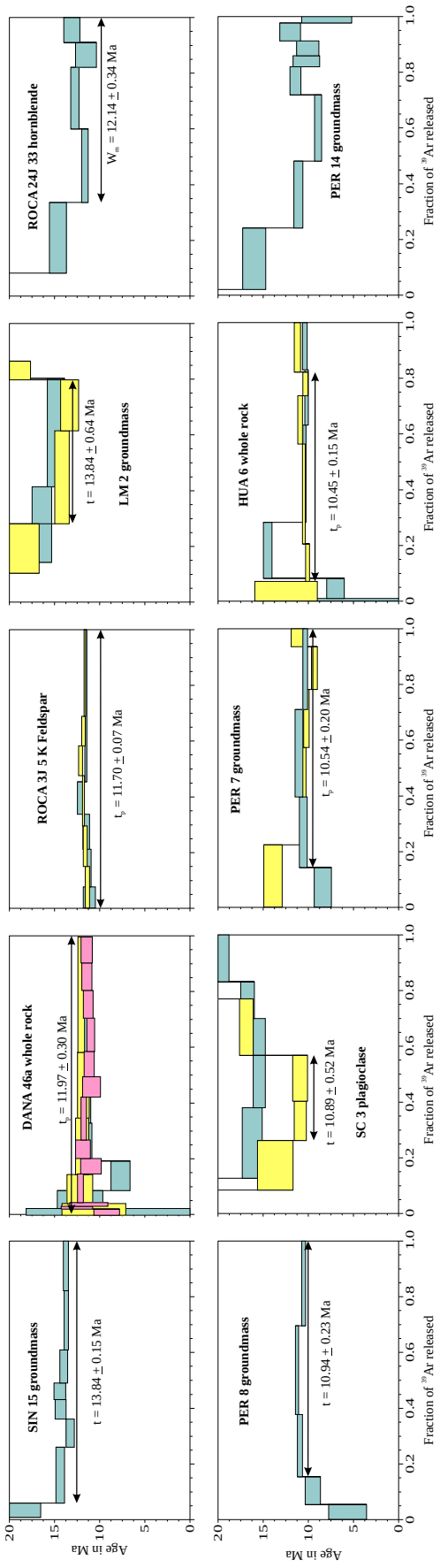

Figure 5 (*continued*).

antecrystic inheritance, as observed elsewhere in the SMO (e.g., Bryan et al., 2008).

Several other silicic domes are emplaced in the hanging wall of the Huajicori-Picachos fault system. The Cuchara and Caramota domes are particularly interesting because they were emplaced above one of the north-south faults without being obviously cut; 28 zircons with acceptable discordance (i.e., <10% of deviation from concordia) from the Cuchara dome gave a $^{206}Pb/^{238}U$ weighted mean age of 25.9 ± 0.2 Ma (MSWD = 1.7, n = 28) (sample MdCH 05; Table 1). The somewhat high MSWD is indicative of age dispersion and the presence of multiple grain ages or populations, confirmed by ^{40}Ar-^{39}Ar dating. A groundmass concentrate from the same sample was laser step-heated and a well-defined plateau (14 fractions of 19 steps) gave an age of 17.41 ± 0.07 Ma (Fig. 5; Table 1). Given the high quality of this age datum, it must be concluded that all zircons in this dome are inherited from previous igneous episodes (i.e., antecrysts) as represented by other dated rocks exposed in proximity to this unit (e.g., ignimbrite HUA1 and dacite lava MdCH 03; Table 1). For the Caramota dome (sample MdCH 6; Table 1), two ^{40}Ar-^{39}Ar experiments yielded a reproducible age spectra, with a wide plateau age of 20.54 ± 0.79 Ma and an isochron age of 20.25 ± 0.64 Ma, which we consider to be the best age estimate. We also dated a microporphyritic olivine basaltic lava vented from one of the approximately north-south faults 15 km east of Huajicori (sample MdCH 09; Table 1). A plagioclase concentrate from this lava was laser step-heated, and yielded a plateau age of 18.34 ± 0.39 Ma defined by 5 consecutive fractions with 72.06% of the ^{39}Ar released, identical to the isochron age of 18.32 ± 0.40 Ma obtained with the combined data of the two experiments. We dated a poorly indurated and poorly welded ignimbrite exposed in the Acaponeta River near Huajicori. This ignimbrite is tilted as much as 25° to the east but is not exposed in the footwall of the Huajicori-Picachos fault system, where the topmost ignimbrite was dated as 21.1 ± 0.7 Ma (sample ESC 3; Ferrari et al., 2002). A plagioclase concentrate from the Huajicori ignimbrite (sample HUA 5; Table 1) was laser step-heated and yielded an isochron age of 18.98 ± 0.30 Ma, considered to be our best age estimate. Further age relations are deduced 45 km northwest of Huajicori near the coast, where basaltic andesitic lavas vented from an approximately north-south fault cover, in angular unconformity, ignimbrites tilted to the east (Fig. 6). A plagioclase concentrate from these basaltic andesite lavas (sample ESC 7; Table 1), was dated by the ^{40}Ar-^{39}Ar method by step-

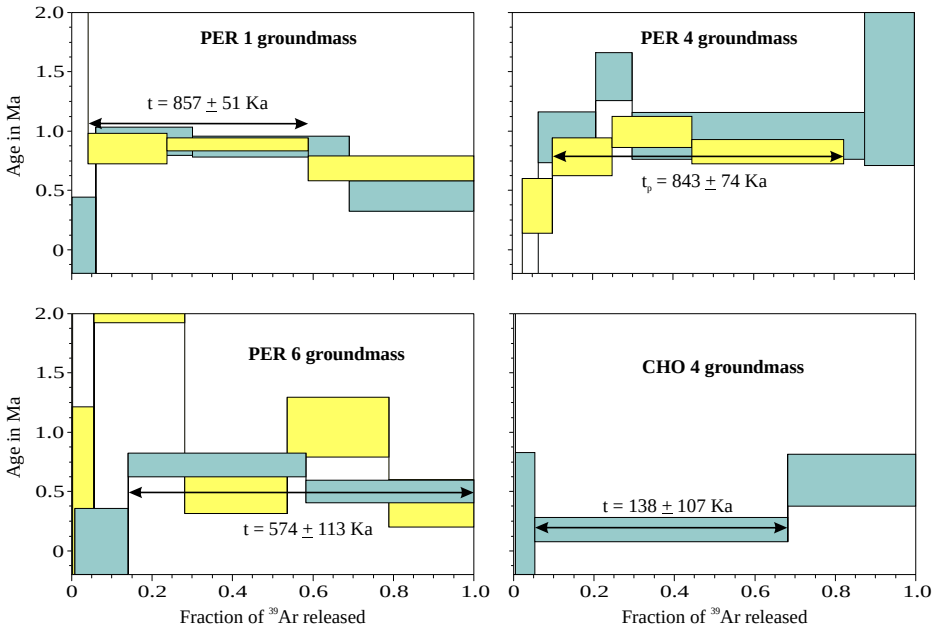

Figure 5 (*continued*).

heating in a temperature-controlled Ta furnace, yielding a plateau age of 22.39 ± 2.56 Ma.

In summary, the new ages obtained in the Huajicori area, as well as the geologic relations, indicate that a significant part of displacement along the approximately north-south faults of the Huajicori-Picachos system occurred before the emplacement of the ca. 18.98 Ma Huajicori ignimbrite and was waning by ca. 17.4 Ma, when the Cuchara dome was emplaced on one side of the fault escarpment. Basalts dated as ca. 18.3 Ma vented from the north-south faults were likely providing the thermal input to promote small-volume crustal melting and emplacement of rhyolitic domes. This suggests that extensional faulting in the area began before the Early Miocene and was likely waning by the time the mafic lavas were emplaced (youngest age within error, 19.83 Ma).

Pochotitán and San Pedro–Acaponeta Fault Systems

Two major systems of north-northwest–striking normal faults postdate the north-south fault systems and form a major breakaway zone bounding the Gulf of California (Figs. 6, 7A, 7B, and 7D). They consist of a series of normal faults that tilt ignimbrites of the Nayar succession as much as 35° to the east-northeast (Ferrari et al., 2002). Geologic maps of the SGM interpret some of the rocks cropping out at the base of the tilted succession as Paleocene to Oligocene. However our new ages indicate that in most cases they are Miocene in age. We dated a tilted ignimbrite near the southern end of the Pochotitán fault system (sample ORO 2; Table 1), and the lowermost ignimbrite in the hanging wall of the southern part of the San Pedro fault system (sample RUIZ 7; Table 1). Sample ORO 2 is from a moderately welded, indurated lithic ignimbrite with feldspar, quartz, and biotite, tilted 15° to the east-northeast. A biotite concentrate from the ignimbrite was laser step-heated and we conclude that the resulting isochron age of 20.74 ± 0.44 Ma is the best eruption age estimate (Fig. 4; Table 1). Sample RUIZ 7 is a pink, well-indurated, moderately welded ignimbrite with quartz and sanidine, dipping 20° to the east-northeast. Zircons separated from the ignimbrite yielded 17 acceptable ages in the range 23–24 Ma, with an inherited crystal of ca. 57 Ma. The $^{206}Pb/^{238}U$ weighted mean yields an age of 23.6 ± 0.2 Ma (MSWD = 1.5, n = 15) (Fig. 3). We have also dated zircons from a porphyritic intrusion crosscut by north-northwest faults 30 km south of Acaponeta, in the coastal plain (sample MicBarr 01; Table 1). The rock is silicic, with quartz, feldspar, and biotite in a glassy matrix, which locally shows flow banding and probably represents the inner part of a dome; 27 zircons yielded ages in the range of 20–22.5 Ma, with a $^{206}Pb/^{238}U$ weighted mean of 20.8 ± 0.2 Ma (MSWD = 1.9, n = 25). Other shallow intrusive bodies exposed by the Pochotitán and San Pedro–Acaponeta fault systems yielded ages between ca. 20 and 17 Ma (Ferrari et al., 2002; Duque-Trujillo et al., 2013). The described relations indicate that approximately east-northeast extension associated with the Pochotitán and San Pedro–Acaponeta fault systems began after ca. 21 Ma and that the faults served as an ascent path for discrete batches of silicic magmas between 20 and 17 Ma that either reached the surface as domes or crystallized at shallow depth. The upper limit of this extensional episode is constrained by undeformed basaltic lavas emplaced along the coast. A 28-km-wide and 35-km-long basaltic plateau is exposed northwest of Tepic and west of the Pochotitán fault system (Ferrari et al., 2000a, 2000b; Figs. 6 and 7A). The plateau consists of a succession of basaltic lavas as much as 300 m thick with an almost constant dip of 4°–5° toward the northwest, in striking contrast to the 20°–35° dipping ignimbrites exposed to the north and to the east. The uppermost lavas were dated as between 8.9 and 9.9 Ma (Gastil et al., 1979; Righter et al., 1995), and paleomagnetic studies indicate that they were not affected by significant tectonic deformation after their emplacement (Goguitchaichvili et al., 2002). An even clearer angular unconformity can be observed at Cerro Peñitas, 5 km west of Estación Ruiz (Figs. 6 and 7B), where flat-lying basaltic andesite lavas emplaced in the coastal plain surround a block of ignimbrites tilted 25° to the west-southwest (Fig. 7B). Laser step-heating experiments on a whole-rock sample from this basaltic andesite (sample HUA 6) yielded a plateau age of 10.45 ± 0.15 Ma (Table 1; Fig. 5). In addition, many ca. 11–10 Ma and north-northwest–striking mafic dikes are emplaced along and parallel to the Pochotitán and San Pedro–Acaponeta extensional fault systems (Ferrari et al., 2002; Frey et al., 2007). Most of the dikes are vertical, and although some of them dip as much as 70°, they are not sheared, indicating that their inclination is due to the intrusion into preexisting normal fault planes that were already inactive. We thus conclude that extension associated with the north-northwest–striking Pochotitán and San Pedro–Acaponeta fault systems must have ended before ca. 10.5 Ma.

EXTENSIONAL FAULTING AND SYNEXTENSIONAL MAGMATISM IN THE SOUTHERN SINALOA DOMAIN

Geologic and Tectonic Setting

North of the Río Mezquital lineament the general architecture of the rift is dominated by west-southwest–tilted ignimbrites and north-northwest–striking normal faults (Figs. 8, 11A, and 11B), which define a hanging-wall segment in the Axen (1995) terminology. This style of faulting continues to the north up to the Piaxtla River valley, where ignimbrites are tilted to the east-northeast (Figs. 2 and 8).

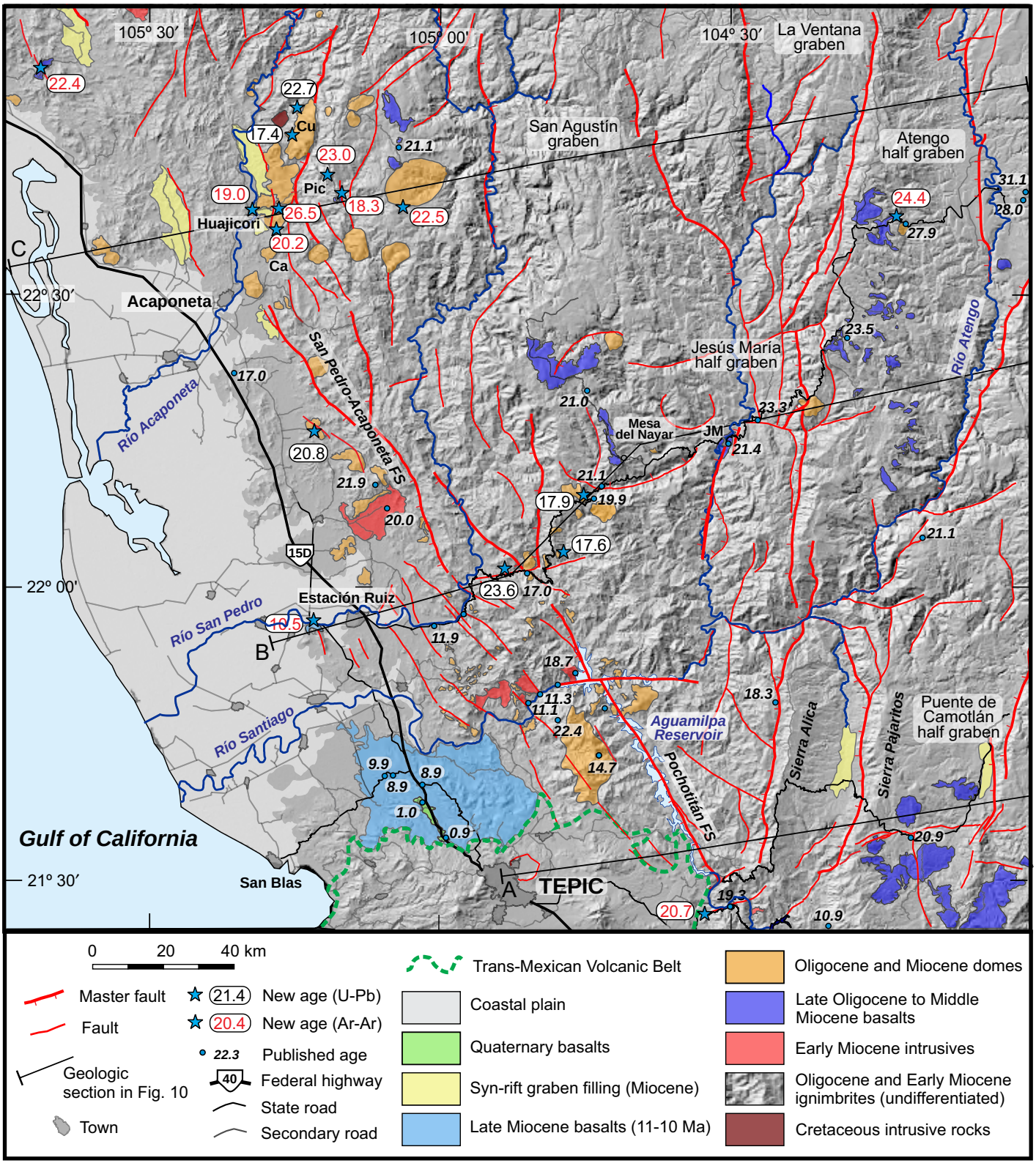

Figure 6. Regional geologic map of northern Nayarit showing the main extensional structures and new and published ages (rounded at the closest decimal). JM—Jesús María, Pic—Picachos, Ca—Caramota dome, Cu—Cuchara dome.

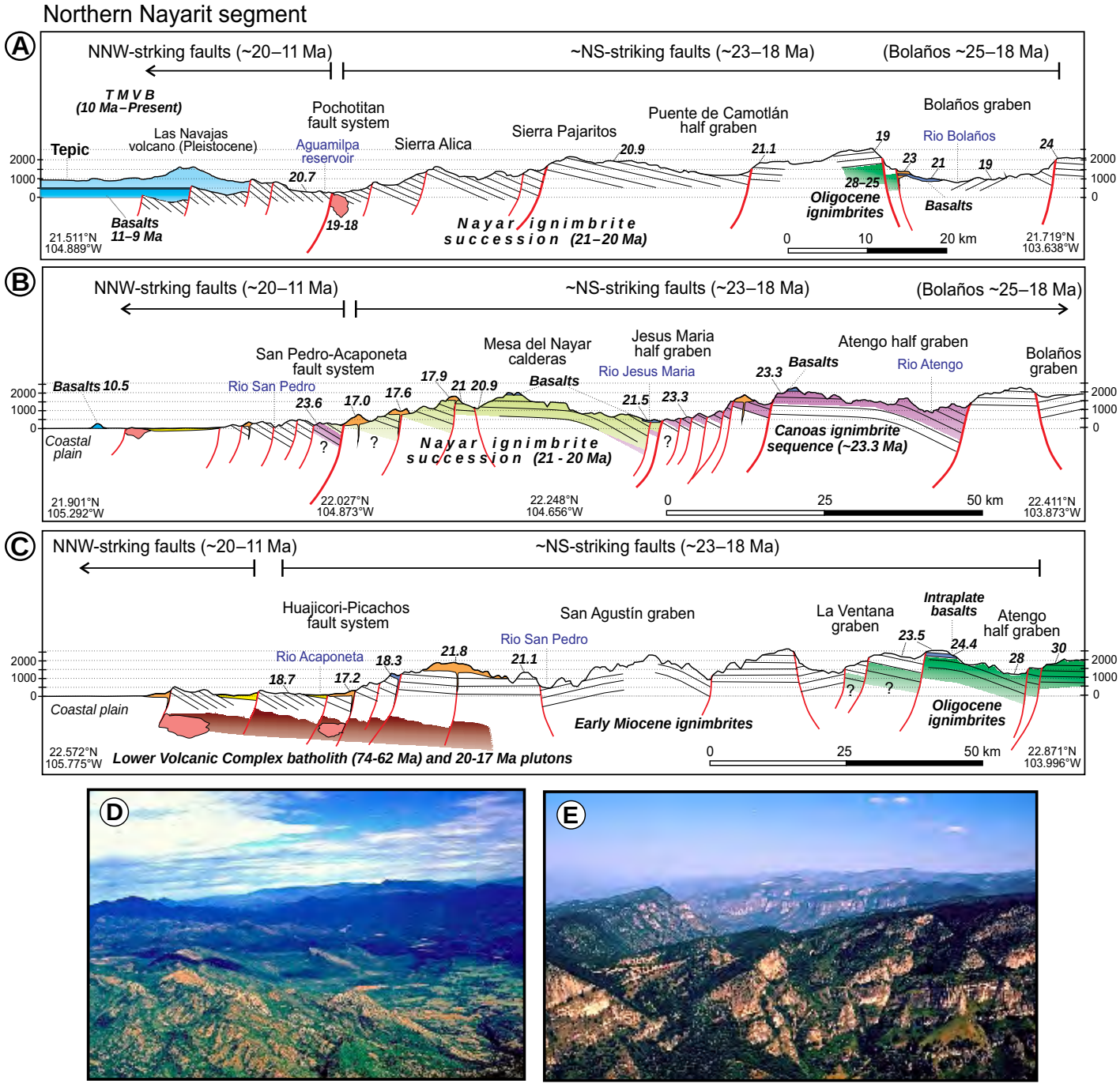

Figure 7. (A, B, and C) Gulf-orthogonal geologic sections showing rifting style, tilting of strata, and synextensional volcanism for northern Nayarit (locations in Fig. 6). Note variable vertical exaggeration. Color of geologic units same as geologic maps except for ignimbrites. (D) Aerial picture of the Pochotitán fault system (geologic section A). Picture taken at ~20°31′00″N, 104°35′00″W looking north before the construction of the Aguamilpa reservoir. Note 21–20 Ma ignimbrites tilted as much as 35° to the east-northeast. (E) Aerial picture of the western side of the north-south–trending San Agustín graben (geologic section C). Picture taken at ~22°35′40″N, 104°46′00″W looking N35°W.

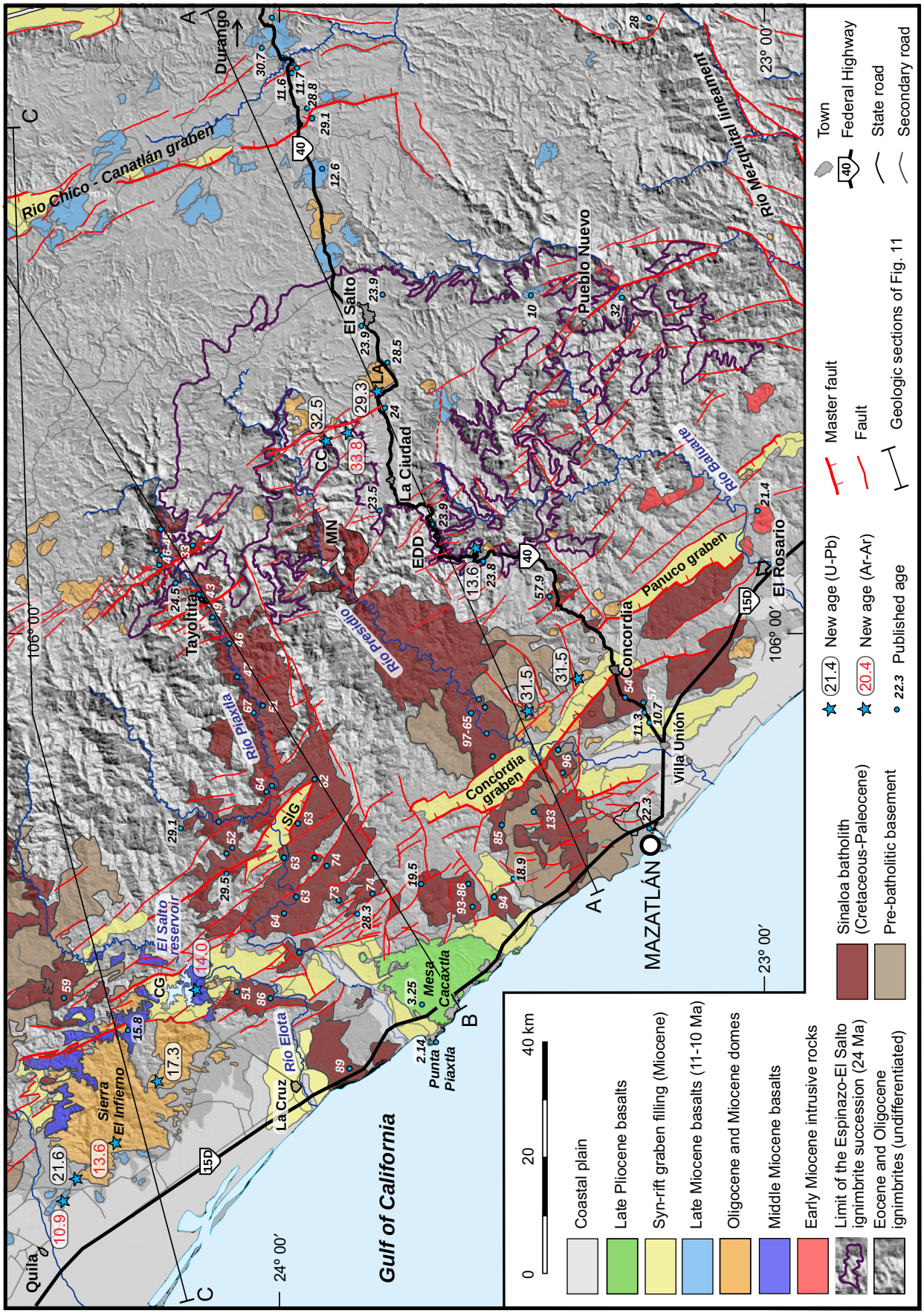

Figure 8. Regional geologic map of southern and central Sinaloa showing the main extensional structures and new and published ages. SIG—San Ignacio graben; CG—Conitaca graben; EDD—Espinazo del Diablo; LA—Las Adjuntas dome; MN—Mala Noche; CC—Cerro Cuadrado.

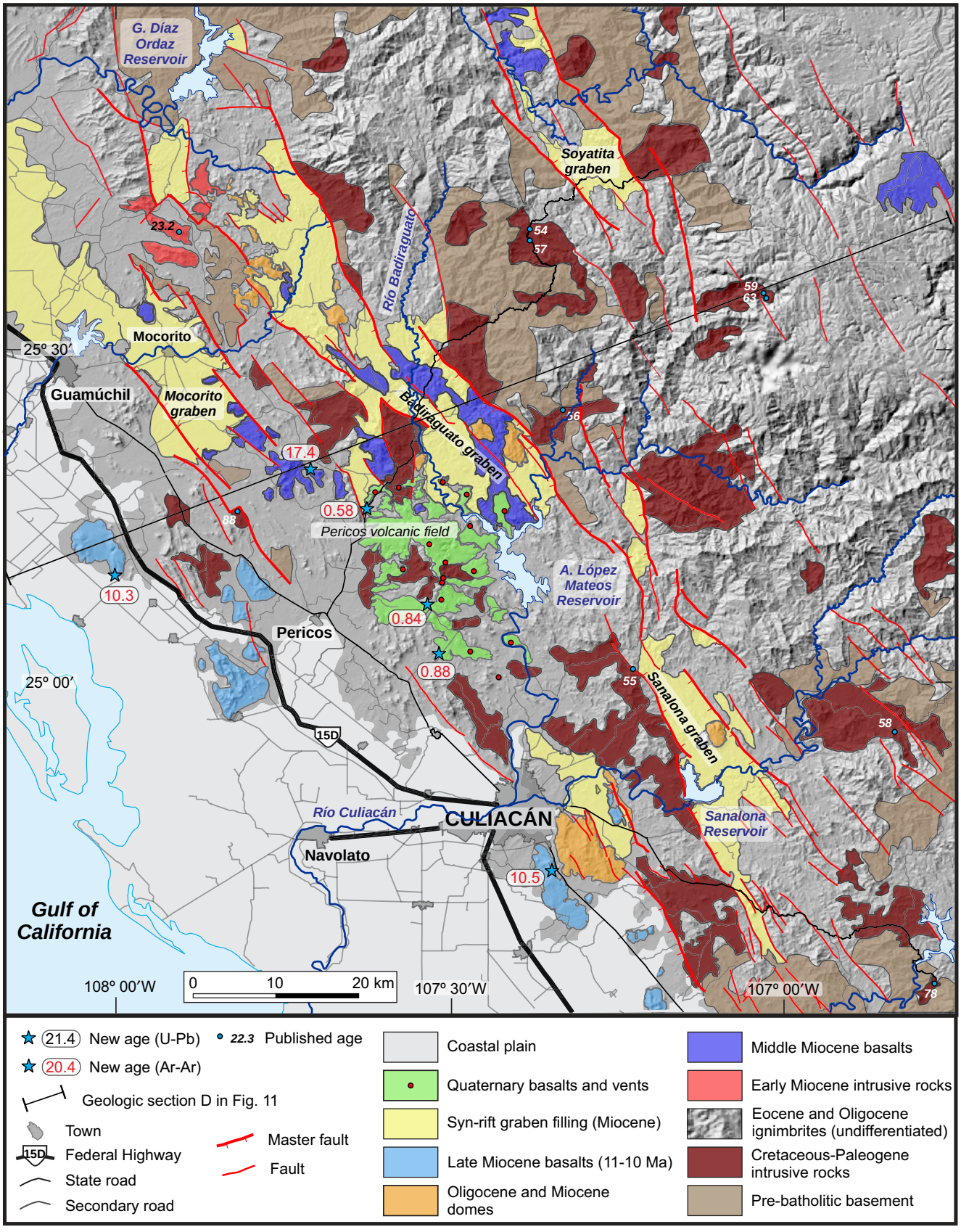

Figure 9. Regional geologic map of Culiacán and Pericos areas (northern Sinaloa) showing selected geologic units, the main extensional structures, and new and published ages.

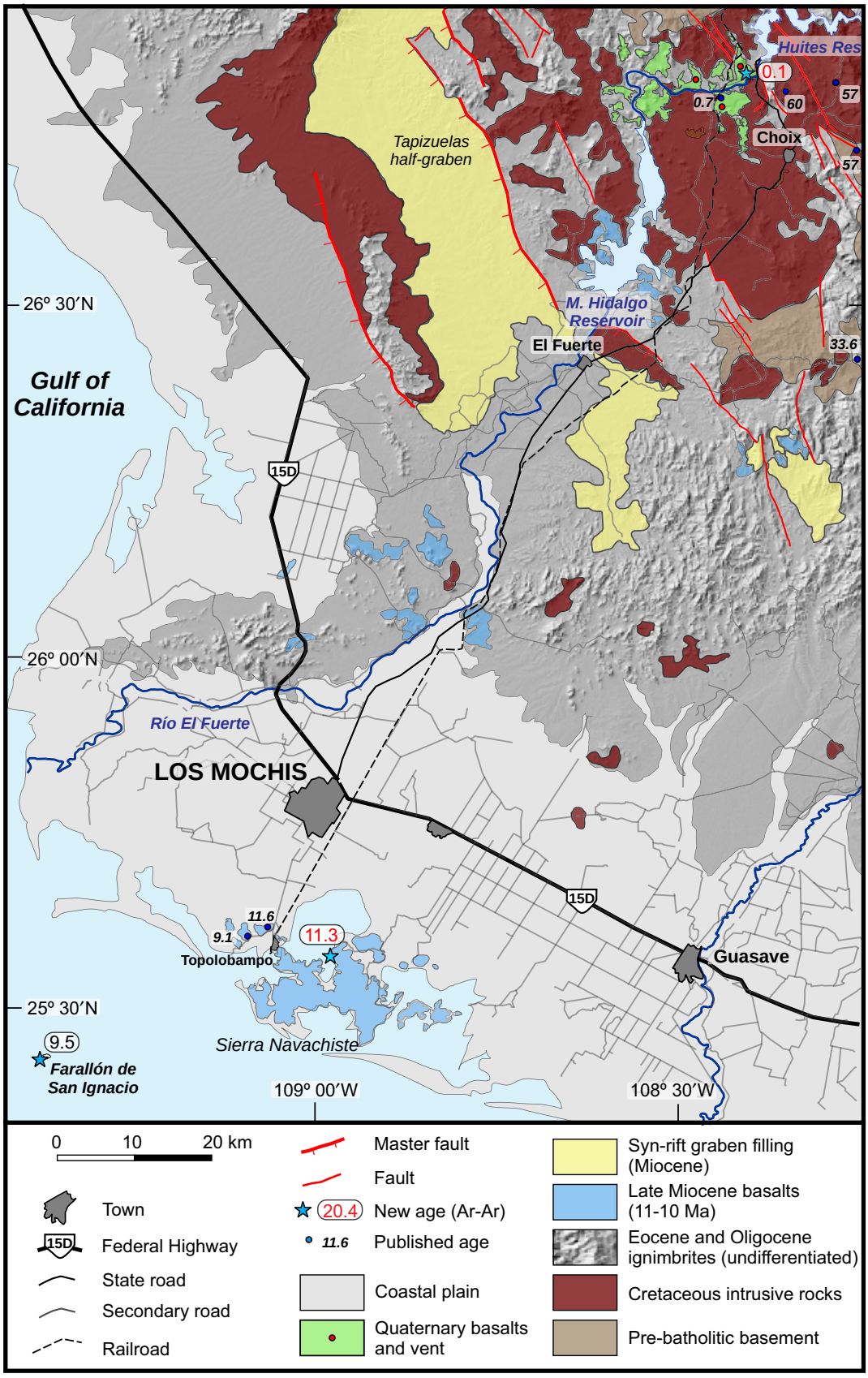

Figure 10. Regional geologic map of Los Mochis–El Fuerte areas (northern Sinaloa) showing selected geologic units, the main extensional structures, and new and published ages.

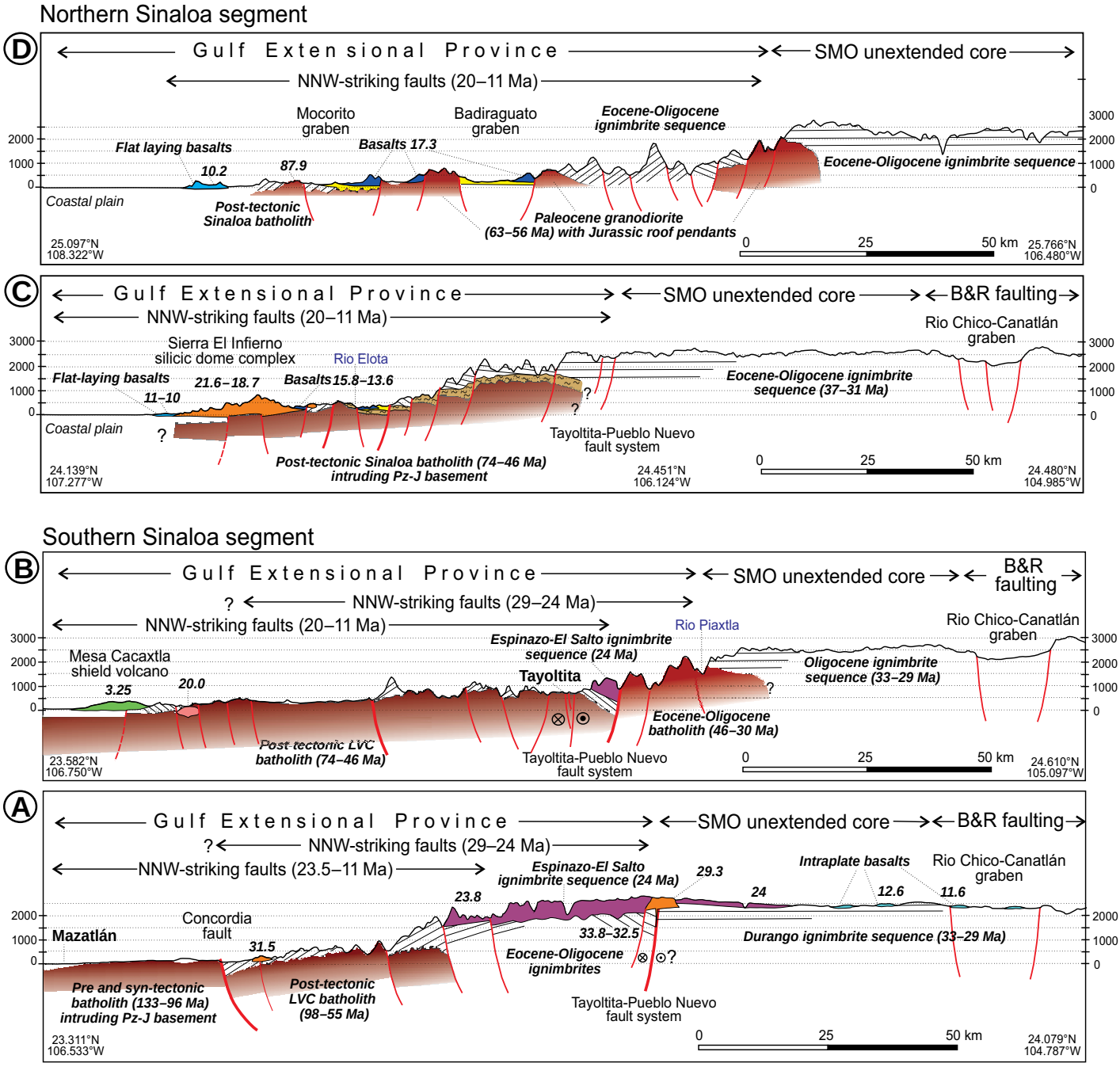

Figure 11. Gulf-orthogonal geologic sections showing rifting style, tilting of strata, and synextensional volcanism for Sinaloa (locations shown in Figs. 8 and 9). Note variable vertical exaggeration. Color of geologic units same as geologic maps except for ignimbrites. SMO—Sierra Madre Occidental; B&R—Basin and Range.

A smaller domain of east-northeast–tilted ignimbrites is observed farther inland in the Tayoltita and Mala Noche mining areas (Enríquez and Rivera, 2001; Aranda-Gómez et al., 2003; this work). The Mezquital lineament also marks the southern limit of a basement high, because to the north, the lower volcanic complex and its host rocks are well exposed or at shallower depths than in the northern Nayarit segment (Fig. 8). In Sinaloa, Cretaceous to Paleogene intrusive rocks likely constitute a large composite batholith, the oldest parts of which were deformed during the Laramide orogeny. Henry et al. (2003) dated a syntectonic intrusion as ca. 105 Ma (TIMS U-Pb on zircon). A more recent study using both U-Pb dating of zircons and ^{40}Ar-^{39}Ar dating of muscovite constrains the deformation in the Mazatlán area between ca. 98 and 93 Ma (Cuéllar Cardenas et al., 2012). Post-tectonic intrusions consist of granodiorite to dioritic bodies that thickened the batholith toward the east in Campanian to Eocene time (Figs. 8 and 11). These are covered by ignimbrites and domes of the Oligocene pulse dated west of Durango between 31.7 and 28.5 Ma and by the 24–23.9 Ma Espinazo–El Salto volcanic sequence (Fig. 8) (McDowell and Keizer, 1977;

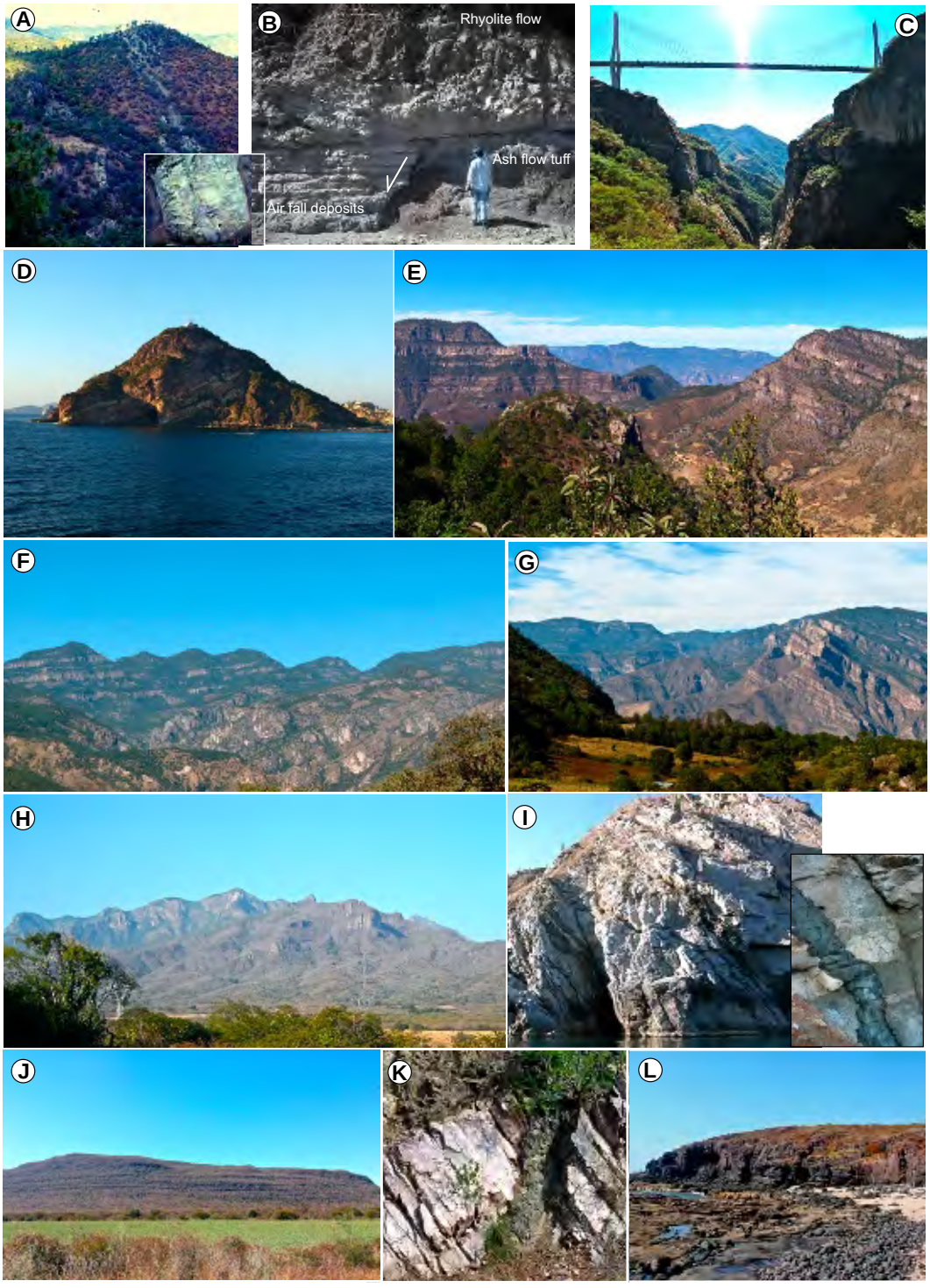

Figure 12. Geologic and tectonic relations described in the text. (A) Rhyolitic dike feeding a large dome dated as 27.9 Ma (Ar-Ar; Ferrari et al., 2002) in the western part of the Atengo half-graben. Dikes are 10–15 m thick (person in inset for scale). Picture taken at 22°37′51″N, 104°13′29″W, looking north. (B) North-south–striking normal fault covered by a rhyolitic dome dated as 17.6 Ma (sample RUIZ 34b; see Table 1 for coordinates). (C) View of the Baluarte bridge (world's second-highest bridge). Note the 400-m-deep canyon cut into the massive, flat-lying, basal unit of the Espinazo–El Salto ignimbrite sequence. Picture taken at 23°32′39″N, 105°46′13″W, looking south-southeast. (D) View looking north of west-dipping Oligocene ignimbrites at Mazatlán lighthouse (Cerro El Crestón). Picture taken at 23°10′25″N, 106°25′33″W, looking N15W. (E) View to the north-northwest of an angular unconformity between flat-lying Espinazo–El Salto ignimbrite sequence (Cerro Cuadrado to left) and Early Oligocene ignimbrites (32.5 Ma, sample ES 11, to right) in the Presidio River canyon. Picture taken at 23°51′00″N, 105°35′30″W. (F) Angular unconformity between slightly tilted El Salto–Espinazo ignimbrite sequence and strongly tilted pre-Miocene ignimbrites in foreground. Picture taken at 23°32′28″N, 105°45′22″W, looking north-northwest from the eastern side of Baluarte River canyon. (G) Angular unconformity (as in E), but north of the Presidio River canyon looking north-northwest from Ejido San Pablo (23°53′32″N, 105°37′22″W). (H) View of the southeastern dome complex of Sierra El Infierno. The base of the Sierra is at 50 m and the highest peak reaches 1400 m above sea level. Picture taken at 24°04′02″N, 106°48′21″W, looking north. (I) North-northwest–striking mafic dikes crosscutting Late Cretaceous granites and aplite dikes at Santa Catalina Island, Baja California Sur. The dike is dated as 10.9 Ma (sample SC 3; see Table 1 for coordinates). (J) Flat-lying mafic lavas along the Sinaloa coast south of Guamuchil dated as 10.3 Ma (sample PER 14; Table 1). Picture taken at 25°12′31″N, 107°59′26″W, looking west. Height of lava pile is 290 m. (K) Subvertical, north-northwest–striking mafic dike cutting a tilted ignimbrite succession near Pericos (Fig. 9). Dike likely fed flat-lying basaltic lavas like those dated as 10.3 Ma nearby (Fig. 12J). (L) Late Pliocene hawaiite sill at Punta Piaxtla. The sill contains xenoliths of spinel lherzolite, granulites, pyroxenites, and megacrysts. Picture taken at 23°38′54″N, 106°48′15″W, looking north-northwest.

McDowell and McIntosh, 2012). Late Miocene mafic dikes and late Pliocene lavas are observed along the coast. Scattered Late Miocene intraplate basalts are also exposed in the eastern part of the SMO in the Río Chico–Canatlán graben (Fig. 8) (Henry and Aranda-Gómez, 2000).

Extensional structures affect the western half of the SMO, in Sinaloa state, as well as a narrow belt on its eastern side, just west of Durango. As in the northern Nayarit segment, two episodes of extension can be recognized: (1) approximately east-west to west-southwest extension responsible for north-northwest–striking faults observed in the Piaxtla, Presidio, and Baluarte river valleys and, possibly, the coastal area; and (2) subsequent west-southwest extension restricted to the coastal area (Pánuco, Concordia, and Villa Unión half-grabens) and a belt east of the SMO (Río Chico–Canatlán graben) (Fig. 7). Timing of faulting can be inferred from geologic relations in a number of areas described in the following.

Early Extension-Transtension in Westernmost Durango: Tayoltita–Pueblo Nuevo Fault System

To the northwest of Mazatlán, the Piaxtla and Presidio Rivers cut ~2-km-deep incisions orthogonal to the Gulf of California coast into the SMO igneous succession. The top of the succession is made by the Espinazo–El Salto volcanic sequence, making a plateau at an average 2700 m of elevation. Originally recognized and dated as ca. 23.5 Ma by McDowell and Keizer (1977), the sequence has been recently redated as 23.8–24 Ma (by ^{40}Ar-^{39}Ar; McDowell and McIntosh, 2012). It consists of a thick package of ignimbrites and tuffs (unit A), covered by massive rhyolites (unit B), basaltic lavas (unit C), and three ignimbrite packages (unit D, E, and F, or plateau series), briefly described in Aranda-Gómez et al. (2003). The sequence can reach 1000 m in thickness in the La Ciudad area (Figs. 8 and 11A) and along the Baluarte River (Fig. 12C), but toward the east, in the El Salto area, only the uppermost three units can be recognized, with an approximate thickness of 350 m. East of La Ciudad, the Espinazo–El Salto sequence is essentially flat lying and only affected by minor faulting. However, our reconnaissance field work shows that it clearly filled a topographic trough that resulted from a previous episode of normal faulting. Along the Presidio River valley, between Mala Noche and Cerro Cuadrado (MN and CC in Fig. 8), a thick succession of ignimbrites and andesites is tilted as much as 35° to the east-northeast, making a spectacular angular unconformity with the ca. 24 Ma Espinazo–El Salto succession, which is almost horizontal (Figs. 12E–12G). We dated a sample of an ignimbrite at ~350 m below the top of the tilted sequence near Ejido San Pablo (sample ES 11; Table 1). The 22 dated zircons range between 31.4 and 33.4 Ma. The ^{206}Pb/^{238}U weighted mean yields an age of 32.5 ± 0.2 Ma (MSWD = 0.89, n = 21) (Fig. 5). This ignimbrite could be correlative with the Registro tuff and other ignimbrites dated by McDowell and Keizer (1977) and McDowell and McIntosh (2012) west of Durango City that underlie the El Salto sequence. Andesitic lavas underlying the ignimbrites were also dated (sample ES 10; Table 1). A plagioclase concentrate from these lavas yielded an isochron of 33.82 ± 0.28 Ma, confirming the Early Oligocene age of this succession.

Tilting of this Oligocene ignimbrite and andesite succession occurs to the west of a north-northwest–striking and west-dipping breakaway fault zone northwest of El Salto that is part of a regional structure, here named the Tayoltita–Pueblo Nuevo fault system (see following). A prominent north-northwest alignment of rhyolitic domes occurs along this fault zone (Fig. 8). Among them is the massive Las Adjuntas dome (LA in Fig. 8), intersected by highway 40 west of El Salto (Figs. 8 and 11A), previously dated as 28.5 Ma by K-Ar (McDowell and Keizer, 1977; age corrected for modern decay constants); 15 zircons separated from this dome yielded a ^{206}Pb/^{238}U weighted mean age of 29.5 ± 0.3 Ma (MSWD = 1.3, n = 15) (sample SIN 18; Table 1) with single ages between 30.5 and 28 Ma; in comparison to the K/Ar age, this may indicate the occurrence of antecrysts. The emplacement of large-volume, viscous rhyolitic domes coupled with the occurrence of inherited zircons is consistent with stratigraphic, structural, and zircon age relationships observed elsewhere in the SMO (e.g., Bryan et al., 2008; Ramos-Rosique, 2013; Murray et al., 2013), and is indicative of an extensional regime allowing the remelting of upper crustal, potentially still partially molten, plutons as well as an easy ascent of these viscous rhyolitic magmas. On this basis, we consider the Las Adjuntas dome to mark the initial extensional activity along the Tayoltita–Pueblo Nuevo fault system.

Toward the north, this pre-Miocene faulting episode is also reported in the Piaxtla River valley, the next valley to the north (Fig. 8). Here, in the Tayoltita mining district, Eocene to Middle Oligocene rocks are tilted as much as 70° to the east-northeast, whereas Early Miocene ignimbrite tilts do not exceed 30° (Enríquez and Rivera, 2001). Microstructural studies established that the first episode formed a negative flower structure defined by north-south– to north-northwest–striking faults with right-lateral extensional kinematics, distributed in a 4-km-wide belt east of Tayoltita (Horner and Enríquez, 1999). This right-lateral transtensional corridor is the northern prolongation of the breakaway fault zone observed in the Presidio River valley (Tayoltita–Pueblo Nuevo fault system). At Tayoltita, transtensional faults displace the mineralized veins dated as between ca. 38 and ca. 32 Ma (Horner and Enríquez, 1999). This constrains this first extensional episode as Late Oligocene, as inferred in the Presidio valley. The second episode of extension must have occurred after the emplacement of the capping ignimbrite sequence, dated as between ca. 24.5 and 20.3 Ma (Enríquez and Rivera, 2001).

Coastal Belt of Extensional Faults

Between Espinazo del Diablo (EDD in Fig. 8) and the coast, the ca. 24 Ma volcanic sequence is also faulted and tilted due to a subsequent extensional episode. In a 60-km-wide belt parallel to the coast, volcanic successions are tilted to the west-southwest by northwest-striking and northeast-dipping normal faults. Pre–ca. 24 Ma rocks are tilted as much as 40° whereas the Espinazo–El Salto ignimbrites dip more gently, not exceeding 20° (Fig. 12F). Approximately 12 km southwest of Espinazo del Diablo, two rhyolite domes aligned along strike of a northwest-striking fault are crossed by highway 40 (Fig. 8). The northernmost dome covers part of the Early Miocene succession and has a subhorizontal base. The lava is a coherent porphyritic rhyolite with plagioclase, lesser alkali feldspar, and hornblende that was considered part of the Espinazo–El Salto succession by McDowell and Keizer (1977; their unit B, undated). However, zircons separated from the rhyolites gave 16 acceptable ages in the range 12.7–14.7 Ma. The ^{206}Pb/^{238}U weighted mean yields an age of 13.7 ± 0.3 Ma (sample SIN 21, MSWD = 1.4, n = 16; Table 1). Because the dome does not appear to be faulted, this age can be taken as a minimum age for the activity of the northwest-striking faults in this area.

Near the coast, northwest-striking faults form several asymmetric grabens. The largest of these extensional basins are the Villa Unión and the Concordia half-grabens (Fig. 8). In the eastern part of the Villa Unión half-graben, gravel fills are tilted as much as 24° and unconformably overlie a 22.6 Ma dacitic lava that is titled as much as 40° (Henry and Fredikson, 1987; Aranda-Gómez et al., 2003). The graben fill is intruded by ca. 11 Ma, north-south– to north-northwest–trending mafic dikes dipping 65° to the east, suggesting that extension began sometime in the Middle Miocene and continued for a short time after 11 Ma (Aranda-Gómez et al., 2003). We tried to constrain the age of the Concordia half-graben by dating two rhyolitic domes

in the eastern part of this structure (Fig. 8). Sample SIN 05 (Table 1) comes from a block and ash flow deposit associated with a dome that appears to be cut in half by a normal fault parallel to, and antithetic with, the Concordia fault. Zircons separated from glassy rhyolite lava blocks from this deposit yielded 34 acceptable ages in the range 35–30 Ma. The large age range is indicative of antecrystic inheritance, so we consider the $^{206}Pb/^{238}U$ weighted mean age of 31.5 ± 0.4 Ma as the maximum age for the emplacement of this dome. Sample SIN 07 (Table 1) was collected from a rhyolite dome apparently vented along a northeast-striking and southeast-dipping normal fault that put metamorphic basement in contact with ignimbrites tilted to the southwest, and is in turn cut by a fault parallel to the Concordia fault. This dome yielded an age identical to SIN 05, with a $^{206}Pb/^{238}U$ weighted mean age of 31.5 ± 0.4 Ma (MSWD = 1.5, n = 20). Although these ages do not help to narrow the age range of the Concordia half-graben, they nevertheless indicate the presence of Oligocene magmatism in this area, which would thus extend along an ~150-km-wide belt from Durango to coastal Sinaloa. However, the alignment of these rhyolitic domes in proximity to the Concordia fault suggests early activity of this structure, which can be thus contemporaneous with the Tayoltita–Pueblo Nuevo fault zone. In this case, the two fault zones would define a 75-km-wide graben, a hypothesis supported by the occurrence of polymictic conglomerates with reworked tuffs at the base of the Espinazo–El Salto sequence at several places within this inferred tectonic depression.

EXTENSIONAL FAULTING AND SYNEXTENSIONAL MAGMATISM IN THE NORTHERN SINALOA DOMAIN

Geologic and Tectonic Setting

The Piaxtla and Elota Rivers mark a tectonic boundary that apparently displaces the prevolcanic basement and the lower volcanic complex batholith in a more inland position (Fig. 8). Whereas in southern Sinaloa these rocks crop out along the coast, to the north of these rivers they are separated from the Gulf of California by a 35–60-km-wide coastal plain. In this region, extensional structures form a 65–85-km-wide belt of northwest-striking normal faults with block tilting both to the southwest and the northeast. They bound a series of grabens and half-grabens cut into the Late Eocene and Oligocene silicic volcanic succession of the upper volcanic supergroup, batholiths of the lower volcanic complex and their roof pendants, as well as the prevolcanic basement (Figs. 8, 9, 10, 11C, and 11D). These tectonic basins are filled by continental sediments and by concurrent bimodal volcanism, a geologic setting similar to that of Sonora to the north, where intracontinental extensional basins were developed since the Early Miocene (Gans, 1997; McDowell et al., 1997). The timing of extension in northern Sinaloa, however, has remained unknown. Our reconnaissance study allows documenting the age of extension in two areas.

Conitaca Graben and Sierra El Infierno Dome Complex

Sierra El Infierno is a huge silicic complex made of domes, lavas, ignimbrites, and shallow subvolcanic intrusions that rises from low-lying alluvial deposits of the coastal plain. There have been no previous studies of this silicic complex; it covers an ~600 km^2 area and some peaks reach 1400 m above sea level (Figs. 8 and 12H). This voluminous amount of silicic magma was fed, at least in part, by large north-south–trending silicic dikes, which are clearly seen in aerial imagery and were observed in the field. Lavas are glassy and flow-banded rhyolites have variable crystal content (commonly K-feldspar, quartz, and plagioclase, sometimes biotite and hornblende) and occasional fragments of preexisting intermediate lavas. The Sierra El Infierno is emplaced in the northwestern part of the Conitaca graben, a tectonic depression bounded toward the east by a series of north-northwest–striking and west-dipping normal faults (CG in Fig. 8). The graben is filled by indurated sandstone and polymictic conglomerate interleaved with and capped by basaltic lavas that abut the silicic rocks of the Sierra El Infierno. Sandstone and conglomerate are crudely stratified and dip 10°–25°, whereas capping basalts are only gently tilted. The time of faulting is clearly established by the ages of the Sierra El Infierno silicic complex and the basaltic lavas intercalated and capping the continental sedimentary succession.

We dated two domes in the southern and western parts of Sierra El Infierno. Sample SIN 39 is a porphyritic to glomeroporphyritic coherent rhyolite with plagioclase, biotite, and alkali feldspar exposed at the northwestern tip of the Sierra. Dated zircons (n = 25) range between 24 and 21 Ma with a $^{206}Pb/^{238}U$ weighted mean age of 21.6 ± 0.1 Ma (MSWD = 1.17, n = 22) (Table 1; Fig. 3). Sample SIN 09 comes from a crystal-rich rhyolite with plagioclase and biotite, from which we dated 26 zircons in the range 21–16 Ma with a dominant population yielding a $^{206}Pb/^{238}U$ weighted mean age of 18.6 ± 0.3 Ma (MSWD = 1.00, n = 25) Ma. If these ages are representative of the entire Sierra El Infierno, the silicic volcanism in this area would overlap with that of northern Nayarit, although with a much larger volume.

A previous age of 15.8 Ma was reported in Iriondo et al. (2004) for a basaltic lava in the Conitaca graben, although the geologic context of this sample was not provided. We dated a sample located at 17 km to the southeast near the dam of the El Salto reservoir (Fig. 8) that belongs to the upper part of the basaltic lavas inside the graben. The lava is a fine-grained microporphyritic basalt with plagioclase, clinopyroxene, and olivine (sample SIN 25; Table 1; Fig. 4). The laser step-heating experiment performed on whole rock yielded an isochron age of 14.01 ± 0.23 Ma, which we consider the best estimation for this rock. Sample SIN 15 is also a plagioclase, clinopyroxene, and olivine-phyric basaltic lava that covers rhyolitic lavas in the western part of Sierra El Infierno. Laser step-heating experiments of the groundmass gave an isochron age of 13.62 ± 0.17 Ma for this sample, which within error almost overlaps the age of SIN 25 (Table 1; Fig. 4).

Basaltic lavas also crop out along the coast just southwest of Sierra el Infierno. These lavas are petrographically similar to those exposed farther inland in the Conitaca graben fill but are generally flat lying. We dated a groundmass concentrate of a basaltic andesite lava from a quarry near the western tip of Sierra el Infierno (sample PER 8; Table 1; Fig. 5). One laser step-heating experiment was performed on a groundmass concentrate from the sample and our preferred age of 10.94 ± 0.23 Ma is taken from the weighted mean of three consecutive fractions with 84.57% of the ^{39}Ar released (see the Supplemental File [see footnote 1] for details). The geologic relations coupled with our new ages constrain extension in the Conitaca–Sierra El Infierno area to the Early to Middle Miocene.

Several other remnants of flat-lying, fissure-fed basaltic lavas are distributed along the coast between Sierra El Infierno and Culiacán (Figs. 8 and 9). The similarity in the mineralogy and composition of the lavas suggests that these outcrops could have been part of a single 60-km-long belt of mafic lavas. We dated a sample from the lower part of a 380-m-thick succession south of Culiacán (Fig. 8; La Pedrera microwave peak). A groundmass concentrate from a basaltic andesite lava (sample PER 7; Table 1; Fig. 5) was laser step-heated and the two experiments yielded reproducible results with a plateau age of 10.54 ± 0.20 Ma.

Badiraguato Graben

This is a composite tectonic trough bounded by northwest-striking normal faults cut into Late Cretaceous to Paleocene intrusions of the

lower volcanic complex and their roof pendants (Fig. 9). To the south, the graben is covered by middle Pleistocene basaltic lavas of the Pericos volcanic field (see following). The Badiraguato graben is filled by sandstone and polymictic conglomerate with intercalations of basaltic lavas and some rhyolitic domes and lavas. The conglomerate is tilted 15°–38° both to the southwest and the northeast (Figs. 9 and 11D). We dated a basaltic andesite lava collected from an eroded succession of lavas between the Badiraguato and Mocorito grabens (sample PER 12; Table 1; Fig. 4). Although the lava is not in direct contact with the conglomerate it is considered equivalent to the basaltic lavas within the graben on a petrographic basis. A groundmass concentrate was step-heated with the temperature-controlled Ta furnace and we take the isochron age of 17.42 ± 0.77 Ma as the best estimate for this sample. Other basaltic lavas are exposed along the coast, ~30 km to the southwest. Similar to those more to the south, these coastal lavas are flat lying. We dated a basaltic andesite (sample PER 14; Table 1; Figs. 4 and 12J) by step-heating using the temperature-controlled Ta furnace. The age spectrum is somewhat perturbed, but an isochron age of 10.33 ± 0.88 Ma can be confidently calculated. In summary, the ages of the graben fill and the postextension lavas indicate that extension in this part of Sinaloa is Early to Middle Miocene in age.

LATE MIOCENE VOLCANISM OF NORTHERN SINALOA AND OFFSHORE AREAS

Our new age data define a regional pulse of mafic magmatism just after the end of subduction across the entire Gulf of California region. Previously, mafic lavas in the range ca. 11–9 Ma were reported from western Sonora (Mora-Klepeis and McDowell, 2004) and in the Bahía de Los Angeles, Jaraguay, and Santa Rosalía areas in Baja California (Benoit et al., 2002; Calmus et al., 2003; Conly et al., 2005; Pallares et al., 2007). In addition to those described in the previous section, we have recognized additional Late Miocene (ca. 12–10.5 Ma) mafic lavas and dikes in the northernmost part of Sinaloa at Sierra de Navachiste, at the small Farallón de San Ignacio Island southwest of Los Mochis (Fig. 10), within the Gulf of California at Santa Catalina Island and in submerged rifted blocks (Fig. 2).

Sierra de Navachiste is an erosional remnant of a volcanic field made of basaltic, andesitic, and dacitic lavas and some intermediate domes that currently cover an area of 170 km^2 along the coast. Epiclastic deposits produced by the erosion of the lavas are also widespread. The lavas are essentially flat lying and their base is at sea level. We dated a groundmass concentrate from a dacitic lava interbedded with more mafic lavas (sample LM 2; Table 1; Fig. 4). The preferred age is taken from the isochron age of 11.34 ± 0.79 Ma calculated excluding the fractions of suspected excess Ar (see the Supplemental File [see footnote 1]). Similar ages were obtained by the K-Ar method by Pallares et al. (2007) and Gastil et al. (1979) for andesitic lavas in the northwestern part of the field near Topolobampo (Fig. 10).

Farallón de San Ignacio is a 0.3 km^2 island 25 km offshore Sierra de Navachiste and just north of the northwest fault scarp bounding the Farallon Basin (Figs. 2 and 10). On the island, a massive rhyolitic lava is covered by 2 basaltic lavas 5–8 m in thickness. The tops of the basaltic lavas are horizontal, and they cover the original irregular morphology of the rhyolite without any visible paleosol. The rocks are too altered to be dated by ^{40}Ar-^{39}Ar, but we separated 11 zircons from the underlying rhyolitic lava. Single zircon ages of sample ROCA F6 range from 9 to 10 Ma with a ^{206}Pb/^{238}U weighted mean age of 9.5 ± 0.3 Ma (MSWD = 1.9, n = 9) . Despite this age not being very precise, it nevertheless suggests that the overlying flat-lying basalts may be correlative with those of coastal Sinaloa. In the seismic images provided by Miller and Lizarralde (2013) in the nearby Guaymas Basin, a 2-km-thick evaporite deposit overlies seaward-dipping reflectors. We interpret the seaward-dipping reflectors to correlate with the ca. 12–10 Ma basaltic lavas at Farallón de San Ignacio and along the coast of Sinaloa. Similar basalts, dated as ca. 11–9.1 Ma (Conly et al., 2005), were also found in the Santa Rosalia area (Fig. 2) below the Boleo evaporites that Miller and Lizarralde (2013) correlated with those seen on seismic sections.

Santa Catalina Island is part of a rifted continental block at the latitude of Sierra de Navachiste in the western part of the Gulf of California (Fig. 2). The bulk of the island consists of Late Cretaceous granite of the Peninsular Ranges batholith heavily intruded by Miocene granitoids and aplitic dikes (Piñero-Lajas, 2009). Many northwest-striking, southwest-dipping mafic dikes exposed in the cliffs of the northwestern part of the island cut all other rocks (Fig. 12I). A plagioclase concentrate from one mafic dike was laser step-heated and analyzed in two experiments (sample SC 3; Table 1; Figs. 4 and 5); although the sample shows evidence of excess argon, we obtained a plateau age of 10.89 ± 0.52 Ma consistent with the less-precise isochron age of 10.14 ± 2.59 Ma (see the Supplemental File [see footnote 1] for details) that we consider representative of the mafic dike swarm at Santa Catalina Island.

Mafic dikes and silicic rocks of similar ages were also found in the rifted blocks submerged in the Gulf of California. Sample ROCA 3J 5 (Table 1; Figs. 4 and 5) is a lithic tuff that was collected using the remotely operated vehicle (ROV) *Jason* at the top of the Tamayo dome (also called Tamayo Bank; Sutherland et al., 2012), a 30 × 40-km-wide, ~1000-m-high volcanic structure 80 km offshore Mazatlán (Fig. 2). Two laser step-heating experiments were performed on a feldspar concentrate defining a plateau age of 11.70 ± 0.07 Ma indistinguishable from the isochron age obtained by combining all the data points from the two experiments. Silicic volcanism of Late Miocene age is widespread in Sonora (Mora Alvarez and McDowell, 2000; Vidal-Solano et al., 2005, 2007), but has never been reported to the south. The sample from the Tamayo dome is the first evidence of Late Miocene silicic pyroclastic rocks in the southern part of the Gulf of California. Sample ROCA 24J-33 was also collected using the ROV on a rifted continental block cut by a transform fault bounding the Pescadero Basin to the south (Fig. 2). It is a porphyritic, fine-grained subvolcanic microdiorite with plagioclase and hornblende (0.25–3.5 mm), scarce biotite and opaque minerals, probably representing a shallow sill. A hornblende concentrate was laser step-heated and we consider the isochron age of 11.29 ± 0.37 Ma as the best estimation for this sample.

Sample DANA 46a was dredged from a prominent north-northeast–striking and 800-m-high fault scarp offshore northern Nayarit, ~90 km southeast of the Tamayo dome (Fig. 2). The sample is a mafic aphyric lava (either a flow or a dike) presumably associated with the fault scarp. Four experiments with different mass spectrometers and heating methods gave very consistent results, yielding a 11.96 ± 0.26 Ma isochron age (Table 1; Fig. 4; Supplemental File [see footnote 1]). This age overlaps with those obtained for northwest-striking mafic dikes in southern Sinaloa and northern Nayarit (Henry and Aranda-Gómez, 2000; Frey et al., 2007). In seismic profiles, Sutherland et al. (2012) recognized an irregular, ropey layer mantling the seismic basement offshore of northern Nayarit that they interpreted as a volcanic layer of the Comondú Group (24–12 Ma). Our dated samples ROCA 3J 5 and DANA 46a, collected close to the trace of the seismic profile, provide a direct constraint of the nature and age of the uppermost part of this volcanic layer.

LATE PLIOCENE AND PLEISTOCENE INTRAPLATE VOLCANISM

Onshore post–Late Miocene volcanism is rare in the southeastern Gulf of California. The only previously known occurrences were the 3.4 Ma Mesa Cacaxtla shield volcano and

the 2.1 Ma mafic lavas at Punta Piaxtla (Aranda-Gómez et al., 2003), both located along the coast ~60 km northwest of Mazatlán (Fig. 8). The geologic maps of the SGM also report two other mafic volcanic fields with young morphologic appearance, Pericos and Choix. The only previous age available was a K-Ar age of 0.7 Ma (Clark, 1976) for a lava in the Choix volcanic field, but no geochronologic information was available for the Pericos volcanic field and there was no geochemical study for either field.

The Pericos volcanic field covers an area of ~20 × 32 km, and is ~25 km north of Culiacán (Fig. 9). Lava flows, small shield volcanoes, and cinder cones of basaltic composition unconformably overlie Paleocene granodiorite and Oligocene ignimbrites, which are mostly tilted to the west-southwest. Lavas are porphyritic and contain olivine, plagioclase, and clinopyroxene in a microcrystalline matrix. Some lavas contain abundant megacrysts of green clinopyroxene (to 8 cm), olivine (to 1 cm), and/or plagioclase (to 1 cm), or aggregates of olivine and clinopyroxene. We recognized at least 16 cinder cones and maars, all with a well-preserved morphology, suggesting a Pleistocene age for this volcanism. We dated three samples, trying to cover the entire age range of the field. The samples (PER1, PER4, and PER 6) are hawaiitic in composition and have low K contents, so Ar had to be released in a few steps. Nevertheless, they provide consistent middle Pleistocene ages ranging between 884 ± 97 and 585 ± 82 ka (Figs. 4 and 5; Table 1, see the Supplemental File [see footnote 1] for details). Rocks from the late Pliocene Punta Piaxtla sills and Mesa Cacaxtla shield volcano, 200 km to the south-southeast along the Sinaloa coast, show remarkably similar compositions, mineralogies, and megacryst contents (see following), suggesting that the mantle of this wide region achieved a homogeneous composition that has been maintained during the past 3.4 m.y.

The Choix volcanic field consists of a few cinder cones and lava flows 120 km north-northeast of Los Mochis in the northernmost corner of Sinaloa, near the boundary with Sonora and Chihuahua (Fig. 9). Lavas are emplaced on top of Paleocene granodiorite and ignimbrites that are undated, but probably Oligocene. Sample CHO 4 comes from an alkali-basalt lava from a very well preserved cinder cone near the Huites reservoir dam (Fig. 9). The lava is vesiculated with phenocrysts of plagioclase, olivine, and pyroxene, and megacrysts of pyroxene (to 3 cm) and olivine (to 0.5 cm). Due to the very low K content and the presumed young age, only four fractions were collected. The bulk of the ^{39}Ar was released in the last two fractions and no plateau can be defined. This also yielded an imprecise isochron age of 29 ± 181 ka. The best estimate for this sample is 138 ± 107 ka, taken from the third fraction containing the bulk of the ^{39}Ar released (see the Supplemental File [see footnote 1] for further details). Although imprecise, this age confirms the very young age of the Choix volcanic field.

GEOCHEMISTRY

Major and trace element analyses were obtained for volcanic rocks of latest Oligocene to Early Miocene, Late Miocene, and Pleistocene age (Table 2) distributed along the southeastern margin of the Gulf of California.

Late Oligocene to Early Miocene (28–16 Ma)

Late Oligocene to Early Miocene samples display a bimodal distribution in the total alkali versus silica diagram (Fig. 13A; LeBas et al., 1986). Samples with low silica content (SiO_2 = 48.7–55.2 wt%) are lavas and dikes that are classified as hypersthene-normative basalts and quartz-normative basaltic andesite, whereas silicic samples (SiO_2 = 68.2–83.0 wt%) from domes, lavas, and ignimbrite are classified as peraluminous (molar $Al_2O_3/CaO + Na_2O + K_2O$, A/CKN >1), corundum-normative dacite and rhyolite, with a predominance of rhyolitic compositions. Most samples plot in the field of subalkaline rocks of Irvine and Baragar (1971), with the exception of one basaltic lava from the Atengo half-graben (TS 16), which has the lowest SiO_2 content and plots in the field of alkaline rocks (Fig. 13A). None of the mafic samples can be regarded as primitive mantle melts, as they have relatively low MgO and Cr contents (Figs. 13B, 13D) and low Mg# (100 × molar MgO/MgO + FeO_{total}) of 42.1–52.5 (Table 2). The TiO_2 content is variable (Fig. 13C), and is highest for the alkaline sample (TS 16; 2.39 wt%).

Mafic rocks have variable trace element patterns in multielement diagrams normalized to primitive mantle values (Sun and McDonough, 1989) (Fig. 14E). Negative anomalies in Nb and Ta are absent in the TiO_2-rich alkaline sample (basalt TS 16), and are variably developed in the subalkaline basalts and basaltic andesite. Positive Pb and Sr anomalies are present in all samples, but are more pronounced in the basaltic andesite. The lack of a Nb-Ta anomaly in sample TS 16 indicates an origin in an intraplate setting; nevertheless, the enrichment in Pb and Sr, which is not a common feature of intraplate magmas, could reflect assimilation of crustal material (feldspar contamination) by the mafic magma. Trace element patterns of the subalkaline samples have typical features of subduction-related rocks; however, in this sample group, crustal assimilation processes can have also contributed to generate signatures similar to those found in arc volcanic rocks. Alternatively, the subduction signature can be inherited from mantle domains previously modified by subduction components, which partially melted under the extensional regime that generated the intraplate magmas. Consequently, the subduction-related geochemical signatures are unlikely to provide unequivocal constraints on tectonic setting.

Silicic rocks are enriched in the most incompatible elements (Rb-U) and display well- developed negative Nb-Ta and positive Pb anomalies (Fig. 14F). Despite the high silica content of these rocks, negative Ba anomalies, which result from the fractionation of K-feldspar, are absent. Eu and Sr negative anomalies are small in dacitic rocks, implying negligible plagioclase fractionation. The trace element behavior indicates that crystal fractionation had a restricted role in the early evolution of the silicic magmas; this is supported by the fact that inherited zircons remained in the melt. This feature is often associated with crustally derived magmas (e.g., Miller et al., 2003; Bryan et al., 2008). An origin in the crust is also consistent with the bimodal composition of the magmas emplaced in this period.

It is important to note that intermediate rocks comparable with the middle and upper members of the Comondú Group (19–12 Ma) observed in Baja California were not observed along the eastern margins of the Gulf of California through Nayarit and Sinaloa. In this region volcanism is essentially bimodal, represented by rhyolitic domes and surrounding basalts in the range ca. 21–13.5 Ma and thus overlapping with peak activity of intermediate composition volcanism of the Comondú Group. This supports the observation of Bryan et al. (2013) that, regionally, bimodal volcanism persisted during the Middle Miocene and to the east of the locus of Comondú Group volcanism.

Late Miocene (11.6–9 Ma)

Volcanic rocks emplaced in the Late Miocene have mainly a bimodal compositional distribution (Fig. 13A). Mafic to intermediate samples (SiO_2 = 51.4–57.2 wt%) are classified as subalkaline quartz-normative basaltic andesite, low-silica andesite, and potassic trachybasalt. Unlike rocks emplaced in the previous event, basalts are absent and more differentiated compositions with lower MgO and Cr contents (Figs. 13B, 13D) and Mg# (36.7–53.5) occur. Analyses of scarce rocks with SiO_2 > 62 wt% indicate metaluminous (A/CKN < 1) high-silica andesite, dacite, and rhyolite compositions.

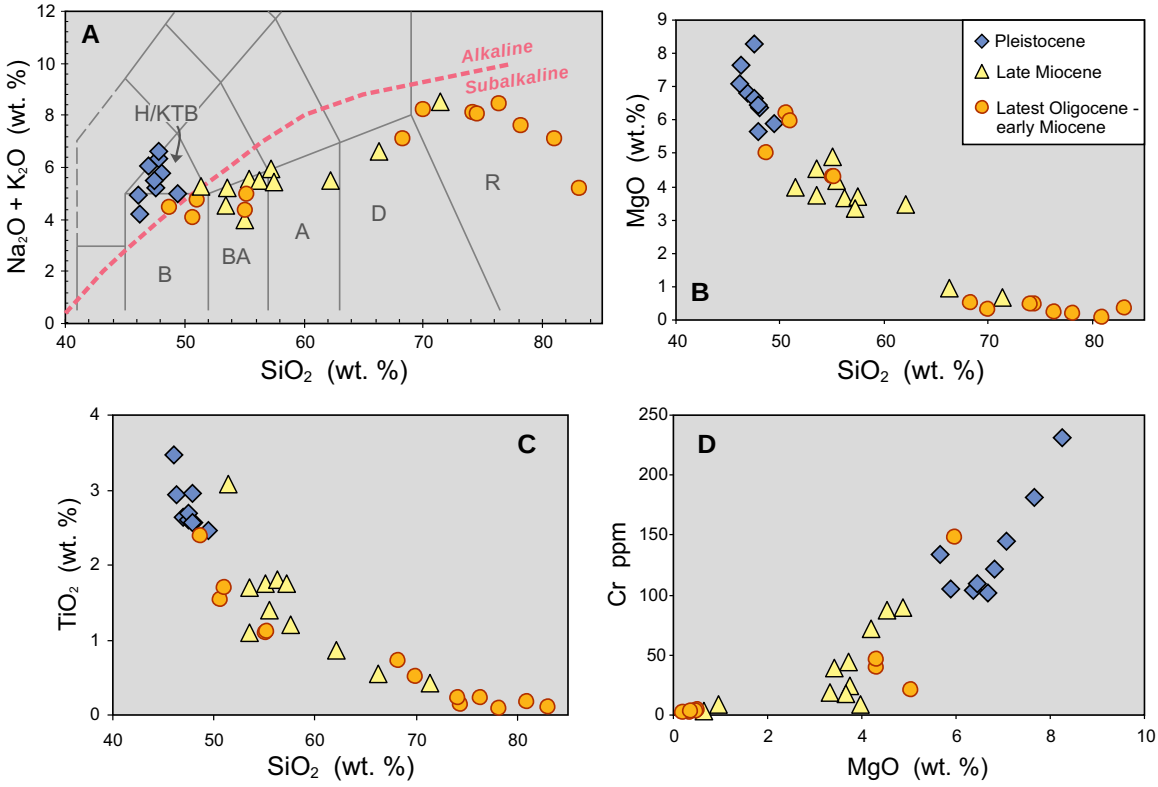

Figure 13. Composition of volcanic rocks of latest Oligocene to Early Miocene, Late Miocene, and Pleistocene age, from the eastern margin of the Gulf of California. (A) Total silica versus alkalis classification diagram (LeBas et al., 1986), showing the line dividing alkaline from subalkaline compositions (Irvine and Baragar, 1971); A—andesite, B—basalt; BA—basaltic andesite; D—dacite; H—hawaiite; KTB—potassic trachybasalt; R—rhyolite. (B) Variation of SiO_2 versus MgO. (C) Variation of SiO_2 versus TiO_2. (D) Variation of MgO versus Cr. Number of analyses is 33.

Low-silica rocks from the coastal area and Farallón de San Ignacio display relatively similar, subparallel trace element patterns in a mantle normalized multielement diagram (Fig. 14B), with weakly developed Nb-Ta anomalies, positive anomalies of Ba, Pb, and Sr, and relatively flat rare earth element (REE) patterns (chondrite normalized La/Yb_n = 3.7–5.3). Very similar compositions are reported for the nearest known outcrops of similar age to the north of the study area, in the central Sonora coast (Till et al., 2009), and for the Santa Rosalía area in Baja California (Conly et al., 2005) (Figs. 1 and 14B). Regional compositional variations are suggested by one potassic trachybasalt from the submarine Nayarit scarp in the southeastern Gulf of California (Fig. 2), which has the lowest SiO_2 content (51.4 wt%) and is more enriched in most trace elements, resulting in a more pronounced Nb-Ta anomaly. In addition, a basaltic andesite collected northeast of Pueblo Nuevo (Fig. 8), within the SMO, has an Nb-Ta anomaly similar to that of the coastal lavas, but is more enriched in the most incompatible elements (Rb to Sr), and has a stronger depletion in the heavy REEs with respect to the light REEs (La/Yb_n = 11.5). A more marked difference is observed in Late Miocene mafic lavas from the Río Chico–Canatlán graben, located in the eastern part of the SMO (Fig. 8) (Henry and Aranda-Gómez, 2000); the lavas have the high Nb contents of intraplate rocks. Differences in composition from east to west indicate changes in the mantle source composition from the Gulf of California to the eastern SMO, probably related to decreasing contributions of subduction components to the mantle and to increasing magma segregation depth.

Late Miocene silicic rocks from coastal and offshore areas display well-developed negative Nb-Ta and positive Pb anomalies, but differ in the abundance of trace elements (Figs. 14C, 14D). Rhyolite R-F6 from Farallón de San Ignacio (Fig. 10) and high-silica andesite R 24J 33 from the South Pescadero transform (Fig. 2) show a pattern similar to those of the latest Oligocene to Early Miocene, with less enrichment in all elements, no Ba anomaly, and less pronounced Sr and Eu anomalies, despite its high SiO_2 content (71% and 62%, respectively). A dacitic tuff (R3J-4a) from the submarine Tamayo dome (Fig. 2) has a higher abundance of most elements and displays pronounced negative anomalies in Ba, Sr, and Eu that indicate extensive feldspar fractionation. Similar differences are observed in Middle to Late Miocene silicic rocks (SiO_2 >70 wt%) from the central Sonora coast (Till et al., 2009), and from the Santa Rosalía area in Baja California (Conly et al., 2005) (Figs. 2 and 14D). A markedly different trace element pattern characterizes a Sierra Navachiste dacite sample (Figs. 10 and 14C), which has a much lower Nb-Ta abundance, positive Ba and Sr anomalies, no Eu anomaly, and stronger depletion toward the heavy REEs (La/Yb_n = 13.3). The composition of this sample is similar to those of samples from Sierra Libre, in the central Sonora coast (Till et al., 2009), and also coincides relatively well with that of clinopyroxene-bearing andesite from Santa Rosalía (Conly et al., 2005), and Mg-andesite reported for the Borja and Jaraguay volcanic fields (Pallares et al., 2008) in the central Baja California peninsula. The variable composition of the Late

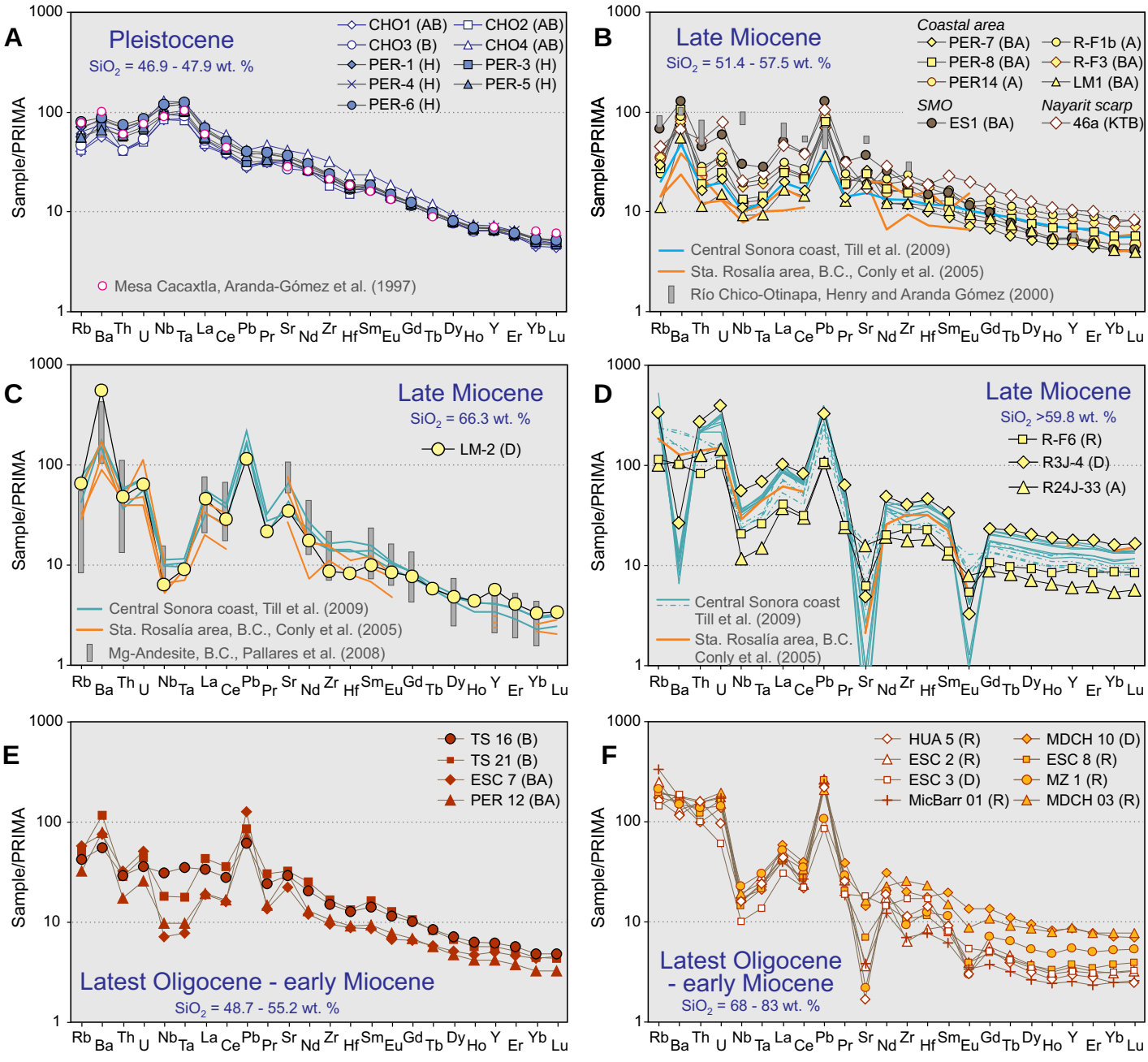

Figure 14. Multielement diagrams of volcanic rocks from the eastern margin of the Gulf of California, normalized to primitive mantle (PRIMA) values of Sun and McDonough (1989). (A) Pleistocene (0.884–0.138 Ma) mafic lavas. Late Miocene (11.96–9.5 Ma) (B) mafic lavas, and (C, D) silicic rocks. Latest Oligocene to Early Miocene (24.38–17.4 Ma) (E) mafic rocks, and (F) silicic rocks. Letters in parentheses next to sample numbers indicate rock composition, A—andesite; AB—alkali basalt; B—basalt; BA—basaltic andesite; D—dacite; H—hawaiite; KTB—potassic trachybasalt; R—rhyolite. In A–D, data compiled from the literature for rocks of similar age in mainland Mexico and Baja California peninsula are shown for comparison. SMO—Sierra Madre Occidental.

Miocene silicic rocks points to variable magma generation processes acting during this event. These processes may have involved crustal melting and assimilation, or differentiation of mafic rocks through crystal fractionation, but further studies are needed to better constrain the origin of the observed differences.

Middle to Late Pleistocene (Younger Than 1 Ma)

Lava samples from the Pleistocene Choix and Pericos volcanic fields (Figs. 9 and 10) plot in the field of alkaline rocks (Fig. 13A). One sample classifies as hypersthene-normative basalt, and the rest are nepheline-normative hawaiite and alkali basalt. The samples have the highest MgO, TiO_2, and Cr contents of all studied samples (Figs. 13B–13D), and Mg# of 48.2–57.9, but these values are lower than those expected for primary magmas derived from the mantle, implying that differentiation occurred during their ascent.

The samples have quite uniform trace element patterns (Fig. 14A), which resemble those of oceanic island basalts (OIB), with the highest normalized abundances in Nb and Ta and strong enrichment of the light REEs with respect to the heavy REEs (La/Yb_n = 9.4–13.5). The trace element pattern of a late Pliocene hawaiite from Mesa Cacaxtla (Figs. 8 and 14A), reported by Aranda-Gómez et al. (1997), is also remarkably similar to that of Choix and Pericos, considering the different emplacement times (Cacaxtla at 3.2 Ma; Aranda-Gómez et al., 1997; Pericos at 0.585–0.884 Ma; Choix at 0.138 Ma, this work) and the distance between them.

The alkaline character and the trace element composition suggest that the Pleistocene magmas originated in a deeper, enriched OIB-like mantle source in the stability field of garnet, and differentiated at crustal levels.

DISCUSSION

Timing of Extension in the Southern Gulf Extensional Province

Figure 15 summarizes the ages of extension documented in this work and the literature. A precise determination of the direction of extension awaits a structural study of the kinematics of the various fault systems that is in progress and will be published later. Although a strike-slip component of motion has been observed along some of the faults, the large vertical displacement and the consistent tilting of blocks indicate a dominant normal motion and an almost fault-orthogonal direction of extension. At a regional scale, we recognize a fairly consistent pattern along the ~700 km of length of the southeastern to central GEP with episodes of extension since ca. 29 Ma.

A Late Oligocene (ca. 29–24 Ma) phase of extension is documented in the central part of the study region (southern Sinaloa domain) in the area bounded by the Tayoltita–Pueblo Nuevo fault system to the east and the Concordia fault to the west (Fig. 8). This early extension would be only slightly younger than that reported in the Rodeo and Nazas area (Luhr et al., 2001) and in the northern part of the Rio Chico–Canatlán graben (Loza-Aguirre et al., 2012) to the east of the SMO unextended core (Fig. 15). We expect a similar Late Oligocene extensional phase to have affected areas to the north (northern Sinaloa domain, Fig. 9), particularly in the more inland part of the GEP, which we did not study directly. Supporting this is that extension of this age has recently been documented further to the north in the Guazapares area of southernmost Chihuahua (Murray et al., 2013). Because of the extensive cover of Early Miocene ignimbrites, the existence of a Late Oligocene phase of extension is difficult to prove in the northern Nayarit domain. However, Late Oligocene normal faulting is documented at least in the central Bolaños graben (Fig. 2), where some of the faults (e.g., the prominent Ballena and Cabreras faults) are also northwest trending and served as mineralization pathways during the Early Miocene (Ramos-Rosique, 2013). The direction of extension during this first phase is not well constrained but, considering the right-lateral component of motion reported in the northern part of the Tayoltita–Pueblo Nuevo fault system (Horner and Enríquez, 1999), it may be slightly oblique with respect to the main faults, i.e., west-northwest–east-southeast directed (Fig. 15).

Extension continued during the Early and Middle Miocene (ca. 24–12 Ma) in Sinaloa and northern Nayarit. In Nayarit, this phase can be further divided into two main episodes with different directions of extension. Normal faulting with approximately north-south trends affected a 180-km-wide area between Bolaños and Huajicori (Fig. 15) between ca. 24 and 18 Ma and was postdated by north-northwest–trending fault systems (Pochotitán and San Pedro–Acaponeta) active between before 18 to 11 Ma along the coast (Fig. 6). In Sinaloa, Early to Middle Miocene extensional faults strike essentially north-northwest, forming grabens and half-grabens filled by 21–17 Ma dome complexes and volcaniclastic sediments interlayered with ca. 17–13 Ma basalts. This last phase of extension is postdated by flat-lying basaltic lavas fed by north-northwest–trending dikes dated as between 11.3 and 10.3 Ma. These geologic and geochronologic relations make the Sinaloa area the southern prolongation of the latest Oligocene–Middle Miocene extensional belt of Sonora, where high-angle faulting and volcaniclastic sedimentation of the Baucarit Formation occurred from 24 Ma and was essentially over by ca. 12 Ma (McDowell et al., 1997).

The western limit of this early extension is poorly constrained due to the superposed subsequent faulting in the southern Gulf of California. Textural and geologic evidence indicate that Early to Middle Miocene (ca. 21–15 Ma) plutons exposed along the Nayarit coast, the islands offshore southern Baja California, and recovered in the rifted blocks inside the southern Gulf of California were emplaced at shallow depths (Duque-Trujillo et al., 2012). The short time span between U-Pb zircon ages and hornblende and biotite ages also suggest rapid cooling and the possibility that they were emplaced into an extending crust (Duque-Trujillo et al., 2012), but more thermochronologic studies are needed to better constrain this inference. However, Mark et al. (2012) found apatite U-Th(He) exhumation ages of 25–17 Ma in the Loreto area that are in agreement with the early extension of the southern GEP evident from our study. In southernmost Baja California, the Cretaceous batholithic rocks of the eastern part of the Los Cabos block show a geochronologic, geochemical, and isotope similarity with those of the Jalisco block in mainland Mexico (Schaaf et al., 2000) and those exposed in the Maria Madre Island in between (Pompa-Mera et al., 2013), suggesting that the two blocks were contiguous in a north-northwest alignment prior to rifting (Fig. 15). The normal faults of the Los Cabos block are mostly north-south striking, thus parallel to the Early and Middle Miocene faults of Nayarit and Jalisco described in this work. The onset of faulting is constrained by the oldest sediments in the Los Cabos basin (Fig. 15) that consist of red terrestrial sandstone and conglomerate (Calera Formation; Martínez-Gutiérrez and Sethi, 1997). These sediments are not dated, but they overlie tilted silicic volcanic rocks correlative with the ca. 21–19 Ma ignimbrites of the La Paz area. They are also conformably covered by the marine Trinidad Formation, assigned to the Late Miocene on a paleontological basis (Martínez-Gutiérrez and Sethi, 1997). Based on these stratigraphic constraints, the approximately north-south normal faults in the Los Cabos blocks might be partly coeval with the last extensional faulting in the northern Nayarit domain (ca. 18–12 Ma). However, thermochronologic studies indicate that rapid cooling of the footwall of the Los Cabos fault initiated at the beginning of the Late Miocene (Fletcher et al., 2000; Lovera et al., 2010). In summary, despite the fact that the onset of extension cannot be precisely determined, we consider that the available data do not preclude the possibility that by Middle Miocene time, the area now occupied by southern Gulf of California was already an extending basin.

Pre–Late Miocene Extension in the Northern Gulf Extensional Province

The early extension we have documented in this work cannot be limited to the southern-central GEP. Early to Middle Miocene extension is well documented in eastern and central Sonora (McDowell et al., 1997; Gans, 1997; Gonzalez-León et al., 2000; Vega-Granillo and Calmus, 2003; Nourse et al., 1994; Wong and Gans, 2003; Wong et al., 2010), and constitutes the obvious prolongation to the north of the extensional belt of Nayarit and Sinaloa described in this work. However, the western boundary of this extensional belt is uncertain. Micropaleontological studies of several deep wells drilled in the Wagner, Consag, and Tiburón

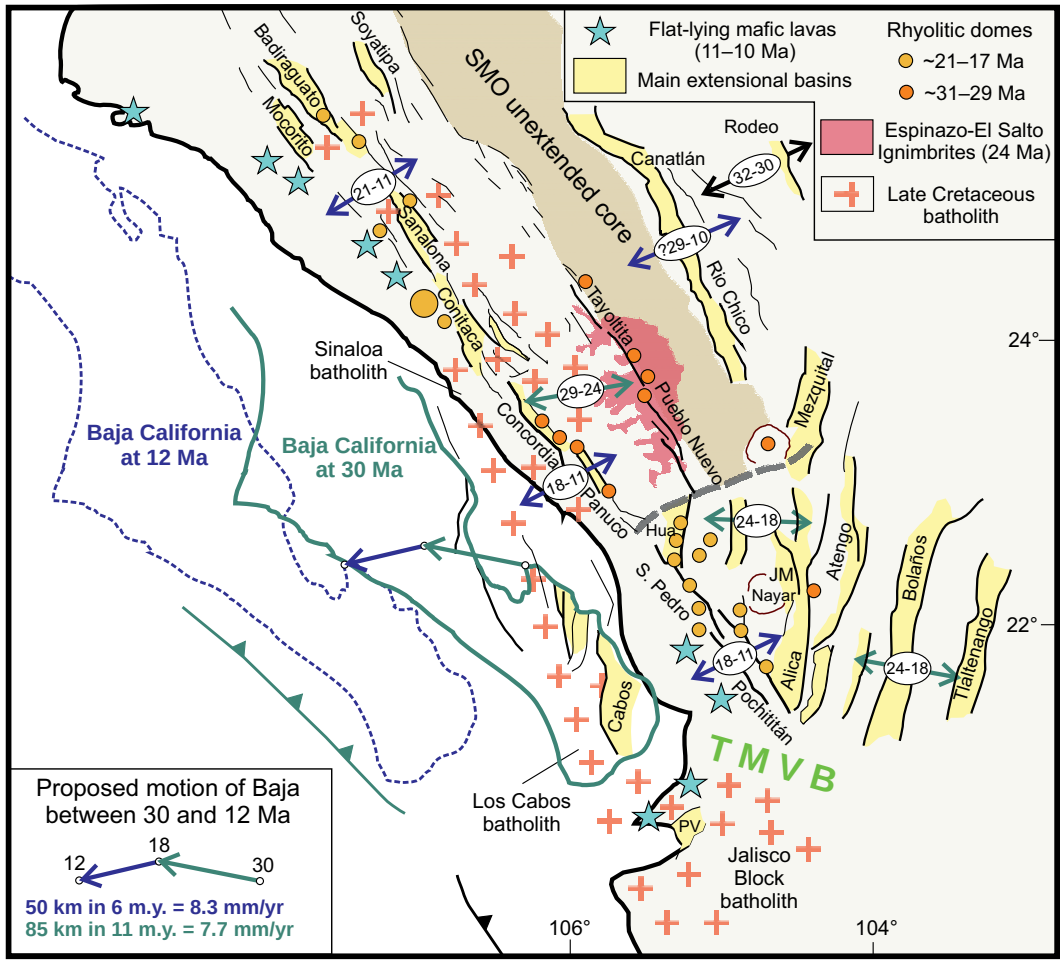

Figure 15. Regional tectonic map summarizing the main structures and age of extension of the conjugate margins of the southern Gulf of California. Geographic coordinates refer to present position of Mexico mainland. Position of Baja California at 12 Ma is obtained by moving the southern tip of Baja California (Cabo San Lucas) 350 km to the southeast parallel to the Tamayo transform, removing all the oceanic crust accreted at the East Pacific Rise to the south. The position at 30 Ma is obtained by aligning the paleotrench off Baja California with the present trench off the Jalisco block and joining the Late Cretaceous batholith of the Los Cabos block in Baja California with the Sinaloa and Jalisco block batholith (see text for discussion). Abbreviations: PV—Puerto Vallarta; Hua—Huajicori; JM—Jesús María.

Basins (Fig. 1) reported the occurrence of >1 km of marine sediments with shallow-water (<200 m) foraminifera, dinoflagellates, and nanofossils older than 11.2 Ma (Helenes et al., 2009). Recent reinterpretation of these data by J. Helenes and A. Carreño (2013, written commun.) indicates that part of the recovered well material is reworked, a feature already reported for other sites in the northern Gulf of California (e.g., Imperial Formation, McDougall et al., 1999; Laguna Salada, Martín-Barajas, 2001; Isla Tiburón, Gastil et al., 1999). Given that the Peninsular Range Batholith of Baja California was uplifted in the Early Eocene (e.g., Axen et al., 2000) the widespread occurrence of reworked Middle Miocene marine microfossils requires the existence and proximity of shallow-marine environments within the northern Gulf of California by the Middle Miocene. This interpretation is apparently at odds with the geology of Isla Tiburón (Fig. 1) (Oskin and Stock, 2003; Bennett et al., 2012), where marine incursion has been well dated as latest Miocene. However, we note that Isla Tiburón is at the southeastern margin of a basin that, in its central part, has >7 km of sediments overlying the Late Cretaceous basement (Martín-Barajas et al., 2013). The well T-1 drilled by PEMEX near the deepest part of the Tiburón Basin encountered ~4.8 km of marine deposits (Helenes et al., 2009), which in their lower part are considered not reworked and have an upper age limit of 11.9 Ma based on the microfossils *Ciclycargolithus floridanus* (known range 37–11.9 Ma), *Cribroperdinium tenuitabulatum* (69.9–11.63 Ma), *Paleocystodinium golzowense* (56–9.2 Ma), and *Dapsilidinium pseudocolligerum* (56–7.12 Ma) (J. Helenes, 2013, written commun.). The recent seismic profiles of Martín-Barajas et al. (2013) show that the lowermost sedimentary package pinches out to the south and is not deposited on the basement high at the southeastern margin of the basin (Tiburon shelf and Isla Tiburón).

Therefore, the latest Miocene age of marine incursion at Isla Tiburón does not contradict the pre–11.9 Ma marine sediments in the deepest part of Tiburón Basin and simply records the widening development of marine conditions in the gulf in the Late Miocene. A definitive answer on the existence and extent of localized marine basins of pre–Late Miocene age in the northern Gulf of California awaits further studies of well stratigraphy and seismic data from the deeper part of the Tiburón and other basins, but the possibility of an early extension in this part of the gulf cannot be ruled out.

Pre–Late Miocene Lithospheric Thinning and Motion of Baja California

The data reported in this work provide important constraints on the magnitude of pre–Late Miocene rifting in the southern GEP. Different seismic methods consistently indicate that the crust along the Nayarit and Sinaloa coast is significantly thinner than in the core of the SMO. Estimations of the Moho depth from receiver functions and seismic refraction along the coast range between ~21 km west of Culiacán to ~18 km in northern Nayarit (Persaud et al., 2007; Lizarralde et al., 2007; Savage and Wang, 2012) (Fig. 2). By contrast, the crustal thickness in the unextended core of the SMO is estimated to be 55 km northeast of Culiacán (Bonner and Herrin, 1999), ~40 km northeast of Mazatlán

(Couch et al., 1991), and almost 30 km in the unfaulted part of the Los Cabos block (Páramo et al., 2008). The presence of 11.3–10.3 Ma flat-lying mafic lavas at or near sea level along the coast of Nayarit and Sinaloa indicates that no significant tectonic activity occurred in this area after ca. 11 Ma. This implies that the thickness of the crust was substantially reduced by early extension occurring well before the end of subduction. This crustal thinning would have greatly aided the subsequent rupture, limiting the elastic thickness of the lithosphere to the uppermost crust, typical of a so-called "crème bruleé" rheology (Jackson, 2002).

The recognition of this early phase of extension in the GEP has important implications for the mode of extension and lithospheric rupture that led to the formation of the Gulf of California. Although the kinematics of opening are debated, studies in the past 20 yr essentially assumed a ca. 14–12.5 Ma initiation of the rifting process (e.g., Stock and Hodges, 1989; Gans, 1997; Umhoefer et al., 2001; Oskin et al., 2001; Fletcher et al., 2007; Sutherland et al., 2012), implying a very fast rate of crustal thinning and the initiation of seafloor spreading only ~6–10 m.y. after the onset of extension (Umhoefer, 2011). This is a very short time span for complete rupturing of the lithosphere, which is commonly accomplished over 25–30 m.y. in other examples (see review in Umhoefer, 2011). Our results indicate a more reasonable time span of ~25 m.y. between the initiation of extension and the initial formation of oceanic crust.

An early phase of extension across the GEP beginning ca. 29 Ma also reconciles the apparent discrepancy between the 275–300 km of offset across the northern Gulf of California since 12.5 Ma estimated by correlative geologic units (Gastil et al., 1973, 1991; Oskin et al., 2001; Miller and Lizarralde, 2013) and the ~450–500 km of offset needed to close the southern Gulf of California based on palinspastic reconstructions using an Airy isostatic model of crustal thickness (Fletcher et al., 2003). In fact, the total offset estimated by Fletcher et al. (2003) can be accounted for by the sum of the post–12.5 Ma rifting plus the early extension documented in this work to have initiated ca. 29 Ma. We have tried to estimate the amount of this early extension by looking at the motion of Baja California during this period (Fig. 15). The position of Baja California before extension at 30 Ma is chosen in a way that realigns the Late Cretaceous batholiths of Puerto Vallarta (Jalisco block), Los Cabos, and Sinaloa, as well as by bringing the paleotrench west of Baja California in line with the present trench west of Puerto Vallarta (Fig. 15). In this reconstruction, the southern tip of Baja California is 475 km southeast of its present position, essentially eliminating all the crustal stretching estimated by Fletcher et al. (2003) at the mouth of the Gulf of California. The position of Baja California at 12 Ma is obtained by removing the 245 km of oceanic crust accreted at the East Pacific Rise (Lizarralde et al., 2007) plus 110 km of extension on both sides of the oceanic crust: 35 km in the stretched crust southeast of the Los Cabos block (Páramo et al., 2008) and 75 km of extension in the 200-km-long area of stretched crust between Puerto Vallarta and the continental slope west of Tres Marías Islands (Lizarralde et al., 2007) (Fig. 2). In this scenario, the motion of Baja California between ca. 30 and 12 Ma would amount to 135 km, which, based on the age and geometry of faults, we propose was accommodated by west-northwest to east-west extension between ca. 30 and ca. 18 Ma and by west-southwest extension between ca. 18 and 12 Ma. Our reconstruction implies a moderate rate of separation of Baja California of 7.7 mm/yr during the first phase and 8.3 mm/yr in the second. Of note is that these values are consistent with the rate of extension of the East African Rift (7 mm/yr; Fernandes et al., 2004). The subsequent 355 km of northwestward motion would have been accomplished with a higher average rate of 29.5 mm/yr. However, if we consider the spreading rate for the past 3.6 m.y. in the southern Gulf of California (45.1 ± 0.8 to 51.1 ± 2.5 mm/yr; DeMets, 1995), the rate of motion during the Late Miocene phase of northwestward rifting would reduce to ~21 mm/yr. This progressive increase in the rate of separation (7.7–8.3 mm/yr prior to 12 Ma to ~21 mm/yr 12–3.6 Ma) is likely related to the decreasing yield strength of the continental lithosphere as it is mechanically and thermally thinned and, eventually, completely severed by the onset of transtension.

Our reconstruction for the original position of Baja California relative to mainland Mexico ca. 30 Ma (Fig. 15) approximates those of Fletcher et al. (2007) and Sutherland et al. (2012) at 12.5–14 Ma. Those reconstructions implicitly imply no extension prior to 14 Ma and a high rate of separation of 32–35 mm/yr, uncommon for continental rifts where geodetically measured rates of opening are typically <10 mm/yr (Calais et al., 1998; Fernandes et al., 2004; Bendick et al., 2006). An implication of our reconstruction of ~475 km of northwest motion of Baja California since ca. 30 Ma is that little dextral shear is required to be accommodated within the Gulf of California after 12.5 Ma other than the ~275–300 km estimated from the correlation of geologic units (Oskin et al., 2001; Miller and Lizarralde, 2013). However, according to global plate circuit reconstructions, since 12.3 Ma, the Pacific plate has moved ~600 km to the northwest relative to stable North America at the latitude of southern Baja California (Atwater and Stock, 1998). This implies that ~300 km of additional oblique shear must have been accommodated since that time between the Pacific plate and stable North America. One possibility is that this deformation occurred in the belt of faults on the western margin of Baja California (Tosco-Abreojos and San Benito faults) that currently accommodates 10% of the Pacific–North America relative motion (Plattner et al., 2009). This possibility would agree with an early estimation of right-lateral motion along this fault belt (Stock and Hodges, 1989), but contrasts with the more limited motion estimates by Fletcher et al. (2007) through correlation of the Magdalena Fan (Fig. 1) with its most probable source. Another place where Late Miocene extension may have been accommodated is in the Basin and Range east of the SMO unextended core. Henry and Aranda-Gomez (2000) reported an extensional episode in this wide area (Fig. 1) between 12 and 6 Ma, although this is not quantified. A third possibility is that deformation has been underestimated in the GEP and some additional motion may be distributed within the Gulf of California in faults buried in the wide coastal plain and shelf of the Nayarit and Sinaloa margin. All these options may contribute to account for the missing ~300 km of displacement between the Pacific and North America plates, but more structural, geochronologic, and geophysical data are needed to assess their respective balance.

Genesis of Magmatism

The significant pre–Late Miocene extensional deformation documented in this work for western Mexico has important implications for the genesis of magmatism in the Gulf of California region. The overall calc-alkaline geochemical character, relatively primitive isotopic signature, and the suprasubduction position of the SMO and the Comondú volcanic rocks have traditionally led to interpretations of these provinces as being the manifestation of arc volcanism, whereas volcanism related to the rifting process would have appeared only after subduction ceased. This view needs to be revised in light of the results presented here and elsewhere (see Bryan et al., 2008, 2013). As we have shown, extension and crustal thinning spatially associated with volcanism occurred for at least 15 m.y. prior to the end of subduction.

Geologically observable extension began in the southern SMO just after the major Oligocene ignimbrite flare-up. For example, the ca. 24 Ma El Salto–Espinazo ignimbrite succession

filled a tectonic depression bounded by this early normal faulting. Extension continued during the Early Miocene, likely triggering the last major sequence of ignimbrite eruptions ca. 21–20 Ma (Nayar ignimbrite succession). At the same time, volcanism became bimodal and was characterized by more effusive activity. A belt of rhyolitic domes was emplaced along north-northwest–trending normal faults that bound extensional basins localized along the site of the opening of the Gulf of California. Mafic lavas and rhyolitic domes filled major grabens along the coast of Sinaloa. Geochemistry of Early Miocene silicic volcanism as well as the zircon antecrystic signature of many samples is consistent with significant crustal assimilation and melting induced by the arrival of mafic magmas in the crust. Similarly to Sinaloa, in southern Baja California the middle member of the Comondú Group was likely emplaced in actively extending tectonic basins, as suggested by the dominance of volcaniclastic sediments with respect to primary volcanic materials (Dorsey and Burns, 1994; Umhoefer et al., 2001; Drake, 2005). The dacitic-andesitic nature of the volumetrically modest Comondú volcanism has alternatively been explained by mixing of basaltic and rhyolitic magmas rather than by fluid fluxing of the mantle wedge above the subducting Guadalupe and Magdalena plates (Bryan et al., 2013). By ca. 16 Ma, the subducting plate at the trench may have been as young as 3–5 Ma (Ferrari et al., 2012, Fig. 18 therein) and thus too dry and hot to release any meaningful amount of fluids once it reached the appropriate depth to flux the mantle wedge (i.e., 105 km; Syracuse and Abers, 2006; see also Peacock and Wang, 1999). In this scenario, melting of sublithospheric mantle was essentially driven by decompression, induced by the significant lithosphere thinning going on at this time. The apparent subduction-related signature of SMO and Comondú volcanics is most likely a feature inherited by the previous >100 m.y. history of subduction, and was acquired by lithospheric assimilation and melting. It is interesting that our easternmost Early Miocene basaltic sample (TS 16, 24 Ma) has an intraplate signature (albeit with some crustal assimilation), suggesting that by that time, at least beneath the eastern part of the SMO, the mantle was already devoid of any subduction influence. We conclude that since the Late Oligocene, crustal extension and magmatism were intrinsically linked and decompression melting progressively overwhelmed any flux melting of the mantle wedge.

A widespread mafic pulse of volcanism occurred ca. 12–10.5 Ma along the Sinaloa and Nayarit coasts, as well as on the conjugate margin of Baja California and in the rifted continental blocks submerged in the Gulf of California. Although this volcanism postdates the end of subduction off Baja California, it still shows a variable subduction signature and a striking difference with the OIB-like late Pliocene to Pleistocene basalts emplaced in the same areas. The regional distribution of this volcanism over a 700-km-long belt from Sinaloa to Nayarit in a narrow time frame points to a common mechanism of mantle melting, albeit modulated by different degrees of fractional crystallization and crustal assimilation. We propose that this mafic volcanism is related to the acceleration of the rate of separation between Baja California and mainland Mexico once subduction ended and the peninsula started to be dragged northwest by the Pacific plate. The increasing northwestward motion of Baja California follows its coupling with the shallow part of the subducted Magdalena plate once the lower part of the slab had detached and started foundering in the mantle (Ferrari, 2004). The precise location of slab detachment in the Gulf of California area is debated, but it is thought to have initiated 13–12 Ma (Calmus et al., 2003; Pallares et al., 2007; Brothers et al., 2012). The ascent of hot asthenospheric mantle into the slab gap that formed after the slab detachment may have triggered extensive melting of the subduction-modified former mantle wedge, which ultimately led to the ca. 12–10.5 Ma mafic pulse. However, the scrubbing of a subduction signature from the mantle and the consequent melting of undepleted asthenosphere in the Nayarit-Sinaloa margin was delayed until the late Pliocene, whereas calc-alkaline melts are still being generated in some locations in eastern Baja California.

CONCLUSIONS

The data presented in this work show that the GEP represents the last and most visible phase of rifting in the Gulf of California driven by the oblique divergence of the Baja California peninsula from the Mexican mainland. Although there are different views on how oblique divergence was partitioned between the San Benito–Tosco–Abreojos fault system and the Gulf of California on the two sides of the peninsula (Stock and Hodges, 1989; Gans, 1997; Oskin and Stock, 2003; Fletcher et al., 2007), there is no doubt that this last episode of rifting and its associated volcanism were primarily controlled by plate boundary forces, namely the progressive dragging of Baja California to the northwest by the Pacific plate and the upwelling of asthenosphere into the slab gap produced by the detachment of the lower part of the subducted slab.

The causes of the early Basin and Range–type extension, however, are not completely understood. The onset of extension in western Mexico was considered to be Oligocene in the eastern part of the SMO and to have subsequently migrated to the west to reach the Gulf of California area at the end of the Middle Miocene (Cameron et al., 1989; McDowell and Mauger, 1994; Henry and Aranda-Gómez, 2000; Luhr et al., 2001; Umhoefer et al., 2001; Aranda-Gómez et al., 2003). By contrast, our work indicates that a sustained period of lithospheric stretching affected the entire western Mexico, from the eastern part of the SMO to the region of the future Gulf of California, since the Late Oligocene. The first part of this extensional history, producing the Mexican Basin and Range, occurred during the last period of subduction beneath North America, and broadly coincided with the silicic volcanism of the SMO and the intermediate volcanism of the Comondú Group. The initial wide zone of rifting between ca. 30 and 20 Ma subsequently focused in the westernmost part of the SMO and the Gulf of California region ca. 20–18 Ma to form a narrower rift where the Comondú Group was being deposited. Subduction of the Magdalena microplate started waning by 15 Ma, and ultimately ceased by ca. 12–11.5 Ma, to be replaced by oblique divergence (Lonsdale, 1991; Tian et al., 2011). Therefore, a significant part of extension in the southern Gulf of California (the proto–Gulf of California) occurred prior to subduction termination and cannot be directly associated with the interaction between the Pacific and North America plates.

Previous studies (e.g., Ferrari et al., 2002, 2007; Bryan et al., 2008, 2013), confirmed by this work, showed that the outbursts of silicic volcanism in the SMO (the ignimbrite flare-ups) cannot be explained by an assimilation and fractional crystallization process alone, but were dominantly produced by intrusion of large amount of mafic melt in the crust. The accumulation of mafic magma in the crust had to be sufficiently rapid to produce enough silicic melt to feed many large-volume ignimbrite eruptions in a short time span (typically 1–2 m.y.). The occurrence in the SMO of two ignimbrite flare-ups suggests that mantle melting and the production of mafic magmas also occurred in two main pulses, ruling out a steady-state flux melting process related to a normal subduction regime.

Silicic magmatism and extension in the U.S. part of the Basin and Range province has been attributed to boundary forces (i.e., trench retreat, rollback, and steepening of the subducting Farallon plate; Dickinson and Snyder, 1978; Best and Christiansen, 1991; Ward, 1991; Bohannon and Parsons, 1995; Dickinson, 2002; McQuarrie and Oskin, 2010) or body forces (i.e., active rifting induced by upwelling of hot asthenosphere

within a slab window or gravitational collapse of a thickened crust; e.g., Houseman et al., 1981; Gans et al., 1989; Harry et al., 1993; Leeman and Harry, 1993; Axen et al., 1993; Wilson et al., 2005; Wong et al., 2010). As shown by Sonder and Jones (1999), a single mechanism is unable to explain all the extensional deformation of the western United States and a combination of both groups of forces is required. The cause of the Basin and Range extension and the ignimbrite flare-ups in the SMO is probably related to a similar combination of processes, but assessing the role and weight of each factor needs a more complete data set on fault activity, magmatic evolution, and crustal structure.

We conclude that, in the past 30 m.y., western Mexico has been dominated by lithospheric extension that was produced by different geodynamic mechanisms. The real change ca. 12.5 Ma was the direct interaction between the Pacific and North America plates that resulted in rifting focusing on the westernmost part of a wide and already thinned belt of lithosphere and in changing the kinematics of deformation, imposing a high degree of obliquity. In this context, the GEP can be only distinguished from the previous episodes of extension by its right-lateral component of deformation and thus should be more properly called the Gulf transtensional province.

ACKNOWLEDGMENTS

Research was supported by CONACYT (Consejo Nacional de Ciencia y Technologia) grants 82378 and 121513 (to Ferrari) and CONACYT P46600-F (to López-Martínez). We thank M. Cerca for information and discussions on the tectonics of Baja California Sur, C. Ortega for assistance in U-Pb dating, O. Pérez Arvizu for inductively coupled plasma–mass spectrometry trace element analysis, M.A. García Gracía for help in the Ar-Ar mass spectrometry, L. Luna for helping with map preparation, A.S. Rosas Montoya, V.M. Pérez Arroyo, G. Rendón, and L. Gradilla for Ar-Ar sample preparation, and A. Ramos-Rosique, J. Pelaez, G. Antillón Mata, V. Reyes, C. Cornejo-Jiménez, Y. González Romo, J. González Romo, V. Reyes Orozco, M. García Sierra, and J.C. Castro Climaco for field assistance and zircon separation. DANA and ROCA samples were collected during research cruises by R/V *Revelle* and R/V *Atlantis* (funded by National Science Foundation grants 0203348 and 0646563 to Lonsdale); we thank the Government of Mexico for operating permission, and the ships' officers and crews for their expert help. Detailed and constructive reviews by Axel Schmitt, Joann Stock, and guest editor Cathy Busby improved the original submission.

APPENDIX 1. U-Pb LA-ICP-MS DATING METHODOLOGY

U-Pb ages on separate zircons were obtained by laser ablation–inductively coupled plasma–mass spectrometry (LA-ICP-MS) at the Laboratorio de Estudios Isotópicos, Centro de Geociencias, Universidad Nacional Autónoma de México, according to the procedures reported in Solari et al. (2010). The analytical data are reported in the Supplemental File [see footnote 1]. The Plešovice reference zircon (ca. 337 Ma; Sláma et al., 2008) was used in combination with NIST 610 standard glass to correct for instrumental drift and downhole fractionation and to recalculate elemental concentrations, using Iolite software (Paton et al., 2010) in combination with the VisuaAge data reduction scheme of Petrus and Kamber (2012). Precision on the measured $^{207}Pb/^{206}Pb$, $^{206}Pb/^{238}U$, and $^{208}Pb/^{232}Th$ ratios typically was ~0.95%, 0.7%, and 1.1% 1σ relative standard deviation, respectively. Replicate analyses of the Plešovice zircon (Sláma et al., 2008) indicate an external reproducibility of 0.95%, 0.7%, and 1.6% on the measured $^{207}Pb/^{206}Pb$, $^{206}Pb/^{238}U$, and $^{208}Pb/^{232}Th$ ratios, respectively. These errors are quadratically included in the quoted uncertainties for individual analyses of the analyzed zircons. Because its signal is swamped by the ^{204}Hg contained in the carrier gases, ^{204}Pb was not analyzed during this study. When needed, the common Pb correction was performed, employing the algebraic method of Andersen (2002). With this method, the analysis of Cenozoic zircons is a complex task, due to the tiny signal of ^{207}Pb, which yields somewhat imprecise (i.e., discordant) analyses, difficult to correct with the Andersen (2002) algorithm. A concordance filter is therefore not applied, because this would eliminate most of the obtained ages. The concordia, weighted mean ages, as well as age error calculations, were performed using Isoplot v. 3.70 (Ludwig, 2008). The $^{206}Pb/^{238}U$ ages are preferred for grains younger than 1000 Ma because of the uncertainty involved in determining the ^{207}Pb isotope in young crystals.

APPENDIX 2 . ^{40}Ar-^{39}Ar METHODOLOGY

The 29 new ages presented here were obtained over a period of 6 years. All the samples were step-heated. The temperature-controlled Ta furnace was used to extract the argon of four samples; for these, the argon isotopes were analyzed with a MS10 mass spectrometer. The rest of the samples were step-heated using an argon-ion laser beam and the extracted argon was analyzed with a VG5400 mass spectrometer. With the exception of samples ESC 7, MdCH 10, LM 2, PER 12, and PER 14, which were prepared at the mineral separation laboratory of the Centro de Geociencias, Universidad Nacional Autónoma de México (CGEO-UNAM), the samples were prepared at Departamento de Geología, Centro de Investigación Científica y de Educación Superior de Ensenada (CICESE). The basic sample preparation consisted of crushing and sieving, then rinsing with distilled water followed by 98% acetone. The rock fragments were dried overnight at ~60° C. The rock fragments or mineral crystals selected for analysis were generally ~500 µm; only 5 samples were smaller: feldspar ROCA 3J 5 was ~300 µm, and samples ESC 7, LM 2, PER 12, and PER 14 were ~200 µm. The fraction selected to prepare the samples was chosen from the fraction where the fragment size was closest to the size of the minerals to be separated or where it could be observed that the groundmass fragments were free of phenocrysts. Mineral-separation procedure consisted of magnetic Frantz separation, heavy liquids if necessary, and final examination of the samples under the microscope to ensure >99% purity of the concentrate. For some samples, no mineral concentrate could be separated; these samples were examined under the microscope and the phenocrysts were eliminated by hand; these were labeled groundmass. If no phenocrysts were observed, the sample was labeled whole rock.

The majority of rock fragments and minerals were irradiated in position 5C and sample ES 10 was irradiated in position 8C. The irradiations were performed in the U-enriched research reactor of McMaster University in Hamilton, Ontario, Canada. Because the project was conducted over several years, the samples were irradiated in different groups. Samples DANA 46a and ES 10 received 40 MWh; the rest of the samples received 30 MWh. With the exception of sample DANA 46a, which was irradiated without a Cd liner, rock fragments were covered with a Cd liner to block thermal neutrons. The irradiation monitors used were: TCR-2 (split G93) sanidine (28.34 ± 0.28 Ma; Renne et al., 1998); FCT-2 sanidine (28.201 ± 0.046 Ma; Kuiper et al., 2008); HD-B1 biotite (24.18 ± 0.09 Ma; Schwarz and Trieloff, 2007); CATAV 7-4 biotite (89.13 ± 0.35 Ma; internal standard calibrated with hornblende hb 3gr at the University of Toronto, with hornblende MMhb 1 at the University of Nice and at CICESE with sanidine TCR-2, sanidine FCT-2, biotite HD-B1, and 128.1 Ma biotite LP-6; Roddick, 1983). The irradiation monitors were distributed among the samples. The irradiation monitors were fused in one step to calculate J. The J value used for the samples came from the monitor that was closest to the sample during irradiation.

All the argon experiments were preceded by a blank measurement of all the argon masses. Upon blank subtraction, the argon isotopes were corrected for mass discrimination, calcium, potassium, and chlorine neutron-induced interference reactions. The parameters used to correct for neutron-induced interference reactions were: $(^{39}Ar/^{37}Ar)Ca = 6.51 \times 10^{-4}$; $(^{36}Ar/^{37}Ar)Ca = 2.54 \times 10^{-4}$; $(^{40}Ar/^{39}Ar)K = 2.87 \times 10^{-2}$ for DANA 46a. For the rest of the samples, which had Cd liners, the parameters were: $(^{39}Ar/^{37}Ar)Ca = 6.50 \times 10^{-4}$; $(^{36}Ar/^{37}Ar)Ca = 2.55 \times 10^{-4}$; $(^{40}Ar/^{39}Ar)K = 0$. Mass 36 was also corrected for chlorine-derived ^{36}Ar [^{35}Cl (n, γ) $^{36}Cl \rightarrow {}^{36}Ar + \beta$ with a half life of 3.1×10^5 yr]. Isotopes ^{37}Ar and ^{39}Ar were corrected for radioactive decay. The constants recommended by Steiger and Jäger (1977) were used in all the calculation, while all the straight line calculations were performed with the equations presented in York et al. (2004). All errors are reported at 1σ level. The errors in the integrated, plateau, isochron, and weighted mean age include the uncertainty in the J parameter. In addition, for the plateau, isochron, and weighted mean ages, the goodness of fit was included in the age uncertainty whenever the mean square of weighted deviates was >1. The integrated ages were calculated adding the fractions of the step-heating experiments. Plateau ages were calculated with the weighted mean of three or more consecutive fractions, which were in agreement within 1 σ errors excluding the uncertainty in J. All the data were plotted on an $^{36}Ar/^{40}Ar$ versus $^{39}Ar/^{40}Ar$ correlation diagram to determine the composition of the $(^{40}Ar/^{36}Ar)i$ of the samples. Tables with the relevant ^{40}Ar-^{39}Ar data of all the experiments are given here. A brief discussion of the ^{40}Ar-^{39}Ar results follows, tables with the relevant ^{40}Ar-^{39}Ar data of all the experiments and the figures with age spectrum, $^{37}Ar_{Ca}/^{39}Ar_K$ diagram, and the $^{36}Ar/^{40}Ar$ versus $^{39}Ar/^{40}Ar$ correlation diagram for each sample are given in the Supplemental File [see footnote 1].

APPENDIX 3. SAMPLE PREPARATION FOR TRACE ELEMENT ANALYSIS

Mafic to intermediate samples were analyzed using the procedure described in Mori et al. (2007). For silicic samples (SiO_2 > 60%), two additional digestion steps were carried out, in order to achieve complete dissolution of refractory minerals (e.g., zircon) The same amount of sample (50 mg) was weighted in 15 mL Teflon vials, and after an initial overnight attack

with 1 mL HF and 0.5 mL 8 N HNO_3 on a hot plate at 90 °C, followed by evaporation to almost dryness, samples were transferred to 1.5 mL Teflon vials with 1 mL HF and 0.5 mL 8 N HNO_3. Closed vials were then placed inside the Teflon liner of metal-jacketed Parr pressure bombs, to which 3 mL of a 2:1 HF-8N HNO_3 mixture were added in order to equalize the pressure inside and outside the vials and prevent solution loss. The bomb was sealed and heated in an oven at 190 °C for 5 days. Thereafter, the bomb was allowed to cool to room temperature and the vials were removed, opened, and placed on a hot plate to evaporate the acids to almost dryness. After addition of 1.5 mL HCl, the vials were placed again in Parr bombs and 3 mL of 6N HCl were added to the Teflon liner. The bombs were heated at 190 °C in an oven for 24 h. This step is required in order to decompose the fluoride that might have formed in the previous steps. After cooling, vials were removed from the bombs and the samples were transferred to the original 15 mL vials, which have a larger surface area that allows faster evaporation. The final steps consisted in evaporating the samples to dryness, fluxing the samples twice with 16N HNO_3, evaporating the sample to dryness after each step. Then, 2 mL deionized water and 2 mL 8N HNO_3 were added to the samples and the closed vials were left overnight on a hot plate at 90 °C. For analysis, the samples were diluted by weight to 100 g (1:2000 dilution) with an internal standard solution containing Ge (10 ppb), In (5 ppb), Tm (5 ppb), and Bi (5 ppb). Calibration was performed with the international rock standards AGV-2, BHVO-2, BCR-2, JB-2, and JR-1.

Samples DANA 46a, ROCA 3J 4a, and ROCA 24J 33 were analyzed by X-ray fluorescence spectrometry and by inductively coupled plasma–mass spectrometry at the GeoAnalytical Laboratory of Washington State University with the methods described in Castillo et al. (2010).

REFERENCES CITED

Albrecht, A., and Goldstein, S., 2000, Effects of basement composition and age on silicic magmas across an accreted terrane-Precambrian crust boundary: Journal of South American Earth Sciences, v. 13, p. 255–273, doi:10.1016/S0895-9811(00)00014-6.

Andersen, T., 2002, Correction of common lead in U-Pb analyses that do not report ^{204}Pb: Chemical Geology, v. 192, p. 59–79, doi:10.1016/S0009-2541(02)00195-X.

Aranda-Gómez, J.J., Henry, C.D., Luhr, J.F., and McDowell, F.W., 1997, Cenozoic volcanism and tectonics in NW Mexico—A transect across the Sierra Madre Occidental volcanic field and observations on extension-related magmatism in the southern Basin and Range and Gulf of California tectonic provinces, *in* Aguirre-Díaz, G.J., et al., eds., Magmatism and tectonics in the central and northwestern Mexico—A selection of the 1997 IAVCEI General Assembly Excursions: México, D.F., Universidad Nacional Autónoma de México, Instituto de Geología, p. 41–84.

Aranda-Gómez, J.J., Henry, C.D., Luhr, J.F., and McDowell, F.W., 2003, Cenozoic volcanic-tectonic development of northwestern Mexicó; a transect across the Sierra Madre Occidental volcanic field and observations on extension-related magmatism in the southern Basin and Range and Gulf of California tectonic provinces, *in* Geologic transects across Cordilleran Mexico: Guidebook for the field trips of the 99th Geological Society of America Cordilleran Section Annual Meeting, Puerto Vallarta, Mexico: Mexico, D.F., Universidad Nacional Autónoma de México, Instituto de Geología, Publicación Especial 1, p. 71–121.

Atwater, T., and Stock, J., 1998, Pacific–North America plate tectonics of the Neogene southwestern United States: An update: International Geology Review, v. 40, p. 375–402, doi:10.1080/00206819809465216.

Axen, G., 1995, Extensional segmentation of the Main Gulf Escarpment, Mexico and United States: Geology, v. 23, p. 515–518, doi:10.1130/0091-7613(1995)023<0515:ESOTMG>2.3.CO;2.

Axen, G., 2003, Late Oligocene(?)–Early Miocene extension in the Bahía de Guadalupe region, north-central Baja California: Geological Society of America, Cordilleran Section, 99th Annual Meeting, abs. 5-7.

Axen, G.J., Taylor, W.J., and Bartley, J.M., 1993, Space-time patterns and tectonic controls of Tertiary extension and magmatism in the Great Basin of the western United States: Geological Society of America Bulletin, v. 105, p. 56–76.

Axen, G., Grove, M., Stockli, D., and Lovera, O., 2000, Thermal evolution of Monte Blanco dome: Low-angle normal faulting during Gulf of California rifting and late Eocene denudation of the eastern Peninsular Ranges: Tectonics, v. 19, p. 197–212, doi:10.1029/1999TC001123.

Bendick, R., McClusky, S., Bilham, R., Asfaw, L., and KLEMPERER, S., 2006, Distributed Nubia–Somalia relative motion and dike intrusion in the Main Ethiopian Rift. Geophysical Journal International, v. 165, p. 303–310. doi:10.1111/j.1365-246X.2006.02904.x

Bennett, S.E.K., Oskin, M.E., Dorsey, R.J., and Iriondo, A., 2012, Volcanic rocks and microfossils confirm a Late Miocene age for marine strata on Isla Tiburón, Gulf of California: Geological Society of America Abstracts with Programs, v. 44, no. 3, p. 19.

Benoit, M., Robles, A.A., and Calmus, T., 2002, Geochemical diversity of Late Miocene volcanism in southern Baja California, Mexico: Implication of mantle and crustal sources during the opening of an asthenospheric window: Journal of Geology, v. 110, p. 627–648, doi:10.1086/342735.

Best, M.G., and Christiansen, E.H., 1991, Limited extension during peak Tertiary volcanism, Great Basin of Nevada and Utah: Journal of Geophysical Research, v. 96, p. 13,509–13,528, doi:10.1029/91JB00244.

Bigioggero, B., Chiesa, S., Zanchi, A., Montrasio, A., and Vezzoli, L., 1995, The Cerro Mencenares volcanic center, Baja California Sur: Source and tectonic control on postsubduction magmatism within the Gulf Rift: Geological Society of America Bulletin, v. 107, p. 1108–1122, doi:10.1130/0016-7606(1995)107<1108:TCMVCB>2.3.CO;2.

Bohannon, R., and Parsons, T., 1995, Tectonic implications of post–30 Ma Pacific and North American relative plate motions: Geological Society of America Bulletin, v. 107, p. 937–959, doi:10.1130/0016-7606(1995)107<0937:TIOPMP>2.3.CO;2.

Bonneau, M., 1970, Una nueva área cretácica fosilífera en el Estado de Sinaloa: Boletín de la Sociedad Geológica Mexicana, v. 32, no. 2, p. 159–167.

Bonner, J.L., and Herrin, E.T., 1999, Surface wave study of the Sierra Madre Occidental of northern Mexico: Seismological Society of America Bulletin, v. 89, p. 1323–1337.

Brothers, D., Harding, A., González-Fernández, A., Holbrook, W.S., Kent, G., Driscoll, N., Fletcher, J., Lizarralde, D., Umhoefer, P., and Axen, G., 2012, Farallon slab detachment and deformation of the Magdalena Shelf, southern Baja California: Geophysical Research Letters, v. 39, no. 9, doi:10.1029/2011GL050828.

Bryan, S.E., Ferrari, L., Reiners, P.W., Allen, C.M., Petrone, C.M., Ramos-Rosique, A., and Campbell, I.H., 2008, New Insights into crustal contributions to large-volume rhyolite generation in the mid-Tertiary Sierra Madre Occidental Province, Mexico, revealed by U-Pb geochronology: Journal of Petrology, v. 49, p. 47–77, doi:10.1093/petrology/egm070.

Bryan, S.E., Orozco-Esquivel, M.T., Ferrari, L., and Lopez-Martinez, M., 2013, Pulling apart the mid to late Cenozoic magmatic record of the Gulf of California: Is there a Comondú Arc?, *in* Gomez-Tuena A., et al., eds., Orogenic andesites and crustal growth: Geological Society of London Special Publication 385, doi:10.1144/SP385.8.

Calais, E., Lesne, O., Déverchère, J., San'kov, V., Lukhnev, A., Miroshnitchenko, A., Buddo, V., Levi, K., Zalutzky, V., Bashkuev, Y., and Bashkuev, Y., 1998, Crustal deformation in the Baikal rift from GPS measurements: Geophysical Research Letters, v. 25, no. 21, p. 4003–4006, doi:10.1029/1998GL900067.

Calmus, T., Aguillón-Robles, A., Maury, R.C., Bellon, H., Benoit, M., Cotten, J., Bourgois, J., and Michaud, F., 2003, Spatial and temporal evolution of basalts and magnesian andesites ("bajaites") from Baja California, Mexico: The role of slab melts: Lithos, v. 66, p. 77–105, doi:10.1016/S0024-4937(02)00214-1.

Calmus, T., Pallares, C., Maury, R.C., Aguillón-Robles, A., Bellon, H., Benoit, M., and Michaud, F., 2010, Volcanic markers of the post-subduction evolution of Baja California and Sonora, Mexico: Slab tearing versus lithospheric rupture of the Gulf of California: Pure and Applied Geophysics, v. 168, p. 1303–1330, doi:10.1007/s00024-010-0204-z.

Cameron, K.L., Nimz, G.J., Kuentz, D., Niemeyer, S., and Gunn, S., 1989, Southern Cordilleran basaltic andesite suite, southern Chihuahua, Mexico: A link between Tertiary continental arc and flood basalt magmatism in North America: Journal of Geophysical Research, v. 94, p. 7817–7840, doi:10.1029/JB094iB06p07817.

Castillo, P.R., Clague, D.A., Davis, A.S., and Lonsdale, P.F., 2010, Petrogenesis of Davidson Seamount lavas and its implications for fossil spreading center and intraplate magmatism in the eastern Pacific: Geochemistry Geophysics Geosystems, v. 11, no. 2, doi:10.1029/2009GC002992.

Charlier, B., Wilson, C., Lowenstern , J.B., Blake, S., Van Calsteren, P.W., and Davidson, J.P., 2005, Magma generation at a large, hyperactive silicic volcano (Taupo, New Zealand) revealed by U–Th and U–Pb systematics in zircons: Journal of Petrology, v. 46, p. 3–32.

Conly, A.G., Brenan, J.M., Bellon, H., and Scott, S.D., 2005, Arc to rift transitional volcanism in the Santa Rosalía region, Baja California Sur, Mexico: Journal of Volcanology and Geothermal Research, v. 142, p. 303–341, doi:10.1016/j.jvolgeores.2004.11.013.

Couch, R.W., Ness, G.E., Sanchez-Zamora, O., Calderon-Riveroll, G., Doguin, P., Plawman, T., Coperude, S., Huehn, B., and Gumma, W., 1991, Gravity anomalies and crustal structure of the Gulf and Peninsular Province of the Californias, *in* Dauphin, J.P., and Simoneit, B.R.T., eds., The Gulf and the Peninsular Province of the Californias: American Association of Petroleum Geologists Memoir 47, p. 47–70.

Cuéllar-Cárdenas, M.A., Nieto-Samaniego, A.F., Levresse, G., Alaniz Alvarez, S.A., Solari, L., Ortega-Obregón, C., and López-Martínez, M., 2012, Límites temporales de la deformación por acortamiento Laramide en el centro de México: Revista Mexicana de Ciencias Geológicas, v. 29, p. 179–203.

Damon, P.E., Nieto-Obregón, J., and Delgado-Argote, L., 1979, Un plegamiento neogénico en Nayarit y Jalisco y evolución geomórfica del Río Grande de Santiago: Asociación Ingenieros de Minas, Metalurgistas y Geólogos de México, Memoria Técnica, v. XIII, p. 156–191.

DeMets, C., 1995, A reappraisal of seafloor spreading lineations in the Gulf of California: Implications for the transfer of Baja California to the Pacific plate and estimates of Pacific–North America motion: Geophysical Research Letters, v. 22, p. 3545–3548, doi:10.1029/95GL03323.

Dickinson, W.R., 2002, The Basin and Range Province as a composite extensional domain: International Geology Review, v. 44, p. 1–38, doi:10.2747/0020-6814.44.1.1.

Dickinson, W.R., and Snyder, W.S., 1978, Plate tectonics of the Laramide orogeny. Geological Society of America Memoir 151, p. 355–366.

Dorsey, R.J., and Burns, B., 1994, Regional stratigraphy, sedimentology, and tectonic significance of Oligocene-Miocene sedimentary and volcanic rocks, northern Baja California, Mexico. Sedimentary Geology, v. 88, p. 231–251.

Drake, W., 2005, Structural analysis, stratigraphy, and geochronology of the San José Island accommodation zone, Baja California Sur, Mexico [M.S. thesis]: Flagstaff, Northern Arizona University, 271 p.

Duque-Trujillo, J., Ferrari, L., Orozco-Esquivel, T., López Martínez, M., and Lonsdale, P., 2012, Rapid exhumation of Early to Middle Miocene intrusive rocks in the southern Gulf of California: The early stages of

continental breakup. Geological Society of America Abstracts with Programs, v. 44, no. 3, p. 14.

Duque-Trujillo, J., Ferrari, L., López Martínez, M., Orozco-Esquivel, T., and Lonsdale, P., 2013, Early to Middle Miocene syn-extensional magmatism in the southern Gulf of California: Geological Society of America Abstracts with Programs, v. 45, no. 6, p. 15.

Enríquez, E., and Rivera, R., 2001, Timing of magmatic and hydrothermal activity in the San Dimas District, Durango, Mexico, *in* Albinson, T., and Nelson, C.E., eds., New mines and mineral discoveries in Mexico and Central America: Society of Economic Geologists Special Publication 8, p. 33–38.

Faure, G., and Mensing, T.M., 2005, Isotopes; principles and applications: New York, Wiley, 897 p.

Fernandes, R.M.S., Ambrosius, B.A.C., Noomen, R., Bastos, L., Combrinck, L., Miranda, J.M., and Spakman, W., 2004, Angular velocities of Nubia and Somalia from continuous GPS data: Implications on present-day relative kinematics: Earth and Planetary Science Letters, v. 222, p. 197–208, doi:10.1016/j.epsl.2004.02.008.

Ferrari, L., 1995, Miocene shearing along the northern boundary of the Jalisco block and the opening of the southern Gulf of California: Geology, v. 23, p. 751–754, doi:10.1130/0091-7613(1995)023<0751:MSATNB>2.3.CO;2.

Ferrari, L., 2004, Slab detachment control on mafic volcanic pulse and mantle heterogeneity in central Mexico: Geology, v. 32, p. 77–80, doi:10.1130/G19887.1.

Ferrari, L., Conticelli, S., Vaggelli, G., Petrone, C.M., and Manetti, P., 2000a, Late Miocene volcanism and intra-arc tectonics during the early development of the Trans-Mexican Volcanic Belt: Tectonophysics, v. 318, p. 161–185, doi:10.1016/S0040-1951(99)00310-8.

Ferrari, L., Pasquaré, G., Venegas Salgado, S., and Romero-Rios, F., 2000b, Geology of the western Mexican volcanic belt and adjacent Sierra Madre Occidental and Jalisco block, *in* Delgado-Granados, H., et al., eds., Cenozoic tectonics and volcanism of Mexico: Geological Society of America Special Paper 334, p. 65–83, doi:10.1130/0-8137-2334-5.65.

Ferrari, L., López-Martínez, M., and Rosas-Elguera, J., 2002, Ignimbrite flare-up and deformation in the southern Sierra Madre Occidental, western Mexico—Implications for the late subduction history of the Farallon Plate: Tectonics, v. 21, 1035, doi:10.1029/2001TC001302.

Ferrari, L., Valencia-Moreno, M., and Bryan, S., 2007, Magmatism and tectonics of the Sierra Madre Occidental and its relation with the evolution of the western margin of North America, *in* Alaniz-Álvarez, S.A., and Nieto-Samaniego, A.F., eds., Geology of México: Celebrating the Centenary of the Geological Society of México: Geological Society of America Special Paper 422, p. 1–39, doi:10.1130/2007.2422(01).

Ferrari, L., Orozco-Esquivel, T., Manea, V., and Manea, M., 2012, The dynamic history of the Trans-Mexican Volcanic Belt and the Mexico subduction zone: Tectonophysics, v. 522–523, p. 122–149, doi:10.1016/j.tecto.2011.09.018.

Fletcher, J.M., Kohn, B.P., Foster, D.A., and Gleadow, A.J.W., 2000, Heterogeneous Neogene cooling and exhumation of the Los Cabos block, southern Baja California: Evidence from fission-track thermochronology: Geology, v. 28, p. 107–110, doi:10.1130/0091-7613(2000)28<107:HNCAEO>2.0.CO;2.

Fletcher, J.M., Martin-Atienza, B., Axen, G.J., González-Fernández, A., Hollbrook, W.S., Kent, G., Lizarralde, D., Harding, A., and Umhoefer, P., 2003, Palinspastic reconstructions of the Gulf of California based on Airy isostatic profiles: Evidence for one kinematic phase of Neogene shearing: American Geophysical Union Fall Meeting, abs. T32D-06.

Fletcher, J.M., Grove, M., Kimbrough, D., Lovera, O., and Gehrels, G.E., 2007, Ridge-trench interactions and the Neogene tectonic evolution of the Magdalena Shelf and southern Gulf of California; insights from detrital zircon U-Pb ages from the Magdalena Fan and adjacent areas: Geological Society of America Bulletin, v. 119, p. 1313–1336, doi:10.1130/ B26067.1.

Frey, H.M., Lange, R.A., Hall, C.M., Delgado Granados, H., and Carmichael, I.S.E., 2007, A Pliocene ignimbrite flare-up along the Tepic-Zacoalco rift: Evidence for the initial stages of rifting between the Jalisco block (Mexico) and North America: Geological Society of America Bulletin, v. 119, p. 49–64, doi:10.1130/B25950.1.

Gans, P., 1997, Large-magnitude Oligo-Miocene extension in southern Sonora: Implications for the tectonic evolution of northwest Mexico: Tectonics, v. 16, p. 388–408, doi:10.1029/97TC00496.

Gastil, R.G., 1975, Plutonic zones in the Peninsular Ranges of southern California and northern Baja California: Geology, v. 3, p. 361–363, doi:10.1130/0091-7613(1975)3<361:PZITPR>2.0.CO;2.

Gastil, R.G., Lemone, D.V., and Stewart, W.J., 1973, Permian fusilinids from near San Felipe, Baja California: American Association of Petroleum Geologists Bulletin, v. 57, p. 746–747.

Gastil, R.G., Phillips, R.P., and Allison, E.C., 1975, Reconnaissance geology of the state of Baja California: Geological Society of America Memoir 140, 201 p., doi:10.1130/MEM140-p1.

Gastil, R.G., Krummenacher, D., and Minch, J., 1979, The record of Cenozoic volcanism around the Gulf of California: Geological Society of America Bulletin, v. 90, p. 839–857, doi:10.1130/0016-7606(1979)90<839:TROCVA>2.0.CO;2.

Gastil, R.G., Miller, R., Anderson, P., Crocker, J., Campbell, M., Buch, P., Lothringer, C., Leier- Engelhardt, P., DeLattre, M., Hobbs, J., and Roldán-Quintana, J., 1991, The relation between the Paleozoic strata on opposite sides of the Gulf of California, *in* Jacques-Ayala, C., ed., Studies of Sonoran geology: Geological Society of America Special Paper 254, p. 7–18, doi:10.1130/SPE254-p7.

Gastil, R.G., Neuhaus, J., Cassidy, M., Smith, J.T., Ingle, J.C., and Krummenacher, D., 1999, Geology and paleontology of southwestern Isla Tiburón, Sonora, Mexico: Revista Mexicana de Ciencias Geológicas, v. 16, p. 1–34.

Goguitchaichvili, A., Alva-Valdivia, L.M., Rosas-Elguera, J., Urrutia-Fucugauchi, J., Cervantes, M.A., and Caballero, C., 2002, Magnetic mineralogy, paleomagnetism, and magnetostratigraphy of Nayarit volcanic formations, western Mexico: A pilot study: International Geology Review, v. 44, p. 264–276, doi:10.2747/0020-6814.44.3.264.

González León, C.M., McIntosh, W.C., Lozano-Santacruz, R., Valencia-Moreno, M., Amaya-Martínez, R., and Rodríguez-Castañeda, J.L., 2000, Cretaceous and Tertiary sedimentary, magmatic, and tectonic evolution of north-central Sonora (Arizpe and Bacanuchi quadrangles), northwest Mexico: Geological Society of America Bulletin, v. 112, p. 600–610, doi:10.1130/0016-7606(2000)112<600:CATSMA>2.0.CO;2.

Harry, D.L., Sawyer, D.S., and Leeman, W.P., 1993, The mechanics of continental extension in western North America: Implications for the magmatic and structural evolution of the Great Basin: Earth and Planetary Science Letters, v. 117, p. 59–71, doi:10.1016/0012-821X(93)90117-R.

Hausback, B.P., 1984, Cenozoic volcanic and tectonic evolution of Baja California Sur, Mexico, *in* Frizzel, V.A., Jr., ed., Geology of the Baja California Peninsula: Pacific Section, Society of Economic Paleontologists and Mineralogists, p. 219–236.

Helenes, J., Carreño, A.L., and Carrillo, R.M., 2009, Middle to late Miocene chronostratigraphy and development of the northern Gulf of California: Marine Micropaleontology, v. 72, p. 10–25, doi:10.1016/j.marmicro.2009.02.003.

Henry, C.D., 1989, Late Cenozoic Basin and Range structure in western Mexico adjacent to the Gulf of California: Geological Society of America Bulletin, v. 101, p. 1147–1156, doi:10.1130/0016-7606(1989)101<1147:LCBARS>2.3.CO;2.

Henry, C.D., and Aranda-Gomez, J.J., 1992, The real southern Basin and Range: Mid-to late Cenozoic extension in Mexico: Geology, v. 20, p. 701–704, doi:10.1130/0091-7613(1992)020<0701:TRSBAR>2.3.CO;2.

Henry, C.D., and Aranda-Gómez, J.J., 2000, Plate interactions control middle-late Miocene, proto-Gulf and Basin and Range extension in the southern Basin and Range: Tectonophysics, v. 318, p. 1–26, doi:10.1016/S0040-1951(99)00304-2.

Henry, C.D., and Fredrikson, G., 1987, Geology of part of southern Sinaloa, Mexico, adjacent to the Gulf of California: Geological Society of America Map and Chart Series MCH063, 1 sheet, 14 p.

Henry, C.D., McDowell, F.W., and Silver, L.T., 2003, Geology and geochronology of granitic batholithic complex, Sinaloa, México: Implications for Cordilleran magmatism and tectonics, *in* Johnson, S.E., et al., eds., Tectonic evolution of northwestern México and the southwestern USA: Geological Society of America Special Paper 374, p. 237–273, doi:10.1130/0-8137-2374-4.237.

Horner, J.T., and Enríquez, E., 1999, Epithermal precious metal mineralization in a strike-slip corridor: The San Dimas district, Durango, Mexico: Economic Geology and the Bulletin of the Society of Economic Geologists, v. 94, p. 1375–1380, doi:10.2113/gsecongeo.94.8.1375.

Houseman, G.A., McKenzie, D.P., and Molnar, P., 1981, Convective instability of a thickened boundary layer and its relevance for the thermal evolution of continental convergent belts: Journal of Geophysical Research, v. 86, p. 6115–6132, doi:10.1029/JB086iB07p06115.

Iriondo, A., Kunk, M.J., Winick, J., and CRM, 2003, $^{40}Ar/^{39}Ar$ dating studies of minerals and rocks in various areas in Mexico: USGS/CRM scientific collaboration (Part 1): U.S. Geological Survey Open-File Report 03-020, 79 p., http://pubs.usgs.gov/of/2003/ofr-03-020/OFR-03-020-508eng.pdf.

Iriondo, A., Kunk, M.J., Winick, J., and CRM, 2004, $^{40}Ar/^{39}Ar$ dating studies of minerals and rocks in various areas in Mexico: USGS/CRM scientific collaboration (Part II): U.S. Geological Survey Open-File Report 04-1444, 46 p., http://pubs.usgs.gov/of/2004/1444/.

Irvine, T., and Baragar, W., 1971, A guide to the chemical classification of the common volcanic rocks: Canadian Journal of Earth Sciences, v. 8, p. 523–548, doi:10.1139/e71-055.

Jackson, J., 2002, Strength of the continental lithosphere: Time to abandon the jelly sandwich?: GSA Today, v. 12, p. 4–9, doi:10.1130/1052-5173(2002)012<0004:SOTCLT>2.0.CO;2.

Keppie, J., Dostal, J., Miller, B., Ortega-Rivera, A., Roldán-Quintana, J., and Lee, J.W.K., 2006, Geochronology and geochemistry of the Francisco Gneiss: Triassic continental rift tholeiites on the Mexican margin of Pangea metamorphosed and exhumed in a Tertiary core complex: International Geology Review, v. 48, p. 1–16, doi:10.2747/0020-6814.48.1.1.

Kuiper, K.F., Deino, A., Hilgen, F.J., Krijgsman, W., Renne, P.R., and Wijbrans, J.R., 2008, Synchronizing rock clocks of Earth history: Science, v. 320, p. 500–504, doi:10.1126/science.1154339.

Le Bas, M., Le Maitre, R., Streckeisen, A., and Zanettin, B., 1986, A chemical classification of volcanic rocks on the total alkali-silica diagram: Journal of Petrology, v. 27, p. 745–750, doi:10.1093/petrology/27.3.745.

Lee, J., Miller, M.M., Crippen, R., Hacker, B., and Ledesma-Vázquez, J., 1996, Middle Miocene extension in the Gulf Extensional Province, Baja California: Evidence from the southern Sierra Juarez: Geological Society of America Bulletin, v. 108, p. 505–525, doi:10.1130/0016-7606(1996)108<0505:MMEITG>2.3.CO;2.

Leeman, W.P., and Harry, D.L., 1993, A binary source model for extension-related magmatism in the Great Basin, western North America: Science, v. 262, p. 1550–1554, doi:10.1126/science.262.5139.1550.

Lizarralde, D., Axen, G.J., Brown, H.E., Fletcher, J.M., González-Fernández, A., Harding, A.J., Holbrook, W.S., Kent, G.M., Paramo, P., Sutherland, F., and Umhoefer, P.J., 2007, Variable styles of rifting in the Gulf of California: Nature, v. 448, p. 466–469, doi:10.1038/nature06035.

Lonsdale, P., 1991, Structural patterns of the Pacific floor offshore of peninsular California, *in* Dauphin, J.P., and Simoneit, B.R.T., eds., The Gulf and the Peninsular Province of the Californias: American Association of Petroleum Geologists Memoir 47, p. 87–125.

Lovera, O.M., Grove, M., Kimbrough, D.L., and Peterman, E.M., 2010, Implications of Eocene subduction refrigeration of southern Baja California for the late

Miocene geotherm during initial rifting of the Gulf of California: Geological Society of America Abstracts with Programs, v. 42, no. 5, p. 577.

Loza-Aguirre, I., Nieto-Samaniego, Á., Alaniz Alvarez, S.A., and Ortega-Obregón, C., 2012, Cenozoic volcanism and extension in northwestern Mesa Central, Durango, México: Boletín de la Sociedad Geológica Mexicana, v. 64, no. 2, p. 243–263.

Lozano-Santa Cruz, R., Verma, S.P., Girón, P., Velasco-Tapia, F., Morán-Zenteno, D., Viera, F., and Chávez, G., 1995, Calibración preliminar de fluorescencia de rayos X para análisis cuantitativo de elementos mayores en rocas ígneas: Actas INAGEQ, v. 1, p. 203–208.

Ludwig, K.R., 2008, User's manual for Isoplot 3.7. A geochronological toolkit for Microsoft Excel: Berkeley Geochronology Center Special Publication 4, 77 p.

Luhr, J., Henry, C., and Housh, T., 2001, Early extension and associated mafic alkalic volcanism from the southern Basin and Range Province: Geology and petrology of the Rodeo and Nazas volcanic fields, Durango, México: Geological Society of America Bulletin, v. 113, p. 760–773, doi:10.1130/0016-7606(2001)113<0760:EEAAMA>2.0.CO;2.

Mark, C., Gupta, S., Carter, A., Mark, D., Gautheron, C., and Martin-Barajas, A., 2012, Temporal constraints on the landscape response to rifting in the Loreto region of Baja California Sur, Mexico: Geological Society of America Abstracts with Programs, v. 44, no. 3, p. 6.

Martín-Barajas, A., 2001, Late Neogene stratigraphy and tectonic control on facies evolution in the Laguna Salada Basin, northern Baja California, Mexico: Sedimentary Geology, v. 144, p. 5–35, doi:10.1016/S0037-0738(01)00133-6.

Martín-Barajas, A., Stock, J.M., Layer, P., Hausback, B., Renne, P., and López-Martínez, M., 1995, Arc-rift transition volcanism in the Puertecitos volcanic province, northeastern Baja California, Mexico: Geological Society of America Bulletin, v. 107, p. 407–424, doi:10.1130/0016-7606(1995)107<0407:ARTVIT>2.3.CO;2.

Martín-Barajas, A., González Escobar, M., Fletcher, J.M., Pacheco, M., Oskin, M., and Dorsey, R., 2013, Thick deltaic sedimentation and detachment faulting delay the onset of continental rupture in the northern Gulf of California: Analysis of seismic reflection profiles: Tectonics, doi:10.1002/tect.20063.

Martínez-Gutiérrez, G., and Sethi, P.S., 1997, Miocene–Pleistocene sediments within the San José del Cabo Basin, Baja California Sur, Mexico, *in* Johnson, M.E., and Ledesma-Vázquez, J., eds., Pliocene carbonates and related facies flanking the Gulf of California, Baja California, Mexico: Geological Society of America Special Paper 318, p. 141–166, doi:10.1130/0-8137-2318-3.141.

McDougall, K.A., Poore, R.Z., and Matti, J.C., 1999, Age and paleoenvironment of the Imperial Formation near San Gorgonio Pass, southern California: Journal of Foraminiferal Research, v. 29, p. 4–25.

McDowell, F., and Keizer, R.P., 1977, Timing of mid-Tertiary volcanism in the Sierra Madre Occidental between Durango city and Mazatlán, Mexico: Geological Society of America Bulletin, v. 88, p. 1479–1487, doi:10.1130/0016-7606(1977)88<1479:TOMVIT>2.0.CO;2.

McDowell, F.W., and Mauger, R.L., 1994, K-Ar and U-Pb zircon chronology of Late Cretaceous and Tertiary magmatism in central Chihuahua State, Mexico: Geological Society of America Bulletin, v. 106, p. 118–132, doi:10.1130/0016-7606(1994)106<0118:KAAUPZ>2.3.CO;2.

McDowell, F.W., and McIntosh, W.C., 2012, Timing of intense magmatic episodes in the northern and central Sierra Madre Occidental, western Mexico: Geosphere, v. 8, p. 1505–1526, doi:10.1130/GES00792.1.

McDowell, F., Roldán-Quintana, J., and Amaya-Martínez, R., 1997, Interrelationship of sedimentary and volcanic deposits associated with Tertiary extension in Sonora, Mexico: Geological Society of America Bulletin, v. 109, p. 1349–1360, doi:10.1130/0016-7606(1997)109<1349:IOSAVD>2.3.CO;2.

McQuarrie, N., and Oskin, M., 2010, Palinspastic restoration of NAVDat and implications for the origin of magmatism in southwestern North America: Journal of Geophysical Research, v. 115, no. B10, doi:10.1029/2009JB006435.

Miller, C.F., Meschter McDowell, S., and Mapes, R.W., 2003, Hot and cold granites? Implications of zircon saturation temperatures and preservation of inheritance: Geology, v. 31, p. 529–532, doi:10.1130/0091-7613(2003)031<0529:HACGIO>2.0.CO;2.

Miller, N.C., and Lizarralde, D., 2013, Thick evaporites and early rifting in the Guaymas Basin, Gulf of California: Geology, v. 41, p. 283–286, doi:10.1130/G33747.1.

Mora-Alvarez, G., and McDowell, F.W., 2000, Miocene volcanism during late subduction and early rifting in the Sierra Santa Ursula of western Sonora, Mexico, *in* Delgado-Granados, H., et al., eds., Cenozoic tectonics and volcanism of Mexico: Geological Society of America Special Paper 334, p. 123–141, doi:10.1130/0-8137-2334-5.123.

Mora-Klepeis, G., and McDowell, F., 2004, Late Miocene calc-alkalic volcanism in northwestern Mexico: An expression of rift or subduction-related magmatism?: Journal of South American Earth Sciences, v. 17, p. 297–310, doi:10.1016/j.jsames.2004.08.001.

Mori, L., Gomez-Tuena, A., Cai, Y., and Goldstein, S., 2007, Effects of prolonged flat subduction on the Miocene magmatic record of the central Trans-Mexican Volcanic Belt: Chemical Geology, v. 244, p. 452–473, doi:10.1016/j.chemgeo.2007.07.002.

Mullan, H.S., 1978, Evolution of the Nevadan orogen in northwestern Mexico: Geological Society of America Bulletin, v. 89, p. 1175–1188, doi:10.1130/0016-7606(1978)89<1175:EOPOTN>2.0.CO;2.

Murray, B.P., Busby, C.J., Ferrari, L., and Solari, L., 2013, Synvolcanic crustal extension during the mid-Cenozoic ignimbrite flare-up in the northern Sierra Madre Occidental, Mexico: Geosphere, doi: 10.1130/GES862.1.

Nourse, J., Anderson, T., and Silver, L., 1994, Tertiary metamorphic core complexes in Sonora, northwestern Mexico: Tectonics, v. 13, p. 1161–1182, doi:10.1029/93TC03324.

Ortega-Rivera, A., 2003, Geochronological constraints on the tectonic history of the Peninsular Ranges batholith of Alta and Baja California: Tectonic implications for western Mexico, *in* Johnson, S.E., et al., eds., Tectonic evolution of northwestern Mexico and the southwestern USA: Geological Society of America Special Paper 374, p. 297–336, doi:10.1130/0-8137-2374-4.297.

Oskin, M., and Stock, J., 2003, Pacific–North America plate motion and opening of the Upper Delfín basin, northern Gulf of California, Mexico: Geological Society of America Bulletin, v. 115, p. 1173–1190, doi:10.1130/B25154.1.

Oskin, M.E., Stock, J.M., and Martín-Barajas, A., 2001, Rapid localization of Pacific–North America plate motion in the Gulf of California: Geology, v. 29, p. 459–462, doi:10.1130/0091-7613(2001)029<0459:RLOPNA>2.0.CO;2.

Pallares, C., Maury, R.C., Bellon, H., Royer, J.-Y., Calmus, T., Aguillón-Robles, A., Cotten, J., Benoit, M., Michaud, F., and Bourgois, J., 2007, Slab-tearing following ridge-trench collision: Evidence from Miocene volcanism in Baja California, México: Journal of Volcanology and Geothermal Research, v. 161, p. 95–117, doi:10.1016/j.jvolgeores.2006.11.002.

Pallares, C., Bellon, H., Benoit, M., Maury, R.C., Aguillón-Robles, A., Calmus, T., and Cotten, J., 2008, Temporal geochemical evolution of Neogene volcanism in northern Baja California (27°–30° N): Insights on the origin of post-subduction magnesian andesites: Lithos, v. 105, p. 162–180, doi:10.1016/j.lithos.2008.03.004.

Páramo, P., Holbrook, W.S., Brown, H.E., Lizarralde, D., Fletcher, J., Umhoefer, P., Kent, G., Harding, A., Gonzalez, A., and Axen, G., 2008, Seismic structure of the southern Gulf of California from Los Cabos block to the East Pacific Rise: Journal of Geophysical Research, v. 113, no. B3, doi:10.1029/2007JB005113.

Paton, C., Woodhead, J.D., Hellstrom, J.C., Hergt, J.M., Greig, A., and Maas, R., 2010, Improved laser ablation U-Pb zircon geochronology through robust downhole fractionation correction: Geochemistry Geophysics Geosystems, v. 11, Q0AA06, doi:10.1029/2009GC002618.

Peacock, S., and Wang, K., 1999, Seismic consequences of warm versus cool subduction metamorphism: Examples from southwest and northeast Japan: Science, v. 286, p. 937–939, doi:10.1126/science.286.5441.937.

Persaud, P., Pérez-Campos, X., and Clayton, R.W., 2007, Crustal thickness variations in the margins of the Gulf of California from receiver functions: Geophysical Journal International, v. 170, p. 687–699, doi:10.1111/j.1365-246X.2007.03412.x.

Petrus, J.A., and Kamber, B.S., 2012, VizualAge: A novel approach to laser ablation ICP-MS U-Pb geochronology data reduction: Geostandards and Geoanalytical Research, v. 36, p. 247–270, doi:10.1111/j.1751-908X.2012.00158.x.

Piñero-Lajas, D., 2009, Seismic reflection and ^{40}Ar-^{39}Ar dating of continental basement in the western margin of Farallon basin (southern Gulf of California, Mexico) [M.S. thesis]: Ensenada, Mexico, Centro de Investigación Científica y de Educación Superior de Ensenada, 155 p.

Plattner, C., Malservisi, R., and Govers, R., 2009, On the plate boundary forces that drive and resist Baja California motion: Geology, v. 37, p. 359–362, doi:10.1130/G25360A.1.

Pompa-Mera, V., Schaaf, P., Hernández-Treviño, T., Weber, B., Solís-Pichardo, G., Villanueva-Lascurain, D., and Layer, P., 2013, Geology, geochronology, and geochemistry of Isla María Madre, Nayarit, Mexico: Revista Mexicana de Ciencias Geológicas, v. 30, p. 1–23.

Ramos-Rosique, A., 2013, Timing and evolution of Late Oligocene to early Miocene magmatism and epithermal mineralization in the central Bolaños Graben, southern Sierra Madre Occidental, México [Ph.D. thesis]: London, UK, Kingston University, 215 p.

Renne, P.R., Swisher, C.C., Deino, A.L., Karner, D.B., Owens, T.L., and De Paolo, D.J., 1998, Intercalibration of standards, absolute ages and uncertainties in ^{40}Ar/^{39}Ar dating: Chemical Geology, v. 145, p. 117–152, doi:10.1016/S0009-2541(97)00159-9.

Righter, K., Carmichael, I.S.E., Becker, T.A., and Renne, P.R., 1995, Pliocene-Quaternary volcanism and faulting at the intersection of the Gulf of California and the Mexican Volcanic Belt: Geological Society of America Bulletin, v. 107, p. 612–626, doi:10.1130/0016-7606(1995)107<0612:PQVAFA>2.3.CO;2.

Roddick, J.C., 1983, High-precision intercalibration of ^{40}Ar-^{39}Ar standards: Geochimica et Cosmochimica Acta, v. 47, p. 887–898, doi:10.1016/0016-7037(83)90154-0.

Roldán-Quintana, J., Mora-Klepeis, G., Calmus, T., Valencia-Moreno, M., and Lozano-Santacruz, R., 2004, El graben de Empalme, Sonora, México: magmatismo y tectónica extensional asociados a la ruptura inicial del Golfo de California: Revista Mexicana de Ciencias Geológicas, v. 21, p. 320–334.

Ruiz, J., Patchett, P., and Arculus, R.J., 1988, Nd-Sr isotope composition of lower crustal xenoliths—Evidence for the origin of mid-Tertiary felsic volcanics in Mexico: Contributions to Mineralogy and Petrology, v. 99, p. 36–43, doi:10.1007/BF00399363.

Ruiz, J., Patchett, P., and Arculus, R.J., 1990, Nd-Sr isotopic compositions of lower crustal xenoliths—Evidence for the origin of mid-Tertiary felsic volcanics in Mexico: Reply: Contributions to Mineralogy and Petrology, v. 104, p. 615–618, doi:10.1007/BF00306669.

Savage, B., and Wang, Y., 2012, Integrated model of the crustal structure in the Gulf of California Extensional Province: Seismological Society of America Bulletin, v. 102, p. 878–885, doi:10.1785/0120110196.

Sawlan, M.G., 1991, Magmatic evolution of the Gulf of California rift, *in* Dauphin, J.P., and Simoneit, B.R., eds., The Gulf and Peninsular Province of the Californias: American Association of Petroleum Geologists Memoir 47, p. 301–369.

Sawlan, M.G., and Smith, J.G., 1984, Petrologic characteristics, age and tectonic setting of Neogene volcanic rocks in northern Baja California Sur, Mexico, *in* Frizzell, V.A., Jr., ed., Geology of the Baja California Peninsula: Pacific Section, Society of Economic Paleontologists and Mineralogists, p. 237–251.

Schaaf, P., Böhnel, H., and Pérez-Venzor, J., 2000, Pre-Miocene palaeogeography of the Los Cabos block, Baja California Sur: Geochronological and palaeomagnetic constraints: Tectonophysics, v. 318, p. 53–69, doi:10.1016/S0040-1951(99)00306-6.

Schmitt, A., Stockli, D.F., and Hausback, B.P., 2006, Eruption and magma crystallization ages of Las Tres Vírgenes (Baja California) constrained by combined $^{230}Th/^{238}U$ and (U-Th)/He dating of zircon: Journal of Volcanology and Geothermal Research, v. 158, p. 281–295, doi:10.1016/j.jvolgeores.2006.07.005.

Schmitt, A.K., Stockli, D.F., Lindsay, J.M., Robertson, R., Lovera, O., and Kislitsyn, R., 2010, Episodic growth and homogenization of plutonic roots in arc volcanoes from combined U-Th and (U-Th)/He zircon dating: Earth and Planetary Science Letters, v. 295, p. 91–103, doi:10.1016/j.epsl.2010.03.028.

Schwarz, W.H., and Trieloff, M., 2007, Intercalibration of ^{40}Ar-^{39}Ar age standards NL-25, HB3gr hornblende, GA1550, SB-3, HD-B1 biotite and BMus/2 muscovite: Chemical Geology, v. 242, p. 218–231, doi:10.1016/j.chemgeo.2007.03.016.

Seiler, C., Fletcher, J.M., Kohn, B.P., Gleadow, A.J.W., and Raza, A., 2011, Low-temperature thermochronology of northern Baja California, Mexico: Decoupled slip-exhumation gradients and delayed onset of oblique rifting across the Gulf of California: Tectonics, v. 30, TC3004, doi:10.1029/2009TC002649.

Servicio Geológico Mexicano, 1999a, Carta Geológico-Minera Pericos, G13-7 Sinaloa, Durango y Chihuahua: Pachuca, México, Instituto Nacional de Estadística, Geografía e Informática (INEGI), scale 1:250,000.

Servicio Geológico Mexicano, 1999b, Carta Geológico-Minera Escuinapa, F13-5 Nayarit, Durango, Zacatecas, Sinaloa y Jalisco: Aguascalientes, México, Instituto Nacional de Estadística, Geografía e Informática (INEGI), scale 1:250,000.

Servicio Geológico Mexicano, 2000, Carta Geológico-Minera Huatabampo G 12-6, Sonora, Sinaloa, Chihuahua: Pachuca, México, Instituto Nacional de Estadística, Geografía e Informática (INEGI), scale 1:250,000.

Sláma, J., and 13 others, 2008, Plešovice zircon—A new natural reference material for U-Pb and Hf isotopic microanalysis: Chemical Geology, v. 249, p. 1–35, doi:10.1016/j.chemgeo.2007.11.005.

Solari, L.A., Gómez-Tuena, A., Bernal, J.P., Pérez-Arvizu, O., and Tanner, M., 2010, U-Pb zircon geochronology by an integrated LA-ICPMS microanalytical workstation: Achievements in precision and accuracy: Geostandards and Geoanalytical Research, v. 34, p. 5–18, doi:10.1111/j.1751-908X.2009.00027.x.

Solé, J., Salinas, J.C., Gonzalez-Torres, E., and Cendejas Cruz, J.E., 2007, Edades K/Ar de 54 rocas ígneas y metamórficas del occidente, centro y sur de México: Revista Mexicana de Ciencias Geológicas, v. 24, p. 104–119.

Sonder, L.J., and Jones, C.H., 1999, Western United States extension: How the west was widened: Annual Review of Earth and Planetary Sciences, v. 27, no. 1, p. 417–462.

Steiger, R.H., and Jäger, E., 1977, Subcommission on Geochronology: Convention on the use of decay constants in geo and cosmochronology: Earth and Planetary Science Letters, v. 36, p. 359–362, doi:10.1016/0012-821X(77)90060-7.

Stewart, J.H., 1978, Basin-range structure in western North America: A review: Geological Society of America, v. 152, p. 1–32, doi:10.1130/MEM152-p1.

Stock, J.M., and Hodges, K.V., 1989, Pre-Pliocene extension around the Gulf of California and the transfer of Baja California to the Pacific plate: Tectonics, v. 8, p. 99–115, doi:10.1029/TC008i001p00099.

Sun, S.S., and McDonough, J.D., 1989, Chemical and isotopic systematics of oceanic basalts: implications for mantle compositions and process, *in* Saunders, A.D., and Norry, M.J., eds., Magmatism in the ocean basins: Geological Society of London Special Publication 42, p. 313–345, doi:10.1144/GSL.SP.1989.042.01.19.

Sutherland, F.H., Kent, G.M., Harding, A.J., Umhoefer, P.J., Driscoll, N.W., Lizarralde, D., Fletcher, J.M., Axen, G.J., Holbrook, W.S., González-Fernández, A., and Lonsdale, P., 2012, Middle Miocene to early Pliocene oblique extension in the southern Gulf of California: Geosphere, v. 8, p. 752–770, doi:10.1130/GES00770.1.

Syracuse, E.M., and Abers, G.A., 2006, Global compilation of variations in slab depth beneath arc volcanoes and implications: Geochemistry Geophysics Geosystems, v. 7, no. 5, doi:10.1029/2005GC001045.

Tian, L., Castillo, P.R., Lonsdale, P.F., Hahm, D., and Hilton, D.R., 2011, Petrology and Sr-Nd-Pb-He isotope geochemistry of postspreading lavas on fossil spreading axes off Baja California Sur, Mexico: Geochemistry Geophysics Geosystems, v. 12, doi:10.1029/2010GC003319.

Till, C.B., Gans, P.B., Spera, F.J., MacMillan, I., and Blair, K.D., 2009, Perils of petrotectonic modeling: A view from southern Sonora, Mexico: Journal of Volcanology and Geothermal Research, v. 186, p. 160–168, doi:10.1016/j.jvolgeores.2009.06.014.

Umhoefer, P.J., 2011, Why did the Southern Gulf of California rupture so rapidly?—Oblique divergence across hot, weak lithosphere along a tectonically active margin: GSA Today, v. 21, no. 11, p. 4–10, doi:10.1130/G133A.1.

Umhoefer, P., Dorsey, R., Willsey, S., Mayer, L., and Renne, P., 2001, Stratigraphy and geochronology of the Comondu group near Loreto, Baja California Sur, Mexico: Sedimentary Geology, v. 144, p. 125–147, doi:10.1016/S0037-0738(01)00138-5.

Vega-Granillo, R., and Calmus, T., 2003, Mazatán metamorphic core complex (Sonora, Mexico): Structures along the detachment fault and its exhumation evolution: Journal of South American Earth Sciences, v. 16, p. 193–204, doi:10.1016/S0895-9811(03)00066-X.

Vega-Granillo, R., and Vidal-Solano, J.R., 2012, Island arc tholeiites of Early Silurian, Late Jurassic and Late Cretaceous ages in the El Fuerte region, northwestern Mexico: Revista Mexicana de Ciencias Geológicas, v. 29, p. 492–513.

Vega-Granillo, R., Salgado-Souto, S., Herrera-Urbina, S., Valencia, V., Ruiz, J., Meza-Figueroa, D., and Talavera-Mendoza, O., 2008, U-Pb detrital zircon data of the Río Fuerte Formation (NW Mexico): Its peri-Gondwanan provenance and exotic nature in relation to southwestern North America: Journal of South American Earth Sciences, v. 26, p. 343–354, doi:10.1016/j.jsames.2008.08.011.

Vidal-Solano, J.R., Paz-Moreno, F.A., Iriondo, A., Demant, A., and Cochemé, J.-J., 2005, Middle Miocene peralkaline ignimbrites in the Hermosillo region (Sonora, México). Geodynamic implications: Comptes Rendus Geoscience, v. 337, p. 1421–1430, doi:10.1016/j.crte.2005.08.007.

Vidal-Solano, J.R., Paz-Moreno, F.A., Demant, A., and Lopez-Martínez, M., 2007, Ignimbritas hiperalcalinas del Mioceno medio en Sonora Central: revaluación de la estratigrafía y significado del volcanismo terciario: Revista Mexicana de Ciencias Geológicas, v. 24, p. 47–67.

Ward, P.L., 1991, On plate tectonics and the geologic evolution of southwestern North America: Journal of Geophysical Research, v. 96, no. B7, p. 12479–12496, doi:10.1029/91JB00606.

Wesnousky, S.G., 2005, Active faulting in the Walker Lane: Tectonics, v. 24, no. 3, doi:10.1029/2004TC001645.

Wilson, D.S., McCrory, P.A., and Stanley, R.G., 2005, Implications of volcanism in coastal California for the Neogene deformation history of western North America: Tectonics, v. 24, no. 3, doi:10.1029/2003TC001621.

Wong, M.S., and Gans, P.B., 2003, Tectonic implications of early Miocene extensional unroofing of the Sierra Mazatán metamorphic core complex, Sonora, Mexico: Geology, v. 31, p. 953–956, doi:10.1130/G19843.1.

Wong, M.S., Gans, P.B., and Scheier, J., 2010, The $^{40}Ar/^{39}Ar$ thermochronology of core complexes and other basement rocks in Sonora, Mexico: Implications for Cenozoic tectonic evolution of northwestern Mexico: Journal of Geophysical Research, v. 115, no. B7, B07414, doi:10.1029/2009JB007032.

York, D., Evensen, N.M., López-Martínez, M., and De Basabe-Delgado, J., 2004, Unified equations for the slope, intercept, and standard errors of the best straight line: American Journal of Physics, v. 72, p. 367–375, doi:10.1119/1.1632486.

3

Edad del proceso de rifting en la parte sur del Golfo de California a partir del estudio del registro plutónico

Articulo:

Duque-Trujillo, J., Ferrari, L., Orozco-Esquivel, T., López-Martínez, M., Lonsdale, P., Bryan, S., Kluesner, J., Piñero-Lajas, D., Solari, L. 2014. Timing of rifting in the Southern Gulf of California and its conjugate margins: insights from the plutonic record: Geological Society of America Bulletin, B31008-1; doi:10.1130/B31008.1

Contribuciones individuales de los autores:

- **Jose Duque-Trujillo:** Concepción y planteamiento del trabajo; muestreo de los intrusivos en tierra y durante el crucero BEKL; participación en la preparación de muestras y obtención de datos geocronológicos (U-Pb y $^{40}Ar/^{39}Ar$) y geoquímicos; petrografía de intrusivos; análisis y presentación de los datos analíticos; revisión bibliográfica y escritura de la versión inicial del trabajo.
- **Luca Ferrari:** Consecución del financiamiento; concepción y planteamiento del trabajo; coordinación general del proyecto; participación en el crucero ROCA y supervisión del trabajo de campo; participación en el análisis y presentación de los datos geocronológicos, geoquímicos, petrográficos y termobarométricos; revisión e integración de las diversas versiones del trabajo.
- **Teresa Orozco-Esquivel:** Participación en los cruceros ROCA y BEKL; asesoría en la obtención de datos geoquímicos y termobarométricos; participación en la preparación, análisis y presentación de datos geoquímicos; realización, análisis y presentación de datos termobarométricos; revisión del manuscrito.
- **Margarita López-Martínez:** Consecución del financiamiento; concepción y planteamiento del trabajo; participación en los cruceros ROCA y BEKL; tutoría en el proceso de preparación de muestras y fechamiento por el método $^{40}Ar/^{39}Ar$; participación en el análisis y presentación de edades $^{40}Ar/^{39}Ar$; colaboración en la preparación de anexos geocronológicos; revisión del manuscrito.
- **Peter Lonsdale:** Consecución del financiamiento; concepción, planeación y dirección de los cruceros ocenanográficos DANA y ROCA; preparación y revisión de los datos geológicos obtenidos durante los cruceros ROCA y BEKL; colaboración en la presentación de los datos batimétricos del Golfo de California.
- **Scott Bryan:** Contribución en la interpretación de la información, particularmente en la

discusión relacionada con el arco Comondú; revisión y aporte en las versiones finales del manuscrito.

- **Jared Kluesner:** Consecución del financiamiento; concepción, planeación y dirección de el crucero oceanográfico BEKL; participación en el crucero oceanográfico ROCA; elaboración y presentación de los datos batimétricos del Golfo de California.
- **Doris Piñero-Lajas:** Participación en la recolección de muestras en la Península de Baja California; participación en los cruceros oceanográficos ROCA y BEKL; participación de la obtención de algunas edades $^{40}Ar/^{39}Ar$.
- **Luigi Solari:** Tutoría en el proceso de preparación de muestras y fechamiento por el método U-Pb; reducción de datos de LA-ICP-MS.

Geological Society of America Bulletin, published online on 4 December 2014 as doi:10.1130/B31008.1

Timing of rifting in the southern Gulf of California and its conjugate margins: Insights from the plutonic record

Jose Duque-Trujillo[1], Luca Ferrari[1,†], Teresa Orozco-Esquivel[1], Margarita López-Martínez[2], Peter Lonsdale[3], Scott E. Bryan[4], Jared Kluesner[3,§], Doris Piñero-Lajas[2,#], and Luigi Solari[1]

[1]*Centro de Geociencias, Universidad Nacional Autónoma de México, Campus Juriquilla, Querétaro, 76230 Querétaro, México*
[2]*Departamento de Geología, Centro de Investigación Científica y de Educación Superior de Ensenada (CICESE), Carretera Ensenada-Tijuana No. 3918, 22860 Ensenada, Baja California, México*
[3]*Scripps Institution of Oceanography, University of California at San Diego, La Jolla, California 92093, USA*
[4]*School of Earth, Environmental and Biological Sciences, Queensland University of Technology, Brisbane, Queensland 4001, Australia*

ABSTRACT

The Gulf of California is a young example of crustal stretching and transtensional shearing leading to the birth of a new oceanic basin at a formerly convergent margin. Previous studies focused along the southwestern rifted margin in Baja California indicated rifting was initiated after subduction and related magmatism ceased at ca. 14–12.5 Ma. However, the geologic record on the Mexico mainland (Sinaloa and Nayarit States) indicates crustal stretching in the region began as early as late Oligocene. The timing of cooling and exhumation of pre- and synrift plutonic rocks can provide constraints on the timing and rate of rifting. Here, we present results of a regional study on intrusive rocks in the southern Gulf of California sampled along the conjugate Baja California and Nayarit-Sinaloa rift margins, as well as plutonic rocks now exposed on submerged rifted blocks inside the gulf. Forty-one samples were dated via U/Pb zircon and $^{40}Ar/^{39}Ar$ mineral ages, providing emplacement age and thermochronological constraints on timing and rate of cooling. We found an extensive suite of early and middle Miocene plutons emplaced at shallow depths within the basement Cretaceous–Paleocene Peninsular Range and Sinaloa-Jalisco Batholiths. Early Miocene granitoids occur in an elongated WNW-ESE belt crossing the entire southern gulf from southern Baja California to Nayarit and Sinaloa. Most have an intermediate composition (<67 SiO_2 wt%), but a distinctive group of high-silica granites (>75 SiO_2 wt%) was emplaced 20.1–18.3 Ma, near the end of the early Miocene. Age span and chemical composition of the early Miocene silicic plutons essentially overlap ignimbrites and domes exposed in the southern Sierra Madre Occidental and in southern Baja California, suggesting that eruptive sources for the early Miocene ignimbrite flare-up may also have been located within the southern Gulf of California. Early Miocene plutons cooled below the ^{40}Ar-^{39}Ar biotite closure temperature (350–400 °C) in less than 2.5 m.y., which we interpret as evidence of a regional extensional event leading to the opening of the Gulf of California. A less widely distributed suite of intermediate-composition, middle Miocene granitoids (15–13 Ma) was sampled from the central-western part of the gulf, west of the Pescadero Basin, and these correspond to an episode of scarce volcanism recorded by the middle and upper members of the onshore Comondú Group in Baja California. Our widely spaced sampling of the generally sediment-covered igneous crust suggests that middle Miocene primary volcanic rocks are much less abundant than implied by previous models in which the gulf was the site of a robust Comondú arc. Thermobarometry data also indicate a very shallow depth (<5 km) of emplacement for the middle Miocene plutonic rocks. Some of these rocks also show a distinctive inequigranular texture indicative of at least two crystallization stages at different pressure. Early and middle Miocene granitoids away from the gulf axis yielded ^{40}Ar-^{39}Ar cooling ages very close to U-Pb zircon ages, demonstrating rapid cooling to <350 °C, which we attribute to their shallow emplacement and, possibly, to exhumation soon after intrusion. Since Comondú-age and middle Miocene magmatism in the gulf region coincided with rapid cooling of young plutons that predate the end of subduction, we suggest that intense crustal stretching controlled the pattern and timing of Comondú-age magmatism, rather than the middle Miocene magmatism controlling the locus of <12 Ma extension.

INTRODUCTION

The geologic record shows that, in continental extensional systems, the process of complete lithosphere rupture can take from 25 to 80 m.y. before the onset of seafloor spreading (Bohannon et al., 1989; Menzies et al., 1997; Abbate et al., 2001; Ziegler and Cloetingh, 2004; Omar and Steckler, 1995; Pik et al., 2008; Corti, 2009). The main factors controlling the time scale of continental breakup are crustal thickness, lithospheric rheology, thermal structure, and the magnitude and rate of forces applied to the lithosphere (e.g., Ziegler and Cloetingh, 2004; Nagel and Buck, 2007). In this context, the Gulf of California has been considered an anomalously fast rift, in which rupture of the continental lithosphere is thought to have been accomplished in only 6–10 m.y. (see review in Umhoefer, 2011). Despite early studies recognizing that Basin and Range extension may have affected the eastern margin of the future gulf well before the end of subduction (e.g., Henry, 1989), virtually all literature over the past two decades has reinforced the view that rifting in the gulf area only began once subduction of

[†]luca@unam.mx.
[§]Present address: Department of Earth and Planetary Sciences, University of California, Santa Cruz, California 95064, USA.
[#]Present address: Departamento de Oceanografía Física, Centro de Investigación Científica y de Educación Superior de Ensenada (CICESE), Carretera Ensenada-Tijuana No. 3918, 22860 Ensenada, Baja California, México.

 doi: 10.1130/B31008.1; 13 figures; 3 tables; Data Repository item 2015022.

Geological Society of America Bulletin, published online on 4 December 2014 as doi:10.1130/B31008.1

the last remnants of the Farallon plate finished at ca. 14–12.5 Ma and the Baja California peninsula started to move with the Pacific plate (Stock and Hodges, 1989; Henry and Aranda-Gomez, 2000; Umhoefer et al., 2002; Fletcher et al., 2007; Lizarralde et al., 2007; Sutherland et al., 2012). To explain this apparently rapid rifting, three main factors have been invoked (Umhoefer, 2011, and references therein): (1) focusing of rifting along an inherited long, narrow belt of hot, weak crust generated by the preceding arc volcanism, (2) relatively rapid plate motions and high strain rates, and (3) a dominant role of strike-slip faulting and highly oblique-divergent setting.

A precise estimation of the timing of rift initiation is crucial to confirm if the Gulf of California is an anomaly among continental rifts. Restoration of the ~300 km of dextral offset estimated in the northern gulf since ca. 6.5 Ma (Oskin and Stock, 2003; Oskin et al., 2001) still leaves 250 km of orthogonal separation between the western (Baja California) and eastern (Mexico mainland) borders of the rift in the southern Gulf of California (Fig. 1; see fig. 2 of Stock and Hodges, 1989) that has to be accommodated in just ~6 m.y. at a high rate of 41 mm/yr. The alternative kinematic model for gulf opening of Fletcher et al. (2007) requires ~460 km of combined transtensional shear within the southern gulf since 12.3 Ma, which translates to a slightly lower rate of separation of ~37 mm/yr. Both values approximate the present-day, postrift rate of opening in the southern gulf (45.1 ± 0.8–51.1 ± 2.5 mm/yr; DeMets, 1995), but they are otherwise uncommon for continental rifts, where geodetically measured rates of opening are typically <10 mm/yr (Calais et al., 1998; Fernandes et al., 2004; Bendick et al., 2006).

It can be misleading to use the subaerial part of just one of the conjugate margins to estimate the timing of rifting and pattern of magmatism. For the Gulf of California, a late Miocene onset of rifting is supported by structural and thermochronology studies, mostly along the narrow onshore part of the Baja California margin and Tiburón Island in the northern Gulf of California (e.g., Stock and Hodges, 1989; Martín-Barajas et al., 1995; Fletcher et al., 2000; Oskin et al., 2001; Umhoefer et al., 2002; Oskin and Stock, 2003; Seiler et al., 2011; Mark et al., 2014). In contrast, studies along the much broader eastern margin side of the Gulf Extensional Province have shown that extension began as early as the late Oligocene (Gans, 1997; McDowell et al., 1997; Wong et al., 2010; Murray et al., 2013) in a wide region and that by ca. 18 Ma, extension had focused toward the present Gulf of California (Ferrari et al., 2013; Bryan et al., 2014).

Insights on the timing of rifting can be obtained by studying plutonic rocks emplaced in the gulf region and their exhumation driven by extensional and transtensional tectonics. In particular, the timing of exhumation, and also the relative timing of emplacement to exhumation, can provide more direct constraints on the onset of rifting in the Gulf of California. In this paper, we present the first integrated geologic, geochronologic, and geochemical study targeted at intrusive rocks exposed on both the subaerial and submarine continental margins of the two sides of the southern Gulf of California rift. Samples from continental blocks submerged in the southern Gulf of California were collected during the DANA (2004), ROCA (2008), and BEKL (2009) cruises. A principal result of our study is that significant amounts of early Miocene and, to a lesser extent, middle Miocene intrusive rocks, initially emplaced in the upper continental crust, are now exposed on the floor of the Gulf of California and along the subaerial margins. Petrographic and geochronologic characteristics of these rocks support an exhumation and crustal thinning phase between ca. 18 and 12 Ma. Our study rekindles early interpretations (e.g., Henry, 1989) that Oligocene to middle Miocene volcanism (Sierra Madre Occidental and Comondú Group) within the southern gulf region, despite being concurrent with the closing phases of subduction off Baja California, was essentially related to continental rifting that led to the opening of the Gulf of California.

MAGMATISM AND TECTONICS OF THE GULF REGION

Western Mexico consists of a series of magmatic and tectonic provinces recording a prolonged history of subduction and extensional tectonics that have affected this segment of the western North American margin since the Cretaceous. Continental magmatism prior to the cessation of subduction off Baja California at ca. 12.5 Ma consisted of three main igneous episodes: (1) the Late Cretaceous–Paleogene, when the Peninsular Range Batholith, which outcrops in Baja California and in adjacent parts of mainland Mexico, was constructed; (2) the late Eocene–early Miocene, when the silicic to bimodal Sierra Madre Occidental silicic large igneous province was emplaced; and (3) the middle Miocene, when volumetrically subordinate intermediate volcanism (the Comondú Group) developed principally along eastern Baja California. These igneous episodes are summarized next, followed by a brief synthesis of the tectonic setting of the Gulf of California.

Peninsular Range and Western Mexico Cretaceous–Paleogene Batholiths

The Peninsular Range Batholith is a N-NW–trending and almost continuous series of batholith-sized intrusive complexes, which form the backbone of Baja California peninsula. The batholith is well exposed for over ~800 km along strike in northern Baja California, it continues beneath the Cenozoic cover in southern Baja California, and it is exposed again south of La Paz in the Los Cabos block (Gastil, 1975) (Fig. 1). Intrusion ages and compositions have formed the basis for correlating the Peninsular Range Batholith with batholiths exposed in mainland Mexico in the states of Sinaloa and Jalisco (Fig. 1; Gastil, 1975; Schaaf et al., 2000; Ortega-Rivera, 2003; Henry et al., 2003), making a 150–200-km-wide igneous belt of Cretaceous to Paleogene age.

The Peninsular Range Batholith has been divided into western and eastern zones on the basis of pluton composition, depth of emplacement, age, host rock geology, and magnetic and gravimetric signatures (Gastil, 1975; Gastil et al., 1990; Silver and Chappell, 1988; Langenheim et al., 2014). Western intrusions have an island-arc geochemical affinity, range in composition between gabbro and monzogranite, and were intruded between ca. 140 and 105 Ma (Gastil, 1975). This part of the batholith is interpreted as the plutonic underpinnings of a Jurassic to Early Cretaceous fringing volcanic arc developed on older oceanic crust that was accreted to the North American plate in Albian times (Silver and Chappell, 1988; Gastil, 1993; Todd et al., 1988, Busby et al., 1998; Busby, 2004). The eastern part of the batholith is composed of nested tonalites and low-K granodiorites plus other smaller, isolated intrusions. This part of the batholith is dominated by La Posta–type tonalite-granodiorite intrusions (Silver and Chappell, 1988; Walawender et al., 1990) with U/Pb zircon ages indicating a short interval of intrusion (ca. 99–92 Ma). Rocks partly overlapping in age with the Peninsular Range Batholith are extensively exposed in Sinaloa (Henry at al., 2003), and in southern Nayarit (Fig. 1). Published ages for the composite and long-lived Sinaloa Batholith span between 101 and 45 Ma, with compositions from gabbro to granite, although granodiorite is the most common rock type (Henry et al., 2003). Intrusive rocks in southern Nayarit are part of the Puerto Vallarta Batholith, which yielded intrusion ages between ca. 92 and 65 Ma (Gastil et al., 1979; Köhler et al., 1988; Zimmermann et al., 1988; Schaaf et al., 1995). On the basis of geochemical and isotopic data, the Puerto Vallarta Batholith is considered equivalent to the Peninsular Range Batholith exposed in the Los Cabos block (Schaaf et al., 2000).

Geological Society of America Bulletin, published online on 4 December 2014 as doi:10.1130/B31008.1

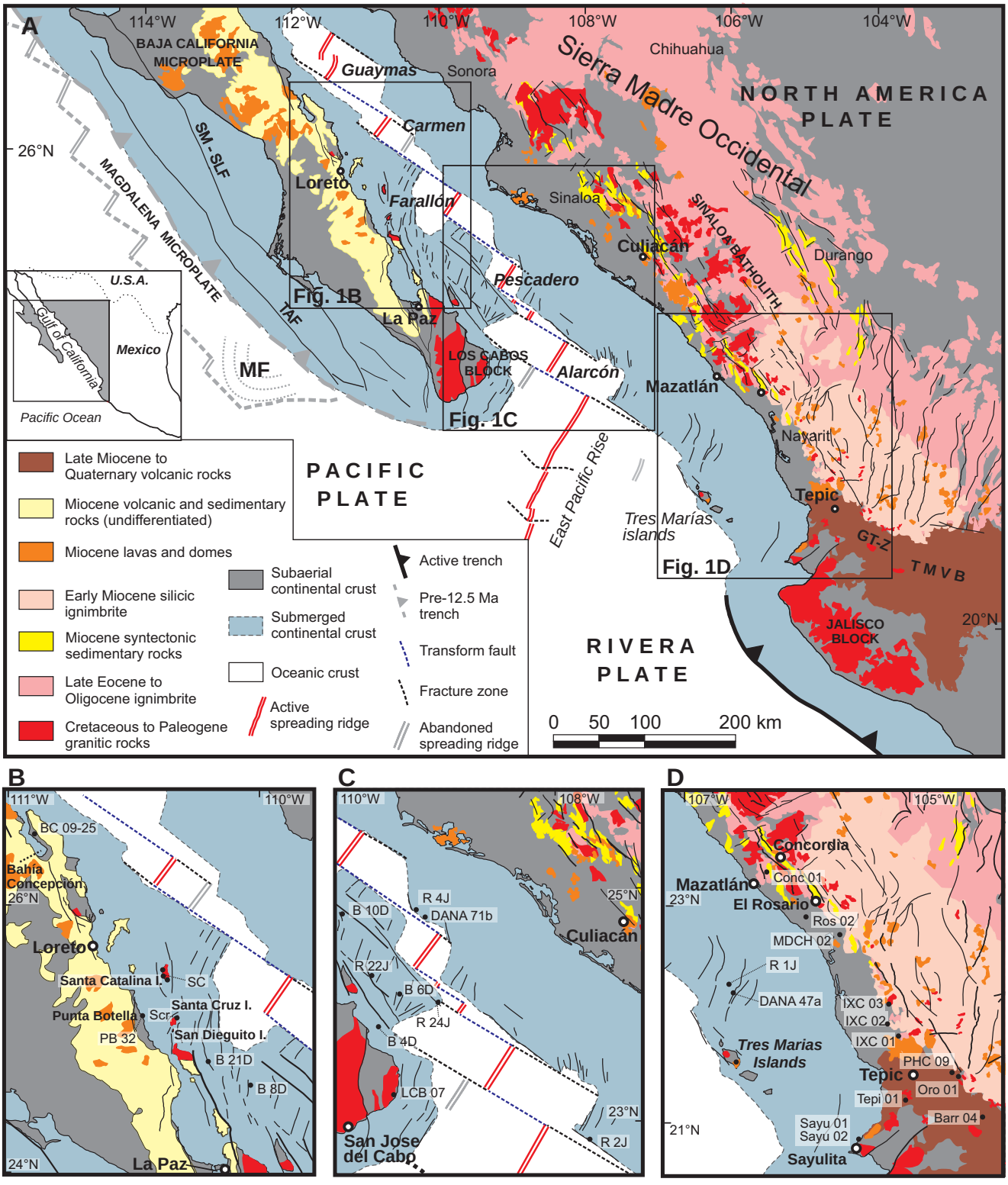

Figure 1. (A) Regional geology and tectonic map of the southern Gulf of California and adjacent margins showing the distribution of submerged continental crust (blue) from Ferrari et al., (2013). Geology is compiled from Ferrari et al. (2007, 2013). Location of the ocean-continent boundary is taken from Lonsdale and Kluesner (2010). (B–D) Detailed areas and location of sampling sites, with samples listed in Tables 1, 2, and 3. Remotely operated vehicle (ROV) dives are indicated with the letter R (sample prefix ROCA), and *Jason* dive number (e.g., R 4J); BEKL dredges are indicated with letter B and dredge number (e.g., B 21D); SC includes all samples from Santa Catalina Island; SCr includes all samples from Santa Cruz Island. GT-Z—Graben Tepic-Zacoalco; MF—Magdalena Fan; SM-SLF—Santa Margarita–San Lorenzo fault; TAF—Tosco-Abreojos fault; TMVB—Trans-Mexican volcanic belt.

Geological Society of America Bulletin, published online on 4 December 2014 as doi:10.1130/B31008.1

Sierra Madre Occidental

The Sierra Madre Occidental preserves the record of continental magmatism preceding the opening of the Gulf of California (Ferrari et al., 2007; Bryan et al., 2014). The province extends from the United States–Mexico border to the Trans-Mexican volcanic belt and constitutes a 1200-km-long and 200–400-km-wide, elongated high plateau with average elevations over 2000 m above sea level (asl; Ferrari et al., 2007). Underlying the Sierra Madre Occidental succession, there are latest Cretaceous to early Eocene intermediate volcanic rocks partly coeval with the Peninsular Range Batholith and traditionally called the Lower Volcanic Complex (McDowell and Clabaugh, 1979; McDowell et al., 1997). However, recent studies indicate that some mafic-intermediate volcanic rocks previously ascribed to the Lower Volcanic Complex are actually interbedded within the Sierra Madre Occidental succession and are thus much younger in age (Murray et al., 2013). The widespread Upper Volcanic Supergroup (McDowell and Keizer, 1977), which defines the Sierra Madre Occidental succession, is mainly composed of voluminous silicic ignimbrites (85%–90% of the total erupted volume) and lesser rhyolitic domes and basaltic lavas. The Upper Volcanic Supergroup makes the Sierra Madre Occidental one of the largest silicic igneous provinces in North America and the most recent of such an event on Earth (Bryan, 2007; Ferrari et al., 2007; Bryan and Ferrari, 2013). Two main "ignimbrite flare-ups" were identified at ca. 34–28 Ma and ca. 24–18 Ma (Ferrari et al., 2007). The Oligocene pulse covers an ~400,000 km^2, NW-trending area and is responsible for at least three quarters (300,000 km^3) of the total erupted volume. The early Miocene ignimbrite flare-up (ca. 24–18 Ma) is essentially concentrated in the southern Sierra Madre Occidental, with a tendency to migrate to the southwest in time (Ferrari et al., 2002, 2007; Bryan et al., 2008).

Geochronologic studies in different areas of the Sierra Madre Occidental have revealed that the emplacement of the ignimbrite successions, locally reaching over 1000 m of thickness, occurred in 1 m.y. or less, hinting at notable high rates of generation of silicic magma (McDowell and Keizer, 1977; Ferrari et al., 2002, 2007; Bryan et al., 2008). Generally, basaltic to basaltic-andesitic lavas are intercalated with or cap the youngest ignimbrite units and have previously been referred to as the Southern Cordillera basaltic andesite suite (SCORBA) in Chihuahua and northern Sinaloa, where they show a transitional to alkaline geochemical signature, more akin to an intraplate environment than to a magmatic arc (Cameron et al., 1989; Luhr et al., 2001).

The Sierra Madre Occidental has been affected by several episodes of extensional deformation since the late Eocene (Henry and Aranda-Gomez, 1992, 2000; Aranda-Gómez and McDowell, 1998; Ferrari et al., 2007, 2013). The central core of the Sierra Madre Occidental, however, is flat-lying and unextended, and it has been used to define the limit between the so-called "Mexican Basin and Range" to the east and the Gulf Extensional Province to the west (Henry and Aranda-Gomez, 2000; Ferrari et al., 2007). The Gulf Extensional Province is widely thought to encapsulate all extension related to the opening of the Gulf of California, which has long been considered to have initiated at ca. 14–13 Ma, when subduction waned and eventually ceased off Baja California (Stock and Hodges, 1989; Henry and Aranda-Gomez, 2000; Umhoefer et al., 2001; Fletcher et al., 2007; Umhoefer, 2011). However, new field and geochronologic studies have shown that the onset of extension in the southern and central part of the Gulf Extensional Province dates back to the late Oligocene and occurred over a broad region up to 350 km from the plate boundary (Ferrari et al., 2013; Bryan and Ferrari, 2013; Bryan et al., 2014). A similar age of extension has been recognized in the northern Sierra Madre Occidental (e.g., Gans, 1997; McDowell et al., 1997; Wong et al., 2010; Murray et al., 2013).

Comondú Group

The Comondú Group consists of volcanic and volcano-sedimentary rocks of latest Oligocene to middle Miocene age, deposited on the northwestern margin of Mexico before the separation of Baja California (Hausback, 1984; Sawlan and Smith, 1984; Sawlan, 1991; Umhoefer et al., 2001). At present, the group is mainly exposed on the eastern side of Baja California, where it has been divided into three members (Umhoefer et al., 2001). The lower Comondú member is a clastic succession of fluvial, eolian, and resedimented tuffaceous sandstones and conglomerates interbedded with silicic ignimbrites. In the Loreto area (Fig. 1), detrital zircon U/Pb data on eolian sandstones indicate a maximum depositional age of ca. 25 Ma (Godinez et al., 2010), and tuffs intercalated in the unit yielded ^{40}Ar-^{39}Ar ages of 22.2–20.2 Ma (Umhoefer et al., 2001). Hausback (1984) reported similar ages (ca. 24–18 Ma) for ignimbrites exposed along the coast north of La Paz. The middle member of the Comondú Group is composed of massive sedimentary breccias and minor andesite-dacite lavas and domes with ages mainly between ca. 19 and 15 Ma. Breccia units are interpreted to thicken to the east and have locally been found to interfinger with the lower member (Hausback, 1984; McLean, 1988). An eastward coarsening is inferred to reflect increasing proximity to arc volcanoes or stratocones now submerged within the gulf. The upper member is dominated by lavas and massive volcanic breccias with a few reported ages between ca. 15 and 12 Ma (Hausback, 1984; Umhoefer et al., 2001; Godinez et al., 2010). The middle and upper Comondú members have a composite thickness exceeding 1 km (Umhoefer et al., 2001). Some shallow intermediate plutons and andesitic porphyry intrusions are associated with the Comondú Group. McFall (1968) reported a 20 ± 0.2 Ma K/Ar age for a tonalitic intrusion in Bahía Concepción. An andesite porphyry at Las Parras, west of Loreto, yielded a U/Pb intrusion age of 19.9 ± 0.7 Ma (Godinez et al., 2010) and a K/Ar (hornblende) age of 19.4 ± 0.9 Ma (McLean, 1988). Godinez et al. (2010) also described a pluton along the Loreto–La Purisima road that yielded several Cretaceous zircon xenocrysts and an intrusion age of 16.3 ± 0.5 Ma. Hypabyssal porphyritic intrusions in the Bahía Concepción and Loreto and east of La Paz (Pichilingüe) have been interpreted to represent core facies of an andesitic arc that, for the most part, extended to the east of the peninsula, within the present gulf (Hausback, 1984).

The ages and lithology of the lower member of the Comondú Group indicate that it represents the distal deposits of the last (early Miocene) ignimbrite flare-up of the Sierra Madre Occidental and therefore can be ascribed to the Sierra Madre Occidental magmatic episode (Umhoefer et al., 2001; Ferrari et al., 2007). By contrast, the middle and upper members of the Comondú Group represent a distinct igneous episode of early to middle Miocene age, characterized by a dominantly effusive style of volcanism (domes, lava flows, and related dikes and subvolcanic intrusion), more intermediate magma compositions, and extensive volcaniclastic and epiclastic deposits.

Southern Gulf of California

The present Gulf of California is an ~1500-km-long, active oblique rift separating mainland Mexico (North American plate) from the Baja California peninsula (Lonsdale, 1989). The rift contains oceanic basins with short NE-striking spreading axes linked by long NW-striking transform faults, which, in many places, bound actively shearing continental margins (Figs. 1 and 2A). Recent geologic and geodetic studies show that Baja California is not completely attached to the Pacific plate, as ~10% of the total Pacific–North America motion is accommodated along its western margin; therefore, the peninsula is defined as a microplate

Geological Society of America Bulletin, published online on 4 December 2014 as doi:10.1130/B31008.1

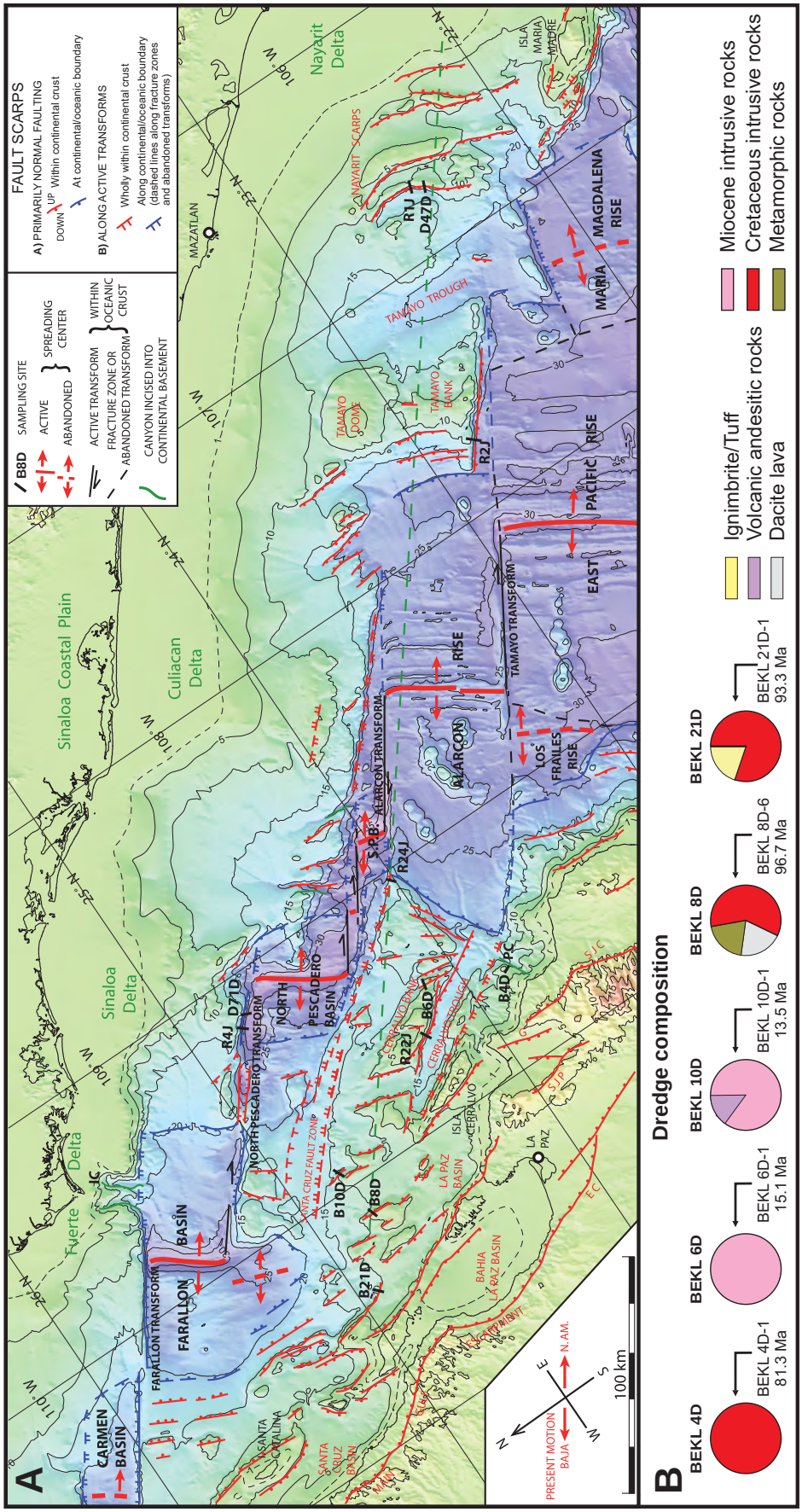

Figure 2. (A) Topographic map of southern Gulf of California, oriented parallel to present geodetically determined motion of the Baja California microplate with respect to the North American plate (Plattner et al., 2007), showing location of DANA dredges (D), BEKL dredges (B), and ROCA dives (R). Bathymetry is from multibeam survey, supplemented in shallow water by contour interpolation of archival soundings; subaerial relief is from satellite altimetry. The green dashed line from northwest to southeast near the middle of the map locates the seismic profile of Sutherland et al. (2012). SJP—San Juan de los Planes fault; SJC—San Jose del Cabo fault; G—La Gata fault; EC—El Carrizal fault; SPB—southern Pescadero Basin; IC—Ignacio Canyon; PC—Pescadero Canyon. (B) Relative abundance of different rock types in BEKL dredges 4D, 6D, 10D, 8D, and 21D, shown in pie charts, together with the ages of intrusive rocks reported in this work.

Geological Society of America Bulletin, published online on 4 December 2014 as doi:10.1130/B31008.1

(Fletcher and Munguía, 2000; Plattner et al., 2007; Fletcher et al., 2007).

The extent and composition of the continental crust in the southern Gulf of California (Figs. 1 and 2A) have been only indirectly inferred by interpretation of structures and wide-angle, multichannel seismic (MCS), and seismic-refraction profiles collected during the National Science Foundation (NSF) MARGINS program in the past decade (Lizarralde et al., 2007; Páramo et al., 2008; Lonsdale and Kluesner, 2010; Kluesner, 2011; Sutherland et al., 2012). Based on seismic velocities, these studies have roughly defined the limits of newly accreted oceanic crust in the Farallón, Pescadero, and Alarcón Basins, as well as southeast of the Los Cabos block (Fig. 2A). The Farallón and Pescadero spreading centers have produced much less oceanic crust than the Alarcón Rise, where the formation of new oceanic crust began between ca. 3.7 and 3.5 Ma (south to north; Lonsdale, 1989, 1995). In all MCS profiles, the prerift basement displays seismic velocities typical of crystalline rocks, which are interpreted to be intrusive rocks of the Peninsular Range Batholith (Páramo et al., 2008; Sutherland et al., 2012). On the conjugate margins of the Alarcón Basin, Sutherland et al. (2012) also recognized a distinctive, reflective "ropey layer," which they interpreted as a volcanic or volcaniclastic succession of the Comondú Group that predated basin formation. Direct information about prerift continental crustal rocks in the mouth of the Gulf of California comes from exposures in the Tres Marías islands, located ~100 km west of Nayarit coast. Mid-Jurassic (163–170 Ma) migmatites and orthogneisses define the crystalline basement of the island, which is cut by Cretaceous intrusions (80.8–83.4 Ma) of tonalitic to granitic composition that are in turn overlain by ignimbrites, volcanic breccias, and lavas of Cretaceous (71.6–80.6 Ma) and Eocene (55.4 Ma) age (Pompa-Mera et al., 2013). Undeformed or slightly deformed sediments that postdate the main rift phase are also recognized in all basins along the gulf, with thicknesses typically increasing toward the center of the gulf. Significant subsidence and marine sedimentation are well documented as early as ca. 8 Ma at Isla Tiburón (Oskin and Stock, 2003), Tres Marías Islands (McCloy et al., 1988), and Isla San José (Carreño, 1992; Fletcher et al., 2000; McTeague, 2006).

METHODS

Introduction

In this work, we sampled the two conjugate rift margins both onshore and offshore to examine the evolving geographic distribution of magmatism and exhumation across the entire southern Gulf of California. Whenever possible, intrusive rocks were dated by both U-Pb (on zircon) and Ar-Ar (hornblende, biotite, or feldspar) methods to provide insight into the rate at which they were exhumed. The samples were analyzed for major and trace elements for correlative purposes relative to onshore intrusive and volcanic suites. Mineral chemistry was also determined on selected samples suitable to apply hornblende geothermobarometry. A brief description of the methodological procedures followed during the present study is presented here. Further details on laboratory procedures are summarized in supplemental file 1 (GSA Data Repository).[1]

Onshore and Submarine Sampling

Subaerial samples used in this work were selected to be representative of the Cretaceous and Miocene intrusive bodies exposed (1) on the southeastern Baja California peninsula and two of its offshore islands (Santa Catalina and Santa Cruz), and (2) on the mainland side of the margin, along the coastal plain and the Sierra Madre Occidental foothills of Nayarit and Sinaloa (Fig. 1). Sampling was guided by the 1:250,000 and 1:50,000 geological maps published by the Mexican Geological Survey (Servicio Geológico Mexicano [SGM]) and by our own mapping (Piñero-Lajas, 2008; Ferrari et al., 2013).

Submarine rock sampling first required locating and mapping patches of rock and talus slopes that crop out through the muddy sediment that covers >90% of the submerged continental crust of the southern gulf, thwarting several earlier sampling attempts. This was accomplished by a multibeam bathymetry and reflectivity survey during the 2004 DANA cruise of R/V *Revelle* (Lonsdale, chief scientist). Steep, highly reflective slopes likely to be good sampling targets included the sides of subaerially incised, now submerged canyons, the steep scarps of sheared continental margins, especially the walls of transtensional rifts along active transform faults, and extensional fault scarps, as well as some steep volcanic slopes. An exploratory DANA dredging campaign immediately after the multibeam survey included 18 successful sampling sites on the submerged continental crust of the Sinaloa-Nayarit margin, six of them yielding granitic intrusive rocks. The 2008 ROCA cruise of R/V *Atlantis* (Lonsdale, chief scientist), with the remote operated vehicle (ROV) *Jason* as its rock-sampling tool, made 11 dives on the mainland continental margin of the southern gulf (including ROCA 1J, 2J, and 4J; Figs. 2 and 3), and three dives on the Baja California margin (including ROCA 22J and ROCA24J; Figs. 2 and 3). The 2009 BEKL cruise of R/V *New Horizon* (Kluesner, chief scientist) dredge-sampled the continental borderland of the southwestern side of the gulf, much of which was geologically unexplored, except for its islands, despite having less obscuring sediment cover than the northeastern margin. Only around the tip of Baja California, south of our study area, was the offshore continental geology relatively well known from interpretations of many previous dredge hauls (Shepard, 1964; Normark and Curray, 1968). We collected granitic rocks from the steep side of Pescadero Canyon and between Pescadero Canyon and Isla Santa Catalina (Fig. 2). Specific objectives were to test how well submarine basement geology could be extrapolated from the adjacent peninsula and its offshore islands, with special attention to testing hypotheses about the geologic history and significance of the Comondú Group.

The steps used for dredging during the DANA and BEKL cruises were (1) to maintain the ship's position as the dredge was lowered to the seafloor, (2) to slowly move the ship 400–600 m directly upslope across rocky terrain while keeping the dredge stationary, and (3) to stop the ship while winching in the dredge until it left the seafloor, 150–200 m shallower than where it landed. With this method, the depth and location are precisely known for the beginning of the dredge track, but less well determined for the end. In addition, the precise depth and location at which individual stones were collected along the 400–600 m dredging track are unknown.

During the ROCA cruise, the ROV *Jason* was operated in a somewhat similar fashion, as a "smart dredge." It was slowly driven, in tandem with its support ship, for 0.5–4.5 km along straight-uphill dive tracks selected using the multibeam imagery while maintaining visual (video) contact with the seafloor. On some dives (e.g., ROCA 1J and 2J; Fig. 3), we conducted two or three uphill profiles spaced along the same fault scarp, separated by "midwater" transits out of sight of the seafloor. Ultrashort-baseline transponder navigation continuously recorded ROV position (±10 m) with respect to the global positioning system (GPS)–positioned ship, and the vehicle's precision depth gauge and echo-sounder recorded its depth and altitude. When ROV video, transmitted in real time to the ship, showed suitable sites, the vehicle was stopped and rocks were grabbed by a manipulator, photographed, and placed in

[1]GSA Data Repository item 2015022, Details on the methodology, thermobarometry, and geochronology, is available at http://www.geosociety.org/pubs/ft2015.htm or by request to editing@geosociety.org.

Geological Society of America Bulletin, published online on 4 December 2014 as doi:10.1130/B31008.1

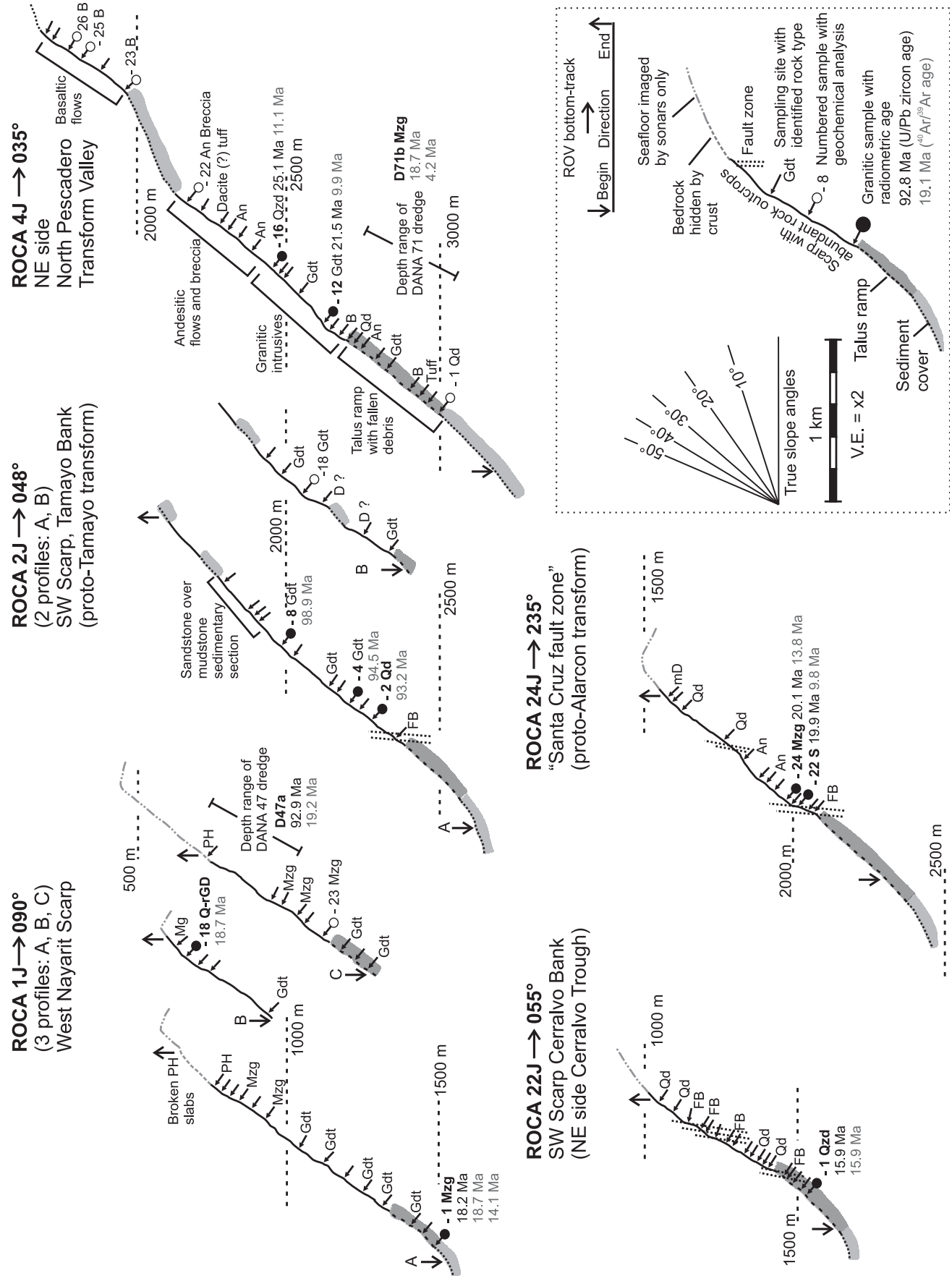

Figure 3. Altimetry profiles from ROCA dive sites from which selected samples were dated. Geomorphologic characteristics and lithologies observed during remotely operated vehicle (ROV) *Jason* dive, and sites of sample collection are shown at each profile.

Geological Society of America Bulletin, published online on 4 December 2014 as doi:10.1130/B31008.1

numbered compartments of a collecting basket so that each one (15–35 per dive) could be identified when brought aboard ship.

Although ROV rock sampling has many advantages over dredge sampling, allowing recovery of selected specimens from visually well-characterized sites at precisely known depths and locations, it does have its limitations. The manipulators are not strong enough to break samples off sound outcrops of intrusive rock, especially if they are cemented with ferromanganese crusts. Along several of our dive tracks, especially along tectonically active plate-boundary fault zones (e.g., ROCA 4J), superficial rocks are pervasively fractured, and fresh fracture-bounded slabs could easily be taken from outcrops. Where samples could not be plucked from true outcrops, we collected rock fragments that appeared to be locally derived, e.g., from narrow ledges within steep outcrops, but a few of these samples may have fallen from outcrops further upslope. On several dives, samples were deliberately collected from scarp-foot talus ramps where loose rocks were clearly not in situ, but very easy to gather; this happened mostly where our initial landing site proved to be at or below a steep talus ramp (e.g., ROCA 4J and 22J), where we grabbed a few stones just to ensure that we brought some samples back even if technical problems curtailed the dive. Stones recovered from the upper surface of active talus ramps, having recently been shaken off upslope outcrops, proved to be among the least altered specimens we collected. Thick ferromanganese oxide encrustation did not prove to be a major problem in the gulf, where bottom waters are lower in dissolved oxygen than in the open ocean, but the shallowest parts of the ROCA 1J profiles were encased in impenetrable phosphorite crusts.

Petrography and Geochemistry

The modal composition and textural features of collected samples were determined in thin sections under the microscope, and results are reported in Table 1. Twenty-nine of the freshest samples were analyzed for major and trace elements and provide a representative characterization of the compositional variability of intrusive rocks in the southern Gulf of California. Onshore samples were collected as far as possible from deformation and alteration zones. Offshore samples were selected among those without strong oxidization and mineral alteration. Major elements were analyzed by X-ray fluorescence (XRF) using a Siemens SRS3000 instrument at Instituto de Geología, Universidad Nacional Autónoma de Mexico (UNAM), according to the procedures outlined in Bernal and Lozano-Santacruz (2005). Sample preparation for trace-element analysis was carried out at Centro de Geociencias (CGEO), UNAM, Campus Juriquilla, Queretaro, Mexico, in a clean laboratory, following the procedures outlined by Mori et al. (2007), incorporating two additional digestion steps in Parr® vessels in order to achieve complete dissolution of refractory minerals (e.g., zircon). Samples were analyzed with a Thermo X Series II quadrupole inductively coupled plasma–mass spectrometer (ICP-MS) at Laboratorio de Estudios Isotópicos, at CGEO, UNAM. Major- and trace-element analyses of DANA and ROCA samples were performed at GeoAnalytical Laboratory, Washington State University. A detailed description of the procedure is presented in supplemental File 1 (see footnote 1). Results of major- and trace-element analyses are presented in Table 2.

Mineral Chemistry

Amphibole and plagioclase analysis for thermobarometric calculations were obtained at Dipartimento di Scienze della Terra, Università degli Studi di Milano, with a JEOL JXA 8200 Superprobe equipped with five wavelength-dispersive spectrometers (WDS), using a 1 µm beam at 15 kV, and 15 nA beam current. Natural and synthetic minerals used as calibration standards were: omphacite and albite (Na), olivine (Mg), anorthite (Al), wollastonite (Ca, Si), apatite (P), K-feldspar (K), ilmenite (Ti), chromite (Cr), rodonite (Mn), and fayalite (Fe). Mineral compositions are listed in supplemental file 2 (see footnote 1).

Geochronology

Forty-one samples (39 plutonic rocks and two dikes) were dated, generating a total of 72 mineral ages using the U/Pb method (laser ablation [LA] ICP-MS) for zircon, and ^{40}Ar-^{39}Ar step-heating method on different materials (hornblende, biotite, muscovite, K-feldspar, and groundmass). Dating using both U/Pb and ^{40}Ar-^{39}Ar techniques was performed when possible, especially for the youngest samples, which required a confirmation of the middle Miocene intrusion age. Twenty samples were dated by both methods, and more than one mineral was analyzed by ^{40}Ar-^{39}Ar on 11 samples (Table 3).

U/Pb geochronological zircon analyses were carried out at Laboratorio de Estudios Isotópicos, Centro de Geociencias, UNAM. Details on the methodology can be found in supplemental file 1 (see footnote 1), and U/Pb analytical data are presented in supplemental file 3 (see footnote 1).

The ^{40}Ar-^{39}Ar analyses were carried out at Laboratorio de Geocronología, Departamento de Geología, Centro de Investigación Científica y de Educación Superior de Ensenada (CICESE), Baja California, Mexico. Information on the ^{40}Ar-^{39}Ar dating process is presented in supplemental file 1 (see footnote 1). Tables with relevant ^{40}Ar-^{39}Ar data for all analyzed samples, as well as a discussion of each age are presented in supplemental file 4 (see footnote 1).

In plutonic rocks, U/Pb zircon ages are usually considered to reflect the age of intrusion, because the closure temperature of the U/Pb systematics in zircon (>900 °C) is comparable with the initial crystallization temperatures of a differentiated magma (Cherniak and Watson, 2001). On the other hand, the ^{40}Ar-^{39}Ar ages are used to constrain the cooling of the sample through different temperatures, which can be interpreted to reflect tectonic and/or erosional exhumation. The most used ^{40}Ar-^{39}Ar closure temperatures are as follows: hornblende (400–600 °C), biotite (350–400 °C), muscovite (300–350 °C), and K-feldspar (150–350 °C) (Reiners et al., 2005, and references therein).

FIELD CONTEXT OF SOUTHERN GULF PLUTONS

The intrusive rocks analyzed in this study were sampled both onshore and offshore on the two rifted margins of the southern Gulf of California. Subaerial sampling sites include: (1) Bahía Concepción, Punta Botella, and some islands off the eastern coast of Baja California and (2) the western Mexico margin in the states of Sinaloa, Nayarit, and Jalisco (Figs. 1 and 2). Submarine sampling was concentrated on rifted continental crust on the northwest and southeast flanks of the Alarcón Basin (Fig. 2A). This basin has accreted a 190–160-km-wide strip of oceanic lithosphere in the past 3.7 m.y. (Castillo et al., 2010), and it is flanked by broad zones of extended continental crust (Lizarralde et al., 2007; Páramo et al., 2008; Sutherland et al., 2012). We also report analyses of intrusive rocks sampled from sites in the deep North Pescadero transform valley, which exposes part of the southeast rifted flank of Farallón Basin (Fig. 2A).

Western Rifted Margin in Eastern Baja California and Adjacent Islands

In the Baja California peninsula, intrusive rocks are exposed to the east of the Main Gulf Escarpment, a morphologic feature formed by a series of E-dipping, high-angle normal faults that mark the western boundary of the Gulf Extensional Province, and extend from Bahía Concepción in the north to La Paz in the south. Bahía Concepción, a bay apparently formed by the displacement of the Main Gulf Escarpment,

TABLE 1. PETROGRAPHIC DATA OF INTRUSIVE ROCKS FROM THE SOUTHERN GULF OF CALIFORNIA AND ITS ADJACENT MARGINS

	Location	QAP	Q′-ANOR	General texture	Pl	Afs	Qz	Amp	Bt	Ms	Px	Ap	Zrn	Ttn	Op
Cretaceous															
PB 32	Punta Botella, Baja California Sur	Qzd	D	E, C-g	63	18	7	4	8			<1	<1	<1	1
SC 17	Santa Catalina Island	Gdt	Gdt	E, M-g	49	15	23	7	6			<1	<1	<1	1
SCr 09-21	Santa Cruz Island	Qd		E, C-g (def)	65	5	5	15	10			<1	<1	<1	<1
SCr 09-20	Santa Cruz Island	T		E, C-g	48.5	4	25	7.5	15			<1	<1	<1	<1
SCr 27	Santa Cruz Island	Mzg	Gdt	E, M-g	18	16	46	15	5				<1		<1
BEKL 21D-1	San Jose scarp	Qzd		I, C-g (def)	63	11	18	2	6			<1	<1		<1
BEKL 8D-6	East of Partida bank	Mzg	Mzg	E, M-g	36	22	28	6	8			<1	<1	<1	1
BEKL 4D-1	Pescadero Canyon	Mzg	Mzg	I, M-g	35	30	22		13			<1	<1		<1
BEKL 4D-2	Pescadero Canyon	Mzg	Gdt	I, C-g	38	27	23		12			<1	<1		<1
ROCA 2J-2	Tamayo fracture zone	Qd		E, C-g (def)	60	3	6	20	11			<1	<1	1	<1
ROCA 2J-4	Tamayo fracture zone	Gdt	Qzd	E, C-g (def)	50	8	16	20	6			<1	<1	1	<1
ROCA 2J-8	Tamayo fracture zone	Gdt	Mzg	E, M-g	47	20	21	12				<1	<1	<1	<1
DANA 47D-1	West Nayarit Ridge fault scarp	Mzg	Mzg	I, M-g	35	19	37.5		8.5			<1	<1	<1	<1
Conc 01	Concordia, Sinaloa	Mzg	Gdt	E, M-g	25	32.5	25	4	13.5			<1	<1	<1	<1
MDCH 02	Mineral de Cucharas, Nayarit	Gdt		E, M-g	45	10	33	5	7			<1	<1		<1
Tepi 01	Tepic, Nayarit	Gdt	Mzg	I, M-g	46	22.5	21.5	1	9			<1	<1		<1
Sayu 01	Sayulita, Nayarit	Gdt	Qd	E, M-g (def)	38	19	15	3	25			1	<1	<1	
Sayu 02	Sayulita, Nayarit	Mzg	Gdt	E, M-g (def)	25	27.5	37.5		10			<1	<1	<1	
Early Miocene															
BC 09-25	Bahía Concepción, Baja California Sur	Mzg		I, M-g	33	22.5	20		7		17.5	<1	<1		1
SC 09-08	Santa Catalina Island	Qzd		E, M-g	58.5	11	7.5	11.5	9		2.5	<1	<1	<1	<1
SC 09-03	Santa Catalina Island	Qzd		I, M-g	55	11	11.5	15	7.5			<1	<1	<1	<1
SC 24	Santa Catalina Island	Qzd		I, M-g	50	25	15	4	6				<1	<1	<1
SC 09-04	Santa Catalina Island	QMz		I, M-g	39	22.5	13.5	10	15			<1	<1	<1	<1
DANA 71D-2	North Pescadero transform	Mzg	QMz	E, M-g	43	23	22	11	1			<1	<1		<1
ROCA 4J-12	North Pescadero transform	Mzg	QMz	I, M-g	33.5	19	30		17.5				<1	<1	<1
ROCA 4J-16	North Pescadero transform	Qzd	Qzd	I, M-g	59	12	12	7	10			<1	<1	<1	<1
ROCA 24J-22	South Pescadero transform	S	S	I, M-g	22	45	31		2				<1		
ROCA 24J-24	South Pescadero transform	Mzg	S	E, C-g	37	31	27		5			<1	<1		<1
ROCA 1J-1	West Nayarit Ridge fault scarp	Mzg	S	E, C-g	27	21	43		9				<1		<1
ROCA 1J-18	West Nayarit Ridge fault scarp	Q-rGD	AG	I, F-g	14	21	60.5		2	2.5			<1		<1
Ros 02	SW of El Rosario, Sinaloa	Qzd	Gdt	E, F-g	51	24	14	11				<1	<1	<1	<1
IXC 01	Santiago Ixcuintla, Nayarit	Qd	QMz	I, M-g	77	0	10	2	8		3	<1	<1		<1
IXC 02	Santiago Ixcuintla, Nayarit	Qd	Qzd	I, M-g	55	5	10	9	3.5		17.5	<1	<1		<1
IXC 03	Santiago Ixcuintla, Nayarit	T	Gdt	I, M-g	43	5	20	19	13			<1	<1		<1
PHC 09	El Cajon dam, Nayarit	Qzd	Qd	I, VF-g (Ph)	60	8	5	5	7		15	<1	<1		5
Oro 1	Santa Maria del Oro, Nayarit	Mzg		E, C-g	25	40	26		9				<1		2
Barr 04	Barrancas, Jalisco	T	Gdt	I, M-g	50	5	25	15	5			<1	<1	<1	<1
Middle Miocene															
BEKL 10D-1	Bank east of Partida Bank	Mzg		I, C-g	37	21	20	2	20		<1	<1	1	<1	<1
BEKL 10D-3	Bank east of Partida Bank	Mzg	Mzg	I, C-g	32.5	22.5	27.5	4	13.5			<1	<1	<1	<1
ROCA 22J-1	Cerralvo Bank	Qzd	Qzd	I, M-g	42.5	20	15	12	10.5				<1		<1
BEKL 6D-1	Cerralvo Bank	Mzg	Qzd	I, M-g	36	23	26	6	9			1	1	<1	<1
BEKL 6D-2	Cerralvo Bank	QMz	QS	I, C-g	32	50	11		7			<1	<1	<1	<1

Note: Mineral modal contents are expressed in vol%. QAP—classification based on the modal content of quartz, alkali feldspar, and plagioclase (QAP diagram for plutonic rocks of Streckeisen, 1976). Q′-ANOR—classification based on the Cross, Iddings, Pirsson and Washington (CIPW) normative composition after Streckeisen and LeMaitre (1979). Grain size after Gillespie and Styles (1999): coarse crystalline (>2 mm), medium crystalline (2–0.25 mm), fine crystalline (<0.25 mm). Geographic coordinates for samples not included in other tables: IXC 01 (21.7827°N, 105.0914°W), IXC 02 (21.9008°N, 105.1759°W), IXC 03 (22.1250°N, 105.1291°W). Abbreviations: Pl—plagioclase; Afs—alkali feldspar; Qz—quartz; Amp—amphibole; Bt—Biotite; Ms—muscovite; Px—pyroxene; Ap—apatite; Zrn—zircon; Ttn—titanite; Op—opaque minerals; Qzd—quartz monzodiorite; Gdt—granodiorite; Qd—quartz diorite; T—tonalite; Mzg—monzogranite; QMz—quartz monzonite; S—syenogranite; Q-rGD—quartz-rich granitoid dike; D—diorite; AG—alkali feldspar granite; QS—quartz syenite; E—equigranular; I—inequigranular; C-g—coarse grained; M-g—medium grained; F-g—fine grained; VF-g—very fine grained; Ph—porphyritic.

Geological Society of America Bulletin, published online on 4 December 2014 as doi:10.1130/B31008.1

TABLE 2. MAJOR AND TRACE ELEMENT ANALYSIS

	Cretaceous												Early Miocene					
Sample:	PB 32	ROCA 2J-4	SC 17	Sayu 01	Conc 01	SCr 27	Tepi 01	Sayu 02	ROCA 2J-8	DANA 47a	BEKL 4D-1	BEKL 8D-6	SC 09-03	PHC 09	SC 09-08	SC 09-04	IXC 02	ROCA 4J-16
Age (Ma):	100.4±1.3	94.5±1.5	96.9±0.9	77.7±0.5	59.4±0.5	98.2±1.5	65.7±0.8	75.2±0.5	98.9±1.4	92.9±0.9	82.4±0.7	96.7±1.1	18.7 ± 0.2	18.2±0.2	22.2±0.4	19.0±0.4		25.1±0.7
Rock type: *	D	QMd	Gdt	QD	Gdt	Gdt	Mg	Gdt	Mg	Mg	Mg	Mg	QMd	QD	QMd	QMd	QMd	QMd
Major elements (wt%)																		
SiO_2	52.79	59.49	63.1	63.63	66.63	67.48	67.87	71.58	72.08	71.96	75.27	75.82	56.51	56.74	58.22	60.29	60.37	62.70
TiO_2	0.922	0.686	0.606	0.441	0.519	0.387	0.429	0.293	0.214	0.177	0.132	0.133	0.811	1.096	1.015	0.622	0.964	0.681
Al_2O_3	18.95	17.2	16.06	18.32	15.46	15.29	15.23	14.89	15.56	15.43	14.07	13.24	17.86	18.07	17.188	17.315	16.24	16.70
Fe_2O_3†	9.45	6.09	6.08	4.44	3.61	4.61	3.86	2.26	1.51	1.38	1.53	1.04	7.06	7.87	6.97	5.53	6.34	5.46
MnO	0.155	0.117	0.089	0.121	0.066	0.055	0.062	0.047	0.027	0.044	0.031	0.029	0.078	0.129	0.109	0.092	0.097	0.102
MgO	3.87	3.20	2.10	0.67	1.6	1.24	1.16	0.65	0.80	0.54	0.13	0.36	4.39	3.06	3.23	3.03	2.69	2.35
CaO	7.56	5.4	4.5	3.87	3.39	3.42	2.55	2.42	1.99	2.17	1.33	1.68	6.37	6.66	5.38	5.64	5.04	3.73
Na_2O	3.76	3.99	3.9	5.51	3.34	3.84	3.35	3.53	4.77	4.71	3.85	3.39	3.93	3.48	4.03	4.28	3.55	4.49
K_2O	1.86	2.2	2.51	1.96	3.85	2.65	3.94	3.52	2.95	3.11	3.66	3.35	2.03	2.10	2.98	2.57	3.42	2.71
P_2O_5	0.276	0.244	0.152	0.141	0.129	0.106	0.100	0.102	0.069	0.062	0.041	0.030	0.168	0.347	0.264	0.186	0.246	0.206
LOI	0.39	1.31	0.56	0.63	0.87	0.7	1.24	0.64	0.72	0.46	0.58	0.6	0.89	0.19	0.51	0.48	0.84	1.13
Total	99.98	99.93	99.66	99.73	99.46	99.78	99.79	99.93	100.69	100.04	100.62	99.67	100.09	99.74	99.90	100.04	99.80	100.26
Trace elements (ppm)																		
Li	17.4		17.9	14.8	26.5	13.5	34.4	24.9			36.2	15.7		13.2			24.4	
Be	1.9		1.6	2.2	2.4	1.2	2	2.1			2.7	2		1.8			2.5	
Sc	4	13	8	4	9	5	7	3	3	3	2	2		17			15	12
V	58	152	93	17	83	61	48	28	25	24	13	20		183			116	101
Cr	429	28	322	3	20	387	6	6	13	5	4	5		13			29	6
Ni	44	8	66	1	9	69	2	2	2	5	1	2		9			18	
Rb	61.7	50.0	53.6	59.2	186.4	25.9	222.5	138.2	69.8	82.8	113.4	114		56.7			169	45.9
Sr	293	800	383	548	337	351	261	425	832	633	173	177		596			422	396
Y	14.4	13.7	15.3	13.9	28.2	6.0	26.1	12.1	4.4	7.5	22	8		29			32.2	23.6
Zr	176	103	180	338	219	126	181	163	89	57	96	114		181			473	292
Nb	12.44	6.92	9.99	9.45	12.86	5.05	9.53	8.17	4.04	3.91	7.05	7.29		8.31			14.69	9.3
Cs	2.21	1.00	2.11	3.89	3.48	1.08	9.37	11.08	3.03	3.57	3.01	2.74		5.02			10.1	0.45
Ba	831	1323	877	937	920	1143	862	1410	1436	1081	1041	395		607			825	974
La	22.03	18.55	20.46	27.66	26.03	26.46	30.09	29.82	12.53	7.87	25.51	17.94		23.34			33.22	26.84
Ce	36.5	36.45	32.71	48.02	55.01	30.68	60.67	53.74	22.89	14.84	47.02	32.71		48.53			67.79	53.19
Pr	4.59	4.59	4.32	5.48	6.94	4.12	7.38	6.14	2.65	1.78	5.51	3.58		7.08			8.9	6.55
Nd	16.52	18.69	16.74	19.14	26.01	13.04	26.41	20.85	9.68	7.24	19.54	11.97		29.03			33.99	25.8
Sm	3.11	4.12	3.38	3.15	5.53	1.98	5.23	3.44	1.85	1.80	4.01	1.75		6.53			6.96	5.43
Eu	0.85	1.38	0.94	1.86	0.89	0.69	0.87	0.87	0.58	0.47	0.57	0.5		1.54			1.32	1.15
Gd	2.68	3.57	2.96	2.64	4.78	1.55	4.55	2.6	1.33	1.56	3.60	1.27		5.86			6.13	4.86
Tb	0.41	0.51	0.46	0.39	0.75	0.22	0.7	0.37	0.16	0.23	0.58	0.18		0.87			0.91	0.76
Dy	2.32	2.83	2.61	2.25	4.48	1.08	4.21	1.99	0.89	1.35	3.60	1.06		5.04			5.24	4.56
Ho	0.46	0.53	0.51	0.48	0.89	0.23	0.84	0.4	0.17	0.27	0.73	0.25		0.97			1.03	0.91
Er	1.35	1.37	1.44	1.39	2.57	0.62	2.38	1.13	0.44	0.70	2.09	0.81		2.62			2.88	2.5
Yb	1.51	1.17	1.51	1.57	2.56	0.65	2.46	1.32	0.40	0.10	2.23	1.26		2.44			2.69	2.36
Lu	0.229	0.18	0.234	0.26	0.371	0.109	0.367	0.215	0.067	0.616	0.329	0.223		0.359			0.404	0.378
Hf	4.28	2.85	4.40	7.10	5.89	3.06	4.94	4.3	2.7	0.09	3.17	4.8		4.34			11.52	7.69
Ta	1.048	0.537	0.742	0.534	1.426	0.373	0.881	0.799	0.283	1.867	0.715	0.955		0.516			0.971	0.671
Pb	9.67	5.30	10.12	11.99	9.15	10.49	23.19	22.91	16.08	20.01	26.82	22.09		9.62			17.21	8.31
Th	8.95	3.03	6.48	7.08	21.33	8.04	21.84	10.69	3.83	3.23	11.88	43.59		6.77			20.56	7.61
U	1.73	1.13	2.19	1.69	7.07	1.12	4.7	3.28	0.85	0.88	3.05	11.4		1.98			9.59	2.34

(*continued*)

TABLE 2. MAJOR AND TRACE ELEMENT ANALYSIS (*continued*)

	Early Miocene													Middle Miocene			
Sample:	IXC 03	DANA 71b	IXC 01	Ros 02	BC 09-25	Barr 04	ROCA 4J-12	SC 24	Oro 01	ROCA 1J-1	ROCA 24J-22	ROCA 24J-24	ROCA 1J-18	ROCA 22J-1	BEKL 6D-1	BEKL 6D-2	BEKL 10D-3
Age (Ma):	20±2[§]	18.7±1.0		21.5±0.2	19.9±0.6	22.7±0.4	21.6±0.4	18.1±0.2	21.3±0.5	18.2±0.2	19.9±0.3	20.1±0.2	18.8±0.07	15.9±0.4	15.4±0.2	14.8±0.1	14.1±0.2
Rock type:*	Gdt	QM	QM	Gdt	QMd	Gdt	QM	Gdt	AFG	Sg	Sg	Sg	Kfs-G	QMd	QMd	QS	Mg
Major elements (wt%)																	
SiO_2	62.74	63.11	63.55	64.2	64.33	65.53	66.19	67.115	73.421	75.59	75.51	75.44	77.08	62.89	63.84	67.86	71.26
TiO_2	0.586	0.801	1.007	0.582	0.527	0.682	0.668	0.476	0.107	0.125	0.151	0.136	0.063	0.878	0.661	0.434	0.521
Al_2O_3	16.69	16.29	15.85	16.48	16.856	15.93	15.17	16.899	13.37	13.59	13.33	12.98	12.64	15.45	16.4	16.02	15.31
Fe_2O_3[†]	5.27	5.83	5.54	4.46	4.22	4.14	3.96	3.43	1.01	0.81	0.88	1.47	0.62	5.49	4.37	2.25	2.10
MnO	0.095	0.111	0.087	0.121	0.068	0.11	0.083	0.04	0.03	0.106	0.045	0.043	0.048	0.083	0.072	0.024	0.045
MgO	2.651	2.58	1.51	1.58	2.015	1.3	2	1.409	0.052	0.2	0.32	0.25	0.07	2.5	1.98	0.52	0.49
CaO	5.029	3.13	3.09	4.03	4.388	3.14	1.59	3.156	0.549	0.74	0.96	0.93	0.44	4.02	3.82	1.32	2.15
Na_2O	3.003	4.21	3.6	4.63	4.241	4.16	5.41	4.217	3.971	3.96	3.84	3.5	4.04	3.29	3.7	3.92	4
K_2O	2.694	3.63	4.9	2.22	2.686	3.39	3.08	3.254	4.498	5.15	4.6	4.54	4.48	3.89	3.91	5.98	4.13
P_2O_5	0.147	0.204	0.239	0.192	0.156	0.206	0.156	0.101	0.039	0.03	0.038	0.035	0.015	0.214	0.154	0.067	0.08
LOI	0.85	1.36	0.69	0.69	0.34	0.61	2.26	0.14	2.94	0.37	0.51	0.4	0.29	0.74	0.47	0.76	0.65
Total	99.76	101.26	100.06	99.19	99.83	99.20	100.56	100.23	99.98	100.67	100.18	99.72	99.79	99.45	99.38	99.16	100.74
Trace elements (ppm)																	
Li	17.8		15.4	8.5		8.6									20.5	15.2	11.3
Be	1.6		3.6	2		2.3									3.5	2.4	2
Sc	14	15	12	10		8	10			5	3	3	6	16	11	7	3
V	123	109	74	79		70	82			5	7	7		119	86	17	33
Cr	34	15	15	9		8	32			4	4	4	4	41	34	4	9
Ni	15	12	10	4		3	14							14	18	2	4
Rb	137.2	74.7	270.6	55.1		87.9	42.4			185.8	129.8	173.8	253.9	169.4	221.4	226.1	129
Sr	372	365	310	417		308	152			60	105	87	12	337	341	181	292
Y	23.6	36.7	36.4	19		25.5	17			29.7	24.6	33.7	39.1	28.1	25.6	25.7	9.4
Zr	152	332	478	198		241	288			65	105	101	56	236	132	434	106
Nb	8.95	14.44	16.55	10.53		11.81	11.47			18.52	8.8	9.26	20.42	13.89	18.94	23.75	7.7
Cs	7.54	0.64	12.47	1.45		1.56	0.21			4.06	0.84	2.22	10.46	9.82	11.43	7.47	2.97
Ba	688	1297	996	1020		1034	1005			410	915	778	63	917	706	1052	1063
La	24.15	26.12	42.55	19.45		38.38	24.93			23.07	28.13	27.73	16.1	34.73	39.92	32.26	15.82
Ce	48.82	55.66	89.68	39.6		65.3	49.39			44.81	55.43	55.54	40.12	71.39	79.85	62.36	27.93
Pr	6.09	7.15	11.53	5.01		8.4	6.01			5.08	6.32	6.42	5.15	8.78	9.24	7.88	3.02
Nd	22.47	30.44	43.34	19.27		29.92	23.35			17.29	22.36	23.13	18.19	33.52	31.56	29.09	10.57
Sm	4.61	7.22	8.8	3.88		5.54	4.54			3.75	4.49	5.25	5.35	6.73	5.82	5.94	1.97
Eu	0.94	1.23	1.31	1.13		1.36	0.89			0.29	0.46	0.44	0.08	1.41	1.09	1.12	0.67
Gd	4.14	6.45	7.36	3.49		4.86	3.92			3.52	3.85	4.92	5.23	5.88	4.79	5.01	1.76
Tb	0.64	1.07	1.1	0.53		0.72	0.6			0.71	0.66	0.89	1.03	0.94	0.72	0.77	0.26
Dy	3.82	6.6	6.21	3.19		4.2	3.39			4.77	4.04	5.6	6.57	5.43	4.16	4.48	1.52
Ho	0.76	1.35	1.19	0.65		0.84	0.68			0.99	0.87	1.17	1.32	1.09	0.82	0.88	0.32
Er	2.16	3.56	3.31	1.83		2.38	1.77			2.98	2.58	3.38	3.67	2.89	2.33	2.46	0.86
Yb	2.17	3.108	3.17	1.92		2.37	1.83			3.69	2.7	3.52	3.68	2.57	2.39	2.43	0.94
Lu	0.326	0.47	0.466	0.296		0.362	0.295			0.605	0.432	0.545	0.563	0.409	0.35	0.359	0.149
Hf	4.37	8.901	11.34	4.57		5.88	7.92			2.79	3.73	3.86	3.23	6.57	3.43	9.8	2.79
Ta	0.838	0.85	1.071	0.692		0.836	0.67			2.693	0.999	1.168	2.692	1.039	1.518	1.22	0.743
Pb	12.84	8.56	20.72	6.14		13.39	8.25			24.54	12.84	16.22	20.78	18.09	10.45	10	10.6
Th	19.49	9.05	40.05	5.64		9.62	9.04			18.96	18.51	21.29	14.4	18.45	22.21	21.02	19.6
U	6.59	3.05	14.26	1.45		1.98	2.72			4.85	5.28	7.04	4.42	4.9	6.37	6.42	4.78

Note: DANA and ROCA samples were analyzed at GeoAnalytical Laboratory, Washington State University; major elements of all other samples were determined by X-ray fluorescence (XRF) at Instituto de Geología, UNAM, and trace elements by inductively coupled plasma–mass spectrometry at Laboratorio de Estudios Isotópicos, Centro de Geociencias, UNAM. Location of sampling sites are given in Tables 1 and 3. Abbreviations: D—diorite; QMd—quartz monzodiorite; Gdt-granodiorite; QD—Quartz diorite; Mg—Monzogranite; QM—Quartz Monzonite; AFG—Alkali feldspar granites; QS—Quarz syenite; Sg—Syenogranite; Kfs-G—Alkali feldspar granite. LOI—Loss on ignition.

*Chemical classification after Streckeisen and LeMaitre (1979).

[†]Values given are total Fe expressed as Fe_2O_3.

[§]Age from Ferrari et al. (2002) for a sample from the same intrusive body (sample ESC 1).

Geological Society of America Bulletin, published online on 4 December 2014 as doi:10.1130/B31008.1

TABLE 3. U/Pb AND $^{40}Ar/^{39}Ar$ AGES OBTAINED FOR INTRUSIVE ROCKS FROM THE SOUTHERN GULF OF CALIFORNIA AND ITS ADJACENT SUBAERIAL MARGINS

Sample	Rock type		Latitude (°N)	Longitude (°W)	Elevation/depth (masl)	Sampling	Age (Ma)	Error (Ma)	Method	Material	Age type	Inherited zircons (Ma)
Cretaceous												
PB 32	Qzd		25.2911	110.9345	0	Field	100.4	1.3	U-Pb	Zrn	wm	110 and 114
							99.86	1.72	$^{40}Ar/^{39}Ar$	Bt	tc	
SCr 09-21	Qd		25.3082	110.6957	0	Field	99.12	1.53	$^{40}Ar/^{39}Ar$	Hbl	tc	
ROCA 2J-8	Gdt		22.8116	107.7310	–1991	ROV	98.93	1.45	$^{40}Ar/^{39}Ar$	Bt	tc	
SCr 27	Mzg		25.3058	110.6997	0	Field	98.2	1.5	U-Pb	Zrn	wm	110 and 115
SC 17	Gdt		25.6832	110.7969	0	Field	96.94	0.86	U-Pb	Zrn	wm	104
							90.97	0.65	$^{40}Ar/^{39}Ar$	Hbl	ofa	
							88.52	0.45	$^{40}Ar/^{39}Ar$	Bt	tp	
BEKL 8D-6	Mzg	(b)	24.7758	110.1308	–1205	Dredge	96.7	1.1	U-Pb	Zrn	wm	108 and 127
		(e)	24.7745	110.1350	–900		96.77	0.35	$^{40}Ar/^{39}Ar$	Bt	tc	
ROCA 2J-4	Gdt		22.8104	107.7336	–2219	ROV	94.53	1.47	$^{40}Ar/^{39}Ar$	Hbl	tc	
BEKL 21D-1	Qzd	(b)	24.9331	110.4116	–1392	Dredge	95.4	2.2	U-Pb	Zrn	wm	119 and 130
		(e)	24.9308	110.4146	–1250							
ROCA 2J-2	Qd		22.8096	107.7347	–2297	ROV	93.18	1.88	$^{40}Ar/^{39}Ar$	Hbl	tc	
DANA 47A	Mzg	(b)	22.5167	106.6992	–1079	Dredge	92.92	0.9	U-Pb	Zrn	wm	130 to 168
		(e)	22.5167	106.6940	–780		19.16	0.06	$^{40}Ar/^{39}Ar$	Bt	wm	
SCr 09-20	T		25.2959	110.7005	0	Field	93.83	0.93	$^{40}Ar/^{39}Ar$	Bt	tc	
BEKL 4D-1	Mzg	(b)	23.8280	109.6020	–1020	Dredge	82.42	0.68	U-Pb	Zrn	wm	95 and 104
		(e)	23.8320	109.6040	–850		75.65	2.39	$^{40}Ar/^{39}Ar$	Bt	tc	
BEKL 4D-2	Mzg	(b)	23.8280	109.6020	–1020	Dredge	81.24	0.7	U-Pb	Zrn	wm	
		(e)	23.8320	109.6040	–850		77.93	0.09	$^{40}Ar/^{39}Ar$	Bt	tp	
LCB 7	Gdt		23.2697	109.4420	0	Field	79.96	0.73	U-Pb	Zrn	wm	160
Sayu 01	Gdt		20.8823	105.4177	114	Field	77.71	0.53	U-Pb	Zrn	wm	
							70.85	0.74	$^{40}Ar/^{39}Ar$	Hbl	wm	
							48.71	0.29	$^{40}Ar/^{39}Ar$	Bt	tp	
Sayu 02	Mzg		20.8685	105.4411	19	Field	75.22	0.53	U-Pb	Zrn	wm	112 to 161
							43.91	0.23	$^{40}Ar/^{39}Ar$	Bt	tp	
Tepi 01	Gdt		21.3161	104.9928	750	Field	65.73	0.83	U-Pb	Zrn	wm	
MDCH 02	Gdt		22.8124	105.2630	377	Field	65.38	0.46	U-Pb	Zrn	wm	
Conc 01	Mzg		23.2725	106.1171	113	Field	59.43	0.51	U-Pb	Zrn	wm	
							55.72	0.47	$^{40}Ar/^{39}Ar$	Hbl	tp	
							56.26	0.34	$^{40}Ar/^{39}Ar$	Bt	tp	
Early Miocene												
ROCA 4J-16	Qzd		24.7899	109.2008	–2455	ROV	25.12	0.67	U-Pb	Zrn	wm	30 - 35
							11.13	0.85	$^{40}Ar/^{39}Ar$	K-fsp	wm	
SC 15	AD		25.6589	110.7649	0	Field	22.8	0.27	$^{40}Ar/^{39}Ar$	Gms	tp	
Barr 04	T		21.0204	104.1917	947	Field	22.67	0.4	U-Pb	Zrn	wm	61
							19.8	0.48	$^{40}Ar/^{39}Ar$	Hbl	wm	
							19.65	0.11	$^{40}Ar/^{39}Ar$	Bt	tp	
SC 09-08	Qzd		25.6387	110.8004	0	Field	22.19	0.42	U-Pb	Zrn	wm	
							18.89	0.47	$^{40}Ar/^{39}Ar$	Hbl	tc	
							18.38	0.08	$^{40}Ar/^{39}Ar$	Bt	tp	

(*continued*)

is bounded toward the gulf by a NNW-trending peninsula, where regional mapping by the Mexican Geological Survey (SGM, 2000) reports several Cretaceous granite to tonalite bodies. However, the highest peaks in Bahía Concepción are formed by an inequigranular medium-grained plutonic rock that intrudes Oligocene ignimbrites. McFall (1968) reported an early Miocene age (ca. 20 Ma, K-Ar) for one sample from this intrusive body, and Godinez et al. (2010) also reported an early Miocene age for an intrusive rock west of Loreto, suggesting the presence of younger magmatism after the Cretaceous in this area. South of Bahía Concepción, intrusive rocks are mainly exposed at Santa Catalina and Santa Cruz islands (Figs. 1 and 4A–4D) and were mapped as Cretaceous in the regional geologic maps of Mexican Geological Survey (SGM, 2000). At Santa Catalina Island, the plutonic rocks intrude a greenish-black metasedimentary sequence with a poorly developed schistose texture overlain by an ~150-m-thick limestone strongly affected by contact metamorphism, which forms marble and an ~1.5-m-thick skarn layer. At Santa Cruz Island, the host rocks are high-grade gneiss, which could have reached migmatitic conditions. These basement rocks could be correlated with the Paleozoic to Late Jurassic basement of the El Fuerte Group, found in northern Sinaloa (Mullan, 1978; Keppie et al., 2006; Vega-Granillo et al., 2008, 2012). Plutonic rocks found on these islands are quite similar and consist of a coarse- to medium-grained granodiorite, which locally passes from quartz-diorite to granite, and in some cases shows ductile deformation at both microscopic and macroscopic scales. Mafic enclaves are common, which are mostly rounded and show a broad range of shapes and sizes (Fig. 4A). At Santa Catalina Island, the main pluton is intruded by younger quartz-monzonite to quartz-monzodiorite rocks with distinctive finer-grained texture (Fig. 4B), which yielded early Miocene U-Pb ages (Dave Kimbrough and Marty Grove [unpublished data], *in* Piñero-Lajas, 2008). A younger set of aplitic dikes and then a series of mafic dikes, which mainly intrude along normal faults, crosscut both plutonic units (Fig. 4C).

Eastern Rifted Margin in Nayarit and Sinaloa (Western Mexico Mainland)

Onshore geology of the Nayarit and Sinaloa margin has been recently described by Ferrari et al. (2013) and is only briefly summarized here. The Sierra Madre Occidental ignimbrite plateau is cut toward the gulf by a series of N-S– and NNW-striking normal faults forming grabens and half grabens. No Cretaceous intrusive rocks have been reported for this margin in northern Nayarit, which is extensively covered by early Miocene ignimbrites of the second Sierra Madre Occidental flare-up (Fig. 1). This area of the Sierra Madre Occidental is affected by several

Geological Society of America Bulletin, published online on 4 December 2014 as doi:10.1130/B31008.1

TABLE 3. U/Pb AND $^{40}Ar/^{39}Ar$ AGES OBTAINED FOR INTRUSIVE ROCKS FROM THE SOUTHERN GULF OF CALIFORNIA AND ITS ADJACENT SUBAERIAL MARGINS (*continued*)

Sample	Rock type		Latitude (°N)	Longitude (°W)	Elevation/depth (masl)	Sampling	Age (Ma)	Error (Ma)	Method	Material	Age type	Inherited zircons (Ma)
Early Miocene (*continued*)												
ROCA 4J-12	Mzg		24.7865	109.2023	–2641	ROV	21.56	0.44	U-Pb	Zrn	wm	
							9.91	0.57	$^{40}Ar/^{39}Ar$	K-fsp	tc	
Ros 02	Qzd		23.0011	105.7498	98	Field	21.46	0.15	U-Pb	Zrn	wm	
Oro 1	Mzg		21.4640	104.5020	381	Field	21.29	0.46	U-Pb	Zrn	wm	
							19.07	0.16	$^{40}Ar/^{39}Ar$	Bt	tp	
							17.65	0.13	$^{40}Ar/^{39}Ar$	K-fsp	tp	
ROCA 24J-24	Mzg		24.0190	109.0390	–1983	ROV	20.13	0.23	U-Pb	Zrn	wm	24
							13.77	0.13	$^{40}Ar/^{39}Ar$	Bt	tp	
ROCA 24J-22	S		24.0200	109.0390	–2009	ROV	19.90	0.27	U-Pb	Zrn	wm	590
							9.84	0.18	$^{40}Ar/^{39}Ar$	K-fsp	wm	
BC 09-25	Mzg		26.7827	111.7911	2	Field	19.89	0.57	U-Pb	Zrn	wm	31, 40, 88 and 89
							19.32	0.35	$^{40}Ar/^{39}Ar$	Bt	tp	
SC 09-04	QMz		25.6275	110.7934	0	Field	18.96	0.35	$^{40}Ar/^{39}Ar$	Hbl	tp	
							19.52	0.2	$^{40}Ar/^{39}Ar$	Bt	tc	
ROCA 1J-18	Q-rGD		22.5541	106.6978	–670	ROV	18.76	0.07	$^{40}Ar/^{39}Ar$	Musc	tp	
DANA 71B	Mzg	(b)	24.7463	109.1667	–3050	Dredge	18.73	1.03	$^{40}Ar/^{39}Ar$	Hbl	tc	
		(e)	24.7487	109.1625	–2780		4.17	0.10	$^{40}Ar/^{39}Ar$	K-fsp		
SC 09-03	Qzd		25.5954	110.1541	1	Field	18.66	0.22	$^{40}Ar/^{39}Ar$	Hbl	tp	
							19.73	0.61	$^{40}Ar/^{39}Ar$	Bt	tc	
ROCA 1J-1	Mzg		22.5564	106.7101	–1486	ROV	18.21	0.22	U-Pb	Zrn	wm	
							18.68	0.1	$^{40}Ar/^{39}Ar$	Bt	tp	
							14.05	0.43	$^{40}Ar/^{39}Ar$	K-fsp	tp	
PHC 09	Qzd		21.5123	104.5179	289	Field	18.16	0.18	U-Pb	Zrn	wm	
SC 24	Qzd		25.6242	110.7931	0	Field	18.10	0.15	$^{40}Ar/^{39}Ar$	Bt	tp	
Middle Miocene												
ROCA 22J-1	Qzd		24.2510	109.6760	–1516	ROV	15.86	0.35	U-Pb	Zrn	wm	
							15.93	0.08	$^{40}Ar/^{39}Ar$	Bt	tp	
BEKL 6D-1	Mzg	(b)	24.1140	109.4586	–1205	Dredge	15.38	0.17	U-Pb	Zrn	wm	
		(e)	24.1148	109.4638	–900		13.71	0.31	$^{40}Ar/^{39}Ar$	Hbl	tp	
							13.45	0.22	$^{40}Ar/^{39}Ar$	Bt	tc	
BEKL 6D-2	QMz	(b)	24.1140	109.4253	–1205	Dredge	14.85	0.14	U-Pb	Zrn	wm	
		(e)	24.1148	109.4638	–900							
BEKL 10D-1	Mzg	(b)	24.8081	109.9233	–1498	Dredge	13.73	0.18	U-Pb	Zrn	wm	
		(e)	24.8050	109.9285	–1200		12.57	0.09	$^{40}Ar/^{39}Ar$	Bt	tp	
BEKL 10D-3	Mzg	(b)	24.8081	109.9233	–1498	Dredge	14.06	0.22	U-Pb	Zrn	wm	
		(e)	24.8050	109.9285	–1200							

Note: U/Pb age errors are expressed in 2σ and $^{40}Ar/^{39}Ar$ errors are in 1σ. Complete data for all the experiments performed are given in supplemental files 4 and 5 (see text footnote 1); (b) begin and (e) end coordinates of dredge track; masl—meters above sea level. Abbreviations: Qzd—quartz monzodiorite; Mzg—monzogranite; Qd—quartz diorite; Gdt—granodiorite; T—tonalite; AD—andesite dike; S—syenogranite; QMz—quartz monzonite; Q-rGD—quartz-rich granitoid dike; Zrn—zircon; Bt—biotite; Hbl—hornblende; K-fsp—K-feldspar; Gms—groundmass; Musc—muscovite; wm—weighted mean; tc—correlation age; ofa—one fraction age; tp—plateau age; ROV—remotely operated vehicle.

NNE to N-S grabens produced by extension between 24 and 18 Ma (Ferrari et al., 2002), which has been related to the onset of rifting of the Gulf of California (Ferrari et al., 2013). The grabens are subsequently cut by NNW extensional fault systems active since ca. 20 Ma that locally expose early Miocene intrusive bodies at very low elevation along the main rivers (Ferrari et al., 2007, 2013; samples Ros 02, Oro 01, and PHC 09; Fig. 1). These plutons are typically inequigranular, with medium- to fine-crystalline and even porphyritic texture (e.g., sample PHC 09). These textural characteristics, and the fact that these plutons intrude the Oligocene ignimbrites, are suggestive of a very shallow depth of emplacement (<5 km). Intrusive rocks were also sampled southwest of Tepic along the NE-striking scarp bounding the mouth of the Gulf of California near Sayulita (samples Sayu 01, Sayu 02, and Tepi 01; Fig. 1). These rocks are equigranular and coarse grained and intrude a metasedimentary or metavolcanic succession of Jurassic to Early Cretaceous age (Valencia et al., 2013), indicating that they are part of the Late Cretaceous Puerto Vallarta Batholith.

Submerged Rifted Margins

Continental Crust on the Flanks of Alarcón Basin

Most of the northwestern boundary of Alarcón Basin has an abrupt contact between oceanic crust with clear magnetic anomalies of the C2An sequence (DeMets, 1995) and a steep continental slope from which silicic lavas and tuffs were dredged. At the northwest end of this continental slope, an orthogonal intersection with a NW-striking fault scarp provides a window into the interior of the slope, and ROCA 24J dive (Figs. 2 and 3) sampled a mainly granitic and andesitic section here (Figs. 4E–4F). The intersecting NW-striking scarp is at the southern end of a major structural lineament, which Lyle and Ness (1991) named the Santa Cruz fault zone and speculated that it was an extinct intracontinental transform fault zone that after ca. 3.7 Ma linked the northeast end of the Alarcón spreading axis to actual or incipient spreading centers in Farallón Basin before opening of the Pescadero Basin. Near the western corner of Alarcón Basin, the rifted continental slope is similarly intersected by the NW-striking Cerralvo Trough, a 10–20-km-wide depression that extends for 75 km to just beyond the northern tip of Cerralvo Island. There is clear geomorphic evidence of an inactive strike-slip fault with at least 30 km of right-lateral offset along the Cerralvo Island (southwest) side of the trough (Lonsdale and Kluesner, 2010; Kluesner, 2011), and we infer that the trough was a transtensional fault zone that, before the Alarcón Basin opened, linked Baja–North America spreading in the mouth of the gulf (i.e., the axes of the Los Frailes and Maria Magdalena Rises, predecessors of the East Pacific Rise; Castillo et al., 2010) to sites of oblique extension within the gulf. The

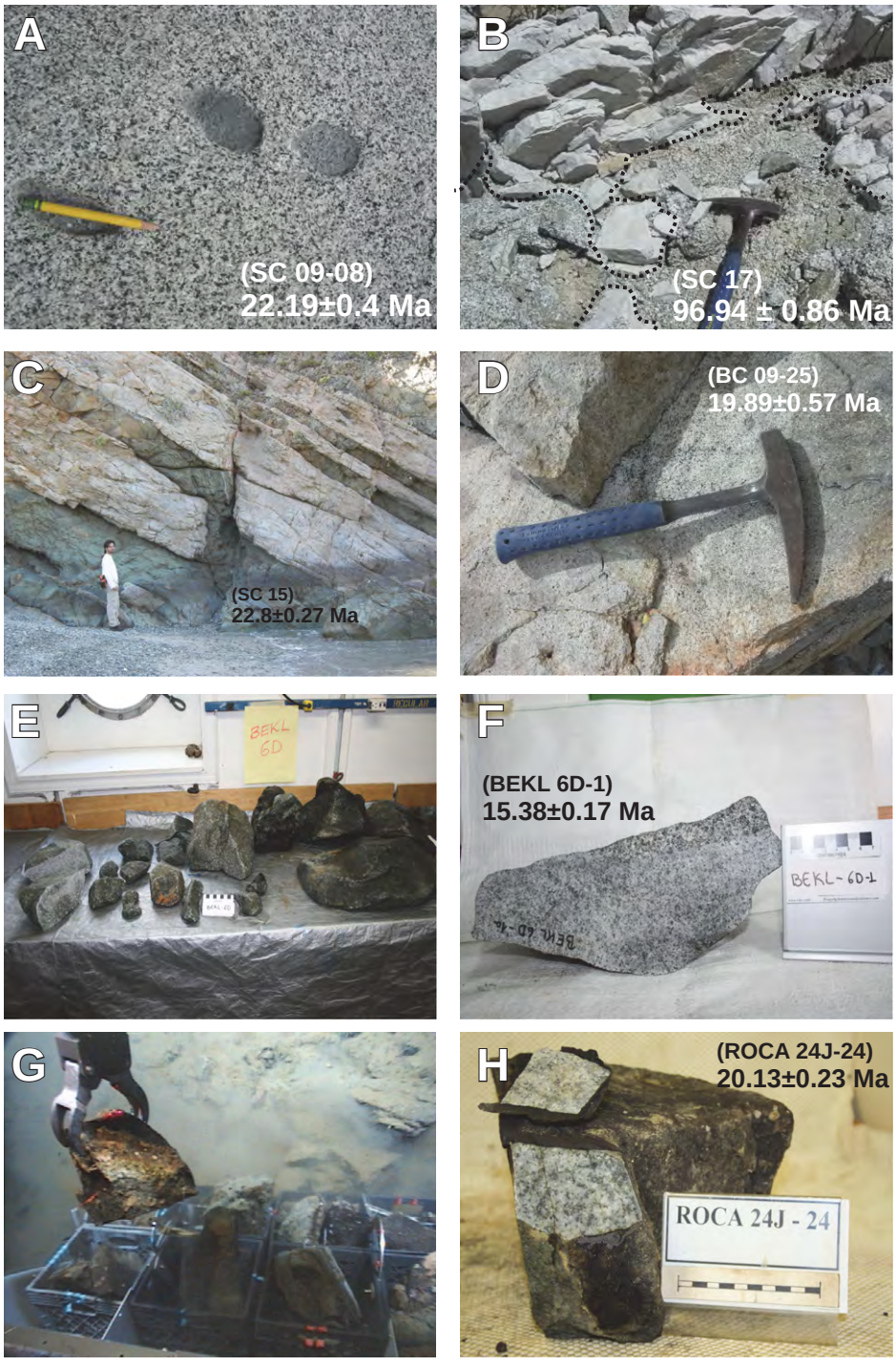

Figure 4. Field and megascopic aspect of studied samples. (A) Detail of early Miocene quartz monzodiorite (SC 09–08) from Santa Catalina Island (25.6387°N, 110.8004°W). (B) Early Miocene quartz monzodiorite (similar to SC 09–08) intruding a Cretaceous tonalite (SC 17) at Santa Catalina Island (25.6832°N, 110.7969°W). (C) Early Miocene mafic dike (SC 15) cutting a Cretaceous tonalite (similar to SC 17), Santa Catalina Island (25.6589°N, 110.7649°W). (D) Early Miocene subvolcanic granite intrusion (BC 09–25) from Bahía Concepción, Baja California (26.7827°N, 111.7911°W). (E) Samples recovered from dredge site BEKL 6D along a fault scarp in the southern part of the East Cerralvo Basin. (F) Megascopic view of the texture of middle Miocene monzogranite sampled at site BEKL 6D-1. (G) Sampling of ROCA 24J-24 sample with the remotely operated vehicle (ROV) *Jason* along the fault scarp bounding the Pescadero Basin to the west (24.0190°N, 109.0390°W, 1983 m below sea level); sample size: 26 × 23 × 13 cm. (H) Megascopic view of the texture of the early Miocene monzogranite recovered at site ROCA 24J-24.

northeast side of Cerralvo Trough is the scarp of a W-dipping, seismically active (Munguía et al., 2006) normal fault; it rises to the rift shoulder named Cerralvo Bank (with a wave-planed summit now at 200–300 m depth), one of the family of large-offset E- and W-dipping faults at the margins of the uplifted Cabo block. ROCA 22J climbed the steep lower part of this scarp, a few kilometers from where a U.S. Geological Survey (USGS) cruise in 1976 had dredged Cretaceous quartz-diorite and an altered middle Miocene hypabyssal rock of andesitic composition (M. Grove, 2007, personal commun.). The dive crossed a young fault scarp in the talus ramp and then climbed a highly altered and fault-brecciated granitic section (Fig. 3). Cerralvo Bank, indeed the whole 35-km-wide block of continental crust between Cerralvo Trough and Santa Cruz fault zone, is cut by extensional faults that strike 005°–015°, 45° oblique to the bounding NW-striking fault zones, and define shallow but steep-walled grabens; BEKL 6D dredged granitic rocks from one of the larger (500-m-high) examples of these N-striking graben-bounding scarps (Figs. 4G–4H). North of ~24.5°N, beyond Cerralvo Trough and the Cerralvo Bank block, most fault scarps maintain a northerly strike, but they tend to define short, isolated horsts rather than well-defined grabens; their lack of parallelism to the main rift-bounding faults (e.g., those of the Main Gulf Escarpment and other faults defining Santa Cruz Basin and Bahía La Paz Basin) may result from rotation of small fault blocks by distributed right-lateral shearing, as demonstrated by fault blocks in similar situations in the northern gulf (Seiler et al., 2011). Dredges BEKL 8D and 10D recovered Cretaceous and Miocene granites from two small N-striking horsts in this distal part of the northwest flank of Alarcón Basin, south of Farallón Basin (Fig. 2). Nearby dredge BEKL 21D collected Cretaceous granite from a very steep, ~650-m-high cliff formed by an E-dipping fault parallel to the Main Gulf Escarpment.

The continental slope at the southeast boundary of the oceanic Alarcón Basin is not quite as steep as the one on the northwest side, and Tamayo Bank (Fig. 2A) is not as shallow as its

Geological Society of America Bulletin, published online on 4 December 2014 as doi:10.1130/B31008.1

conjugate Cerralvo Bank, but it has an equally abrupt contact with the oceanic crust. The sheared-margin scarp at the southwest side of Tamayo Bank, which prior to Alarcón Basin spreading was continuous with the northeast side of Cerralvo Trough (the site of ROCA 22J), was explored by ROCA 2J. Its two upslope profiles (Fig. 3), located 17 km and 20 km southeast of the truncation of the scarp by oceanic crust at the southern corner of Alarcón Basin, climbed a Cretaceous granitic outcrop overlain by sandstone and mudstone. The dredging sites of Niemitz and Bischoff (1981, p. 388–389) are ~10 km southeast of ROCA 2J profile B, near where the sheared-margin scarp intersects the top of the rifted continental margin of Alarcón Basin; they reported a "granodiorite-tonalite suite" plus "a transitional suite of andesitic rocks, recovered from the lowermost part of the slope"; neither suite has been dated. At the ROCA 2J dive sites, the sheared margin of the "proto–Tamayo transform," a largely intracontinental shear zone that extended into Cerralvo Trough, is ~5 km north of the Tamayo fracture zone. The trail of the present Tamayo transform, and the intervening strip, is conjugate to the turbidite-smothered floor of Cerralvo Trough. Fitting the dredging profile shown in figure 9 of Niemitz and Bischoff (1981) to our multibeam bathymetry, it is clear that this strip, sampled at the steep step down to the west flank of the East Pacific Rise, is the source of the reported andesite suite.

Southeast of Tamayo Bank, seismic-refraction profiles (Lizarralde et al., 2007) show dramatic crustal thinning beneath an elongate depression known as Tamayo Trough (Fig. 2). However, seismic-reflection profiles indicate only minor faulting of the discontinuously reflective "basement" layer, which Sutherland et al. (2012) attributed to a volcanic or volcaniclastic section, beneath the trough floor and margins. This could easily be explained if the volcanic section postdated major basin-formation faulting, but if it is part of the lower to middle Miocene Comondú Group, the interpretation favored by Sutherland et al. (2012), this would imply large-scale faulting and basin extension there in the early Miocene. ROCA dive 3J onto Tamayo Dome, a major but mostly sediment-smothered, 40-km-diameter volcanic structure at the northern end of Tamayo Trough, sampled rhyolitic lithic ignimbrite that could have been a source of the structure-obscuring layer in Tamayo Trough. The tuff yielded a ^{40}Ar-^{39}Ar age of 11.70 ± 0.07 Ma (Ferrari et al., 2013), right at the middle-late Miocene boundary, providing a minimum age for this layer.

Further to the southeast, three large (50–70-km-long, up to 1-km-high) fault-bounded ridges, horsts, and half-horsts that strike N-NE (020°), curving to N-NW (340°) near their northern ends, rise above the muddy seafloor. These Nayarit Ridges have wave-planed summits, which step up from 500–600 m deep at the western ridge to 200–300 m deep at the central ridge, and 140–250 m deep at the eastern ridge, and their basement rocks crop out on their sides, especially at the W-dipping fault scarps on their western sides. The fresh granitic samples collected at the DANA 47 site, and the contrast between Cretaceous (U/Pb zircon; M. Grove, 2006, personal commun.) and Neogene ^{40}Ar-^{39}Ar mica cooling ages (published here) observed on some samples prompted us to resample this site during the ROCA cruise (ROCA 1J; Fig. 3).

Continental Crust on the Southeastern Flank of Farallón Basin

Subsided continental crust at the margin of Farallón Basin, which is mostly buried by thick turbidites, is well exposed at a scarp along the North Pescadero Transform (Fig. 2). This transform is a relatively recent link between the spreading center in the broad Farallón Basin and a younger spreading center that has accreted the floor of the much narrower North Farallón Basin. Because of its youth, all of this transform is bounded by continental crust on one or both sides, and because it is significantly oblique to present Baja California–North America relative plate motion (Fig. 2A), a deep transtensional transform valley has opened along these actively shearing continental margins.

The part of the transform valley that extends northwest from the northeastern tip of the North Pescadero spreading axis is relatively protected from terrigenous sediment filling, and it has a valley wall that rises steeply from 3300 m to 1200 m on its northeastern (continental) side. Of course, not all of this 2-km-high wall exposes igneous basement: It has a partly sediment-covered talus ramp that accounts for 600 m of relief at the foot of the scarp, and on the ROCA 4J profile (Fig. 3), we encountered only sedimentary rock at depths shallower that 1700 m. The DANA 71 dredge included Miocene granitic intrusive rocks in its diverse rock collection from the scarp-foot talus, and ROCA 4J was targeted to a nearby site to get more samples of this rock type to define the vertical extent of its outcrop and to attempt to define the stratigraphy of the overlying volcanic sections.

RESULTS

The plutonic rocks of the southern Gulf of California analyzed in this work yielded three separate groups of intrusion (U/Pb) ages: Cretaceous to early Paleocene (ca. 100–60 Ma), early Miocene (ca. 25–18 Ma), and middle Miocene (ca. 15.5–13.5 Ma). Significantly, no Oligocene age of intrusion was found in the study area, supporting the general conclusions of previous studies that the first ignimbrite flare-up of the Sierra Madre Occidental was sourced from areas to the east of the present-day Gulf of California (e.g., Ferrari et al., 2007). These three age groups are used in the description of the petrographic, geochemical, and geochronological results, which are summarized in Tables 1, 2, and 3 and Figures 5, 6, and 7. A brief explanation of each age obtained for the dated sample is given in the supplemental file 4 (see footnote 1).

Petrography and Geochronology

Cretaceous–Paleocene Magmatic Episode

Nineteen samples within and around the Gulf of California yielded Cretaceous to early Paleocene ages (100 and 60 Ma; Fig. 1; Table 3), with younger ages mostly toward the east (Fig. 8). On the western rifted margin, rocks of this group are all older than 80 Ma. They are found to the south of Loreto (Punta Botella; Fig. 1) and along the rifted continental crust offshore southern Baja California at the western border of the Farallón, Pescadero, and Alarcón Basins (Santa Cruz and Santa Catalina Islands, Partida Bank, Los Cabos block). On the eastern rifted margin, dated rocks range between ca. 100 and ca. 60 Ma and were found at the western Nayarit scarp (dredge DANA 47A), along the Tamayo fracture zone (dive ROCA 2J), and in the southern Sinaloa and northern Nayarit coastal area on the mainland (Sayu 01, Sayu 02, MDCH 02, Tepi 1, and Conc 01; Figs. 1 and 2A; Table 3).

Figure 5 (*on following three pages*). U/Pb concordia and ^{40}Ar-^{39}Ar age spectra or ^{36}Ar-^{40}Ar vs. ^{39}Ar-^{40}Ar correlation diagrams for Cretaceous plutons; the obtained age is given for each sample. In the U/Pb concordia diagrams, dashed ellipses indicate data not taken into account for age calculation. In the ^{40}Ar-^{39}Ar ages spectra, t_p and W_m indicate plateau and weighted mean ages, respectively; these ages were calculated using the fractions identified with the horizontal arrow. The value t_c indicates the isochron age, calculated using the fractions identified with the dotted line in the age spectra diagrams. Detailed information on the geochronological analysis is given in supplemental file 4 (see text footnote 1). MSWD—mean square of weighted deviates.

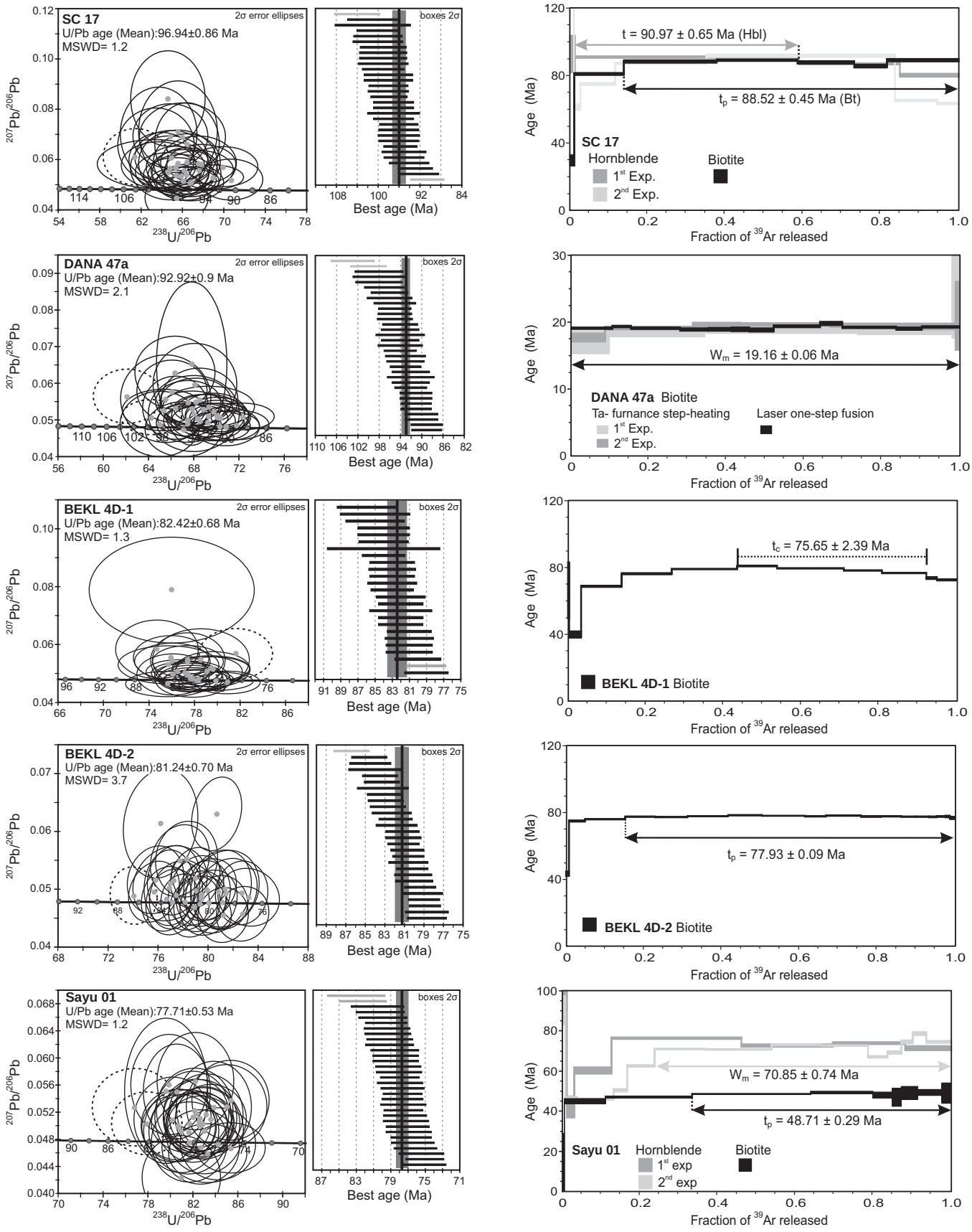
SC 17
U/Pb age (Mean):96.94±0.86 Ma
MSWD= 1.2
2σ error ellipses
boxes 2σ
Best age (Ma)
t = 90.97 ± 0.65 Ma (Hbl)
t_p = 88.52 ± 0.45 Ma (Bt)
SC 17
Hornblende
Biotite
1st Exp.
2nd Exp.
DANA 47a
U/Pb age (Mean):92.92±0.9 Ma
MSWD= 2.1
W_m = 19.16 ± 0.06 Ma
DANA 47a Biotite
Ta- furnance step-heating
Laser one-step fusion
BEKL 4D-1
U/Pb age (Mean):82.42±0.68 Ma
MSWD= 1.3
t_c = 75.65 ± 2.39 Ma
BEKL 4D-1 Biotite
BEKL 4D-2
U/Pb age (Mean):81.24±0.70 Ma
MSWD= 3.7
t_p = 77.93 ± 0.09 Ma
BEKL 4D-2 Biotite
Sayu 01
U/Pb age (Mean):77.71±0.53 Ma
MSWD= 1.2
W_m = 70.85 ± 0.74 Ma
t_p = 48.71 ± 0.29 Ma
Sayu 01
Hornblende
Biotite
1st exp
2nd exp
Age (Ma)
Fraction of 39Ar released
207Pb/206Pb
238U/206Pb

Figure 5.

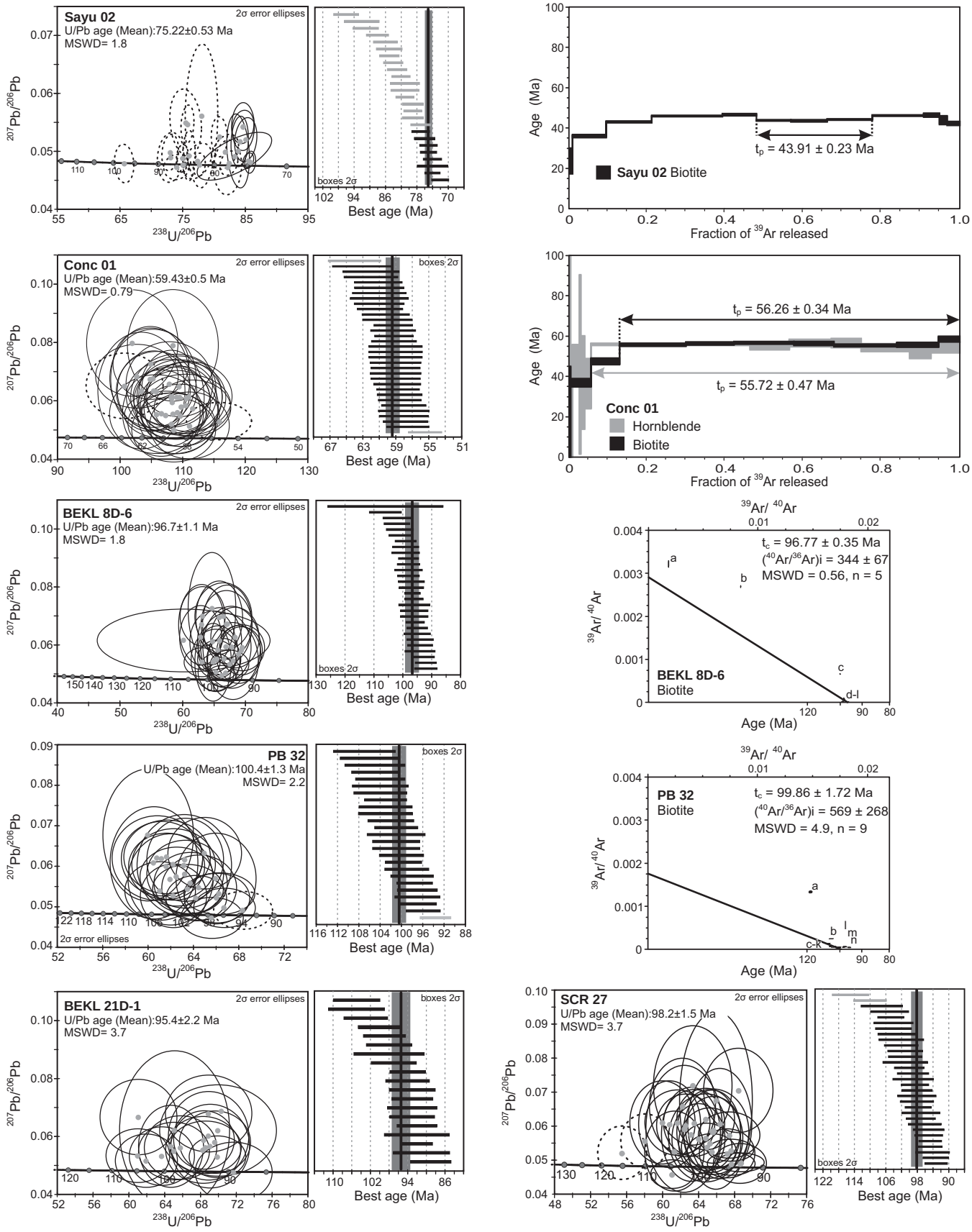

Figure 5 (*continued*).

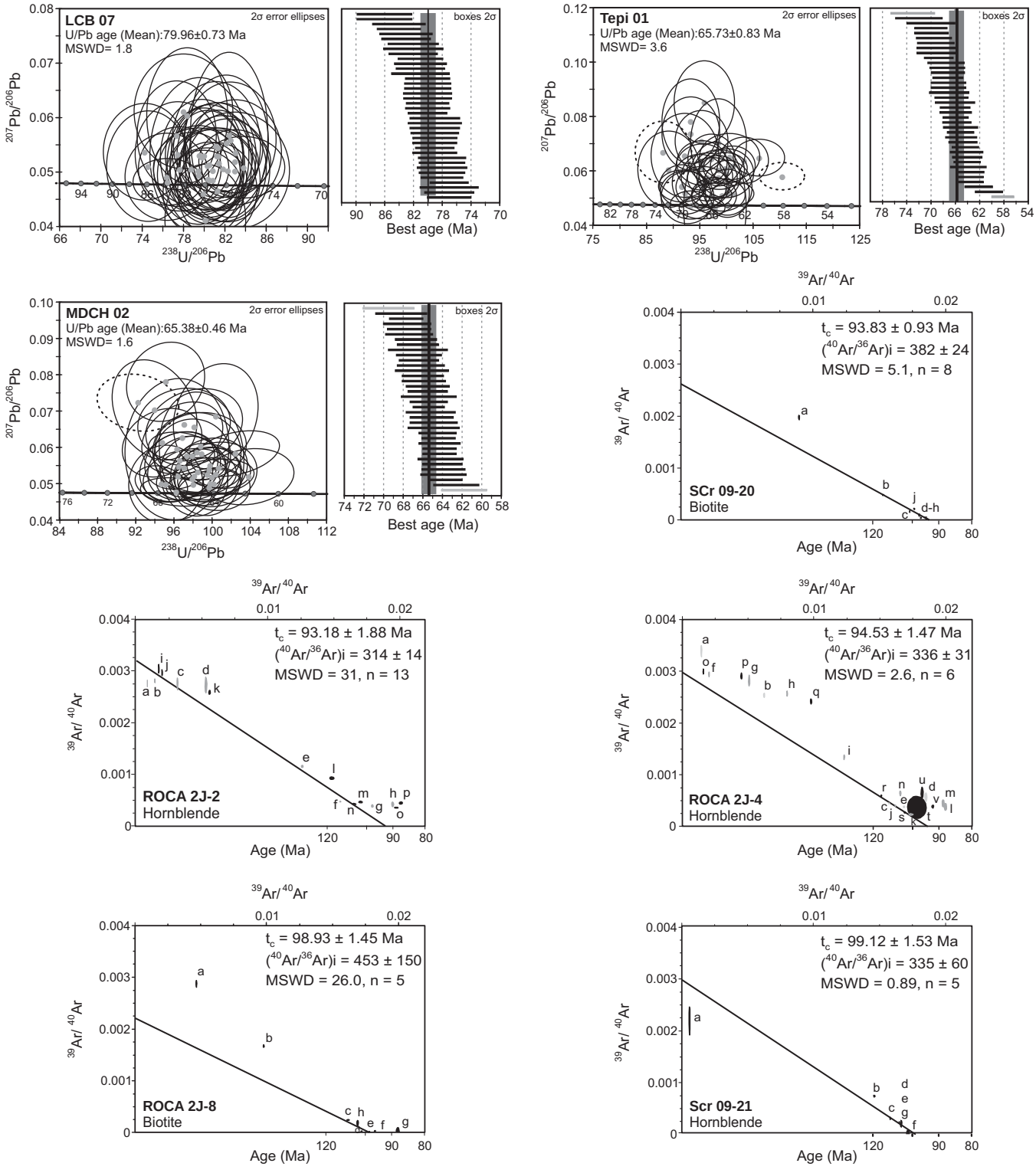

Figure 5 (*continued*).

The studied samples are defined as quartz monzodiorite, granodiorite, quartz diorite, tonalite, and monzogranite in the Streckeisen (1976) classification scheme (Table 1). Samples are mainly equigranular, with hypidiomorphic granular texture and medium to coarse grain size (Table 1). Some samples display an inequigranular texture characterized by an older generation of larger crystals (plagioclase and K-feldspar) and a second generation of medium- to coarse-grained crystals, arranged in a hypidiomorphic granular texture. A factor of note is that all samples from the Mexican mainland are medium grained; coarse-grained samples were found along the lower part of the Tamayo fracture zone at depths

Geological Society of America Bulletin, published online on 4 December 2014 as doi:10.1130/B31008.1

of 2297 and 2219 m below sea level (bsl; ROCA 2J-2 and ROCA 2J-4, respectively; Figs. 2A and 3), and in the western rifted margin (dredges BEKL 4D, 8D, and 21D, depths between 850 and 1392 mbsl; Santa Cruz Island, SCr 09–20, SCr 09–21; Punta Botella, PB 32; Figs. 2 and 3). In the Cretaceous–Paleocene samples, amphibole and biotite are the main ferromagnesian minerals, whereas apatite, zircon, titanite, and Fe-Ti oxides are common accessory minerals. Some Cretaceous samples display mineral lineations, possibly related to the syntectonic older intrusions in southern Baja California and Sinaloa (Henry and Fredrikson, 1987; Henry et al., 2003; Cuéllar-Cárdenas et al., 2012).

Most Cretaceous–Paleocene samples have ^{40}Ar-^{39}Ar ages 5–10 m.y. younger than the corresponding U/Pb age (Figs. 5 and 8). Nevertheless, some samples from western Nayarit and its offshore region (Fig. 1D) yielded a much larger time gap between intrusion and cooling age (Sayu 01, Sayu 02, DANA 47A; Table 3; Fig. 8). Samples Sayu 01 and Sayu 02 represent two different magmatic facies from the same pluton, and they have similar intrusion ages of ca. 76 Ma (Figs. 5 and 8). However, Sayu 01 yielded a ^{40}Ar-^{39}Ar age on hornblende of 70.85 ± 0.74 Ma, and a ^{40}Ar-^{39}Ar biotite age of 48.71 ± 0.29 Ma, similar to the 43.91 ± 0.23 Ma age obtained for a biotite from Sayu 02 (Fig. 5). Sample DANA 47A, dredged on the western Nayarit scarp (Figs. 1D, 2, and 3), has a U/Pb age of 92.92 ± 0.90 Ma, but a ^{40}Ar-^{39}Ar biotite age of 19.16 ± 0.06 Ma. This latter age is similar to the 18.21 ± 0.22 Ma U/Pb age and the 18.68 ± 0.1 Ma ^{40}Ar-^{39}Ar biotite ages of sample ROCA 1J-1 (Figs. 5 and 8), as well as the 18.76 ± 0.07 Ma ^{40}Ar-^{39}Ar muscovite age of sample ROCA 1J-18 (Figs. 5 and 8). These three samples (DANA 47A, ROCA 1J-1, and ROCA 1J-18) were recovered within a few kilometers in the same area of the western Nayarit scarp (Figs. 1D, 2, and 3), which we interpret as formed by a Cretaceous batholith (sampled by DANA 47A) that was subsequently intruded by a series of younger bodies during the early Miocene (ca. 18–19 Ma). The intrusion of these early Miocene rocks likely generated a thermal anomaly, potentially perturbing the ^{40}Ar-^{39}Ar systematics of surrounding rocks. The Cretaceous U/Pb age of sample DANA 47A contrasts with the early Miocene biotite ^{40}Ar-^{39}Ar age obtained on the same sample (19.16 ± 0.06 Ma), which approaches Ar cooling ages for samples ROCA 1J-1 and ROCA 1J-18 (Figs. 5 and 6). These age differences suggest that the DANA 47A biotite was reheated by the intrusion of a plutonic body represented by ROCA 1J-1 and ROCA 1J-18 samples. The age spectra of DANA 47A (Fig. 5) does not show any evidence of perturbation, indicating that the Ar system was completely reset. Furthermore, samples Sayu 01 and Sayu 02, which yield Cretaceous U/Pb ages (ca. 76 Ma), also yielded Eocene (48.71 ± 0.29 Ma and 43.91 ± 0.23 Ma) ^{40}Ar-^{39}Ar biotite ages, which probably are geologically meaningless. In fact, these samples have a so-called "Turner profile" spectra, which is typical of biotites that has undergone incomplete Ar loss (York and López-Martinez, 1986). This is confirmed by the fact that no intrusive or extrusive rocks of Eocene age are found in the surrounding region, which is in turn affected by widespread late Miocene mafic volcanism. We thus interpret the Sayulita pluton to have been only mildly reheated by a younger igneous event causing only partial Ar loss.

Early Miocene Magmatic Episode

Seventeen samples yielded U/Pb zircon ages between 25 and 18 Ma. They span the whole southern gulf from the eastern side of the Baja California peninsula and its neighboring islands, to the submerged rifted blocks, and Mexico mainland in Nayarit and Sinaloa (Table 3; Fig. 6). On the western rifted margin of the gulf, early Miocene plutons were found at Bahía Concepción, on Santa Catalina Island, and in the submerged continental blocks to the east (Figs. 1B–1D and 2). The early Miocene plutons are commonly medium grained, and inequigranular textures predominate over equigranular ones (Table 1), whereas fine-grained and porphyritic rocks were only found in the southeastern part of the gulf. Inequigranular samples are mostly medium grained, with the exception of a fine-grained sample from the western Nayarit scarp collected at 670 mbsl (ROCA 1J-18) and a porphyritic subvolcanic intrusion with very fine-grained matrix from the southwestern foothills of the Sierra Madre Occidental (PHC 09; Fig. 1D). Equigranular samples are hypidiomorphic granular with variable grain size (coarse to fine grained). The only fine-grained equigranular sample (Ros 02) comes from southern Sinaloa, in mainland Mexico. Coarse-grained, equigranular samples were found only at three localities: the southern Pescadero transform fault at depths of 1983 mbsl (ROCA 24J-24), the western Nayarit scarp at depths of 1486 mbsl (ROCA 1J-1), and east of Tepic in the Sierra Madre Occidental foothills (Oro 1) at 381 masl (Figs. 1, 2, and 3).

The least-differentiated early Miocene rocks are quartz diorite, quartz monzodiorite, monzogranite, and tonalite that contain amphibole and biotite as the main ferromagnesian minerals, and titanite, zircon, apatite, and Fe-Ti oxides as accessory minerals. Within the more-evolved rocks, which classify as monzogranite, syenogranite, and granite, the main ferromagnesian mineral is biotite, whereas amphibole and titanite are absent (except for DANA 71B, which has 11% of amphibole). Muscovite, along with biotite, was observed only in a granite sample from the western Nayarit scarp (ROCA 1J-18). In some early Miocene samples, pyroxene constitutes 2%–17.5% of the rock. Usually, pyroxene is found as subhedral crystals exhibiting resorption textures that in some cases obliterate the original crystal structure; the presence of orthopyroxene and clinopyroxene crystals, even in highly differentiated samples (e.g., monzogranite BC 09–25), along with resorption textures, indicates that pyroxene was not in equilibrium with the melt.

Several early Miocene plutonic rocks show little difference between intrusion and cooling ages. A fine-grained monzogranite in the eastern side of Bahía Concepción (sample BC 09–25) yielded almost identical U/Pb and ^{40}Ar-^{39}Ar biotite ages of 19.89 ± 0.57 Ma and 19.32 ± 0.35 Ma, respectively. This indicates that in this area, the pluton cooled very quickly (within ~0.5 m.y.) from emplacement (~900 °C) to below 350–400 °C, the closure temperature of biotite (Reiners et al., 2005; Fig. 6). A rapid cooling at ca. 19–18 Ma can be also inferred at Santa Catalina Island. The quartz-monzonite that crops out in the western part of the island yielded a U/Pb age of 22.19 ± 0.42 Ma (sample SC 09–08; Table 3; Fig. 6), a hornblende age of 18.89 ± 0.47 Ma, and a biotite age of 18.38 ± 0.08 Ma. A dike intruding the Cretaceous pluton in the eastern side of the island (SC 15) yielded a ^{40}Ar-^{39}Ar age of 22.8 ± 0.27 Ma (groundmass), but the rest of early Miocene granitoids sampled at the island (SC 09–03, SC 09–04, and SC 24) all fall in a narrow ^{40}Ar-^{39}Ar age range at ca. 19–18 Ma (Table 3; Fig. 6).

Figure 6 (*on following three pages*). U/Pb concordia and ^{40}Ar-^{39}Ar age spectra or ^{36}Ar-^{40}Ar vs. ^{39}Ar-^{40}Ar correlation diagrams for early Miocene plutons; the obtained age is given for each sample. In the U/Pb concordia diagrams, dashed ellipses indicate data not taken into account for age calculation. In the ^{40}Ar-^{39}Ar age spectra, t_p and W_m indicate plateau and weighted mean ages, respectively; these ages were calculated with the fractions identified with the horizontal arrow. The value t_c indicates the isochron age, calculated using the fractions identified with the dotted line in the age spectra diagrams. Detailed information on the geochronological analysis is given in supplemental file 4 (see text footnote 1). MSWD—mean square of weighted deviates.

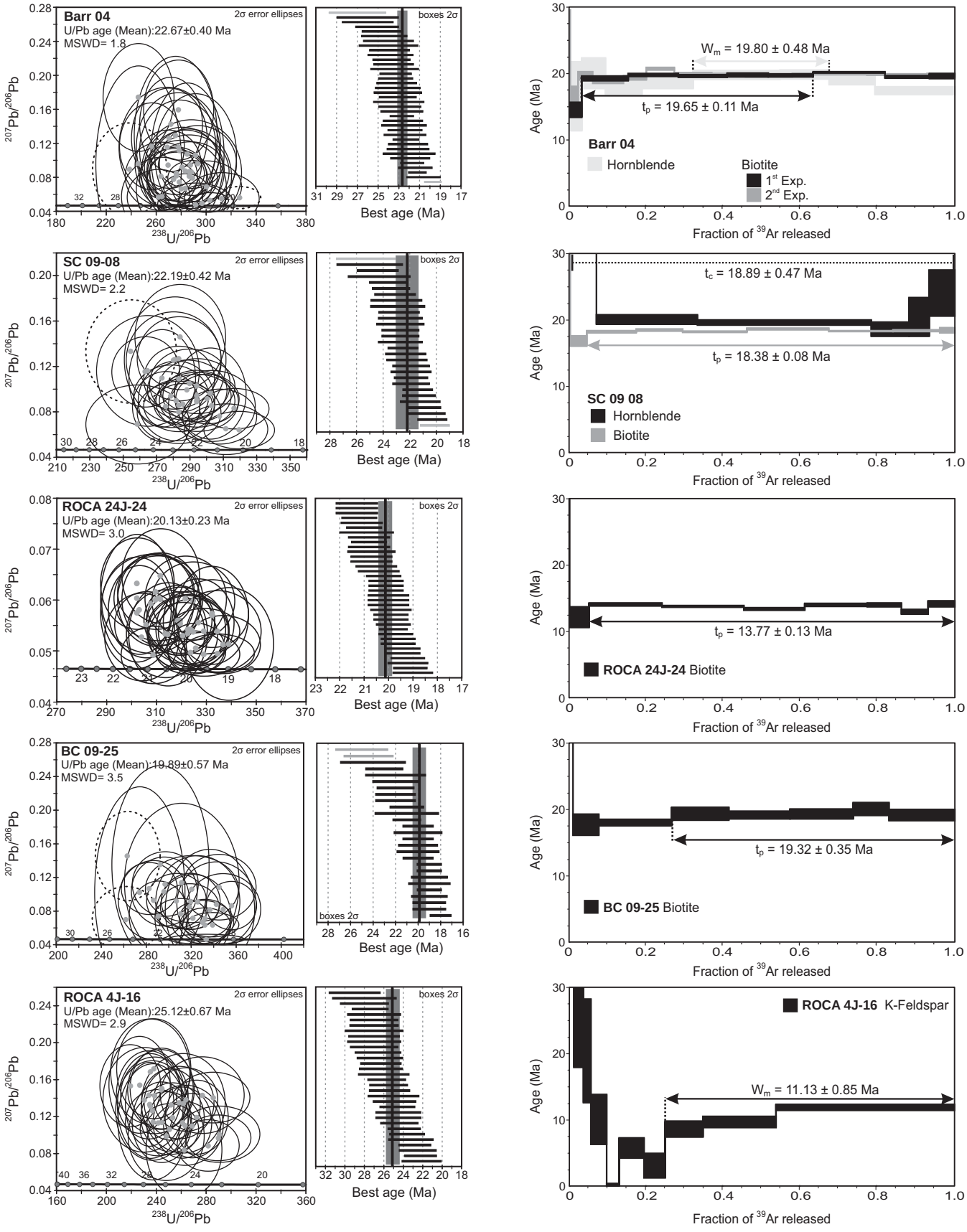
Barr 04
U/Pb age (Mean):22.67±0.40 Ma
MSWD= 1.8
2σ error ellipses
boxes 2σ
Best age (Ma)
$^{207}Pb/^{206}Pb$
$^{238}U/^{206}Pb$
W_m = 19.80 ± 0.48 Ma
t_p = 19.65 ± 0.11 Ma
Hornblende
Biotite
1st Exp.
2nd Exp.
Age (Ma)
Fraction of ^{39}Ar released
SC 09-08
U/Pb age (Mean):22.19±0.42 Ma
MSWD= 2.2
t_c = 18.89 ± 0.47 Ma
t_p = 18.38 ± 0.08 Ma
SC 09 08
ROCA 24J-24
U/Pb age (Mean):20.13±0.23 Ma
MSWD= 3.0
t_p = 13.77 ± 0.13 Ma
ROCA 24J-24 Biotite
BC 09-25
U/Pb age (Mean):19.89±0.57 Ma
MSWD= 3.5
t_p = 19.32 ± 0.35 Ma
BC 09-25 Biotite
ROCA 4J-16
U/Pb age (Mean):25.12±0.67 Ma
MSWD= 2.9
ROCA 4J-16 K-Feldspar
W_m = 11.13 ± 0.85 Ma

Figure 6.

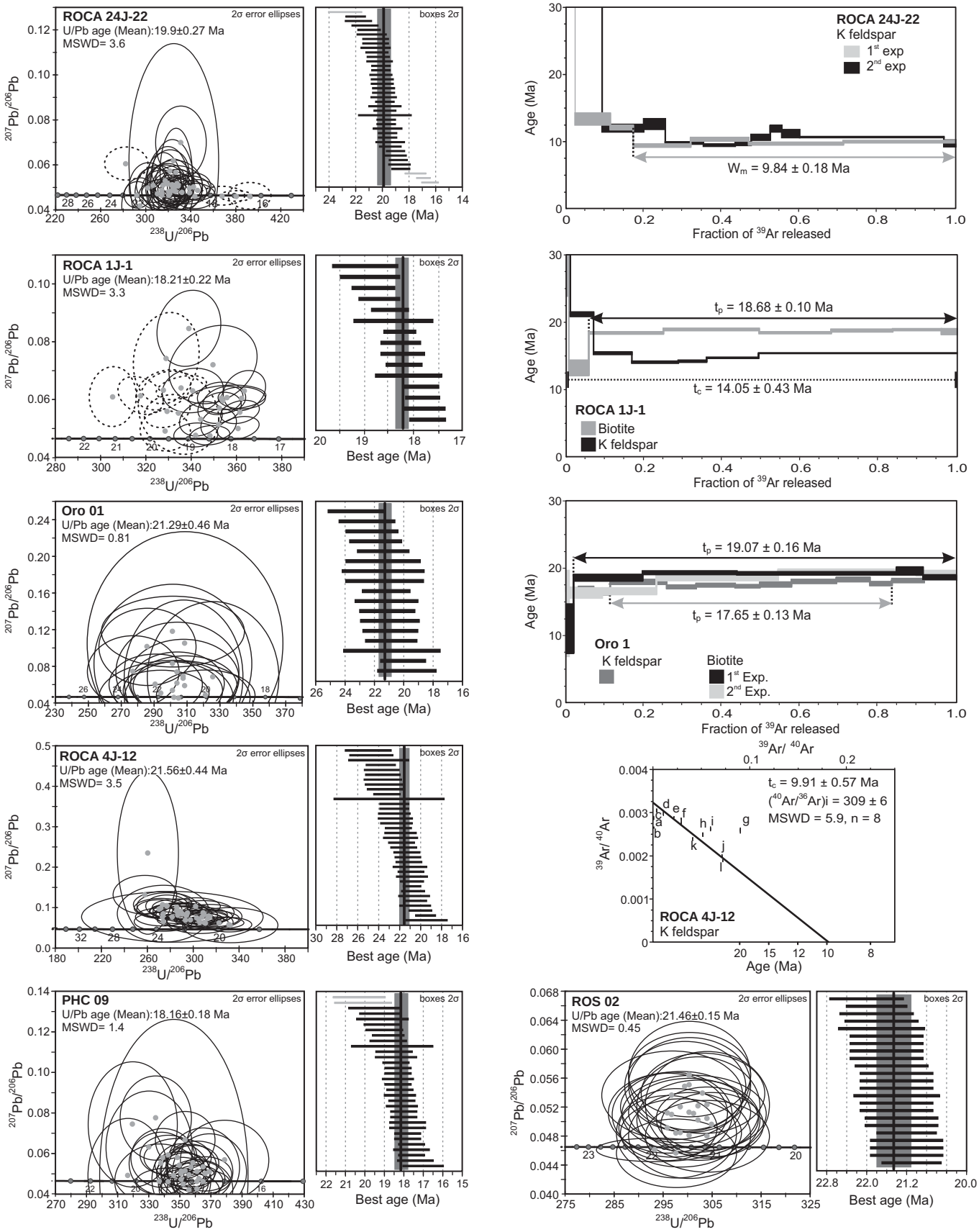

Figure 6 (*continued*).

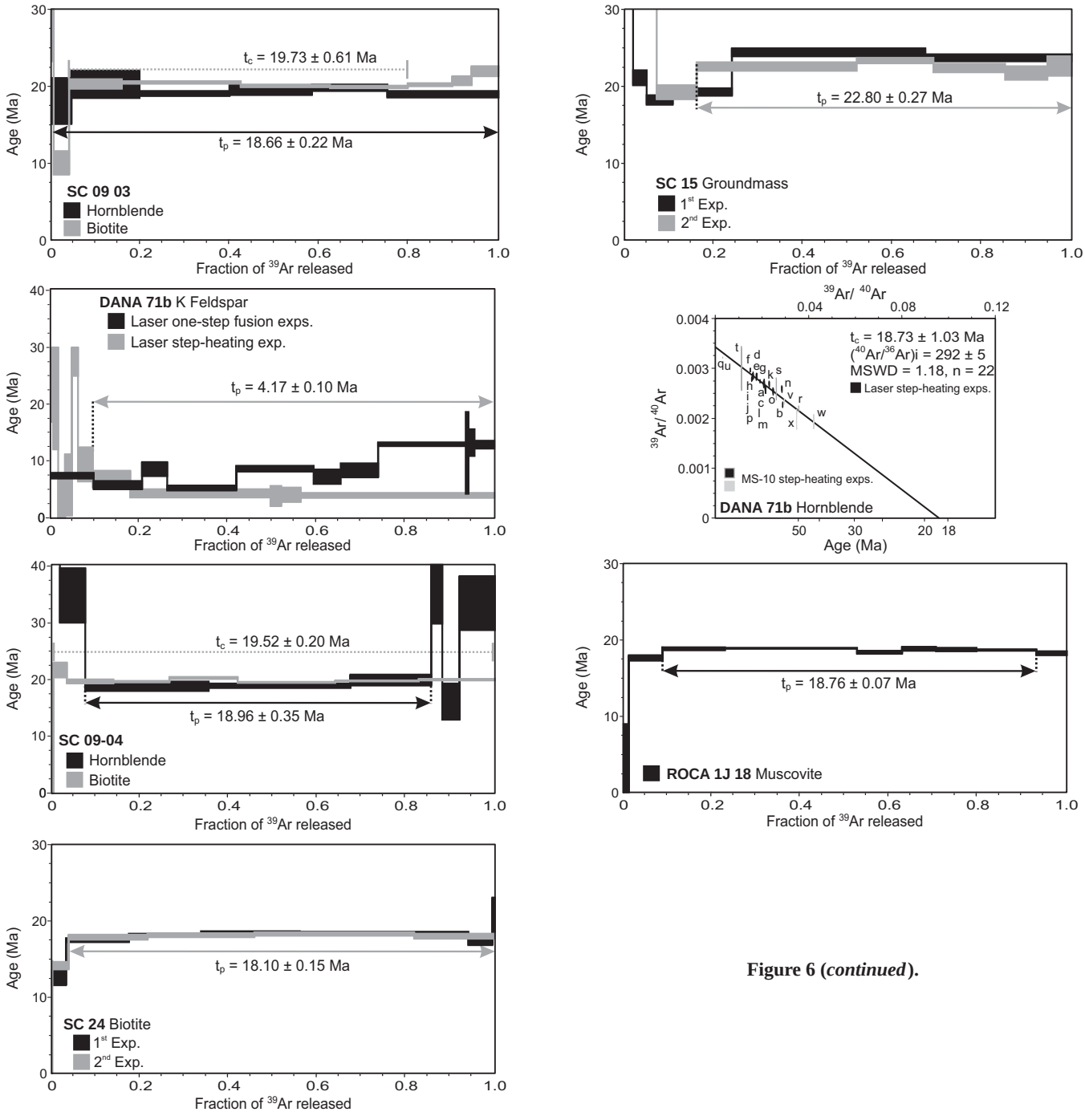

Figure 6 (*continued*).

On mainland Mexico, samples collected in two outcrops 5 km apart from the same pluton along the Río Santiago (northern Nayarit) yielded a U/Pb age of 18.16 ± 0.18 Ma (sample PH 09), a ^{40}Ar-^{39}Ar biotite age of 19.07 ± 0.16 Ma, and a 17.65 ± 0.13 Ma K-feldspar age (sample Oro 01). A sample from an inequigranular, medium-grained granodiorite further to the southeast in the Tepic-Zacoalco rift (Barr 04) yielded a zircon U/Pb age of 22.67 ± 0.4 Ma, with younger and very close ^{40}Ar-^{39}Ar hornblende and biotite ages of 19.8 ± 0.48 Ma and 19.65 ± 0.11 Ma, respectively. Intrusive rocks sampled at the fault scarps bounding the Pescadero Basin (Fig. 2A) show a pervasive alteration that prevented their dating by the ^{40}Ar-^{39}Ar method but yielded consistent early Miocene emplacement ages. Samples ROCA 4J-16 and ROCA 4J-12, recovered north of the Pescadero Basin, yielded U/Pb ages of 25.12 ± 0.67 Ma and 21.56 ± 0.44 Ma, respectively (Fig. 6). Samples from the southwestern scarps of the same basin (ROCA 24J-24 and ROCA 24J-22) yielded slightly younger ages of 20.13 ± 0.23 Ma and 19.90 ± 0.27 Ma.

Samples from sites ROCA 4J and ROCA 24J all have early Miocene U/Pb ages but yielded middle to late Miocene ^{40}Ar-^{39}Ar ages between 13.7 and 9.8 Ma (Table 3; Fig. 6). Sample DANA 71B was dredged very close to ROCA 4J site and yielded a very young ^{40}Ar-^{39}Ar age of 4.17 ± 0.10 Ma on K-feldspar (Table 3; Fig. 6). Experimental results from

Geological Society of America Bulletin, published online on 4 December 2014 as doi:10.1130/B31008.1

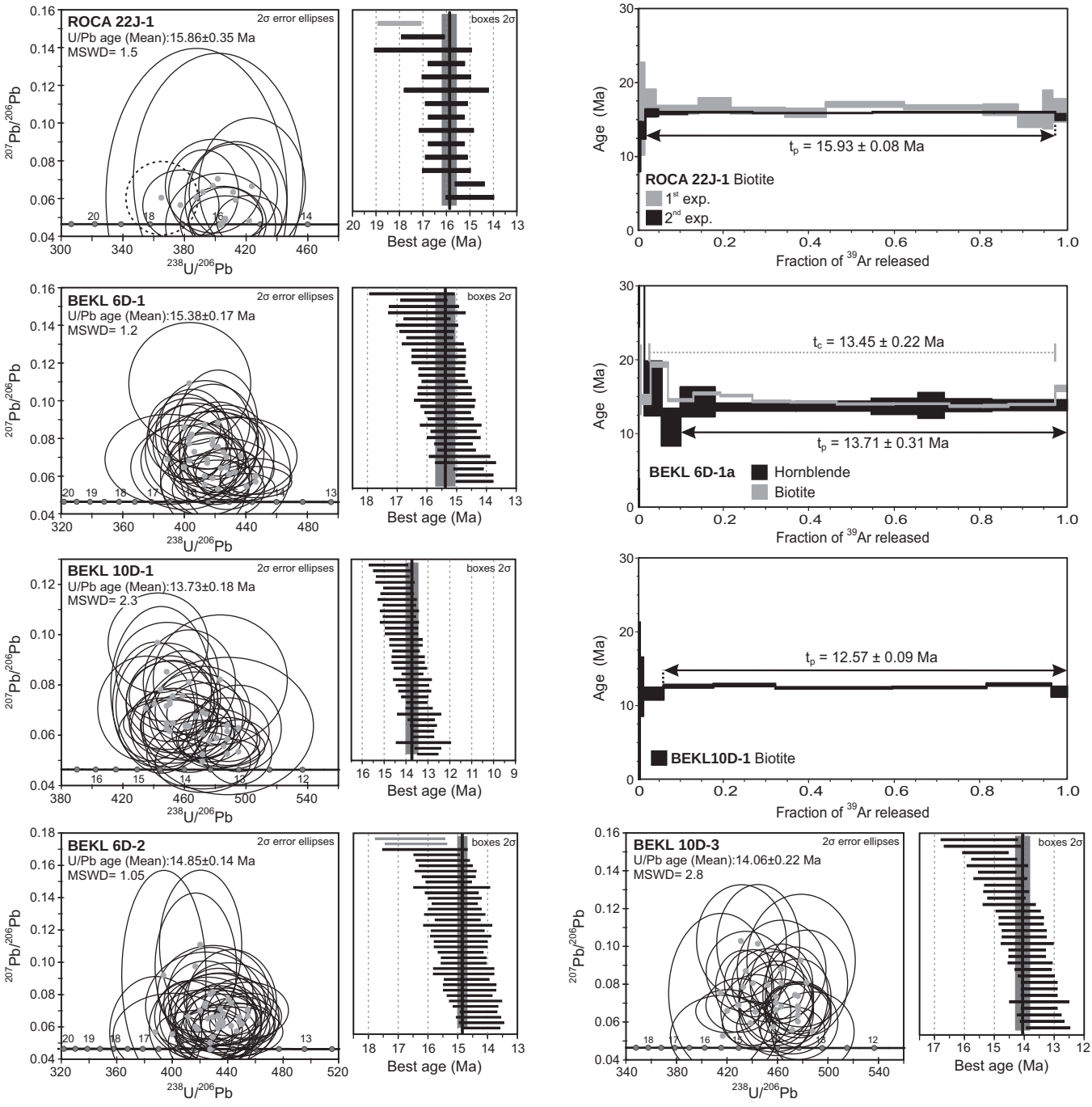

Figure 7. U/Pb concordia and ^{40}Ar-^{39}Ar age spectra or ^{36}Ar-^{40}Ar vs. ^{39}Ar-^{40}Ar correlation diagrams for middle Miocene plutons; the obtained age is given for each sample. In the U/Pb concordia diagrams, dashed ellipses indicate data not taken into account for age calculation. In the ^{40}Ar-^{39}Ar age spectra, t_p indicates plateau ages; these ages were calculated with the fractions identified with the horizontal arrow. Value t_c indicates the isochron age, calculated using the fractions identified with the dotted line in the age spectra diagrams. Detailed information on the geochronological analysis is given in supplemental file 4 (see text footnote 1). MSWD—mean square of weighted deviates.

these samples show evidence of perturbation in the Ar systematics (Fig. 6). All these samples are located around the Pescadero Basin in the central Gulf of California, an area with subsequent middle Miocene magmatism and where late Miocene mafic volcanism (12–10 Ma) has been also reported (Ferrari et al., 2013), suggesting that these early Miocene plutons underwent various degrees of resetting due to later igneous activity.

Middle Miocene Magmatic Episode

Only five samples out of 41 yielded U/Pb zircon ages between 15.8 Ma and 13.4 Ma, providing an indirect indication that middle Miocene plutons are less widespread than early

Geological Society of America Bulletin, published online on 4 December 2014 as doi:10.1130/B31008.1

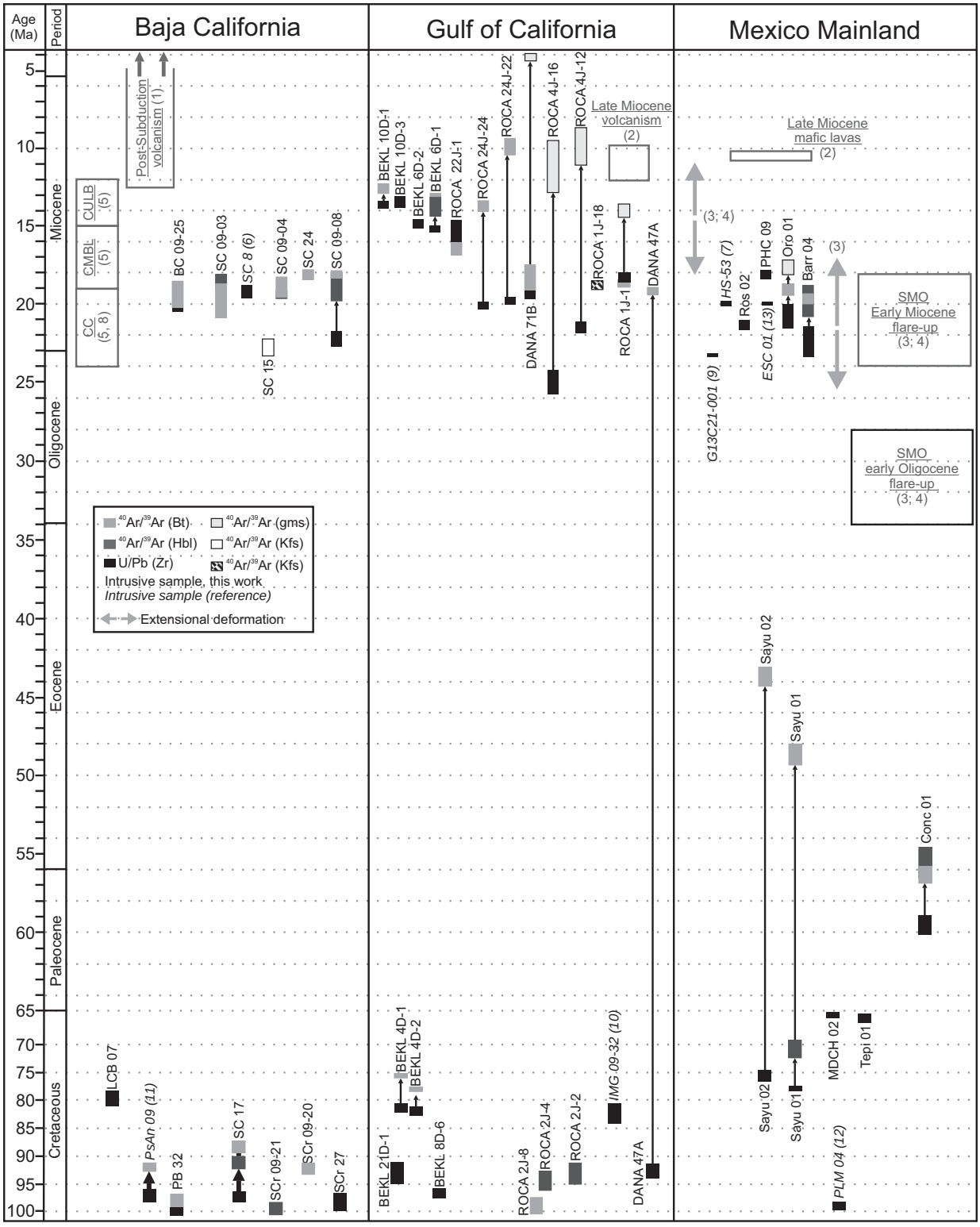

Figure 8. Distribution of U/Pb and ^{40}Ar-^{39}Ar ages obtained in this work for intrusive samples from the southern Gulf of California area and its adjacent margins; ages from the literature for plutons in the area are also included (sample numbers in italics); sample location is given in Figure 1. Main volcanic and tectonic events registered in the area are also shown. (1) Calmus et al. (2011); (2) Ferrari et al. (2013); (3) Ferrari et al. (2002); (4) Ferrari et al. (2007) and references therein; (5) Umhoefer et al. (2001); (6) Piñero-Lajas (2008); (7) Henry et al. (2003); (8) Hausback (1984); (9) Iriondo et al. (2003); (10) Pompa-Mera et al. (2013); (11) Iriondo et al. (2005); (12) Cuéllar-Cárdenas et al. (2012); (13) our unpublished data. CC—Clastic Comondú; CMBL—Comondú middle breccia and lava unit; CULB—Comondú upper lava and breccia unit; SMO—Sierra Madre Occidental; Bt—biotite; Hbl—hornblende; Zr—zircon; Kfs—K-feldspar; gms—groundmass.

Geological Society of America Bulletin, published online on 4 December 2014 as doi:10.1130/B31008.1

Miocene plutons. Middle Miocene intrusive rocks seem to be restricted to the western rifted blocks submerged in the gulf (Fig. 1C), and thus most proximal to the onshore Comondú Group exposures. The dated samples come from three sites along a topographic high, situated halfway between the Pescadero Basin and Baja California margin (Fig. 2A). Sample ROCA 22J-1 was recovered at 1516 mbsl at the southwestern side of the Cerralvo Bank, and four other samples were dredged at sites BEKL 6D (southeast end of Cerralvo Bank at 900–1205 mbsl) and 10D (northernmost part of La Paz Basin at 1200–1498 mbsl; Figs. 1 and 2; Table 1). Studied samples show a peculiar inequigranular texture with phenocrysts of plagioclase and K-feldspar surrounded by finer plagioclase, K-feldspar, quartz, and minor mafic minerals (Table 1), which indicates at least two crystallization stages at different pressure. A group of four samples has similar alkali feldspar content (20%–23%) and classifies as quartz monzodiorite and monzogranite (Table 1); they contain amphibole and biotite as ferromagnesian minerals, as well as apatite, zircon, titanite, and Fe-Ti oxides as accessory minerals. Sample BEKL 6D-2 has a distinctly different composition, with 50% alkali feldspar and a quartz monzonite composition; this sample has biotite as the only ferromagnesian mineral.

Paired U-Pb and Ar-Ar ages could only be obtained for three middle Miocene samples. In these cases, as for the early Miocene samples, the rocks yielded very close U/Pb zircon, hornblende, and/or biotite ages, suggesting very rapid cooling to <375 °C (Table 3; Figs. 7 and 8). Sample ROCA 22J-1 has a U/Pb age of 15.86 ± 0.35 Ma and a ^{40}Ar-^{39}Ar biotite plateau age of 15.86 ± 0.08 Ma (Fig. 6). Sample BEKL 6D-1 yielded a U/Pb zircon age of 15.38 ± 0.17 Ma, a ^{40}Ar-^{39}Ar hornblende plateau age of 13.71 ± 0.31 Ma, and a ^{40}Ar-^{39}Ar biotite plateau age of 13.4 ± 0.22 Ma. Sample BEKL 10D-1 yielded a U/Pb age of 14.06 ± 0.22 Ma and a biotite ^{40}Ar-^{39}Ar plateau age of 12.57 ± 0.09 Ma (Table 3). The middle Miocene samples show no inherited zircons, but they commonly have antecrysts as defined in Ferrari et al. (2013) (Table 3; Fig. 7).

Thermobarometry

To obtain further constraints on magma emplacement depth, thermobarometric calculations were performed on samples representative of each magmatic episode: one Paleocene equigranular, medium-grained monzogranite (Conc 01), one early Miocene inequigranular, medium-grained tonalite (IXC 03), and three middle Miocene inequigranular, medium- to coarse-grained monzogranites (BEKL 6D-1, BEKL 10D-1, BEKL 10D-3). Pressure and temperature of magma crystallization were estimated through iteration of pressure calculated with the Al-in-hornblende barometers of Schmidt (1992) and Anderson and Smith (1995), at temperatures obtained with the Holland and Blundy (1994) hornblende-plagioclase thermometer (reaction edenite + albite = richterite + anorthite), using the spreadsheet published by Anderson et al. (2008). In the analyzed samples, hornblende coexists with the full buffering assemblage required for Al-in-hornblende barometry (quartz + alkali feldspar + plagioclase + biotite + Fe-Ti oxide + titanite; see Table 1). Estimates of pressure and temperature were also obtained with the empirical calibration based on the composition of amphibole recently proposed by Ridolfi and Renzulli (2012). Results obtained with both procedures are plotted in Figure 9 and listed in supplemental file 2 (see footnote 1).

Pressures obtained with the first method (Anderson et al., 2008) for the Paleocene sample range mainly between 231 and 308 MPa, which correspond to 8.8–11.8 km depth for an upper-crustal density of 2.7 g/cm^3, whereas the early Miocene sample yielded lower values between 150 and 196 MPa (5.7–7.5 km depth). Temperatures for these samples plot close to the granite water-saturated solidus and span a broader range for the Paleocene sample (567–720 °C) than for the early Miocene sample (689–722 °C). Middle Miocene samples span over a larger pressure range, with a group plotting close to the granite solidus at 165–309 MPa (6.3–8.8 km depth) and temperatures between 636 °C and 735 °C, and a second group yielding low pressures and temperatures (32–145 MPa, 1.2–5.5 km; 573–665 °C) that plot well below the granite solidus. Amphibole in all samples is classified as magnesiohornblende, but analyses that yield pressure-temperature values below the solidus have lower Al_{tot} (<1.0) and higher Si/Al and Mg/Fe, pointing to subsolidus reequilibration to actinolitic hornblende. Subsolidus reactions have been related to vapor-phase saturation at shallow levels (Hammarstrom and Zen, 1986) or to the infiltration of high-temperature contact aureole fluids (Anderson et al., 2012). These values are therefore not further considered in the discussion.

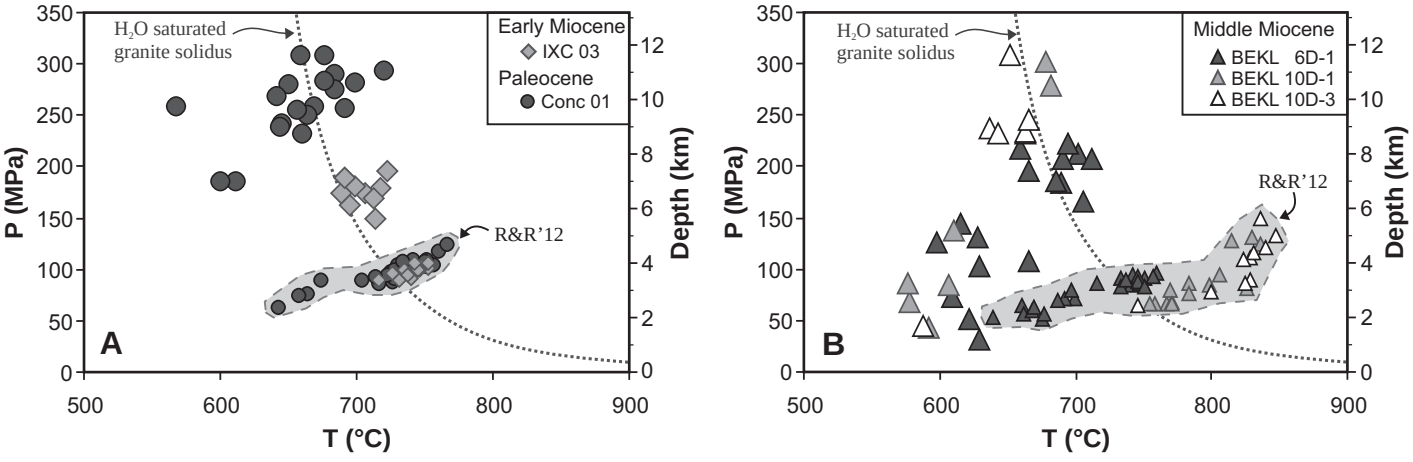

Figure 9. Estimated pressures and temperatures for (A) Paleocene and early Miocene and (B) middle Miocene intrusive rocks from submerged blocks of the Gulf of California. Large symbols correspond to pressure estimates based on the Al-in-hornblende calibration of Schmidt (1992) and Anderson and Smith (1995) and temperatures from the hornblende-plagioclase calibration of Holland and Blundy (1994). Small symbols within the gray fields labeled R&R'12 correspond to pressures and temperature estimates after the Ridolfi and Renzulli (2012) formulation based on amphibole composition.

Geological Society of America Bulletin, published online on 4 December 2014 as doi:10.1130/B31008.1

The empirical thermobarometer of Ridolfi and Renzulli (2012) yielded quite different results for samples plotting close to the solidus, with lower pressures for all samples and higher temperatures for some of the middle Miocene samples (Fig. 9). For the Paleocene sample, pressures between 86 and 125 MPa (3.3–4.8 km depth) and temperatures of 704–767 °C were obtained, whereas the early Miocene sample yielded similar values with slightly lower maxima values at 89–106 MPa (3.4–4.1 km depth) and 716–742 °C. For the middle Miocene, two samples from the same site (BEKL 10D) spanned a large pressure range between 64 and 150 MPa (2.5–5.7 km depth) and had the highest temperatures among the analyzed samples (746– 847 °C). For the third middle Miocene sample (BEKL 6D-1), pressures was between 83 and 97 MPa (3.1–3.7 km depth) and temperatures were between 733 °C and 759 °C. Noteworthy with the Ridolfi and Renzulli (2012) calibration, subsolidus pressure-temperature values were obtained only for some hornblende analyses of a middle Miocene sample (BEKL 6D-1) and of the Paleocene sample.

The discrepancy in the results obtained with the two methods may be ascribed to differences in the calibration approaches. The Al-in-hornblende barometer was experimentally calibrated for pressures between 250 and 1300 MPa (Schmidt, 1992; Anderson and Smith, 1995), corresponding to 9.5–50 km crustal depths, and may thus be inadequate to estimate crystallization pressures of shallow intrusive rocks like those presented here (pressure <308 MPa). On the other hand, the calibration proposed by Ridolfi and Renzulli (2012) is based in a multivariate least-square regression of selected experimental calcic amphibole compositions synthesized in a broader pressure range (130–2200 MPa). A drawback of the barometer formulation is the lack of the required temperature correction; nevertheless, according to Anderson and Smith (1995), such correction would result in even lower pressure values than those obtained with the present formulation. For the pressure range of the studied samples, the calibration of Ridolfi and Renzulli (2012) is probably the most adequate. Variable crystallization pressures down to 64 MPa (2.5 km depth) for the middle Miocene samples also are consistent with the distinct inequigranular textures that characterize these samples (Table 1).

Geochemistry

Cretaceous–Paleocene Magmatic Episode

Cretaceous–Paleocene samples plot in the diorite, quartz monzodiorite, granodiorite, and monzogranite fields in the Q′-ANOR diagram of Streckeisen and Le Maitre (1979), which is based on the parameters Q′ [= 100 × q/(q + or + ab + an)] and ANOR [= 100 × an/(or + an)], derived from the normative proportions of quartz (q), orthoclase (or), albite (ab) and anorthite (an), and belong to the calcic and calc-alkalic series of Frost and Frost (2008) (Figs. 10A and 10B). Most samples have SiO_2 contents in the range of 60–77 wt%, except for one diorite sample, with 53.3 wt% SiO_2, which plots in the field of high-K calc-alkalic series in the SiO_2 versus K_2O diagram (Fig. 10C; Peccerillo and Taylor, 1976).

Trace-element variation is shown in primitive mantle–normalized multi-element diagrams (Fig. 11A; Sun and McDonough, 1989). All studied samples are enriched in large ion lithophile elements (LILEs; e.g., Rb, Ba) and light rare earth elements (LREEs; e.g., La, Ce) with respect to the high field strength elements (HFSEs; e.g., Nb, Ta) and display positive Pb anomalies, features commonly considered characteristic of subduction-related rocks. The enrichment of the middle and heavy rare earth elements (MREEs and HREEs, respectively), as well as Y, is quite variable but cannot be ascribed to the degree of differentiation (expressed as SiO_2 content). In part, the variations result from the stronger HREE depletion found in some of the oldest dated rocks (99.1–92.8 Ma) from Santa Cruz Island and submerged continental blocks offshore southern Baja California and Sinaloa (ROCA 2J-8, SCr 27, BEKL 8D-6, DANA 47A; Fig. 1). The age and composition (e.g., high Sr/Y and La/Yb, low Nb and Ta, absence of negative Eu anomaly) of these rocks resemble those of La Posta–type plutons, which were emplaced in southern California and northern Baja California peninsula between 99 and 92 Ma (Walawender et al., 1990; Kimbrough et al., 2001) and dominate the eastern Peninsular Ranges Batholith. These samples from the southern Gulf of California constitute the southernmost exposures of La Posta–type plutons yet identified.

Early Miocene Magmatic Episode

Intrusive rocks emplaced in the early Miocene show compositional trends distinctive from those of Cretaceous–Paleocene plutons. These rocks can be divided in two groups on the basis of differentiation. A group of samples of intermediate composition, in the range of 61–68 wt% SiO_2, plots in the quartz diorite, quartz-monzodiorite, quartz-monzonite, and granodiorite fields in the Q′-ANOR diagram (Fig. 10A). The narrow range of silica content is reflected in a restricted variation of Q′ at variable ANOR values. A further intermediate-composition sample from a subvolcanic, porphyritic intrusive body (PHC 09) has lower SiO_2 content (57.3 wt%) and lower Q′ value, and it plots in the quartz diorite field (Fig. 10A); this less-evolved sample also yielded the youngest emplacement age (18.1 Ma, U/Pb; Table 3) among the early Miocene rocks. A second group of samples is composed of high-silica granitoids with 75–77 wt% SiO_2, which classify as syenogranite and alkali feldspar granite in the Q′-ANOR diagram (Fig. 10A); this group of samples yielded U/Pb ages in a narrow age range between 20.1 Ma and 18.3 Ma (Table 3; Fig. 10A).

Part of the intermediate and the high-silica intrusive rocks plot in the alkali-calcic field, whereas some of the least-differentiated samples are calc-alkalic (Fig. 10B); also, early Miocene rocks tend to have higher K_2O contents than the Cretaceous ones, and they mostly plot in the field of high-K calc-alkalic rocks (Fig. 10C).

Primitive mantle–normalized trace-element patterns of intermediate early Miocene samples are quite similar (Fig. 11B), despite the fact that they were collected over a broad area both onshore and offshore of Sinaloa and Nayarit States. They are characterized by the enrichment of LILEs and LREEs with respect to HFSEs, positive Pb anomalies, and weakly developed Eu anomalies (Fig. 11B); when compared with the Cretaceous intrusions, they have less prominent negative Nb-Ta and positive Pb anomalies, but REE patterns comparable to those of the less HREE-depleted Cretaceous samples. In the group of high-silica granites, the geochemical features are in part comparable to those of the intermediate magmas, but they are distinguished by stronger Sr, Eu, and Ti depletions, as well as by comparatively higher abundances of MREEs, HREEs and Y, and flat MREE to HREE patterns (Fig. 11B).

Middle Miocene Magmatic Episode

The four analyzed samples belonging to this episode have silica contents between 64 wt% and 71 wt% SiO_2 and classify as quartz monzodiorite, monzogranite, and quartz syenite in the Q′-ANOR diagram (Fig. 10A), where they display a similar trend as the early Miocene rocks. Three samples are high-K calc-alkalic, and one is alkalic with a shoshonitic character, in agreement with the high percentage of alkali feldspar observed in thin section for these rocks.

Among the middle Miocene rocks, the quartz monzodiorite and quartz syenite have trace-element compositions similar to those of the intermediate-composition early Miocene rocks, except for higher Rb, Th, and U abundances (Fig. 11C). A monzogranite sample from submerged crustal blocks offshore southern Baja California (BEKL 10D-3; Fig. 1) displays a different pattern, defined by a strong depletion in REEs, and slightly positive Eu and Sr anomalies (Fig. 11C).

Geological Society of America Bulletin, published online on 4 December 2014 as doi:10.1130/B31008.1

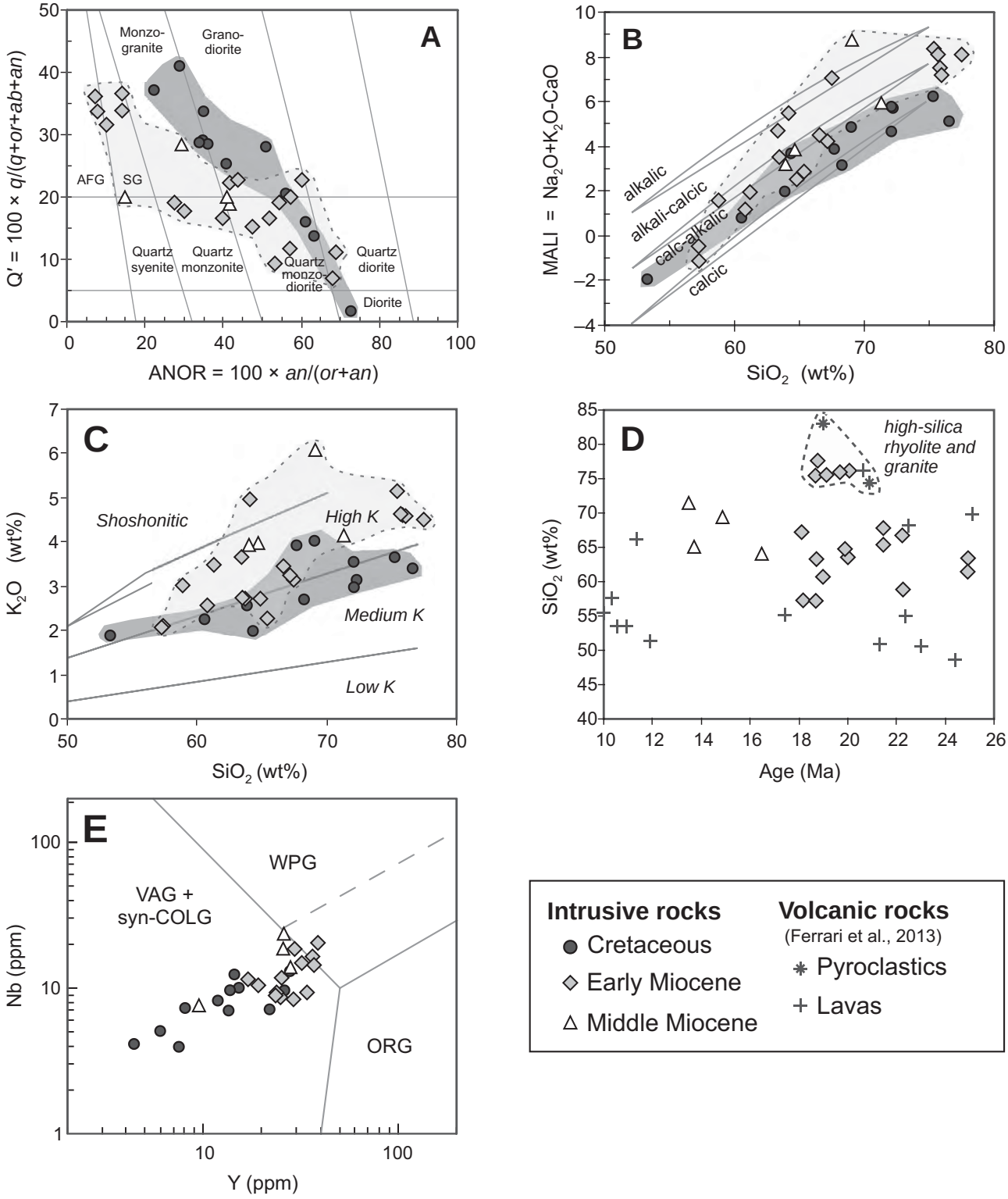

Figure 10. Compositional characterization of analyzed samples. (A) Q′ vs. ANOR diagram (Streckeisen and Le Maitre, 1979) showing rock types according to their normative mineral proportions (q—quartz; or—orthoclase; ab—albite; an—anorthite). SG—syenogranites, AFG—alkali feldspar granites. (B) $Na_2O + K_2O$–CaO vs. SiO_2 diagram showing the approximate ranges for the alkalic, alkali-calcic, calc-alkalic, and calcic rock series (modified after Frost and Frost, 2008). (C) K_2O vs. SiO_2 diagram (Peccerillo and Taylor, 1976). (D) SiO_2 vs. age diagram for Miocene plutons (this work) and Miocene volcanic rocks from Ferrari et al. (2013). (E) Nb vs. Y tectonic discrimination diagram (after Pearce et al., 1984). VAG—volcanic arc granitoids; syn-COLG—syncollisional granitoids; WPG—within-plate granitoids; ORG—ocean-ridge granitoids.

Geological Society of America Bulletin, published online on 4 December 2014 as doi:10.1130/B31008.1

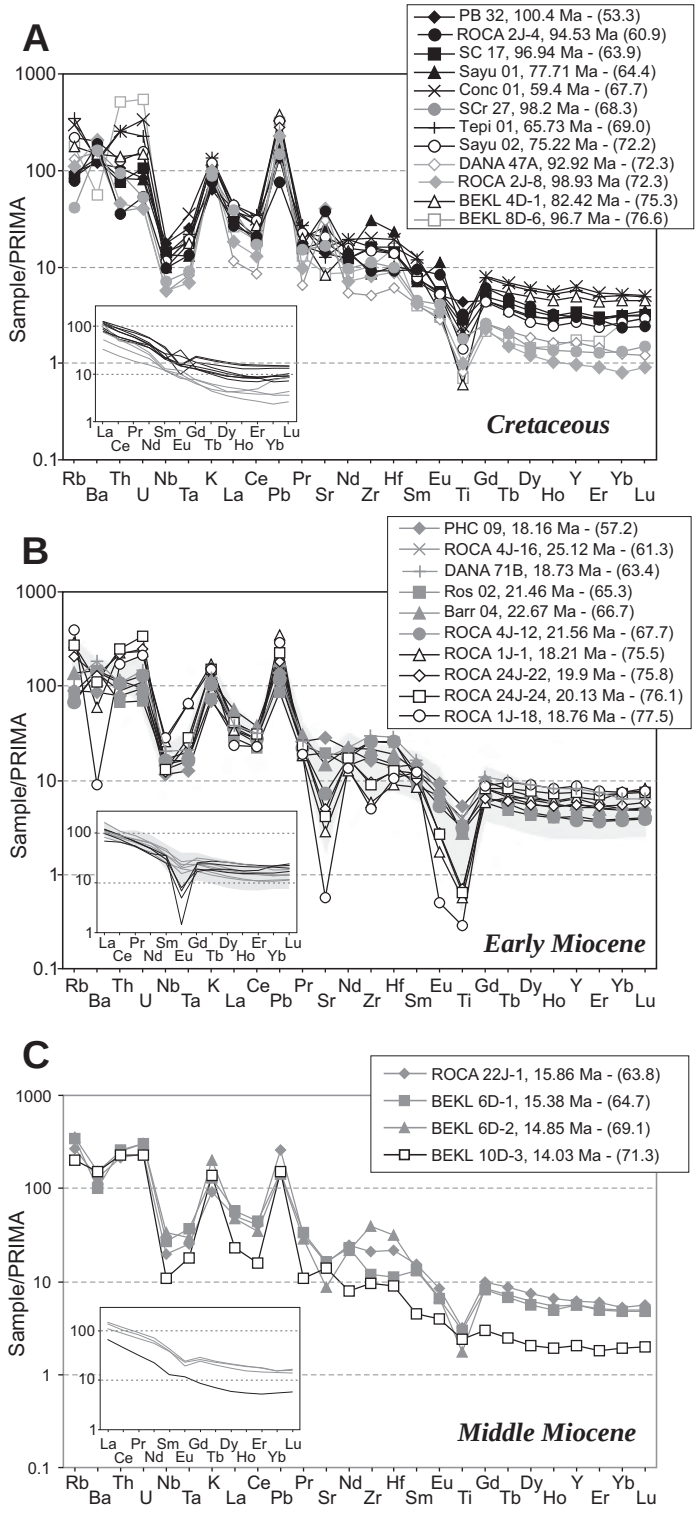

Figure 11. Multi-element diagrams normalized to primitive mantle values of Sun and McDonough (1989) for the intrusive samples. (A) Cretaceous samples. (B) Early Miocene samples; the gray field denotes the compositional range of early Miocene silicic tuffs and lavas reported by Ferrari et al. (2013). (C) Middle Miocene samples. Inserted in each diagram is the chondrite-normalized rare earth element (REE) diagram for the same samples. The legend in each diagram indicates sample name, followed by the U/Pb age (except for sample Roca 1J-18, which is a ^{40}Ar-^{39}Ar age on K-feldspar), and then the SiO_2 content in parenthesis in wt%.

DISCUSSION AND CONCLUSIONS

Geographic Distribution of Miocene Magmatism in the Southern Gulf: Relationships with the Sierra Madre Occidental and the Comondú Group

The geologic, geochemical, and geochronologic results of our study indicate the presence of an extensive silicic plutonic province of early Miocene age across the southern Gulf of California (Figs. 8, 12, and 13) nested within Late Cretaceous to early Paleocene batholiths. Previous studies assumed a progressive westward migration of the locus of Cenozoic magmatism, with the early Miocene silicic pulse of the Sierra Madre Occidental located to the west of the Oligocene pulse, in southern Sinaloa and Nayarit (Ferrari et al., 2002, 2007), and subsequent middle Miocene volcanism of the Comondú Group centered in the gulf just east of Baja California (Hausback, 1984; Umhoefer et al., 2001). However, the occurrence of 24–18 Ma granitic intrusive rocks on both sides of the gulf, as well as in submerged rifted blocks within the gulf, indicates that silicic-dominant early Miocene magmatism of the Sierra Madre Occidental was located not only on the Mexican mainland but spanned a much larger area, elongated in a WNW-ESE direction (Figs. 12 and 13). The composition and age range of these plutons are essentially coincident with those of the ignimbrites exposed in the southern Sierra Madre Occidental and in southern Baja California between La Paz and Loreto (Fig. 12; Hausback, 1984; Umhoefer et al., 2001; Ferrari et al., 2002, 2013; Drake, 2005; Bryan et al., 2008; Ramos-Rosique, 2013). The two compositional groups of the early Miocene plutons also compare well with the silicic volcanic rocks emplaced during the same age span in the southern Sierra Madre Occidental (Fig. 10D; Ferrari et al., 2013). For early Miocene ignimbrites and lavas, two similar compositional groups of high-K rocks are recognized: an older dacite and low-silica rhyolite (SiO_2 < 70 wt%) suite and a younger, high-silica rhyolite (SiO_2 > 74 wt%) suite. Also, trace-element compositions and patterns of volcanic and plutonic rocks are strikingly similar (Fig. 11B) and indicate a limited role for crystal fractionation in the evolution of early Miocene silicic magmas (Ferrari et al., 2013). Zircon inheritance also points to a significant role of crustal melting in the genesis of these rocks, as shown for other onshore Sierra Madre Occidental ignimbrites (e.g., Bryan et al., 2008). Our data add weight to the interpretation that the early Miocene plutonic rocks across the southern gulf region represent intrusive underpinnings to part of the early Miocene Sierra Madre Occidental silicic volcanism.

Geological Society of America Bulletin, published online on 4 December 2014 as doi:10.1130/B31008.1

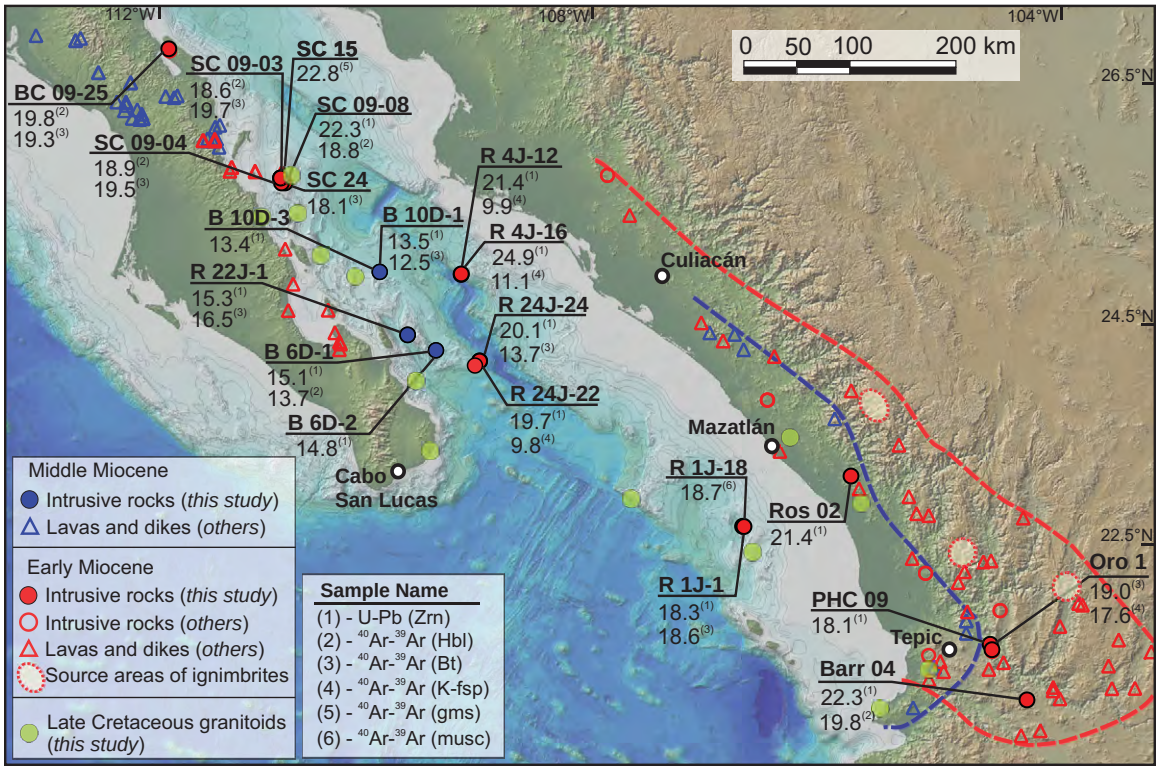

Figure 12. Location and ages of plutonic rocks reported in this work, and distribution of early and middle Miocene intrusive (this work) and volcanic samples compiled from the literature. Sample prefixes of ROCA and BEKL sample names are abbreviated to R and B, respectively. Base map data are from GeoMapApp. Abbreviations: Zrn—zircon; Hbl—hornblende; Bt—biotite; K-fsp—K-feldspar; gms—groundmass; musc—muscovite.

Scarce middle Miocene plutonic rocks were encountered across the southern gulf, and particularly in fault scarps bounding the Cerralvo Bank (Figs. 2 and 12), in the western rifted margin of the southern gulf. These sites lie on the southward prolongation of the few lavas and domes of the same age exposed in Baja California, near Loreto and in Bahía Concepción, which have been assigned to the middle and upper members of the Comondú Group (Figs. 1 and 12; Umhoefer et al., 2001; Drake, 2005). No intrusive rocks of middle Miocene age have been found on the eastern rifted margin, but a few basalts of this age are interlayered with continental sedimentary rocks between Mazatlán and Culiacán (Fig. 1; Ferrari et al., 2013). The distribution of middle Miocene rocks defines a NNW-trending belt in the central and western part of the wider region occupied by the early Miocene intrusive rocks (Fig. 12). As this belt is superimposed on early Miocene magmatism, rather than a westward migration of magmatism, the distribution of middle Miocene igneous rocks suggests the narrowing of the magmatic belt in a position coincident with the future gulf axis.

Two arguments have been that: (1) the Gulf of California opened along a line/zone of hot, thermally weakened crust resulting from igneous activity of the Comondú "arc" (Umhoefer, 2011, and references therein), and (2) thick epiclastic deposits that constitute the bulk of the middle and upper members of the Comondú Group were shed westward from a series of high-standing andesitic stratocones located within the area of the present-day gulf and just east of Baja California peninsula (Hausback, 1984; Umhoefer et al., 2001). We would also expect that rapid subsidence in the gulf region at 12 Ma, allowing a marine incursion by at least 8 Ma, would have enhanced preservation and burial of the arc volcanoes. If this was the case, extensive outcrops of volcanic, resedimented volcaniclastic ± intrusive rocks associated with the core of this volcanic arc should be present in the submerged rifted blocks on both sides of the newly formed oceanic basins within the gulf. However, visual inspection of the submerged blocks during the ROCA dives indicates that the normal fault scarps bounding the Alarcón and Pescadero Basins are dominated by Late Cretaceous or early Miocene intrusive rocks (Figs. 2 and 12). These observations thus require complete removal of any arc volcanic constructs and sedimentary accumulations of the middle Miocene Comondú Group, as well as of thick (at least 1 km) volcanic accumulations of early Miocene age to expose underlying early Miocene and older plutonic rocks; this is despite the requirement for rapid crustal thinning, subsidence, and gulf flooding within a few million years. The scarcity of middle Miocene rocks in the southern gulf casts doubts on the prevailing model of substantial andesitic volcanism occurring along the gulf axis that was sufficiently vigorous to form a significant volume of new arc igneous crust and to thermally weaken the crust (with a prerift thickness of ~40 km, i.e., the present thickness of the unextended part of the Sierra Madre Occidental) prior to the onset of rifting (e.g., Umhoefer, 2011). The geology of the submerged rift flanks in the southern gulf region therefore indicates that Comondú-age magmatism and related sedimentation were not volumetrically significant and not a major tectonomagmatic feature in the middle Miocene. The submarine geology supports recent interpretations of Comondú-age magmatism being synextensional in origin, primarily related to continued lithosphere extension that had affected western Mexico since the late Oligocene and culminated in the opening of the Gulf

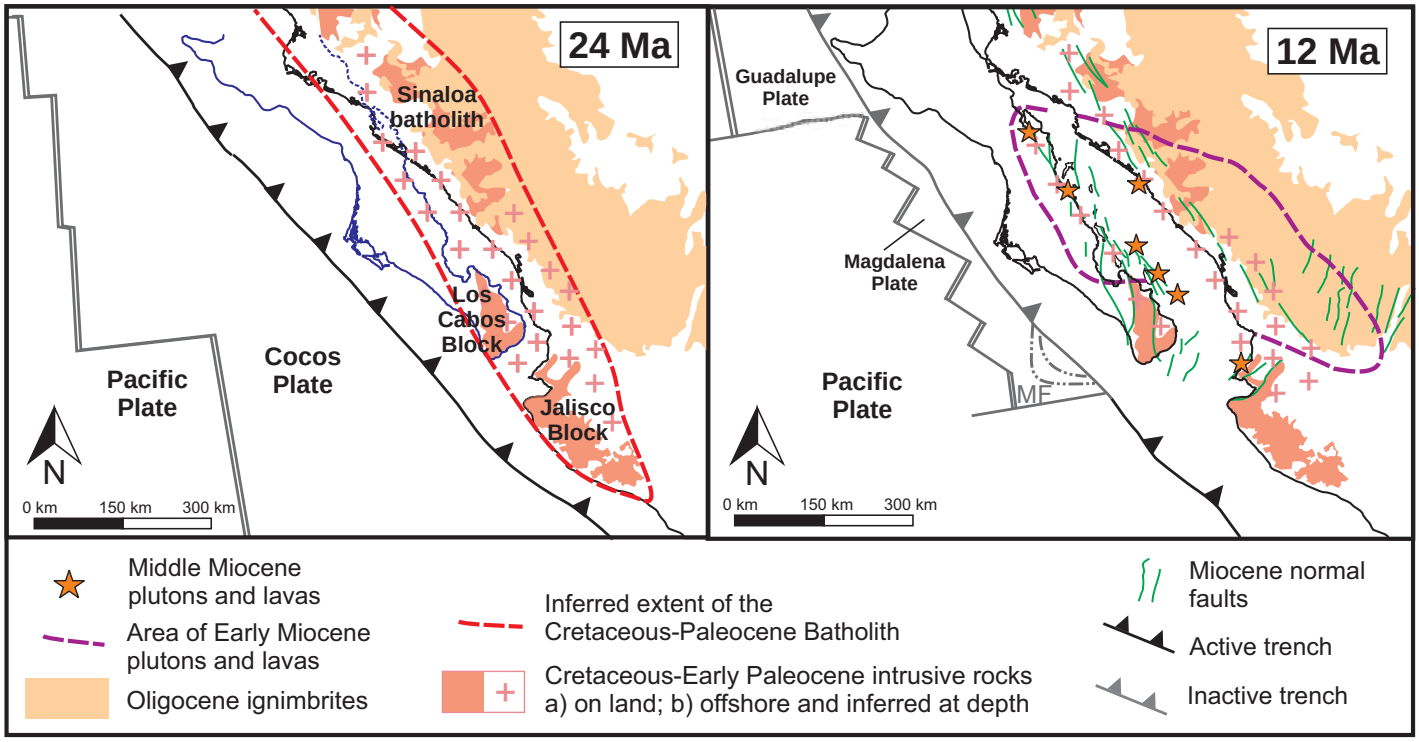

Figure 13. Paleotectonic reconstructions at 24 and 12 Ma showing the distribution of the Late Cretaceous–Paleocene, early Miocene, and middle Miocene magmatic events based on data presented in this work and from the literature. Main extensional faults formed prior to 12 Ma are shown as green lines. Pacific-Cocos plate boundary configuration with respect to North America at 24 Ma is from Atwater and Stock (1998). Magdalena and Guadalupe microplate configuration and location of Magdalena Fan (MF) at 12 Ma are from Fletcher et al. (2007). Geology is modified from Ferrari et al. (2007, 2013). Baja California position is as in Ferrari et al. (2013).

of California in the late Miocene (Bryan et al., 2014; Ferrari et al., 2013).

Previous models also require rapid extension after ca. 12.5 Ma that would produce significant thinning of an almost unextended crust (Stock and Hodges, 1989; Umhoefer et al., 2002; Fletcher et al., 2007; Lizarralde et al., 2007; Sutherland et al., 2012). In such a scenario, one would also expect a significant amount of post–ca. 12 Ma volcanism associated with mantle decompression induced by a high rate of extensional deformation. However, post-Comondú volcanism is scarce in the southern gulf and western Mexico. In fact, after a widespread pulse of basaltic volcanism at ca. 11–10 Ma (Ferrari et al., 2013), an ~7 m.y. gap in volcanism is observed until the late Pliocene and Quaternary on the eastern rifted margin (Ferrari et al., 2013), just when prevailing models predict the main episode of rifting. Alternatively, if a significant part of crustal thinning occurred before the end of subduction, as we propose here and in Ferrari et al. (2013), then the rate of extension after ca. 12 Ma would be much lower and the associated volcanism less abundant, as actually observed (Lizarralde et al., 2007).

Synextensional Nature of Miocene Magmatism

An examination of the thermal evolution of intrusive rocks provides a useful chronometric bracket on the tectonic event responsible for the opening of the Gulf of California. A complete modeling of the thermal history awaits low-temperature geochronologic approaches, such as fission tracks or U-Th/He dating, which are in progress. However, an analysis of the time span between zircon U/Pb and hornblende, biotite, and feldspar ^{40}Ar-^{39}Ar ages obtained in this study consistently indicates that the early and middle Miocene plutons were rapidly cooled after intrusion. All dated early Miocene intrusive rocks emplaced between 25 and 18 Ma (Fig. 8) were cooled below the ^{40}Ar-^{39}Ar biotite closure temperature of 350–400 °C within ~2.5 m.y., with one exception being sample ROCA 24J-24, which, as discussed already, has been likely reset. Significantly, in all cases, ^{40}Ar-^{39}Ar biotite ages are restricted to the 19.7–18.1 Ma interval, and, in the samples where we were able to date both hornblende and biotite, the ^{40}Ar-^{39}Ar ages almost completely overlap in the ca. 19–18 Ma interval (Barr 04, SC 09–08, SC 09–04, SC 09–03; Table 3). Meanwhile, middle Miocene plutons show an even more restricted cooling window of <1.5 m.y. from emplacement defined by the U-Pb zircon age (15.8–13.4 Ma) to the ^{40}Ar-^{39}Ar biotite age (<375 °C), and, as for the early Miocene plutons, almost overlapping hornblende and biotite ages. Middle Miocene intrusive rocks have also distinctive inequigranular textures (Table 1), defined by at least two generations of crystals with grain sizes that change from coarse to fine grained. The presence of crystals formed at different stages and the variable crystallization pressures between 64 and 150 MPa (2.5–5.7 km depth) obtained with the hornblende barometer (Fig. 9; supplemental file 2 [see footnote 1]) support a polybaric crystallization of these intrusive rocks. Consistent with this is the fact that in the three analyzed samples, we consistently obtained higher pressure estimates for core domains (88–150 MPa, 3.4–5.7 km) than for the crystal rims (supplemental file 2 [see footnote 1]). The cooling behavior of the Miocene plutons therefore contrasts with that of spatially related Cretaceous plutons into which they intrude, with the Cretaceous plutons showing a protracted period of intrusion (ca. 100–65 Ma)

Geological Society of America Bulletin, published online on 4 December 2014 as doi:10.1130/B31008.1

and variable cooling time spans to the ^{40}Ar-^{39}Ar biotite age of between 4 and 10 m.y. (Fig. 8).

The time span between U/Pb zircon ages and the ^{40}Ar-^{39}Ar ages indicates cooling rates of 52–130 °C/m.y. for the Late Cretaceous–Paleocene rocks, ~210 °C/m.y. for the early Miocene plutons, and ~350 °C/m.y. or more for the middle Miocene rocks. Such a rapid cooling can be explained by a shallow level of intrusion (comparable to those observed in porphyry copper intrusions; Ballard et al., 2001), by ongoing extensional tectonics at the time of emplacement (as observed in synextensional granitoids in core complexes; Ring and Collins, 2005), or both. Geobarometric data from the four Miocene samples that we analyzed are not conclusive in this respect. The Al-in-hornblende barometer of Anderson and Smith (1995) yielded pressure estimates corresponding to a 6.3–11.8 km depth range, but this barometer was calibrated for a range of pressures corresponding to greater depths (>9.5 km). With the empirical thermobarometer of Ridolfi and Renzulli (2012), we obtained pressure estimates corresponding to a 2.5–5.7 km depth range for a subset of data that plot close to the granite subsolidus. If the depth range obtained using the Anderson and Smith (1995) geobarometer is used, then rapid unroofing by extension is required to explain the fast cooling of the plutonic rocks. However, a shallow level of emplacement is suggested by the textural characteristics of most Miocene samples and is confirmed by field evidence both in Baja California (Bahia Concepción) and in Nayarit, where fine-grained granitoids are found intruding <2.5-km-thick volcanic successions only 2–8 m.y. older. Ferrari et al. (2013) estimated significant crustal thinning (up to ~100%) along the southeastern margin of the gulf between ca. 18 and 11 Ma, which importantly corresponds to the period of intrusion and rapid cooling of our studied plutonic samples. A critical factor here is that the remarkably uniform ca. 19–18 Ma ^{40}Ar-^{39}Ar biotite ages obtained for early Miocene granitoids point to regional extension across the southern gulf region to explain widely spaced plutonic samples simultaneously crossing the 375 °C isotherm. Although more data are required, we consider that extension in the southern gulf was ongoing in the middle Miocene, even though thermochronological data from the now subaerial part of the Baja California margin indicated that cooling through the apatite annealing zone (<110 °C) occurred principally in the late Miocene (e.g., Fletcher et al., 2000; Seiler et al., 2011).

Some early Miocene plutons (sites ROCA 24J, 4J, and DANA 71B) show a wider time span between U-Pb zircon crystallization and ^{40}Ar-^{39}Ar cooling ages (7–13 m.y.; Fig. 8). These samples are all located in the central part of the Gulf of California along the scarps of the Pescadero Basin. At these sites, the ^{40}Ar-^{39}Ar cooling ages are interpreted as being thermally perturbed by the younger magmatism and high heat flow that were focused along the pull-apart basins of the central part of the Gulf of California rift since the late Miocene (e.g., Wang et al., 2009). Thermal perturbation of some ^{40}Ar-^{39}Ar age spectra is also observed for some Cretaceous plutons located near the axis of the gulf. In other samples away from the rift axis (Sayu 01 and Sayu 02), we only observed an incomplete resetting, possibly due to the distance from local heat sources (plutons). A similar resetting of the ^{40}Ar-^{39}Ar system is reported for Paleozoic and Jurassic basement gneisses and granites found near the northern Sinaloa coast (El Fuerte area), for which Keppie et al. (2006) reported muscovite and biotite ages of 16.5 ± 1 Ma and 13 ± 1 Ma, respectively.

Evolution of Miocene Magmatism: A Drying Mantle?

On the basis of limited whole-rock chemical and isotope signatures, early to middle Miocene volcanism in the southern Gulf of California area has traditionally been related to suprasubduction arc volcanism during the final stages of subduction beneath this part of the North America plate (e.g., Hausback, 1984; Sawlan and Smith, 1984; Wark et al., 1990; Umhoefer et al., 2001). Recent studies have shown that the silicic rocks of the Sierra Madre Occidental are largely the product of crustal melting (Bryan et al., 2008, and reference therein; see also Ruiz et al., 1988, 1990). Bryan et al. (2014) further showed that the intermediate-composition Comondú-age igneous rocks can be explained by mixing and hybridization of crustal silicic melts and mantle magmas. The geochemical signature of the early and middle Miocene rocks may have been inherited from the crust or by the past ~100 m.y. of subduction and provide no unambiguous constraint on early and middle Miocene tectonic setting and mantle source.

The onset of extensional faulting in the western part of the Sierra Madre Occidental (southwestern Chihuahua, Sinaloa, and Nayarit States) has been recently documented to have initiated at the end of the Oligocene (Ferrari et al., 2013; Bryan et al., 2014), concurrent with the well-documented extension that took place in central and western Sonora (McDowell et al., 1997; Gans, 1997; González-León et al., 2000; Vega-Granillo and Calmus, 2003; Wong et al., 2010; Bryan et al., 2014). In this study, we have further shown evidence for an important extensional event also taking place in the gulf area in the early to middle Miocene. In this context, the Sierra Madre Occidental and Comondú magmatic episodes can be seen as the manifestation of the initial and continuing stages, respectively, of lithosphere stretching that led to the formation of the Gulf of California. We propose that during this long period of rifting (>25 m.y.), extension-induced decompression melting prevailed, overwhelming any partial melting of the mantle in response to the fluxing of fluids derived from the subducting plates (Fig. 10E). Since the late Oligocene, the age of the subducting plate at the trench off Baja California was less than 15 m.y. old, and progressively decreased to 1–5 m.y. old at ca. 12.5 Ma. This is because the age of the oceanic lithosphere entering the subduction zone was extremely young as the East Pacific Rise approached the trench, being only 4.5–1 m.y. old for the Magdalena microplate and 5–4 m.y. old for the Guadalupe microplate at 12.5 Ma (Lonsdale, 1991; Stock and Lee, 1994). It has been long recognized that when a young plate is thin and warm, slab dehydration reactions occur at shallow depth (Stern, 2002). Numerical modeling and experimental petrology show that for a plate younger than ca. 15 Ma entering the subduction zone, dehydration will occur mostly before the slab reaches 100 km depth, strongly limiting the volatile flux to the mantle wedge (e.g., Peacock and Wang, 1999; Green and Harry, 1999). Consequently, fluid fluxing of the mantle beneath western Mexico due to slab dehydration became increasingly limited, and instead, decompression of previously hydrated mantle, induced by lithosphere thinning, was the dominant melting mechanism. At the same time, infiltration of dry and hot asthenosphere from the slab window that was forming to the north (Atwater and Stock, 1998) and the widespread melting associated with the Sierra Madre Occidental may have resulted in a dry and hotter mantle.

CONCLUDING REMARKS

The results of our study are consistent with an early Miocene broad extensional region developing across the area of the future Gulf of California between the relatively undeformed belt of the Peninsular Range Batholith of Baja California and the Sierra Madre Occidental core. The widespread occurrence of middle Miocene (ca. 19–13 Ma) ^{40}Ar-^{39}Ar cooling ages for both early and middle Miocene intrusions across the southern gulf region is incompatible with all gulf extension and thus with crustal cooling and exhumation only occurring after ca. 12.3 Ma (e.g., Stock and Hodges, 1989; Fletcher et al., 2007; Lizarralde et al., 2007; Umhoefer, 2011). Rather, our study indicates that early and middle

Miocene plutons intruded into a belt of extending crust, thinning up to ~100% at ca. 18–12 Ma (Ferrari et al., 2013; Bryan et al., 2014), which was subsequently exploited by transtensional deformation in the central part of the gulf since the late Miocene.

A significant volume of intermediate-composition and high-silica granitic plutons intruded this area in the early Miocene, forming plutonic equivalents to the ignimbrite flare-up recorded in the southern Sierra Madre Occidental. Volumetrically subordinate intrusions were emplaced during the middle Miocene, and these temporally correlate with the onshore middle and upper member of the Comondú Group.

The rifting process envisaged here for the pre–late Miocene deformation in the southern gulf agrees with models and observations in other rifts that pass from a wide to a narrow rift and where extension controls the locus of volcanism (e.g., Parsons et al., 1998; Corti et al., 2003). A rapid opening of the gulf had been inferred by considering that extension in the Gulf Extensional Province only began at the end of the middle Miocene and was guided by the presence of an active Comondú "arc." Our results suggest not only that rifting began much earlier, but also that crustal extension guided the location of volcanism and not the other way round.

ACKNOWLEDGMENTS

This research was supported by grant CONACYT (Consejo Nacional de Ciencia y Tecnología) 82378 (to Ferrari), UC-MEXUS CN-09-312 (to Ferrari and Lonsdale), CONACYT P46600-F (to López-Martinez), and National Science Foundation (NSF) grant OCE-11-44558 to Lonsdale. S. Bryan was in part supported by a Vice Chancellor's fellowship at Queensland University of Technology. We thank M. Grove and D. Kimborough for providing unpublished U-Pb ages that helped us in selecting samples sites at Santa Catalina Island and several dive sites. We thank J. Aranda for providing a sample from Los Cabos block. We also acknowledge the help of many individuals in field and laboratory work: C. Ortega for assistance in U/Pb dating, O. Pérez Arvizu for inductively coupled plasma–mass spectrometry trace-element analysis, R. Lozano-Santacruz for X-ray fluorescence analysis, M.A. García for help with Ar-Ar mass spectrometry, A.S. Rosas Montoya, V.M. Pérez Arroyo, G. Rendón, and L. Gradilla for Ar-Ar sample preparation, J.T. Vázquez for thin section preparation, and G. Norini, G. Antillón Mata, Y. González Romo, J. González Romo, J.C. Castro Climaco, Iisel Calderón Durán, and M. Michell for field assistance and mineral separation. We also thank S. Poli for providing access to the microprobe laboratory at Università di Milano and A. Risplendente for assistance with the electron microprobe analysis. DANA and ROCA samples were collected during research cruises by R/V *Revelle* and R/V *Atlantis* (funded by NSF grants 0203348 and 0646563 to Lonsdale); BEKL samples were collected during a R/V *New Horizon* cruise funded by an award from the State of California to Kluesner. We thank the government of Mexico for operating permission, and the ships' officers and crews for their expert help. Cathy Busby, Lawford Anderson, and Associate Editor Calvin Miller provided critical reviews that helped to improve the final version of the manuscript. We also appreciate the editorial support of Nancy Riggs.

REFERENCES CITED

Abbate, E.P., Balestrieri, M.L., and Bigazzi, G., 2001, Uplifted rift-shoulder of the Gulf of Aden in northwestern Somalia: Palinspastic reconstructions supported by apatite fission-track data, *in* Ziegler, P.A., et al., eds., Peri-Tethys Memoir 6: Peri-Tethyan Rift/Wrench Basins and Passive Margins. Memoires du Museum National d'Histoire Naturelle 186, p. 629–640.

Anderson, J.L., and Smith, D.R., 1995, The effects of temperature and fO_2 on the Al-in-hornblende barometer. The American Mineralogist, v. 80, p. 549–559.

Anderson, J.L., Barth, A.P., Wooden, J.L., and Mazdab, F., 2008, Thermometers and thermobarometers in granitic systems. Reviews in Minerology and Geochemistry, v. 69, p. 121–142.

Anderson, J.L., Morrison, J., and Paterson, S.R., 2012, Post-emplacement fluids and pluton thermobarometry: Mount Stuart batholith, Washington Cascades. International Geology Review, v. 54, no. 5, p. 491–508.

Aranda-Gómez, J.J., and McDowell, F.W., 1998, Paleogene extension in the southern Basin and Range Province of Mexico: Syndepositional tilting of Eocene red beds and Oligocene volcanic rocks in the Guanajuato Mining District. International Geology Review, v. 40, no. 2, p. 116–134, doi:10.1080/00206819809465201.

Atwater, T., and Stock, J., 1998, Pacific–North America plate tectonics of the Neogene southwestern United States: An update. International Geology Review, v. 40, no. 5, p. 375–402, doi:10.1080/00206819809465216.

Ballard, J.R., Palin, J.M., Williams, I.S., Campbell, I.H., and Faunes, A., 2001, Two ages of porphyry intrusion resolved for the super-giant Chuquicamata copper deposit of northern Chile by ELA-ICPMS and SHRIMP. Geology, v. 29, n. 5, p. 383–386.

Bendick, R., McClusky, S., Bilham, R., Asfaw, L., and Klemperer, S., 2006, Distributed Nubia–Somalia relative motion and dike intrusion in the Main Ethiopian Rift. Geophysical Journal International, v. 165, no. 1, p. 303–310, doi:10.1111/j.1365-246X.2006.02904.x.

Bernal, J.P., and Lozano-Santacruz, R., 2005, Characterization of a new set of eight geochemical reference materials for XRF major and trace element analysis. Revista Mexicana de Ciencias Geológicas, v. 22, no. 3, p. 329–344.

Bohannon, R.G., Naeser, C.W., Schmidt, D.L., and Zimmermann, R.A., 1989, The timing of uplift, volcanism, and rifting peripheral to the Red Sea: A case for passive rifting? Journal of Geophysical Research–Solid Earth, v. 94, no. B2, p. 1683–1701, doi:10.1029/JB094iB02p01683.

Bryan, S., 2007, Silicic large igneous provinces. Episodes, v. 30, no. 1, p. 20.

Bryan, S.E., and Ferrari, L., 2013, Large igneous provinces and silicic large igneous provinces: Progress in our understanding over the last 25 years. Geological Society of America Bulletin, v. 125, p. 1053–1078, doi:10.1130/B30820.1.

Bryan, S.E., Ferrari, L., Reiners, P.W., Allen, C.M., Petrone, C.M., Ramos-Rosique, A., and Campbell, I.H., 2008, New insights into crustal contributions to large volume rhyolite generation at the mid-Tertiary Sierra Madre Occidental Province, Mexico, revealed by U/Pb geochronology. Journal of Petrology, v. 49, no. 1, p. 47–77, doi:10.1093/petrology/egm070.

Bryan, S.E., Orozco-Esquivel, T., Ferrari, L., and López-Martínez, M., 2014, Pulling apart the mid to late Cenozoic magmatic record of the Gulf of California: Is there a Comondú arc?, *in* Gómez-Tuena, A., Straub, S.M., and Zellmer, G.F., eds., Orogenic Andesites and Crustal Growth. Geological Society of London Special Publication 385, p. 389–407.

Busby, C., 2004, Continental growth at convergent margins facing large ocean basins: A case study from Mesozoic convergent-margin basins of Baja California, Mexico. Tectonophysics, v. 392, no. 1, p. 241–277, doi:10.1016/j.tecto.2004.04.017.

Busby, C., Smith, D., Morris, W., and Fackler-Adams, B., 1998, Evolutionary model for convergent margins facing large ocean basins: Mesozoic Baja California, Mexico. Geology, v. 26, no. 3, p. 227–230, doi:10.1130/0091-7613(1998)026<0227:EMFCMF>2.3.CO;2.

Calais, E., Lesne, O., Déverchère, J., San'kov, V., Lukhnev, A., Miroshnitchenko, A., Buddo, V., Levi, K., Zalutzky, V., Bashkuev, Y., and Bashkuev, Y., 1998, Crustal deformation in the Baikal rift from GPS measurements. Geophysical Research Letters, v. 25, no. 21, p. 4003–4006.

Calmus, T., Pallares, C., Maury, R.C., Aguillón-Robles, A., Bellon, H., Benoit, M., and Michaud, F., 2011, Volcanic markers of the post-subduction evolution of Baja California and Sonora, Mexico: Slab tearing versus lithospheric rupture of the Gulf of California. Pure and Applied Geophysics, v. 168, no. 8–9, p. 1303–1330.

Cameron, K.L., Nimz, G.J., Kuentz, D., Niemeyer, S., and Gunn, S., 1989, Southern Cordilleran basaltic andesite suite, southern Chihuahua, Mexico: A link between Tertiary continental arc and flood basalt magmatism in North America. Journal of Geophysical Research, v. 94, no. B6, p. 7817–7840, doi:10.1029/JB094iB06p07817.

Carreño, A.L., 1992, Neogene microfossils from the Santiago Diatomite, Baja California Sur, Mexico. Paleontología Mexicana, v. 59, p. 1–37.

Castillo, P.R., Clague, D.A., Davis, A.S., and Lonsdale, P.F., 2010, Petrogenesis of Davidson Seamount lavas and its implications for fossil spreading center and intraplate magmatism in the eastern Pacific. Geochemistry Geophysics Geosystems, v. 11, no. 2, p. 1297, doi:10.1029/2009GC002992.

Cherniak, D.J., and Watson, E.B., 2001, Pb diffusion in zircon. Chemical Geology, v. 172, no. 1, p. 5–24, doi:10.1016/S0009-2541(00)00233-3.

Corti, G., 2009, Continental rift evolution: From rift initiation to incipient break-up in the Main Ethiopian Rift, East Africa. Earth-Science Reviews, v. 96, no. 1, p. 1–53.

Corti, G., Van Wijk, J., Bonini, M., Sokoutis, D., Cloetingh, S., Innocenti, F., and Manetti, P., 2003, Transition from continental break-up to punctiform seafloor spreading: How fast, symmetric and magmatic. Geophysical Research Letters, v. 30, no. 12, p. 1604, doi:10.1029/2003GL017374.

Cuéllar-Cárdenas, M.A., Nieto-Samaniego, Á.F., Levresse, G., Alaniz-Álvarez, S.A., Solari, L., Ortega-Obregón, C., and López-Martínez, M., 2012, Límites temporales de la deformación por acortamiento Laramide en el centro de México. Revista Mexicana de Ciencias Geológicas, v. 29, no. 1, p. 179–203.

DeMets, C., 1995, A reappraisal of seafloor spreading lineations in the Gulf of California: Implications for the transfer of Baja California to the Pacific plate and estimates of Pacific–North America motion. Geophysical Research Letters, v. 22, no. 24, p. 3545–3548, doi:10.1029/95GL03323.

Drake, W.R., 2005, Structural Analysis, Stratigraphy, and Geochronology of the San José Island Accommodation Zone, Baja California Sur, Mexico [M.S. thesis]. Flagstaff, Arizona, Northern Arizona University, 271 p.

Fernandes, R.M.S., Ambrosius, B.A.C., Noomen, R., Bastos, L., Combrinck, L., Miranda, J.M., and Spakman, W., 2004, Angular velocities of Nubia and Somalia from continuous GPS data: Implications on present-day relative kinematics. Earth and Planetary Science Letters, v. 222, no. 1, p. 197–208.

Ferrari, L., López-Martínez, M., and Rosas-Elguera, J., 2002, Ignimbrite flare-up and deformation in the southern Sierra Madre Occidental, western Mexico—Implications for the late subduction history of the Farallon plate. Tectonics, v. 21, no. 4, doi:10.1029/2001TC001302.

Ferrari, L., Valencia-Moreno, M., and Bryan, S.E., 2007, Magmatism and tectonics of the Sierra Madre Occidental and its relation with the evolution of the western margin of North America, *in* Alaniz-Álvarez, S.A., and Nieto-Samaniego, A.F., eds., Geology of México:

Celebrating the Centenary of the Geological Society of México. Geological Society of America Special Paper 422, p. 1–39, doi:10.1130/2007.2422(01).

Ferrari, L., López-Martínez, M., Orozco-Esquivel, T., Bryan, S.E., Duque-Trujillo, J., Lonsdale, P., and Solari, L., 2013, Late Oligocene to middle Miocene rifting and syn-extensional magmatism in the southwestern Sierra Madre Occidental, Mexico: The beginning of the Gulf of California rift. Geosphere, v. 9, p. 1161–1200, doi:10.1130/GES00925.1.

Fletcher, J.M., and Munguía, L., 2000, Active continental rifting in southern Baja California, Mexico: Implications for plate motion partitioning and the transition to seafloor spreading in the Gulf of California. Tectonics, v. 19, no. 6, p. 1107–1123, doi:10.1029/1999TC001131.

Fletcher, J.M., Kohn, B.P., Foster, D.A., and Gleadow, A.J.W., 2000, Heterogeneous Neogene cooling and exhumation of the Los Cabos block, southern Baja California: Evidence from fission-track thermochronology. Geology, v. 28, no. 2, p. 107–110, doi:10.1130/0091-7613(2000)28<107:HNCAEO>2.0.CO;2.

Fletcher, J.M., Grove, M., Kimbrough, D., Lovera, O., and Gehrels, G.E., 2007, Ridge-trench interactions and the Neogene tectonic evolution of the Magdalena Shelf and southern Gulf of California; insights from detrital zircon U/Pb ages from the Magdalena Fan and adjacent areas. Geological Society of America Bulletin, v. 119, no. 11–12, p. 1313–1336, doi:10.1130/B26067.1.

Frost, B.R., and Frost, C.D., 2008, Geochemical classification for feldspathic igneous rocks. Journal of Petrology, v. 49, no. 11, p. 1955–1969, doi:10.1093/petrology/egn054.

Gans, P.B., 1997, Large-magnitude Oligo-Miocene extension in southern Sonora: Implications for the tectonic evolution of northwest Mexico. Tectonics, v. 16, no. 3, p. 388–408, doi:10.1029/97TC00496.

Gastil, R.G., 1975, Plutonic zones in the Peninsular Ranges of southern California and northern Baja California. Geology, v. 3, no. 7, p. 361–363, doi:10.1130/0091-7613(1975)3<361:PZITPR>2.0.CO;2.

Gastil, R.G., 1993, Prebatholithic history of peninsular California, *in* Gastil, R.G., and Miller, R.H., eds., The Prebatholithic Stratigraphy of Peninsular California. Geological Society of America Special Paper 279, p. 145–156, doi:10.1130/SPE279-p145.

Gastil, R.G., Krummenacher, D., and Jensky, W.A., 1979, Reconnaissance geology of west-central Nayarit, Mexico: Summary. Geological Society of America Bulletin, v. 90, no. 1, p. 15–18, doi:10.1130/0016-7606(1979)90<15:RGOWNM>2.0.CO;2.

Gastil, R.G., Diamond, J., Knaack, C., Walawender, M., Marshall, M., Boyles, C., Chadwick, B., and Erskine, B., 1990, The problem of the magnetite/ilmenite boundary in southern and Baja California, *in* Anderson, J., ed., The Nature and Origin of Cordilleran Magmatism. Geological Society of America Memoir 174, p. 19–32.

Gillespie, M.R., and Styles, M.T., 1999, Classification of Igneous Rocks: Keyworth, Nottingham, U.K., British Geological Survey, Research Report RR 99-06, 2nd edition, 52 p.

Godinez, N.S., Kimbrough, D.L., and Kohel, C., 2010, Stratigraphy and petrologic evolution of the Oligocene–Miocene Comondú Group near Bahia Concepcion and Loreto, Baja California Sur, Mexico. Geological Society of America Abstracts with Programs, v. 42, no. 4, p. 66.

González-León, C.M., McIntosh, W.C., Lozano-Santacruz, R., Valencia-Moreno, M., Amaya-Martínez, R., and Rodríguez-Castañeda, J.L., 2000, Cretaceous and Tertiary sedimentary, magmatic, and tectonic evolution of north-central Sonora (Arizpe and Bacanuchi quadrangles), northwest Mexico. Geological Society of America Bulletin, v. 112, no. 4, p. 600–610, doi:10.1130/0016-7606(2000)112<600:CATSMA>2.0.CO;2.

Green, N.L., and Harry, D.L., 1999, On the relationship between subducted slab age and arc basalt petrogenesis, Cascadia subduction system, North America. Earth and Planetary Science Letters, v. 171, no. 3, p. 367–381, doi:10.1016/S0012-821X(99)00159-4.

Hammarstrom, J.M., and Zen, E., 1986, Aluminum in hornblende: An empirical igneous geobarometer. American Mineralogist, v. 71, p. 1297–1313.

Hausback, B.P., 1984, Cenozoic volcanic and tectonic evolution of Baja California Sur, Mexico, *in* Frizzell, V.A., ed., Geology of the Baja California Peninsula. Pacific Section, Society of Economic Paleontologists and Mineralogists Book 39, p. 219–236.

Henry, C.D., 1989, Late Cenozoic Basin and Range structure in western México adjacent to the Gulf of California. Geological Society of America Bulletin, v. 101, p. 1147–1156, doi:10.1130/0016-7606(1989)101<1147:LCBARS>2.3.CO;2.

Henry, C.D., and Aranda-Gomez, J.J., 1992, The real southern Basin and Range: Mid- to late Cenozoic extension in Mexico. Geology, v. 20, no. 8, p. 701–704, doi:10.1130/0091-7613(1992)020<0701:TRSBAR>2.3.CO;2.

Henry, C.D., and Aranda-Gomez, J.J., 2000, Plate interactions control middle-late Miocene, proto–Gulf and Basin and Range extension in the southern Basin and Range. Tectonophysics, v. 318, no. 1, p. 1–26, doi:10.1016/S0040-1951(99)00304-2.

Henry, C.D., and Fredrikson, G., 1987, Geology of Part of Southern Sinaloa, Mexico, Adjacent to the Gulf of California. Geological Society of America Maps and Chart MCH063, 1 sheet, 14 p. text.

Henry, C.D., McDowell, F.W., and Silver, L.T., 2003, Geology and geochronology of the granitic batholithic complex, Sinaloa, México: Implications for Cordilleran magmatism and tectonics, *in* Johnson, S.E., Paterson, S.R., Fletcher, J.M., Girty, G.H., Kimbrough, D.L., and Martín-Barajas, A., eds., Tectonic Evolution of Northwestern México and the Southwestern USA. Geological Society of America Special Paper 374, p. 237–273.

Holland, T., and Blundy, J., 1994, Non-ideal interactions in calcic amphiboles and their bearing on amphibole-plagioclase thermometry. Contributions to Mineralogy and Petrology, v. 116, p. 433–447, doi:10.1007/BF00310910.

Iriondo, A., Kunk, M.J., Winick, J.A., and Consejo de Recursos Minerales (CRM), 2003, $^{40}Ar/^{39}Ar$ Dating Studies of Minerals and Rocks in Various Areas in Mexico: USGS/CRM scientific collaboration (Part I). U.S. Geological Survey Open-File Report 03–020, 79 p.

Iriondo, A., Nieto-Samaniego, A.F., Alaniz-Alvarez, S.A., and Tolson-Jones, G., 2005, Time constraints for a pseudotachylyte event hosted by the Late Cretaceous Las Cruces granite near La Paz, B.C.S., Mexico. Actas INAGEQ, v.11, p. 101–102.

Keppie, J.D., Dostal, J., Miller, B.V., Ortega-Rivera, A., Roldán-Quintana, J., and Lee, J.W., 2006, Geochronology and geochemistry of the Francisco Gneiss: Triassic continental rift tholeiites on the Mexican margin of Pangea metamorphosed and exhumed in a Tertiary core complex. International Geology Review, v. 48, no. 1, p. 1–16, doi:10.2747/0020-6814.48.1.1.

Kimbrough, D.L., Smith, D.P., Mahoney, J.B., Moore, T.E., Grove, M., Gastil, R.G., Ortega-Rivera, A., and Fanning, C.M., 2001, Forearc-basin sedimentary response to rapid Late Cretaceous batholith emplacement in the Peninsular Ranges of southern and Baja California. Geology, v. 29, no. 6, p. 491–494, doi:10.1130/0091-7613(2001)029<0491:FBSRTR>2.0.CO;2.

Kluesner, J., 2011, Marine Geophysical Study of Cyclic Sedimentation and Shallow Sill Intrusion in the Floor of the Central Gulf of California [Ph.D. dissertation]. San Diego, California, University of California, 232 p.

Köhler, H., Schaaf, P., Müller-Sohnius, D., Emermann, R., Negendank, J.F.W., and Tobschall, H.J., 1988, Geochronological and geochemical investigations on plutonic rocks from the complex of Puerto Vallarta, Sierra Madre del Sur. Geofísica Internacional, v. 27, p. 579–592.

Langenheim, V.E., Jachens, R.C., and Aiken, C., 2014, Geophysical framework of the Peninsular Ranges batholith—Implications for tectonic evolution and neotectonics, *in* Morton, D.M., and Miller, F.K., eds., Peninsular Ranges Batholith, Baja California and Southern California. Geological Society of America Memoir 211, p. 1–20.

Lizarralde, D., Axen, G.J., Brown, H.E., Fletcher, J.M., González-Fernández, A., Harding, A.J., Holbrook, W.S., Kent, G.M., Paramo, P., Sutherland, F., and Umhoefer, P.J., 2007, Variation in styles of rifting in the Gulf of California. Nature, v. 448, p. 466–469, doi:10.1038/nature06035.

Lonsdale, P.F., 1989, Geology and tectonic history of the Gulf of California, *in* Winterer, E.L., Hussong, D.M., and Decker, R.W., eds., The Eastern Pacific Ocean and Hawaii. Boulder, Colorado, Geological Society of America, Decade of North American Geology, v. N, p. 499–521.

Lonsdale, P.F., 1991, Structural patterns of the Pacific floor offshore of peninsular California, *in* Dauphin, J.P., and Simoneit, B.R.T., The Gulf and Peninsular Province of the Californias. American Association of Petroleum Geologists Memoir 47, p. 87–125.

Lonsdale, P.F., 1995, Segmentation and disruption of the East Pacific Rise in the mouth of the Gulf of California. Marine Geophysical Researches, v. 17, no. 4, p. 323–359, doi:10.1007/BF01227039.

Lonsdale, P.F., and Kluesner, J., 2010, Routing of terrigenous clastics to oceanic basins in the Southern Gulf of California, inherited from features of the pre-spreading protogulf. San Francisco, California, American Geophysical Union, fall meeting supplement, abstract T33C-2265.

Luhr, J.F., Henry, C.D., Housh, T.B., Aranda-Gómez, J.J., and McIntosch, W.C., 2001, Early extension and associated mafic alkalic volcanism from the southern Basin and Range Province: Geology and petrology of the Rodeo and Nazas volcanic fields, Durango, México. Geological Society of America Bulletin, v. 113, no. 6, p. 760–773, doi:10.1130/0016-7606(2001)113<0760:EEAAMA>2.0.CO;2.

Lyle, M., and Ness, G.E., 1991, The opening of the southern Gulf of California, *in* Dauphin, J.P., and Simoneit, B.R.T., eds., The Gulf and Peninsular Province of the Californias. American Association of Petroleum Geologists Memoir 47, p. 403–423.

Mark, C., Gupta, S., Carter, A., Mark, D.F., Gautheron, C., and Martín, A., 2014, Rift flank uplift at the Gulf of California: No requirement for asthenospheric upwelling. Geology, v. 42, p. 259–262.

Martín-Barajas, A., Stock, J.M., Layer, P., Hausback, B., Renne, P., and López-Martínez, M., 1995, Arc-rift transition volcanism in the Puertecitos volcanic province, northeastern Baja California, Mexico. Geological Society of America Bulletin, v. 107, no. 4, p. 407–424.

McCloy, C., Ingle, J.C., and Barron, J.A., 1988, Neogene stratigraphy, foraminifera, diatoms, and depositional history of Maria Madre Island, Mexico: Evidence of early Neogene marine conditions in the southern Gulf of California. Marine Micropaleontology, v. 13, no. 3, p. 193–212, doi:10.1016/0377-8398(88)90003-5.

McDowell, F.W., and Clabaugh, S.E., 1979, Ignimbrites of the Sierra Madre Occidental and their relation to the tectonic history of western Mexico, *in* Chapin, C.E., and Elston, W.E., eds., Ash-Flow Tuffs. Geological Society of America Special Paper 180, p. 113–124, doi:10.1130/SPE180-p113.

McDowell, F.W., and Keizer, R.P., 1977, Timing of mid-Tertiary volcanism in the Sierra Madre Occidental between Durango City and Mazatlán, Mexico. Geological Society of America Bulletin, v. 88, no. 10, p. 1479–1487, doi:10.1130/0016-7606(1977)88<1479:TOMVIT>2.0.CO;2.

McDowell, F.W., Roldán-Quintana, J., and Amaya-Martínez, R., 1997, Interrelationship of sedimentary and volcanic deposits associated with Tertiary extension in Sonora, Mexico. Geological Society of America Bulletin, v. 109, no. 10, p. 1349–1360, doi:10.1130/0016-7606(1997)109<1349:IOSAVD>2.3.CO;2.

McFall, C.C., 1968, Reconnaissance Geology of the Concepcion Bay Area, Baja California, Mexico. Stanford University Publications in Geological Sciences 10, no. 5, 25 p.

McLean, H., 1988, Reconnaissance Geologic Map of the Loreto and Part of the San Javier Quadrangles, Baja California Sur, Mexico. U.S. Geological Survey Miscellaneous Field Studies Map MF-2000, scale 1:50,000, 10 p. text.

McTeague, M.S., 2006, Marginal Strata of the East Central San Jose del Cabo Basin, Baja California Sur, Mexico [Ph.D. thesis]. Flagstaff, Arizona, Northern Arizona University, 152 p.

Menzies, M., Gallagher, K., Yelland, A., and Hurford, A.J., 1997, Volcanic and nonvolcanic rifted margins of the Red Sea and Gulf of Aden: Crustal cooling and margin evolution in Yemen. Geochimica et Cosmochimica Acta, v. 61, no. 12, p. 2511–2527, doi:10.1016/S0016-7037(97)00108-7.

Mori, L., Gómez-Tuena, A., Cai, Y., and Goldstein, S.L., 2007, Effects of prolonged flat subduction on the Miocene magmatic record of the central Trans-Mexican volcanic belt. Chemical Geology, v. 244, no. 3, p. 452–473, doi:10.1016/j.chemgeo.2007.07.002.

Mullan, H.S., 1978, Evolution of part of the Nevadan orogen in northwestern Mexico. Geological Society of America Bulletin, v. 89, no. 8, p. 1175–1188, doi:10.1130/0016-7606(1978)89<1175:EOPOTN>2.0.CO;2.

Munguía, L., González, M., Mayer, S., and Aguirre, A., 2006, Seismicity and state of stress in the La Paz–Los Cabos region, Baja California Sur, Mexico. Bulletin of the Seismological Society of America, v. 96, no. 2, p. 624–636, doi:10.1785/0120050114.

Murray, B.P., Busby, C.J., Ferrari, L., and Solari, L.A., 2013, Synvolcanic crustal extension during the mid-Cenozoic ignimbrite flare-up in the northern Sierra Madre Occidental, Mexico: Evidence from the Guazapares Mining District region, western Chihuahua. Geosphere, v 9, p. 1201–1235, doi:10.1130/GES00862.1.

Nagel, T.J., and Buck, W.R., 2007, Control of rheological stratification on rifting geometry: A symmetric model resolving the upper plate paradox. International Journal of Earth Sciences, v. 96, no. 6, p. 1047–1057.

Niemitz, J.W., and Bischoff, J.L., 1981, Tectonic elements of the southern part of the Gulf of California. Geological Society of America Bulletin, Part II, v. 92, no. 3, p. 360–407.

Normark, W.R., and Curray, J.R., 1968, Geology and structure of the tip of Baja California, Mexico. Geological Society of America Bulletin, v. 79, no. 11, p. 1589–1600, doi:10.1130/0016-7606(1968)79[1589:GASOTT]2.0.CO;2.

Omar, G.I., and Steckler, M.S., 1995, Fission track evidence on the initial rifting of the Red Sea: Two pulses, no propagation. Science, v. 270, no. 5240, p. 1341–1344, doi:10.1126/science.270.5240.1341.

Ortega-Rivera, A., 2003, Geochronological constraints on the tectonic history of the Peninsular Ranges Batholith of Alta and Baja California: Tectonic implications for western Mexico, *in* Johnson, S.E., Paterson, S.R., Fletcher, J.M., Girty, G.H., Kimbrough, D.L., and Martín-Barajas, A., eds., Tectonic Evolution of Northwestern Mexico and the Southwestern USA. Geological Society of America Special Paper 374, p. 297–336.

Oskin, M., and Stock, J., 2003, Pacific–North America plate motion and opening of the upper Delfin basin, northern Gulf of California, Mexico. Geological Society of America Bulletin, v. 115, no. 10, p. 1173–1190, doi:10.1130/B25154.1.

Oskin, M., Stock, J., and Martín-Barajas, A., 2001, Rapid localization of Pacific–North America plate motion in the Gulf of California. Geology, v. 29, no. 5, p. 459–462, doi:10.1130/0091-7613(2001)029<0459:RLOPNA>2.0.CO;2.

Páramo, P., Holbrook, W.S., Brown, H.E., Lizarralde, D., Fletcher, J.M., Umhoefer, P., Kent, G., Harding, A., Gonzalez, A., and Axen, G., 2008, Seismic structure of the southern Gulf of California from Los Cabos block to the East Pacific Rise. Journal of Geophysical Research, v. 113, no. B3, p. B03307, doi:10.1029/2007JB005113.

Parsons, T., Thompson, G.A., and Smith, R.P., 1998, More than one way to stretch: A tectonic model for extension along the plume track of the Yellowstone hotspot and adjacent Basin and Range Province. Tectonics, v. 17, no. 2, p. 221–234, doi:10.1029/98TC00463.

Peacock, S.M., and Wang, K., 1999, Seismic consequences of warm versus cool subduction metamorphism: Examples from southwest and northeast Japan. Science, v. 286, no. 5441, p. 937–939, doi:10.1126/science.286.5441.937.

Pearce, J.A., Harris, N.B., and Tindle, A.G., 1984, Trace element discrimination diagrams for the tectonic interpretation of granitic rocks. Journal of Petrology, v. 25, no. 4, p. 956–983.

Peccerillo, A., and Taylor, S.R., 1976, Geochemistry of Eocene calc-alkaline volcanic rocks from the Kastamonu area, northern Turkey. Contributions to Mineralogy and Petrology, v. 58, p. 63–81, doi:10.1007/BF00384745.

Pik, R., Marty, B., Carignan, J., Yirgu, G., and Ayalew, T., 2008, Timing of East African Rift development in southern Ethiopia: Implication for mantle plume activity and evolution of topography. Geology, v. 36, p. 167–170, doi:10.1130/G24233A.1.

Piñero-Lajas, D., 2008, Sísmica de Reflexión y Fechamiento 40Ar-39Ar del Basamento Continental en el Margen Oeste de la Cuenca Farallón (Sur del Golfo de California, México) [Ms.C. thesis]. Ensenada, Baja California, Mexico, Centro de Investigación Científica y de Educación Superior de Ensenada (CICESE), 183 p.

Plattner, C.R., Malservisi, R., Dixon, T.H., LaFemina, P., Sella, G.F., Fletcher, J.M., and Suarez-Vidal, F., 2007, New constraints on relative motion between the Pacific plate and Baja California microplate (Mexico) from GPS measurements. Geophysical Journal International, v. 170, no. 3, p. 1373–1380, doi:10.1111/j.1365-246X.2007.03494.x.

Pompa-Mera, V., Schaaf, P., Hernández-Treviño, T., Weber, B., Solís-Pichardo, G., Villanueva-Lascurain, D., and Layer, P., 2013, Geology, geochronology, and geochemistry of Isla María Madre, Nayarit, Mexico. Revista Mexicana de Ciencias Geológicas, v. 30, p. 1–23.

Ramos-Rosique, A., 2013, Timing and evolution of Late Oligocene to early Miocene magmatism and epithermal mineralization in the central Bolaños Graben, southern Sierra Madre Occidental, México [Ph.D. thesis]. London, UK, Kingston University, 215 p.

Reiners, P.W., Ehlers, T.A., and Zeitler, P.K., 2005, Past, present, and future of thermochronology. Reviews in Mineralogy and Geochemistry, v. 58, no. 1, p. 1–18, doi:10.2138/rmg.2005.58.1.

Ridolfi, F., and Renzulli, A., 2012, Calcic amphiboles in calc-alkaline and alkaline magmas: Thermobarometric and chemometric empirical equations valid up to 1,130 °C and 2.2 GPa. Contributions to Mineralogy and Petrology, v. 163, p. 877–895.

Ring, U., and Collins, A.S., 2005, U-Pb SIMS dating of synkinematic granites: Timing of core-complex formation in the northern Anatolide belt of western Turkey. Journal of the Geological Society of London, v. 162, p. 289–298, doi:10.1144/0016-764904-016.

Ruiz, J., Patchett, P., and Arculus, R.J., 1988, Nd-Sr isotope composition of lower crustal xenoliths—Evidence for the origin of mid-Tertiary felsic volcanics in Mexico. Contributions to Mineralogy and Petrology, v. 99, p. 36–43, doi:10.1007/BF00399363.

Ruiz, J., Patchett, P.J., and Arculus, R.J., 1990, Reply to "Comments on Nd-Sr isotopic compositions of lower crustal xenoliths—Evidence for the origin of mid-Tertiary felsic volcanics in Mexico" by K.L. Cameron and J.V. Robinson. Contributions to Mineralogy and Petrology, v. 104, no. 5, p. 615–618, doi:10.1007/BF00306669.

Sawlan, M.G., 1991, Magmatic evolution of the Gulf of California rift, *in* Dauphin, J.P., and Simoneit, B.R., eds., The Gulf and Peninsular Province of the Californias. American Association of Petroleum Geologists Memoir 47, p. 301–369.

Sawlan, M.G., and Smith, J.G., 1984, Petrologic characteristics, age and tectonic setting of Neogene volcanic rocks in northern Baja California Sur, Mexico, *in* Frizzell, V.A., ed., Geology of the Baja California Peninsula. Pacific Section, Society of Economic Paleontologists and Mineralogists Book 39, p. 237–251.

Schaaf, P., Morán-Zenteno, D., Hernández-Bernal, M.D.S., Solís-Pichardo, G., Tolson, G., and Köhler, H., 1995, Paleogene continental margin truncation in southwestern Mexico: Geochronological evidence. Tectonics, v. 14, no. 6, p. 1339–1350.

Schaaf, P., Böhnel, H., and Pérez-Venzor, J.A., 2000, Pre-Miocene palaeogeography of the Los Cabos block, Baja California Sur: Geochronological and palaeomagnetic constraints. Tectonophysics, v. 318, no. 1, p. 53–69, doi:10.1016/S0040-1951(99)00306-6.

Schmidt, M.W., 1992, Amphibole composition in tonalite as a function of pressure: An experimental calibration of the Al-in-hornblende barometer. Contributions to Mineralogy and Petrology, v. 110, p. 304–310, doi:10.1007/BF00310745.

Seiler, C., Fletcher, J.M., Kohn, B.P., Gleadow, A.J., and Raza, A., 2011, Low temperature thermochronology of northern Baja California, Mexico: Decoupled slip exhumation gradients and delayed onset of oblique rifting across the Gulf of California. Tectonics, v. 30, no. 3, TC3004, doi:10.1029/2009TC002649.

Servicio Geológico Mexicano (SGM), 2000, Carta Geológico-Minera Villa Constitución. Servicio Geológico Mexicano Map G12–7-8, scale 1:250,000, 1 sheet.

Shepard, F.P., 1964, Sea-floor valleys of Gulf of California, *in* van Andel, T.H., and Shor, G.G., eds., Marine Geology of the Gulf of California. American Association of Petroleum Geologists Memoir 3, p. 1157–1192.

Silver, L.T., and Chappell, B.W., 1988, The Peninsular Ranges Batholith: An insight into the evolution of the Cordilleran batholiths of southwestern North America. Transactions of the Royal Society of Edinburgh–Earth Sciences, v. 79, p. 105–121, doi:10.1017/S0263593300014152.

Stern, R.J., 2002, Subduction zones. Reviews of Geophysics, v. 40, no. 4, p. 3-1–3-38, doi:10.1029/2001RG000108.

Stock, J.M., and Hodges, K.V., 1989, Pre-Pliocene extension around the Gulf of California and the transfer of Baja California to the Pacific plate. Tectonics, v. 8, no. 1, p. 99–115, doi:10.1029/TC008i001p00099.

Stock, J.M., and Lee, J., 1994, Do microplates in subduction zones leave a geological record? Tectonics, v. 13, no. 6, p. 1472–1487, doi:10.1029/94TC01808.

Streckeisen, A.L., 1976, To each plutonic rock its proper name. Earth-Science Reviews, v. 12, p. 1–33.

Streckeisen, A.L., and LeMaitre, R.W., 1979, Chemical approximation to modal QAPF classification of the igneous rocks. Neues Jahrbuch für Mineralogie, Abhandlungen, v. 136, p. 169–206.

Sun, S.S., and McDonough, W.F., 1989, Chemical and isotopic systematics of oceanic basalts: Implications for mantle composition and processes, *in* Saunders, A.D., and Norry, M.J., eds., Magmatism in the Ocean Basins. Geological Society of London Special Publication 42, p. 313–345, doi:10.1144/GSL.SP.1989.042.01.19.

Sutherland, F.H., Kent, G.M., Harding, A.J., Umhoefer, P.J., Driscoll, N.W., Lizarralde, D., Fletcher, J.M., Axen, G.J., Holbrook, W.S., González-Fernández, A., and Lonsdale, P.F., 2012, Middle Miocene to early Pliocene oblique extension in the southern Gulf of California. Geosphere, v. 8, no. 4, p. 752–770, doi:10.1130/GES00770.1.

Todd, V.R., Erskine, B.G., and Morton, D.M., 1988, Metamorphic and tectonic evolution of the northern Peninsular Ranges Batholith, southern California, *in* Ernst, W.G., ed., Metamorphism and Crustal Evolution of the Western United States (Rubey Volume VII). Englewood Cliffs, New Jersey, Prentice-Hall, p. 894–937.

Umhoefer, P.J., 2011, Why did the southern Gulf of California rupture so rapidly?—Oblique divergence across hot, weak lithosphere along a tectonically active margin. GSA Today, v. 21, no. 11, p. 1–10.

Umhoefer, P., Dorsey, R., Willsey, S., Mayer, L., and Renne, P., 2001, Stratigraphy and geochronology of the Comundú Group near Loreto, Baja California Sur, Mexico. Sedimentary Geology, v. 144, no. 1, p. 125–147, doi:10.1016/S0037-0738(01)00138-5.

Umhoefer, P.J., Mayer, L., and Dorsey, R.J., 2002, Evolution of the margin of the Gulf of California near Loreto, Baja California Peninsula, Mexico. Geological Society of America Bulletin, v. 114, p. 849–868, doi:10.1130/0016-7606(2002)114<0849:EOTMOT>2.0.CO;2.

Valencia, V.A., Righter, K., Rosas-Elguera, J., López-Martínez, M., and Grove, M., 2013, The age and composition of the pre-Cenozoic basement of the Jalisco block: Implications for and relation to the Guerrero composite terrane. Contributions to Mineralogy and Petrology, v. 166, p. 1–24, doi:10.1007/s00410-013-0908-z.

Vega-Granillo, R.V., and Calmus, T., 2003, Mazatan metamorphic core complex (Sonora, Mexico): Structures

along the detachment fault and its exhumation evolution. Journal of South American Earth Sciences, v. 16, no. 4, p. 193–204, doi:10.1016/S0895-9811(03)00066-X.

Vega-Granillo, R., Salgado-Souto, S., Herrera-Urbina, S., Valencia, V., Ruiz, J., Meza-Figueroa, D., and Talavera-Mendoza, O., 2008, U-Pb detrital zircon data of the Río Fuerte Formation (NW Mexico): Its peri-Gondwanan provenance and exotic nature in relation to southwestern North America. Journal of South American Earth Sciences, v. 26, no. 4, p. 343–354, doi:10.1016/j.jsames.2008.08.011.

Vega-Granillo, R., Vidal-Solano, J., and Herrera-Urbina, S., 2012, Island arc tholeiites of Early Silurian, Late Jurassic and Late Cretaceous ages in the El Fuerte region, northwestern Mexico. Revista Mexicana de Ciencias Geológicas, v. 29, no. 2, p. 492–513.

Walawender, M.J., Gastil, R.G., Clinkenbeard, J.P., McCormick, W.V., Eastman, B.G., Wernicke, R.S., Wardlaw, M.S., Gunn, S.H., and Smith, B.M., 1990, Origin and evolution of the zoned La Posta–type plutons, eastern Peninsular Ranges Batholith, southern and Baja California, *in* Anderson, J., ed., The Nature and Origin of Cordilleran Magmatism. Geological Society of America Memoir 174, p. 1–18.

Wang, Y., Forsyth, D.W., and Savage, B., 2009, Convective upwelling in the mantle beneath the Gulf of California. Nature, v. 462, no. 7272, p. 499–501, doi:10.1038/nature08552.

Wark, D.A., Kempter, K.A., and McDowell, F.W., 1990, Evolution of waning subduction-related magmatism, northern Sierra Madre Occidental, Mexico. Geological Society of America Bulletin, v. 102, no. 11, p. 1555–1564, doi:10.1130/0016-7606(1990)102<1555:EOWSRM>2.3.CO;2.

Wong, M.S., Gans, P.B., and Scheier, J., 2010, The $^{40}Ar/^{39}Ar$ thermochronology of core complexes and other basement rocks in Sonora, Mexico: Implications for Cenozoic tectonic evolution of northwestern Mexico. Journal of Geophysical Research, v. 115, no. B7, B07414, doi:10.1029/2009JB007032.

York, D., and López-Martinez, M., 1986, The two-faced mica. Geophysical Research Letters, v. 13, no. 9, p. 973–975, doi:10.1029/GL013i009p00973.

Ziegler, P.A. and Cloetingh, S., 2004, Dynamic processes controlling evolution of rifted basins. Earth-Sciences Reviews, v. 64, p. 1–50.

Zimmermann, J.L., Stussi, J.M., Gonzalez Partida, E., and Arnold, M., 1988, K-Ar evidence for age and compositional zoning in the Puerto Vallarta–Río Santiago Batholith (Jalisco, Mexico). Journal of South American Earth Sciences, v. 1, no. 3, p. 267–274, doi:10.1016/0895-9811(88)90005-3.

Science Editor: Nancy Riggs
Associate Editor: Calvin F. Miller

Manuscript Received 8 October 2013
Revised Manuscript Received 2 September 2014
Manuscript Accepted 29 October 2014

Printed in the USA

4

Caracterización del fallamiento mioceno de la parte suroccidental de la Sierra Madre Occidental (SMO), México: cinemática y segmentación durante el rifting inicial de la porción sur del Golfo de California.

Articulo:

Duque-Trujillo, J., Ferrari, L., Norini, G., López-Martínez, M., 2014. Miocene faulting in the southwestern Sierra Madre Occidental, Nayarit, Mexico: kinematics and segmentation during the initial rifting of the southern Gulf of California. Revista Mexicana de Ciencias Geológicas. v.31, # 3, p. 283-302.

Contribuciones individuales de los autores:

- **Jose Duque-Trujillo:** Concepción y planteamiento del trabajo; trabajo de campo, obtención de datos estructurales, estratigráficos y toma de muestras; preparación, análisis y presentación de datos estructurales; obtención y análisis de paleotensores de esfuerzo; preparación de muestras y obtención de datos geocronológicos (U-Pb y $^{40}Ar/^{39}Ar$); petrografía de rocas volcánicas de la SMO; recopilación bibliográfica; preparación de mapas y perfiles geológicos; redacción del manuscrito.
- **Luca Ferrari:** Consecución del financiamiento; concepción y planteamiento del trabajo; tutoría general del proyecto; supervisión del trabajo de campo; participación en el análisis y presentación de los datos geocronológicos y estructurales; revisión y participación en la preparación del manuscrito.
- **Gianluca Norini:** Participación en el trabajo de campo y la recolección de los datos estructurales; tutoría en el procesado, análisis y presentación de los datos estructurales; revisión del manuscrito.
- **Margarita López-Martínez:** Tutoría en el proceso de preparación de muestras y fechamiento por el método $^{40}Ar/^{39}Ar$; participación en el análisis y presentación de edades $^{40}Ar/^{39}Ar$.

Miocene faulting in the southwestern Sierra Madre Occidental, Nayarit, Mexico: kinematics and segmentation during the initial rifting of the southern Gulf of California

Jose Duque-Trujillo[1,*], Luca Ferrari[1], Gianluca Norini[2], and Margarita López-Martínez[3]

[1] *Centro de Geociencias, Universidad Nacional Autónoma de México, Campus Juriquilla, Blvd. Juriquilla 3001, 76230 Querétaro, Qro., Mexico.*
[2] *Istituto per la Dinamica dei Processi Ambientali – Sezione di Milano, Consiglio Nazionale delle Ricerche, via Pasubio 5, 24044 Dalmine (BG), Italy.*
[3] *División de Ciencias de la Tierra, Centro de Investigación Científica y de Educación Superior de Ensenada (CICESE), Carretera Ensenada-Tijuana No. 3918, 22860 Ensenada, B.C., Mexico.*
** jduquetr@gmail.com*

ABSTRACT

Crustal stretching affecting western Mexico during the Neogene, and its relationship with the opening of the Gulf of California, has been widely studied and discussed for several decades. Nevertheless, the timing and kinematics of the opening is a matter of debate. Most authors essentially agree in considering the rupture of the lithosphere around the Gulf of California, as a fast process that began at ~12.5 Ma and became successful in the early Pliocene, when new oceanic crust began to form in the southern Gulf of California. However, recent studies demonstrated that the crustal stretching processes leading to the Gulf opening began in Late Oligocene as a wide rift, which subsequently focused into the present Gulf area in the early Miocene, accompanied by a slight change in the direction of extension. Eventually, after subduction ceased, highly oblique transtensional deformation broke the previously extended lithosphere.

In this work we present a structural study of the kinematics and time of faulting, and of mafic dikes along three transects in the southern Sierra Madre Occidental, along the southeastern margin of the Gulf. We found that the deformation associated with the beginning of the Gulf of California rifting can be grouped in three sets: 1) normal faults formed during a first phase of deformation, beginning at ~24 Ma, characterized by E-W extension; 2) normal faults and dikes formed between ~20 and 11 Ma, associated with a second deformation phase, with ENE-WSW extension; 3) E-W to NE-SW oblique slip and strike-slip faults and dikes, associated with rift accommodation zones that segment the Gulf of California rift. No significant deformation occurred in the study area after 11 Ma, time at which the extension focused in the present Gulf region. The kinematics of faulting in the study area excludes that significant oblique or lateral deformation might have occurred during the initial phase of rifting in the southern Gulf of California, coincident with the last phase of subduction.

Key words: Sierra Madre Occidental; extensional tectonics; kinematics; Miocene; Gulf of California; Mexico.

RESUMEN

El proceso de extensión cortical de la margen occidental de México durante el Neógeno y su relación con la apertura del Golfo de California ha sido estudiado y discutido por varias décadas. Sin embargo la temporalidad y la cinemática de esta apertura son temas todavía debatidos. La mayoría de los autores concuerdan en que la ruptura de la litósfera en el Golfo de California fue un proceso rápido que inició a los ~12.5 Ma, para culminar al principio del Plioceno, cuando comienza el proceso de oceanización en las cuencas de la parte sur del Golfo. Sin embargo, trabajos recientes han demostrado que el proceso de extensión cortical que llevó a la apertura del Golfo comenzó desde el Oligoceno tardío a manera de un rift amplio, para posteriormente focalizarse en la zona del futuro Golfo de California en el Mioceno inferior, acompañado de un ligero cambio en el dirección de extensión. Finalmente, después del termino de la subducción, la deformación transtensional fuertemente oblicua terminó de romper la franja de litósfera previamente extendida.

En este trabajo se presenta un estudio estructural de la cinemática y la temporalidad del fallamiento, y de los diques máficos a lo largo de tres transectos en la zona suroccidental de la Sierra Madre Occidental, la cual constituye la margen suroriental del Golfo. Los resultados indican que las estructuras observadas se pueden agrupar en tres familias: 1) fallas normales asociadas a una primera fase de deformación que comienza hacia los ~24 Ma, y se caracteriza por una extensión con dirección E-W; 2) fallas normales y diques, entre ~20 y 11 Ma, asociados a una extensión orientada en dirección ENE-WSW, ortogonal al eje del Golfo de California; 3) fallas oblicuas y laterales, y diques de dirección E-W a NE-SW que se asocian a zonas de acomodo que segmentan transversalmente al rift del Golfo de California. Cabe mencionar que no hay deformación significativa después de los 11 Ma, tiempo en que la extensión se concentra en la región actualmente ocupada por el Golfo. La cinemática asociada al fallamiento observado indica movimientos dominantemente de tipo normal, lo cual excluye la posibilidad de que se hayan acomodado movimientos oblicuos o laterales durante las primeras etapas de apertura del Golfo de California, ocurridas durante la fase final de la subducción.

Palabras clave: Sierra Madre Occidental; tectónica extensional; cinemática; Mioceno; Golfo de California; México.

Duque-Trujillo, J., Ferrari, L., Norini, G., López-Martínez, M., 2014, Miocene faulting in the southwestern Sierra Madre Occidental, Nayarit, Mexico: kinematics and segmentation of the initial rifting in the southern Gulf of California: Revista Mexicana de Ciencias Geológicas, v. 31, núm. 3, p. 283-302.

INTRODUCTION

The age and kinematics of the extensional deformation that led to the formation of the Gulf of California is a matter of debate. Early studies proposed that in the middle to late Miocene the lithosphere in the area, called "proto-Gulf", was rheologically weakened by the previous (early/middle Miocene) arc-volcanism, a feature that was subsequently exploited by strike-slip and extensional faulting that led to the Gulf of California opening (Karig and Jensky, 1972; Umhoefer, 2011). Later, Stock and Hodges (1989) proposed that the initial phase of opening of the Gulf of California began in late Miocene (*ca.* 12 Ma) and was partitioned into strike-slip motion along the Tosco-Abreojos fault system, west of Baja California, and orthogonal extension (WSW-ENE) in a broadly NNW belt along the main Gulf axis. Subsequently, beginning near the end of the late Miocene (*ca.* 6 Ma), the main deformation focused east of Baja California and transtensional deformation produced the final rupture of the lithosphere and the oblique opening of new oceanic basins.

Further studies in Sonora and Baja California questioned the initial partitioning of deformation proposed by Stock and Hodges (1989) and led to alternative models, which state that the deformation inside the Gulf was characterized by right-lateral transtension since ~12.5 Ma, with a smaller component of right lateral motion accommodated west of Baja California along the Tosco-Abreojos fault system (*e.g.* Gans, 1997; Fletcher *et al.*, 2007). Recently, Bennett *et al.* (2013) proposed a hybrid model of rifting, in which the deformation along the northern Gulf was focused on a right-lateral shear zone, which later evolved into a transtensional plate limit, forming the Gulf of California rift (Bennett, *et al.*, 2013; Bennett and Oskin, 2014). All these models, however, agree on placing the initiation of the regional dextral-oblique Pacific-North America relative plate motion at ~12.5 Ma, when the subduction of the Farallon plate remnants under North America ceased and Baja California began to be transferred to the Pacific Plate (Atwater and Stock, 1998).

More recent studies of the regional geology of northern Nayarit and Sinaloa demonstrated that extensional faulting began much earlier than the end of subduction at ~12.5 Ma (Ferrari *et al.*, 2013). These authors shown that extension in the south-western part of the Sierra Madre Occidental (SMO) is as old as late Oligocene to early Miocene and likely controlled the style and composition of volcanism. Based on the reconstruction of the paleo-position of Baja California, Ferrari *et al.* (2013) also proposed that the early extension (24 to 18 Ma) in northern Nayarit and southern Sinaloa was almost orthogonal to the margin of the southern Gulf (southern Sinaloa and Nayarit) (see their fig. 15) predicting a minor component of right lateral motion, if any, in this region. This deformation is very similar to that of Sonora, where a 250 km wide belt in the western SMO was extended between late Oligocene and middle Miocene (McDowell *et al.*, 1997; González-León *et al.*, 2000; Vega-Granillo and Calmus, 2003; Nourse *et al.*, 1994; Wong *et al.*, 2010; Murray *et al.*, 2013). Following Ferrari *et al.* (2013), in this work we consider that the Gulf of California rift is the result of a long period of crustal thinning that began in the late Oligocene, and became highly oblique once Baja California started moving with the Pacific plate after the end of subduction (*ca.* 12.5 Ma).

Here, we present a geologic and structural study of the southwestern part of the SMO in Nayarit, which constrains the kinematics of the early deformation in the southeastern flank of the Gulf of California rift. We describe the stratigraphy, as well as the geometry, kinematics and age of faulting along three transects that run almost orthogonal to the main fault systems of this part of the SMO. We found that faulting and volcanism occurred concurrently during the early Miocene under an E-W to ENE-WSW extensional stress regime. Strike slip deformation is very minor, apart from the accommodation zones that segmented this part of the rift.

GEOLOGICAL AND TECTONIC SETTING

The study area is located within the SMO, which constitutes the largest silicic igneous province in North America and the most recent event of this kind on Earth (Ferrari *et al.*, 2007, Bryan and Ferrari, 2013). A distinctive trait of the SMO is the thick late Eocene to early Miocene ignimbrite cover that caps most of the province, traditionally known as the Upper Volcanic Supergroup (UVS, McDowell and Keizer, 1977). The UVS overlies the so-called Lower Volcanic Complex (LVC), constituted by a series of Late Cretaceous to early Eocene batholitic rocks and intermediate lavas, partly coeval with the Peninsular Range Batholiths of Baja California (McDowell and Clabaugh, 1979; McDowell *et al.*, 1997).

The UVS was emplaced approximately between 38 and 18 Ma, with a minimum estimated volume of ~400,000 km^3 of dominantly rhyolitic ignimbrites (~85%) and lesser rhyolitic domes and basaltic lavas. Geochronologic studies have revealed that ignimbrites were erupted in short time spans, with peaks of over 1 km thick ignimbrite sequences emplaced in less than 1 m.y. (Swanson *et al.*, 2006; Ferrari *et al.*, 2002, 2007), implying a high rate of magma generation and eruption (Bryan *et al.*, 2008; Bryan and Ferrari, 2013). Two main flare-up episodes are recognized at ~34–28 Ma and ~24–18 Ma (Ferrari *et al.*, 2007). The Oligocene episode (~34–28 Ma) forms three-quarters of the total erupted volume, covering ~400,000 km^2 of the SMO (Figure 1). The Miocene ignimbritic pulse (~24–18 Ma) is concentrated in the southwestern and western part of the SMO and Baja California (Figure 1) (Sawlan and Smith, 1984; Umhoefer *et al.*, 2001; Drake, 2005; Ferrari *et al.*, 2002, 2007). During this period, volcanism was bimodal, with massive rhyolitic ignimbrites and rhyolitic domes accompanied by basaltic lavas that erupted from fissures, concurrently with extensional faulting (Ferrari *et al.*, 2013). Recent studies in the southern Gulf of California documented the occurrence of early Miocene granitoids and ignimbrites on continental blocks that make up the submerged rifted margins of the Gulf of California rift, suggesting that the source area of the Miocene ignimbrites was located not only in the western side of the SMO but also within the proto-Gulf area (Ferrari *et al.*, 2013; Duque-Trujillo *et al.*, in press).

The central part of the SMO in western Durango and southwestern Chihuahua is characterized by a plateau of flat lying ignimbrites, which appear unfaulted (Henry and Aranda-Gómez. 2000; Ferrari *et al.*, 2007). On both flanks of this unextended core, extensional fault systems tilted the ignimbrite succession in different directions. Geophysical studies indicate a crustal thickness of 40 to 55 km in the unextended core of the SMO (Couch *et al.*, 1991; Bonner and Herrin, 1999), which decreases to ~22–26 km on the extended western flank, adjacent to the Gulf of California (Persaud *et al.*, 2007; Lizarralde *et al.*, 2007; Savage and Wang, 2012) (Figure 1). The extensional fault systems along the western flank of the SMO, in Sonora, Sinaloa, and northern Nayarit are part of the so-called Gulf Extensional Province (GEP), whose onset has been now dated as early as late Oligocene (Murray *et al.*, 2013; Ferrari *et al.*, 2013). Along this belt, ignimbrites are tilted to the ENE or WSW in domains separated by ~ENE-WSW accommodation zones (Stewart, 1998; Ferrari *et al.*, 2007, 2013). Based on the dominant dip direction, tectonic transport direction during rifting, and the type of basement, Ferrari *et al.* (2013) divided the southern SMO into three different domains bounded by accommodation zones where the structural style changes and dip polarity reverses. The studied area is located in the northern Nayarit domain

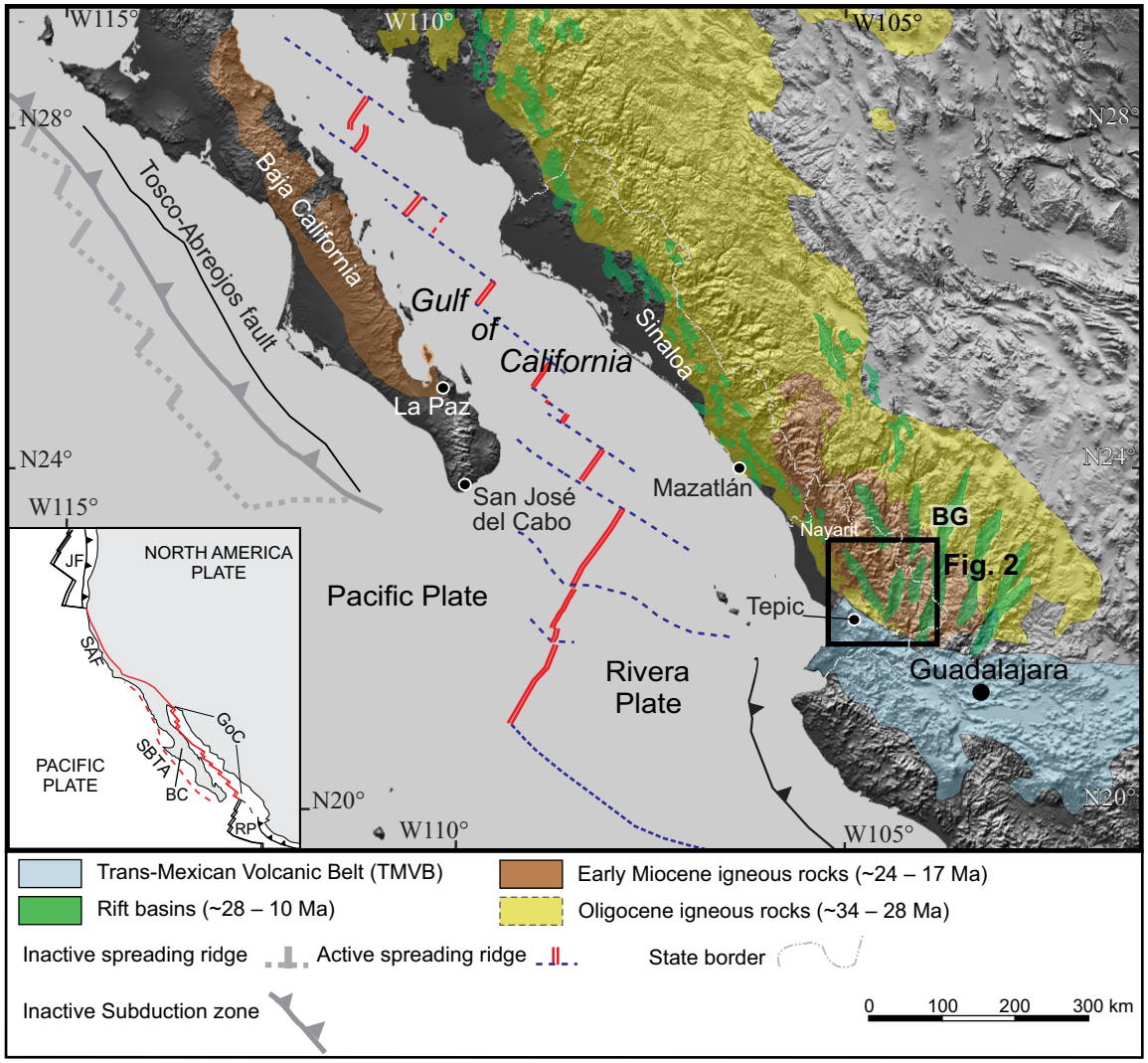

Figure 1. Geodynamic map of western Mexico showing the distribution of the main volcanic provinces and the main regional tectonic features. BG = Bolaños graben. Modified from Duque *et al.* (in press), Bryan and Ferrari (2013), and Ferrari *et al.* (2002). Insert shows the regional geodynamic setting of the Gulf of California. BC: Baja California; SBTA: San Benito-Tosco Abreojos fault system; GoC: Gulf of California; RP: Rivera Plate; JF: Juan de Fuca plate; SAF: San Andreas Fault.

as defined in Ferrari *et al.* (2013), which is bounded to the south by El Roble accommodation zone (Figure 2), a left-lateral shear zone, and to the north, by the Mezquital accommodation zone, which separates opposite tilting of strata (ENE to the south and WSW to the north). Within the northern Nayarit domain, ignimbrites dominantly dip E to ENE due to N-S to NNW-SSE striking west dipping normal faults (Figure 2). Deformation within the northern Nayarit domain can be further separated into eastern and western zones.

The eastern part of the northern Nayarit domain is characterized by N-S striking high-angle normal faults that affect almost the entire domain, forming several graben and half graben structures(Figure 1). This deformation, bracketed between *ca.* 24 and 18 Ma, took place during the first phase of rifting that affected a wide region of the SMO (Ferrari *et al.*, 2013). The western limit of this early extension is difficult to establish because of younger faulting affecting the southeastern margin of the Gulf of California and because structures are probably buried in the coastal plain and offshore in the continental platform. Nevertheless, early Miocene plutons, exposed along the Nayarit coast, on islands just offshore of southeastern Baja California, and on the rifted blocks submerged under the Gulf of California waters, indicate rapid cooling before ~18 Ma, during a major phase of crustal thinning (Duque-Trujillo *et al.*, in press).

The western deformation zone of the northern Nayarit domain is characterized by a 20 km wide and ~160 km long NNW striking belt of extensional fault systems developed along the western margin of the SMO (Pochotitán and San Pedro-Acaponeta fault systems, Figure 2), which accommodated up to ~1.7 km of vertical displacement. These fault systems tilt the 21 to 18 Ma old ignimbrites and rhyolitic lavas up to 35° down to the ENE. The observed field relationships and available ages, indicate that the activity of these fault systems began after ~21 Ma, and they possibly acted as conduits for easy ascent to the surface of small volumes of silicic magmas that extruded as domes or formed subvolcanic intrusions dated between 20 and 17 Ma (Ferrari *et al.*, 2002, 2013). The upper age of these faults is constrained by several 11 to 10 Ma old flat-lying basaltic lavas emplaced along the Nayarit coast that unconformably overlie the SMO ignimbrites. Vertical to very gently dipping, NNW striking mafic dikes of the same age are also intruded parallel to the Pochotitán and San Pedro-Acaponeta fault systems (Righter *et al.*, 1995; Henry and Aranda-Gómez, 2000; Ferrari *et al.*, 2000a, 2002, 2013).

LOCAL GEOLOGY

We closely examined the fault systems along the western flank of the southern SMO, following three transects, which cross the main structures along roads that were recently enlarged and paved, so that fault planes are well exposed along roadcuts (Figure 2 and 3a–3m). A brief description of the geology along these transects (Figures 4 to 6) is given in the following. Geological cross sections (Figure 7) were drawn using information gathered during fieldwork, Google Earth observations, and information compiled from previous works (Ferrari *et al.*, 2002, 2013; SGM, 1998 and 1999).

Northern transect: Estación Ruiz – Jesús María

The Estación Ruiz-Jesús María transect runs approximately in a WSW-ENE direction between the coastal plain and the core of the SMO (Figure 2). It crosses the San Pedro-Acaponeta fault system and the southern part of the Nayar caldera, ending in the Jesús María half graben (Figures 2, 4 and 7a), The oldest rocks of the SMO province are exposed in the lowest part of the sequence on both western and eastern sides of the transect (Figure 7a). These are composed of reddish sandstones and conglomerates (Emvs) rich in andesitic clasts, conglomeratic sandstones, and sandstones interbedded with andesitic lava flows and some thin ignimbrites (Emig) (Figure 3a-3b). Based on crude layering, it can be inferred that this sequence dips ~20° to the east, both on the western and eastern sides of the transect. These deposits are usually too weathered to be dated and are inferred to be of Paleocene to Eocene age in the Mexican Geological Survey geologic maps (SGM, 1996, 1998, 1999, 2006). However, a sample from a 2 m thick ignimbrite (Emig) interbedded with red sandstones (Emvs) along this transect (Figure 3b) has been recently dated at 23.6±0.2 Ma (Ferrari *et al.*, 2013). This age correspond to the onset of the early Miocene ignimbrite pulse in the southern SMO (Scheubel *et al.*, 1988; Ferrari *et al.*, 2002, 2007, 2013; McDowell and McIntosh, 2012). Particularly, ignimbrites of this age make up the Las Canoas ignimbrite succession (Ferrari *et al.*, 2002) exposed in the eastern part of the transect, which covers the reddish volcano-sedimentary sequence. Las Canoas succession is composed of a series of pink to grey, moderately indurated and slightly weathered ignimbrites (Emig), that contain small phenocrysts of plagioclase, biotite, alkali-feldspar and scarce hornblende (Figure 3c). Therefore, the volcaniclastic succession observed in the western part of the transect represents distal facies of the early Miocene volcanic succession exposed in the SMO core (Figure 7a).

A series of mafic dikes (Md), which vary in thickness and orientation, is observed at several locations along the transect cutting the Las Canoas ignimbrites and the volcaniclastic succession. The dikes are dark green, aphyric to porphyritic in texture, with plagioclase and less common hornblende phenocrysts. Most of them have been intruded along fault planes (Figure 3d). Striae and fault gouge (Fg) were observed along some dike walls, indicating that faults remained active after dike intrusion (Figure 3d). In some cases, dikes were cut and displaced by faults (Figure 3e). Intense alteration prevented radiometric dating on most of these mafic dikes. Nevertheless, we were able to obtain a ^{40}Ar-^{39}Ar age for one dike located ~6 km west of Jesús María (site Nay-21, Figure 4). This dike has an E-W orientation and cut an ignimbrite succession that can be correlated with the Las Canoas ignimbrite succession. Two laser step-heating experiments on groundmass concentrates (Figure 8a) yielded similar age spectra, with a decreasing staircase pattern. A plateau age of 23.44±0.23 Ma is defined by five consecutive fractions representing more than 70% of the ^{39}Ar released. The staircase shaped age spectrum suggest the presence of excess argon, for this reason the preferred age was obtained combining all gas fractions obtained from both experiments on a correlation diagram (Figure 8b), which yields a 23.01±0.24 Ma isochron age. A summary of relevant information about ^{40}Ar-^{39}Ar dating is presented in Supplemental file 1. East of Jesús María, a N-S trending mafic dike was also observed cutting the Las Canoas ignimbrite succession and feeding a lava flow (Figure 3c). This dike was too altered to be dated but similar basaltic lavas were dated by Ferrari *et al.* (2002) at 21.3±0.3 Ma just 1.5 km East from this site (their sample TS-21). Based on these two ages and crosscutting relations, we consider that the mafic dikes observed along the eastern part of the transect are early Miocene in age. Basaltic dikes and flows of this age have been also reported for the Bolaños graben (Figure 1) (Nieto-Obregon *et al.*, 1981; Scheubel *et al.*, 1988; Ramos Rosique, 2013) and at the boundary between the SMO and the Trans-Mexican Volcanic Belt north of Guadalajara (Rossotti *et al.*, 2002).

In the central part of the transect, the Las Canoas ignimbrite succession is overlain by the younger Nayar ignimbrite (Nig) succession (Figure 7a) (Ferrari, *et al.*, 2002), which consists of a series of welded ash-flow and air fall tuffs, characterized by white to light yellow colors, composed of ash with phenocrysts of quartz, plagioclase, alkali-feldspar and biotite (Figure 3f). Several rhyolitic domes (Rd) are intercalated with or cap the Nayarit ignimbritic succession (Figure 3g to 3i; Figure 7a). These domes, which post-date the Nayar succession, yielded ages between ~17.5 and 18.4 Ma (Figure 4) (Ferrari *et al.*, 2002; 2013). In the Mesa del Nayar area most layers of this succession are horizontal or show only minor tilting (<10°), whereas they are tilted up to 35° to the west (Figures 2 and 3f). The maximum thickness of the Nayar succession is observed in the Mesa del Nayar area (Figure 3i), with at least ~800 m of ignimbrites (Figure 7a). The top and the base of the unit were dated by Ferrari *et al.* (2002) at 19.9±0.4 Ma and 21.1±0.3 Ma, respectively, implying that a thickness of almost 1 km was emplaced within *ca.* 1 m.y. The source of this succession has been associated with the formation of a series of NNW aligned calderas, interpreted on the basis of landforms, domes, and sedimentary deposits found in the Mesa del Nayar area (Ferrari *et al.*, 2002).

Central transect: Aguamilpa dam

This relatively short transect runs for ~12 km in a WSW-ENE direction along roads following both sides of the Santiago river, downstream and west of the Aguamilpa dam (Figures 2 and 5). In this area, the Santiago river follows a complex accommodation zone, which separates the San Pedro-Acaponeta fault system to the north from the Pochotitán fault system to the south (Figure 2). The geology of the Aguamilpa dam area is dominated by a succession of well indurated, pink colored ignimbrites, typically rich in phenocrysts of plagioclase and/or biotite. The succession dips 26° to 50° to the W and WSW due to normal faulting (Figure 7b). Available ages for these ignimbrites range between 22.4 and 18.7 Ma (Rodríguez-Castañeda and Rodríguez-Torres, 1992, and references therein; Frey *et al.*, 2007), making them broadly correlative with the Las Canoas and the Nayar successions.

A series of subvolcanic bodies, which vary in composition from intermediate to felsic, are found below the ignimbrites (Figure 7b). Although field relations are not always clear, some of them are clearly intrusive and seem to have exploited the normal faults to ascend to a shallow level. Rodríguez-Castañeda and Rodríguez-Torres (1992) report a K-Ar age of 18.3 Ma for an granite body. Duque-Trujillo *et al.* (in press) report many subvolcanic intrusives along the SMO piedmont with ages between 22.3 and 18.1 Ma. Based on their geographical distribution, mineralogy, and field relationship with the ignimbrites, we consider that the subvolcanic bodies exposed near the Aguamilpa dam are part of the same subvolcanic suite.

Several rhyolitic domes cap the ignimbrites (Figures 2, 5 and 7b). Although no dates have been obtained, their stratigraphic position

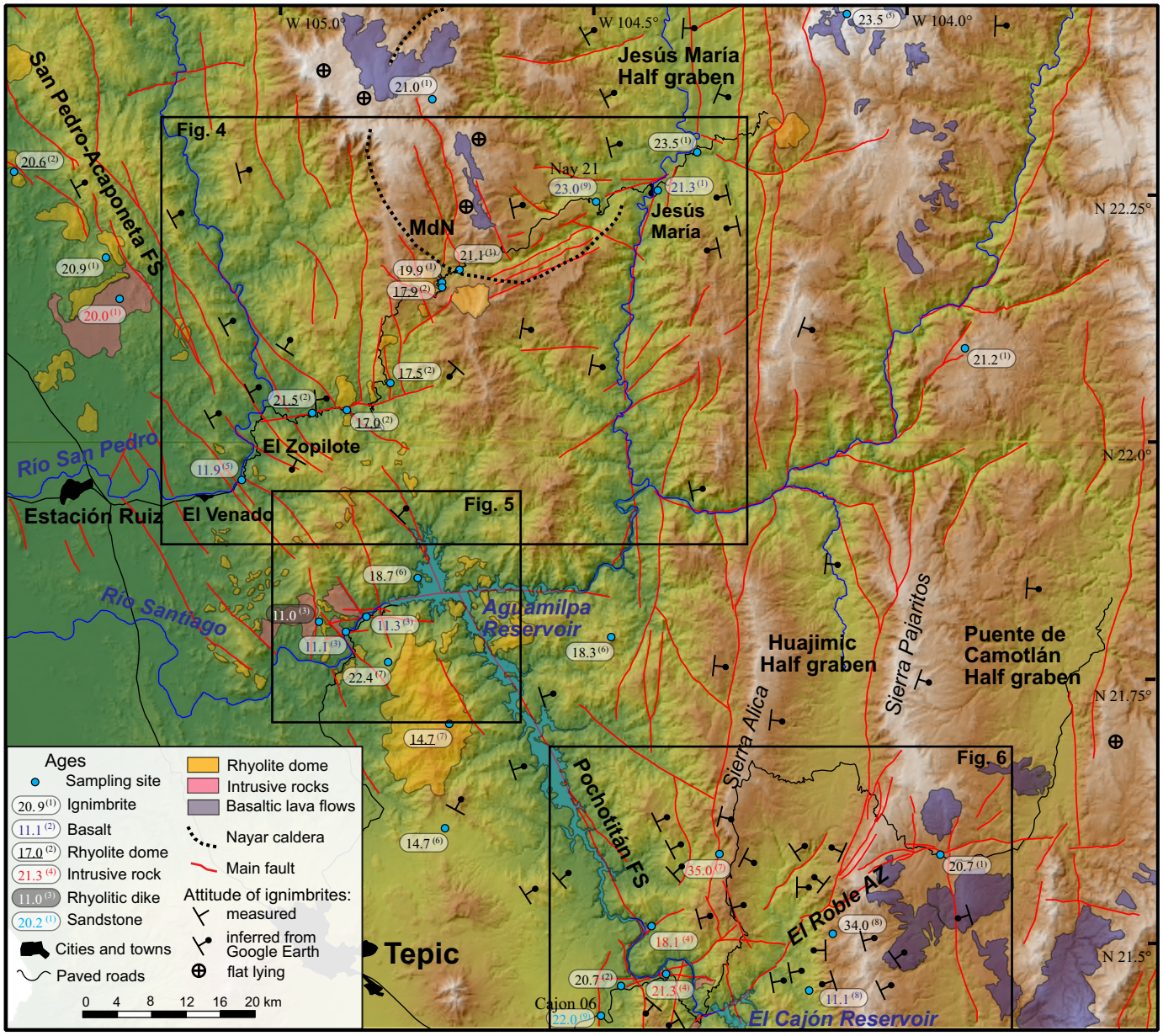

Figure 2. Map of the study area showing selected geological features and isotopic ages described in the text. Minor faults interpreted during the present work; main fault traces from Ferrari *et al.* (2013). Dip directions from Ferrari *et al.* (2002, 2013), 1:250.000 scale geologic maps of Servicio Geológico Méxicano (Escuinapa and Tepic sheets), and Google Earth observations. Reference for geochronologic dates, shown in parentheses on each date: (1) Ferrari *et al.* (2002); (2) Ferrari *et al.* (2013); (3) Frey *et al.* (2007); (4) Duque-Trujillo *et al.* (in press); (5) Clark *et al.* (1981); (6) Soto and Ortega (1982); (7) Rodríguez-Castañeda and Rodríguez-Torres (1992); (8) Damon *et al.*, 1979; (9) This study. FS: Fault system, AZ: Accommodation zone.

suggests that they could correlate with those observed in the Estación Ruiz-Jesús María transect east of Mesa del Nayar, with ages between ~17.5 and 18.4 Ma. A large dome complex is also observed on the southwestern side of the Aguamilpa reservoir. Rodríguez-Castañeda and Rodríguez-Torres (1992) report a K-Ar age of 14.7 Ma for an andesite making up the peak of the complex (Picachos andesite). Although these domes were not mapped in detail, they do not appear faulted, suggesting they post-date the NNW striking normal fault systems.

A swarm of mafic dikes cross-cut the early Miocene ignimbrites along this transect. They are fine grained to aphyric, dark green in color and range between 1 to 4 m in thickness. Many of these dikes were dated both by K-Ar and ^{40}Ar-^{39}Ar methods, yielding ages between 11.5 and 11 Ma (Damon *et al.*, 1979; Soto and Ortega, 1982; Frey *et al.*, 2007). These dikes are thus part of the regional pulse of mafic magmatism recognized along the whole eastern side of the Gulf, as described and discussed in Ferrari *et al.* (2013).

Southern transect: El Cajón – Sierra de Pajaritos

This transect goes from Santa María del Oro-El Cajón area, at the boundary between the Trans Mexican Volcanic Belt (TMVB) and the SMO (Figure 7c), to the Sierra de Pajaritos fault system, which bounds the eastern side of the Huajimic half graben (Figures 2 and 7d). This transect passes across the NNW striking Pochotitán fault system and the N-S striking Sierra de Alica fault system and, in its

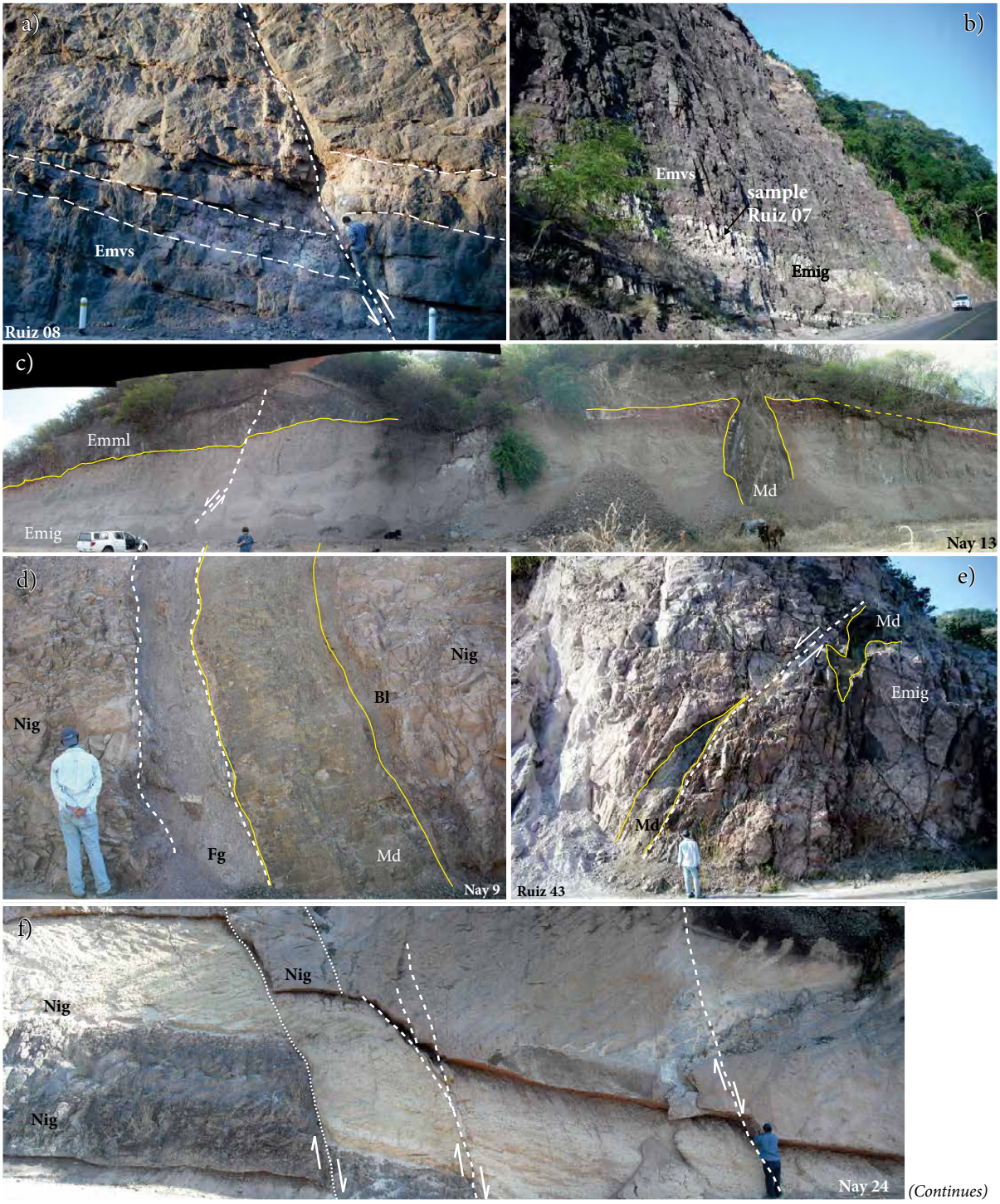

(Continues)

Figure 3. a) NE-verging oblique reverse fault affecting volcanoclastic deposits (Emvs) at the base of the El Nayar ignimbrite succession; site Ruiz-08. Picture taken at 22.0345°N, 104.9063°W, looking north. b) Ignimbrite (Emig), dated at 23.6±0.2 Ma (sample Ruiz 07; Ferrari *et al.*, 2013), interbedded with a volcanoclastic deposit (Emvs). Picture taken at 22.0295°N, 104.8869°W, looking north. c) A mafic dike (Md) cutting an ignimbrite (Emig) correlative with the Canoas succession and feeding a basaltic lava flow (Emml), cut by a small E-dipping normal fault; site Nay-13. Picture taken at 22.2515°N, 104.5263°W, looking southeast. d) Fault gouge at the contact between a mafic dike (Md) and the El Nayar ignimbrites (Nig) at site Nay-09. Picture taken at 22.1893°N, 104.6782°W, looking south. Fg: Fault gauge; Bl: baked layer. e) Mafic dike (Md) intruding early Miocene ignimbrite (Emig) and displaced by a W-dipping normal fault at site Ruiz-43. Picture taken at 22.0377° N, 104.8406°W, looking northwest. f) A series of SW-dipping normal faults cutting the El Nayar ignimbrites (Nig) at site Nay-24. Picture taken at 22.2316°N, 104.6174°W, looking east. (*continues*)

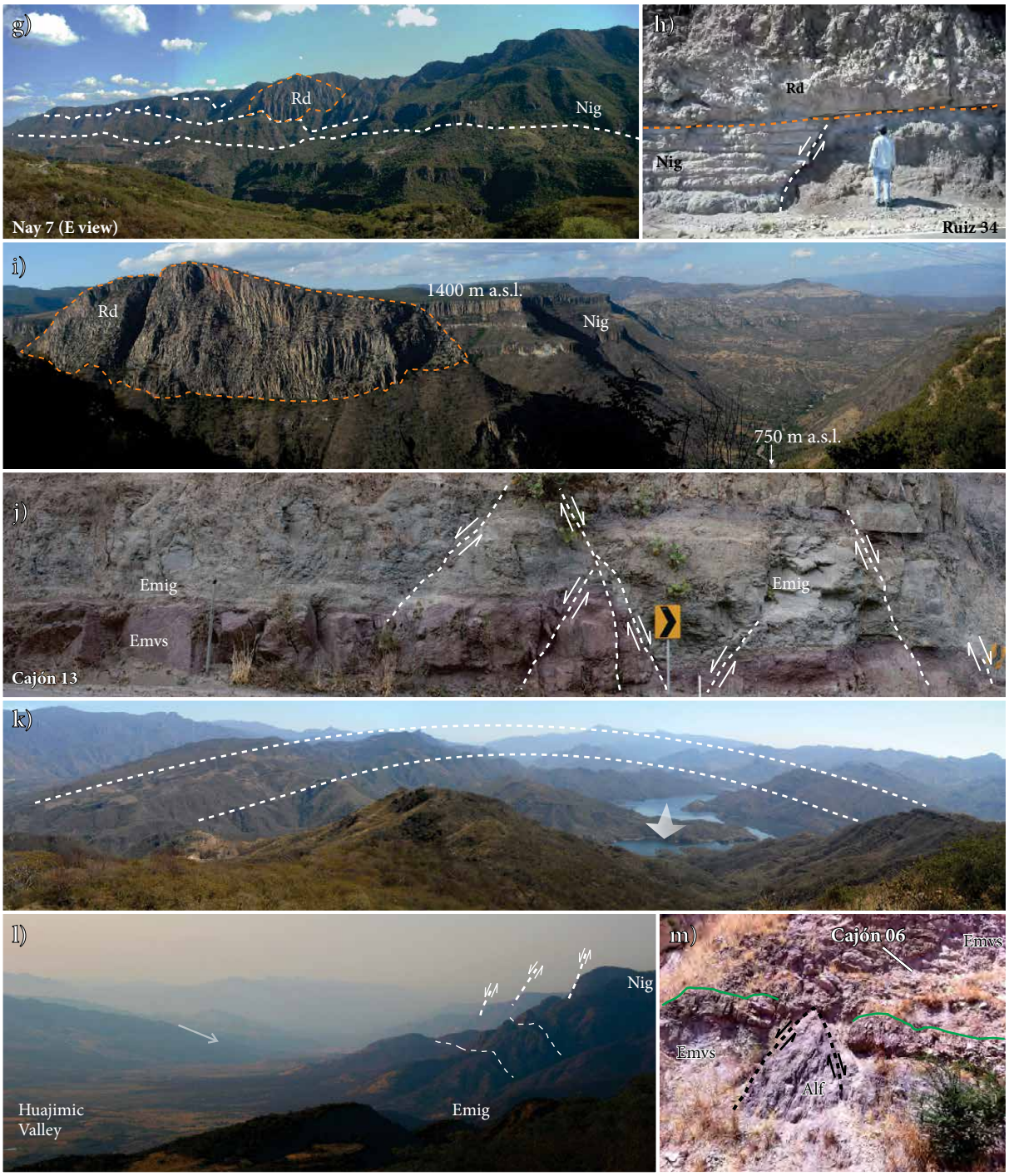

Figure 3 (cont.). g) Traces (white doted lines) of N-dipping normal faults affecting the upper part of the El Nayar succession (Nig). Picture taken at 22.18702°N, 104.69260°W, looking east. h) E-dipping normal fault covered by a rhyolitic dome (Rd) dated at 17.57±0.19 Ma by ^{40}Ar-^{39}Ar in biotite (Ferrari *et al.* 2013), site Ruiz-34. Picture taken at 22.18702°N, 104.69260°W, looking east. i) The ~800 m thick El Nayar ignimbritic sequence (Nig), capped by a rhyolitic dome (Rd) at Mesa del Nayar. Picture taken at 22.2189°N, 104.6412°W, looking northeast. m a.s.l.: meters above sea level. j) Eocene volcano-sedimentary sequence (Emvs) underlying early Miocene ignimbrite and affected by conjugate normal faulting near Santiago river, site Cajón 13. Picture taken at 22.4381°N, 104.4876°W, looking east. k) Broad anticline formed by the Miocene ignimbrites in the El Cajón reservoir zone. Picture taken at 21.4541°N, 104.4454°W, looking southwest. Fold axis and plunging north (white arrow). l) Trace and vertical projection of some west-dipping normal faults on the Sierra de Pajaritos escarpment. On the west side of the Huajimic valley, the El Nayar ignimbrite sequences (Nig) dip to the east (arrow). Picture taken at 21.6268°N, 104.2698°W, looking north. m) Normal fault affecting an andesitic lava flow (Alf) and covered by a reddish volcano-sedimetary deposit (Emvs; sample Cajón 06). La línea verde marca el límite entre la secuencia afectada por el fallamiento y la no afectada. Picture taken at 22.4278°N, 104.5761°W, looking east.

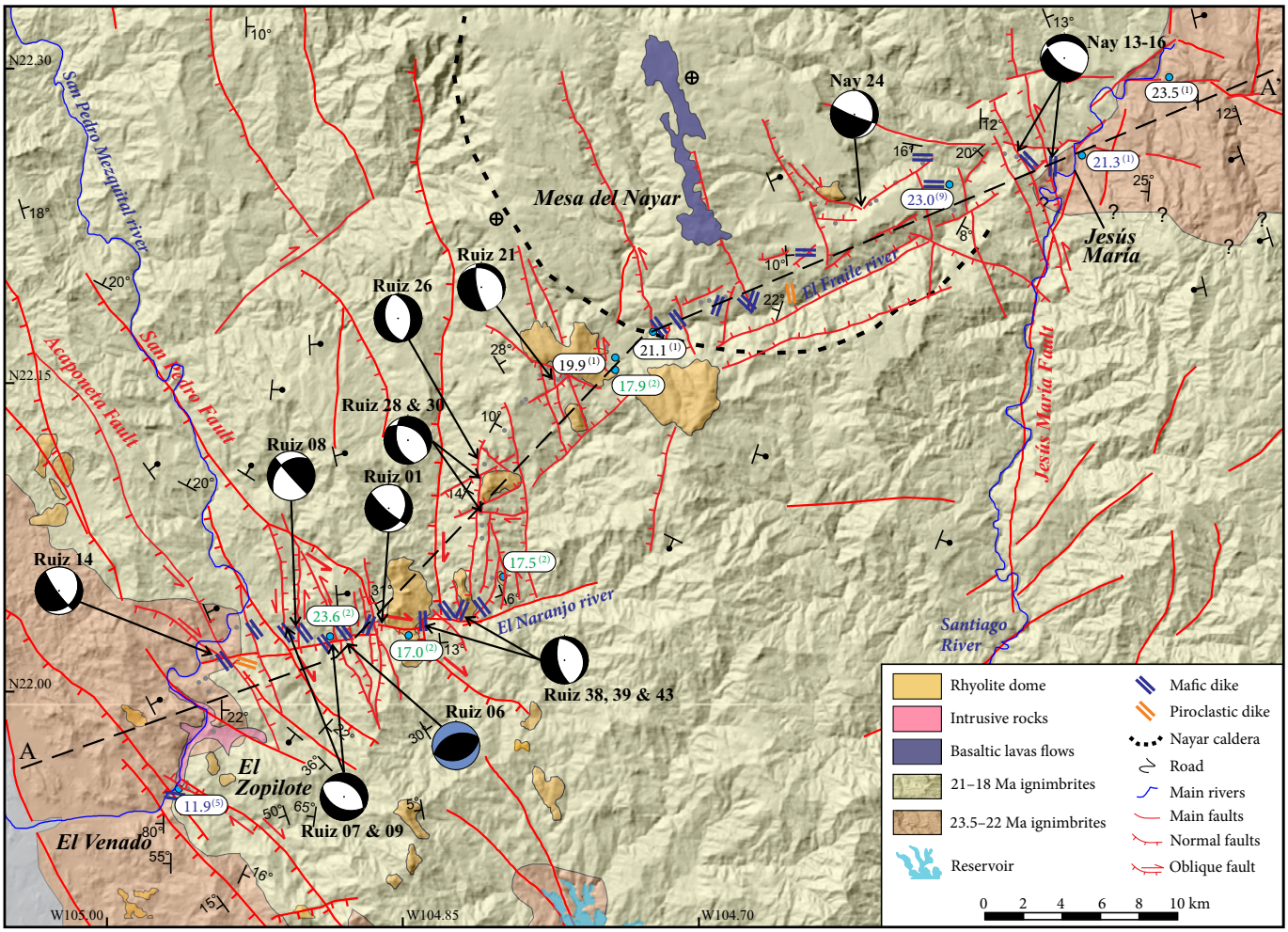

Figure 4. Geological map of the Estación Ruiz – Jesús María transect showing fault kinematics and right-dihedra solution obtained from field data. On the right-dihedra diagrams, black quadrants indicate tension and white quadrants indicate compression. The Ruiz 06 dihedra diagram (blue compressive quadrants) represents a local situation (see text for explanation). Minor faults interpreted in this work, and main fault traces from Ferrari *et al.* (2013). Dip directions from Ferrari *et al.* (2002, 2013), 1:250.000 scale geologic maps of Servicio Geológico Mexicano, Escuinapa and Tepic sheets, (SGM, 1998, 1999), and Google Earth observations. Key for ages as in Figure 2.

eastern part, intersects the Sierra de Pajaritos fault system and El Roble accommodation zone (Figures 6 and 7c-7d). The geologic units observed along this transect are similar to those described in the other two transects.

The lower part of the sequence observed along this transect is constituted by a reddish volcano-sedimentary sequence (Emvs), mainly composed of sandstones and conglomeratic sandstones with abundant clasts of andesitic volcanic rocks (Figures 3j and 7c). Interbedded within this sequence are ignimbrites (Emig) that range in thickness from 2 to >50 m, which become dominant up-section. Ignimbrites vary in composition; they are characterized by different matrix color, phenocrysts, fiammes and lithics of different compositions. Also, interbedded in the volcano-sedimentary sequence are andesitic lava flows, usually less than 5 m thick. These are fine to medium grained, usually porphyritic with hornblende and plagioclase phenocrysts. On the western side of the El Cajón reservoir, the dip of this sequence varies greatly, but does not exceed 30°; strata mainly dips west with variation from WSW to NNW. On the eastern side of the El Cajón reservoir, rocks dips mostly to the east, defining a broad anticline with a N-S striking axial plane parallel to the valley (Figures 3k and 7c). This is part of a series of left-stepping en-echelon folds developed by left-lateral transpression along the boundary between the SMO and the TMVB, which would have been active between 14.5 and 11.5 Ma (Ferrari, 1995; Ferrari *et al.*, 2002). North of the transect, at Sierra de Alica and Sierra de Pajaritos, rocks dip monotonously to the east because of N-S striking west-dipping normal faults (Figures 2, 3l and 7d).

Despite the lack of radiometric ages, in the geologic maps of the Mexican Geological Survey (SGM, 1996, 1998), the lower part of the succession in this area is interpreted as Paleocene to Oligocene in age. Middle and late Eocene ages have been reported for a rhyolite lava and an ignimbrite northwest of Santa María del Oro and southern Sierra de Pajaritos, respectively (Damon, *et al.*, 1979; Frey *et al.*, 2007), but the geologic context of these samples is unknown. We dated detrital zircons separated from the sandy matrix of the reddish volcano-sedimentary succession toward the base of the succession (sample Cajón 06, Figure 9). The dated layer include well rounded green and red clasts of porphyritic volcanic rocks and overlies a faulted sequence of red sandstones and siltstones (Emvs), in turn deposited over a basaltic lava flow (Figures 3m and 8). Twenty-seven grains yielded ages in the range between 26 and 22 Ma, with a peak at ~23.5 Ma, indicating that this sequence is correlative with that found in the lower part of the Estación Ruiz-Jesús María transect.

The upper part of the sequence is dominated by several ignimbrites that resemble the Nayar succession (Figure 7c). These are white to light yellow ash flow tuffs, with phenocrysts of plagioclase, K-feldspar, quartz and biotite in a matrix composed mainly of ash and, less commonly, pumice, which may constitute up to 30% of the rock. ^{40}Ar-^{39}Ar ages of 20.5±0.4 Ma and 20.7±0.2 Ma (Ferrari *et al.*, 2002; 2013) confirm that these ignimbrites are distal facies of the Nayar succession.

On the deepest part of the Santiago river, several subvolcanic bodies were found intruding the ignimbrites. Using U-Pb in zircon geochronology, Duque-Trujillo *et al.* (in press) dated a quartz-dioritic and a granitic subvolcanic body from the footwall of the Pochotitán fault system at 18.1±0.2 and 21.3±0.43 Ma, respectively (Figure 6).

A series of mafic dikes cuts the whole volcanic sequence in the El Cajón-Sierra de Pajaritos region. These dikes vary in width and orientation, but have similar appearance, being dark green in color, aphyric to porphyritic, with plagioclase and less often hornblende phenocrysts. Most of them are moderately altered and are surrounded by baked layers of country rock, as in the Estación Ruiz-Jesús María transect (Figure 3d). Dike intrusion mostly occurred along faults, which in some cases were also active after the intrusion, displacing some of the dikes. Damon *et al.* (1979) reported an age of 11.1 Ma for a mafic dike east of El Cajón reservoir. This age, and the fact that the mafic dikes were observed cutting all the early Miocene ignimbrites, indicate that they are coeval with those observed in the Aguamilpa dam area to the north (Figure 5) and with the regional pulse of late Miocene mafic volcanism recognized on the eastern side of the Gulf (Ferrari *et al.*, 2002; 2013).

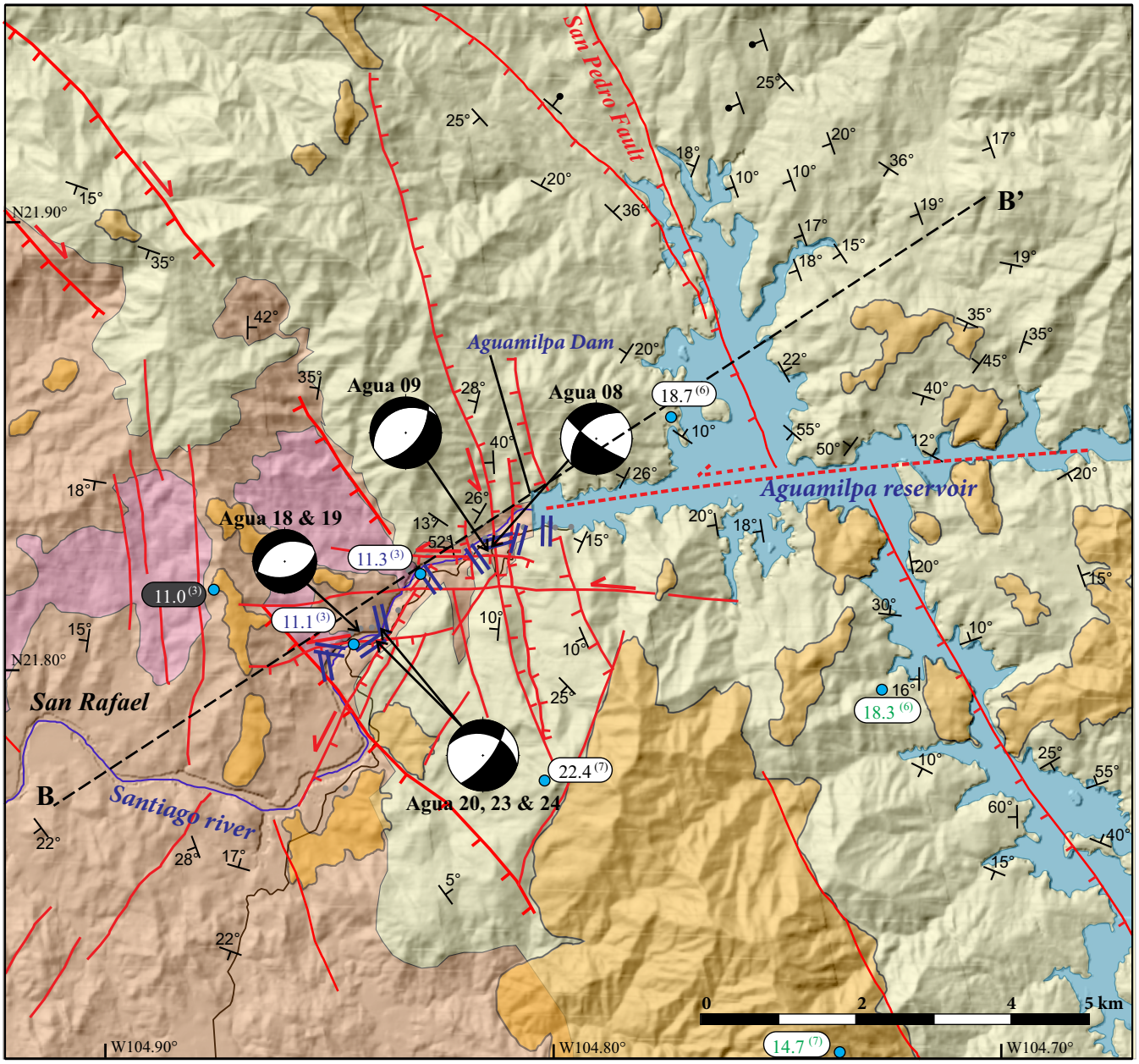

Figure 5. Geological map of the Aguamilpa Dam transect. Minor faults interpreted in this work, and main fault traces from Ferrari *et al.* (2013). On the right-dihedra diagrams, black quadrants indicate tension and white quadrants indicate compression. Dip directions from Ferrari *et al.* (2002, 2013), 1:250.000 scale geologic maps of Servicio Geológico Méxicano, Escuinapa and Tepic sheets, (SGM, 1998; 1999), and Google Earth observations. Key for ages as in Figure 2.

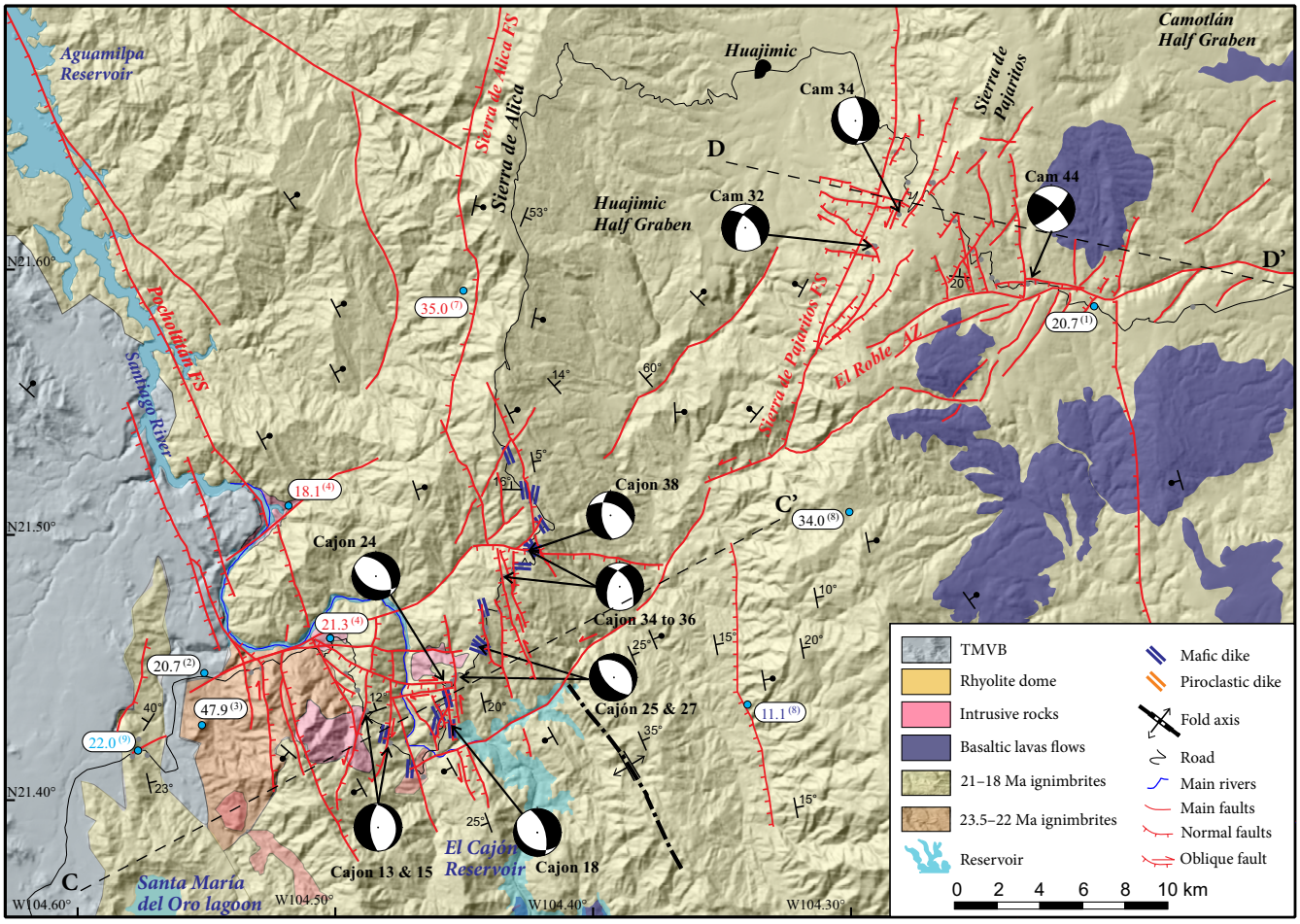

Figure 6. Geological map of the El Cajón – Sierra de Pajaritos transect. On the right-dihedra diagrams, black quadrants indicate tension and white quadrants indicate compression. Dip directions from Ferrari *et al.* (2002, 2013), 1:250.000 scale geologic maps of Servicio Geológico Méxicano, Escuinapa and Tepic sheets, (SGM, 1998; 1999), and Google Earth observations. Key for ages as in Figure 4.

FIELD MEASUREMENTS

A total of 160 faults and 144 dikes were measured along the three transects described in the previous section. Faults and fractures were identified at the outcrop scale, paying particular attention to areas where the roads cross the main fault systems. The orientation of faults and fractures were measured using a stratum compass, and fault planes were inspected for fault-slip kinematic indicators (*e.g.*, slickenlines). Each fault-slip measurement consisted of strike and dip of the fault plane and trend and plunge of the slickenlines. Faults and kinematic indicators were observed at 24 structural outcrops allowing for a dynamic analysis. We performed a paleo-stress analysis using the right-dihedra method of Angelier (1979, 1984) (Table 1; Figures 4-6, and 10) using the tectonicsFP software (Ortner *et al.* 2002). The sum of right-dihedra diagrams defines tension and compression quadrants similar to those used in the visualization of earthquake focal mechanisms. The maximum and minimum stress tensors axis, σ1 and σ3, should be located inside these quadrants (Angelier, 1994). To define the degree of fitting of the data set, right-dihedra density plot from each transect (obtained using the stereo32 software) are shown together with the fault-slip data in Figure 10. The right-dihedra method was applied only at sites where a minimum of four faults with kinematic indicators was observed. However we included three sites (Ruiz 26, Nay 24, and Cam 32) where less than four kinematic indicators were measured because at these sites a major fault plane with homogeneous kinematic indicators was present. All the measured faults and kinematic indicators are contained in the 23.5 Ma and younger volcano-sedimentary sequence, ignimbrites, and mafic dikes. A synthesis of faults, slikenlines, and mafic dikes measurements is presented in Figure 11.

Faults

We summarize the orientations of faults measured along each of the three transects and illustrate the three broad categories of observed fault orientations (Figure 11a–11c). The dominant orientation is N-S to NNW-SSE, which corresponds to the main extensional structures affecting the southern SMO (Ferrari *et al.*, 2007, 2013), and produced up to 100 km long and 20 km wide grabens and half grabens. In the study area, these faults displace the early Miocene ignimbrite succession, forming the Jesús María, Sierra de Alica, and Huajimic half grabens, with offsets up to 1.5 km (Figures 1, 7a, 7c and 7d).

The second dominant fault orientation is NW-SE and corresponds to the San Pedro-Acaponeta and Pochotitán fault systems, located on the westernmost part of the SMO, bordering the coastal plain (Figures 2 and 6). The offset along these faults systems is at least 1 km as they lower the SMO ignimbrites beneath the coastal plain (Figure 7b).

A third group of faults, almost orthogonal to the previous two groups has E-W and NE-SW orientation. These faults correspond to accommodation zones, which separate different segments of the rift

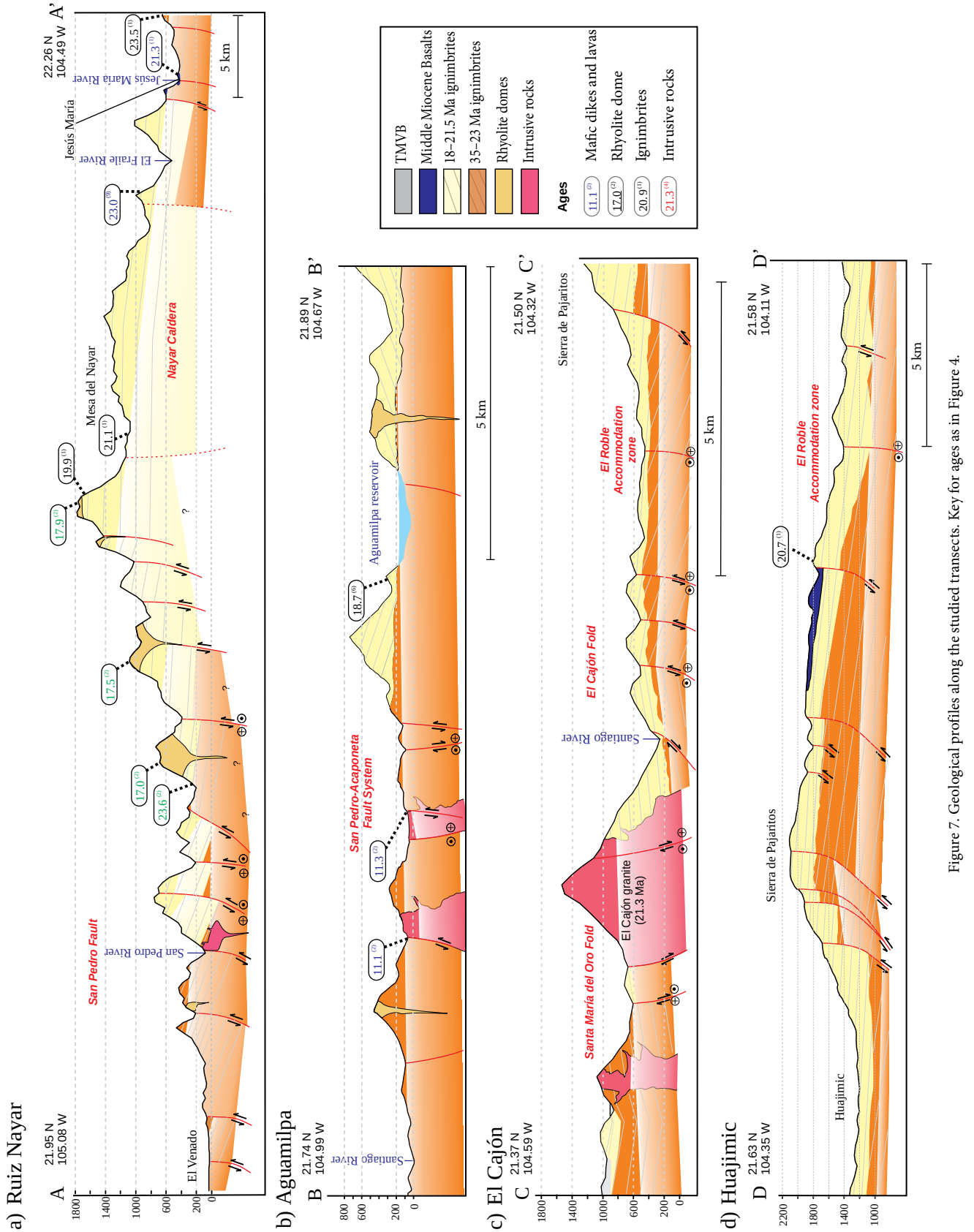

Figure 7. Geological profiles along the studied transects. Key for ages as in Figure 4.

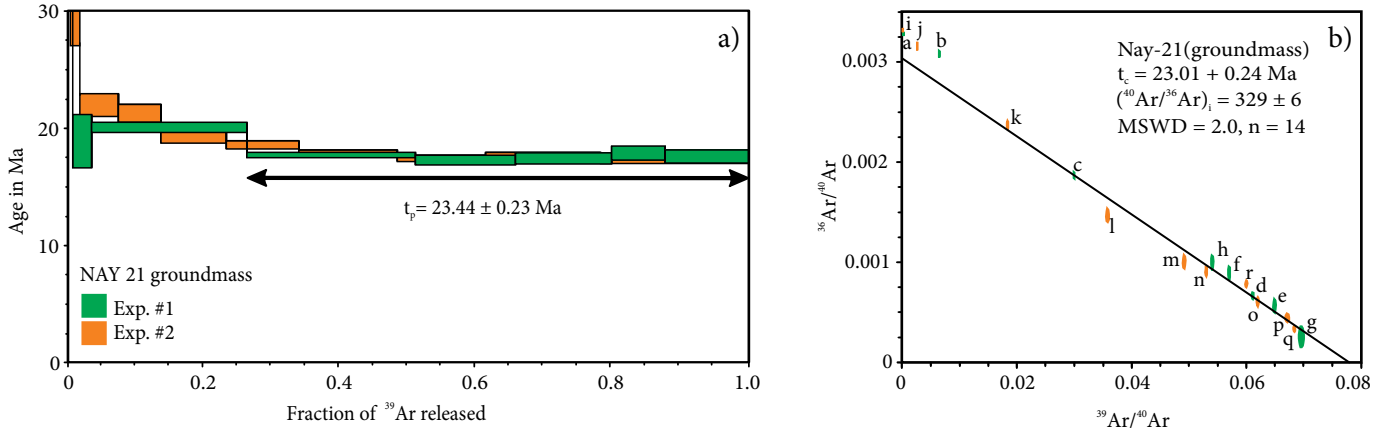

Figure 8. a) ^{40}Ar-^{39}Ar age spectra and b) ^{36}Ar-^{40}Ar versus ^{39}Ar-^{40}Ar correlation diagram for sample Nay 21 (22.24161°N; 104.57821°W). Colors in B represent the two experiments shown in (a). Analytical data are provided in Supplemental file 1.

characterized by opposite tilting direction (Ferrari *et al.*, 2002; 2013). Axen (1995) also observed that the Main Gulf Escarpment in Baja California is segmented by similar accommodation zones.

The field measurements (Figure 11a-11c) show some variation with respect to the large-scale faults and lineations (Figures 4 to 6). This difference is likely due to the presence of several second order structures seen at outcrop scale, such as Riedel shears and tension gashes, which are normally associated with the main structures.

Estación Ruiz-Mesa del Nayar transect

Along this transect, the dominant fault orientation is N-S to NNW-SSE with a dominant dip to the west (Figure 4, Figure 11a). Large blocks of the SMO ignimbrite sequence are tilted ~20° down to the east, with offsets varying from meters to hundreds of meters (Figure 7a). Most faults have normal dip-slip kinematics, but a right-lateral(?) strike-slip component can be observed near the San Pedro-Pochotitán fault system, and is not observed further east (Figure 4). One of the N-S striking faults is capped and sealed by a rhyolitic dome (site Ruiz-34) (Figures 3h and 4) dated at 18.4±0.3 Ma by U-Pb in zircon and 17.57±0.19 Ma by ^{40}Ar-^{39}Ar in biotite (Ferrari *et al.*, 2013). Assuming this single fault is representative of the population of N-S striking faults, this relation implies that the N-S faults where not active after ~18 Ma.

The San Pedro-Pochotitán fault system is present on the westernmost portion of this transect. The faults belonging to this system are characterized by a NW-SE orientation with primarily normal dip-slip kinematics, although a dextral strike-slip component was observed in many of the measured faults. Most of the faults dip to the west, tilting the ignimbrites and sediments of the SMO ~20° down to the east (Figure 7a).

NE-SW and E-W striking faults are also present in this transect. These faults control the El Fraile and El Naranjo rivers (Figure 4). From the western part of Mesa del Nayar to Jesús María, the dominant structures are NE-SW striking faults, NW dipping normal faults located on the southern side of the El Fraile river (Figure 3g), and shorter faults with variable dip on the northern side (Figure 4). The El Fraile river faults have a prominent morphological expression, and Ferrari *et al.* (2002; 2007) interpreted them as part of a caldera rim, with the area to the north of the river forming the caldera interior, filled by numerous ignimbrite sheets (Figure 4). On the western part of the transect, along El Naranjo river, we observed a series of E-W striking and south dipping faults, with a dominant right-lateral strike-slip motion (Figure 4). Some minor reverse faults (blue stereoplot in Figure 4) affecting the volcano-sedimentary and ignimbrite rocks have been interpreted as local restraining segments within the strike-slip system (sites Ruiz-05 and 06 in Figures 3a and 4). The ENE-WSW striking El Fraile fault system and the E-W striking El Naranjo fault system could represent an accommodation zone, likely related to basement discontinuities. At least in some part of the transect, these transverse structures represent a boundary between zones with opposite tilting of the volcano-sedimentary sequence (Figure 2).

Aguamilpa Dam transect

Although the Aguamilpa Dam transect runs along the northern part of the NNW striking Pochotitán fault system, several fault orientations where found. NNE-SSW striking faults are the most abundant structures observed in outcrops (Figure 11b). Most of them are minor faults, with only one major fault showing normal kinematics with a left-lateral strike-slip component of motion (Figure 5). We speculate that these faults could be Riedel structures (R') formed by the activity of the Pochotitán fault system. E-W faults were also observed with dominant normal dip-slip kinematics and a consistent left-lateral component of motion. The E-W faults are arranged in a left stepping array (Figures 2 and 4). Together with the NE-SW faults, they inter-

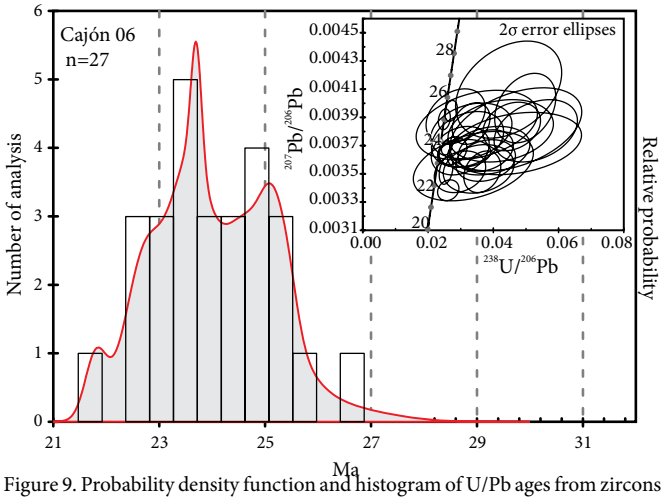

Figure 9. Probability density function and histogram of U/Pb ages from zircons from sample Cajón 06 (21.42845°N; 104.57444°W). Upper right insert shows U/Pb Concordia diagram of analyzed grains. Analytical data are provided in Supplemental file 2.

Table 1. Summary of structural sites, observed lithology and right-dihedra-based paleo-stress tensors (σ1, σ2, and σ3) orientations calculated for each site.

Site	Lat. N	Long. W	Lithology	Lithology age (Ma)	*n*	σ1		σ2		σ3	
Ruiz - Mesa del Nayar Transect						**pl**	**az**	**pl**	**az**	**pl**	**az**
Ruiz 01	22.0378°	-104.8627°	Pink ignimbrite with fiammes	Early Miocene	9	47	009	30	138	28	246
Ruiz 06	22.0326°	-104.8811°	Pink ignimbrite with fiammes	Early Miocene	9	05	340	02	250	85	136
Ruiz 07 and 09	22.0295°	-104.8869°	2 m thick ignimbrites interbedded with redish fluviovolcanic sequence	>21. 5 Ma (1)	4	84	320	06	120	02	211
	22.0344°	-104.9081°									
Ruiz 08	22.0345°	-104.9063°	2 m thick ignimbrites interbedded with redish fluviovolcanic sequence	Early Miocene	9	31	195	40	081	34	081
Ruiz 14	22.0203°	-104.9466°	Andesitic subvolcanic intrusive	Early Miocene	6	46	025	28	148	31	257
Ruiz 21	22.1512°	-104.7755°	White ignimbrite (El Nayar) over fluviovolcanic redish sequence	Early Miocene (18 to 20 Ma)	10	57	099	16	343	28	245
Ruiz 26	22.1174°	-104.8097°	White ignimbrite (El Nayar sequence)	Early Miocene (18 to 20 Ma)	3	86	344	04	169	00	079
Ruiz 28 and 30	22.1037°	-104.8119°	White and pink ignimbrites (El Nayar sequence)	Early Miocene (18 to 20 Ma)	5	68	135	22	325	03	234
	22.0878°	-104.8120°									
Ruiz 38, 39 and 40	22.0399°	-104.8214°	White and pink ignimbrites (El Nayar sequence)	Early Miocene (18 to 20 Ma)	9	69	086	04	346	20	255
	22.0411°	-104.8246°									
Nay 13 to 16	22.2515°	-104.5263°	Brown and pink ignimbrite succession	Oligocene?	6	63	071	18	301	19	204
	22.2534°	-104.5441°									
Nay 24	22.2316°	-104.6174°	Light yellow and pink ignimbrites	Miocene	2	47	359	22	114	35	221
Aguamilpa Transect											
Agua 08	21.8314°	-104.8082°	Light pink ignimbrite	Early Miocene	8	35	077	49	294	19	180
Agua 09	21.8331°	-104.8120°	Light pink ignimbrite	Early Miocene	9	72	276	12	046	13	139
Agua 18 and 19	21.8249°	-104.8439°	Gray lithic ignimbrite	Early Miocene	4	87	104	03	267	01	357
	21.8132°	-104.8412°									
Agua 20, 23 and 24	21.8135°	-104.8396°	Gray lithic ignimbrite	Early Miocene	5	48	268	35	50	20	155
	21.8106°	-104.8404°									
El Cajón-Sierra de Pajaritos Transect											
Cajón 13 and 15	21.4381°	-104.4876°	Fluvio-volcanic sequence with interbedded ignimbrites	Early Miocene	6	70	105	06	358	19	266
	21.4264°	-104.4783°									
Cajón 18	21.4326°	-104.4545°	Well indurated lithic ignimbrite	Early Miocene	9	65	286	17	153	17	058
Cajón 24	21.4487°	-104.4543°	Fluvio-volcanic sequence	Early Miocene	15	74	310	16	131	00	041
Cajón 25 and 27	21.4496°	-104.4530°	Pink ignimbrites over basaltic andesite lava flow	Early Miocene	9	79	64	3	317	11	227
	21.4606°	-104.4436°									
Cajón 34 to 36	21.4865°	-104.4343°	White crystal rich ignimbrite	Early Miocene	7	56	182	34	358	03	088
	21.4889°	-104.4304°									
Cajón 38	21.4960°	-104.4246°	White crystal rich ignimbrite	Early Miocene	4	54	139	36	329	05	238
Cam 32	21.6061°	-104.2899°	White to pale yellow ignimbrite	Early Miocene	1	50	168	40	350	01	259
Cam 34	21.6175°	-104.2807°	White to pale yellow ignimbrite	Early Miocene	9	65	307	18	172	16	076
Cam 44	21.5924°	-104.2306°	Pink well indurated ignimbrite	Early Miocene	4	01	179	66	086	24	270

Note: N: Number of faults used for paloe-stress calculations; pl: plunge; az:azimuth. (1) Ferrari *et al.* (2013).

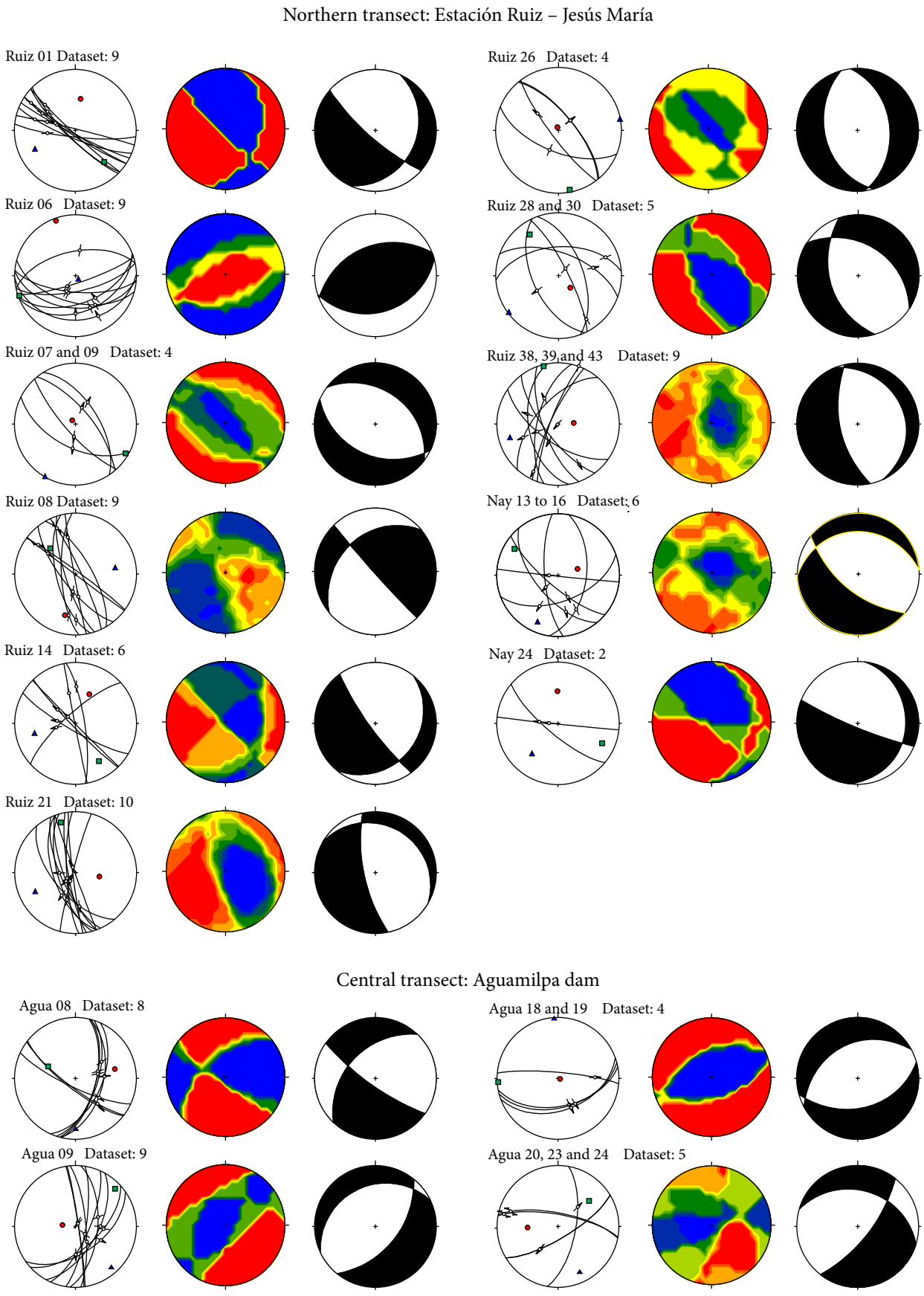

Figure 10. Fault planes with fault-slip data, dihedral density plot and resultant right-dihedra calculations for each structural site shown in Figures 4 to 6.

rupt the continuity of the Pochotitán fault system, which to the south consists of a series NNW-SSE striking west dipping normal faults. To the north, the northern termination of the Pochotitán fault system is slightly rotated counterclockwise and display a minor right-lateral strike-slip component of motion. As a whole, these structures define a complex accommodation zone along which the Santiago river found its way to the coast. The N-S faults observed on this transect are minor normal faults, mostly dipping east, and some of them show a small left-lateral component (Figure 5).

El Cajón Dam-Sierra de Pajaritos transect

Along the El Cajón-Sierra de Pajaritos transect, the dominant faults strike from NNW to NNE (Figure 11c). These faults are primarily normal, with occasionally right lateral strike-slip component (Figure 6). This group of faults is parallel to the main ~N-S structure forming the Huajimic and Camotlán half grabens (Figures 3l, 6 and 7d). The westernmost part of the transect is dominated by the NNW-SSE striking Pochotitán fault system, which tilt early Miocene ignimbrites down to the SWS (Figure 7c). These early Miocene ignimbrites are covered by younger mafic lavas (11 to 10 Ma) of the TMVB (Ferrari *et al.*, 2000b; 2002).

In the eastern part of the transect (Figure 7d), the Sierra de Pajaritos is bounded by two main fault systems: the N-S to NNE-SSW west-dipping faults which form the eastern edge of the Huajimic half graben and the E-W to ENE-WSW faults of El Roble accommodation zone (Figure 6, Figure 11c). These two fault patterns was also observed at outcrop scale. The kinematics of these faults were difficult to establish due to the lack of kinematic indicators. Nevertheless, at site Cam 44 (Figure 6) kinematic indicators corroborate the left lateral strike-slip motion of these faults (Table 1).

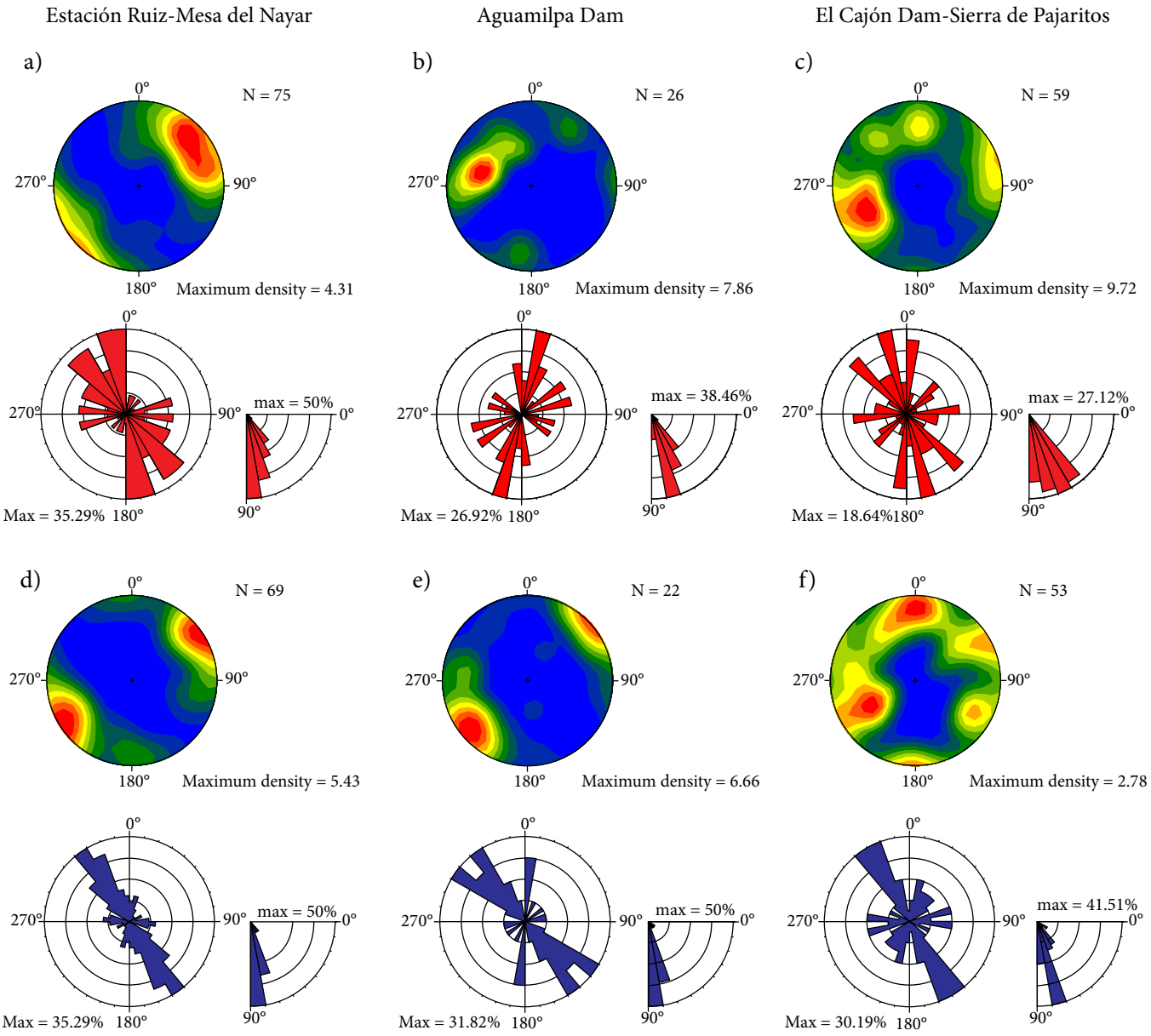

Figure 11. Pole density plot and rose diagram for faults (panels a-c) and dikes (panels d-f) measured in the study area. Diagrams are equal angle projection, lower hemisphere. Rose diagram interval: 20°, dip angle interval: 10°, maximum values represent the percentage of the data grouped in the maximum value.

Mafic dikes

Along the three transects we observed a large number of mafic dikes. The most common dike orientation is NNW-SSE to NW-SE, although other orientations were found locally (Figure 11d-11f). Dike orientation is important to estimate the least principal stress at the time of intrusion, which tends to be normal to the strike of a subvertical dike (Pollard, 1987). We recognized three groups of dike orientations: NNW to NW striking, E-W striking and N-S to NNE-SSW striking.

Dikes striking NW to NNW are by far the most common (Figure 11d–11f). These are mostly located along the western part of the northern and southern transects (Estación Ruiz-Jesús María and El Cajón Dam–Sierra de Pajaritos transects) (Figure 4 and 6). They are also common in the Aguamilpa dam transect (Figure 5). Most of these mafic dikes have subvertical dip (between 80 and 90°) and usually intrude along previously existing normal faults, which commonly remain inactive after intrusion. Only some of the faults show evidence of reactivation, such as fault gouges and striated dike walls (Figure 3d), and at least in one case a dike was observed to be cut by the same fault it intruded (Figure 3e). Several of these dikes have been dated between 11.5 and 11 Ma (Damon *et al.*, 1979; Clark *et al.*, 1981; Soto and Ortega, 1982; Frey *et al.*, 2007).

A second group of dikes, striking E-W and dipping 70-90° (dipping both N and S) was found in the eastern part of the Estación Ruiz-Jesús María transect and, to a lesser extent, in the El Cajón dam-Sierra de Pajaritos transect (Figure 9d and 9f). They cut the lower ignimbrite and volcano-sedimentary sequence and do not seem to have intruded along pre-existing faults. At site Nay 13 an E-W striking dike was observed cutting the ignimbrite sequence and feeding into an overlying basaltic lava flow (Figure 3c).

Some scattered dikes, striking NNE-SSW and NE-SW were also found locally in the Aguamilpa Dam and the El Cajón-Sierra de Pajaritos transects (Figure 11e and 11f). Usually, these dikes are associated with faults observed in these two areas (Figure 11b and 11c).

DISCUSSION

The meso-scale faults observed along the studied transects can be grouped into three sets, and can be associated to the two extensional phases that have occurred since the late Oligocene, defined in Ferrari *et al.* (2013). The dominant fault orientation is ~N-S striking, with subordinate NNW-SSE to NW-SE and ~E-W to NE-SW orientations (Figure 11a–11c).

The N-S fault set corresponds to the major N-S striking structures located in the eastern part of the study areas: the Jesús María, Sierra de Alíca, Sierra de Pajaritos, and Puente de Camotlán half-grabens. The kinematic analysis of these N-S striking faults indicates that they have a dominantly normal motion with a minor strike-slip component. We illustrate the relationship between fault plane dip and the striae plunge contained on each fault plane (Figure 10), which determine the kinematics of the faults (Figure 12). The data from the eastern and western part of the northern and southern transects were plotted separately. Faults measured in the eastern part of these transects (Mesa del Nayar and Sierra de Pajaritos areas) are dominated by pure normal motion and, to a lesser extent, by almost pure strike-slip motion, with very rare oblique slip faults (Figures 12b and 11e). Field relations of dated units show that the activity of the N-S striking faults began during the emplacement of the ~23.5 Ma Las Canoas ignimbrite succession and was complete by ~18 Ma (Ferrari *et al.*, 2013). The direction of the minimum principal stress (σ3) calculated for the ~N-S structures indicate that this deformation phase was characterized by E-W to ENE-WSW crustal stretching (Figure 13).

The second set of faults, characterized by NNW to NW orientations is mostly found in the western part of the transects (Figure 11a-11c) and correspond to the San Pedro-Acaponeta and Pochotitán fault systems. These fault systems defines the western limit of the SMO (Figure 2) and tilt the ignimbrite sequence as much as 35° down to the E-NE. We consider that the activity of these NNW to NW faults began at *ca.* 21

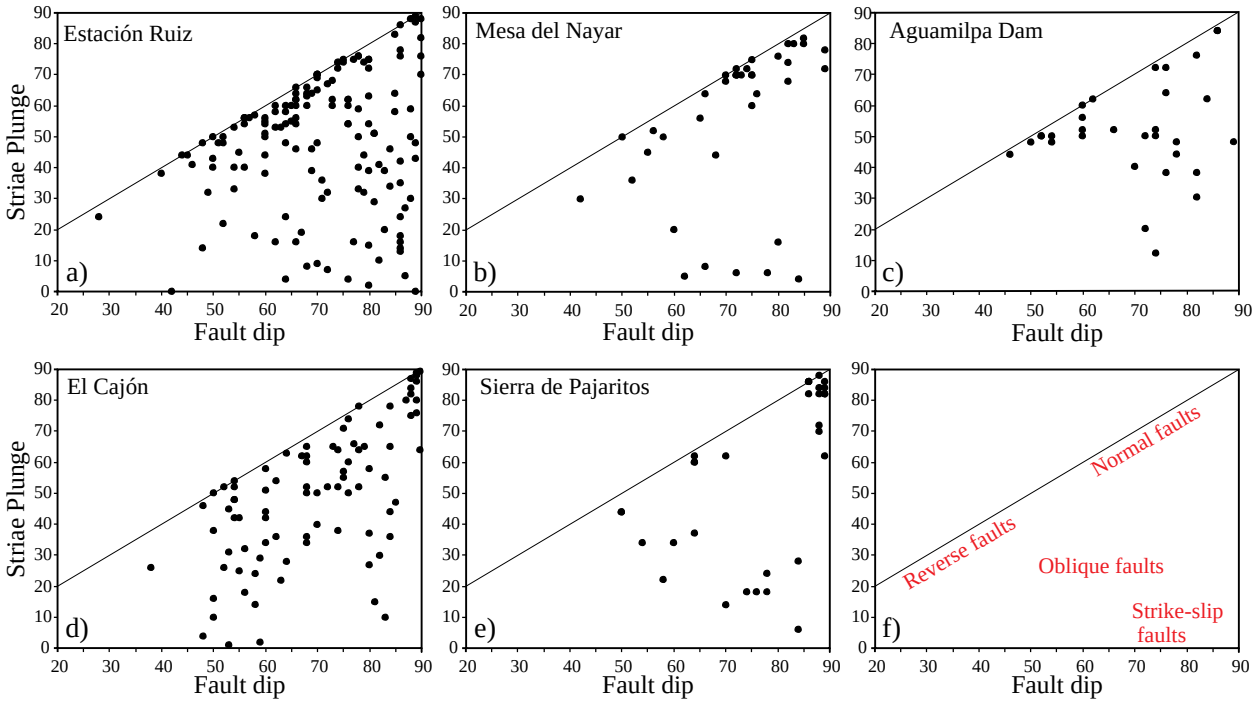

Figure 12. Fault classification diagram based on the fault dip *vs.* striae plunge values, for different zones of the study transects. a) and b), data from Estación Ruiz-Jesús María transect; c), data from Aguamilpa Dam transect; d) and e), from El Cajón-Sierra de Pajaritos transect; f), classification of fault kinematics.

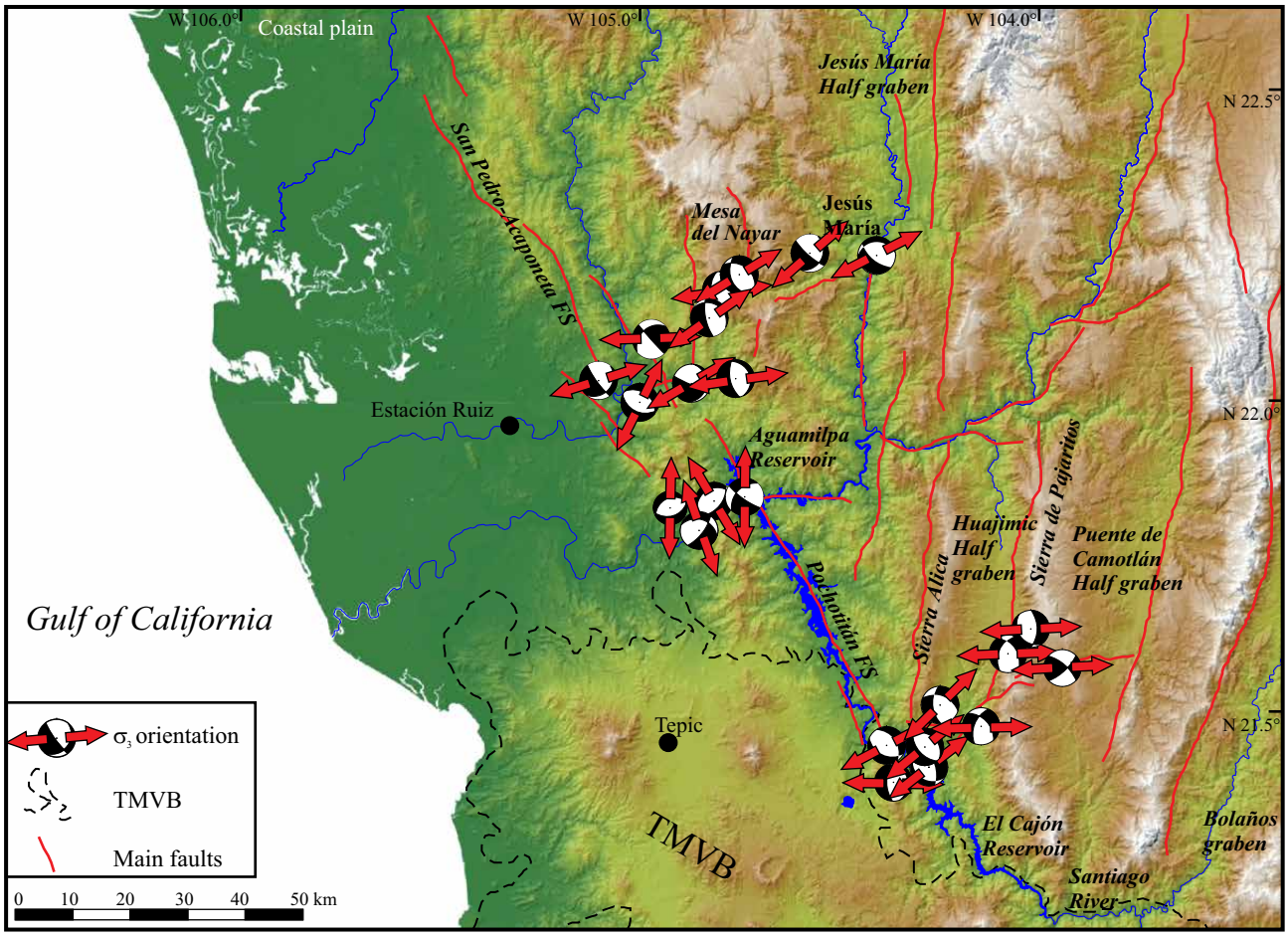

Figure 13. Regional map showing the calculated σ3 orientation at each structural site for which a right-dihedra was calculated.

Ma because they cut the El Nayar ignimbrite sequence and expose some shallow intrusive bodies with ages between *ca.* 20 and 17 Ma (Ferrari *et al.*, 2002; Duque-Trujillo, *et al.*, in press). The minimum age estimate for the activity of these faults is constrained by a series of flat-lying basaltic lavas as old as 10.5 Ma that are found covering the tilted ignimbrites along the coastal plain (Ferrari *et al.*, 2013, and references therein). Several of these faults have a pure normal displacement (Figures 12a, 11c and 11d), with an ENE-WSW orientation of the minimum principal stress (σ3), indicating a slight counterclockwise rotation from the E-W stretching direction determined on the N-S striking faults mapped in the eastern part of the study area (Figure 13). Several faults measured along the San Pedro-Acaponeta and Pochotitán fault system are oblique-slip with a right-lateral strike-slip component (Figure 12a, 12c and 12d). The majority of these faults are found in proximity of accommodation zones (El Naranjo, Aguamilpa, and El Roble; Figures 4, 5, 6) and can be associated to block rotation and/or interaction with transverse structures of these shear zones. Alternatively, if these systems were active at the same time of the ~N-S fault systems, the E-W extension that characterize the early Miocene regime may have induced a right-lateral oblique motion on these NNW striking planes.

The younger group of mafic dikes emplaced along the western SMO, support the dominant extensional kinematics deduced for the San Pedro-Acaponeta and Pochotitán fault systems. These dikes are NNW to NW striking (Figure 11d-11f). Assuming that they were emplaced orthogonal to the former σ3 (Delaney, *et al.*, 1986), they indicate an ENE or NE trending minimum principal stress (σ3) at the time of emplacement. As mentioned before, these dikes were emplaced between 11.5 and 11 Ma, at the end of the period of activity of the San Pedro-Acaponeta and Pochotitán fault systems. Due to the preferred orientation of the San Pedro-Acaponeta and Pochotitán fault systems (NNW to NW), a ENE to NE oriented minimum principal stress would had been expressed with normal kinematic faults along them, instead of right-lateral. This implies that these fault systems had a minimum oblique, right-lateral motion until ca. 11 Ma. This also suggests that if right-lateral transtension began within the Gulf area prior to ~11 Ma (*e.g.*, Fletcher *et al.*, 2007; Sutherland *et al.*, 2012), the southeastern margin of the Gulf was not significantly affected. Such hypothesized dextral transtensional deformation must have occurred further west of our study area, and possibly preserved beneath that coastal plain or the offshore rifted continental shelf. At a regional scale, an initial ~E-W extension was accommodated along N-S striking faults, which then turned into a more ENE extension, accommodated along NNW faults which only affected the westernmost flank of the SMO. Ferrari *et al.* (2013) and Bryan *et al.* (2014) proposed that this tectonic change could have taken place between 21 and 18 Ma, which is now confirmed by the counterclockwise rotation of the minimum principal stress (σ3) determined in this work.

The third set of faults observed strikes E-W, ENE-WSW or NE-SW and have a transverse orientation with respect to the other two sets (Figure 2). Although this kind of structures has already been reported for the southern SMO (Henry and Aranda-Gómez, 2000; Ferrari, *et al.* 2002), they are uncommon. The ~23.01 Ma age for a ~E-W striking

dike found in the Mesa del Nayar-Jesús María area suggest that these faults may be the oldest structures in the study area. However, in other cases these faults appear contemporaneous with the other two sets, which suggest that they represent transfer or accommodation zones, which separate different domains of extension along the western SMO. Transfer zones are mostly formed along a sharp contrast in amount or style of deformation between rift domains (Faulds and Varga, 1998). Nevertheless, the location of these zones could be controlled by the presence of ancient shear zones, as observed in other rifts (*e.g.*, East African Rift and Gulf of Suez, Rosendahl, 1987; Moustafa, 1996). In the study area, the location of these ~E-W to NE-SW structures may be related to pre-existing basement structures, which could have been reactivated during the progressive E-W to WSW-ENE extension that accompanied the initial rifting of the Gulf of California. Indeed, several E-W to NE-SW striking structures affecting the Cretaceous to Paleogene basement have been reported in the SMO (Henry, 1986; Horner and Enriquez, 1999; Horner and Steyrer, 2005). These structures include folds, thrust faults, foliations, tension gashes, shear fractures, and fault zones, which constitute structural weaknesses prone to be reactivated as rift-related accommodation zones (Henry and Aranda-Gómez, 2000; Ferrari, *et al.* 2002). Although some of the ~E-W structures mark a reversal in the tilting direction of the ignimbrites (*e.g.*, El Roble accommodation zone), this is not a rule in the study area (*e.g.*, Aguamilpa and El Naranjo), where some transverse fault zones seem to locally relay the deformation rather than represent a change in the structural style, as defined by Axen (1995) in Baja California. In particular, the El Naranjo (Figure 5) and Aguamilpa (Figure 6) accommodation zones serve as the structural connection across a broad, ~10 km-wide left step between the Pochotitán and San Pedro-Acaponeta fault systems, while block tilting is everywhere down to the E and ENE. In the case of the El Roble fault zone (Figure 6), it separates the extensional structures associated to the Gulf of California with a complex transpressional zone associated with the interaction between the Jalisco block and the southernmost end of the SMO (Ferrari, 1995; Ferrari *et al.*, 2002).

CONCLUDING REMARKS

We have presented the first detailed structural study of the fault systems that affect the southwestern part of the SMO in northern Nayarit, which constrains the kinematics of the initial rifting of the southeastern margin of the Gulf of California rift. Three main families of faults were identified: 1) A group of ~N-S striking faults, associated to the province bounding structure along the western edge of the SMO, with activity bracketed between 24 and 18 Ma; 2) a family of NNW-SSE to NW-SE striking faults associated to the San Pedro-Acaponeta and Pochotitán fault systems in the western part of the SMO, whose activity is constrained between ~21 and 11 Ma; 3) an E-W to ENE-WSW striking group of faults, which seems to be associated to pre-existing basement structures reactivated as accommodation zones during early and middle Miocene rifting phases.

The kinematic analysis and right-dihedra calculation based on the collected fault dataset, the orientation of extension-related dikes, in addition to the age of rocks affected and unaffected by faults allow us to infer that the minimum principal stress ($\sigma 3$) was oriented ~E-W during the early Miocene (24–18 Ma) phase and subsequently rotated slightly counterclockwise to ENE-WSW during the middle Miocene (18–11 Ma) phase. Deformation kinematics indicates a dominant normal faulting and, to a lesser extent, oblique faulting regime along the southeastern SMO. Fault obliquity can be associated to fault interaction in proximity to accommodation zones as observed near the El Roble accommodation zone in Sierra de Pajaritos. Also, some transtensional motion along NNW striking faults during the early Miocene ~E-W extension cannot be excluded. Our data do not support the hypothesis that significant right-lateral transtensional motion was accommodated in the early to middle Miocene (24–11 Ma) in the southeastern margin of the Gulf of California. Rather, these data support the hypothesis that the onset of dextral transtension in the Gulf of California was delayed until the onset of regional dextral oblique motion between the Pacific and North American plates at *ca.* 12.5 Ma (*e.g.*, Stock and Hodges, 1989; Bennett and Oskin, 2014).

ACKNOWLEDGMENTS

The present work was supported by grant CONACYT 82378 (to Ferrari), CONACYT also supported Duque-Trujillo PhD scholarship. We thank I. Loza Aguirre, P. Botero Santa, G. Antillón Mata, M. Michell for discussion and field assistance. C. Ortega, M.A. García are thanked for assistance in U-Pb and Ar-Ar dating, respectively. A.S. Rosas Montoya, V.M. Pérez Arroyo, G. Rendón and L. Gradilla helped with Ar-Ar sample preparation. Reviews by Scott Bennett, an anonymous reviewer and associated editor Angel Nieto Samaniego greatly helped to improve the quality of the manuscript. T. Orozco-Esquivel is thanked for thoroughly reviewing the final version of the paper.

APPENDIX A. SUPPLEMENTARY MATERIAL

Supplementary files 1 and 2 can be found at the journal web site <http://rmcg.unam.mx/>, in the table of contents of this issue.

REFERENCES

Angelier, J., 1979, Determination of the mean principal directions of stresses for a given fault population: Tectonophysics, 56(3), T17-T26.

Angelier, J., 1984, Tectonic analysis of fault slip data sets: Journal of Geophysical Research, Solid Earth, 89(B7), 5835-5848.

Angelier, J., 1994, Fault slip analysis and palaeostress reconstruction, *in* Hancock, L. (ed.), Continental deformation: Oxford, UK, Pergamon Press, 53-100.

Atwater, T., Stock, J., 1998, Pacific-North America plate tectonics of the Neogene southwestern United States: An update: International Geology Review, 40, 375-402.

Axen, G., 1995, Extensional segmentation of the Main Gulf Escarpment, Mexico and United States: Geology, 23, 515-518, doi:10.1130/0091-7613(1995)023<0515:ESOTMG>2.3.CO;2.

Bennett, S.E., Oskin, M.E., 2014, Oblique rifting ruptures continents: Example from the Gulf of California shear zone: Geology, 42(3), 215-218.

Bennett, S.E.K., Oskin, M.E., Iriondo, A., 2013, Transtensional rifting in the proto-Gulf of California near Bahia Kino, Sonora, Mexico: Geological Society of America Bulletin, 125(11-12), 1752-1782. doi:10.1130/B30676.1

Bonner, J.L., Herrin, E.T., 1999, Surface wave studies of the Sierra Madre Occidental of northern Mexico: Bulletin of the Seismological Society of America, 89(5), 1323-1337.

Bryan, S.E., Ferrari L., 2013, Large igneous provinces and silicic large igneous provinces: Progress in our understanding over the last 25 years: Geological Society of America Bulletin, 125(7/8), 1053-1078, doi: 10.1130/B30820.1.

Bryan, S.E., Ferrari, L., Reiners, P.W., Allen, C.M., Petrone, C.M., Ramos-Rosique, A., Campbell, I.H., 2008, New insights into crustal contributions to large volume rhyolite generation at the mid-Tertiary Sierra Madre Occidental Province, Mexico, revealed by U/Pb geochronology: Journal of Petrology, 49(1), 47-77.

Bryan, S.E., Orozco-Esquivel, T., Ferrari, L., López-Martínez, M., 2014, Pulling apart the Mid to Late Cenozoic magmatic record of the Gulf of California: Is there a Comondú arc?, *in* Gómez-Tuena, A., Straub, S.M., Zellmer,

G.F. (eds.), Orogenic Andesites and Crustal Growth: Geological Society, London, Special Publication 385, 389-407, doi:10.1144/SP385.8

Clark, K.F., Damon, P. E., Shafiquillah, M., Ponce, B.F. Cárdenas, D., 1981, Sección geológica-estructural a través de la parte sur de la Sierra Madre Occidental, entre Fresnillo y la costa de Nayarit: Asociación de Ingenieros Mineros, Metalúrgicos y Geólogos de México, Memoria Técnica XIV, 69-99.

Couch, R.W., Ness, G.E., Sanchez-Zamora, O., Calderón-Riveroll, G., Doguin, P., Plawman, T., Coperude, S., Huehn, B., Gumma, W., 1991, Gravity anomalies and crustal structure of the Gulf and Peninsular Province of the Californias, *in* Dauphin, J.P., Simoneit, B.R.T. (eds), The Gulf and the Peninsular Province of the Californias: American Association of Petroleum Geologists, Memoir 47, 25-45.

Damon, P.E., Nieto-Obregón, J., Delgado-Argote, L., 1979, Un plegamiento neogénico en Nayarit y Jalisco y evolución geomórfica del Río Grande de Santiago: Asociación de Ingenieros Mineros, Metalúrgicos y Geólogos de México, Memoria Técnica, XIII, 156-191.

Delaney, P., Pollard, D., Ziony, J., McKee, E., 1986, Field relations between dikes and joints: Emplacement processes and paleostress analysis: Journal of Geophysical Research, 9., 4920-4938.

Drake, W.R, 2005, Structural analysis, stratigraphy, and geochronology of the San José Island accommodation zone, Baja California Sur, Mexico: Northern Arizona University, M. Sc. Thesis, 271 pp.

Duque-Trujillo, J., Ferrari, L., Orozco-Esquivel, T., López-Martinez, M., Lonsdale, P., Bryan, S., Kluesner, J., Piñero-Lajas, D., Solari, L., in press, Timing of rifting in the Southern Gulf of California and its conjugate margins: insights from the plutonic record: Geological Society of America Bulletin.

Faulds, J.E., Varga, R.J.,1998, The role of accommodation zones and transfer zones in the regional segmentation of extended terranes: Geological Society of America, Special Paper 323, 1-45.

Ferrari, L., 1995, Miocene shearing along the northern boundary of the Jalisco block and the opening of the southern Gulf of California: Geology, 23, 751–754, doi:10.1130/0091-7613(1995)023<0751:MSATNB>2.3.CO;2.

Ferrari, L., Pasquaré, G., Venegas-Salgado, S., Romero-Rios, F., 2000a, Geology of the western Mexican Volcanic Belt and adjacent Sierra Madre Occidental and Jalisco block: Geological Society of America Special Paper, 334, 65-84.

Ferrari, L., Conticelli, S., Vaggelli, G., Petrone, C., Manetti, P., 2000b, Late Miocene mafic volcanism and intraarc tectonics during the early development of the Trans-Mexican Volcanic Belt: Tectonophysics, 318, 161-185.

Ferrari, L., López-Martínez, M., Rosas-Elguera, J., 2002, Ignimbrite flare-up and deformation in the southern Sierra Madre Occidental, western Mexico-implications for the late subduction history of the Farallón Plate: Tectonics, 21(4), doi: 10.1029/2001TC001302.

Ferrari, L., Valencia-Moreno, M., Bryan, S.E, 2007, Magmatism and tectonics of the Sierra Madre Occidental and its relation with the evolution of the western margin of North America, *in* Alaniz-Álvarez, S.A., Nieto-Samaniego, A.F. (eds.), Geology of México: Celebrating the Centenary of the Geological Society of México: Geological Society of America, Special Paper 422, 1-39, doi: 10.1130/2007.2422(01).

Ferrari, L., López-Martínez, M., Orozco-Esquivel, T., Bryan, S.E, Duque-Trujillo, J., Lonsdale, P.F., 2013, Late Oligocene to middle Miocene rifting and syn-extensional magmatism in the southwestern Sierra Madre Occidental, Mexico: the beginning of the Gulf of California rift: Geosphere, 9(5), 1-40.

Fletcher, J.M., Grove, M., Kimbrough, D., Lovera, O., Gehrels, G.E., 2007, Ridge-trench interactions and the Neogene tectonic evolution of the Magdalena Shelf and southern Gulf of California; insights from detrital zircon U/Pb ages from the Magdalena Fan and adjacent areas: Geological Society of America Bulletin, 119(11-12), 1313-1336, doi: 10.1130/ B26067.1.

Frey, H.M., Lange, R.A., Hall, C.M., Delgado Granados, H., Carmichael, I.S.E., 2007, A Pliocene ignimbrite flare-up along the Tepic-Zacoalco rift: Evidence for the initial stages of rifting between the Jalisco block (Mexico) and North America: Geological Society of America Bulletin, 119, 49-64, doi:10.1130/B25950.1.

Gans, P.B., 1997, Large magnitude Oligo-Miocene extension in southern Sonora: Implications for the tectonic evolution of northwest Mexico: Tectonics, 16(3), 388-408.

González-León, C.M., McIntosh, W.C., Lozano-Santacruz, R., Valencia-Moreno, M., Amaya-Martínez, R., Rodríguez-Castañeda, J.L., 2000, Cretaceous and Tertiary sedimentary, magmatic, and tectonic evolution of north-central Sonora (Arizpe and Bacanuchi Quadrangles), northwest Mexico: Geological Society of America Bulletin, 112, 600-610.

Henry, C.D., 1986, East-Northeast-trending structures in western Mexico: evidence for oblique convergence in the late Mesozoic: Geology, 14, 314-317.

Henry, C.D., Aranda-Gómez, J.J., 2000, Plate interactions control middle-late Miocene, proto-Gulf and Basin and Range extension in the southern Basin and Range: Tectonophysics, 318(1), 1-26.

Horner, J. T., Enriquez, E., 1999, Epithermal precious metal mineralization in a strike-slip corridor; the San Dimas District, Durango, Mexico: Economic Geology, 94(8), 1375-1380.

Horner, J.T., Steyrer, H.P., 2005, An analogue model of a crustal-scale fracture zone in West-Central Mexico: Evidence for a possible control of ore forming processes. Neues Jahrbuch fur Geologie und Palaontologie-Abhandlungen, 236(3), 185-206.

Karig, D. E., Jensky, W., 1972, The proto-Gulf of California: Earth and Planetary Science Letters, 17(1), 169-174.

Lizarralde, D., Axen, G.J., Brown, H.E., Fletcher, J.M., González-Fernández, A., Harding, A.J., Holbrook, W.S., Kent, G.M., Paramo, P., Sutherland, F., Umhoefer, P.J., 2007, Variable styles of rifting in the Gulf of California: Nature, 448, 466-469, doi:10.1038/nature06035.

McDowell, F.W., Keizer, R.P., 1977, Timing of mid-Tertiary volcanism in the Sierra Madre Occidental between Durango City and Mazatlán, Mexico: Geological Society of America Bulletin, 88(10), 1479–1487.

McDowell, F.W., Clabaugh, S.E., 1979, Ignimbrites of the Sierra Madre Occidental and their relation to the tectonic history of western Mexico: Geological Society of America, Special Paper 180, 113-124.

McDowell, F.W., McIntosh, W.C., 2012, Timing of intense magmatic episodes in the northern and central Sierra Madre Occidental, western Mexico: Geosphere, 8, 1505–1526, doi:10.1130/GES00792.1.

McDowell, F.W, Roldán-Quintana, J., Amaya-Martínez, R., 1997, Interrelationship of sedimentary and volcanic deposits associated with Tertiary extension in Sonora, Mexico: Geological Society of America Bulletin, 109(10), 1349-1360.

Moustafa, A. R., 1996, Internal structure and deformation of an accommodation zone in the northern part of the Suez rift: Journal of Structural Geology, 18, 93-108.

Murray, B.P., Busby, C.J., Ferrari, L., Solari, L.A., 2013, Synvolcanic crustal extension during the mid-Cenozoic ignimbrite flare-up in the northern Sierra Madre Occidental, Mexico: Evidence from the Guazapares Mining District region, western Chihuahua: Geosphere, 9, doi:10.1130/GES00862.1.

Nieto-Obregón, J., Delgado-Argote, L., Damon, P.E., 1981, Relaciones petrológicas y geocronológicas del magmatismo de la Sierra Madre Occidental y el Eje Neovolcánico en Nayarit, Jalisco y Zacatecas: Asociación de Ingenieros Mineros, Metalúrgicos y Geólogos de México, Memoria Técnica XIV, 327-361.

Nourse, J., Anderson, T., Silver, L., 1994, Tertiary metamorphic core complexes in Sonora, Northwestern Mexico: Tectonics, 13(5), 1161-1182.

Ortner, H., Reiter, F., Acs, P., 2002, Easy handling of tectonic data: the programs TectonicVB for Mac and TectonicsFP for Windows™: Computers & Geosciences, 28(10), 1193-1200.

Persaud, P., Pérez-Campos, X., Clayton, R.W., 2007, Crustal thickness variations in the margins of the Gulf of California from receiver functions: Geophysical Journal International, 170(2), 687-699.

Pollard, D.D., 1987, Elementary fracture mechanics applied to the structural interpretation of dykes, *in* Halls H.C., Fahrig W.F. (eds.), Mafic dyke swarms: Geological Association of Canada, Special Paper 34, 5-24.

Ramos-Rosique, A., 2013, Timing and evolution of Late Oligocene to Early Miocene magmatism and epithermal mineralization in the central Bolaños Graben, southern Sierra Madre Occidental, México: London, UK, Kingston University, Ph.D. thesis, 215 pp.

Righter, K., Carmichael, I.S.E., Becker, T., 1995, Pliocene-Quaternary faulting and volcanism at the intersection of the Gulf of California and the Mexican Volcanic Belt: Geological Society of America Bulletin, 107, 612-626.

Rodríguez-Castañeda, J.L., Rodríguez-Torres, R., 1992, Geología estructural y estratigrafía del área entre Guadalajara y Tepic, Estados de Jalisco y

Nayarit, México: Revista del Instituto de Geología UNAM, 10, 99-110.
Rosendahl, B.R., 1987, Architecture of continental rifts with special reference to East Africa: Annual Review of Earth and Planetary Science Letters, 15, 445-504.
Rossotti, A., Ferrari, L., López-Martinez, M., Rosas-Elguera, J., 2002, Geology of the boundary between the Sierra Madre Occidental and the Trans-Mexican Volcanic Belt in the Guadalajara region, western Mexico: Revista Mexicana de Ciencias Geológicas, 19, 1-15.
Savage, B., Wang, Y., 2012, Integrated model of the crustal structure in the Gulf of California Extensional Province: Bulletin of the Seismological Society of America, 102(2), 878-885.
Sawlan, M.G., Smith, J.G., 1984, Petrologic characteristics, age and tectonic setting of Neogene volcanic rocks in northern Baja California Sur, Mexico, *in* Frizzell, V.A. (ed.), Geology of the Baja California Peninsula: Society of Economic Paleontologists and Mineralogists, Pacific Section, 39, 237-251.
Scheubel, F.R., Clark, K.F., Porter, E.W., 1988, Geology, tectonic environment and structural controls in the San Martin de Bolaños district, Jalisco, Mexico: Economic Geology, 83, 1703-1720.
SGM (Servicio Geológico Mexicano), 1996, Carta Geológico-Minera Santa María del Oro F13-D32, Nayarit, scale 1:50.000: Pachuca, Mexico, Servicio Geológico Mexicano, 1 map.
SGM (Servicio Geológico Mexicano), 1998, Carta Geológico-Minera Tepic F13-8, Nayarit y Jalisco, scale 1:250.000: Pachuca, Mexico, Servicio Geológico Mexicano, 1 map.
SGM (Servicio Geológico Mexicano), 1999, Carta Geológico-Minera Escuinapa F13-5, Nayarit y Jalisco, scale 1:250.000: Pachuca, Mexico, Servicio Geológico Mexicano, 1 map.
SGM (Servicio Geológico Mexicano), 2006, Carta Geológico-Minera El Venado F13-D11, Nayarit y Jalisco, scale 1:50.000: Pachuca, Mexico, Servicio Geológico Mexicano, 1 map.
Soto, M.A., Ortega J.G., 1982, Geología del Río Santiago en los estados de Jalisco y Nayarit, México: México City, XII Convención de la Sociedad Geológica Mexicana, Memoria, 20 pp.
Stewart, J., 1998, Regional characteristics, tilt domains, and extensional history of the later Cenozoic Basin and Range Province, western North America, *in* Faulds, J. E., Stewart, J. H. (eds.), Accommodation Zones and Transfer Zones: The Regional Segmentation of the Basin and Range Province: Geological Society of America, Special Paper, 323, 47-74,
Stock, J.M., Hodges, K.V., 1989, Pre-Pliocene extension around the Gulf of California and the transfer of Baja California to the Pacific plate: Tectonics, 8(1), 99-115.
Sutherland, F.H., Kent, G.M., Harding, A.J., Umhoefer, P.J., Driscoll, N.W., Lizarralde, D., Fletcher, J.M., Axen, G.J., Holbrook, W.S., González-Fernández, A., Lonsdale, P., 2012, Middle Miocene to early Pliocene oblique extension in the southern Gulf of California: Geosphere, 8, 752-770, doi:10.1130/GES00770.1.
Swanson, E.R., Kempter, K.A., McDowell, F.W., McIntosh, W.C., 2006, Major ignimbrites and volcanic centers of the Copper Canyon area: A view into the core of Mexico's Sierra Madre Occidental: Geosphere, 2(3), 125-141.
Umhoefer, P.J., 2011, Why did the Southern Gulf of California rupture so rapidly?—Oblique divergence across hot, weak lithosphere along a tectonically active margin: GSA Today, 21(11), 1-10.
Umhoefer, P., Dorsey, R., Willsey, S., Mayer, L., Renne, P., 2001, Stratigraphy and geochronology of the Comundú Group near Loreto, Baja California Sur, Mexico: Sedimentary Geology, 144(1), 125-147.
Vega-Granillo, R., Calmus, T., 2003, Mazatán metamorphic core complex (Sonora, Mexico): structures along the detachment fault and its exhumation evolution: Journal of South American Earth Sciences, 16(4), 193-204.
Wong, M.S., Gans, P.B., Scheier, J., 2010, The $^{40}Ar/^{39}Ar$ thermochronology of core complexes and other basement rocks in Sonora, Mexico: Implications for Cenozoic tectonic evolution of northwestern Mexico: Journal of Geophysical Research, 115(B7), doi: 10.1029/2009JB007032.

Manuscript received: April 9, 2014
Corrected manuscript received: September 22, 2014
Manuscript accepted: September 26, 2014

5

Discusión y conclusiones

El presente trabajo presenta evidencias geológicas de extensión temprana en la Provincia Extensional del Golfo de California, anterior a los 12.5 Ma como hasta ahora lo han postulado los modelos clásicos de apertura del golfo. Así mismo se presentan evidencias para concluir que al menos en la parte sur del golfo existieron al menos dos fases de extensión durante la apertura del Golfo de California. Con la evidencia presentada en los tres artículos que constituyen esta tesis se puede afirmar que:

- Los resultados del presente trabajo son coincidentes con la hipótesis de que durante el Mioceno temprano habría existido un extenso proceso de extensión litosférica en el occidente de México, donde posteriormente se formaría el actual del Golfo de California. Este proceso extensional habría afectado la zona geográfica comprendida entre el cinturón de batolitos de las Sierras Peninsulares de Baja California y la Sierra Madre Occidental (SMO). Las actuales teorías sobre el inicio de la extensión en las margenes del Golfo de California (e.g. Stock and Hodges 1989; Fletcher et al., 2007; Lizarralde et al., 2007; Umhoefer, 2011) son incompatibles con las altas tasas de enfriamiento durante el Mioceno medio (~19-13 Ma) ($^{40}Ar/^{39}Ar$) obtenidas en plutones con edades de cristalización tanto del Mioceno temprano como del Mioceno medio encontrados en la zona sur del Golfo de California. Por el contrario, los datos obtenidos durante el presente trabajo, sugieren que estos plutones intruyeron a nivel somero durante el Mioceno temprano y medio, a lo largo de una región que estaba sujeta a un importante proceso de extensión, y que esta amplia franja de extensión y magmatismo se concentraría hacia la región del Golfo durante el Mioceno medio para posteriormente ser aprovechada por la deformación transtensional a partir del Mioceno superior con el desarrollo del actual Golfo de California.

- Los intrusivos muestreados en la corteza continental sumergida bajo las aguas del Golfo de California, indican que un volumen considerable de magmas de composición intermedia a félsica se originaron en la región del Golfo durante el Mioceno temprano, representando el equivalente plutónico del “flare-up” ignimbrítico registrado en la SMO. Las muestras de intrusivos con edades del Mioceno medio, recuperadas en esta zona, representan aparentemente un volumen menor y temporalmente son correlacionables con los miembros medio y superior del Grupo Comondú.

- El modelo de rifting propuesto en este trabajo, y que habría iniciado antes del Mioceno tardío, concuerda con los modelos globales de evolución del proceso de rifting, en el cual un rift amplio evoluciona a un rift estrecho y la distribución del magmatismo es controlada por el régimen de esfuerzos (e.g. Parsons, et al., 1998; Corti et al., 2003). La apertura rápida del Golfo de California (Umhoefer, 2011) se basa en considerar que la extensión en la Provincia Extensional del Golfo inicia a finales del Mioceno medio, propiciada por la actividad del “arco” Comondú. Mientras que nuestros resultados muestran que el proceso de extensión habría comenzado sustancialmente antes que lo propuesto por los modelos clásicos y además indican que el proceso de extensión de la litósfera habría guiado la localización del magmatismo y no de manera contraria.

- Este trabajo presenta el primer estudio estructural detallado de los sistemas de fallas que afectan la parte suroccidental de la SMO en el norte de Nayarit, constriñendo la cinemática del proceso inicial de extensión en la margen suroccidental del rift del Golfo de California. En esta zona fueron identificadas tres familias de fallas principales: 1) Un grupo de fallas con dirección predominante ~N-S, con una edad de actividad entre los 24 y 18 Ma, asociadas con la provincia extensional que limita la margen oeste de la SMO; 2) Una familia de fallas con direcciones entre NNW-SSE a NW-SE, con actividad entre los ~21 y 11 Ma, asociadas con los sistemas de falla San Pedro Acaponeta y Pocholtitán en la parte occidental de la SMO; 3) Un grupo de fallas con orientación E-W a ENE-WSW, las cuales parecen estar asociadas a estructuras antiguas del basamento y que fueron reactivadas como zonas de acomodación durante las primeras fases del proceso de rifting en el Mioceno temprano a medio.

- El análisis cinemático y los cálculos de diedros rectos, estimados a partir de los datos tomados en fallas, orientación a partir de direcciones de intrusión de diques, además de edades que acotan la actividad de fallas, nos permiten inferir que el esfuerzo principal mínimo (σ_3) estaba orientado ~E-W durante el Mioceno temprano (~24-18 Ma) y que posteriormente habría rotado ligeramente en sentido contrario a las manecillas del reloj al estar orientado ENE-WSW durante el Mioceno medio (~18-11 Ma).

- La cinemática de deformación indica un fallamiento dominantemente normal, con una ligera componente oblicua extensional a lo largo de la zona suroccidental de la SMO. No se descarta que la oblicuidad observada en estas fallas pudiera estar asociada a la cercanía de zonas de acomodo, tal como fue observado cerca a la zona de cizalla El Roble, en la Sierra de Pajaritos. Por otro lado, una componente transtensional a lo largo de las fallas con dirección NNW es compatible con la extensión E-W del Mioceno temprano. El presente trabajo excluye que movimientos transtensionales de tipo lateral-derecho puedan haber sido acomodados en la margen sureste del Golfo durante el Mioceno temprano a medio. Por el contrario, los datos que aquí se presentan soportan la hipótesis de que una extensión transtensional en el Golfo de California habría ocurrido solo después de los ~12.5 Ma, una vez iniciada la divergencia oblicua dextral entre las placas Pacífico y Norteamérica (e.g. Stock and Hodges, 1989; Oskin et al., 2001; Oskin and Stock, 2003; Bennett et al., 2013; Bennet and Oskin, 2014).

- Los datos que aquí se presentan, permiten concluir que durante los últimos 30 m.a. el occidente de México ha estado dominado por una extensión litosférica, producto de varios mecanismos geodinámicos y que el proceso que se ha observado a partir de ~12.5 Ma, es la interacción directa entre las placas Pacífico y Norteamérica, la cual genera la focalización del proceso de rifting en la zona del Golfo de California. Por lo tanto, la Provincia Extensional del Golfo solo sería identificable por su componente dextro-lateral de deformación y debería más bien ser llamada Provincia Transtensional del Golfo.

- Se considera que la extensión en el occidente de México haya empezado en el Oligoceno en la parte oriente de la SMO y posteriormente haber migrando hacia el oeste hasta llegar en el Mioceno medio a la zona del actual Golfo de California (Cameron et al., 1989; McDowell y Mauger, 1994; Henry y Aranda-Gómez, 2000; Luhr et al., 2001; Umhoefer et al., 2001; Aranda-Gómez et al., 2003). Sin embargo, los datos obtenidos durante el presente trabajo, indican que una extensión generalizada afectó todo el occidente de México a partir del Oligoceno, desde la parte oriental de la SMO hasta la región que posteriormente se convertiría en el Golfo de California. Esta primera fase de extensión (~29 a 20 Ma) coincide con el volcanismo silícico de la SMO. Esta deformación de tipo rift amplio habría sido posteriormente focalizada en un rift estrecho entre los ~20 y 11 Ma, localizado en la parte más occidental de la SMO y el Golfo de California, generando una cuenca estrecha y alargada donde habría sido depositado el Grupo Comondú. Esta temporalidad en el proceso de extensión implica que parte de la extensión en la zona sur del Golfo de California habría ocurrido antes del cese de la subducción y que no puede ser considerada como debida a la interacción entre la Placa Pacífico y Norteamérica.

6

Bibliografía

- Abbate, E.P., Balestrieri, M.L. y Bigazzi, G., 2001, Uplifted rift-shoulder of the Gulf of Aden in northwestern Somalia: Palinspastic reconstructions supported by apatite fission-track data, in Peri-Tethys Memoir 6: Peri-Tethyan Rift/Wrench Basins and Passive Margins, edited by Ziegler, P. A. et al., Mem. Mus. Natl. Hist. Nat., 186, p. 629–640.

- Angelier, J., 1979, Determination of the mean principal directions of stresses for a given fault population: Tectonophysics, v. 56, no. 3, p. T17-T26.

- Angelier, J., 1984, Tectonic analysis of fault slip data sets. Journal of Geophysical Research: Solid Earth, v. 89, no. B7, p. 5835-5848.

- Angelier, J., 1994, Fault slip analysis and palaeostress reconstruction, in Hancock, L., ed., Continental deformation: Oxford, UK, Pergamon Press, p. 53–100.

- Aranda-Gómez, J.J., Henry, C.D., Luhr, J.F., y McDowell, F.W., 2003, Cenozoic volcanic-tectonic development of northwestern México; a transect across the Sierra Madre Occidental volcanic field and observations on extension-related magmatism in the southern Basin and Range and Gulf of California tectonic provinces, in Geologic transects across Cordilleran Mexico: Guidebook for the field trips of the 99th Geological Society of America Cordilleran Section Annual Meeting, Puerto Vallarta, Mexico: Mexico, D.F., Universidad Nacional Autónoma de México, Instituto de Geología, Publicación Especial 1, p. 71–121.

- Baker, B. y Morgan, P., 1981, Continental rifting: progress and outlook. Eos, Transactions of the American Geophysical Union. v. 62, p. 585–586.

- Bennett, S. E., Oskin, M. E., e Iriondo, A., 2013, Transtensional rifting in the proto–Gulf of California near Bahía Kino, Sonora, México: Geological Society of America Bulletin, v. 125, no. 11-12, p. 1752-1782.

- Bennett, S. E., y Oskin, M. E., 2014, Oblique rifting ruptures continents: Example from the Gulf of California shear zone: Geology, v. 42, no. 3, p. 215-218.

- Bernal, J.P., y Lozano-Santacruz, R., 2005, Characterization of a new set of eight geochemical reference materials for XRF major and trace element analysis: Revista Mexicana de Ciencias Geológicas, v. 22, no. 3, p. 329–344.

- Bohannon, R.G., Naeser, C.W., Schmidt, D.L., y Zimmermann, R.A., 1989, The timing of uplift, volcanism, and rifting peripheral to the Red Sea: A case for passive rifting?: Journal of Geophysical Research. Solid Earth, v. 94, no. B2, p. 1683-1701.

- Bryan, S. E., Orozco-Esquivel, T., Ferrari, L., y López-Martínez, M., 2014, Pulling apart the Mid to Late Cenozoic magmatic record of the Gulf of California: is there a Comondú Arc?: Geological Society, London, Special Publications, v. 385, no. 1, p. 389-407.

- Bryan, S., 2007, Silicic large igneous provinces: Episodes, v. 30, no. 1, p. 20.

- Bryan, S.E., Ferrari, L., Reiners, P.W., Allen, C.M., Petrone, C.M., Ramos-Rosique, A., y Campbell, I.H., 2008, New insights into crustal contributions to large volume rhyolite generation at the mid-Tertiary Sierra Madre Occidental Province, Mexico, revealed by U/Pb geochronology: Journal of Petrology, v. 49, no. 1, p. 47-77.

- Bryan, S.E., Orozco-Esquivel, T., Ferrari, L., y López-Martínez, M., 2014, Pulling Apart the Mid to Late Cenozoic Magmatic Record of the Gulf of California: Is there a Comondú Arc?, in Gómez-Tuena, A., Straub, S.M., Zellmer, G.F., eds. Orogenic andesites and crustal growth: Geological Society, London, Special Publications, v. 385, no. 1, p. 389-407.

- Bryan, S.E., y Ferrari L., 2013, Large igneous provinces and silicic large igneous provinces: Progress in our understanding over the last 25 years: Geological Society of America Bulletin, doi: 10.1130/B30820.1.

- Calmus, T., Pallares, C., Maury, R.C., Aguillón-Robles, A., Bellon, H., Benoit, M., y Michaud, F., 2010, Volcanic markers of the post-subduction evolution of Baja California and Sonora, Mexico: Slab tearing versus lithospheric rupture of the Gulf of California: Pure and Applied Geophysics, v. 168, p. 1303–1330, doi:10.1007/s00024-010-0204-z.

- Cameron, K.L., Nimz, G.J., Kuentz, D., Niemeyer, S., y Gunn, S., 1989, Southern Cordilleran basaltic ande site suite, southern Chihuahua, Mexico: A link between Tertiary continental arc and flood basalt magmatism in North America: Journal of Geophysical Research, v. 94, p. 7817–7840, doi:10.1029/JB094iB06p07817.

- Conly, A.G., Brenan, J.M., Bellon, H. y Scott, S.D. 2005, Arc to rift transitional volcanism in the Santa Rosalía Region, Baja California Sur, Mexico: Journal of Volcanology and Geothermal Research, v. 142, p. 303–341.

- Corti, G., 2009, Continental rift evolution: from rift initiation to incipient break-up in the Main Ethiopian Rift, East Africa: Earth-Science Reviews, v. 96, no. 1, p, 1-53.

- Corti, G., Bonini, M., Innocenti, F., Manetti, P., Mulugeta, G., Sokoutis, D., y Cloetingh, S. 2003, Rift-parallel magma migration and localization of magmatic activity in transfer zones: Acta Vulcanologica, v. 14, no. 17.

- Cherniak, D.J., y Watson, E.B., 2001, Pb diffusion in zircon: Chemical Geology, v. 172, no.1, p. 5-24.

- Duque-Trujillo, J., Ferrari, L., Orozco-Esquivel, T., Lopez-Martinez, M., Lonsdale, P., Bryan, S., Kluesner, J., Pinero-Lajas, D., Solari, L., 2014, Timing of rifting in the Southern Gulf of California and its conjugate margins: insights from the plutonic record: Geological Society of America Bulletin, B31008-1; doi:10.1130/B31008.1.

- Ferrari, L., López-Martínez, M., y Rosas-Elguera, J., 2002, Ignimbrite flare-up and deformation in the southern Sierra Madre Occidental, western Mexico-implications for the late subduction history of the Farallón Plate: Tectonics, v. 21, no. 4, doi: 10.1029/2001TC001302.

- Ferrari, L., Valencia-Moreno, M., y Bryan, S.E, 2007, Magmatism and tectonics of the Sierra Madre Occidental and its relation with the evolution of the western margin of North America, in Alaniz-Álvarez, S.A., and Nieto-Samaniego, A.F., eds., Geology of México: Celebrating the Centenary of the Geological Society of México: Geological Society of America Special Paper 422, p. 1–39, doi: 10.1130/2007.2422(01).

- Fletcher, J.M., Grove, M., Kimbrough, D., Lovera, O., y Gehrels, G.E., 2007, Ridge-trench interactions and the Neogene tectonic evolution of the Magdalena Shelf and southern Gulf of California; insights from detrital zircon U/Pb ages from the Magdalena Fan and adjacent areas: Geological Society of America Bulletin, v. 119, no. 11-12, p. 1313-1336, doi: 10.1130/B26067.1.

- Fletcher, J.M., y Munguía, L., 2000, Active continental rifting in southern Baja California, Mexico: Implications for plate motion partitioning and the transition to seafloor spreading in the Gulf of California: Tectonics, v. 19, no. 6, p. 1107-1123.

- Gans, P.B., 1997, Large-magnitude Oligo-Miocene extension in southern Sonora: Implications for the tectonic evolution of northwest Mexico: Tectonics, v. 16, no. 3, p. 388-408.

- Gastil, R.G., 1975, Plutonic zones in the Peninsular Ranges of southern California and northern Baja California: Geology, v. 3, no. 7, p. 361–363, doi: 10.1130/0091-7613(1975)3<361:PZITPR>2.0.CO;2.

- Godinez. N.S., Kimbrough, D.L., y Kohel, C., 2010, Stratigraphy and petrologic evolution of the Oligocene-Miocene Comondú Group near Bahia Concepcion and Loreto, Baja California Sur, Mexico: Geological Society of America Abstracts with Programs, v. 42, no. 4, p. 66.

- Hausback, B.P., 1984, Cenozoic volcanic and tectonic evolution of Baja California Sur, Mexico, in Frizzell, V.A., ed., Geology of the Baja Peninsula: Pacific Section, Society of Economic Paleontologists and Mineralogists, v. 39, p. 219–236.

- Henry, C.D., 1989, Late Cenozoic Basin and Range structure in western México adjacent to the Gulf of California: Geological Society of America Bulletin, v. 101, p. 1147–1156.

- Henry, C.D., McDowell, F.W., y Silver, L.T., 2003, Geology and geochronology of the granitic batholithic complex, Sinaloa, México: Implications for Cordilleran magmatism and tectonics, in Johnson, S.E, Paterson, S.R., Fletcher, J.M., Girty, G.H., Kimbrough, D.L., y Martín-Barajas, A., eds., Tectonic Evolution of Northwestern México and the Southwestern USA: Geological Society of America Special Paper. v. 374, p. 237–273.

- Henry, C.D., y Aranda-Gomez, J.J., 1992, The real southern Basin and Range: Mid-to late Cenozoic extension in Mexico: Geology, v. 20, no. 8, p. 701-704.

- Henry, C.D., y Aranda-Gomez, J.J., 2000, Plate interactions control middle-late Miocene, proto-Gulf and Basin and Range extension in the southern Basin and Range: Tectonophysics, v. 318, no. 1, p. 1-26.

- Huismans, R.S., Podladchikov, Y.Y.y Cloetingh, S., 2001, Transition from passive to active rifting: relative importance of asthenospheric doming and passive extension of the lithosphere: Journal of Geophysical Research. v. 106, p. 11271–11291.

- Karig, D. E., y Jensky, W., 1972, The proto-gulf of California: Earth and Planetary Science Letters, v. 17, no. 1, 169-174.

- Lizarralde, D., Axen, G.J., Brown, H.E., Fletcher, J.M., González-Fernández, A., Harding, A.J., Holbrook, W.S., Kent, G.M., Paramo, P., Sutherland, F., y Umhoefer, P.J., 2007, Variation in styles of rifting in the Gulf of California: Nature, v. 448, p. 466–469.

- Ludwig, K.R., 2004, Isoplot/Ex, ver. 3. A geochronological toolkit for Microsoft Excel: Berkeley Geochronology Center, Special Publication, 4, 70 pp.

- Luhr, J.F., Henry, C.D., Housh, T.B., Aranda-Gómez, J.J., y McIntosch, W.C., 2001, Early extension and associated mafic alkalic volcanism from the southern Basin and Range Province: Geology and petrology of the Rodeo and Nazas volcanic fields, Durango, México: Geological Society of America Bulletin, v. 113, no. 6, p. 760-773.

- Mark, C., Gupta, S., Carter, A., Mark, D., Gautheron, C.,y Martin-Barajas, A., 2012, Temporal constraints on the landscape response to rifting in the Loreto region of Baja California Sur, Mexico: Geological Society of America Abstracts with Programs, v. 44, no. 3, p. 6.

- Martín-Barajas, A., Stock, J. M., Layer, P., Hausback, B., Renne, P., y López-Martínez, M., 1995, Arc-rift transition volcanism in the Puertecitos volcanic province, northeastern Baja California, Mexico: Geological Society of America Bulletin, v.107, no. 4, p, 407-424.

- McDowell, F.W, Roldán-Quintana, J., y Amaya-Martínez, R., 1997, Interrelationship of sedimentary and volcanic deposits associated with Tertiary extension in Sonora, Mexico: Geological Society of America Bulletin, v. 109, no. 10, p. 1349-1360.

- McDowell, F.W., y Keizer, R.P., 1977, Timing of mid-Tertiary volcanism in the Sierra Madre Occidental between Durango City and Mazatlán, Mexico: Geological Society of America Bulletin, v. 88, no. 10, p. 1479–1487, doi: 10.1130/0016-7606(1977)88<1479:TOMVIT>2.0.CO;2.

- McDowell, F.W., y Mauger, R.L., 1994, K-Ar and U-Pb zircon chronology of Late Cretaceous and Tertiary magmatism in central Chihuahua State, Mexico: Geological Society of America Bulletin, v. 106, p. 118–132, doi:10.1130/0016-7606(1994)106<0118: KAAUPZ>2.3.CO;2.

- Menzies, M., Gallagher, K., Yelland, A., y Hurford, A. J., 1997, Volcanic and nonvolcanic rifted margins of the Red Sea and Gulf of Aden: Crustal cooling and margin evolution in Yemen: Geochimica et Cosmochimica Acta, v. 61, no.12, p. 2511-2527.

- Miller, N.C., y Lizarralde, D., 2013, Thick evaporites and early rifting in the Guaymas Basin, Gulf of California: Geology, v. 41, no. 2, p. 283-286.

- Morgan, P. y Baker, B.H. (Eds.), 1983, Processes of Continental Rifting: Tectonophysics, v. 94, p. 680.

- Mori, L., Gómez-Tuena, A., Cai, Y., y Goldstein, S.L., 2007, Effects of prolonged flat subduction on the Miocene magmatic record of the central Trans-Mexican Volcanic Belt: Chemical Geology, v. 244, no. 3, p. 452–473, doi: 10.1016/j.chemgeo.2007.07.002.

- Mulugeta, G., 1985, Dynamic models of continental rift valley systems: Tectonophysics. v. 113, p. 49– 73.

- Murray, B.P., Busby, C.J., Ferrari, L., y Solari, L.A., 2013, Synvolcanic crustal extension during the mid-Cenozoic ignimbrite flare-up in the northern Sierra Madre Occidental, Mexico: Evidence from the Guazapares Mining District region, western Chihuahua: Geosphere. GES00862-1.

- Nourse, J. A., Anderson, T. H., y Silver, L. T., 1994, Tertiary metamorphic core complexes in Sonora, northwestern Mexico: Tectonics, v. 13, no. 5, p.1161-1182.

- Neumann, E.-R. y Ramberg, I.B. (Eds.), 1978, Petrology and Geochemistry of Continental Rifts. Reidel, Dordrecht, 296 pp.

- Omar, G. I., y Steckler, M. S., 1995, Fission track evidence on the initial rifting of the Red Sea: two pulses, no propagation: Science, v. 270, no. 5240, p. 1341 1344.

- Ortega-Rivera, A., 2003, Geochronological constraints on the tectonic history of the Peninsular Ranges batholith of Alta and Baja California: Tectonic implications for western Mexico: Geological Society of America Special Paper. v. 374, p. 297–336.

- Oskin, M., Stock, J., y Martín-Barajas, A., 2001, Rapid localization of Pacific–North America plate motion in the Gulf of California: Geology, v. 29, no. 5, p. 459-462.

- Oskin, M., y Stock, J., 2003, Pacific–North America plate motion and opening of the upper Delfín basin, northern Gulf of California, Mexico: Geological Society of America Bulletin, v. 115, no. 10, p. 1173-1190, doi:10.1130 /B25154.1.

- Parsons, T., Thompson, G.A., y Smith. R.P., 1998, More than one way to stretch: a tectonic model for extension along the plume track of the Yellowstone hotspot and adjacent Basin and Range Province: Tectonics, v. 17, no. 2, p. 221-234.

- Paton, C., Hellstrom, J., Paul, B., Woodhead, J., y Hergt, J., 2011, Iolite: Freeware for the visualization and processing of mass spectrometric data: Journal of Analytical Atomic Spectrometry, v. 26, no. 12, p. 2508-2518.

- Pik, R., Marty, B., Carignan, J., Yirgu, G., y Ayalew, T., 2008, Timing of East African Rift development in southern Ethiopia: Implication for mantle plume activity and evolution of topography: Geology, v. 36, p. 167-170.

- Reiners, P.W., Ehlers, T.A., y Zeitler, P.K., 2005, Past, present, and future of thermochronology: Reviews in Mineralogy and Geochemistry, v. 58, no. 1, p. 1-18.

- Ruppel, C., 1995, Extensional processes in continental lithosphere: Journal of Geophysical Research. v. 100, p. 24187– 24215.

- Sawlan, M.G., 1991, Magmatic evolution of the Gulf of California rift, in Dauphin, J.P., Simoneit, B.R., eds., The Gulf and Peninsular Province of the Californias: American Association of Petroleum Geologists Memoir 47, p. 301-369.

- Sawlan, M.G., y Smith, J.G., 1984, Petrologic characteristics, age and tectonic setting of Neogene volcanic rocks in northern Baja California Sur, Mexico, in Frizzell, V.A., ed., Geology of the Baja California Peninsula: Pacific Section, Society of Economic Paleontologists and Mineralogists, v. 39, p. 237-251.

- Schaaf, P., Böhnel, H., y Pérez-Venzor, J.A., 2000, Pre-Miocene palaeogeography of the Los Cabos Block, Baja California Sur: geochronological and palaeomagnetic constraints: Tectonophysics, v. 318, no. 1, p. 53-69.

- Seiler, C., Fletcher, J. M., Kohn, B. P., Gleadow, A. J., y Raza, A., 2011, Low temperature thermochronology of northern Baja California, Mexico: Decoupled slip exhumation gradients and delayed onset of oblique rifting across the Gulf of California: Tectonics, v. 30, no. 3, TC3004, DOI: 10.1029/2009TC002649.

- Sengör, A.M.C. y Burke, K., 1978, Relative timing of rifting and volcanism on Earth and its tectonic implications: Geophysical Research Letters 5, p. 419–421.
- Sláma, J., Košler, J., Condon, D.J., Crowley, J.L., Gerdes, A., Hanchar, J.M., Horstwood, M.S.A., Morris, G.A., Nasdala, L., Norberg, N., Schaltegger, U., Schoene, B., Tubrett, M.N., y Whitehouse, M.J., 2008, Plešovice zircon—a new natural reference material for U–Pb and Hf isotopic microanalysis: Chemical Geology, v. 249, no. 1-2, p. 1-35.

- Solari, L. A, Gómez-Tuena, A., Bernal, J.P., Pérez-Arvizu, O., y Tanner, M., 2010, U/Pb zircon geochronology with an integrated LA-ICP-MS Microanalytical Workstation: Achievements in precision and accuracy: Geostandards and Geoanalytical Research, v. 34, no.1, p. 5-18.

- Solari, L.A., y Tanner, M., 2011, UPb.age, a fast data reduction script for LA-ICP-MS U/Pb geochronology: Revista Mexicana de Ciencias Geológicas, v. 28, no. 1, p. 83-91.

- Stewart, J., 1998, Regional characteristics, tilt domains, and extensional history of the later Cenozoic Basin and Range Province, western North America: Geological Society of America Special Papers, 323, p. 47-74.

- Stock, J. M. y Hodges, K. V., 1989, Pre-Pliocene extension around the Gulf of California and the transfer of Baja California to the Pacific plate: Tectonics. v. 8, no.1, p. 99-115.

- Sutherland, F.H., Kent, G.M., Harding, A.J., Umhoefer, P.J., Driscoll, N.W., Lizarralde, D., Fletcher, J.M., Axen, G.J., Holbrook, W.S., González-Fernández, A., y Lonsdale P.F., 2012, Middle Miocene to early Pliocene oblique extension in the southern Gulf of California: Geosphere, v. 8, no.4, p. 752-770, doi: 10.1130/GES00770.1.

- Umhoefer, P., Dorsey, R., Willsey, S., Mayer, L., y Renne, P., 2001, Stratigraphy and geochronology of the Comundú Group near Loreto, Baja California Sur, Mexico: Sedimentary Geology, v. 144, no. 1, p. 125-147.

- Umhoefer, P.J., 2011, Why did the Southern Gulf of California rupture so rapidly?—Oblique divergence across hot, weak lithosphere along a tectonically active margin: GSA Today, v. 21, no. 11, p. 1-10.

- Umhoefer, P.J., Mayer, L., y Dorsey, R.J., 2002, Evolution of the margin of the Gulf of California near Loreto, Baja California Peninsula, Mexico: Geological Society of America Bulletin, v. 114, p. 849–868.

- Veevers, J. y Hansen, L. 1981, Volcanism in the rift−valley system that evolved into the western margin of Australia: J. of the Geological Society of Australia, v. 28, no.3-4, p. 377-384.

- Granillo, R. V., y Calmus, T., 2003, Mazatan metamorphic core complex (Sonora, Mexico): structures along the detachment fault and its exhumation evolution: Journal of South American Earth Sciences, v. 16, no. 4, p. 193-204.

- Wong, M.S., Gans, P.B., y Scheier, J., 2010, The $^{40}Ar/^{39}Ar$ thermochronology of core complexes and other basement rocks in Sonora, Mexico: Implications for Cenozoic tectonic evolution of northwestern Mexico: Journal of Geophysical Research, v. 115, no. B7, doi: 10.1029/2009JB007032.

- Ziegler, P. A. y Cloetingh, S., 2004, Dynamic processes controlling evolution of rifted basins: Earth-Sciences Reviews, v. 64, p, 1-50.

7

Anexos

Anexo 1

Material suplementario publicado en línea como parte del articulo:

Ferrari, L., López-Martínez, M., Orozco-Esquivel, T., Bryan, S., Duque-Trujillo, J., Lonsdale, P., Solari, L. 2013. Late Oligocene to Middle Miocene rifting and synextensional magmatism in the southwestern Sierra Madre Occidental, México: The beginning of the Gulf of California rift. Geosphere, v. 9, n. 5. doi:10.1130/GES00925.1

Secciones:

1) Datos analíticos de edades U-Pb.

2) Discusión de experimentos de fechamiento por ^{30}Ar-^{40}Ar

Appendix 1. U-Pb analytical data

				CORRECTED RATIOS [2,3]									CORRECTED AGES (Ma)						Best age (Ma)	±2σ
Spot Name	U (ppm)[1]	Th (ppm)[1]	Th/U	207Pb/206Pb	±2σ [3]	207Pb/235U	±2σ [3]	206Pb/238U	±2σ [3]	208Pb/232Th	±2σ [3]	Rho	206Pb/238U	±2σ	207Pb/235U	±2σ	207Pb/206Pb	±2σ		
Sample: ES 11																				
ES-11	1430	1022	0.71	0.046695	0.00037	0.03182	0.000936	0.004942	0.00014	N.D.	N.D.	0.963036	31.78	0.93	31.8	0.935427	33.63	0.19	31.78	0.93
_28	494	300	0.61	0.04827	0.00084	0.0331	0.000968	0.005106	0.00012	N.D.	N.D.	0.803665	32.83	0.8	33.1	0.967951	111	41	32.83	0.8
_29	263	160	0.61	0.046848	0.00024	0.03149	0.000262	0.004874	0.000032	N.D.	N.D.	0.788392	31.34	0.21	31.48	0.262154	41.5	1.2	31.34	0.21
_30	190.1	107.37	0.56	0.046699	0.00056	0.03203	0.000674	0.004975	0.000086	N.D.	N.D.	0.821653	31.99	0.55	32.01	0.673446	33.85	0.29	31.99	0.55
_31	357	214	0.60	0.046723	0.00049	0.03318	0.00079	0.00515	0.00011	N.D.	N.D.	0.897636	33.11	0.73	33.14	0.788565	35.09	0.25	33.11	0.73
_33	390.1	345.3	0.89	0.046692	0.00055	0.03284	0.000654	0.005103	0.000082	N.D.	N.D.	0.806514	32.81	0.53	32.81	0.653706	33.5	0.28	32.81	0.53
_34	757	460	0.61	0.046702	0.00034	0.03294	0.000687	0.005115	0.0001	N.D.	N.D.	0.937134	32.89	0.67	32.91	0.686563	34.03	0.17	32.89	0.67
_35	277	170	0.61	0.0478	0.00059	0.03263	0.000919	0.005135	0.00013	N.D.	N.D.	0.898858	33.02	0.85	32.6	0.918183	87	29	33.02	0.85
_36	450	358	0.80	0.04674	0.00083	0.03327	0.000658	0.005162	0.000045	N.D.	N.D.	0.440673	33.19	0.29	33.23	0.657367	35.94	0.42	33.19	0.29
_37	274.2	205.6	0.75	0.046752	0.0008	0.03335	0.000861	0.005173	0.0001	N.D.	N.D.	0.748788	33.26	0.67	33.31	0.85995	36.59	0.41	33.26	0.67
_38	111.2	47.83	0.43	0.046711	0.00071	0.03351	0.001036	0.005203	0.00014	N.D.	N.D.	0.870686	33.45	0.87	33.46	1.034043	34.5	0.36	33.45	0.87
_39	175	97.6	0.56	0.046814	0.00063	0.03328	0.000786	0.005156	0.0001	N.D.	N.D.	0.821592	33.15	0.64	33.24	0.784678	39.76	0.32	33.15	0.64
_40	393.4	309.6	0.79	0.046863	0.0002	0.03227	0.000287	0.004994	0.000039	N.D.	N.D.	0.877513	32.11	0.25	32.25	0.287007	42.2	1	32.11	0.25
_41	94.82	48.71	0.51	0.04702	0.0001	0.03276	0.000478	0.005053	0.000073	N.D.	N.D.	0.989337	32.49	0.47	32.73	0.477942	50.4	5.2	32.49	0.47
_42	108.35	97.2	0.90	0.046903	0.00038	0.03223	0.0005	0.004982	0.000066	N.D.	N.D.	0.853109	32.04	0.42	32.21	0.50018	44.3	1.9	32.04	0.42
_43	248.8	113.93	0.46	0.046725	0.0008	0.03276	0.001174	0.005084	0.00016	N.D.	N.D.	0.87842	32.69	1	32.73	1.172623	35.19	0.41	32.69	1
_44	388.6	249.3	0.64	0.046768	0.00014	0.03252	0.000234	0.00505	0.000033	N.D.	N.D.	0.909146	32.47	0.21	32.54	0.233887	37.42	0.72	32.47	0.21
_46	144.8	71.1	0.49	0.047044	0.00012	0.03206	0.000783	0.004943	0.00012	N.D.	N.D.	0.994525	31.79	0.79	32.04	0.782109	51.48	0.63	31.79	0.79
_47	183.5	104.2	0.57	0.046733	0.0004	0.03192	0.000943	0.004953	0.00014	N.D.	N.D.	0.957082	31.85	0.91	31.9	0.942109	35.61	0.21	31.85	0.91
_48	111.4	57.2	0.51	0.046745	0.00064	0.03232	0.001005	0.005015	0.00014	N.D.	N.D.	0.897833	32.25	0.88	32.3	1.004301	36.22	0.33	32.25	0.88
_49	468.4	342.2	0.73	0.046865	0.00012	0.03234	0.00078	0.005005	0.00012	N.D.	N.D.	0.994346	32.18	0.78	32.32	0.779312	42.35	0.61	32.18	0.78
ES-11_1	175	86.8	0.50	0.04716	0.00021	0.0326	0.001049	0.00502	0.00016	N.D.	N.D.	0.990381	32.3	1	32.6	1.049135	57	11	32.3	1

1: U and Th concentrations are calculated employing an external standard zircon as in Paton, C., Woodhead, J. D., Hellstrom, J. C., Hergt, J. M., Greig, A., and Maas, R., 2010, Improved laser ablation U-Pb zircon geochronology through robust downhole fractionation correction. Geochemistry, Geophysics, Geosystems, vol., 11, no. 3.
2: 2σ uncertainties propagated according to Paton, C., Woodhead, J. D., Hellstrom, J. C., Hergt, J. M., Greig, A., and Maas, R., 2010, Improved laser ablation U-Pb zircon geochronology through robust downhole fractionation correction. Geochemistry, Geophysics, Geosystems, vol., 11, no. 3.
3: $^{207}Pb/^{206}Pb$ ratios, ages and errors are calculated according to Petrus, J. A., and Kamber, B. S., 2012, VizualAge: A Novel Approach to Laser Ablation ICP-MS U-Pb Geochronology Data Reduction. Geostandards and Geoanalytical Research, vol. 36, no. 3, pags 247-270. Analyzed spot is 23 micrometer, using an analytical protocol modified from Solari, L. A., Gómez-Tuena, A., Bernal, J. P., Pérez-Arvizu, O., and Tanner, M., 2010, U-Pb Zircon Geochronology with an Integrated LA-ICP-MS Microanalytical Workstation: Achievements in Precision and Accuracy. Geostandards and Geoanalytical Research, vol. 34, no. 1, pags 5-18. Data measured employing a Neptune Plus MC-ICPMS coupled to a Resonetics, Resolution M050 excimer laser workstation. N.D.: Not determined.

				CORRECTED RATIOS [†,*]									CORRECTED AGES (Ma)						Best age (Ma)	±2σ
Spot Name	U (ppm) [§]	Th (ppm) [§]	Th/U	207Pb/206Pb	±2σ [*]	207Pb/235U	±2σ [*]	206Pb/238U	±2σ [*]	208Pb/232Th	±2σ [*]	Rho	206Pb/238U	±2σ	207Pb/235U	±2σ	207Pb/206Pb	±2σ		
Sample: MdCh 03																				
Z_1_Mdch003	268	106	0.40	0.121	0.014	0.0595	0.0076	0.00364	0.00019	0.00266	0.00042	0.27411	23.4	1.2	58.6	7.2	1970	120	23.4	1.2
Zircon_2	199	126	0.63	0.177	0.012	0.084	0.0067	0.00345	0.0002	0.00213	0.00031	0.18919	22.2	1.3	81.8	6.3	2558	68	22.2	1.3
Zircon_4	350	215	0.61	0.0937	0.0064	0.0504	0.004	0.0039	0.00019	0.00165	0.00021	0.613846	25.1	1.2	49.9	3.8	1507	87	25.1	1.2

Zircon_6	289	312	1.08	0.114	0.012	0.0566	0.0071	0.00356	0.0002	0.00151	0.00029	0.16472	22.9	1.3	58.4	7.1	1930	110	22.9	1.3
Zircon_7	152	106	0.70	0.357	0.026	0.257	0.045	0.00537	0.00051	0.0064	0.0012	0.37177	~~34.5~~	~~3.3~~	232	32	3760	80	34.5	3.3
Zircon_8	65	59	0.91	0.227	0.036	0.139	0.025	0.00443	0.0003	0.002	0.00044	0.376524	~~28.5~~	~~1.9~~	131	21	3010	180	28.5	1.9
Zircon_9	75	25	0.33	0.152	0.031	0.097	0.025	0.0046	0.00033	0.0032	0.001	0.09894	~~29.6~~	~~2.1~~	94	22	2390	210	29.6	2.1
Zircon_10	126	61	0.48	0.093	0.018	0.06	0.013	0.00469	0.00025	0.00215	0.0004	0.246023	~~30.1~~	~~1.6~~	59	13	1490	200	30.1	1.6
Zircon_11	67	21	0.31	0.057	0.02	0.027	0.014	0.00356	0.00025	0.00234	0.00041	0.135433	22.9	1.6	27	13	890	240	22.9	1.6
Zircon_12	135	51	0.38	0.063	0.015	0.0302	0.0072	0.00348	0.00019	0.00142	0.00024	0.229007	22.4	1.2	30.1	7	1000	170	22.4	1.2
Zircon_16	110	53	0.48	0.131	0.039	0.077	0.054	0.00461	0.00074	0.0022	0.0011	0.2142	~~29.7~~	~~4.7~~	75	41	2110	240	29.7	4.7
Zircon_18	26	22	0.85	0.195	0.062	0.155	0.051	0.00588	0.00056	0.00252	0.00073	0.289449	~~37.8~~	~~3.6~~	143	41	2910	240	37.8	3.6
Zircon_19	74	41	0.55	0.095	0.017	0.058	0.011	0.00449	0.00029	0.0015	0.00028	0.340555	28.9	1.9	57	10	1700	140	28.9	1.9
Zircon_21	185	65	0.35	0.113	0.017	0.0583	0.0093	0.00401	0.00022	0.00204	0.00029	0.091803	25.8	1.4	57.2	8.9	1850	120	25.8	1.4
Zircon_23	120	37	0.31	0.144	0.041	0.086	0.044	0.00425	0.00052	0.0028	0.0011	0.239144	27.3	3.3	83	36	2350	300	27.3	3.3
Zircon_24	150	61	0.41	0.057	0.014	0.027	0.0066	0.00359	0.00022	0.00133	0.00019	0.250696	23.1	1.4	26.9	6.4	1190	180	23.1	1.4
Zircon_26	109	52	0.48	0.101	0.03	0.055	0.02	0.00411	0.00027	0.00163	0.00037	0.180657	26.5	1.7	54	19	1650	280	26.5	1.7
Zircon_27	125	42	0.34	0.087	0.02	0.046	0.011	0.00411	0.00025	0.00165	0.00036	0.009139	26.4	1.6	45	10	1380	200	26.4	1.6

				CORRECTED RATIOS [†,*]									CORRECTED AGES (Ma)						Best age (Ma)	±2σ
Spot Name	**U (ppm) [§]**	**Th (ppm) [§]**	**Th/U**	**207Pb/206Pb**	**±2σ [*]**	**207Pb/235U**	**±2σ [*]**	**206Pb/238U**	**±2σ [*]**	**208Pb/232Th**	**±2σ [*]**	**Rho**	**206Pb/238U**	**±2σ**	**207Pb/235U**	**±2σ**	**207Pb/206Pb**	**±2σ**		
Sample: MdCh 10																				
Z_1_Mdch010	641	465	S	0.073	0.016	0.0392	0.0088	0.00392	0.00012	0.00145	0.0002	0.136364	25.25	0.79	39	8.6	1010	160	25.25	0.79
Zircon_2	663	1119	1.69	0.078	0.023	0.038	0.01	0.00389	0.00013	0.00118	0.00013	0.126992	25.05	0.82	38	10	1300	180	25.05	0.82
Zircon_3	268	368	1.37	0.083	0.013	0.0448	0.0063	0.00395	0.00014	0.00135	0.00016	0.252039	25.43	0.9	44.5	6.2	1340	200	25.43	0.9
Zircon_4	407	422	1.04	0.0826	0.0082	0.0422	0.0043	0.00368	0.00013	0.00125	0.00015	0.24717	23.7	0.8	41.9	4.2	1290	110	23.7	0.8
Zircon_5	225	128	0.57	0.07	0.017	0.0369	0.008	0.00384	0.00018	0.00122	0.00019	0.216211	24.7	1.2	36.6	7.9	1000	270	24.7	1.2
Zircon_7	417	146	0.35	0.069	0.011	0.0349	0.0056	0.00384	0.00019	0.00118	0.0002	0.41003	24.7	1.2	34.8	5.5	900	170	24.7	1.2
Zircon_8	653	559	0.86	0.0754	0.0058	0.0383	0.003	0.003663	0.000096	0.00127	0.00012	0.2315	23.57	0.61	38.2	3	1112	66	23.57	0.61
Zircon_10	375	296	0.79	0.074	0.016	0.0436	0.0097	0.00418	0.00023	0.0015	0.00019	0.032942	26.9	1.5	43.1	9.4	1170	260	26.9	1.5
Zircon_11	684	614	0.90	0.0653	0.0053	0.0334	0.0028	0.00371	0.00011	0.00123	0.00012	0.353677	23.89	0.68	33.4	2.7	840	120	23.89	0.68
Zircon_12	767	710	0.93	0.068	0.0065	0.0356	0.0035	0.003698	0.000097	0.00121	0.00011	0.032454	23.8	0.62	35.5	3.5	950	110	23.8	0.62
Zircon_13	619	502	0.81	0.068	0.011	0.0356	0.0058	0.00374	0.00012	0.00126	0.00016	0.59854	24.05	0.76	35.4	5.7	890	200	24.05	0.76
Zircon_14	1002	951	0.95	0.0565	0.006	0.0274	0.0028	0.00365	0.000093	0.0011	0.00011	0.16953	23.49	0.6	27.5	2.8	460	110	23.49	0.6
Zircon_16	466	340	0.73	0.071	0.013	0.0349	0.0064	0.00377	0.00015	0.00121	0.00013	0.19216	24.28	0.97	34.7	6.3	1040	140	24.28	0.97
Zircon_17	767	464	0.60	0.0755	0.0058	0.0367	0.0029	0.003554	0.000071	0.00127	0.00011	0.30248	22.87	0.46	36.5	2.9	1070	110	22.87	0.46
Zircon_18	563	514	0.91	0.0667	0.0084	0.0322	0.004	0.003548	0.000086	0.00108	0.00011	0.195124	22.83	0.55	32.2	3.9	920	110	22.83	0.55
Zircon_19	300	371	1.24	0.078	0.011	0.0419	0.0055	0.00403	0.00014	0.00132	0.00012	0.264651	25.94	0.91	41.6	5.3	1230	140	25.94	0.91
Zircon_20	355	233	0.66	0.079	0.01	0.0423	0.005	0.00398	0.00013	0.00137	0.00014	0.276332	25.61	0.81	42	4.9	1220	120	25.61	0.81
Zircon_21	792	780	0.98	0.055	0.0044	0.0293	0.0026	0.003842	0.000087	0.00117	0.00011	0.2891	24.72	0.56	29.3	2.6	483	81	24.72	0.56
Zircon_22	548	548	1.00	0.0672	0.0079	0.0328	0.0038	0.00356	0.00012	0.00107	0.00013	0.14098	22.9	0.75	32.7	3.8	940	140	22.9	0.75
Zircon_24	558	465	0.83	0.0584	0.0065	0.0289	0.0031	0.003678	0.000084	0.00113	0.00011	0.212914	23.66	0.54	28.9	3.1	600	140	23.66	0.54

Zircon_25	585	467	0.80	0.0628	0.0073	0.0321	0.0038	0.0037	0.00012	0.00123	0.00012	0.17482	23.79	0.78	32	3.8	700	71	23.79	0.78
Zircon_26	214	130	0.61	0.073	0.012	0.0357	0.0066	0.00378	0.00019	0.0015	0.00021	0.18506	24.3	1.2	36.9	6.1	890	150	24.3	1.2
Zircon_30	554	256	0.46	0.0705	0.007	0.039	0.0038	0.00394	0.00013	0.00159	0.00018	0.338632	25.33	0.82	38.8	3.7	920	180	25.33	0.82
Zircon_31	1571	1499	0.95	0.0508	0.0027	0.0257	0.0015	0.003671	0.000079	0.001064	0.000087	0.29948	23.62	0.51	25.7	1.5	307	66	23.62	0.51
Zircon_33	186	153	0.82	0.073	0.012	0.0424	0.0071	0.00419	0.00014	0.00126	0.00014	0.017831	26.98	0.87	42.1	6.9	1110	170	26.98	0.87
Zircon_35	400	438	1.10	0.057	0.011	0.0267	0.0045	0.00361	0.00012	0.00117	0.00012	0.19723	23.25	0.8	26.7	4.4	610	180	23.25	0.8
Zircon_36	159	115	0.72	0.073	0.021	0.045	0.013	0.00445	0.00015	0.00154	0.00028	0.15727	28.6	0.96	44	12	1140	360	28.6	0.96
Zircon_37	605	447	0.74	0.0504	0.0072	0.0257	0.0036	0.003771	0.000098	0.00117	0.00013	0.21211	24.26	0.63	25.8	3.6	410	160	24.26	0.63
Zircon_38	534	459	0.86	0.0536	0.0099	0.0266	0.0048	0.00365	0.00017	0.00137	0.00015	0.051363	23.5	1.1	26.7	4.8	580	190	23.5	1.1
Zircon_39	631	553	0.88	0.0532	0.0057	0.0275	0.0033	0.00368	0.00011	0.001116	0.000097	0.249094	23.7	0.71	27.5	3.2	460	100	23.7	0.71
Zircon_40	489	353	0.72	0.0786	0.0091	0.0406	0.0048	0.003784	0.000091	0.00142	0.00015	0.203411	24.35	0.59	40.3	4.7	1160	190	24.35	0.59

				CORRECTED RATIOS [†,*]									CORRECTED AGES (Ma)							
Spot Name	**U (ppm) [§]**	**Th (ppm) [§]**	**Th/U**	**207Pb/206Pb**	**±2σ [*]**	**207Pb/235U**	**±2σ [*]**	**206Pb/238U**	**±2σ [*]**	**208Pb/232Th**	**±2σ [*]**	**Rho**	**206Pb/238U**	**±2σ**	**207Pb/235U**	**±2σ**	**207Pb/206Pb**	**±2σ**	**Best age (Ma)**	**±2σ**
Sample: MdCH 05																				
Z_1_Mdch005	568	1012	1.78	0.049	0.016	0.027	0.01	0.00393	0.00016	0.00118	0.00021	0.39326	25.3	1	26.6	9.6	200	280	25.3	1
Zircon_2	394	1336	3.39	0.0594	0.0095	0.0332	0.0058	0.00417	0.00014	0.00141	0.0001	0.192177	26.81	0.93	33.2	5.6	760	180	26.81	0.93
Zircon_4	353	245	0.69	0.079	0.017	0.045	0.011	0.00407	0.0002	0.00209	0.00048	0.201027	26.2	1.3	44	11	1180	280	26.2	1.3
Zircon_5	345	210	0.61	0.0603	0.0081	0.02549	0.00095	0.00409	0.00015	0.00156	0.00015	0.27632	26.28	0.99	25.56	0.94	760	130	26.28	0.99
Zircon_6	322	136	0.42	0.0872	0.0086	0.0488	0.0051	0.00407	0.00013	0.00141	0.00021	0.204	26.21	0.85	48.2	4.9	1450	120	26.21	0.85
Zircon_7	448	302	0.67	0.055	0.011	0.0298	0.0074	0.00394	0.00013	0.00121	0.00027	0.19953	25.37	0.84	29.8	7.1	430	230	25.37	0.84
Zircon_8	455	348	0.76	0.05	0.0081	0.0277	0.0047	0.00403	0.00011	0.00122	0.00014	0.077458	25.91	0.7	27.7	4.6	460	140	25.91	0.7
Zircon_9	243	182	0.75	0.103	0.014	0.0578	0.0077	0.00412	0.00015	0.00154	0.00011	0.273295	26.5	0.98	56.8	7.4	1530	210	26.5	0.98
Zircon_10	208	95	0.46	0.052	0.012	0.0305	0.0071	0.00417	0.00015	0.0008	0.00022	0.073628	26.86	0.98	30.4	6.9	710	210	26.86	0.98
Zircon_11	341	155	0.45	0.0466	0.0088	0.0251	0.005	0.00407	0.00012	0.00139	0.00013	0.14801	26.18	0.78	25.9	4.9	600	170	26.18	0.78
Zircon_12	230	94	0.41	0.0483	0.0088	0.0294	0.0056	0.00412	0.00013	0.00158	0.00019	0.48082	26.52	0.81	29.2	5.5	820	160	26.52	0.81
Zircon_13	318	135	0.42	0.057	0.016	0.0316	0.0088	0.00407	0.00017	0.00156	0.00035	0.006113	26.2	1.1	31.5	8.4	620	290	26.2	1.1
Zircon_14	423	168	0.40	0.0484	0.0053	0.0269	0.0031	0.00408	0.0001	0.00123	0.000097	0.098563	26.25	0.67	26.9	3	328	68	26.25	0.67
Zircon_15	1062	529	0.50	0.055	0.0057	0.0286	0.0035	0.00391	0.0001	0.00145	0.00012	0.19331	25.15	0.66	28.6	3.5	520	150	25.15	0.66
Zircon_16	327	173	0.53	0.0557	0.0081	0.0305	0.0044	0.003993	0.000095	0.001257	0.000099	0.164919	25.69	0.61	29.8	4.3	730	110	25.69	0.61
Zircon_18	689	274	0.40	0.0479	0.0041	0.0261	0.0026	0.00397	0.00012	0.001214	0.000082	0.31977	25.53	0.78	26.1	2.6	272	81	25.53	0.78
Zircon_20	259	101	0.39	0.0562	0.0083	0.0309	0.0047	0.00407	0.00012	0.00118	0.00014	0.193842	26.17	0.76	30.8	4.6	760	110	26.17	0.76
Zircon_21	388	195	0.50	0.095	0.01	0.0568	0.0062	0.00417	0.00014	0.00224	0.00016	0.28641	26.85	0.9	56	6	1630	170	26.85	0.9
Zircon_22	511	393	0.77	0.0621	0.0081	0.0335	0.0047	0.00405	0.00011	0.0014	0.00012	0.32618	26.03	0.73	33.3	4.6	880	150	26.03	0.73
Zircon_24	474	167	0.35	0.0735	0.0073	0.0408	0.0041	0.00406	0.00012	0.00156	0.00012	0.294125	26.11	0.78	40.5	4	959	98	26.11	0.78
Zircon_25	464	326	0.70	0.0583	0.0083	0.0322	0.0048	0.00407	0.00013	0.00137	0.00012	0.096228	26.16	0.83	32.1	4.7	630	110	26.16	0.83
Zircon_28	274	98	0.36	0.0524	0.0079	0.0284	0.0045	0.0039	0.00013	0.00145	0.00011	0.21037	25.11	0.81	28.4	4.4	680	140	25.11	0.81
Zircon_29	338	132	0.39	0.0574	0.0069	0.0292	0.0035	0.00386	0.00011	0.00126	0.00012	0.23775	24.81	0.74	29.2	3.5	580	140	24.81	0.74
Zircon_31	287	188	0.66	0.12	0.01	0.0683	0.006	0.00409	0.00014	0.00218	0.00021	0.28881	26.34	0.9	66.9	5.7	1907	94	26.34	0.9

Zircon_33	598	318	0.53	0.0524	0.0063	0.0286	0.0033	0.00393	0.00011	0.0015	0.00011	0.242578	25.31	0.7	28.7	3.3	620	130	25.31	0.7
Zircon_34	479	289	0.60	0.0748	0.0089	0.0414	0.0054	0.00393	0.00012	0.00169	0.00015	0.55662	25.26	0.8	41.1	5.2	1120	140	25.26	0.8
Zircon_35	463	328	0.71	0.084	0.012	0.0458	0.0062	0.00393	0.00013	0.00151	0.00015	0.244357	25.27	0.85	47.1	6.1	1490	260	25.27	0.85
Zircon_40	555	408	0.74	0.0934	0.0094	0.0533	0.0055	0.00414	0.00013	0.00173	0.00016	0.304304	26.63	0.85	52.6	5.4	1590	140	26.63	0.85

				CORRECTED RATIOS [†,*]									CORRECTED AGES (Ma)						Best age (Ma)	±2σ
Spot Name	**U (ppm) [§]**	**Th (ppm) [§]**	**Th/U**	**207Pb/206Pb**	**±2σ [*]**	**207Pb/235U**	**±2σ [*]**	**206Pb/238U**	**±2σ [*]**	**208Pb/232Th**	**±2σ [*]**	**Rho**	**206Pb/238U**	**±2σ**	**207Pb/235U**	**±2σ**	**207Pb/206Pb**	**±2σ**		
Sample: MicBarr 01																				
Z_05_micbar01	1046	544	0.52	0.0501	0.0044	0.0221	0.002	0.003288	0.000054	0.000997	0.00006	0.34961	21.16	0.35	22.2	2	325	76	21.16	0.35
Zircon_08	432	1050	2.43	0.0498	0.0091	0.0233	0.0041	0.003283	0.000085	0.00091	0.00011	0.147136	21.13	0.54	23.4	4.1	640	160	21.13	0.54
Zircon_09	563	535	0.95	0.0493	0.0073	0.0223	0.003	0.003328	0.000083	0.001003	0.000057	0.185387	21.42	0.53	22.3	3	420	140	21.42	0.53
Zircon_12	343	324	0.94	0.0536	0.0081	0.0231	0.0036	0.003159	0.000086	0.000902	0.000071	0.174686	20.33	0.55	23.1	3.6	520	140	20.33	0.55
Zircon_14	260	175	0.67	0.061	0.01	0.0263	0.0043	0.003303	0.000094	0.00099	0.00009	0.2015	21.26	0.6	26.3	4.2	940	160	21.26	0.6
Zircon_15	204	142	0.70	0.056	0.013	0.0257	0.0057	0.0032	0.00012	0.00107	0.0001	0.15998	20.61	0.8	25.6	5.6	630	250	20.61	0.8
Zircon_16	281	208	0.74	0.0709	0.0087	0.0322	0.004	0.00333	0.0001	0.001059	0.000087	0.241742	21.4	0.66	32.1	3.9	1070	120	21.4	0.66
Zircon_17	178	80	0.45	0.057	0.021	0.025	0.01	0.00317	0.00016	0.00119	0.00013	0.06871	20.4	1	25.3	9.7	1030	270	20.4	1
Zircon_18	396	448	1.13	0.0575	0.0064	0.026	0.003	0.003154	0.000088	0.000959	0.000065	0.241809	20.3	0.57	26	3	700	150	20.3	0.57
Zircon_19	390	249	0.64	0.059	0.015	0.0243	0.0075	0.0031	0.00016	0.00092	0.00013	0.167226	20	1	24.4	7.2	550	260	20	1
Zircon_20	220	118	0.54	0.055	0.023	0.022	0.011	0.00318	0.00015	0.00096	0.00013	0.09434	20.49	0.99	22	11	1080	290	20.49	0.99
Zircon_21	361	192	0.53	0.0506	0.0086	0.0226	0.0037	0.0032	0.00011	0.001086	0.000091	0.38415	20.61	0.7	22.7	3.7	760	170	20.61	0.7
Zircon_23	563	327	0.58	0.0496	0.0041	0.0212	0.0018	0.003205	0.000081	0.000953	0.000069	0.38357	20.63	0.52	21.3	1.8	370	94	20.63	0.52
Zircon_24	334	373	1.12	0.0479	0.007	0.0218	0.003	0.003195	0.000079	0.000945	0.000062	0.179677	20.57	0.51	21.8	3	540	110	20.57	0.51
Zircon_25	176	116	0.66	0.049	0.012	0.023	0.0049	0.00331	0.00013	0.001099	0.000091	0.24316	21.32	0.81	23	4.8	590	190	21.32	0.81
Zircon_26	818	452	0.55	0.0533	0.0058	0.0232	0.0025	0.003264	0.000081	0.001	0.000066	0.230294	21.01	0.52	23.2	2.4	630	110	21.01	0.52
Zircon_27	295	254	0.86	0.076	0.013	0.0335	0.0055	0.00313	0.00011	0.0011	0.000088	0.54964	20.15	0.71	33.3	5.4	1310	190	20.15	0.71
Zircon_28	1651	879	0.53	0.0459	0.0028	0.0209	0.0011	0.003237	0.000042	0.001015	0.000055	0.246525	20.84	0.27	21	1.1	243	75	20.84	0.27
Zircon_30	474	240	0.51	0.0526	0.0092	0.0231	0.004	0.003173	0.000085	0.001003	0.000089	0.16341	20.43	0.55	23.2	3.9	760	180	20.43	0.55
Zircon_31	845	588	0.70	0.0487	0.0066	0.0223	0.0028	0.003355	0.00007	0.00096	0.000061	0.16617	21.59	0.45	22.4	2.7	510	110	21.59	0.45
Zircon_32	633	340	0.54	0.0602	0.0074	0.027	0.0033	0.003254	0.000066	0.000984	0.00007	0.16595	20.94	0.42	27	3.2	770	130	20.94	0.42
Zircon_33	1117	555	0.50	0.0496	0.0046	0.0205	0.002	0.003101	0.000047	0.001115	0.000063	0.12042	~~19.96~~	~~0.3~~	21.5	2	243	85	19.96	0.3
Zircon_34	493	257	0.52	0.049	0.0069	0.0222	0.003	0.003144	0.000083	0.001015	0.000071	0.11453	20.23	0.53	22.3	3	560	120	20.23	0.53
Zircon_35	880	618	0.70	0.0466	0.0049	0.0204	0.002	0.003191	0.000046	0.000973	0.000062	0.076801	20.54	0.3	20.5	2	240	120	20.54	0.3
Zircon_36	648	254	0.39	0.0515	0.0056	0.0219	0.0022	0.0032	0.000062	0.00102	0.000077	0.192869	20.6	0.4	22	2.2	360	100	20.6	0.4
Zircon_37	584	254	0.43	0.0475	0.0049	0.0215	0.0019	0.003265	0.00006	0.001114	0.000071	0.207947	21.01	0.39	21.6	1.9	514	99	21.01	0.39
Zircon_39	361	341	0.94	0.085	0.012	0.0378	0.0049	0.00322	0.000095	0.001058	0.000068	0.007593	20.73	0.61	37.6	4.8	1340	100	20.73	0.61

Spot Name	U (ppm) §	Th (ppm) §	Th/U	CORRECTED RATIOS †,* 207Pb/206Pb	±2σ *	207Pb/235U	±2σ *	206Pb/238U	±2σ *	208Pb/232Th	±2σ *	Rho	CORRECTED AGES (Ma) 206Pb/238U	±2σ	207Pb/235U	±2σ	207Pb/206Pb	±2σ	Best age (Ma)	±2σ
Sample: ROCA F6																				
Zircon_2	158	73	0.46	0.118	0.027	0.021	0.005	0.001429	0.000084	0.000472	0.000087	0.04	9.2	0.54	21	4.9	1970	150	9.2	0.54
Zircon_4	269	147	0.55	0.093	0.019	0.0183	0.0037	0.001479	0.000076	0.000556	0.000086	0.32	9.53	0.49	18.4	3.6	1610	160	9.53	0.49
Zircon_10	385	231	0.60	0.097	0.011	0.017	0.0019	0.001246	0.000057	0.000419	0.000045	0.08	~~8.03~~	~~0.36~~	17.1	1.9	1440	110	8.03	0.36
Zircon_11	198	109	0.55	0.071	0.018	0.0137	0.004	0.001472	0.000082	0.000372	0.000087	0.04	9.48	0.53	13.8	3.9	1250	170	9.48	0.53
Zircon_17	486	326	0.67	0.088	0.011	0.017	0.0025	0.001412	0.000065	0.000549	0.000076	0.31	9.09	0.42	17.1	2.5	1490	120	9.09	0.42
Zircon_18	215	105	0.49	0.082	0.022	0.0163	0.004	0.001473	0.00007	0.000626	0.000081	0.19	9.49	0.45	16.3	4	1470	190	9.49	0.45
Zircon_19	181	108	0.60	0.064	0.021	0.014	0.0068	0.00157	0.0001	0.00055	0.00028	0.10	10.09	0.66	14.1	6.7	1170	380	10.09	0.66
Zircon_20	190	101	0.53	0.07	0.027	0.0153	0.0067	0.001533	0.000094	0.00059	0.00027	0.18	9.87	0.61	15.3	6.8	1130	300	9.87	0.61
Zircon_23	203	90	0.44	0.064	0.022	0.0147	0.0043	0.001514	0.000067	0.00084	0.00011	0.05	9.76	0.43	14.8	4.3	1220	250	9.76	0.43
Zircon_24	344	227	0.66	0.077	0.013	0.014	0.0024	0.001326	0.000065	0.000422	0.000082	0.29	~~8.54~~	~~0.42~~	14.1	2.4	1260	180	8.54	0.42
Zircon_25	453	411	0.91	0.076	0.016	0.0147	0.0032	0.001399	0.00007	0.000661	0.000097	0.20	9.01	0.45	14.7	3.2	1520	150	9.01	0.45

Spot Name	U (ppm) §	Th (ppm) §	Th/U	CORRECTED RATIOS †,* 207Pb/206Pb	±2σ *	207Pb/235U	±2σ *	206Pb/238U	±2σ *	208Pb/232Th	±2σ *	Rho	CORRECTED AGES (Ma) 206Pb/238U	±2σ	207Pb/235U	±2σ	207Pb/206Pb	±2σ	Best age (Ma)	±2σ
Sample: Ruiz 34b																				
Zircon_68	1269	1442	1.14	0.0739	0.0061	0.0287	0.0031	0.00284	0.000079	0.00099	0.00012	0.47417	18.25	0.51	28.8	3	1020	120	18.25	0.51
Zircon_69	145	97	0.67	0.121	0.025	0.044	0.014	0.00304	0.0002	0.00103	0.0004	0.16022	19.6	1.3	43	12	1920	160	19.6	1.3
Zircon_71	326	286	0.88	0.0455	0.0065	0.0182	0.0024	0.00287	0.0001	0.00077	0.00006	0.2211	18.47	0.65	18.3	2.4	500	100	18.47	0.65
Zircon_72	197	128	0.65	0.075	0.023	0.032	0.013	0.00304	0.00016	0.00105	0.00033	0.47081	19.6	1	32	12	1250	250	19.6	1
Zircon_73	302	335	1.11	0.128	0.018	0.054	0.0098	0.00308	0.00012	0.00115	0.0002	0.11887	19.84	0.76	53.4	9.5	2120	150	19.84	0.76
Zircon_74	284	131	0.46	0.0591	0.0099	0.0224	0.0038	0.00277	0.00011	0.00091	0.0001	0.36137	17.86	0.68	22.5	3.7	850	140	17.86	0.68
Zircon_75	259	263	1.02	0.075	0.011	0.0304	0.0043	0.00302	0.00011	0.00105	0.000091	0.25751	19.45	0.7	30.4	4.2	1070	170	19.45	0.7
Zircon_76	560	795	1.42	0.0599	0.0064	0.0257	0.0028	0.00311	0.000089	0.00118	0.000081	0.42791	20.03	0.57	25.7	2.8	710	130	20.03	0.57
Zircon_77	384	172	0.45	0.114	0.011	0.0491	0.0052	0.00297	0.00011	0.00193	0.0002	0.37496	19.12	0.72	48.6	5	1980	110	19.12	0.72
Zircon_78	163	136	0.83	0.114	0.013	0.0467	0.0051	0.003	0.00011	0.00119	0.00014	0.10562	19.28	0.72	46.2	5	1990	110	19.28	0.72
Zircon_79	137	89	0.65	0.089	0.017	0.0421	0.008	0.00333	0.00013	0.00159	0.00016	0.10823	21.44	0.83	41.7	7.7	1510	170	21.44	0.83
Zircon_80	254	225	0.89	0.076	0.023	0.031	0.012	0.0031	0.00014	0.00101	0.00027	0.00173	19.95	0.87	31	11	1070	280	19.95	0.87
Zircon_82	1857	779	0.42	0.0475	0.0029	0.0233	0.0014	0.00356	0.000083	0.00111	0.000079	0.38791	22.91	0.53	23.4	1.4	201	51	22.91	0.53
Zircon_84	818	1448	1.77	0.0468	0.005	0.0207	0.0026	0.00326	0.00023	0.00088	0.000074	0.5617	21	1.4	20.8	2.6	400	100	21	1.4
Zircon_86	393	342	0.87	0.1037	0.0069	0.042	0.0029	0.00288	0.000094	0.00127	0.000094	0.2752	18.54	0.6	41.8	2.8	1704	69	18.54	0.6
Zircon_88	426	513	1.20	0.0946	0.0095	0.0374	0.0039	0.0029	0.00008	0.00119	0.000088	0.04757	18.66	0.52	37.3	3.8	1525	98	18.66	0.52
Zircon_89	165	109	0.66	0.072	0.015	0.0303	0.0071	0.00314	0.00015	0.00102	0.00018	0.20387	20.23	0.95	30.3	6.9	1050	240	20.23	0.95
Zircon_90	236	252	1.07	0.063	0.026	0.024	0.019	0.00285	0.00023	0.0009	0.00041	0.00146	18.4	1.4	24	17	850	330	18.4	1.4
Zircon_91-2	497	630	1.27	0.125	0.013	0.0521	0.0082	0.003	0.00012	0.00134	0.00016	0.4715	19.28	0.79	51.5	7.7	2010	130	19.28	0.79
Zircon_92	554	692	1.25	0.0486	0.0079	0.0194	0.0033	0.00288	0.000087	0.00099	0.000093	0.17734	18.57	0.56	19.5	3.2	260	190	18.57	0.56

Zircon_93	301	204	0.68	0.061	0.01	0.0273	0.0053	0.00303	0.00013	0.00101	0.00018	0.38257	19.5	0.81	27.3	5.2	960	180	19.5	0.81
Zircon_94	461	362	0.79	0.0535	0.0064	0.0234	0.0029	0.00322	0.00011	0.00117	0.0001	0.27565	20.72	0.7	23.5	2.9	498	94	20.72	0.7
Zircon_97	1021	1710	1.67	0.0515	0.0094	0.0198	0.0039	0.00283	0.000076	0.00095	0.000073	0.32617	18.24	0.49	19.9	3.8	350	210	18.24	0.49
Zircon_98	331	332	1.00	0.106	0.011	0.0463	0.0056	0.00296	0.00013	0.00127	0.00016	0.60916	19.04	0.83	45.9	5.4	1790	120	19.04	0.83
Zircon_99	393	443	1.13	0.0515	0.008	0.019	0.0029	0.00282	0.000087	0.00089	0.000071	0.20198	18.17	0.56	19.1	2.9	530	140	18.17	0.56
Z_101_Ruiz34b	1171	380	0.32	0.077	0.025	0.03	0.012	0.00289	0.00013	0.00181	0.00071	0.49427	18.57	0.82	30	12	1180	280	18.57	0.82

				CORRECTED RATIOS †,*									CORRECTED AGES (Ma)						Best age (Ma)	±2σ
Spot Name	**U (ppm) §**	**Th (ppm) §**	**Th/U**	**207Pb/206Pb**	**±2σ ***	**207Pb/235U**	**±2σ ***	**206Pb/238U**	**±2σ ***	**208Pb/232Th**	**±2σ ***	**Rho**	**206Pb/238U**	**±2σ**	**207Pb/235U**	**±2σ**	**207Pb/206Pb**	**±2σ**		
Sample: Ruiz 07																				
Z_01_Ruiz07	2689	1109	0.41	0.0524	0.0024	0.0259	0.0014	0.003636	0.000083	0.00121	0.000074	0.49	23.4	0.53	25.9	1.4	330	52	23.4	0.53
Zircon_02	560	238	0.43	0.0485	0.0038	0.0255	0.0021	0.00387	0.0001	0.001189	0.000098	0.31	24.93	0.67	25.5	2.1	294	64	24.93	0.67
Zircon_04	350	159	0.45	0.0513	0.0029	0.0603	0.004	0.00885	0.00021	0.00274	0.0002	0.50	56.8	1.4	59.4	3.8	356	56	56.8	1.4
Zircon_05	661	288	0.44	0.0527	0.0045	0.0266	0.0023	0.003698	0.000097	0.001212	0.000098	0.30	23.8	0.62	26.6	2.3	490	100	23.8	0.62
Zircon_07	965	292	0.30	0.0481	0.0037	0.0242	0.0019	0.003641	0.000083	0.001238	0.000091	0.15	23.43	0.53	24.3	1.8	150	110	23.43	0.53
Zircon_09	466	217	0.47	0.055	0.012	0.0276	0.0076	0.00359	0.00014	0.00124	0.00025	0.14	23.07	0.89	27.6	7.3	540	220	23.07	0.89
Zircon_10	502	140	0.28	0.0497	0.0039	0.0257	0.0021	0.00373	0.0001	0.00123	0.0001	0.33	24.01	0.64	25.7	2.1	299	84	24.01	0.64
Zircon_11	244	163	0.67	0.0617	0.0052	0.0314	0.0027	0.003731	0.000095	0.001282	0.000091	0.30	24	0.61	31.3	2.7	738	82	24	0.61
Zircon_12	681	206	0.30	0.0482	0.0028	0.0236	0.0015	0.003585	0.000087	0.0012	0.000082	0.38	23.07	0.56	23.6	1.5	206	52	23.07	0.56
Zircon_13	541	143	0.26	0.0497	0.0038	0.0254	0.0021	0.003807	0.000095	0.00123	0.00011	0.41	24.49	0.61	25.5	2	249	76	24.49	0.61
Zircon_16	1105	498	0.45	0.0549	0.0028	0.028	0.0014	0.003665	0.000085	0.001279	0.000089	0.33	23.58	0.55	28	1.4	413	76	23.58	0.55
Zircon_20	759	268	0.35	0.0501	0.0022	0.0254	0.0013	0.003684	0.000087	0.001194	0.000082	0.46	23.7	0.56	25.4	1.3	290	51	23.7	0.56
Zircon_22	431	181	0.42	0.0654	0.003	0.0333	0.0019	0.00367	0.00011	0.00136	0.0001	0.08	23.64	0.68	33.3	1.9	836	82	23.64	0.68
Zircon_24	1280	439	0.34	0.0492	0.0022	0.0253	0.0013	0.003665	0.000083	0.001223	0.000085	0.23	23.58	0.53	25.4	1.3	197	69	23.58	0.53
Zircon_25	657	229	0.35	0.0525	0.0029	0.0255	0.0017	0.00365	0.00009	0.001184	0.000088	0.05	23.49	0.58	25.6	1.6	433	63	23.49	0.58
Zircon_26	904	432	0.48	0.0542	0.0035	0.0271	0.002	0.003658	0.000089	0.00121	0.00011	0.33	23.54	0.57	27.2	2	387	94	23.54	0.57
Z_30_Ruiz07	262	176	0.67	0.0662	0.0074	0.0334	0.0044	0.00366	0.00012	0.00118	0.00012	0.10	23.56	0.76	33.3	4.3	840	140	23.56	0.76

				CORRECTED RATIOS †,*									CORRECTED AGES (Ma)						Best age (Ma)	±2σ
Spot Name	**U (ppm) §**	**Th (ppm) §**	**Th/U**	**207Pb/206Pb**	**±2σ ***	**207Pb/235U**	**±2σ ***	**206Pb/238U**	**±2σ ***	**208Pb/232Th**	**±2σ ***	**Rho**	**206Pb/238U**	**±2σ**	**207Pb/235U**	**±2σ**	**207Pb/206Pb**	**±2σ**		
Sample: Sin 07																				
Zircon_03	462	217	0.47	0.0559	0.0043	0.037	0.0035	0.00476	0.00019	0.00156	0.00029	0.22029	30.6	1.2	36.9	3.6	435	95	30.6	1.2
Zircon_04	107	80	0.75	0.0856	0.0091	0.0584	0.0078	0.00502	0.00026	0.0018	0.0004	0.387782	32.3	1.6	57.6	7.4	1380	110	32.3	1.6
Zircon_05	405	208	0.51	0.0603	0.0044	0.0392	0.0037	0.00493	0.00021	0.00154	0.0003	0.451291	31.7	1.3	39	3.6	568	94	31.7	1.3
Zircon_06	153	97	0.63	0.084	0.0086	0.0587	0.0073	0.0051	0.00026	0.00185	0.00041	0.21422	32.8	1.6	57.8	6.9	1220	110	32.8	1.6
Zircon_08	455	239	0.53	0.0571	0.0044	0.0371	0.0039	0.00476	0.0002	0.00143	0.00028	0.27876	30.6	1.3	37	3.8	480	110	30.6	1.3
Zircon_09	133	109	0.82	0.128	0.018	0.096	0.016	0.00547	0.0003	0.00273	0.00063	0.43044	35.2	1.9	93	14	2080	140	35.2	1.9
Zircon_12	204	155	0.76	0.0646	0.0056	0.0427	0.0049	0.00493	0.00023	0.00161	0.00031	0.11588	31.7	1.5	42.4	4.8	728	98	31.7	1.5

Zircon_13	1333	784	0.59	0.0619	0.0035	0.0397	0.0031	0.00463	0.00018	0.00191	0.00034	0.43333	29.8	1.2	39.6	3	718	92	29.8	1.2
Zircon_14	63	41	0.65	0.106	0.022	0.081	0.023	0.00531	0.00038	0.00254	0.00095	0.252027	34.1	2.4	78	22	1760	230	34.1	2.4
Zircon_17	120	62	0.52	0.085	0.023	0.057	0.025	0.00506	0.00035	0.0021	0.0011	0.24816	32.5	2.3	56	22	1280	290	32.5	2.3
Zircon_18	479	274	0.57	0.1064	0.0057	0.0724	0.0062	0.00504	0.00021	0.00301	0.00056	0.13913	32.4	1.3	71	5.8	1724	66	32.4	1.3
Zircon_19	206	127	0.62	0.055	0.011	0.0369	0.0086	0.00484	0.00024	0.00152	0.00039	0.212762	31.1	1.6	36.8	8.2	570	200	31.1	1.6
Zircon_20	175	106	0.61	0.0491	0.0083	0.0334	0.006	0.00485	0.00023	0.00172	0.00029	0.263986	31.2	1.5	33.4	5.8	550	130	31.2	1.5
Zircon_21	166	100	0.60	0.128	0.013	0.093	0.012	0.00542	0.00028	0.00286	0.00086	0.6369	34.8	1.8	90	11	2050	100	34.8	1.8
Zircon_22	256	125	0.49	0.0632	0.008	0.0431	0.0069	0.00483	0.00025	0.00187	0.00046	0.079303	31.1	1.6	42.7	6.6	810	140	31.1	1.6
Zircon_23	316	162	0.51	0.0519	0.004	0.0355	0.0035	0.00489	0.00019	0.00152	0.00027	0.29872	31.4	1.2	35.3	3.4	510	110	31.4	1.2
Zircon_24	76	41	0.54	0.097	0.011	0.0688	0.0096	0.005	0.00031	0.00198	0.00043	0.36673	32.2	2	67.3	9.1	1660	100	32.2	2
Zircon_25	140	96	0.69	0.0913	0.0095	0.0635	0.0072	0.00497	0.00025	0.00189	0.00038	0.25545	32	1.6	62.4	6.8	1574	99	32	1.6
Zircon_26	234	237	1.01	0.128	0.02	0.087	0.02	0.00512	0.00032	0.00254	0.00067	0.58317	32.9	2.1	85	18	2080	180	32.9	2.1
Zircon_27	329	165	0.50	0.089	0.01	0.0591	0.0089	0.00486	0.00021	0.00237	0.00058	0.286933	31.2	1.4	58.3	8.4	1280	180	31.2	1.4
Zircon_29	219	180	0.82	0.076	0.012	0.049	0.013	0.00487	0.0003	0.00173	0.00046	0.31228	31.3	1.9	48	12	1020	170	31.3	1.9
Zircon_31	138	65	0.47	0.096	0.013	0.065	0.013	0.00508	0.00031	0.00242	0.00065	0.305118	32.7	2	64	12	1570	160	32.7	2

				CORRECTED RATIOS †,*									CORRECTED AGES (Ma)							
Spot Name	**U (ppm) §**	**Th (ppm) §**	**Th/U**	**207Pb/206Pb**	**±2σ ***	**207Pb/235U**	**±2σ ***	**206Pb/238U**	**±2σ ***	**208Pb/232Th**	**±2σ ***	**Rho**	**206Pb/238U**	**±2σ**	**207Pb/235U**	**±2σ**	**207Pb/206Pb**	**±2σ**	**Best age (Ma)**	**±2σ**
Sample: Sin 09																				
Z_01_SIN_09	372	502	1.35	0.0752	0.0075	0.0318	0.0046	0.00296	0.00024	0.00102	0.00015	0.095503	19	1.5	31.7	4.5	1190	110	19	1.5
Zircon_02	710	986	1.39	0.0524	0.0082	0.0218	0.004	0.00297	0.00022	0.0009	0.00014	0.403704	19.1	1.4	21.9	3.9	340	170	19.1	1.4
Zircon_03	710	898	1.26	0.0543	0.0043	0.0234	0.0024	0.00301	0.00023	0.001	0.00015	0.31871	19.4	1.5	23.5	2.4	409	99	19.4	1.5
Zircon_04	781	1081	1.38	0.0536	0.0049	0.0221	0.0023	0.00282	0.00022	0.00094	0.00013	0.749615	18.2	1.4	22.2	2.3	564	77	18.2	1.4
Zircon_05	563	837	1.49	0.0492	0.0044	0.0209	0.0024	0.00287	0.00022	0.00093	0.00013	0.667538	18.5	1.4	20.9	2.3	520	62	18.5	1.4
Zircon_07	1730	2642	1.53	0.1001	0.0045	0.0398	0.0035	0.00283	0.00023	0.00113	0.00016	0.31648	18.2	1.5	39.7	3.4	1598	67	18.2	1.5
Zircon_08	392	324	0.83	0.0705	0.0057	0.0287	0.0031	0.0029	0.00022	0.00093	0.00014	0.702336	18.7	1.4	28.7	3	1039	91	18.7	1.4
Zircon_10	1023	1698	1.66	0.0467	0.0038	0.0186	0.0019	0.00286	0.00021	0.00092	0.00013	0.30108	18.4	1.4	18.7	1.9	302	80	18.4	1.4
Zircon_11	576	1068	1.85	0.0581	0.0048	0.0231	0.0025	0.00285	0.00021	0.00087	0.00012	0.31248	18.3	1.4	23.1	2.5	526	93	18.3	1.4
Zircon_12	1075	1374	1.28	0.0573	0.0033	0.023	0.0024	0.00288	0.00024	0.00095	0.00013	0.44845	18.6	1.6	23	2.4	500	70	18.6	1.6
Zircon_13	1778	2999	1.69	0.0551	0.0035	0.0194	0.0017	0.00249	0.00019	0.0008	0.00011	0.870777	16	1.2	19.5	1.7	368	84	16	1.2
Zircon_14	669	655	0.98	0.0691	0.0073	0.0276	0.0035	0.00291	0.00023	0.00095	0.00016	0.62327	18.7	1.5	27.7	3.5	870	130	18.7	1.5
Zircon_15	732	1085	1.48	0.0735	0.0045	0.0308	0.0026	0.00303	0.00023	0.00106	0.00014	0.10238	19.5	1.4	30.8	2.6	1038	67	19.5	1.4
Zircon_16	597	539	0.90	0.0667	0.0056	0.0277	0.0031	0.00303	0.00023	0.00102	0.00015	0.678271	19.5	1.5	27.7	3	926	99	19.5	1.5
Zircon_17	878	1115	1.27	0.0595	0.0043	0.0233	0.0025	0.00282	0.00021	0.00089	0.00012	0.2669	18.2	1.4	23.4	2.4	639	85	18.2	1.4
Zircon_18	489	364	0.74	0.071	0.0079	0.0306	0.004	0.00313	0.00025	0.00116	0.00018	0.611022	20.1	1.6	30.6	3.9	990	120	20.1	1.6
Zircon_21	528	475	0.90	0.0541	0.005	0.0218	0.0024	0.00292	0.00022	0.00093	0.00014	0.684361	18.8	1.4	21.9	2.4	460	110	18.8	1.4
Zircon_24	605	945	1.56	0.0518	0.0041	0.0208	0.0023	0.00288	0.00022	0.00091	0.00013	0.690821	18.5	1.4	20.8	2.3	380	91	18.5	1.4
Zircon_25	687	584	0.85	0.0529	0.0043	0.0217	0.0023	0.00295	0.00022	0.00091	0.00013	0.30006	19	1.4	21.8	2.3	480	110	19	1.4
Zircon_26	488	411	0.84	0.0626	0.0069	0.0257	0.0035	0.00297	0.00024	0.00092	0.00015	0.22272	19.1	1.5	25.8	3.4	730	120	19.1	1.5

Zircon_27	626	918	1.47	0.0709	0.0055	0.0256	0.0025	0.00272	0.00021	0.00087	0.00012	0.790588	17.5	1.3	25.7	2.5	898	80	17.5	1.3
Zircon_29	1457	2143	1.47	0.0578	0.0036	0.0211	0.0018	0.0026	0.0002	0.00079	0.00012	0.19951	16.8	1.3	21.2	1.8	467	83	16.8	1.3
Zircon_31	338	290	0.86	0.0704	0.0081	0.0279	0.0044	0.00291	0.00023	0.00096	0.00016	0.034163	18.7	1.5	27.9	4.3	1000	130	18.7	1.5
Zircon_32	361	342	0.95	0.0668	0.0059	0.0262	0.0031	0.00274	0.00022	0.00088	0.00014	0.44202	17.6	1.4	26.3	3.1	910	100	17.6	1.4
Zircon_33	589	503	0.85	0.0727	0.0055	0.0285	0.003	0.00287	0.00021	0.00105	0.00016	0.695122	18.5	1.4	28.5	3	1047	75	18.5	1.4
Zircon_34	870	1371	1.58	0.0528	0.0047	0.0195	0.0023	0.0028	0.00021	0.0009	0.00012	0.63587	18	1.3	19.6	2.3	310	120	18	1.3

				CORRECTED RATIOS †,*									CORRECTED AGES (Ma)						Best age (Ma)	±2σ
Spot Name	**U (ppm) §**	**Th (ppm) §**	**Th/U**	**207Pb/206Pb**	**±2σ ***	**207Pb/235U**	**±2σ ***	**206Pb/238U**	**±2σ ***	**208Pb/232Th**	**±2σ ***	**Rho**	**206Pb/238U**	**±2σ**	**207Pb/235U**	**±2σ**	**207Pb/206Pb**	**±2σ**		
Sample: Sin 18																				
Z_01_SIN_18_009	305	163	0.48	0.06041	0.015349	0.03756	0.010103	0.00451	0.000184	0.00139	0.00007	0.15	29	1.2	37	10.0	618	157.0	28.1	1.2
Zircon_02_010	155	84	0.49	0.07424	0.010315	0.04648	0.007079	0.00454	0.000184	0.00137	0.00005	0.27	29.2	1.2	46	7.0	1048	145.6	27.7	1.2
Zircon_03_011	348	158	0.41	0.05506	0.004786	0.03349	0.003297	0.00441	0.000133	0.00138	0.00005	0.31	28.4	0.9	33	3.2	415	36.1	27.8	0.9
Zircon_04_012	464	207	0.40	0.05539	0.004788	0.03319	0.003123	0.00435	0.000118	0.00135	0.00003	0.29	28	0.8	33	3.1	428	37.0	27.4	0.8
Zircon_05_013	149	64	0.39	0.08205	0.016716	0.0524	0.011389	0.00463	0.000185	0.00138	0.00007	0.18	29.8	1.2	52	11.3	1247	254.1	27.9	1.2
Zircon_06_015	138	91	0.59	0.06191	0.010288	0.03828	0.006817	0.00448	0.000166	0.00138	0.00005	0.21	28.8	1.1	38	6.8	671	111.5	27.9	1.1
Zircon_07_016	181	137	0.68	0.06449	0.009546	0.04191	0.007033	0.00471	0.000203	0.00144	0.00005	0.26	30.3	1.3	42	7.0	758	112.2	29.2	1.3
Zircon_08_017	165	94	0.51	0.05676	0.008964	0.03556	0.006055	0.00454	0.00015	0.00141	0.00005	0.19	29.2	1.0	35	6.0	482	76.1	28.5	1.0
Zircon_09_018	148	94	0.57	0.07648	0.01698	0.04959	0.011834	0.0047	0.000186	0.00141	0.00007	0.17	30.2	1.2	49	11.7	1108	246.0	28.5	1.2
Zircon_10_019	171	126	0.66	0.06924	0.006457	0.04393	0.004345	0.00459	0.000151	0.00147	0.00009	0.33	29.5	1.0	44	4.4	906	84.5	29.7	1.0
Zircon_11_021	434	316	0.65	0.0505	0.005145	0.0321	0.003572	0.00461	0.000122	0.00145	0.00004	0.24	29.7	0.8	32	3.6	218	22.2	29.4	0.8
Zircon_12_022	264	175	0.59	0.0587	0.007062	0.03735	0.00489	0.00462	0.000136	0.00143	0.00005	0.23	29.7	0.9	37	4.8	556	66.9	28.9	0.9
Zircon_13_023	204	86	0.38	0.06196	0.021272	0.04043	0.01463	0.00473	0.000203	0.00146	0.00014	0.12	30.4	1.3	40	14.5	673	231.1	29	1.3
Zircon_14_024	283	228	0.72	0.05864	0.009465	0.03723	0.006694	0.00461	0.000185	0.00143	0.00005	0.22	29.6	1.2	37	6.7	554	89.4	28.8	1.2
Zircon_16_027	178	117	0.59	0.05886	0.007553	0.03811	0.005051	0.00469	0.000169	0.0015	0.00009	0.27	30.2	1.1	38	5.0	562	72.1	30.3	1.1

				CORRECTED RATIOS †,*									CORRECTED AGES (Ma)						Best age (Ma)	±2σ
Spot Name	**U (ppm) §**	**Th (ppm) §**	**Th/U**	**207Pb/206Pb**	**±2σ ***	**207Pb/235U**	**±2σ ***	**206Pb/238U**	**±2σ ***	**208Pb/232Th**	**±2σ ***	**Rho**	**206Pb/238U**	**±2σ**	**207Pb/235U**	**±2σ**	**207Pb/206Pb**	**±2σ**		
Sample: Sin 21																				
Z_01_SIN21_008	118	55	0.50	0.09678	0.02092	0.02889	0.008727	0.00216	0.000125	0.00063	4.19376E-05	0.19	13.9	0.8	29	9	1563	338	13.9	0.8
Zircon_02_009	120	56	0.50	0.04611	0.037643	0.01257	0.011597	0.00198	0.000143	0.00071	0.000500202	0.08	12.7	0.9	13	12	3	2	12.7	0.9
Zircon_03_010	74	26	0.37	0.08908	0.042808	0.02731	0.014797	0.00222	0.000164	0.00066	8.10817E-05	0.14	14.3	1.1	27	15	1406	676	14.3	1.1
Zircon_05_012	132	70	0.56	0.10716	0.028898	0.0298	0.010354	0.00202	0.000144	0.00058	4.1648E-05	0.20	13	0.9	30	10	1752	472	13	0.9
Zircon_06_014	100	51	0.54	0.07001	0.027408	0.02107	0.009562	0.00218	0.000125	0.00066	6.14348E-05	0.13	14.1	0.8	21	10	929	364	14.1	0.8
Zircon_07_015	133	72	0.57	0.08482	0.022414	0.0247	0.008448	0.00211	0.000144	0.00063	4.19376E-05	0.20	13.6	0.9	25	9	1311	346	13.6	0.9
Zircon_08_016	103	46	0.47	0.10028	0.021681	0.03136	0.009486	0.00227	0.000184	0.00066	4.21217E-05	0.27	14.6	1.2	31	9	1629	352	14.6	1.2
Zircon_10_018	100	43	0.45	0.06661	0.037785	0.02013	0.012579	0.00219	0.000164	0.00067	0.000180498	0.12	14.1	1.1	20	12	826	469	14.1	1.1
Zircon_12_021	94	39	0.44	0.11778	0.048393	0.03662	0.017568	0.00225	0.000164	0.00065	8.10494E-05	0.15	14.5	1.1	37	18	1923	790	14.5	1.1

Zircon_14_023	127	66	0.56	0.11433	0.030019	0.03195	0.010775	0.00203	0.000144	0.00058	4.1648E-05	0.21	13.1	0.9	32	11	1869	491	13.1	0.9
Zircon_15_024	128	70	0.59	0.09113	0.068625	0.02546	0.021853	0.00203	0.000262	0.0006	0.0001804	0.15	13	1.7	26	22	1449	1091	13	1.7
Zircon_16_026	63	43	0.73	0.10996	0.038974	0.03463	0.014435	0.00228	0.000203	0.00066	6.14348E-05	0.21	14.7	1.3	35	15	1799	638	14.7	1.3
Zircon_19_029	119	71	0.63	0.09098	0.030172	0.02593	0.010163	0.00207	0.000144	0.00061	4.18191E-05	0.18	13.3	0.9	26	10	1446	480	13.3	0.9
Zircon_20_030	125	68	0.58	0.09166	0.026274	0.02681	0.009447	0.00212	0.000125	0.00063	4.19376E-05	0.17	13.7	0.8	27	10	1460	419	13.7	0.8
Zircon_22_033	137	69	0.54	0.06973	0.02067	0.02069	0.007362	0.00215	0.000106	0.00065	4.20595E-05	0.14	13.9	0.7	21	7	921	273	13.9	0.7
Zircon_04_011	121	59	0.52	0.06742	0.039845	0.01939	0.012734	0.00209	0.000203	0.00064	0.000180455	0.15	13.4	1.3	19	12	851	503	13.4	1.3

				CORRECTED RATIOS [†,*]									CORRECTED AGES (Ma)						Best age (Ma)	±2σ
Spot Name	**U (ppm) [§]**	**Th (ppm) [§]**	**Th/U**	**207Pb/206Pb**	**±2σ [*]**	**207Pb/235U**	**±2σ [*]**	**206Pb/238U**	**±2σ [*]**	**208Pb/232Th**	**±2σ [*]**	**Rho**	**206Pb/238U**	**±2σ**	**207Pb/235U**	**±2σ**	**207Pb/206Pb**	**±2σ**		
Sample: Sin 39																				
Z_01_SIN39	2296	4938	2.15	0.0525	0.0026	0.0244	0.0015	0.003401	0.000075	0.001039	5.4E-05	0.36	21.89	0.5	24.4	1.5	324	56	21.89	0.48
Zircon_02	1987	1840	0.93	0.0525	0.0036	0.0249	0.0024	0.003432	0.000083	0.001098	6.9E-05	0.35	22.08	0.5	25	2.3	330	110	22.08	0.53
Zircon_03	1409	3430	2.43	0.0589	0.0033	0.0281	0.0019	0.00349	0.000087	0.001094	5.8E-05	0.37	22.46	0.6	28.1	1.7	563	74	22.46	0.56
Zircon_06	1361	1960	1.44	0.0627	0.0059	0.0288	0.0043	0.003364	0.000092	0.001176	7.1E-05	0.18	21.65	0.6	28.8	4.2	700	120	21.65	0.59
Zircon_07	2813	4404	1.57	0.0598	0.0032	0.0278	0.0016	0.00334	0.00007	0.001118	5.7E-05	0.36	21.5	0.5	27.8	1.6	600	100	21.5	0.45
Zircon_08	2982	4327	1.45	0.0509	0.0037	0.0227	0.0019	0.003279	0.000067	0.001064	5.9E-05	0.24	21.1	0.4	22.8	1.8	240	120	21.1	0.43
Zircon_10	2230	4825	2.16	0.0474	0.0026	0.022	0.0014	0.003349	0.000078	0.001059	5.5E-05	0.07	21.55	0.5	22	1.3	133	82	21.55	0.5
Zircon_11	2470	4405	1.78	0.0571	0.0029	0.0252	0.0016	0.00327	0.000075	0.001036	5.5E-05	0.39	21.04	0.5	25.3	1.6	459	76	21.04	0.48
Zircon_12	4419	8919	2.02	0.0483	0.002	0.0219	0.0012	0.003339	0.000065	0.00103	5.2E-05	0.23	21.49	0.4	22	1.2	140	50	21.49	0.42
Zircon_16	2137	2341	1.1	0.0502	0.0029	0.0227	0.0018	0.003323	0.000084	0.001102	6.2E-05	0.15	21.38	0.5	22.8	1.8	188	95	21.38	0.54
Zircon_17	1778	4107	2.31	0.0486	0.0031	0.0229	0.0017	0.003425	0.000083	0.001092	5.7E-05	0.44	22.04	0.5	23	1.6	172	81	22.04	0.53
Zircon_18	2590	3269	1.26	0.0504	0.0025	0.0231	0.0014	0.003327	0.000082	0.001064	5.5E-05	0.47	21.41	0.5	23.1	1.4	244	59	21.41	0.52
Zircon_20	994	1309	1.32	0.0508	0.0032	0.0239	0.0017	0.003397	0.000084	0.001064	6.2E-05	0.27	21.86	0.5	24	1.7	253	58	21.86	0.54
Zircon_22	2998	5080	1.69	0.0481	0.0025	0.0219	0.0014	0.003342	0.000066	0.001102	5.5E-05	0.31	21.51	0.4	22	1.3	138	69	21.51	0.42
Zircon_23	2299	4393	1.91	0.0554	0.0025	0.026	0.0015	0.00335	0.000075	0.001043	5.3E-05	0.59	21.56	0.5	26.1	1.5	423	70	21.56	0.48
Zircon_24	1947	2463	1.27	0.0499	0.0026	0.0235	0.0015	0.003373	0.000067	0.00109	5.7E-05	0.23	21.71	0.4	23.6	1.5	225	64	21.71	0.43
Zircon_27	1610	2300	1.43	0.0546	0.0025	0.0252	0.0013	0.003376	0.000073	0.001059	5.4E-05	0.64	21.73	0.5	25.3	1.3	366	68	21.73	0.47
Zircon_28	2368	3313	1.4	0.051	0.0026	0.0237	0.0015	0.003338	0.000076	0.001045	5.5E-05	0.21	21.48	0.5	23.7	1.5	335	65	21.48	0.49
Zircon_31	720	914	1.27	0.0562	0.0029	0.0265	0.0021	0.00345	0.00024	0.001099	5.9E-05	0.24	22.2	1.6	26.5	2.1	377	59	22.2	1.6
Zircon_32	2172	2426	1.12	0.0517	0.0026	0.0234	0.0015	0.003305	0.000076	0.001092	5.8E-05	0.33	21.27	0.5	23.5	1.4	252	69	21.27	0.49
Zircon_33	571	944	1.65	0.0549	0.0069	0.0266	0.0043	0.0035	0.00011	0.001167	7.7E-05	0.75	22.53	0.7	26.6	4.2	440	160	22.53	0.68
Zircon_34	1870	2815	1.51	0.05	0.0024	0.0231	0.0015	0.003332	0.000076	0.001105	6.3E-05	0.35	21.44	0.5	23.2	1.5	209	66	21.44	0.49
Zircon_35	2495	4301	1.72	0.0513	0.0024	0.0237	0.0013	0.00337	0.000072	0.00105	5.3E-05	0.39	21.69	0.5	23.8	1.2	280	51	21.69	0.46
Zircon_36	4248	9091	2.14	0.0495	0.0021	0.0228	0.0012	0.003337	0.000064	0.001034	5.2E-05	0.22	21.48	0.4	22.9	1.2	194	50	21.48	0.41
Zircon_37	1090	1912	1.75	0.0575	0.0052	0.0266	0.004	0.003501	0.000098	0.001181	7.1E-05	0.3	22.53	0.6	26.6	3.9	530	140	22.53	0.63

Spot Name	U (ppm) §	Th (ppm) §	Th/U	CORRECTED RATIOS †,* 207Pb/206Pb	±2σ *	207Pb/235U	±2σ *	206Pb/238U	±2σ *	208Pb/232Th	±2σ *	Rho	CORRECTED AGES (Ma) 206Pb/238U	±2σ	207Pb/235U	±2σ	207Pb/206Pb	±2σ	Best age (Ma)	±2σ
Sample: Sin 05																				
Z_01_SIN-05	69	31	0.45	0.089	0.013	0.0625	0.0094	0.00523	0.00031	0.00192	0.0002	0.24732	33.7	2	61.3	9	1400	170	33.7	2
Zircon_02	150	95	0.63	0.088	0.0064	0.0611	0.0055	0.00511	0.00026	0.00227	0.00015	0.565238	32.9	1.7	60.2	5.3	1415	96	32.9	1.7
Zircon_03	260	118	0.45	0.061	0.02	0.041	0.018	0.00481	0.00032	0.00199	0.00084	0.082681	30.9	2	41	17	720	300	30.9	2
Zircon_04	363	207	0.57	0.059	0.0037	0.0389	0.0031	0.00482	0.00024	0.00162	0.00011	0.624816	31	1.5	38.7	3.1	626	66	31	1.5
Zircon_05	361	408	1.13	0.047	0.052	0.031	0.071	0.00481	0.00067	0.0016	0.0018	0.15554	30.9	4.3	31	56	360	470	30.9	4.3
Zircon_06	47	39	0.83	0.094	0.015	0.073	0.011	0.00531	0.00033	0.00201	0.0002	0.412429	34.2	2.1	70	11	1660	210	34.2	2.1
Zircon_07	161	79	0.49	0.057	0.0069	0.0399	0.0058	0.0054	0.00028	0.00176	0.00022	0.17102	34.7	1.8	39.6	5.6	600	150	34.7	1.8
Zircon_08	179	85	0.47	0.0875	0.0069	0.059	0.0055	0.00517	0.00028	0.00241	0.00017	0.580974	33.2	1.8	58.2	5.2	1310	100	33.2	1.8
Zircon_09	686	286	0.42	0.051	0.0032	0.0339	0.0028	0.00481	0.00023	0.001496	0.000091	0.578928	30.9	1.5	33.9	2.7	356	86	30.9	1.5
Zircon_10	140	70	0.50	0.0486	0.0064	0.0322	0.0047	0.00476	0.00027	0.00148	0.00013	0.388611	30.6	1.7	32.2	4.6	580	140	30.6	1.7
Zircon_11	828	702	0.85	0.0495	0.0028	0.0333	0.0029	0.00493	0.00025	0.00159	0.000096	0.58229	31.7	1.6	33.2	2.8	346	54	31.7	1.6
Zircon_12	275	120	0.44	0.0664	0.0064	0.0441	0.006	0.00473	0.00029	0.00193	0.00018	0.450634	30.4	1.9	43.8	5.8	810	140	30.4	1.9
Zircon_13	96	63	0.66	0.0786	0.0098	0.054	0.0076	0.00509	0.0003	0.00182	0.00015	0.418778	32.7	1.9	53.2	7.3	1260	120	32.7	1.9
Zircon_14	193	129	0.67	0.0731	0.0078	0.0479	0.0061	0.00479	0.00028	0.0015	0.00014	0.459016	30.8	1.8	47.5	5.9	1020	160	30.8	1.8
Zircon_15	115	88	0.77	0.095	0.031	0.067	0.036	0.00511	0.00045	0.00196	0.00091	0.163894	32.8	2.9	66	30	1530	240	32.8	2.9
Zircon_17	218	100	0.46	0.0648	0.0053	0.0419	0.0045	0.00473	0.00025	0.0015	0.00012	0.492131	30.4	1.6	41.7	4.4	869	90	30.4	1.6
Zircon_18	284	111	0.39	0.0745	0.005	0.0485	0.0041	0.00481	0.00025	0.00194	0.00014	0.614827	30.9	1.6	48	4	1010	100	30.9	1.6
Zircon_19	35	20	0.57	0.106	0.055	0.073	0.068	0.00536	0.00064	0.002	0.0014	0.50941	34.5	4.1	71	54	1650	420	34.5	4.1
Zircon_20	91	43	0.47	0.064	0.017	0.043	0.016	0.00488	0.00033	0.00171	0.00026	0.41426	31.4	2.1	42	15	890	280	31.4	2.1
Zircon_21	104	24	0.23	0.069	0.0065	0.0464	0.0053	0.00493	0.00028	0.00166	0.00017	0.063001	31.7	1.8	46	5.2	996	98	31.7	1.8
Zircon_22	90	31	0.34	0.0674	0.0073	0.0455	0.0059	0.00488	0.00029	0.00163	0.00016	0.088277	31.4	1.9	45.1	5.8	940	120	31.4	1.9
Zircon_23	120	52	0.43	0.092	0.019	0.063	0.019	0.00503	0.00032	0.00202	0.00048	0.210945	32.4	2.1	62	17	1480	180	32.4	2.1
Zircon_24	240	92	0.38	0.0618	0.0046	0.0388	0.0039	0.00482	0.00024	0.00156	0.00013	0.25625	31	1.6	38.7	3.8	657	72	31	1.6
Zircon_25	154	54	0.35	0.106	0.035	0.074	0.039	0.00545	0.00042	0.0028	0.0011	0.146224	35	2.7	73	34	1630	260	35	2.7
Zircon_26	147	73	0.50	0.0568	0.0076	0.0386	0.0055	0.00494	0.00025	0.00156	0.00012	0.355171	31.8	1.6	38.4	5.3	630	130	31.8	1.6
Zircon_27	87	108	1.24	0.123	0.04	0.087	0.093	0.00491	0.00069	0.0022	0.00045	0.34689	31.5	4.4	85	57	2000	120	31.5	4.4
Zircon_28	182	105	0.58	0.0609	0.0041	0.041	0.004	0.00485	0.00025	0.00182	0.00013	0.24693	31.2	1.6	40.8	3.9	644	85	31.2	1.6
Zircon_29	611	401	0.66	0.0607	0.0027	0.0399	0.0029	0.00471	0.00023	0.00165	0.0001	0.027431	30.3	1.5	39.7	2.9	640	56	30.3	1.5
Zircon_30	176	107	0.61	0.059	0.0057	0.0407	0.0048	0.00496	0.00027	0.00163	0.00013	0.461568	31.9	1.8	40.4	4.7	652	73	31.9	1.8
Zircon_31	277	191	0.69	0.0499	0.0079	0.0326	0.0064	0.00477	0.00025	0.00165	0.00015	0.266968	30.7	1.6	32.6	6.2	440	160	30.7	1.6
Zircon_32	949	575	0.61	0.0581	0.0035	0.0383	0.0034	0.00476	0.00023	0.00165	0.00012	0.045109	30.6	1.5	38.2	3.3	486	80	30.6	1.5
Zircon_33	7030	2905	0.41	0.0587	0.0035	0.0451	0.0042	0.00556	0.00027	0.00234	0.00022	0.6066	35.7	1.7	44.8	4.1	550	120	35.7	1.7
Zircon_34	201	127	0.63	0.064	0.011	0.0434	0.0083	0.00485	0.00029	0.00167	0.0002	0.043091	31.2	1.8	43	8	1150	150	31.2	1.8
Zircon_35	131	109	0.83	0.079	0.032	0.052	0.033	0.00487	0.00047	0.0016	0.0012	0.24758	31.3	3	52	28	1330	310	31.3	3

§: U and Th concentrations are calculated employing the NIST 610 glass as external standard.

†: 2σ uncertainties propagated according to Paton, C., Woodhead, J. D., Hellstrom, J. C., Hergt, J. M., Greig, A., and Maas, R., 2010, Improved laser ablation U-Pb zircon geochronology through robust downhole fractionation correction. Geochemistry, Geophysics, Geosystems, vol., 11, no. 3.

*: $^{207}Pb/^{206}Pb$ ratios, ages and errors are calculated according to Petrus, J. A., and Kamber, B. S., 2012, VizualAge: A Novel Approach to Laser Ablation ICP-MS U-Pb Geochronology Data Reduction. Geostandards and Geoanalytical Research, vol. 36, no. 3, pags 247-270. Analyzed spot is 23 micrometer, using an analytical protocol modified from Solari, L. A., Gómez-Tuena, A., Bernal, J. P., Pérez-Arvizu, O., and Tanner, M., 2010, U-Pb Zircon Geochronology with an Integrated LA-ICP-MS Microanalytical Workstation: Achievements in Precision and Accuracy. Geostandards and Geoanalytical Research, vol. 34, no. 1, pags 5-18. Data measured employing a Thermo X-series quadrupole ICPMS coupled to a Resonetics, Resolution M050 excimer laser workstation. N.D.: Not determined.

Discussion of ^{40}Ar-^{39}Ar dating experiments

A brief discussion of the ^{40}Ar-^{39}Ar results is given here for each simple, providing basis for the selection of the preferred age reported in the text (i.e. isochron or plateau). The samples are reported in the same order as in Table 1 (oldest to newest).

ES 10 basaltic andesite
Two laser step-heating experiments were performed on plagioclase with 6 and 8 fractions collected. Well defined plateaux are displayed in both experiments. The plateau age of 34.17 ± 0.31 Ma (MSWD = 0.53) was calculated with 5 consecutive fractions representing 86.66% of the ^{39}Ar released. The preferred age for this simple is the isochron age 33.82 ± 0.28 Ma using the combined fractions of the two experiments (MSWD = 1.1 for n =14). The isochron age is slightly younger than the plateau age because the $(^{40}Ar/^{36}Ar)_i$ = 298 ± 2 is slightly above the atmospheric value; for this reason the isochron age was selected as the best age estimate for sample ES 10.

HUA 1 crystal rich ignimbrite
Two laser step-heating experiments were performed on biotite. The two experiments yielded reproducible results. The plateau age of 26.48 ± 0.15 Ma was obtained from the weighted mean of the last four fractions of the second experiment, which gave a MSWD = 0.18 for 96.61% of the ^{39}Ar released. The isochron calculated with the fractions representing the bulk of the ^{39}Ar from both experiments (92.19% and 86.83% respectively) yields an age of 26.51 ± 0.69 Ma with a $(^{40}Ar/^{36}Ar)_i$ = 295 ± 69, and an MSWD = 0.32 for n = 5, in very good agreement with the plateau age. We chose the plateau age of 26.48 ± 0.15 Ma as our best estimate for the age of this sample.

TS 16 basalt
A plagioclase concentrate was laser step-heated. Six fractions were collected. Because this plagioclase is calcium-rich but has very low K content we obtained a low precision results. Applying 12 watts of laser power over 50% of the ^{39}Ar was released in the last fraction collected. The individual ages for the 6 fractions define a plateau age of 24.38 ± 0.75 Ma (MSWD = 0.54). The plateau age is practically identical to the isochron age of 24.43 ± 0.87 Ma obtained using all the data points.

HUA 2 lithic ignimbrite
Two laser step-heating experiments were performed on a biotite concentrate. No age information could be obtained for the last fraction of the first experiment because the signal of mass 36 was not measured correctly. The data of this experiment are presented in the Electronic Supplementary Material, only for illustrative purpose. For the second experiment a broad, well defined plateau age of 22.99 ± 0.14 Ma (MSWD = 0.63), was obtained for 94% of the ^{39}Ar released in five steps. Combining the six fractions, released with more than 1.5 Watts of laser power from both experiments, an isochron age of 23.19 ± 0.27 Ma was obtained. The straight line is well defined with MSWD = 0.35, but due to the point distribution, the y-intercept is poorly constrained with $(^{40}Ar/^{36}Ar)_i$ = 282 ± 21. The isochron and plateau ages are statistically indistinguishable but we favour the more precise plateau age of 22.99 ± 0.14 Ma for this sample.

ESC 7 basaltic andesite

Two step-heating experiments were performed using the temperature controlled Ta-furnace on ~0.2 and ~0.3 gr. of plagioclase. The two experiments yielded reproducible results. Because the plagioclase had low K content the ages obtained were not very precise. For the second experiment a well defined plateau age of 22.39 ± 2.56 Ma (MSWD < 0.01 for n = 5) was obtained. This was calculated with the fractions released between 700 and 1350ºC, which represent 97.2% of the ^{39}Ar released. The plateau age is statistically indistinguishable from the isochron age of 22.35 ± 2.73 Ma (MSWD = 0.11 for n = 11), obtained combining the fractions of the two experiments. We favour the plateau age of 22.39 ± 2.56 Ma because os its slightly lower error.

MdCH10 dacite

A plagioclase concentrate was laser step-heated. The two experiments performed yielded reproducible results. Because the plagioclase had very low K content, the experiments were not detailed. Due to analytical dificulties, on three of the low temperature fractions, mass 36 was not measured correctly; no age information could be obtained from them. However, since the bulk of the ^{39}Ar was released at high temperature, the low temperature fractions were not significant. With the fractions measured correctly a well-defined plateau age of 22.15 ± 0.93 Ma (MSWD = 0.59 for n= 3), was obtained for 88.50% of the ^{39}Ar released. The isochron age of 22.51 ± 0.90 Ma, calculated with the combined fractions of the two experiments (MSWD = 0.73 for n = 6) is the preferred age for dacite MdCH10.

ORO 2 ignimbrite

A laser step-heating experiment was performed on a biotite concentrate. The biotite displays a flat age spectrum with a wide plateau of 20.88 ± 0.12 Ma (MSWD = 0.85 for n = 6) for 99.73% of the ^{39}Ar released. In the ^{36}Ar/^{40}Ar versus ^{39}Ar/^{40}Ar correlation diagram, the bulk of the ^{39}Ar released in the last four fractions define a straight line (MSWD = 0.19) with a $(^{40}Ar/^{36}Ar)_i$ = 325 ± 59, suggesting the presence of some excess argon. Therefore we chose the isochron age of 20.74 ± 0.44 Ma as our best estimate for this sample.

MdCH 06 rhyolite

Two laser step-heating experiments were performed on a plagioclase concentrate. During the first experiment, more than 50% of the ^{39}Ar was released in one fraction. To insure that this result was realiable, a different heating schedule was chosen for the second experiment, in which we obtained a wide plateau age of 20.54 ± 0.79 Ma (MSWD = 0.45 for n =4) representing 78.72% of the ^{39}Ar released. The age spectra display a small saddle suggesting the presence of excess argon. The combined data of the two experiments constrain an isochron age of 20.25 ± 0.64 Ma (MSWD = 0.98 for n= 22), with $(^{40}Ar/^{36}Ar)_i$ = 304 ± 2 confirming the presence of excess argon. For this reason, we favour the isochron age of 20.25 ± 0.64 Ma for this sample.

HUA 5 ash flow tuff

Two laser step-heating experiments were performed on a plagioclase concentrate with reproducible results. In the two experiments, the bulk of the ^{39}Ar was released in the last fraction. The weighted mean of two fractions from the second experiment yielded an age of 18.99 ± 0.27 Ma (MSWD = 0.09 for 91.75% of ^{39}Ar released), in complete agreement with the isochron age of 18.98 ± 0.30 Ma (MSWD = 1.57 for n=5) obtained with the combined the data of the two experiments. The preferred age is the isochron age because combined data from the two experiments.

MdCH 09 olivine basalt

A plagioclase concentrate from this sample was laser step-heated obtaining reproducible results. The plagioclase analyzed is Ca-rich, with Ca/K ~30 and a high temperature release of ^{39}Ar. For this reason it needed more than 8 watts of laser power to release the bulk of ^{39}Ar. From the second experiment, a plateau age of 18.34 ± 0.39 Ma is defined by the last five fractions, which represent 72.06% of the ^{39}Ar released. The same age was obtained plotting the data of the two experiments in the $^{36}Ar/^{40}Ar$ versus $^{39}Ar/^{40}Ar$ correlation diagram. An isochron age of 18.32 ± 0.40 Ma was calculated with an MSWD = 1.6 for the 11 points fitted. The plateau and isochron ages obtained are statistically indistinguishable but we favour the isochron age as our best estimate because it incorporates the data of the two experiments.

RUIZ 16 rhyolite

Two laser step-heating experiments were performed on plagioclase concentrate yielding reproducible results and almost flat age spectra. The 7 fractions collected in the second experiment fullfill the criteria to calculate a plateau age. The weigthted mean of their individual ages yields a plateau age of 17.76 ± 0.12 Ma (MSWD = 0.5). The plateau age is statistically indistinguishable from the isochron age of 17.91 ± 0.20 Ma, obtained with the combined fractions of the two experiments. The isochron age is taken as the best estimate for this rhyolite since it contains the data of the two experiments.

RUIZ 34B rhyolite

A biotite concentrate was laser step-heated. The experiment yielded a flat age spectra, with a broad plateau defined by seven fractions with 86.74% of the ^{39}Ar released and an age of 17.82 ± 0.07 Ma. Because the best straight line (MSWD = 0.79) defined by 9 out of the 12 fractions collected yields a $(^{40}Ar/^{36}Ar)_i$ = 357 ± 40, the isochron age of 17.57 ± 0.19 Ma is taken as the preferred age for this sample.

PER 12 basaltic andesite

One gram of groundmass concentrate was step-heated with the temperature controlled Ta-furnace and the argon isotopes were analized with the MS-10 mass spectrometer. The ^{39}Ar was released evenly over the 10 fractions collected between 500 and 1350°C. Six fractions representing 62.65% of the ^{39}Ar released fulfill the criteria to calculate a plateau. The weighted mean of the individual ages yields a plateau of 17.78 ± 0.37 Ma. The age spectrum displays a descending staircase pattern, which may be indicative of excess argon. The data were plotted in the $^{36}Ar/^{40}Ar$ versus $^{39}Ar/^{40}Ar$ correlation diagram, where

7 consecutive fractions representing more than 88% of the ^{39}Ar released, define a straight line with a y-intercept confirming the presence of excess argon with an $(^{40}Ar/^{36}Ar)_i$ = 335 ± 19. The x-intercept defines an isochron age of 17.42 ± 0.77 Ma, which is our preferred age given that the presence of excess argon was confirmed.

MdCH 05 rhyolite

For this sample we carried out a laser step heating experiment on groundmass collecting a total of 19 fractions. The first third of the ^{39}Ar released yielded an age spectrum with a decreasing staircase pattern. The remaining fractions define a plateau age of 17.41 ± 0.07 Ma with the ^{39}Ar evenly distributed in 14 fractions. The plateau fractions (identified with letters f to s) align in the $^{36}Ar/^{40}Ar$ versus $^{39}Ar/^{40}Ar$ correlation diagram defining an isochron age of 17.52 ± 0.24. However the points are

narrowly distributed close to the x-axis, so that the y-intercept (292 ± 9) is not well constrained. Because of this we favour the well-defined plateau age of 17.41 ± 0.07 Ma for this rhyolite.

SIN 25 basalt

Twelve fractions were collected in the laser step-heating experiment performed on whole rock. The sample displays an almost flat age spectrum with a slight negative slope. Ten consecutive fractions representing more than 98% of the ^{39}Ar released fulfill the criteria to calculate the plateau age of 14.31 ± 0.11 Ma. However the plateau segment displays variable composition in the $^{37}Ar_{Ca}/^{39}Ar_K$ diagram. An iscohron age of 14.01 ± 0.23 Ma was calculated with the last 9 fractions (MSWD = 0.82). The $(^{40}Ar/^{36}Ar)_i$ = 315 ± 11, obtained in the correlation diagram indicates excess argon and explains the subtle negative slope displayed in the age spectrum. Therefore our prefered age for this basalt is the isochron age.

SIN 15 basalt

A groundmass concentrate was laser step-heated. The weighted mean of the individual ages of 7 consecutive fractions representing 94.03% of the ^{39}Ar released yield a 13.84 ± 0.15 Ma plateau age. However, the older ages for the fractions released at low temperature suggest the presence of excess argon. This is confirmed by the $(^{40}Ar/^{36}Ar)_i$ = 304 ± 4 calculated from the y-intercept of the straight line defined with all the data in the $^{36}Ar/^{40}Ar$ vs $^{39}Ar/^{40}Ar$ correlation diagram. For this reason we favour the isochron age of 13.62 ± 0.17 Ma for this basalt.

DANA 46a basalt

This whole rock sample was analyzed in detail. The first set of experiments, from irradiation labeled CIC 41A, consisted of a step-heating experiment with the temperature controlled Ta-furnace and 8 one-step laser fusion experiments. For the step-heating experiment the argon isotopes were measured with the MS-10 mass spectrometer while the argon isotopes of the laser fusion experiments were measured with the VG5400 mass spectrometer. A flat age spectrum was obtained yielding a plateau age of 11.97 ± 0.30 Ma, for 100% of the ^{39}Ar released in five fractions. The results from the one-step experiments were remarkably similar and yielded statistically undistinguishable ages. The sample was irradiated again and another set of one-step laser fusion runs was performed plus a laser-step-heating experiment. The second group of experiments yielded reproducible results in agreement with the first data set. The weighted mean of all the one-step laser fusions yields an age of 11.59 ± 0.31 Ma (MSWD = 0.89 for n=13). The 21 data points from all the experiments are well distributed and aligned in the $^{36}Ar/^{40}Ar$ versus $^{39}Ar/^{40}Ar$ correlation diagram. The well defined straight line (MSWD = 0.50) yields a $(^{40}Ar/^{36}Ar)_i$ = 291 ± 3 and an isochron age of 11.96 ± 0.26 Ma. This group of experiments is a good example of the reproducibility of results produced at CICESE's Geochronology Laboratory applying different heating techniques and two mass spectrometers. We favour the 11.96 ± 0.26 Ma isochron age as the best estimate for basalt DANA 46a, because it incorporates the data from all the experiments performed with this sample.

ROCA 3J 5 lithic tuff

Two laser step-heating experiments were performed on feldspar concentrate yielding reproducible and flat age spectra. The six fractions collected in the second experiment yield individual ages statistically indistinguishable within 1σ errors, defining a plateau age of 11.70 ± 0.07 Ma. The same age was obtained combining the data from the two experiments, in the $^{36}Ar/^{40}Ar$ versus $^{39}Ar/^{40}Ar$ correlation diagram: 11.69 ± 0.08 Ma. We chose the more precise plateau age as the best estimate for this sample.

LM 2 dacite

Two laser step-heating experiments were performed on a groundmass concentrate. The pronounced and reproducible saddle shaped age spectra obtained suggests the presence of excess argon. With the purpose of improving the results, a different heating schedule was selected in the second experiment. The weighted mean of the individual ages of the fractions that define the base of the saddle yield an age of 13.38 ± 0.61 Ma. This U-shaped age spectra is also displayed in the $^{37}Ar_{Ca}/^{39}Ar_K$ diagram indicating a homogeneous composition in the calcium and potasium composition for the fractions collected at intermediate laser power, that is between 0.5 and 4 Watts. The data of the two experiments were plotted in the $^{36}Ar/^{40}Ar$ versus $^{39}Ar/^{40}Ar$ correlation diagram. The 8 fractions with $^{37}Ar_{Ca}/^{39}Ar_K$ values ≤ 0.6 define a straight line with $(^{40}Ar/^{36}Ar)_i = 400 \pm 10$, corroborating the presence of excess argon. Therefore we prefer the isochron age of 11.34 ± 0.79 Ma as the best age estimate for this dacite.

ROCA 24J 33 microdiorite

A hornblende concentrate was laser step-heated. The sample displays a perturbed age spectrum with a pronounced saddle shape, which suggests the presence of excess argon. The weighted mean of the last four fractions yields an age of 12.14 ± 0.34 Ma. These fractions represent 66.40% of the ^{39}Ar released and have variable values of $^{37}Ar_{Ca}/^{39}Ar_K$, suggesting inhomogeneous composition for the hornblende. The data are very well distributed and aligned in the $^{36}Ar/^{40}Ar$ versus $^{39}Ar/^{40}Ar$ correlation diagram. The straight line defined by the data intercepts the y-axis at $(^{40}Ar/^{36}Ar)_i = 313 \pm 4$, confirming the presence of excess argon. For this reason, the isochron age of 11.29 ± 0.37 Ma is our preferred age for this sample.

PER 8 basaltic andesite

One laser step-heating experiment was performed on a groundmass concentrate. Only five fractions were collected, with the bulk of the ^{39}Ar released in the last three fractions. The weighted mean of the individual ages of these three fractions yielded a 10.94 ± 0.23 Ma age. The data aligns in the $^{36}Ar/^{40}Ar$ versus $^{39}Ar/^{40}Ar$ correlation diagram defining a $(^{40}Ar/^{36}Ar)_i$ below the atmospheric value of 295.5. Since the data do not plot close to the x-axis, the abcissa intercept is not well constrained. For this reason we favour the weighted mean age of 10.94 ± 0.23 Ma, calculated with the individual ages of three fractions representing 84.57% of the ^{39}Ar released.

SC 3 mafic dike

Two laser step-heating experiments were performed on a plagioclase. The sample yielded a pronounced saddle-shaped age spectra, typical of excess argon and was also characterized by low content of radiogenic ^{40}Ar. On the basis of the results of the first experiment, a more suitable heating schedule was selected for the second experiment. This allowed us to obtain an age of 10.89 ± 0.52 Ma, using the two fractions (representing 30.61% of the ^{39}Ar released) that define the base of the saddle. We have confidence in this age, because the combined data of the two experiments, when plotted in the $^{36}Ar/^{40}Ar$ vs $^{39}Ar/^{40}Ar$ correlation diagram yielded a not so precise, but similar, age of 10.74 ± 2.59 Ma. Additionally the $(^{40}Ar/^{36}Ar)_i = 322 \pm 13$, confirms the presence of excess argon in the sample. We therefore prefer the 10.89 ± 0.52 Ma age as the best age estimate for this mafic dike.

PER 7 basaltic andesite

A groundmass concentrate was laser step-heated. With the exception of the first fractions of each experiment, similar ^{40}Ar-^{39}Ar results were obtained for the remaining part of the experiments. The

discrepancy observed in the age spectra may be attributed to tiny inhomogeneities undetectable under the binocular microscope. Despite that in the two experiments the first fraction was obtained applying 0.5 Watts of laser power, different amounts of ^{39}Ar were released: ~14% and 22.4%. Furthermore the $^{37}Ar_{Ca}/^{39}Ar_K$ diagram displays an ascending staircase pattern, indicating that the composition is variable with respect to the calcium and potassium content or that there is more than one mineral phase releasing the argon isotopes. The data cluster in the central part of the $^{36}Ar/^{40}Ar$ versus $^{39}Ar/^{40}Ar$ correlation diagram. Their distribution does not define a well-constrained isochron age (t_c = 9.76 ± 0.90 Ma with MSWD = 3.57 for n = 9). For this reason the plateau age of 10.54 ± 0.20 Ma calculated with the weighted mean of three consecutive fractions representing 86.73% of the ^{39}Ar released is our best estimate for this basaltic andesite.

HUA 6 basaltic andesite

Two laser step-heating experiments were performed on whole rock. For the first experiment, the three fractions released applying up to 1.7 Watts of laser power yielded discordant ages. For the second experiment a modified heating schedule was chosen and an almost flat age espectrum was obtained. The discrepancies between the two experiments in the ages obtained applying ≤ 1.7 Watts of laser power can be attributed to the different heating schedules used, because when the amount of argon released in them is added, similar ages are obtained: 11.5 ± 0.8 Ma and 10.8 ±1.2 Ma, respectively, for the first and second experiment. Therefore, we focus on the argon isotopes released at higer temperature. The weighted mean of the last four fractions of the second experiment yielded an age of 10.45 ± 0.15 Ma for 75.13% of the ^{39}Ar released. This age is statistically indistinguishable from the isochron age of 10.61 ± 0.15 Ma calculated combining the data of the two experiments. Because the straight line defined by the data in the correlation diagram yields a $(^{40}Ar/^{36}Ar)_i$ below the atmospheric value of 295.5, we favour the plateau age of 10.45 ± 0.15 Ma, as our best estimate for basaltic andesite HUA 6.

PER 14 basaltic andesite

More that one gram of groundmass concentrate was step-heated using the temperature controlled Ta-furnace and the argon isotopes were measured with the MS-10 mass spectrometer. The argon was released in nine fractions between 500 to 1350 ℃. More than 70% of the argon was released below 800 ℃. The age spectrum is somewhat perturbed and saddle-shaped, suggesting the presence of excess argon. The ages obtained for individual fractions does not fulfill the criteria to calculate a plateau age. When plotted in the $^{36}Ar/^{40}Ar$ versus $^{39}Ar/^{40}Ar$ correlation diagram, the data are scattered about the best straight line (MSWD = 28) calculated with all the fractions. The y-intercept of $(^{40}Ar/^{36}Ar)_i$ = 310 ± 4 confirms the presence of excess argon. In spite of the data being scattered, we consider the isochron age 10.33 ± 0.88 Ma to be reliable. Furthermore, on the basis on field observations and geochemical similarity it is posible to correlate basaltic andesite PER 14 with similar samples in the area.

PER 1 hawaiite

A groundmass concentrate was laser step-heated in two experiments. Because of the low argon content of the sample, only four fractions were collected on each experiment. The $^{37}Ar_{Ca}/^{39}Ar_K$ diagram indicates homogeneous composition with respect to calcium to potassium content for ~60% of the ^{39}Ar released. The last fractions of each experiment yield younger ages with significantly higher values of $^{37}Ar_{Ca}/^{39}Ar_K$ (greater than 2), which can be attributed to a different mineral phase. The weighted mean of two fractions with $^{37}Ar_{Ca}/^{39}Ar_K$ ~0.6, representing 54.79% of the ^{39}Ar released, yielded an age of

857 ± 51 Ka. The isochron age of 884 ± 97 Ka (MSWD = 0.14) was obtained with four fractions, the two intermediate fractions of each experiment with $^{37}Ar_{Ca}/^{39}Ar_K$ ~0.6. Our preferred age for sample PER 1 is 884 ± 97 Ka because it integrates the results of two experiments and uses fractions that have homogeneous composition with respect to $^{37}Ar_{Ca}/^{39}Ar_K$.

PER 4 hawaiite

A groundmass concentrate was laser step-heated in two experiments yielding reproducible results. To improve the precision of the experiment, in the second experiment a larger amount of sample was used. For the last fraction of the second experiment the signal of mass 36 was not measured correctly, therfore no age information can be reported for this fraction. Because the only information missing for this fraction is mass ^{36}Ar, it is possible to draw the age spectrum with the available fractions. For both experiments, the bulk of the ^{39}Ar was released applying more than 2 watts of laser power and these were the fractions with the highest $^{40}Ar^*$ content. With the combined data of the two experiments we were able to construct an isochron with age of 853 ± 80 Ka (MSWD = 2.56 for n = 7). The isochron age is statistically indistinguishable from the plateau age of 843 ± 74 Ka calculated with the weighted mean of the individual ages of three fractions form the second experiment (72.53% of the ^{39}Ar released). We favour the plateau age of 843 ± 74 Ka because it is better constrained as it has a MSWD = 0.68

PER 6 hawaiite

A groundmass concentrate was laser step-heated in two experiments. Due to the low content of radiogenic ^{40}Ar, the indivual ages obtained are not very precise. For the first experiment the bulk of the ^{39}Ar was released in the last two fractions. The weighted mean of their individual ages yielded a 574 ± 113 Ka age. A diferent heating schedule was selected for the second experiment and in this case the ^{39}Ar was distributed evenly in the five fractions collected. The results from the second experiment are more scattered and less precise than the experiment performed in less detail. The data of the two experiments were combined in the $^{36}Ar/^{40}Ar$ versus $^{39}Ar/^{40}Ar$ correlation diagram. Due to the low radiogenic ^{40}Ar the data cluster close to the y-axis. Two fractions of the second experiment (in the figure, these are identified with letters g and i) were ignored to calculate the isochron age of 585 ± 82 Ka. We favour the isochron age because is well defined (MSWD = 1.36 for n = 8) and it incorportates data from the two experiments performed.

CHO 4 basalt

One gram of groundmass was step-heated with the Ta-furnace and the argon isotopes were measured with the MS-10 mass spectrometer. Only four fractions were collected. The content of radiogenic ^{40}Ar was very low, with a $^{40}Ar/^{36}Ar$ close to atmospheric composition. The bulk of the ^{39}Ar was released in the last two fractions. Due to the lack of detail, no plateau can be defined for this sample. The data cluster very close to the y- axis in the $^{36}Ar/^{40}Ar$ versus $^{39}Ar/^{40}Ar$ correlation diagram and display an almost horizontal distribution, yielding an unprecise and unreliable isocrhon age of 29 ± 181 Ka. Therefore the best estimate for the sample is taken from the third fraction released at 1000ºC, which contains the bulk of the ^{39}Ar released with an age of 138 ± 107 Ka.

ES 10

Basltic andesite

Long W	Lat N
-105.600	23.862

Laser step-heating experiments on plagioclase concentrate

Pwr	$^{39}Ar \times 10^{-6}$	F ^{39}Ar	$^{40}Ar^*/^{39}Ar_K$	1σ	Age in Ma	1σ		% $^{40}Ar^*$	$^{40}Ar/^{36}Ar$	$^{37}Ar_{Ca}/^{39}Ar_K$
1.00	37.752	0.1072	6.11	0.68	43.87	4.80	a	8.11	321.59	0.871
2.80	57.198	0.1620	4.72	0.22	33.95	1.60	b	33.57	444.86	5.114
5.50	52.556	0.1487	4.37	0.15	31.46	1.05	c	60.66	751.08	6.692
7.50	24.994	0.0707	4.68	0.32	33.70	2.26	d	66.18	873.77	6.867
10.00	45.306	0.1282	4.58	0.15	32.98	1.08	e	73.41	1111.22	6.868
13.00	135.418	0.3831	4.67	0.08	33.59	0.56	f	83.45	1785.19	7.308
0.50	6.958	0.0128	7.31	3.35	52.36	23.61	g	2.34	302.57	1.486
1.10	27.083	0.0498	5.10	0.54	36.71	3.86	h	10.05	328.53	1.070
2.40	38.572	0.0708	4.24	0.40	30.53	2.83	i	15.76	350.80	4.383
4.50	60.510	0.1109	4.64	0.19	33.42	1.32	j	52.22	618.51	7.404
8.00	85.797	0.1573	4.64	0.11	33.42	0.79	k	65.57	858.29	7.271
12.00	90.086	0.1652	4.66	0.10	33.54	0.75	l	62.08	779.17	7.017
13.00	106.614	0.1955	4.79	0.07	34.50	0.49	m	81.44	1591.80	7.137
14.00	129.701	0.2377	4.70	0.07	33.83	0.49	n	79.83	1465.28	7.505

Integrated results

$^{39}Ar \times 10^{-6}$	$^{40}Ar^*/^{39}Ar_K$	1σ	Age in Ma	1σ	% $^{40}Ar^*$	$^{40}Ar/^{36}Ar$	$^{37}Ar_{Ca}/^{39}Ar_K$
35.18	4.78	0.10	34.37	0.71	32.11	435.28	6.083
54.30	4.72	0.08	33.95	0.57	32.92	440.51	6.685

$J = 0.004027 \pm 0.000012$

$t_p = 33.92 \pm 0.30$ Ma

plateau age was calculated with the weighted mean of fractions j to n; 86.66% of ^{39}Ar released in 5 consecutive fractions, MSWD = 0.53

Preferred age t_c = 33.58 ± 0.28 Ma, $(^{40}Ar/^{36}Ar)_i = 298 \pm 2$, MSWD = 1.1 for n = 14

HUA 1
Crystal rich ignimbrite Huajicori-Picachos road

Long W	Lat N
-105.28105	22.65721

laser step-heating experiments on biotite concentrate

Pwr	$^{39}Ar \times 10^{-6}$	F ^{39}Ar	$^{40}Ar^*/^{39}Ar_K$	1σ	Age in Ma	1σ			% $^{40}Ar^*$	$^{40}Ar/^{36}Ar$	$^{37}Ar_{Ca}/^{39}Ar_K$
0.30	56.99	0.0069	1.81	0.42	10.73	2.48	a	‡	8.33	322.35	0.075
0.80	304.36	0.0370	4.10	0.14	24.20	0.82	b	‡	57.36	693.04	0.033
1.60	280.72	0.0341	4.33	0.11	25.54	0.66	c	‡	74.86	1175.19	0.038
2.80	2015.58	0.2450	4.53	0.06	26.70	0.36	d		87.00	2272.21	0.046
5.00	5568.78	0.6769	4.51	0.04	26.58	0.26	e		91.06	3305.52	0.025
0.50	121.61	0.0181	2.52	0.27	14.93	1.57	f	‡	19.05	365.05	0.121
1.00	106.50	0.0158	4.19	0.13	24.69	0.77	g	‡	55.28	660.72	0.049
2.00	657.81	0.0978	4.46	0.09	26.28	0.54	h	‡	83.58	1799.79	0.035
3.00	2008.99	0.2988	4.50	0.08	26.52	0.44	i		89.54	2824.72	0.025
4.00	1695.25	0.2522	4.49	0.02	26.45	0.12	j		90.10	2983.59	0.019
6.00	2132.97	0.3173	4.53	0.07	26.73	0.38	k		93.29	4400.73	0.023

Integrated results

$^{39}Ar \times 10^{-6}$	$^{40}Ar^*/^{39}Ar_K$	1σ	Age in Ma	1σ	% $^{40}Ar^*$	$^{40}Ar/^{36}Ar$	$^{37}Ar_{Ca}/^{39}Ar_K$
8226	4.47	0.03	26.38	0.24	85.38	2021.28	0.031
6723	4.46	0.03	26.31	0.23	86.14	2131.31	0.026

J = 0.0032919 ± 0.0000168

Preferred age t_p = 26.48 ± 0.15 Ma

the plateau age was calculated with the weighted mean of fractions h to k; 96.61% of ^{39}Ar released in 4 consecutive fractions, MSWD = 0.18

t_c = 26.51 ± 0.69 Ma, $(^{40}Ar/^{36}Ar)_i$ = 295 ± 69, MSWD = 0.32 for n = 5

‡ Fractions ignored in the isochron

TS 16

Basaltic lava flow, underlying 23.5 ignimbrite east of Las Canoas, Zacatecas

Long W	Lat N
-104.23	22.63

laser step-heating experiment on plagioclase concentrate

Pwr	$^{39}Ar \times 10^{-6}$	F ^{39}Ar	$^{40}Ar^*/^{39}Ar_K$	1 σ	Age in Ma	1 σ		% $^{40}Ar^*$	$^{40}Ar/^{36}Ar$	$^{37}Ar_{Ca}/^{39}Ar_K$
1.30	14.483	0.0862	3.52	1.44	23.65	9.61	a	14.57	345.91	16.86
2.70	26.421	0.1571	3.32	0.35	22.32	2.33	b	70.38	997.50	17.28
4.70	19.403	0.1154	4.27	0.60	28.71	3.99	c	91.96	3676.80	17.68
5.85	8.413	0.0500	2.99	1.27	20.12	8.52	d	61.22	761.91	18.12
7.95	9.761	0.0580	4.30	0.95	28.88	6.30	e	93.38	4465.59	18.83
12.00	89.875	0.5334	3.63	0.12	24.42	0.82	f	82.04	1645.73	20.34

Integrated results

$^{39}Ar \times 10^{-6}$	$^{40}Ar^*/^{39}Ar_K$	1 σ	Age in Ma	1 σ	% $^{40}Ar^*$	$^{40}Ar/^{36}Ar$	$^{37}Ar_{Ca}/^{39}Ar_K$
166.30	3.65	0.19	24.56	1.25	58.66	714.78	19.055

J = 0.003753 ± 0.000011

Preferred age t_p = 24.38 ± 0.75 Ma

Weighted mean of fractions a to f; 100% of ^{39}Ar released in 6 consecutive fractions,
MSWD = 0.54

t_c = 24.43 ± 0.87 Ma, $(^{40}Ar/^{36}Ar)_i$ = 293 ± 21, MSWD = 0.68 for n = 6

HUA 2
Lithic ignimbrite near Picachos

Long W	Lat N
-105.19123	22.70874

laser step-heating experiments on biotite concentrate

Pwr	$^{39}Ar \times 10^{-6}$	F ^{39}Ar	$^{40}Ar^*/^{39}Ar_K$	1σ	Age in Ma	1σ			% $^{40}Ar^*$	$^{40}Ar/^{36}Ar$	$^{37}Ar_{Ca}/^{39}Ar_K$
0.25	196.65	0.0224	4.66	0.50	27.48	2.93	a	‡	53.22	631.65	0.095
0.80	515.45	0.0588	3.70	0.11	21.86	0.67	b	‡	60.97	757.19	0.288
1.60	1359.49	0.1551	3.88	0.05	22.89	0.27	c		78.86	1397.60	0.108
2.80	3722.85	0.4246	3.92	0.04	23.12	0.22	d		91.41	3441.81	0.046
5.00	2973.21	0.3391	----	----	----	----	e		----	----	0.044
0.50	978.41	0.0600	3.55	0.18	20.94	1.07	f	‡	46.63	553.73	0.128
1.00	1592.75	0.0977	3.84	0.05	22.64	0.29	g	‡	73.45	1113.06	0.072
2.00	6321.62	0.3879	3.90	0.04	22.99	0.22	h		87.17	2303.44	0.053
2.70	3217.38	0.1974	3.95	0.04	23.31	0.26	i		89.74	2879.45	0.063
4.00	3227.12	0.1980	3.89	0.06	22.95	0.32	j		93.04	4244.08	0.054
6.00	960.41	0.0589	3.89	0.06	22.97	0.38	k		93.48	4534.33	0.086

Integrated results

$^{39}Ar \times 10^{-6}$	$^{40}Ar^*/^{39}Ar_K$	1σ	Age in Ma	1σ	% $^{40}Ar^*$	$^{40}Ar/^{36}Ar$	$^{37}Ar_{Ca}/^{39}Ar_K$
8768.0	----	----	----	----	----	----	0.071
16300.0	3.88	0.02	22.89	0.18	83.54	1794.92	0.064

J = 0.0032919 ± 0.0000168

Preferred age t_p = 22.99 ± 0.14 Ma

the plateau age was calculated with the weighted mean of fractions g to k; 94.00% of ^{39}Ar released in 5 consecutive fractions, MSWD = 0.63

t_c = 23.19 ± 0.27 Ma, $(^{40}Ar/^{36}Ar)_i$ = 282 ± 21, MSWD = 0.35 for n = 6

‡ Fractions ignored in the isochron

for fraction "**e**" mass 36 was not tuned properly, no age information can be obtained.

ESC 7
Basaltic andesite lava
Escuinapa-Corral de Piedras road, Sinaloa

Long W	Lat N
-105.68	22.889

Ta furnace step-heating experiments on plagioclase concentrate

Temp ºC	^{39}Ar cc STP/g	F ^{39}Ar	^{40}Ar*/^{39}Ar$_K$	1 σ	Age in Ma	1 σ		% ^{40}Ar*	^{40}Ar/^{36}Ar	^{37}Ar$_{Ca}$/^{39}Ar$_K$
600	3.20E-09	0.0431	0.43	7.67	2.65	47.84	a	0.65	297.43	11.11
800	2.35E-08	0.3133	4.14	1.07	25.67	6.61	b	19.32	366.25	43.82
1000	2.95E-08	0.3932	3.26	0.80	20.24	4.97	c	22.65	382.02	30.79
1100	9.60E-09	0.1282	2.69	2.60	16.72	16.10	d	6.68	316.64	28.36
1350	9.20E-09	0.1221	3.80	3.02	23.61	18.62	e	2.93	304.41	31.80
550	2.30E-09	0.0280	0.73	7.09	4.54	44.20	f	0.84	298.02	12.48
700	9.70E-09	0.1187	3.59	1.67	22.28	10.33	g	17.59	358.56	34.59
850	2.63E-08	0.3216	3.66	0.63	22.71	3.89	h	26.33	401.11	38.52
1000	2.32E-08	0.2832	3.54	0.70	21.97	4.35	i	30.63	425.96	26.77
1150	1.46E-08	0.1789	3.67	1.11	22.76	6.87	j	22.39	380.73	22.57
1350	5.70E-09	0.0696	3.32	2.95	20.62	18.23	k	4.30	308.77	33.05

Integrated results

^{39}Ar ccSTP/g	^{40}Ar*/^{39}Ar$_K$	1 σ	Age in Ma	1 σ	% ^{40}Ar*	^{40}Ar/^{36}Ar	^{37}Ar$_{Ca}$/^{39}Ar$_K$
7.503E-08	3.40	0.82	21.15	5.05	9.40	326.15	33.84
8.178E-08	3.51	0.53	21.81	3.26	16.82	355.24	30.48

J = 0.0034640 ± 0.0000196

1st exp. sample weight = 0.1987 g
2nd exp. sample weight = 0.3202 g

Preferred age t_p = 22.39 ± 2.56 Ma

the plateau age was calculated with the weighted mean of fractions g to k; 97.20% of ^{39}Ar released in 5 consecutive fractions, MSWD < 0.01

t_c = 22.35 ± 2.73 Ma, (^{40}Ar/^{36}Ar)$_i$ = 295 ± 6, MSWD = 0.10 for n = 11

MdCH 10 Dacite

Nuevo León dome, on top of 21.1 Ma ignimbrite plateau, Nayarit

Long W	Lat N
-105.06	22.652

laser step-heating experiments on plagioclase sample

Pwr	$^{39}Ar \times 10^{-6}$	F ^{39}Ar	$^{40}Ar^*/^{39}Ar_K$	1 σ	Age in Ma	1 σ			% $^{40}Ar^*$	$^{40}Ar/^{36}Ar$	$^{37}Ar_{Ca}/^{39}Ar_K$
0.20	2.167	0.0133	12.99	9.44	79.60	56.59	a		16.81	355.19	0.466
0.50	7.012	0.0431	----	----	----	----	b	‡	----	----	2.595
0.70	9.508	0.0584	----	----	----	----	c	‡	----	----	3.920
1.00	15.127	0.0929	3.99	0.99	24.84	6.09	d		93.79	4755.49	4.985
2.50	37.561	0.2307	3.32	0.27	20.69	1.70	e		74.19	1144.71	4.941
7.00	91.584	0.5614	3.65	0.18	22.71	1.14	f		86.37	2168.57	7.965
1.00	3.395	0.0366	----	----	----	----	g	‡	----	----	3.226
3.00	22.052	0.2372	3.60	0.50	22.42	3.09	h		55.53	664.56	6.203
9.00	67.594	0.7262	3.78	0.14	23.54	0.84	i		87.14	2297.16	8.362

Integrated results

$^{39}Ar \times 10^{-6}$	$^{40}Ar^*/^{39}Ar_K$	1 σ	Age in Ma	1 σ	% $^{40}Ar^*$	$^{40}Ar/^{36}Ar$	$^{37}Ar_{Ca}/^{39}Ar_K$
162.3	----	----	----	----	----	----	6.422
92.58	----	----	----	----	----	----	7.662

J = 0.003473 ± 0.000013

t_p = 22.15 ± 0.93 Ma; calculated with the weighted mean of fractions d to f; 88.50% of ^{39}Ar released in 3 consecutive fractions, MSWD = 0.59

Preferred age t_c = 22.51 ± 0.90 Ma

$(^{40}Ar/^{36}Ar)_i$ = 322 ± 39, MSWD = 0.73 for n = 6

‡ fraction ignored in the isochron

for fractions "**a, b, c, g**" mass 36 was not tuned properly, no age information can be obtained and in consequence only ^{39}Ar and ^{37}Ar data can be reported in the integrated results.

ORO 2
Ignimbrite, Road to El Cajón Hydro plant

Long W	Lat N
-104.55067	21.45178

laser step-heating experiments on biotite concentrate

Pwr	$^{39}Ar \times 10^{-6}$	F ^{39}Ar	$^{40}Ar^*/^{39}Ar_K$	1 σ	Age in Ma	1 σ			% $^{40}Ar^*$	$^{40}Ar/^{36}Ar$	$^{37}Ar_{Ca}/^{39}Ar_K$
0.30	24.410	0.0027	-1.28	2.73	-7.59	16.28	a	‡	-6.52	277.42	0.021
0.73	123.496	0.0134	3.30	0.33	19.48	1.91	b	‡	52.31	619.56	0.289
1.20	500.643	0.0544	3.43	0.06	20.26	0.37	c	‡	69.86	980.46	0.024
1.80	2288.553	0.2489	3.57	0.04	21.06	0.26	d		86.93	2261.76	0.036
2.40	2928.183	0.3185	3.56	0.04	21.02	0.22	e		92.20	3790.20	0.033
3.00	2105.753	0.2290	3.53	0.04	20.85	0.24	f		92.65	4020.00	0.036
6.00	1223.813	0.1331	3.53	0.04	20.87	0.24	g		91.53	3490.50	0.027

Integrated results

$^{39}Ar \times 10^{-6}$	$^{40}Ar^*/^{39}Ar_K$	1 σ	Age in Ma	1 σ	% $^{40}Ar^*$	$^{40}Ar/^{36}Ar$	$^{37}Ar_{Ca}/^{39}Ar_K$
9195.0	3.53	0.02	20.83	0.17	87.30	2326.75	0.036

J = 0.0032919 ± 0.0000168

t_p = 20.88 ± 0.12 Ma, calculated with the weighted mean of fractions b to g; 99.73% of ^{39}Ar released in 6 consecutive fractions, MSWD = 0.85

Preferred age t_c = 20.74 ± 0.44 Ma, $(^{40}Ar/^{36}Ar)_i$ = 325 ± 59, MSWD = 0.19 for n = 4

‡ Fractions ignored in the isochron

MdCH 06

Rhyolite dome

Laser step-heating experiments on plagioclase concentrate

Pwr	$^{39}Ar \times 10^{-6}$	F ^{39}Ar	$^{40}Ar^*/^{39}Ar_K$	1σ	Age in Ma	1σ		% $^{40}Ar^*$	$^{40}Ar/^{36}Ar$	$^{37}Ar_{Ca}/^{39}Ar_K$
0.30	0.107	0.0009	19.38	59.05	112.68	332.74	a	4.43	309.21	5.48
0.90	4.250	0.0363	15.93	5.45	93.13	31.07	b	3.22	305.34	7.14
1.20	6.970	0.0593	2.25	1.95	13.45	11.60	c	3.59	306.50	14.79
1.70	6.838	0.0580	3.16	1.57	18.88	9.30	d	7.71	320.19	18.72
2.30	6.870	0.0582	5.93	0.97	35.24	5.72	e	57.71	698.73	21.49
4.00	9.960	0.0852	3.74	0.73	22.30	4.32	f	27.87	409.68	7.18
6.00	8.901	0.0761	3.05	0.84	18.18	4.98	g	50.57	597.83	7.25
9.00	10.368	0.0887	2.74	0.73	16.37	4.36	h	37.84	475.36	7.02
12.00	62.841	0.5372	3.47	0.14	20.69	0.83	i	49.33	583.22	7.54
1.00	7.748	0.0584	14.21	3.77	83.31	21.58	j	4.40	309.11	16.24
3.00	24.290	0.1833	4.50	0.80	26.80	4.72	k	14.94	347.42	13.75
6.00	10.118	0.0766	2.95	0.74	17.58	4.41	l	31.27	429.93	8.17
7.00	7.811	0.0592	4.33	0.64	25.81	3.77	m	79.72	1457.34	7.61
9.50	10.937	0.0829	3.39	0.44	20.21	2.58	n	52.73	625.07	7.25
10.50	22.592	0.1711	3.60	0.33	21.45	1.96	o	54.89	655.11	7.97
11.50	21.155	0.1602	3.52	0.36	21.01	2.16	p	42.34	512.48	7.75
12.50	5.023	0.0380	4.53	0.78	26.96	4.61	q	73.37	1109.53	8.30
13.00	22.487	0.1703	3.28	0.29	19.56	1.72	r	51.39	607.86	8.06

Integrated results

$^{39}Ar \times 10^{-6}$	$^{40}Ar^*/^{39}Ar_K$	1σ	Age in Ma	1σ	% $^{40}Ar^*$	$^{40}Ar/^{36}Ar$	$^{37}Ar_{Ca}/^{39}Ar_K$
116.4	3.92	0.30	23.34	1.79	12.60	338.10	9.31
131.4	4.33	0.30	25.78	1.78	14.56	345.87	9.44

J = 0.003325 ± 0.000013

t_p = 20.54 ± 0.79 Ma, calculated with the weighted mean of fractions f to i; 78.72% of ^{39}Ar released in 4 consecutive fractions, MSWD = 0.45

Preferred age t_c = 20.25 ± 0.64 Ma, $(^{40}Ar/^{36}Ar)_i$ = 304 ± 2, MSWD = 0.98 for n = 18

HUA 5
Poorly welded ash flow, Huajicori

Long W	Lat N
-105.31948	22.64773

laser step-heating experiments on plagioclase concentrate

Pwr	$^{39}Ar \times 10^{-6}$	F ^{39}Ar	$^{40}Ar^*/^{39}Ar_K$	1 σ	Age in Ma	1 σ			% $^{40}Ar^*$	$^{40}Ar/^{36}Ar$	$^{37}Ar_{Ca}/^{39}Ar_K$
1.00	16.54	0.0069	0.40	1.69	2.37	10.00	a	‡	1.02	298.53	0.345
2.00	16.99	0.0071	2.67	0.51	15.81	3.00	b	‡	29.99	422.07	0.619
4.20	116.06	0.0482	3.60	0.20	21.28	1.16	c		82.12	1653.06	1.674
6.50	176.69	0.0734	3.37	0.10	19.92	0.58	d		98.71	22828.40	1.920
8.00	2082.41	0.8645	3.24	0.04	19.15	0.23	e		97.61	12350.26	2.057
3.00	71.81	0.0403	2.63	0.18	15.54	1.08	f	‡	17.77	359.35	0.885
5.00	75.00	0.0421	3.75	0.19	22.14	1.11	g	‡	48.77	2768.21	1.688
7.00	112.56	0.0632	3.18	0.11	18.80	0.67	h		89.26	2752.04	2.015
8.00	1521.12	0.8543	3.22	0.05	19.02	0.27	i		94.28	5165.73	2.061

Integrated results

$^{39}Ar \times 10^{-6}$	$^{40}Ar^*/^{39}Ar_K$	1 σ	Age in Ma	1 σ	% $^{40}Ar^*$	$^{40}Ar/^{36}Ar$	$^{37}Ar_{Ca}/^{39}Ar_K$
2409.0	3.25	0.04	19.17	0.24	88.51	2571.02	2.006
1780.0	3.22	0.04	19.00	0.26	82.57	1695.11	1.995

J = 0.0032919 ± 0.0000168

t = 18.99 ± 0.27 Ma, calculated with the weighted mean of fractions h and i; 91.75% of ^{39}Ar released in 2 consecutive fractions, MSWD = 0.09

Preferred age t_c = 18.98 ± 0.30 Ma, $(^{40}Ar/^{36}Ar)_i$ = 356 ± 79, MSWD = 1.57 for n = 5

‡ Fractions ignored in the isochron

MdCH 09

Olivine Basalt
El Ryito, Nayarit

Long W	Lat N
-105.17	22.669

laser step-heating experiments on plagioclase concentrate

Pwr	$^{39}Ar \times 10^{-6}$	F ^{39}Ar	$^{40}Ar^*/^{39}Ar_K$	1 σ	Age in Ma	1 σ			% $^{40}Ar^*$	$^{40}Ar/^{36}Ar$	$^{37}Ar_{Ca}/^{39}Ar_K$
0.50	16.481	0.0525	-1.35	0.90	-8.55	5.71	a	‡	-2.07	289.51	2.241
1.50	32.939	0.1043	2.63	1.19	16.52	7.43	b		4.55	309.59	12.793
3.00	38.602	0.1218	2.68	0.32	16.85	2.02	c		26.86	404.03	17.736
4.50	8.219	0.0259	3.69	0.98	23.13	6.13	d		45.58	542.96	17.227
12.00	220.482	0.6954	3.01	0.07	18.93	0.44	e		65.59	858.88	18.876
1.00	46.837	0.1194	4.88	0.72	30.53	4.49	f		5.42	312.45	4.704
3.00	63.306	0.1600	2.18	0.33	13.70	2.06	g		18.07	360.66	17.872
5.00	12.943	0.0327	3.64	0.73	22.81	4.57	h		45.56	542.76	16.050
7.00	8.890	0.0225	3.14	0.86	19.72	5.38	i		41.34	503.73	14.937
8.40	8.704	0.0220	2.08	0.73	13.06	4.56	j		34.64	452.11	15.960
10.00	40.834	0.1032	2.82	0.18	17.71	1.15	k		54.59	650.81	17.965
13.00	213.901	0.5402	2.93	0.06	18.41	0.39	l		68.02	924.02	18.551

Integrated results

$^{39}Ar \times 10^{-6}$	$^{40}Ar^*/^{39}Ar_K$	1 σ	Age in Ma	1 σ	% $^{40}Ar^*$	$^{40}Ar/^{36}Ar$	$^{37}Ar_{Ca}/^{39}Ar_K$
313.2	2.72	0.15	17.10	0.97	19.33	366.32	17.186
391.2	3.04	0.12	19.10	0.77	18.90	364.38	16.509

J = 0.003498 ± 0.000030

t_p = 18.34 ± 0.39 Ma, calculated with the weighted mean of fractions h to l; 72.06% of ^{39}Ar released in 5 consecutive fractions, MSWD = 0.67

Preferred age t_c = 18.32 ± 0.40 Ma, $(^{40}Ar/^{36}Ar)_i$ = 300 ± 3, MSWD = 1.63 for n = 11

‡ fraction ignored in the isochron

RUIZ 16

Rhyolitic dome

Long W	Lat N
-104.745	22.155

Laser step-heating experiments on plagioclase concentrate

Pwr	$^{39}Ar \times 10^{-6}$	F ^{39}Ar	$^{40}Ar^*/^{39}Ar_K$	1σ	Age in Ma	1σ			% $^{40}Ar^*$	$^{40}Ar/^{36}Ar$	$^{37}Ar_{Ca}/^{39}Ar_K$
0.50	0.54	0.0009	-57.13	36.53	-317.69	222.12	a	‡	-10.44	267.58	0.734
1.20	7.68	0.0129	5.60	0.68	28.35	3.41	b		30.88	427.54	0.960
2.40	29.89	0.0501	3.19	0.20	16.17	1.00	c		62.44	786.79	1.159
3.00	22.42	0.0376	3.45	0.25	17.51	1.25	d		89.19	2734.58	1.467
4.00	48.58	0.0814	3.59	0.15	18.23	0.76	e		95.41	6436.68	1.562
5.00	37.37	0.0626	3.86	0.12	19.56	0.62	f		98.18	16260.36	1.670
7.00	43.73	0.0733	3.68	0.14	18.69	0.73	g		90.74	3192.09	1.691
8.00	406.33	0.6811	3.60	0.03	18.25	0.16	h		84.67	1927.56	1.875
2.00	42.96	0.0796	3.39	0.33	17.22	1.69	i		21.09	374.46	1.220
5.00	103.84	0.1923	3.53	0.07	17.90	0.36	j		79.15	1417.20	1.573
6.80	54.20	0.1003	3.63	0.12	18.42	0.60	k		87.76	2414.92	1.804
7.50	30.28	0.0561	3.60	0.22	18.27	1.10	l		89.59	2838.27	1.895
8.50	13.18	0.0244	3.07	0.42	15.56	2.12	m		81.19	1570.64	1.806
10.50	55.49	0.1027	3.40	0.12	17.26	0.61	n		78.85	1397.34	1.896
13.00	240.14	0.4446	3.50	0.03	17.74	0.14	o		83.73	1815.85	1.893

Integrated results

$^{39}Ar \times 10^{-6}$	$^{40}Ar^*/^{39}Ar_K$	1σ	Age in Ma	1σ	% $^{40}Ar^*$	$^{40}Ar/^{36}Ar$	$^{37}Ar_{Ca}/^{39}Ar_K$
595.9	3.56	0.05	18.08	0.24	73.09	1098.08	1.759
539.5	3.49	0.04	17.73	0.21	67.57	911.24	1.767

J = 0.002826 ± 0.000003

the plateau age was calculated with the weighted mean of fractions i to o

t_p = 17.76 ± 0.12 Ma, 100 % of ^{39}Ar released in 7 consecutive fractions, MSWD = 0.5

t_c = 17.91 ± 0.20 Ma, $(^{40}Ar/^{36}Ar)_i$ = 301 ± 11, MSWD = 2.4 for n = 14

‡ fraction ignored in the isochron given in the figure

RUIZ 34B

Rhyolitic dome

Long W Lat N
-104.8 22.059

Laser step-heating experiments on biotite concentrate

Pwr	$^{39}Ar \times 10^{-6}$	F ^{39}Ar	$^{40}Ar^*/^{39}Ar_K$	1σ	Age in Ma	1σ			% $^{40}Ar^*$	$^{40}Ar/^{36}Ar$	$^{37}Ar_{Ca}/^{39}Ar_K$
0.30	11.533	0.0080	1.81	1.02	9.22	5.16	a	‡	6.45	315.86	0.029
0.60	32.261	0.0225	3.48	0.28	17.67	1.42	b	‡	33.05	441.40	0.019
0.90	32.964	0.0230	3.08	0.23	15.62	1.14	c	‡	60.85	754.87	0.012
1.40	56.261	0.0392	3.80	0.13	19.26	0.67	d		85.25	2003.91	0.006
1.80	57.326	0.0399	3.46	0.10	17.55	0.51	e		83.73	1816.22	0.005
2.40	124.181	0.0865	3.62	0.06	18.35	0.31	f		89.85	2911.61	0.003
3.00	133.674	0.0931	3.51	0.05	17.81	0.26	g		91.14	3334.62	0.002
3.80	472.930	0.3295	3.51	0.02	17.79	0.10	h		93.31	4413.78	0.001
4.40	311.826	0.2173	3.52	0.02	17.84	0.12	i		95.85	7117.52	0.001
5.00	131.532	0.0917	3.48	0.04	17.64	0.22	j		95.15	6093.75	0.001
6.00	14.266	0.0099	3.34	0.41	16.93	2.06	k		84.06	1854.36	0.000
9.00	56.388	0.0393	3.57	0.13	18.11	0.66	l		79.35	1430.94	0.002

Integrated results

$^{39}Ar \times 10^{-6}$	$^{40}Ar^*/^{39}Ar_K$	1σ	Age in Ma	1σ	% $^{40}Ar^*$	$^{40}Ar/^{36}Ar$	$^{37}Ar_{Ca}/^{39}Ar_K$
1435.0	3.50	0.02	17.77	0.10	83.14	1752.75	0.002

J = 0.002826 ± 0.000003

the plateau age was calculated with the weighted mean of fractions f to l

t_p = 17.82 ± 0.07 Ma, 86.74 % of ^{39}Ar released in 7 consecutive fractions, MSWD = 0.68

t_c = 17.57 ± 0.19 Ma, $(^{40}Ar/^{36}Ar)_i$ = 357 ± 40, MSWD = 0.79 for n = 9

‡ fraction ignored in the isochron given in the figure

PER 12

Basaltic andesite, Batequitos-El Divisadero road

Long W	Lat N
-107.71	25.31

Ta furnace step-heating experiment on groundmass sample

Temp ºC	^{39}Ar ccSTP/g	F ^{39}Ar	^{40}Ar*/^{39}Ar$_K$	1 σ	Age in Ma	1 σ			%^{40}Ar*	^{40}Ar/^{36}Ar	^{37}Ar$_{Ca}$/^{39}Ar$_K$
500	5.257E-09	0.0132	2.52	2.54	16.33	16.41	a	‡	2.77	303.93	0.98
600	1.170E-08	0.0294	2.49	0.72	16.10	4.66	b	‡	10.27	329.32	1.58
700	3.521E-08	0.0884	3.23	0.19	20.92	1.25	c		42.57	514.50	1.65
800	9.660E-08	0.2426	2.97	0.08	19.21	0.49	d		68.15	927.77	1.66
850	6.572E-08	0.1651	2.84	0.08	18.38	0.54	e		77.35	1304.75	1.90
900	4.805E-08	0.1207	2.72	0.11	17.59	0.71	f		72.11	1059.70	2.16
950	3.288E-08	0.0826	2.83	0.15	18.29	0.98	g		73.63	1120.53	2.32
1000	2.849E-08	0.0716	2.68	0.18	17.39	1.13	h		66.33	877.55	2.36
1100	4.610E-08	0.1158	2.66	0.12	17.20	0.77	i		62.90	796.50	2.63
1350	2.816E-08	0.0707	2.50	0.20	16.21	1.29	j	‡	48.01	568.37	13.10

Integrated results

^{39}Ar ccSTP/g	^{40}Ar*/^{39}Ar$_K$	1 σ	Age in Ma	1 σ	% ^{40}Ar*	^{40}Ar/^{36}Ar	^{37}Ar$_{Ca}$/^{39}Ar$_K$
3.982E-07	2.82	0.12	18.25	0.85	45.73	544.48	2.78

J = 0.003608 ± 0.000078

sample weight = 1.035 g; estimated 0.58%K

t_p = 17.78 ± 0.37 Ma; plateau age calculated with the weighted mean of fractions e to j; 62.65% of ^{39}Ar released in 6 consecutive fractions, MSWD = 0.75

Preferred age t_c = 17.42 ± 0.77 Ma, (^{40}Ar/^{36}Ar)$_i$ = 335 ± 19, MSWD = 1.8 for n = 7

‡ fractions ignored in the isochron given in the figure

MDCH 05

Rhyolite,Cucharas dome

Long W	Lat N
-105.261	22.777

laser step-heating experiments on groundmass sample

Pwr	$^{39}Ar \times 10^{-6}$	F ^{39}Ar	$^{40}Ar^*/^{39}Ar_K$	1 σ	Age in Ma	1 σ			% $^{40}Ar^*$	$^{40}Ar/^{36}Ar$	$^{37}Ar_{Ca}/^{39}Ar_K$
0.40	64.619	0.0057	11.60	1.27	75.08	8.05	a	‡	6.70	316.70	0.003
0.84	493.293	0.0438	5.09	0.19	33.35	1.25	b	‡	16.12	352.30	0.009
1.00	819.131	0.0727	3.15	0.07	20.68	0.43	c	‡	36.41	464.70	0.003
1.40	1308.110	0.1160	2.98	0.03	19.58	0.22	d	‡	48.03	568.55	0.002
1.80	1774.455	0.1574	2.80	0.02	18.42	0.12	e	‡	66.43	880.14	0.002
2.22	1084.352	0.0962	2.69	0.02	17.65	0.10	f		79.48	1440.36	0.002
2.40	558.693	0.0496	2.63	0.03	17.29	0.17	g		79.16	1418.28	0.002
2.90	565.139	0.0501	2.61	0.03	17.13	0.18	h		75.53	1207.39	0.002
3.50	489.728	0.0434	2.60	0.03	17.13	0.23	i		71.85	1049.80	0.002
4.20	525.565	0.0466	2.61	0.03	17.19	0.19	j		72.32	1067.38	0.001
5.20	477.472	0.0423	2.58	0.03	16.93	0.21	k		67.27	902.98	0.001
6.20	509.033	0.0451	2.67	0.03	17.57	0.20	l		66.00	869.23	0.001
7.22	548.891	0.0487	2.68	0.03	17.64	0.22	m		60.87	755.17	0.001
8.20	512.379	0.0454	2.65	0.03	17.41	0.19	n		62.23	782.36	0.001
9.20	412.571	0.0366	2.67	0.05	17.53	0.33	o		62.32	784.14	0.001
10.20	283.356	0.0251	2.64	0.04	17.36	0.28	p		65.12	847.30	0.001
12.00	243.442	0.0216	2.60	0.05	17.08	0.32	q		63.91	818.82	0.001
12.50	316.356	0.0281	2.72	0.03	17.86	0.18	r		74.35	1152.26	0.001
13.00	288.197	0.0256	2.59	0.05	17.01	0.36	s		58.73	715.93	0.002

Integrated results

$^{39}Ar \times 10^{-6}$	$^{40}Ar^*/^{39}Ar_K$	1 σ	Age in Ma	1 σ	% $^{40}Ar^*$	$^{40}Ar/^{36}Ar$	$^{37}Ar_{Ca}/^{39}Ar_K$
11270.0	2.90	0.02	19.07	0.15	43.38	521.87	0.002

J = 0.003662 ± 0.000013

Preferred age t_p = 17.41 ± 0.07 Ma

calculated with the weighted mean of fractions f to s; 60.44% of ^{39}Ar released in 14 consecutive fractions, MSWD = 1.8

t_c = 17.52 ± 0.24 Ma, $(^{40}Ar/^{36}Ar)_i$ = 292 ± 9, MSWD = 2.4 for n = 14

‡ fraction ignored in the isochron

SIN 25

Basalt, El Salto reservoir

Long W	Lat N
-106.701	24.1201

laser step-heating experiments on whole rock sample

Pwr	$^{39}Ar \times 10^{-6}$	F ^{39}Ar	$^{40}Ar^*/^{39}Ar_K$	1 σ	Age in Ma	1 σ			% $^{40}Ar^*$	$^{40}Ar/^{36}Ar$	$^{37}Ar_{Ca}/^{39}Ar_K$
0.20	4.403	0.0023	-11.28	4.80	-72.62	31.55	a	‡	-6.37	277.79	0.660
0.50	29.089	0.0150	1.58	0.49	9.97	3.08	b	‡	3.06	304.82	0.772
0.80	88.192	0.0456	2.17	0.22	13.62	1.40	c	‡	20.25	370.53	0.825
1.20	194.186	0.1004	2.35	0.05	14.76	0.28	d		55.85	669.30	0.815
1.60	224.761	0.1162	2.35	0.06	14.77	0.38	e		67.69	914.60	0.985
2.00	285.318	0.1475	2.29	0.03	14.36	0.19	f		78.42	1369.35	1.062
2.50	283.876	0.1468	2.31	0.04	14.50	0.25	g		85.17	1991.96	1.087
3.00	212.498	0.1099	2.23	0.06	14.00	0.37	h		84.09	1857.29	1.005
3.60	198.112	0.1025	2.20	0.05	13.84	0.30	i		79.26	1424.82	0.916
5.00	220.311	0.1139	2.25	0.04	14.14	0.25	j		83.13	1751.27	1.133
6.00	76.585	0.0396	2.24	0.11	14.10	0.69	k		78.86	1397.58	2.090
8.00	116.464	0.0602	2.17	0.10	13.65	0.65	l		66.73	888.31	2.263

Integrated results

$^{39}Ar \times 10^{-6}$	$^{40}Ar^*/^{39}Ar_K$	1 σ	Age in Ma	1 σ	% $^{40}Ar^*$	$^{40}Ar/^{36}Ar$	$^{37}Ar_{Ca}/^{39}Ar_K$
1932.0	2.23	0.03	14.00	0.20	49.33	583.23	1.116

J = 0.003498 ± 0.000030

t_p = 14.31 ± 0.11 Ma, calculated with the weighted mean of fractions c to l; 98.27% of ^{39}Ar released in 10 consecutive fractions, MSWD = 1.07

Preferred age t_c = 14.01 ± 0.23 Ma, $(^{40}Ar/^{36}Ar)_i$ = 315 ± 11, MSWD = 0.8 for n = 9

‡ Fractions ignored in the isochron

SIN15

Basaltic lava

Long W	Lat N
-107.001	24.269

Laser step-heating experiments on groundmass concentrate

Pwr	$^{39}Ar \times 10^{-6}$	F ^{39}Ar	$^{40}Ar^*/^{39}Ar_K$	1σ	Age in Ma	1σ		% $^{40}Ar^*$	$^{40}Ar/^{36}Ar$	$^{37}Ar_{Ca}/^{39}Ar_K$
0.2	7.342	0.0088	6.37	1.95	32.18	9.77	a	6.56	316.24	1.11
0.5	42.597	0.0509	3.72	0.47	18.89	2.36	b	8.60	323.31	0.46
1.0	167.794	0.2004	2.83	0.09	14.38	0.47	c	41.64	506.34	0.42
1.3	84.817	0.1013	2.61	0.09	13.27	0.44	d	62.07	778.96	0.61
1.6	58.648	0.0700	2.82	0.12	14.33	0.61	e	64.30	827.74	0.91
2.1	50.021	0.0597	2.84	0.13	14.42	0.64	f	71.49	1036.48	0.97
3.2	98.767	0.1179	2.76	0.09	13.99	0.44	g	76.24	1243.43	0.69
4.8	178.338	0.2129	2.70	0.05	13.70	0.26	h	75.93	1227.69	1.06
8.0	149.327	0.1781	2.71	0.06	13.75	0.29	i	69.46	967.66	2.15

Integrated results

$^{39}Ar \times 10^{-6}$	$^{40}Ar^*/^{39}Ar_K$	1σ	Age in Ma	1σ	% $^{40}Ar^*$	$^{40}Ar/^{36}Ar$	$^{37}Ar_{Ca}/^{39}Ar_K$
837.1	2.83	0.04	14.35	0.23	38.91	483.69	0.98

J = 0.002826 ± 0.000003

the plateau age was calculated with the weighted mean of fractions c to i

t_p = 13.84 ± 0.15 Ma, 94.03 % of ^{39}Ar released in 7 consecutive fractions, MSWD = 0.82

t_c = 13.62 ± 0.17 Ma, $(^{40}Ar/^{36}Ar)_i$ = 304 ± 3, MSWD = 0.56 for n = 9

DANA 46a

Basalt, Nayarit scarp

Long W	Lat N
-106.63	22.44

laser one-step fusion experiments on whole rock, irradiation CIC 41

Pwr	$^{39}Ar \times 10^{-6}$	$^{40}Ar^*/^{39}Ar_K$	1 σ	Age in Ma	1 σ			% $^{40}Ar^*$	$^{40}Ar/^{36}Ar$	$^{37}Ar_{Ca}/^{39}Ar_K$
3.00	506.308	1.06	0.17	9.26	1.44	a	‡	22.20	379.83	8.619
3.00	238.204	1.44	0.20	12.58	1.76	b		38.98	484.24	3.569
3.00	284.893	1.29	0.24	11.27	2.13	c		20.29	370.73	4.879
5.00	2289.683	1.40	0.04	12.18	0.33	d		55.37	662.06	0.543
4.00	1228.054	1.26	0.13	11.02	1.16	e		24.22	389.96	3.499
4.00	1454.440	1.37	0.09	11.91	0.82	f		29.92	421.64	2.287
3.00	3417.317	1.35	0.03	11.82	0.29	g		39.90	491.71	1.265
3.00	1613.156	1.26	0.12	10.96	1.01	h		21.34	375.66	3.386

J = 0.004851 ± 0.000007

laser one-step fusion experiments on whole rock, irradiation CIC 44

Pwr	$^{39}Ar \times 10^{-6}$	F ^{39}Ar	$^{40}Ar^*/^{39}Ar_K$	1 σ	Age in Ma	1 σ		% $^{40}Ar^*$	$^{40}Ar/^{36}Ar$	$^{37}Ar_{Ca}/^{39}Ar_K$
5.00	2023.918	0.1819	1.41	0.07	11.16	0.57	i	26.95	404.50	2.274
6.00	2638.512	0.2372	1.39	0.05	10.99	0.42	j	32.72	439.21	1.690
6.13	2212.066	0.1989	1.43	0.07	11.28	0.53	k	32.26	436.26	1.359
4.07	2181.523	0.1960	1.45	0.07	11.43	0.55	l	32.84	440.02	2.467
6.00	2069.463	0.1860	1.45	0.08	11.45	0.63	m	26.32	401.05	2.275

J = 0.004389 ± 0.000015

Weighted mean of fractions a to m; t = 11.59 ± 0.31 Ma; MSWD = 0.89

laser step-heating experiments on whole rock, irradiation CIC 44

Pwr	$^{39}Ar \times 10^{-6}$	F ^{39}Ar	$^{40}Ar^*/^{39}Ar_K$	1 σ	Age in Ma	1 σ			% $^{40}Ar^*$	$^{40}Ar/^{36}Ar$	$^{37}Ar_{Ca}/^{39}Ar_K$
0.18	102.766	0.0252	0.87	1.43	6.91	11.25	n		1.29	299.36	2.698
0.41	263.267	0.0646	1.55	0.32	12.20	2.52	o		12.43	337.43	1.352
0.77	432.804	0.1061	0.97	0.13	7.68	1.05	p	‡	16.75	354.94	1.333
1.10	555.221	0.1362	1.48	0.10	11.68	0.81	q		48.92	578.49	1.032
6.00	2723.589	0.6679	1.44	0.05	11.34	0.36	r		46.87	556.14	1.483

Integrated results

$^{39}Ar \times 10^{-6}$	$^{40}Ar^*/^{39}Ar_K$	1 σ	Age in Ma	1 σ	% $^{40}Ar^*$	$^{40}Ar/^{36}Ar$	$^{37}Ar_{Ca}/^{39}Ar_K$
4074.0	1.39	0.06	10.94	0.45	24.83	393.09	1.428

J = 0.004389 ± 0.000015

DANA 46a

Basalt, Nayarit scarp

Long W	Lat N
-106.63	22.44

Ta furnace step-heating experiment on whole rock sample, irradiation CIC 41

Temp ºC	^{39}Ar cc STP/g	F ^{39}Ar	^{40}Ar*/^{39}Ar$_K$	1 σ	Age in Ma	1 σ		% ^{40}Ar*	^{40}Ar/^{36}Ar	^{37}Ar$_{Ca}$/^{39}Ar$_K$
600	4.454E-08	0.0429	1.23	0.41	10.71	3.55	s	6.83	317.17	0.97
700	1.085E-07	0.1044	1.40	0.17	12.25	1.43	t	26.47	401.87	0.50
900	2.104E-07	0.2025	1.37	0.09	11.98	0.74	u	39.17	485.82	1.01
1000	2.448E-07	0.2356	1.36	0.07	11.86	0.63	v	56.49	679.09	0.64
1350	4.308E-07	0.4146	1.39	0.04	12.10	0.38	w	37.50	472.80	2.74

Integrated results

^{39}Ar cc STP/g	^{40}Ar*/^{39}Ar$_K$	1 σ	Age in Ma	1 σ	% ^{40}Ar*	^{40}Ar/^{36}Ar	^{37}Ar$_{Ca}$/^{39}Ar$_K$
1.040E-06	1.37	0.04	11.98	0.36	33.20	442.38	1.59

J = 0.004851 ± 0.000007

sample weight = 0.3107 g; estimated 1.12%K

t_p = 11.97 ± 0.30 Ma, calculated with the weighted mean of fractions s to w; 100% of ^{39}Ar released in 5 consecutive fractions, MSWD = 0.08

Preferred age t_c = 11.96 ± 0.26 Ma, (^{40}Ar/^{36}Ar)$_i$ = 291 ± 3, MSWD = 0.50 for n = 21

‡ Fractions ignored in the isochron

Roca 3J 5

Lithic crystal tuff, Tamayo Dome

Long W	Lat N
-107.34	23.06

laser step-heating experiments on feldspar concentrate

Pwr	$^{39}Ar \times 10^{-6}$	F ^{39}Ar	$^{40}Ar^*/^{39}Ar_K$	1 σ	Age in Ma	1 σ		% $^{40}Ar^*$	$^{40}Ar/^{36}Ar$	$^{37}Ar_{Ca}/^{39}Ar_K$
2.00	165.055	0.0769	1.68	0.10	11.14	0.66	a	46.75	554.93	0.192
3.70	289.830	0.1350	1.69	0.04	11.22	0.26	b	75.28	1195.18	0.159
5.20	271.057	0.1262	1.73	0.05	11.49	0.35	c	87.31	2328.46	0.142
6.70	247.692	0.1154	1.83	0.05	12.15	0.34	d	97.72	12955.00	0.126
12.00	1173.434	0.5465	1.74	0.01	11.54	0.09	e	95.77	6993.56	0.127
3.00	415.658	0.1507	1.71	0.03	11.36	0.23	f	57.08	688.57	0.213
4.50	398.701	0.1446	1.75	0.03	11.60	0.21	g	82.56	1694.40	0.154
6.00	500.087	0.1813	1.78	0.02	11.79	0.11	h	89.32	2766.32	0.144
7.50	293.994	0.1066	1.83	0.03	12.12	0.22	i	99.13	33993.77	0.145
9.80	292.731	0.1061	1.78	0.03	11.79	0.18	j	99.05	31065.67	0.136
13.00	856.988	0.3107	1.75	0.01	11.63	0.08	k	96.18	7728.28	0.132

Integrated results

$^{39}Ar \times 10^{-6}$	$^{40}Ar^*/^{39}Ar_K$	1 σ	Age in Ma	1 σ	% $^{40}Ar^*$	$^{40}Ar/^{36}Ar$	$^{37}Ar_{Ca}/^{39}Ar_K$
2147.0	1.74	0.02	11.53	0.12	85.25	2003.76	0.138
2758.0	1.76	0.01	11.68	0.09	84.99	1968.15	0.152

J = 0.003689 ± 0.000018

Preferred age t_p = 11.70 ± 0.07 Ma,

calculated with the weighted mean of fractions f to k; 100% of ^{39}Ar released in 6 consecutive fractions, MSWD = 1.5

t_c = 11.69 ± 0.08 Ma, $(^{40}Ar/^{36}Ar)_i$ = 284 ± 8, MSWD = 1.5 for n = 11

LM 2
Dacite, Sierra Navachiste, El Muellecito

Long W	Lat N
-108.98	25.58

laser step-heating experiments on groundmass sample

Pwr	$^{39}Ar \times 10^{-6}$	F ^{39}Ar	$^{40}Ar^*/^{39}Ar_K$	1 σ	Age in Ma	1 σ			% $^{40}Ar^*$	$^{40}Ar/^{36}Ar$	$^{37}Ar_{Ca}/^{39}Ar_K$
0.50	71.743	0.0365	66.04	3.60	298.84	15.00	a	‡	34.52	451.27	1.201
0.90	208.660	0.1061	9.45	0.65	45.92	3.10	b		31.49	431.32	0.644
1.70	534.693	0.2719	3.35	0.22	16.41	1.08	c		51.75	612.40	0.455
3.50	764.359	0.3887	3.03	0.19	14.85	0.94	d		57.79	700.06	0.503
6.00	387.392	0.1969	5.39	0.70	26.33	3.41	e	‡	51.88	614.06	1.046
0.30	87.116	0.0297	58.41	8.66	266.73	36.77	f	‡	24.50	391.40	3.793
0.60	217.370	0.0743	17.84	2.16	85.73	10.14	g		32.30	436.48	0.695
1.20	519.138	0.1775	3.97	0.56	19.43	2.70	h		49.25	582.31	0.291
2.00	976.263	0.3338	2.89	0.16	14.16	0.80	i		75.91	1226.58	0.311
3.00	532.749	0.1821	2.72	0.21	13.34	1.01	j		53.68	638.00	0.448
4.00	196.403	0.0671	4.12	0.51	20.16	2.50	k		64.97	843.66	0.460
5.00	194.278	0.0664	5.51	0.69	26.89	3.35	l	‡	73.79	1127.49	0.730
7.00	201.825	0.0690	6.39	0.81	31.20	3.94	m	‡	65.51	856.69	1.401

Integrated results

$^{39}Ar \times 10^{-6}$	$^{40}Ar^*/^{39}Ar_K$	1 σ	Age in Ma	1 σ	% $^{40}Ar^*$	$^{40}Ar/^{36}Ar$	$^{37}Ar_{Ca}/^{39}Ar_K$
1966.0	6.56	0.31	32.00	1.55	40.99	500.78	0.637
2924.0	6.31	0.40	30.79	1.96	38.45	480.12	0.577

J = 0.002728 ± 0.000040

t = 13.84 ± 0.64 Ma,

calculated with the weighted mean of fractions i and j; 51.59% of ^{39}Ar released in 2 consecutive fractions, MSWD = 0.4

Preferred age t_c = 11.34 ± 0.79 Ma, $(^{40}Ar/^{36}Ar)_i$ = 400 ± 10, MSWD = 1.22 for n = 8

‡ Fractions ignored in the isochron

Roca 24J 33

Microdiorite, S of Pescadero transform

Long W	Lat N
-109.04	24.02

laser step-heating experiments on hornblende concentrate

Pwr	$^{39}Ar \times 10^{-6}$	F ^{39}Ar	$^{40}Ar^*/^{39}Ar_K$	1σ	Age in Ma	1σ		% $^{40}Ar^*$	$^{40}Ar/^{36}Ar$	$^{37}Ar_{Ca}/^{39}Ar_K$
0.20	3.467	0.0033	31.33	7.76	185.17	43.60	a	7.16	318.30	2.118
0.80	83.358	0.0791	4.83	0.95	29.80	5.79	b	8.78	323.94	1.635
1.40	267.240	0.2536	2.36	0.15	14.63	0.95	c	19.68	367.90	1.952
2.00	278.722	0.2643	1.88	0.06	11.65	0.37	d	47.13	558.91	2.757
2.80	232.719	0.2208	2.05	0.08	12.74	0.47	e	59.69	733.03	2.030
4.00	94.286	0.0894	1.86	0.18	11.52	1.14	f	40.90	499.96	3.114
6.00	94.584	0.0895	2.11	0.15	13.08	0.91	g	28.83	415.19	6.289

Integrated results

$^{39}Ar \times 10^{-6}$	$^{40}Ar^*/^{39}Ar_K$	1σ	Age in Ma	1σ	% $^{40}Ar^*$	$^{40}Ar/^{36}Ar$	$^{37}Ar_{Ca}/^{39}Ar_K$
1053.0	2.39	0.10	14.80	0.62	20.41	371.26	2.649

J = 0.00345 ± 0.000025

Preferred age t_c = 11.29 ± 0.37 Ma

$(^{40}Ar/^{36}Ar)_i$ = 313 ± 4, MSWD = 1.12 for n = 7

W_m = 12.14 ± 0.34 Ma, calculated with the weighted mean of fractions d to g; 66.40% of ^{39}Ar released in 4 consecutive fractions, MSWD = 1.53

PER 8
Basaltic andesite, S of Culiacán

Long W	Lat N
-107.12	24.38

laser step-heating experiments on groundmass sample

Pwr	$^{39}Ar \times 10^{-6}$	F ^{39}Ar	$^{40}Ar^*/^{39}Ar_K$	1 σ	Age in Ma	1 σ		% $^{40}Ar^*$	$^{40}Ar/^{36}Ar$	$^{37}Ar_{Ca}/^{39}Ar_K$
0.40	412.642	0.0542	0.95	0.35	5.65	2.10	a	5.67	313.28	0.602
0.80	762.979	0.1001	1.60	0.14	9.50	0.85	b	21.27	375.31	1.173
1.40	1705.234	0.2236	1.85	0.05	10.93	0.29	c	48.82	577.36	1.679
3.00	2431.496	0.3188	1.90	0.03	11.25	0.17	d	66.10	871.64	2.095
7.00	2316.772	0.3033	1.78	0.03	10.52	0.20	e	54.41	648.11	4.195

Integrated results

$^{39}Ar \times 10^{-6}$	$^{40}Ar^*/^{39}Ar_K$	1 σ	Age in Ma	1 σ	% $^{40}Ar^*$	$^{40}Ar/^{36}Ar$	$^{37}Ar_{Ca}/^{39}Ar_K$
7617.0	1.77	0.03	10.48	0.19	40.07	493.07	2.466

J = 0.0032919 ± 0.0000168

Preferred age t = 10.94 ± 0.23 Ma

calculated with the weighted mean of fractions c to e; 84.57% of ^{39}Ar released in 3 consecutive fractions, MSWD = 3.74

t_c = 11.44 ± 0.28 Ma, $(^{40}Ar/^{36}Ar)_i$ = 276 ± 8, MSWD = 2.26 for n = 5

SC 3

Santa Catalina Island andesite

Long W	Lat N
-110.797	25.683

laser step-heating experiments on plagioclase concentrate

Pwr	$^{39}Ar \times 10^{-6}$	F ^{39}Ar	$^{40}Ar^*/^{39}Ar_K$	1 σ	Age in Ma	1 σ		% $^{40}Ar^*$	$^{40}Ar/^{36}Ar$	$^{37}Ar_{Ca}/^{39}Ar_K$
1.00	222.636	0.1262	5.83	0.70	33.19	3.92	a	13.21	340.47	4.168
1.90	446.253	0.2530	2.84	0.19	16.22	1.10	b	16.56	354.14	4.509
3.00	565.409	0.3205	2.70	0.12	15.44	0.67	c	24.59	391.88	4.689
4.00	234.360	0.1327	2.93	0.14	16.74	0.77	d	28.60	413.86	6.739
6.00	296.281	0.1676	3.42	0.13	19.52	0.75	e	23.45	386.03	7.915
0.50	60.708	0.0845	4.41	0.74	25.17	4.22	f	8.60	323.29	2.785
1.00	127.514	0.1772	2.39	0.35	13.66	1.98	g	9.86	327.83	5.729
1.60	101.989	0.1419	1.90	0.12	10.88	0.67	h	19.96	369.21	4.011
2.50	117.970	0.1642	1.90	0.14	10.90	0.82	i	18.08	360.71	3.623
4.00	145.792	0.2025	2.95	0.13	16.84	0.76	j	21.92	378.44	7.077
6.00	165.553	0.2297	3.92	0.28	22.38	1.56	k	22.93	383.41	8.488

Integrated results

$^{39}Ar \times 10^{-6}$	$^{40}Ar^*/^{39}Ar_K$	1 σ	Age in Ma	1 σ	% $^{40}Ar^*$	$^{40}Ar/^{36}Ar$	$^{37}Ar_{Ca}/^{39}Ar_K$
1759.0	3.28	0.12	18.74	0.69	19.04	365.00	5.390
716.8	2.87	0.13	16.44	0.72	15.66	350.38	5.797

J = 0.003185 ± 0.000011

Preferred age t = 10.89 ± 0.52 Ma

Weighted mean age calculated with fractions h and i, which define the base of the saddle. 30.61% of ^{39}Ar released in 2 consecutive fractions, MSWD < 0.01

t_c = 10.14 ± 2.59 Ma, $(^{40}Ar/^{36}Ar)_i$ = 322 ± 13, MSWD = 8.4 for n = 11

PER 7
Basaltic andesite, S of Culiacán

Long W	Lat N
-107.35	24.71

laser step-heating experiments on groundmass sample

Pwr	$^{39}Ar \times 10^{-6}$	F ^{39}Ar	$^{40}Ar^*/^{39}Ar_K$	1 σ	Age in Ma	1 σ		% $^{40}Ar^*$	$^{40}Ar/^{36}Ar$	$^{37}Ar_{Ca}/^{39}Ar_K$
0.50	1037.845	0.1427	1.41	0.16	8.38	0.95	a	13.05	339.84	0.535
1.20	1846.448	0.2538	1.79	0.07	10.57	0.44	b	29.13	416.97	1.309
2.40	2286.918	0.3142	1.86	0.07	11.03	0.43	c	37.79	474.97	1.963
7.00	2108.358	0.2892	1.75	0.04	10.35	0.25	d	36.66	466.55	4.387
0.50	1346.814	0.2240	2.35	0.17	13.92	1.03	e	24.72	392.52	0.720
1.10	2102.762	0.3495	1.78	0.05	10.55	0.30	f	33.23	442.57	1.540
1.80	1258.608	0.2091	1.72	0.05	10.21	0.30	g	38.75	482.48	2.516
3.80	922.477	0.1530	1.58	0.06	9.33	0.34	h	35.11	455.38	5.201
7.00	388.459	0.0644	1.88	0.14	11.10	0.81	i	40.51	496.76	6.323

Integrated results

$^{39}Ar \times 10^{-6}$	$^{40}Ar^*/^{39}Ar_K$	1 σ	Age in Ma	1 σ	% $^{40}Ar^*$	$^{40}Ar/^{36}Ar$	$^{37}Ar_{Ca}/^{39}Ar_K$
7269.0	1.75	0.04	10.34	0.25	28.95	415.91	2.294
6010.0	1.87	0.05	11.08	0.29	31.62	432.12	2.428

J = 0.0032919 ± 0.0000168

Preferred age t_p = 10.54 ± 0.20 Ma

the plateau age was calculated with the weighted mean of fractions b to d; 86.73% of ^{39}Ar released in 3 consecutive fractions, MSWD = 0.93

t_c = 9.76 ± 0.90 Ma, $(^{40}Ar/^{36}Ar)_i$ = 304 ± 13, MSWD = 3.57 for n = 9

HUA 6
Basaltic andesite, Road to Las Peñitas microwave st

Long W	Lat N
-105.22	21.94

laser step-heating experiments on whole rock sample

Pwr	$^{39}Ar \times 10^{-6}$	F ^{39}Ar	$^{40}Ar^*/^{39}Ar_K$	1 σ	Age in Ma	1 σ			% $^{40}Ar^*$	$^{40}Ar/^{36}Ar$	$^{37}Ar_{Ca}/^{39}Ar_K$
0.40	39.84	0.0107	-1.74	3.46	-10.39	20.69	a		-1.77	290.36	5.387
1.10	266.93	0.0717	1.18	0.16	6.98	0.97	b		18.84	364.08	4.968
1.70	746.60	0.2005	2.45	0.08	14.52	0.48	c	‡	95.33	6323.27	3.051
2.70	1302.03	0.3497	1.76	0.03	10.43	0.18	d		78.42	1369.52	2.148
3.90	738.48	0.1983	1.72	0.03	10.18	0.20	e		80.75	1535.19	2.939
6.00	629.82	0.1691	1.75	0.04	10.39	0.26	f		80.71	1532.25	4.111
1.00	402.09	0.0719	2.11	0.59	12.49	3.46	g		10.73	331.02	5.033
1.50	752.26	0.1344	1.71	0.04	10.10	0.23	h		59.36	727.06	3.511
2.50	2004.26	0.3582	1.77	0.03	10.49	0.16	i		75.84	1222.90	2.355
3.50	972.17	0.1737	1.84	0.04	10.90	0.25	j		87.00	2273.12	2.416
4.50	475.07	0.0849	1.74	0.05	10.33	0.28	k		84.18	1868.06	2.776
6.00	989.38	0.1768	1.89	0.06	11.21	0.35	l		91.12	3328.69	3.650

Integrated results

$^{39}Ar \times 10^{-6}$	$^{40}Ar^*/^{39}Ar_K$	1 σ	Age in Ma	1 σ	% $^{40}Ar^*$	$^{40}Ar/^{36}Ar$	$^{37}Ar_{Ca}/^{39}Ar_K$
3724.0	1.81	0.05	10.73	0.27	50.39	595.68	3.055
5595.0	1.82	0.05	10.77	0.28	51.26	606.30	2.978

J = 0.0032919 ± 0.0000168

Preferred age t_p = 10.45 ± 0.15 Ma,

calculated with the weighted mean of fractions h to k; 75.13% of ^{39}Ar released in 4 consecutive fractions, MSWD = 1.95

t_c = 10.61 ± 0.15 Ma, $(^{40}Ar/^{36}Ar)_i$ = 279 ± 10, MSWD = 2.85 for n = 11

‡ Fraction ignored in the isochron

PER 14
Basaltic andesite, W of Pericos VF

Long W	Lat N
-108.00	25.15

Ta furnace step-heating experiment on groundmass sample

Temp ºC	^{39}Ar cc STP/g	F ^{39}Ar	^{40}Ar*/^{39}Ar$_K$	1 σ	Age in Ma	1 σ		% ^{40}Ar*	^{40}Ar/^{36}Ar	^{37}Ar$_{Ca}$/^{39}Ar$_K$
500	9.555E-09	0.0208	9.50	3.92	60.83	24.68	a	4.29	308.75	0.489
600	1.015E-07	0.2205	2.47	0.20	16.00	1.30	b	19.37	366.50	0.269
700	1.103E-07	0.2396	1.71	0.08	11.09	0.50	c	34.11	448.50	0.774
800	1.094E-07	0.2377	1.37	0.06	8.91	0.39	d	38.78	482.65	2.287
850	4.690E-07	0.1019	1.76	0.09	11.44	0.60	e	51.46	608.75	2.877
900	1.815E-08	0.0394	1.57	0.23	10.21	1.47	f	32.45	437.47	3.260
1000	2.418E-08	0.0525	1.55	0.19	10.08	1.24	g	23.60	386.81	3.173
1100	2.982E-08	0.0648	1.85	0.18	12.00	1.14	h	23.96	388.63	3.524
1350	1.051E-08	0.0228	1.23	0.43	7.97	2.78	i	10.65	330.71	0.188

Integrated results

^{39}Ar ccSTP/g	^{40}Ar*/^{39}Ar$_K$	1 σ	Age in Ma	1 σ	% ^{40}Ar*	^{40}Ar/^{36}Ar	^{37}Ar$_{Ca}$/^{39}Ar$_K$
4.604E-07	1.95	0.18	12.64	1.19	17.56	358.44	2.076

J = 0.0035828 ± 0.0000775

sample weight = 1.1410 g; estimated 0.67%K

Preferred age t_c = 10.33 ± 0.88 Ma, (^{40}Ar/^{36}Ar)$_i$ = 310 ± 4, MSWD = 28 for n = 9

PER 1
Hawaiite lava, Pericos Volcanic field

Long W	Lat N
-107.52	25.04

laser step-heating experiments on groundmass sample

Pwr	$^{39}Ar \times 10^{-6}$	F ^{39}Ar	$^{40}Ar^*/^{39}Ar_K$	1 σ	Age in Ka	1 σ			% $^{40}Ar^*$	$^{40}Ar/^{36}Ar$	$^{37}Ar_{Ca}/^{39}Ar_K$
0.80	379.17	0.0606	-0.08	0.15	- 434	839	a	‡	-1.86	290.12	0.804
1.50	1502.84	0.2401	0.16	0.02	890	122	b		34.98	454.50	0.585
2.50	2436.37	0.3893	0.15	0.02	844	90	c		36.85	467.92	0.760
8.00	1939.88	0.3100	0.07	0.02	418	131	d	‡	8.17	321.78	4.138
0.80	589.67	0.0410	4.52	0.36	25091	1974	e	‡	82.92	1730.48	0.926
1.50	2814.98	0.1955	0.15	0.02	827	132	f		32.22	436.00	0.623
2.50	5074.98	0.3524	0.15	0.01	863	55	g		46.94	556.97	0.640
8.05	5919.98	0.4111	0.12	0.02	656	107	h	‡	21.62	377.01	2.188

Integrated results

$^{39}Ar \times 10^{-6}$	$^{40}Ar^*/^{39}Ar_K$	1 σ	Age in Ka	1 σ	% $^{40}Ar^*$	$^{40}Ar/^{36}Ar$	$^{37}Ar_{Ca}/^{39}Ar_K$
6258.0	0.12	0.01	646	80	14.33	344.94	1.768
14400.0	0.32	0.02	1769	102	48.57	574.52	1.285

J = 0.0030998 ± 0.000017

t = 857 ± 51 Ka, calculated with the weighted mean of fractions f and g; 54.79% of ^{39}Ar released in 2 consecutive fractions, MSWD = 0.06

Preferred age t_c = 884 ± 97 Ka, $(^{40}Ar/^{36}Ar)_i$ = 288 ± 23, MSWD = 0.14 for n = 4

‡ Fractions ignored in the isochron

PER 4
Hawaiite lava, Pericos Volcanic field

Long W	Lat N
-107.54	25.11

laser step-heating experiments on groundmass sample

Pwr	$^{39}Ar \times 10^{-6}$	F ^{39}Ar	$^{40}Ar^*/^{39}Ar_K$	1 σ	Age in Ka	1 σ			% $^{40}Ar^*$	$^{40}Ar/^{36}Ar$	$^{37}Ar_{Ca}/^{39}Ar_K$
0.70	299.98	0.0642	-0.42	0.14	-2334	780	a	‡	-10.23	268.08	1.511
1.20	671.32	0.1438	0.17	0.04	926	219	b		30.91	427.68	1.135
2.00	420.10	0.0900	0.26	0.04	1447	207	c		59.36	727.06	0.874
5.00	2701.74	0.5782	0.17	0.04	936	201	d		34.90	453.94	2.394
8.00	578.43	0.1238	0.34	0.22	1913	1234	e		1.98	301.46	2.591
0.50	308.14	0.0245	-0.45	0.14	-2537	762	f	‡	-5.54	279.99	1.716
1.00	942.28	0.0750	0.06	0.04	332	238	g	‡	8.07	321.44	1.132
2.00	1871.69	0.1490	0.13	0.03	754	164	h		31.04	428.50	1.032
4.00	2487.30	0.1980	0.17	0.02	971	135	i		50.62	598.43	1.624
6.00	4754.56	0.3783	0.14	0.02	801	105	j		43.35	521.60	2.298
8.00	2202.06	0.1752	----	----	----	----	k		----	----	2.501

Integrated results

$^{39}Ar \times 10^{-6}$	$^{40}Ar^*/^{39}Ar_K$	1 σ	Age in Ka	1 σ	% $^{40}Ar^*$	$^{40}Ar/^{36}Ar$	$^{37}Ar_{Ca}/^{39}Ar_K$
4665.0	0.16	0.04	891	209	5.70	313.36	2.04
12550.0	----	----	----	----	----	----	1.91

J = 0.0030998 ± 0.000017

Preferred age t_p = 843 ± 74 Ka

calculated with the weighted mean of fractions h to j; 72.53% of ^{39}Ar released in 3 consecutive fractions, MSWD = 0.68

t_c = 853 ± 80 Ka, $(^{40}Ar/^{36}Ar)_i$ = 300 ± 9, MSWD = 2.56 for n = 7

‡ Fractions ignored in the isochron

for fraction k mass 36 was not tuned properly, no age information can be obtained.

PER 6
Hawaiite lava, Pericos Volcanic field

Long W	Lat N
-107.63	25.25

laser step-heating experiments on groundmass sample

Pwr	$^{39}Ar \times 10^{-6}$	F ^{39}Ar	$^{40}Ar^*/^{39}Ar_K$	1 σ	Age in Ka	1 σ			% $^{40}Ar^*$	$^{40}Ar/^{36}Ar$	$^{37}Ar_{Ca}/^{39}Ar_K$
0.10	17.47	0.0020	2.52	2.09	14025	11606	a		1.57	300.21	1.724
0.25	51.28	0.0059	-2.05	1.14	-11521	6417	b		-3.16	286.44	1.159
0.80	1159.98	0.1330	-0.02	0.07	-92	412	c		-0.29	294.64	0.875
1.50	3851.78	0.4417	0.12	0.02	694	102	d		14.22	344.47	0.740
8.00	3645.13	0.4174	0.08	0.02	467	97	e		7.91	320.90	2.959
0.55	560.595	0.0555	-0.03	0.24	-172	1369	f		-0.12	295.15	0.972
1.00	2278.277	0.2256	0.45	0.10	2496	574	g	‡	32.44	437.42	0.871
1.70	2575.058	0.2550	0.08	0.03	442	166	h		10.72	331.00	0.825
3.00	2553.623	0.2529	0.18	0.05	1021	256	i	‡	31.10	428.85	0.865
7.00	2137.154	0.2111	0.06	0.04	363	204	j		8.73	323.77	4.743

Integrated results

$^{39}Ar \times 10^{-6}$	$^{40}Ar^*/^{39}Ar_K$	1 σ	Age in Ka	1 σ	% $^{40}Ar^*$	$^{40}Ar/^{36}Ar$	$^{37}Ar_{Ca}/^{39}Ar_K$
8716.0	0.08	0.02	450	99	3.52	306.30	1.688
10090.0	0.18	0.03	1001	176	7.99	321.16	1.680

J = 0.0030998 ± 0.000017

t = 574 ± 113 Ka

calculated with the weighted mean of fractions d and e; 85.91% of ^{39}Ar released in 2 consecutive fractions, MSWD = 2.59

Preferred age t_c = 585 ± 82 Ka, $(^{40}Ar/^{36}Ar)_i$ = 292 ± 3, MSWD = 1.36 for n = 8

‡ Fractions ignored in the isochron

CHO 4

Volcanic field Los Choix

Long W	Lat N
-108.389	26.825

Ta furnace step-heating experiment on groundmass sample

Temp ºC	^{39}Ar cc STP/g	F ^{39}Ar	^{40}Ar*/^{39}Ar$_K$	1 σ	Age in Ka	1 σ		% ^{40}Ar*	^{40}Ar/^{36}Ar	^{37}Ar$_{Ca}$/^{39}Ar$_K$
350	3.5668E-09	0.0041	5.59	2.78	36044	17741	a	6.05	314.52	0.931
600	4.2325E-08	0.0487	-0.06	0.18	-368	1172	b	-1.18	292.07	0.625
1000	5.4710E-07	0.6289	0.02	0.02	138	107	c	4.44	309.02	0.599
1350	2.7698E-07	0.3184	0.09	0.03	563	225	d	9.11	325.11	3.600

Integrated results

^{39}Ar ccSTP/g	^{40}Ar*/^{39}Ar$_K$	1 σ	Age in Ka	1 σ	% ^{40}Ar*	^{40}Ar/^{36}Ar	^{37}Ar$_{Ca}$/^{39}Ar$_K$
8.700E-07	0.06	0.04	397	232	5.02	311.13	1.557

J = 0.003608 ± 0.000078

sample weight = 0.9834 g; estimated 1.27%K

t_c = 29 ± 181 Ka, (^{40}Ar/^{36}Ar)$_i$ = 311 ± 10, MSWD = 5.0 for n = 4

Preferred age: t = 138 ± 107 Ka

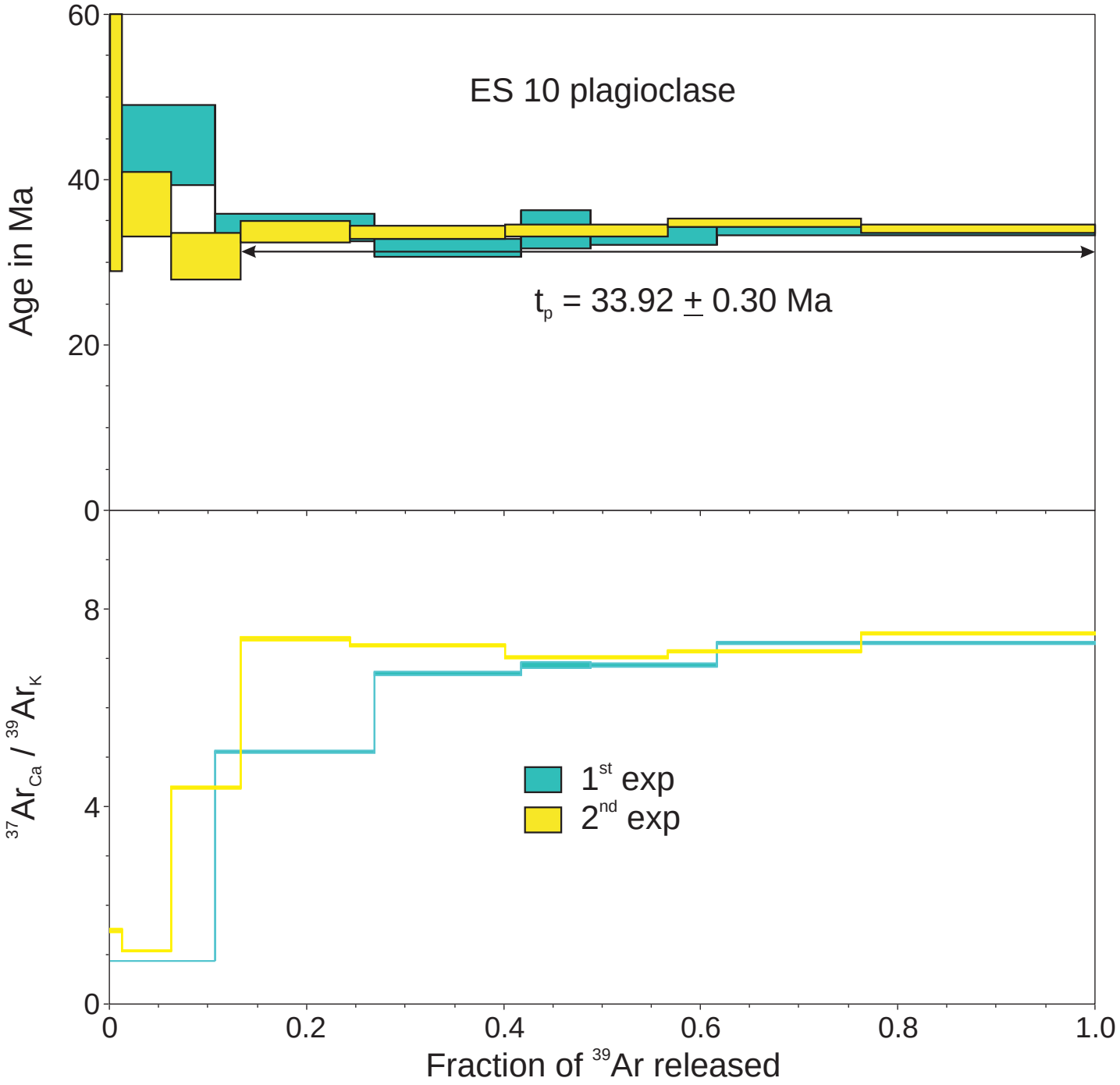

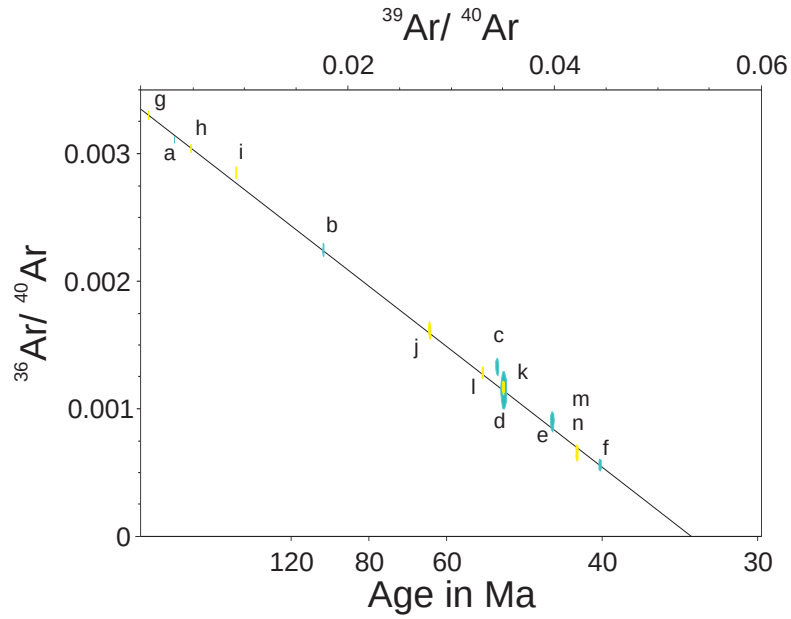

t_c = 33.58 ± 0.28 Ma

$(^{40}Ar / ^{36}Ar)_i$ = 298 ± 2

MSWD = 1.1, n = 14

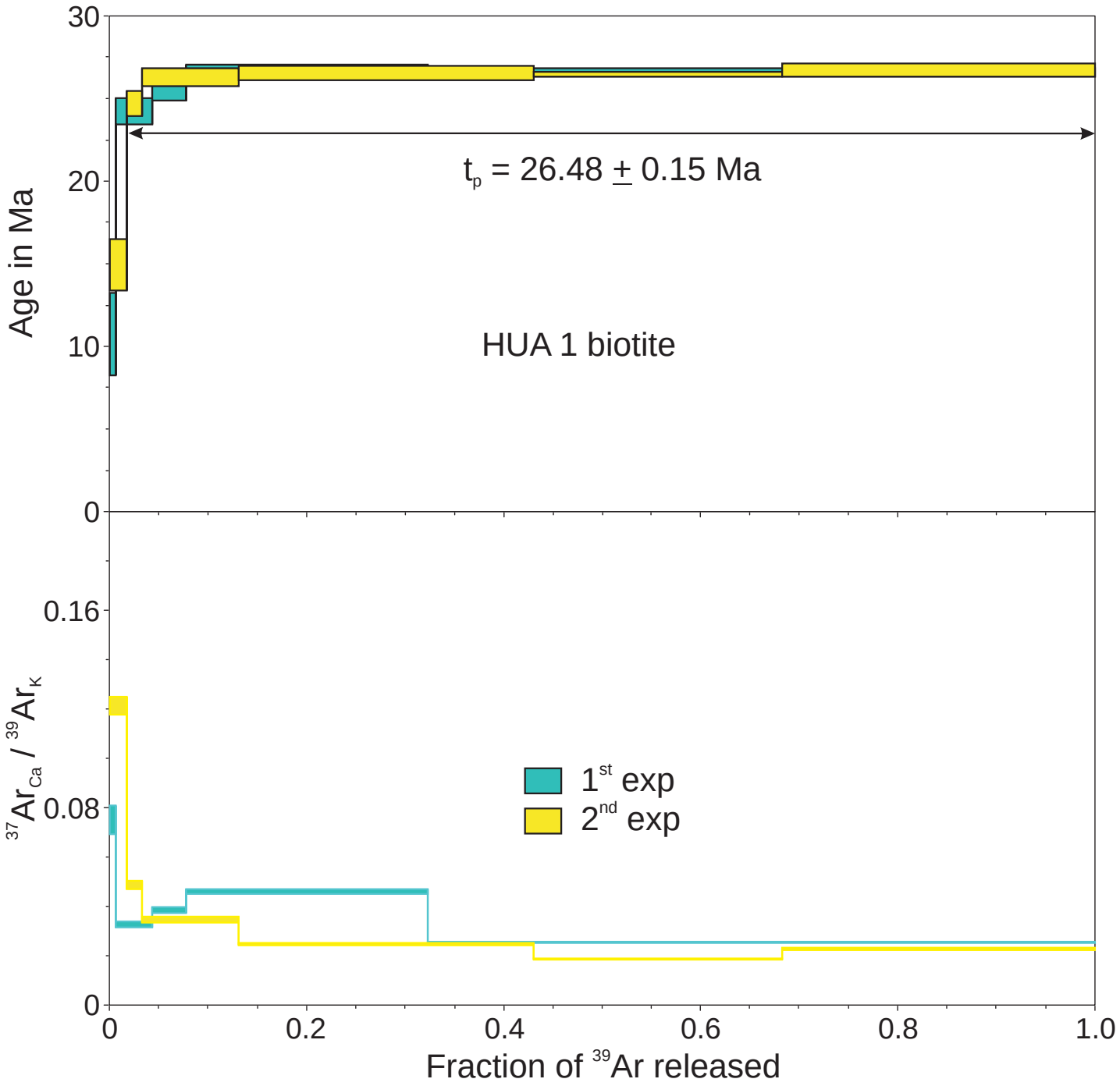

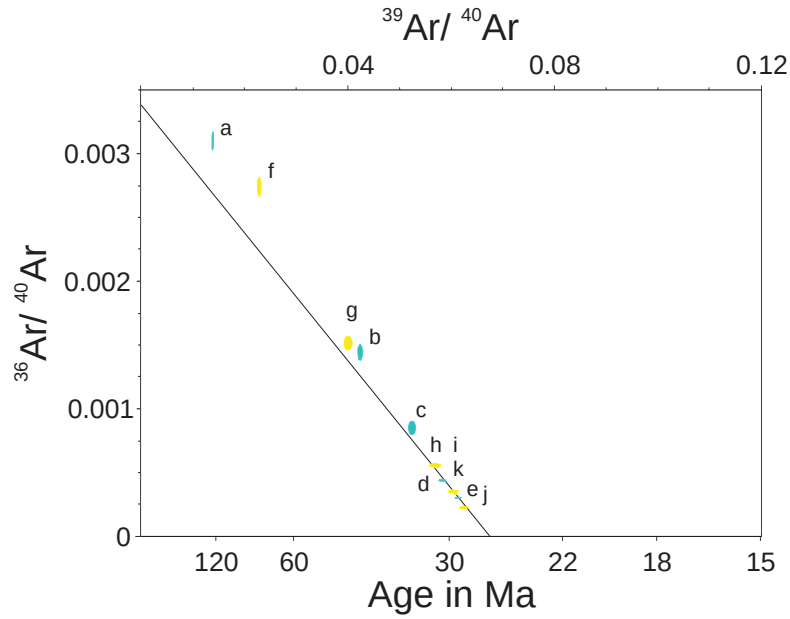

t_c = 26.51 ± 0.69 Ma

$(^{40}Ar / ^{36}Ar)_i$ = 295 ± 69

MSWD = 0.32, n = 5

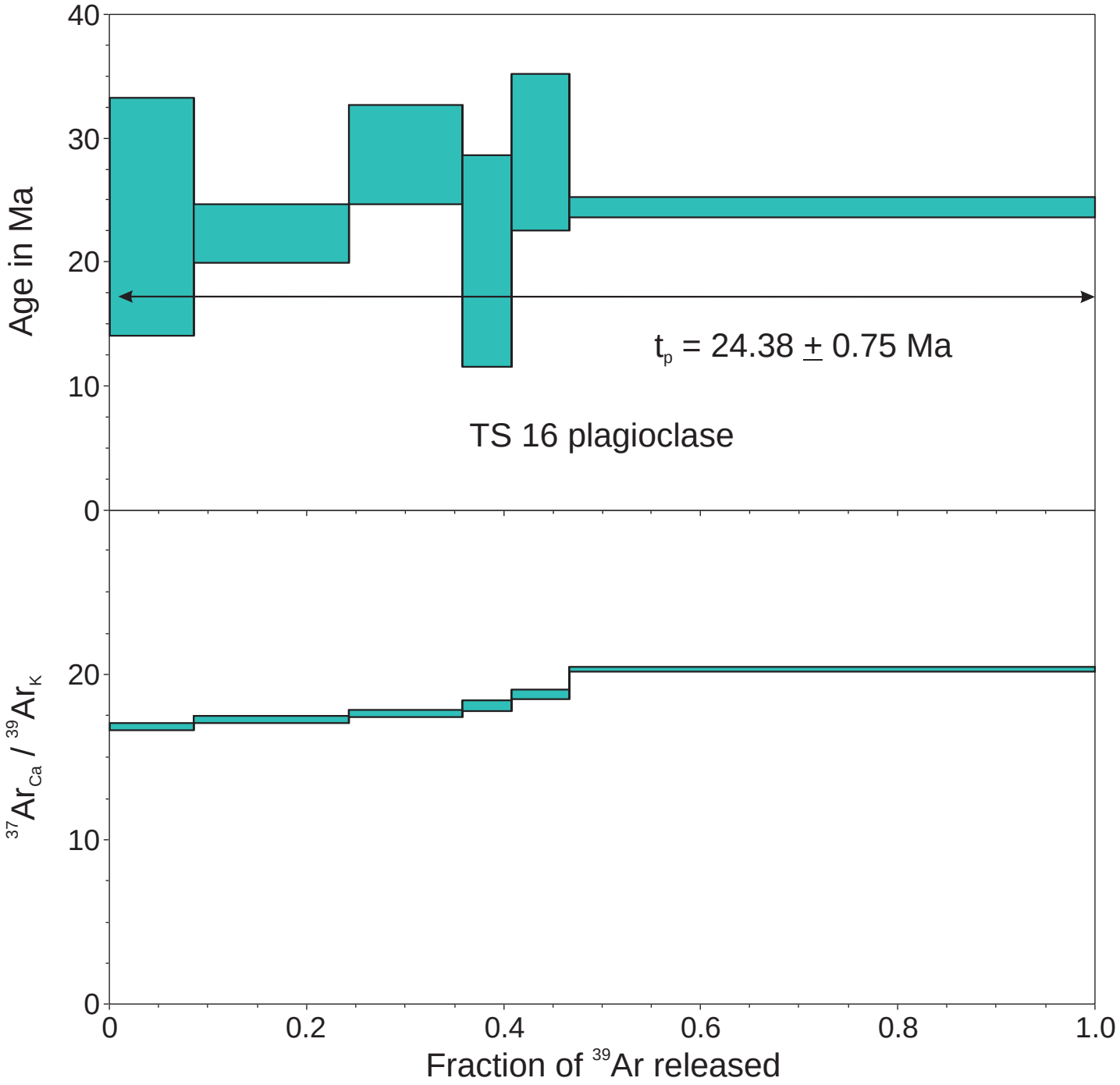

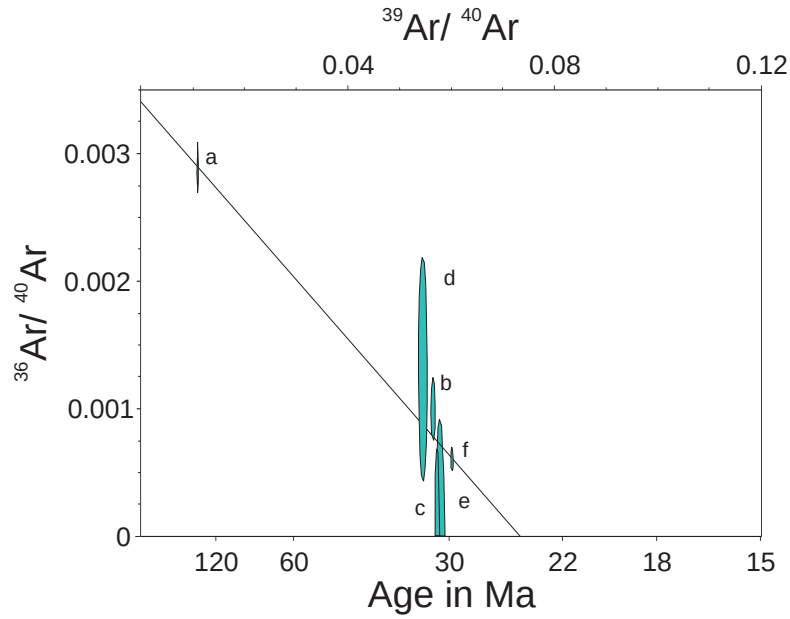

t_c = 24.43 ± 0.87 Ma

$(^{40}Ar / ^{36}Ar)_i$ = 293 ± 21

MSWD = 0.68, n = 6

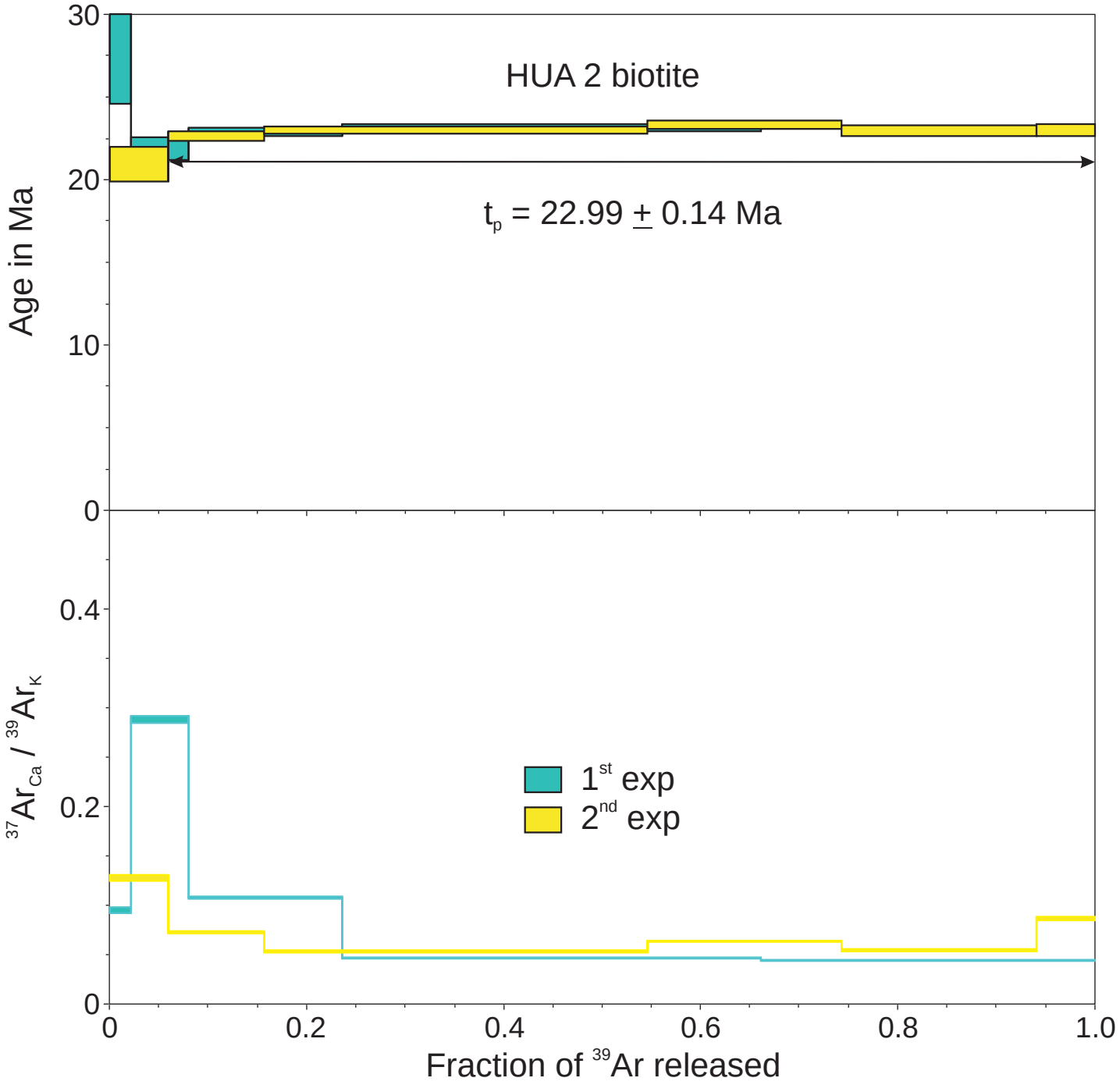

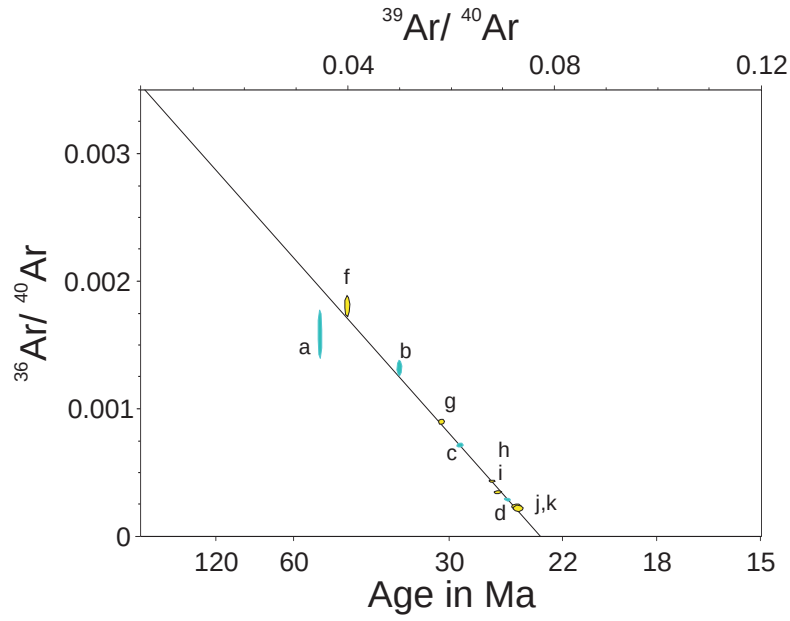

t_c = 23.19 ± 0.27 Ma

$(^{40}Ar / ^{36}Ar)_i$ = 282 ± 21

MSWD = 0.35, n = 6

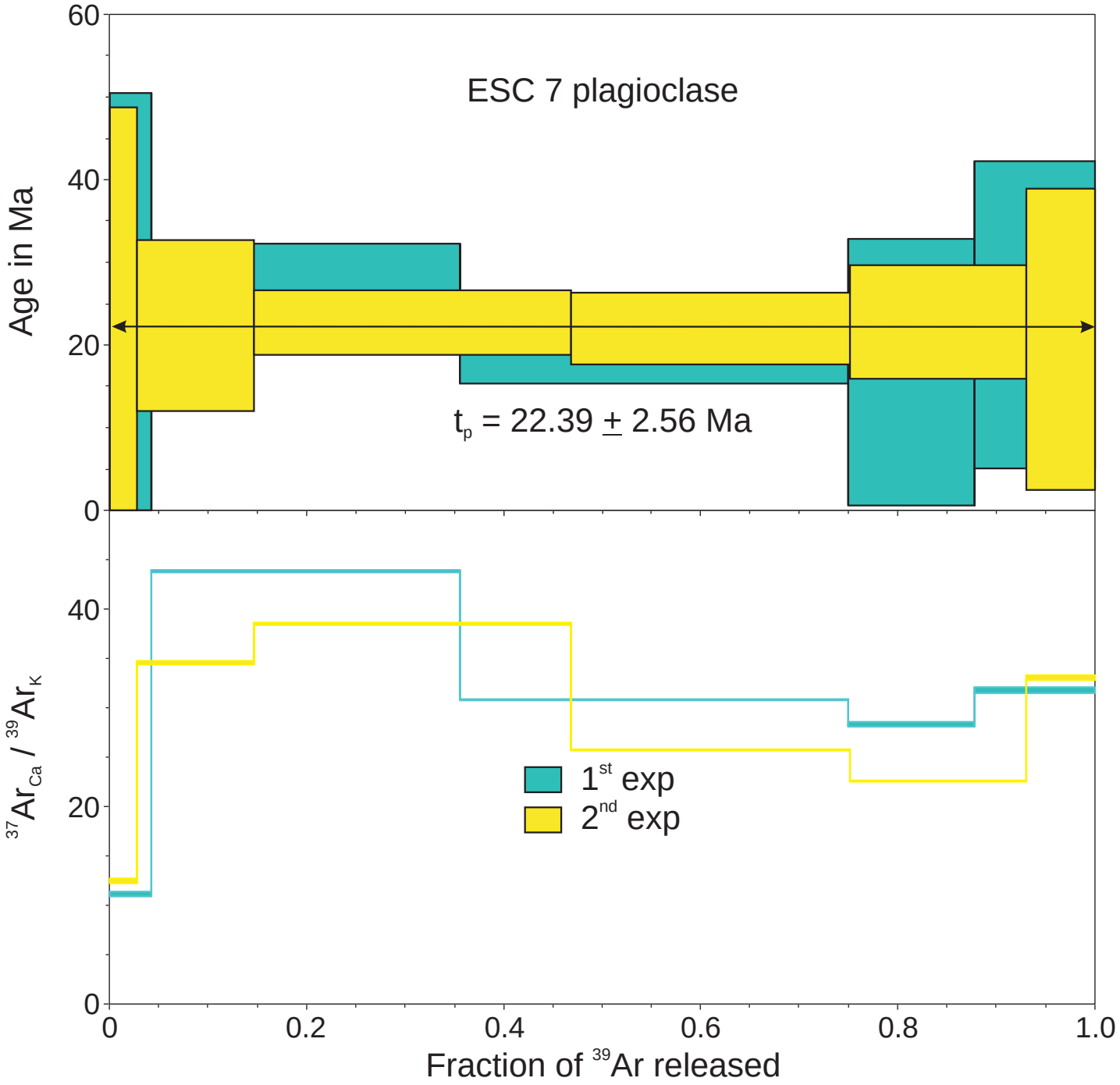

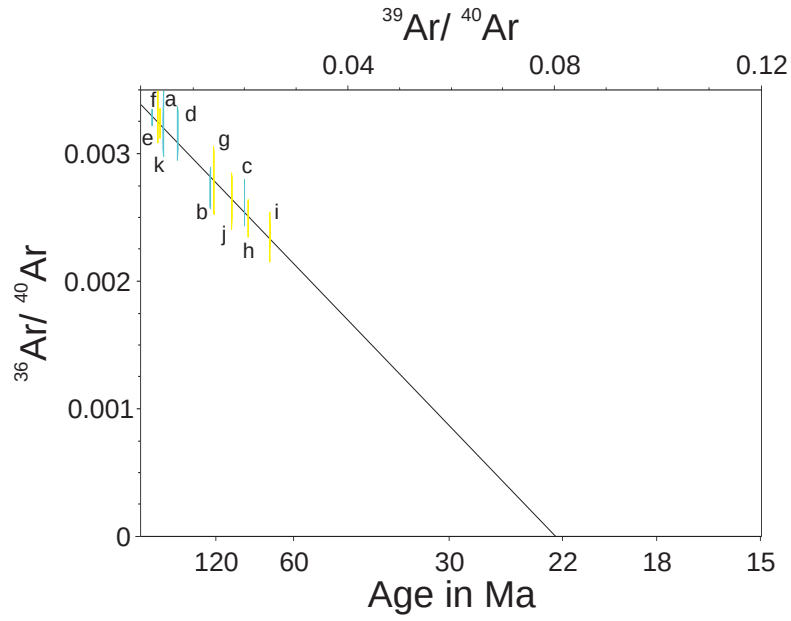

t_c = 22.35 ± 2.73 Ma

$(^{40}Ar / ^{36}Ar)_i$ = 295 ± 6

MSWD = 0.10, n = 11

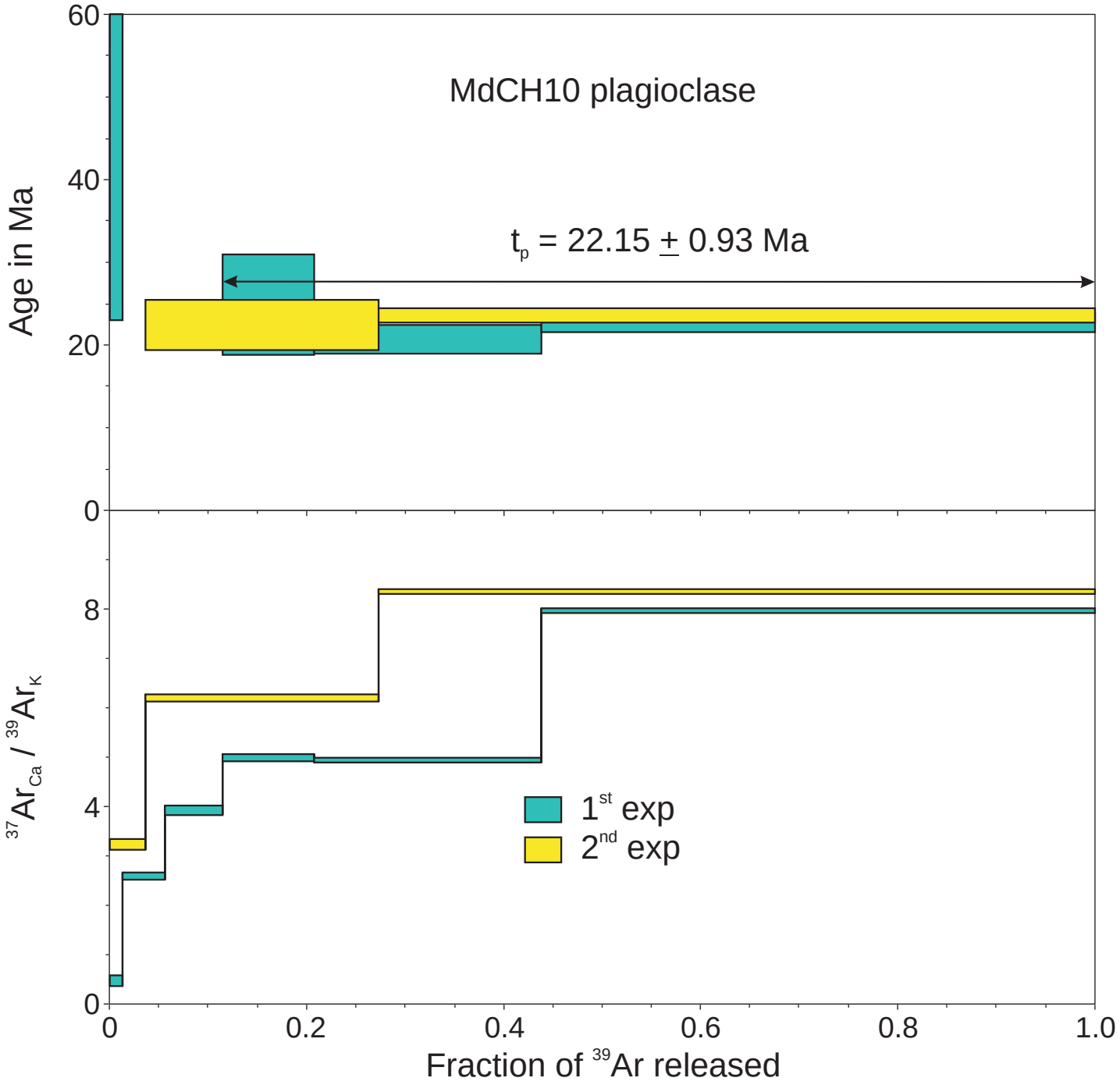

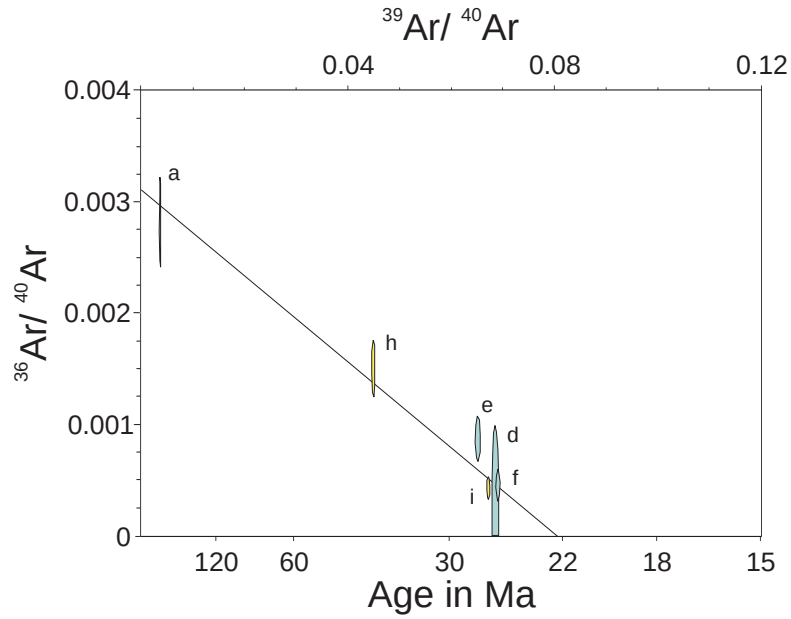

t_c = 22.51 ± 0.90 Ma

$(^{40}Ar / ^{36}Ar)_i$ = 322 ± 39

MSWD = 0.73, n = 6

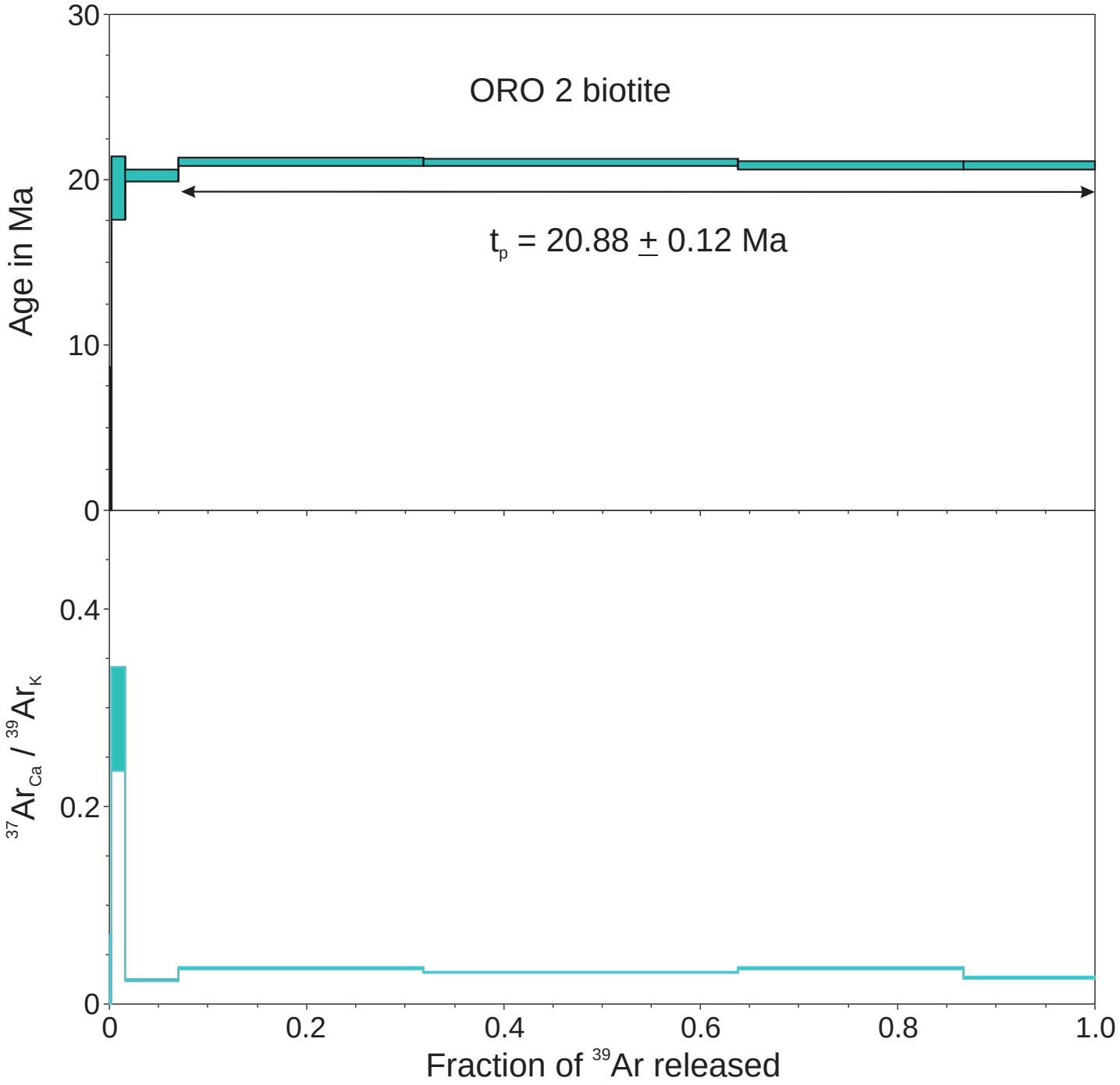

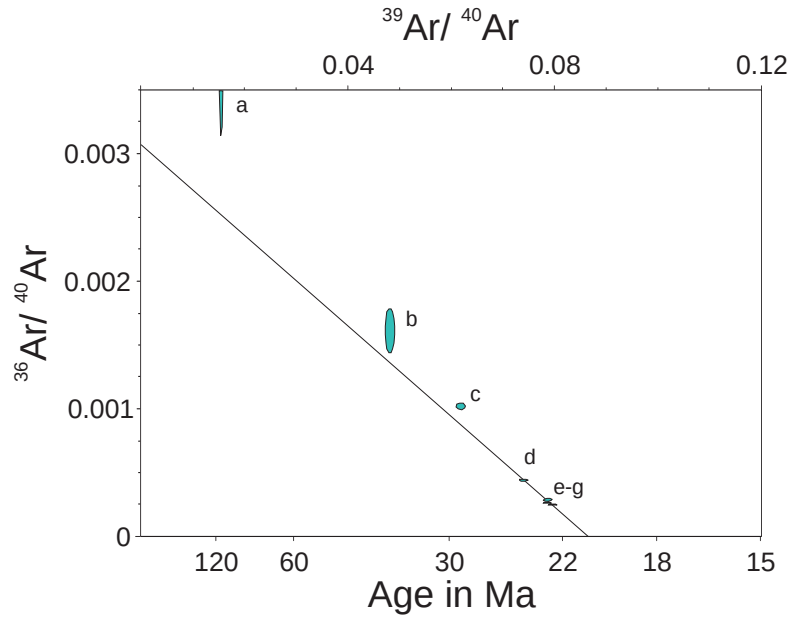

t_c = 20.74 ± 0.44 Ma

$(^{40}Ar / ^{36}Ar)_i$ = 325 ± 59

MSWD = 0.19, n = 4

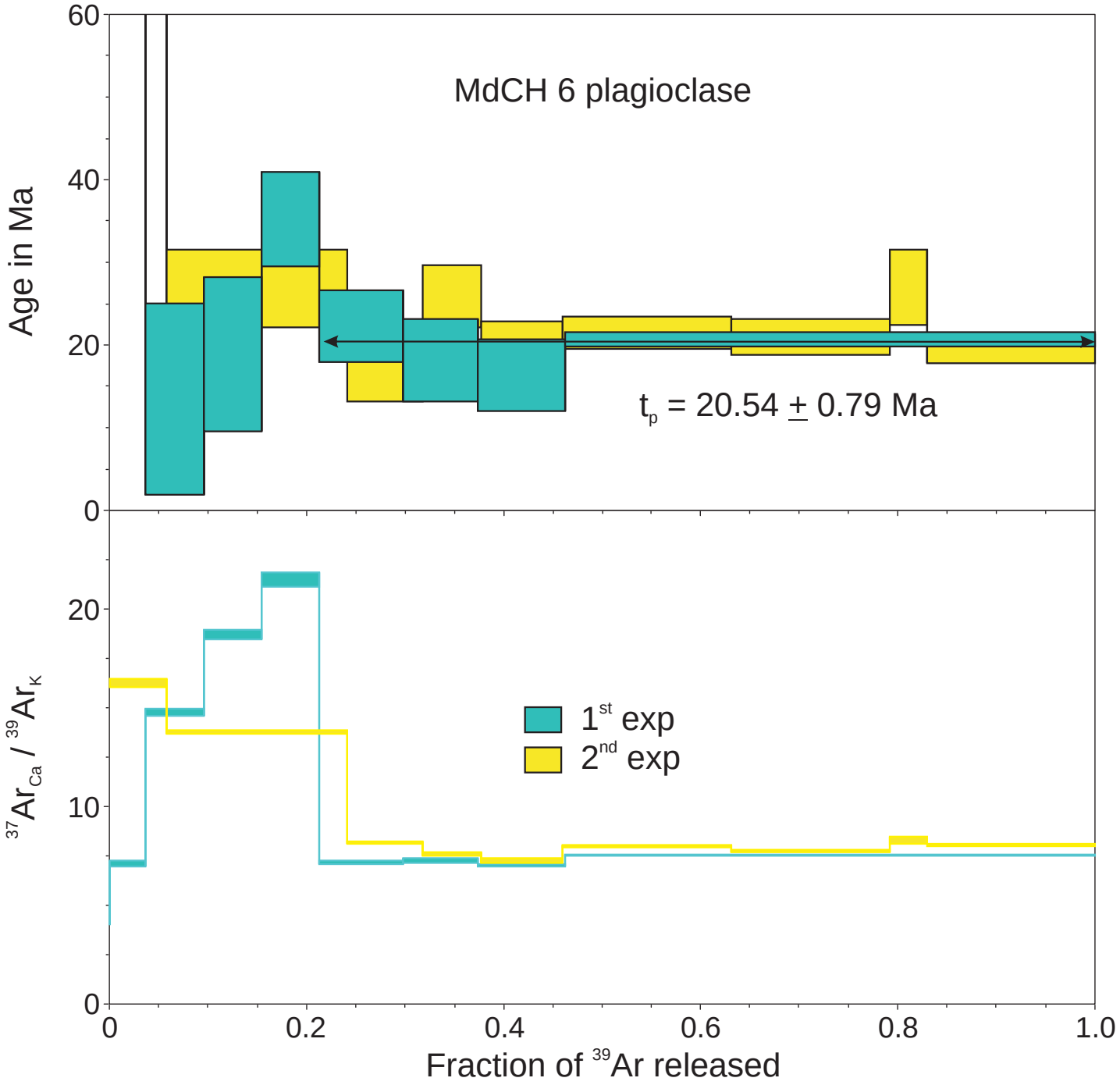

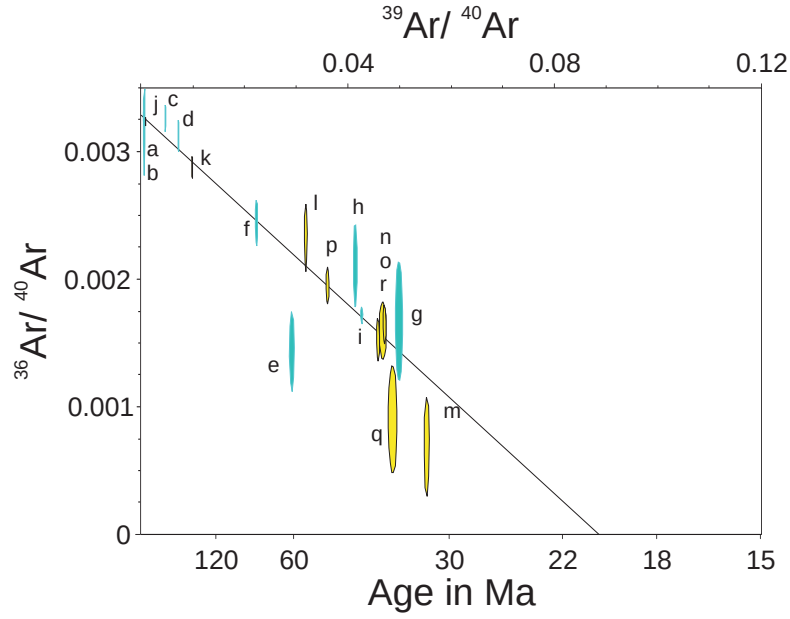

t_c = 20.25 ± 0.64 Ma

$(^{40}Ar / ^{36}Ar)_i$ = 304 ± 2

MSWD = 0.98, n = 18

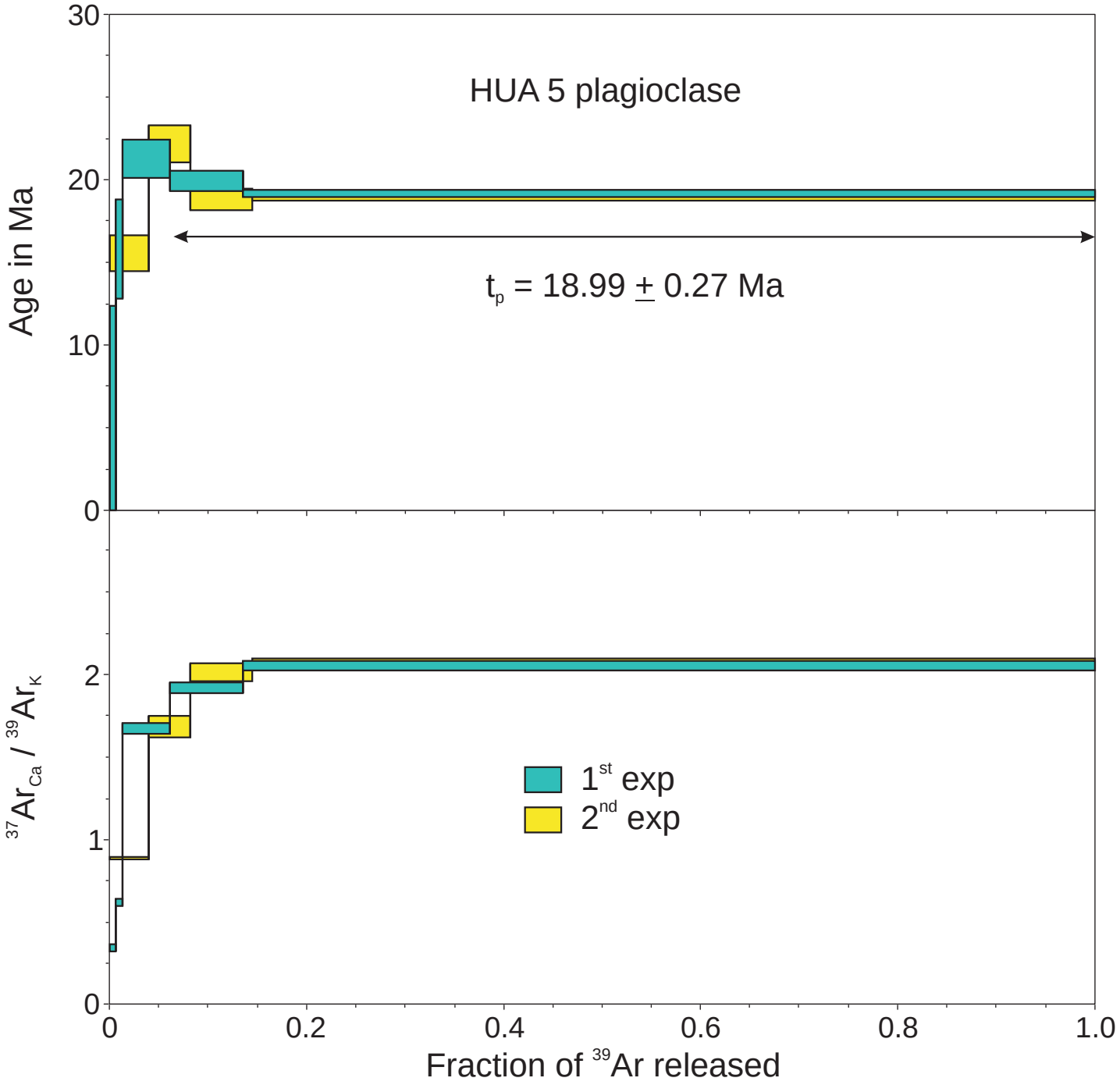

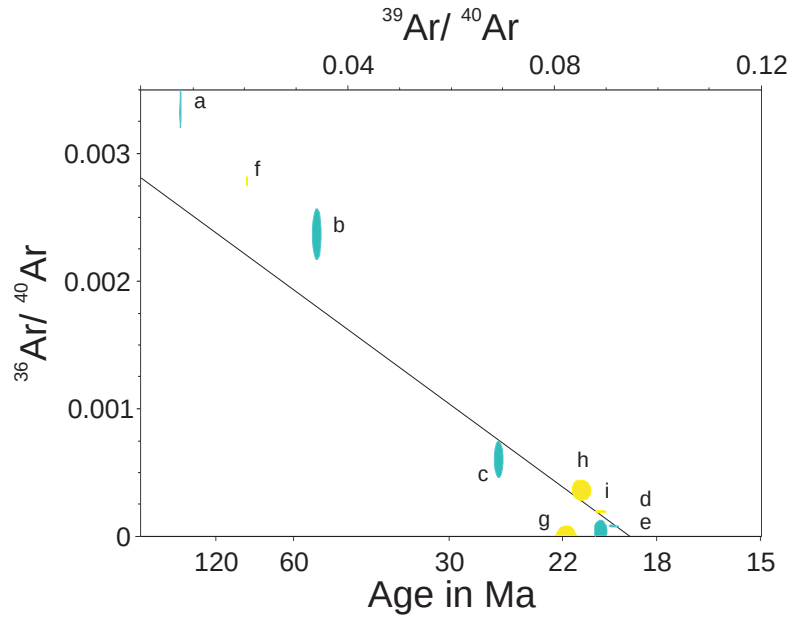

t_c = 18.98 ± 0.30 Ma

$(^{40}Ar / ^{36}Ar)_i$ = 356 ± 79

MSWD = 1.57, n = 5

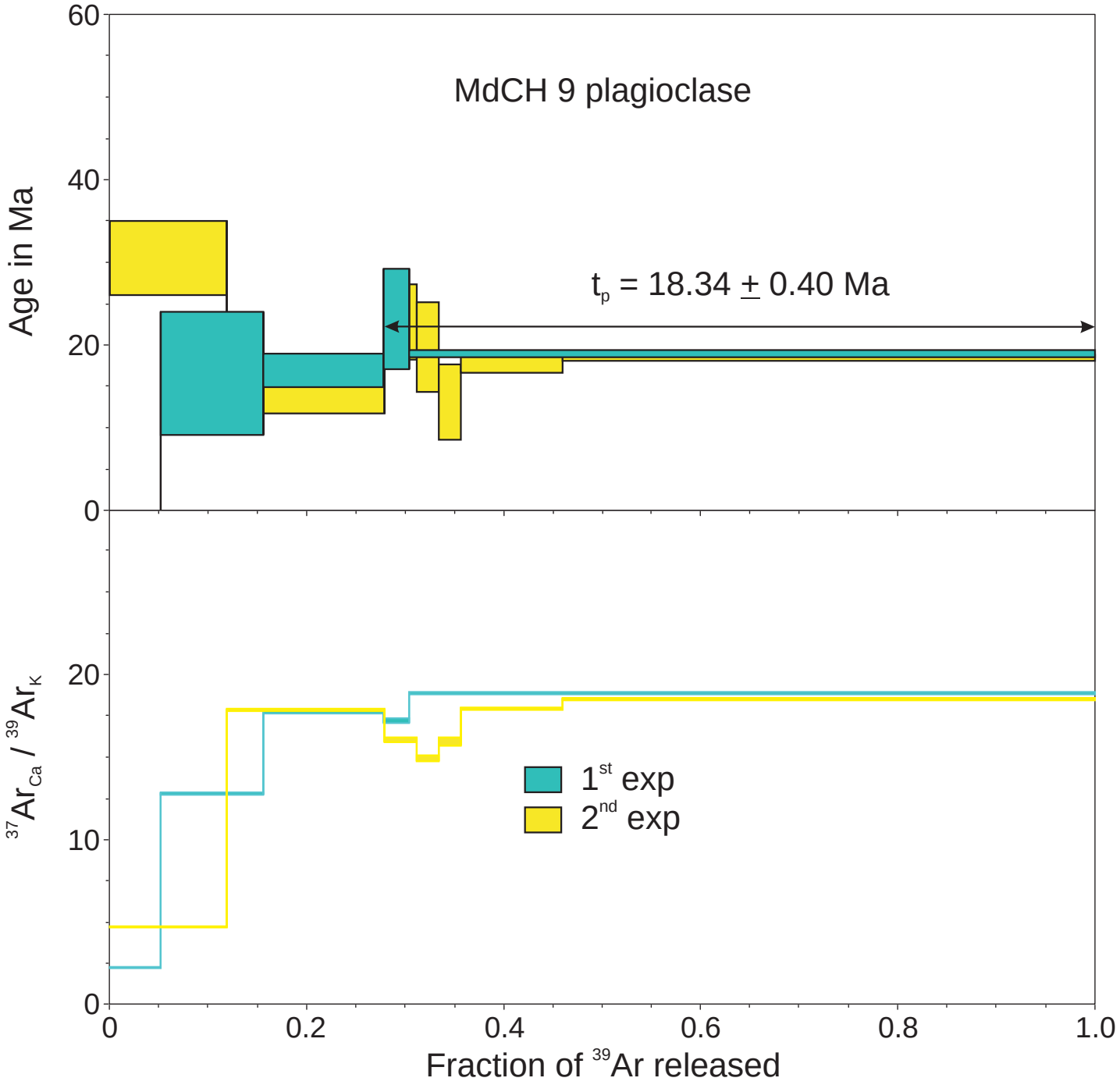

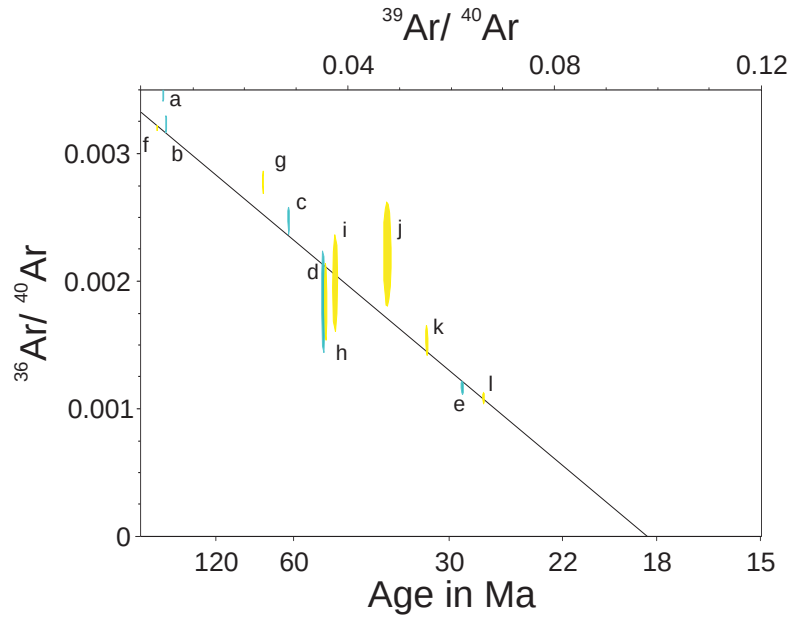

t_c = 18.32 ± 0.40 Ma

$(^{40}Ar / ^{36}Ar)_i$ = 300 ± 3

MSWD = 1.63, n = 11

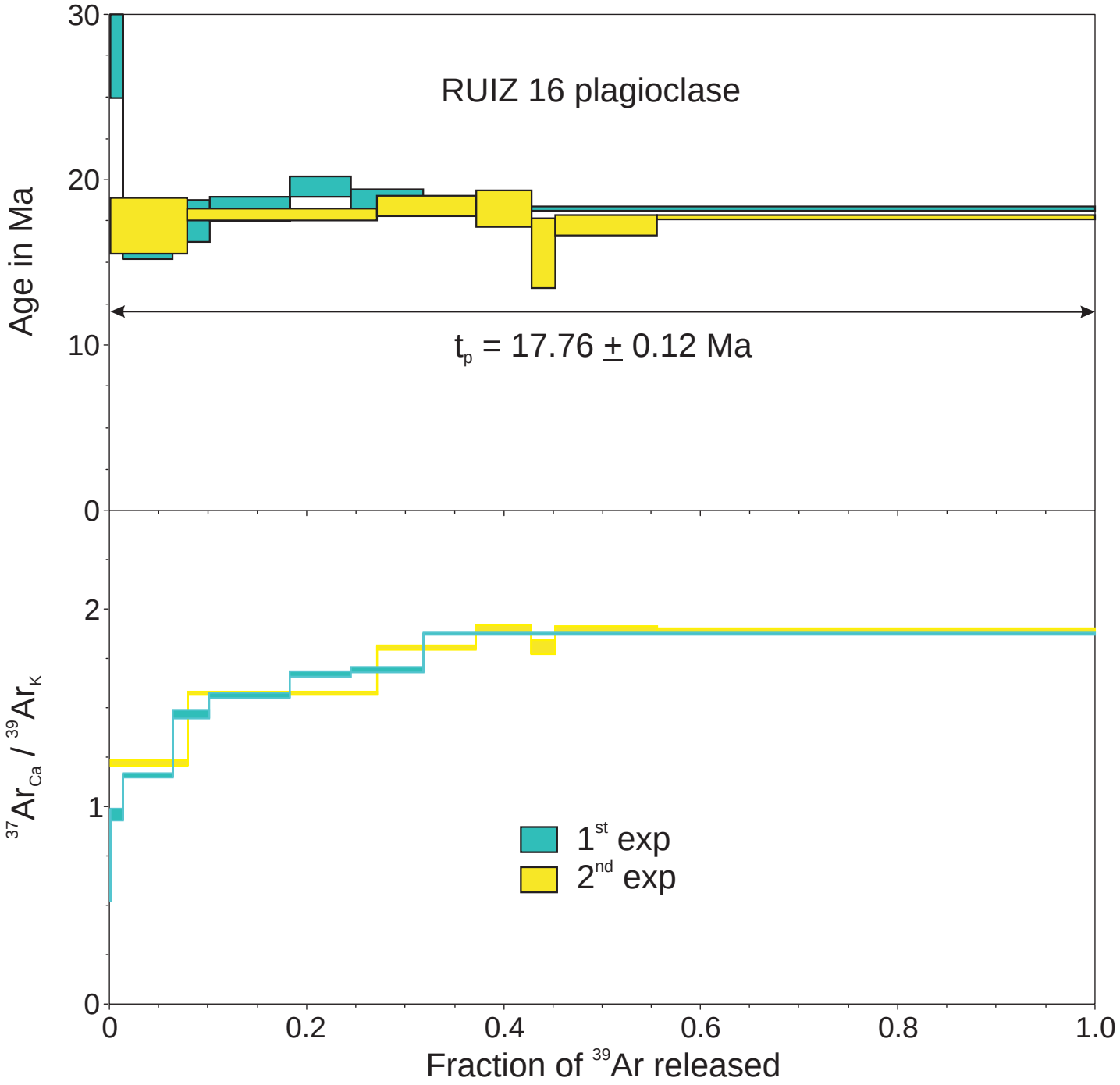

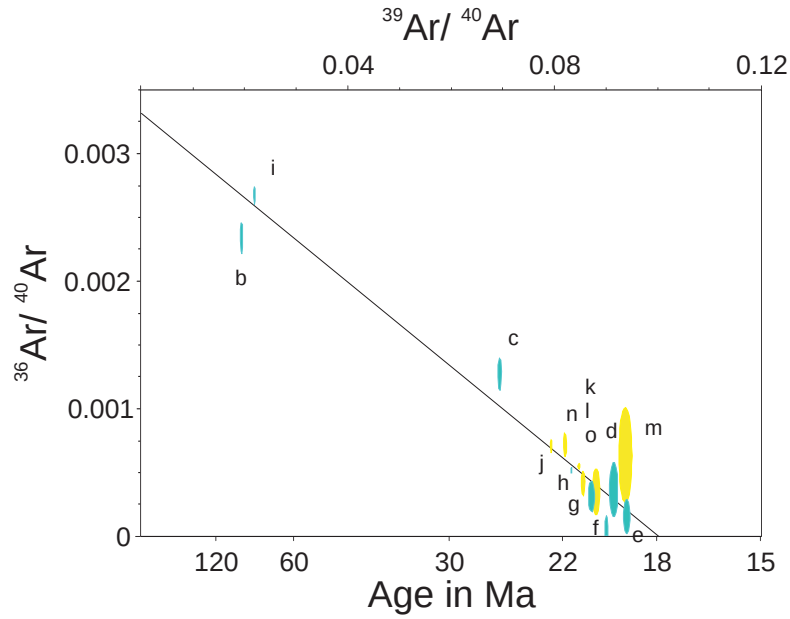

t_c = 17.91 ± 0.29 Ma

$(^{40}Ar / ^{36}Ar)_i$ = 301 ± 11

MSWD = 2.4, n = 14

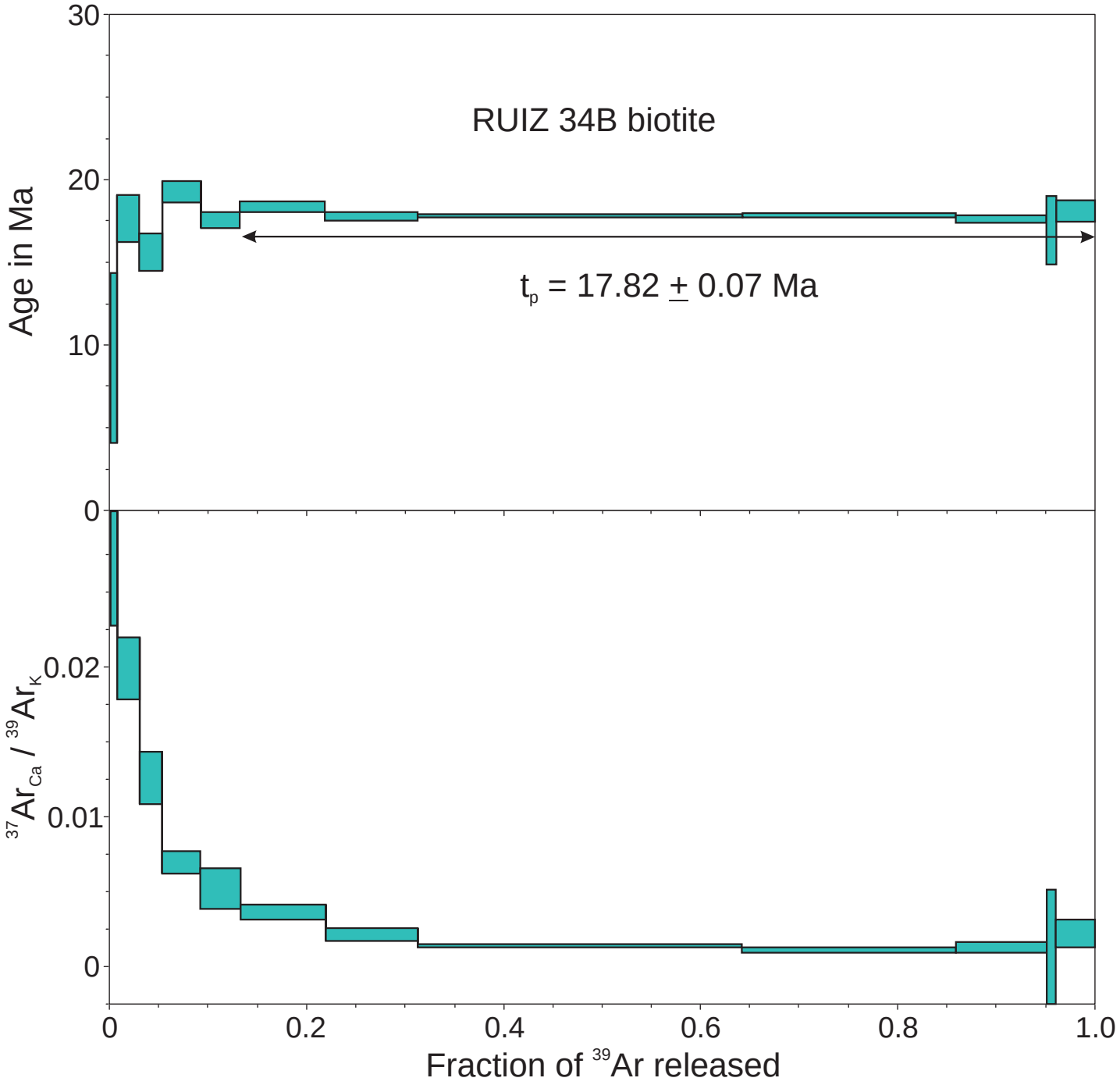

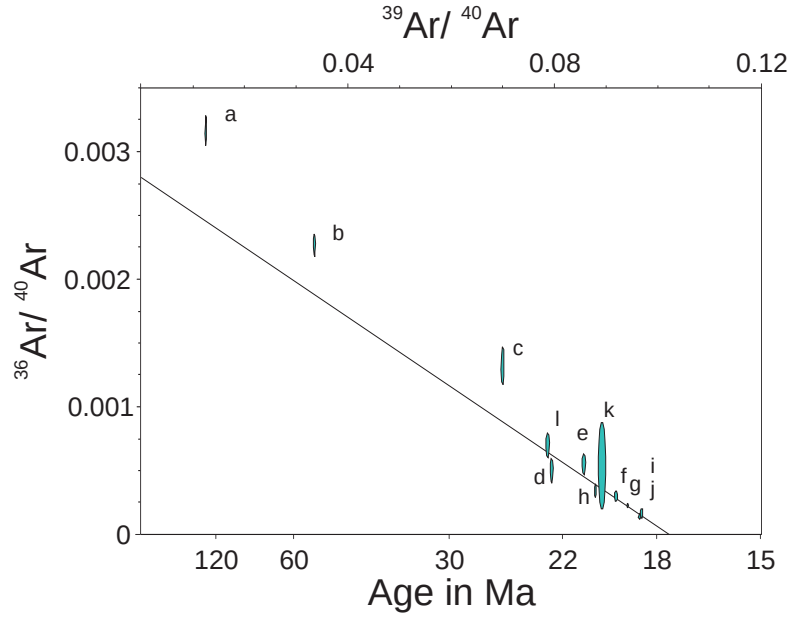

t_c = 17.57 ± 0.19 Ma

$(^{40}Ar / ^{36}Ar)_i$ = 357 ± 40

MSWD = 0.79, n = 9

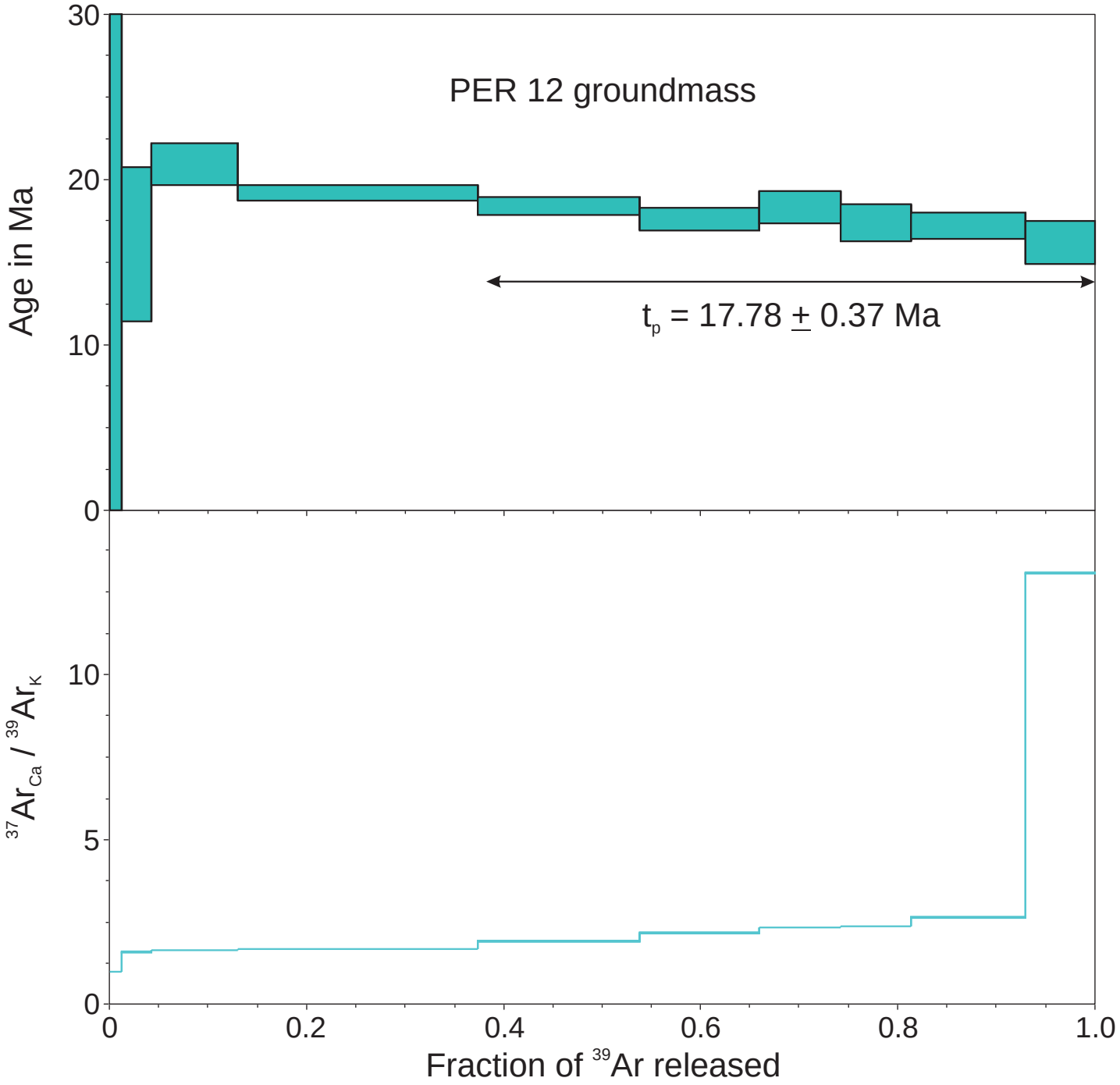

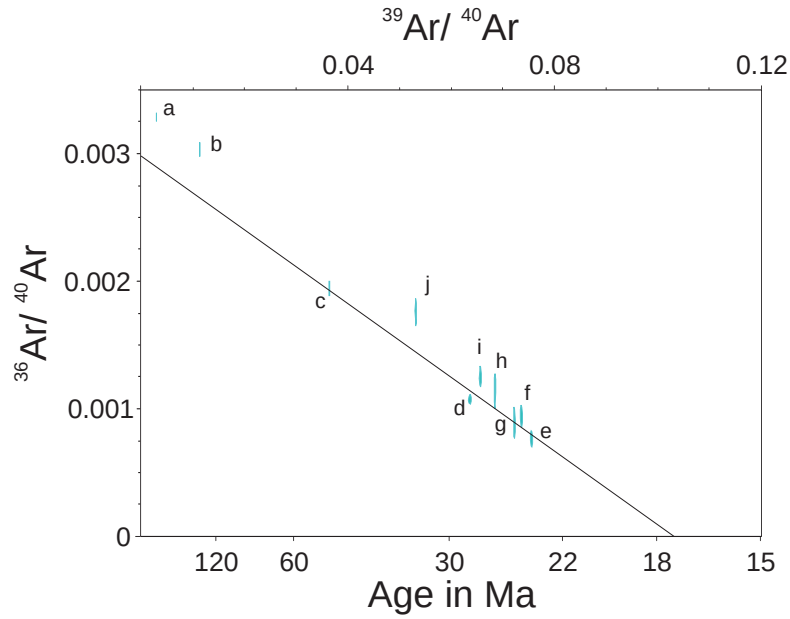

t_c = 17.42 ± 0.77 Ma

$(^{40}Ar / ^{36}Ar)_i$ = 335 ± 19

MSWD = 1.8, n = 7

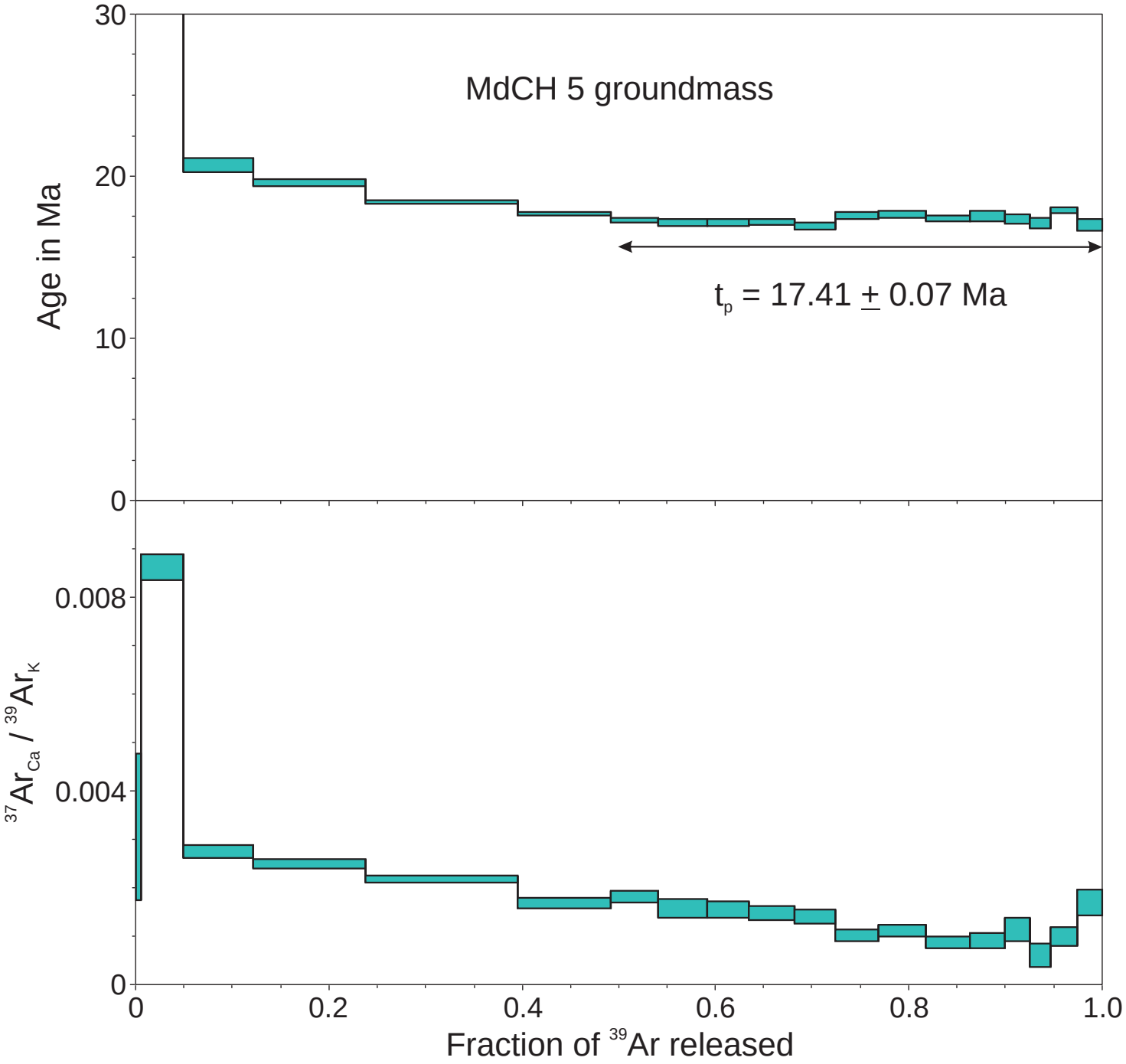

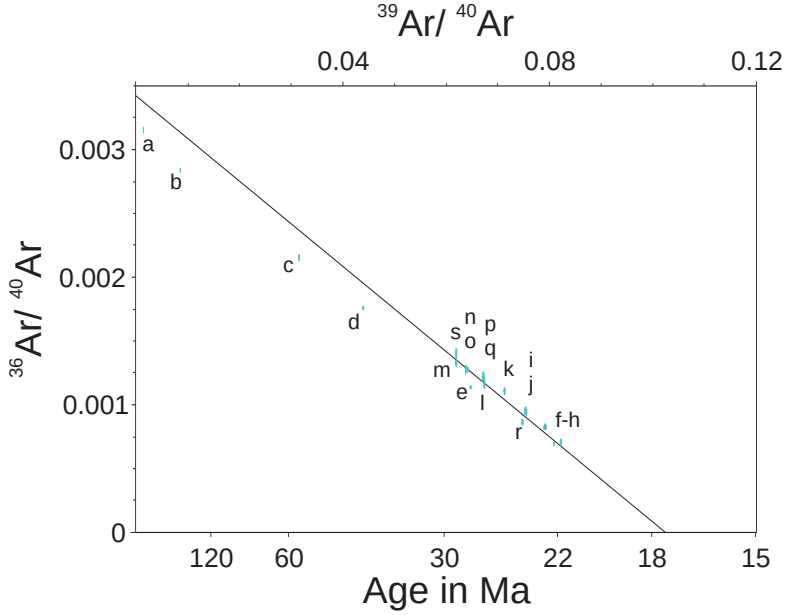

t_c = 17.52 ± 0.24 Ma

(^{40}Ar / ^{36}Ar)$_i$ = 292 ± 9

MSWD = 2.4, n = 14

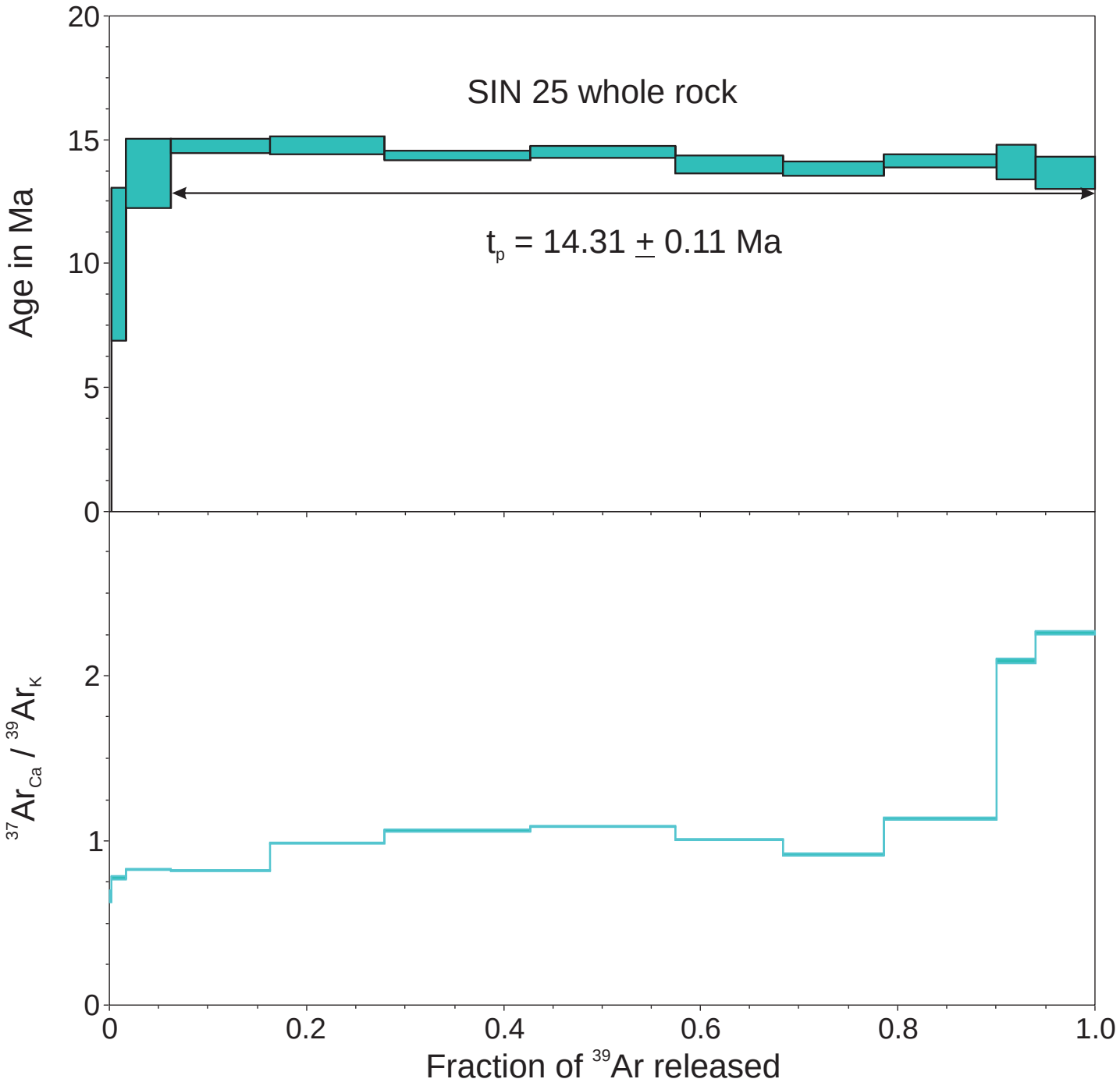

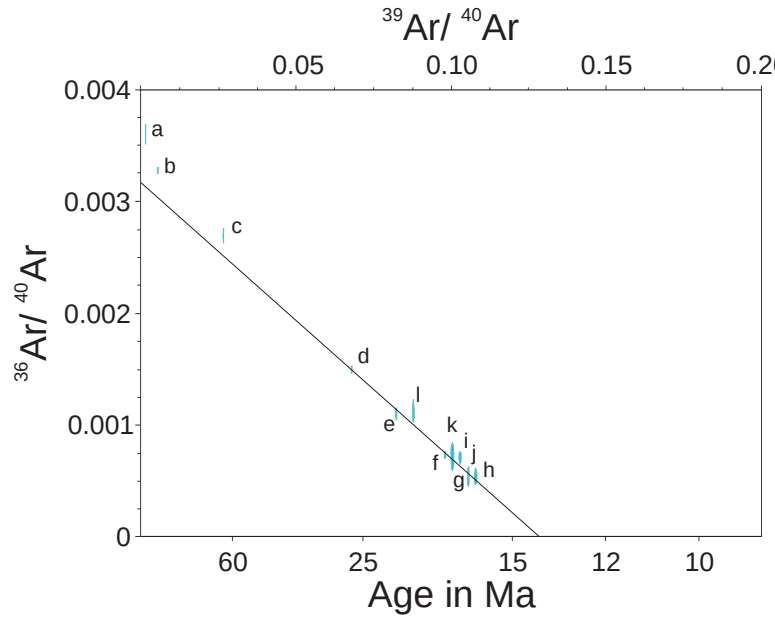

t_c = 14.01 ± 0.23 Ma

$(^{40}Ar / ^{36}Ar)_i$ = 315 ± 11

MSWD = 0.8, n = 9

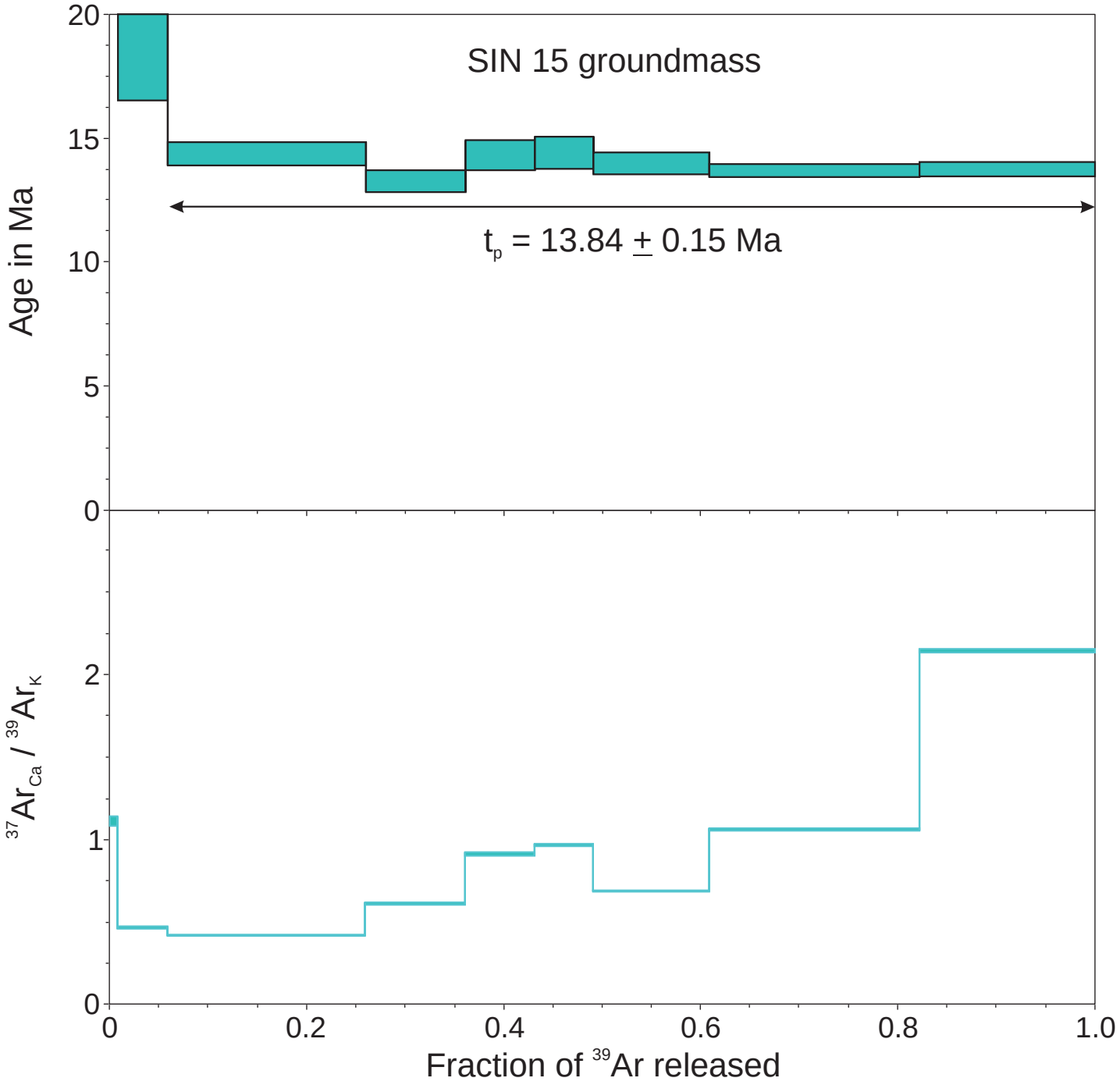

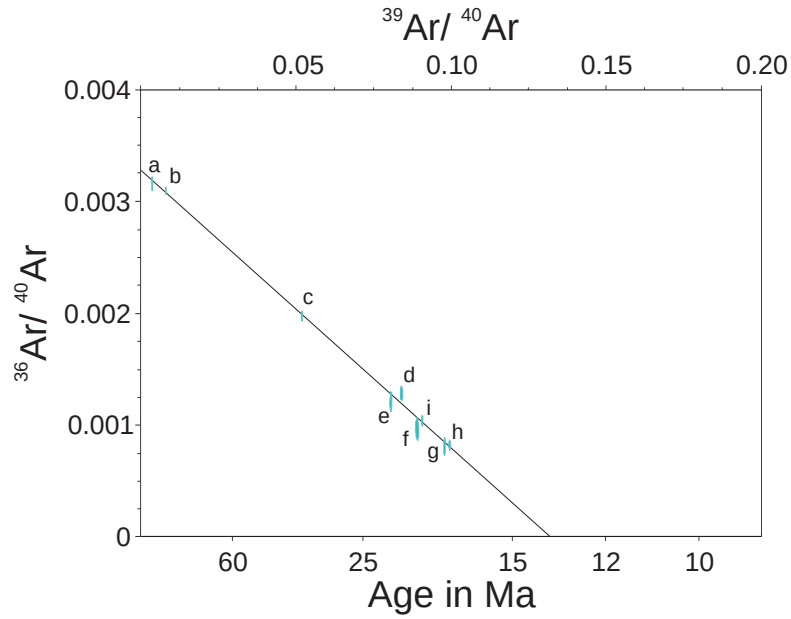

t_c = 13.62 ± 0.17 Ma

$(^{40}Ar / ^{36}Ar)_i$ = 304 ± 3

MSWD = 0.56, n = 9

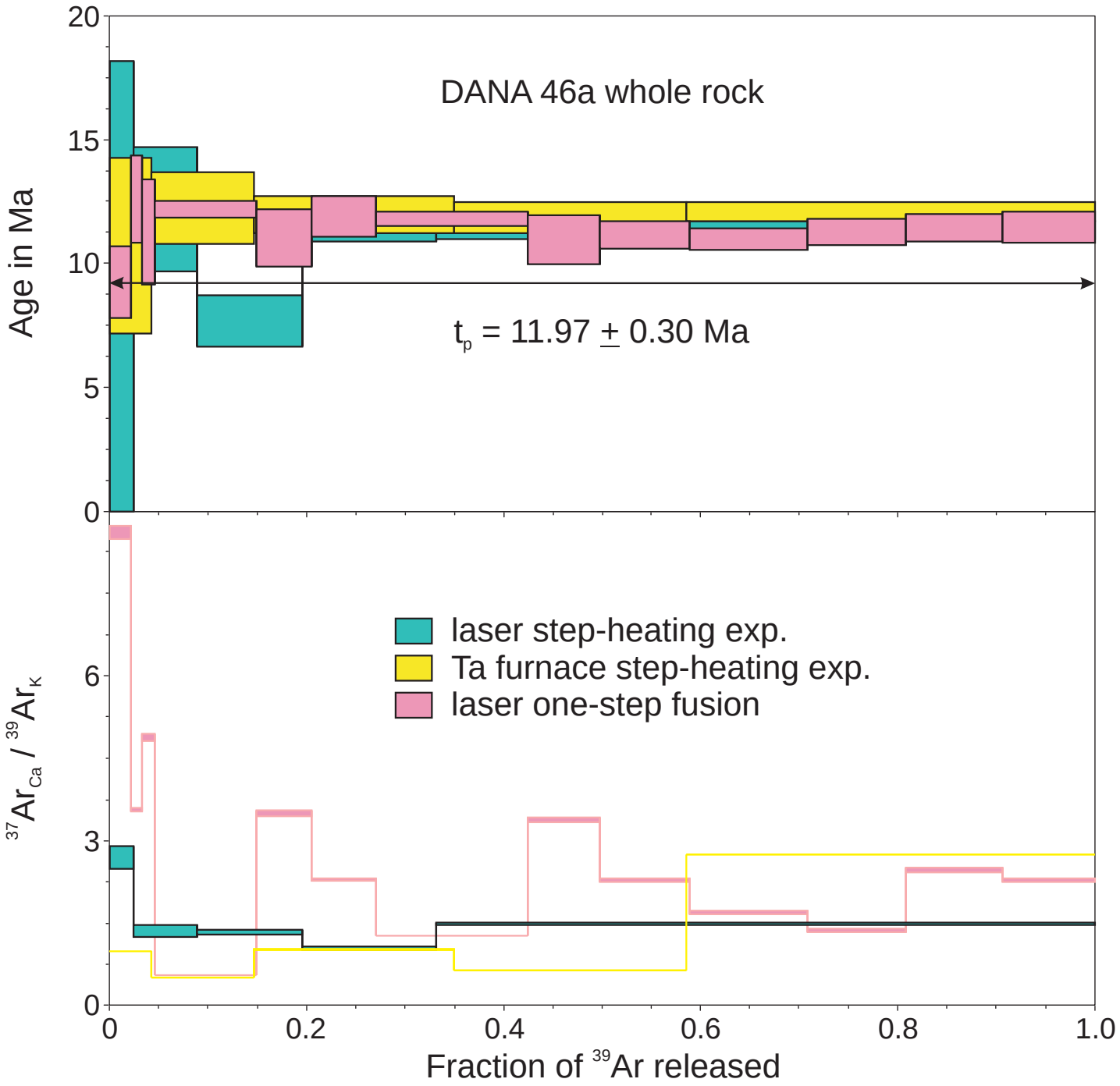

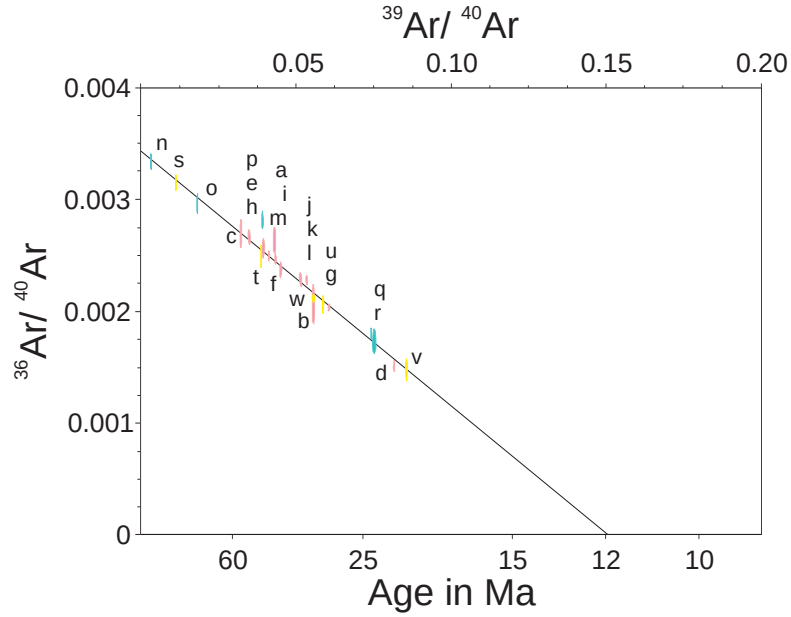

t_c = 11.96 ± 0.26 Ma

$(^{40}Ar / ^{36}Ar)_i$ = 291 ± 3

MSWD = 0.50, n = 21

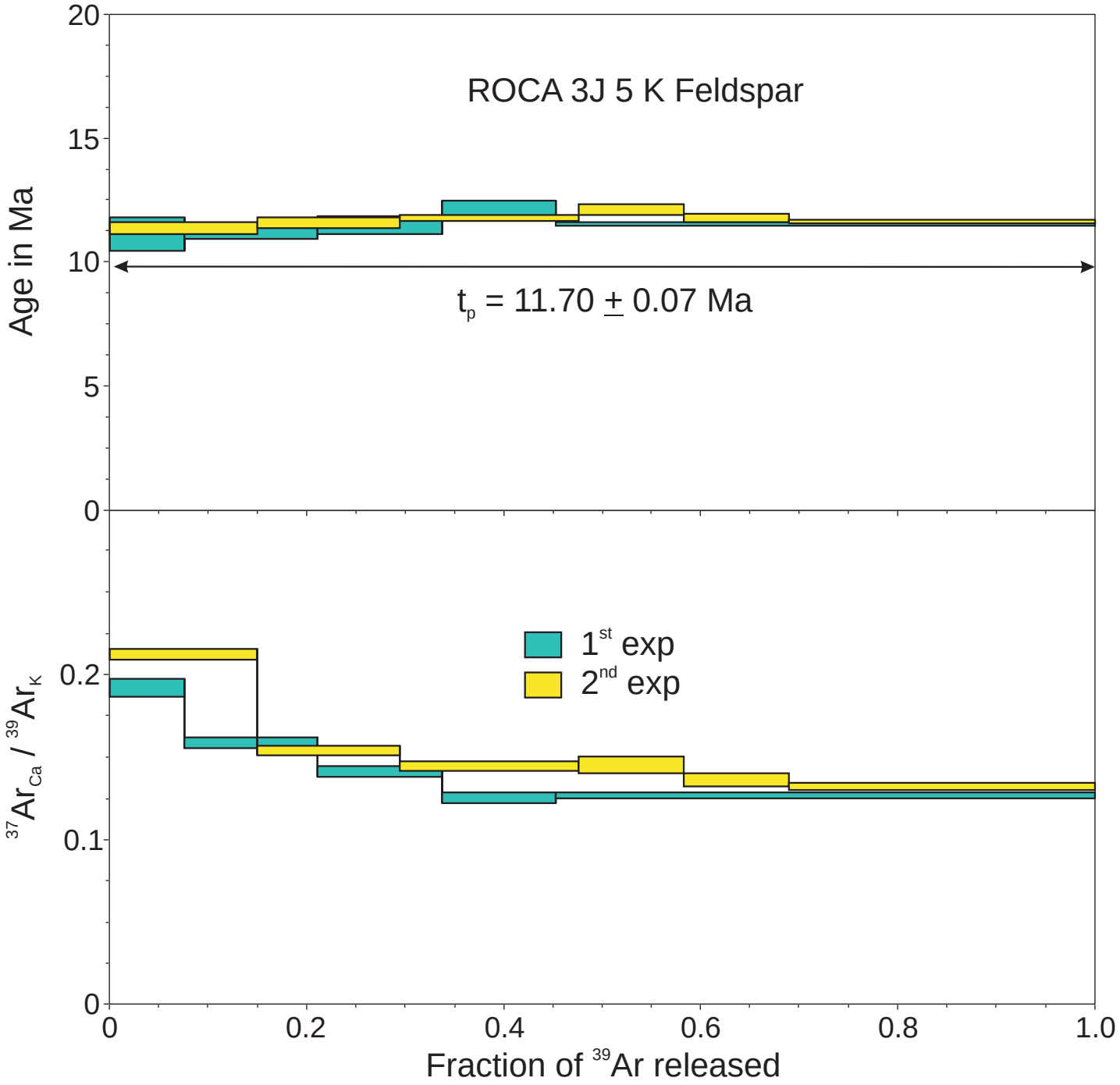

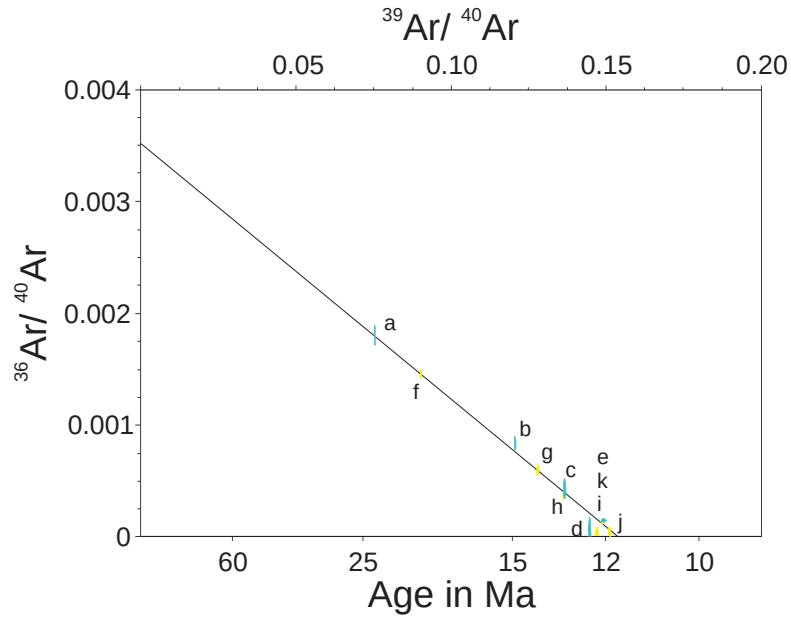

t_c = 11.69 ± 0.08 Ma

$(^{40}Ar / ^{36}Ar)_i$ = 284 ± 8

MSWD = 1.5, n = 11

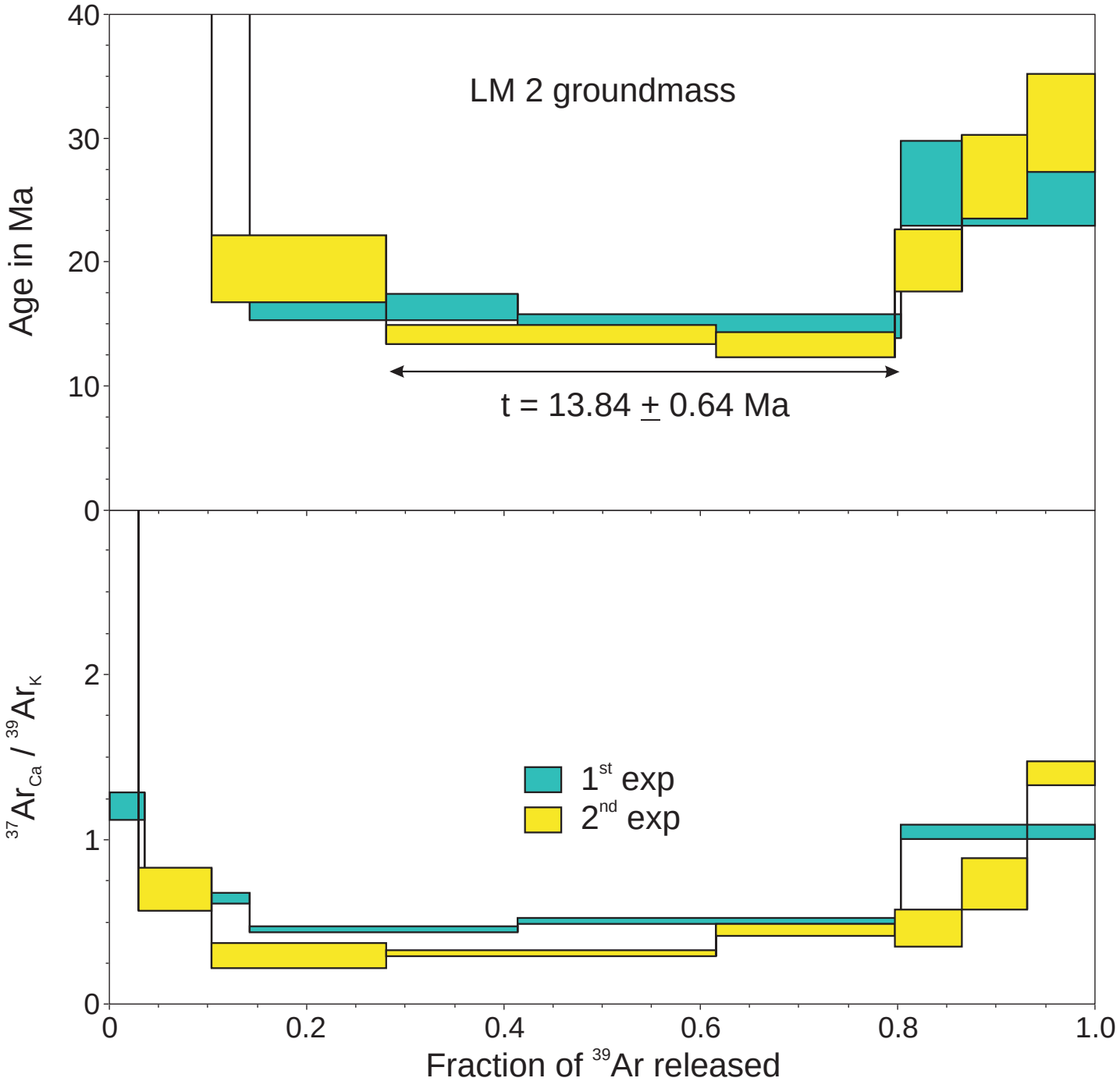

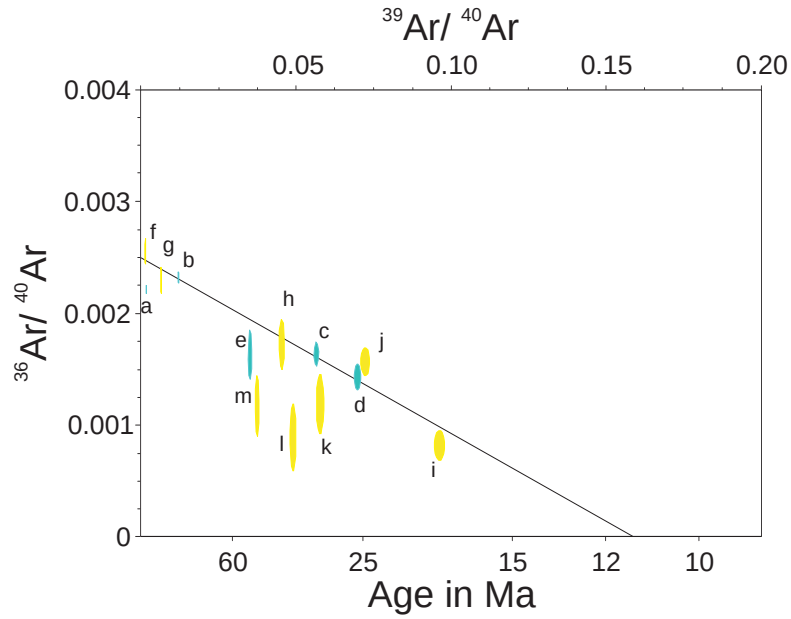

t_c = 11.34 ± 0.79 Ma

$(^{40}Ar / ^{36}Ar)_i$ = 400 ± 10

MSWD = 1.22, n = 8

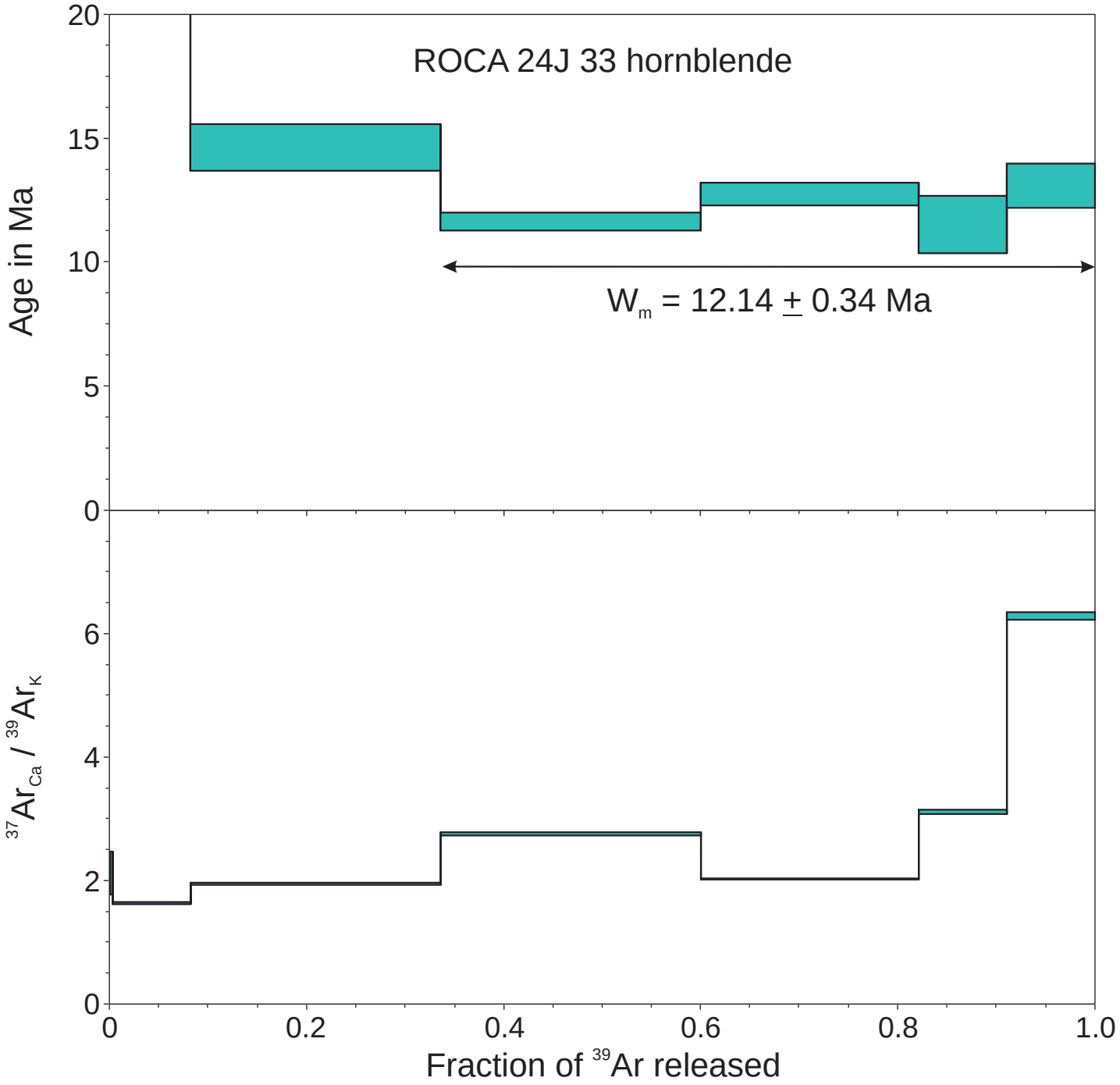

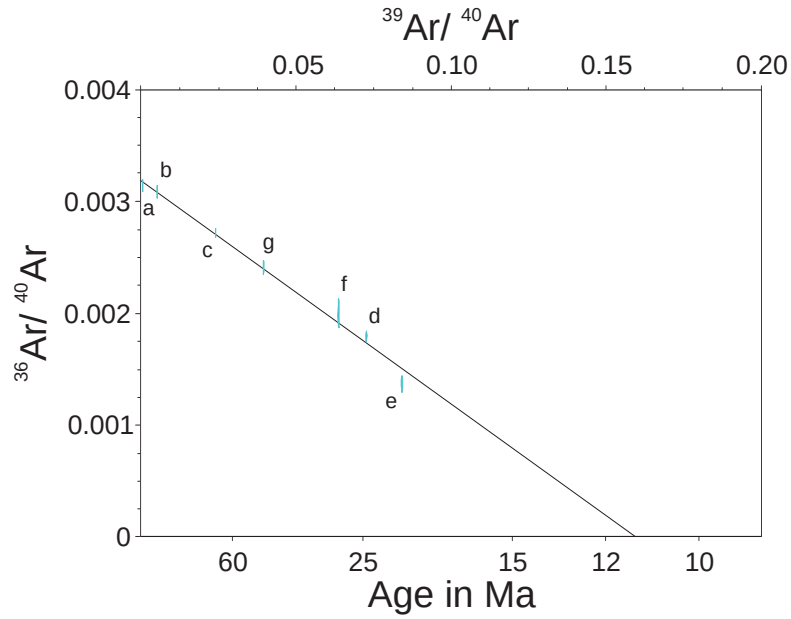

t_c = 11.29 ± 0.37 Ma

$(^{40}Ar / ^{36}Ar)_i$ = 313 ± 4

MSWD = 1.12, n = 7

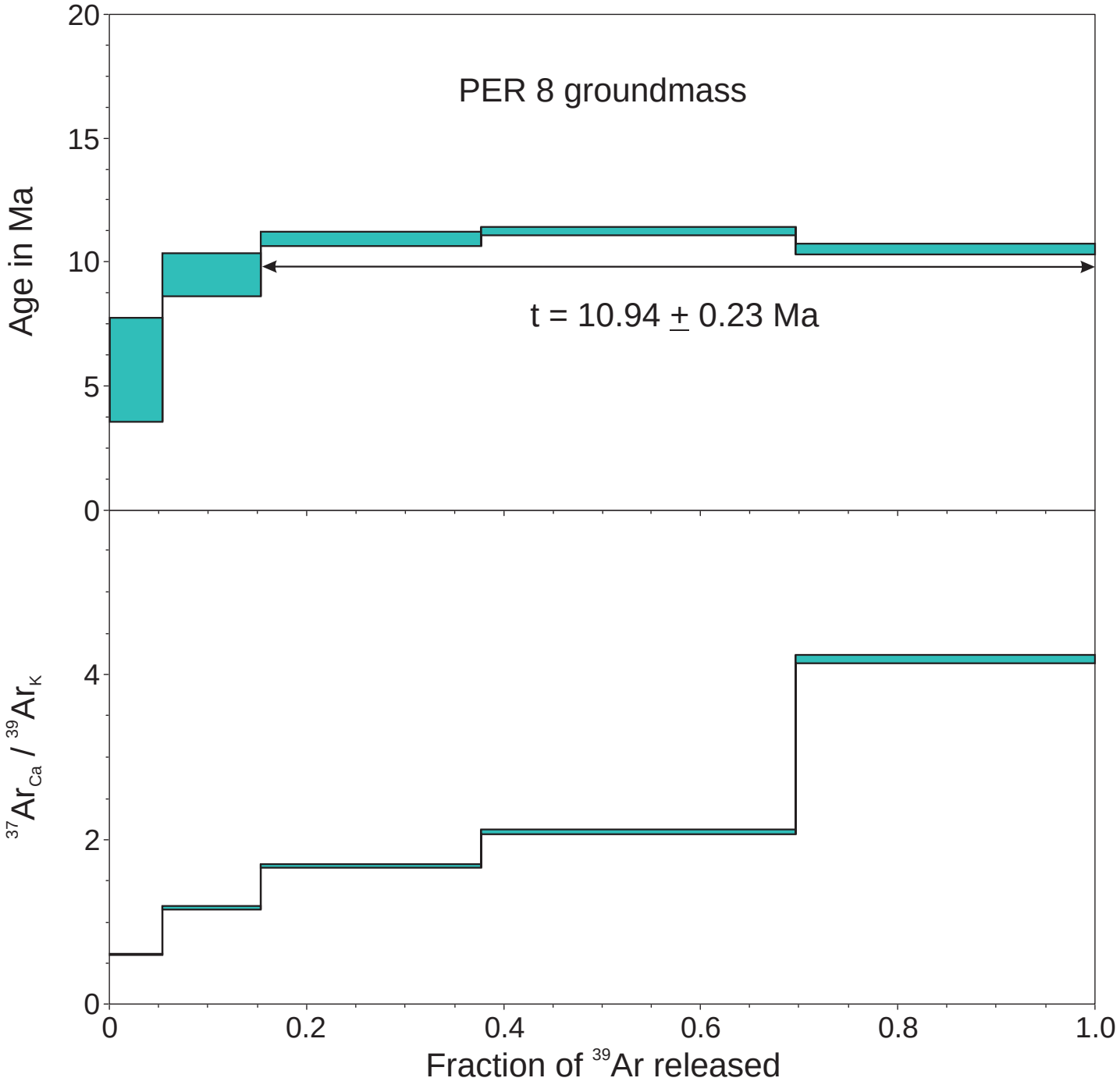

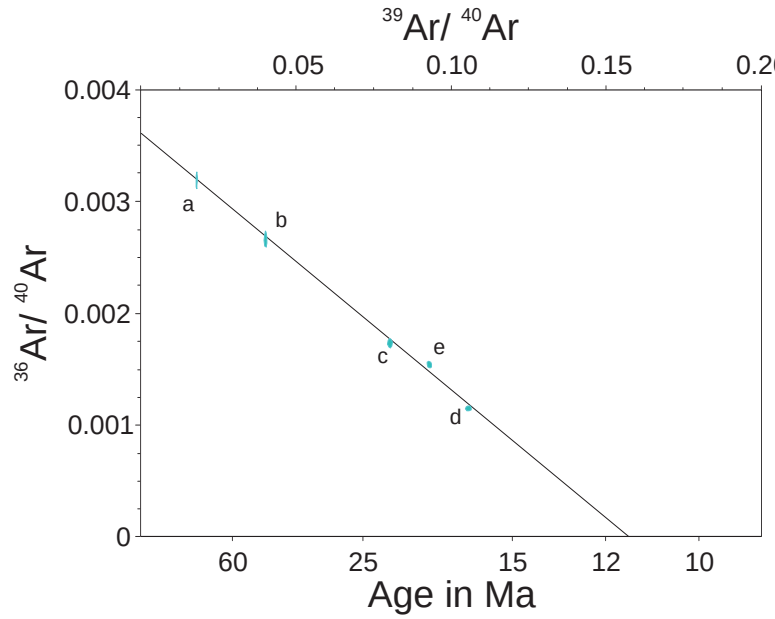

t_c = 11.44 ± 0.28 Ma

$(^{40}Ar / ^{36}Ar)_i$ = 276 ± 8

MSWD = 2.26, n = 5

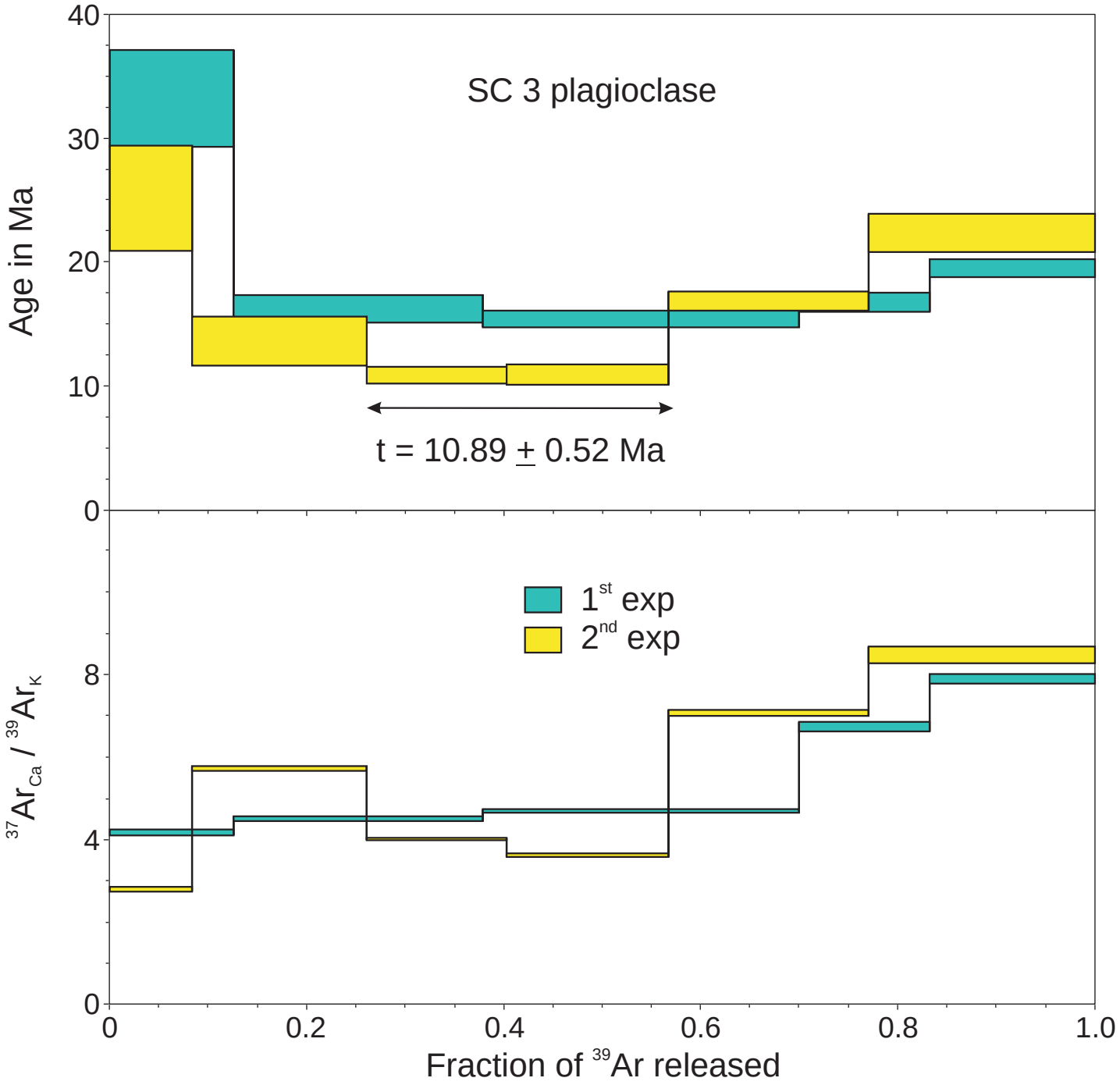

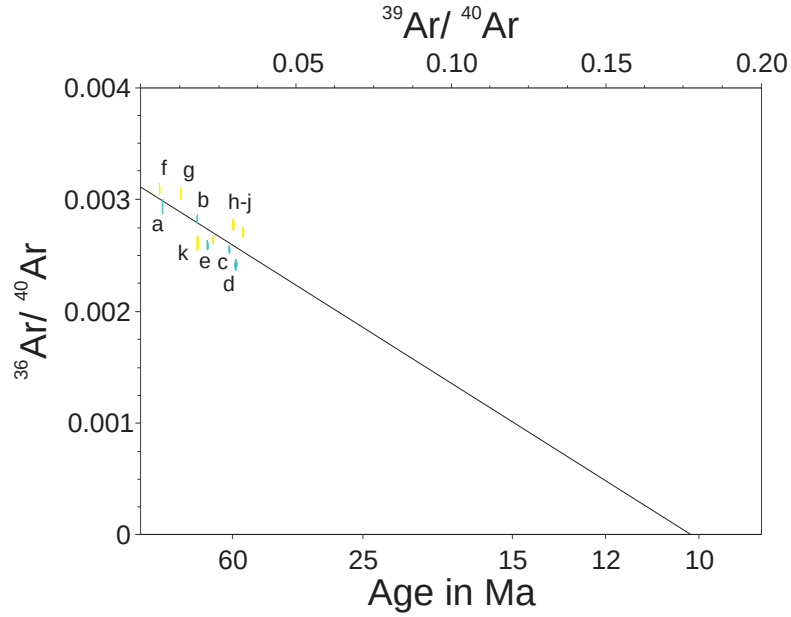

t_c = 10.14 ± 2.59 Ma

$(^{40}Ar / ^{36}Ar)_i$ = 322 ± 13

MSWD = 8.4, n = 11

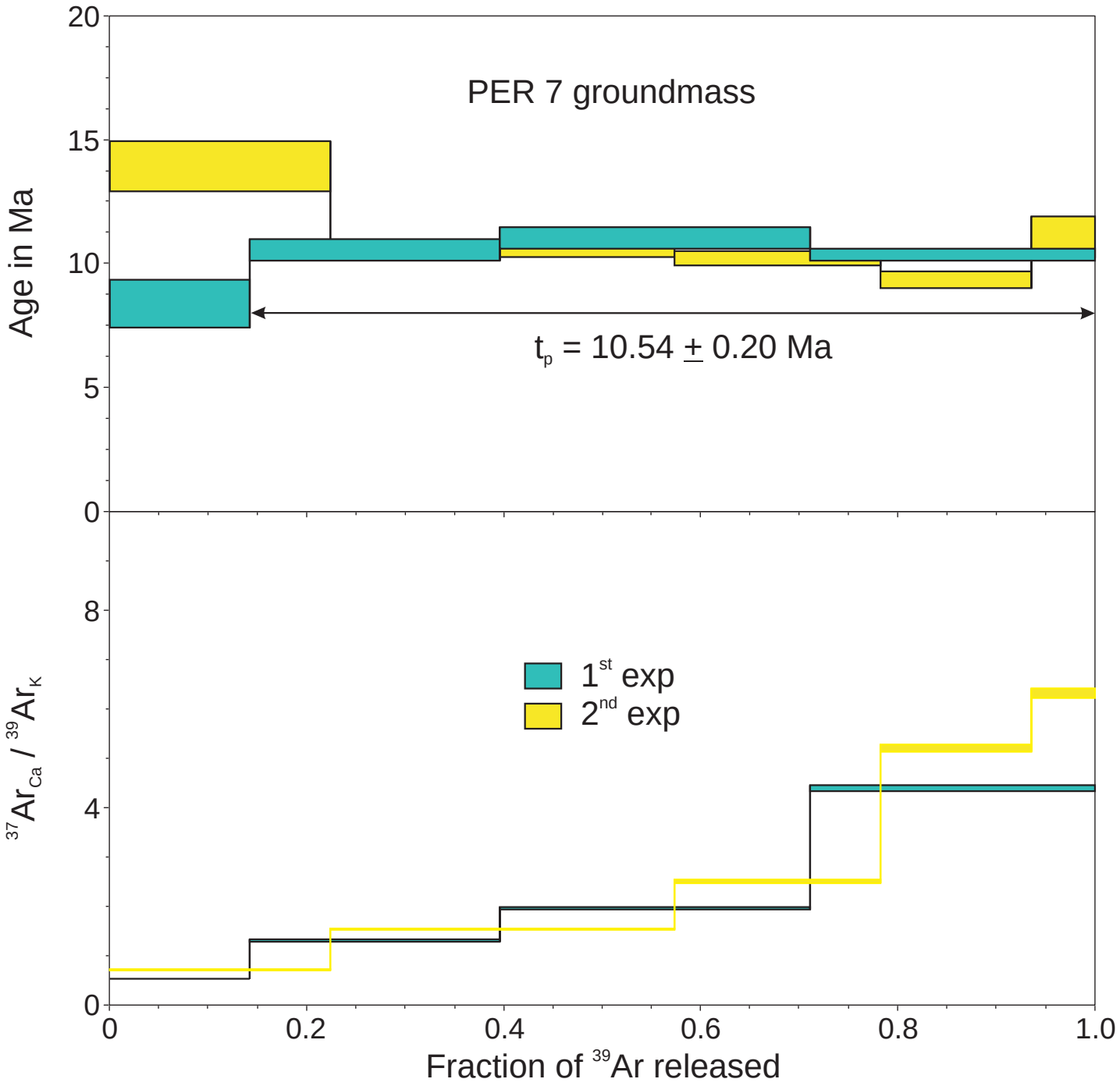

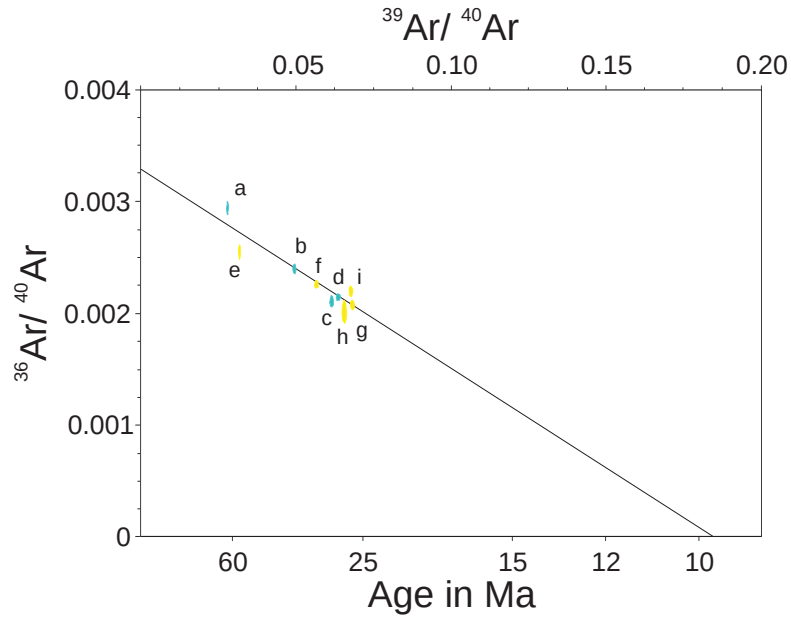

t_c = 9.76 ± 0.90 Ma

$(^{40}Ar / ^{36}Ar)_i$ = 304 ± 13

MSWD = 3.57, n = 9

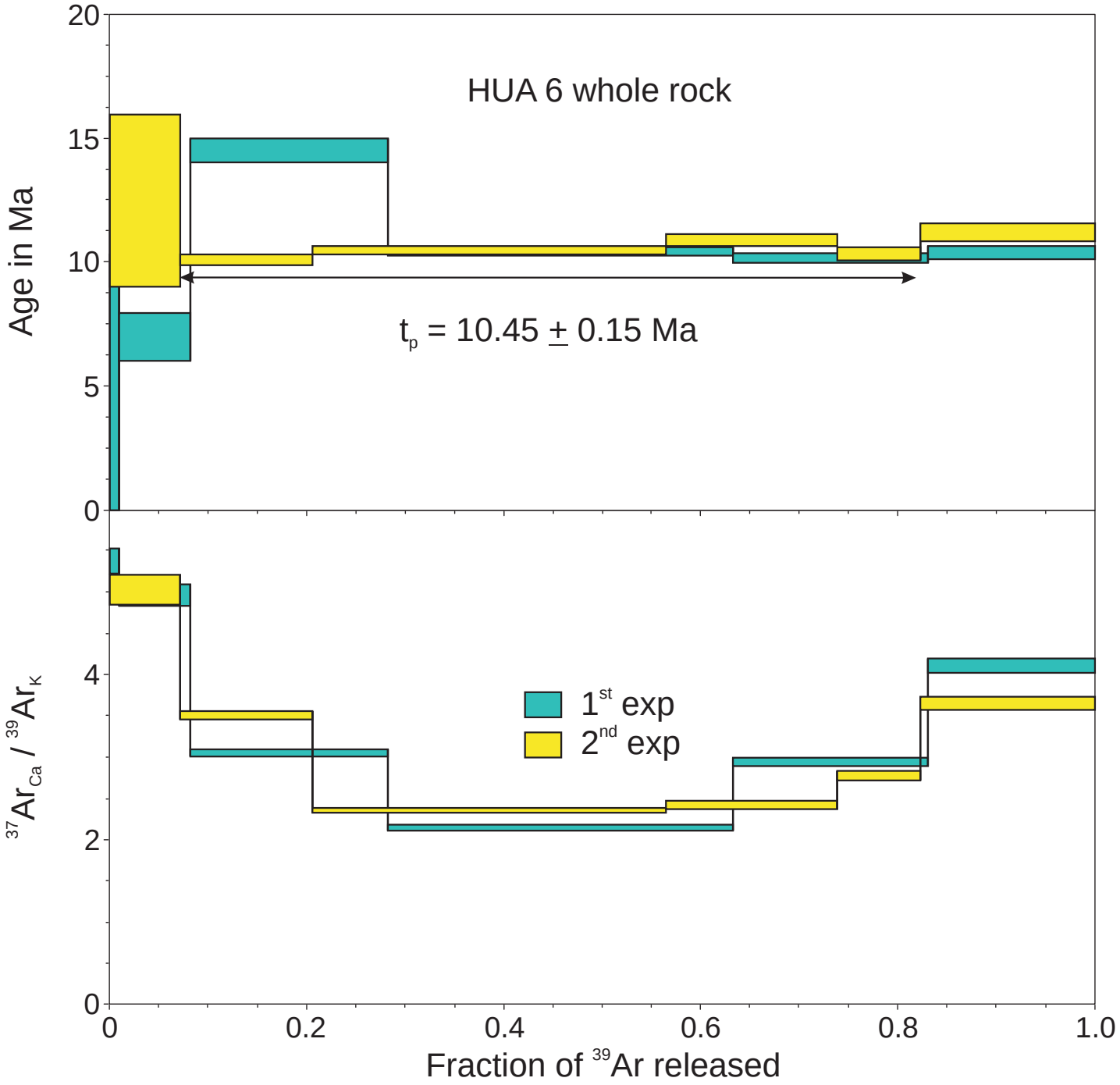

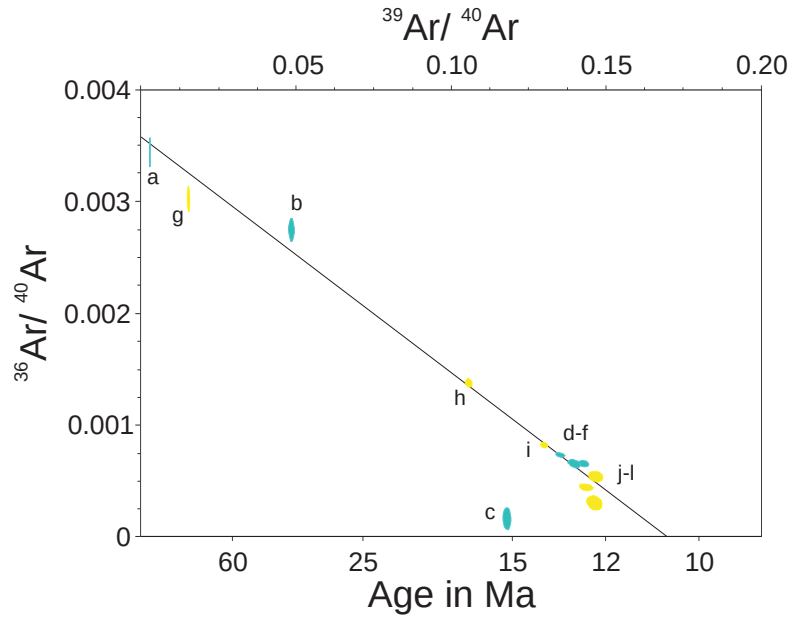

t_c = 10.61 ± 0.15 Ma

$(^{40}Ar / ^{36}Ar)_i$ = 279 ± 10

MSWD = 2.85, n = 11

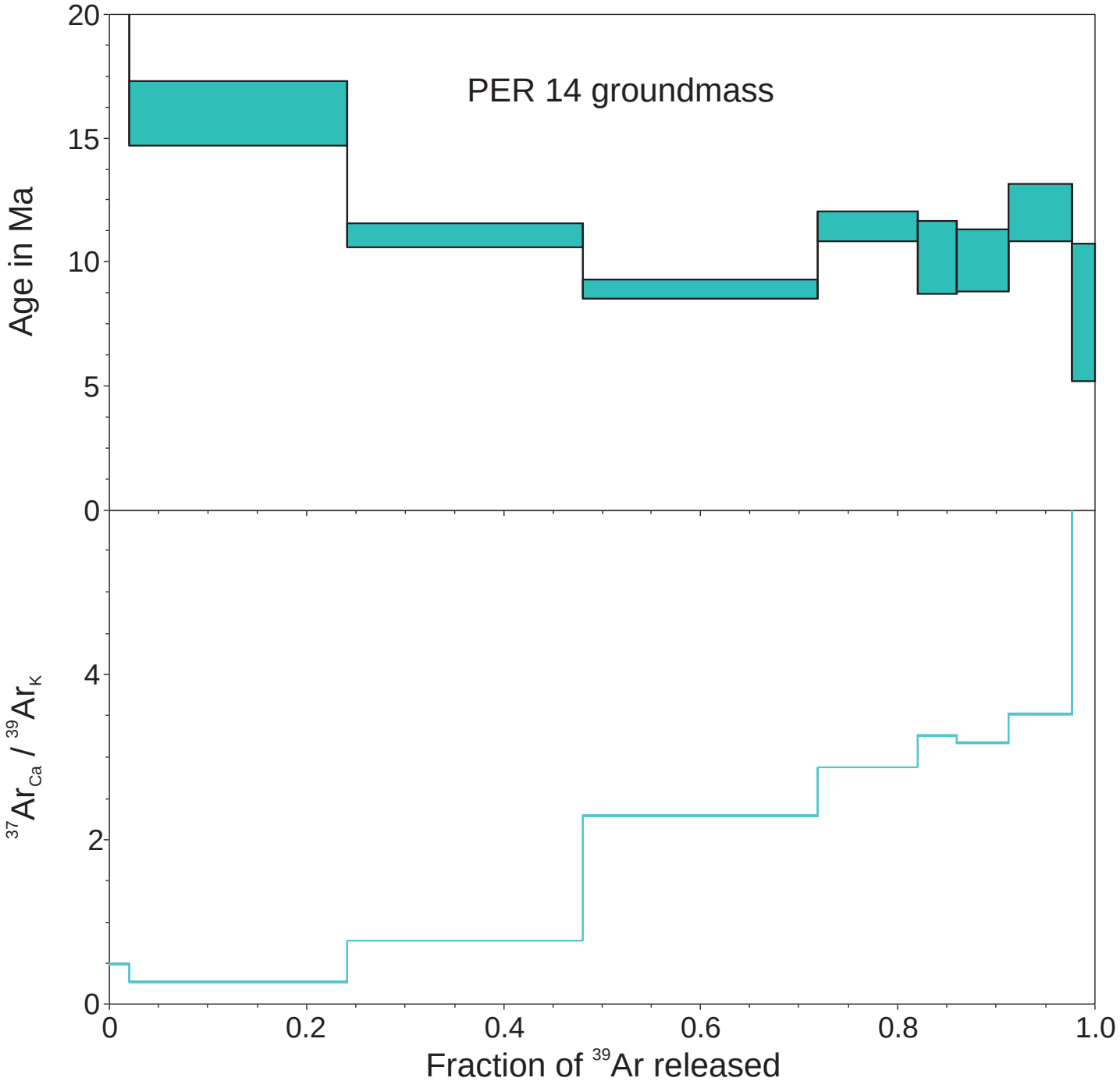

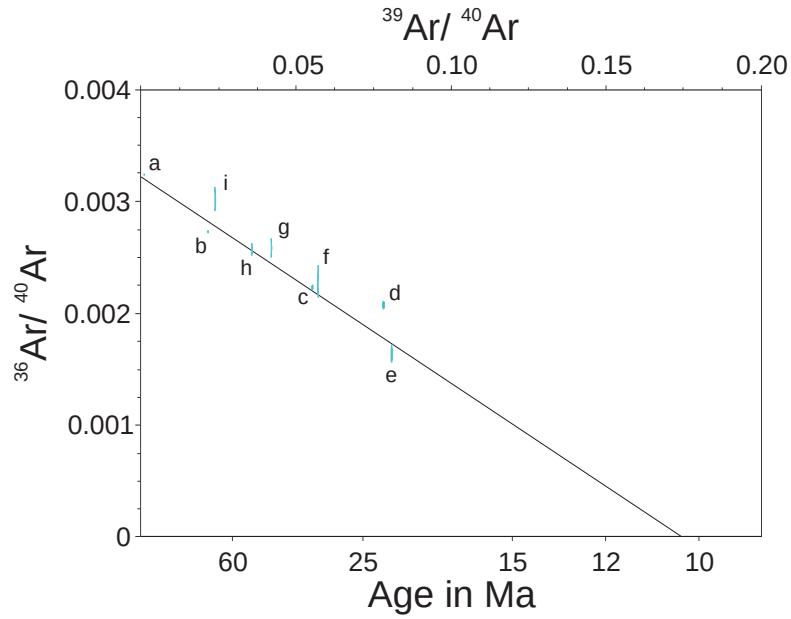

t_c = 10.33 ± 0.88 Ma

$(^{40}Ar / ^{36}Ar)_i$ = 310 ± 4

MSWD = 28, n = 9

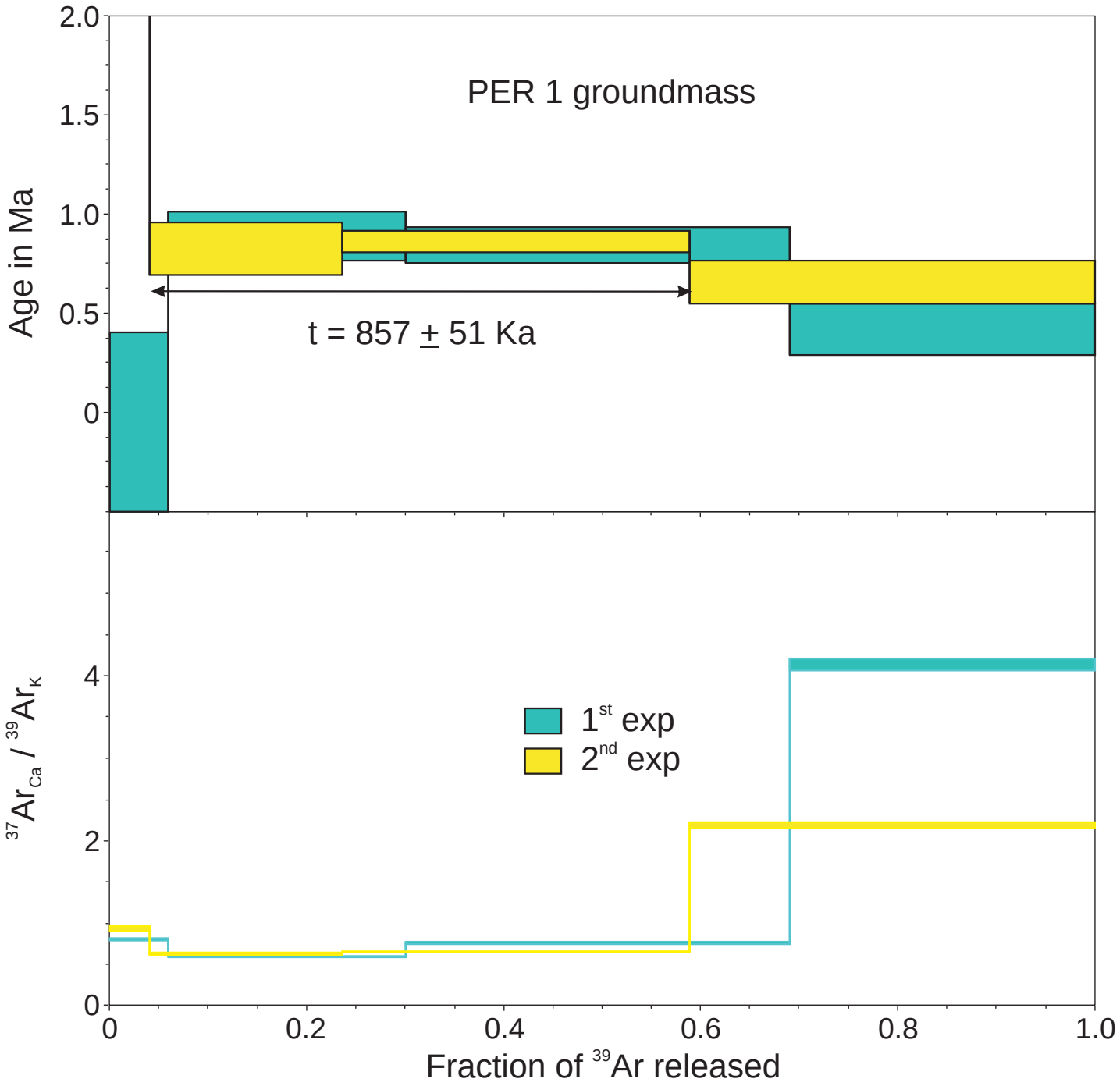

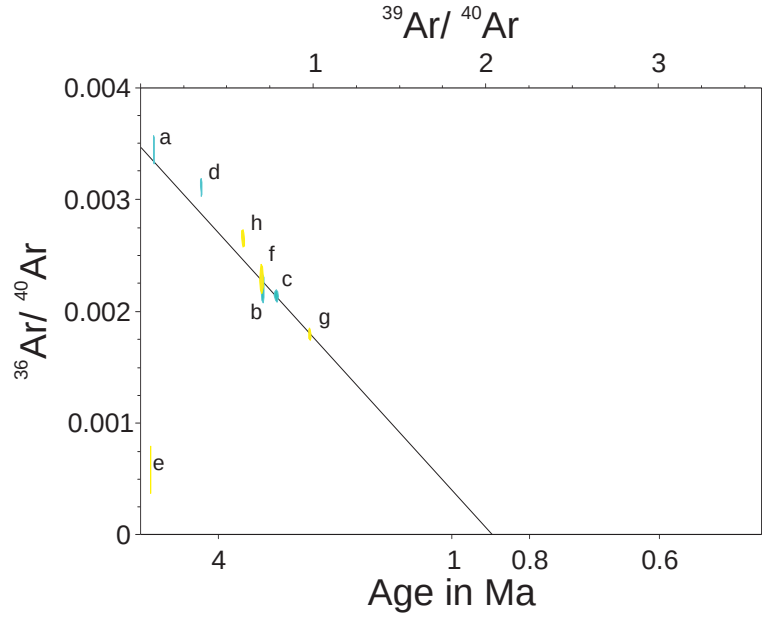

t_c = 884 ± 97 Ka

$(^{40}Ar / ^{36}Ar)_i$ = 288 ± 23

MSWD = 0.14, n = 4

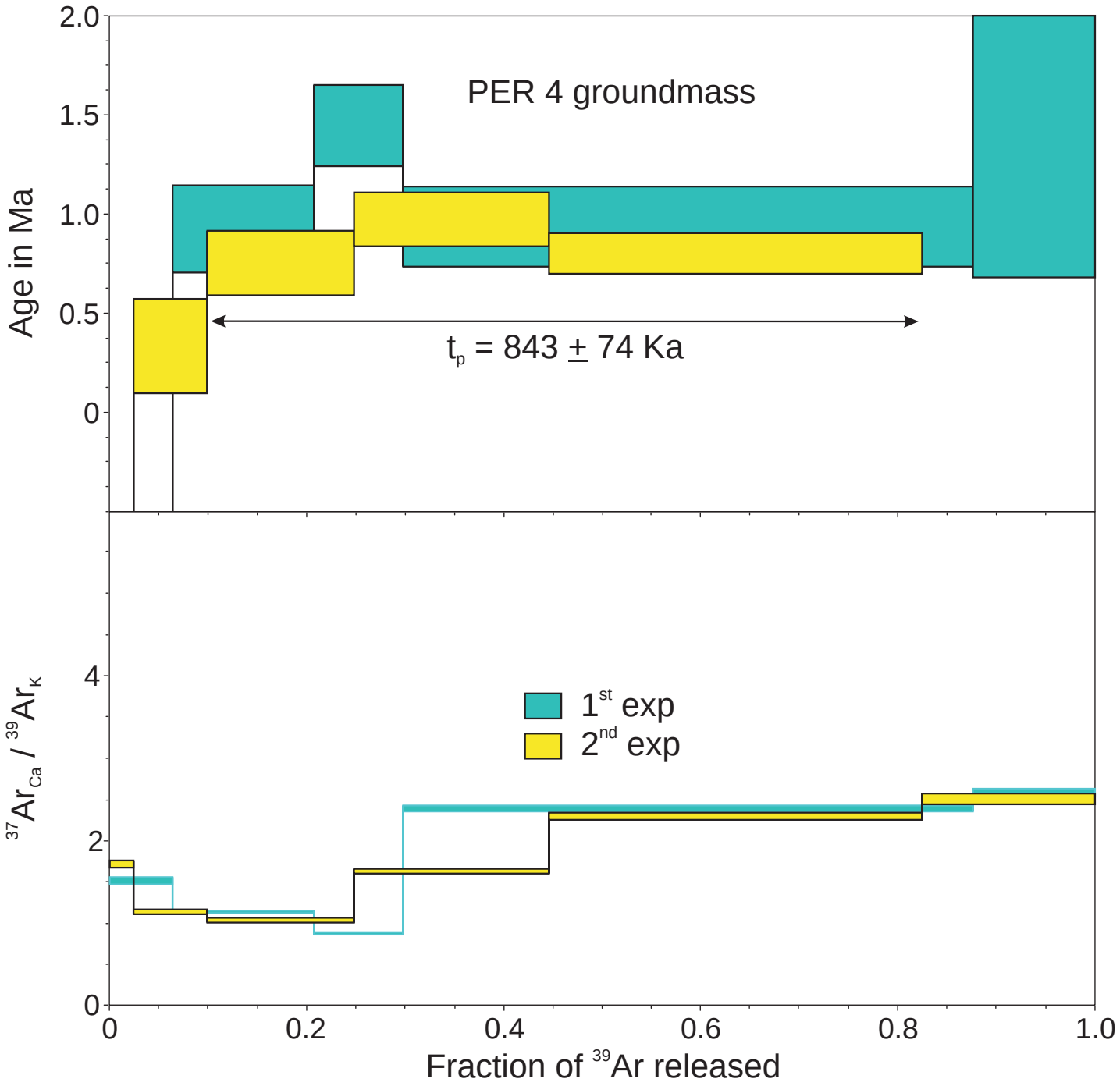

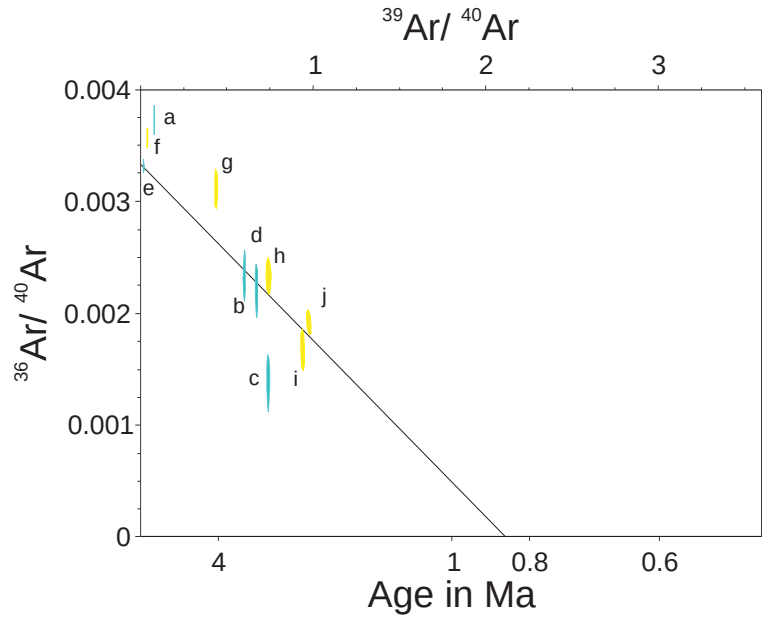

t_c = 853 ± 80 Ka

$(^{40}Ar / ^{36}Ar)_i$ = 300 ± 9

MSWD = 2.56, n = 7

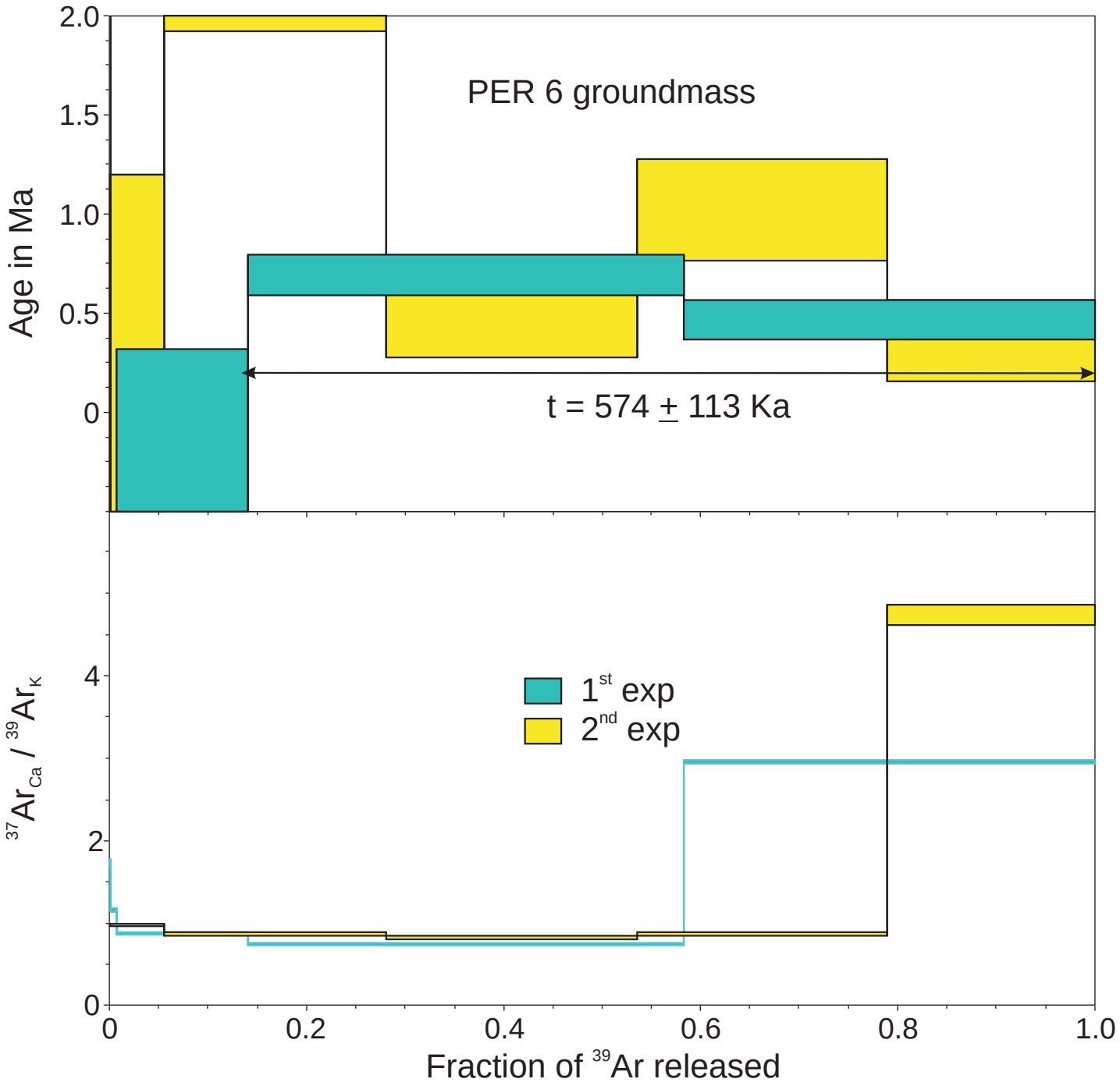

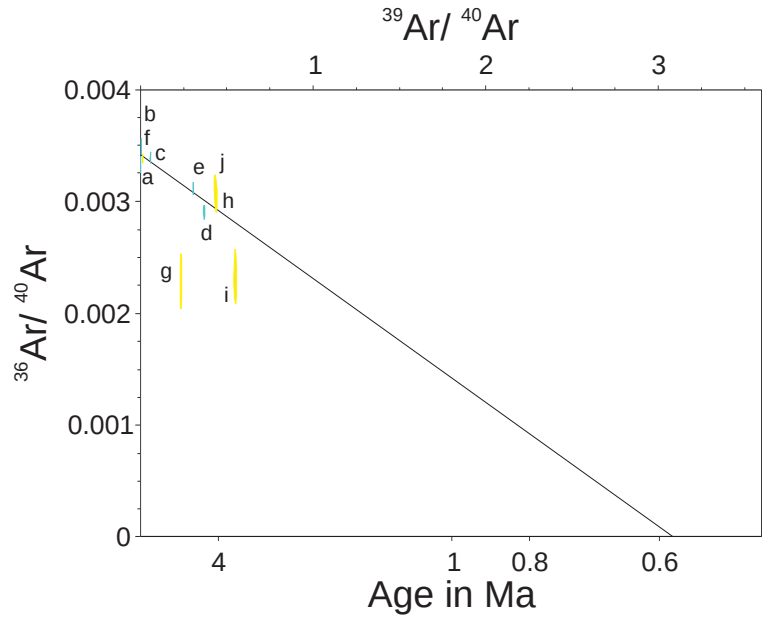

t_c = 585 ± 82 Ka

$(^{40}Ar / ^{36}Ar)_i$ = 292 ± 3

MSWD = 1.36, n = 8

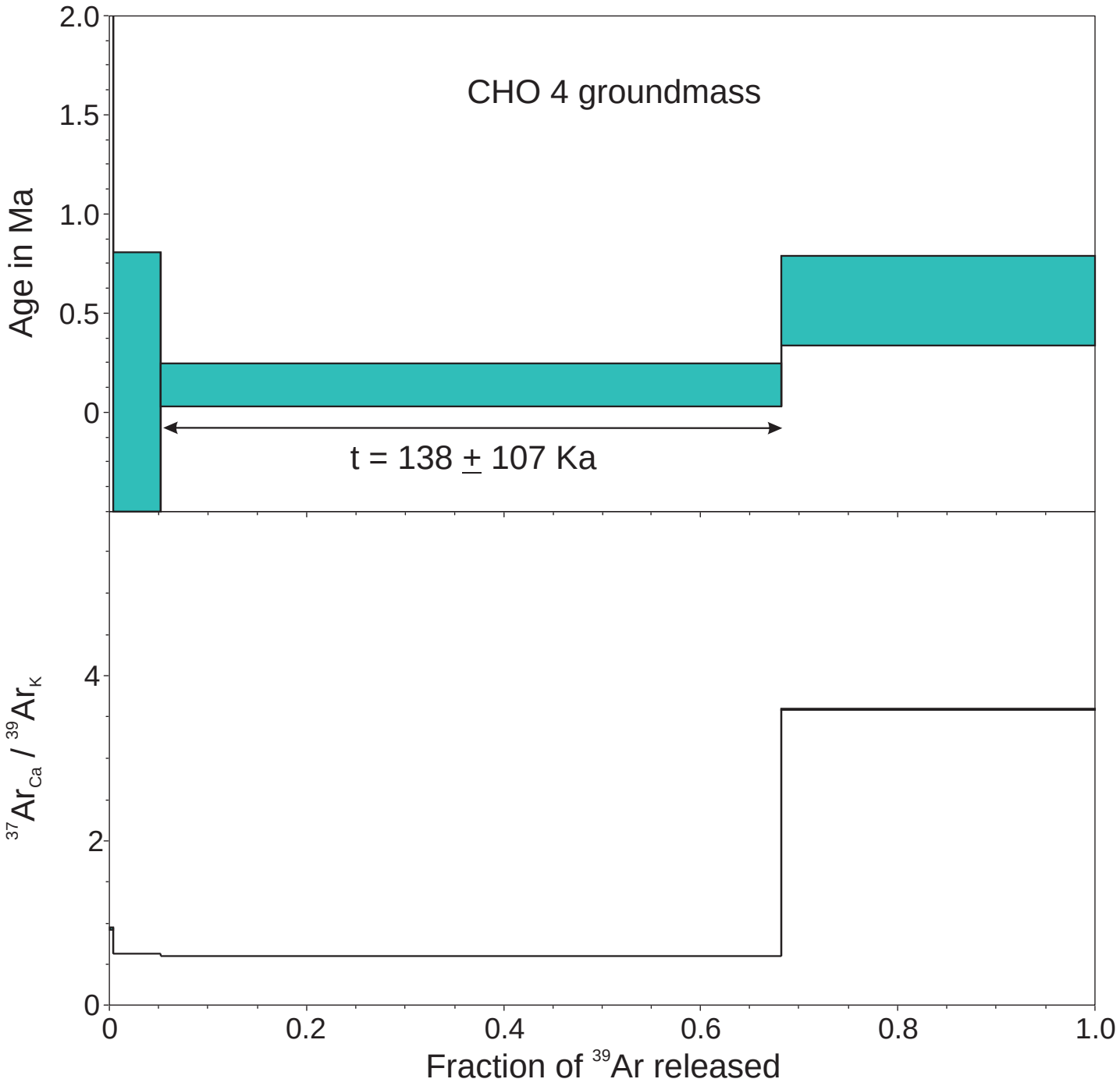

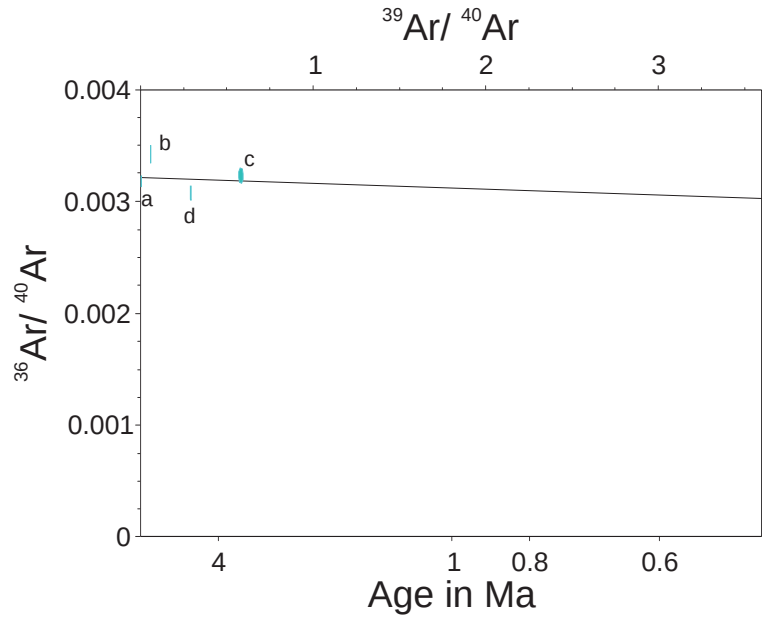

t_c = 29 ± 181 Ka

$(^{40}Ar / ^{36}Ar)_i$ = 311 ± 10

MSWD = 5, n = 4

Anexo 2

Material suplementario publicado en línea como parte del articulo:

Duque-Trujillo, J., Ferrari, L., Orozco-Esquivel, T., López-Martínez, M., Lonsdale, P., Bryan, S., Kluesner, J., Piñero-Lajas, D., Solari, L. 2014. Timing of rifting in the Southern Gulf of California and its conjugate margins: insights from the plutonic record: Geological Society of America Bulletin, en prensa.

Secciones:

1) Información metodologica adicional

2) Datos de química mineral

3) Datos analíticos de edades U-Pb

4) Resultados geocronológicos

Duque-Trujillo, et al., Timing of rifting and exhumation in the Southern Gulf of California and its conjugate margins: insights from the plutonic record

Supplemental File 1. Additional information on methodology

U/Pb LA-ICP-MS dating

Zircon crystals were separated using conventional techniques of rock crushing, sieving, Frantz isodynamic magnetic separator, panning, and heavy liquid separation. Zircon crystals were then hand-picked from the final heavy minerals concentrate. Selected crystals were mounted on 1-inch epoxy resin mounts and then sanded down and polished to expose internal planes of the crystals. Cathodoluminiscence (CL) images were obtained using a binocular microscope attached to an ELM-3R luminoscope. Crystal ablation was performed using an ArF excimer laser (Resolution M-50) operated at 193nm, 5 Hz and ~6 J/cm^2.

U/Pb ages on separate zircons were obtained by laser ablation–inductively coupled plasma–mass spectrometry (LA-ICP-MS) at the Laboratorio de Estudios isotópicos, Centro de Geociencias (CGEO), Universidad Nacional Autónoma de México (UNAM), according to the procedure described in Solari et al. (2010). The Plešovice reference zircon (ca. 337 Ma; Sláma et al., 2008) was used in combination with NIST 610 standard glass to correct for instrumental drift and down-hole fractionation and to recalculate elemental concentrations, using the UPb.age script for R (Solari and Tanner, 2011), or employing Iolite (Paton et al., 2010). The internal 1SE on the measured $^{207}Pb/^{206}Pb$, $^{206}Pb/^{238}U$, and $^{208}Pb/^{232}Th$ ratios typically was ~0.8%, 0.7%, and 0.9%, respectively. Replicate analyses of the Plešovice zircon indicate an external reproducibility of1.1%, 0.9%, and 1.6% on the measured $^{207}Pb/^{206}Pb$, $^{206}Pb/^{238}U$, and $^{208}Pb/^{232}Th$ ratios, respectively. These errors are quadratically included in the quoted uncertainties for individual analyses of the analyzed zircons.

Because its signal is swamped by the ^{204}Hg contained in the carrier gases, ^{204}Pb was not analyzed during this study. Common Pb correction, where needed, was thus performed employing the algebraic method of Andersen (2002). A filter was then applied to ensure the quality of selected analyses, which consisted in the evaluation of the concordance. For grains with ages younger than 1000 Ma, the analysis was considered meaningful if the $^{206}Pb/^{238}U$ and $^{207}Pb/^{235}U$ ages differed by <10%. The concordia and age distribution plots, as well as age error calculations, were performed using Isoplot v. 3.70 (Ludwig, 2004). The $^{206}Pb/^{238}U$ ages are preferred for grains younger than 1000 Ma because of the uncertainty involved in determining the ^{207}Pb isotope in young crystals. The U-Pb analytical data are reported in Supplemental File 2, and the concordia and age distribution plots, along with a brief discussion on age calculation, are presented in Supplemental File 3.

^{40}Ar-^{39}Ar dating

Mineral concentrates were obtained at the mineral separation laboratories of CGEO-UNAM, and Department of Geology, CICESE, using conventional procedures of rock crushing, sieving, rinsing with deionized water, drying at 60 °C and concentration with a Frantz isodynamic magnetic separator. For mineral concentration, fractions with grain size similar to that of the crystals of interest were selected for magnetic separation. The obtained mineral concentrate was examined under the microscope to ensure a >99% purity. For groundmass separation, fractions with phenocryst-free fragments were selected; the fraction was examined under the microscope to check for homogeneity and the concentrate was labeled groundmass. The groundmass samples or mineral crystals selected for analysis were generally ~500μ in size.

Groundmass and minerals were irradiated in position 5C of the U-enriched research reactor of McMaster University in Hamilton, Ont. Canada. Since the project was conducted over several years, the samples were irradiated in different groups. Sample DANA 47a and DANA 71b received 40 MWH and were irradiated without a Cd-liner. The rest of the samples received 30 MWH and were covered with a Cd-liner to block thermal neutrons. For the experiments conducted with the VG5400 mass spectrometer, the irradiation monitors used were: sanidine TCR-2 (28.34 ± 0.28 Ma, Renne et al., 1998); sanidine FCT-2 (28.201 ± 0.046 Ma; Kuiper et al., 2008). For the two experiments conducted in the MS-10 mass spectrometer, the irradiation monitors used were biotite HD-B1 (24.18 ± 0.09 Ma; Schwarz and Trieloff, 2007) and biotite CATAV 7-4 (89.13 ± 0.35 Ma; internal standard calibrated with hornblende hb-3gr at the University of Toronto, with hornblende MMhb-1 at the University of Nice, and at CICESE with sanidine TCR-2, sanidine FCT-2, biotite HD-B1 and 128.1 Ma biotite LP-6, Roddick 1983). For the irradiation, the samples were distributed at regular distances to the monitors. The irradiation monitors were fused in one-step to calculate the parameter J. The J value used to calculate the ^{40}Ar-^{39}Ar ages came from the monitor that was located closest to the sample during irradiation.

Most ^{40}Ar-^{39}Ar ages presented in this paper were obtained by laser step-heating and determination of the extracted argon isotopic composition with a VG5400 mass spectrometer. For samples DANA 47a and DANA 71b, two step-heating experiments were performed using a temperature controlled Ta-furnace attached to an MS-10 mass spectrometer; additional one-step heating experiments were performed on these two samples with the VG5400 mass spectrometer.

Each argon step measurement was preceded by a blank measurement; all argon masses were measured in each case. Upon blank subtraction, the argon isotopes were corrected for mass discrimination, calcium, potassium and chlorine neutron induced interference reactions. For samples DANA 47a and DANA 71b, which were irradiated without Cd liner, the parameters used to correct for intereference reactions were:

$(^{39}Ar/^{37}Ar)Ca = 6.51 \times 10^{-4}$;

$(^{36}Ar/^{37}Ar)Ca = 2.54 \times 10^{-4}$;

$(^{40}Ar/^{39}Ar)K = 2.87 \times 10^{-2}$.

For the rest of the samples, irradiated with Cd-liner, the parameters used were:

$(^{39}Ar/^{37}Ar)Ca = 6.50 \times 10^{-4}$;

$(^{36}Ar/^{37}Ar)Ca = 2.55 \times 10^{-4}$;

$(^{40}Ar/^{39}Ar) = 0$.

Mass 36 was also corrected for chlorine derived ^{36}Ar (^{35}Cl (n, γ) $^{36}Cl \rightarrow {}^{36}Ar$ + ß, with $t_{1/2} = 3.1 \times 10^5$ a). Isotopes ^{37}Ar and ^{39}Ar were corrected for radioactive decay.

Data reduction and graphic presentation was done using the RaDan and AgeCalcVG5400 software specially designed for the irradiation and corrections parameters used at the CICESE's Geochronology Laboratory, including the equations proposed by York et al. (2004) for best straight line calculations, the Steiger and Jäger (1977) constants, and the Neutron fluence monitor ages recommended by Renne et al. (1998).

Errors for integrated, plateau, isochron and weighted mean ages include the uncertainty in the J parameter. Additionally for the plateau, isochron and weighted mean ages, the goodness of fit was included in the age uncertainty whenever the MSWD exceeded 1. The integrated ages were calculated by adding the fractions of the step-heating experiments. Plateau ages were calculated with the weighted mean of three or more consecutive fractions, which were in agreement within 1σ errors excluding the uncertainty in J. All the data were plotted in the $^{36}Ar/^{40}Ar$ versus $^{39}Ar/^{40}Ar$ correlation diagram to determine the composition of the ($^{40}Ar/^{36}Ar$)i of the samples. Tables with the relevant ^{40}Ar-^{39}Ar data of all the experiments and the figures with age spectrum, $^{37}ArCa/^{39}ArK$ diagram, the $^{36}Ar/^{40}Ar$ versus $^{39}Ar/^{40}Ar$ correlation diagram for each sample, and the interpretation of each ^{40}Ar-^{39}Ar experiment are given in Supplemental File 3.

Trace element analysis

Trace element contents of the intrusive sampes were determined at Laboratorio de Estudios Isotópicos, Centro de Geociencias, UNAM. Mafic to intermediate samples were analyzed using the procedure described in Mori et al. (2007). For silicic samples (SiO_2 > 60%), two additional digestion steps were carried out, in order to achieve complete dissolution of refractory minerals (e.g., zircon). The same amount of sample (50 mg) was weighted in 15 mL teflon vials, and after an initial overnight attack with 1mL of HF and 0.5 mL of 8 N HNO_3 on a hot plate at 90 °C, followed by evaporation to almost dryness, samples were transferred to 1.5 mL Teflon vials with 1 mL of HF and 0.5 mL of 8 N HNO_3. Closed vials were then placed inside the teflon liner of metal-jacketed Parr pressure bombs, to which

3 mL of a 2:1 HF-8 N HNO_3 mixture were added in order to equalize the pressure inside and outside the vials and prevent solution loss. The bomb was sealed and heated in an oven at 190 °C for five days. Thereafter, the bomb was allowed to cool to room temperature and the vials were removed, opened and placed on a hot plate to evaporate the acids to almost dryness. After addition of 1.5 mL of HCl, the vials were placed again in Parr bombs and 3 mL of 6N HCl were added to the teflon liner. Parr bombs were heated at 190°C in an oven for 24 hrs. This step is required in order to decompose the fluoride that might have formed in the previous steps. After cooling, vials were removed from the bombs and the samples were transferred to the original 15 mL vials, which have a larger surface area that allows faster evaporation. The final steps consisted in evaporating the samples to dryness, fluxing the samples twice with 16N of HNO_3, evaporating the sample to dryness after each step. Then, 2 mL of deionized water and 2 mL of 8N HNO_3 were added to the samples and the closed vials were left overnight on a hot plate at 90 °C. For analysis, the samples were diluted by weight to 100 g (1:2000 dilution) with an internal standard solution containing

Ge (10 ppb), In (5 ppb), Tm (5 ppb) and Bi (5 ppb). Calibration was performed with the international rock standards AGV-2, BHVO-2, BCR-2, JB-2, and JR.

References

Andersen, T., 2002, Correction of common lead in U–Pb analyses that do not report 204Pb. Chemical geology, v. 192, no. 1, p, 59-79.

Kuiper, K.F., Deino, A., Hilgen, F.J., Krijgsman W., Renne P.R., and Wijbrans J.R., 2008, Synchronizing rock clocks of Earth history: Science, v. 320, p. 500-504.

Ludwig, K.R., 2004, Isoplot/Ex, ver. 3. A geochronological toolkit for Microsoft Excel: Berkeley Geochronology Center, Special Publication, 4, 70 p.

Mori, L., Gómez-Tuena, A., Cai, Y., and Goldstein, S.L., 2007, Effects of prolonged flat subduction on the Miocene magmatic record of the central Trans-Mexican Volcanic Belt: Chemical Geology, v. 244, no. 3, p. 452–473, doi: 10.1016/j.chemgeo.2007.07.002.

Renne, P.R., Swisher, C.C., Deino, A.L., Karner, D.B., Owens, T.L., and De Paolo, D.J., 1998, Intercalibration of standards, absolute ages and uncertainties in ^{40}Ar-^{39}Ar dating: Chemical Geology, v. 145, p. 117-152.

Roddick, J.C., 1983, High precision intercalibration of ^{40}Ar-^{39}Ar standards: Geochimica et Cosmochimica Acta, 47, 887-898.

Schwarz, W.H., and Trieloff, M., 2007, Intercalibration of ^{40}Ar-^{39}Ar age standards NL-25, HB3gr hornblende, GA1550, SB-3, HD-B1 biotite and BMus/2 muscovite: Chemical Geology, v. 242, p. 218-231.

Solari, L. A., and Tanner, M., 2011, UPb.age, a fast data reduction script for LA-ICP-MS U/Pb geochronology: Revista Mexicana de Ciencias Geológicas, v. 28, no. 1, p. 83-91.

Solari, L. A, Gómez-Tuena, A., Bernal, J.P., Pérez-Arvizu, O., and Tanner, M., 2010, U/Pb zircon geochronology with an integrated LA-ICP-MS Microanalytical Workstation: Achievements in precision and accuracy: Geostandards and Geoanalytical Research, v. 34, no.1, p. 5-18.

Steiger, R.H., and Jäger, E., 1977, Subcommission on Geochronology: Convention on the use of decay constants in Geo and Cosmochronology: Earth and Planetary Science Letters, 36, 359-362.

York, D., Evensen, N.M., López-Martínez, M., and De Basabe-Delgado, J., 2004, Unified equations for the slope, intercept, and standard errors of the best straight line: American Journal of Physics, v. 72, no. 3, p. 367.

Supplemental file 2. Composition of hornblende and plagioclase in selected samples and thermobarometric results.

	Middle Miocene																						
Sample	BEKL-10D1	BEKL-10D1	BEKL-10D1	BEKL-10D1	BEKL-10D1	BEKL-10D1	BEKL-10D1	BEKL-10D1	BEKL-10D1	BEKL-10D1	BEKL-10D1	BEKL-10D1	BEKL-10D1	BEKL-10D1		BEKL-10D3	BEKL-10D3	BEKL-10D3	BEKL-10D3	BEKL-10D3	BEKL-10D3	BEKL-10D3	BEKL-10D3	BEKL-10D3	BEKL-10D3
Hornblende composition (wt%)																							
Analysis nr.	C1-1	C1-3	C1-9	C2-1	C2-3	C2-5	C2-7	C2-9	C3-1	C3-3	C3-5	C6-1	C6-3	C6-7		C1-1	C2-1	C2-3	C3-2	C3-4	C6-1	C6-3	C6-5	C7-1	C7-3
Location	rim	rim	rim	rim	rim	rim	rim	core	rim	rim	rim	rim	rim	rim		core	rim	core	rim	rim	rim	rim	rim	rim	rim
SiO_2	47.82	47.29	52.06	51.74	49.66	51.15	50.88	47.95	51.50	50.23	50.27	51.50	52.07	52.22		46.72	46.96	49.89	48.77	51.86	48.34	47.99	47.73	52.04	50.81
TiO_2	1.290	1.338	0.603	0.540	0.956	0.323	0.836	1.223	0.335	0.720	0.544	0.707	0.611	0.678		1.604	1.220	0.904	1.350	0.790	1.110	1.040	1.136	0.518	0.765
Al_2O_3	7.12	7.32	3.54	3.73	5.26	4.69	4.30	6.53	3.47	4.67	4.84	4.08	3.65	3.61		8.23	7.25	4.90	6.38	4.40	6.42	6.61	6.23	3.62	4.56
Cr_2O_3	0.000	0.005	0.037	0.008	0.000	0.010	0.024	0.022	0.027	0.000	0.022	0.057	0.000	0.000		0.044	0.052	0.039	0.000	0.020	0.040	0.153	0.067	0.051	0.000
FeO_{tot}	15.52	15.25	13.69	13.96	14.82	14.95	14.89	15.58	14.15	14.85	15.06	14.51	14.07	13.87		14.68	15.51	14.51	15.43	14.40	15.46	15.93	15.80	14.00	15.04
MgO	12.07	11.92	14.54	13.94	13.54	13.47	13.72	12.52	14.84	13.78	13.19	13.41	14.09	14.55		12.84	12.80	13.89	12.36	14.00	12.45	12.66	12.22	14.26	13.44
MnO	0.786	0.782	0.984	1.036	1.024	1.077	1.143	1.008	1.017	1.069	1.058	1.181	1.055	0.902		0.385	0.793	1.019	0.878	0.997	0.927	0.822	0.864	0.851	1.147
CaO	11.16	11.23	11.14	11.01	11.34	11.49	10.90	11.16	11.19	11.16	11.12	11.28	11.26	10.98		11.09	11.43	11.00	11.10	10.97	11.08	11.17	11.15	11.06	10.63
Na_2O	1.460	1.670	0.905	1.015	1.028	0.968	1.234	1.126	0.817	0.941	0.919	0.780	0.835	0.908		1.980	1.520	1.238	1.610	1.278	1.380	1.390	1.410	0.955	1.213
K_2O	0.637	0.639	0.320	0.297	0.457	0.355	0.374	0.564	0.284	0.405	0.394	0.362	0.307	0.322		0.624	0.687	0.443	0.518	0.401	0.555	0.519	0.506	0.277	0.383
Sum	97.86	96.10	97.82	97.28	98.09	98.48	98.30	97.66	97.63	97.83	97.42	97.87	97.95	98.04		98.15	98.22	97.79	98.40	99.12	97.76	98.28	97.11	97.63	97.99
Plagioclase composition (wt%)																							
Analysis nr.	C1-2	C1-4			C2-4	C2-6				C3-4	C3-6					C1-4		C3-3			C6-2	C6-4	C6-6		C7-4
Location	rim	rim			rim	rim				rim	rim					rim		rim			rim	rim	rim		rim
SiO_2	62.82	64.02			66.05	65.74				65.30	66.33					66.29		66.79			64.80	64.84	66.15		67.45
TiO_2	0.065	0.050			0.083	0.000				0.017	0.000					0.011		0.000			0.070	0.000	0.000		0.000
Al_2O_3	24.00	23.35			21.76	22.18				22.21	21.68					21.99		22.20			22.76	22.79	22.20		21.08
FeO_{tot}	0.207	0.168			0.251	0.184				0.128	0.163					0.145		0.304			0.199	0.471	0.215		0.234
CaO	5.11	4.78			2.47	2.77				2.75	2.64					2.49		3.09			3.91	3.39	2.85		1.79
Na_2O	8.61	8.92			9.67	10.06				9.86	10.10					9.98		10.48			9.01	9.29	9.82		10.22
K_2O	0.192	0.197			0.193	0.177				0.177	0.123					0.089		0.224			0.343	0.244	0.313		0.457
BaO	0.089	0.040			0.000	0.000				0.000	0.182					0.048		0.067			0.044	0.060	0.097		0.011
SrO	0.010	0.063			0.000	0.035				0.000	0.000					0.000		0.022			0.000	0.016	0.047		0.000
Sum	101.10	101.59			100.48	101.15				100.44	101.22					101.04		103.18			101.14	101.10	101.69		101.24
Thermobarometry																							
Holland and Blundy (1994); Schmidt (1992); Anderson and Smith (1995)																							
T (°C)	682	678	–	–	610	578	–	–	–	606	576	–	–	–		–	652	–	636	–	663	666	642	–	575
P (MPa)	279	302	–	–	138	69	–	–	–	85	87	–	–	–		–	309	–	237	–	234	246	232	–	57
Depth (km)	10.6	11.5	–	–	5.3	2.6	–	–	–	3.3	3.3	–	–	–		–	11.8	–	9.0	–	8.9	9.4	8.8	–	2.2
Ridolfi and Renzulli (2012).																							
T (°C)	815	830	767	770	806	770	826	836	771	799	784	783	759	755		837	847	829	828	800	831	840	824	746	825
P (MPa)	128	132	67	69	94	80	81	125	66	85	87	77	67	66		150	133	90	110	78	117	121	109	64	86
Depth (km)	4.9	5.0	2.5	2.6	3.6	3.1	3.1	4.8	2.5	3.2	3.3	2.9	2.6	2.5		5.7	5.1	3.4	4.2	3.0	4.5	4.6	4.2	2.5	3.3

(Continues)

Supplemental file 2 (cont.)

	Middle Miocene																						Early Miocene	
Sample	BEKL-6D1	BEKL-6D1	BEKL-6D1	BEKL-6D1	BEKL-6D1	BEKL-6D1	BEKL-6D1	BEKL-6D1	BEKL-6D1	BEKL-6D1	BEKL-6D1	BEKL-6D1	BEKL-6D1	BEKL-6D1	BEKL-6D1	BEKL-6D1	BEKL-6D1	BEKL-6D1	BEKL-6D1	BEKL-6D1	BEKL-6D1	BEKL-6D1	IXC-03	IXC-03
Hornblende composition (wt%)																								
Analysis nr.	C1-1	C1-6	C1-17	C2-1	C2-3	C2-5	C2-9	C3-1	C3-3	C3-6	C4-2	C4-3	C4-6	C4-7	C4-9	C4-11	C4-13	C4-14	C4-15	C4-20	C5-1	C5-3	C1-2	C2-1
Location	rim	rim	rim	rim	rim	rim	rim	rim	rim	rim	rim	rim	rim	rim	rim	rim	core	core	core	rim	rim	rim	rim	core
SiO_2	47.97	50.06	48.77	50.38	49.59	48.86	47.83	50.27	49.59	51.29	47.82	47.64	47.93	47.19	47.50	47.19	47.70	47.04	46.55	49.33	48.44	47.10	49.23	49.04
TiO_2	1.125	0.944	0.900	0.428	0.715	0.819	1.101	0.697	0.904	0.593	1.177	1.228	1.282	1.384	1.388	1.341	1.135	1.432	1.428	0.549	1.280	1.546	1.050	0.885
Al_2O_3	5.97	4.92	6.19	4.20	5.11	5.23	5.89	4.47	5.08	4.01	6.34	5.92	5.93	6.45	6.25	6.48	6.15	6.38	6.63	4.73	5.97	6.53	6.41	5.79
Cr_2O_3	0.000	0.007	0.042	0.000	0.068	0.026	0.000	0.000	0.028	0.000	0.068	0.000	0.000	0.000	0.000	0.000	0.038	0.042	0.019	0.000	0.042	0.000	0.009	0.057
FeO_{tot}	17.99	16.61	17.14	16.51	16.71	17.59	17.82	16.51	17.01	16.21	17.47	17.24	17.49	18.00	17.63	17.82	17.47	17.94	18.39	17.71	17.83	18.15	13.77	14.63
MgO	11.35	12.00	11.64	12.82	12.13	11.68	11.18	12.29	11.77	13.04	11.21	11.96	11.19	11.03	11.14	11.08	11.57	11.14	10.79	11.76	11.14	10.96	14.07	13.76
MnO	0.550	0.384	0.388	0.496	0.504	0.486	0.463	0.465	0.488	0.535	0.441	0.374	0.533	0.497	0.472	0.456	0.460	0.403	0.424	0.549	0.457	0.430	0.394	0.401
CaO	11.12	11.41	11.15	11.57	11.38	11.27	11.46	11.30	11.28	11.35	11.21	11.07	10.93	11.04	10.89	11.15	11.09	11.32	10.84	11.38	10.84	10.97	11.41	11.13
Na_2O	1.370	1.041	1.400	0.941	1.107	1.053	1.116	1.064	1.085	1.025	1.370	1.440	1.500	1.296	1.540	1.520	1.470	1.420	1.590	0.890	1.720	1.650	1.216	1.117
K_2O	0.637	0.466	0.604	0.379	0.518	0.506	0.614	0.429	0.497	0.378	0.699	0.599	0.668	0.683	0.686	0.691	0.647	0.713	0.726	0.426	0.657	0.716	0.576	0.545
Sum	98.08	97.84	98.22	97.72	97.83	97.52	97.47	97.49	97.73	98.43	97.81	97.47	97.45	97.57	97.50	97.73	97.73	97.83	97.39	97.32	98.38	98.05	98.14	97.35
Plagioclase composition (wt%)																								
Analysis nr.	C1-2	C1-7	C1-18	C2-2	C2-4	C2-6	C2-10	C3-2	C3-4	C3-7	C4-1	C4-4	C4-5	C4-8	C4-10	C4-12				C4-21		C5-4	C1-3	
Location	rim	rim	rim	rim	rim	rim	rim	rim	rim	rim	rim	rim	rim	rim	rim	rim				rim		rim	rim	
SiO_2	63.81	62.48	63.70	64.61	66.67	65.88	63.40	65.64	64.71	65.16	64.24	63.63	64.20	63.03	63.62	63.18				64.02		64.00	60.52	
TiO_2	0.018	0.047	0.023	0.007	0.000	0.000	0.000	0.010	0.000	0.000	0.008	0.035	0.000	0.004	0.025	0.003				0.059		0.000	0.026	
Al_2O_3	23.17	24.96	23.73	22.68	21.81	22.22	23.25	22.42	22.33	22.52	22.85	23.52	22.99	24.16	23.12	23.50				23.60		23.14	25.34	
FeO_{tot}	0.115	0.161	0.078	0.246	0.077	0.210	0.277	0.110	0.178	0.175	0.105	0.161	0.154	0.138	0.236	0.167				0.097		0.214	0.236	
CaO	4.51	6.06	4.66	3.54	2.60	2.78	4.40	3.23	3.89	3.80	4.17	4.32	4.42	4.98	4.29	4.40				4.25		4.39	7.24	
Na_2O	9.16	8.22	9.08	9.40	9.94	9.40	8.66	9.68	9.29	9.28	9.15	8.60	8.80	8.54	8.94	8.71				9.18		8.59	7.26	
K_2O	0.126	0.134	0.180	0.241	0.347	0.210	0.277	0.356	0.282	0.354	0.288	0.248	0.252	0.124	0.269	0.242				0.303		0.248	0.378	
BaO	0.018	0.000	0.000	0.000	0.009	0.000	0.005	0.000	0.078	0.000	0.000	0.000	0.072	0.000	0.031	0.000				0.001		0.047	0.098	
SrO	0.000	0.026	0.000	0.000	0.072	0.000	0.016	0.038	0.010	0.006	0.041	0.006	0.086	0.044	0.063	0.029				0.085		0.041	0.013	
Sum	100.93	102.09	101.45	100.72	101.53	100.70	100.29	101.48	100.77	101.29	100.85	100.52	100.97	101.02	100.59	100.23				101.60		100.67	101.11	
Thermobarometry																								
Holland and Blundy (1994); Schmidt (1992); Anderson and Smith (1995)																								
T (°C)	689	665	659	622	598	615	665	609	628	629	663	705	685	702	690	695	–	–	–	630	–	712	717	–
P (MPa)	183	108	217	51	126	145	196	72	131	32	233	165	186	213	208	223	–	–	–	103	–	208	178	–
Depth (km)	7.0	4.1	8.3	1.9	4.8	5.5	7.5	2.8	5.0	1.2	8.9	6.3	7.1	8.1	7.9	8.5	–	–	–	3.9	–	7.9	6.8	–
Ridolfi and Renzulli (2012)																								
T (°C)	740	660	715	661	699	691	697	668	687	676	734	733	747	742	751	745	746	738	759	669	751	758	747	740
P (MPa)	85	64	86	56	71	71	80	60	69	56	91	83	86	95	91	92	88	89	97	63	84	93	102	91
Depth (km)	3.2	2.5	3.3	2.2	2.7	2.7	3.0	2.3	2.6	2.2	3.5	3.1	3.3	3.6	3.5	3.5	3.4	3.4	3.7	2.4	3.2	3.6	3.9	3.5

(Continues)

Supplemental file 2 (cont.)

	Early Miocene											Paleocene											
Sample	IXC-03	IXC-03	IXC-03	IXC-03	IXC-03	IXC-03	IXC-03	IXC-03	IXC-03	IXC-03	IXC-03	CONC-01	CONC-01	CONC-01	CONC-01	CONC-01	CONC-01	CONC-01	CONC-01	CONC-01	CONC-01	CONC-01	CONC-01
Hornblende composition (wt%)																							
Analysis nr.	C2-6	C3-1	C3-3	C4-3	C4-8	C5-1	C5-3	C5-5	C6-1	C6-3	C6-5	C1-3	C1-5	C1-7	C2-2	C2-3	C2-5	C2-7	C2-9	C4-3	C5-1	C5-3	C5-5	C6-1
Location	rim	rim	rim	rim	core	rim	rim	core	rim	rim	rim	rim	rim	core	rim	rim	rim	rim	rim	rim	rim	rim	rim	rim
SiO_2	49.17	49.12	48.83	49.54	50.01	49.62	48.86	49.62	49.33	50.19	48.74	47.47	48.21	46.49	47.70	49.15	48.60	47.09	47.40	48.20	47.13	47.31	47.29	48.99
TiO_2	0.891	0.909	1.029	0.907	0.929	0.924	1.014	0.924	0.985	0.989	1.119	1.134	1.128	1.170	1.124	0.690	0.855	1.223	1.170	1.124	1.222	1.104	1.147	0.375
Al_2O_3	5.94	6.12	6.49	5.96	5.64	6.17	6.17	6.17	6.18	5.92	6.70	6.68	6.33	7.44	6.64	5.72	6.34	7.18	7.01	6.36	7.03	6.78	6.87	5.74
Cr_2O_3	0.000	0.027	0.000	0.000	0.029	0.000	0.021	0.014	0.003	0.068	0.000	0.077	0.000	0.000	0.000	0.000	0.000	0.000	0.064	0.004	0.000	0.049	0.056	0.000
FeO_{tot}	14.29	13.97	14.31	13.04	13.03	14.43	14.26	14.43	13.10	13.50	14.78	17.85	17.45	17.58	17.30	17.25	17.51	17.64	17.69	18.02	17.76	18.06	17.94	17.63
MgO	13.84	13.69	13.92	14.53	0.44	13.47	13.75	13.47	14.37	14.12	13.23	10.85	11.19	10.99	11.08	11.44	11.00	10.71	10.60	10.60	10.75	10.44	10.87	11.52
MnO	0.402	0.525	0.495	0.501	14.560	0.476	0.459	0.476	0.430	0.464	0.459	0.523	0.553	0.461	0.457	0.429	0.481	0.463	0.484	0.511	0.443	0.481	0.554	0.440
CaO	11.61	11.22	11.54	11.38	11.49	11.23	11.34	11.23	11.65	11.52	11.55	11.24	11.22	11.11	11.12	11.61	11.42	11.13	11.28	11.26	11.08	11.20	11.12	11.70
Na_2O	0.995	1.087	1.040	0.967	0.975	1.126	1.047	1.126	1.011	1.011	1.129	1.217	1.284	1.490	1.303	0.925	1.200	1.450	1.360	1.360	1.680	1.303	1.460	0.985
K_2O	0.523	0.606	0.648	0.516	0.546	0.583	0.573	0.583	0.604	0.581	0.688	0.727	0.657	0.850	0.759	0.506	0.651	0.754	0.737	0.680	0.816	0.702	0.738	0.469
Sum	97.66	97.27	98.30	97.34	97.65	98.03	97.49	98.04	97.66	98.36	98.39	97.77	98.02	97.58	97.48	97.72	98.06	97.64	97.79	98.12	97.91	97.43	98.04	97.85
Plagioclase composition (wt%)																							
Analysis nr.	C2-5	C3-2	C3-4	C4-4		C5-2	C5-4		C6-2	C6-4	C6-6	C1-4	C1-6		C2-1	C2-4	C2-6	C2-8	C2-10	C4-4	C5-2	C5-4	C5-6	C6-2
Location	rim	rim	rim	rim		rim	rim		rim	rim	rim	rim	rim		rim	rim	rim	rim	rim	rim	rim	rim	rim	rim
SiO_2	59.31	60.28	58.66	60.85		60.62	59.35		58.72	59.85	59.33	63.23	63.35		64.78	64.02	63.23	64.66	61.36	64.49	64.18	64.11	63.23	65.16
TiO_2	0.047	0.051	0.006	0.000		0.024	0.000		0.015	0.026	0.000	0.004	0.006		0.011	0.000	0.043	0.003	0.000	0.019	0.036	0.036	0.051	0.000
Al_2O_3	26.28	25.56	26.21	25.85		25.69	25.98		26.01	25.95	26.26	23.50	23.08		22.94	23.06	23.56	23.25	24.51	22.96	23.13	23.09	23.31	22.63
FeO_{tot}	0.241	0.278	0.259	0.255		0.220	0.226		0.206	0.219	0.316	0.128	0.203		0.103	0.108	0.152	0.198	0.156	0.229	0.161	0.129	0.164	0.148
CaO	8.08	7.40	7.97	7.07		7.25	7.64		7.59	7.82	7.89	4.83	4.37		3.83	4.31	5.10	4.30	6.10	4.24	4.38	4.46	5.10	3.51
Na_2O	6.98	7.32	7.09	7.24		7.42	7.17		6.83	7.02	6.89	8.73	8.72		9.42	9.20	8.80	9.32	8.12	9.13	9.12	9.31	8.59	9.43
K_2O	0.300	0.408	0.341	0.405		0.413	0.373		0.349	0.275	0.335	0.264	0.300		0.167	0.149	0.245	0.238	0.216	0.202	0.176	0.089	0.226	0.129
BaO	0.000	0.024	0.074	0.000		0.047	0.053		0.118	0.000	0.052	0.075	0.000		0.000	0.000	0.000	0.043	0.000	0.000	0.031	0.000	0.122	0.055
SrO	0.000	0.109	0.042	0.029		0.016	0.032		0.038	0.038	0.067	0.035	0.000		0.000	0.038	0.035	0.054	0.073	0.000	0.101	0.044	0.000	0.095
Sum	101.24	101.43	100.65	101.70		101.70	100.82		99.88	101.20	101.14	100.80	100.03		101.25	100.88	101.16	102.06	100.53	101.27	101.31	101.27	100.79	101.16
Thermobarometry																								
Holland and Blundy (1994); Schmidt (1992); Anderson and Smith (1995)																								
T (°C)	714	699	722	689	–	691	713	–	707	695	722	669	660	–	642	611	644	659	684	645	676	650	691	600
P (MPa)	150	180	180	174	–	189	169	–	174	162	196	259	231	–	269	186	239	308	275	242	284	281	257	185
Depth (km)	5.7	6.9	6.8	6.6	–	7.2	6.5	–	6.6	6.2	7.5	9.9	8.8	–	10.2	7.1	9.1	11.8	10.5	9.2	10.8	10.7	9.8	7.1
Ridolfi and Renzulli (2012)																								
T (°C)	716	753	753	746	731	736	744	726	735	737	742	739	731	760	725	663	704	742	730	727	752	728	757	658
P (MPa)	89	101	106	99	90	98	99	95	99	95	106	101	93	117	98	76	89	109	104	91	103	100	104	74
Depth (km)	3.4	3.9	4.0	3.8	3.4	3.7	3.8	3.6	3.8	3.6	4.1	3.9	3.5	4.5	3.7	2.9	3.4	4.1	4.0	3.5	3.9	3.8	4.0	2.8

(Continues)

Supplemental file 2 (cont.)

	Paleocene						
Sample	CONC-01	CONC-01	CONC-01	CONC-01	CONC-01	CONC-01	CONC-01
Hornblende composition (wt%)							
Analysis nr.	C6-3	C7-1	C7-5	C8-1	C8-3	C10-1	C10-3
Location	rim	rim	rim	rim	rim	rim	rim
SiO_2	48.08	48.30	48.06	46.43	47.12	46.27	45.87
TiO_2	0.674	1.241	0.997	1.315	1.266	1.339	1.249
Al_2O_3	6.66	6.62	6.57	7.75	7.20	7.28	7.12
Cr_2O_3	0.039	0.058	0.078	0.000	0.000	0.005	0.000
FeO_{tot}	17.93	17.57	17.72	17.31	18.11	18.67	18.30
MgO	10.59	10.95	10.84	11.07	10.46	10.21	9.97
MnO	0.425	0.450	0.504	0.453	0.434	0.445	0.546
CaO	11.61	11.21	11.36	11.28	11.29	11.23	11.11
Na_2O	1.159	1.420	1.288	1.520	1.380	1.480	1.440
K_2O	0.642	0.694	0.661	0.958	0.837	0.926	0.888
Sum	97.81	98.51	98.08	98.09	98.10	97.85	96.49
Plagioclase composition (wt%)							
Analysis nr.	C6-4	C7-2	C7-6	C8-2	C8-4	C10-2	C10-4
Location	rim	rim	rim	rim	rim	rim	rim
SiO_2	66.52	63.95	63.71	61.52	62.72	64.21	62.27
TiO_2	0.004	0.000	0.000	0.046	0.001	0.000	0.024
Al_2O_3	21.46	23.50	23.51	25.13	24.52	22.62	24.29
FeO_{tot}	0.049	0.197	0.241	0.166	0.194	0.223	0.135
CaO	2.47	4.51	4.75	6.47	5.58	4.00	5.81
Na_2O	10.28	8.91	7.59	8.18	8.46	8.94	8.49
K_2O	0.109	0.117	0.114	0.177	0.168	0.237	0.113
BaO	0.000	0.000	0.021	0.000	0.014	0.012	0.000
SrO	0.085	0.000	0.000	0.000	0.099	0.073	0.070
Sum	100.98	101.18	99.94	101.69	101.76	100.32	101.20
Thermobarometry							
Holland and Blundy (1994); Schmidt (1992); Anderson and Smith (1995)							
T (°C)	567	656	664	720	684	676	699
P (MPa)	259	256	251	293	291	308	281
Depth (km)	9.9	9.8	9.6	11.2	11.1	11.8	10.7
Ridolfi and Renzulli (2012).							
T (°C)	674	723	714	767	734	751	750
P (MPa)	89	94	93	125	107	109	109
Depth (km)	3.4	3.6	3.6	4.8	4.1	4.2	4.1

Note: Analysis were obtained at Dipartimento di Scienze della Terra, Università degli Studi di Milano with a JEOL JXA 8200 Superprobe equipped with five WDS-wavelength-dispersive spectrometers, using a 1 mm beam at 15 kV, and 15 nA beam current.

Natural and synthetic minerals and glasses were used as calibration standards.

Hornblende-plagioclase pairs used for temperature calculations after Holland and Blundy (1994) are in the same column.

Depth calculated with a crustal density of 2.7 g/cm^3.

Supplemental file 3. U-Pb analytical data

Spot Name	U (ppm)	Th (ppm)	Th/U	CORRECTED RATIOS							CORRECTED AGES (Ma)						Best age (Ma)	±1s
				207Pb/206Pb	±1s	207Pb/235U	±1s	206Pb/238U	±1s	Rho	206Pb/238U	±1s	207Pb/235U	±1s	207Pb/206Pb	±1s		
Sample: PB 32																		
Zircon_22_033	684	347	0.47	0.04927	0.00148	0.09901	0.00306	0.01463	0.00011	0.24	93.6	0.7	96	3	161	69	93.6	0.7
Zircon_03_010	717	429	0.56	0.0497	0.00154	0.10274	0.00331	0.01499	0.00013	0.27	95.9	0.8	99	3	181	69	95.9	0.8
Zircon_27_039	277	98	0.33	0.0523	0.00204	0.10882	0.00438	0.01514	0.00015	0.25	96.9	1	105	4	299	90	96.9	1.0
Zircon_09_017	218	205	0.87	0.05706	0.00405	0.11898	0.00861	0.01516	0.00021	0.19	97	1	114	8	494	161	97.0	1.0
Zircon_23_034	334	124	0.34	0.05351	0.00166	0.11067	0.00364	0.01509	0.00017	0.33	97	1	107	3	350	71	97.0	1.0
Zircon_12_021	507	292	0.53	0.04726	0.00165	0.09921	0.00358	0.01524	0.00014	0.25	97.5	0.9	96	3	62	72	97.5	0.9
Zircon_20_030	127	34	0.25	0.06319	0.0029	0.13408	0.00666	0.01539	0.00019	0.26	98	1	128	6	715	99	98.0	1.0
Zircon_25_036	153	65	0.39	0.05501	0.00281	0.11699	0.00616	0.01551	0.0002	0.24	99	1	112	6	413	116	99.0	1.0
Zircon_04_011	409	160	0.36	0.05231	0.00183	0.11184	0.00404	0.01557	0.00014	0.25	99.6	0.9	108	4	299	76	99.6	0.9
Zircon_06_014	316	113	0.33	0.0558	0.00244	0.1207	0.00585	0.01569	0.0002	0.3	100	1	116	5	444	92	100.0	1.0
Zircon_08_016	189	147	0.72	0.05847	0.00292	0.12647	0.00657	0.01581	0.00022	0.28	101	1	121	6	547	104	101.0	1.0
Zircon_14_023	105	51	0.45	0.06137	0.00362	0.1342	0.00814	0.01581	0.00022	0.23	101	1	128	7	652	121	101.0	1.0
Zircon_18_028	66	47	0.67	0.06135	0.00466	0.13136	0.01029	0.01583	0.0003	0.24	101	2	125	9	652	169	101.0	2.0
Zircon_19_029	300	156	0.48	0.05457	0.00202	0.11794	0.00459	0.01575	0.00019	0.31	101	1	113	4	395	84	101.0	1.0
Zircon_26_038	138	71	0.48	0.05757	0.00248	0.12663	0.00569	0.016	0.00021	0.28	102	1	121	5	513	96	102.0	1.0
Zircon_07_015	86	36	0.39	0.05709	0.00411	0.12623	0.00934	0.01614	0.00027	0.23	103	2	121	8	495	152	103.0	2.0
Zircon_15_024	126	53	0.39	0.06114	0.00312	0.13387	0.00716	0.01607	0.00026	0.3	103	2	128	6	644	104	103.0	2.0
Zircon_24_035	185	90	0.45	0.05298	0.00275	0.11667	0.0062	0.01607	0.00018	0.21	103	1	112	6	328	118	103.0	1.0
Zircon_10_018	66	36	0.51	0.06173	0.00321	0.13931	0.00758	0.01634	0.00026	0.29	104	2	132	7	665	106	104.0	2.0
Zircon_13_022	77	39	0.47	0.06323	0.00322	0.13928	0.00749	0.01622	0.00028	0.32	104	2	132	7	716	103	104.0	2.0
Zircon_16_026	120	68	0.52	0.0602	0.00283	0.13414	0.00658	0.01623	0.00023	0.29	104	1	128	6	611	97	104.0	1.0
Zircon_11_020	296	156	0.49	0.05383	0.00248	0.12164	0.00581	0.01638	0.00021	0.26	105	1	117	5	364	99	105.0	1.0
Zircon_28_040	139	76	0.51	0.06173	0.0037	0.14065	0.00885	0.01645	0.00031	0.3	105	2	134	8	665	131	105.0	2.0
Zircon_17_027	74	48	0.60	0.06194	0.0052	0.1386	0.01191	0.01653	0.0003	0.21	106	2	132	11	672	172	106.0	2.0
Zircon_01_PB32_008	110	33	0.28	0.06856	0.0061	0.15557	0.01416	0.01667	0.00032	0.21	107	2	147	12	886	193	107.0	2.0
Zircon_05_012	118	50	0.39	0.05589	0.00307	0.13285	0.00769	0.0172	0.00031	0.32	110	2	127	7	448	116	110.0	2.0
Zircon_02_009	148	60	0.37	0.06026	0.00289	0.14851	0.00743	0.01787	0.00025	0.28	114	2	141	7	613	104	114.0	2.0

Spot Name	U (ppm)	Th (ppm)	Th/U	CORRECTED RATIOS							CORRECTED AGES (Ma)						Best age (Ma)	±1s
				207Pb/206Pb	±1s	207Pb/235U	±1s	206Pb/238U	±1s	Rho	206Pb/238U	±1s	207Pb/235U	±1s	207Pb/206Pb	±1s		
Sample: SCr 27																		
Zircon_31_043	2863	1788	0.59	0.04915	0.00074	0.09847	0.00164	0.01455	0.00011	0.43	93.1	0.7	95	2	155	34	93.1	0.70
Zircon_28_040	334	237	0.67	0.04894	0.00196	0.09803	0.00403	0.01457	0.00014	0.23	93.2	0.9	95	4	145	88	93.2	0.90
Zircon_25_036	238	198	0.78	0.07053	0.00444	0.1417	0.00918	0.01461	0.00022	0.24	94	1	135	8	944	128	94.0	1.00

Zircon_01_SCR-27_008	1296	846	0.61	0.04874	0.00097	0.09929	0.00215	0.01478	0.00012	0.39	94.6	0.8	96	2	135	45	94.6	0.80
Zircon_06_014	1225	2067	1.58	0.05275	0.0009	0.10743	0.00199	0.01479	0.00011	0.39	94.6	0.7	104	2	318	39	94.6	0.70
Zircon_18_028	255	136	0.50	0.0522	0.00251	0.10622	0.00523	0.01488	0.00016	0.22	95	1	103	5	294	107	95.0	1.00
Zircon_22_033	399	74	0.17	0.05743	0.0023	0.11691	0.00492	0.01483	0.00019	0.31	95	1	112	4	508	86	95.0	1.00
Zircon_21_032	132	75	0.53	0.06195	0.00619	0.12577	0.0127	0.01506	0.00021	0.14	96	1	120	11	672	214	96.0	1.00
Zircon_19_029	162	62	0.36	0.0591	0.00349	0.12327	0.0074	0.01523	0.00017	0.18	97	1	118	7	571	126	97.0	1.00
Zircon_26_038	87	31	0.33	0.06742	0.00976	0.14093	0.02115	0.01516	0.00026	0.18	97	2	134	19	851	310	97.0	2.00
Zircon_10_018	438	396	0.85	0.0525	0.00168	0.11019	0.00366	0.01527	0.00014	0.27	97.7	0.9	106	3	307	71	97.7	0.90
Zircon_13_022	129	68	0.49	0.05504	0.00374	0.11579	0.00804	0.01532	0.00021	0.21	98	1	111	7	414	149	98.0	1.00
Zircon_17_027	131	48	0.34	0.05811	0.00446	0.12214	0.00994	0.01524	0.00026	0.27	98	2	117	9	534	166	98.0	2.00
Zircon_32_044	168	63	0.35	0.05827	0.00417	0.12263	0.00934	0.01526	0.00018	0.26	98	1	117	8	540	156	98.0	1.00
Zircon_07_015	210	103	0.46	0.05394	0.00237	0.114	0.00514	0.0154	0.00015	0.22	98.5	1	110	5	369	97	98.5	1.00
Zircon_14_023	133	85	0.60	0.05686	0.00483	0.11985	0.01041	0.01543	0.00028	0.21	99	2	115	9	486	186	99.0	2.00
Zircon_15_024	185	108	0.55	0.06261	0.00319	0.1317	0.0069	0.01543	0.00019	0.23	99	1	126	6	695	106	99.0	1.00
Zircon_29_041	160	100	0.58	0.05687	0.00375	0.12084	0.00809	0.01562	0.00017	0.17	100	1	116	7	487	144	100.0	1.00
Zircon_02_009	74	25	0.31	0.07409	0.00674	0.15628	0.01456	0.01578	0.00032	0.22	101	2	147	13	1044	187	101.0	2.00
Zircon_03_010	105	80	0.71	0.05866	0.00522	0.12528	0.01127	0.01583	0.00021	0.15	101	1	120	10	555	197	101.0	1.00
Zircon_09_017	124	95	0.72	0.06147	0.0035	0.13182	0.00774	0.01574	0.00022	0.24	101	1	126	7	656	120	101.0	1.00
Zircon_05_012	150	64	0.40	0.06029	0.00326	0.13225	0.00735	0.01598	0.00021	0.23	102	1	126	7	614	118	102.0	1.00
Zircon_24_035	66	26	0.36	0.06073	0.00729	0.1304	0.01586	0.01602	0.00032	0.16	102	2	124	14	630	264	102.0	2.00
Zircon_30_042	100	51	0.47	0.06574	0.00478	0.14567	0.01164	0.01607	0.00026	0.29	103	2	138	10	798	152	103.0	2.00
Zircon_12_021	133	72	0.50	0.05241	0.00418	0.11788	0.00986	0.01631	0.00023	0.2	104	1	113	9	303	175	104.0	1.00
Zircon_20_030	120	63	0.49	0.06172	0.00346	0.13607	0.00792	0.01622	0.00026	0.27	104	2	130	7	664	118	104.0	2.00
Zircon_11_020	764	532	0.65	0.04587	0.00133	0.10309	0.0031	0.01638	0.00013	0.27	104.7	0.8	100	3	-9	55	104.7	0.80
Zircon_23_034	69	44	0.59	0.0612	0.00471	0.137	0.01075	0.01645	0.00025	0.2	105	2	130	10	646	166	105.0	2.00
Zircon_08_016	96	40	0.38	0.06075	0.00443	0.14003	0.0105	0.01667	0.00028	0.23	107	2	133	9	630	155	107.0	2.00
Zircon_27_039	338	204	0.56	0.05568	0.00273	0.13187	0.00662	0.01723	0.00019	0.21	110	1	126	6	440	107	110.0	1.00
Zircon_04_011	206	98	0.45	0.05214	0.00276	0.12904	0.00701	0.01802	0.00022	0.22	115	1	123	6	292	121	115.0	1.00

				CORRECTED RATIOS							CORRECTED AGES (Ma)						Best age (Ma)	±1s
Spot Name	**U (ppm)**	**Th (ppm)**	**Th/U**	**207Pb/206Pb**	**±1s**	**207Pb/235U**	**±1s**	**206Pb/238U**	**±1s**	**Rho**	**206Pb/238U**	**±1s**	**207Pb/235U**	**±1s**	**207Pb/206Pb**	**±1s**		
Sample: SC 17																		
Zircon_18_035	259	247	0.88	0.05241	0.00288	0.1009	0.00563	0.01414	0.00014	0.17	90.5	0.9	98	5	303	125	90.5	0.90
Zircon_10_025	285	105	0.34	0.05688	0.00273	0.1122	0.00555	0.0143	0.00017	0.24	92	1	108	5	487	97	92.0	1.00
Zircon_04_011	547	343	0.58	0.05299	0.00154	0.10537	0.00323	0.0145	0.00014	0.32	92.8	0.9	102	3	328	66	92.8	0.90
Zircon_06_021	180	147	0.75	0.05883	0.00271	0.11783	0.0056	0.01474	0.00018	0.25	94	1	113	5	561	101	94.0	1.00
Zircon_09_024	162	105	0.59	0.05558	0.00267	0.11331	0.00561	0.01479	0.00018	0.24	95	1	109	5	436	107	95.0	1.00
Zircon_23_041	129	81	0.58	0.05867	0.00393	0.11894	0.00814	0.0148	0.00021	0.2	95	1	114	7	555	133	95.0	1.00
Zircon_05_012	246	102	0.38	0.05122	0.002	0.10498	0.0042	0.01496	0.00013	0.22	95.7	0.8	101	4	251	91	95.7	0.80

Zircon_08_023	160	99	0.57	0.05099	0.00255	0.10443	0.00537	0.01498	0.00018	0.23	96	1	101	5	240	114	96.0	1.00
Zircon_16_033	239	91	0.35	0.0539	0.0036	0.11196	0.00794	0.01506	0.00019	0.21	96	1	108	7	367	151	96.0	1.00
Zircon_26_045	223	160	0.66	0.05902	0.00401	0.12212	0.00843	0.01505	0.00018	0.18	96	1	117	8	568	135	96.0	1.00
Zircon_31_050	115	65	0.52	0.0661	0.00602	0.13713	0.01257	0.01505	0.00017	0.11	96	1	130	11	810	174	96.0	1.00
Zircon_02_009	330	203	0.57	0.05159	0.00175	0.10708	0.00386	0.01513	0.00018	0.34	97	1	103	4	267	78	97.0	1.00
Zircon_20_037	87	45	0.47	0.06866	0.00488	0.14383	0.01053	0.01515	0.00027	0.24	97	2	136	9	889	148	97.0	2.00
Zircon_22_040	222	153	0.63	0.05393	0.00297	0.11167	0.00629	0.01518	0.00018	0.21	97	1	107	6	368	124	97.0	1.00
Zircon_28_047	229	167	0.67	0.0555	0.00283	0.11567	0.00606	0.01511	0.00018	0.23	97	1	111	6	432	104	97.0	1.00
Zircon_17_034	223	90	0.37	0.05677	0.0029	0.11958	0.00621	0.0153	0.00015	0.18	97.9	1	115	6	483	113	97.9	1.00
Zircon_03_010	150	69	0.42	0.05402	0.00232	0.1131	0.00505	0.01529	0.00018	0.27	98	1	109	5	372	98	98.0	1.00
Zircon_11_027	203	130	0.59	0.04562	0.00374	0.09397	0.00777	0.01528	0.00017	0.13	98	1	91	7	-22	174	98.0	1.00
Zircon_21_039	91	46	0.46	0.07102	0.00729	0.14932	0.01599	0.01525	0.00024	0.16	98	2	141	14	958	214	98.0	2.00
Zircon_29_048	161	113	0.64	0.0584	0.00479	0.12289	0.01027	0.01525	0.00024	0.19	98	2	118	9	545	164	98.0	2.00
Zircon_07_022	237	155	0.60	0.05502	0.00264	0.11691	0.00578	0.01547	0.00019	0.24	99	1	112	5	413	107	99.0	1.00
Zircon_14_030	105	71	0.62	0.05643	0.00436	0.12005	0.01016	0.01543	0.00025	0.24	99	2	115	9	469	172	99.0	2.00
Zircon_15_031	108	76	0.65	0.08493	0.00705	0.17947	0.01514	0.01548	0.00023	0.18	99	1	168	13	1314	162	99.0	1.00
Zircon_24_042	118	85	0.66	0.06996	0.00469	0.14699	0.01009	0.01542	0.00023	0.22	99	1	139	9	927	126	99.0	1.00
Zircon_25_043	129	90	0.64	0.06068	0.00382	0.12874	0.00831	0.0154	0.00022	0.22	99	1	123	7	628	124	99.0	1.00
Zircon_13_029	150	94	0.57	0.06944	0.00687	0.15158	0.0152	0.0157	0.00025	0.16	100	2	143	13	912	207	100.0	2.00
Zircon_19_036	231	132	0.53	0.05785	0.0033	0.12443	0.00733	0.0157	0.00024	0.25	100	2	119	7	524	125	100.0	2.00
Zircon_30_049	143	61	0.39	0.06066	0.004	0.12831	0.00861	0.01563	0.00019	0.19	100	1	123	8	627	130	100.0	1.00
Zircon_01_SC17_008	86	49	0.52	0.05978	0.00359	0.12632	0.00836	0.0158	0.00044	0.42	101	3	121	8	596	132	101.0	3.00
Zircon_12_028	109	50	0.42	0.06667	0.00553	0.14231	0.01203	0.01576	0.00025	0.19	101	2	135	11	827	175	101.0	2.00
Zircon_27_046	171	63	0.34	0.06143	0.00405	0.13641	0.00918	0.01627	0.00021	0.2	104	1	130	8	654	129	104.0	1.00

				CORRECTED RATIOS							CORRECTED AGES (Ma)						Best age (Ma)	±1s
Spot Name	**U (ppm)**	**Th (ppm)**	**Th/U**	**207Pb/206Pb**	**±1s**	**207Pb/235U**	**±1s**	**206Pb/238U**	**±1s**	**Rho**	**206Pb/238U**	**±1s**	**207Pb/235U**	**±1s**	**207Pb/206Pb**	**±1s**		
Sample: BEKL 8D-6																		
Zircon_02_009	6691	651	0.09	0.04964	0.00092	0.08585	0.00185	0.01254	0.0001	0.43	80.4	0.6	84	2	178	42	80.4	0.6
Zircon_29_041	2133	318	0.14	0.05029	0.00136	0.0874	0.00257	0.01261	0.00009	0.4	80.8	0.6	85	2	208	62	80.8	0.6
Zircon_24_035	175	136	0.71	0.05959	0.00274	0.1172	0.0056	0.01439	0.00019	0.27	92	1	113	5	589	95	92.0	1.0
Zircon_34_047	147	100	0.62	0.05834	0.00286	0.11538	0.00582	0.01442	0.00017	0.24	92	1	111	5	543	106	92.0	1.0
Zircon_08_016	106	63	0.54	0.05728	0.00355	0.11358	0.0072	0.01451	0.00019	0.21	93	1	109	7	502	136	93.0	1.0
Zircon_01_8d6a_008	92	57	0.56	0.05928	0.00477	0.12055	0.01086	0.01475	0.00029	0.29	94	2	116	10	577	176	94.0	2.0
Zircon_26_038	126	87	0.62	0.0632	0.00373	0.12629	0.00769	0.01463	0.00022	0.25	94	1	121	7	715	124	94.0	1.0
Zircon_32_045	117	78	0.60	0.0545	0.00465	0.11049	0.01006	0.0147	0.00024	0.25	94	2	106	9	392	189	94.0	2.0
Zircon_15_024	108	66	0.55	0.06804	0.00497	0.13794	0.01031	0.0149	0.00024	0.21	95	2	131	9	870	146	95.0	2.0
Zircon_35_048	285	145	0.46	0.05318	0.0016	0.1088	0.00348	0.01482	0.00016	0.34	95	1	105	3	336	67	95.0	1.0
Zircon_31_044	445	193	0.39	0.05049	0.00157	0.10372	0.00333	0.01496	0.00013	0.25	95.7	0.8	100	3	218	70	95.7	0.8

Zircon_25_036	73	44	0.55	0.06782	0.00421	0.13811	0.00888	0.01493	0.00025	0.26	96	2	131	8	863	128	96.0	2.0
Zircon_28_040	103	69	0.61	0.06059	0.0043	0.12226	0.00893	0.01495	0.00025	0.24	96	2	117	8	625	152	96.0	2.0
Zircon_33_046	77	51	0.60	0.0705	0.00416	0.14478	0.00902	0.01504	0.0003	0.32	96	2	137	8	943	120	96.0	2.0
Zircon_30_042	270	155	0.52	0.0555	0.00239	0.11425	0.00501	0.01502	0.00013	0.19	96.1	0.8	110	5	432	95	96.1	0.8
Zircon_13_022	1432	366	0.23	0.04945	0.00104	0.10282	0.00225	0.0151	0.00009	0.28	96.6	0.6	99	2	169	46	96.6	0.6
Zircon_09_017	102	50	0.44	0.06139	0.00385	0.12852	0.00878	0.01518	0.00021	0.24	97	1	123	8	653	134	97.0	1.0
Zircon_11_020	114	69	0.55	0.0697	0.00453	0.14546	0.0097	0.01519	0.00023	0.22	97	1	138	9	920	129	97.0	1.0
Zircon_14_023	196	93	0.43	0.05542	0.00222	0.11609	0.00482	0.01528	0.00017	0.26	98	1	112	4	429	85	98.0	1.0
Zircon_16_026	94	49	0.48	0.05568	0.0039	0.1159	0.00832	0.01533	0.00025	0.22	98	2	111	8	440	149	98.0	2.0
Zircon_18_028	130	71	0.50	0.05919	0.00296	0.12236	0.00629	0.01524	0.00018	0.23	98	1	117	6	574	104	98.0	1.0
Zircon_19_029	965	143	0.13	0.05058	0.00214	0.10677	0.00478	0.01531	0.00015	0.33	98	1	103	4	222	96	98.0	1.0
Zircon_03_010	92	49	0.48	0.07204	0.00713	0.15463	0.01551	0.01546	0.00025	0.16	99	2	146	14	987	204	99.0	2.0
Zircon_21_032	118	60	0.46	0.06146	0.00381	0.13015	0.0083	0.01544	0.00023	0.23	99	1	124	7	655	128	99.0	1.0
Zircon_23_034	294	135	0.42	0.05414	0.00477	0.11509	0.01055	0.01542	0.00016	0.18	99	1	111	10	377	182	99.0	1.0
Zircon_04_011	511	66	0.12	0.05432	0.00158	0.11826	0.00367	0.01585	0.00017	0.35	101	1	113	3	384	64	101.0	1.0
Zircon_07_015	92	89	0.87	0.07048	0.00359	0.15251	0.00811	0.01583	0.00024	0.29	101	2	144	7	942	103	101.0	2.0
Zircon_12_021	147	58	0.36	0.06365	0.00395	0.13738	0.00873	0.01591	0.00022	0.22	102	1	131	8	730	126	102.0	1.0
Zircon_20_030	84	43	0.46	0.06807	0.00511	0.14662	0.01124	0.01587	0.00025	0.2	102	2	139	10	871	150	102.0	2.0
Zircon_10_018	53	30	0.51	0.09926	0.00933	0.22039	0.02128	0.01627	0.00036	0.23	104	2	202	18	1610	177	104.0	2.0
Zircon_05_012	85	32	0.33	-0.00831	-0.0049	-0.01887	-0.01114	0.01652	0.0003	0.05	106	2	-19.3	-11.5	-2694	1198	106.0	2.0
Zircon_17_027	90	46	0.47	0.06649	0.00426	0.14124	0.01514	0.01663	0.00143	0.8	106	9	134	13	822	129	106.0	9.0
Zircon_27_039	606	139	0.21	0.04786	0.00158	0.11122	0.00378	0.01696	0.00014	0.24	108.4	0.9	107	3	92	73	108.4	0.9
Zircon_22_033	150	37	0.22	0.05576	0.0029	0.15054	0.00811	0.01987	0.00028	0.26	127	2	142	7	443	110	127.0	2.00

				CORRECTED RATIOS							CORRECTED AGES (Ma)						Best age (Ma)	±1s
Spot Name	**U (ppm)**	**Th (ppm)**	**Th/U**	**207Pb/206Pb**	**±1s**	**207Pb/235U**	**±1s**	**206Pb/238U**	**±1s**	**Rho**	**206Pb/238U**	**±1s**	**207Pb/235U**	**±1s**	**207Pb/206Pb**	**±1s**		
Sample: BEKL 21D-1																		
Zircon_07_015	368	145	0.39	0.04754	0.00361	0.09146	0.00744	0.01395	0.00023	0.29	89	1	89	7	77	153	89	1.0
Zircon_21_032	196	92	0.46	0.06867	0.01332	0.13463	0.02664	0.01422	0.00036	0.18	91	2	128	24	889	405	91	2.0
Zircon_13_022	455	97	0.21	0.05289	0.00234	0.10432	0.00496	0.01431	0.00015	0.29	91.6	0.9	101	5	324	94	92	0.9
Zircon_02_009	260	72	0.27	0.06197	0.00533	0.12219	0.0122	0.0143	0.00043	0.47	92	3	117	11	673	175	92	3.0
Zircon_29_041	190	102	0.52	0.05816	0.0039	0.11473	0.00788	0.01437	0.00022	0.22	92	1	110	7	536	144	92	1.0
Zircon_18_028	119	59	0.49	0.05656	0.0052	0.11291	0.0109	0.01448	0.00026	0.25	93	2	109	10	475	199	93	2.0
Zircon_28_040	180	118	0.64	0.06892	0.00489	0.13574	0.01005	0.01452	0.0003	0.29	93	2	129	9	896	144	93	2.0
Zircon_30_042	176	99	0.55	0.05652	0.00322	0.11286	0.00668	0.01459	0.00023	0.27	93	1	109	6	473	124	93	1.0
Zircon_34_047	108	45	0.41	0.0601	0.00555	0.12032	0.01159	0.01452	0.00027	0.25	93	2	115	11	607	197	93	2.0
Zircon_20_030	137	91	0.65	0.05609	0.00426	0.11157	0.00869	0.01465	0.00025	0.22	94	2	107	8	456	166	94	2.0
Zircon_22_033	247	169	0.67	0.05903	0.0036	0.11833	0.00736	0.01463	0.00018	0.2	94	1	114	7	568	130	94	1.0
Zircon_32_045	157	93	0.58	0.05664	0.00402	0.11752	0.00858	0.01521	0.00026	0.23	97	2	113	8	478	154	97	2.0

Zircon_05_012	71	48	0.65	0.06209	0.00985	0.13159	0.02279	0.01537	0.00047	0.31	98	3	126	20	677	327	98	3.0
Zircon_19_029	140	70	0.49	0.0555	0.00361	0.1163	0.00781	0.01538	0.00026	0.25	98	2	112	7	432	142	98	2.0
Zircon_12_021	144	82	0.56	0.05715	0.00532	0.12041	0.01134	0.01546	0.00023	0.15	99	1	115	10	497	194	99	1.0
Zircon_23_034	157	59	0.37	0.05313	0.00352	0.11506	0.00807	0.01571	0.00024	0.26	100	2	111	7	334	147	100	2.0
Zircon_33_046	155	84	0.53	0.05246	0.00336	0.11468	0.00754	0.01615	0.00024	0.23	103	2	110	7	306	142	103	2.0
Zircon_03_010	128	53	0.41	0.06685	0.00475	0.15034	0.01113	0.01638	0.00034	0.28	105	2	142	10	833	140	105	2.0
Zircon_10_018	123	62	0.49	0.05403	0.00335	0.12044	0.00771	0.0164	0.00026	0.25	105	2	115	7	372	131	105	2.0
Zircon_24_035	237	70	0.29	0.05201	0.00244	0.13351	0.00648	0.01867	0.00022	0.26	119	1	127	6	286	105	119	1.0
Zircon_16_026	170	91	0.52	0.0549	0.00313	0.1552	0.00901	0.02044	0.00022	0.19	130	1	146	8	408	120	130.0	1.00

				CORRECTED RATIOS							CORRECTED AGES (Ma)						Best age (Ma)	±1s
Spot Name	**U (ppm)**	**Th (ppm)**	**Th/U**	**207Pb/206Pb**	**±1s**	**207Pb/235U**	**±1s**	**206Pb/238U**	**±1s**	**Rho**	**206Pb/238U**	**±1s**	**207Pb/235U**	**±1s**	**207Pb/206Pb**	**±1s**		
Sample: DANA 47a																		
Zircon_35_048	1369	614	0.41	0.04817	0.00101	0.08989	0.00203	0.01354	0.00011	0.37	86.7	0.7	87	2	108	43	87	0.70
Zircon_32_045	795	357	0.41	0.05065	0.00106	0.09671	0.00218	0.01382	0.00011	0.37	88.5	0.7	94	2	225	42	89	0.70
Zircon_38_052	843	421	0.46	0.04861	0.00126	0.09306	0.00254	0.01393	0.00012	0.31	89.2	0.8	90	2	129	53	89	0.80
Zircon_04_011	671	220	0.30	0.04819	0.00125	0.09374	0.00258	0.01411	0.00013	0.33	90.3	0.8	91	2	109	58	90	0.80
Zircon_13_022	499	193	0.36	0.04806	0.00173	0.09344	0.00347	0.01411	0.00013	0.25	90.3	0.8	91	3	102	80	90	0.80
Zircon_06_014	839	388	0.43	0.05048	0.00116	0.09895	0.0024	0.01421	0.00011	0.32	91	0.7	96	2	217	51	91	0.70
Zircon_28_040	928	520	0.52	0.04812	0.00125	0.09437	0.00256	0.01422	0.00011	0.29	91	0.7	92	2	105	53	91	0.70
Zircon_07_015	499	229	0.42	0.05118	0.00159	0.10035	0.00322	0.01427	0.00012	0.25	91.3	0.8	97	3	249	68	91	0.80
Zircon_22_033	659	251	0.35	0.05062	0.00142	0.09949	0.00291	0.01426	0.00012	0.28	91.3	0.8	96	3	224	64	91	0.80
Zircon_20_030	543	440	0.75	0.05231	0.00157	0.10304	0.00321	0.01433	0.00012	0.27	91.7	0.8	100	3	299	68	92	0.80
Zircon_21_032	525	158	0.28	0.04915	0.00167	0.09804	0.0035	0.01444	0.00016	0.31	92	1	95	3	155	78	92	1.00
Zircon_27_039	475	452	0.88	0.05351	0.00182	0.10635	0.004	0.01442	0.00023	0.43	92	1	103	4	350	66	92	1.00
Zircon_03_010	487	149	0.28	0.05098	0.00179	0.10144	0.00402	0.01443	0.00016	0.3	92.4	1	98	4	240	77	92	1.00
Zircon_31_044	748	387	0.48	0.05278	0.00116	0.10572	0.00245	0.01452	0.00011	0.32	92.9	0.7	102	2	319	43	93	0.70
Zircon_17_027	342	121	0.33	0.04965	0.00154	0.09973	0.00328	0.01459	0.00016	0.33	93	1	97	3	179	71	93	1.00
Zircon_18_028	321	86	0.25	0.05539	0.00285	0.11142	0.0062	0.01459	0.00018	0.25	93	1	107	6	428	99	93	1.00
Zircon_37_051	652	309	0.44	0.05032	0.00106	0.10144	0.00228	0.01463	0.00012	0.35	93.6	0.8	98	2	210	42	94	0.80
Zircon_15_024	176	91	0.48	0.05956	0.00388	0.12053	0.00834	0.01468	0.00021	0.21	94	1	116	8	588	140	94	1.00
Zircon_23_034	221	216	0.90	0.066	0.00858	0.13256	0.01729	0.01474	0.00016	0.08	94	1	126	16	806	276	94	1.00
Zircon_29_041	94	43	0.42	0.05153	0.00349	0.10444	0.00783	0.0147	0.00024	0.27	94	2	101	7	264	133	94	2.00
Zircon_33_046	318	261	0.76	0.05508	0.00215	0.11079	0.00449	0.01466	0.00016	0.27	94	1	107	4	415	75	94	1.00
Zircon_11_020	500	178	0.33	0.05291	0.00148	0.10753	0.00317	0.01473	0.00014	0.32	94.3	0.9	104	3	325	63	94	0.90
Zircon_01_Dana47a_008	340	101	0.27	0.05488	0.00192	0.11171	0.00404	0.01481	0.00014	0.25	94.8	0.9	108	4	407	75	95	0.90
Zircon_19_029	347	100	0.27	0.0492	0.00172	0.10005	0.00361	0.01482	0.00013	0.25	94.8	0.8	97	3	157	80	95	0.80
Zircon_36_050	489	152	0.29	0.05009	0.0014	0.10194	0.00297	0.01482	0.00012	0.28	94.8	0.8	99	3	199	56	95	0.80
Zircon_08_016	144	71	0.45	0.04796	0.00269	0.09708	0.00558	0.0149	0.00019	0.22	95	1	94	5	97	116	95	1.00

Zircon_25_036	110	83	0.69	0.06322	0.00354	0.13037	0.00753	0.01507	0.00021	0.25	96	1	124	7	716	118	96	1.00
Zircon_09_017	483	189	0.36	0.05314	0.00284	0.11032	0.00638	0.01506	0.00015	0.26	96.3	1	106	6	335	116	96	1.00
Zircon_05_012	266	261	0.91	0.05801	0.00296	0.12028	0.00628	0.01513	0.00017	0.21	97	1	115	6	530	107	97	1.00
Zircon_02_009	126	65	0.48	0.04955	0.00327	0.10326	0.00697	0.01538	0.00022	0.21	98	1	100	6	174	140	98	1.00
Zircon_24_035	119	80	0.62	0.05559	0.00439	0.11699	0.00945	0.01526	0.00026	0.21	98	2	112	9	436	175	98	2.00
Zircon_30_042	299	115	0.36	0.05214	0.00188	0.1108	0.00432	0.0153	0.00023	0.38	98	1	107	4	292	71	98	1.00
Zircon_26_038	480	170	0.33	0.05029	0.00151	0.10845	0.0034	0.01556	0.00014	0.29	99.5	0.9	105	3	208	60	100	0.90
Zircon_16_026	270	84	0.29	0.05625	0.00253	0.12491	0.00582	0.0161	0.00019	0.26	103	1	120	5	462	99	103	1.00
Zircon_12_021	392	302	0.71	0.04717	0.00132	0.13331	0.00388	0.02042	0.00016	0.27	130	1	127	3	58	60	130	1.00
Zircon_14_023	1069	223	0.19	0.04785	0.001	0.13534	0.003	0.02045	0.00014	0.33	130.5	0.9	129	3	92	49	131	0.90
Zircon_10_018	1023	154	0.14	0.05074	0.00101	0.16575	0.00356	0.02372	0.00019	0.38	151	1	156	3	229	45	151	1.00
Zircon_34_047	466	163	0.32	0.05102	0.00143	0.18583	0.00542	0.02647	0.00021	0.28	168	1	173	5	242	56	168	1.00

				CORRECTED RATIOS							CORRECTED AGES (Ma)						Best age (Ma)	±1s
Spot Name	**U (ppm)**	**Th (ppm)**	**Th/U**	**207Pb/206Pb**	**±1s**	**207Pb/235U**	**±1s**	**206Pb/238U**	**±1s**	**Rho**	**206Pb/238U**	**±1s**	**207Pb/235U**	**±1s**	**207Pb/206Pb**	**±1s**		
Sample: BEKL 4D-1																		
Zircon_15_024	6597	672	0.09	0.05118	0.00165	0.0751	0.00253	0.01064	0.00009	0.31	68.2	0.6	74	2	249	81	68	0.60
Zircon_12_021	4984	848	0.16	0.04911	0.00079	0.0814	0.00141	0.01202	0.00008	0.37	77	0.5	79	1	153	41	77	0.50
Zircon_08_016	3025	724	0.22	0.04839	0.00082	0.08116	0.00147	0.01218	0.00008	0.35	78	0.5	79	1	118	43	78	0.50
Zircon_36_049	818	300	0.34	0.05698	0.00302	0.09608	0.00515	0.01225	0.0001	0.15	78.5	0.6	93	5	491	116	79	0.60
Zircon_13_022	3946	788	0.19	0.04933	0.00074	0.08359	0.00138	0.01229	0.00008	0.42	78.7	0.5	82	1	164	38	79	0.50
Zircon_16_026	1321	613	0.43	0.04723	0.00118	0.08009	0.00207	0.01236	0.00008	0.26	79.2	0.5	78	2	61	60	79	0.50
Zircon_03_010	4721	2272	0.45	0.04742	0.00071	0.08097	0.00133	0.01238	0.00008	0.41	79.3	0.5	79	1	70	34	79	0.50
Zircon_17_027	3741	862	0.21	0.04989	0.00075	0.0861	0.00141	0.01252	0.00008	0.4	80.2	0.5	84	1	190	38	80	0.50
Zircon_20_030	1610	592	0.34	0.04756	0.0009	0.08188	0.00172	0.01252	0.00011	0.43	80.2	0.7	80	2	77	43	80	0.70
Zircon_11_020	841	257	0.28	0.05156	0.00134	0.08911	0.00243	0.01256	0.00011	0.3	80.5	0.7	87	2	266	65	81	0.70
Zircon_27_039	618	225	0.34	0.05156	0.00201	0.08926	0.00357	0.01256	0.00011	0.22	80.5	0.7	87	3	266	85	81	0.70
Zircon_06_014	593	169	0.26	0.05197	0.00135	0.08996	0.00249	0.01259	0.00012	0.35	80.7	0.8	87	2	284	65	81	0.80
Zircon_02_009	566	120	0.20	0.05081	0.00168	0.08853	0.003	0.01264	0.0001	0.22	81	0.6	86	3	232	73	81	0.60
Zircon_25_036	1529	510	0.31	0.048	0.00106	0.08441	0.00197	0.01276	0.0001	0.32	81.7	0.6	82	2	99	50	82	0.60
Zircon_26_038	1478	592	0.37	0.04756	0.00109	0.08376	0.00204	0.01279	0.0001	0.34	81.9	0.6	82	2	77	50	82	0.60
Zircon_22_033	249	88	0.33	0.05484	0.00367	0.09625	0.00689	0.01273	0.00018	0.27	82	1	93	6	406	145	82	1.00
Zircon_28_040	1163	200	0.16	0.04841	0.00116	0.08553	0.00215	0.01285	0.0001	0.3	82.3	0.6	83	2	119	54	82	0.60
Zircon_29_041	618	301	0.45	0.0481	0.00203	0.08524	0.00383	0.01285	0.00012	0.22	82.3	0.7	83	4	104	89	82	0.70
Zircon_34_047	761	241	0.29	0.04825	0.00145	0.08576	0.00264	0.01288	0.00009	0.22	82.5	0.6	84	2	112	68	83	0.60
Zircon_09_017	807	518	0.59	0.05463	0.00318	0.09732	0.00603	0.01292	0.00012	0.22	82.7	0.8	94	6	397	143	83	0.80
Zircon_32_045	999	316	0.29	0.0498	0.00124	0.08829	0.0023	0.01291	0.0001	0.29	82.7	0.6	86	2	186	55	83	0.60
Zircon_30_042	574	224	0.36	0.05439	0.00179	0.09649	0.00329	0.01292	0.00011	0.26	82.8	0.7	94	3	387	71	83	0.70
Zircon_21_032	958	349	0.34	0.0503	0.00116	0.08979	0.00218	0.01296	0.0001	0.31	83	0.6	87	2	209	51	83	0.60

Zircon_31_044	3423	363	0.10	0.05052	0.00111	0.09079	0.00207	0.01297	0.00008	0.27	83.1	0.5	88	2	219	49	83	0.50
Zircon_19_029	989	220	0.21	0.05065	0.00127	0.09129	0.00237	0.01307	0.00009	0.26	83.7	0.6	89	2	225	55	84	0.60
Zircon_04_011	63	16	0.24	0.08123	0.00699	0.14322	0.01309	0.01316	0.00041	0.34	84	3	136	12	1227	165	84	3.00
Zircon_05_012	710	326	0.43	0.04977	0.00229	0.09016	0.00447	0.01314	0.00012	0.24	84.1	0.8	88	4	184	114	84	0.80
Zircon_07_015	393	117	0.28	0.05437	0.00207	0.09845	0.00386	0.01315	0.00013	0.24	84.2	0.8	95	4	386	94	84	0.80
Zircon_35_048	316	163	0.48	0.05589	0.00263	0.10078	0.00484	0.01317	0.00013	0.2	84.3	0.8	97	4	448	103	84	0.80
Zircon_18_028	902	273	0.28	0.04658	0.0014	0.08474	0.00274	0.01322	0.00016	0.37	85	1	83	3	28	68	85	1.00
Zircon_23_034	283	59	0.19	0.05307	0.00214	0.09668	0.00437	0.01321	0.00021	0.36	85	1	94	4	332	88	85	1.00
Zircon_37_050	294	106	0.33	0.05842	0.00336	0.10785	0.00675	0.01339	0.00016	0.3	86	1	104	6	546	124	86	1.00
Zircon_24_035	392	79	0.19	0.052	0.00312	0.10737	0.00655	0.01486	0.00016	0.18	95	1	104	6	285	131	95	1.00
Zircon_33_046	200	36	0.17	0.05109	0.0033	0.11422	0.00792	0.01621	0.00023	0.27	104	1	110	7	245	143	104	1.00

				CORRECTED RATIOS							CORRECTED AGES (Ma)						Best age (Ma)	±1s
Spot Name	**U (ppm)**	**Th (ppm)**	**Th/U**	**207Pb/206Pb**	**±1s**	**207Pb/235U**	**±1s**	**206Pb/238U**	**±1s**	**Rho**	**206Pb/238U**	**±1s**	**207Pb/235U**	**±1s**	**207Pb/206Pb**	**±1s**		
Sample: LCB 7																		
Zircon_31_044	571	268	0.42	0.05076	0.00188	0.08343	0.00325	0.01193	0.00014	0.31	76.5	0.9	81	3	230	82	77	0.9
Zircon_01_Jose7_008	328	172	0.47	0.05364	0.00349	0.08872	0.0059	0.01204	0.00017	0.21	77	1	86	6	356	150	77	1.0
Zircon_24_035	168	80	0.43	0.05051	0.00399	0.08322	0.00674	0.01205	0.00022	0.22	77	1	81	6	219	158	77	1.0
Zircon_28_040	703	464	0.60	0.05175	0.00191	0.08609	0.00328	0.01205	0.00011	0.25	77.2	0.7	84	3	274	76	77	0.7
Zircon_11_020	428	255	0.54	0.05652	0.00565	0.0948	0.00954	0.01213	0.00013	0.12	77.7	0.8	92	9	473	219	78	0.8
Zircon_07_015	358	202	0.51	0.05014	0.00326	0.08399	0.00581	0.01215	0.00015	0.2	77.8	1	82	5	202	148	78	1.0
Zircon_08_016	200	75	0.34	0.05578	0.00368	0.09317	0.00654	0.01211	0.00017	0.26	78	1	90	6	444	151	78	1.0
Zircon_12_021	234	111	0.43	0.05522	0.00449	0.09264	0.00778	0.01217	0.00015	0.19	78	0.9	90	7	421	162	78	0.9
Zircon_30_042	692	430	0.56	0.0505	0.00329	0.08506	0.00602	0.01222	0.00016	0.22	78	1	83	6	218	141	78	1.0
Zircon_35_048	460	253	0.50	0.05162	0.00217	0.08725	0.00379	0.01228	0.00014	0.25	78.7	0.9	85	4	269	93	79	0.9
Zircon_19_029	564	204	0.33	0.05283	0.00283	0.08953	0.00503	0.01229	0.00011	0.25	78.8	0.7	87	5	321	109	79	0.7
Zircon_37_051	246	119	0.43	0.04661	0.00317	0.07874	0.00542	0.0123	0.00014	0.15	78.8	0.9	77	5	29	140	79	0.9
Zircon_23_034	356	223	0.56	0.05286	0.00331	0.08973	0.00602	0.01231	0.00014	0.29	78.9	0.9	87	6	323	127	79	0.9
Zircon_16_026	435	256	0.53	0.05065	0.00263	0.08554	0.00459	0.01237	0.00016	0.25	79	1	83	4	225	106	79	1.0
Zircon_20_030	203	103	0.46	0.05467	0.00414	0.09287	0.00744	0.01232	0.00017	0.25	79	1	90	7	399	151	79	1.0
Zircon_33_046	221	144	0.59	0.04838	0.00348	0.08254	0.00607	0.01237	0.00019	0.21	79	1	81	6	118	152	79	1.0
Zircon_36_050	267	125	0.42	0.05532	0.00293	0.09213	0.00505	0.01229	0.00017	0.26	79	1	89	5	425	114	79	1.0
Zircon_05_012	398	145	0.33	0.04839	0.00231	0.08289	0.00414	0.01242	0.00011	0.19	79.6	0.7	81	4	119	107	80	0.7
Zircon_15_024	474	287	0.55	0.04832	0.00188	0.08335	0.00338	0.01244	0.00014	0.28	79.7	0.9	81	3	115	79	80	0.9
Zircon_14_023	328	195	0.54	0.05107	0.00351	0.08767	0.00632	0.01245	0.00013	0.21	79.8	0.8	85	6	244	138	80	0.8
Zircon_27_039	236	110	0.42	0.05261	0.0037	0.09089	0.00676	0.01253	0.00016	0.25	80	1	88	6	312	142	80	1.0

Zircon_34_047	361	139	0.35	0.05124	0.00379	0.08775	0.00695	0.01242	0.00016	0.24	80	1	85	6	252	160	80	1.0
Zircon_40_LCB7_054	235	106	0.41	0.04085	0.00376	0.07065	0.00655	0.01248	0.00015	0.12	80	1	69	6	-241	163	80	1.0
Zircon_03_010	333	131	0.35	0.04615	0.00282	0.07922	0.00493	0.01251	0.00015	0.19	80.1	1	77	5	5	132	80	1.0
Zircon_06_014	622	279	0.40	0.05287	0.00293	0.09117	0.0054	0.0125	0.00014	0.24	80.1	0.9	89	5	323	128	80	0.9
Zircon_10_018	247	120	0.44	0.05293	0.00496	0.09176	0.00938	0.01257	0.00021	0.3	81	1	89	9	326	206	81	1.0
Zircon_18_028	322	169	0.47	0.04977	0.00329	0.08551	0.00575	0.01258	0.00016	0.18	81	1	83	5	184	132	81	1.0
Zircon_32_045	254	119	0.42	0.05043	0.00277	0.087	0.00494	0.01259	0.00018	0.25	81	1	85	5	215	120	81	1.0
Zircon_26_038	593	258	0.39	0.05052	0.00227	0.08834	0.00409	0.0127	0.00014	0.24	81.4	0.9	86	4	219	92	81	0.9
Zircon_02_009	257	113	0.39	0.06028	0.00437	0.10604	0.00808	0.01276	0.00016	0.22	82	1	102	7	614	162	82	1.0
Zircon_09_017	185	92	0.45	0.06201	0.00384	0.10784	0.00693	0.01282	0.00022	0.27	82	1	104	6	674	136	82	1.0
Zircon_29_041	250	117	0.42	0.051	0.00275	0.08948	0.00497	0.01288	0.00017	0.24	82	1	87	5	241	118	82	1.0
Zircon_21_032	380	179	0.42	0.0566	0.00343	0.10088	0.0065	0.01293	0.00016	0.26	83	1	98	6	476	120	83	1.0
Zircon_39_053	223	52	0.21	0.05369	0.00349	0.0946	0.00629	0.01291	0.00018	0.21	83	1	92	6	358	141	83	1.0
Zircon_25_036	818	500	0.55	0.04815	0.00135	0.08659	0.00257	0.01308	0.00013	0.33	83.8	0.8	84	2	107	58	84	0.8
Zircon_38_052	255	128	0.45	0.04961	0.00288	0.08838	0.00527	0.01309	0.00018	0.23	84	1	86	5	177	126	84	1.0
Zircon_13_022	579	274	0.43	0.05093	0.00351	0.09414	0.00695	0.01341	0.00019	0.31	86	1	91	6	238	139	86	1.0
Zircon_17_027	255	141	0.50	0.0538	0.00317	0.09944	0.00603	0.01347	0.00019	0.24	86	1	96	6	363	119	86	1.0
Zircon_04_011	363	153	0.38	0.05391	0.00183	0.18648	0.00661	0.02507	0.00025	0.29	160	2	174	6	367	78	160	2

				CORRECTED RATIOS							CORRECTED AGES (Ma)						Best age (Ma)	±1s
Spot Name	**U (ppm)**	**Th (ppm)**	**Th/U**	**207Pb/206Pb**	**±1s**	**207Pb/235U**	**±1s**	**206Pb/238U**	**±1s**	**Rho**	**206Pb/238U**	**±1s**	**207Pb/235U**	**±1s**	**207Pb/206Pb**	**±1s**		
Sample: Sayu 1																		
Zircon_02_009	461	154	0.31	0.05394	0.00194	0.08668	0.0032	0.01171	0.0001	0.23	75	0.6	84	3	369	79	75.0	0.60
Zircon_08_016	1016	600	0.54	0.04683	0.00112	0.07526	0.00187	0.01171	0.00008	0.27	75	0.5	74	2	41	50	75.0	0.50
Zircon_18_028	406	154	0.35	0.05306	0.00207	0.08555	0.00343	0.01176	0.00011	0.23	75.4	0.7	83	3	331	84	75.4	0.70
Zircon_30_042	495	161	0.30	0.04768	0.00176	0.07729	0.00294	0.01187	0.0001	0.24	76.1	0.6	76	3	83	76	76.1	0.60
Zircon_06_014	411	147	0.33	0.05268	0.00218	0.08657	0.00382	0.01192	0.0001	0.25	76.4	0.6	84	4	315	91	76.4	0.60
Zircon_04_011	763	373	0.45	0.05089	0.00163	0.08397	0.00276	0.01196	0.00009	0.22	76.6	0.6	82	3	236	72	76.6	0.60
Zircon_07_015	600	338	0.52	0.04591	0.00138	0.07586	0.00238	0.012	0.00011	0.29	76.9	0.7	74	2	-7	56	76.9	0.70
Zircon_01_Sayu01_008	393	117	0.27	0.05146	0.00196	0.08556	0.00333	0.01202	0.0001	0.21	77	0.6	83	3	261	85	77.0	0.60
Zircon_32_045	477	208	0.40	0.04921	0.00202	0.08169	0.00369	0.01204	0.00011	0.28	77.2	0.7	80	3	158	84	77.2	0.70
Zircon_16_026	504	210	0.38	0.05037	0.00171	0.08356	0.00292	0.01206	0.0001	0.24	77.3	0.6	81	3	212	74	77.3	0.60
Zircon_10_018	1014	420	0.38	0.05027	0.00131	0.08338	0.00224	0.01209	0.00008	0.24	77.5	0.5	81	2	207	58	77.5	0.50
Zircon_33_046	447	217	0.45	0.04685	0.00183	0.07794	0.00313	0.01209	0.00011	0.23	77.5	0.7	76	3	42	76	77.5	0.70
Zircon_19_029	667	346	0.48	0.05059	0.00132	0.08432	0.00227	0.01211	0.00009	0.25	77.6	0.6	82	2	222	57	77.6	0.60
Zircon_22_033	831	368	0.41	0.05028	0.00156	0.08356	0.00266	0.01211	0.00008	0.22	77.6	0.5	81	2	208	68	77.6	0.50

Zircon_35_048	540	207	0.35	0.05103	0.00175	0.08516	0.00318	0.0121	0.0001	0.26	77.6	0.6	83	3	242	70	77.6	0.60
Zircon_03_010	352	131	0.34	0.05657	0.00243	0.09474	0.00416	0.01216	0.00011	0.21	77.9	0.7	92	4	475	93	77.9	0.70
Zircon_14_023	700	280	0.37	0.0517	0.0016	0.08664	0.00275	0.01215	0.00008	0.22	77.9	0.5	84	3	272	68	77.9	0.50
Zircon_23_034	431	154	0.33	0.05219	0.002	0.08761	0.00356	0.01217	0.00011	0.23	78	0.7	85	3	294	81	78.0	0.70
Zircon_24_035	386	109	0.26	0.05125	0.00225	0.08612	0.00392	0.01219	0.00011	0.2	78.1	0.7	84	4	252	94	78.1	0.70
Zircon_13_022	304	90	0.27	0.04785	0.00201	0.08017	0.00344	0.01224	0.00011	0.2	78.4	0.7	78	3	92	90	78.4	0.70
Zircon_27_039	606	206	0.31	0.05035	0.00136	0.08484	0.00241	0.01224	0.00011	0.31	78.4	0.7	83	2	211	58	78.4	0.70
Zircon_25_036	375	139	0.34	0.04908	0.00211	0.08276	0.00365	0.01225	0.00012	0.22	78.5	0.8	81	3	152	92	78.5	0.80
Zircon_20_030	301	60	0.18	0.04253	0.00213	0.07199	0.00367	0.01235	0.00012	0.19	79.1	0.8	71	3	-148	104	79.1	0.80
Zircon_29_041	411	117	0.26	0.04927	0.00207	0.08363	0.00359	0.01235	0.00011	0.21	79.1	0.7	82	3	161	90	79.1	0.70
Zircon_34_047	535	227	0.39	0.04983	0.00154	0.0848	0.00274	0.01238	0.00011	0.29	79.3	0.7	83	3	187	64	79.3	0.70
Zircon_26_038	546	232	0.39	0.05021	0.00176	0.08531	0.00307	0.01239	0.00011	0.23	79.4	0.7	83	3	205	76	79.4	0.70
Zircon_21_032	901	371	0.38	0.055	0.00223	0.09407	0.00409	0.01241	0.00009	0.27	79.5	0.6	91	4	412	86	79.5	0.60
Zircon_36_049	439	137	0.29	0.05081	0.00199	0.08739	0.00371	0.01247	0.00012	0.29	79.9	0.7	85	3	232	80	79.9	0.70
Zircon_05_012	336	107	0.29	0.05608	0.00252	0.0967	0.00445	0.01252	0.00012	0.22	80.2	0.8	94	4	456	97	80.2	0.80
Zircon_09_017	208	51	0.22	0.05506	0.00377	0.09539	0.00678	0.01256	0.00014	0.21	80.5	0.9	93	6	415	148	80.5	0.90
Zircon_15_024	611	264	0.40	0.05047	0.00146	0.08897	0.00269	0.01284	0.00011	0.29	82.2	0.7	87	3	217	63	82.2	0.70
Zircon_28_040	370	78	0.19	0.05293	0.00191	0.09452	0.00359	0.01302	0.00016	0.31	83	1	92	3	326	76	83.0	1.00

				CORRECTED RATIOS							CORRECTED AGES (Ma)						Best age (Ma)	±1s
Spot Name	**U (ppm)**	**Th (ppm)**	**Th/U**	**207Pb/206Pb**	**±1s**	**207Pb/235U**	**±1s**	**206Pb/238U**	**±1s**	**Rho**	**206Pb/238U**	**±1s**	**207Pb/235U**	**±1s**	**207Pb/206Pb**	**±1s**		
Sample: Sayu 2																		
Zircon_02_009	691	902	1.20	0.05351	0.00139	0.08319	0.00224	0.01128	0.00008	0.26	72.3	0.5	81	2	350	58	72	0.50
Zircon_27_039	4502	311	0.06	0.04816	0.00067	0.07663	0.00114	0.01154	0.00006	0.35	74	0.4	75	1	107	32	74	0.40
Zircon_31_044	852	490	0.53	0.046	0.00244	0.07173	0.00402	0.01151	0.00021	0.32	74	1	70	4	-2	109	74	1.00
Zircon_13_022	901	507	0.52	0.04607	0.00216	0.0735	0.00364	0.01157	0.00009	0.18	74.2	0.6	72	3	1	95	74	0.60
Zircon_21_032	1258	479	0.35	0.04877	0.00107	0.07812	0.00178	0.01163	0.00007	0.27	74.5	0.4	76	2	137	51	75	0.40
Zircon_10_018	535	366	0.63	0.04659	0.00172	0.07528	0.00283	0.01175	0.00008	0.19	75.3	0.5	74	3	28	75	75	0.50
Zircon_14_023	510	202	0.36	0.05097	0.00214	0.08323	0.00375	0.01184	0.00011	0.22	75.9	0.7	81	4	239	95	76	0.70
Zircon_16_026	590	136	0.21	0.04895	0.00197	0.08108	0.00339	0.01201	0.00008	0.19	77	0.5	79	3	146	91	77	0.50
Zircon_25_036	858	317	0.34	0.04648	0.00143	0.07727	0.00259	0.01206	0.0001	0.31	77.3	0.6	76	2	23	61	77	0.60
Zircon_23_034	586	167	0.26	0.05194	0.00178	0.08805	0.00325	0.01229	0.00011	0.27	78.8	0.7	86	3	283	78	79	0.70
Zircon_26_038	1411	264	0.17	0.04795	0.00101	0.08175	0.00179	0.01235	0.00008	0.27	79.1	0.5	80	2	97	49	79	0.50
Zircon_15_024	450	212	0.43	0.04718	0.00208	0.0799	0.00359	0.01239	0.00011	0.19	79.4	0.7	78	3	58	93	79	0.70
Zircon_20_030	1186	272	0.21	0.04914	0.00143	0.08542	0.00254	0.01261	0.00008	0.21	80.8	0.5	83	2	155	67	81	0.50
Zircon_01_Sayu02_008	103	46	0.42	0.06013	0.00542	0.10516	0.00997	0.01268	0.00018	0.21	81	1	102	9	608	194	81	1.00
Zircon_29_041	177	64	0.33	0.05316	0.00287	0.09283	0.0052	0.01269	0.00019	0.27	81	1	90	5	336	122	81	1.00
Zircon_19_029	9779	2969	0.28	0.04776	0.00057	0.08447	0.00113	0.01281	0.00008	0.45	82.1	0.5	82	1	87	28	82	0.50
Zircon_12_021	484	136	0.26	0.04895	0.00191	0.08738	0.00346	0.01301	0.00009	0.17	83.3	0.6	85	3	145	88	83	0.60

Zircon_24_035	550	218	0.36	0.05118	0.00158	0.09201	0.00306	0.01304	0.00009	0.26	83.5	0.6	89	3	249	70	84	0.60
Zircon_11_020	782	306	0.36	0.05049	0.00106	0.09235	0.00204	0.0133	0.00009	0.31	85.2	0.6	90	2	218	48	85	0.60
Zircon_32_045	925	117	0.12	0.04479	0.00139	0.08087	0.00266	0.01331	0.00015	0.33	85.2	1	79	2	-30	63	85	1.00
Zircon_30_042	1322	301	0.21	0.0476	0.00105	0.08841	0.00214	0.01347	0.00013	0.41	86.3	0.8	86	2	79	49	86	0.80
Zircon_04_011	1098	289	0.24	0.0502	0.00131	0.09557	0.0026	0.0138	0.00011	0.28	88.4	0.7	93	2	204	59	88	0.70
Zircon_33_046	1346	661	0.45	0.05117	0.00184	0.10128	0.00378	0.01425	0.00014	0.27	91.2	0.9	98	3	248	82	91	0.90
Zircon_18_028	1809	198	0.10	0.04734	0.00095	0.09299	0.00238	0.01438	0.00023	0.62	92	1	90	2	66	44	92	1.00
Zircon_03_010	441	58	0.12	0.0455	0.00177	0.09429	0.00377	0.01494	0.00013	0.23	95.6	0.8	91	3	-28	77	96	0.80
Zircon_17_027	576	84	0.13	0.05035	0.00176	0.13405	0.00492	0.01923	0.00021	0.3	123	1	128	4	211	80	123	1.00
Zircon_28_040	362	77	0.20	0.05544	0.00172	0.14914	0.00496	0.01986	0.00024	0.36	127	2	141	4	430	69	127	2.00
Zircon_09_017	357	127	0.33	0.04934	0.00168	0.14764	0.00523	0.02204	0.00022	0.28	141	1	140	5	164	78	141	1.00
Zircon_07_015	958	320	0.31	0.049	0.00118	0.15184	0.00401	0.02247	0.00014	0.27	143.3	0.9	144	4	148	55	143	0.90
Zircon_08_016	237	98	0.38	0.05004	0.0015	0.16993	0.00532	0.02468	0.00022	0.29	157	1	159	5	197	68	157	1.00
Zircon_06_014	264	159	0.55	0.05313	0.00175	0.18334	0.00628	0.02494	0.00023	0.27	159	1	171	5	334	73	159	1.00
Zircon_05_012	589	306	0.48	0.05046	0.00116	0.17425	0.00416	0.02506	0.00016	0.27	160	1	163	4	216	52	160	1.00
Zircon_22_033	204	113	0.51	0.05648	0.00198	0.19634	0.00714	0.02517	0.00025	0.27	160	2	182	6	471	77	160	2.00

				CORRECTED RATIOS							CORRECTED AGES (Ma)						Best age (Ma)	±1s
Spot Name	**U (ppm)**	**Th (ppm)**	**Th/U**	**207Pb/206Pb**	**±1s**	**207Pb/235U**	**±1s**	**206Pb/238U**	**±1s**	**Rho**	**206Pb/238U**	**±1s**	**207Pb/235U**	**±1s**	**207Pb/206Pb**	**±1s**		
Sample: Tepi 1																		
Zircon_42_057	1421	1493	1.18	0.05757	0.00155	0.07193	0.00202	0.00905	0.00007	0.28	58.1	0.4	71	2	513	58	58.1	0.4
Zircon_44_063	718	418	0.65	0.06448	0.00219	0.08384	0.003	0.00942	0.0001	0.32	60.4	0.6	82	3	757	70	60.4	0.6
Zircon_40_062	446	242	0.61	0.06384	0.00294	0.08473	0.00399	0.00968	0.0001	0.21	62.1	0.6	83	4	736	96	62.1	0.6
Zircon_04_011	949	816	0.78	0.05139	0.00144	0.06977	0.00202	0.00988	0.00008	0.25	63.4	0.5	68	2	258	60	63.4	0.5
Zircon_09_017	663	339	0.46	0.03654	0.00186	0.05003	0.00259	0.00989	0.00008	0.18	63.4	0.5	50	3	-12	261	63.4	0.5
Zircon_34_055	517	195	0.42	0.06146	0.0024	0.08387	0.00337	0.00988	0.00009	0.24	63.4	0.6	82	3	655	82	63.4	0.6
Zircon_32_053	341	198	0.65	0.06559	0.00295	0.08893	0.00422	0.00994	0.00015	0.32	63.8	1	87	4	793	95	63.8	1.0
Zircon_17_035	357	119	0.37	0.05137	0.003	0.07066	0.00435	0.00998	0.00009	0.22	64	0.6	69	4	257	134	64.0	0.6
Zircon_27_047	260	183	0.79	0.05378	0.00366	0.07344	0.00506	0.00998	0.00011	0.16	64	0.7	72	5	362	155	64.0	0.7
Zircon_30_050	412	171	0.47	0.05879	0.00298	0.08107	0.00448	0.01	0.00013	0.27	64.1	0.8	79	4	560	111	64.1	0.8
Zircon_37_059	772	334	0.49	0.06048	0.00181	0.08381	0.00262	0.01002	0.00009	0.29	64.3	0.6	82	2	621	63	64.3	0.6
Zircon_15_024	417	135	0.29	0.05149	0.00201	0.0705	0.00284	0.01008	0.0001	0.25	64.7	0.6	69	3	263	86	64.7	0.6
Zircon_20_038	432	164	0.43	0.06072	0.00249	0.08406	0.00359	0.01014	0.00012	0.28	65	0.8	82	3	629	89	65.0	0.8
Zircon_22_041	417	237	0.64	0.05718	0.00269	0.08029	0.00385	0.01015	0.00009	0.19	65.1	0.6	78	4	499	104	65.1	0.6
Zircon_10_018	207	107	0.47	0.07113	0.00597	0.09819	0.00836	0.01015	0.00014	0.17	65.1	0.9	95	8	961	167	65.1	0.9
Zircon_07_015	374	150	0.36	0.05129	0.00231	0.0712	0.00328	0.01024	0.0001	0.21	65.7	0.6	70	3	254	97	65.7	0.6
Zircon_24_043	835	411	0.55	0.05075	0.00142	0.07165	0.00207	0.01028	0.00008	0.25	65.9	0.5	70	2	229	65	65.9	0.5
Zircon_01_Tepi01_008	439	175	0.36	0.05713	0.00251	0.0809	0.00369	0.01027	0.00012	0.27	65.9	0.8	79	3	497	91	65.9	0.8
Zircon_29_049	295	122	0.46	0.06456	0.0031	0.09112	0.00449	0.01029	0.00011	0.22	66	0.7	89	4	760	102	66.0	0.7

Zircon_25_044	537	227	0.47	0.04607	0.0087	0.06491	0.0133	0.01022	0.00017	0.34	66	1	64	13	1	307	66.0	1.0
Zircon_08_016	271	132	0.44	0.05741	0.00295	0.08218	0.00454	0.01038	0.00013	0.27	66.6	0.8	80	4	507	106	66.6	0.8
Zircon_35_056	141	66	0.52	0.08488	0.00552	0.1222	0.00818	0.01043	0.00017	0.24	67	1	117	7	1313	125	67.0	1.0
Zircon_06_014	295	119	0.37	0.05392	0.00264	0.0775	0.00393	0.01047	0.00014	0.26	67.1	0.9	76	4	368	104	67.1	0.9
Zircon_38_060	327	162	0.55	0.06157	0.00296	0.08815	0.00438	0.01047	0.00014	0.25	67.1	0.9	86	4	659	102	67.1	0.9
Zircon_23_042	539	393	0.82	0.04607	0.00119	0.06658	0.00202	0.01048	0.00011	0.34	67.2	0.7	65	2	1	50	67.2	0.7
Zircon_14_023	278	114	0.37	0.06336	0.00285	0.09044	0.00421	0.01048	0.00013	0.26	67.2	0.8	88	4	720	92	67.2	0.8
Zircon_33_054	275	110	0.45	0.07116	0.00399	0.10223	0.00588	0.01049	0.00014	0.22	67.3	0.9	99	5	962	113	67.3	0.9
Zircon_03_010	172	108	0.57	0.05622	0.00382	0.08028	0.00557	0.01053	0.00015	0.2	67.5	1	78	5	461	142	67.5	1.0
Zircon_12_021	394	189	0.44	0.04729	0.0017	0.06943	0.00259	0.01071	0.0001	0.27	68.7	0.6	68	2	64	74	68.7	0.6
Zircon_19_037	146	77	0.59	0.07792	0.00569	0.11522	0.00861	0.01072	0.00017	0.21	69	1	111	8	1145	147	69.0	1.0
Zircon_28_048	185	86	0.52	0.07436	0.00491	0.10855	0.00737	0.01072	0.00017	0.23	69	1	105	7	1051	134	69.0	1.0
Zircon_05_012	147	84	0.52	0.0504	0.00353	0.07402	0.00528	0.01079	0.00015	0.19	69.2	1	73	5	213	148	69.2	1.0
Zircon_11_020	375	138	0.33	0.05165	0.00267	0.07718	0.0043	0.01084	0.00014	0.27	69.5	0.9	75	4	270	113	69.5	0.9
Zircon_41_039	894	333	0.42	0.05401	0.00194	0.08125	0.00308	0.01091	0.00013	0.32	69.9	0.8	79	3	371	79	69.9	0.8
Zircon_02_009	490	171	0.32	0.05416	0.00254	0.0815	0.00408	0.01091	0.00012	0.32	70	0.7	80	4	378	99	70.0	0.7
Zircon_18_036	134	80	0.68	0.06599	0.00581	0.09779	0.00882	0.01085	0.00022	0.22	70	1	95	8	806	187	70.0	1.0
Zircon_13_022	202	100	0.45	0.06099	0.00525	0.09319	0.00821	0.01122	0.00021	0.21	72	1	90	8	639	180	72.0	1.0
Zircon_39_061	459	235	0.58	0.06659	0.00354	0.10423	0.00658	0.01135	0.00019	0.49	73	1	101	6	825	110	73	1.00

				CORRECTED RATIOS							CORRECTED AGES (Ma)							
Spot Name	**U (ppm)**	**Th (ppm)**	**Th/U**	**207Pb/206Pb**	**±1s**	**207Pb/235U**	**±1s**	**206Pb/238U**	**±1s**	**Rho**	**206Pb/238U**	**±1s**	**207Pb/235U**	**±1s**	**207Pb/206Pb**	**±1s**	**Best age (Ma)**	**±1s**
Sample: Conc 01																		
Zircon_10_018	367	295	0.73	0.05281	0.00217	0.06283	0.00265	0.00863	0.00009	0.23	55.4	0.6	62	3	321	92	55.4	0.6
Zircon_30_042	151	125	0.76	0.05738	0.00344	0.07071	0.00437	0.00896	0.00013	0.24	57.5	0.8	69	4	506	137	57.5	0.8
Zircon_20_030	137	92	0.61	0.05126	0.00401	0.06361	0.00533	0.009	0.00014	0.2	57.8	0.9	63	5	253	172	57.8	0.9
Zircon_02_009	134	92	0.63	0.0626	0.00444	0.07612	0.00558	0.00901	0.00016	0.25	58	1	74	5	695	150	58.0	1.0
Zircon_09_017	142	95	0.61	0.06003	0.0039	0.07279	0.00493	0.00905	0.00017	0.28	58	1	71	5	605	140	58.0	1.0
Zircon_17_027	108	82	0.70	0.06077	0.00444	0.07576	0.00566	0.00904	0.00014	0.21	58	0.9	74	5	631	155	58.0	0.9
Zircon_15_024	112	83	0.68	0.05873	0.00517	0.07265	0.00647	0.00911	0.00013	0.15	58.5	0.8	71	6	557	190	58.5	0.8
Zircon_32_045	264	214	0.74	0.05471	0.00354	0.06882	0.00499	0.00912	0.00014	0.29	58.5	0.9	68	5	400	150	58.5	0.9
Zircon_04_011	146	95	0.59	0.0655	0.00373	0.08164	0.00479	0.00914	0.00013	0.24	58.7	0.8	80	4	790	118	58.7	0.8
Zircon_22_033	180	122	0.62	0.05593	0.00506	0.07061	0.00681	0.00916	0.00015	0.2	58.8	1	69	6	450	198	58.8	1.0
Zircon_01_SC17_008	130	99	0.70	0.06218	0.00473	0.07694	0.00601	0.00913	0.00016	0.23	59	1	75	6	680	162	59.0	1.0
Zircon_05_012	89	36	0.37	0.06645	0.00538	0.08392	0.00696	0.00927	0.00017	0.22	59	1	82	7	821	169	59.0	1.0
Zircon_13_022	108	70	0.60	0.05031	0.00413	0.06333	0.0053	0.00921	0.00016	0.19	59	1	62	5	209	179	59.0	1.0
Zircon_16_026	101	54	0.49	0.05252	0.00383	0.06618	0.00498	0.00924	0.00017	0.25	59	1	65	5	308	161	59.0	1.0
Zircon_27_039	105	57	0.50	0.06191	0.00464	0.07819	0.00607	0.00924	0.00018	0.26	59	1	76	6	671	158	59.0	1.0
Zircon_33_046	116	61	0.48	0.06118	0.00516	0.07732	0.00702	0.00917	0.00018	0.22	59	1	76	7	646	190	59.0	1.0

Zircon_35_048	93	49	0.48	0.07945	0.00715	0.10027	0.00924	0.00922	0.00018	0.22	59	1	97	9	1183	186	59.0	1.0
Zircon_07_015	144	110	0.70	0.05969	0.00466	0.0756	0.00601	0.00923	0.00014	0.19	59.2	0.9	74	6	592	169	59.2	0.9
Zircon_08_016	290	134	0.42	0.05587	0.00246	0.0704	0.00321	0.00922	0.00011	0.26	59.2	0.7	69	3	447	97	59.2	0.7
Zircon_11_020	115	67	0.53	0.06142	0.00369	0.07784	0.00481	0.00924	0.00014	0.23	59.3	0.9	76	5	654	126	59.3	0.9
Zircon_19_029	143	72	0.46	0.06072	0.00594	0.0774	0.00784	0.00924	0.00011	0.17	59.3	0.7	76	7	629	209	59.3	0.7
Zircon_28_040	152	113	0.68	0.05487	0.00285	0.07061	0.00386	0.00932	0.00016	0.31	60	1	69	4	407	121	60.0	1.0
Zircon_25_036	125	89	0.65	0.05518	0.00552	0.07186	0.00728	0.00938	0.00015	0.16	60.2	1	70	7	420	219	60.2	1.0
Zircon_24_035	126	53	0.38	0.06334	0.00474	0.08286	0.00663	0.00949	0.00014	0.27	60.9	0.9	81	6	720	156	60.9	0.9
Zircon_06_014	131	105	0.73	0.06559	0.00518	0.08222	0.00664	0.00945	0.00016	0.21	61	1	80	6	793	165	61.0	1.0
Zircon_18_028	73	34	0.42	0.05613	0.00511	0.07195	0.00672	0.00945	0.0002	0.22	61	1	71	6	458	199	61.0	1.0
Zircon_23_034	113	66	0.54	0.0686	0.00638	0.08843	0.00839	0.0095	0.00018	0.2	61	1	86	8	887	190	61.0	1.0
Zircon_36_049	93	41	0.41	0.06973	0.00697	0.08853	0.00898	0.00954	0.00016	0.17	61	1	86	8	920	216	61.0	1.0
Zircon_03_010	87	48	0.50	0.07365	0.00442	0.09531	0.00592	0.00953	0.00015	0.26	61.1	1	92	5	1032	120	61.1	1.0
Zircon_12_021	230	147	0.59	0.06923	0.00395	0.09169	0.00548	0.00974	0.00018	0.3	62	1	89	5	906	115	62.0	1.0
Zircon_34_047	97	54	0.51	0.06622	0.00795	0.08443	0.01027	0.00967	0.00019	0.16	62	1	82	10	813	265	62.0	1.0
Zircon_21_032	78	37	0.43	0.07998	0.0068	0.10777	0.00944	0.00981	0.00021	0.24	63	1	104	9	1196	166	63.0	1.0
Zircon_29_041	90	47	0.48	0.06575	0.00408	0.0889	0.00572	0.00993	0.00017	0.26	64	1	86	5	798	136	64.0	1.0

				CORRECTED RATIOS							CORRECTED AGES (Ma)						Best age (Ma)	±1s
Spot Name	**U (ppm)**	**Th (ppm)**	**Th/U**	**207Pb/206Pb**	**±1s**	**207Pb/235U**	**±1s**	**206Pb/238U**	**±1s**	**Rho**	**206Pb/238U**	**±1s**	**207Pb/235U**	**±1s**	**207Pb/206Pb**	**±1s**		
Sample: ROCA 4J-16																		
Zircon_01_4J-16_008	281	119	0.39	0.07622	0.00685	0.03537	0.00346	0.00337	0.00007	0.29	21.7	0.5	35	3	1101	192	21.7	0.5
Zircon_06_014	149	110	0.69	0.10068	0.01058	0.04772	0.00578	0.00344	0.00013	0.36	22.1	0.8	47	6	1637	184	22.1	0.8
Zircon_10_018	110	56	0.47	0.09665	0.00868	0.04599	0.0046	0.00345	0.0001	0.33	22.2	0.6	46	4	1560	157	22.2	0.6
Zircon_05_012	108	61	0.52	0.14829	0.01068	0.06773	0.00539	0.0035	0.00012	0.43	22.5	0.8	67	5	2326	114	22.5	0.8
Zircon_24_035	134	72	0.50	0.09309	0.01117	0.04327	0.00532	0.00355	0.0001	0.22	22.8	0.6	43	5	1490	227	22.8	0.6
Zircon_12_021	81	41	0.47	0.14291	0.01474	0.07115	0.00837	0.00361	0.00015	0.39	23.2	0.9	70	8	2263	167	23.2	0.9
Zircon_03_010	93	45	0.45	0.11893	0.01446	0.06024	0.00793	0.00367	0.00011	0.27	23.6	0.7	59	8	1940	237	23.6	0.7
Zircon_20_030	94	53	0.52	0.11266	0.01352	0.05635	0.00693	0.00372	0.0001	0.22	23.9	0.6	56	7	1843	217	23.9	0.6
Zircon_17_027	82	66	0.75	0.14261	0.01326	0.07223	0.0071	0.00379	0.00012	0.32	24.4	0.8	71	7	2259	150	24.4	0.8
Zircon_32_045	94	50	0.50	0.11022	0.01532	0.05778	0.00906	0.0038	0.00015	0.42	24.5	0.9	57	9	1803	243	24.5	0.9
Zircon_35_048	73	39	0.50	0.08378	0.01986	0.04399	0.01096	0.00381	0.00015	0.2	24.5	0.9	44	11	1287	474	24.5	0.9
Zircon_16_026	112	58	0.48	0.12006	0.01561	0.0598	0.00796	0.00383	0.00011	0.21	24.6	0.7	59	8	1957	221	24.6	0.7
Zircon_09_017	65	36	0.51	0.14878	0.01637	0.07202	0.00834	0.00387	0.00014	0.31	24.9	0.9	71	8	2332	177	24.9	0.9
Zircon_25_036	50	31	0.57	0.13417	0.01884	0.07068	0.01139	0.00382	0.00017	0.36	25	1	69	11	2153	246	25.0	1.0
Zircon_15_024	68	56	0.76	0.11551	0.01386	0.0647	0.00805	0.00395	0.00013	0.26	25.4	0.8	64	8	1888	204	25.4	0.8
Zircon_02_009	58	46	0.73	0.1386	0.01525	0.07264	0.00828	0.00397	0.00012	0.26	25.5	0.8	71	8	2210	206	25.5	0.8
Zircon_29_041	83	39	0.44	0.11059	0.01073	0.0584	0.00595	0.00399	0.00012	0.31	25.7	0.8	58	6	1809	175	25.7	0.8
Zircon_38_052	67	56	0.79	0.09925	0.01886	0.05477	0.01065	0.00403	0.00017	0.21	26	1	54	10	1610	351	26.0	1.0

Zircon_27_039	59	41	0.65	0.15822	0.0174	0.08471	0.00978	0.00409	0.00014	0.3	26.3	0.9	83	9	2437	185	26.3	0.9
Zircon_28_040	65	48	0.68	0.11373	0.01565	0.06409	0.00967	0.00409	0.00013	0.25	26.3	0.9	63	9	1860	250	26.3	0.9
Zircon_22_033	68	56	0.77	0.15936	0.01753	0.08422	0.00975	0.0041	0.00015	0.31	26.4	1	82	9	2449	185	26.4	1.0
Zircon_23_034	67	35	0.48	0.11311	0.01242	0.06454	0.00814	0.00414	0.00015	0.37	26.6	1	64	8	1850	198	26.6	1.0
Zircon_18_028	61	35	0.54	0.1433	0.01669	0.08433	0.01118	0.00427	0.00016	0.34	27	1	82	10	2267	200	27.0	1.0
Zircon_31_044	42	26	0.58	0.18772	0.02253	0.09939	0.01267	0.0042	0.00018	0.34	27	1	96	12	2722	188	27.0	1.0
Zircon_33_046	63	28	0.41	0.11415	0.02347	0.06621	0.01453	0.00421	0.00017	0.29	27	1	65	14	1866	371	27.0	1.0
Zircon_34_047	43	30	0.64	0.18139	0.02358	0.09872	0.01361	0.00425	0.0002	0.33	27	1	96	13	2666	206	27.0	1.0
Zircon_36_050	59	45	0.71	0.14282	0.01571	0.08247	0.00963	0.00419	0.00016	0.34	27	1	80	9	2262	180	27.0	1.0
Zircon_37_051	49	26	0.49	0.1311	0.02045	0.07687	0.01321	0.00425	0.00016	0.32	27	1	75	12	2113	265	27.0	1.0
Zircon_39_053	75	37	0.45	0.12638	0.01945	0.0735	0.01257	0.00422	0.00018	0.33	27	1	72	12	2048	263	27.0	1.0
Zircon_07_015	72	36	0.46	0.14218	0.01848	0.07817	0.01038	0.00426	0.00011	0.2	27.4	0.7	76	10	2254	213	27.4	0.7
Zircon_13_022	37	19	0.48	0.16434	0.02136	0.0937	0.01266	0.00441	0.00016	0.27	28	1	91	12	2501	207	28.0	1.0
Zircon_19_029	47	24	0.48	0.13796	0.02029	0.08249	0.01377	0.00434	0.00022	0.35	28	1	80	13	2202	257	28.0	1.0
Zircon_08_016	50	37	0.67	0.15315	0.01685	0.09626	0.01117	0.00456	0.00017	0.32	29	1	93	10	2381	176	29.0	1.0
Zircon_21_032	42	24	0.53	0.16265	0.02318	0.10508	0.01697	0.00469	0.00023	0.35	30	1	101	16	2483	241	30.0	1.0
Zircon_30_042	42	22	0.50	0.1902	0.02282	0.12779	0.01638	0.00504	0.00023	0.35	32	1	122	15	2744	188	32.0	1.0
Zircon_04_011	33	14	0.38	0.1472	0.01766	0.09853	0.01237	0.00519	0.00019	0.29	33	1	95	11	2314	223	33.0	1.0
Zircon_11_020	37	18	0.45	0.14108	0.03483	0.10108	0.02652	0.0052	0.00028	0.25	33	2	98	24	2241	440	33.0	2.0
Zircon_14_023	30	15	0.47	0.16728	0.02509	0.10803	0.01677	0.00509	0.0002	0.26	33	1	104	15	2531	241	33.0	1.0
Zircon_26_038	30	14	0.44	0.21188	0.02966	0.15259	0.02279	0.00546	0.00028	0.35	35	2	144	20	2920	227	35.0	2.0

				CORRECTED RATIOS							CORRECTED AGES (Ma)						Best age (Ma)	±1s
Spot Name	**U (ppm)**	**Th (ppm)**	**Th/U**	**207Pb/206Pb**	**±1s**	**207Pb/235U**	**±1s**	**206Pb/238U**	**±1s**	**Rho**	**206Pb/238U**	**±1s**	**207Pb/235U**	**±1s**	**207Pb/206Pb**	**±1s**		
Sample: Barr 04																		
Zircon_38_052	729	420	0.52	0.05599	0.00455	0.02363	0.00205	0.00306	0.00004	0.22	19.7	0.3	24	2	452	178	19.7	0.3
Zircon_17_027	172	211	1.12	0.05492	0.01126	0.02421	0.00534	0.0032	0.0001	0.16	20.6	0.7	24	5	409	404	20.6	0.7
Zircon_13_022	892	555	0.57	0.05283	0.00304	0.02404	0.00151	0.0033	0.00004	0.25	21.2	0.3	24	1	322	127	21.2	0.3
Zircon_21_032	154	90	0.53	0.07759	0.01319	0.03163	0.00546	0.00333	0.0001	0.17	21.4	0.6	32	5	1136	351	21.4	0.6
Zircon_28_040	166	88	0.48	0.05009	0.00852	0.02292	0.00392	0.00337	0.00006	0.1	21.7	0.4	23	4	199	331	21.7	0.4
Zircon_06_014	120	106	0.80	0.09614	0.01667	0.04514	0.00836	0.00341	0.00012	0.24	21.9	0.8	45	8	1550	343	21.9	0.8
Zircon_12_021	71	44	0.57	0.08605	0.0233	0.04115	0.0119	0.00347	0.00017	0.32	22	1	41	12	1339	568	22.0	1.0
Zircon_03_010	71	58	0.75	0.10695	0.02888	0.0501	0.01365	0.00343	0.00013	0.13	22.1	0.8	50	13	1748	581	22.1	0.8
Zircon_33_046	89	58	0.60	0.04764	0.00928	0.02253	0.00477	0.00343	0.00012	0.22	22.1	0.8	23	5	82	349	22.1	0.8
Zircon_27_039	186	121	0.59	0.07962	0.00772	0.03774	0.00373	0.00346	0.00007	0.19	22.3	0.4	38	4	1188	205	22.3	0.4
Zircon_04_011	94	62	0.60	0.08664	0.01643	0.04164	0.00829	0.00349	0.00013	0.2	22.4	0.8	41	8	1352	390	22.4	0.8
Zircon_39_053	166	113	0.62	0.09735	0.01071	0.04529	0.00516	0.00348	0.0001	0.26	22.4	0.6	45	5	1574	205	22.4	0.6
Zircon_36_050	76	69	0.83	0.08473	0.02288	0.03911	0.01067	0.00349	0.00014	0.14	22.5	0.9	39	10	1309	563	22.5	0.9
Zircon_08_016	112	110	0.89	0.10099	0.03131	0.05193	0.01619	0.00351	0.00012	0.11	22.6	0.8	51	16	1642	652	22.6	0.8

Zircon_11_020	218	115	0.48	0.06846	0.0065	0.0326	0.00315	0.00353	0.00006	0.19	22.7	0.4	33	3	883	195	22.7	0.4
Zircon_40_054	116	123	0.96	0.08721	0.01792	0.04247	0.00935	0.00353	0.00013	0.24	22.7	0.8	42	9	1365	416	22.7	0.8
Zircon_14_023	114	117	0.94	0.09608	0.01922	0.04508	0.00916	0.00356	0.00013	0.18	22.9	0.8	45	9	1549	400	22.9	0.8
Zircon_23_034	84	59	0.64	0.0665	0.02151	0.03272	0.01127	0.00357	0.00016	0.24	23	1	33	11	822	672	23.0	1.0
Zircon_05_012	127	120	0.86	0.07429	0.01369	0.03674	0.00723	0.00359	0.00011	0.21	23.1	0.7	37	7	1049	391	23.1	0.7
Zircon_29_041	111	72	0.59	0.1158	0.02331	0.05741	0.01269	0.0036	0.00015	0.28	23.1	0.9	57	12	1892	427	23.1	0.9
Zircon_31_044	101	102	0.92	0.11139	0.02186	0.05514	0.01173	0.00359	0.00014	0.22	23.1	0.9	55	11	1822	417	23.1	0.9
Zircon_20_030	131	142	0.98	0.15922	0.02149	0.07908	0.01155	0.0036	0.00012	0.28	23.2	0.8	77	11	2447	230	23.2	0.8
Zircon_30_042	110	71	0.59	-0.00328	-0.01574	-0.00081	-0.0039	0.00361	0.0001	0.58	23.2	0.6	-0.8	-4	-2269	1256	23.2	0.6
Zircon_22_033	101	87	0.78	0.08851	0.01416	0.04074	0.00661	0.00362	0.0001	0.17	23.3	0.6	41	6	1394	341	23.3	0.6
Zircon_37_051	191	117	0.56	0.08451	0.00878	0.04223	0.00483	0.00362	0.00009	0.28	23.3	0.6	42	5	1304	201	23.3	0.6
Zircon_07_015	99	80	0.74	0.12918	0.03557	0.06469	0.01864	0.00363	0.00015	0.2	23.4	1	64	18	2087	596	23.4	1.0
Zircon_02_009	76	66	0.79	0.08047	0.01448	0.03904	0.00715	0.00365	0.00012	0.19	23.5	0.8	39	7	1209	373	23.5	0.8
Zircon_19_029	85	61	0.65	0.1547	0.02321	0.07229	0.01104	0.00368	0.00011	0.19	23.7	0.7	71	10	2399	259	23.7	0.7
Zircon_10_018	88	59	0.62	0.12606	0.0215	0.06428	0.01196	0.0037	0.00014	0.28	23.8	0.9	63	11	2044	311	23.8	0.9
Zircon_32_045	112	83	0.68	0.09431	0.01519	0.04822	0.00834	0.00371	0.00012	0.21	23.9	0.8	48	8	1514	339	23.9	0.8
Zircon_01_Barr04_008	72	61	0.77	0.11542	0.02567	0.05915	0.01463	0.00372	0.00019	0.44	24	1	58	14	1887	450	24.0	1.0
Zircon_16_026	78	52	0.61	0.0702	0.02246	0.02989	0.00965	0.00378	0.00016	0.13	24	1	30	10	934	656	24.0	1.0
Zircon_35_048	91	48	0.48	0.08121	0.01486	0.0424	0.00834	0.00379	0.00014	0.24	24.4	0.9	42	8	1226	408	24.4	0.9
Zircon_18_028	119	88	0.68	0.05661	0.01255	0.0298	0.00681	0.00382	0.00012	0.15	24.6	0.8	30	7	476	435	24.6	0.8
Zircon_26_038	94	57	0.55	0.11347	0.01929	0.06267	0.01086	0.0039	0.00013	0.19	25.1	0.8	62	10	1856	355	25.1	0.8
Zircon_15_024	83	73	0.80	0.18013	0.02522	0.09778	0.01424	0.00407	0.00016	0.28	26	1	95	13	2654	234	26.0	1.0
Zircon_24_035	45	41	0.84	0.10241	0.04916	0.05395	0.02603	0.00407	0.0002	0.1	26	1	53	25	1668	1085	26.0	1.0
Zircon_09_017	52	34	0.59	0.1016	0.02438	0.05164	0.01259	0.00419	0.00018	0.18	27	1	51	12	1654	485	27.0	1.0
Zircon_34_047	279	132	0.43	0.04978	0.00244	0.06522	0.00329	0.00956	0.00011	0.24	61.3	0.7	64	3	185	115	61.3	0.7

				CORRECTED RATIOS							CORRECTED AGES (Ma)						Best age (Ma)	±1s
Spot Name	**U (ppm)**	**Th (ppm)**	**Th/U**	**207Pb/206Pb**	**±1s**	**207Pb/235U**	**±1s**	**206Pb/238U**	**±1s**	**Rho**	**206Pb/238U**	**±1s**	**207Pb/235U**	**±1s**	**207Pb/206Pb**	**±1s**		
Sample: SC 09-08																		
Zircon_26_038	260	180	0.65	-0.02021	-0.01111	-0.0079	-0.00435	0.00293	0.00007	0.06	18.9	0.4	-8.1	-4.5	-199	1196	18.9	0.40
Zircon_30_042	293	164	0.52	0.01662	0.0098	0.00712	0.00421	0.00305	0.00006	0.1	19.6	0.4	7	4	-942	529	19.6	0.40
Zircon_03_010	184	151	0.77	0.06569	0.00624	0.02772	0.00269	0.00313	0.00006	0.2	20.1	0.4	28	3	797	212	20.1	0.40
Zircon_05_012	299	306	0.96	0.08434	0.00658	0.0362	0.00291	0.00316	0.00006	0.24	20.3	0.4	36	3	1300	160	20.3	0.40
Zircon_28_040	297	213	0.67	0.0651	0.00797	0.0288	0.00382	0.00321	0.00008	0.21	20.7	0.5	29	4	777	265	20.7	0.50
Zircon_29_041	283	117	0.39	0.07607	0.00875	0.03413	0.00417	0.00325	0.00007	0.23	20.9	0.5	34	4	1097	236	20.9	0.50
Zircon_07_015	177	122	0.65	0.08519	0.01193	0.03888	0.00554	0.0033	0.00009	0.18	21.2	0.6	39	5	1320	295	21.2	0.60
Zircon_24_035	187	99	0.50	0.10243	0.01639	0.04395	0.0071	0.00331	0.00007	0.14	21.3	0.4	44	7	1669	310	21.3	0.40
Zircon_01_SC-09-08_008	176	109	0.58	0.09196	0.00809	0.042	0.00377	0.00333	0.00006	0.2	21.4	0.4	42	4	1467	177	21.4	0.40
Zircon_08_016	163	131	0.75	0.1049	0.00913	0.04821	0.00434	0.0034	0.00008	0.26	21.9	0.5	48	4	1713	170	21.9	0.50

Zircon_11_020	189	110	0.55	0.09593	0.00854	0.04408	0.00404	0.0034	0.00007	0.24	21.9	0.4	44	4	1546	178	21.9	0.40
Zircon_14_023	194	138	0.67	0.09156	0.01007	0.04172	0.00472	0.0034	0.00009	0.23	21.9	0.6	42	5	1458	224	21.9	0.60
Zircon_31_043	292	107	0.34	0.09003	0.00822	0.04224	0.00417	0.0034	0.00008	0.27	21.9	0.5	42	4	1426	176	21.9	0.50
Zircon_22_033	203	160	0.74	0.10486	0.01054	0.04991	0.00562	0.00345	0.00009	0.29	22.2	0.6	49	5	1712	188	22.2	0.60
Zircon_21_032	180	145	0.76	0.10066	0.01007	0.04753	0.0049	0.00347	0.00009	0.24	22.3	0.6	47	5	1636	189	22.3	0.60
Zircon_06_014	243	115	0.45	0.08686	0.0064	0.04188	0.00329	0.0035	0.00006	0.24	22.5	0.4	42	3	1357	150	22.5	0.40
Zircon_02_009	128	102	0.75	0.08298	0.01079	0.03887	0.00518	0.00353	0.0001	0.22	22.7	0.6	39	5	1269	276	22.7	0.60
Zircon_04_011	168	135	0.75	0.11141	0.01103	0.05308	0.00541	0.00353	0.00008	0.24	22.7	0.5	53	5	1823	191	22.7	0.50
Zircon_09_017	198	155	0.73	0.08582	0.00858	0.04172	0.00427	0.00353	0.00008	0.21	22.7	0.5	42	4	1334	206	22.7	0.50
Zircon_19_029	142	118	0.78	0.14847	0.01782	0.07085	0.0088	0.00352	0.00011	0.26	22.7	0.7	70	8	2328	210	22.7	0.70
Zircon_23_034	141	111	0.74	0.12336	0.01357	0.06173	0.00702	0.00353	0.0001	0.25	22.7	0.6	61	7	2005	199	22.7	0.60
Zircon_15_024	156	123	0.74	0.09502	0.01425	0.04396	0.00668	0.00355	0.00009	0.16	22.8	0.6	44	6	1528	309	22.8	0.60
Zircon_25_036	155	116	0.71	0.12608	0.02077	0.06188	0.01075	0.00356	0.00013	0.19	22.9	0.8	61	10	2044	305	22.9	0.80
Zircon_13_022	160	118	0.69	0.12942	0.01682	0.06173	0.00829	0.00357	0.00012	0.25	23	0.8	61	8	2090	246	23.0	0.80
Zircon_10_018	133	103	0.72	0.09546	0.0105	0.04652	0.00525	0.00359	0.00009	0.22	23.1	0.6	46	5	1537	221	23.1	0.60
Zircon_27_039	234	153	0.61	0.09087	0.01272	0.04238	0.00601	0.00363	0.00008	0.16	23.4	0.5	42	6	1444	276	23.4	0.50
Zircon_20_030	158	131	0.78	0.11713	0.01757	0.05537	0.00839	0.00366	0.00008	0.14	23.6	0.5	55	8	1913	280	23.6	0.50
Zircon_17_027	97	64	0.62	0.1163	0.01788	0.06057	0.01009	0.00378	0.00015	0.27	24.3	1	60	10	1900	302	24.3	1.00
Zircon_16_026	163	96	0.56	0.11954	0.01195	0.06047	0.00623	0.0038	0.00009	0.24	24.4	0.6	60	6	1949	190	24.4	0.60
Zircon_18_028	116	46	0.37	0.0691	0.01287	0.03691	0.00737	0.00387	0.00016	0.26	25	1	37	7	902	405	25.0	1.00
Zircon_12_021	113	71	0.59	0.13281	0.01727	0.07227	0.00975	0.00393	0.00014	0.27	25.3	0.9	71	9	2135	245	25.3	0.90

				CORRECTED RATIOS							CORRECTED AGES (Ma)							
Spot Name	**U (ppm)**	**Th (ppm)**	**Th/U**	**207Pb/206Pb**	**±1s**	**207Pb/235U**	**±1s**	**206Pb/238U**	**±1s**	**Rho**	**206Pb/238U**	**±1s**	**207Pb/235U**	**±1s**	**207Pb/206Pb**	**±1s**	**Best age (Ma)**	**±1s**
Sample: Ros 02																		
Zircon_31_044	622	602	0.88	0.05768	0.00388	0.02368	0.00176	0.00298	0.00004	0.29	19.2	0.3	24	2	518	153	19.2	0.3
Zircon_09_017	1240	1310	0.96	0.03891	0.00253	0.01718	0.00114	0.00322	0.00004	0.2	20.7	0.3	17	1	-354	174	20.7	0.3
Zircon_22_033	1645	1326	0.73	0.03781	0.0017	0.01692	0.00078	0.00326	0.00003	0.22	21	0.2	17	0.8	-421	223	21.0	0.2
Zircon_26_038	3244	6536	1.83	0.04994	0.00135	0.02244	0.00063	0.00328	0.00002	0.28	21.1	0.1	22.5	0.6	192	60	21.1	0.1
Zircon_12_021	1572	1134	0.66	0.04804	0.00159	0.02178	0.00075	0.00329	0.00003	0.28	21.2	0.2	21.9	0.7	101	74	21.2	0.2
Zircon_20_030	1421	1284	0.82	0.05239	0.00251	0.02374	0.00116	0.00329	0.00003	0.2	21.2	0.2	24	1	302	105	21.2	0.2
Zircon_24_035	1706	1172	0.63	0.05413	0.00179	0.02454	0.00084	0.0033	0.00003	0.26	21.2	0.2	24.6	0.8	376	71	21.2	0.2
Zircon_28_040	3396	7588	2.03	0.05037	0.00131	0.02288	0.00062	0.00329	0.00002	0.29	21.2	0.1	23	0.6	212	62	21.2	0.1
Zircon_07_015	999	621	0.57	0.0526	0.00231	0.02381	0.00107	0.00331	0.00003	0.21	21.3	0.2	24	1	312	101	21.3	0.2
Zircon_11_020	1420	1862	1.19	0.05025	0.00181	0.02292	0.00085	0.00331	0.00003	0.24	21.3	0.2	23	0.8	207	84	21.3	0.2
Zircon_05_012	1557	1287	0.75	0.06023	0.00229	0.0277	0.00107	0.00332	0.00002	0.18	21.4	0.1	28	1	612	83	21.4	0.1
Zircon_13_022	1705	1633	0.87	0.05152	0.00149	0.02355	0.00071	0.00333	0.00003	0.28	21.4	0.2	23.6	0.7	264	67	21.4	0.2
Zircon_15_024	1954	3381	1.58	0.0568	0.00187	0.02594	0.00089	0.00333	0.00003	0.28	21.4	0.2	26	0.9	484	73	21.4	0.2
Zircon_17_027	1610	1578	0.89	0.05085	0.00173	0.0234	0.00084	0.00332	0.00004	0.32	21.4	0.3	23.5	0.8	234	75	21.4	0.3

Zircon_18_028	1595	1563	0.89	0.04817	0.00197	0.02209	0.00093	0.00333	0.00003	0.24	21.4	0.2	22.2	0.9	108	86	21.4	0.2
Zircon_19_029	1819	1466	0.73	0.0552	0.00215	0.02529	0.00102	0.00333	0.00003	0.26	21.4	0.2	25	1	420	83	21.4	0.2
Zircon_25_036	1408	1790	1.16	0.05631	0.00253	0.02588	0.00119	0.00333	0.00003	0.21	21.4	0.2	26	1	465	96	21.4	0.2
Zircon_02_009	1378	1224	0.81	0.0551	0.00204	0.02527	0.00097	0.00334	0.00003	0.27	21.5	0.2	25.3	1	416	78	21.5	0.2
Zircon_14_023	1502	1449	0.88	0.04592	0.00152	0.02115	0.00073	0.00336	0.00003	0.28	21.6	0.2	21.3	0.7	-6	66	21.6	0.2
Zircon_23_034	1687	1737	0.94	0.05216	0.00156	0.02404	0.00075	0.00335	0.00003	0.28	21.6	0.2	24.1	0.7	292	65	21.6	0.2
Zircon_29_041	1584	1814	1.04	0.04835	0.0015	0.02239	0.00072	0.00335	0.00003	0.26	21.6	0.2	22.5	0.7	116	72	21.6	0.2
Zircon_30_042	1452	1193	0.75	0.04865	0.00209	0.02243	0.00098	0.00336	0.00003	0.18	21.6	0.2	22.5	1	131	98	21.6	0.2
Zircon_06_014	1076	718	0.61	0.05386	0.00205	0.02493	0.00099	0.00337	0.00004	0.29	21.7	0.3	25	1	365	87	21.7	0.3
Zircon_08_016	1547	988	0.58	0.05098	0.00194	0.02369	0.00092	0.00337	0.00003	0.2	21.7	0.2	23.8	0.9	240	89	21.7	0.2
Zircon_21_032	1345	1146	0.78	0.05139	0.0018	0.02386	0.00086	0.00338	0.00003	0.24	21.8	0.2	23.9	0.9	258	77	21.8	0.2
Zircon_27_039	2947	5575	1.72	0.04904	0.00137	0.0229	0.00066	0.00338	0.00002	0.25	21.8	0.1	23	0.7	150	63	21.8	0.1
Zircon_03_010	1323	856	0.59	0.04607	0.00035	0.02169	0.00024	0.00341	0.00003	0.28	22	0.2	21.8	0.2	1	16	22.0	0.2
Zircon_16_026	1363	1656	1.11	0.06282	0.00476	0.02959	0.00241	0.00342	0.00004	0.2	22	0.2	30	2	702	157	22.0	0.2
Zircon_04_011	1435	1699	1.08	0.06219	0.00454	0.02987	0.0024	0.00348	0.00005	0.22	22.4	0.3	30	2	681	159	22.4	0.3
Zircon_32_045	202	79	0.35	0.0652	0.00698	0.03151	0.00358	0.0035	0.00008	0.25	22.6	0.5	31	4	781	239	22.6	0.5
Zircon_01_Ros02_008	139	60	0.39	0.08953	0.01482	0.04847	0.00828	0.00393	0.0001	0.18	25.3	0.7	48	8	1416	317	25.3	0.7

				CORRECTED RATIOS							CORRECTED AGES (Ma)						Best age (Ma)	±1s
Spot Name	**U (ppm)**	**Th (ppm)**	**Th/U**	**207Pb/206Pb**	**±1s**	**207Pb/235U**	**±1s**	**206Pb/238U**	**±1s**	**Rho**	**206Pb/238U**	**±1s**	**207Pb/235U**	**±1s**	**207Pb/206Pb**	**±1s**		
Sample: ROCA 4J-12																		
Zircon_91_116	162	68	0.47	0.05623	0.01565	0.02337	0.00719	0.00301	0.00013	0.43	19.4	0.8	23	7	462	481	19.4	0.8
Zircon_96_122	303	136	0.50	0.05772	0.00636	0.02407	0.00287	0.00302	0.00005	0.26	19.5	0.3	24	3	519	227	19.5	0.3
Zircon_86_110	599	250	0.46	0.0621	0.00507	0.02659	0.00237	0.0031	0.00006	0.25	20	0.4	27	2	678	156	20.0	0.4
Zircon_81_104	248	103	0.46	0.07769	0.01064	0.03407	0.00513	0.00318	0.00009	0.32	20.5	0.6	34	5	1139	245	20.5	0.6
Zircon_105_132	223	99	0.49	0.08041	0.00571	0.0348	0.00257	0.00319	0.00006	0.28	20.5	0.4	35	3	1207	131	20.5	0.4
Zircon_99_125	156	79	0.56	0.07259	0.00725	0.03201	0.00366	0.0032	0.00009	0.34	20.6	0.6	32	4	1003	191	20.6	0.6
Zircon_83_106	281	120	0.47	0.06137	0.00548	0.02726	0.00263	0.00322	0.00006	0.22	20.7	0.4	27	3	652	171	20.7	0.4
Zircon_78_100	383	173	0.50	0.0644	0.00432	0.02827	0.00193	0.00323	0.00004	0.19	20.8	0.3	28	2	755	126	20.8	0.3
Zircon_87_111	278	115	0.46	0.08311	0.00573	0.037	0.00279	0.00323	0.00006	0.25	20.8	0.4	37	3	1272	120	20.8	0.4
Zircon_100_126	132	87	0.73	0.08739	0.01035	0.03899	0.00518	0.00324	0.00009	0.28	20.8	0.6	39	5	1369	216	20.8	0.6
Zircon_75_096	230	159	0.77	0.07652	0.00587	0.03427	0.00302	0.00325	0.00007	0.28	20.9	0.5	34	3	1109	137	20.9	0.5
Zircon_106_134	127	70	0.61	0.06353	0.00982	0.02864	0.00493	0.00327	0.0001	0.32	21	0.7	29	5	726	315	21.0	0.7
Zircon_74_095	293	122	0.46	0.07049	0.00568	0.03184	0.00282	0.00328	0.00007	0.31	21.1	0.5	32	3	943	169	21.1	0.5
Zircon_77_099	216	152	0.78	0.07655	0.00475	0.03403	0.00224	0.0033	0.00007	0.33	21.2	0.4	34	2	1109	111	21.2	0.4
Zircon_102_129	129	107	0.92	0.10391	0.00779	0.04697	0.00365	0.00331	0.00007	0.26	21.3	0.4	47	4	1695	129	21.3	0.4
Zircon_95_120	208	95	0.51	0.06965	0.00833	0.0323	0.00419	0.00336	0.00007	0.26	21.6	0.5	32	4	918	234	21.6	0.5
Zircon_104_131	165	109	0.74	0.08837	0.00636	0.04054	0.00304	0.00339	0.00007	0.28	21.8	0.4	40	3	1391	129	21.8	0.4
Zircon_98_124	178	70	0.44	0.0807	0.01005	0.0378	0.00534	0.0034	0.0001	0.41	21.9	0.7	38	5	1214	233	21.9	0.7

Zircon_101_128	357	110	0.34	0.06883	0.00654	0.0323	0.00318	0.00341	0.00009	0.26	21.9	0.6	32	3	894	185	21.9	0.6
Zircon_80_102	204	100	0.54	0.08658	0.00736	0.03991	0.00349	0.00344	0.00007	0.23	22.1	0.4	40	3	1351	146	22.1	0.4
Zircon_89_113	166	86	0.58	0.09325	0.00821	0.04332	0.00396	0.00346	0.00009	0.27	22.3	0.6	43	4	1493	149	22.3	0.6
Zircon_93_118	114	46	0.45	0.09499	0.00741	0.04385	0.00365	0.00348	0.0001	0.35	22.4	0.6	44	4	1528	138	22.4	0.6
Zircon_76_098	189	89	0.52	0.0935	0.00701	0.04381	0.00346	0.0035	0.00009	0.31	22.5	0.6	44	3	1498	127	22.5	0.6
Zircon_85_108	132	66	0.56	0.10394	0.00769	0.04866	0.00377	0.0035	0.00008	0.3	22.5	0.5	48	4	1696	122	22.5	0.5
Zircon_90_114	178	85	0.53	0.08127	0.00715	0.03913	0.00386	0.00349	0.00008	0.3	22.5	0.5	39	4	1228	154	22.5	0.5
Zircon_84_107	97	62	0.71	0.077	0.0195	0.03767	0.01286	0.00355	0.00038	0.75	23	2	38	13	1121	464	23.0	2.0
Zircon_82_105	120	63	0.58	0.10692	0.01059	0.05156	0.00521	0.00361	0.00007	0.2	23.2	0.4	51	5	1748	162	23.2	0.4
Zircon_97_123	93	77	0.92	0.10477	0.01062	0.05222	0.00619	0.00361	0.00011	0.32	23.3	0.7	52	6	1710	176	23.3	0.7
Zircon_103_130	101	55	0.60	0.0688	0.00963	0.03281	0.0047	0.00365	0.00011	0.21	23.5	0.7	33	5	893	277	23.5	0.7
Zircon_73Roca4j-12_094	96	68	0.78	0.10725	0.01115	0.05418	0.00632	0.00366	0.00011	0.32	23.6	0.7	54	6	1753	196	23.6	0.7
Zircon_88_112	133	105	0.88	0.08165	0.00898	0.03869	0.00438	0.00366	0.0001	0.24	23.6	0.6	39	4	1237	193	23.6	0.6
Zircon_79_101	93	48	0.58	0.09971	0.00897	0.04997	0.0047	0.00368	0.0001	0.29	23.7	0.6	50	5	1619	149	23.7	0.6
Zircon_92_117	141	68	0.54	0.09624	0.00784	0.04908	0.00449	0.0037	0.00008	0.29	23.8	0.5	49	4	1552	143	23.8	0.5
Zircon_108_36	86	68	0.89	0.08457	0.02514	0.04259	0.01424	0.00365	0.00019	0.28	24	1	42	14	1306	584	24.0	1.0
Zircon_94_119	56	26	0.52	0.14513	0.02032	0.07041	0.01016	0.00388	0.00014	0.24	25	0.9	69	10	2289	230	2289	230.0
Zircon_107_135	93	49	0.59	0.26465	0.08998	0.12436	0.04248	0.00384	0.00013	0.1	24.7	0.8	119	38	3275	619	3275.0	619.0

				CORRECTED RATIOS							CORRECTED AGES (Ma)						Best age (Ma)	±1s
Spot Name	**U (ppm)**	**Th (ppm)**	**Th/U**	**207Pb/206Pb**	**±1s**	**207Pb/235U**	**±1s**	**206Pb/238U**	**±1s**	**Rho**	**206Pb/238U**	**±1s**	**207Pb/235U**	**±1s**	**207Pb/206Pb**	**±1s**		
Sample: ROCA 24J-24																		
Zircon_07_015	1205	734	0.57	0.05135	0.00378	0.02088	0.00167	0.00295	0.00004	0.2	19	0.3	21	2	257	158	19.0	0.3
Zircon_10_018	2017	884	0.41	0.05156	0.00191	0.02098	0.0008	0.00297	0.00003	0.24	19.1	0.2	21.1	0.8	266	80	19.1	0.2
Zircon_03_010	1639	783	0.44	0.04272	0.00162	0.01748	0.00069	0.00298	0.00003	0.28	19.2	0.2	17.6	0.7	-138	81	19.2	0.2
Zircon_04_011	933	388	0.39	0.05389	0.00257	0.02219	0.00119	0.00299	0.00004	0.27	19.2	0.3	22	1	367	103	19.2	0.3
Zircon_14_023	4084	2450	0.56	0.0498	0.0012	0.0204	0.00052	0.00299	0.00003	0.33	19.2	0.2	20.5	0.5	186	52	19.2	0.2
Zircon_01_24J-24_008	1443	454	0.29	0.0573	0.00204	0.02379	0.00095	0.00301	0.00003	0.32	19.4	0.2	23.9	0.9	503	75	19.4	0.2
Zircon_36_050	1170	914	0.73	0.05703	0.00314	0.02365	0.00143	0.00301	0.00003	0.4	19.4	0.2	24	1	493	118	19.4	0.2
Zircon_12_021	2064	1025	0.46	0.05418	0.00141	0.02258	0.00062	0.00304	0.00003	0.32	19.6	0.2	22.7	0.6	379	55	19.6	0.2
Zircon_23_034	2647	917	0.32	0.04943	0.00138	0.02067	0.0006	0.00304	0.00003	0.28	19.6	0.2	20.8	0.6	168	68	19.6	0.2
Zircon_08_016	1005	318	0.29	0.05562	0.00284	0.02345	0.00128	0.00306	0.00003	0.21	19.7	0.2	24	1	437	109	19.7	0.2
Zircon_02_009	2820	1150	0.38	0.05052	0.00141	0.02139	0.00067	0.00307	0.00002	0.32	19.8	0.1	21.5	0.7	219	62	19.8	0.1
Zircon_20_030	1737	630	0.34	0.05427	0.00223	0.02282	0.00096	0.00308	0.00003	0.21	19.8	0.2	22.9	1	382	87	19.8	0.2
Zircon_21_032	2793	1287	0.43	0.04978	0.00134	0.02116	0.0006	0.00309	0.00003	0.32	19.9	0.2	21.3	0.6	185	59	19.9	0.2
Zircon_27_039	1297	517	0.37	0.05433	0.00235	0.02311	0.00111	0.00309	0.00003	0.33	19.9	0.2	23	1	385	101	19.9	0.2
Zircon_39_053	1002	258	0.24	0.05975	0.00254	0.02541	0.00116	0.00308	0.00004	0.31	19.9	0.2	25	1	595	89	19.9	0.2
Zircon_05_012	934	305	0.30	0.05385	0.00258	0.02285	0.00113	0.0031	0.00004	0.25	20	0.3	23	1	365	104	20.0	0.3
Zircon_28_040	1203	470	0.36	0.05468	0.00235	0.02318	0.00103	0.0031	0.00004	0.26	20	0.3	23	1	399	100	20.0	0.3

Zircon_34_047	1021	417	0.38	0.06017	0.00278	0.02584	0.00129	0.00311	0.00004	0.28	20	0.2	26	1	610	97	20.0	0.2
Zircon_06_014	521	171	0.31	0.05315	0.00218	0.02279	0.00097	0.00312	0.00003	0.27	20.1	0.2	22.9	1	335	89	20.1	0.2
Zircon_09_017	1574	433	0.26	0.05662	0.00215	0.02417	0.00096	0.00313	0.00003	0.3	20.1	0.2	24.2	1	477	79	20.1	0.2
Zircon_24_035	1293	465	0.33	0.05631	0.00208	0.02389	0.00092	0.00313	0.00003	0.29	20.1	0.2	24	0.9	465	85	20.1	0.2
Zircon_18_028	1628	796	0.46	0.05623	0.00231	0.02424	0.00102	0.00314	0.00003	0.22	20.2	0.2	24	1	461	85	20.2	0.2
Zircon_22_033	885	276	0.29	0.05333	0.00346	0.02335	0.00163	0.00318	0.00004	0.27	20.4	0.3	23	2	343	152	20.4	0.3
Zircon_26_038	1093	351	0.30	0.0534	0.00287	0.02347	0.00137	0.00319	0.00004	0.27	20.5	0.3	24	1	346	126	20.5	0.3
Zircon_16_026	835	270	0.30	0.06008	0.00301	0.02663	0.00145	0.00321	0.00004	0.27	20.7	0.3	27	1	607	102	20.7	0.3
Zircon_25_036	633	237	0.35	0.06566	0.00328	0.02866	0.00147	0.00321	0.00004	0.23	20.7	0.3	29	1	796	109	20.7	0.3
Zircon_33_046	681	421	0.58	0.06102	0.00293	0.02679	0.00135	0.00322	0.00005	0.3	20.7	0.3	27	1	640	100	20.7	0.3
Zircon_30_042	984	365	0.35	0.0621	0.00248	0.02743	0.00115	0.00323	0.00004	0.3	20.8	0.3	27	1	678	89	20.8	0.3
Zircon_31_044	1418	555	0.36	0.04923	0.00174	0.02197	0.00086	0.00324	0.00003	0.31	20.8	0.2	22.1	0.9	159	83	20.8	0.2
Zircon_35_048	817	341	0.39	0.06041	0.0032	0.02674	0.00146	0.00323	0.00004	0.24	20.8	0.3	27	1	618	111	20.8	0.3
Zircon_17_027	534	214	0.37	0.06042	0.00356	0.02655	0.00163	0.00325	0.00006	0.28	20.9	0.4	27	2	619	120	20.9	0.4
Zircon_11_020	1031	591	0.53	0.05541	0.00216	0.02486	0.001	0.00327	0.00003	0.25	21	0.2	24.9	1	429	81	21.0	0.2
Zircon_32_045	1721	863	0.47	0.05275	0.00279	0.0239	0.00141	0.00329	0.00004	0.32	21.1	0.3	24	1	318	125	21.1	0.3
Zircon_37_051	624	139	0.21	0.06928	0.00363	0.03138	0.00172	0.00328	0.00004	0.26	21.1	0.2	31	2	907	105	21.1	0.2
Zircon_29_041	765	402	0.49	0.05852	0.00304	0.02642	0.0014	0.0033	0.00003	0.2	21.2	0.2	26	1	549	118	21.2	0.2
Zircon_19_029	872	350	0.37	0.05746	0.00376	0.02624	0.00183	0.00331	0.00004	0.23	21.3	0.3	26	2	509	136	21.3	0.3
Zircon_38_052	471	134	0.26	0.06032	0.00444	0.02755	0.00211	0.00331	0.00004	0.23	21.3	0.3	28	2	615	154	21.3	0.3
Zircon_40_054	842	289	0.32	0.0639	0.00313	0.02887	0.00146	0.00331	0.00004	0.25	21.3	0.3	29	1	738	101	21.3	0.3
Zircon_13_022	121	58	0.44	0.09646	0.00878	0.04758	0.00453	0.00374	0.0001	0.29	24.1	0.6	47	4	1557	162	24.1	0.6

				CORRECTED RATIOS							CORRECTED AGES (Ma)							
Spot Name	**U (ppm)**	**Th (ppm)**	**Th/U**	**207Pb/206Pb**	**±1s**	**207Pb/235U**	**±1s**	**206Pb/238U**	**±1s**	**Rho**	**206Pb/238U**	**±1s**	**207Pb/235U**	**±1s**	**207Pb/206Pb**	**±1s**	**Best age (Ma)**	**±1s**
Sample: BC 09-25																		
Zircon_41_056	289	37	0.12	0.0863	0.01051	0.03343	0.00429	0.00281	0.00005	0.36	18.1	0.3	33	4	1345	237	18	0.3
Zircon_56_074	163	146	0.84	0.08196	0.01537	0.03242	0.00662	0.00287	0.00009	0.24	18.5	0.5	32	7	1245	365	19	0.5
Zircon_51_068	121	88	0.68	0.10853	0.01361	0.04333	0.00614	0.0029	0.00009	0.35	18.6	0.6	43	6	1775	222	19	0.6
Zircon_65_084	212	158	0.70	0.08803	0.01832	0.03547	0.00805	0.00292	0.0001	0.23	18.8	0.6	35	8	1383	399	19	0.6
Zircon_39_053	287	381	1.24	0.06351	0.00485	0.0258	0.00223	0.00295	0.00006	0.24	19	0.4	26	2	725	159	19	0.4
Zircon_40_054	129	97	0.70	0.08147	0.02651	0.03341	0.01175	0.00297	0.00012	0.45	19.1	0.8	33	12	1233	647	19	0.8
Zircon_37_051	245	300	1.15	0.04609	0.00186	0.0191	0.00107	0.003	0.0001	0.37	19.3	0.6	19	1	3	81	19	0.6
Zircon_33_046	189	116	0.58	0.07116	0.00813	0.02954	0.0036	0.00301	0.00006	0.25	19.4	0.4	30	4	962	234	19	0.4
Zircon_45_060	230	213	0.87	0.06416	0.0077	0.02634	0.0032	0.00301	0.00006	0.16	19.4	0.4	26	3	747	246	19	0.4
Zircon_34_047	126	102	0.76	0.06668	0.00928	0.02788	0.00417	0.00303	0.00008	0.27	19.5	0.5	28	4	828	284	20	0.5
Zircon_48_064	139	96	0.65	0.09085	0.01958	0.03851	0.00926	0.00307	0.00012	0.45	19.8	0.7	38	9	1443	412	20	0.7
Zircon_57_075	98	52	0.50	0.07149	0.01929	0.03063	0.00887	0.00311	0.00011	0.21	20	0.7	31	9	971	531	20	0.7
Zircon_47_063	83	66	0.74	0.09343	0.01308	0.03942	0.00561	0.00313	0.00008	0.18	20.1	0.5	39	5	1497	259	20	0.5

Zircon_59_077	74	44	0.57	0.10616	0.0139	0.04561	0.00692	0.00312	0.00014	0.37	20.1	0.9	45	7	1734	233	20	0.9
Zircon_44_059	94	50	0.50	0.08503	0.00984	0.03686	0.00457	0.00314	0.00008	0.27	20.2	0.5	37	4	1316	225	20	0.5
Zircon_64_083	121	82	0.64	0.0769	0.00669	0.03405	0.00306	0.00322	0.00007	0.25	20.7	0.4	34	3	1119	166	21	0.4
Zircon_42_057	86	69	0.75	0.11398	0.03376	0.0504	0.01689	0.00321	0.00019	0.45	21	1	50	16	1864	571	21	1.0
Zircon_60_078	75	59	0.75	0.09198	0.01151	0.04137	0.00573	0.00326	0.00009	0.27	21	0.6	41	6	1467	230	21	0.6
Zircon_36_050	106	58	0.51	0.11188	0.01387	0.05206	0.00703	0.00337	0.00011	0.32	21.7	0.7	52	7	1830	226	22	0.7
Zircon_52_069	121	71	0.55	0.1031	0.01427	0.0481	0.00755	0.00338	0.00011	0.39	21.8	0.7	48	7	1681	249	22	0.7
Zircon_38_052	54	33	0.57	0.07666	0.01687	0.03508	0.00778	0.00344	0.0001	0.12	22.1	0.6	35	8	1112	454	22	0.6
Zircon_35_048	54	33	0.57	0.09289	0.01761	0.04463	0.009	0.00349	0.00013	0.3	22.4	0.8	44	9	1486	370	22	0.8
Zircon_58_076	61	41	0.63	0.10872	0.01196	0.05201	0.00589	0.00354	0.0001	0.24	22.8	0.6	51	6	1778	193	23	0.6
Zircon_61_080	83	50	0.56	0.10221	0.04872	0.05151	0.02547	0.00365	0.00019	0.14	24	1	51	25	1665	979	24	1.0
Zircon_31_bc0925_044	70	72	0.97	0.06981	0.0144	0.03677	0.00825	0.00382	0.00015	0.29	24.6	0.9	37	8	923	429	25	0.9
Zircon_46_062	127	75	0.55	0.08613	0.03572	0.05805	0.04023	0.00489	0.00116	0.96	31	7	57	39	1341	834	31	7.0
Zircon_53_070	82	47	0.54	0.06373	0.00878	0.05536	0.00846	0.0063	0.0002	0.3	40	1	55	8	733	279	40	1.0
Zircon_62_081	293	172	0.55	0.05241	0.00241	0.09924	0.00492	0.01373	0.00011	0.2	87.9	0.7	96	5	303	99	88	0.7
Zircon_63_082	236	148	0.59	0.05634	0.00203	0.10781	0.00403	0.01387	0.00014	0.27	88.8	0.9	104	4	466	75	89	0.9
Zircon_49_065	121	89	0.69	0.13549	0.04131	0.06386	0.0224	0.00342	0.00018	0.58	22	1	63	21	2170	603	22	1
Zircon_50_066	147	31	0.20	0.1457	0.01962	0.07624	0.01107	0.0038	0.00014	0.31	24.4	0.9	75	10	2296	225	24.4	0.9

				CORRECTED RATIOS							CORRECTED AGES (Ma)						Best age (Ma)	±1s
Spot Name	**U (ppm)**	**Th (ppm)**	**Th/U**	**207Pb/206Pb**	**±1s**	**207Pb/235U**	**±1s**	**206Pb/238U**	**±1s**	**Rho**	**206Pb/238U**	**±1s**	**207Pb/235U**	**±1s**	**207Pb/206Pb**	**±1s**		
Sample: ROCA 24J-22																		
Zircon_22_033	3281.15	2982.64	0.85	0.04626	0.00181	0.01625	0.00073	0.00255	0.00003	0.29	16.4	0.2	16.4	0.7	11	75	16.4	0.2
Zircon_31_044	6773.18	3200.09	0.44	0.04616	0.00053	0.01673	0.00025	0.00263	0.00002	0.33	16.9	0.1	16.8	0.2	6	23	16.9	0.1
Zircon_21_032	1397.55	358.88	0.24	0.04624	0.0012	0.01735	0.00056	0.00272	0.00004	0.43	17.5	0.3	17.5	0.6	10	48	17.5	0.3
Zircon_37_051	2141.09	968.32	0.42	0.0488	0.00142	0.01946	0.00061	0.00289	0.00003	0.37	18.6	0.2	19.6	0.6	138	66	18.6	0.2
Zircon_4_011	744.92	394.17	0.49	0.04617	0.00181	0.01853	0.00081	0.00291	0.00004	0.29	18.7	0.3	18.6	0.8	6	79	18.7	0.3
Zircon_14_023	1439.07	586.53	0.38	0.05044	0.00185	0.02029	0.00084	0.00292	0.00003	0.3	18.8	0.2	20.4	0.8	215	82	18.8	0.2
Zircon_19_029	1242.20	1136.65	0.85	0.04977	0.00174	0.02029	0.00075	0.00295	0.00004	0.33	19	0.3	20.4	0.7	184	77	19	0.3
Zircon_6_014	1526.96	610.88	0.37	0.0478	0.00158	0.01945	0.00071	0.00295	0.00003	0.29	19	0.2	19.6	0.7	89	73	19	0.2
Zircon_12_021	623.14	233.83	0.35	0.04791	0.00258	0.0199	0.00114	0.00301	0.00004	0.19	19.4	0.3	20	1	95	114	19.4	0.3
Zircon_9_017	268.34	96.00	0.33	0.07083	0.00602	0.02916	0.00255	0.00302	0.00006	0.24	19.4	0.4	29	3	953	175	19.4	0.4
Zircon_17_027	1024.58	618.09	0.56	0.05173	0.00202	0.02182	0.00088	0.00305	0.00003	0.25	19.6	0.2	21.9	0.9	273	85	19.6	0.2
Zircon_36_050	1035.60	597.92	0.54	0.05091	0.00244	0.0213	0.00105	0.00304	0.00003	0.24	19.6	0.2	21	1	237	108	19.6	0.2
Zircon_7_015	489.27	154.70	0.30	0.0523	0.00314	0.02144	0.00136	0.00305	0.00006	0.32	19.6	0.4	22	1	299	135	19.6	0.4
Zircon_25_036	1614.30	578.16	0.33	0.05752	0.00748	0.02397	0.00313	0.00306	0.00003	0.09	19.7	0.2	24	3	512	278	19.7	0.2
Zircon_40_054	1566.22	579.29	0.35	0.04835	0.00182	0.02038	0.00084	0.00306	0.00003	0.31	19.7	0.2	20.5	0.8	116	83	19.7	0.2
Zircon_10_018	739.90	327.31	0.41	0.06199	0.01923	0.02632	0.00885	0.00308	0.00013	0.27	19.8	0.8	26	9	674	599	19.8	0.8
Zircon_13_022	563.79	379.28	0.63	0.05189	0.00441	0.02159	0.00186	0.00308	0.00004	0.16	19.8	0.3	22	2	281	185	19.8	0.3

Zircon_16_026	875.16	516.51	0.55	0.05021	0.00389	0.02126	0.00192	0.00307	0.00007	0.39	19.8	0.5	21	2	205	165	19.8	0.5
Zircon_27_039	931.37	358.32	0.36	0.04923	0.00182	0.02086	0.00081	0.00308	0.00003	0.31	19.8	0.2	21	0.8	159	81	19.8	0.2
Zircon_24_035	631.88	360.59	0.53	0.05132	0.00732	0.02187	0.00327	0.00309	0.00005	0.15	19.9	0.3	22	3	255	285	19.9	0.3
Zircon_28_040	773.10	376.84	0.46	0.05078	0.00203	0.0217	0.00092	0.00309	0.00004	0.33	19.9	0.3	21.8	0.9	231	88	19.9	0.3
Zircon_38_052	841.90	240.18	0.27	0.04963	0.00233	0.0208	0.00101	0.00309	0.00004	0.26	19.9	0.3	21	1	178	105	19.9	0.3
Zircon_3_010	515.37	244.56	0.44	0.05743	0.00327	0.02461	0.00144	0.00311	0.00004	0.23	20	0.3	25	1	508	120	20	0.3
Zircon_8_016	1384.61	834.48	0.56	0.04751	0.0019	0.02035	0.00086	0.00311	0.00004	0.32	20	0.3	20.5	0.9	75	86	20	0.3
Zircon_15_024	428.25	154.49	0.34	0.05229	0.00309	0.02241	0.00135	0.00313	0.00004	0.2	20.1	0.3	23	1	298	128	20.1	0.3
Zircon_20_030	1003.82	544.30	0.51	0.04842	0.00179	0.02078	0.0008	0.00312	0.00003	0.28	20.1	0.2	20.9	0.8	120	80	20.1	0.2
Zircon_5_012	1568.72	2116.35	1.26	0.04694	0.00197	0.02008	0.00087	0.00312	0.00003	0.25	20.1	0.2	20.2	0.9	46	88	20.1	0.2
Zircon_30_042	495.95	215.87	0.41	0.05159	0.00605	0.02229	0.00272	0.00313	0.00005	0.21	20.2	0.3	22	3	267	248	20.2	0.3
Zircon_26_038	625.39	348.51	0.52	0.05307	0.00234	0.02305	0.00106	0.00315	0.00004	0.28	20.3	0.3	23	1	332	95	20.3	0.3
Zircon_11_020	936.95	638.92	0.64	0.05109	0.00508	0.02235	0.00235	0.00317	0.00004	0.2	20.4	0.3	22	2	245	216	20.4	0.3
Zircon_2_009	557.64	371.08	0.62	0.04706	0.00245	0.02045	0.00113	0.00318	0.00006	0.34	20.5	0.4	21	1	52	105	20.5	0.4
Zircon_32_045	834.81	266.00	0.30	0.04729	0.00213	0.0208	0.00099	0.00318	0.00005	0.32	20.5	0.3	20.9	1	64	91	20.5	0.3
Zircon_34_047	541.41	205.35	0.35	0.0489	0.00304	0.02145	0.00143	0.00318	0.00005	0.25	20.5	0.3	22	1	143	136	20.5	0.3
Zircon_33_046	534.24	201.10	0.35	0.04726	0.00433	0.02101	0.00209	0.00322	0.00006	0.32	20.8	0.4	21	2	62	190	20.8	0.4
Zircon_29_041	702.45	234.63	0.31	0.05098	0.0027	0.02295	0.00125	0.00326	0.00004	0.23	21	0.3	23	1	240	115	21	0.3
Zircon_18_028	827.48	323.08	0.36	0.04992	0.00375	0.0228	0.00187	0.00331	0.00005	0.38	21.3	0.3	23	2	191	160	21.3	0.3
Zircon_23_034	702.17	521.78	0.69	0.04315	0.00475	0.01961	0.00217	0.00339	0.00005	0.11	21.8	0.3	20	2	-115	184	21.8	0.3
Zircon_24J-22_1_008	1098.61	491.75	0.42	0.04683	0.00197	0.02202	0.00095	0.00342	0.00003	0.22	22	0.2	22.1	0.9	41	83	22	0.2
Zircon_39_053	1105.59	1860.49	1.57	0.06004	0.00252	0.02959	0.00136	0.00354	0.00007	0.41	22.8	0.4	30	1	605	90	22.8	0.4
Zircon_35_048	86	62	0.67	0.09626	0.00221	1.2761	0.03147	0.09577	0.00085	0.37	590	5	835	14	1553	42	1553.0	42.0

				CORRECTED RATIOS							CORRECTED AGES (Ma)							
Spot Name	**U (ppm)**	**Th (ppm)**	**Th/U**	**207Pb/206Pb**	**±1s**	**207Pb/235U**	**±1s**	**206Pb/238U**	**±1s**	**Rho**	**206Pb/238U**	**±1s**	**207Pb/235U**	**±1s**	**207Pb/206Pb**	**±1s**	**Best age (Ma)**	**±1s**
Sample: ROCA 1J-1																		
Zircon_27_039	5993	1485	0.26	0.04613	0.00028	0.01604	0.00016	0.00252	0.00002	0.3	16.2	0.1	16.2	0.2	4	13	16.2	0.1
Zircon_31_044	3998	959	0.25	0.04658	0.00129	0.01661	0.00049	0.00259	0.00002	0.21	16.6	0.1	16.7	0.5	28	56	16.6	0.1
Zircon_07_015	4461	873	0.20	0.04612	0.00056	0.01663	0.00024	0.00261	0.00002	0.31	16.8	0.1	16.7	0.2	4	24	16.8	0.1
Zircon_11_020	4628	1728	0.39	0.04635	0.00105	0.01675	0.00042	0.00262	0.00002	0.26	16.9	0.1	16.9	0.4	16	44	16.9	0.1
Zircon_13_022	1409	419	0.31	0.05085	0.0029	0.01839	0.0011	0.00262	0.00002	0.24	16.9	0.1	19	1	234	126	16.9	0.1
Zircon_08_016	1295	857	0.69	0.05143	0.00305	0.01878	0.00122	0.00265	0.00003	0.27	17	0.2	19	1	260	131	17.0	0.2
Zircon_15_024	4655	1185	0.26	0.04845	0.00097	0.01772	0.00037	0.00266	0.00002	0.29	17.1	0.1	17.8	0.4	121	46	17.1	0.1
Zircon_17_027	1300	381	0.30	0.05142	0.00296	0.01925	0.00116	0.00271	0.00003	0.24	17.5	0.2	19	1	260	121	17.5	0.2
Zircon_32_Roca1j1_045	1631	584	0.37	0.04844	0.00214	0.01851	0.00095	0.00277	0.00004	0.41	17.8	0.3	18.6	0.9	121	97	17.8	0.3
Zircon_21_032	5882	2186	0.39	0.05234	0.00275	0.0202	0.00109	0.0028	0.00002	0.16	18	0.1	20	1	300	110	18.0	0.1
Zircon_06_014	2643	1271	0.50	0.05306	0.00281	0.02017	0.00108	0.00281	0.00002	0.15	18.1	0.1	20	1	331	118	18.1	0.1
Zircon_22_033	1755	636	0.38	0.04787	0.00149	0.01856	0.00064	0.00281	0.00003	0.27	18.1	0.2	18.7	0.6	93	65	18.1	0.2

Zircon_16_026	1207	390	0.34	0.05026	0.0026	0.01971	0.00108	0.00284	0.00003	0.27	18.3	0.2	20	1	207	109	18.3	0.2
Zircon_20_030	1084	567	0.54	0.04809	0.00181	0.0188	0.00075	0.00284	0.00002	0.21	18.3	0.1	18.9	0.7	103	79	18.3	0.1
Zircon_24_035	1506	324	0.22	0.04618	0.00265	0.01808	0.00108	0.00284	0.00002	0.19	18.3	0.1	18	1	7	112	18.3	0.1
Zircon_25_036	318	195	0.64	0.05597	0.01026	0.02199	0.00425	0.00285	0.00007	0.22	18.3	0.4	22	4	451	355	18.3	0.4
Zircon_14_023	371	255	0.71	0.07246	0.00598	0.02868	0.00251	0.00287	0.00004	0.21	18.5	0.3	29	2	999	168	18.5	0.3
Zircon_26_038	1798	428	0.25	0.04903	0.00188	0.01947	0.0008	0.00288	0.00003	0.32	18.5	0.2	19.6	0.8	149	82	18.5	0.2
Zircon_30_042	458	386	0.87	0.05396	0.00372	0.02143	0.00161	0.00288	0.00003	0.27	18.5	0.2	22	2	369	143	18.5	0.2
Zircon_19_029	345	180	0.54	0.04609	0.00413	0.01852	0.00166	0.00291	0.00006	0.25	18.8	0.4	19	2	2	173	18.8	0.4
Zircon_05_012	1231	1295	1.09	0.05152	0.00201	0.02075	0.00083	0.00295	0.00003	0.22	19	0.2	20.9	0.8	264	87	19.0	0.2
Zircon_04_011	174	276	1.64	0.0462	0.01021	0.01892	0.00452	0.00297	0.00007	0.17	19.1	0.5	19	5	8	349	19.1	0.5
Zircon_02_009	522	379	0.75	0.04875	0.00282	0.0202	0.00131	0.00301	0.00004	0.32	19.3	0.3	20	1	136	125	19.3	0.3
Zircon_03_010	374	295	0.82	0.05335	0.00315	0.02191	0.00132	0.00302	0.00004	0.2	19.4	0.3	22	1	344	131	19.4	0.3
Zircon_29_041	293	171	0.61	0.04621	0.00703	0.01945	0.0032	0.00305	0.00008	0.28	19.7	0.5	20	3	8	269	19.7	0.5
Zircon_23_034	2256	702	0.32	0.05146	0.00108	0.0218	0.00049	0.00309	0.00003	0.36	19.9	0.2	21.9	0.5	261	44	19.9	0.2
Zircon_12_021	496	454	0.95	0.06374	0.00357	0.02725	0.00155	0.00311	0.00003	0.17	20	0.2	27	2	733	117	20.0	0.2
Zircon_18_028	473	208	0.46	0.04616	0.00291	0.01975	0.00133	0.0031	0.00004	0.23	20	0.3	20	1	6	124	20.0	0.3
Zircon_01_Roca1j1_008	718	568	0.82	0.05596	0.00252	0.02387	0.0011	0.00312	0.00003	0.21	20.1	0.2	24	1	451	98	20.1	0.2
Zircon_09_017	1467	653	0.46	0.05631	0.00152	0.02486	0.00072	0.00324	0.00003	0.37	20.9	0.2	24.9	0.7	465	58	20.9	0.2
Zircon_10_018	450	254	0.58	0.06424	0.00373	0.02846	0.00169	0.00325	0.00004	0.21	20.9	0.3	28	2	750	121	20.9	0.3

				CORRECTED RATIOS							CORRECTED AGES (Ma)						Best age (Ma)	±1s
Spot Name	**U (ppm)**	**Th (ppm)**	**Th/U**	**207Pb/206Pb**	**±1s**	**207Pb/235U**	**±1s**	**206Pb/238U**	**±1s**	**Rho**	**206Pb/238U**	**±1s**	**207Pb/235U**	**±1s**	**207Pb/206Pb**	**±1s**		
Sample: PHC 09																		
Zircon_16_026	1557	1683	0.99	0.05593	0.00497	0.02038	0.00196	0.00264	0.00003	0.22	17	0.2	20	2	450	190	17.0	0.2
Zircon_28_040	694	217	0.29	0.05684	0.00728	0.02071	0.00277	0.00264	0.00006	0.2	17	0.4	21	3	485	293	17.0	0.4
Zircon_30_042	631	211	0.31	0.05102	0.00687	0.01906	0.00272	0.00271	0.00005	0.27	17.4	0.3	19	3	242	280	17.4	0.3
Zircon_20_030	1733	1631	0.87	0.05016	0.00271	0.01888	0.00114	0.00273	0.00003	0.23	17.6	0.2	19	1	202	118	17.6	0.2
Zircon_24_035	331	237	0.66	0.05353	0.00699	0.0202	0.00281	0.00274	0.00005	0.21	17.6	0.3	20	3	351	285	17.6	0.3
Zircon_31_044	1525	1271	0.77	0.04587	0.00197	0.01747	0.00077	0.00274	0.00003	0.23	17.6	0.2	17.6	0.8	-9	87	17.6	0.2
Zircon_08_016	779	754	0.89	0.04725	0.00312	0.01813	0.00122	0.00276	0.00003	0.2	17.8	0.2	18	1	62	137	17.8	0.2
Zircon_21_032	775	797	0.94	0.04628	0.0027	0.01765	0.00113	0.00277	0.00003	0.2	17.8	0.2	18	1	12	123	17.8	0.2
Zircon_22_033	371	307	0.76	0.04376	0.00569	0.01627	0.00214	0.00277	0.00005	0.15	17.8	0.3	16	2	-83	210	17.8	0.3
Zircon_29_041	383	263	0.63	0.05118	0.00533	0.01954	0.0022	0.00277	0.00005	0.2	17.8	0.3	20	2	249	236	17.8	0.3
Zircon_18_028	793	695	0.81	0.05607	0.00308	0.02134	0.0012	0.00279	0.00003	0.22	18	0.2	21	1	455	117	18.0	0.2
Zircon_23_034	980	813	0.76	0.05338	0.00383	0.0206	0.00161	0.0028	0.00003	0.29	18	0.2	21	2	345	163	18.0	0.2
Zircon_14_023	681	390	0.53	0.04324	0.00307	0.01633	0.00118	0.00281	0.00004	0.19	18.1	0.3	16	1	-110	147	18.1	0.3
Zircon_33_046	1683	1614	0.88	0.04949	0.00193	0.01918	0.00078	0.00281	0.00003	0.28	18.1	0.2	19.3	0.8	171	93	18.1	0.2
Zircon_17_027	548	394	0.66	0.06669	0.00465	0.02606	0.00203	0.00283	0.00004	0.37	18.2	0.3	26	2	828	139	18.2	0.3
Zircon_19_029	1038	669	0.59	0.05139	0.00298	0.02008	0.00127	0.00283	0.00003	0.22	18.2	0.2	20	1	258	127	18.2	0.2

Zircon_03_010	643	424	0.61	0.05053	0.00409	0.01971	0.00161	0.00285	0.00003	0.13	18.3	0.2	20	2	219	175	18.3	0.2
Zircon_06_014	1056	811	0.71	0.04733	0.00638	0.01859	0.00266	0.00285	0.00004	0.2	18.3	0.3	19	3	66	250	18.3	0.3
Zircon_07_015	1007	845	0.77	0.05167	0.00243	0.02016	0.00096	0.00285	0.00003	0.17	18.3	0.2	20.3	1	271	104	18.3	0.2
Zircon_13_022	916	646	0.65	0.04571	0.00265	0.01758	0.00104	0.00284	0.00003	0.2	18.3	0.2	18	1	-17	114	18.3	0.2
Zircon_02_009	1044	831	0.73	0.05474	0.0023	0.02139	0.00093	0.00286	0.00003	0.26	18.4	0.2	21.5	0.9	402	91	18.4	0.2
Zircon_26_038	234	123	0.49	-0.03909	-0.01094	-0.01492	-0.00419	0.00286	0.00006	0.08	18.4	0.4	-15.3	-4.3	-706	377	18.4	0.4
Zircon_09_017	614	489	0.73	0.05824	0.00344	0.02297	0.0014	0.00287	0.00005	0.25	18.5	0.3	23	1	539	124	18.5	0.3
Zircon_12_021	806	669	0.76	0.04929	0.02792	0.01962	0.01238	0.00289	0.00014	0.26	18.6	0.9	20	12	162	897	18.6	0.9
Zircon_05_012	383	294	0.70	0.0461	0.00237	0.01857	0.00102	0.00292	0.00005	0.18	18.8	0.3	19	1	3	102	18.8	0.3
Zircon_10_018	578	384	0.61	0.06021	0.00349	0.02389	0.00143	0.00292	0.00004	0.25	18.8	0.3	24	1	611	120	18.8	0.3
Zircon_01_PHC09B_008	493	296	0.55	0.05805	0.00521	0.02357	0.00223	0.00295	0.00005	0.25	19	0.3	24	2	532	193	19.0	0.3
Zircon_15_024	671	504	0.69	0.05518	0.00536	0.02256	0.00238	0.00296	0.00005	0.24	19.1	0.3	23	2	420	208	19.1	0.3
Zircon_27_039	238	175	0.68	0.04644	0.00658	0.01902	0.00294	0.00297	0.00008	0.19	19.1	0.5	19	3	21	256	19.1	0.5
Zircon_25_036	443	251	0.52	0.07571	0.00757	0.03201	0.00326	0.00299	0.00006	0.19	19.2	0.4	32	3	1087	208	19.2	0.4
Zircon_11_020	211	145	0.63	0.06265	0.01065	0.02641	0.00454	0.00303	0.00008	0.15	19.5	0.5	26	4	696	359	19.5	0.5
Zircon_32_045	188	118	0.58	0.07345	0.01175	0.03216	0.00522	0.00313	0.00009	0.17	20.1	0.6	32	5	1026	372	20.1	0.6
Zircon_04_011	323	190	0.54	0.04921	0.01071	0.02144	0.00485	0.00316	0.00008	0.26	20.3	0.5	22	5	158	370	20.3	0.5

				CORRECTED RATIOS							CORRECTED AGES (Ma)						Best age (Ma)	±1s
Spot Name	**U (ppm)**	**Th (ppm)**	**Th/U**	**207Pb/206Pb**	**±1s**	**207Pb/235U**	**±1s**	**206Pb/238U**	**±1s**	**Rho**	**206Pb/238U**	**±1s**	**207Pb/235U**	**±1s**	**207Pb/206Pb**	**±1s**		
Sample: ROCA 22J-1																		
Zircon_43_058	2540	536	0.22	0.04719	0.00245	0.01447	0.00078	0.00222	0.00002	0.18	14.3	0.1	14.6	0.8	59	109	14	0.1
Zircon_49_065	1823	1487	0.85	0.0666	0.01329	0.02167	0.00463	0.00236	0.00006	0.24	15.2	0.4	22	5	825	425	15	0.4
Zircon_54_071	2053	960	0.49	0.04838	0.00476	0.01578	0.00166	0.00237	0.00003	0.29	15.2	0.2	16	2	118	209	15	0.2
Zircon_55_072	2170	622	0.30	0.05924	0.01148	0.01975	0.00406	0.00242	0.00006	0.3	15.6	0.4	20	4	576	400	16	0.4
Zircon_37_051	768	766	1.03	0.06331	0.00911	0.02124	0.00331	0.00243	0.00005	0.28	15.7	0.3	21	3	719	306	16	0.3
Zircon_44_059	1671	1110	0.69	0.04937	0.00422	0.01674	0.00157	0.00246	0.00004	0.25	15.8	0.3	17	2	165	182	16	0.3
Zircon_52_069	1717	738	0.45	0.0461	0.01014	0.01573	0.00372	0.00248	0.00007	0.23	15.9	0.5	16	4	3	352	16	0.5
Zircon_57_075	851	702	0.86	0.04873	0.00622	0.01655	0.00226	0.00246	0.00004	0.3	15.9	0.3	17	2	135	246	16	0.3
Zircon_56_074	580	549	0.98	0.04737	0.00699	0.01612	0.00255	0.00247	0.00005	0.28	15.9	0.4	16	3	68	267	16	0.4
Zircon_35_048	1097	838	0.79	0.07036	0.02402	0.02418	0.00916	0.00249	0.00012	0.32	16	0.8	24	9	939	678	16	0.8
Zircon_45_060	833	449	0.56	0.06663	0.00876	0.02311	0.00332	0.00251	0.00006	0.42	16.2	0.4	23	3	826	274	16	0.4
Zircon_42_057	1207	752	0.65	0.0635	0.00814	0.02231	0.00303	0.00255	0.00004	0.23	16.4	0.2	22	3	725	271	16	0.2
Zircon_46_062	607	503	0.86	0.06048	0.02819	0.02156	0.01132	0.00258	0.00014	0.38	16.6	0.9	22	11	621	863	17	0.9
Zircon_38_052	248	224	0.94	0.05652	0.00677	0.02067	0.00262	0.00265	0.00005	0.18	17.1	0.3	21	3	473	258	17	0.3
Zircon_51_068	365	233	0.66	0.06045	0.00699	0.02283	0.0028	0.00274	0.00005	0.22	17.6	0.3	23	3	620	246	18	0.3
Zircon_39_053	466	810	1.81	0.18078	0.00998	0.07664	0.00529	0.00307	0.00007	0.36	19.8	0.5	75	5	2660	90	19.8	0.5

				CORRECTED RATIOS							CORRECTED AGES (Ma)						Best age (Ma)	±1s
Spot Name	U (ppm)	Th (ppm)	Th/U	207Pb/206Pb	±1s	207Pb/235U	±1s	206Pb/238U	±1s	Rho	206Pb/238U	±1s	207Pb/235U	±1s	207Pb/206Pb	±1s		
Sample: BEKL 6D-1																		
Zircon_24_035	2024	90	0.04	0.05413	0.00193	0.01576	0.00059	0.00211	0.00002	0.29	13.6	0.1	15.9	0.6	377	77	13.6	0.1
Zircon_32_045	1950	867	0.41	0.05036	0.00196	0.01522	0.00061	0.0022	0.00002	0.24	14.2	0.1	15.3	0.6	212	86	14.2	0.1
Zircon_02_009	818	476	0.54	0.05982	0.00329	0.01856	0.00105	0.00224	0.00003	0.23	14.4	0.2	19	1	597	117	14.4	0.2
Zircon_06_014	985	544	0.51	0.0574	0.00287	0.01763	0.00091	0.00224	0.00003	0.25	14.4	0.2	17.7	0.9	507	108	14.4	0.2
Zircon_08_016	1367	425	0.29	0.05522	0.00243	0.01705	0.00077	0.00227	0.00002	0.23	14.6	0.1	17.2	0.8	421	96	14.6	0.1
Zircon_15_024	359	301	0.78	0.07082	0.00739	0.02232	0.00251	0.00229	0.00006	0.22	14.7	0.4	22	2	952	206	14.7	0.4
Zircon_16_026	344	280	0.76	0.06215	0.01089	0.0198	0.00366	0.00231	0.00006	0.15	14.9	0.4	20	4	679	357	14.9	0.4
Zircon_19_029	822	440	0.50	0.06107	0.00497	0.01958	0.00164	0.00233	0.00003	0.14	15	0.2	20	2	642	166	15.0	0.2
Zircon_01_6d1a_008	716	394	0.51	0.06606	0.00377	0.02086	0.00122	0.00234	0.00003	0.22	15.1	0.2	21	1	808	118	15.1	0.2
Zircon_07_015	272	235	0.80	0.07012	0.01015	0.02266	0.00345	0.00234	0.00005	0.14	15.1	0.3	23	3	932	310	15.1	0.3
Zircon_22_033	386	352	0.85	0.07402	0.00888	0.02353	0.00286	0.00235	0.00004	0.16	15.1	0.3	24	3	1042	236	15.1	0.3
Zircon_12_021	288	267	0.86	0.06656	0.00632	0.02089	0.00205	0.00236	0.00006	0.25	15.2	0.4	21	2	824	190	15.2	0.4
Zircon_33_046	399	246	0.57	0.07563	0.00879	0.02469	0.00298	0.00237	0.00004	0.16	15.2	0.3	25	3	1085	229	15.2	0.3
Zircon_04_011	434	297	0.64	0.08968	0.01076	0.02887	0.00349	0.00237	0.00004	0.12	15.3	0.3	29	3	1419	234	15.3	0.3
Zircon_13_022	334	293	0.81	0.05604	0.00616	0.01738	0.00194	0.00237	0.00005	0.17	15.3	0.3	17	2	454	226	15.3	0.3
Zircon_09_017	287	263	0.85	0.08148	0.0057	0.0261	0.00193	0.00239	0.00006	0.32	15.4	0.4	26	2	1233	136	15.4	0.4
Zircon_11_020	335	298	0.83	0.07811	0.0068	0.02525	0.00226	0.00239	0.00005	0.23	15.4	0.3	25	2	1150	165	15.4	0.3
Zircon_21_032	295	239	0.75	0.0847	0.01186	0.02622	0.00372	0.00239	0.00005	0.16	15.4	0.3	26	4	1309	270	15.4	0.3
Zircon_28_040	347	317	0.85	0.06032	0.00513	0.01942	0.00169	0.00239	0.00004	0.21	15.4	0.3	20	2	615	178	15.4	0.3
Zircon_20_030	490	440	0.84	0.06777	0.00583	0.02226	0.00196	0.00241	0.00004	0.21	15.5	0.3	22	2	862	171	15.5	0.3
Zircon_23_034	354	196	0.51	0.0695	0.00542	0.02287	0.00182	0.00241	0.00004	0.2	15.5	0.3	23	2	914	152	15.5	0.3
Zircon_17_027	241	212	0.82	0.09005	0.009	0.02912	0.00298	0.00242	0.00005	0.22	15.6	0.3	29	3	1427	183	15.6	0.3
Zircon_26_038	363	214	0.55	0.06012	0.01025	0.02002	0.00365	0.00242	0.00005	0.17	15.6	0.3	20	4	608	352	15.6	0.3
Zircon_31_044	337	207	0.57	0.0555	0.00567	0.0185	0.00203	0.00242	0.00005	0.19	15.6	0.3	19	2	433	219	15.6	0.3
Zircon_18_028	287	232	0.75	0.07292	0.00943	0.02473	0.00341	0.00246	0.00006	0.2	15.8	0.4	25	3	1012	258	15.8	0.4
Zircon_03_010	341	251	0.68	0.08343	0.00918	0.02796	0.00312	0.00247	0.00004	0.17	15.9	0.3	28	3	1279	218	15.9	0.3
Zircon_05_012	343	305	0.83	0.08367	0.00837	0.02739	0.00279	0.00248	0.00005	0.19	16	0.3	27	3	1285	196	16.0	0.3
Zircon_27_039	300	227	0.70	0.07112	0.00853	0.02335	0.00285	0.00248	0.00006	0.19	16	0.4	23	3	961	241	16.0	0.4
Zircon_30_042	335	179	0.50	0.07798	0.0078	0.02642	0.00268	0.00248	0.00004	0.17	16	0.3	26	3	1146	194	16.0	0.3
Zircon_10_018	322	285	0.82	0.10903	0.01121	0.03735	0.00434	0.00248	0.00008	0.35	16	0.5	37	4	1783	183	16.0	0.5
Zircon_14_023	213	124	0.54	0.06497	0.00808	0.02236	0.00299	0.0025	0.00007	0.27	16.1	0.4	22	3	773	249	16.1	0.4
Zircon_29_041	265	199	0.70	0.08683	0.0066	0.0296	0.0023	0.0025	0.00004	0.21	16.1	0.3	30	2	1357	141	16.1	0.3
Zircon_25_036	233	150	0.60	0.06919	0.00844	0.02449	0.00334	0.00257	0.00009	0.29	16.5	0.6	25	3	904	248	16.5	0.6

				CORRECTED RATIOS							CORRECTED AGES (Ma)						Best age (Ma)	±1s
Spot Name	U (ppm)	Th (ppm)	Th/U	207Pb/206Pb	±1s	207Pb/235U	±1s	206Pb/238U	±1s	Rho	206Pb/238U	±1s	207Pb/235U	±1s	207Pb/206Pb	±1s		
Sample: BEKL 6D-2																		
Zircon_28_040	475	213	0.41	0.06658	0.00498	0.02024	0.00162	0.0022	0.00003	0.24	14.2	0.2	20	2	825	151	14	0.20
Zircon_39_053	401	329	0.75	0.07291	0.00664	0.02139	0.00199	0.0022	0.00004	0.2	14.2	0.3	21	2	1011	175	14	0.30
Zircon_30_042	448	197	0.40	0.06323	0.00563	0.01942	0.00182	0.00223	0.00004	0.17	14.3	0.3	20	2	716	184	14	0.30
Zircon_38_052	556	491	0.81	0.06172	0.00463	0.01894	0.00145	0.00222	0.00003	0.2	14.3	0.2	19	1	664	152	14	0.20
Zircon_01_6d2a_008	501	221	0.41	0.06595	0.00873	0.02032	0.00283	0.00223	0.00004	0.18	14.4	0.3	20	3	805	274	14	0.30
Zircon_37_051	286	189	0.61	0.06045	0.00592	0.0177	0.00179	0.00224	0.00005	0.25	14.4	0.3	18	2	620	201	14	0.30
Zircon_03_010	482	200	0.38	0.06063	0.00505	0.01891	0.00171	0.00226	0.00004	0.25	14.6	0.3	19	2	626	176	15	0.30
Zircon_13_022	497	399	0.74	0.07821	0.0086	0.0242	0.00271	0.00227	0.00005	0.19	14.6	0.3	24	3	1152	225	15	0.30
Zircon_17_027	400	176	0.40	0.07464	0.01199	0.02327	0.00404	0.00226	0.00005	0.31	14.6	0.3	23	4	1059	343	15	0.30
Zircon_22_033	317	117	0.34	0.06305	0.00726	0.01987	0.00237	0.00229	0.00004	0.2	14.7	0.2	20	2	710	252	15	0.20
Zircon_04_011	356	142	0.37	0.06065	0.0086	0.01919	0.00288	0.00229	0.00006	0.2	14.8	0.4	19	3	627	298	15	0.40
Zircon_12_021	270	198	0.67	0.07543	0.00905	0.02256	0.00276	0.0023	0.00006	0.2	14.8	0.4	23	3	1080	249	15	0.40
Zircon_29_041	307	116	0.35	0.06807	0.00689	0.02152	0.00227	0.00229	0.00004	0.17	14.8	0.3	22	2	871	205	15	0.30
Zircon_35_048	510	223	0.40	0.06461	0.00561	0.02047	0.0019	0.0023	0.00004	0.23	14.8	0.3	21	2	762	178	15	0.30
Zircon_11_020	460	180	0.36	0.0592	0.00522	0.01883	0.00176	0.00231	0.00004	0.26	14.9	0.2	19	2	574	196	15	0.20
Zircon_20_030	237	166	0.64	0.06659	0.01102	0.02123	0.00368	0.00231	0.00005	0.17	14.9	0.3	21	4	825	365	15	0.30
Zircon_27_039	299	134	0.41	0.06393	0.00959	0.01962	0.00297	0.00231	0.00005	0.13	14.9	0.3	20	3	739	317	15	0.30
Zircon_14_023	275	119	0.40	0.06671	0.00968	0.02124	0.00329	0.00231	0.00006	0.23	14.9	0.4	21	3	829	292	15	0.40
Zircon_16_026	462	305	0.61	0.06762	0.00676	0.02123	0.00216	0.00233	0.00005	0.19	15	0.3	21	2	857	213	15	0.30
Zircon_21_032	312	132	0.39	0.08175	0.01045	0.02621	0.00363	0.00233	0.00007	0.29	15	0.4	26	4	1240	260	15	0.40
Zircon_33_046	435	292	0.62	0.05371	0.0066	0.01727	0.00227	0.00233	0.00004	0.27	15	0.3	17	2	359	262	15	0.30
Zircon_07_015	296	197	0.61	0.06522	0.00958	0.02113	0.00325	0.00235	0.00006	0.14	15.1	0.4	21	3	782	308	15	0.40
Zircon_18_028	414	165	0.37	0.08012	0.01086	0.0259	0.00363	0.00234	0.00005	0.18	15.1	0.3	26	4	1200	279	15	0.30
Zircon_31_044	374	151	0.37	0.04607	0.00214	0.01489	0.00077	0.00234	0.00004	0.16	15.1	0.3	15	0.8	1	90	15	0.30
Zircon_32_045	329	210	0.59	0.05009	0.0074	0.01619	0.00252	0.00234	0.00005	0.26	15.1	0.3	16	3	199	278	15	0.30
Zircon_02_009	322	135	0.39	0.0745	0.00978	0.0242	0.00335	0.00236	0.00005	0.2	15.2	0.3	24	3	1055	268	15	0.30
Zircon_24_035	191	154	0.74	0.07284	0.01245	0.02369	0.00432	0.00236	0.00008	0.2	15.2	0.5	24	4	1010	354	15	0.50
Zircon_34_047	390	163	0.38	0.07037	0.00464	0.02298	0.00157	0.00238	0.00004	0.26	15.3	0.3	23	2	939	130	15	0.30
Zircon_10_018	189	75	0.37	0.11527	0.01844	0.03639	0.00588	0.00238	0.00005	0.14	15.3	0.3	36	6	1884	280	15	0.30
Zircon_06_014	298	112	0.35	0.0602	0.01087	0.0199	0.00375	0.0024	0.00006	0.18	15.4	0.4	20	4	611	380	15	0.40
Zircon_15_024	706	268	0.35	0.05875	0.00407	0.01934	0.00147	0.00239	0.00005	0.28	15.4	0.3	19	1	558	153	15	0.30
Zircon_23_034	491	262	0.49	0.08768	0.01578	0.03226	0.00585	0.0024	0.00005	0.12	15.5	0.3	32	6	1375	373	16	0.30
Zircon_25_036	393	158	0.37	0.06638	0.00812	0.02226	0.00286	0.00243	0.00004	0.22	15.7	0.3	22	3	818	252	16	0.30
Zircon_19_029	134	75	0.51	0.05981	0.01077	0.01909	0.0035	0.0025	0.00009	0.19	16.1	0.6	19	3	597	389	16	0.60
Zircon_36_050	159	64	0.37	0.09187	0.02526	0.03222	0.00898	0.00254	0.00006	0.09	16.4	0.4	32	9	1465	533	16	0.40
Zircon_09_017	124	56	0.41	0.0605	0.01452	0.02016	0.00487	0.00258	0.00007	0.11	16.6	0.5	20	5	622	481	17	0.50

Zircon_08_016	137	85	0.57	0.11294	0.01073	0.03996	0.00397	0.00263	0.00008	0.29	16.9	0.5	40	4	1847	170	17	0.50
Zircon_26_038	127	74	0.53	0.15873	0.02063	0.05486	0.0076	0.00277	0.00013	0.35	17.8	0.8	54	7	2442	217	18	0.80

				CORRECTED RATIOS							CORRECTED AGES (Ma)						Best age (Ma)	±1s
Spot Name	**U (ppm)**	**Th (ppm)**	**Th/U**	**207Pb/206Pb**	**±1s**	**207Pb/235U**	**±1s**	**206Pb/238U**	**±1s**	**Rho**	**206Pb/238U**	**±1s**	**207Pb/235U**	**±1s**	**207Pb/206Pb**	**±1s**		
Sample: BEKL 10D-1																		
Zircon_15_024	2539	467	0.17	0.05064	0.00309	0.01314	0.00083	0.00191	0.00003	0.26	12.3	0.2	13.3	0.8	224	139	12	0.200
Zircon_03_010	927	741	0.73	0.05433	0.00478	0.01489	0.00132	0.00202	0.00002	0.12	13	0.1	15	1	385	189	13	0.100
Zircon_10_018	624	356	0.52	0.06289	0.00631	0.01752	0.0018	0.00202	0.00003	0.18	13	0.2	18	2	705	220	13	0.200
Zircon_06_014	323	173	0.49	0.06387	0.01011	0.01804	0.00306	0.00205	0.00008	0.3	13.2	0.5	18	3	737	351	13	0.500
Zircon_08_016	959	796	0.76	0.05869	0.00299	0.01653	0.00087	0.00205	0.00002	0.26	13.2	0.1	16.6	0.9	556	112	13	0.100
Zircon_25_036	1391	961	0.63	0.05305	0.00202	0.01486	0.00059	0.00205	0.00002	0.29	13.2	0.1	15	0.6	331	77	13	0.100
Zircon_37_051	483	283	0.54	0.0615	0.00473	0.0174	0.00141	0.00205	0.00003	0.23	13.2	0.2	18	1	657	170	13	0.200
Zircon_21_032	1062	309	0.27	0.05563	0.00267	0.01581	0.00083	0.00206	0.00003	0.31	13.3	0.2	15.9	0.8	438	95	13	0.200
Zircon_17_027	273	117	0.39	0.08206	0.00957	0.02346	0.00286	0.00207	0.00006	0.26	13.4	0.4	24	3	1247	237	13	0.400
Zircon_24_035	768	460	0.55	0.05888	0.00403	0.01686	0.00125	0.00208	0.00003	0.26	13.4	0.2	17	1	563	134	13	0.200
Zircon_11_020	1805	1429	0.72	0.0578	0.00272	0.01669	0.00081	0.0021	0.00002	0.25	13.5	0.1	16.8	0.8	522	104	14	0.100
Zircon_01_10d1a_008	645	394	0.56	0.06983	0.00454	0.01992	0.00133	0.00211	0.00003	0.23	13.6	0.2	20	1	923	127	14	0.200
Zircon_19_029	586	390	0.61	0.0496	0.00428	0.01447	0.00133	0.00212	0.00004	0.23	13.6	0.3	15	1	176	194	14	0.300
Zircon_16_026	512	278	0.50	0.0691	0.00661	0.02024	0.00202	0.00212	0.00004	0.22	13.7	0.3	20	2	902	203	14	0.300
Zircon_28_040	536	305	0.52	0.05238	0.00467	0.01534	0.00153	0.00212	0.00005	0.33	13.7	0.3	15	2	302	179	14	0.300
Zircon_32_045	1043	963	0.85	0.0611	0.00324	0.01769	0.00096	0.00212	0.00002	0.22	13.7	0.1	17.8	1	643	102	14	0.100
Zircon_09_017	528	309	0.54	0.06767	0.00649	0.01994	0.00198	0.00214	0.00004	0.18	13.8	0.3	20	2	859	205	14	0.300
Zircon_13_022	425	209	0.45	0.08329	0.00791	0.02418	0.00234	0.00216	0.00004	0.19	13.9	0.3	24	2	1276	190	14	0.300
Zircon_35_048	397	343	0.79	0.06365	0.00657	0.01896	0.00207	0.00216	0.00004	0.19	13.9	0.3	19	2	730	227	14	0.300
Zircon_12_021	532	319	0.55	0.07559	0.00658	0.02276	0.00201	0.00218	0.00003	0.17	14	0.2	23	2	1084	178	14	0.200
Zircon_27_039	565	370	0.60	0.06552	0.00413	0.01914	0.00125	0.00217	0.00004	0.26	14	0.3	19	1	791	118	14	0.300
Zircon_29_041	677	438	0.59	0.06342	0.00445	0.01896	0.00148	0.00217	0.00004	0.29	14	0.3	19	1	722	134	14	0.300
Zircon_23_034	498	298	0.55	0.0763	0.00519	0.02304	0.00162	0.00221	0.00004	0.25	14.2	0.3	23	2	1103	122	14	0.300
Zircon_38_052	546	341	0.57	0.06667	0.00527	0.01975	0.00159	0.00221	0.00004	0.19	14.2	0.3	20	2	827	169	14	0.300
Zircon_22_033	437	275	0.58	0.06262	0.0047	0.01886	0.00147	0.00222	0.00005	0.27	14.3	0.3	19	1	695	144	14	0.300
Zircon_33_046	478	281	0.54	0.07269	0.0072	0.02217	0.00222	0.00222	0.00004	0.15	14.3	0.3	22	2	1005	183	14	0.300
Zircon_34_047	260	136	0.48	0.0718	0.00929	0.02203	0.00298	0.00223	0.00005	0.23	14.3	0.3	22	3	980	277	14	0.300
Zircon_36_050	414	237	0.52	0.07517	0.00594	0.02253	0.00183	0.00222	0.00004	0.23	14.3	0.3	23	2	1073	163	14	0.300
Zircon_05_012	408	194	0.44	0.08803	0.00748	0.0262	0.00231	0.00223	0.00005	0.27	14.4	0.3	26	2	1383	157	14	0.300
Zircon_20_030	652	378	0.53	0.06515	0.00365	0.01992	0.00117	0.00223	0.00004	0.3	14.4	0.3	20	1	779	119	14	0.300
Zircon_30_042	622	307	0.45	0.06363	0.00573	0.01933	0.00176	0.00223	0.00003	0.15	14.4	0.2	19	2	729	173	14	0.200
Zircon_04_011	312	189	0.56	0.07812	0.0122	0.02424	0.00399	0.00225	0.00005	0.23	14.5	0.3	24	4	1150	308	15	0.300
Zircon_07_015	396	217	0.50	0.07227	0.00904	0.02266	0.00296	0.00227	0.00004	0.2	14.6	0.3	23	3	994	248	15	0.300

Zircon_31_044	351	242	0.63	0.09918	0.00734	0.03016	0.00235	0.00226	0.00005	0.31	14.6	0.3	30	2	1609	124	15	0.300
Zircon_18_028	301	200	0.61	0.07057	0.00764	0.02242	0.00254	0.0023	0.00005	0.21	14.8	0.3	23	3	945	229	15	0.300

				CORRECTED RATIOS							CORRECTED AGES (Ma)						Best age (Ma)	±1s
Spot Name	**U (ppm)**	**Th (ppm)**	**Th/U**	**207Pb/206Pb**	**±1s**	**207Pb/235U**	**±1s**	**206Pb/238U**	**±1s**	**Rho**	**206Pb/238U**	**±1s**	**207Pb/235U**	**±1s**	**207Pb/206Pb**	**±1s**		
Sample: BEKL 10D-3																		
Zircon_24_035	1286	551	0.39	0.073	0.00669	0.01893	0.00186	0.00188	0.00003	0.23	12.1	0.2	19	2	1014	183	12.1	0.2
Zircon_23_034	1667	750	0.41	0.07137	0.00435	0.01936	0.00128	0.00197	0.00002	0.33	12.7	0.1	19	1	968	121	12.7	0.1
Zircon_26_038	1323	1238	0.86	0.06776	0.00379	0.01822	0.00104	0.00197	0.00002	0.2	12.7	0.1	18	1	861	113	12.7	0.1
Zircon_09_017	1194	673	0.52	0.06223	0.00384	0.0174	0.00112	0.00203	0.00002	0.2	13.1	0.1	18	1	682	127	13.1	0.1
Zircon_04_011	668	374	0.51	0.0552	0.00777	0.01559	0.00229	0.00205	0.00004	0.25	13.2	0.3	16	2	420	291	13.2	0.3
Zircon_02_009	1032	701	0.63	0.0644	0.00374	0.01833	0.00109	0.00207	0.00002	0.22	13.3	0.1	18	1	755	118	13.3	0.1
Zircon_37_051	1225	1279	0.96	0.06032	0.0029	0.01714	0.00084	0.00207	0.00002	0.19	13.3	0.1	17.3	0.8	615	101	13.3	0.1
Zircon_39_053	1375	1445	0.97	0.05915	0.00349	0.01661	0.001	0.00206	0.00002	0.2	13.3	0.1	16.7	1	573	126	13.3	0.1
Zircon_21_032	444	254	0.53	0.08072	0.01023	0.02308	0.00306	0.00207	0.00004	0.17	13.4	0.3	23	3	1215	249	13.4	0.3
Zircon_01_10d3a_008	484	278	0.53	0.06023	0.00705	0.01746	0.00221	0.0021	0.00004	0.28	13.5	0.3	18	2	612	241	13.5	0.3
Zircon_17_027	618	415	0.62	0.06906	0.00476	0.0198	0.0014	0.0021	0.00003	0.22	13.5	0.2	20	1	901	139	13.5	0.2
Zircon_20_030	298	206	0.64	0.09255	0.01265	0.0267	0.00394	0.00209	0.00006	0.24	13.5	0.4	27	4	1479	239	13.5	0.4
Zircon_25_036	944	626	0.61	0.06379	0.00625	0.01842	0.00182	0.0021	0.00003	0.13	13.5	0.2	19	2	735	204	13.5	0.2
Zircon_31_044	725	558	0.71	0.0684	0.00547	0.01925	0.00156	0.0021	0.00003	0.16	13.5	0.2	19	2	881	163	13.5	0.2
Zircon_38_052	638	395	0.57	0.07632	0.00763	0.02136	0.00216	0.0021	0.00003	0.15	13.5	0.2	21	2	1103	199	13.5	0.2
Zircon_19_029	470	275	0.54	0.0765	0.00995	0.02164	0.00283	0.00211	0.00003	0.1	13.6	0.2	22	3	1108	260	13.6	0.2
Zircon_11_020	780	614	0.72	0.05577	0.00419	0.01631	0.00135	0.00212	0.00003	0.3	13.7	0.2	16	1	443	161	13.7	0.2
Zircon_36_050	618	398	0.59	0.01665	0.005	0.00492	0.00148	0.00214	0.00004	0.06	13.8	0.3	5	1	-940	270	13.8	0.3
Zircon_03_010	518	332	0.59	0.07033	0.00549	0.02032	0.00161	0.00216	0.00003	0.17	13.9	0.2	20	2	938	156	13.9	0.2
Zircon_18_028	528	279	0.49	0.07997	0.00768	0.02396	0.00233	0.00216	0.00003	0.16	13.9	0.2	24	2	1196	186	13.9	0.2
Zircon_29_041	399	231	0.53	0.08814	0.0093	0.02621	0.00298	0.00216	0.00005	0.32	13.9	0.3	26	3	1386	202	13.9	0.3
Zircon_08_016	446	261	0.54	0.07346	0.00859	0.02209	0.00274	0.00218	0.00004	0.25	14	0.3	22	3	1027	236	14.0	0.3
Zircon_32_045	719	489	0.63	0.07063	0.00848	0.02109	0.00256	0.00218	0.00004	0.15	14	0.3	21	3	947	247	14.0	0.3
Zircon_15_024	550	350	0.59	0.05927	0.00492	0.01734	0.00147	0.00219	0.00004	0.2	14.1	0.3	17	1	577	177	14.1	0.3
Zircon_16_026	579	405	0.64	0.06638	0.00866	0.01997	0.00277	0.00218	0.00004	0.17	14.1	0.3	20	3	818	272	14.1	0.3
Zircon_13_022	568	320	0.52	0.08205	0.00738	0.02426	0.00222	0.00221	0.00004	0.18	14.2	0.3	24	2	1247	172	14.2	0.3
Zircon_06_014	199	87	0.40	0.10124	0.01166	0.03147	0.00374	0.00225	0.00005	0.19	14.5	0.3	31	4	1647	212	14.5	0.3
Zircon_22_033	514	297	0.53	0.08065	0.00606	0.02524	0.00205	0.00227	0.00003	0.25	14.6	0.2	25	2	1213	145	14.6	0.2
Zircon_30_042	693	530	0.70	0.06532	0.007	0.02038	0.00235	0.00226	0.00004	0.23	14.6	0.3	20	2	785	225	14.6	0.3
Zircon_28_040	949	674	0.65	0.0595	0.00404	0.01871	0.00135	0.00228	0.00003	0.24	14.7	0.2	19	1	585	145	14.7	0.2
Zircon_33_046	324	164	0.47	0.08902	0.00801	0.02758	0.00256	0.0023	0.00005	0.25	14.8	0.3	28	3	1405	170	14.8	0.3
Zircon_27_039	525	311	0.55	0.07841	0.00688	0.02502	0.00232	0.00231	0.00003	0.19	14.9	0.2	25	2	1157	171	14.9	0.2
Zircon_35_048	440	258	0.54	0.10303	0.01067	0.03291	0.00368	0.00232	0.00006	0.29	14.9	0.4	33	4	1679	190	14.9	0.4

Zircon_14_023	686	513	0.69	0.07012	0.00526	0.02215	0.0017	0.00233	0.00004	0.21	15	0.3	22	2	932	149	15.0	0.3
Zircon_34_047	570	311	0.50	0.06704	0.00416	0.02165	0.00138	0.00238	0.00004	0.23	15.3	0.3	22	1	839	127	15.3	0.3
Zircon_12_021	249	150	0.56	0.05276	0.00795	0.01743	0.00282	0.0024	0.00008	0.27	15.4	0.5	18	3	318	305	15.4	0.5
Zircon_40_054	294	195	0.61	0.07537	0.01581	0.02505	0.00554	0.00241	0.00008	0.19	15.5	0.5	25	5	1078	406	15.5	0.5
Zircon_07_015	134	63	0.43	0.11491	0.02183	0.03553	0.00687	0.00253	0.00009	0.19	16.3	0.6	35	7	1878	368	16.3	0.6
Zircon_05_012	144	69	0.44	0.14369	0.01724	0.04576	0.00567	0.00242	0.00007	0.25	15.6	0.5	45	6	2272	206	15.6	0.5

				CORRECTED RATIOS							CORRECTED AGES (Ma)						Best age (Ma)	±2s
Spot Name	**U (ppm)**	**Th (ppm)**	**Th/U**	**207Pb/206Pb**	**±2s**	**207Pb/235U**	**±2s**	**206Pb/238U**	**±2s**	**Rho**	**206Pb/238U**	**±2s**	**207Pb/235U**	**±2s**	**207Pb/206Pb**	**±2s**		
Sample: Oro 1																		
Zircon_017	335	69	0.20	0.069	0.026	0.029	0.014	0.00307	0.00013	0.09	19.78	0.86	29	13	990	250	19.78	0.86
Zircon_010	312	114	0.37	0.043	0.012	0.0209	0.0047	0.003113	0.000094	0.13	20.04	0.6	20.8	4.7	1090	330	20.04	0.6
Zircon_015	89	47	0.53	0.115	0.041	0.047	0.022	0.00324	0.00023	0.15	20.8	1.5	45	21	2460	230	20.8	1.5
Zircon_019	377	230	0.61	0.056	0.013	0.0263	0.0058	0.00324	0.00011	0.15	20.85	0.72	26.2	5.7	1010	210	20.85	0.72
Zircon_028	383	344	0.90	0.067	0.016	0.03	0.0076	0.00325	0.00012	0.15	20.91	0.77	29.9	7.3	920	250	20.91	0.77
Zircon_014	147	74	0.50	0.066	0.032	0.031	0.015	0.00325	0.00013	0.08	20.94	0.82	30	14	2170	240	20.94	0.82
Zircon_008	324	123	0.38	0.047	0.017	0.0205	0.0073	0.00328	0.00012	0.10	21.12	0.74	20.4	7.1	1300	220	21.12	0.74
Zircon_021	193	89	0.46	0.073	0.023	0.0335	0.0099	0.00329	0.00014	0.14	21.17	0.92	33.1	9.6	1360	240	21.17	0.92
Zircon_013	373	148	0.40	0.063	0.013	0.028	0.0061	0.00329	0.0001	0.14	21.19	0.66	27.9	6	1100	180	21.19	0.66
Zircon_025	238	121	0.51	0.047	0.017	0.021	0.0075	0.00331	0.00018	0.15	21.3	1.2	20.9	7.4	1240	370	21.3	1.2
Zircon_006	475	240	0.50	0.084	0.028	0.038	0.016	0.00332	0.00019	0.14	21.4	1.2	38	15	1280	230	21.4	1.2
Zircon_022	363	101	0.28	0.115	0.017	0.0541	0.0073	0.00332	0.00017	0.38	21.4	1.1	53.3	6.9	1910	170	21.4	1.1
Zircon_030	590	426	0.72	0.056	0.012	0.0246	0.0057	0.00332	0.00011	0.14	21.4	0.69	26.1	5.7	690	180	21.4	0.69
Zircon_016	267	109	0.41	0.05	0.01	0.0238	0.0047	0.0034	0.00011	0.16	21.91	0.74	23.8	4.6	730	210	21.91	0.74
Zircon_003	540	223	0.41	0.062	0.013	0.0287	0.0062	0.00344	0.00011	0.15	22.16	0.73	28.7	6	920	210	22.16	0.73
Zircon_004	316	120	0.38	0.107	0.018	0.049	0.008	0.0035	0.00012	0.21	22.5	0.78	48.3	7.7	1800	200	22.5	0.78
Zircon_005	219	110	0.50	0.072	0.015	0.0371	0.0077	0.00361	0.00012	0.16	23.24	0.75	36.8	7.4	1310	170	23.24	0.75

Supplemental File 4. Geochronology results.

Sample Name: PB 32

Location: Punta Botella, Baja California
Latitude: 25.2911°
Longitude: -110.9345
Altitude/Depth (m.a.s.l.): 0

Rock type: Granite

U-Pb Age

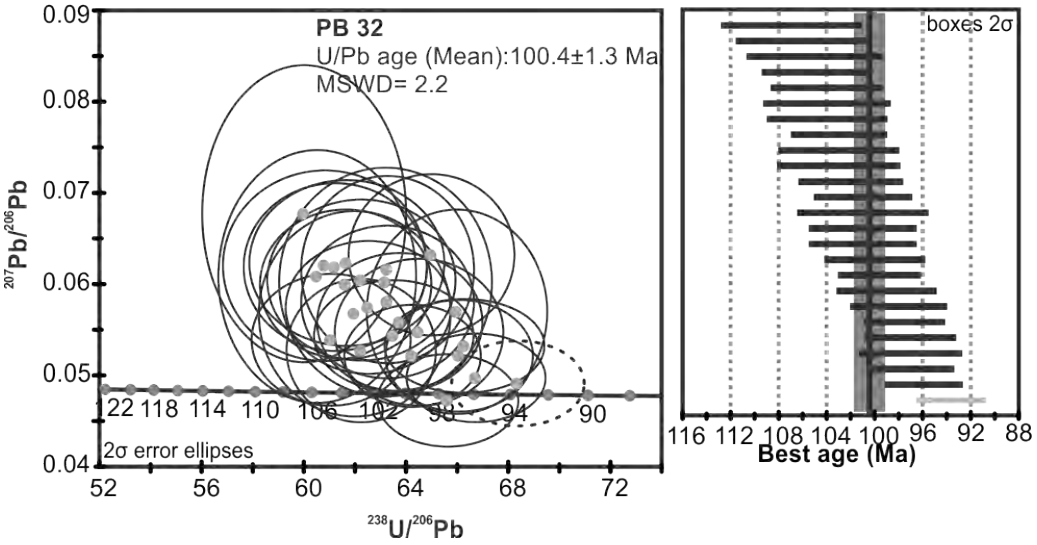

Preferred age: t= 100.4±1.3 Ma

Weighted mean age (95% confidence) calculated with 34 data points. The oldest two points and the youngest were extracted from calculation. Single crystals are in the 107 to 95.5 Ma age range.

Abreviations used in this supplemental file
(i)= Dredge initiation
(e)= Dredge end
(wire)= Dredge wire longitude

^{40}Ar-^{39}Ar age
Sample Name: PB 32
Mineral: Biotite

Laser step-heating experiments on biotite concentrate

Pwr	^{39}Ar × 10^{-6}	F ^{39}Ar	^{40}Ar*/^{39}Ar$_K$	1σ	Age in Ma	1σ			% ^{40}Ar*	^{40}Ar/^{36}Ar	^{37}Ar$_{Ca}$/^{39}Ar$_K$
0.50	189.676	0.0254	12.86	0.21	72.40	1.16	a	‡	60.66	751.20	0.070
0.80	465.854	0.0624	17.45	0.20	97.55	1.07	b	‡	92.84	4129.76	0.014
1.00	892.634	0.1196	18.38	0.20	102.61	1.11	c		96.07	7512.11	0.012
1.20	574.741	0.0770	18.03	0.15	100.74	0.83	d		98.21	16511.76	0.019
1.40	615.279	0.0824	18.09	0.11	101.07	0.60	e		98.16	16047.26	0.021
1.60	879.432	0.1178	18.53	0.12	103.42	0.68	f		98.08	15402.44	0.032
1.80	973.689	0.1304	18.55	0.17	103.56	0.93	g		98.31	17440.76	0.054
2.00	855.483	0.1146	18.46	0.15	103.04	0.82	h		98.76	23888.14	0.067
2.20	443.513	0.0594	17.77	0.13	99.32	0.71	i		98.67	22189.65	0.090
2.40	416.541	0.0558	17.72	0.16	99.01	0.88	j		98.52	19955.73	0.091
2.80	523.080	0.0701	17.86	0.21	99.80	1.12	k		98.82	25126.83	0.103
3.20	301.050	0.0403	17.37	0.10	97.16	0.57	l	‡	98.61	21313.62	0.107
3.70	190.037	0.0255	17.19	0.17	96.15	0.92	m	‡	98.23	16715.73	0.155
6.00	144.052	0.0193	16.91	0.15	94.63	0.80	n	‡	98.76	23896.82	0.164

Integrated results

^{39}Ar × 10^{-6}	^{40}Ar*/^{39}Ar$_K$	1σ	Age in Ma	1σ	% ^{40}Ar*	^{40}Ar/^{36}Ar	^{37}Ar$_{Ca}$/^{39}Ar$_K$
7465.0	17.97	0.05	100.40	0.44	96.69	8919.93	0.055

J = 0.003185 ± 0.000011

Preferred age t_c = 99.86 ± 1.72 Ma

(^{40}Ar/^{36}Ar)$_i$ = 569 ± 268, MSWD = 4.9 for n = 9

t_p = 103.33 ± 0.50 Ma, calculated with the weighted mean of fractions f to h, representing 36.28 % of ^{39}Ar released in 3 consecutive fractions, MSWD = 0.09

‡ fraction ignored in the isochron given in the figure

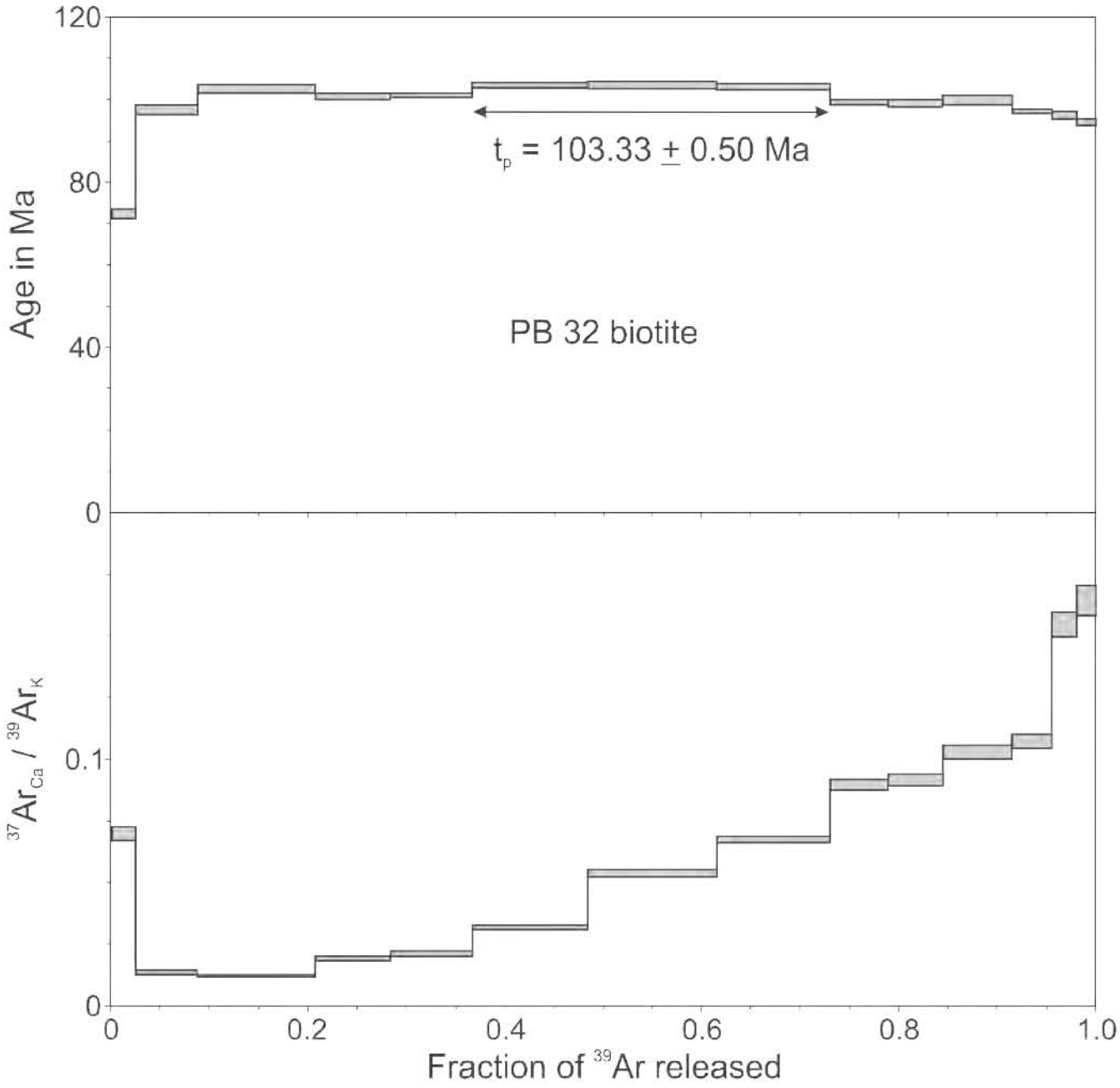

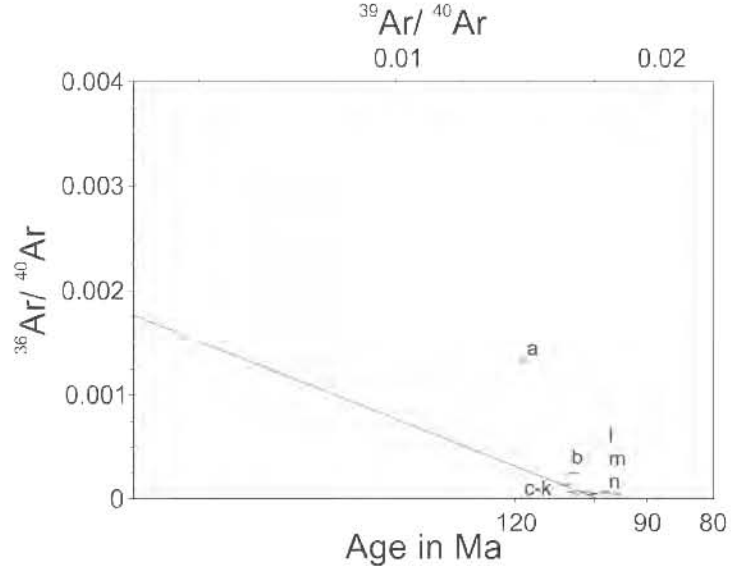

t_c = 99.86 ± 1.72 Ma

$(^{40}Ar / ^{36}Ar)_i$ = 569 ± 268

MSWD = 4.9, n = 9

Sample Name: SCr 27

Location: Santa Cruz Island
Latitude: 25.3058°
Longitude: -110.6997°
Altitude/Depth (m.a.s.l.): 0

Rock type: Granite

U-Pb Age

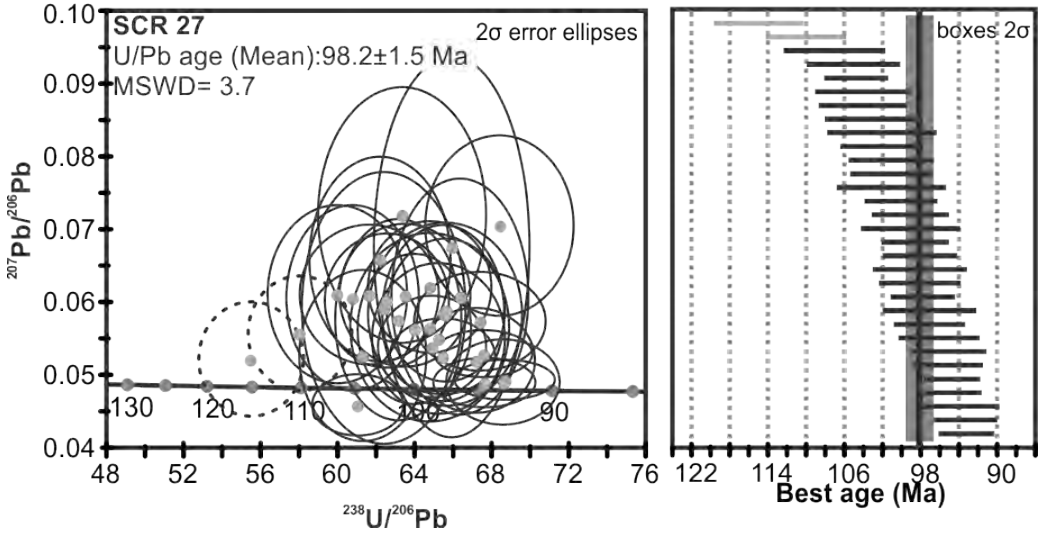

Preferred age: t= 98.2±1.5 Ma

Weighted mean age (95% confidence) calculated with 28 data points. The oldest two points and the youngest were extracted from calculation. Single crystals are in the 93.1 to 105 Ma age range.

Sample Name: SCr 09-21

Location: Santa Cruz Island
Latitude: 25.3082°
Longitude: -110.6957°
Altitude/Depth (m.a.s.l.): 0

Rock type: Granite

^{40}Ar-^{39}Ar age
Sample Name: SCr 09-21
Mineral: Hornblende

Laser step-heating experiments on hornblende concentrate

Pwr	^{39}Ar × 10^{-6}	F ^{39}Ar	^{40}Ar*/^{39}Ar$_K$	1σ	Age in Ma	1σ			% ^{40}Ar*	^{40}Ar/^{36}Ar	^{37}Ar$_{Ca}$/^{39}Ar$_K$
0.20	0.844	0.0008	159.55	39.49	837.68	165.85	a	‡	35.28	456.60	23.959
1.20	188.333	0.1841	14.47	0.12	94.16	0.78	b	‡	78.26	1359.15	0.306
2.00	150.679	0.1469	15.53	0.13	100.91	0.83	c		90.93	3257.27	4.097
2.60	374.150	0.3643	15.37	0.06	99.89	0.41	d		94.49	5363.34	6.578
3.20	176.480	0.1718	15.31	0.10	99.48	0.61	e		93.52	4558.77	6.311
3.90	61.738	0.0601	15.66	0.29	101.74	1.83	f		99.51	60781.44	6.503
11.50	73.928	0.0720	15.25	0.32	99.11	2.02	g		93.97	4902.70	6.725

Integrated results

^{39}Ar × 10^{-6}	^{40}Ar*/^{39}Ar$_K$	1σ	Age in Ma	1σ	% ^{40}Ar*	^{40}Ar/^{36}Ar	^{37}Ar$_{Ca}$/^{39}Ar$_K$
1023.0	15.34	0.06	99.71	0.88	89.56	2829.66	5.033

J = 0.003704 ± 0.000030

Preferred age t_c = 99.12 ± 1.53 Ma

(^{40}Ar/^{36}Ar)$_i$ = 335 ± 60, MSWD = 0.89 for n = 5

t_p = 100.08 ± 0.53 Ma; plateau age calculated with the weighted mean of fractions c to g, representing 81.51% of ^{39}Ar released in 5 consecutive fractions, MSWD = 0.46

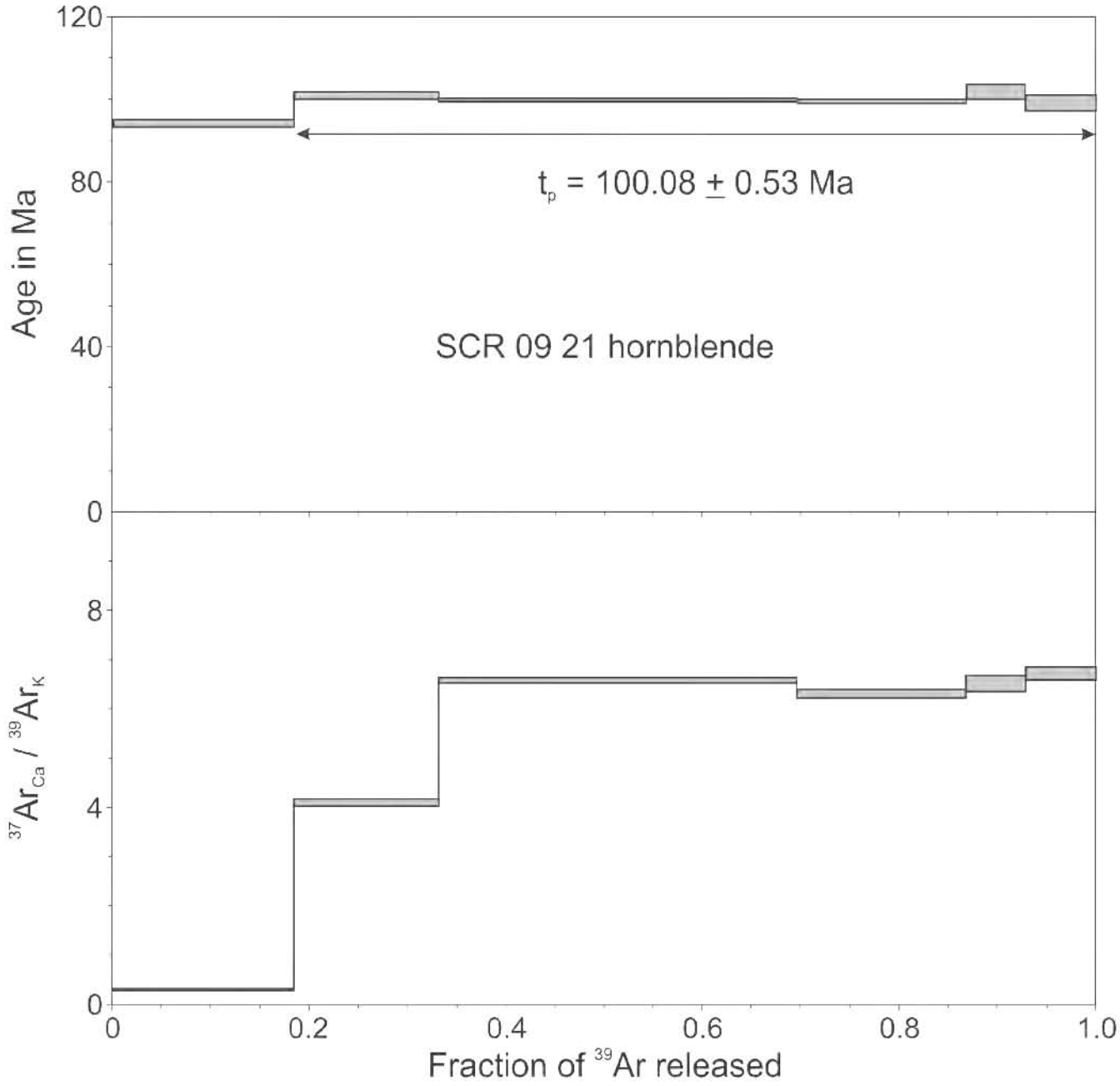

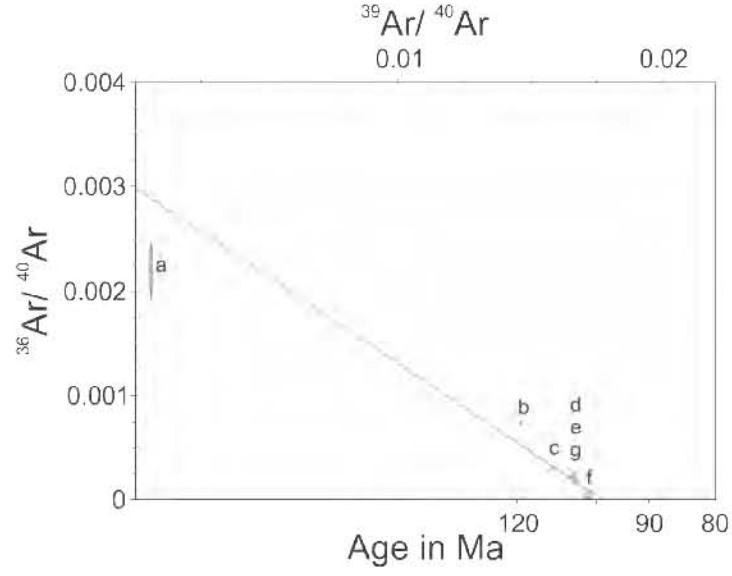

t_c = 99.12 ± 1.53 Ma

(^{40}Ar / ^{36}Ar)$_i$ = 335 ± 60

MSWD = 0.89, n = 5

Sample Name: ROCA 2J-8

Location: Tamayo Fracture Zone fault scarp
Latitude: 22.8116°
Longitude: -107.7310°
Altitude/Depth (m.a.s.l.): -1991

Rock type: Granodiorite

^{40}Ar-^{39}Ar age
Sample Name: ROCA 2J-8
Mineral: Biotite

Laser step-heating experiments on biotite concentrate

Pwr	^{39}Ar × 10^{-6}	F ^{39}Ar	^{40}Ar*/^{39}Ar$_K$	1σ	Age in Ma	1σ			% ^{40}Ar*	^{40}Ar/^{36}Ar	^{37}Ar$_{Ca}$/^{39}Ar$_K$
0.25	55.981	0.0253	8.86	1.26	57.87	8.12	a	‡	15.12	348.13	0.218
0.50	284.701	0.1289	14.13	0.23	91.41	1.46	b	‡	50.70	599.45	0.069
0.80	587.127	0.2658	15.63	0.10	100.90	0.64	c		92.99	4214.68	0.003
1.10	621.641	0.2814	15.71	0.05	101.35	0.32	d		99.35	45186.79	0.024
1.40	332.488	0.1505	15.24	0.06	98.45	0.37	e		99.78	136807.42	0.039
2.00	192.865	0.0873	14.84	0.07	95.89	0.45	f		99.37	47062.29	0.062
2.50	36.781	0.0166	13.65	0.40	88.40	2.55	g	‡	62.94	-175988.45	0.314
3.00	97.779	0.0443	15.25	0.28	98.52	1.73	h		94.81	5696.92	0.166

Integrated results

^{39}Ar × 10^{-6}	^{40}Ar*/^{39}Ar$_K$	1σ	Age in Ma	1σ	% ^{40}Ar*	^{40}Ar/^{36}Ar	^{37}Ar$_{Ca}$/^{39}Ar$_K$
2209.0	15.11	0.06	97.61	0.54	81.54	1600.38	0.046

J = 0.003679 ± 0.000015

t = 101.27 ± 0.49 Ma; weighted mean of fractions c and d, representing 54.72% of ^{39}Ar released in 2 consecutive fractions, MSWD = 0.51

Preferred age t_c = 98.93 ± 1.45 Ma, $(^{40}Ar/^{36}Ar)_i$ = 453 ± 150, MSWD = 26.0 for n = 5

‡ fraction ignored in the isochron age calculation

The integrated results are given just for comparison. It is necessary to take in account that these results are not accurate since for fraction “g” mass 36 could not be estimated. However, since this is a small fraction with only ~1.66% of the ^{39}Ar released, it is likely that it has very little effect in the integrated results.

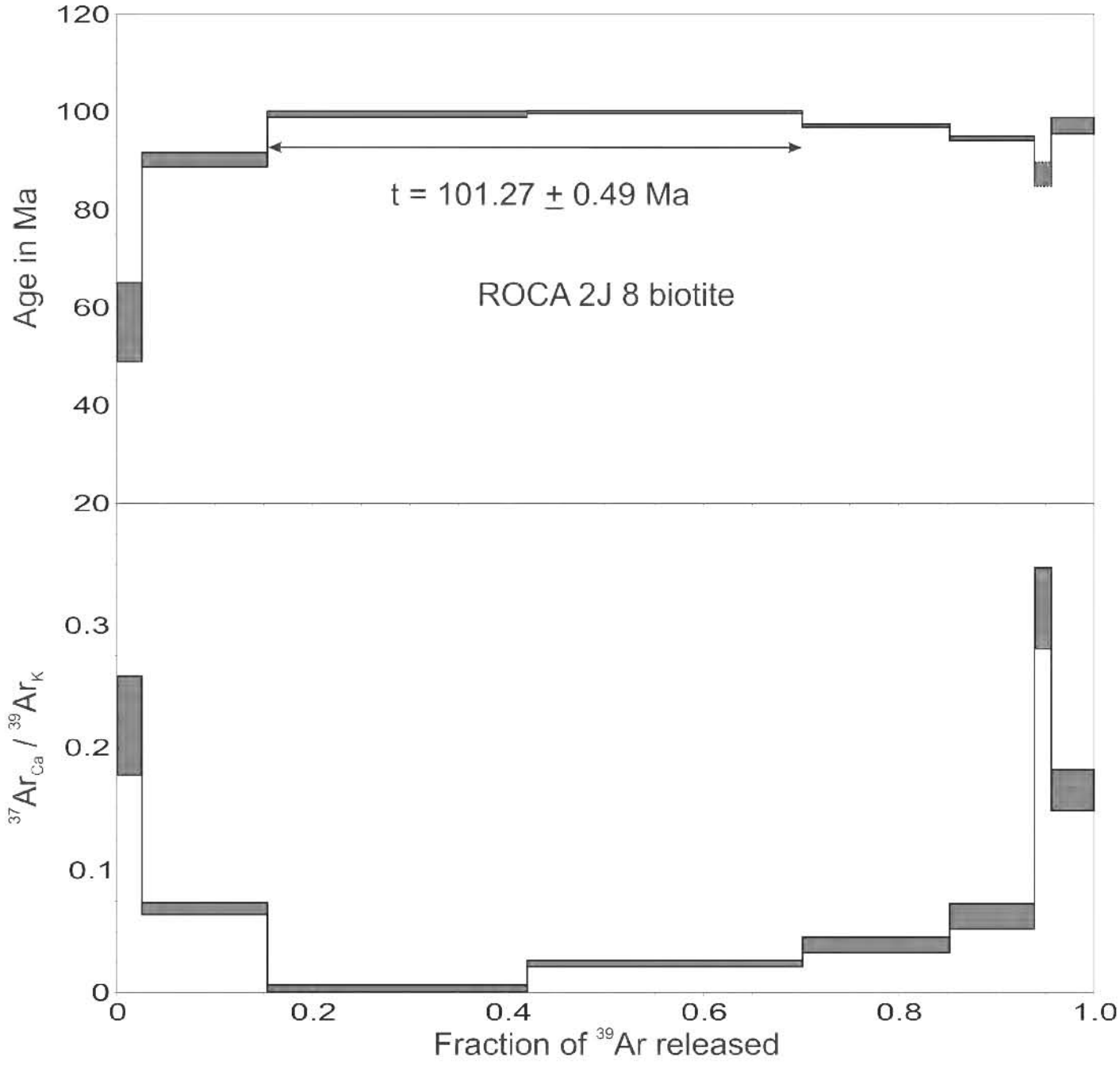

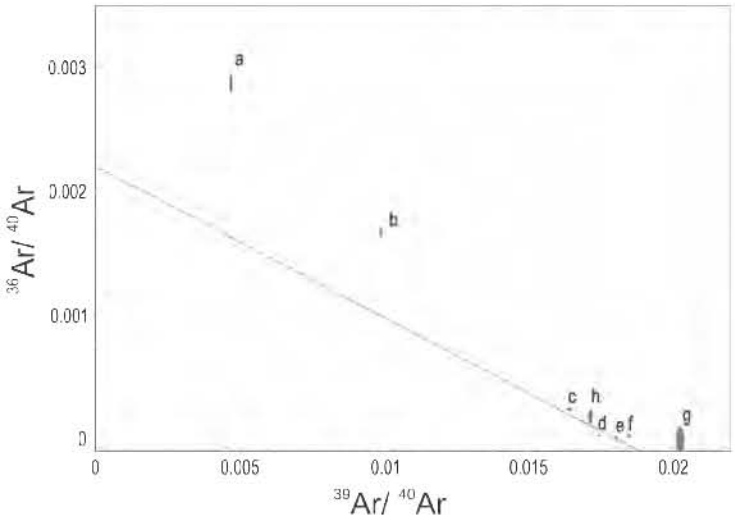

t_c = 98.93 ± 1.45 Ma

$(^{40}Ar / ^{36}Ar)_i$ = 453 ± 150

SumS / (n-2) = 26.0, n = 5

Sample Name: SC 17

Location: Santa Catalina Island
Latitude: 25.6832°
Longitude: -110.7969°
Altitude/Depth (m.a.s.l.): 0

Rock type: Granodiorite

U-Pb Age

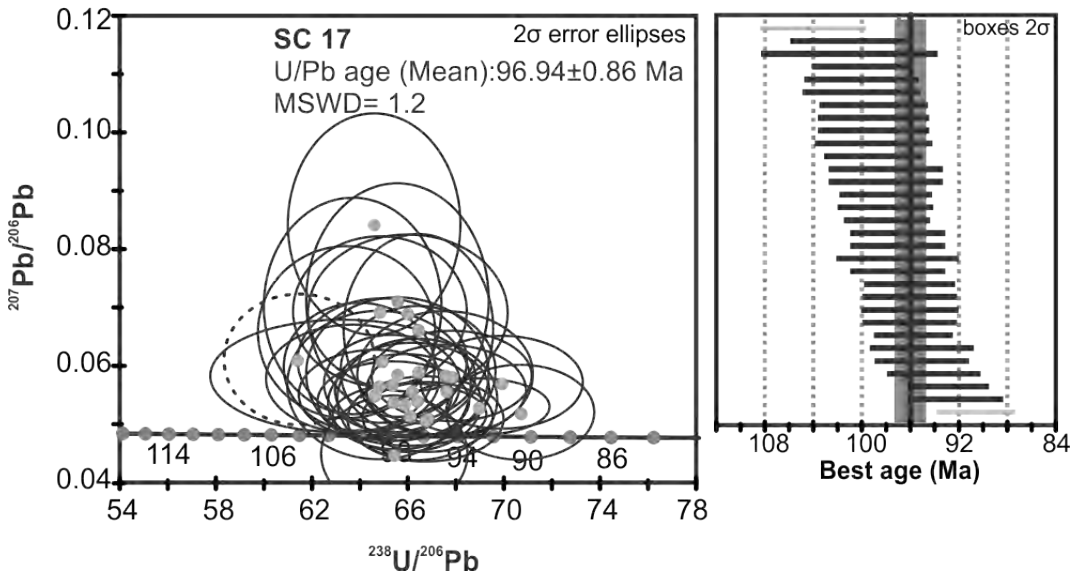

Preferred age: t= 96.94±0.86 Ma

Weighted mean age (95% confidence) calculated with 27 data points. Oldest point and three youngest analyses were removed from analysis. Single crystals are in the 94 to 101 Ma age range.

^{40}Ar-^{39}Ar age
Sample Name: SC 17
Mineral: Hornblende

Laser step-heating experiments on hornblende concentrate

Pwr	^{39}Ar × 10^{-6}	F ^{39}Ar	^{40}Ar*/^{39}Ar$_K$	1σ	Age in Ma	1σ			% ^{40}Ar*	^{40}Ar/^{36}Ar	^{37}Ar$_{Ca}$/^{39}Ar$_K$
0.50	22.659	0.0134	16.54	2.00	92.63	10.93	a		14.10	343.99	1.238
1.20	980.055	0.5763	16.24	0.11	90.97	0.58	b	†	90.75	3194.46	6.545
1.90	440.803	0.2592	15.49	0.06	86.87	0.34	c	†	94.89	5780.13	6.700
5.00	257.145	0.1511	14.26	0.15	80.12	0.81	d		92.61	4000.13	7.739
0.40	8.011	0.0018	109.52	4.05	539.80	17.25	e		27.85	409.56	3.031
0.80	40.474	0.0091	31.33	0.85	171.59	4.42	f		48.75	576.54	2.985
1.10	73.686	0.0166	10.84	0.30	61.24	1.69	g		52.23	618.62	2.119
1.80	393.222	0.0885	13.31	0.12	74.90	0.65	h		67.51	909.63	3.446
2.30	1049.879	0.2359	15.53	0.07	87.09	0.37	i	†	93.82	4784.21	6.090
2.90	2153.243	0.4836	16.37	0.15	91.66	0.80	j	†	96.34	8072.54	6.898
3.80	484.002	0.1090	11.56	0.08	65.20	0.46	k		95.05	5967.44	3.377
7.00	246.571	0.0555	11.23	0.10	63.40	0.56	l		66.44	880.62	4.648

Integrated results

^{39}Ar × 10^{-6}	^{40}Ar*/^{39}Ar$_K$	1σ	Age in Ma	1σ	% ^{40}Ar*	^{40}Ar/^{36}Ar	^{37}Ar$_{Ca}$/^{39}Ar$_K$
1693.0	15.75	0.07	88.30	0.50	85.41	2025.56	6.694
4432.0	15.30	0.07	85.85	0.50	86.12	2129.38	5.771

J = 0.003185 ± 0.000011

Preferred age t = 90.97 ± 0.65 Ma

fraction b, representing 57.6% of the ^{39}Ar

t_c = 85.91 ± 3.74 Ma; $(^{40}Ar/^{36}Ar)_i$ = 420 ± 191, MSWD = 35 for n = 4

† fractions used to calculate the straight line given in the figure

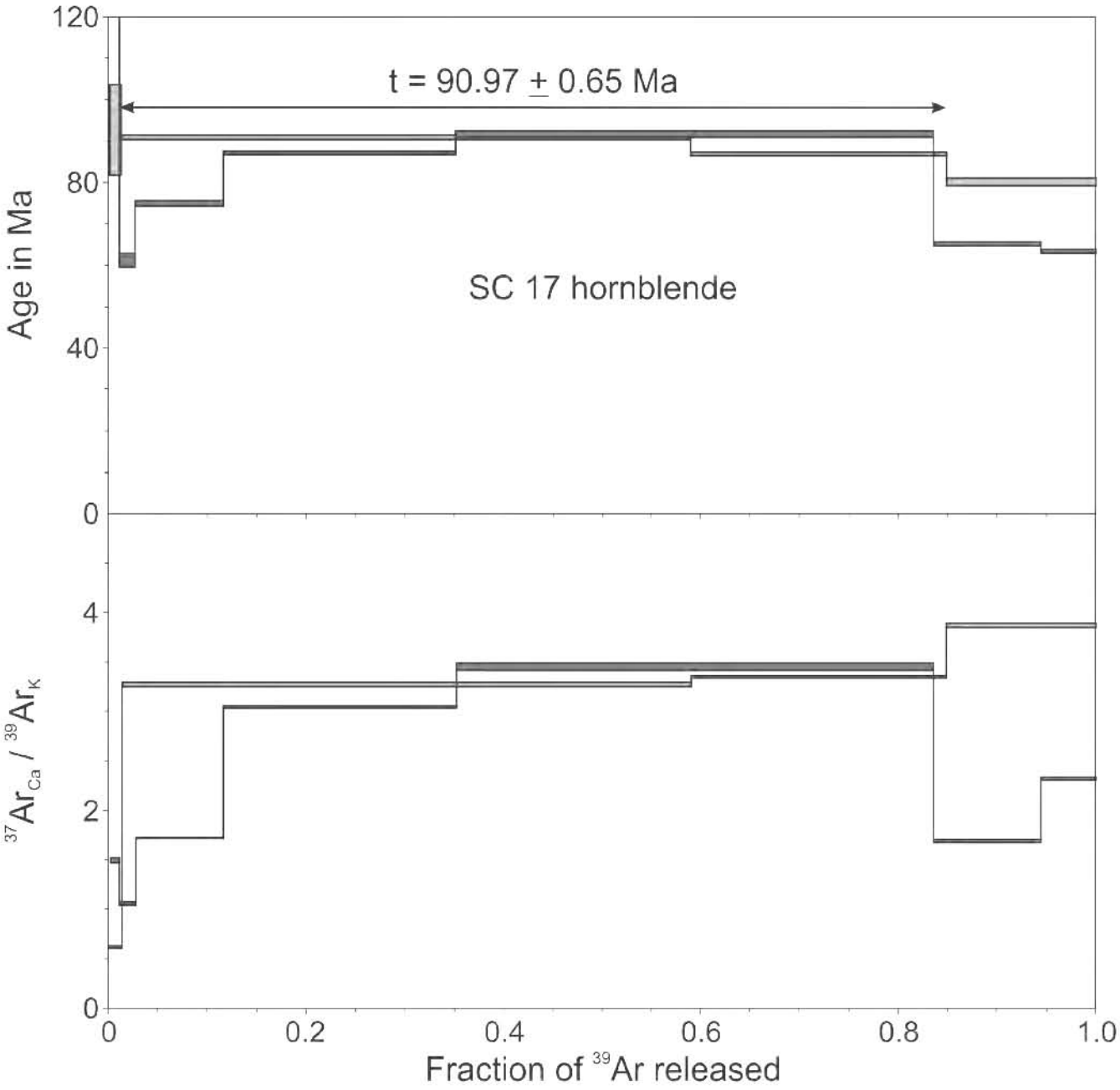

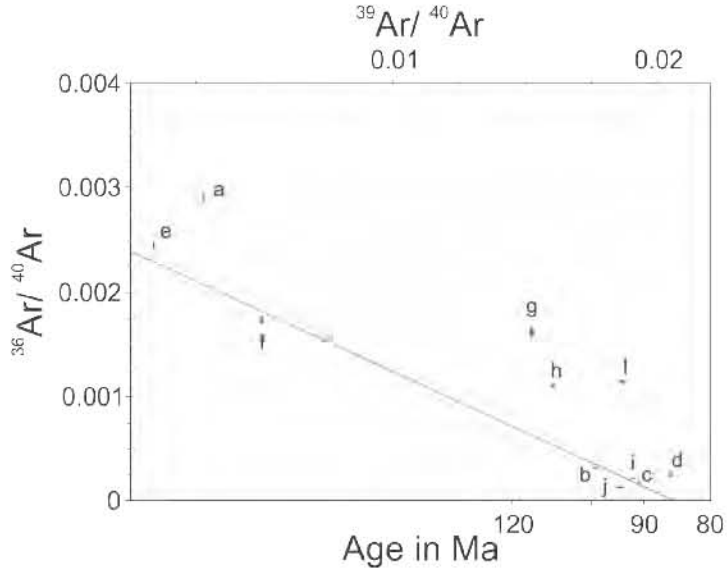

t_c = 85.91 ± 3.74 Ma

$(^{40}Ar / ^{36}Ar)_i$ = 420 ± 191

MSWD = 35, n = 4

^{40}Ar-^{39}Ar age
Sample Name: SC 17
Mineral: Biotite

Laser step-heating experiments on biotite concentrate

Pwr	^{39}Ar × 10^{-6}	F ^{39}Ar	^{40}Ar*/^{39}Ar$_K$	1σ	Age in Ma	1σ			% ^{40}Ar*	^{40}Ar/^{36}Ar	^{37}Ar$_{Ca}$/^{39}Ar$_K$
0.30	86.087	0.0123	5.19	0.55	29.60	3.09	a	‡	11.10	332.41	0.220
0.60	886.064	0.1266	14.41	0.12	80.93	0.68	b	‡	76.07	1234.61	0.049
0.90	1666.643	0.2382	15.76	0.14	88.33	0.74	c		91.03	3292.96	0.071
1.40	1457.278	0.2082	15.89	0.12	89.09	0.64	d		97.78	13311.43	0.108
1.80	1023.963	0.1463	15.68	0.15	87.89	0.80	e		97.03	9961.00	0.292
2.40	580.303	0.0829	15.25	0.15	85.58	0.82	f		94.78	5662.52	0.288
4.00	1297.706	0.1854	15.88	0.13	89.03	0.72	g		96.44	8303.41	0.082

Integrated results

^{39}Ar × 10^{-6}	^{40}Ar*/^{39}Ar$_K$	1σ	Age in Ma	1σ	% ^{40}Ar*	^{40}Ar/^{36}Ar	^{37}Ar$_{Ca}$/^{39}Ar$_K$
6997.0	15.45	0.06	86.68	0.43	89.68	2862.58	0.130

J = 0.003185 ± 0.000011

Preferred age t_p = 88.52 ± 0.45 Ma

Weighted mean of fractions c to e, representing 59.27% of ^{39}Ar released in 3 consecutive fractions, MSWD = 0.62

t_c = 88.71 ± 1.36 Ma; $(^{40}Ar/^{36}Ar)_i$ = 258 ± 84, MSWD = 4.2 for n = 5

‡ fraction ignored in the isochron age calculation

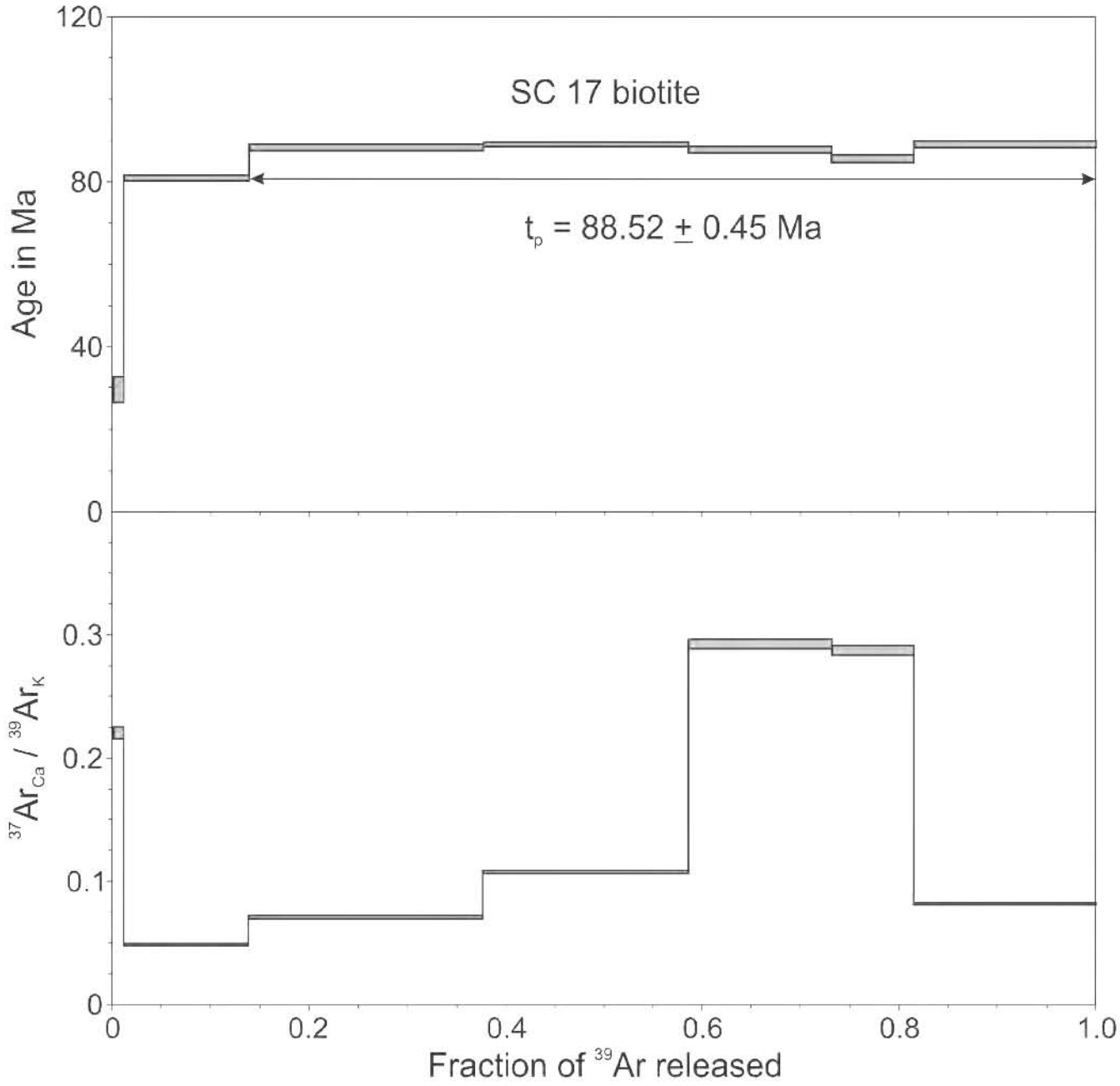

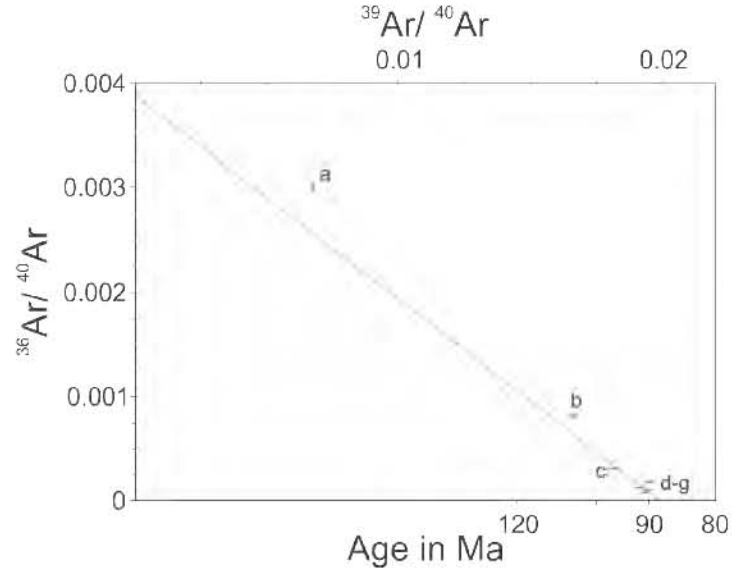

t_c = 88.71 ± 1.36 Ma

$(^{40}Ar / ^{36}Ar)_i$ = 258 ± 84

MSWD = 4.2, n = 5

Sample Name: BEKL 8D-6

Location: East of Partida Bank
Latitude: 24.7758° (i); 24.7745° (e)
Longitude: -110.1308° (i); -110.1350° (e)
Altitude/Depth (m.a.s.l.): 900 (i); 860 (e) (wire)

Rock type: Biotite Granite

U-Pb Age

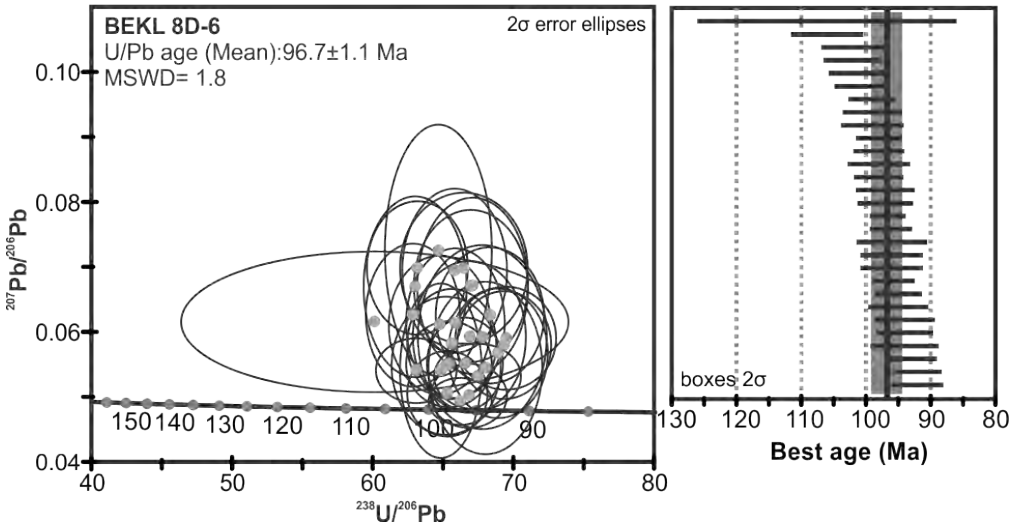

Preferred age: t= 96.7±1.1 Ma

Weighted mean age (95% confidence) calculated with 27 data points. Single crystals are in the 92 to 102 Ma age range.

^{40}Ar-^{39}Ar age
Sample Name: BEKL 8D-6
Mineral: Biotite

Laser step-heating experiments on biotite concentrate

Pwr	^{39}Ar × 10^{-6}	F ^{39}Ar	^{40}Ar*/^{39}Ar$_K$	1σ	Age in Ma	1σ			% ^{40}Ar*	^{40}Ar/^{36}Ar	^{37}Ar$_{Ca}$/^{39}Ar$_K$
0.20	3.912	0.0013	7.74	3.84	47.99	23.50	a	‡	4.94	310.87	0.468
0.50	124.865	0.0415	7.02	0.30	43.58	1.81	b	‡	20.56	372.00	0.145
0.80	371.051	0.1232	13.23	0.06	81.33	0.36	c	‡	80.56	1520.43	0.058
1.20	771.750	0.2563	15.79	0.03	96.61	0.19	d	‡	98.32	17582.74	0.034
1.40	345.871	0.1149	16.07	0.04	98.29	0.23	e	‡	99.43	51864.45	0.028
1.60	221.615	0.0736	16.11	0.06	98.51	0.35	f	‡	99.72	104149.49	0.045
1.85	208.378	0.0692	16.14	0.05	98.73	0.31	g	‡	99.39	48768.43	0.063
2.20	372.658	0.1238	15.84	0.03	96.91	0.19	h		99.43	52033.07	0.051
2.50	175.719	0.0584	15.84	0.05	96.91	0.33	i		99.72	104125.37	0.056
2.90	93.965	0.0312	15.72	0.09	96.23	0.54	j		99.82	160479.26	0.044
3.50	58.946	0.0196	15.75	0.14	96.42	0.82	k		97.86	13778.36	0.098
6.70	262.359	0.0871	15.86	0.04	97.04	0.25	l		98.22	16595.74	0.121

Integrated results

^{39}Ar × 10^{-6}	^{40}Ar*/^{39}Ar$_K$	1σ	Age in Ma	1σ	% ^{40}Ar*	^{40}Ar/^{36}Ar	^{37}Ar$_{Ca}$/^{39}Ar$_K$
3011.0	15.19	0.03	93.06	0.31	89.16	2725.97	0.057

J = 0.003485 ± 0.000010

Preferred age t_c = 96.77 ± 0.35 Ma

(^{40}Ar/^{36}Ar)$_i$ = 344 ± 67, MSWD = 0.56 for n = 5

t_p = 96.85 ± 0.20 Ma calculated with the weighted mean of fractions h to l, representing 32.01% of ^{39}Ar released in 5 consecutive fractions, MSWD = 0.41

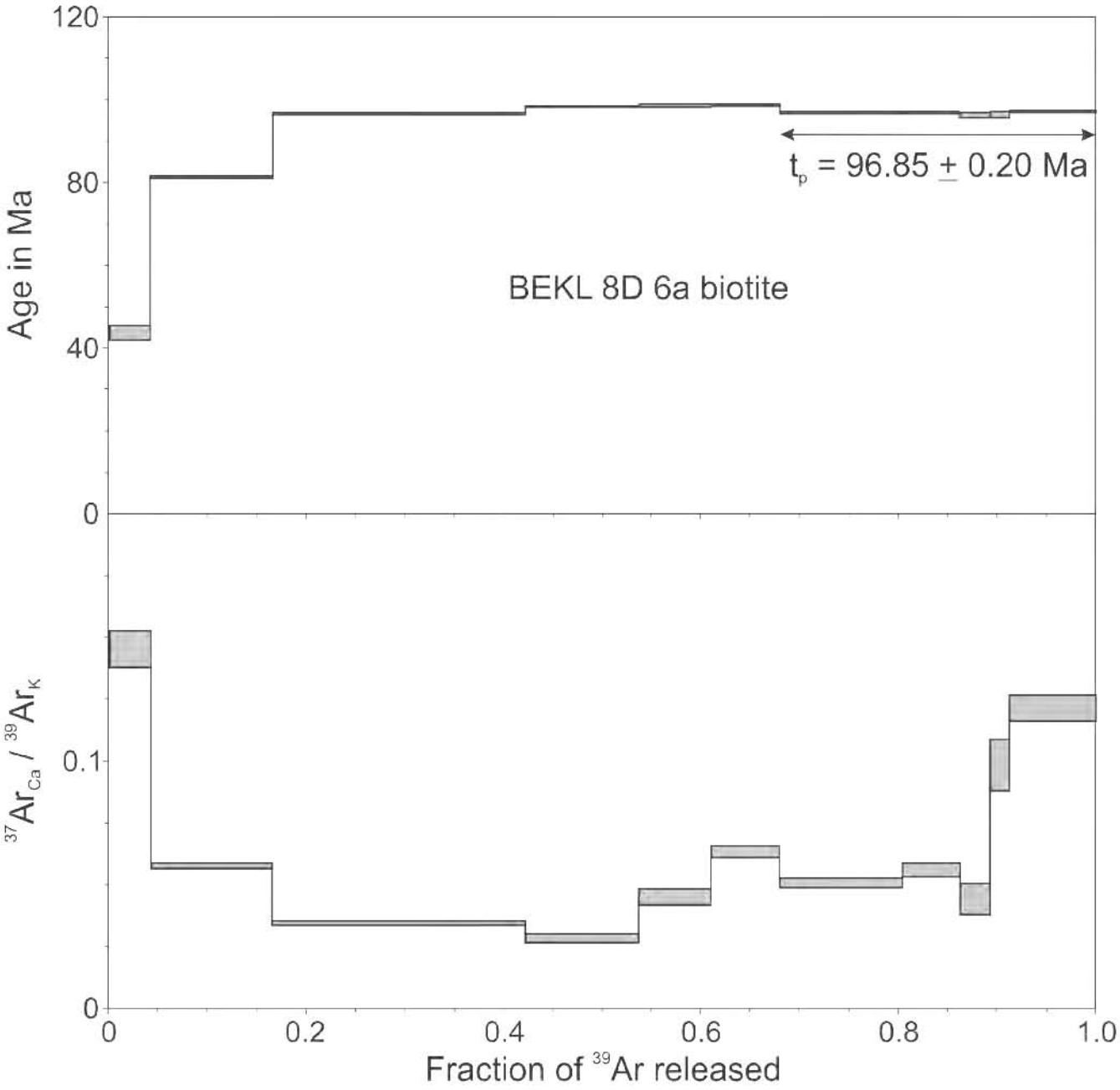

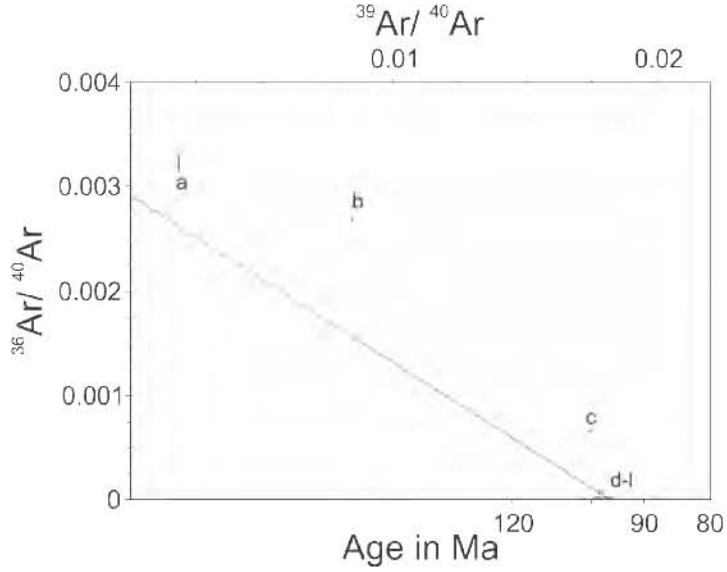

t_c = 96.77 ± 0.35 Ma

(^{40}Ar / ^{36}Ar)$_i$ = 344 ± 67

MSWD = 0.56, n = 5

Sample Name: ROCA 2J-4

Location: Tamayo Fracture Zone
Latitude: 22.8104°
Longitude: -107.7337°
Altitude/Depth (m.a.s.l.): -2219

Rock type: Diorite

^{40}Ar-^{39}Ar age
Sample Name: ROCA 2J-4
Mineral: Hornblende

Laser step-heating experiments on hornblende concentrate

Pwr	^{39}Ar × 10^{-6}	F ^{39}Ar	^{40}Ar*/^{39}Ar$_K$	1σ	Age in Ma	1σ			% ^{40}Ar*	^{40}Ar/^{36}Ar	^{37}Ar$_{Ca}$/^{39}Ar$_K$
0.90	9.855	0.0119	- 0.14	3.59	-0.93	23.93	a	‡	-0.07	295.28	2.784
2.20	51.873	0.0624	11.00	0.52	71.75	3.35	b	‡	25.19	395.03	3.291
3.63	540.165	0.6494	15.01	0.07	97.25	0.44	c		86.91	2257.49	5.201
4.14	45.216	0.0544	12.23	0.37	79.59	2.35	d	‡	83.40	1780.34	5.536
6.00	184.745	0.2219	14.31	0.10	92.83	0.65	e	‡	88.86	2653.54	6.593
0.56	17.326	0.0211	17.59	1.99	113.43	12.44	f	‡	13.16	340.30	2.454
0.87	19.014	0.0231	8.92	1.72	58.41	11.10	g	‡	16.68	354.66	2.176
1.50	43.244	0.0526	8.21	0.54	53.81	3.47	h	‡	24.07	389.20	0.791
2.40	102.308	0.1242	13.36	0.31	86.76	1.98	i	‡	60.51	748.32	4.551
3.00	328.194	0.3982	14.79	0.08	95.80	0.48	j		88.17	2498.53	5.728
3.40	176.982	0.2147	14.56	0.17	94.40	1.08	k		93.24	4369.25	5.830
4.50	37.441	0.0454	12.07	0.30	78.58	1.90	l	‡	88.91	2665.53	5.281
6.00	37.405	0.0454	11.89	0.29	77.45	1.88	m	‡	86.86	2249.07	5.266
10.00	62.071	0.0753	13.30	0.23	86.39	1.45	n	‡	81.15	1567.30	6.224
0.57	15.244	0.0227	19.60	2.56	125.94	15.87	o	‡	11.51	333.93	2.689
0.88	14.042	0.0209	8.52	1.03	55.80	6.66	p	‡	14.09	343.96	1.263
1.50	43.177	0.0643	7.96	0.42	52.22	2.73	q	‡	28.69	414.39	1.389
2.40	227.962	0.3388	14.83	0.11	96.07	0.67	r		82.57	1695.48	4.954
3.00	180.050	0.2676	14.79	0.09	95.83	0.55	s		92.10	3740.87	4.833
3.40	37.340	0.0555	13.58	1.12	88.17	7.11	t		89.17	2727.64	5.195
4.50	54.824	0.0817	12.06	0.50	78.50	3.21	u	‡	80.95	1551.38	0.898
11.50	99.898	0.1484	12.65	0.14	82.26	0.89	v	‡	88.68	2610.53	5.419

Integrated results

^{39}Ar × 10^{-6}	^{40}Ar*/^{39}Ar$_K$	1σ	Age in Ma	1σ	% ^{40}Ar*	^{40}Ar/^{36}Ar	^{37}Ar$_{Ca}$/^{39}Ar$_K$
829.0	14.28	0.08	92.59	0.69	69.48	968.29	5.380
821.2	13.77	0.10	89.39	0.76	65.30	851.51	5.189
670.7	13.73	0.12	89.15	0.86	63.95	819.63	4.315

J = 0.003689 ± 0.000018

t_p = 95.91 ± 1.13 Ma; plateau age calculated with the weighted mean of fractions r to t, representing, 66.19% of ^{39}Ar released in 3 consecutive fractions, MSWD = 0.64

Preferred age t_c = 94.53 ± 1.47 Ma, $(^{40}Ar/^{36}Ar)_i$ = 336 ± 31, MSWD = 2.3 for n = 6

‡ fraction ignored in the isochron given in the figure
‡ fractions ignored in the isochron given in the figure

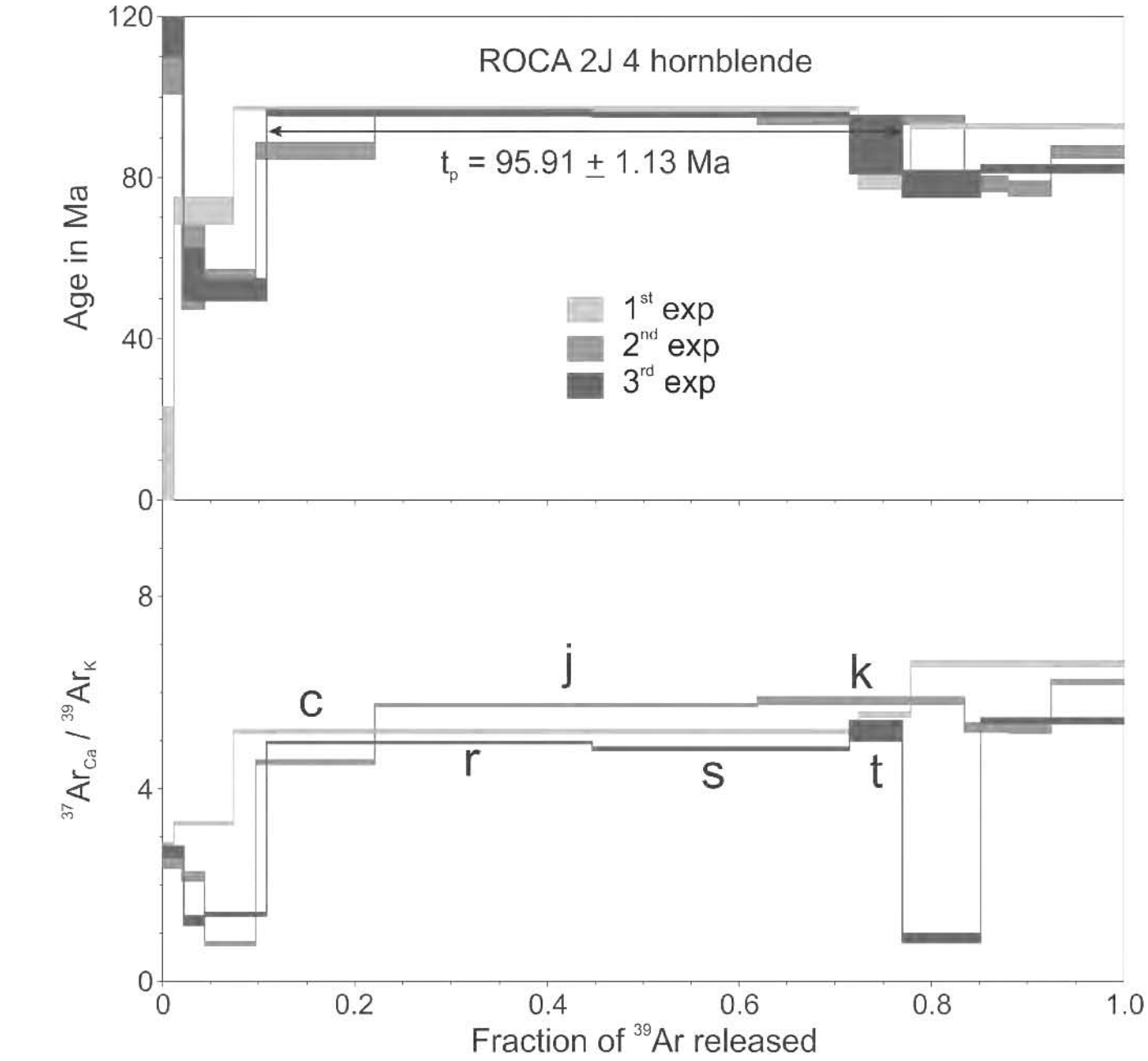
ROCA 2J 4 hornblende
t_p = 95.91 ± 1.13 Ma
1st exp
2nd exp
3rd exp
Age in Ma
$^{37}Ar_{Ca}$ / $^{39}Ar_K$
c
j
k
r
s
t
Fraction of ^{39}Ar released

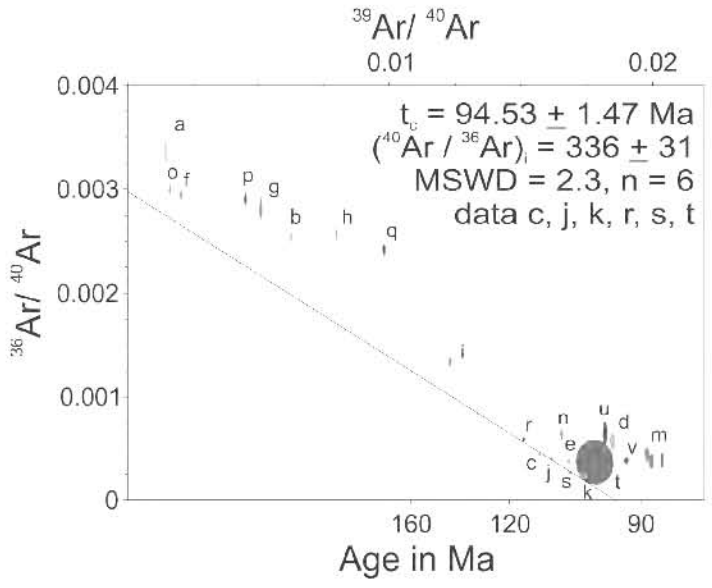
$^{39}Ar/^{40}Ar$
t_c = 94.53 ± 1.47 Ma
$(^{40}Ar / ^{36}Ar)_i$ = 336 ± 31
MSWD = 2.3, n = 6
data c, j, k, r, s, t
$^{36}Ar/^{40}Ar$
Age in Ma

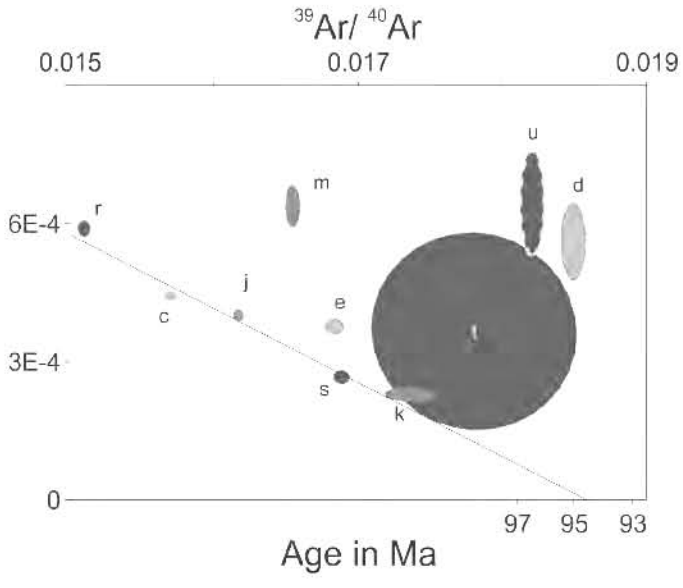
$^{39}Ar/^{40}Ar$
Age in Ma

Sample Name: BEKL 21D-1

Location: San Jose Scarp
Latitude: 24.9331° (i); 24.9308° (e)
Longitude: -110.4116° (i); -110.4146° (e)
Altitude/Depth (m.a.s.l.): 1392 (i); 1250 (e) (wire)

Rock type: Biotite granite

U-Pb Age

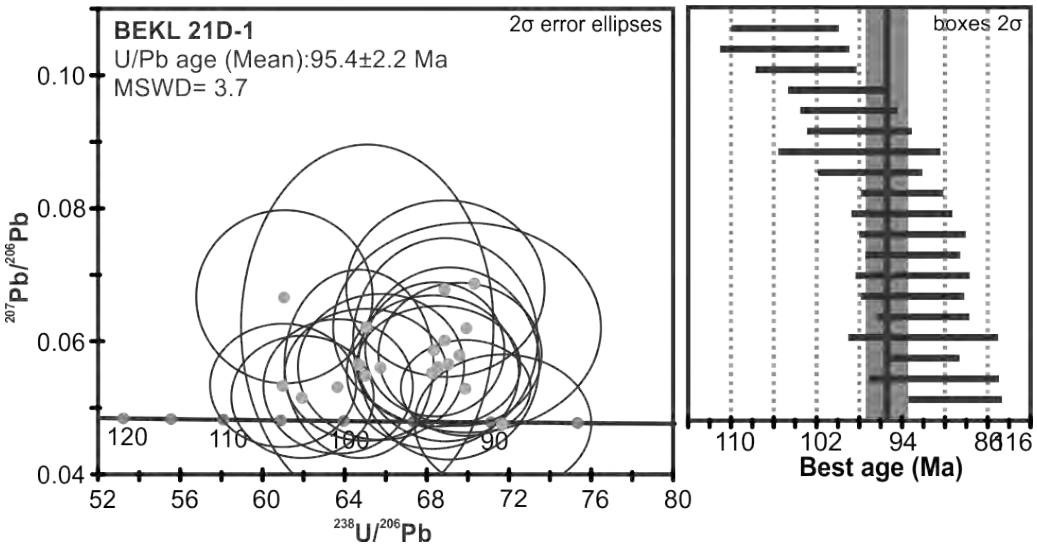

Preferred age: t= 95.4±2.2 Ma

Weighted mean age (95% confidence) calculated with 15 data points. Single crystals are in the 89 to 99 Ma age range.

Sample Name: ROCA 2J-2

Location: Tamayo Fracture Zone
Latitude: 22.8096°
Longitude: -107.7347°
Altitude/Depth (m.a.s.l.): -2297

Rock type: Quartz diorite

^{40}Ar-^{39}Ar age
Sample Name: ROCA 2J-2
Mineral: Hornblende

Laser step-heating experiments on hornblende concentrate

Pwr	^{39}Ar × 10^{-6}	F ^{39}Ar	^{40}Ar*/^{39}Ar$_K$	1σ	Age in Ma	1σ			% ^{40}Ar*	^{40}Ar/^{36}Ar	^{37}Ar$_{Ca}$/^{39}Ar$_K$
0.30	5.448	0.0063	62.39	6.38	373.69	34.53	a		18.79	363.88	1.729
0.75	10.567	0.0122	33.43	2.20	209.79	13.06	b		17.21	356.94	2.896
1.30	13.177	0.0152	16.62	3.03	107.32	18.99	c		19.04	364.99	2.163
1.80	16.569	0.0191	10.13	2.35	66.19	15.09	d		19.68	367.88	4.049
2.80	171.715	0.1976	14.25	0.17	92.42	1.05	e		66.08	871.19	6.044
4.00	460.558	0.5300	15.12	0.07	97.89	0.43	f		86.26	2150.04	5.719
6.20	150.048	0.1726	13.44	0.12	87.30	0.78	g		88.72	2620.01	6.254
10.50	40.864	0.0470	12.25	0.20	79.71	1.27	h	‡	87.79	2420.31	6.772
0.30	5.095	0.0048	16.84	4.47	106.66	27.46	i		10.24	329.21	1.151
0.50	9.820	0.0092	17.87	2.50	112.97	15.30	j		12.51	337.76	1.785
2.00	70.285	0.0661	11.84	0.63	75.64	3.97	k		23.76	387.59	1.926
2.50	140.820	0.1321	13.57	0.22	86.46	1.39	l		72.81	1086.85	4.856
3.00	165.673	0.1554	14.06	0.15	89.49	0.96	m		86.48	2185.79	5.175
3.65	283.382	0.2658	14.67	0.16	93.29	0.97	n		87.63	2389.38	5.173
5.00	206.910	0.1941	12.58	0.12	80.28	0.73	o	‡	89.68	2863.21	4.804
6.50	156.036	0.1464	11.99	0.13	76.59	0.84	p	‡	86.97	2268.10	5.152
7.00	27.672	0.0260	6.14	0.24	39.60	1.53	q	‡	81.22	1573.09	3.440

Integrated results

^{39}Ar × 10^{-6}	^{40}Ar*/^{39}Ar$_K$	1σ	Age in Ma	1σ	% ^{40}Ar*	^{40}Ar/^{36}Ar	^{37}Ar$_{Ca}$/^{39}Ar$_K$
865.7	14.97	0.11	96.96	0.81	63.47	809.00	5.780
1062.0	13.26	0.11	84.54	0.71	67.07	897.29	4.746

J = 0.003689 ± 0.000018 (1st exp. CIC 74B) J = 0.003617 ± 0.000011 (2nd exp. CIC 77 B)

t_c = 93.18 ± 1.88 Ma, $(^{40}Ar/^{36}Ar)_i$ = 314 ± 14, MSWD = 31 for n = 13

‡ fraction ignored in the isochron age calculation

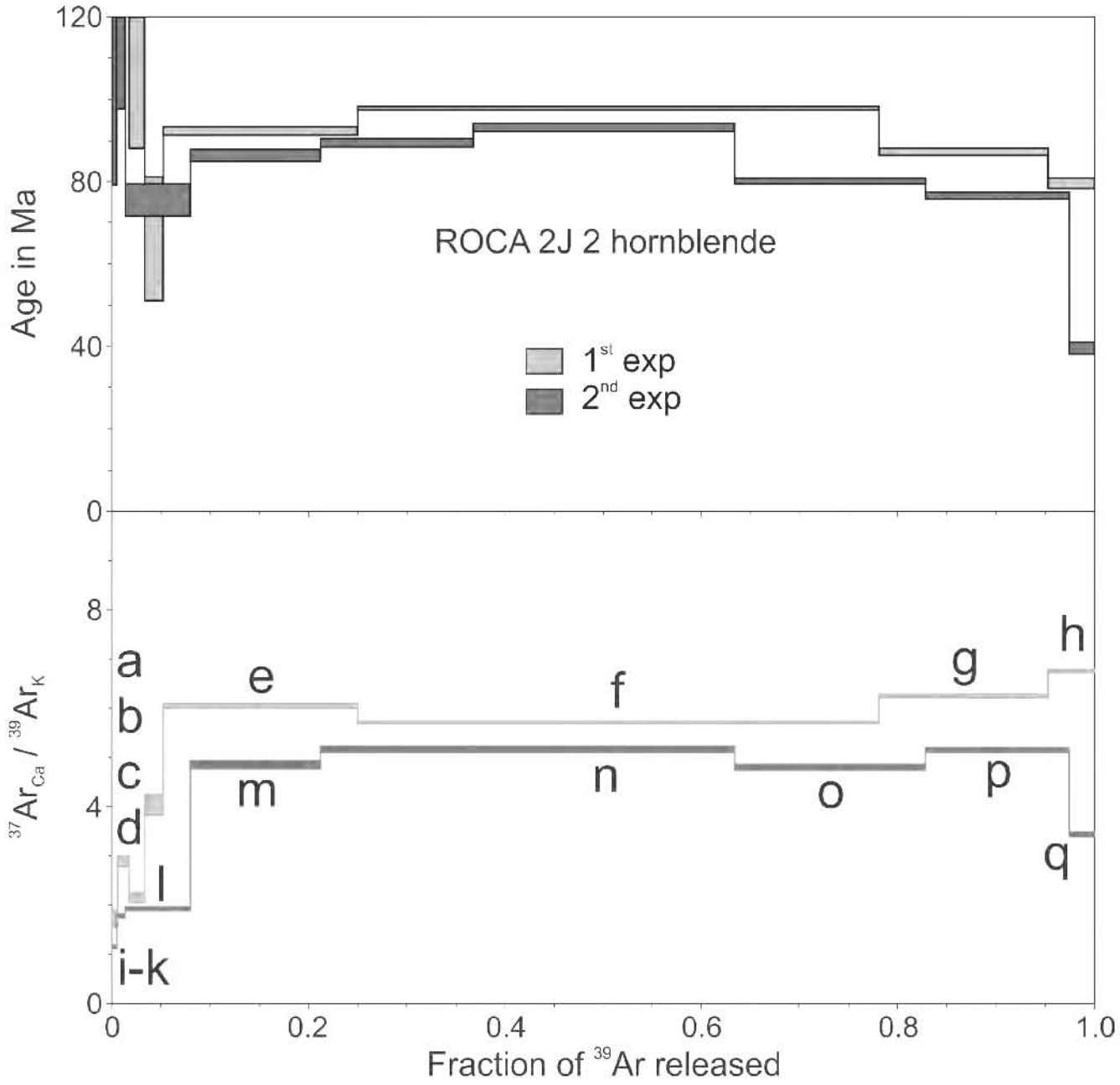
ROCA 2J 2 hornblende
1st exp
2nd exp
Age in Ma
120
80
40
0
$^{37}Ar_{Ca}$ / $^{39}Ar_K$
8
4
0
a
b
c
d
e
f
g
h
i-k
l
m
n
o
p
q
0
0.2
0.4
0.6
0.8
1.0
Fraction of ^{39}Ar released

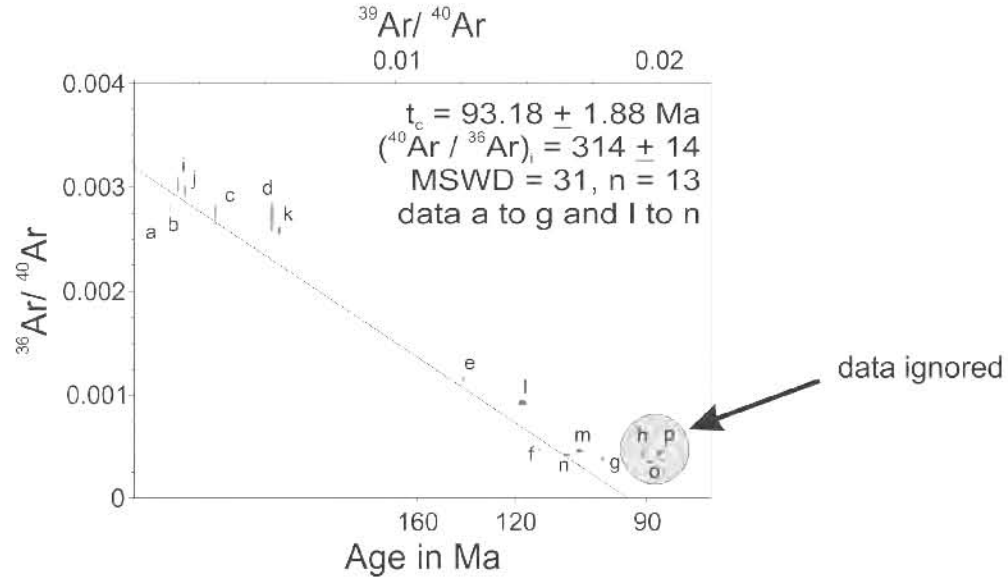
$^{39}Ar/^{40}Ar$
0.01
0.02
t_c = 93.18 ± 1.88 Ma
$(^{40}Ar / ^{36}Ar)_i$ = 314 ± 14
MSWD = 31, n = 13
data a to g and I to n
$^{36}Ar/^{40}Ar$
0.004
0.003
0.002
0.001
0
a
b
c
d
e
f
g
h
i
j
k
l
m
n
o
p
data ignored
160
120
90
Age in Ma

Sample Name: DANA 47a

Location: West Nayarit ridge fault scarp
Latitude: 22.5167°
Longitude: -106.6992°
Altitude/Depth (m.a.s.l.): -1079

Rock type: Biotite granodiorite

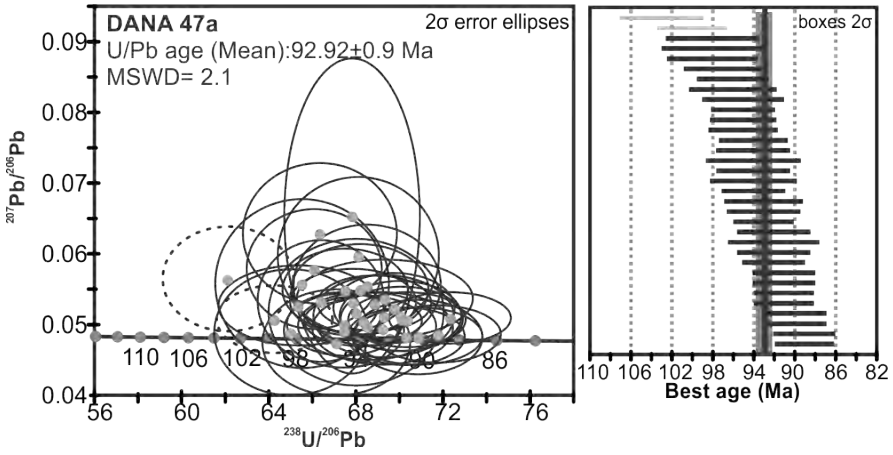

U-Pb Age

Preferred age: t= 92.92 ± 0.90 Ma

Weighted mean age (95% confidence) calculated with 33 data points. Single crystals are in the 87 to 100 Ma age range. Oldest data point was removed from age calculation.

^{40}Ar-^{39}Ar age
Sample Name: DANA 47a
Mineral: Biotite

Laser one-step fusion experiments on biotite crystals

Pwr	^{39}Ar × 10^{-6}	^{40}Ar*/^{39}Ar$_K$	1σ	Age in Ma	1σ		% ^{40}Ar*	^{40}Ar/^{36}Ar	^{37}Ar$_{Ca}$/^{39}Ar$_K$
4.00	5408.015	2.19	0.01	19.09	0.11	a	88.41	2549.72	0.034
2.50	2449.646	2.22	0.02	19.35	0.15	b	89.35	2775.24	0.030
3.00	6388.995	2.19	0.01	19.10	0.12	c	91.37	3424.41	0.047
2.32	3730.795	2.17	0.02	18.91	0.19	d	88.78	2634.30	0.025
1.60	2999.145	2.17	0.03	18.91	0.22	e	77.07	1288.55	0.056
1.60	2336.502	2.17	0.03	18.93	0.26	f	84.99	1968.72	0.062
1.90	3164.871	2.16	0.03	18.82	0.24	g	85.15	1990.03	0.071
2.20	6040.938	2.22	0.02	19.36	0.16	h	85.94	2102.22	0.079
2.00	2947.232	2.27	0.03	19.79	0.25	i	92.94	4182.60	0.121
2.40	7051.199	2.21	0.01	19.24	0.12	j	91.42	3442.08	0.029
2.10	3299.295	2.18	0.02	19.02	0.21	k	88.38	2542.03	0.022
2.00	4955.220	2.22	0.02	19.29	0.14	l	90.05	2968.60	0.037

J = 0.004851 ± 0.000007; CIC-41

Preferred age t = 19.16 ± 0.06 Ma

Weighted mean of one-step fusion experiments a to l, MSWD = 1.61 for n = 12

Ta furnace step-heating experiments on biotite concentrate

Temp °C	^{39}Ar cc STP/g	F ^{39}Ar	^{40}Ar*/^{39}Ar$_K$	1σ	Age in Ma	1σ		% ^{40}Ar*	^{40}Ar/^{36}Ar	^{37}Ar$_{Ca}$/^{39}Ar$_K$
800	0.485 E-06	0.0978	2.23	0.22	16.98	1.67	m	32.57	438.26	0.027
900	1.220 E-06	0.2460	2.43	0.09	18.52	0.66	n	87.91	2444.41	0.013
1050	1.954 E-06	0.3939	2.47	0.05	18.76	0.41	o	93.25	4380.93	0.008
1200	1.207 E-06	0.2432	2.48	0.09	18.87	0.67	p	69.01	953.42	0.088
1350	0.095 E-06	0.0191	3.48	1.16	26.41	8.78	q	6.77	316.95	0.664
800	0.415 E-06	0.0879	2.32	0.08	17.68	0.62	r	32.83	439.90	0.026
875	1.064 E-06	0.2256	2.51	0.03	19.12	0.23	s	87.86	2433.25	0.007
950	0.585 E-06	0.1240	2.56	0.05	19.51	0.41	t	95.23	6200.16	0.005
1025	1.080 E-06	0.2290	2.58	0.03	19.65	0.23	u	96.29	7962.08	0.017
1100	0.989 E-06	0.2098	2.57	0.03	19.57	0.25	v	77.42	1308.51	0.038
1200	0.535 E-06	0.1135	2.55	0.06	19.36	0.45	w	88.11	2485.99	0.172
1305	0.047 E-06	0.0100	2.76	0.67	20.96	5.10	x	19.86	368.72	0.752

Integrated results

^{39}Ar cc STP/g	^{40}Ar*/^{39}Ar$_K$	1σ	Age in Ma	1σ	% ^{40}Ar*	^{40}Ar/^{36}Ar	^{37}Ar$_{Ca}$/^{39}Ar$_K$
4.961E-06	2.46	0.05	18.70	0.44	57.85	701.12	0.043
4.715E-06	2.54	0.02	19.30	0.27	75.06	1184.71	0.044

J = 0.00424 ± 0.000049; CIC-44 sample weight = 0.043 g (1st exp) 0.1487 g (2nd exp)

t_p = 19.44 ± 0.25 Ma, calculated with the weighted mean of fractions s to x, representing 91.21% of ^{39}Ar released in 6 consecutive fractions, MSWD = 0.66

t_c = 19.24 ± 0.14 Ma, (^{40}Ar/^{36}Ar)$_i$ = 289 ± 5, MSWD = 1.52 for n = 24

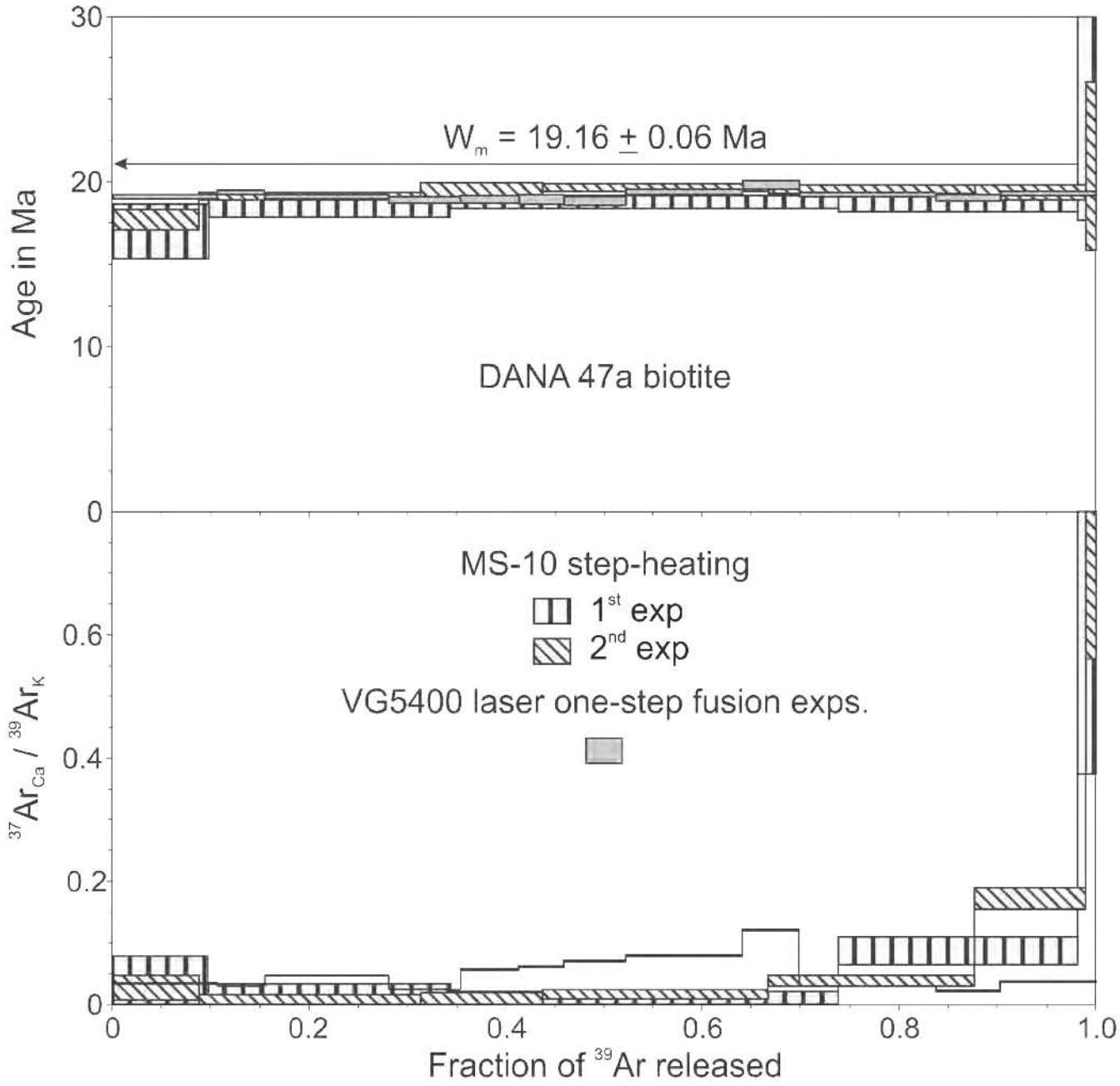

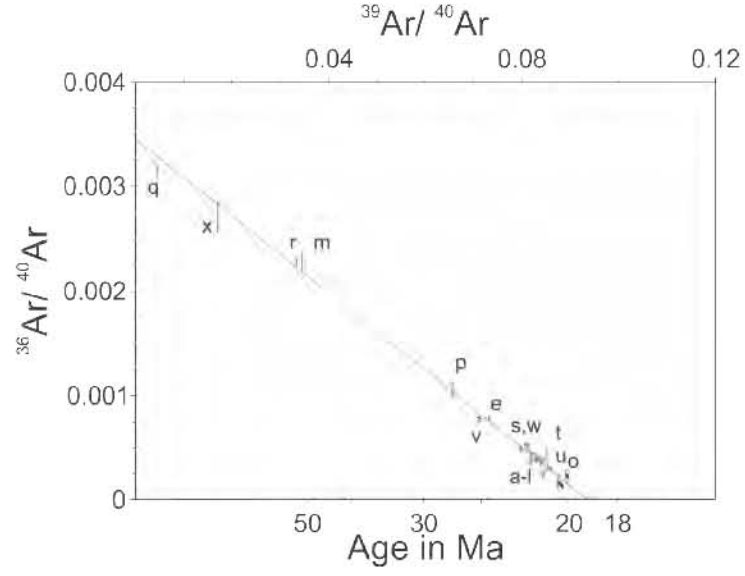

t_o = 19.24 ± 0.14 Ma

$(^{40}Ar / ^{36}Ar)_i$ = 289 ± 5

MSWD = 1.52, n = 24

Sample Name: SCr 09-20

Location: Santa Cruz Island
Latitude: 25.2959°
Longitude: -110.7005°
Altitude/Depth (m.a.s.l.): 0

Rock type: Santa Cruz Island

^{40}Ar-^{39}Ar age
Sample Name: SCr 09-20
Mineral: Biotite

Laser step-heating experiments on biotite concentrate

Pwr	^{39}Ar × 10^{-6}	F ^{39}Ar	^{40}Ar*/^{39}Ar$_K$	1σ	Age in Ma	1σ			% ^{40}Ar*	^{40}Ar/^{36}Ar	^{37}Ar$_{Ca}$/^{39}Ar$_K$
0.20	51.780	0.0167	12.61	0.38	82.35	2.40	a	‡	41.72	507.07	0.069
0.50	966.652	0.3119	15.17	0.07	98.61	0.47	b		85.84	2086.57	0.033
0.60	497.604	0.1606	14.88	0.09	96.81	0.60	c		95.34	6337.82	0.015
0.70	232.664	0.0751	14.45	0.07	94.06	0.44	d		99.90	293668.12	0.170
0.80	227.597	0.0734	14.58	0.10	94.90	0.62	e		97.30	10943.24	0.043
1.10	291.090	0.0939	14.42	0.07	93.89	0.41	f		98.66	22000.25	0.041
1.30	199.845	0.0645	14.45	0.08	94.03	0.48	g		99.32	43591.15	0.140
1.60	251.422	0.0811	14.71	0.08	95.71	0.48	h		98.83	25182.95	0.146
1.90	137.236	0.0443	-----	----	-----	----	i	‡	-----	---------	0.238
5.44	243.088	0.0784	14.36	0.07	93.47	0.44	j		93.75	4728.90	0.222

Integrated results

^{39}Ar × 10^{-6}	^{40}Ar*/^{39}Ar$_K$	1σ	Age in Ma	1σ	% ^{40}Ar*	^{40}Ar/^{36}Ar	^{37}Ar$_{Ca}$/^{39}Ar$_K$
3099.0	14.75	0.04	95.96	0.79	91.70	3558.25	0.082

J = 0.003704 ± 0.000030

Preferred age t_c = 93.83 ± 0.93 Ma

(^{40}Ar/^{36}Ar)$_i$ = 382 ± 24, MSWD = 5.1 for n = 8

t_p = 94.48 ± 0.40 Ma; plateau age calculated with the weighted mean of fractions d to h, representing 38.80% of ^{39}Ar released in 5 consecutive fractions, MSWD = 0.77

Mass 36 was not measured correctly due to analytical problems, for this reason no age information is available. The integrated data are approximate and only reported for illustrative purposes.

‡ fractions ignored in the isochron age calculation

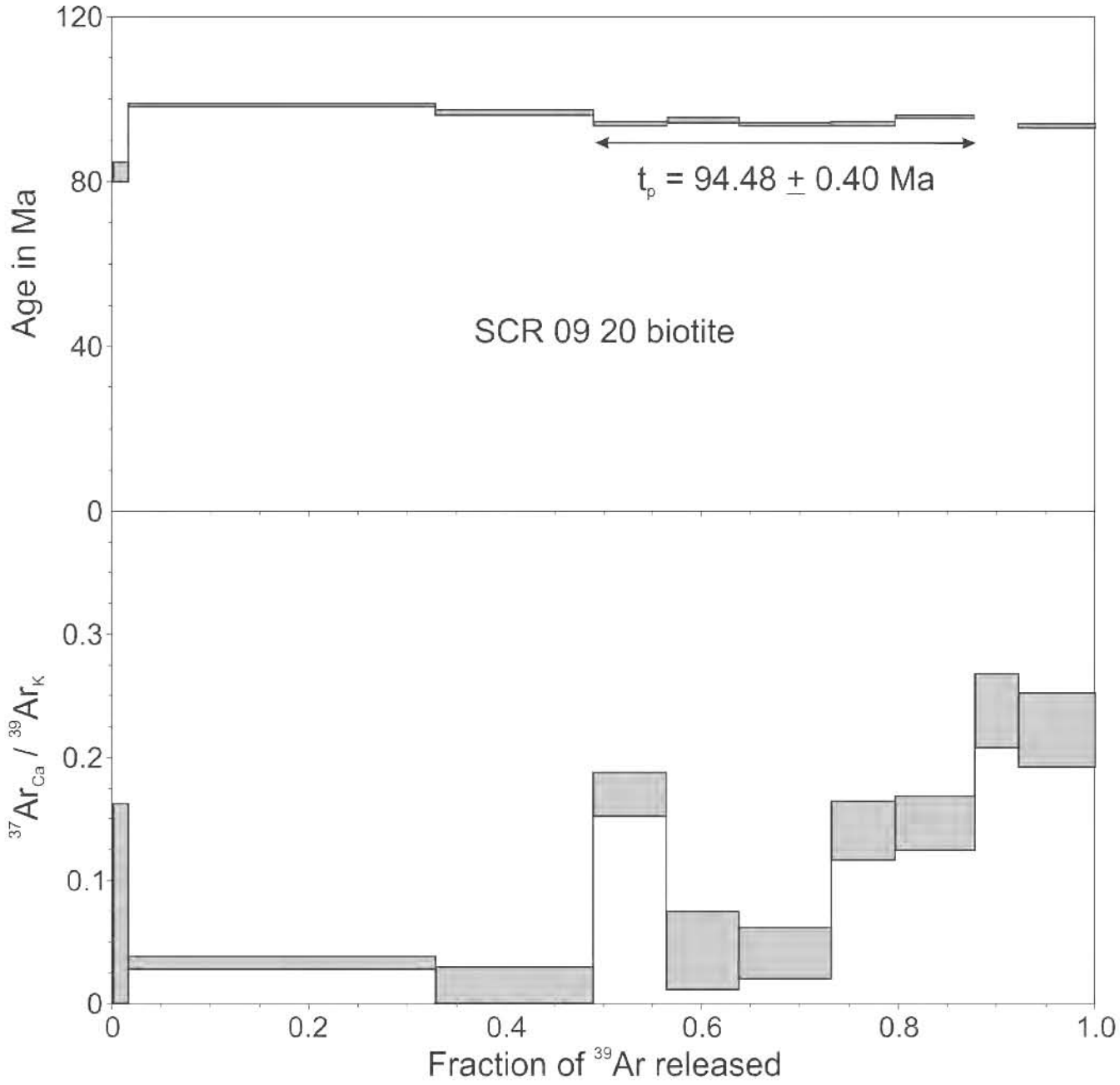

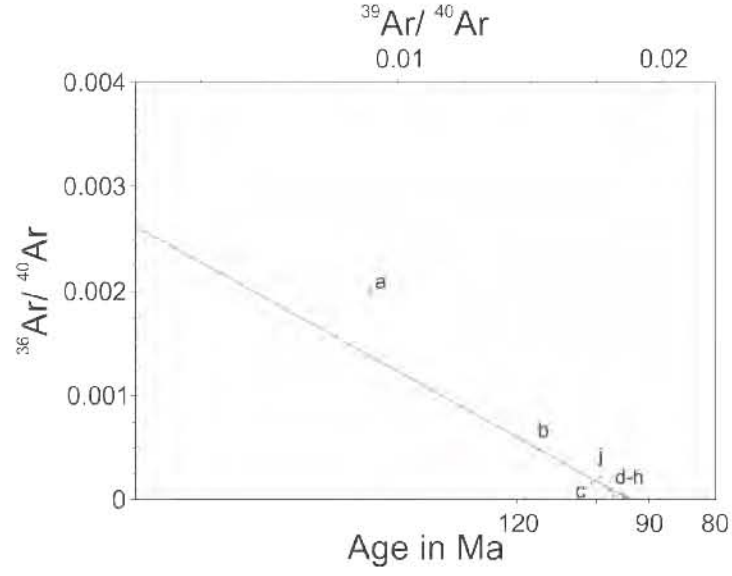

t_c = 93.83 ± 0.93 Ma

$(^{40}Ar / ^{36}Ar)_i$ = 382 ± 24

MSWD = 5.1, n = 8

Sample Name: BEKL 4D-1

Location: Pescadero Canyon
Latitude: 23.8280° (i); 23.8320° (e)
Longitude: -109.6020° (i); -109.8320° (e)
Altitude/Depth (m.a.s.l.): -1020 (i), -850 (e) (wire)

Rock type: Biotite granite

U-Pb Age

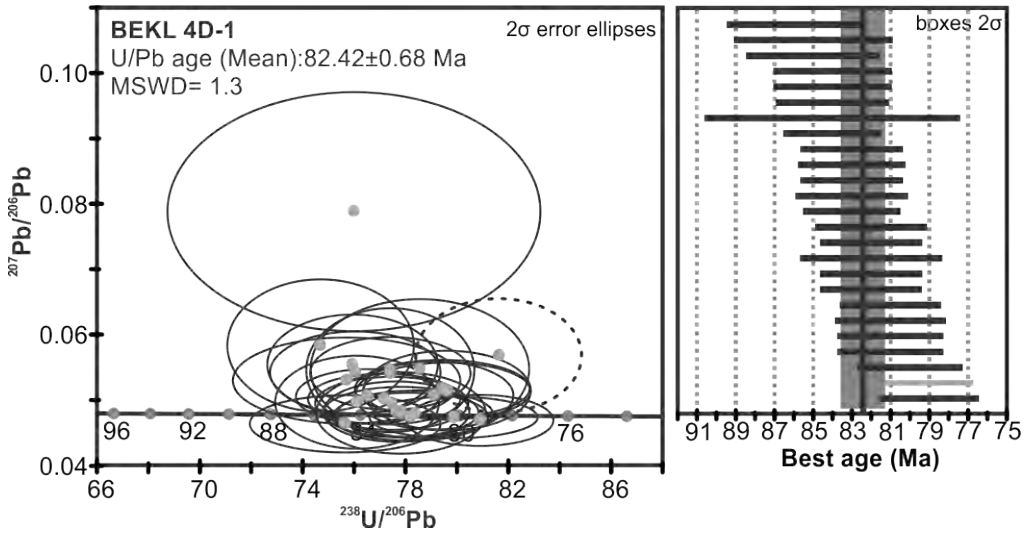

Preferred age: t= 82.42±0.68 Ma

Weighted mean age (95% confidence) calculated with 28 data points. Single crystals are in the 78 to 85 Ma age range. Older and younger analyses were removed from age analysis.

^{40}Ar-^{39}Ar age
Sample Name: BEKL 4D-1
Mineral: Biotite

Laser step-heating experiments on biotite concentrate

Pwr	^{39}Ar × 10^{-6}	F ^{39}Ar	^{40}Ar*/^{39}Ar$_K$	1σ	Age in Ma	1σ			% ^{40}Ar*	^{40}Ar/^{36}Ar	^{37}Ar$_{Ca}$/^{39}Ar$_K$
0.20	11.018	0.0041	10.63	2.76	66.41	16.93	a	‡	23.29	385.24	0.130
0.40	81.991	0.0306	6.33	0.32	39.86	2.01	b	‡	33.34	443.32	0.012
0.60	279.309	0.1043	11.03	0.07	68.83	0.45	c	‡	82.66	1703.94	0.005
0.80	345.048	0.1288	12.26	0.06	76.38	0.37	d	‡	93.22	4361.32	0.006
1.00	451.815	0.1687	12.73	0.03	79.23	0.20	e	‡	95.63	6766.12	0.005
1.20	273.882	0.1022	13.03	0.06	81.10	0.34	f		98.09	15503.27	0.005
1.62	459.052	0.1714	12.78	0.04	79.55	0.22	g		99.37	46797.80	0.026
2.00	263.814	0.0985	12.59	0.04	78.36	0.24	h		99.02	30027.51	0.072
2.50	305.150	0.1139	12.33	0.04	76.78	0.25	i		99.54	64644.73	0.108
3.50	74.346	0.0277	11.85	0.10	73.90	0.63	j	‡	98.02	14892.77	0.244
6.00	133.408	0.0498	11.67	0.08	72.76	0.46	k	‡	95.67	6827.47	0.256

Integrated results

^{39}Ar × 10^{-6}	^{40}Ar*/^{39}Ar$_K$	1σ	Age in Ma	1σ	% ^{40}Ar*	^{40}Ar/^{36}Ar	^{37}Ar$_{Ca}$/^{39}Ar$_K$
2679.0	12.19	0.03	75.95	0.22	91.88	3639.82	0.047

J = 0.003527 ± 0.000007

Preferred age t_c = 75.65 ± 2.39 Ma

(^{40}Ar/^{36}Ar)$_i$ = 1748 ± 1030, MSWD = 3.9 for n = 4

weighted mean of fractions e to h

W_m = 79.37 ± 0.48 Ma, 54.08% of ^{39}Ar released in 4 consecutive fractions, MSWD = 11.54

‡ fraction ignored in the isochron given in the figure

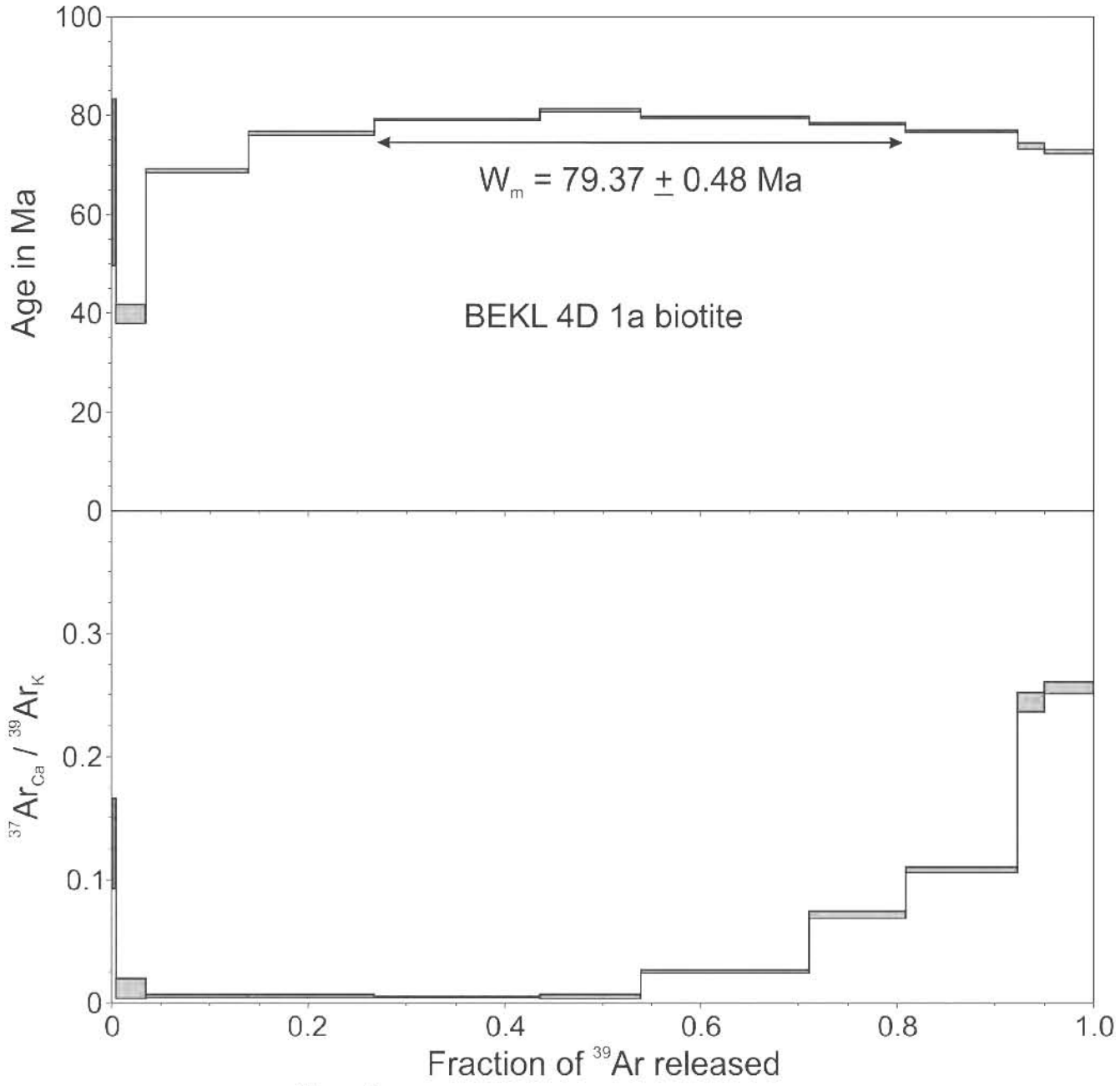

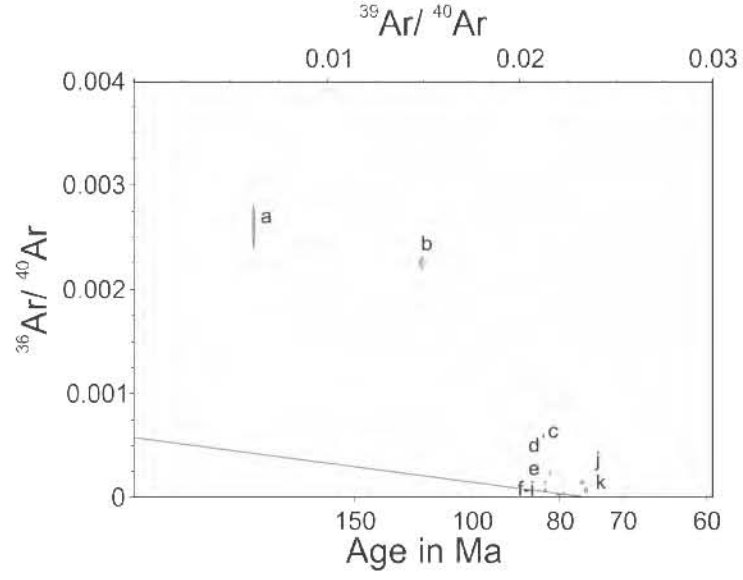

t_c = 75.65 ± 2.39 Ma

$(^{40}Ar / ^{36}Ar)_i$ = 1748 ± 1030

MSWD = 3.9, n = 4

Sample Name: BEKL 4D-2

Location: Pescadero Canyon
Latitude: 23.8280° (i); 23.8320° (e)
Longitude: -109.6020° (i); -109.8320° (e)
Altitude/Depth (m.a.s.l.): -1020 (i), -850 (e) (wire)

Rock type: Biotite granite

U-Pb Age

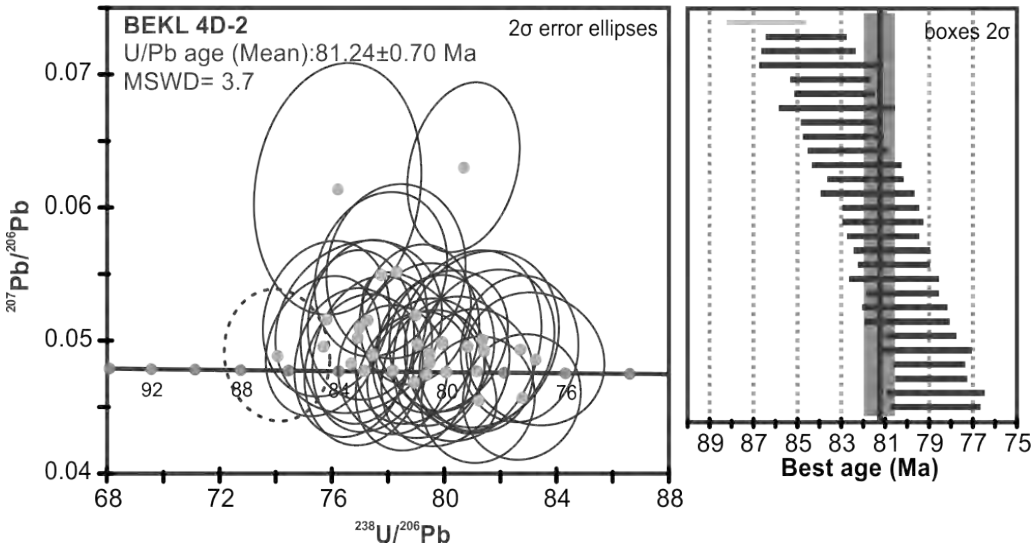

Preferred age: t= 81.24±0.70 Ma

Weighted mean age (95% confidence) calculated with 24 data points. Single crystals are in the 79 to 87 Ma age range. Older and younger analyses were removed from age analysis.

^{40}Ar-^{39}Ar age
Sample Name: BEKL 4D-2
Mineral: Biotite

Laser step-heating experiments on biotite concentrate

Pwr	^{39}Ar × 10^{-6}	F ^{39}Ar	^{40}Ar*/^{39}Ar$_K$	1σ	Age in Ma	1σ			% ^{40}Ar*	^{40}Ar/^{36}Ar	^{37}Ar$_{Ca}$/^{39}Ar$_K$
0.20	5.044	0.0008	11.94	2.93	74.45	17.89	a	‡	10.70	330.89	0.000
0.40	45.607	0.0074	6.89	0.23	43.31	1.41	b	‡	45.12	538.45	0.018
0.60	260.558	0.0422	12.06	0.07	75.13	0.41	c	‡	76.81	1274.18	0.006
0.80	632.992	0.1025	12.23	0.03	76.17	0.19	d	‡	93.68	4674.37	0.002
1.00	473.800	0.0767	12.47	0.04	77.67	0.22	e		99.47	55496.19	0.001
1.20	519.303	0.0841	12.44	0.03	77.48	0.15	f		97.84	13686.97	0.001
1.40	644.945	0.1045	12.53	0.02	78.03	0.15	g		98.24	16766.81	0.003
1.60	532.819	0.0863	12.61	0.03	78.51	0.19	h		99.55	65196.79	0.010
1.80	677.683	0.1098	12.56	0.02	78.19	0.14	i		99.61	75010.99	0.002
2.00	340.092	0.0551	12.53	0.04	78.02	0.22	j		99.63	79306.74	0.004
2.20	554.222	0.0898	12.58	0.03	78.33	0.19	k		99.90	288627.60	0.007
2.40	320.808	0.0520	12.50	0.04	77.84	0.25	l		99.82	164196.58	0.019
2.70	320.611	0.0519	12.50	0.03	77.83	0.21	m		99.48	57027.27	0.037
3.00	234.529	0.0380	12.48	0.04	77.74	0.25	n		99.91	333830.71	0.069
3.40	197.669	0.0320	12.48	0.05	77.71	0.28	o		99.61	76725.40	0.122
3.90	134.238	0.0217	12.45	0.06	77.56	0.34	p		99.39	48204.88	0.146
4.60	130.343	0.0211	12.50	0.07	77.83	0.40	q		99.62	76845.97	0.228
5.44	75.539	0.0122	12.49	0.09	77.76	0.52	r		99.24	38900.42	0.345
6.60	73.053	0.0118	12.34	0.12	76.86	0.74	s		98.15	15971.58	0.382

Integrated results

^{39}Ar × 10^{-6}	^{40}Ar*/^{39}Ar$_K$	1σ	Age in Ma	1σ	% ^{40}Ar*	^{40}Ar/^{36}Ar	^{37}Ar$_{Ca}$/^{39}Ar$_K$
6174.0	12.43	0.02	77.40	0.18	96.43	8269.11	0.029

J = 0.003527 ± 0.000007

Preferred age t_p = 77.93 ± 0.09 Ma

Weighted mean of fractions e to s, representing 84.71% of ^{39}Ar released in 15 consecutive fractions, MSWD = 1.42

‡ fraction ignored in the isochron given in the figure

t_c = 78.05 ± 0.19 Ma, (^{40}Ar/^{36}Ar)$_i$ = 249 ± 40, MSWD = 2.84 for n = 15

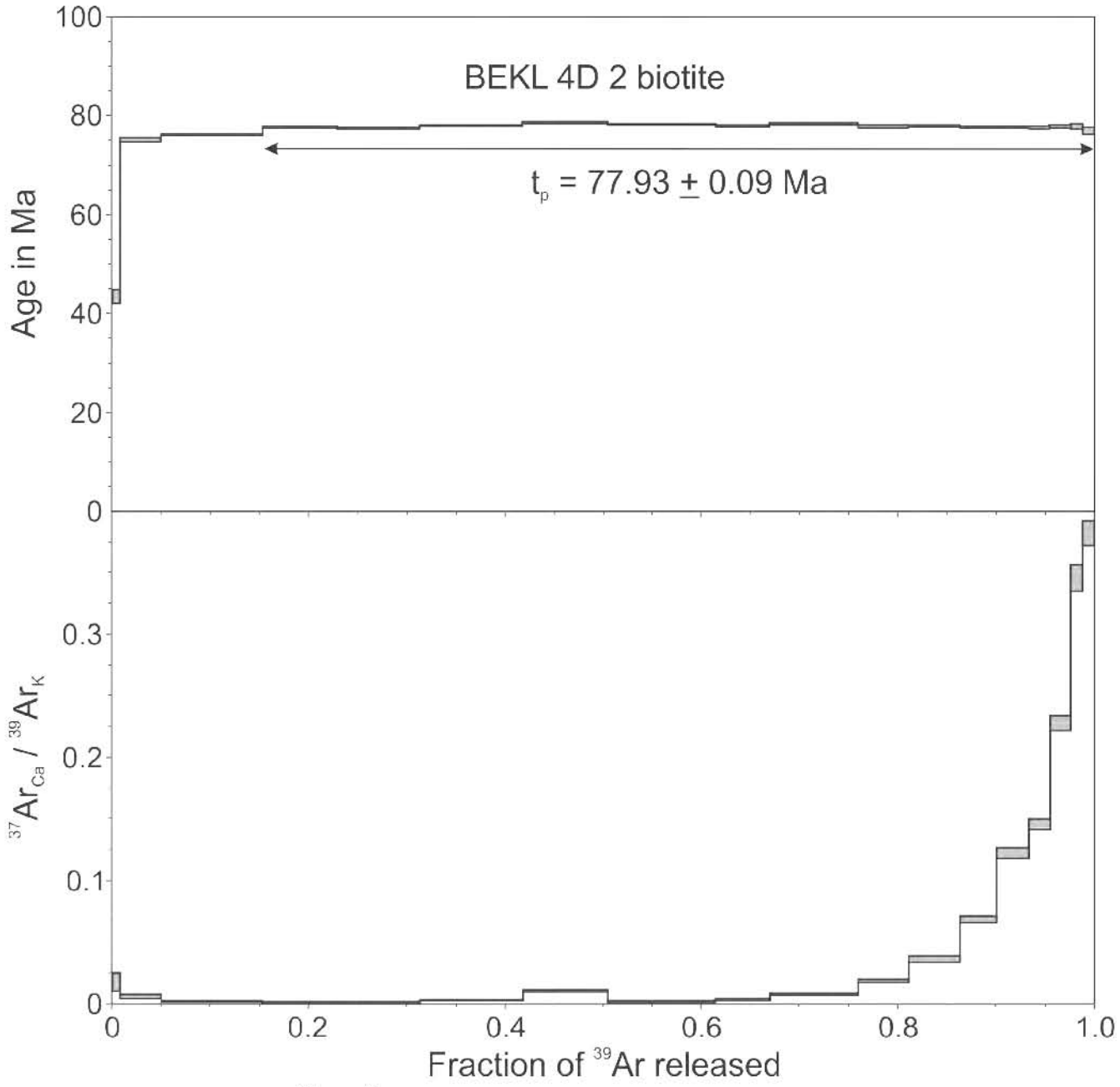

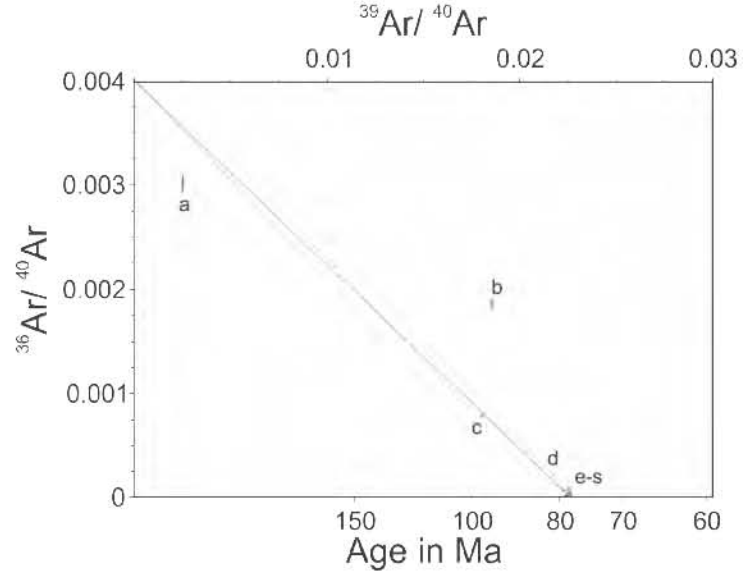

t_c = 78.05 ± 0.19 Ma

$(^{40}Ar / ^{36}Ar)_i$ = 249 ± 40

MSWD = 2.84, n = 15

Sample Name: LCB 7

Location: Los Cabos Block
Latitude: 23.2697°
Longitude: -109.442°
Altitude/Depth (m.a.s.l.): 0

Rock type: Granodiorite

U-Pb Age

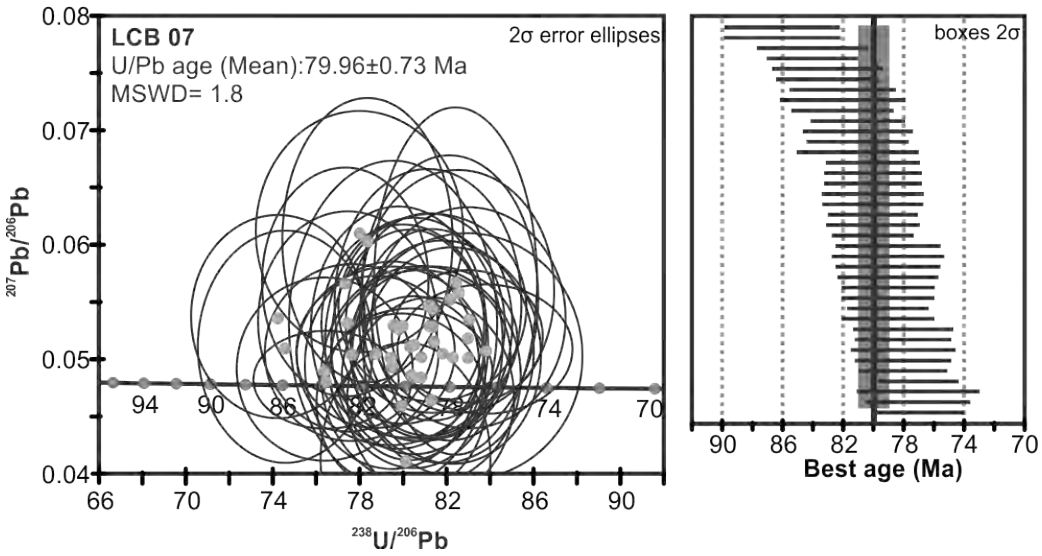

Preferred age: t= 79.96±0.73 Ma

Weighted mean age (95% confidence) calculated with 38 data points. Single crystals are in the 94 to 101 Ma age range. One xenocrystal with an age of 160 Ma was removed from analysis.

Sample Name: Sayu 01

Location: Sayulita, Nayarit
Latitude: 20.8823°
Longitude: -105.4177°
Altitude/Depth (m.a.s.l.): 114

Rock type: Granodiorite

U-Pb Age

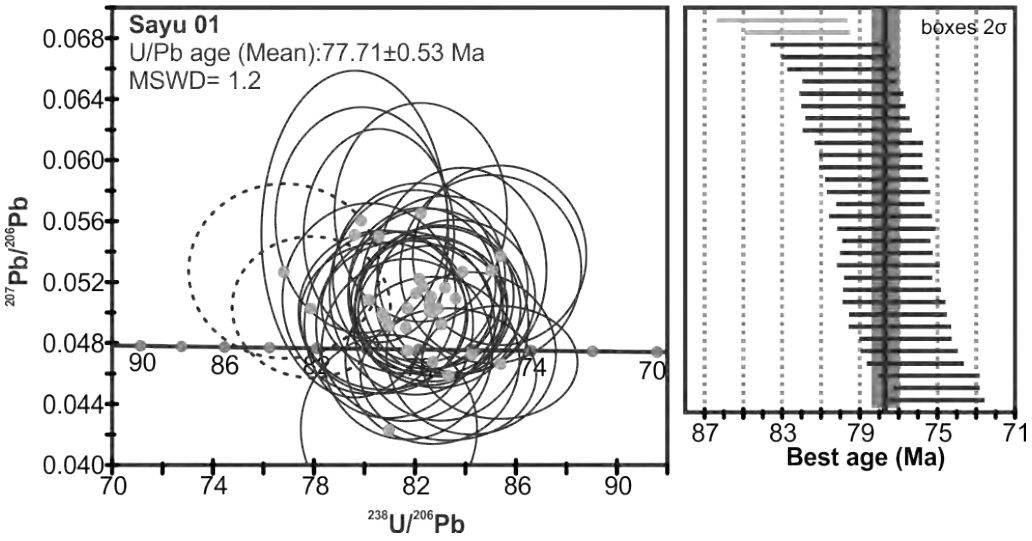

Preferred age: t= 77.71±0.53 Ma

Weighted mean age (95% confidence) calculated with 26 data points. Single crystals are in the 76.1 to 80 Ma age range. The three youngest and the two oldest analyses were removed from age calculation. One analysis with low $^{207}Pb/^{206}Pb$ was also removed.

^{40}Ar-^{39}Ar age
Sample Name: Sayu 01
Mineral: Hornblende

Laser step-heating experiments on hornblende concentrate

Pwr	^{39}Ar × 10^{-6}	F ^{39}Ar	^{40}Ar*/^{39}Ar$_K$	1σ	Age in Ma	1σ			% ^{40}Ar*	^{40}Ar/^{36}Ar	^{37}Ar$_{Ca}$/^{39}Ar$_K$
0.20	2.230	0.0031	30.35	8.34	185.65	48.46	a	‡	13.07	339.93	3.245
0.50	6.472	0.0091	16.92	2.59	105.85	15.76	b	‡	29.00	416.22	4.635
0.75	12.835	0.0180	6.62	0.84	42.14	5.29	c	‡	45.85	545.71	9.344
1.20	67.909	0.0956	9.51	0.25	60.25	1.59	d	‡	88.13	2489.98	4.386
1.50	237.296	0.3341	12.12	0.07	76.43	0.43	e		97.05	10003.13	3.625
1.70	167.114	0.2353	11.51	0.10	72.67	0.63	f		98.31	17469.02	3.396
2.00	132.063	0.1859	11.70	0.09	73.83	0.54	g		98.97	28606.44	3.699
2.50	84.320	0.1187	11.31	0.19	71.43	1.18	h		98.40	18481.48	3.358
0.50	16.250	0.0073	14.40	1.14	90.44	7.00	i	‡	16.51	353.94	3.073
0.80	68.900	0.0310	7.19	0.23	45.72	1.42	j	‡	54.98	656.40	1.655
1.06	207.390	0.0935	7.22	0.04	45.94	0.27	k	‡	94.35	5227.20	0.756
1.25	77.782	0.0351	7.95	0.10	50.51	0.62	l	‡	97.60	12317.15	0.519
1.50	155.518	0.0700	9.89	0.06	62.60	0.38	m	‡	95.35	6349.62	1.855
1.70	290.043	0.1305	11.24	0.04	71.02	0.25	n		97.56	12129.93	2.716
1.90	379.255	0.1706	11.19	0.04	70.69	0.22	o		97.67	12678.82	3.139
2.10	284.512	0.1280	11.56	0.05	73.00	0.30	p		97.78	13328.61	3.315
2.28	265.765	0.1196	11.51	0.04	72.70	0.22	q		97.77	13274.11	3.373
2.50	111.830	0.0503	10.60	0.08	67.06	0.48	r		98.99	29262.59	2.571
2.75	78.511	0.0353	10.96	0.10	69.25	0.61	s		97.48	11722.05	3.049
3.10	66.950	0.0301	11.82	0.12	74.58	0.77	t		97.59	12249.61	3.835
3.70	77.463	0.0348	12.48	0.12	78.66	0.75	u		97.09	10159.16	4.074
7.00	141.850	0.0638	11.83	0.09	74.64	0.56	v		96.45	8316.10	4.191

Integrated results

^{39}Ar × 10^{-6}	^{40}Ar*/^{39}Ar$_K$	1σ	Age in Ma	1σ	% ^{40}Ar*	^{40}Ar/^{36}Ar	^{37}Ar$_{Ca}$/^{39}Ar$_K$
708.5	11.55	0.06	72.94	0.44	88.58	2588.50	3.737
2218.0	10.67	0.02	67.49	0.22	91.37	3424.18	2.772

J = 0.003571 ± 0.000009

Preferred age t = 70.85 ± 0.74 Ma

Weighted mean of fractions n to v, 76.31% of ^{39}Ar released in 9 consecutive fractions, MSWD = 32.8 The sample does not fulfill the criteria for plateau age definition.

t_c = 57.52 ± 5.94 Ma; $(^{40}Ar/^{36}Ar)_i$ = 2869 ± 1048, MSWD = 1.12 for n = 13

‡ fraction ignored in the isochron given in the figure

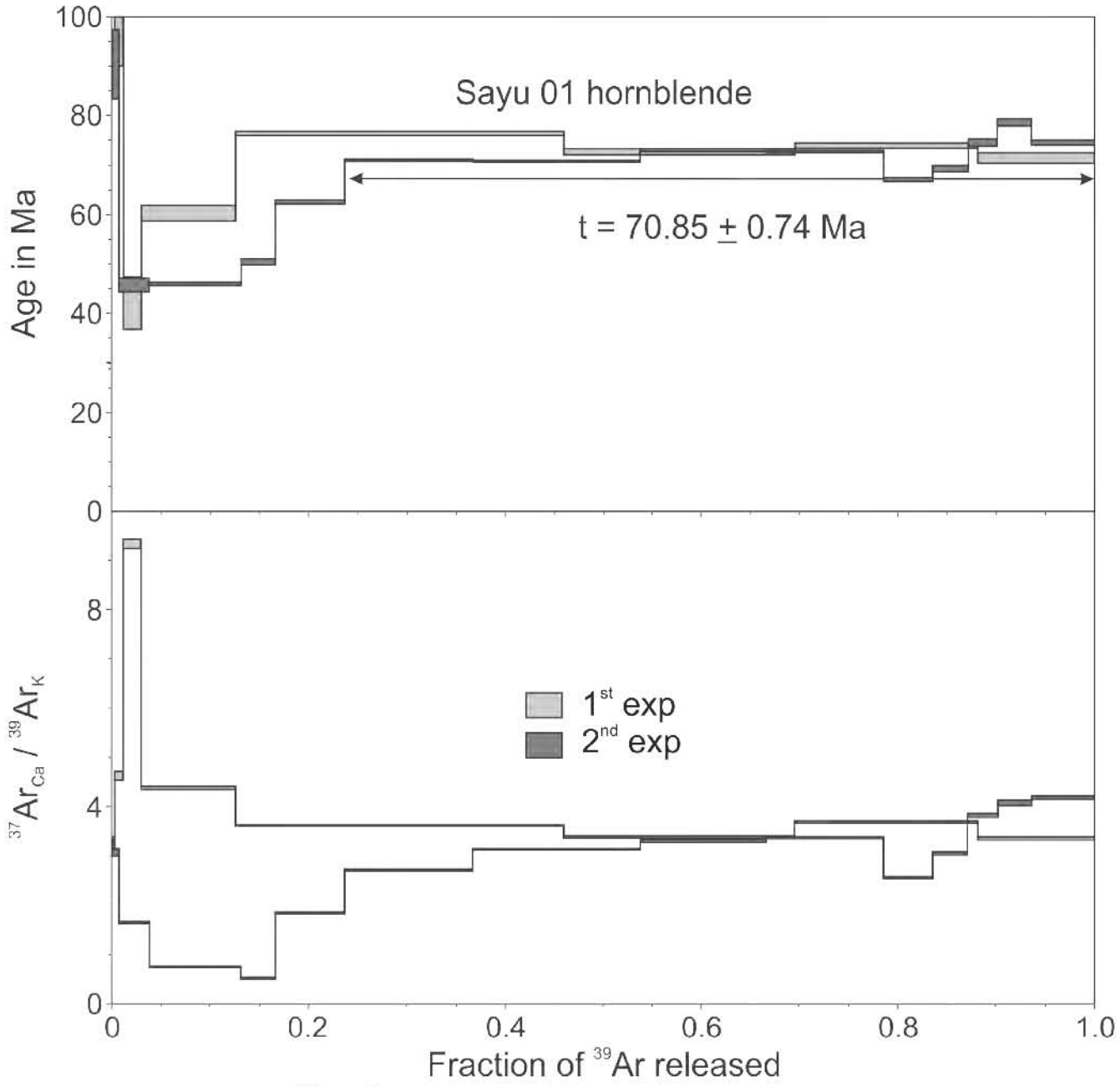

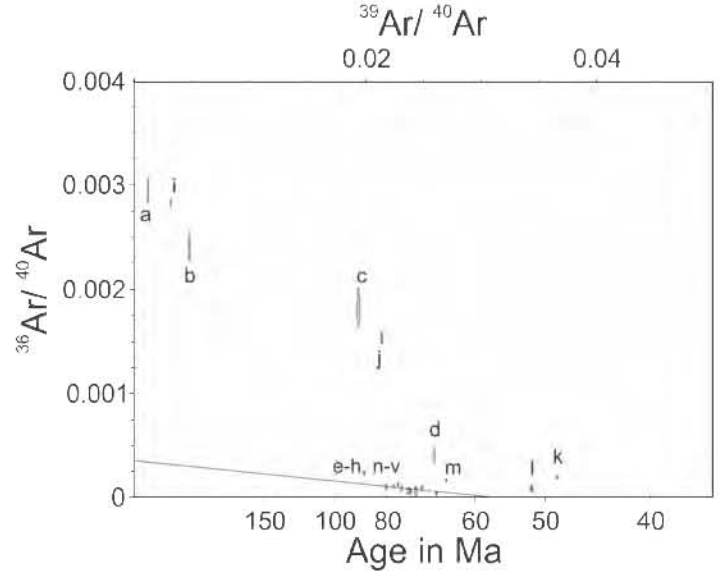

t_c = 57.52 ± 5.94 Ma

$(^{40}Ar / ^{36}Ar)_i$ = 2869 ± 1048

MSWD = 1.12, n = 13

^{40}Ar-^{39}Ar age
Sample Name: Sayu 01
Mineral: Biotite

Laser step-heating experiments on biotite concentrate

Pwr	^{39}Ar × 10^{-6}	F ^{39}Ar	^{40}Ar*/^{39}Ar$_K$	1σ	Age in Ma	1σ			% ^{40}Ar*	^{40}Ar/^{36}Ar	^{37}Ar$_{Ca}$/^{39}Ar$_K$
0.20	3.982	0.0053	1.91	2.63	12.25	16.84	a	‡	17.27	357.17	0.139
0.40	78.355	0.1052	7.08	0.20	45.08	1.26	b	‡	74.47	1157.32	0.018
0.60	166.744	0.2240	7.40	0.09	47.07	0.54	c	‡	97.36	11199.26	0.008
1.00	226.224	0.3038	7.64	0.05	48.55	0.32	d		99.51	60515.51	0.014
1.20	119.123	0.1600	7.77	0.11	49.38	0.67	e		99.78	133627.68	0.021
1.40	37.173	0.0499	7.57	0.25	48.10	1.57	f		97.54	12030.06	0.033
1.60	17.401	0.0234	7.40	0.72	47.05	4.53	g		97.80	13409.22	0.060
2.00	31.922	0.0429	7.73	0.51	49.10	3.18	h		98.68	22429.19	0.058
4.00	45.881	0.0616	7.77	0.24	49.39	1.49	i		98.54	20290.53	0.156
7.00	17.729	0.0238	7.71	0.81	49.01	5.08	j		96.84	9353.89	0.130

Integrated results

^{39}Ar × 10^{-6}	^{40}Ar*/^{39}Ar$_K$	1σ	Age in Ma	1σ	% ^{40}Ar*	^{40}Ar/^{36}Ar	^{37}Ar$_{Ca}$/^{39}Ar$_K$
744.5	7.52	0.06	47.82	0.37	95.02	5929.18	0.030

J = 0.003571 ± 0.000009

Preferred age t_p = 48.71 ± 0.29 Ma

Weighted mean of fractions d to j, representing 66.55% of ^{39}Ar released in 7 consecutive fractions, MSWD = 0.28

t_c = 47.37 ± 6.80 Ma, $(^{40}Ar/^{36}Ar)_i$ = 1762 ± 2586, MSWD = 0.11 for n = 7

‡ fraction ignored in the isochron given in the figure

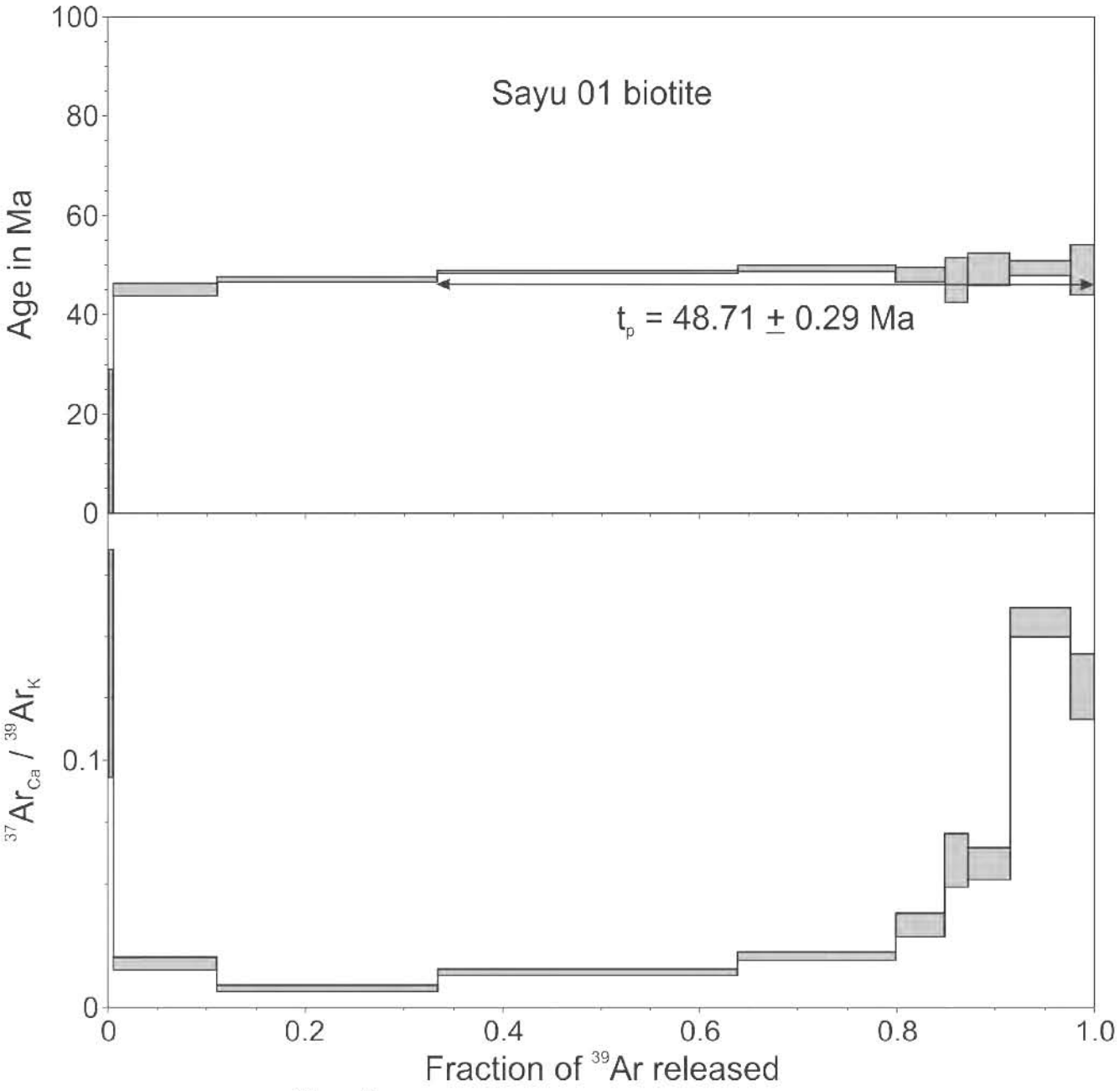

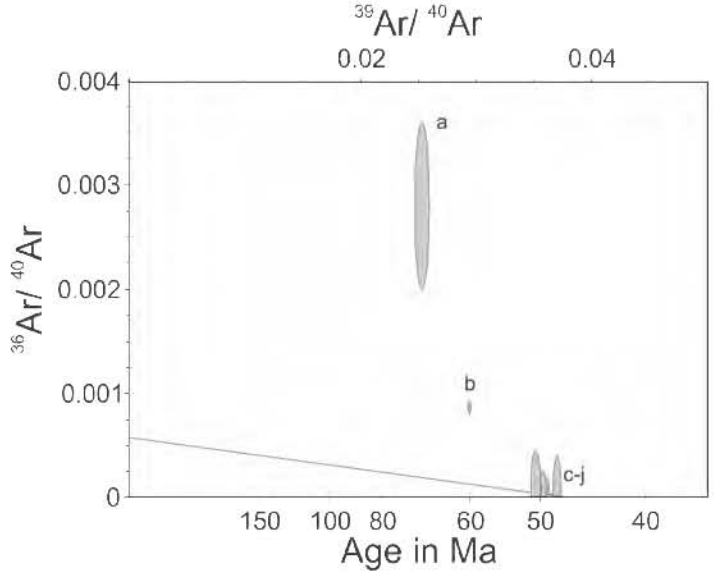

t_c = 47.37 ± 6.80 Ma

$(^{40}Ar / ^{36}Ar)_i$ = 1762 ± 2586

MSWD = 0.11, n = 7

Sample Name: Sayu 02

Location: Sayulita, Nayarit
Latitude: 20.8685°
Longitude: -105.4411°
Altitude/Depth (m.a.s.l.): 19

Rock type:

U-Pb Age

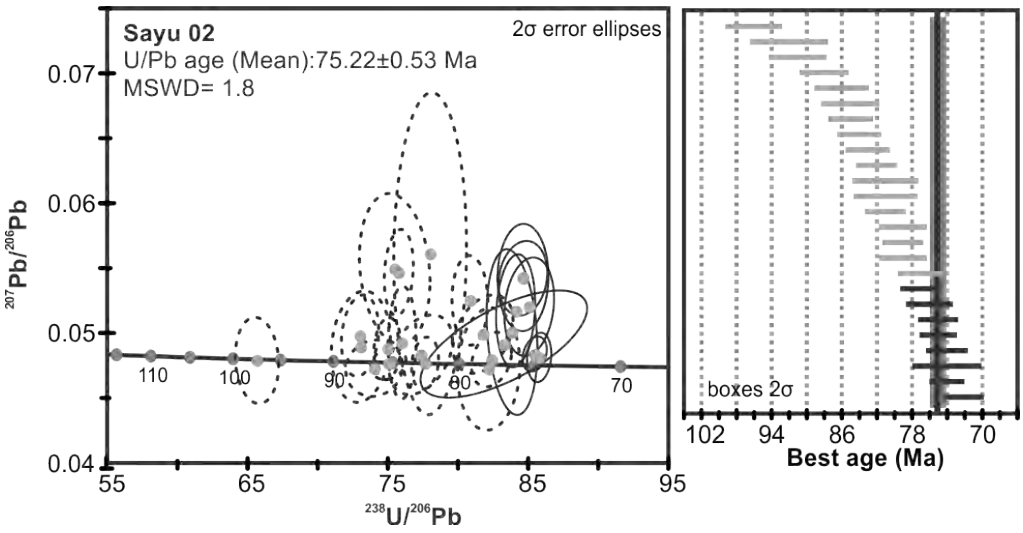

Preferred age: t= 75.22±0.53 Ma

This sample has a wide single crystal age range, from 74 to 96 Ma. The 75.2±1.1 Ma age (Weighted mean age with 95% confidence), the closer age to crystallization, was calculated using the 8 youngest analyses, where the best cluster of ages is present. Several xenocrystic analyses were found with an age span from 123 to 160 Ma.

^{40}Ar-^{39}Ar age
Sample Name: Sayu 02
Mineral: Biotite

Laser step-heating experiments on biotite concentrate

Pwr	^{39}Ar × 10^{-6}	F ^{39}Ar	^{40}Ar*/^{39}Ar$_K$	1σ	Age in Ma	1σ			% ^{40}Ar*	^{40}Ar/^{36}Ar	^{37}Ar$_{Ca}$/^{39}Ar$_K$
0.20	19.104	0.0097	3.71	1.02	23.73	6.47	a		12.69	338.44	0.053
0.50	168.737	0.0859	5.66	0.12	36.08	0.76	b	‡	55.74	667.60	0.022
0.70	228.495	0.1163	6.76	0.06	43.02	0.38	c		84.06	1853.54	0.022
1.00	355.109	0.1807	7.23	0.04	45.96	0.26	d	‡	95.40	6428.74	0.015
1.20	171.756	0.0874	7.32	0.08	46.57	0.53	e	‡	96.78	9178.57	0.027
1.40	172.132	0.0876	6.89	0.05	43.83	0.32	f		94.49	5360.78	0.036
1.60	182.494	0.0929	6.85	0.08	43.61	0.49	g		90.90	3247.99	0.039
2.00	227.568	0.1158	6.95	0.07	44.25	0.41	h		95.80	7039.93	0.051
2.60	258.133	0.1314	7.25	0.05	46.13	0.32	i	‡	97.61	12379.63	0.079
3.00	79.376	0.0404	7.30	0.15	46.41	0.95	j	‡	98.49	19545.73	0.165
4.00	38.423	0.0196	6.91	0.33	43.98	2.10	k		96.64	8788.86	0.325
6.00	63.498	0.0323	6.64	0.17	42.31	1.05	l		87.29	2325.38	0.497

Integrated results

^{39}Ar × 10^{-6}	^{40}Ar*/^{39}Ar$_K$	1σ	Age in Ma	1σ	% ^{40}Ar*	^{40}Ar/^{36}Ar	^{37}Ar$_{Ca}$/^{39}Ar$_K$
1965.0	6.90	0.03	43.89	0.20	86.62	2208.86	0.062

J = 0.003571 ± 0.000009

Preferred age t_p = 43.91 ± 0.23 Ma

Weighted mean of fractions f to h, 29.63% of ^{39}Ar released in 3 consecutive fractions, MSWD = 0.52

t_c = 44.20 ± 0.24 Ma, $(^{40}Ar/^{36}Ar)_i$ = 255 ± 9, MSWD = 0.44 for n = 7

‡ fractions ignored in the isochron given in the figure

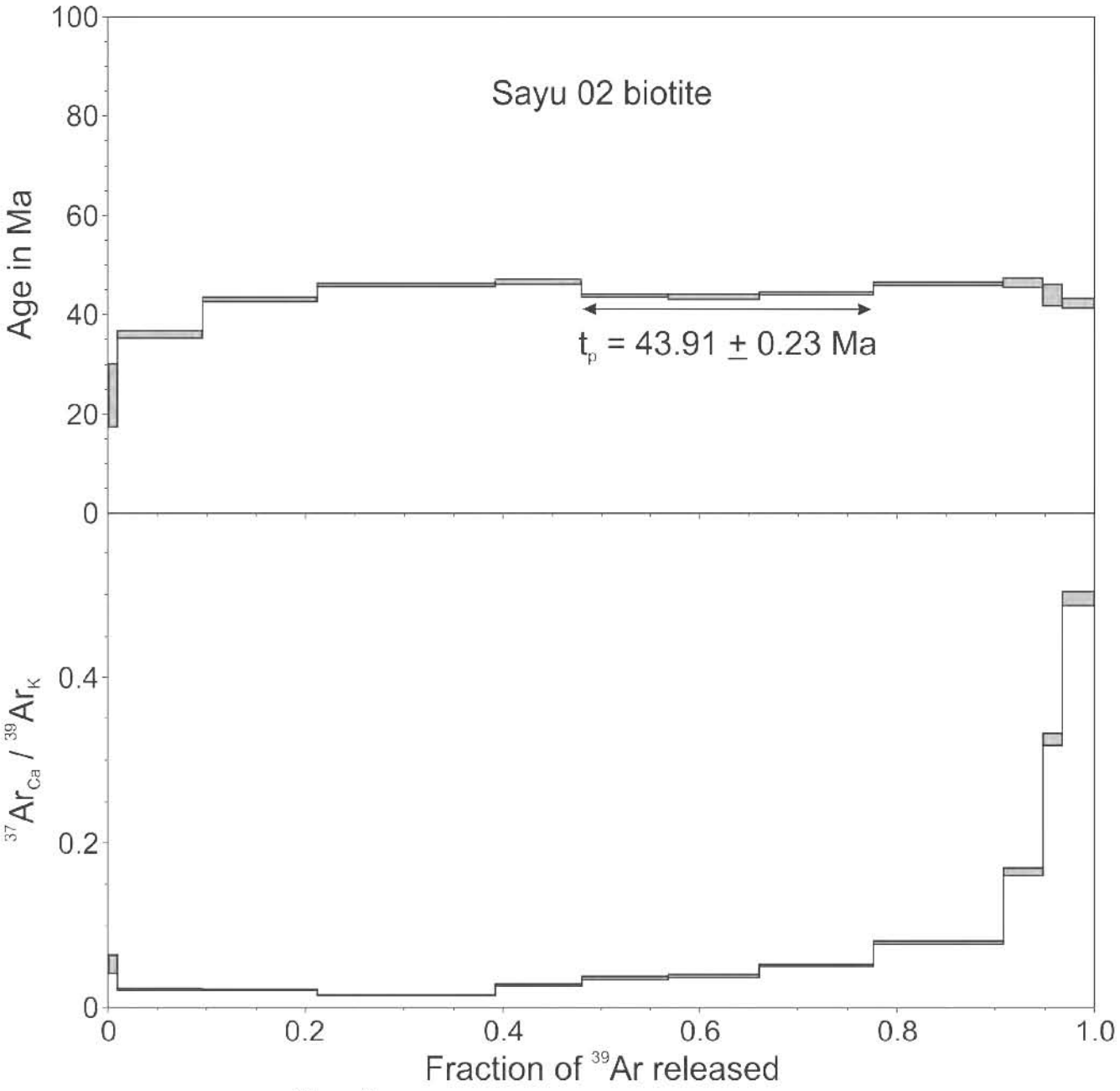

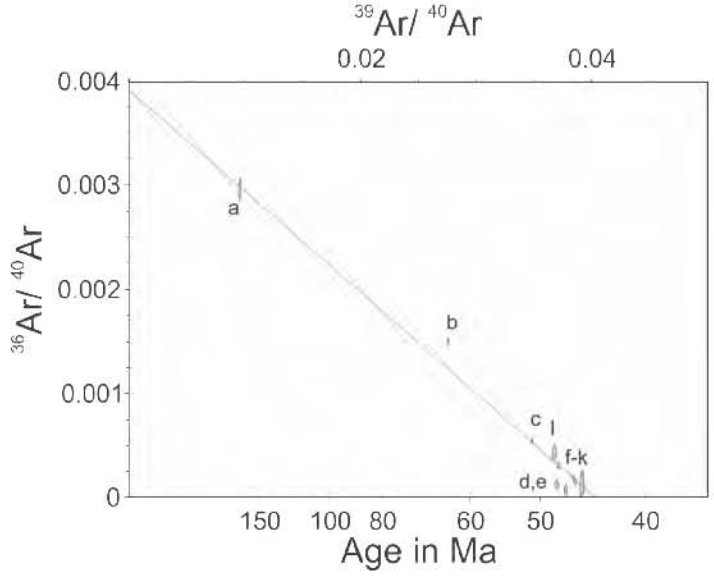

t_c = 44.20 ± 0.24 Ma

$(^{40}Ar / ^{36}Ar)_i$ = 255 ± 9

MSWD = 0.44, n = 7

Sample Name: MDCH 02

Location: Mineral de Cucharas, Nayarit
Latitude: 22.8124°
Longitude: 105.2630°
Altitude/Depth (m.a.s.l.): 377

Rock type: Granodiorite

U-Pb Age

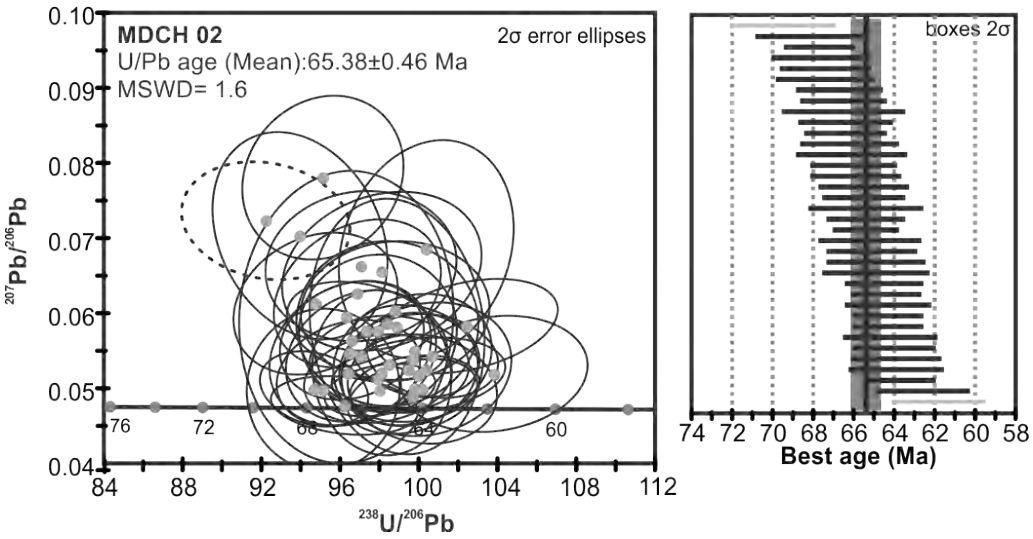

Preferred age: t= 65.38±0.46 Ma

Weighted mean age (95% confidence) calculated with 32 data points. Single crystals are in the 63.4 to 70 Ma age range. The two youngest, the two oldest and a low $^{207}Pb/^{206}Pb$ analyses were removed from age calculation.

Sample Name: Tepi 01

Location: Tepic, Nayarit
Latitude: 21.3161°
Longitude: 104.9928°
Altitude/Depth (m.a.s.l.): 750

Rock type: Granodiorite

U-Pb Age

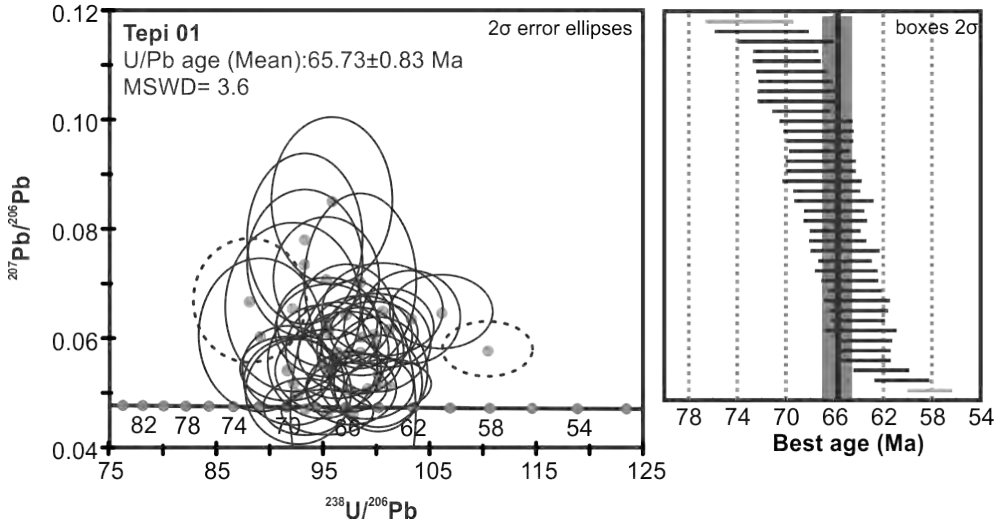

Preferred age: t= 65.73±0.83 Ma

Weighted mean age (95% confidence) calculated with 32 data points. Single crystals are in the 63.4 to 70 Ma age range. The two youngest, the two oldest and a low $^{207}Pb/^{206}Pb$ analyses were removed from age calculation.

Sample Name: Conc 01

Location: Concordia, Sinaloa
Latitude: 23.2725°
Longitude: -106.1171°
Altitude/Depth (m.a.s.l.): 113

Rock type: Granite

U-Pb Age

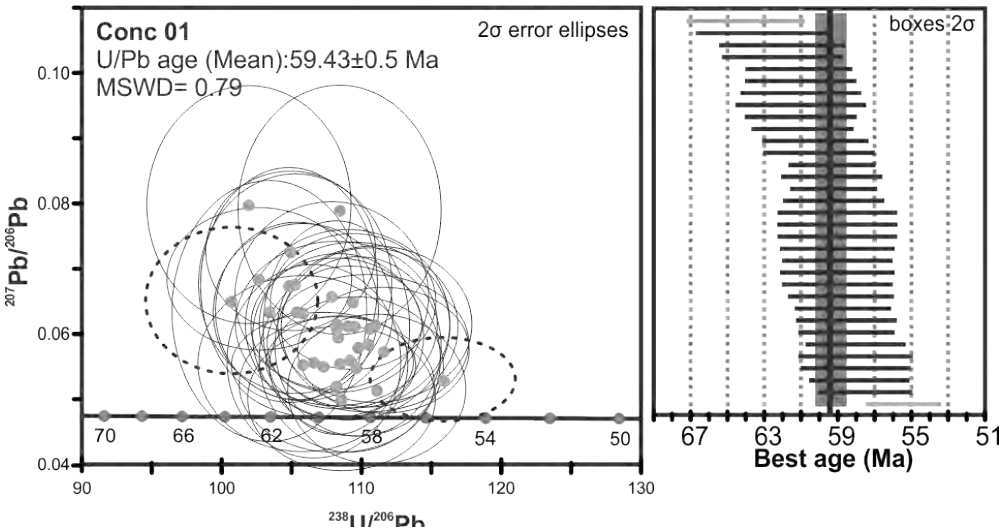

Preferred age: t= 59.43±0.51 Ma

Weighted mean age (95% confidence) calculated with 32 data points. Single crystals are in the 57.5 to 64 Ma age range. The youngest analysis was removed from age calculation.

^{40}Ar-^{39}Ar age
Sample Name: Conc 01
Mineral: Hornblende

Laser step-heating experiments on hornblende concentrate

Pwr	^{39}Ar × 10^{-6}	F ^{39}Ar	^{40}Ar*/^{39}Ar$_K$	1σ	Age in Ma	1σ			% ^{40}Ar*	^{40}Ar/^{36}Ar	^{37}Ar$_{Ca}$/^{39}Ar$_K$
0.20	0.074	0.0002	392.76	343.09	1552.08	909.27	a	‡	47.72	565.21	10.338
0.50	0.704	0.0017	74.20	19.65	413.58	97.87	b	‡	33.84	446.64	3.203
0.70	0.865	0.0021	10.53	14.99	64.82	90.57	c	‡	64.91	842.00	3.858
1.00	2.068	0.0051	0.51	5.19	3.20	32.46	d	‡	3.02	304.71	3.996
1.20	7.339	0.0180	7.37	1.68	45.58	10.26	e	‡	48.56	574.50	2.078
1.50	1.585	0.0039	7.44	7.29	46.01	44.49	f	‡	89.52	2818.97	0.540
1.70	3.945	0.0097	5.96	3.77	36.96	23.11	g	‡	76.78	1272.60	0.419
2.00	6.291	0.0154	5.88	2.02	36.47	12.38	h	‡	62.82	794.79	0.490
2.20	166.413	0.4072	9.07	0.08	55.93	0.51	i		91.30	3398.17	5.702
2.40	40.949	0.1002	8.89	0.28	54.84	1.68	j		94.09	4996.92	5.594
2.60	44.127	0.1080	9.19	0.30	56.69	1.82	k		97.86	13790.98	5.060
3.00	30.970	0.0758	9.18	0.37	56.62	2.27	l		96.07	7511.40	4.766
3.50	50.673	0.1241	8.80	0.32	54.30	1.94	m		93.77	4742.07	4.677
4.00	22.148	0.0542	8.49	0.59	52.42	3.61	n		92.38	3876.82	5.663
7.00	30.331	0.0743	8.81	0.42	54.34	2.56	o		91.59	3513.38	4.334

Integrated results

^{39}Ar × 10^{-6}	^{40}Ar*/^{39}Ar$_K$	1σ	Age in Ma	1σ	% ^{40}Ar*	^{40}Ar/^{36}Ar	^{37}Ar$_{Ca}$/^{39}Ar$_K$
407.1	9.01	0.13	55.60	0.80	87.68	2397.85	5.087

J = 0.003473 ± 0.000013

Preferred age t_p = 55.72 ± 0.47 Ma

Weighted mean of fractions i to o, representing 94.38% of ^{39}Ar released in 7 consecutive fractions, MSWD = 0.42

t_c = 54.08 ± 2.84 Ma; $(^{40}Ar/^{36}Ar)_i$ = 400 ± 175, MSWD = 0.38 for n = 7

‡ fraction ignored in the isochron given in the figure

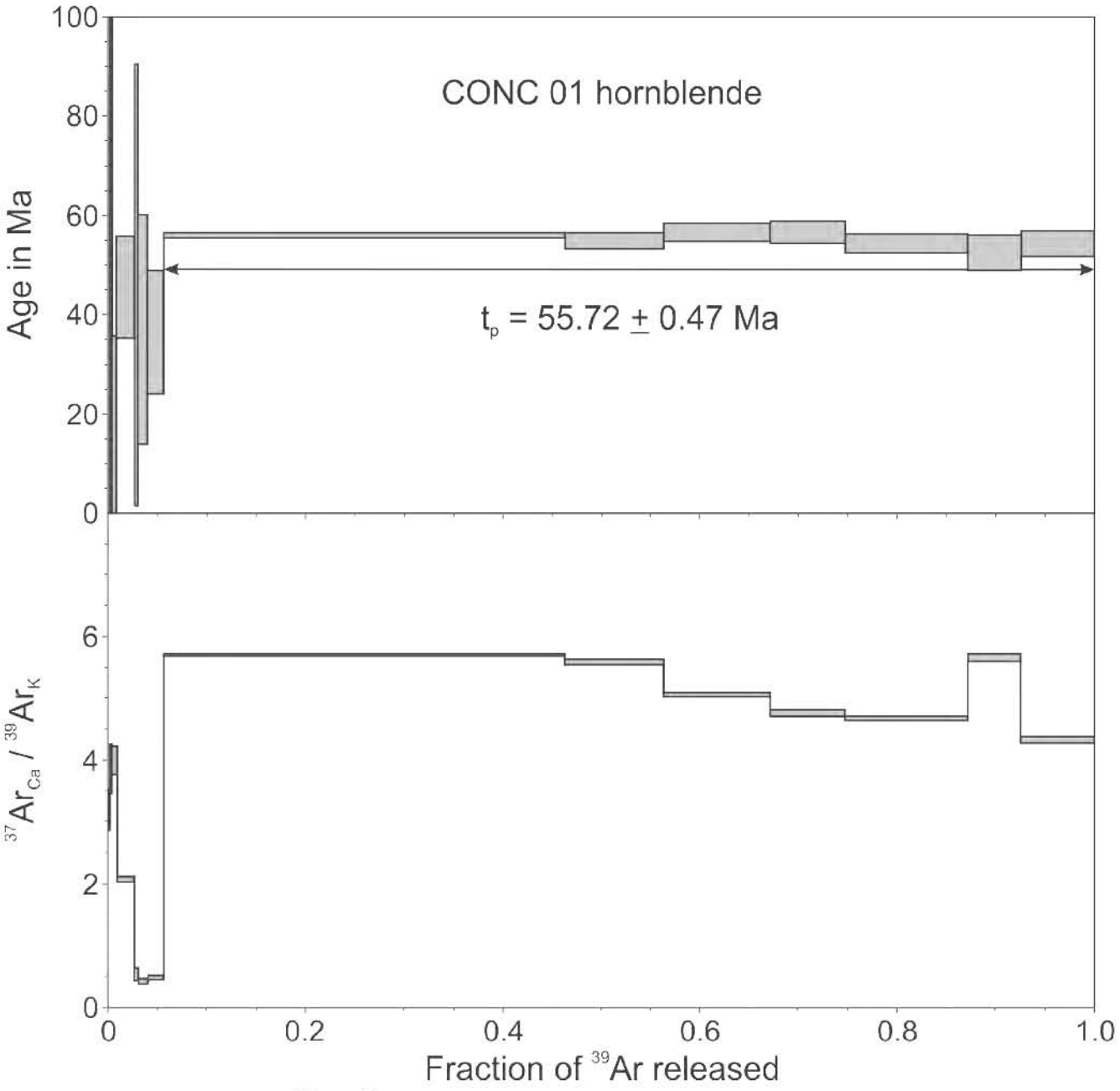

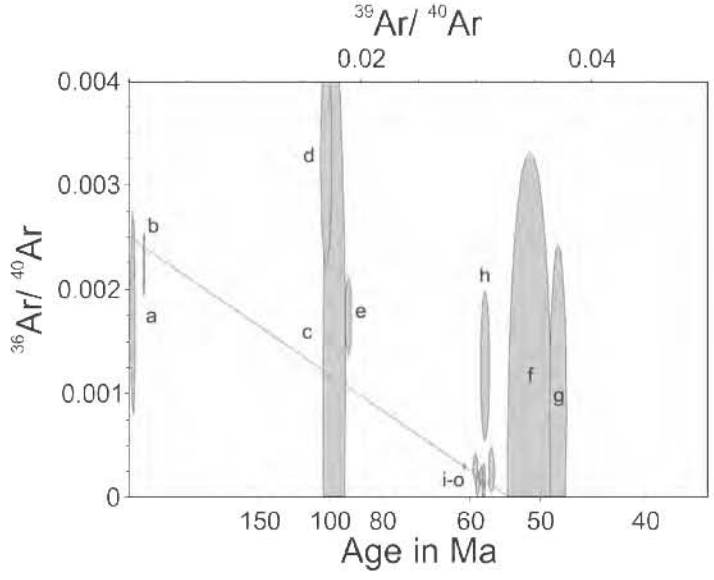

t_c = 54.08 ± 2.84 Ma

$(^{40}Ar / ^{36}Ar)_i$ = 400 ± 175

MSWD = 0.38, n = 7

^{40}Ar-^{39}Ar age
Sample Name: Conc 01
Mineral: Biotite

Laser step-heating experiments on biotite concentrate

Pwr	^{39}Ar × 10^{-6}	F ^{39}Ar	^{40}Ar*/^{39}Ar$_K$	1σ	Age in Ma	1σ			% ^{40}Ar*	^{40}Ar/^{36}Ar	^{37}Ar$_{Ca}$/^{39}Ar$_K$
0.20	2.900	0.0049	3.12	4.13	19.45	25.57	a	‡	22.61	381.85	0.955
0.50	30.556	0.0515	5.94	0.34	36.85	2.08	b	‡	67.72	915.43	0.309
0.70	43.067	0.0726	7.69	0.27	47.55	1.63	c	‡	90.69	3173.92	0.126
1.00	100.588	0.1697	9.05	0.12	55.83	0.74	d		99.20	36856.18	0.068
1.20	72.923	0.1230	9.14	0.13	56.39	0.81	e		96.59	8661.94	0.090
1.60	91.022	0.1535	9.21	0.11	56.78	0.69	f		97.91	14172.21	0.176
2.00	60.958	0.1028	9.14	0.17	56.40	1.02	g		98.41	18625.69	0.247
3.00	95.266	0.1607	8.98	0.12	55.41	0.73	h		99.82	166510.78	0.210
4.00	63.173	0.1066	9.03	0.19	55.72	1.16	i		98.36	18068.88	0.154
6.00	32.396	0.0546	9.51	0.22	58.59	1.34	j		91.57	3507.04	0.236

Integrated results

^{39}Ar × 10^{-6}	^{40}Ar*/^{39}Ar$_K$	1σ	Age in Ma	1σ	% ^{40}Ar*	^{40}Ar/^{36}Ar	^{37}Ar$_{Ca}$/^{39}Ar$_K$
592.8	8.82	0.06	54.42	0.41	95.46	6510.351	0.168

J = 0.003473 ± 0.000013

Preferred age t_p = 56.26 ± 0.34 Ma

Weighted mean of fractions d to j, representing 87.10% of ^{39}Ar released in 7 consecutive fractions, MSWD = 0.87

t_c = 55.54 ± 0.74 Ma; $(^{40}Ar/^{36}Ar)_i$ = 479 ± 128, MSWD = 0.09 for n = 7

‡ fraction ignored in the isochron given in the figure

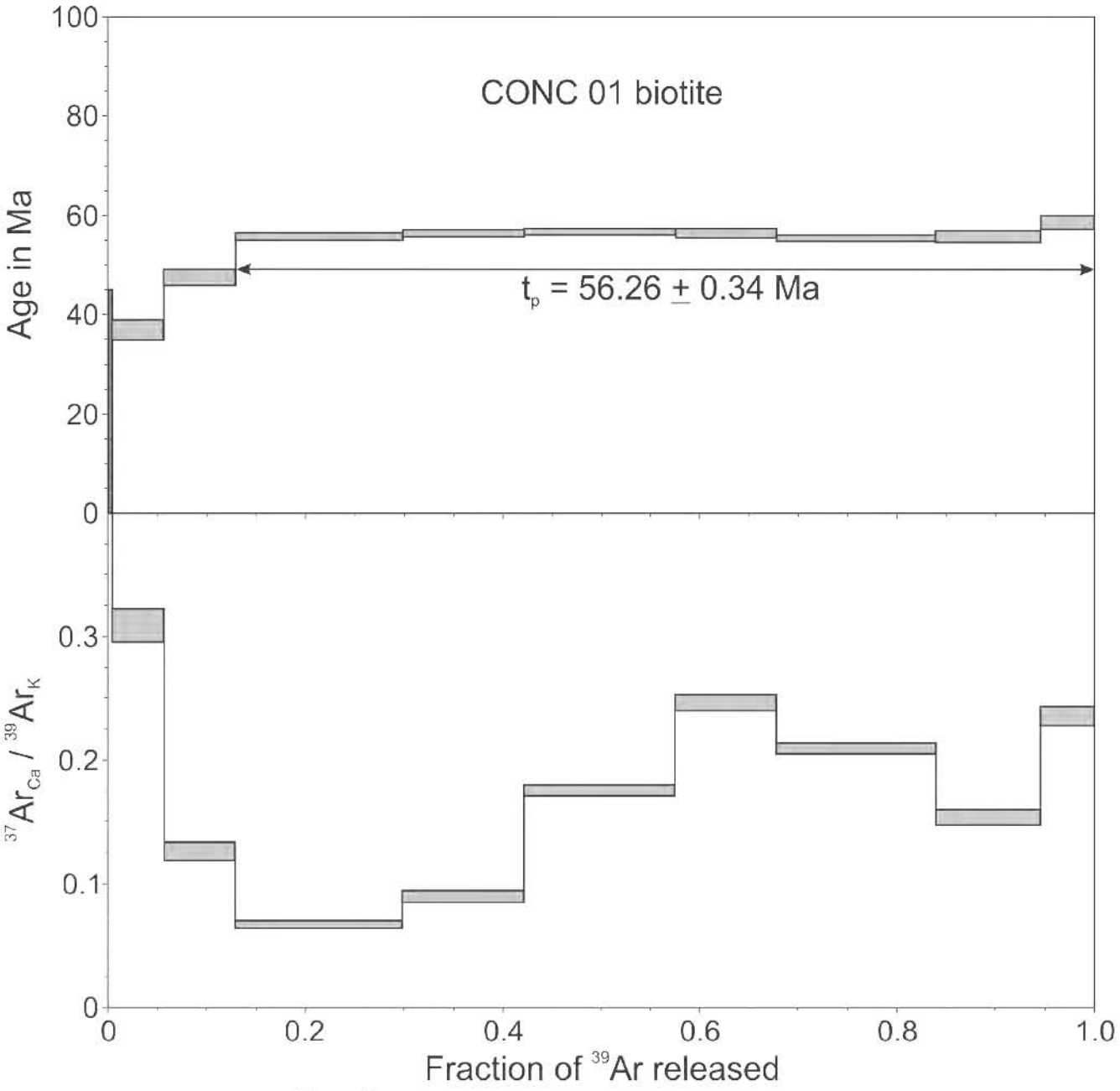

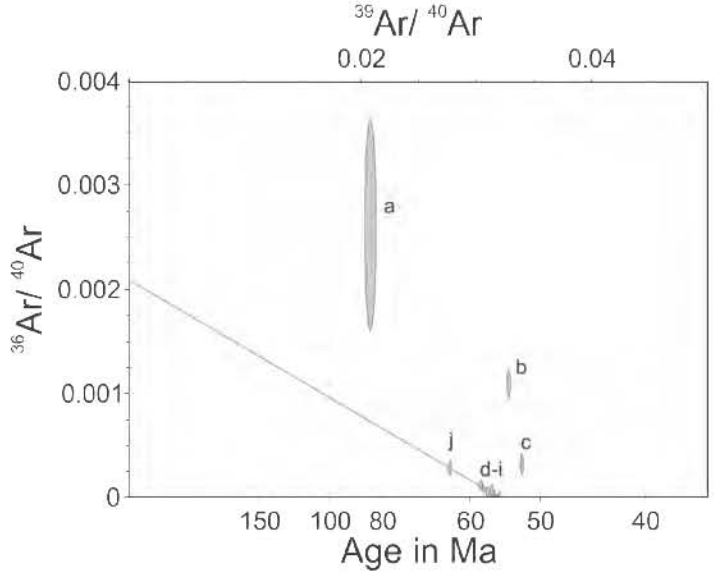

t_c = 55.54 ± 0.74 Ma

$(^{40}Ar / ^{36}Ar)_i$ = 479 ± 128

MSWD = 0.09, n = 7

Sample Name: ROCA 4J-16

Location: North Pescadero Basin East scarp
Latitude: 24.7899 °
Longitude: -109.2008°
Altitude/Depth (m.a.s.l.): -2455

Rock type: Hornblende granodiorite

U-Pb Age

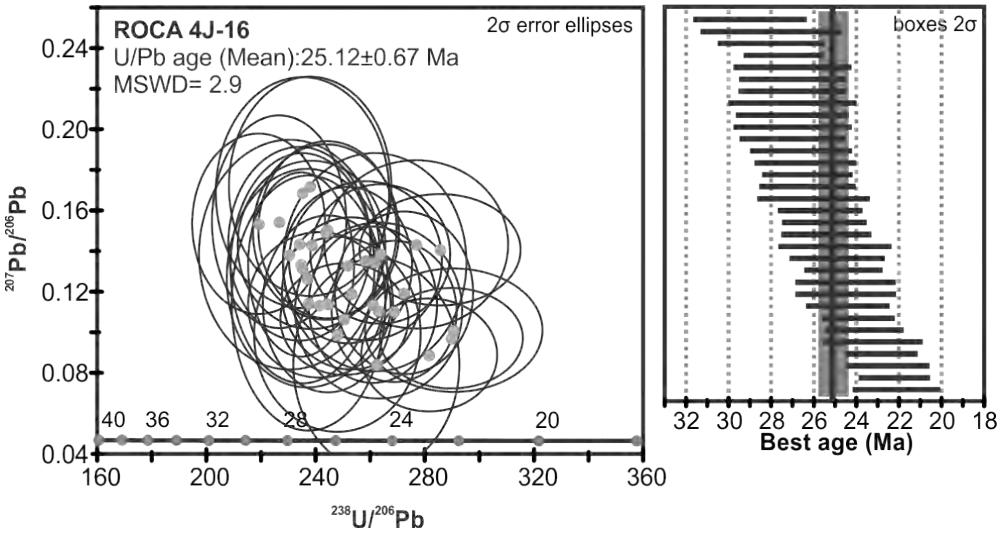

Preferred age: t= 25.12 ± 0.67 Ma

Weighted mean age (95% confidence) calculated with 34 data points. Oldest five points were extracted from calculation. Single crystals are in the 30 to 22 Ma age range. Five oldest analyses were removed from age calculation.

^{40}Ar-^{39}Ar age
Sample Name: ROCA 4J-16
Mineral: K-Feldspar

laser step-heating experiments on feldspar concentrate

Pwr	^{39}Ar × 10^{-6}	F ^{39}Ar	^{40}Ar*/^{39}Ar$_K$	1σ	Age in Ma	1σ			% ^{40}Ar*	^{40}Ar/^{36}Ar	^{37}Ar$_{Ca}$/^{39}Ar$_K$
0.30	2.652	0.0032	24.86	8.95	147.76	51.08	a		7.23	318.53	0.152
0.60	6.720	0.0082	24.62	2.94	146.40	16.77	b		16.14	352.38	0.129
0.90	20.873	0.0254	4.83	1.93	29.64	11.74	c		10.94	331.81	0.170
1.22	16.150	0.0197	3.32	1.28	20.44	7.81	d		14.36	345.04	0.273
1.65	33.117	0.0404	1.63	0.61	10.06	3.74	e	‡	11.06	332.25	0.292
2.05	26.303	0.0321	-0.34	0.41	-2.12	2.52	f	‡	-5.66	279.67	0.424
2.50	52.930	0.0645	0.93	0.25	5.75	1.55	g	‡	9.53	326.63	0.517
2.90	45.122	0.0550	0.50	0.30	3.08	1.82	h	‡	8.83	324.13	0.393
3.90	81.091	0.0988	1.39	0.20	8.60	1.20	i		38.29	478.89	0.191
4.90	155.548	0.1896	1.57	0.14	9.67	0.84	j		36.87	468.06	0.301
9.00	380.142	0.4632	1.92	0.07	11.88	0.44	k		38.41	479.81	0.485

Integrated results

^{39}Ar × 10^{-6}	^{40}Ar*/^{39}Ar$_K$	1σ	Age in Ma	1σ	% ^{40}Ar*	^{40}Ar/^{36}Ar	^{37}Ar$_{Ca}$/^{39}Ar$_K$
820.4	1.94	0.09	11.96	0.57	21.18	374.90	0.392

J = 0.003433 ± 0.000016

Preferred age t = 11.13 ± 0.85 Ma

Weighted mean of fractions i to k, representing 75.16% of the ^{39}Ar released in three consecutive fractions, MSWD = 5.2; the sample does not define a plateau age.

‡ fraction ignored in the isochron age calculation

t_c = 8.64 ± 0.89 Ma, (^{40}Ar/^{36}Ar)$_i$ = 336 ± 9, MSWD = 2.7 for n = 7

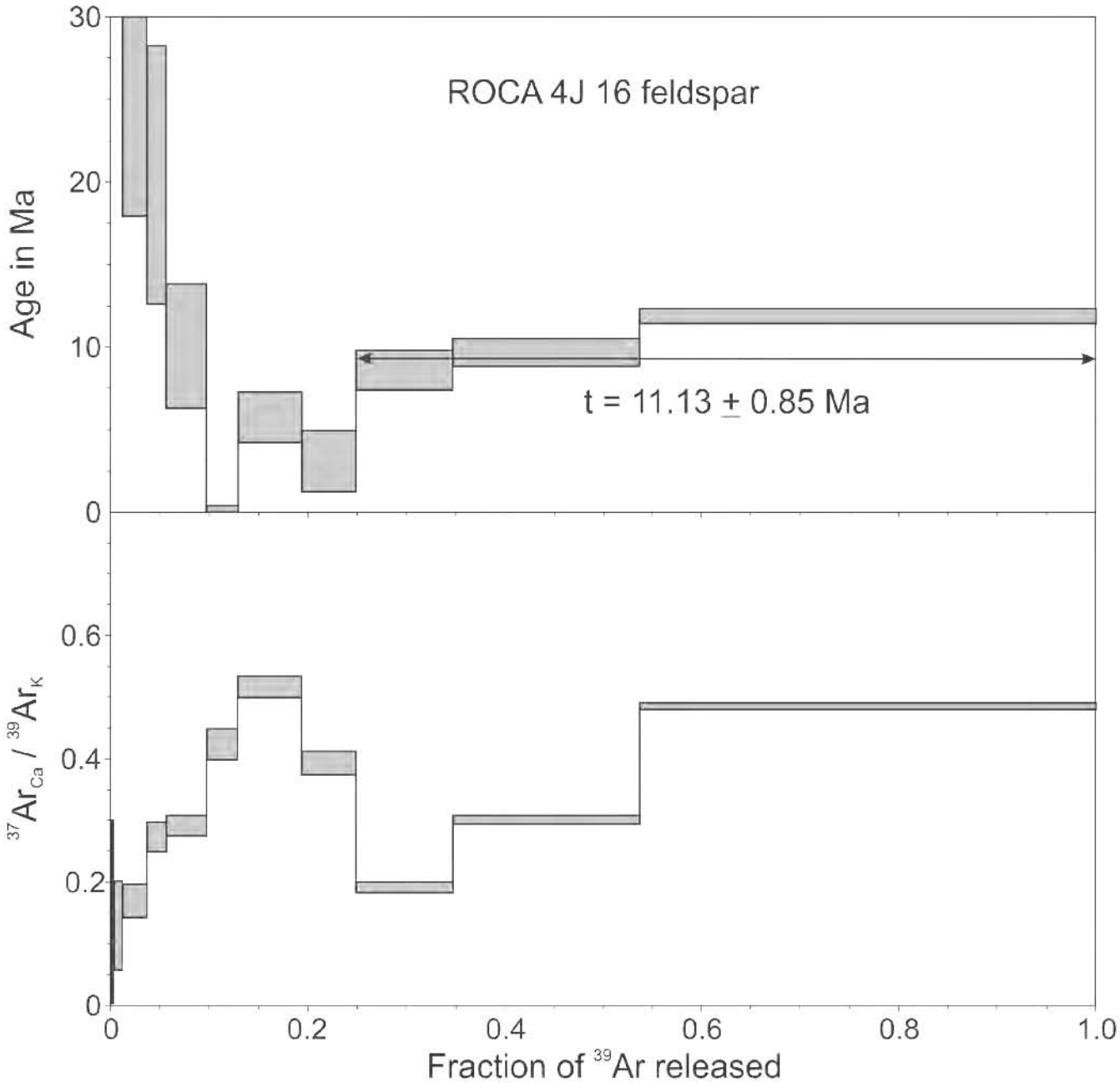

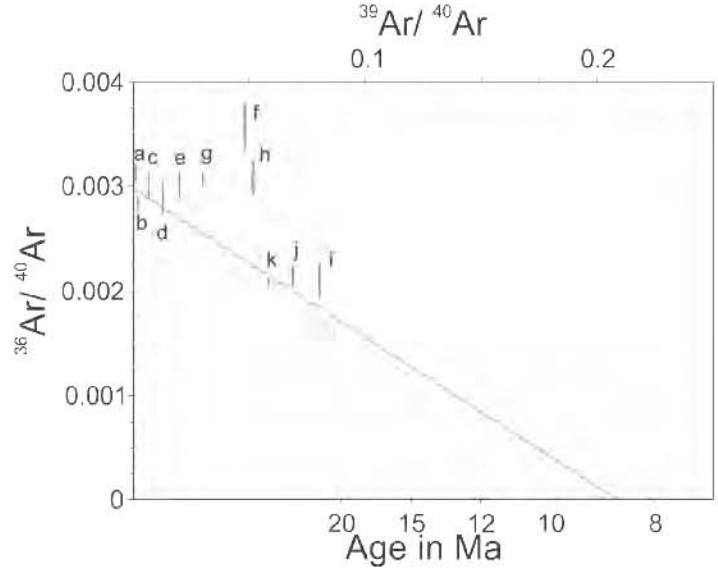

t_c = 8.64 ± 0.89 Ma

$(^{40}Ar / ^{36}Ar)_i$ = 336 ± 9

MSWD = 2.7, n = 7

Sample Name: SC 15

Location: Santa Catalina Island
Latitude: 25.6589°
Longitude: -110.7649°
Altitude/Depth (m.a.s.l.): 0

Rock type: Andesite dike

^{40}Ar-^{39}Ar age
Sample Name: SC 15
Mineral: Grownmass

Laser step-heating experiments on groundmass concentrate

Pwr	^{39}Ar × 10^{-6}	F ^{39}Ar	^{40}Ar*/^{39}Ar$_K$	1σ	Age in Ma	1σ			% ^{40}Ar*	^{40}Ar/^{36}Ar	^{37}Ar$_{Ca}$/^{39}Ar$_K$
0.50	70.881	0.0194	27.12	1.49	149.45	7.86	a	‡	15.15	348.28	2.808
0.80	109.438	0.0299	3.69	0.18	21.10	1.00	b	‡	15.80	350.94	3.333
1.10	212.663	0.0582	3.19	0.11	18.23	0.63	c	‡	24.75	392.71	2.805
1.80	483.018	0.1322	3.37	0.09	19.27	0.49	d	‡	46.24	549.63	2.726
2.60	1582.304	0.4328	4.27	0.09	24.39	0.51	e		59.22	724.59	3.247
6.00	1198.605	0.3275	4.15	0.08	23.71	0.46	f		56.71	682.53	4.857
0.90	155.571	0.0720	12.73	0.53	71.68	2.92	g	‡	17.43	357.89	3.688
1.10	192.019	0.0889	3.36	0.16	19.21	0.91	h	‡	22.89	383.22	3.560
1.90	773.736	0.3580	3.95	0.09	22.55	0.54	i		59.05	721.58	3.522
2.20	371.226	0.1718	4.09	0.07	23.35	0.38	j		73.74	1125.41	3.427
2.80	347.178	0.1606	3.92	0.10	22.38	0.57	k		69.30	962.57	4.278
3.50	203.101	0.0938	3.80	0.16	21.71	0.89	l		48.00	568.27	7.002
6.00	119.269	0.0550	3.96	0.22	22.63	1.27	m		25.62	397.29	9.806

Integrated results

^{39}Ar × 10^{-6}	^{40}Ar*/^{39}Ar$_K$	1σ	Age in Ma	1σ	% ^{40}Ar*	^{40}Ar/^{36}Ar	^{37}Ar$_{Ca}$/^{39}Ar$_K$
3648.0	4.48	0.06	25.55	0.37	39.26	486.48	3.674
2156.0	4.54	0.07	25.87	0.40	36.55	465.71	4.314

J = 0.003185 ± 0.000011

Preferred age t_p = 22.80 ± 0.27 Ma

Weighted mean of fractions i to m, representing 83.91% of ^{39}Ar released in 5 consecutive fractions, MSWD = 1.08

t_c = 23.28 ± 0.67 Ma; $(^{40}Ar/^{36}Ar)_i$ = 295 ± 12, MSWD = 3.1 for n = 7
‡ fraction ignored in the isochron age calculation

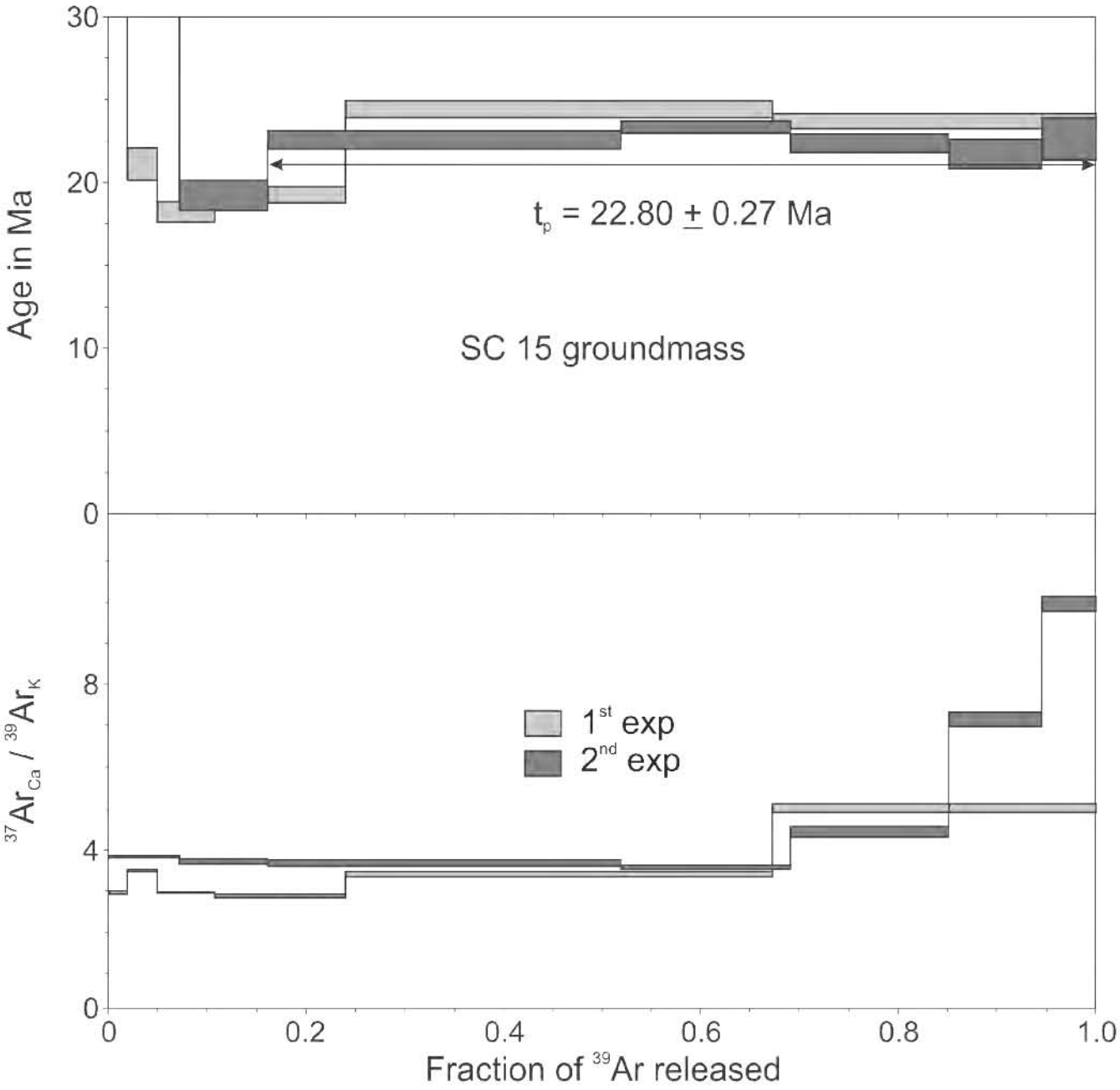

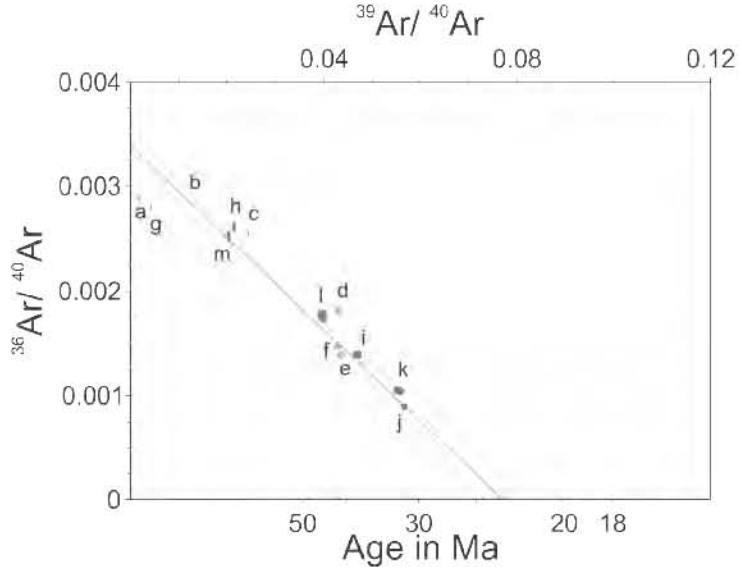

t_c = 23.28 ± 0.27 Ma

$(^{40}Ar / ^{36}Ar)_i$ = 295 ± 12

MSWD = 3.1, n = 7

Sample Name: Barr 04

Location: West Jalisco (Tepic-Zacualco graben)
Latitude: 21.0204°
Longitude: -104.1917°
Altitude/Depth (m.a.s.l.): 947

Rock type: Tonalite

U-Pb Age

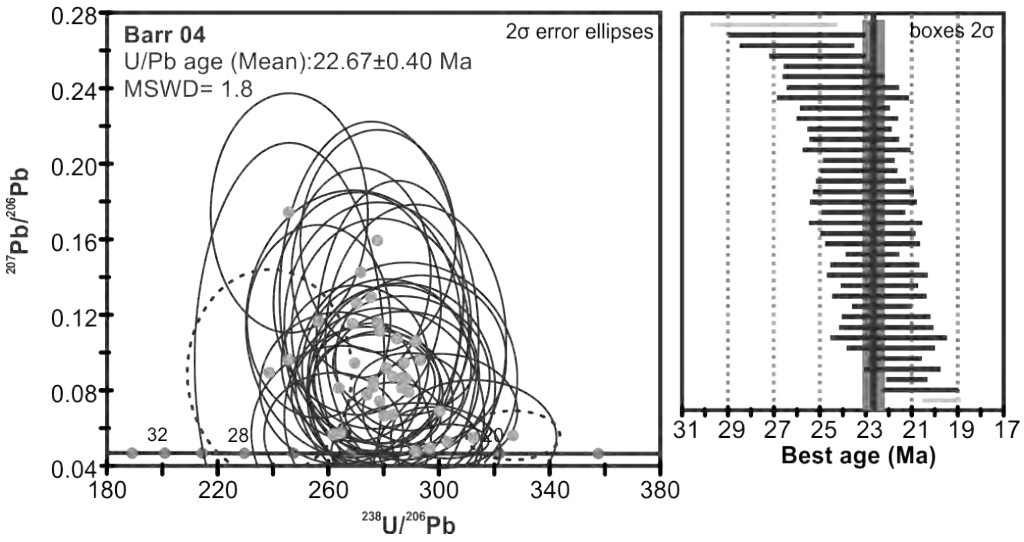

Preferred age: t= 22.67 ± 0.40 Ma

Weighted mean age (95% confidence) calculated with 37 data points. Single crystals are in the 19.7 to 27 Ma age range. One heritage zircon with an age of 61.3 Ma was found.

^{40}Ar-^{39}Ar age
Sample Name: Barr 04
Mineral: Hornblende

Laser step-heating experiments on hornblende concentrate

Pwr	^{39}Ar × 10^{-6}	F ^{39}Ar	^{40}Ar*/^{39}Ar$_K$	1σ	Age in Ma	1σ			% ^{40}Ar*	^{40}Ar/^{36}Ar	^{37}Ar$_{Ca}$/^{39}Ar$_K$
0.20	1.270	0.0024	24.44	7.31	147.48	42.32	a	‡	9.45	326.33	3.637
0.60	15.872	0.0302	2.64	0.83	16.54	5.19	b		7.99	321.15	1.188
0.90	32.623	0.0621	3.20	0.37	20.03	2.32	c		24.31	390.39	0.454
1.25	49.358	0.0938	2.92	0.22	18.29	1.39	d		57.08	688.49	1.427
1.60	70.016	0.1327	2.95	0.12	18.48	0.75	e		55.70	667.05	6.538
1.90	119.201	0.2259	3.16	0.11	19.77	0.69	f		75.31	1196.67	6.758
2.30	67.186	0.1273	3.17	0.11	19.83	0.67	g		80.18	1490.80	6.531
2.90	62.528	0.1186	3.05	0.13	19.10	0.79	h		77.61	1319.93	4.703
6.00	109.034	0.2070	2.78	0.10	17.41	0.61	i	‡	61.81	773.77	3.467

Integrated results

^{39}Ar × 10^{-6}	^{40}Ar*/^{39}Ar$_K$	1σ	Age in Ma	1σ	% ^{40}Ar*	^{40}Ar/^{36}Ar	^{37}Ar$_{Ca}$/^{39}Ar$_K$
525.5	3.06	0.06	19.14	0.39	47.26	560.27	4.708

J = 0.003485 ± 0.000010

Preferred age t = 19.80 ± 0.48 Ma

Weighted mean of fractions f and g, representing 35.32% of ^{39}Ar released in 2 consecutive fractions, MSWD < 0.01

Weighted mean of fractions b to h yields t = 19.29 ± 0.34 Ma; 79.06% of ^{39}Ar released in 7 consecutive fractions, MSWD = 0.54; but the ^{37}Ar$_{Ca}$/^{39}Ar$_K$ displays a range of values from 0.4 to 7 suggesting a inhomogeneous composition, for this reason the preferred age is the segment represented by fractions f and g, these have the highest ^{40}Ar* composition, their ages are in agreement within 1 σ errors and have an homogeneous ^{37}Ar$_{Ca}$/^{39}Ar$_K$ ~ 6.6

t_c = 19.42 ± 0.41 Ma; (^{40}Ar/^{36}Ar)$_i$ = 291 ± 7, MSWD = 0.59 for n = 7

‡ fraction ignored in the isochron given in the figure

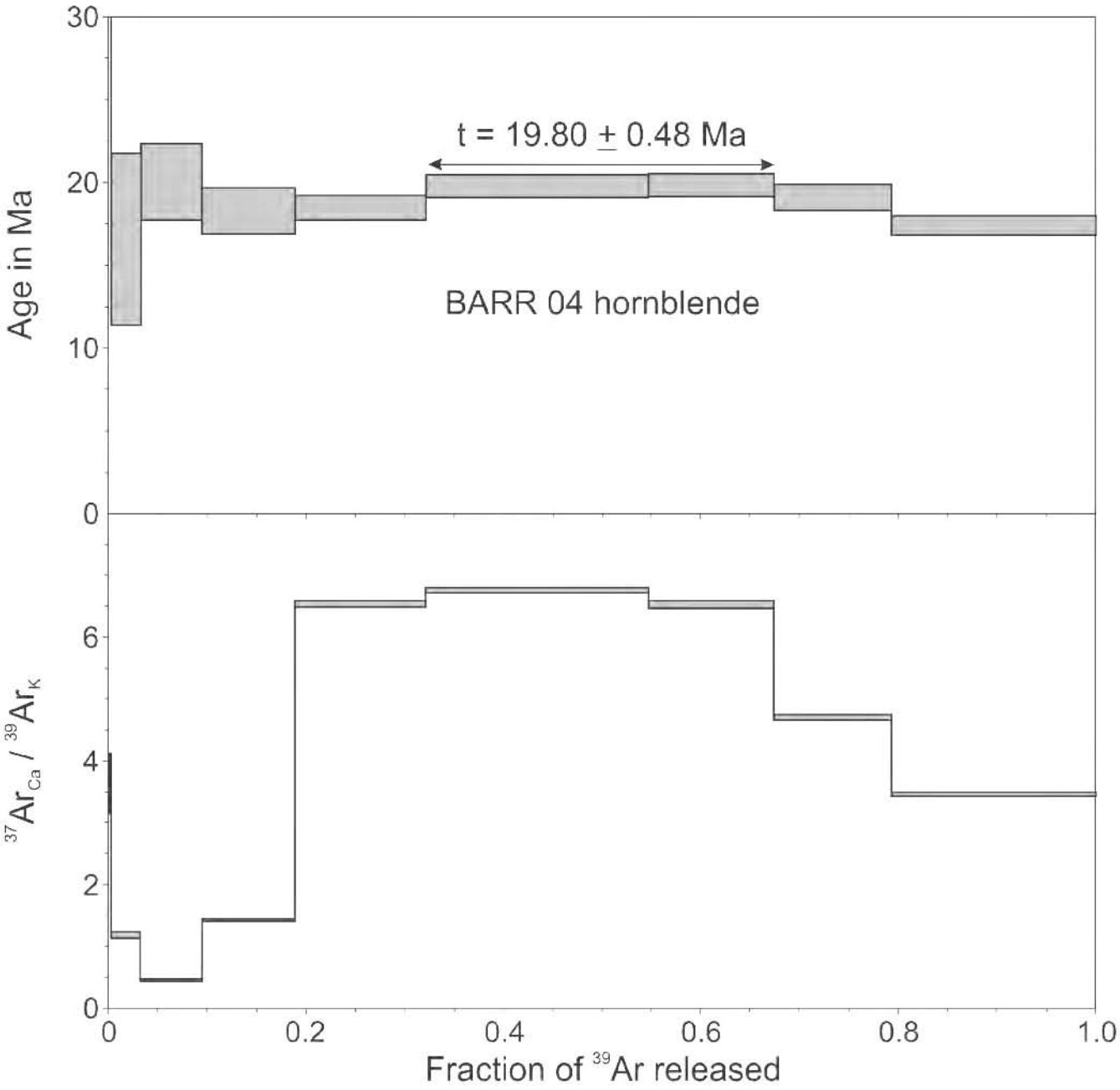

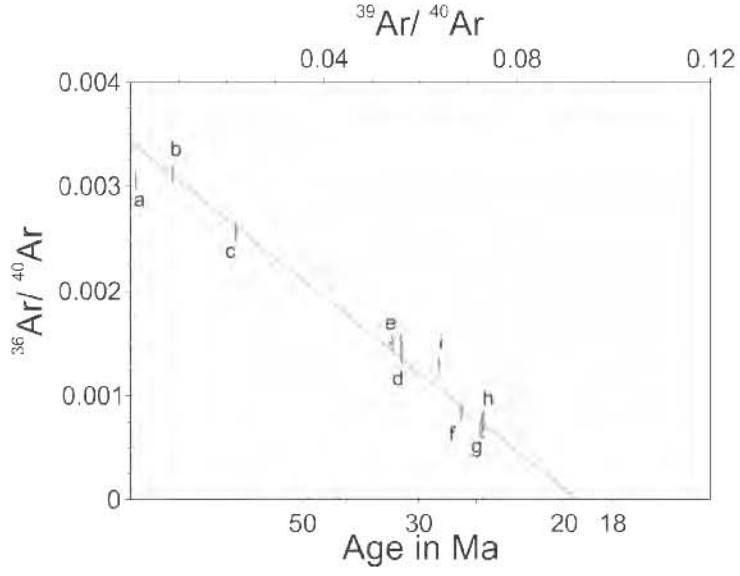

t_c = 19.42 ± 0.41 Ma

$(^{40}Ar / ^{36}Ar)_i$ = 291 ± 7

MSWD = 0.59, n = 7

^{40}Ar-^{39}Ar age
Sample Name: Barr 04
Mineral: Biotite

Laser step-heating experiments on biotite concentrate

Pwr	^{39}Ar × 10^{-6}	F ^{39}Ar	^{40}Ar*/^{39}Ar$_K$	1σ	Age in Ma	1σ			% ^{40}Ar*	^{40}Ar/^{36}Ar	^{37}Ar$_{Ca}$/^{39}Ar$_K$
0.20	3.066	0.0015	1.47	3.32	9.19	20.76	a		5.34	312.16	0.256
0.60	63.106	0.0316	2.32	0.18	14.52	1.14	b	‡	30.84	427.28	0.109
1.00	239.477	0.1199	3.08	0.06	19.26	0.36	c		74.05	1138.68	0.032
1.30	260.166	0.1302	3.16	0.04	19.78	0.25	d		90.90	3247.53	0.029
1.65	252.355	0.1263	3.14	0.03	19.60	0.20	e		89.90	2926.62	0.047
2.00	213.008	0.1066	3.16	0.05	19.75	0.29	f		90.66	3163.44	0.175
2.50	231.855	0.1160	3.15	0.03	19.71	0.21	g		93.58	4606.12	0.298
3.20	373.547	0.1870	3.23	0.02	20.18	0.12	h	‡	97.53	11968.14	0.143
4.00	229.405	0.1148	3.11	0.03	19.47	0.20	i		94.04	4961.44	0.102
7.00	131.714	0.0659	3.13	0.06	19.59	0.38	j		92.51	3947.10	0.074
0.50	8.973	0.0032	3.59	1.16	22.40	7.18	k		7.56	319.65	0.257
1.00	56.467	0.0202	2.61	0.28	16.35	1.74	l		24.40	390.85	0.150
1.50	105.979	0.0380	3.14	0.10	19.65	0.64	m		75.34	1198.21	0.019
2.00	222.101	0.0796	3.00	0.05	18.79	0.31	n		80.14	1487.68	0.033
2.50	166.044	0.0595	3.09	0.05	19.35	0.33	o		88.17	2496.84	0.027
3.00	201.944	0.0723	3.31	0.03	20.68	0.19	p	‡	95.10	6025.26	0.112
3.50	270.557	0.0969	3.19	0.03	19.97	0.17	q		93.64	4643.94	0.157
4.00	245.920	0.0881	3.18	0.03	19.86	0.17	r		94.80	5679.35	0.385
5.00	338.063	0.1210	3.15	0.03	19.68	0.18	s		92.45	3913.65	0.534
6.50	540.472	0.1936	3.19	0.01	19.92	0.09	t		95.99	7370.53	0.255
8.50	435.666	0.1560	3.17	0.02	19.85	0.11	u		94.59	5461.20	0.265
10.00	200.147	0.0717	3.16	0.04	19.76	0.25	v		91.47	3462.49	0.314

Integrated results

^{39}Ar × 10^{-6}	^{40}Ar*/^{39}Ar$_K$	1σ	Age in Ma	1σ	% ^{40}Ar*	^{40}Ar/^{36}Ar	^{37}Ar$_{Ca}$/^{39}Ar$_K$
1998.0	3.12	0.02	19.53	0.11	85.40	2024.44	0.114
2792.0	3.15	0.01	19.73	0.10	84.41	1895.20	0.244

J = 0.003485 ± 0.000010

Preferred age t_p = 19.65 ± 0.11 Ma

Weighted mean of fractions c to g, representing 59.99% of ^{39}Ar released in 5 consecutive fractions, MSWD = 0.40

t_c = 19.83 ± 0.08 Ma; $(^{40}Ar/^{36}Ar)_i$ = 285 ± 6, MSWD = 1.36 for n = 19

‡ fraction ignored in the isochron given in the figure

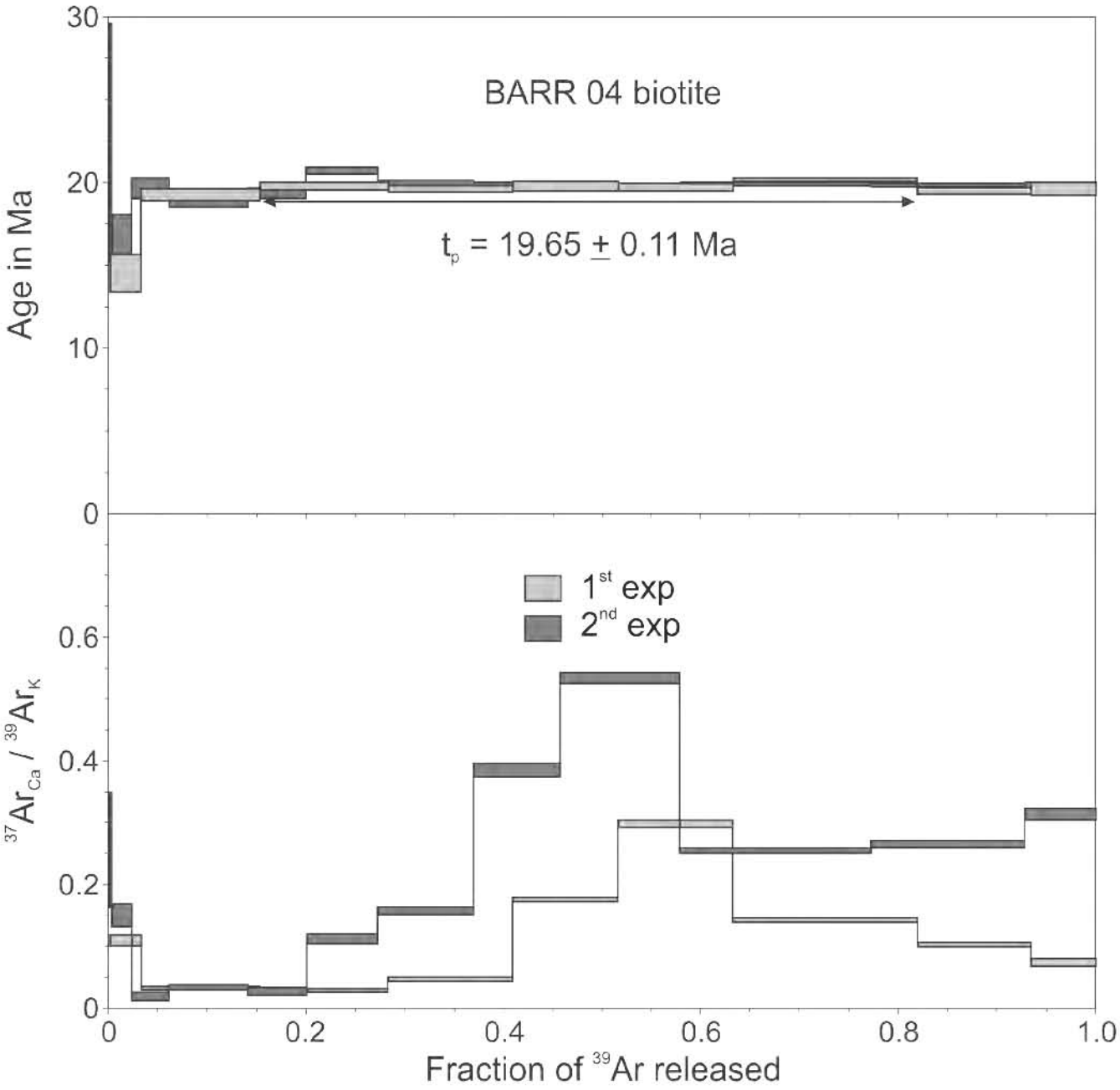

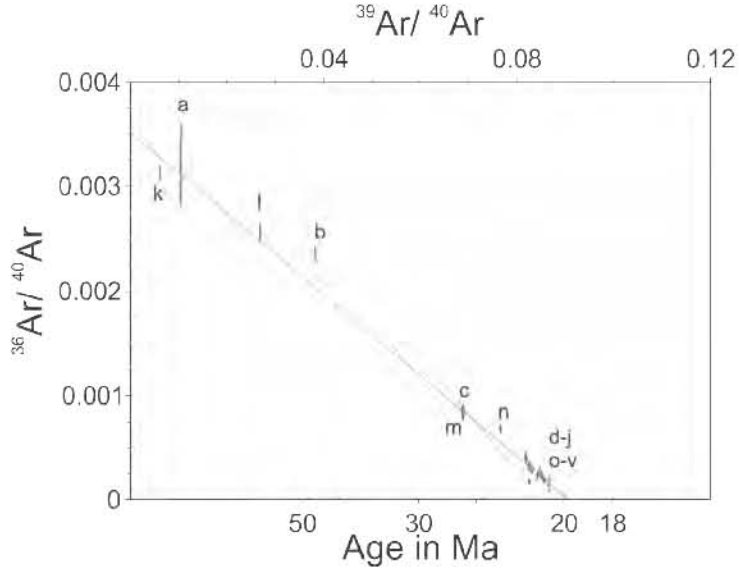

t_c = 19.83 ± 0.08 Ma

$(^{40}Ar / ^{36}Ar)_i$ = 285 ± 6

MSWD = 1.36, n = 19

Sample Name: SC 09-08

Location: Santa Catalina Island
Latitude: 25.6387°
Longitude: -110.8004°
Altitude/Depth (m.a.s.l.): 0

Rock type: Quartz Monzonite

U-Pb Age

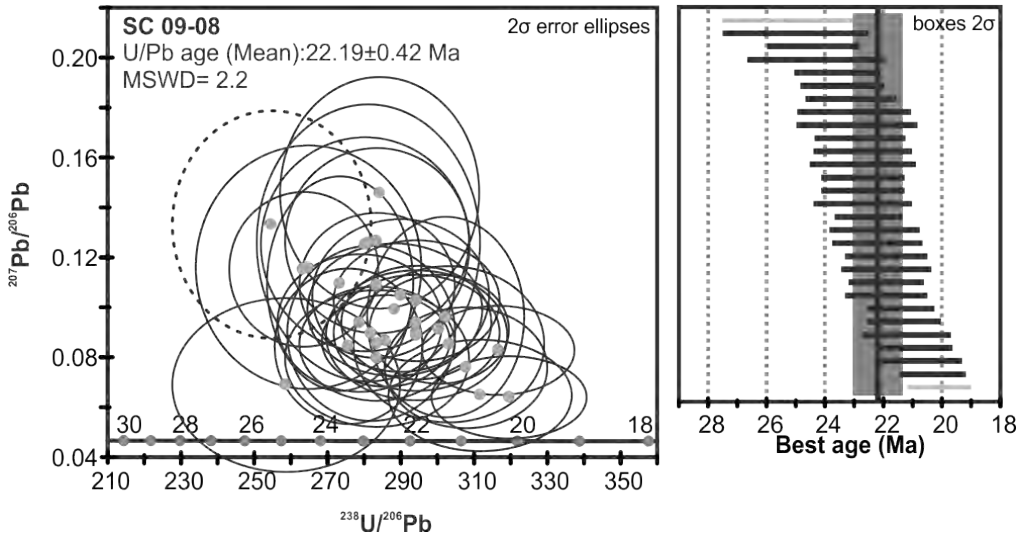

Preferred age: t= 22.19 ± 0.42 Ma

Weighted mean age (95% confidence) calculated with 25 data points. Single crystals are in the 20.7 to 24.4 Ma age range. Two young and two old zircons were removed from the age calculation.

^{40}Ar-3^{9}Ar age
Sample Name: SC 09-08
Mineral: Hornblende

Laser step-heating experiments on hornblende concentrate

Pwr	^{39}Ar × 10^{-6}	F ^{39}Ar	^{40}Ar*/^{39}Ar$_K$	1σ	Age in Ma	1σ			% ^{40}Ar*	^{40}Ar/^{36}Ar	^{37}Ar$_{Ca}$/^{39}Ar$_K$
0.20	0.562	0.0007	-186.10	58.39	-2108.54	1255.41	a	‡	-7.38	275.19	35.660
1.20	58.260	0.0703	10.48	2.39	68.71	15.39	b		14.35	345.02	1.207
1.90	217.677	0.2617	3.02	0.11	20.07	0.70	c		42.86	517.11	6.124
2.60	374.553	0.4504	2.95	0.06	19.59	0.40	d		79.28	1425.86	5.729
3.20	81.477	0.0980	2.80	0.16	18.60	1.09	e		83.42	1781.92	4.764
4.20	43.489	0.0522	3.08	0.44	20.44	2.92	f		82.22	1661.57	8.016
6.00	56.059	0.0668	3.62	0.53	24.04	3.46	g		34.15	448.73	19.793

Integrated results

^{39}Ar × 10^{-6}	^{40}Ar*/^{39}Ar$_K$	1σ	Age in Ma	1σ	% ^{40}Ar*	^{40}Ar/^{36}Ar	^{37}Ar$_{Ca}$/^{39}Ar$_K$
828.6	3.41	0.18	22.63	1.23	29.50	419.12	6.499

J = 0.003704 ± 0.000030

Preferred age t_c = 18.89 ± 0.47 Ma

$(^{40}Ar/^{36}Ar)_i$ = 319 ± 8, MSWD = 0.9 for n = 6

t_c = 19.61 ± 0.35 Ma; plateau age calculated with the weighted mean of fractions c to f, representing 86.22% of ^{39}Ar released in 4 consecutive fractions, MSWD = 0.44

‡ fraction ignored in the isochron age calculation

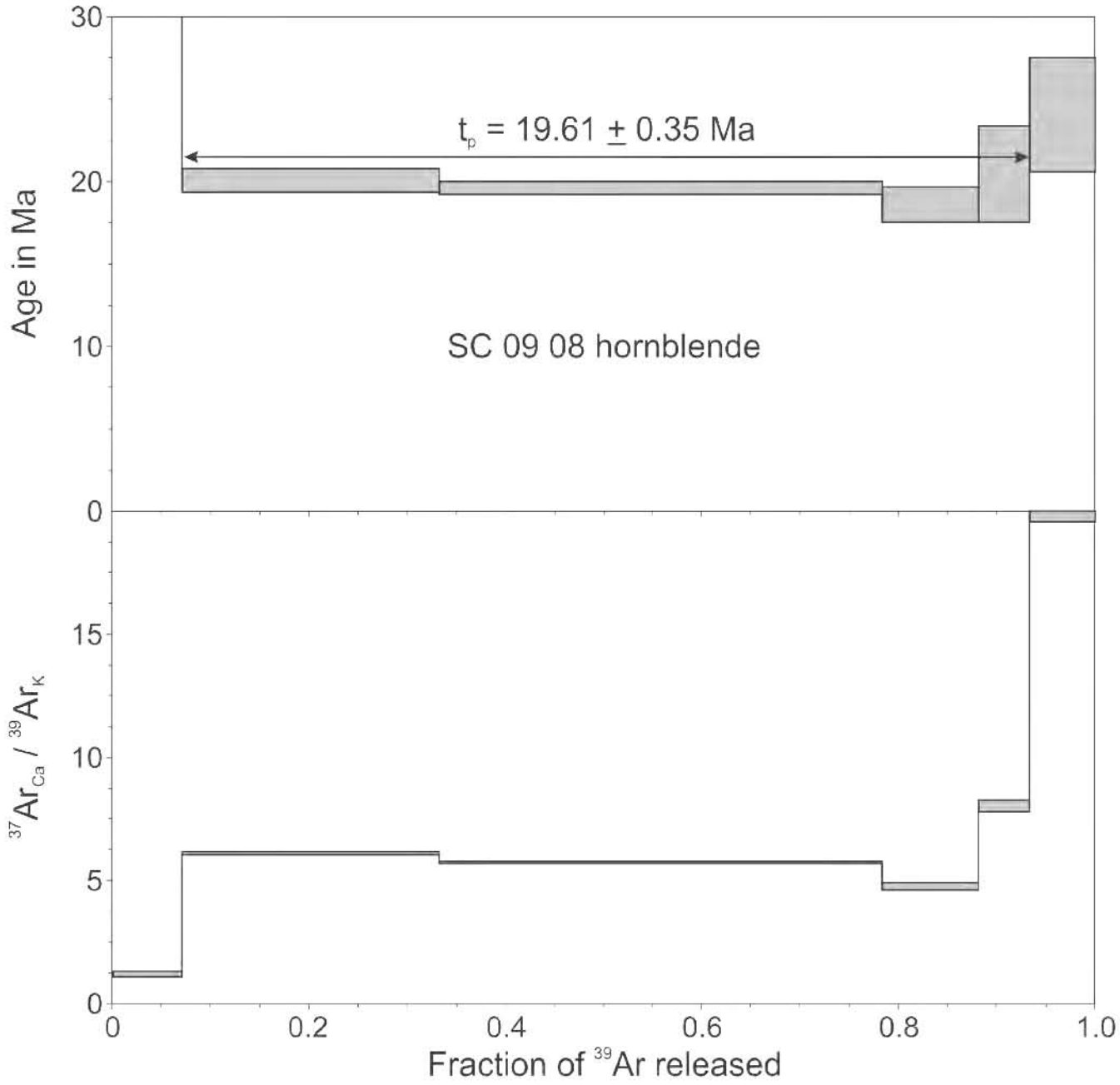

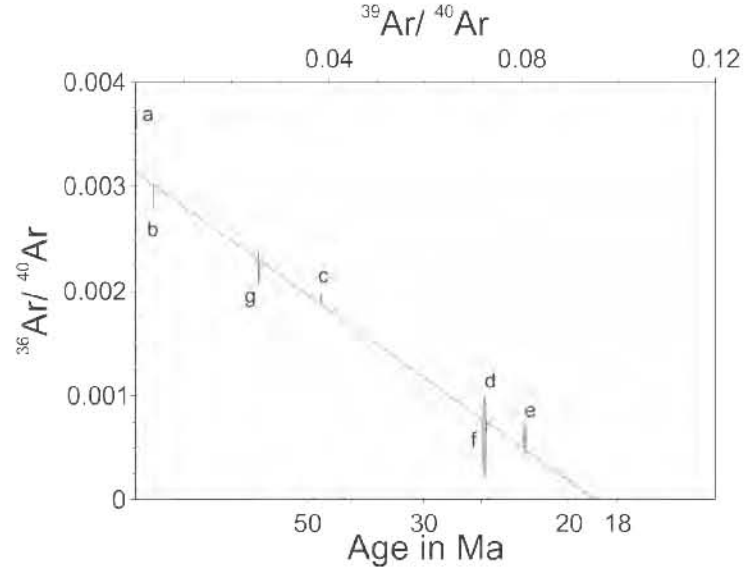

t_c = 18.89 ± 0.47 Ma

$(^{40}Ar / ^{36}Ar)_i$ = 319 ± 8

MSWD = 0.9, n = 6

^{40}Ar-^{39}Ar age
Sample Name: SC 09-08
Mineral: Biotite

Laser step-heating experiments on biotite concentrate

Pwr	^{39}Ar × 10^{-6}	F ^{39}Ar	^{40}Ar*/^{39}Ar$_K$	1σ	Age in Ma	1σ			% ^{40}Ar*	^{40}Ar/^{36}Ar	^{37}Ar$_{Ca}$/^{39}Ar$_K$
0.40	17.098	0.0031	6.84	2.05	43.89	13.01	a	‡	12.10	336.17	0.751
0.90	241.735	0.0433	2.61	0.12	16.84	0.77	b		31.44	431.00	0.085
1.40	716.445	0.1282	2.82	0.03	18.24	0.16	c		70.83	1013.04	0.055
1.90	672.208	0.1203	2.86	0.03	18.47	0.17	d		91.93	3661.45	0.191
2.50	929.500	0.1664	2.82	0.02	18.23	0.11	e		94.82	5705.67	0.028
3.30	1182.925	0.2117	2.89	0.02	18.64	0.10	f		97.24	10698.06	0.034
4.00	930.494	0.1665	2.84	0.01	18.31	0.09	g		97.68	12726.99	0.048
4.80	679.376	0.1216	2.84	0.02	18.36	0.13	h		97.18	10481.18	0.093
8.50	217.800	0.0390	2.86	0.06	18.44	0.40	i		96.01	7397.71	0.293

Integrated results

^{39}Ar × 10^{-6}	^{40}Ar*/^{39}Ar$_K$	1σ	Age in Ma	1σ	% ^{40}Ar*	^{40}Ar/^{36}Ar	^{37}Ar$_{Ca}$/^{39}Ar$_K$
5587.0	2.85	0.01	18.40	0.17	81.51	1598.59	0.079

J = 0.003599 ± 0.000031

Preferred age t_p = 18.38 ± 0.08 Ma

Weighted mean of fractions c to i, representing 95.36% of ^{39}Ar released in 7 consecutive fractions, MSWD = 0.55

t_c = 18.42 ± 0.17 Ma; $(^{40}Ar/^{36}Ar)_i$ = 286 ± 6, MSWD = 1.79 for n = 8

‡ fraction ignored in the isochron age calculation

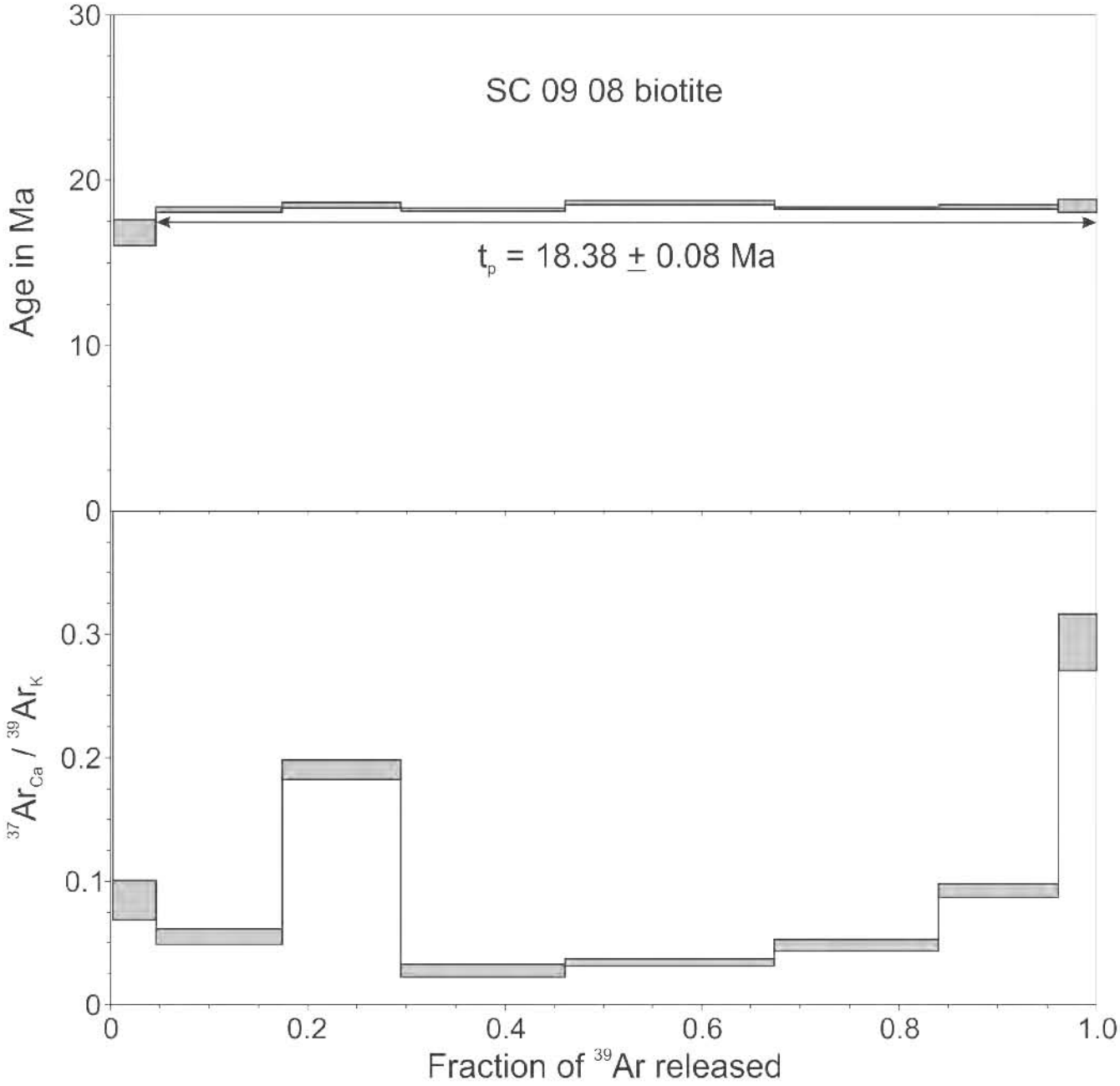

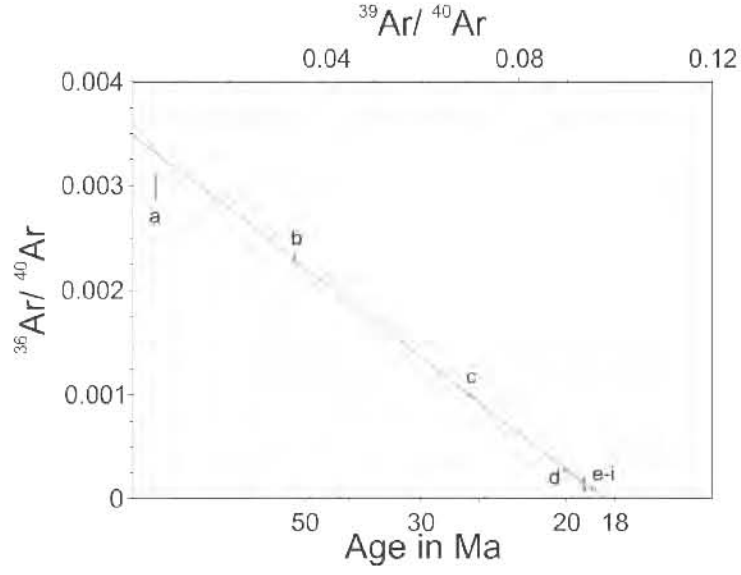

t_c = 18.42 ± 0.17 Ma

$(^{40}Ar / ^{36}Ar)_i$ = 286 ± 6

MSWD = 1.79, n = 8

Sample Name: Ros 02

Location: South Sinaloa
Latitude: 23.0011°
Longitude: -105.7498°
Altitude/Depth (m.a.s.l.): 98

Rock type: Quartz Monzonite

U-Pb Age

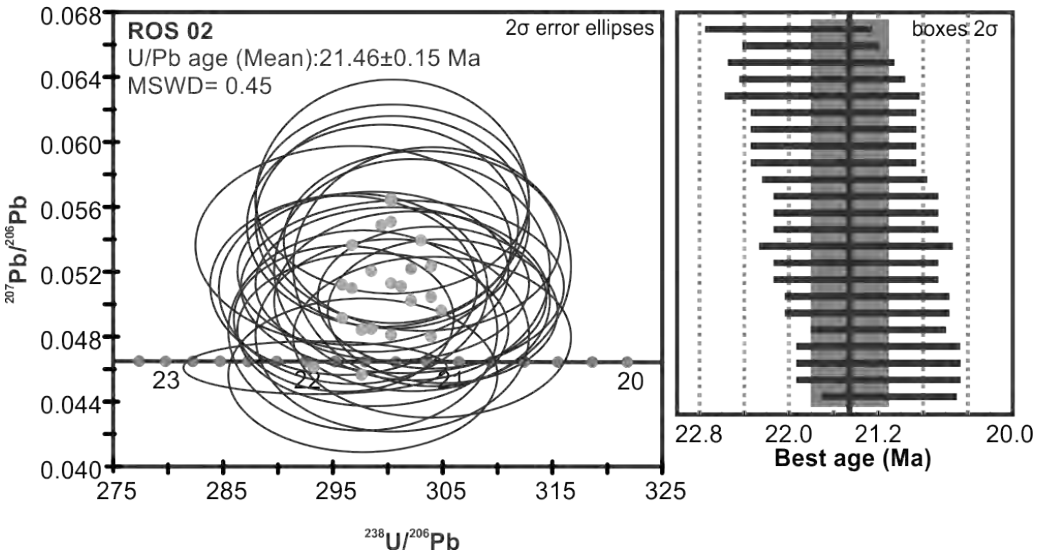

Preferred age: t= 21.46 ± 0.15 Ma

Weighted mean age (95% confidence) calculated with 24 data points. Single crystals are in the 21.1 to 22.0 Ma age range.

Sample Name: ROCA 4J-12

Location: North Pescadero Basin East scarp
Latitude: 24.7865°
Longitude: -109.2023°
Altitude/Depth (m.a.s.l.): -2641

Rock type: Biotite-hornblende granodiorite

U-Pb Age

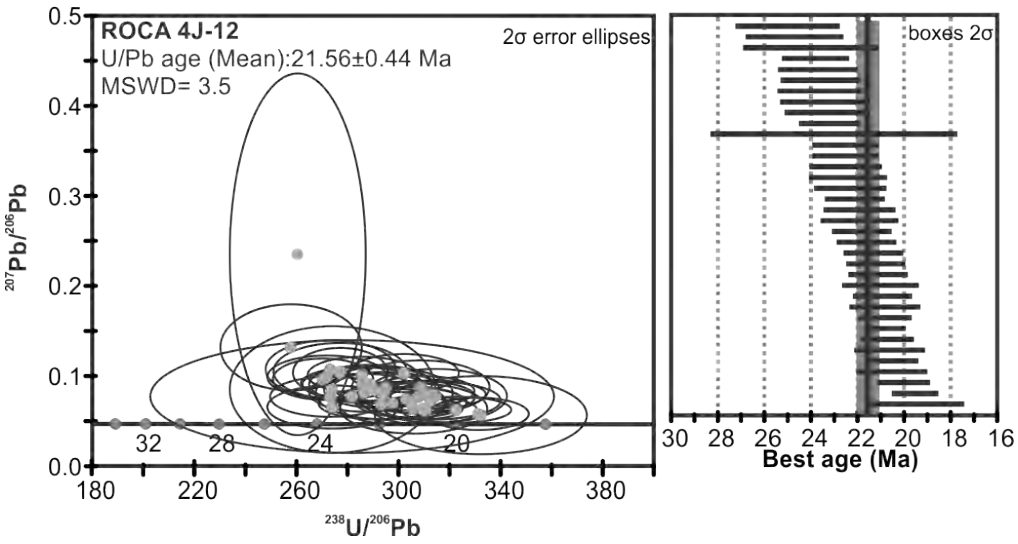

Preferred age: t= 21.56 ± 0.44 Ma

Weighted mean age (95% confidence) calculated with 24 data points. Single crystals are in the 19.4 to 24.0 Ma age range.

^{40}Ar-^{39}Ar age
Sample Name: ROCA 4J-12
Mineral: K Feldspar

laser step-heating experiments on K Feldspar concentrate

Pwr	^{39}Ar × 10^{-6}	F ^{39}Ar	^{40}Ar*/^{39}Ar$_K$	1σ	Age in Ma	1σ			% ^{40}Ar*	^{40}Ar/^{36}Ar	^{37}Ar$_{Ca}$/^{39}Ar$_K$
0.25	4.461	0.0007	92.17	8.26	526.85	40.95	a	‡	15.11	348.12	0.226
0.45	22.929	0.0038	57.64	2.34	347.01	12.83	b	‡	21.59	376.84	< 0.001
0.65	85.583	0.0143	6.82	1.04	44.74	6.74	c		9.82	327.70	0.024
0.95	202.135	0.0338	2.94	0.41	19.44	2.71	d		11.71	334.71	0.078
1.35	523.813	0.0877	1.81	0.10	11.99	0.66	e		14.45	345.40	0.138
1.65	217.979	0.0365	1.62	0.24	10.74	1.60	f		17.48	358.09	0.099
2.00	226.661	0.0380	0.71	0.06	4.72	0.40	g	‡	23.68	387.21	0.062
2.50	531.443	0.0890	1.39	0.08	9.23	0.52	h		26.41	401.57	0.070
3.20	354.330	0.0593	1.02	0.07	6.79	0.47	i	‡	22.44	380.99	0.074
4.20	1007.539	0.1687	1.56	0.04	10.30	0.28	j		40.96	500.49	0.046
5.20	781.375	0.1308	1.95	0.09	12.87	0.57	k		29.39	418.51	0.055
7.00	2013.604	0.3372	1.67	0.03	11.03	0.22	l		44.29	530.40	0.112

Integrated results

^{39}Ar × 10^{-6}	^{40}Ar*/^{39}Ar$_K$	1σ	Age in Ma	1σ	% ^{40}Ar*	^{40}Ar/^{36}Ar	^{37}Ar$_{Ca}$/^{39}Ar$_K$
5972.0	2.00	0.04	13.21	0.28	23.78	387.69	0.085

J = 0.003679 ± 0.000015

Preferred age t_c = 9.91 ± 0.57 Ma

(^{40}Ar/^{36}Ar)$_i$ = 309 ± 6, MSWD = 5.9 for n = 8

‡ fractions ignored in the isochron age calculation

The sample does not define a plateau age.

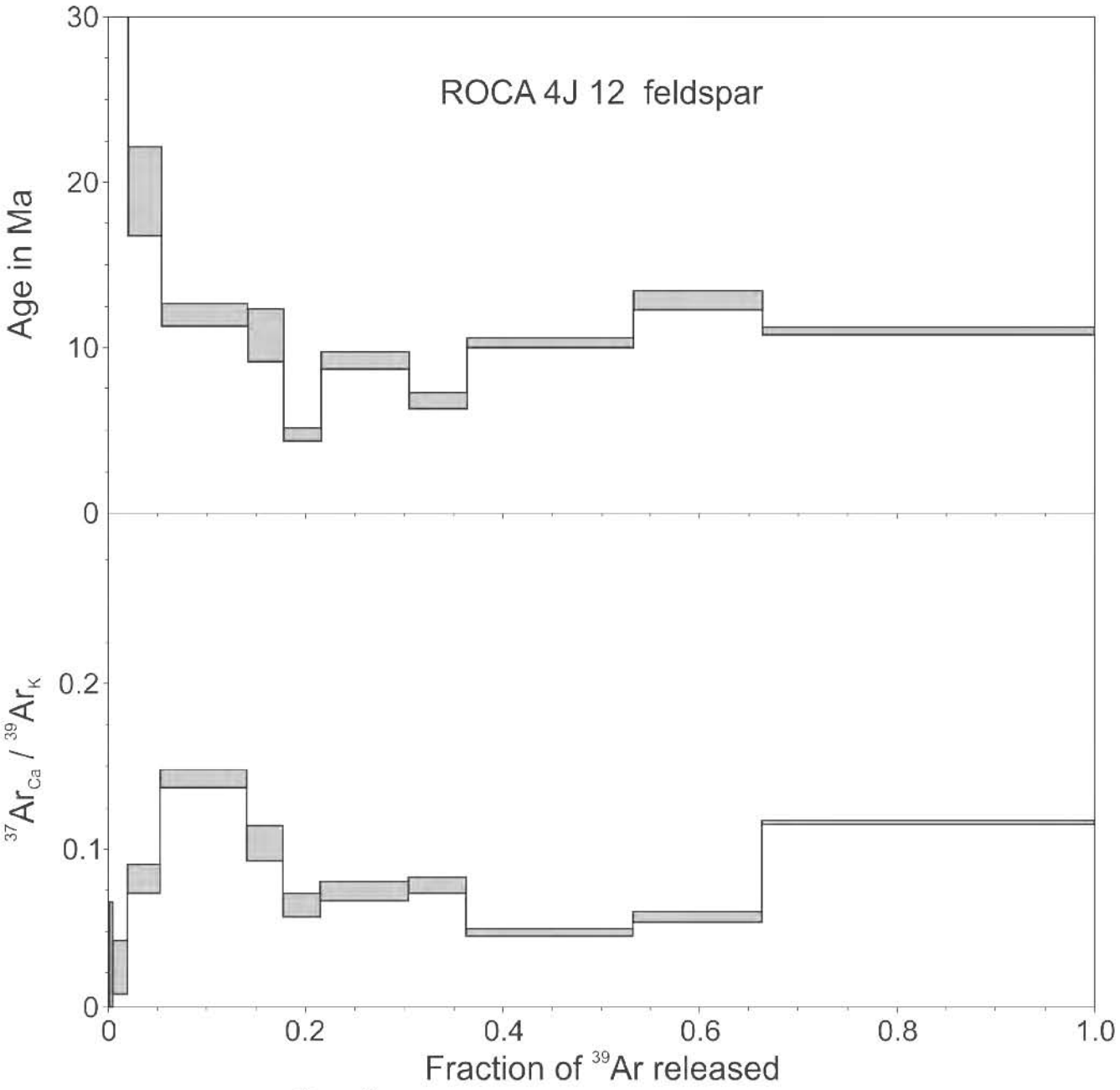

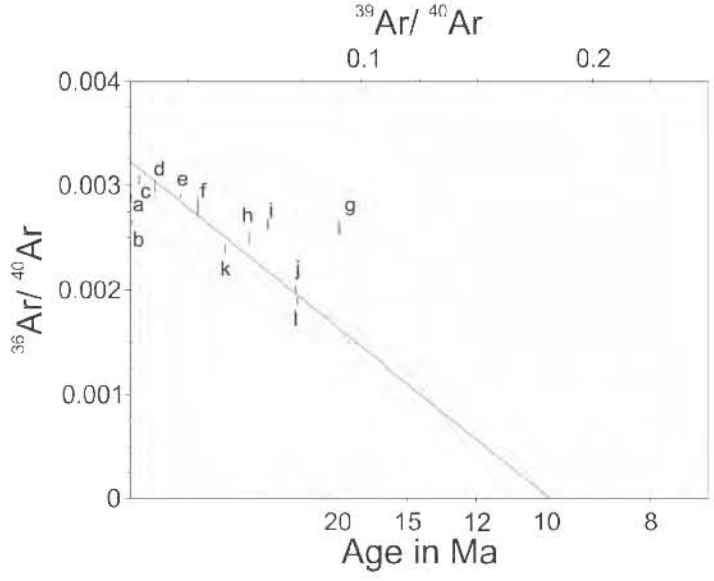

t_c = 9.91 ± 0.57 Ma

$(^{40}Ar / ^{36}Ar)_i$ = 309 ± 6

MSWD = 5.9, n = 8

Sample Sample Name: ROCA 24J-24

Location: South Pescadero transform
Latitude: 24.0190°
Longitude: -109.039°
Altitude/Depth (m.a.s.l.): -1983

Rock type: Hornblende-biotite tonalite

U-Pb Age

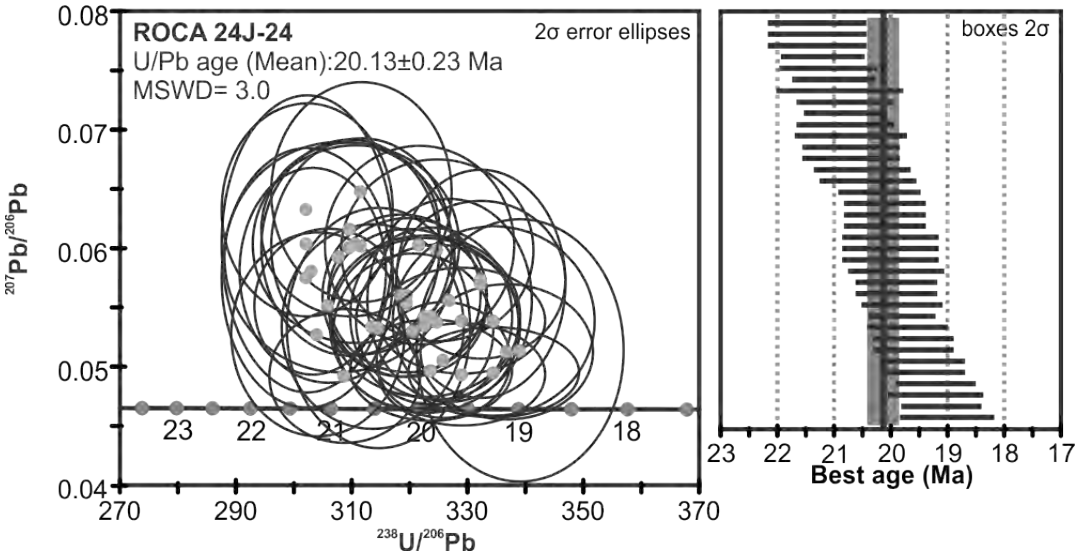

Preferred age: t= 20.13 ± 0.23 Ma

Weighted mean age (95% confidence) calculated with 37 data points. Single crystals are in the 19 to 21 Ma age range. An antecrystal with an age of 24.1 was rejected from the age calculation.

^{40}Ar-^{39}Ar age
Sample Name: ROCA 24J-24
Mineral: Biotite

laser step-heating experiments on biotite concentrate

Pwr	^{39}Ar × 10^{-6}	F ^{39}Ar	^{40}Ar*/^{39}Ar$_K$	1σ	Age in Ma	1σ		% ^{40}Ar*	^{40}Ar/^{36}Ar	^{37}Ar$_{Ca}$/^{39}Ar$_K$
0.20	6.687	0.0020	7.58	2.59	46.33	15.61	a	11.30	333.16	0.142
0.50	164.655	0.0504	1.96	0.26	12.13	1.57	b	12.19	336.51	0.021
0.80	615.982	0.1884	2.28	0.04	14.06	0.22	c	57.07	688.28	0.007
1.10	695.304	0.2127	2.23	0.02	13.78	0.15	d	87.33	2331.97	0.007
1.40	514.882	0.1575	2.17	0.03	13.39	0.20	e	87.79	2419.55	0.014
1.90	530.641	0.1623	2.27	0.04	14.00	0.23	f	94.26	5151.33	0.040
2.30	286.921	0.0878	2.27	0.05	14.01	0.29	g	96.45	8328.17	0.083
2.90	226.750	0.0693	2.10	0.06	12.97	0.36	h	88.90	2662.58	0.138
6.00	227.652	0.0696	2.29	0.07	14.15	0.45	i	91.85	3625.56	0.307

Integrated results

^{39}Ar × 10^{-6}	^{40}Ar*/^{39}Ar$_K$	1σ	Age in Ma	1σ	% ^{40}Ar*	^{40}Ar/^{36}Ar	^{37}Ar$_{Ca}$/^{39}Ar$_K$
3269.0	2.23	0.02	13.78	0.14	62.57	789.54	0.051

J = 0.003433 ± 0.000016

Preferred age t_p = 13.77 ± 0.13 Ma

Weighted mean of fractions c to i, representing 94.76 % of ^{39}Ar released in 7 consecutive fractions, MSWD = 2.0

t_c = 13.73 ± 0.17 Ma, $(^{40}Ar/^{36}Ar)_i$ = 299 ± 7, MSWD = 2.53 for n = 9

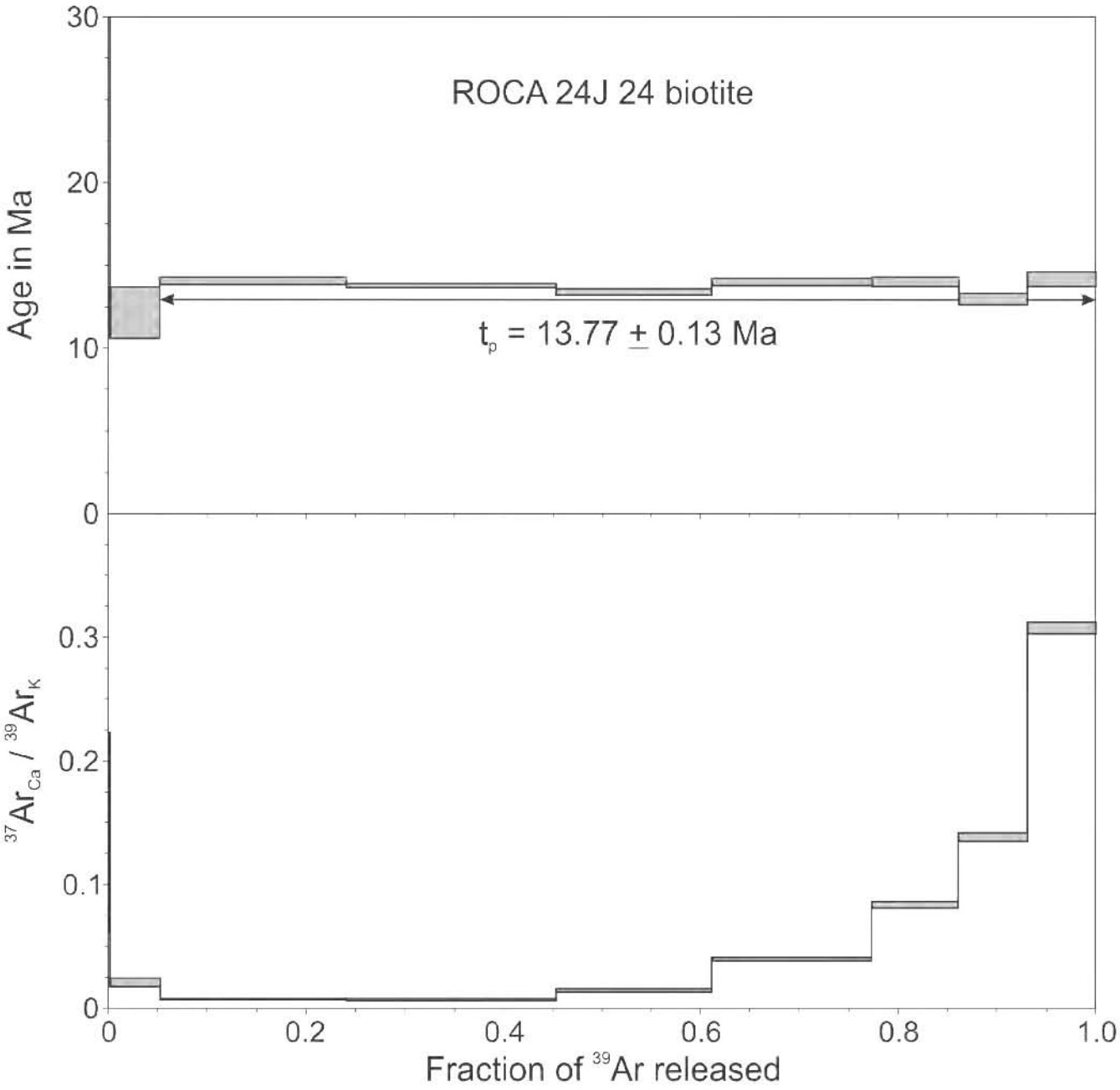

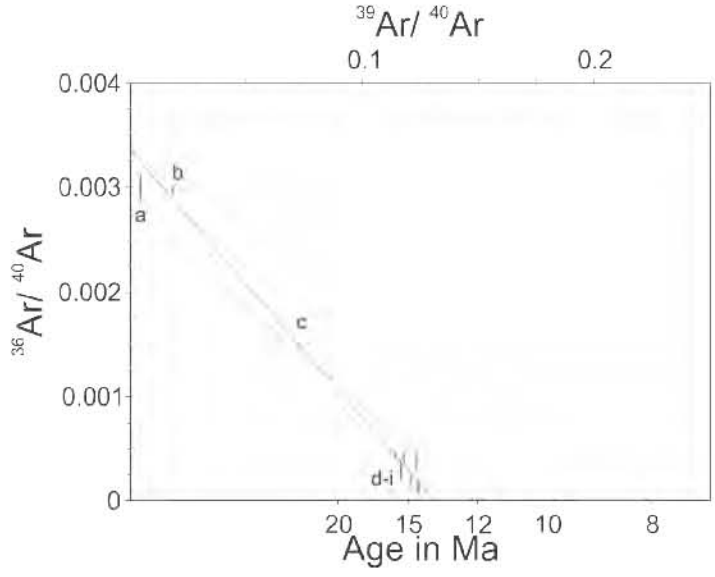

t_c = 13.73 ± 0.17 Ma

(^{40}Ar / ^{36}Ar)$_i$ = 299 ± 7

MSWD = 2.53, n = 9

Sample Name: BC 09-25

Location: Bahia Concepcion
Latitude: 26.7827°
Longitude: -111.7911°
Altitude/Depth (m.a.s.l.): 2

Rock type: Granite

U-Pb Age

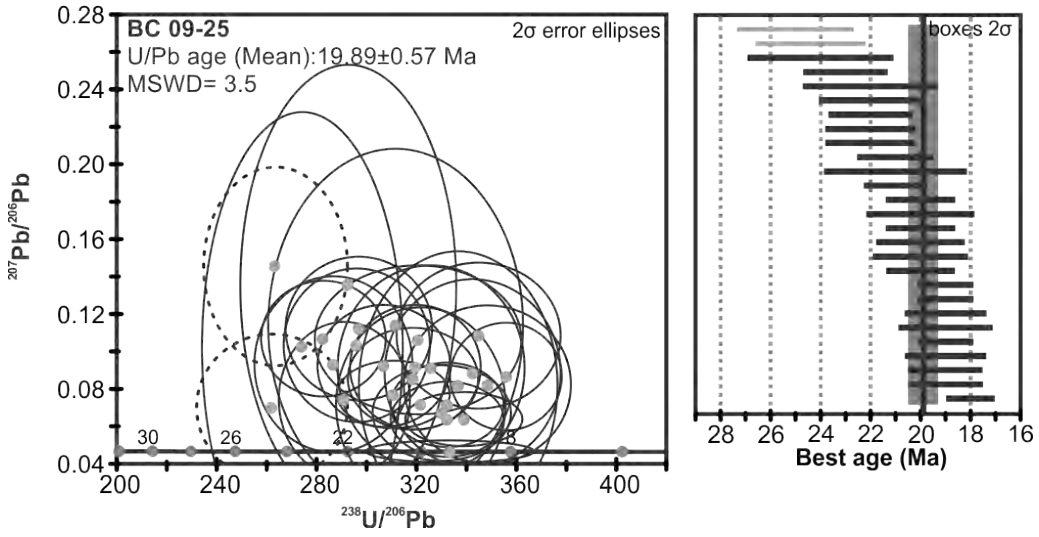

Preferred age: t= 19.80 ± 0.67 Ma

Weighted mean age (95% confidence) calculated with 25 data points. Single crystals are in the 18 to 24.6 Ma age range. Five heritage zircon with ages from 40 to 88 were found.

^{40}Ar-^{39}Ar age
Sample Name: BC 09-25
Mineral: Biotite

Laser step-heating experiments on biotite concentrate

Pwr	^{39}Ar × 10^{-6}	F ^{39}Ar	^{40}Ar*/^{39}Ar$_K$	1σ	Age in Ma	1σ			% ^{40}Ar*	^{40}Ar/^{36}Ar	^{37}Ar$_{Ca}$/^{39}Ar$_K$
0.40	8.295	0.0101	10.01	3.11	63.83	19.51	a	‡	36.91	468.36	1.815
0.90	54.920	0.0668	2.74	0.25	17.70	1.60	b	‡	43.11	519.46	0.333
1.40	155.167	0.1889	2.79	0.07	18.02	0.47	c	‡	85.75	2073.47	0.032
1.90	121.947	0.1484	3.00	0.15	19.36	0.96	d		95.41	6437.34	0.154
2.50	130.413	0.1587	2.96	0.09	19.15	0.56	e		93.93	4869.52	0.121
3.30	134.534	0.1637	2.99	0.12	19.30	0.75	f		99.22	37825.34	0.079
4.00	76.234	0.0928	3.11	0.16	20.07	1.00	g		96.94	9649.43	0.107
7.00	140.108	0.1705	2.97	0.13	19.16	0.84	h		94.18	5077.18	0.027

Integrated results

^{39}Ar × 10^{-6}	^{40}Ar*/^{39}Ar$_K$	1σ	Age in Ma	1σ	% ^{40}Ar*	^{40}Ar/^{36}Ar	^{37}Ar$_{Ca}$/^{39}Ar$_K$
821.6	3.01	0.06	19.44	0.40	83.43	1783.64	0.116

J = 0.003599 ± 0.000031

Preferred age t_p = 19.32 ± 0.35 Ma

Weighted mean of fractions d to h, representing 73.42% of ^{39}Ar released in 5 consecutive fractions, MSWD = 0.17

t_c = 19.09 ± 1.26 Ma; $(^{40}Ar/^{36}Ar)_i$ = 370 ± 391, MSWD = 0.22 for n = 5

‡ fraction ignored in the isochron given in the figure

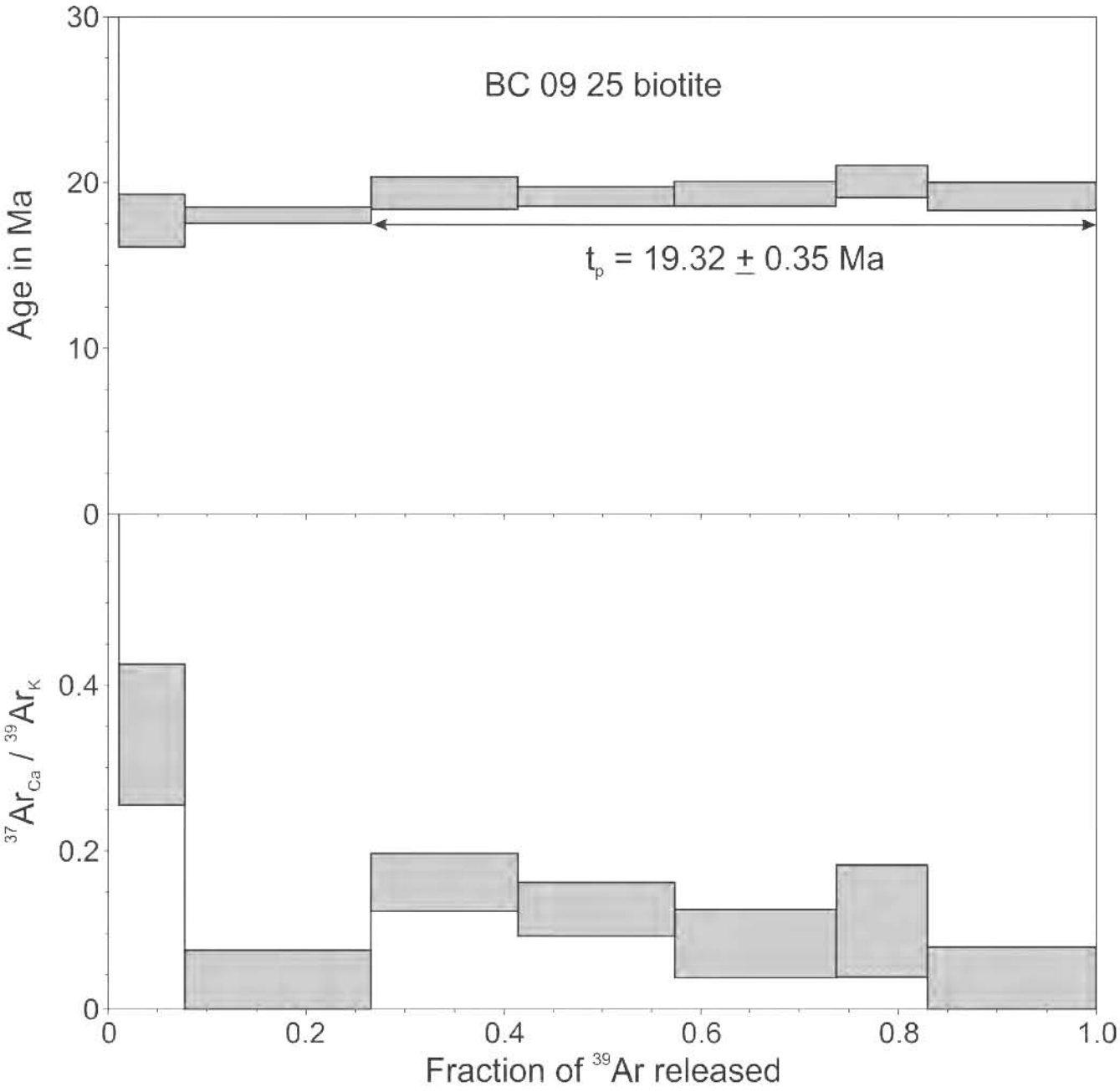

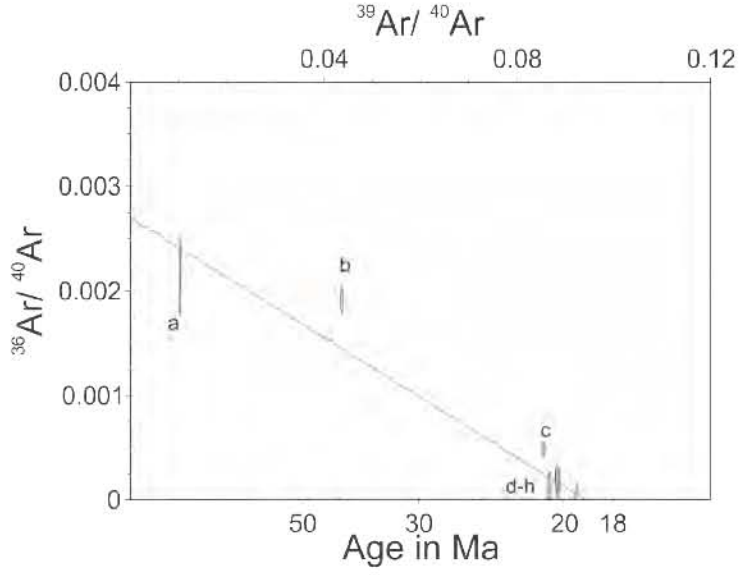

t_c = 19.09 ± 1.26 Ma

$(^{40}Ar / ^{36}Ar)_i$ = 370 ± 391

MSWD = 0.22, n = 5

Sample Sample Name: ROCA 24J-22

Location: South Pescadero transform
Latitude: 24.02°
Longitude: -109.039°
Altitude/Depth (m.a.s.l.): -2009

Rock type: Granite

U-Pb Age

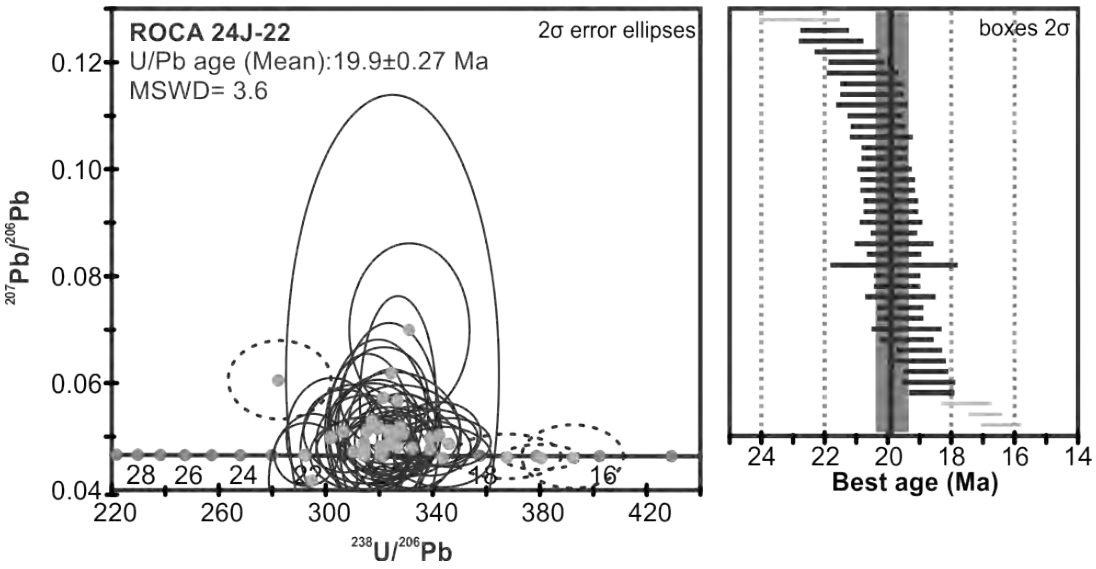

Preferred age: t= 19.9 ± 0.27 Ma

Weighted mean age (95% confidence) calculated with 32 data points. Three young crystals and three oldest crystals were eliminated from calculation.
Single crystals are in the 18.6 to 22 Ma age range.

^{40}Ar-^{39}Ar age
Sample Name: ROCA 24J-22
Mineral: K-feldspar

laser step-heating experiments on K Feldspar concentrate

Pwr	^{39}Ar × 10^{-6}	F ^{39}Ar	^{40}Ar*/^{39}Ar$_K$	1σ	Age in Ma	1σ			% ^{40}Ar*	^{40}Ar/^{36}Ar	^{37}Ar$_{Ca}$/^{39}Ar$_K$
0.80	79.793	0.0234	13.98	0.86	88.57	5.29	a		15.79	350.91	0.039
1.60	306.453	0.0897	2.06	0.14	13.32	0.87	b		38.75	482.42	0.018
2.20	201.976	0.0591	1.87	0.05	12.08	0.30	c	‡	95.62	6747.37	0.025
3.20	503.895	0.1475	1.45	0.03	9.40	0.22	d		71.68	1043.47	< 0.001
4.50	510.084	0.1494	1.59	0.04	10.32	0.23	e		59.84	735.81	0.006
6.10	828.358	0.2426	1.49	0.03	9.66	0.19	f		52.90	627.32	0.002
8.20	984.642	0.2883	1.54	0.03	9.97	0.17	g		53.48	635.25	< 0.001
2.00	922.585	0.0924	5.45	0.30	35.06	1.92	h		21.42	376.04	0.011
3.00	1064.826	0.1066	1.85	0.08	11.96	0.55	i	‡	83.43	1783.12	0.023
4.00	560.097	0.0561	1.95	0.12	12.59	0.80	j	‡	82.07	1648.01	0.025
5.00	972.344	0.0974	1.51	0.03	9.76	0.18	k		67.89	920.36	0.018
6.00	814.039	0.0815	1.46	0.02	9.45	0.15	l		61.17	761.07	0.003
6.50	410.869	0.0412	1.50	0.04	9.68	0.26	m		61.05	758.70	< 0.001
7.00	490.867	0.0492	1.64	0.06	10.61	0.41	n		64.38	829.52	0.010
7.50	291.733	0.0292	1.84	0.08	11.90	0.49	o		70.25	993.28	0.038
8.00	457.427	0.0458	1.72	0.09	11.14	0.59	p		66.40	879.48	0.035
12.00	3694.620	0.3700	1.64	0.01	10.63	0.07	q		68.58	940.62	0.007
11.00	305.177	0.0306	1.50	0.07	9.72	0.46	r		53.45	634.81	< 0.001

Integrated results

^{39}Ar × 10^{-6}	^{40}Ar*/^{39}Ar$_K$	1σ	Age in Ma	1σ	% ^{40}Ar*	^{40}Ar/^{36}Ar	^{37}Ar$_{Ca}$/^{39}Ar$_K$
3415.0	1.88	0.03	12.16	0.21	38.58	481.15	0.005
9985.0	2.00	0.03	12.96	0.24	44.29	530.39	0.013

J = 0.003599 ± 0.000031

Preferred age t = 9.84 ± 0.18 Ma

Weighted mean of fractions d to g, representing 82.78 % of ^{39}Ar released in 4 consecutive fractions, MSWD = 2.9

t_c = 9.35 ± 0.27 Ma, $(^{40}Ar/^{36}Ar)_i$ = 345 ± 10, MSWD = 11.8 for n = 15

‡ fractions ignored in the isochron age calculation

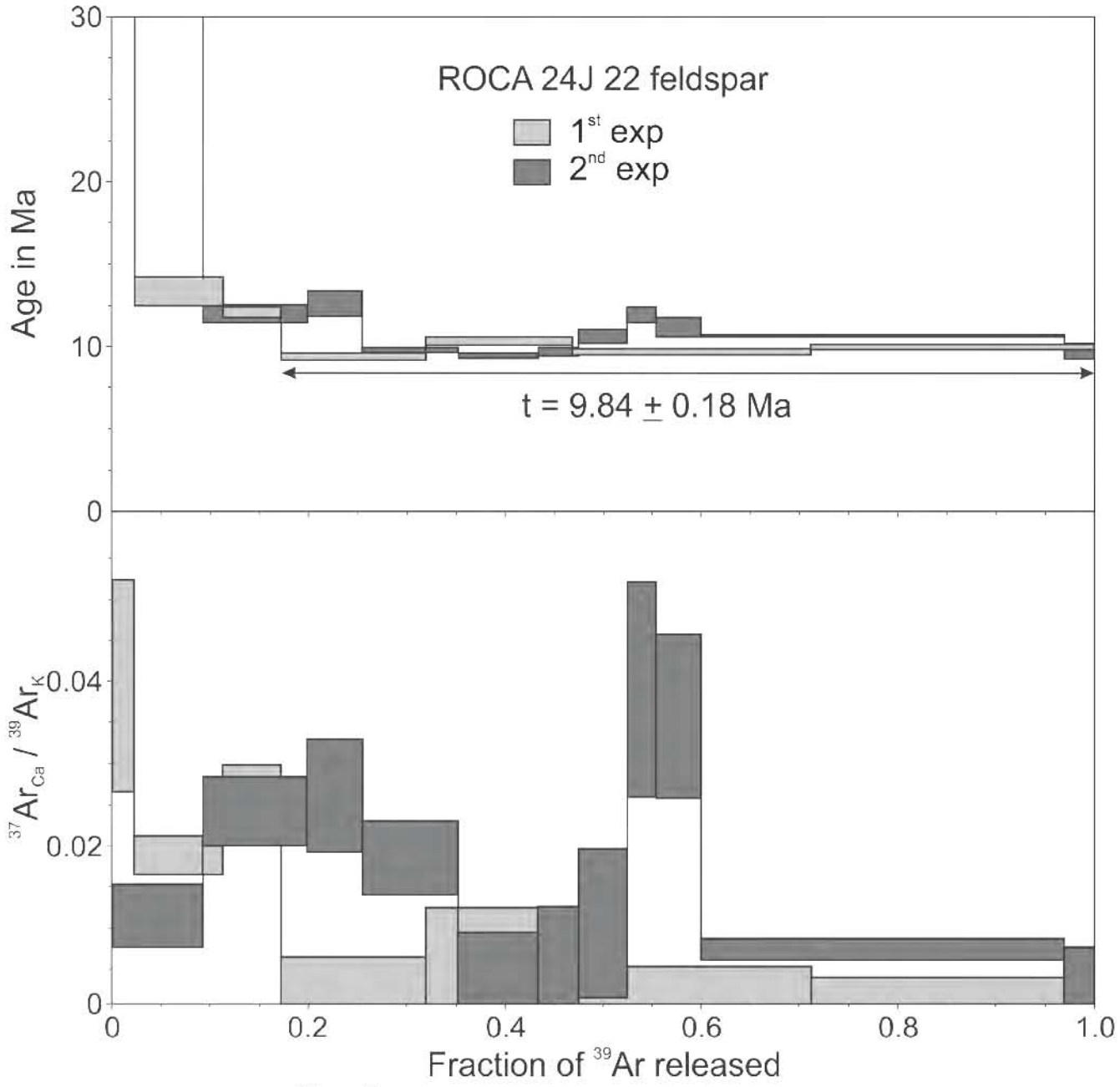

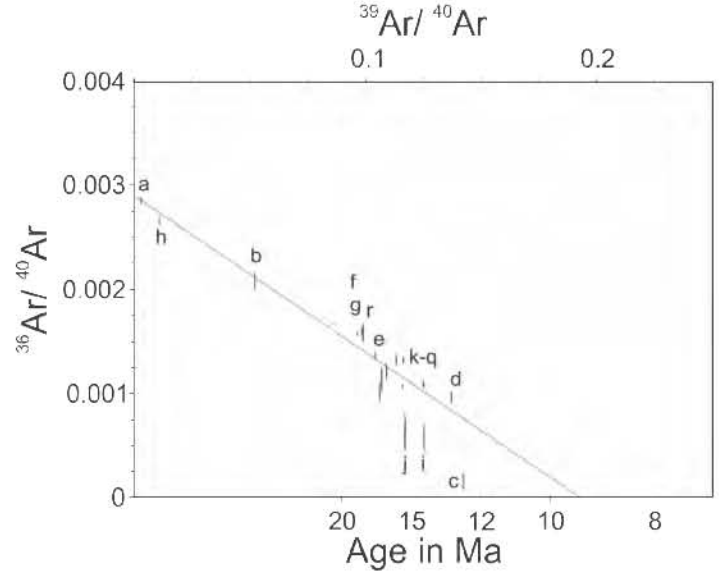

t_c = 9.35 ± 0.27 Ma

$(^{40}Ar / ^{36}Ar)_i$ = 345 ± 10

MSWD = 11.8, n = 15

Sample Name: Oro 01

Location: Santa Maria del Oro, Nayarit
Latitude: 21.464
Longitude: -104.502
Altitude/Depth (m.a.s.l.): 381

Rock type: Granite

U-Pb Age

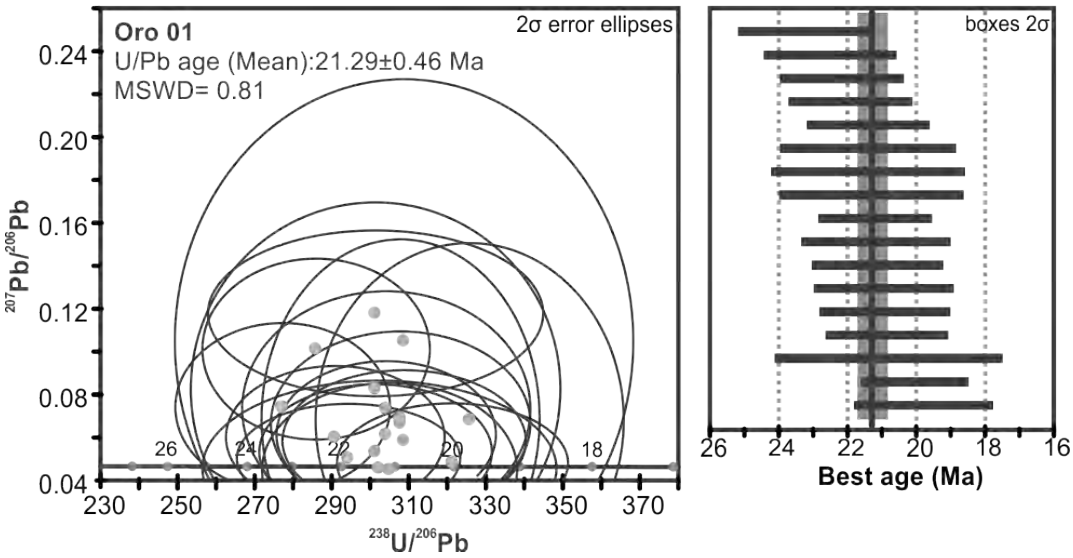

Preferred age: t= 21.29 ± 0.46 Ma

Weighted mean age (95% confidence) calculated with 17 data points. Single crystals are in the 19.7 to 23.2 Ma age range.

^{40}Ar-^{39}Ar age
Sample Name: Oro 01
Mineral: Biotite

laser step-heating experiments on biotite concentrate

Pwr	^{39}Ar × 10^{-6}	F ^{39}Ar	^{40}Ar*/^{39}Ar$_K$	1σ	Age in Ma	1σ			% ^{40}Ar*	^{40}Ar/^{36}Ar	^{37}Ar$_{Ca}$/^{39}Ar$_K$
0.25	232.952	0.0197	1.84	0.62	10.92	3.66	a	‡	6.82	317.14	0.031
0.70	2091.072	0.1769	3.14	0.08	18.55	0.47	b		29.97	421.98	0.014
1.20	2864.299	0.2423	3.26	0.05	19.28	0.27	c		46.28	550.08	0.011
2.05	4830.996	0.4086	3.25	0.04	19.20	0.22	d		56.52	679.58	0.026
2.53	801.748	0.0678	3.31	0.10	19.56	0.57	e		62.88	796.02	0.039
7.00	1001.616	0.0847	3.15	0.06	18.64	0.33	f		54.73	652.68	0.061
0.20	154.471	0.0088	2.23	1.08	13.20	6.39	g	‡	6.96	317.61	0.078
0.70	1492.629	0.0852	2.75	0.13	16.27	0.76	h	‡	18.52	362.65	0.048
1.20	2417.831	0.1380	2.79	0.08	16.52	0.49	i	‡	22.21	379.89	0.026
1.99	5477.917	0.3126	3.14	0.08	18.55	0.45	j		36.95	468.66	0.020
3.00	6183.177	0.3528	3.29	0.06	19.45	0.36	k		51.62	610.81	0.033
6.00	1798.606	0.1026	3.25	0.07	19.22	0.41	l		51.66	611.29	0.051

Integrated results

^{39}Ar × 10^{-6}	^{40}Ar*/^{39}Ar$_K$	1σ	Age in Ma	1σ	% ^{40}Ar*	^{40}Ar/^{36}Ar	^{37}Ar$_{Ca}$/^{39}Ar$_K$
11820.0	3.20	0.03	18.92	0.21	43.93	527.02	0.024
17520.0	3.12	0.04	18.42	0.27	35.27	456.50	0.031

J = 0.003292 ± 0.000017

Preferred age t_p = 19.07 ± 0.16 Ma

calculated with the weighted mean of fractions b to f; 98.03% of ^{39}Ar released in 5 consecutive fractions, MSWD = 1.07

t_c = 19.54 ± 0.36 Ma, $(^{40}Ar/^{36}Ar)_i$ = 289 ± 5, MSWD = 0.73 for n = 8

‡ Fractions ignored in the isochron

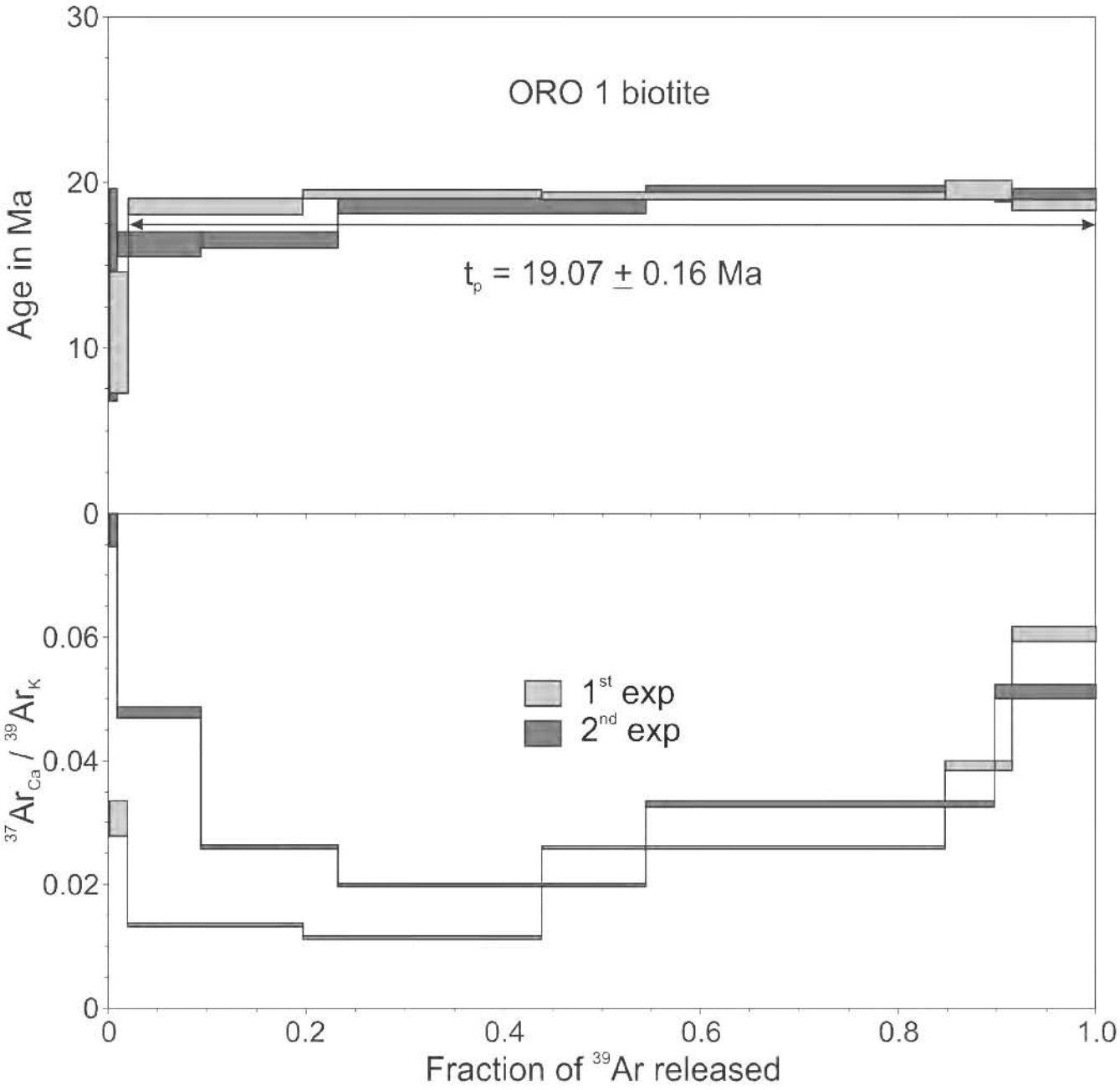

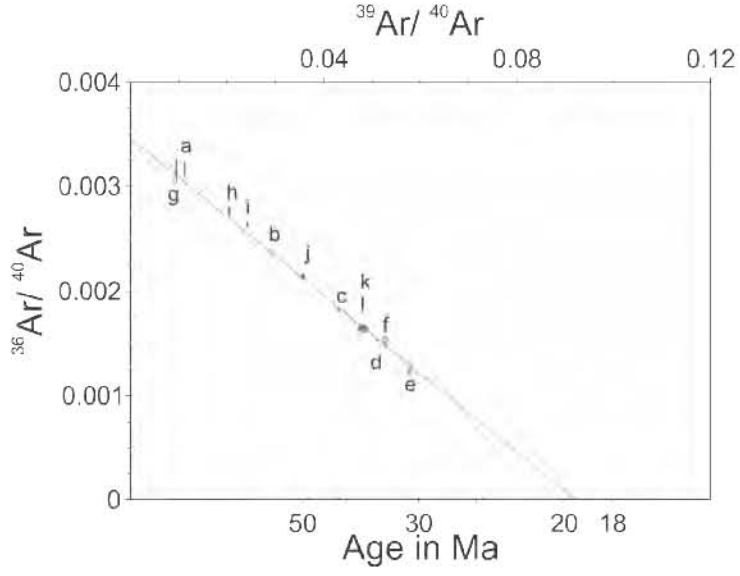

t_c = 19.54 ± 0.36 Ma

$(^{40}Ar / ^{36}Ar)_i$ = 289 ± 5

MSWD = 0.73, n = 8

^{40}Ar-^{39}Ar age
Sample Name: Oro 01
Mineral: K-feldspar

laser step-heating experiments on K Feldspar concentrate

Pwr	^{39}Ar × 10^{-6}	F ^{39}Ar	^{40}Ar*/^{39}Ar$_K$	1σ	Age in Ma	1σ			% ^{40}Ar*	^{40}Ar/^{36}Ar	^{37}Ar$_{Ca}$/^{39}Ar$_K$
1.50	1114.100	0.0327	2.84	0.05	16.81	0.28	a	‡	51.70	611.79	0.030
1.80	1315.559	0.0386	2.88	0.04	17.03	0.23	b	‡	48.54	574.25	0.034
2.20	1425.666	0.0418	2.75	0.04	16.27	0.23	c	‡	46.32	550.47	0.028
2.80	4951.612	0.1453	3.04	0.06	17.95	0.33	d		41.48	504.98	0.021
3.00	2576.536	0.0756	2.91	0.05	17.23	0.27	e		40.20	494.14	0.023
3.40	3391.406	0.0995	2.96	0.04	17.47	0.26	f		38.69	482.01	0.019
3.60	2143.762	0.0629	2.93	0.04	17.31	0.24	g		39.25	486.42	0.015
4.00	2739.267	0.0804	2.97	0.06	17.57	0.35	h		43.57	523.70	0.020
4.70	3932.306	0.1154	3.05	0.05	18.02	0.29	i		47.20	559.70	0.018
5.40	2937.890	0.0862	3.10	0.05	18.31	0.32	j		38.01	476.70	0.025
6.40	1903.100	0.0558	3.00	0.05	17.71	0.30	k		42.48	513.70	0.023
7.00	2815.246	0.0826	3.07	0.05	18.17	0.29	l		43.66	524.51	0.040
7.50	2840.260	0.0833	3.14	0.05	18.56	0.31	m		40.79	499.07	0.038

Integrated results

^{39}Ar × 10^{-6}	^{40}Ar*/^{39}Ar$_K$	1σ	Age in Ma	1σ	% ^{40}Ar*	^{40}Ar/^{36}Ar	^{37}Ar$_{Ca}$/^{39}Ar$_K$
34090.0	3.00	0.02	17.73	0.16	42.18	511.09	0.025

J = 0.003292 ± 0.000017

Preferred age t_p = 17.65 ± 0.13 Ma

calculated with the weighted mean of fractions d to k; 72.10% of ^{39}Ar released in 8 consecutive fractions, MSWD = 1.51

t_c = 17.78 ± 1.46 Ma, $(^{40}Ar/^{36}Ar)_i$ = 295 ± 17, MSWD = 2.18 for n = 10

‡ Fractions ignored in the isochron

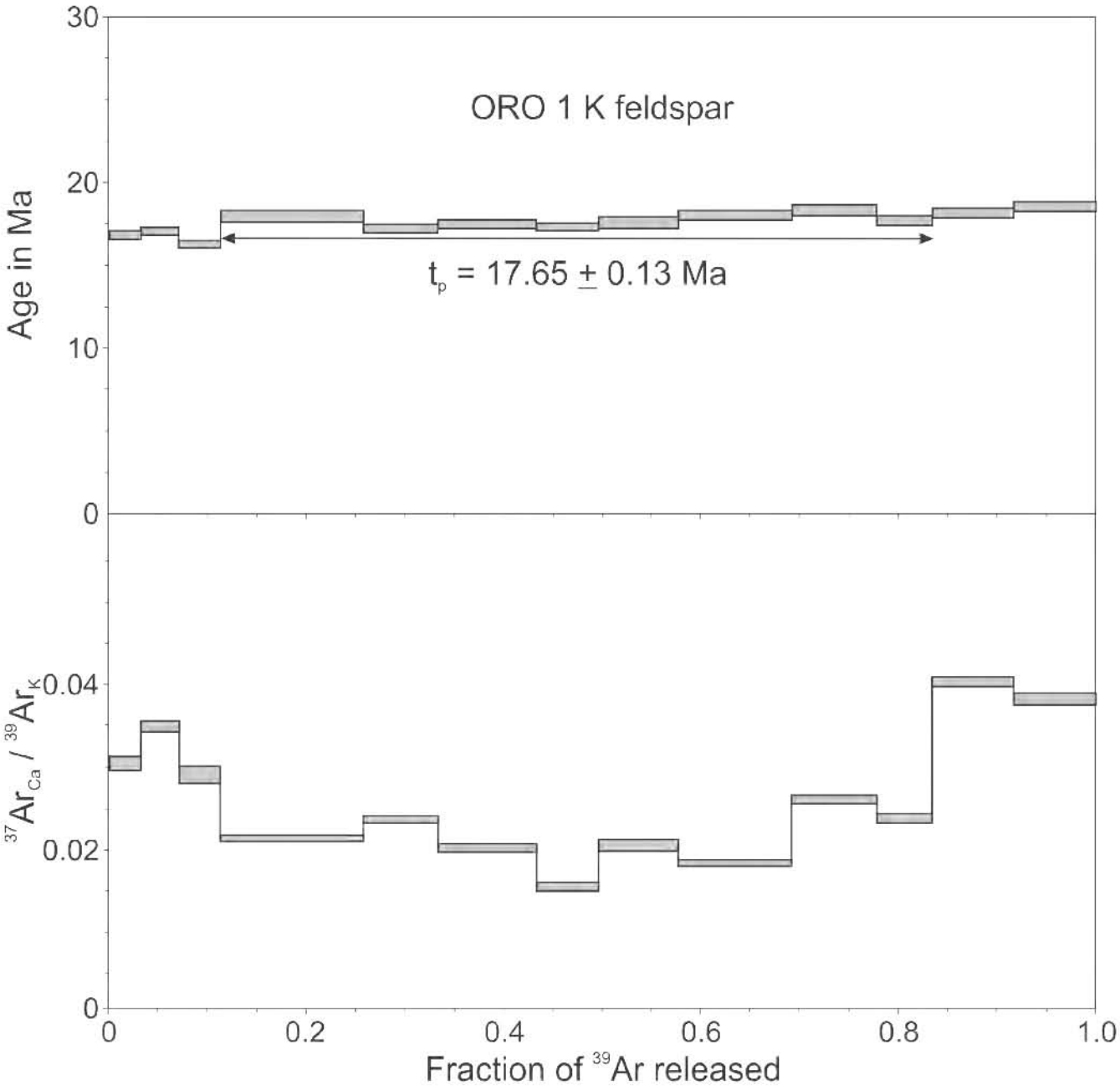

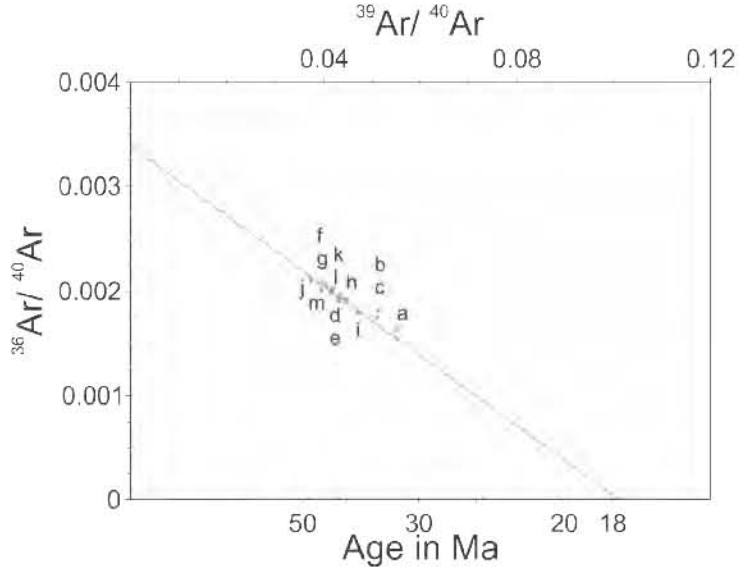

t_c = 17.78 ± 1.46 Ma

$(^{40}Ar / ^{36}Ar)_i$ = 295 ± 17

MSWD = 2.18, n = 10

Sample Name: SC 09-04

Location: Santa Catalina Island
Latitude: 25.6275°
Longitude: -110.7934°
Altitude/Depth (m.a.s.l.): 0

Rock type: Quartz Monzonite

^{40}Ar-^{39}Ar age
Sample Name: SC 09-04
Mineral: Hornblende

Laser step-heating experiments on hornblende concentrate

Pwr	^{39}Ar × 10^{-6}	F ^{39}Ar	^{40}Ar*/^{39}Ar$_K$	1σ	Age in Ma	1σ			% ^{40}Ar*	^{40}Ar/^{36}Ar	^{37}Ar$_{Ca}$/^{39}Ar$_K$
0.50	2.944	0.0053	31.05	9.71	196.41	58.20	a		4.50	309.44	6.554
1.00	7.706	0.0139	11.15	4.77	72.99	30.59	b		23.19	384.73	9.436
1.60	31.549	0.0568	5.23	0.73	34.59	4.76	c		49.25	582.22	8.698
2.20	154.632	0.2782	2.82	0.13	18.77	0.84	d	†	59.47	729.01	9.218
2.80	177.980	0.3201	2.83	0.06	18.84	0.39	e	†	71.27	1028.52	9.426
3.40	101.094	0.1819	2.98	0.15	19.83	0.97	f	†	81.45	1593.33	8.935
4.10	13.914	0.0250	5.32	0.83	35.18	5.45	g		98.05	15165.11	11.934
5.10	21.888	0.0393	2.41	0.48	16.02	3.16	h		48.03	568.59	12.055
6.70	44.196	0.0796	5.03	0.72	33.27	4.70	i		62.60	790.16	8.184

Integrated results

^{39}Ar × 10^{-6}	^{40}Ar*/^{39}Ar$_K$	1σ	Age in Ma	1σ	% ^{40}Ar*	^{40}Ar/^{36}Ar	^{37}Ar$_{Ca}$/^{39}Ar$_K$
552.6	3.48	0.12	23.10	0.84	37.99	476.52	9.290

J = 0.003704 ± 0.000030

Preferred age t_p = 18.96 ± 0.35 Ma

Weighted mean of fractions d to f, representing 78.02% of ^{39}Ar released in 3 consecutive fractions, MSWD = 0.46

t_c = 19.55 ± 1.13 Ma; $(^{40}Ar/^{36}Ar)_i$ = 273 ± 40, MSWD = 0.70 for n = 3

† fractions used to calculate the isochron age

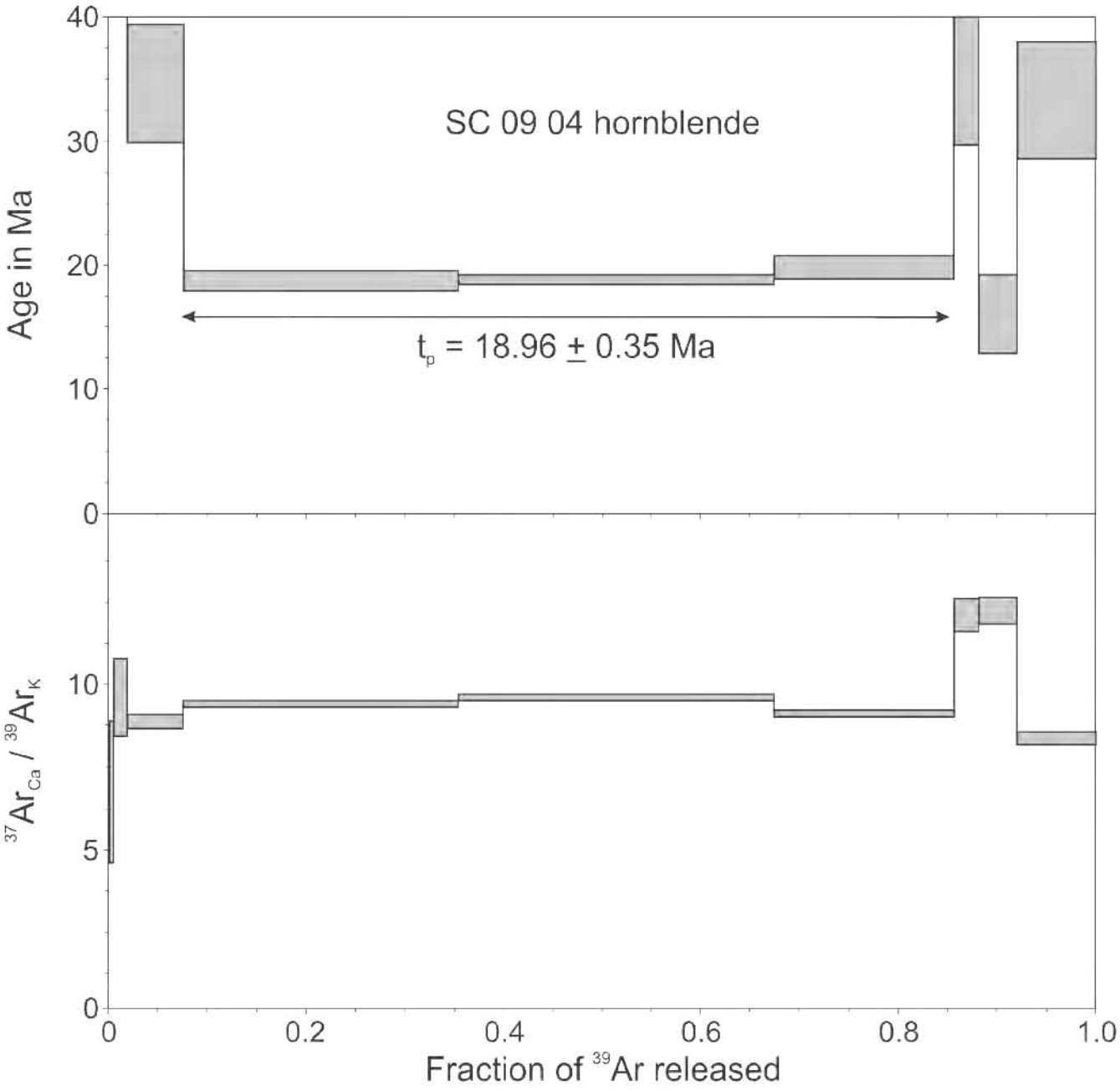

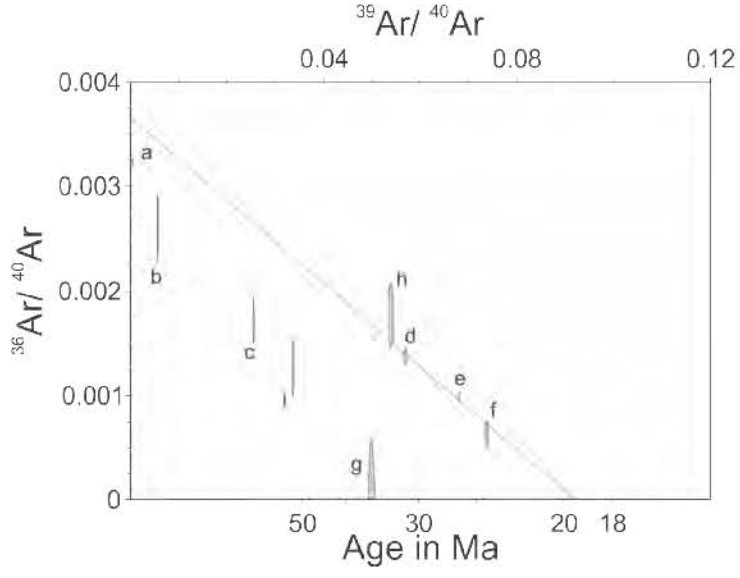

t_c = 19.55 ± 1.13 Ma

$(^{40}Ar / ^{36}Ar)_i$ = 273 ± 40

MSWD = 0.70, n = 3

^{40}Ar-^{39}Ar age
Sample Name: SC 09-04
Mineral: Biotite

Laser step-heating experiments on biotite concentrate

Pwr	^{39}Ar × 10^{-6}	F ^{39}Ar	^{40}Ar*/^{39}Ar$_K$	1σ	Age in Ma	1σ			% ^{40}Ar*	^{40}Ar/^{36}Ar	^{37}Ar$_{Ca}$/^{39}Ar$_K$
0.40	29.406	0.0044	0.35	0.88	2.36	5.84	a	‡	0.88	298.12	0.000
0.90	198.517	0.0300	3.25	0.20	21.59	1.29	b		32.55	438.08	0.091
1.40	691.665	0.1046	2.94	0.06	19.57	0.38	c		72.73	1083.41	0.054
1.90	838.537	0.1268	2.94	0.02	19.53	0.11	d		92.09	3737.68	0.005
2.50	1016.910	0.1537	3.04	0.03	20.18	0.17	e		96.61	8714.06	0.154
3.30	1456.316	0.2201	2.92	0.01	19.38	0.06	f		96.03	7446.26	0.130
4.00	1244.430	0.1881	2.95	0.01	19.62	0.08	g		97.66	12636.07	0.164
7.00	1139.538	0.1723	3.00	0.02	19.91	0.13	h		99.36	46350.81	0.140

Integrated results

^{39}Ar × 10^{-6}	^{40}Ar*/^{39}Ar$_K$	1σ	Age in Ma	1σ	% ^{40}Ar*	^{40}Ar/^{36}Ar	^{37}Ar$_{Ca}$/^{39}Ar$_K$
6615.0	2.96	0.01	19.67	0.18	83.46	1786.45	0.116

J = 0.003704 ± 0.000030

Preferred age t_c = 19.52 ± 0.20 Ma

(^{40}Ar/^{36}Ar)$_i$ = 307 ± 20, MSWD = 6.3 for n = 7

t_p = 19.66 ± 0.12 Ma; plateau age calculated with the weighted mean of fractions c to h, representing 96.56% of ^{39}Ar released in 6 consecutive fractions, MSWD = 1.92

‡ fraction ignored in the isochron age calculation

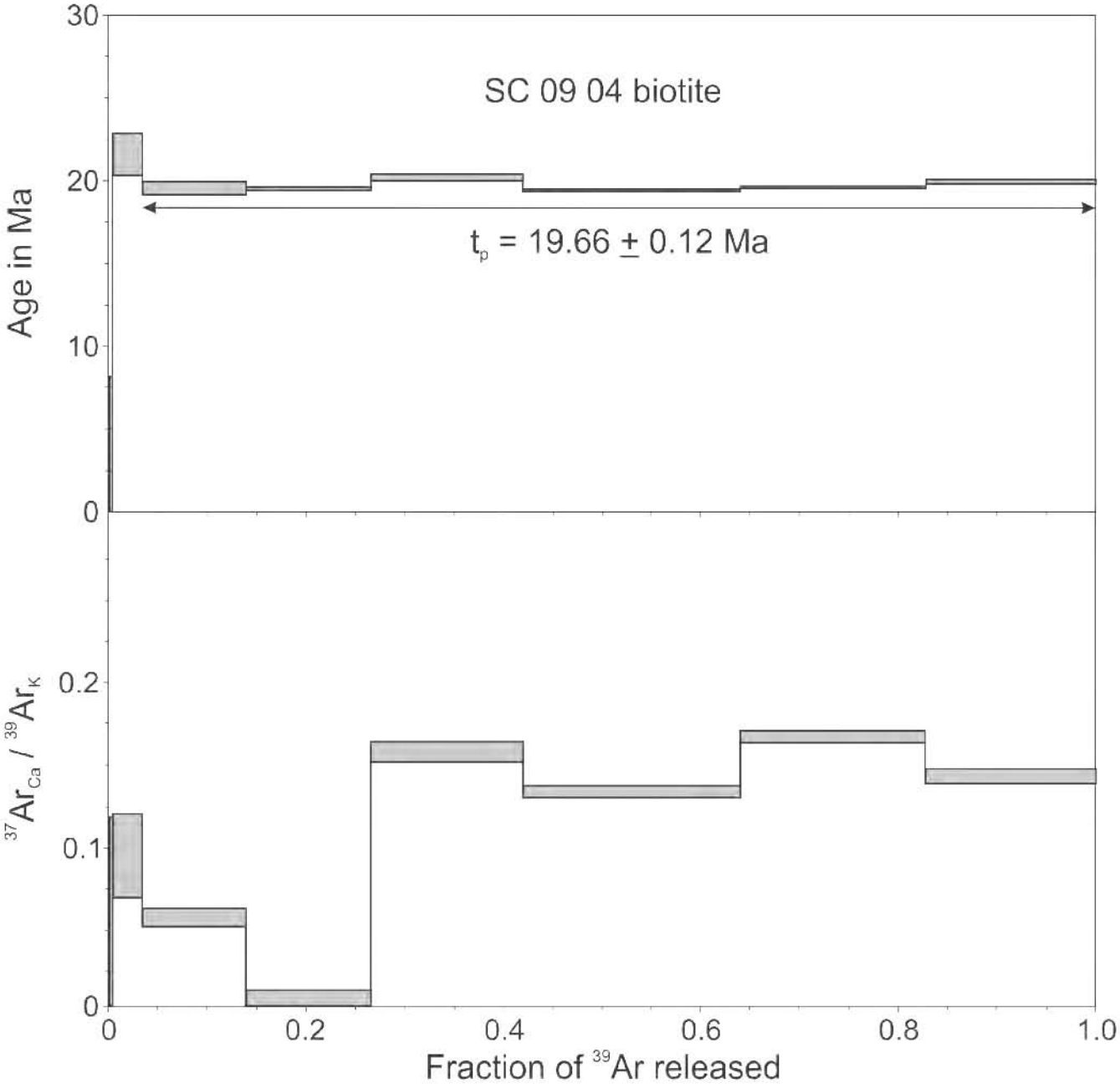

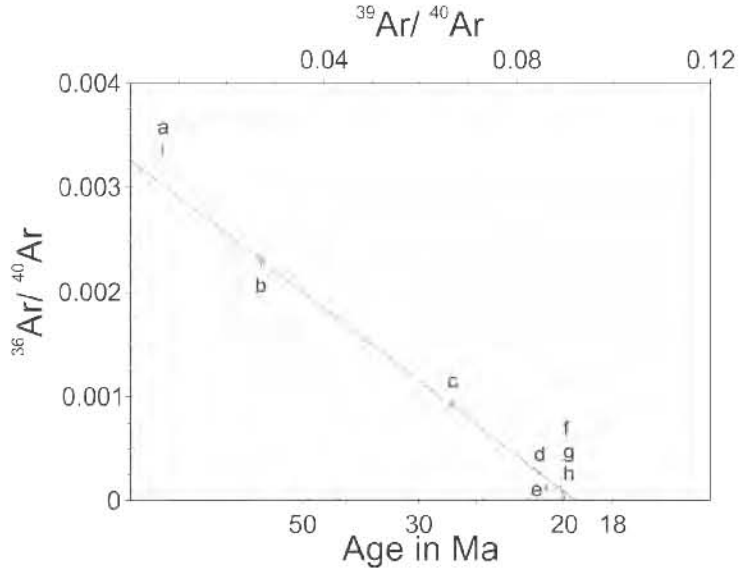

t_c = 19.52 ± 0.20 Ma

$(^{40}Ar / ^{36}Ar)_i$ = 307 ± 20

MSWD = 6.3, n = 7

Sample Name: ROCA 1J-18

Location: North Pescadero Basin East fault scarp
Latitude: 22.5541°
Longitude: -106.6978°
Altitude/Depth (m.a.s.l.): -670

Rock type: Leucocratic granodiorite

^{40}Ar-^{39}Ar age
Sample Name: ROCA 1J-18
Mineral: Muscovite

laser step-heating experiments on muscovite concentrate

Pwr	^{39}Ar × 10^{-6}	F ^{39}Ar	^{40}Ar*/^{39}Ar$_K$	1σ	Age in Ma	1σ			% ^{40}Ar*	^{40}Ar/^{36}Ar	^{37}Ar$_{Ca}$/^{39}Ar$_K$
0.20	3.853	0.0011	15.67	7.59	101.13	47.65	a	‡	29.99	422.08	< 0.001
0.41	41.805	0.0118	0.50	0.86	3.29	5.69	b	‡	2.08	301.76	0.003
0.60	269.126	0.0757	2.67	0.05	17.63	0.35	c	‡	61.78	773.10	0.008
0.80	502.337	0.1413	2.85	0.03	18.81	0.20	d		96.08	7529.77	0.002
1.02	1057.409	0.2974	2.86	0.01	18.90	0.09	e		98.99	29315.77	0.002
1.20	359.979	0.1012	2.79	0.03	18.40	0.20	f		97.51	11877.89	< 0.001
1.45	272.925	0.0768	2.85	0.04	18.83	0.27	g		99.92	373271.10	< 0.001
1.75	324.497	0.0913	2.84	0.03	18.75	0.22	h		100.00	9261103.40	< 0.001
2.30	478.449	0.1346	2.83	0.02	18.67	0.12	i		99.60	74600.67	0.002
3.50	245.040	0.0689	2.76	0.04	18.22	0.26	j	‡	98.88	26442.05	< 0.001

Integrated results

^{39}Ar × 10^{-6}	^{40}Ar*/^{39}Ar$_K$	1σ	Age in Ma	1σ	% ^{40}Ar*	^{40}Ar/^{36}Ar	^{37}Ar$_{Ca}$/^{39}Ar$_K$
3555.0	2.81	0.02	18.55	0.13	85.51	2039.09	0.002

J = 0.003679 ± 0.000015

Preferred age t_p = 18.76 ± 0.07 Ma

Weighted mean of fractions d to i, representing 84.25 % of ^{39}Ar released in 6 consecutive fractions, MSWD = 0.96

t_c = 18.69 ± 0.17 Ma, $(^{40}Ar/^{36}Ar)_i$ = 427 ± 169, MSWD = 1.27 for n = 6

‡ fraction ignored in the isochron age calculation

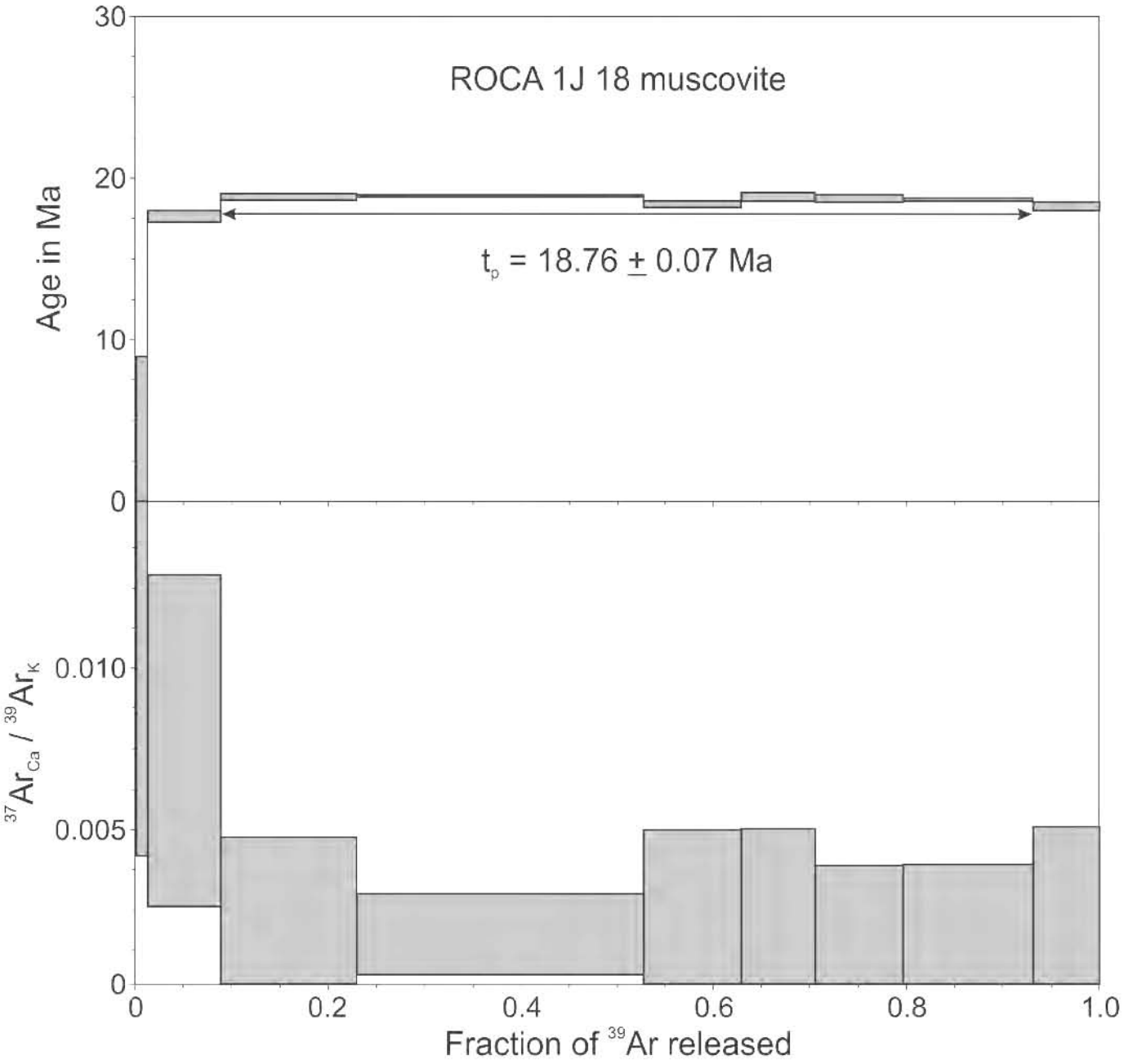

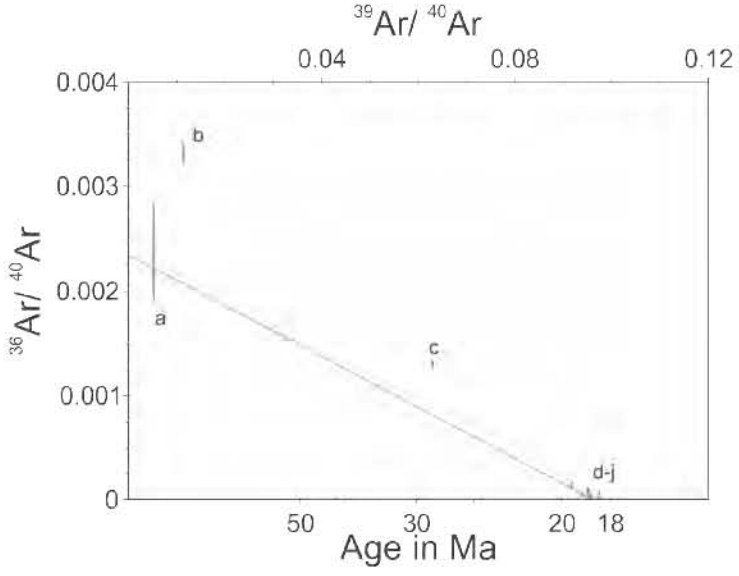

t_c = 18.69 ± 0.17 Ma

$(^{40}Ar / ^{36}Ar)_i$ = 427 ± 169

MSWD = 1.27, n = 6

Sample Name: DANA 71b

Location: North Pescadero Basin East fault scarp
Latitude: 24.7463°
Longitude: -109.1666°
Altitude/Depth (m.a.s.l.): -3050

Rock type: Granodiorite

^{40}Ar-^{39}Ar age
Sample Name: DANA 71b
Mineral: Hornblende

laser one step fusion experiments on hornblende concentrate

Pwr	^{39}Ar × 10^{-6}	F ^{39}Ar	^{40}Ar*/^{39}Ar$_K$	1σ	Age in Ma	1σ		% ^{40}Ar*	^{40}Ar/^{36}Ar	^{37}Ar$_{Ca}$/^{39}Ar$_K$
2.60	329.426	0.0233	2.00	0.27	17.42	2.33	a	20.29	370.74	13.03
2.60	744.235	0.0529	2.35	0.13	20.44	1.09	b	32.94	440.67	7.36
2.50	449.780	0.0319	2.28	0.25	19.81	2.19	c	23.84	388.02	9.63
2.30	481.309	0.0342	1.83	0.22	15.95	1.91	d	15.80	350.96	8.38
4.00	1087.448	0.0772	1.92	0.25	16.72	2.21	e	16.37	353.36	7.07
4.00	1120.820	0.0794	1.68	0.18	14.67	1.58	f	12.27	336.82	10.96
4.00	2087.224	0.1480	2.05	0.11	17.85	0.99	g	19.05	365.05	9.39
4.00	1650.834	0.1171	2.05	0.14	17.83	1.17	h	15.86	351.22	9.48
2.51	558.939	0.0396	1.99	0.29	17.29	2.50	i	15.64	350.29	10.14
2.51	870.599	0.0617	2.35	0.17	20.45	1.44	j	17.81	359.51	11.20
4.00	706.107	0.0501	1.85	0.16	16.11	1.39	k	20.74	372.81	9.02
2.84	698.507	0.0496	2.23	0.20	19.45	1.71	l	23.18	384.68	7.68
4.00	810.027	0.0575	2.06	0.20	17.91	1.77	m	20.67	372.52	8.21
4.00	1086.381	0.0772	1.71	0.14	14.93	1.25	n	23.71	387.36	6.37
3.00	603.835	0.0428	2.08	0.19	18.15	1.65	o	25.08	394.40	9.52
4.00	810.463	0.0575	2.14	0.27	18.63	2.30	p	16.49	353.84	9.60

J = 0.004851 ± 0.000007 CIC 41A

MS-10 Ta furnace step-heating experiment on hornblende concentrate

Temp °C	^{39}Ar cc STP/g	F ^{39}Ar	^{40}Ar*/^{39}Ar$_K$	1σ	Age in Ma	1σ			% ^{40}Ar*	^{40}Ar/^{36}Ar	^{37}Ar$_{Ca}$/^{39}Ar$_K$
1050	0.673	0.2278	3.55	0.00	27.92	7.12	q	‡	5.05	311.21	11.09
1150	1.798	0.6084	2.25	0.91	17.75	1.15	r		35.34	457.03	7.40
1250	0.397	0.1345	2.04	0.15	16.11	4.73	s		23.45	386.04	8.77
1312	0.087	0.0293	2.33	0.60	18.33	21.51	t		11.49	333.84	11.39
1050	0.939	0.3029	2.69	0.00	21.17	3.54	u	‡	5.50	312.71	11.10
1100	1.140	0.3679	2.38	0.45	18.73	1.16	v		30.89	427.55	7.24
1200	0.636	0.2051	2.32	0.15	18.28	1.93	w		42.98	518.21	7.80
1310	0.385	0.1241	2.72	0.25	21.40	3.17	x		41.62	506.15	9.34

Integrated results

^{39}Ar cc STP/g	^{40}Ar*/^{39}Ar$_K$	1σ	Age in Ma	1σ	% ^{40}Ar*	^{40}Ar/^{36}Ar	^{37}Ar$_{Ca}$/^{39}Ar$_K$
2.971E-07	2.52	0.30	19.87	2.32	11.64	334.42	8.54
3.118E-07	2.50	0.19	19.71	1.50	12.80	338.87	8.78

J = 0.004392 ± 0.000017 (CIC 44T); sample weight = 0.2075 g (1st exp); 0.3051 g (2nd exp)

Preferred age t_c = 18.73 ± 1.03 Ma, (^{40}Ar/^{36}Ar)$_i$ = 292 ± 5, MSWD = 1.18 for n = 22

‡ fractions ignored in the isochron age

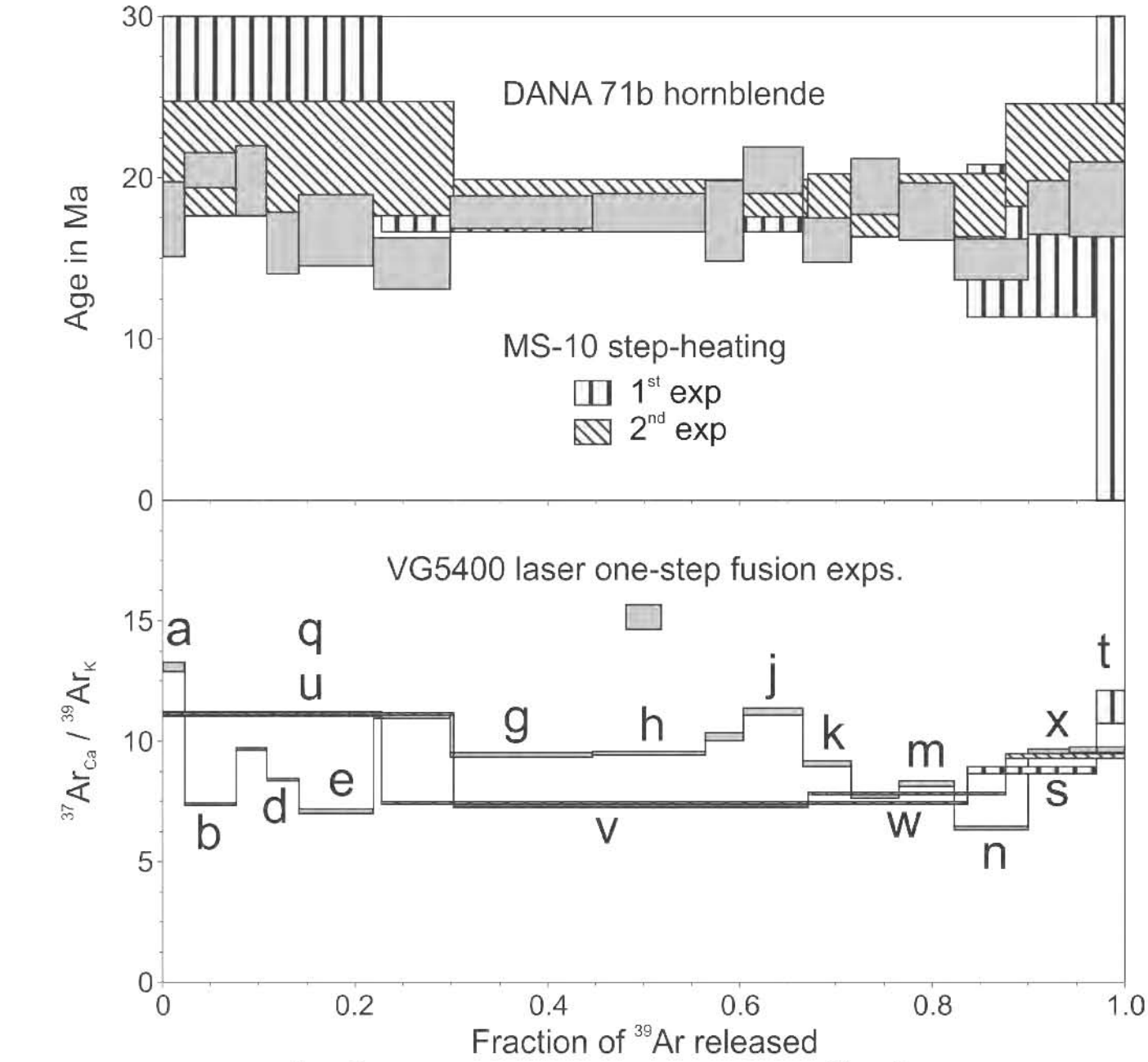
DANA 71b hornblende
MS-10 step-heating
1st exp
2nd exp
Age in Ma
VG5400 laser one-step fusion exps.
37ArCa / 39ArK
Fraction of 39Ar released

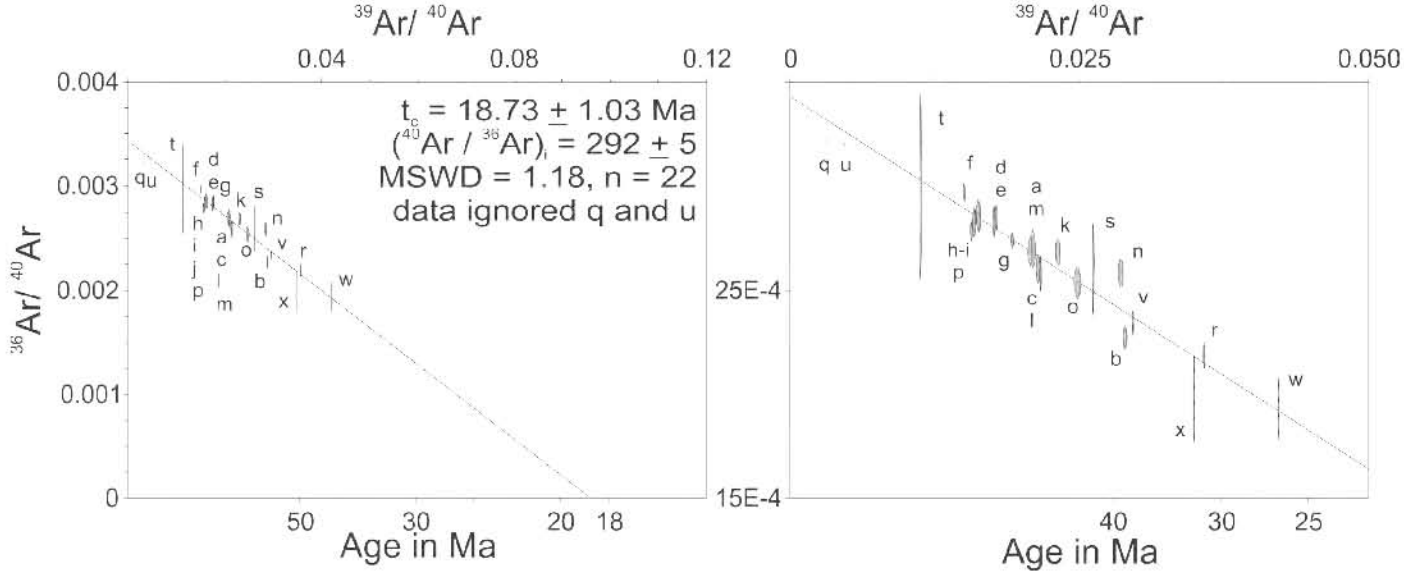
39Ar/ 40Ar
36Ar/ 40Ar
tc = 18.73 ± 1.03 Ma
(40Ar / 36Ar)i = 292 ± 5
MSWD = 1.18, n = 22
data ignored q and u
Age in Ma

^{0}Ar-^{39}Ar age
Sample Name: DANA 71b
Mineral: K Feldspar

laser one step fusion experiments on feldspar concentrate irradiation CIC 41A

Pwr	^{39}Ar × 10^{-6}	^{40}Ar*/^{39}Ar$_K$	1σ	Age in Ma	1σ			% ^{40}Ar*	^{40}Ar/^{36}Ar	^{37}Ar$_{Ca}$/^{39}Ar$_K$
5.30	1960.777	0.85	0.06	7.44	0.54	a		11.27	333.02	0.152
6.00	2228.277	0.66	0.08	5.78	0.73	b		9.35	325.98	0.321
6.00	1146.227	0.99	0.14	8.61	1.26	c		11.02	332.09	0.175
5.60	3171.111	0.60	0.05	5.25	0.44	d		10.93	331.75	0.223
4.83	3552.987	0.99	0.06	8.67	0.50	e	‡	22.38	380.70	0.129
5.20	1245.697	0.83	0.14	7.26	1.26	f		10.12	328.77	0.120
7.00	1720.941	0.96	0.14	8.39	1.21	g		13.19	340.38	0.763
5.00	4015.183	1.49	0.04	12.95	0.33	h	‡	51.39	607.92	0.019
7.00	127.215	1.31	0.83	11.44	7.19	i		4.76	310.27	4.008
4.80	283.341	1.52	0.27	13.25	2.35	j		13.61	342.04	4.430
4.40	909.382	1.48	0.08	12.92	0.67	k	‡	31.20	429.53	0.565

laser step-heating experiments on feldspar concentrate irradiation CIC 44T

Pwr	^{39}Ar × 10^{-6}	F ^{39}Ar	^{40}Ar*/^{39}Ar$_K$	1σ	Age in Ma	1σ			% ^{40}Ar*	^{40}Ar/^{36}Ar	^{37}Ar$_{Ca}$/^{39}Ar$_K$
0.19	18.594	0.0015	33.03	8.19	244.27	56.65	l		5.26	311.89	0.678
0.40	49.394	0.0039	7.16	5.07	55.86	38.95	m		1.79	300.89	0.533
0.55	136.866	0.0108	2.78	1.25	21.86	9.77	n		5.56	312.90	0.392
0.65	194.913	0.0154	0.40	0.48	3.13	3.79	o		2.04	301.67	0.744
0.75	200.186	0.0158	0.74	0.68	5.84	5.39	p		2.33	302.56	1.470
0.89	177.902	0.0140	3.69	0.51	28.99	3.95	q	‡	58.26	707.94	2.341
1.11	428.330	0.0337	1.19	0.38	9.44	3.01	r		5.07	311.28	0.226
1.40	1058.961	0.0834	0.86	0.19	6.80	1.48	s		9.13	325.20	0.339
1.90	4022.800	0.3170	0.55	0.09	4.35	0.71	t		4.22	308.52	0.151
1.80	305.337	0.0241	0.49	0.22	3.85	1.76	u		12.17	336.44	0.253
2.20	556.639	0.0439	0.52	0.16	4.08	1.26	v		12.56	337.94	0.213
7.00	5542.210	0.4367	0.50	0.05	3.98	0.43	w		8.57	323.19	0.337

Integrated results

^{39}Ar × 10^{-6}	^{40}Ar*/^{39}Ar$_K$	1σ	Age in Ma	1σ	% ^{40}Ar*	^{40}Ar/^{36}Ar	^{37}Ar$_{Ca}$/^{39}Ar$_K$
12690.0	0.72	0.07	5.66	0.51	5.75	313.53	0.321

J = 0.004851 ± 0.000007 (CIC 41A); J = 0.004389 ± 0.000015 (CIC 44T)

Preferred age t_p = 4.17 ± 0.32 Ma

plateau age calculated with the weighted mean of fractions s to w; representing 86.12% of ^{39}Ar released in 5 consecutive fractions, MSWD = 0.86

t_c = 3.84 ± 0.80 Ma, $(^{40}Ar/^{36}Ar)_i$ = 304 ± 4, MSWD = 3.6 for n = 19

‡ Fractions ignored in the isochron

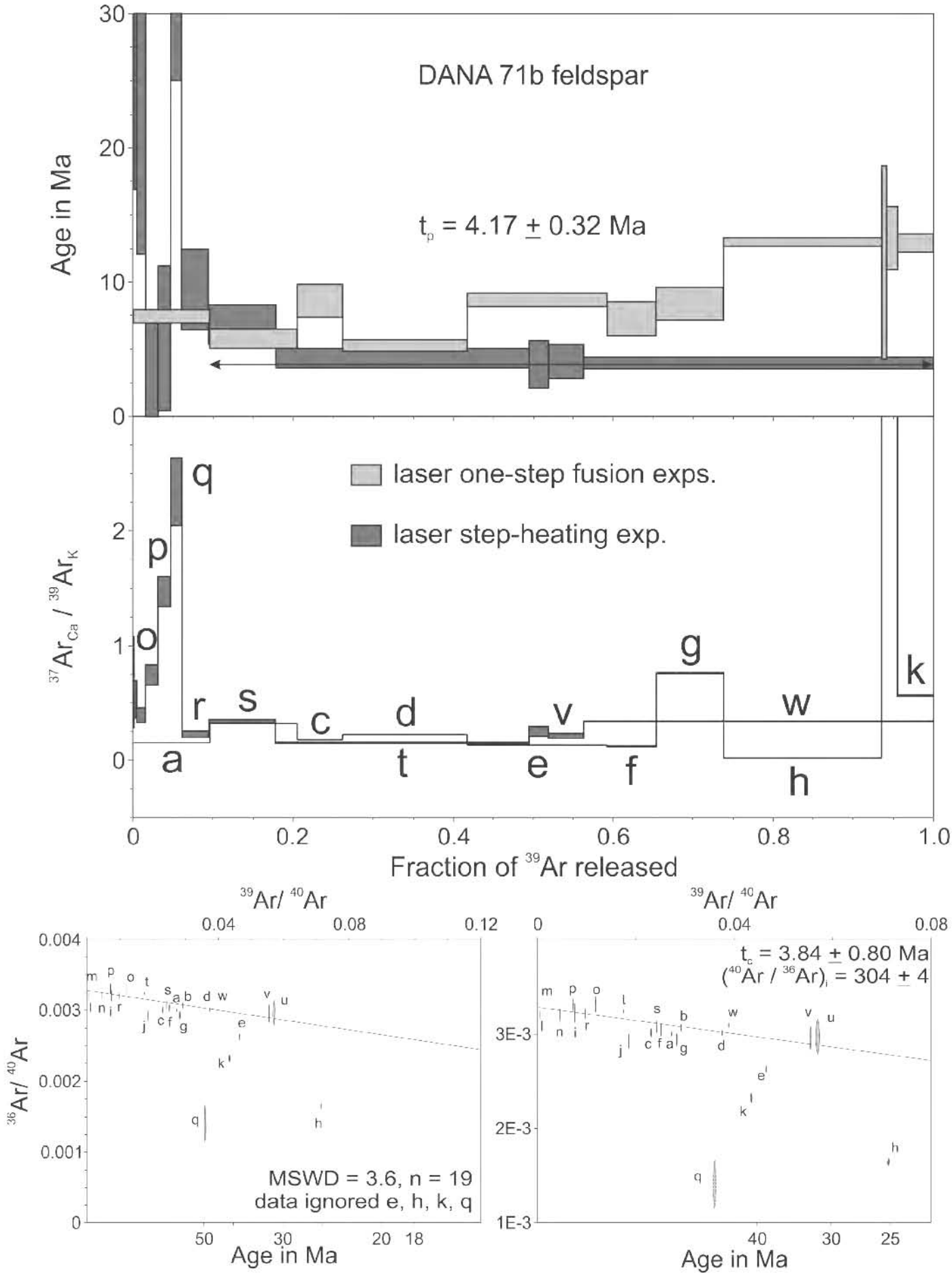
DANA 71b feldspar
t_p = 4.17 ± 0.32 Ma
Age in Ma
laser one-step fusion exps.
laser step-heating exp.
$^{37}Ar_{Ca}$ / $^{39}Ar_K$
Fraction of ^{39}Ar released
$^{39}Ar/^{40}Ar$
$^{36}Ar/^{40}Ar$
MSWD = 3.6, n = 19
data ignored e, h, k, q
t_c = 3.84 ± 0.80 Ma
$(^{40}Ar / ^{36}Ar)_i$ = 304 ± 4
Age in Ma

Sample Name: SC 09-03

Location: Santa Catalina Island
Latitude: 25.5954°
Longitude: -110.7625°
Altitude/Depth (m.a.s.l.): 1

Rock type: Quartz Monzonite

^{40}Ar-^{39}Ar age
Sample Name: SC 09-03
Mineral: Hornblende

Laser step-heating experiments on hornblende concentrate

Pwr	^{39}Ar × 10^{-6}	F ^{39}Ar	^{40}Ar*/^{39}Ar$_K$	1σ	Age in Ma	1σ		% ^{40}Ar*	^{40}Ar/^{36}Ar	^{37}Ar$_{Ca}$/^{39}Ar$_K$
0.20	1.651	0.0012	13.82	10.14	90.05	64.45	a	7.42	319.17	4.851
1.15	62.510	0.0440	2.63	0.45	17.46	2.97	b	7.87	320.74	2.144
2.00	216.912	0.1529	2.96	0.27	19.64	1.80	c	42.10	510.38	1.296
2.65	285.751	0.2011	2.77	0.05	18.44	0.30	d	55.25	660.36	3.899
3.25	261.019	0.1835	2.84	0.10	18.89	0.64	e	71.61	1040.81	6.080
3.90	239.298	0.1684	2.89	0.06	19.21	0.42	f	80.71	1531.78	4.372
7.00	353.479	0.2489	2.76	0.06	18.35	0.42	g	54.47	649.08	3.426

Integrated results

^{39}Ar × 10^{-6}	^{40}Ar*/^{39}Ar$_K$	1σ	Age in Ma	1σ	% ^{40}Ar*	^{40}Ar/^{36}Ar	^{37}Ar$_{Ca}$/^{39}Ar$_K$
1417.0	2.84	0.06	18.85	0.41	44.59	533.30	3.787

J = 0.003704 ± 0.000030

Preferred age t_p = 18.66 ± 0.22 Ma

Weighted mean of fractions b to g, representing 99.88% of ^{39}Ar released in 6 consecutive fractions, MSWD = 0.60

t_c = 18.75 ± 0.30 Ma; $(^{40}Ar/^{36}Ar)_i$ = 293 ± 4, MSWD = 0.87 for n = 7

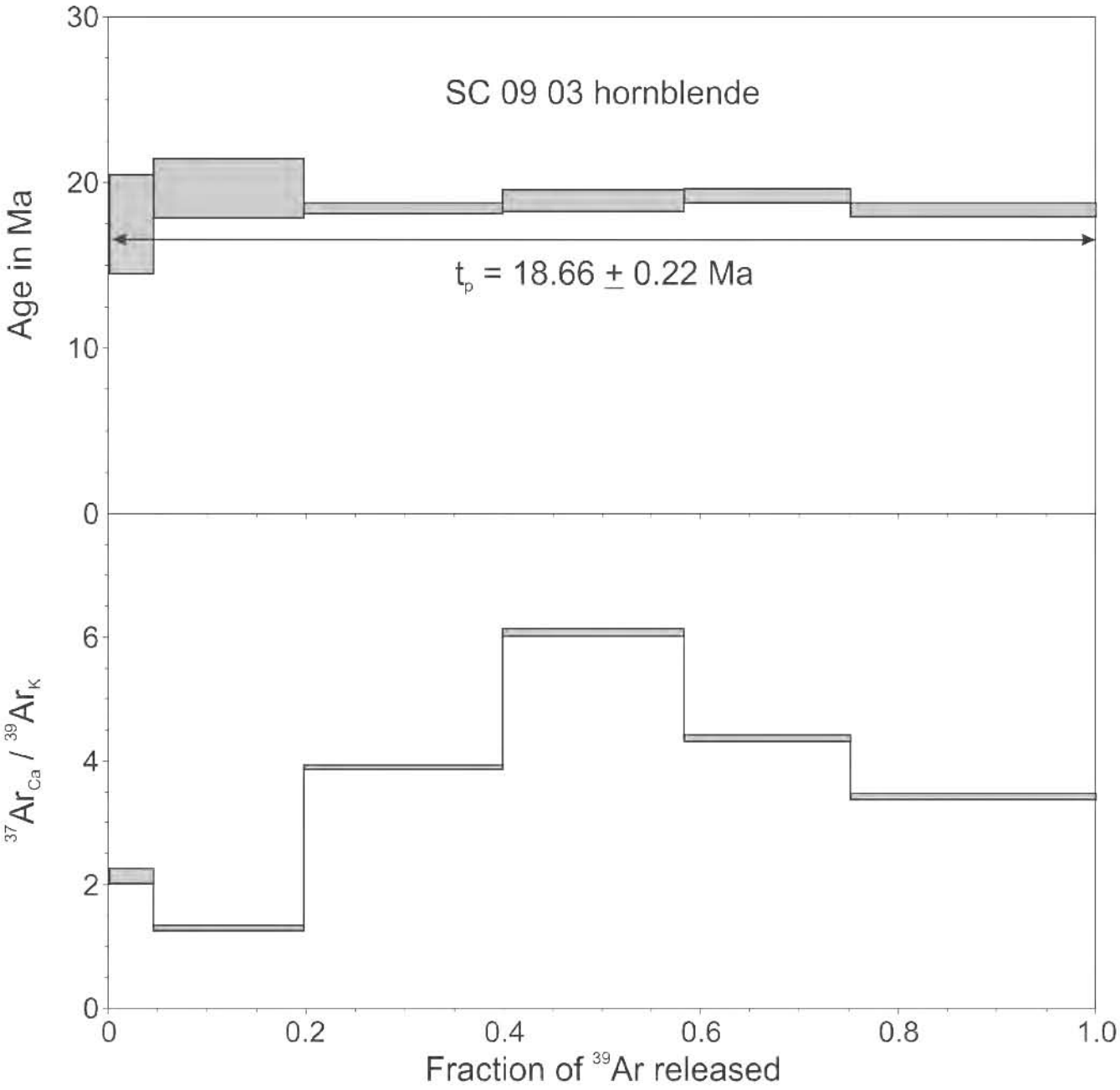

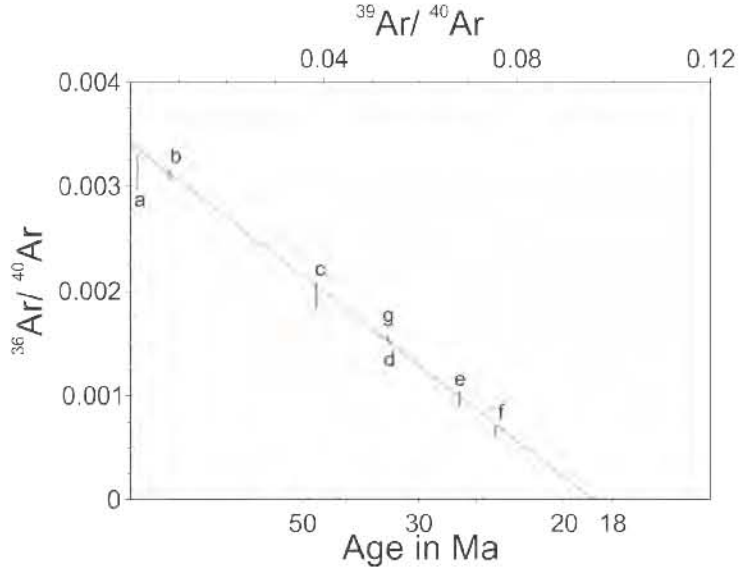

t_c = 18.75 ± 0.30 Ma

$(^{40}Ar / ^{36}Ar)_i$ = 293 ± 4

MSWD = 0.87, n = 7

^{40}Ar-^{39}Ar age
Sample Name: SC 09-03
Mineral: Biotite

Laser step-heating experiments on biotite concentrate

Pwr	^{39}Ar × 10^{-6}	F ^{39}Ar	^{40}Ar*/^{39}Ar$_K$	1σ	Age in Ma	1σ			% ^{40}Ar*	^{40}Ar/^{36}Ar	^{37}Ar$_{Ca}$/^{39}Ar$_K$
0.40	19.252	0.0056	4.90	1.41	32.45	9.24	a		7.60	319.79	1.432
0.90	120.748	0.0351	1.51	0.23	10.04	1.54	b	‡	9.21	325.49	0.295
1.40	403.506	0.1173	3.05	0.09	20.29	0.59	c		66.80	890.18	0.164
1.90	912.985	0.2655	3.08	0.02	20.48	0.14	d		90.65	3160.22	0.196
2.50	686.876	0.1997	3.01	0.02	20.02	0.15	e		91.66	3543.44	0.296
3.30	598.859	0.1741	3.00	0.02	19.92	0.15	f		94.29	5178.42	0.274
4.00	341.232	0.0992	3.04	0.03	20.20	0.21	g		98.78	24296.75	0.129
4.70	150.325	0.0437	3.12	0.09	20.71	0.57	h	‡	98.21	16470.16	0.296
7.00	205.611	0.0598	3.31	0.10	21.96	0.67	i	‡	93.49	4539.66	0.358

Integrated results

^{39}Ar × 10^{-6}	^{40}Ar*/^{39}Ar$_K$	1σ	Age in Ma	1σ	% ^{40}Ar*	^{40}Ar/^{36}Ar	^{37}Ar$_{Ca}$/^{39}Ar$_K$
3439.0	3.02	0.02	20.04	0.21	71.15	1024.13	0.244

J = 0.003704 ± 0.000030

Preferred age t_c = 19.73 ± 0.61 Ma

The saddle shaped age spetrum suggests the presence of excess argon, therefore an isochron age was calculated with fractions e and f, that form the base of the saddle. The straight line calculated (black line in the figure), yields an age of 19.73 ± 0.61 Ma, with a $(^{40}Ar/^{36}Ar)_i$ = 342 ± 112, confirming the presence of initial argon.

t = 19.97 ± 0.15 Ma; calculated with the weighted mean of fractions e and f, representing 37.38% of ^{39}Ar released in 2 consecutive fractions, MSWD = 0.10

t_c = 20.10 ± 0.20 Ma; $(^{40}Ar/^{36}Ar)_i$ = 307 ± 10, MSWD = 2.1 for n = 6 (blue dashed line in the figure)

‡ fraction ignored in the isochron age calculation

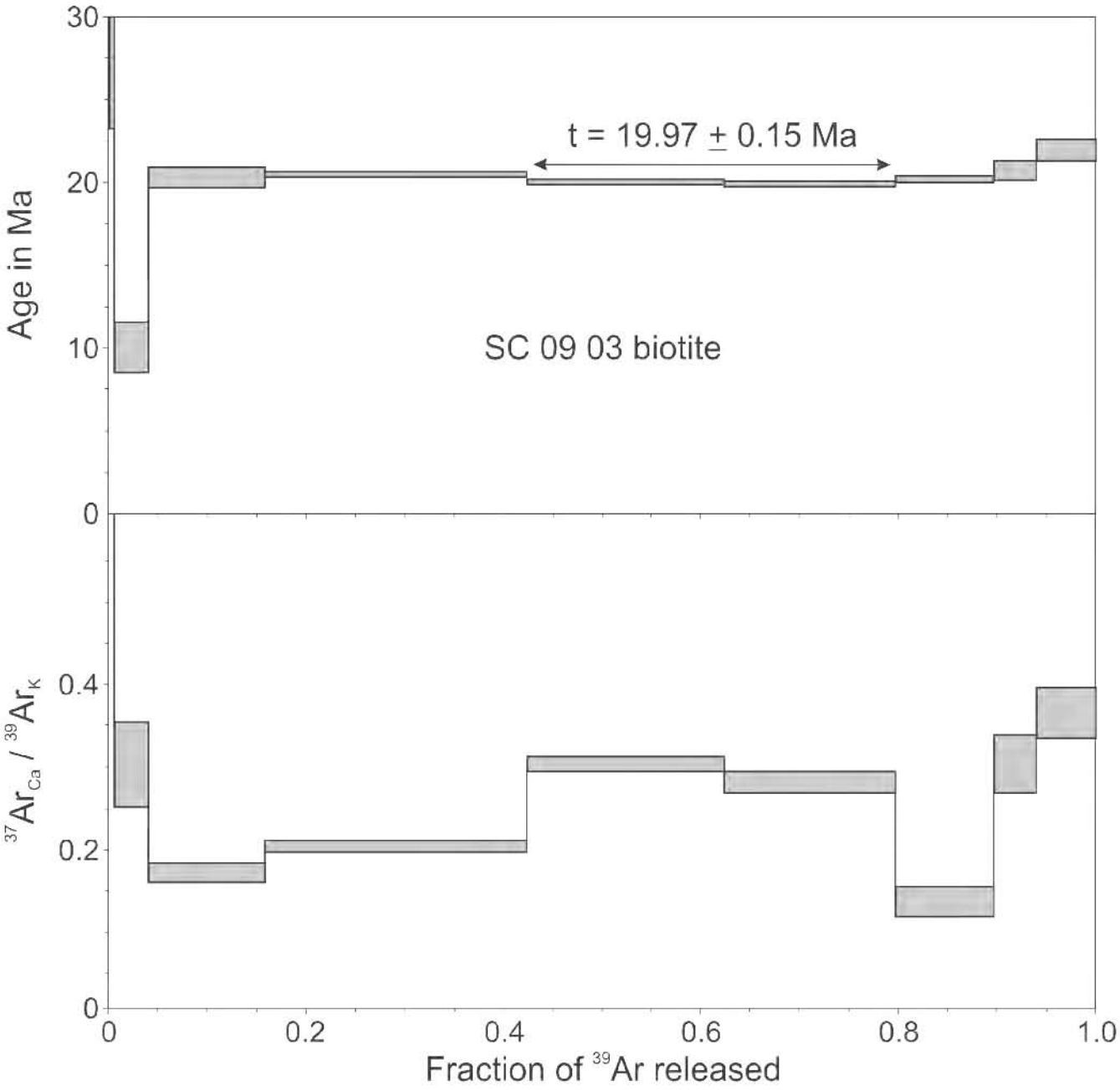

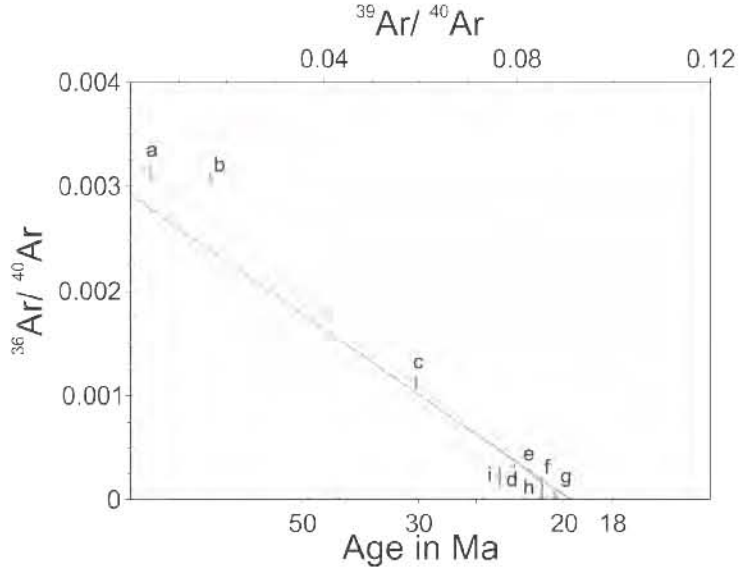

t_o = 19.73 ± 0.61 Ma

$(^{40}Ar / ^{36}Ar)_i$ = 342 ± 112

n = 2

Sample Name: ROCA 1J-1

Location: West Nayarit ridge fault scarp
Latitude: 22.5564°
Longitude: -106.7101°
Altitude/Depth (m.a.s.l.): -1486

Rock type: Biotite granodiorite

U-Pb Age

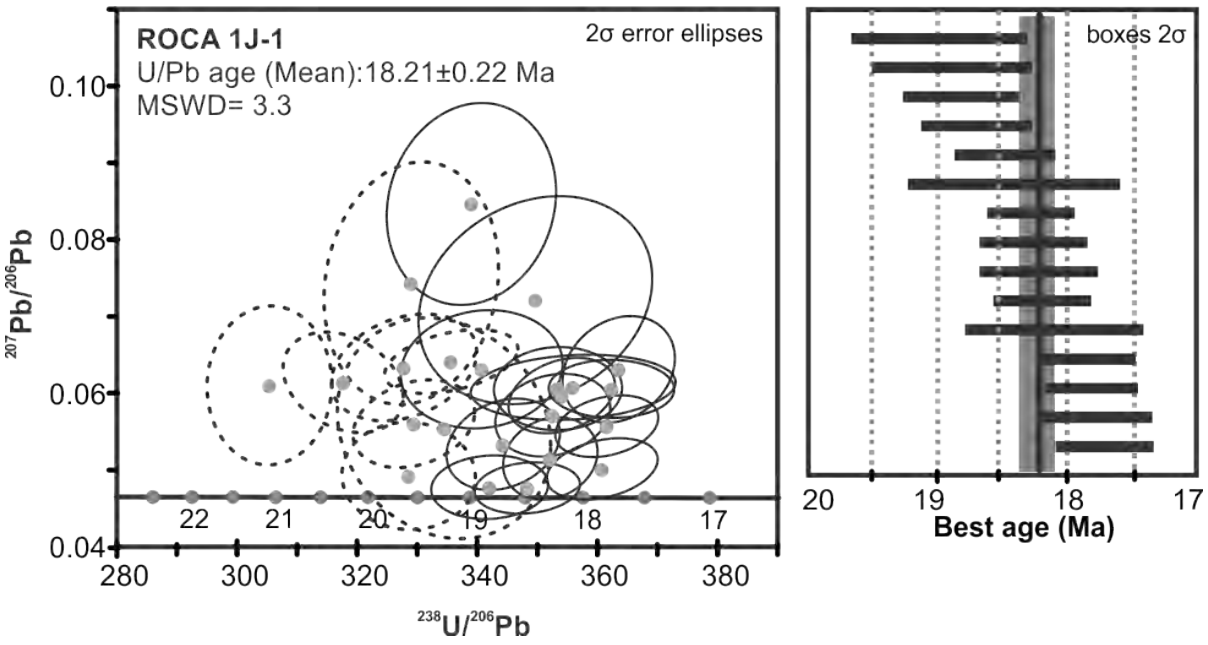

Preferred age: t= 18.21 ± 0.22 Ma

Weighted mean age (95% confidence) calculated with 37 data points. Single crystals are in the 16.2 to 20.9 Ma age range.

^{40}Ar-^{39}Ar age
Sample Name: ROCA 1J-1
Mineral: Biotite

laser step-heating experiments on biotite concentrate

Pwr	^{39}Ar × 10^{-6}	F ^{39}Ar	^{40}Ar*/^{39}Ar$_K$	1σ	Age in Ma	1σ			% ^{40}Ar*	^{40}Ar/^{36}Ar	^{37}Ar$_{Ca}$/^{39}Ar$_K$
0.20	25.993	0.0071	5.07	1.45	33.35	9.44	a	‡	16.82	355.26	0.264
0.50	182.481	0.0501	2.00	0.17	13.22	1.14	b	‡	23.74	387.49	0.050
0.80	697.909	0.1916	2.79	0.03	18.41	0.17	c	‡	85.48	2035.08	0.007
1.10	892.435	0.2449	2.87	0.02	18.93	0.13	d		93.86	4813.17	0.008
1.40	669.831	0.1838	2.79	0.02	18.45	0.12	e		96.05	7474.61	0.030
1.80	574.700	0.1577	2.84	0.03	18.77	0.19	f		98.04	15065.44	0.053
2.30	452.185	0.1241	2.86	0.02	18.89	0.14	g		98.43	18863.05	0.066
2.80	147.965	0.0406	2.81	0.06	18.59	0.41	h		98.89	26689.58	0.156

Integrated results

^{39}Ar × 10^{-6}	^{40}Ar*/^{39}Ar$_K$	1σ	Age in Ma	1σ	% ^{40}Ar*	^{40}Ar/^{36}Ar	^{37}Ar$_{Ca}$/^{39}Ar$_K$
3643.0	2.80	0.02	18.51	0.14	80.62	1524.72	0.036

J = 0.003679 ± 0.000015

Preferred age t_p = 18.68 ± 0.10 Ma

Weighted mean of fractions c to h, representing 94.28 % of ^{39}Ar released in 6 consecutive fractions, MSWD = 1.91

‡ fraction ignored in the isochron given in the figure

t_c = 18.48 ± 0.33 Ma, (^{40}Ar/^{36}Ar)$_i$ = 399 ± 123, MSWD = 2.29 for n = 5

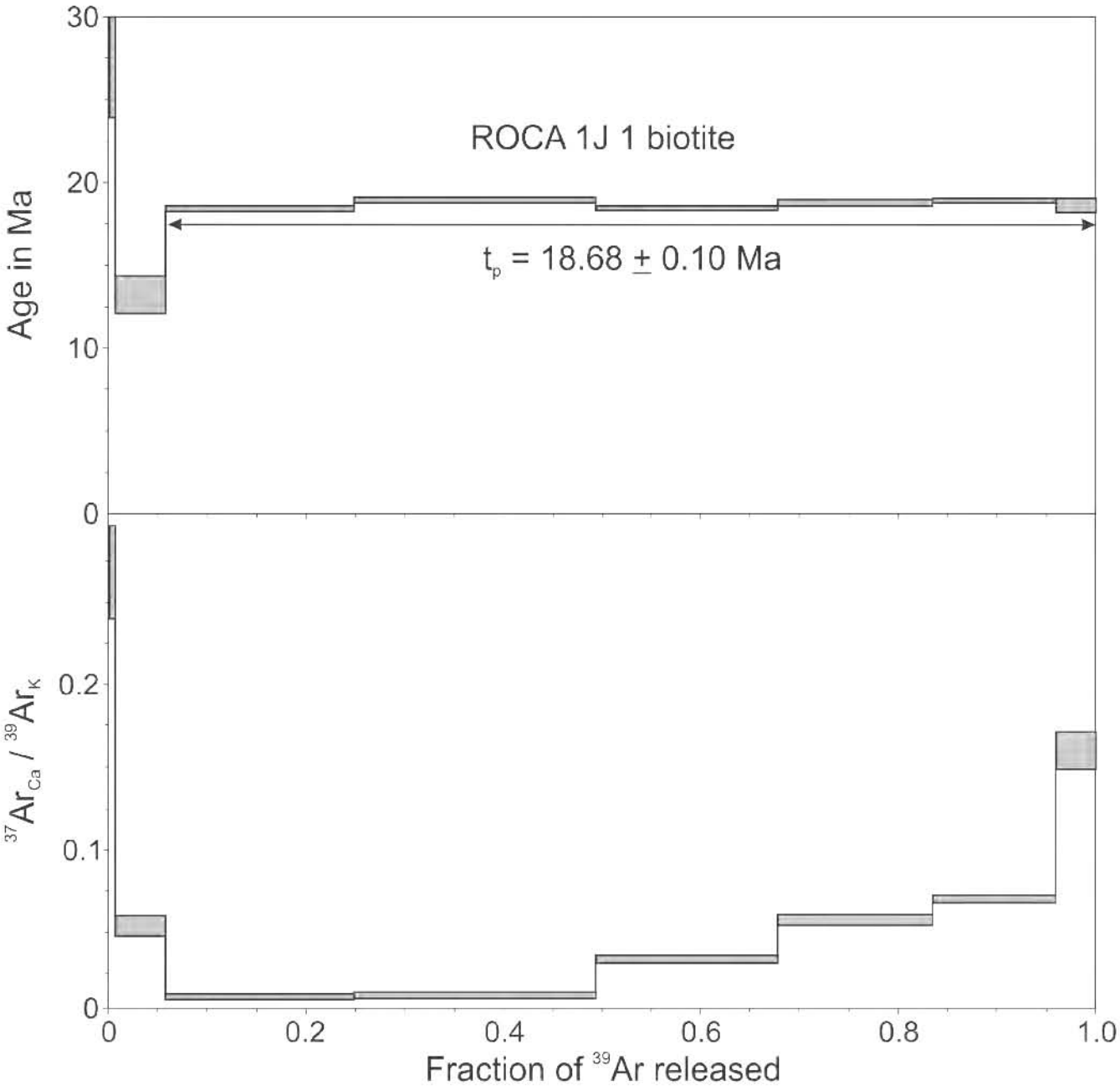

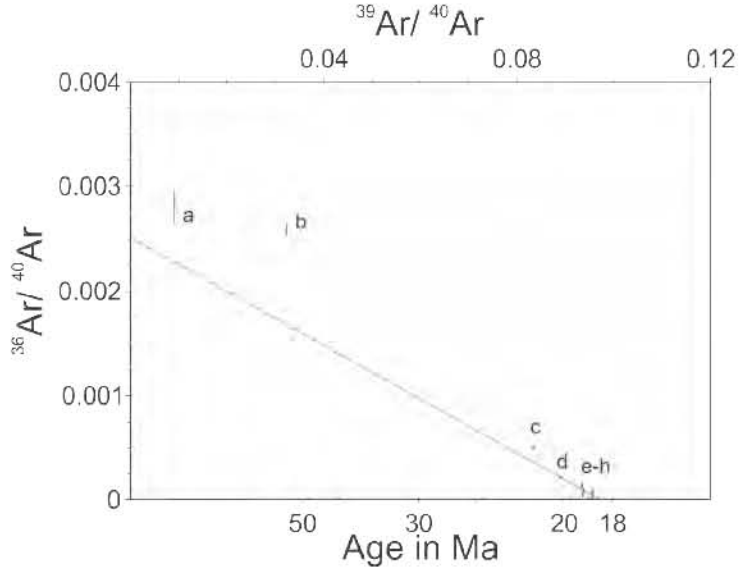

t_c = 18.48 ± 0.33 Ma

$(^{40}Ar / ^{36}Ar)_i$ = 399 ± 123

MSWD = 2.29, n = 5

^{40}Ar-^{39}Ar age
Sample Name: ROCA 1J-1
Mineral: K-feldspar

laser step-heating experiments on K-feldspar concentrate

Pwr	^{39}Ar × 10^{-6}	F ^{39}Ar	^{40}Ar*/^{39}Ar$_K$	1σ	Age in Ma	1σ		% ^{40}Ar*	^{40}Ar/^{36}Ar	^{37}Ar$_{Ca}$/^{39}Ar$_K$
1.50	78.453	0.0112	10.48	0.38	47.60	1.71	a	20.39	371.18	0.013
3.00	419.377	0.0596	4.62	0.07	21.16	0.31	b	42.62	515.02	0.017
6.00	685.272	0.0974	3.35	0.04	15.36	0.20	c	57.06	688.20	0.018
9.00	834.263	0.1186	3.06	0.03	14.04	0.15	d	70.21	991.97	0.015
12.00	512.952	0.0729	3.08	0.03	14.14	0.15	e	68.09	926.01	0.009
13.00	934.813	0.1329	3.20	0.02	14.66	0.08	f	72.43	1071.80	0.010
14.00	3567.568	0.5073	3.35	0.01	15.35	0.06	g	78.35	1365.09	0.015

Integrated results

^{39}Ar × 10^{-6}	^{40}Ar*/^{39}Ar$_K$	1σ	Age in Ma	1σ	% ^{40}Ar*	^{40}Ar/^{36}Ar	^{37}Ar$_{Ca}$/^{39}Ar$_K$
7033.0	3.43	0.01	15.73	0.09	63.60	811.80	0.014

J = 0.002551 ± 0.000010

Preferred age t_c = 14.05 ± 0.43 Ma
(^{40}Ar/^{36}Ar)$_i$ = 353 ± 16, MSWD = 46 for n = 7

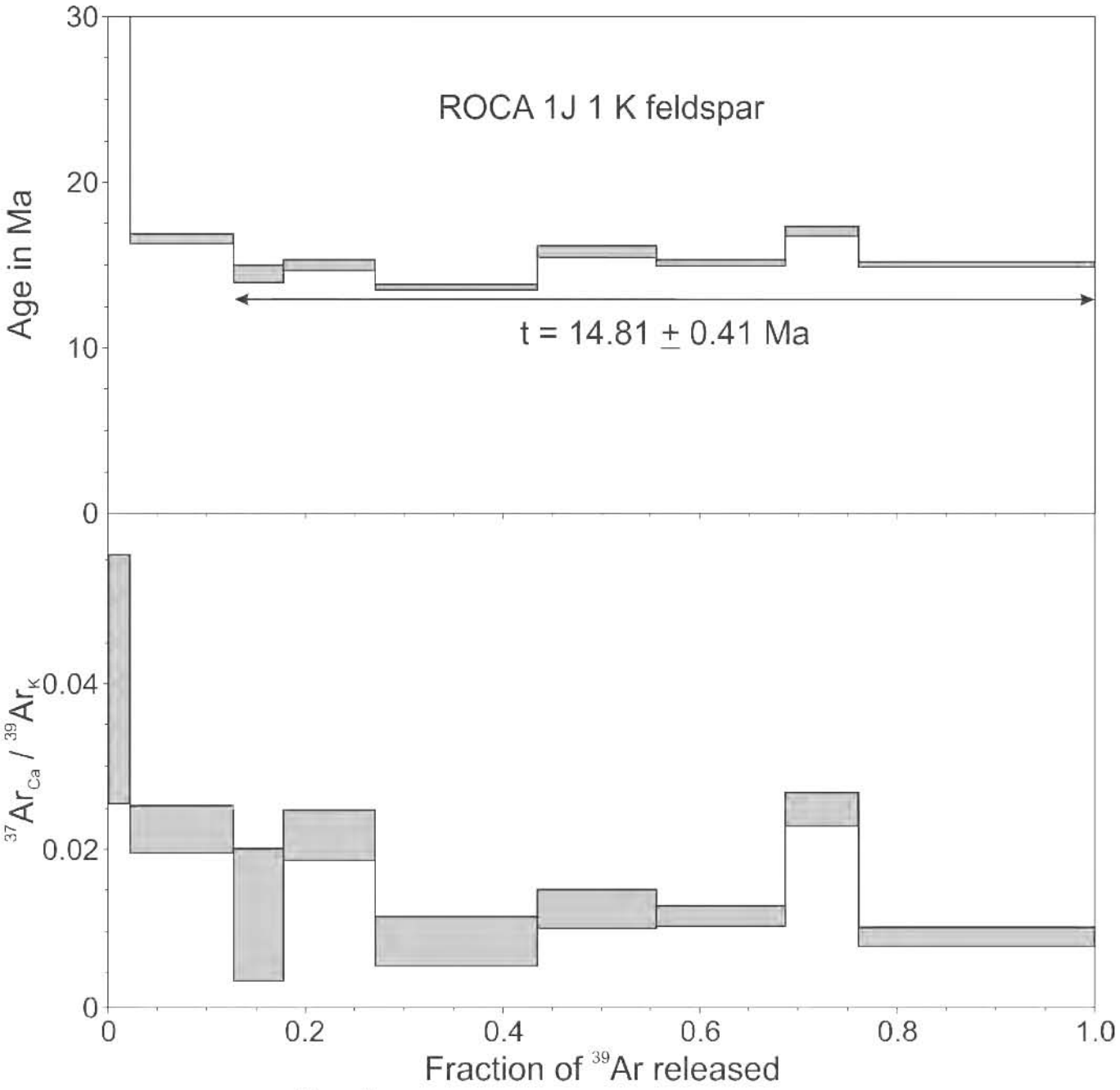
ROCA 1J 1 K feldspar
Age in Ma
30
20
10
0
t = 14.81 ± 0.41 Ma
$^{37}Ar_{Ca}$ / $^{39}Ar_K$
0.04
0.02
0
0
0.2
0.4
0.6
0.8
1.0
Fraction of ^{39}Ar released

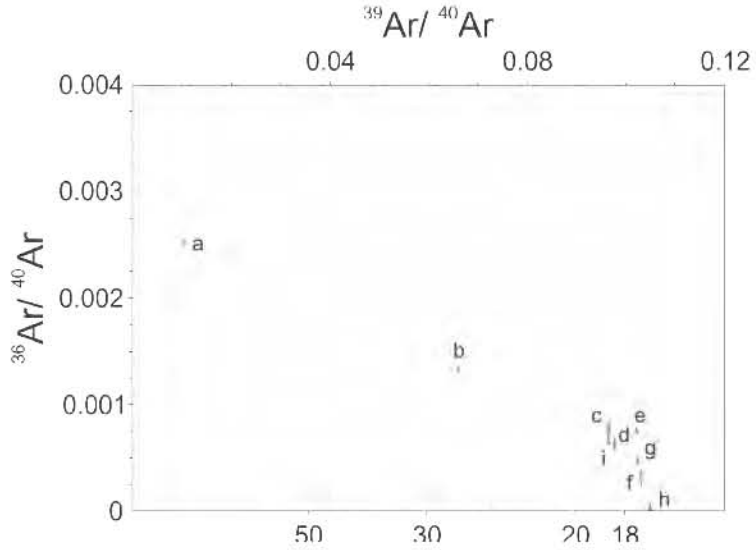
$^{39}Ar/^{40}Ar$
0.04
0.08
0.12
$^{36}Ar/^{40}Ar$
0.004
0.003
0.002
0.001
0
a
b
c
d
e
f
g
h
i
50
30
20
18

Sample Name: PHC 09

Location: El Cajon Dam
Latitude: 21.5123°
Longitude: -104.5179°
Altitude/Depth (m.a.s.l.): 289

Rock type: Diorite Porphyrite

U-Pb Age

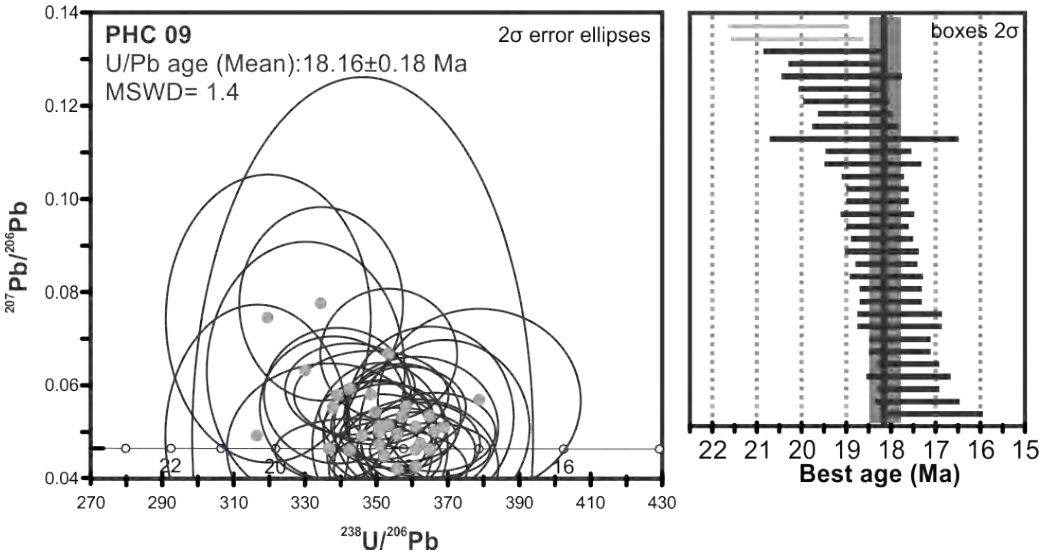

Preferred age: t= 18.16 ± 0.18 Ma

Weighted mean age (95% confidence) calculated with 27 data points. Two youngest and two oldest crystals were eliminated from age calculation.
Single crystals are in the 17.4 to 19.5 Ma age range.

Sample Name: SC 24

Location: Santa Catalina Island
Latitude: 25.6242°
Longitude: -110.7931°
Altitude/Depth (m.a.s.l.): 0

Rock type: Granodiorite

^{40}Ar-^{39}Ar age
Sample Name: SC 24
Mineral: Biotite

Laser step-heating experiments on biotite concentrate

Pwr	^{39}Ar × 10^{-6}	F ^{39}Ar	^{40}Ar*/^{39}Ar$_K$	1σ	Age in Ma	1σ			% ^{40}Ar*	^{40}Ar/^{36}Ar	^{37}Ar$_{Ca}$/^{39}Ar$_K$
0.20	11.804	0.0021	1.06	1.52	6.05	8.71	a	‡	3.60	306.53	0.274
0.60	202.329	0.0363	2.47	0.08	14.12	0.47	b		38.48	480.34	0.056
0.90	990.717	0.1780	3.12	0.06	17.85	0.32	c		82.34	1673.74	0.026
1.40	1339.539	0.2406	3.17	0.05	18.13	0.27	d		93.18	4334.83	0.050
2.50	2006.100	0.3603	3.20	0.04	18.27	0.24	e		93.49	4536.00	0.060
6.00	1016.742	0.1826	3.15	0.06	17.99	0.34	f		91.21	3360.49	0.065
0.50	112.307	0.0326	2.19	0.17	12.52	0.99	g		24.87	393.33	0.103
0.80	489.469	0.1420	3.05	0.04	17.47	0.25	h		79.78	1461.26	0.032
1.00	559.550	0.1624	3.17	0.03	18.10	0.20	i		91.77	3590.07	0.023
1.50	766.573	0.2224	3.22	0.04	18.40	0.25	j		94.87	5762.12	0.082
2.50	1311.536	0.3805	3.21	0.04	18.37	0.23	k		96.36	8110.40	0.048
4.00	187.348	0.0544	3.01	0.06	17.20	0.35	l		92.10	3739.09	0.100
6.00	19.718	0.0057	3.63	0.41	20.71	2.35	m		95.32	6316.18	0.062

Integrated results

^{39}Ar × 10^{-6}	^{40}Ar*/^{39}Ar$_K$	1σ	Age in Ma	1σ	% ^{40}Ar*	^{40}Ar/^{36}Ar	^{37}Ar$_{Ca}$/^{39}Ar$_K$
5567.0	3.14	0.02	17.93	0.15	85.92	2099.268	0.053
3446.0	3.14	0.02	17.96	0.14	86.96	2265.635	0.054

J = 0.003185 ± 0.000011

Preferred age t_p = 18.10 ± 0.15 Ma

Weighted mean of fractions c to f, representing 96.16% of ^{39}Ar released in 4 consecutive fractions, MSWD = 0.39

t_c = 18.35 ± 0.12 Ma; $(^{40}Ar/^{36}Ar)_i$ = 244 ± 5, MSWD = 1.3 for n = 12
‡ fraction ignored in the isochron age calculation

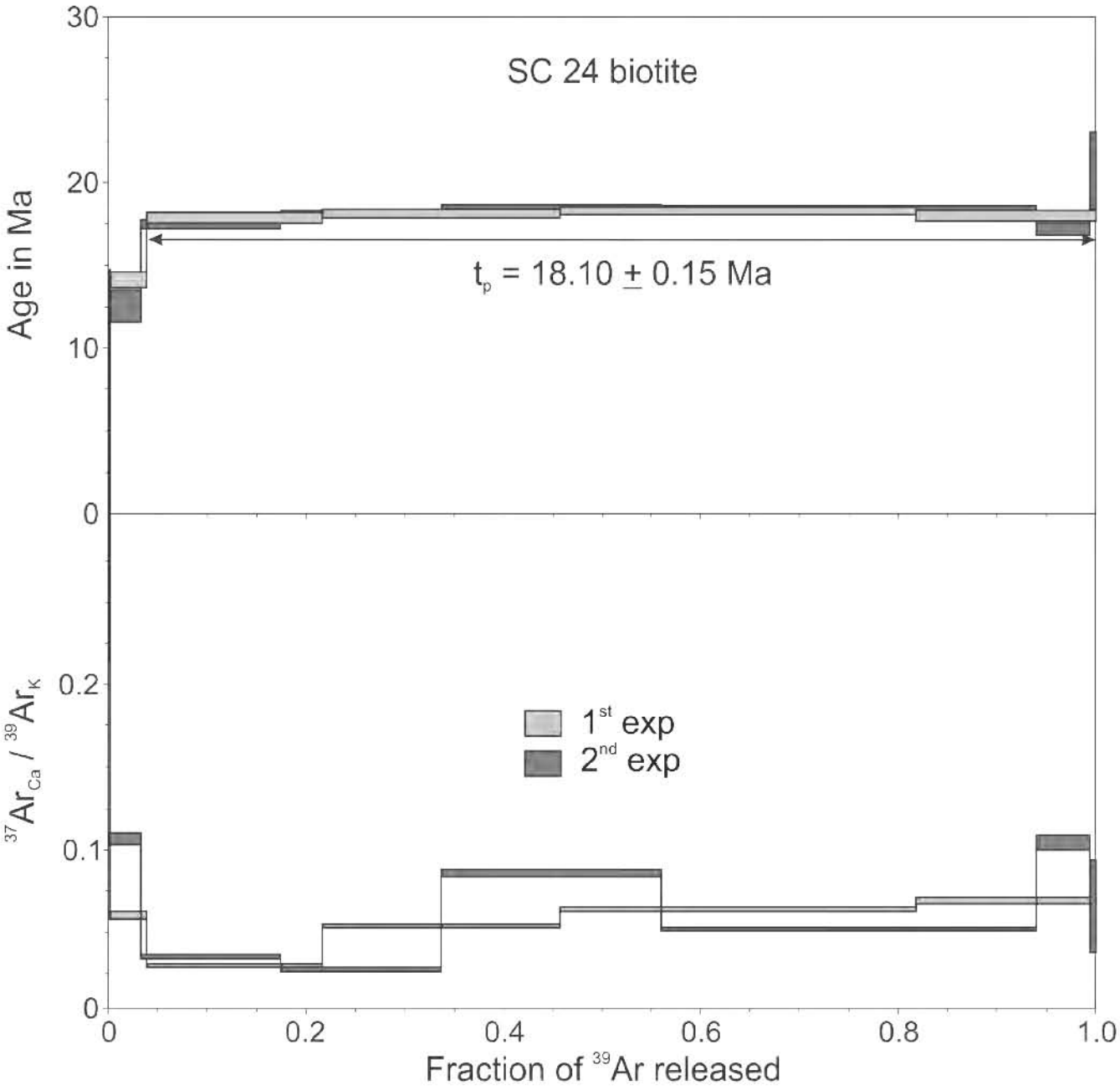

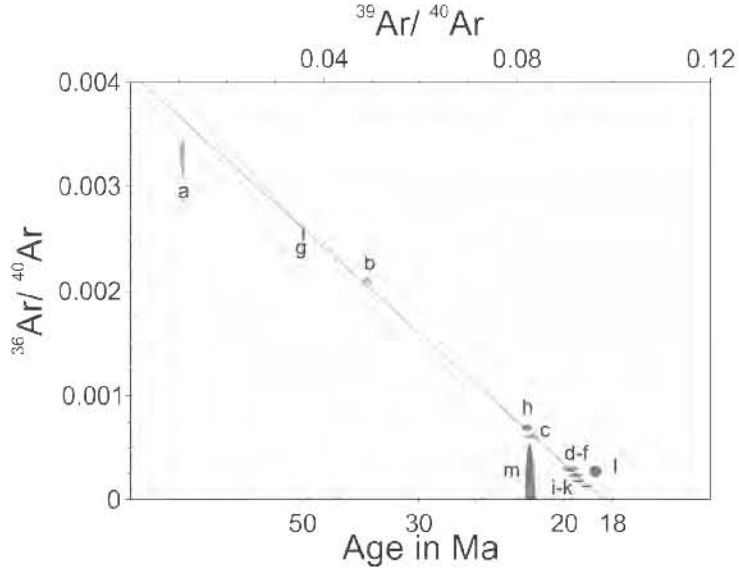

t_c = 18.35 ± 0.12 Ma

$(^{40}Ar / ^{36}Ar)_i$ = 244 ± 5

MSWD = 1.3, n = 12

Sample Name: ROCA 22J-1

Location: Cerralvo Bank
Latitude: 24.251°
Longitude: -109.676°
Altitude/Depth (m.a.s.l.): -1516

Rock type: Biotite-hornblende quartz diorite

U-Pb Age

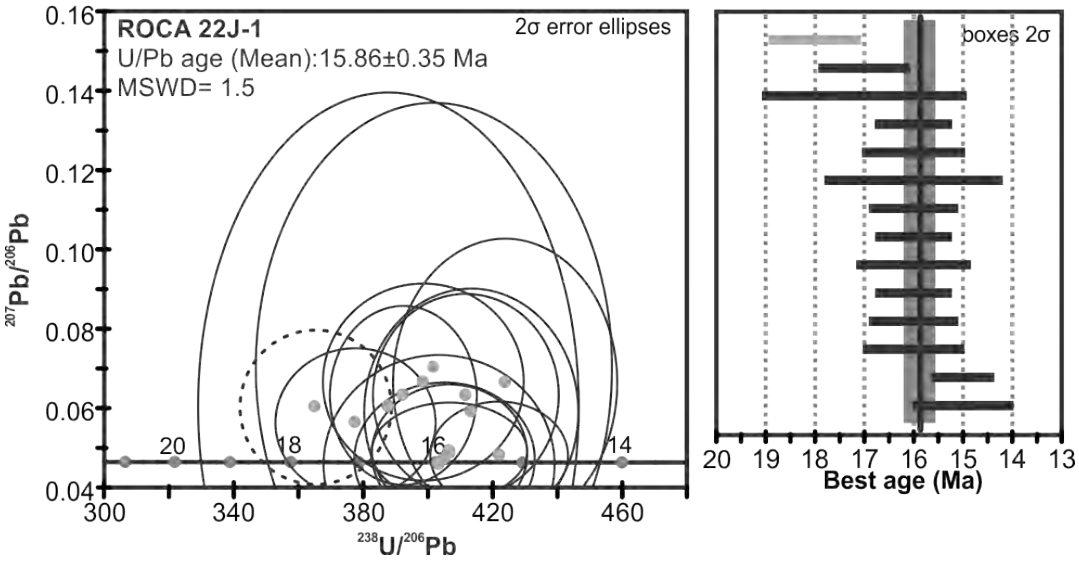

Preferred age: t= 15.86 ± 0.35 Ma

Weighted mean age (95% confidence) calculated with 15 data points. Single crystals are in the 14.3 to 17.6 Ma age range. An antecrystal with an age of 19.8 was rejected from the age calculation.

^{40}Ar-^{39}Ar age
Sample Name: ROCA 22J-1
Mineral: Biotite

laser step-heating experiments on biotite concentrate

Pwr	^{39}Ar × 10^{-6}	F ^{39}Ar	^{40}Ar*/^{39}Ar$_K$	1σ	Age in Ma	1σ		% ^{40}Ar*	^{40}Ar/^{36}Ar	^{37}Ar$_{Ca}$/^{39}Ar$_K$
0.20	1.823	0.0015	3.59	6.38	22.99	40.56	a	10.95	331.85	0.164
0.50	14.517	0.0118	2.57	0.98	16.46	6.27	b	22.46	381.11	0.131
0.70	33.552	0.0274	2.68	0.29	17.18	1.88	c	55.70	667.02	0.027
1.00	122.321	0.0998	2.54	0.09	16.32	0.55	d	83.94	1840.04	0.031
1.20	92.581	0.0755	2.65	0.14	17.02	0.87	e	95.14	6075.65	0.018
1.40	155.885	0.1272	2.53	0.06	16.21	0.41	f	91.61	3520.26	0.014
1.60	117.328	0.0957	2.48	0.09	15.92	0.57	g	90.24	3027.84	0.014
1.90	224.102	0.1828	2.66	0.06	17.06	0.36	h	97.52	11909.21	0.019
2.20	227.754	0.1858	2.59	0.05	16.63	0.30	i	96.78	9162.80	0.020
2.50	99.184	0.0809	2.54	0.12	16.32	0.74	j	94.03	4951.83	0.042
3.00	72.745	0.0593	2.32	0.15	14.91	0.94	k	87.37	2339.22	0.066
3.80	25.687	0.0210	2.55	0.41	16.38	2.61	l	94.37	5248.64	0.061
6.00	38.323	0.0313	2.53	0.25	16.23	1.57	m	95.21	6175.02	0.068
0.50	2.955	0.0012	2.63	3.26	11.80	14.56	n	6.35	315.53	0.165
1.00	6.954	0.0029	2.52	0.75	11.29	3.35	o	16.85	355.37	0.135
1.60	29.921	0.0124	3.00	0.25	13.45	1.12	p	26.77	403.55	0.052
2.60	71.568	0.0298	3.54	0.12	15.84	0.52	q	53.90	640.94	0.022
3.60	162.874	0.0677	3.52	0.04	15.77	0.17	r	81.08	1562.07	0.016
5.60	368.098	0.1530	3.55	0.02	15.90	0.08	s	93.02	4234.68	0.018
7.00	675.496	0.2808	3.53	0.01	15.80	0.05	t	94.87	5762.00	0.021
9.00	684.074	0.2844	3.55	0.01	15.90	0.05	u	96.11	7597.39	0.033
11.00	346.241	0.1439	3.55	0.02	15.90	0.08	v	95.82	7073.77	0.050
13.00	57.461	0.0239	3.40	0.10	15.23	0.43	w	85.39	2023.17	0.133

Integrated results

^{39}Ar × 10^{-6}	^{40}Ar*/^{39}Ar$_K$	1σ	Age in Ma	1σ	% ^{40}Ar*	^{40}Ar/^{36}Ar	^{37}Ar$_{Ca}$/^{39}Ar$_K$
1226.0	2.57	0.03	16.46	0.22	86.83	2244.44	0.028
2406.0	3.53	0.01	15.80	0.09	87.53	2369.12	0.032

J= 0.003571 ± 0.000009 (1st exp. CIC 79RIII); J = 0.002504 ± 0.000011 (2nd exp. CIC 82 RI)

Preferred age t_p = 15.86 ± 0.08 Ma

Weighted mean of fractions q to v, representing 95.96% of ^{39}Ar released in 6 consecutive fractions, MSWD = 0.54

t_c = 15.90 ± 0.07 Ma, (^{40}Ar/^{36}Ar)$_i$ = 286 ± 7, MSWD = 1.55 for n = 23

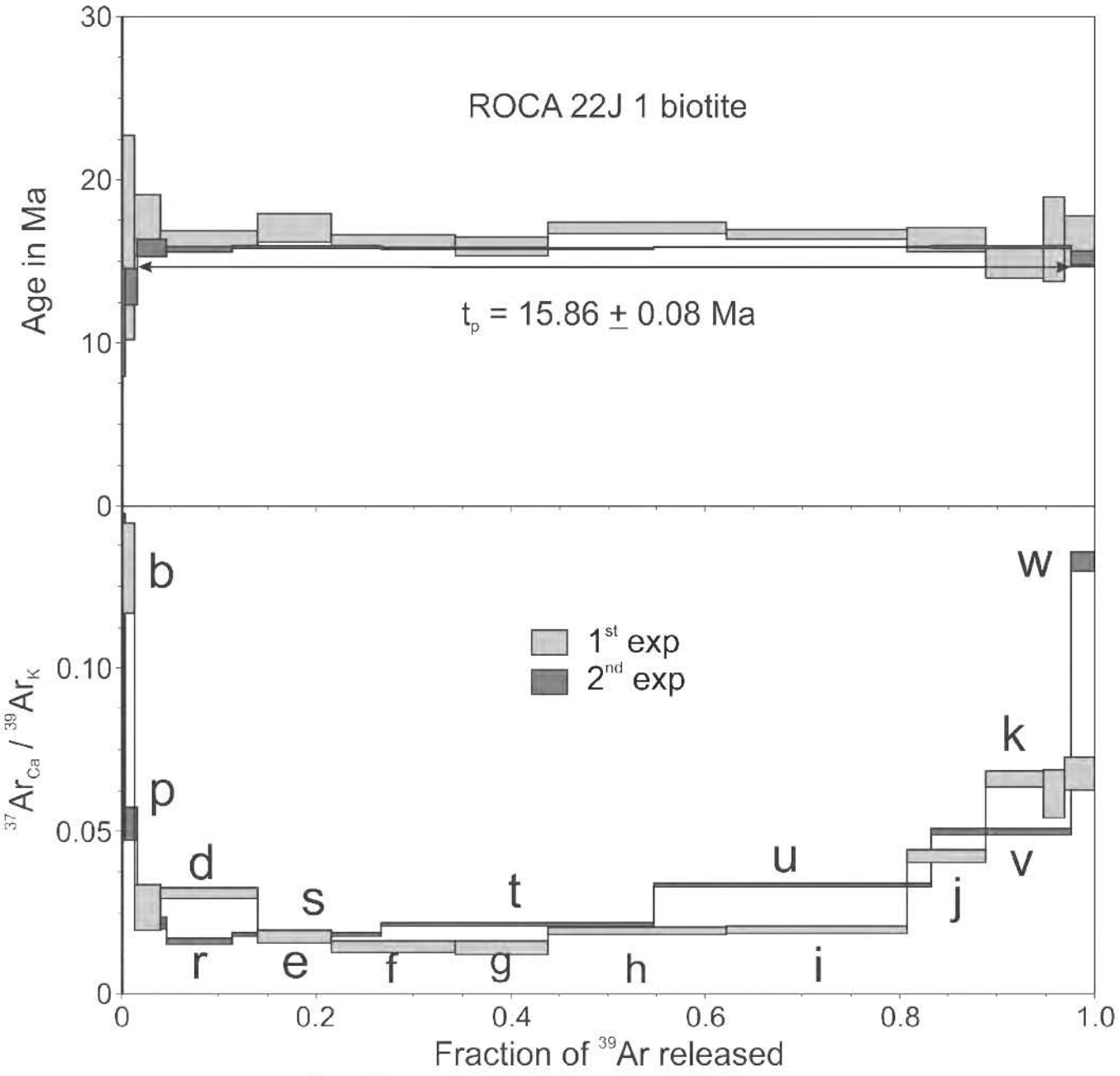

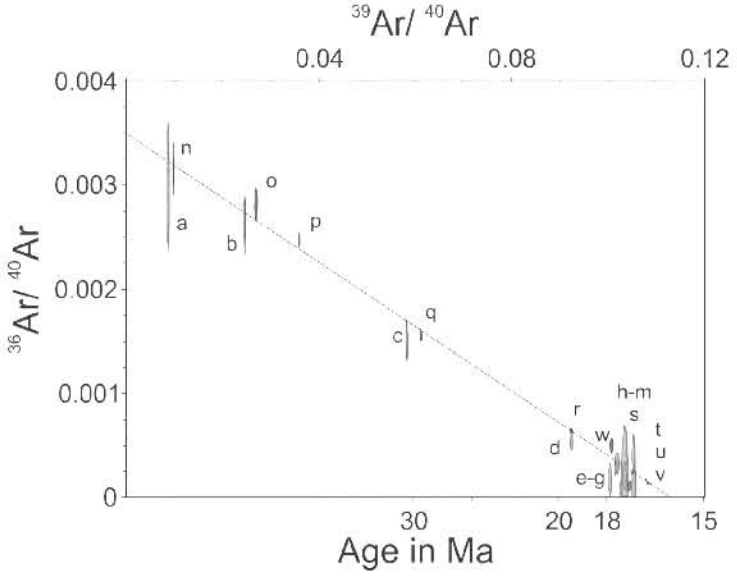

t_c = 15.90 ± 0.07 Ma

$(^{40}Ar / ^{36}Ar)_i$ = 286 ± 7

MSWD = 1.55, n = 23

all data used

Sample Name: BEKL 6D-1

Location: Cerralvo bank
Latitude: 24.1140° (i); 24.1148° (e)
Longitude: -109.4253° (i); -109.4638° (e)
Altitude/Depth (m.a.s.l.): 1205 (i); 900 (e) (wire)

Rock type: Granodiorite

U-Pb Age

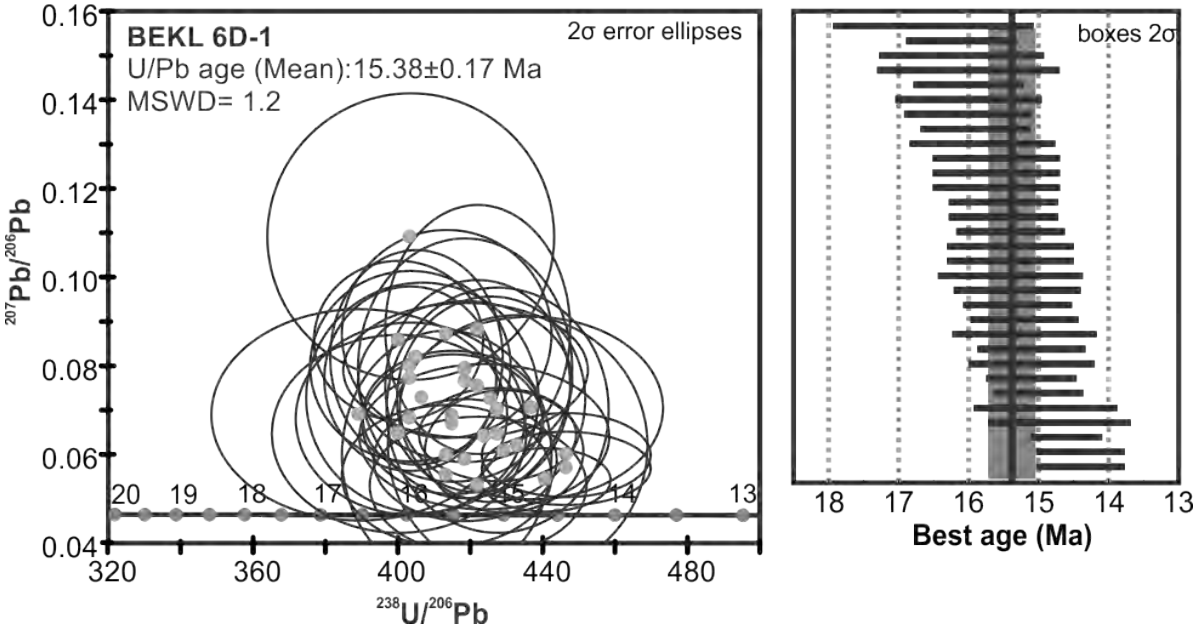

Preferred age: t= 15.38 ± 0.17 Ma

Weighted mean age (95% confidence) calculated with 30 data points. Single crystals are in the 14.3 to 17.6 Ma age range. Three discordant analyses were rejected from the age calculation.

^{40}Ar-^{39}Ar age
Sample Name: BEKL 6D-1
Mineral: Hornblende

Laser step-heating experiments on hornblende concentrate

Pwr	^{39}Ar × 10^{-6}	F ^{39}Ar	^{40}Ar*/^{39}Ar$_K$	1σ	Age in Ma	1σ			% ^{40}Ar*	^{40}Ar/^{36}Ar	^{37}Ar$_{Ca}$/^{39}Ar$_K$
0.20	0.675	0.0014	8.15	13.43	51.16	83.09	a	‡	2.49	303.03	1.134
0.60	5.928	0.0125	7.59	1.69	47.68	10.50	b	‡	18.07	360.67	0.531
1.33	19.098	0.0402	2.54	0.59	16.10	3.69	c		25.05	394.25	0.604
1.70	21.036	0.0443	1.71	0.40	10.83	2.53	d		32.47	437.56	1.882
2.10	38.090	0.0800	2.25	0.32	14.29	2.00	e		50.78	600.41	5.307
2.50	90.527	0.1898	2.14	0.09	13.57	0.54	f		63.39	807.24	7.109
2.80	83.676	0.1755	2.16	0.11	13.70	0.67	g		83.44	1784.23	6.204
3.20	51.936	0.1090	2.16	0.17	13.67	1.06	h		86.57	2199.88	5.019
3.60	28.597	0.0601	2.17	0.27	13.77	1.73	i		91.86	3629.76	3.012
4.60	52.765	0.1110	2.18	0.13	13.82	0.85	j		97.40	11360.37	1.425
7.00	83.857	0.1761	2.18	0.11	13.81	0.71	k		85.56	2046.60	4.464

Integrated results

^{39}Ar × 10^{-6}	^{40}Ar*/^{39}Ar$_K$	1σ	Age in Ma	1σ	% ^{40}Ar*	^{40}Ar/^{36}Ar	^{37}Ar$_{Ca}$/^{39}Ar$_K$
474.7	2.24	0.07	14.21	0.41	53.46	634.979	4.651

J = 0.003527 ± 0.000007

Preferred age t_p = 13.71 ± 0.31 Ma

Plateau age calculated with the weighted mean of fractions e to k, representing 90.16% of ^{39}Ar released in 7 consecutive fractions, MSWD = 0.03

t_c = 13.68 ± 0.41 Ma; $(^{40}Ar/^{36}Ar)_i$ = 296 ± 17, MSWD = 0.27 for n = 9

‡ fraction ignored in the isochron given in the figure

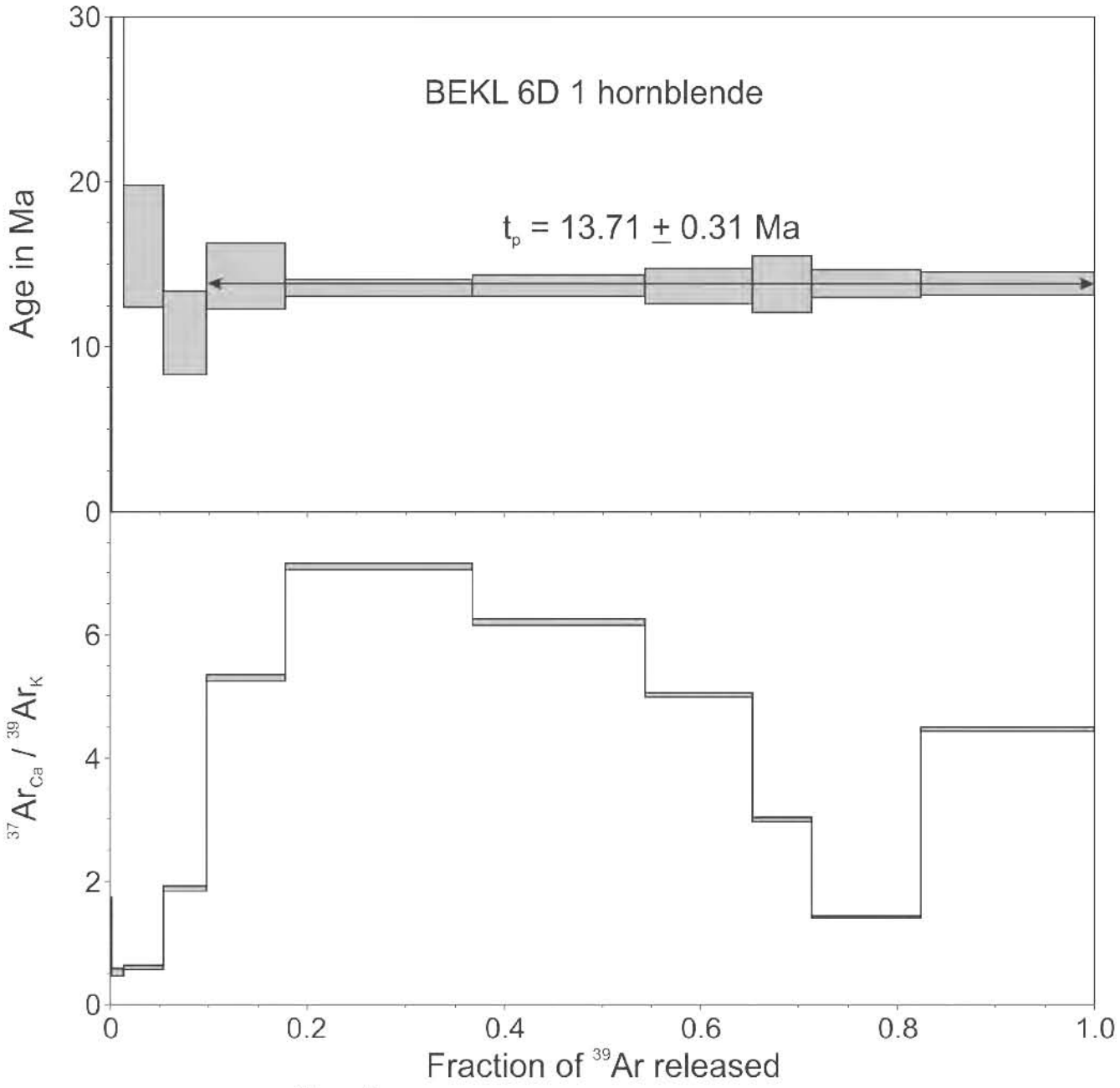

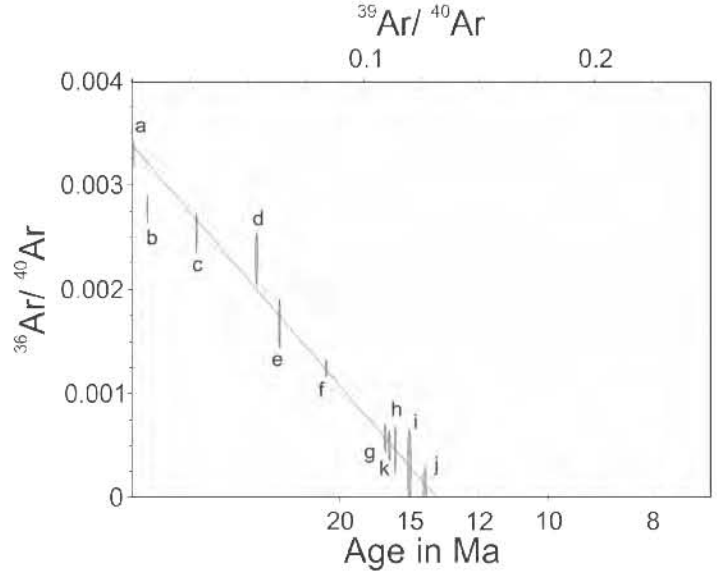

t_c = 13.68 ± 0.41 Ma

(^{40}Ar / ^{36}Ar)$_i$ = 296 ± 17

MSWD = 0.27, n = 9

^{40}Ar-^{39}Ar age
Sample Name: BEKL 6D-1
Mineral: Biotite

Laser step-heating experiments on biotite concentrate

Pwr	^{39}Ar × 10^{-6}	F ^{39}Ar	^{40}Ar*/^{39}Ar$_K$	1σ	Age in Ma	1σ			% ^{40}Ar*	^{40}Ar/^{36}Ar	^{37}Ar$_{Ca}$/^{39}Ar$_K$
0.20	2.296	0.0005	0.31	4.63	1.96	29.44	a	‡	0.41	296.72	0.092
0.40	6.170	0.0013	2.23	1.59	14.16	10.07	b	‡	9.61	326.92	0.058
0.60	15.130	0.0031	2.73	0.74	17.29	4.68	c	‡	12.67	338.36	0.000
0.90	114.214	0.0235	2.30	0.10	14.59	0.64	d	‡	46.82	555.63	0.012
1.20	196.385	0.0404	3.06	0.05	19.34	0.35	e		80.44	1510.84	0.004
1.50	288.652	0.0593	2.29	0.02	14.49	0.15	f		91.24	3372.37	0.003
1.80	307.481	0.0632	2.43	0.02	15.40	0.16	g		96.56	8579.08	0.003
2.10	363.877	0.0748	2.39	0.02	15.15	0.12	h		95.24	6204.79	0.020
2.50	430.903	0.0885	2.26	0.02	14.36	0.12	i		97.06	10048.38	0.041
2.85	527.460	0.1084	2.25	0.02	14.26	0.10	j		96.26	7893.74	0.003
3.15	646.791	0.1329	2.21	0.01	14.00	0.08	k		97.25	10748.85	0.005
3.45	630.958	0.1297	2.22	0.01	14.04	0.07	l		97.18	10461.93	0.011
3.75	389.757	0.0801	2.16	0.02	13.71	0.14	m		96.42	8254.30	0.016
4.20	279.732	0.0575	2.16	0.03	13.71	0.16	n		97.24	10706.63	0.024
5.20	533.141	0.1095	2.19	0.01	13.91	0.09	o		97.56	12090.78	0.062
8.00	133.688	0.0275	2.54	0.06	16.11	0.39	p	‡	98.77	23975.16	0.164

Integrated results

^{39}Ar × 10^{-6}	^{40}Ar*/^{39}Ar$_K$	1σ	Age in Ma	1σ	% ^{40}Ar*	^{40}Ar/^{36}Ar	^{37}Ar$_{Ca}$/^{39}Ar$_K$
4867.0	2.29	0.01	14.51	0.06	88.82	2643.64	0.022

J = 0.003527 ± 0.000007

t = 14.03 ± 0.07 Ma

Weighted mean of fractions i to o, representing 70.66% of ^{39}Ar released in 7 consecutive fractions, MSWD = 3.60; the sample does not define a plateau age

Preferred age t_c = 13.45 ± 0.22 Ma

(^{40}Ar/^{36}Ar)$_i$ = 735 ± 94, MSWD = 2.81 for n = 11

‡ fraction ignored in the isochron given in the figure

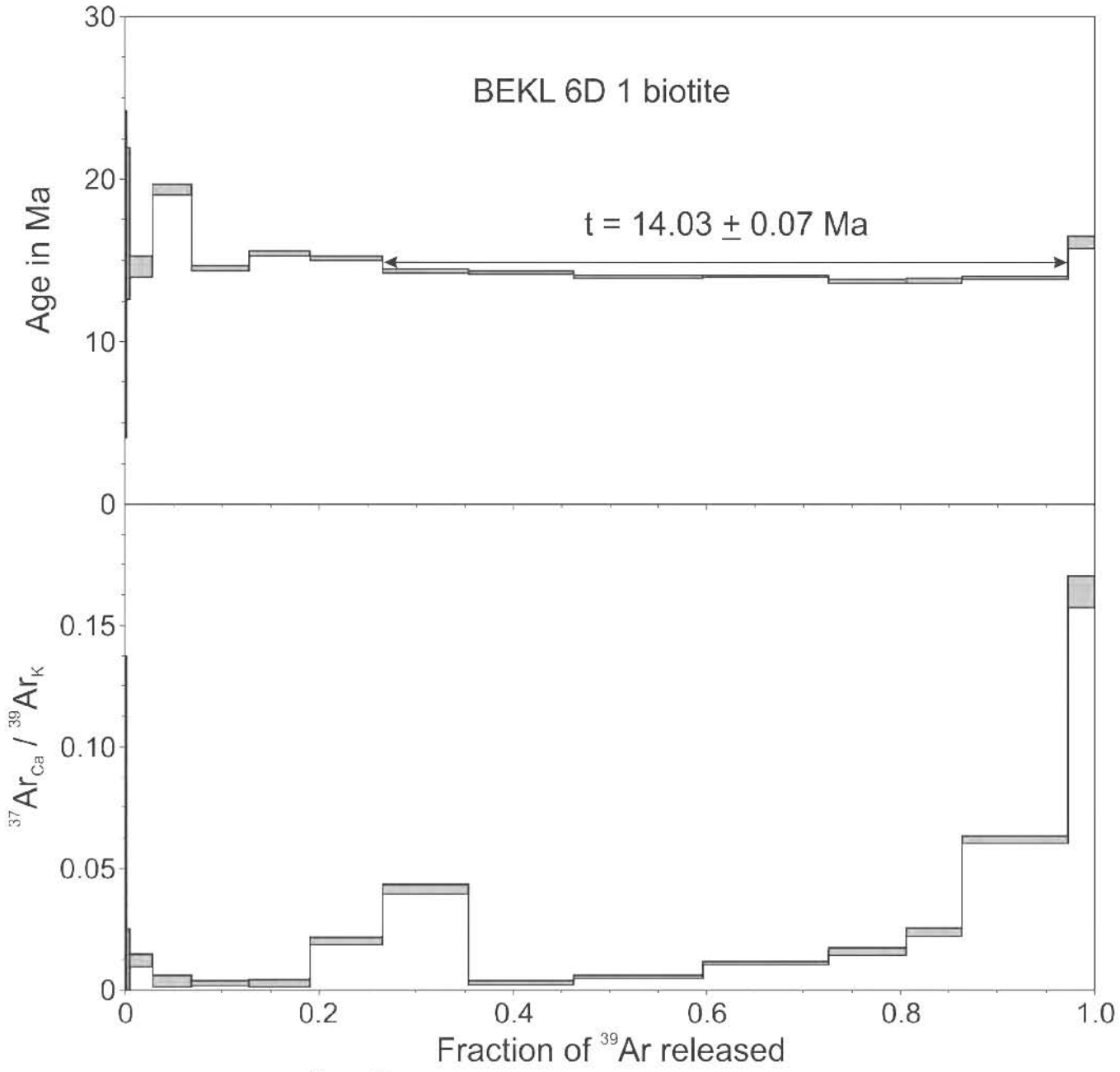

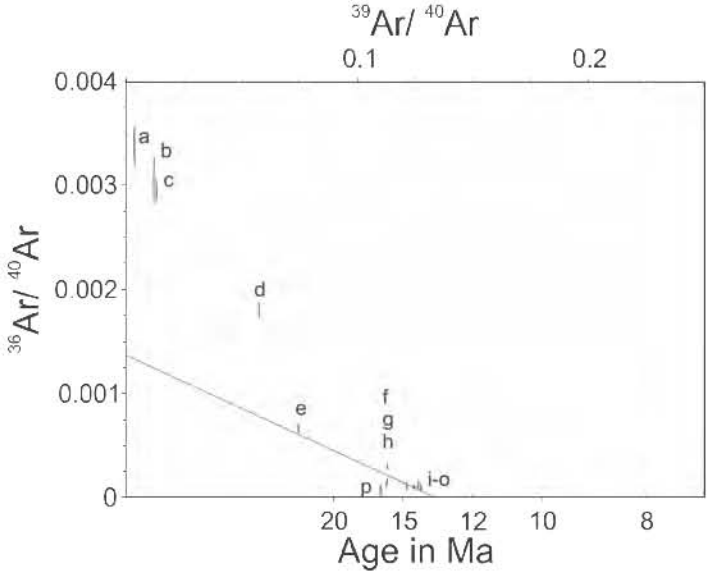

t_c = 13.45 ± 0.22 Ma

$(^{40}Ar / ^{36}Ar)_i$ = 735 ± 94

MSWD = 2.81, n = 11

Sample Name: BEKL 6D-2

Location: Cerralvo bank
Latitude: 24.1140° (i); 24.1148° (e)
Longitude: -109.4253° (i); -109.4638° (e)
Altitude/Depth (m.a.s.l.): 1205 (i); 900 (e) (wire)

Rock type: Granodiorite

U-Pb Age

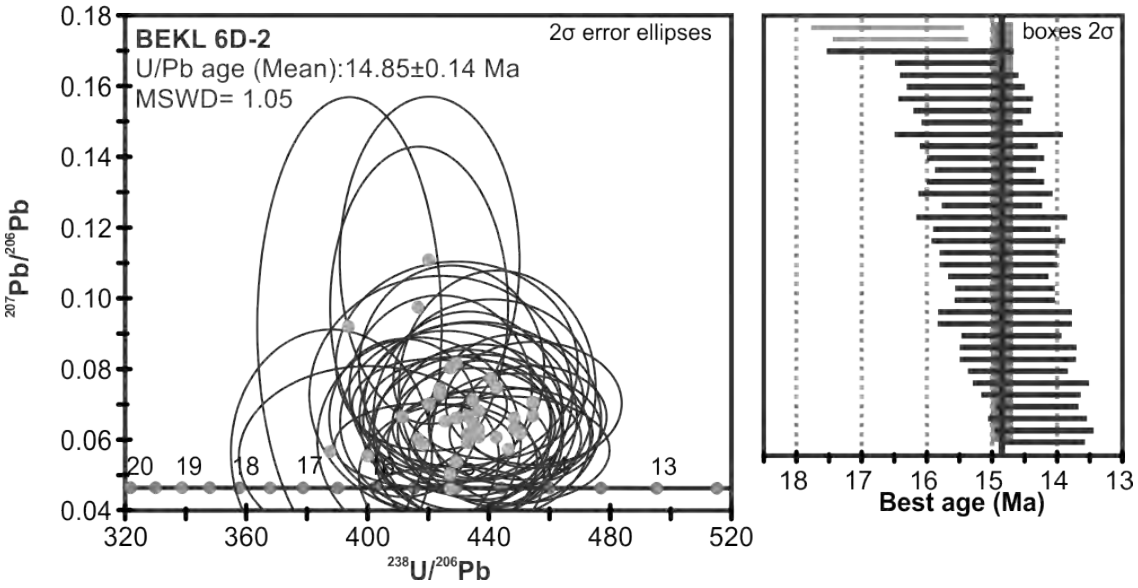

Preferred age: t= 14.86 ± 0.14 Ma

Weighted mean age (95% confidence) calculated with 36 data points. Single crystals are in the 14.2 to 16.6 Ma age range. Two most discordant analyses were rejected from the age calculation.

Sample Name: BEKL 10D-1

Location: Bank East of Partida Bank
Latitude: 24.8081° (i); 24.8050° (e)
Longitude: -109.9233° (i); -109.9285° (e)
Wire Longitud: 1498 (i); 1200 (e) (wire)

Rock type: Biotite Granite

U-Pb Age

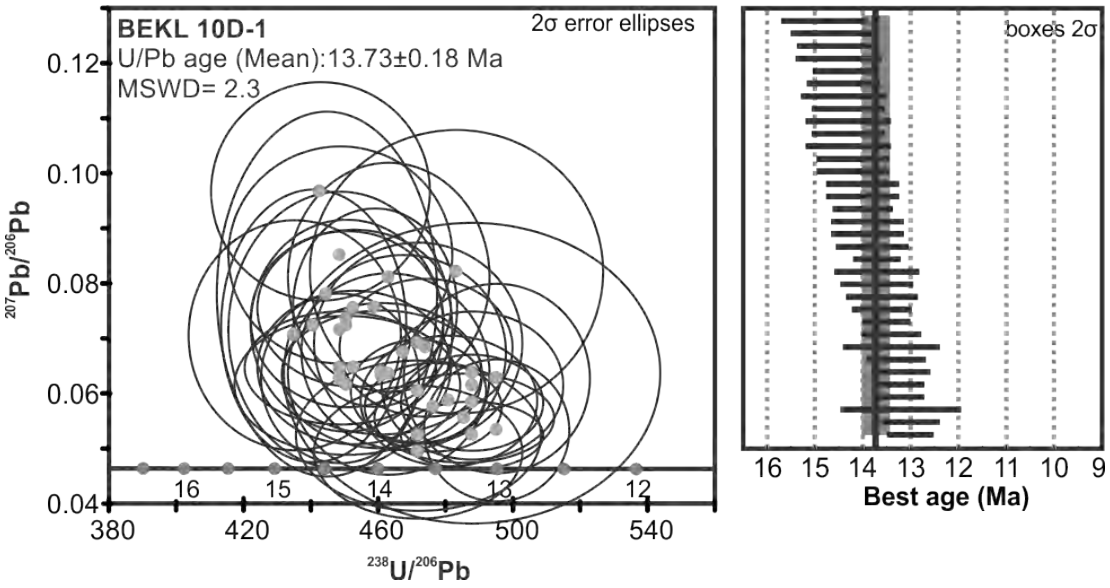

Preferred age: t= 13.73± 0.18 Ma

Weighted mean age (95% confidence) calculated with 35 data points. Single crystals are in the 12.3 to 14.8 Ma age range.

^{40}Ar-^{39}Ar age
Sample Name: BEKL 10D-1
Mineral: Biotite

Laser step-heating experiments on biotite concentrate

Pwr	^{39}Ar × 10^{-6}	F ^{39}Ar	^{40}Ar*/^{39}Ar$_K$	1σ	Age in Ma	1σ		% ^{40}Ar*	^{40}Ar/^{36}Ar	^{37}Ar$_{Ca}$/^{39}Ar$_K$
0.20	5.158	0.0030	1.50	1.91	9.38	11.94	a	5.84	313.83	0.485
0.40	13.680	0.0080	2.01	0.64	12.58	3.98	b	18.16	361.09	0.208
0.70	81.194	0.0477	1.85	0.14	11.61	0.85	c	41.49	505.03	0.037
1.00	197.518	0.1161	2.02	0.04	12.63	0.25	d	84.31	1883.24	0.018
1.30	245.034	0.1440	2.04	0.03	12.80	0.21	e	96.54	8540.65	0.029
1.80	463.342	0.2724	1.98	0.02	12.42	0.14	f	95.95	7301.03	0.060
2.30	375.016	0.2204	1.99	0.02	12.47	0.13	g	97.79	13376.59	0.074
3.20	257.495	0.1514	2.05	0.03	12.86	0.19	h	99.62	77983.11	0.090
7.00	62.775	0.0369	1.90	0.11	11.89	0.72	i	89.42	2792.94	0.051

Integrated results

^{39}Ar × 10^{-6}	^{40}Ar*/^{39}Ar$_K$	1σ	Age in Ma	1σ	% ^{40}Ar*	^{40}Ar/^{36}Ar	^{37}Ar$_{Ca}$/^{39}Ar$_K$
1701.0	2.00	0.02	12.51	0.11	84.48	1904.23	0.060

J = 0.003485 ± 0.000010

Preferred age t_p = 12.57 ± 0.09 Ma

Weighted mean of fractions d to h, representing 90.44% of ^{39}Ar released in 5 consecutive fractions, MSWD = 1.28

t_c = 12.57 ± 0.08 Ma; $(^{40}Ar/^{36}Ar)_i$ = 288 ± 11, MSWD = 1.02 for n = 9

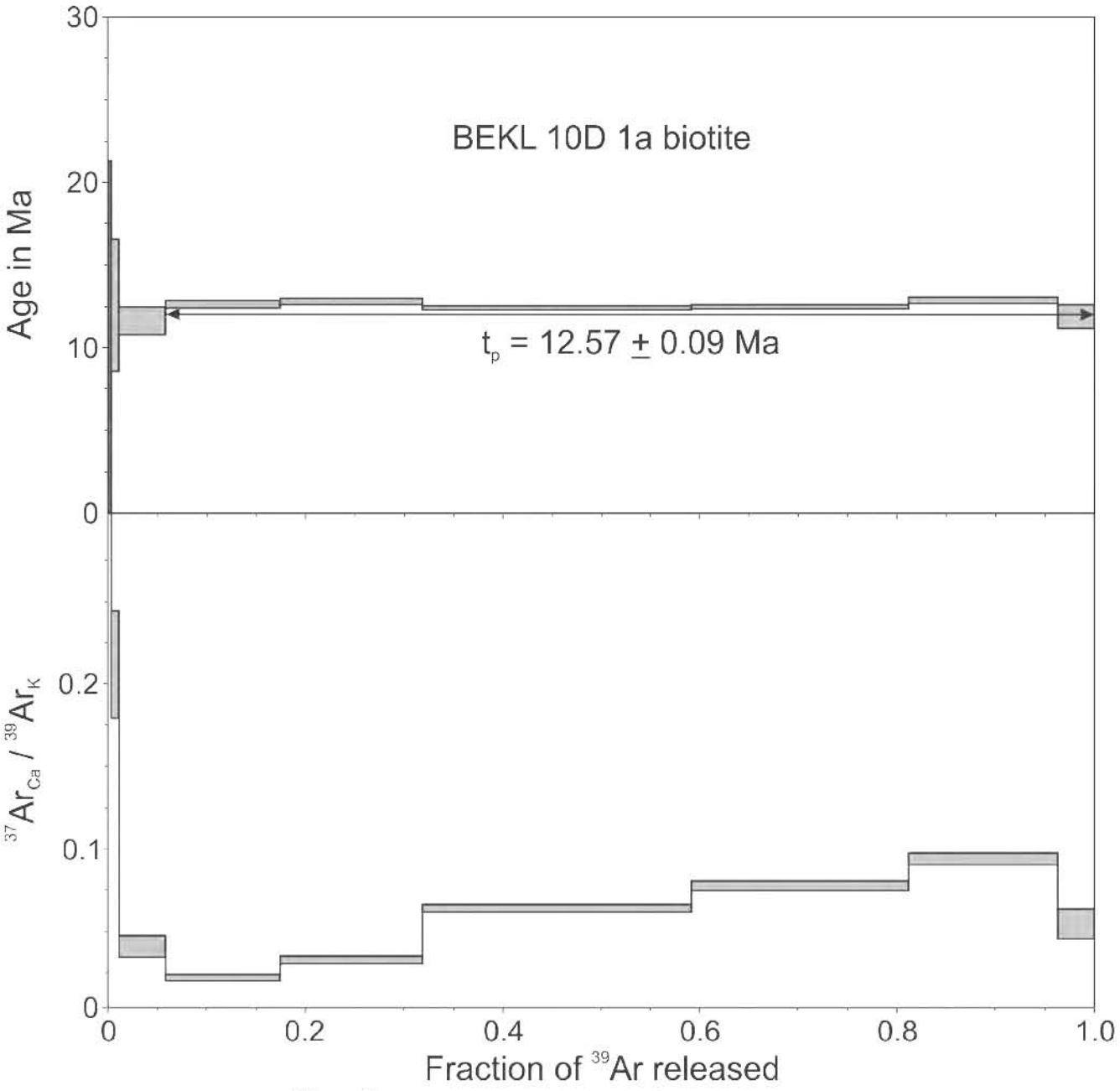

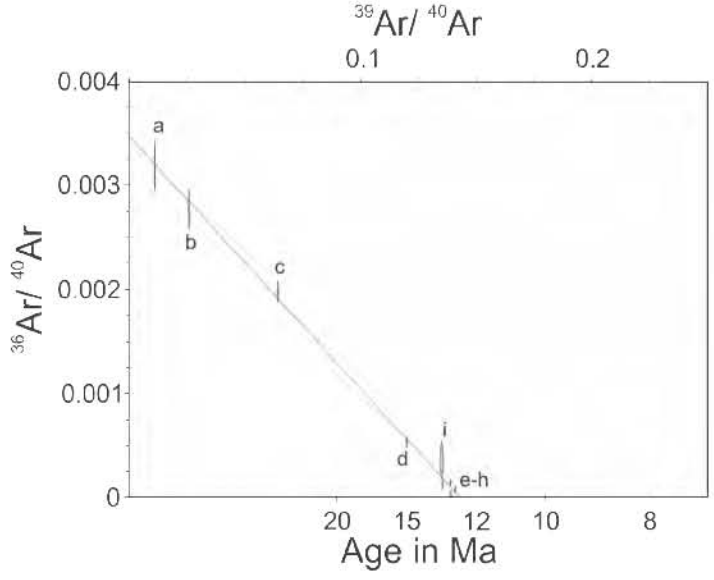

t_c = 12.57 ± 0.08 Ma

$(^{40}Ar / ^{36}Ar)_i$ = 288 ± 11

MSWD = 1.02, n = 9

Sample Name: BEKL 10D-3

Location: Bank East of Partida Bank
Latitude: 24.8081° (i); 24.8050° (e)
Longitude: -109.9233° (i); -109.9285° (e)
Altitude/Depth (m.a.s.l.): -1498 (i); 1200 (e) (wire)

Rock type: Granodiorite

U-Pb Age

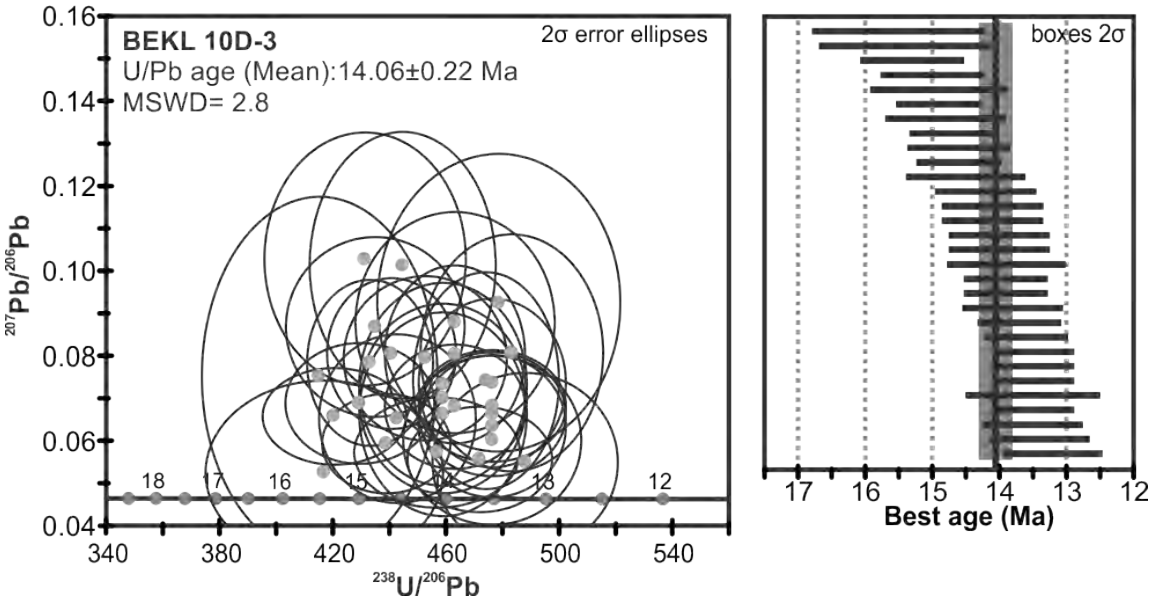

Preferred age: t= 14.06 ± 0.22 Ma

Weighted mean age (95% confidence) calculated with 36 data points. Single crystals are in the 12.1 to 15.5 Ma age range. Three most discordant analyses were rejected from the age calculation.

Anexo 3

Material suplementario publicado en línea como parte del articulo:

Duque-Trujillo, J., Ferrari, L., Norini, G., López-Martínez, M., 2014. Miocene faulting in the southwestern Sierra Madre Occidental, Nayarit, Mexico: kinematics and segmentation of the initial rifting in the southern Gulf of California. Revista Mexicana de Ciencias Geológicas. v. 31, núm. 3, p. 283-302.

Secciones:

1) Información metodologica adicional de fechamiento por ^{30}Ar-^{40}Ar y datos analíticos

2) Datos analíticos de edades U-Pb

Supplementary material to the paper:
Duque-Trujillo, J., Ferrari, L., Norini, G., López-Martínez, M., 2014, Miocene faulting in the southwestern Sierra Madre Occidental, Nayarit, Mexico: kinematics and segmentation of the initial rifting in the southern Gulf of California: Revista Mexicana de Ciencias Geológicas, v. 31, núm. 3, p. 283-302.

Supplemental File 1. Additional information on ^{40}Ar-^{39}Ar methodology and analytical data

Sample NAY 21 was prepared at Departamento de Geología del Centro de Investigación Científica y Educación Superior de Ensenada (CICESE). The sample preparation procedure consisted of crushing and sieving, then rinsing with distilled water followed by 98% acetone. The rock fragments were dried overnight at ~60° C. A groundmass concentrate was obtained by passing the sample through a Frantz isodynamic magnetic separator and final examination under the microscope to ensure purity greater than 99%. The sample was irradiated in position 8E of the U-enriched research reactor of McMaster University in Hamilton, Ont. Canada. During the irradiation the sample and monitor were covered with a Cd liner to block thermal neutrons. The sample was irradiated with sanidine FCT 2 (28.201 ± 0.046 Ma; Kuiper *et al.*, 2008). The ^{40}Ar-^{39}Ar analysis of sample NAY 21 was performed at CICESE's Laboratorio de Geocronología. A Coherent Innova 300 Ar-ion laser was used to heat the samples. The argon extraction chamber was connected in-line with the VG5400 mass spectrometer, where the argon isotopes were measured. The irradiation monitors were fused in one-step. Two step-heating experiments were performed with the groundmass concentrate. Each argon step measurement was preceded by a blank measurement of all argon masses. Upon blank subtraction, the argon isotopes were corrected for mass discrimination, and for calcium, potassium and chlorine neutron induced interference reactions. The parameters used to correct for neutron induced interference reactions were: $(^{39}Ar/^{37}Ar)_{Ca} = 6.50 \times 10^{-4}$; $(^{36}Ar/^{37}Ar)_{Ca} = 2.55 \times 10^{-4}$; $(^{40}Ar/^{39}Ar)_{K} = 0$. Mass 36 was also corrected for chlorine-derived ^{36}Ar (^{35}Cl (n, γ) ^{36}Cl → ^{36}Ar + β with t½ = 3.1×10^{5} a). Isotopes ^{37}Ar and ^{39}Ar were corrected for radioactive decay. The constants recommended by Steiger and Jäger (1977) were used in all the calculations, while all the straight line calculations were performed with the equations presented in York *et al.* (2004). All errors are reported at 1σ level. The errors in the integrated, plateau and isochron age include the uncertainty in the *J* parameter. Additionally, the error of the isochron age includes the goodness of fit since the mean square of weighted deviates (MSWD) exceeded 1. The integrated ages were calculated adding the fractions of the step-heating experiments. The plateau age is calculated with the weighted mean of five consecutive fractions, which are in agreement within 1σ errors excluding the uncertainty in *J*. The data were plotted in a ^{36}Ar/^{40}Ar versus ^{39}Ar/^{40}Ar correlation diagram to determine the isochron age and the initial ^{40}Ar/^{36}Ar composition. A table with the relevant ^{40}Ar-^{39}Ar data follows. The preferred age is highlighted in bold typeface.

NAY 21, Mafic dike west of Jesús María (22.24161°N; 104.57821°W).

Pwr	$^{39}Ar \times 10^{-6}$	F ^{39}Ar	$^{40}Ar^*/^{39}Ar_K$	1σ	Age in Ma	1σ			% $^{40}Ar^*$	$^{40}Ar/^{36}Ar$	$^{37}Ar_{Ca}/^{39}Ar_K$
0.2	3.908	0.72	37.72	8.63	184.70	40.14	a	‡	3.11	304.99	2.65
0.5	15.198	2.79	4.91	0.59	25.15	3.02	b	‡	9.14	325.23	2.43
1.0	123.801	22.74	5.23	0.11	26.75	0.58	c		44.80	535.29	2.83
1.5	135.103	24.84	4.60	0.06	23.58	0.31	d		80.37	1505.69	1.87
2.0	80.001	14.70	4.50	0.11	23.03	0.55	e		83.36	1776.32	2.06
2.8	76.356	14.02	4.53	0.13	23.19	0.65	f		73.74	1125.27	3.36
3.8	43.285	7.94	4.65	0.16	23.82	0.81	g		92.44	3909.55	4.37
6.8	66.691	12.24	4.57	0.15	23.43	0.74	h		70.63	1006.22	4.88
0.2	2.995	0.36	34.41	12.16	169.20	57.10	i	‡	1.99	301.50	2.49
0.5	10.845	1.32	8.81	1.76	44.86	8.85	j	‡	6.73	316.83	2.49
1.0	46.812	5.69	5.72	0.26	29.27	1.31	k		30.12	422.88	2.32
1.3	51.754	6.29	5.54	0.20	28.32	1.02	l		56.69	682.23	2.50
1.6	79.177	9.63	5.01	0.14	25.63	0.72	m		70.34	996.18	2.36
1.9	87.014	10.58	4.83	0.09	24.74	0.47	n		73.17	1101.33	2.36
2.3	119.285	14.50	4.64	0.08	23.75	0.39	o		82.14	1654.70	1.96
2.9	107.076	13.02	4.53	0.07	23.21	0.35	p		86.88	2252.91	1.40
4.0	138.744	16.87	4.62	0.05	23.64	0.23	q		90.15	3000.43	1.64
6.8	179.131	21.73	4.48	0.06	22.96	0.32	r		76.82	1274.56	5.67

Integrated results

$^{39}Ar \times 10^{-6}$	$^{40}Ar^*/^{39}Ar_K$	1σ	Age in Ma	1σ	% $^{40}Ar^*$	$^{40}Ar/^{36}Ar$	$^{37}Ar_{Ca}/^{39}Ar_K$
543.3	4.97	0.09	25.42	0.44	28.98	416.10	2.91
821.3	4.92	0.07	25.21	0.35	33.44	443.95	2.78

Pwr: laser power in Watts applied to heat the sample; $^{39}Ar \times 10^{-6}$ signal output for ^{39}Ar; % ^{39}Ar precentage of ^{39}Ar released; % $^{40}Ar^*$ percentage of radiogenic ^{40}Ar; $^{37}Ar_{Ca}/^{39}Ar_K$ ratio of calcium derived ^{37}Ar over potassium derived ^{39}Ar.

$J = 0.002858 \pm 0.000004$

Plateau age calculated with the weighted mean of fractions d to h

$t_p = 23.45 \pm 0.23$ Ma, 73.74 % of ^{39}Ar released in 5 consecutive fractions, MSWD = 0.24

Isochron age obtained with the combined data of the two experiments

t_c = 23.01 ± 0.24 Ma, $(^{40}Ar/^{36}Ar)_i = 329 \pm 6$, MSWD = 2.0 for $n = 14$

‡ fractions ignored in the isochron age determination

REFERENCES

Kuiper, K.F., Deino, A., Hilgen, F.J., Krijgsman W., Renne P.R., and Wijbrans J.R., 2008, Synchronizing rock clocks of Earth history: Science 320, 500-504.

Steiger, R.H., and Jäger, E., 1977, Subcommission on Geochronology: Convention on the use of decay constants in Geo and Cosmochronology: Earth and Planetary Science Letters, 36, 359-362.

York, D., Evensen, N.M., López-Martínez, M., and De Basabe-Delgado, J., 2004, Unified equations for the slope, intercept, and standard errors of the best straight line: Americam Journal of Physics, 72 (3), 367-375.

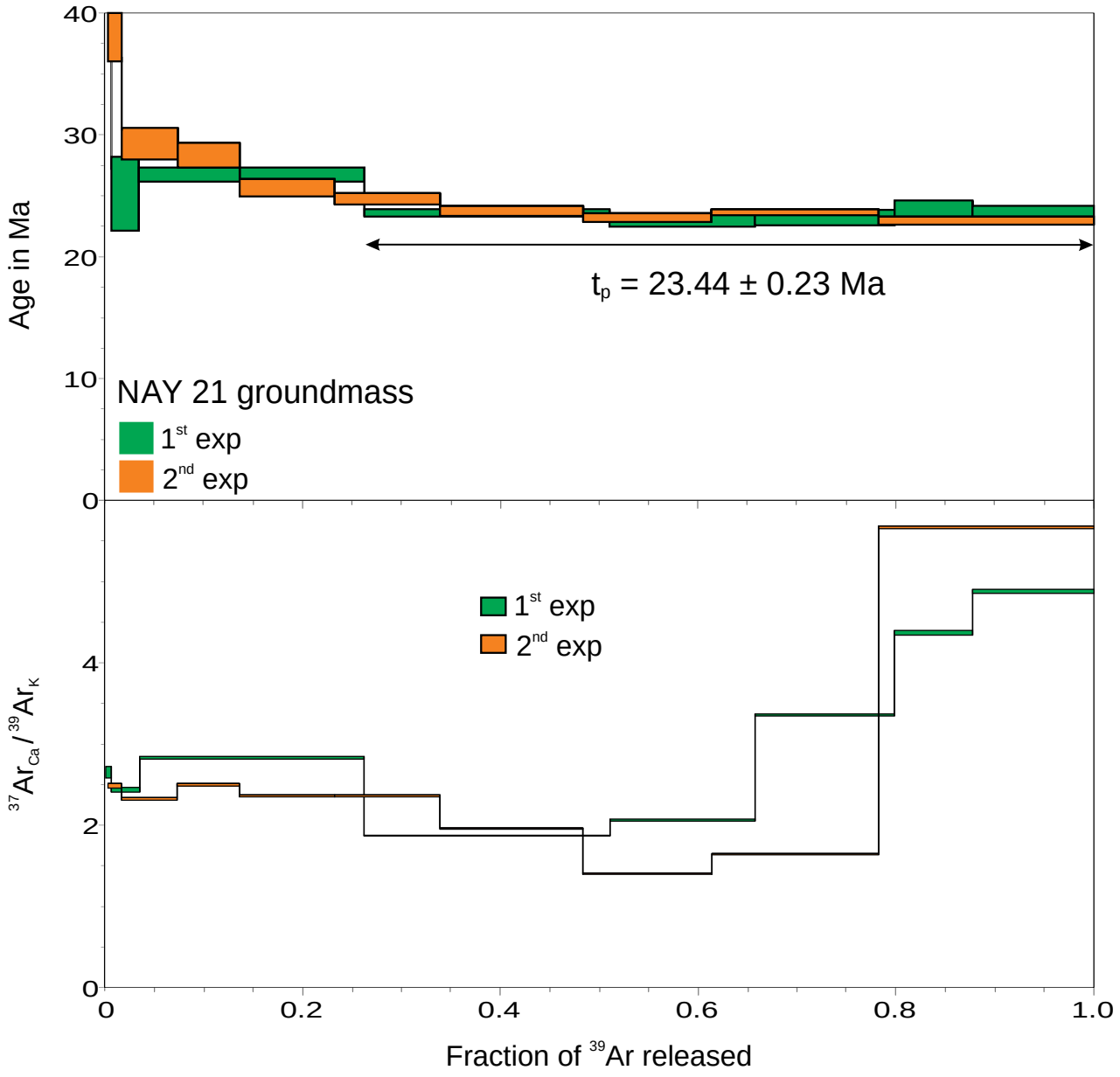

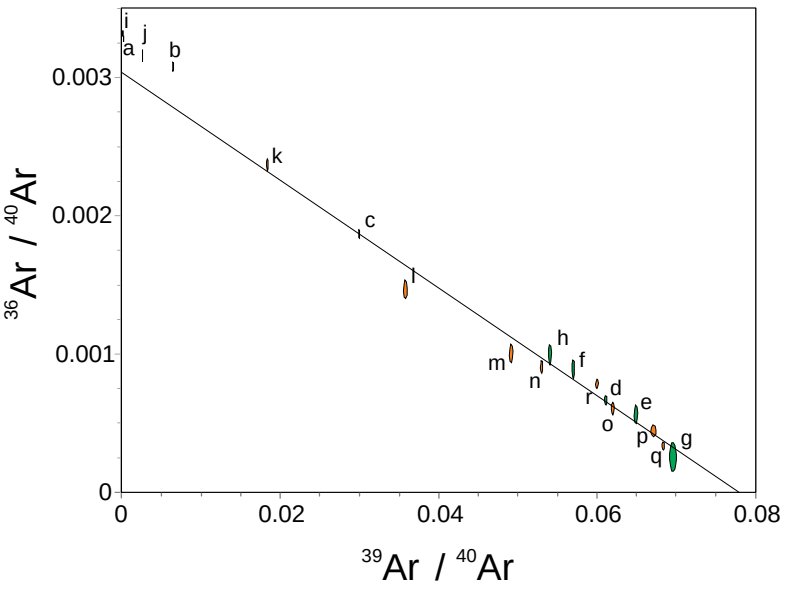

t_c = 23.01 ± 0.24 Ma

$(^{40}Ar / ^{36}Ar)_i$ = 329 ± 6

MSWD = 2.0, n = 14

Supplementary material to the paper:
Duque-Trujillo, J., Ferrari, L., Norini, G., López-Martínez, M., 2014, Miocene faulting in the southwestern Sierra Madre Occidental, Nayarit, Mexico: kinematics and segmentation of the initial rifting in the southern Gulf of California: Revista Mexicana de Ciencias Geológicas, v. 31, núm. 3, p. 283-302.

Supplemental File 2. Additional information on U/Pb methodology and U-Pb analytical data

U/Pb LA-ICP-MS dating

U/Pb ages on individual zircons were obtained by laser ablation–inductively coupled plasma–mass spectrometry (LA-ICP-MS) at Laboratorio de Estudios isotópicos, Centro de Geociencias, Universidad Nacional Autónoma de México (UNAM), according to the procedures described in Solari *et al.* (2010). The Pleišovice reference zircon (*ca.* 337 Ma; Sláma *et al.*, 2008) was used in combination with NIST 610 standard glass to correct for instrumental drift and down-hole fractionation and to recalculate elemental concentrations, using the U-Pb.Age software (Solari and Tanner, 2011). Precision on the measured $^{207}Pb/^{206}Pb$, $^{206}Pb/^{238}U$, and $^{208}Pb/^{232}Th$ ratios was typically ~0.8%, 0.7%, and 0.9% 1σ relative standard deviation, respectively. Replicate analyses of the Pleišovice zircon indicate an external reproducibility of 0.75%, 0.6%, and 1.6% on the measured $^{207}Pb/^{206}Pb$, $^{206}Pb/^{238}U$, and $^{208}Pb/^{232}Th$ ratios, respectively. These errors are quadratically included in the quoted uncertainties for individual analyses of the analyzed zircons. Because its signal is swamped by the ^{204}Hg contained in the carrier gases, ^{204}Pb was not analyzed during this study. Common Pb correction was thus performed employing the algebraic method of Andersen (2002). A filter was then applied to ensure the quality of selected analyses, which consisted in the evaluation of the concordance. For grains with ages younger than 1000 Ma, the analysis was considered concordant if the $^{206}Pb/^{238}U$ and $^{207}Pb/^{235}U$ ages differed by <10%. The concordia and age distribution plots, as well as age error calculations, were performed using Isoplot v. 3.70 (Ludwig, 2004). The $^{206}Pb/^{238}U$ ages are preferred for grains younger than 1000 Ma because of the uncertainty involved in determining the ^{207}Pb isotope in young crystals. The U-Pb analytical data are in the following table.

References

Andersen, T., 2002, Correction of common lead in U–Pb analyses that do not report ^{204}Pb. Chemical Geology, 192(1), 59-79.

Ludwig, K.R., 2004, Isoplot/Ex, ver. 3. A geochronological 2toolkit for Microsoft Excel: Berkeley Geochronology Center, Special Publication, 4, 70 pp.

Solari, L. A., Tanner, M., 2011, UPb.age, a fast data reduction script for LA-ICP-MS U/Pb geochronology: Revista Mexicana de Ciencias Geológicas, 28(1), 83-91.

Sláma, J., Košler, J., Condon, D., Crowley, J., Gerdes, A., Hanchar, J., Horstwood, M., Morris, G., Nasdala, L., Norberg, N., Schaltegger, U., Schoene, B., Tubrett, M., Whitehouse, M., 2008, A new natural reference material for U–Pb and Hf isotopic microanalysis: Chemical Geology, 249(1), 1-35.

Solari, L. A, Gómez-Tuena, A., Bernal, J.P., Pérez-Arvizu, O., Tanner, M., 2010, U/Pb zircon geochronology with an integrated LA-ICP-MS Microanalytical Workstation: Achievements in precision and accuracy: Geostandards and Geoanalytical Research, 34(1), 5-18.

U-Pb analytical data

Spot name	U (ppm)	Th (ppm)	Th/U	CORRECTED RATIOS							CORRECTED AGES (Ma)						Best age (Ma)	±1s
				$^{207}Pb/^{206}Pb$	±1s	$^{207}Pb/^{235}U$	±1s	$^{206}Pb/^{238}U$	±1s	Rho	$^{206}Pb/^{238}U$	±1s	$^{207}Pb/^{235}U$	±1s	$^{207}Pb/^{206}Pb$	±1s		
Sample: Cajón 06 (21.42845°N, 104.57444°W)																		
Zircon_07_015	839	668	0.75	0.05634	0.00282	0.02609	0.00133	0.00339	0.00003	0.19	21.8	0.2	26	1	466	109	22	0.2
Zircon_11_020	237	172	0.69	0.08838	0.02339	0.04214	0.01195	0.00346	0.00012	0.31	22.3	0.8	42	12	1391	580	22	0.8
Zircon_04_011	238	126	0.50	0.06113	0.00623	0.02964	0.00321	0.00352	0.00006	0.24	22.6	0.4	30	3	644	222	23	0.4
Zircon_05_012	254	205	0.76	0.07583	0.00463	0.03651	0.00230	0.00352	0.00006	0.25	22.7	0.4	36	2	1091	121	23	0.4
Zircon_09_017	1097	410	0.35	0.05240	0.00168	0.02542	0.00086	0.00353	0.00004	0.32	22.7	0.3	25.5	0.9	303	71	23	0.3
Zircon_22_033	281	226	0.76	0.07259	0.00850	0.03541	0.00443	0.00354	0.00007	0.19	22.8	0.4	35	4	1003	225	23	0.4
Zircon_31_044	193	149	0.73	0.06871	0.01403	0.03377	0.00751	0.00356	0.00010	0.37	22.9	0.6	34	7	890	393	23	0.6
Zircon_03_010	269	143	0.50	0.07560	0.00705	0.03755	0.00373	0.00360	0.00006	0.22	23.2	0.4	37	4	1084	189	23	0.4
Zircon_18_028	597	291	0.46	0.06143	0.00640	0.03091	0.00332	0.00365	0.00004	0.13	23.5	0.3	31	3	654	210	24	0.3
Zircon_02_009	259	187	0.68	0.07597	0.00952	0.03849	0.00516	0.00367	0.00007	0.25	23.6	0.4	38	5	1094	260	24	0.4
Zircon_12_021	722	235	0.31	0.05426	0.00327	0.02749	0.00174	0.00367	0.00004	0.21	23.6	0.3	28	2	382	133	24	0.3
Zircon_20_030	270	200	0.70	0.07408	0.00619	0.03754	0.00345	0.00367	0.00006	0.26	23.6	0.4	37	3	1044	158	24	0.4
Zircon_27_039	326	185	0.54	0.05886	0.00658	0.02976	0.00362	0.00367	0.00007	0.26	23.6	0.5	30	4	562	228	24	0.5
Zircon_28_040	3627	1832	0.48	0.05053	0.00126	0.02561	0.00066	0.00369	0.00002	0.26	23.7	0.1	25.7	0.7	219	54	24	0.1
Zircon_23_034	177	128	0.69	0.09109	0.01505	0.04666	0.00829	0.00372	0.00009	0.27	23.9	0.5	46	8	1449	305	24	0.5
Zircon_32_045	216	129	0.56	0.06191	0.00800	0.03201	0.00451	0.00375	0.00008	0.28	24.1	0.5	32	4	671	261	24	0.5
Zircon_01_Cajon6_008	264	153	0.55	0.06309	0.00901	0.03316	0.00509	0.00381	0.00008	0.26	24.5	0.5	33	5	711	317	25	0.5
Zircon_08_016	171	142	0.78	0.08025	0.01161	0.04213	0.00660	0.00381	0.00009	0.22	24.5	0.6	42	6	1203	301	25	0.6
Zircon_15_024	130	70	0.51	0.10065	0.00891	0.0529	0.00522	0.00381	0.00009	0.33	24.5	0.6	52	5	1636	165	25	0.6
Zircon_29_041	133	84	0.59	0.08887	0.01416	0.04682	0.00826	0.00382	0.00012	0.42	24.6	0.8	46	8	1401	295	25	0.8
Zircon_19_029	202	199	0.93	0.08625	0.00664	0.04557	0.00361	0.00384	0.00007	0.24	24.7	0.4	45	4	1344	139	25	0.4
Zircon_24_035	136	91	0.64	0.10178	0.01796	0.05377	0.01002	0.00383	0.00011	0.20	24.7	0.7	53	10	1657	318	25	0.7
Zircon_17_027	306	122	0.38	0.06214	0.00405	0.03309	0.00238	0.00386	0.00006	0.27	24.8	0.4	33	2	679	130	25	0.4
Zircon_25_036	190	128	0.64	0.06559	0.01335	0.03482	0.00760	0.00385	0.00010	0.33	24.8	0.6	35	7	793	391	25	0.6
Zircon_06_014	1765	1303	0.70	0.04632	0.00126	0.02488	0.00076	0.00389	0.00003	0.21	25.1	0.2	24.9	0.8	14	51	25	0.2
Zircon_16_026	616	330	0.51	0.05258	0.00634	0.02836	0.00370	0.00391	0.00008	0.31	25.2	0.5	28	4	311	260	25	0.5
Zircon_30_042	1466	1060	0.68	0.04963	0.00144	0.02687	0.00080	0.00395	0.00003	0.23	25.4	0.2	26.9	0.8	178	63	25	0.2
Zircon_14_023	154	78	0.48	0.09316	0.00680	0.04968	0.00382	0.00397	0.00010	0.31	25.5	0.6	49	4	1491	138	26	0.6
Zircon_34_047	93	48	0.49	0.07886	0.01039	0.04458	0.00665	0.00410	0.00014	0.35	26.4	0.9	44	6	1169	248	26	0.9
Zircon_10_018	154	98	0.60	0.08721	0.00524	0.06361	0.00431	0.00529	0.00010	0.32	34.0	0.7	63	4	1365	114	34	0.7